Proceedings of the 4th Brazilian Conference on Composite Materials BCCM4

Edited by
Flávio A. Silva
José Roberto M. d'Almeida
Daniel C. T. Cardoso
Lourdes M. S. Souza

Flávio A. Silva · José Roberto M. d'Almeida · Daniel C. T. Cardoso · Lourdes M. S. Souza

Editors

Proceedings of the 4th Brazilian Conference on Composite Materials BCCM4

1st Edition

Rio de Janeiro

Departamento de Engenharia Civil e Ambiental – PUC-Rio

2018

Editors

Flávio de Andrade Silva
Departamento de Engenharia Civil e Ambiental
Pontifícia Universidade Católica do Rio de Janeiro
Rio de Janeiro
Brazil

Daniel Carlos Taissum Cardoso
Departamento de Engenharia Civil e Ambiental
Pontifícia Universidade Católica do Rio de Janeiro
Rio de Janeiro
Brazil

José Roberto Moraes d'Almeida
Departamento de Engenharia Química e de Materiais
Pontifícia Universidade Católica do Rio de Janeiro
Rio de Janeiro
Brazil

Lourdes Maria Silva de Souza
Instituto Tecgraf
Pontifícia Universidade Católica do Rio de Janeiro
Rio de Janeiro
Brazil

Brazilian Conference on Composite Materials (4. : 2018 : Rio de Janeiro, RJ)

Proceedings of the 4th Brazilian Conference on Composite Materials [recurso eletrônico] : BCCM4 / Flávio A. Silva ... [et al.], editors. – Rio de Janeiro : PUC-Rio, Departamento de Engenharia Civil e Ambiental, 2018.

1 recurso eletrônico (970 p.) : il. color.

Descrição baseada na consulta ao recurso eletrônico em 17 de jul. de 2018

Inclui bibliografia

Exigências do sistema: conexão com a Internet, World Wide Web browser e Adobe Acrobat Reader

Disponível em: http://bccm4.com.br/2018/online-proceedings/

ISBN 978-85-85083-00-7 (e-book)

1. Materiais compósitos – Congressos. I. Silva, Flávio A. II. Pontifícia Universidade Católica do Rio de Janeiro. Departamento de Engenharia Civil e Ambiental.

CDD: 620.11806

SPONSORS:

SUPPORTERS:

PREFACE

The 4th Brazilian Conference on Composite Materials will be hosted by Pontifical Catholic University of Rio de Janeiro in Rio de Janeiro, Brazil, from July 22nd to 25th, 2018. It is the fourth event of a series of biannual international conferences on composite materials. The goal of the event is to bring together Brazilian researchers who work with composites in various areas such as Damage and Fracture, Simulation in Composites, Multifunctional Structures, Durability and Aging, Mechanical and Physicochemical Properties, Nanocomposites, Reclycling, Experimental Techniques, Lignocellulosic Composites, Processing and Manufacturing and Active and Passive Monitoring of Structural Health of Composites and to promote the scientific dissemination of their work in the academic and industrial communities. The conference also aims to promote a forum for discussions among national and international researchers as well as stimulate the formation of critical mass in the country.

TABLE OF CONTENTS

1. ANALYTICAL METHODS AND MULTI-SCALE MODELLING

THERMOELASTIC ANALYTICAL SOLUTION FOR 2D COMPOSITE LAMINATES

André S. de Lima (1) and Alfredo R. de Faria (1)

(1) Department of Mechanical Engineering, Instituto Tecnológico de Aeronáutica, Brazil

https://doi.org/10.21452/bccm4.2018.01.01

Abstract

Thermo-mechanical phenomena are inherently related to composite materials, from manufacturing to service applications. Therefore, analytical and numerical models developed to simulate composite structural behaviour must satisfactorily account for thermal effects. Pagano's solutions for 2D and 3D composite problems are usually the base for comparison of the different theories and finite elements developments, even when thermo-mechanical behaviour is assessed. Although a number of papers in the literature use numerical results based on this solution, the formulation accounting for temperature effects is not explicitly presented, nor discussed. The objective of the present paper is to present Pagano's solution equations for a 2D case of a simply supported beam under a constant temperature field. Results obtained with the derived solution are discussed and compared against a 2D solid Finite Element Model (FEM) generated using a commercial software package.

1. INTRODUCTION

The development of laminate theories and elements to model composite structures has been the focus of many researches. The recent reviews by Sayyad and Ghugal [1], [2] together present more than 800 references on the subject. These extensive studies present an interesting concluding remark for future research: there is a need of studying problems involving thermo-mechanical loads in laminated and sandwich composite structures.

It is important to have reliable references to assess the capacities of newly developed models and theories, such as analytical solutions for 2D and 3D problems. Pagano's works for beams [3] and plates [4] appear as the most common base of comparison for laminated structures. Despite its spread use, thermal effects are not accounted for on the original formulation.

Recent works by Qian *et al*. present the analytical solutions for layered rectangular plates [5] and cylindrical arches [6] subjected to thermo-loads. These works solve the heat conduction equations for the layers, but a simpler approach is proposed in the present work.

The present paper presents the inclusion of a temperature field in Pagano's solution for 2D composite laminates under cylindrical bending [3]. The derived formulation is compared to finite element commercial solutions using 2D elements and the results for this apparently simple problem

are discussed, revealing an important conclusion concerning the modelling of composite structures using solid elements.

2. FORMULATION

The constitutive equation for an orthotropic material considering thermal effects is:

$$\begin{Bmatrix} \varepsilon_x - \alpha_x \Delta T \\ \varepsilon_y - \alpha_y \Delta T \\ \varepsilon_z - \alpha_z \Delta T \\ \gamma_{yz} \\ \gamma_{xz} \\ \gamma_{xy} \end{Bmatrix} = \begin{bmatrix} S_{11} & S_{12} & S_{13} & 0 & 0 & 0 \\ S_{12} & S_{22} & S_{23} & 0 & 0 & 0 \\ S_{13} & S_{23} & S_{33} & 0 & 0 & 0 \\ 0 & 0 & 0 & S_{44} & 0 & 0 \\ 0 & 0 & 0 & 0 & S_{55} & 0 \\ 0 & 0 & 0 & 0 & 0 & S_{66} \end{bmatrix} \begin{Bmatrix} \sigma_x \\ \sigma_y \\ \sigma_z \\ \tau_{yz} \\ \tau_{xz} \\ \tau_{xy} \end{Bmatrix} \quad (1)$$

Where α_i is the expansion coefficient in *i*-direction. The coordinate systems and layer numbering scheme are kept the same [3]. Assuming plane stress, $\sigma_z = \tau_{xz} = \tau_{xz} = 0$, the constitutive relations then become:

$$\varepsilon_x - \alpha_x \Delta T = S_{11}\sigma_x + S_{12}\sigma_y = R_{11}\sigma_x + R_{12}\sigma_y \quad (2)$$

$$\varepsilon_y - \alpha_y \Delta T = S_{12}\sigma_x + S_{22}\sigma_y = R_{12}\sigma_x + R_{22}\sigma_y$$

$$\gamma_{xy} = S_{66}\tau_{xy} = R_{66}\tau_{xy}$$

Therefore the R_{ij} coefficients of Pagano's original work become equal to S_{ij} in Eq. (2). The original paper by Pagano assumes plane strain, therefore the R_{ij} coefficients values are different. The equations developed in the sequence are applicable also for plane strain, requiring only to change the definition of R_{ij}.

The equilibrium equations of the 2D problem are given as:

$$\sigma_{x,x} + \tau_{xy,y} = 0 \; ; \; \sigma_{y,y} + \tau_{xy,x} = 0 \quad (3)$$

The strain displacement relations are assumed according small displacement gradients hypothesis:

$$\varepsilon_x = u_{,x} \; ; \; \varepsilon_y = v_{,y} \; ; \; \gamma_{xy} = u_{,y} + v_{,x} \quad (4)$$

The boundary conditions are the same considered on Pagano's original work [3] for bending, a distributed load q on the upper surface and simply supported edges, according to Eq. (5).

$$\sigma_y\left(x, \frac{h}{2}\right) = q \; ; \; \sigma_y\left(x, -\frac{h}{2}\right) = \tau_{xy}\left(x, \pm\frac{h}{2}\right) = 0 \quad (5)$$

$$\sigma_y(0, y) = \sigma_y(l, y) = 0$$

$$v(0, y) = v(l, y) = 0$$

Where q has a sinusoidal distribution given by:

$$q\,(x) = q_0 \sin px \; ; \; p = p(n) = \frac{n\pi}{l} \quad (6)$$

This shape of the load function is suitable for the solution of the differential equations. If one wants to represent a particular load distribution, it can be expanded as a Fourier series and Pagano's solution is still applicable, as will be discussed in the next section.

In order to include the temperature field the same sinusoidal representation is needed as the same resources of the Fourier series apply for more general fields.

$$\Delta T\ (x) = \Delta T_0 \sin px \tag{7}$$

Although the temperature effects are included, an analogous solution for stresses to the one proposed in Pagano's original work [3] applies:

$$\sigma_x^{(i)} = f_i''(y) \sin px \tag{8}$$
$$\sigma_y^{(i)} = -p^2 f_i(y) \sin px$$
$$\tau_{xy}^{(i)} = -p\, f_i'(y) \cos px$$

Using Eqs. (2), (4) and (8), we find that the new functions $f_i(y)$ are defined by the solution of the following ordinary differential equation:

$$R_{11}^{(i)} f_i''''(y) - \left(R_{66}^{(i)} + 2R_{12}^{(i)}\right) p^2 f_i''(y) + R_{22}^{(i)} p^4 f_i(y) = \alpha_y^{(i)} \Delta T_0 p^2 \tag{9}$$

Where:

$$a_i = R_{66}^{(i)} + 2R_{12}^{(i)}\ ;\ b_i = \left(a_i^2 - 4R_{11}^{(i)} R_{22}^{(i)}\right)^{1/2}\ ;\ c_i = 2R_{11}^{(i)} \tag{10}$$

This is almost the same equation of Pagano's original work; moreover, the coefficients a_i, b_i and c_i remain as previously defined **[1]**. The addition of thermal effects introduces a particular solution for the differential equation, where the homogeneous solution is kept equal to the previously defined by Pagano.

$$f_i(y) = f_{ih}(y) + f_{ip}(y) \tag{11}$$

The particular solution is given by:

$$f_{ip}(y) = \frac{\alpha_y^{(i)} \Delta T_0}{R_{22}^{(i)} p^2} \tag{12}$$

There is a term dependent on α_y but not on α_x because the temperature distribution is assumed constant through y-direction, thus in the derivation of Eq. (9) the term related to α_x vanishes. Therefore the solution for the stresses become:

$$\sigma_x^{(i)} = f_i''(y) \sin px = f_{ih}''(y) \sin px \tag{13}$$
$$\sigma_y^{(i)} = -p^2 \left(f_{ih}(y) + \frac{\alpha_y^{(i)} \Delta T_0}{R_{22}^{(i)} p^2} \right) \sin px = -p^2 f_{ih}(y) \sin px - \frac{\alpha_y^{(i)} \Delta T_0}{R_{22}^{(i)}} \sin px$$
$$\tau_{xy}^{(i)} = -p\, f_i'(y) \cos px = -p\, f_{ih}'(y) \cos px$$

The displacements can be calculated by the integration of the constitutive relations. For the *u* displacement, from Eq. (2) :

$$\varepsilon_x^{(i)} = u_{i,x} = R_{11}^{(i)}\sigma_x + R_{12}^{(i)}\sigma_y + \alpha_x^{(i)}\Delta T \tag{14}$$

Substitution of Eqs. (8) and (11) and (12) into Eq. (14) yields :

$$u_{i,x} = \left[R_{11}^{(i)} f_{ih}''(y) - R_{12}^{(i)} p^2 f_{ih}(y) - R_{12}^{(i)} p^2 f_{ip}(y)\right] \sin px + \alpha_x^{(i)}\Delta T_0 \sin px \tag{15}$$

$$u_{i,x} = \left[R_{11}^{(i)} f_{ih}''(y) - R_{12}^{(i)} p^2 f_{ih}(y) - \left(-\alpha_x^{(i)} + \frac{\alpha_y^{(i)} R_{12}^{(i)}}{R_{22}^{(i)}}\right)\Delta T_0\right] \sin px$$

Integration in *x*-direction yields :

$$u_i = \left[-R_{11}^{(i)} f_{ih}''(y) + R_{12}^{(i)} p^2 f_{ih}(y) + \left(-\alpha_x^{(i)} + \frac{\alpha_y^{(i)} R_{12}^{(i)}}{R_{22}^{(i)}}\right)\Delta T_0\right] \frac{\cos px}{p} \tag{16}$$

Proceeding analogously for the *v* displacement :

$$\varepsilon_y^{(i)} = v_{i,y} = R_{12}^{(i)}\sigma_x + R_{22}^{(i)}\sigma_y + \alpha_y^{(i)}\Delta T \tag{17}$$

Substitution of Eqs. (8) and (11) and (12) into Eq. (17) yields :

$$v_{i,y} = \left[R_{12}^{(i)} f_{ih}''(y) - R_{22}^{(i)} p^2 f_{ih}(y) - R_{22}^{(i)} p^2 f_{ip}(y)\right] \sin px + \alpha_y^{(i)}\Delta T_0 \sin px \tag{18}$$

$$v_{i,y} = \left[R_{12}^{(i)} f_{ih}''(y) - R_{22}^{(i)} p^2 f_{ih}(y)\right] \sin px$$

Integration in *y*-direction yields :

$$v_i = \left[R_{12}^{(i)} f_{ih}'(y) - R_{22}^{(i)} p^2 \int f_{ih}(y)dy\right] \sin px \tag{19}$$

where $\int f_{ih}(y)dy$ is the non-definite integral of $f_i(y)$. These expressions apply to any material that respect the assumed constitutive relations in Eq. (1).

It is important to mention that in Pagano's original work [3], the p^2 coefficient in Eq. (19) is not present in the expression for the isotropic and transversely v_i displacement as it should. This point should be taken into consideretion when implementing Pagano's solution.

The homogeneous solution assumes the different shapes depending on lamina material properties. For orthotropic materials $b_i \neq 0$, then the $f_i(y)$ for the *i*-th layer is:

$$f_i(y) = \sum_{j=1}^{4} A_{ji} \exp\left(m_{ji} y_i\right) \; ; (i = 1,2, \ldots m) \tag{20}$$

where m_{ij} coefficients are given by:

$$\left.\begin{matrix} m_{1i} \\ m_{2i} \end{matrix}\right\} = \pm p \left(\frac{a_i + b_i}{c_i}\right)^{\frac{1}{2}} \tag{21}$$

$$\left.\begin{matrix} m_{3i} \\ m_{4i} \end{matrix}\right\} = \pm p \left(\frac{a_i - b_i}{c_i}\right)^{1/2}$$

The first and second derivatives, and the indefinite integral of the $f_i(y)$, required to calculate displacements, are given by:

$$f'_{ih}(y) = \sum_{j=1}^{4} A_{ji} m_{ji} \exp(m_{ji} y_i) \; ; (i = 1,2, \dots n) \tag{22}$$

$$f'_{ih}(y) = \sum_{j=1}^{4} A_{ji} m_{ji} \exp(m_{ji} y_i) \; ; (i = 1,2, \dots n)$$

$$\int f_{ih}(y) dy = \sum_{j=1}^{4} A_{ji} \frac{1}{m_{ji}} \exp(m_{ji} y_i) \; ; (i = 1,2, \dots n)$$

If the material of a layer is isotropic or transversely isotropic in *xy* plane, b_i vanishes and the homogeneous solution becomes:

$$f_{ih}(y) = (A_{1i} + A_{2i} y_i) \exp(m_{1i} y_i) + (A_{3i} + A_{4i} y_i) \exp(-m_{1i} y_i) \tag{23}$$

with $m_{1i} = p(ai/ci)^{1/2}$. The first and second derivatives, and the indefinite integral of the $f_i(y)$, required to calculate displacements, are given by:

$$\begin{aligned} f'_{ih}(y) &= \big((m_{1i}) A_{1i} + A_{2i}(m_{1i} y_i + 1)\big) \exp(m_{1i} y_i) \\ &\quad + \big((-m_{1i}) A_{3i} + A_{4i}(-m_{1i} y_i + 1)\big) \exp(-m_{1i} y_i) \end{aligned} \tag{24}$$

$$\begin{aligned} f''_{ih}(y) &= \Big((m_{1i}^2) A_{1i} + A_{2i}\big(m_{1i}(m_{1i} y_i + 2)\big)\Big) \exp(m_{1i} y_i) \\ &\quad + \Big((m_{1i}^2) A_{3i} + A_{4i}\big(m_{1i}(m_{1i} y_i - 2)\big)\Big) \exp(-m_{1i} y_i) \end{aligned}$$

$$\begin{aligned} \int f_{ih}(y) dy &= \left(\left(\frac{1}{m_{1i}}\right) A_{1i} + A_{2i}\left(\frac{m_{1i} y_i - 1}{m_{1i}^2}\right)\right) \exp(m_{1i} y_i) \\ &\quad + \left(\left(-\frac{1}{m_{1i}}\right) A_{3i} + A_{4i}\left(\frac{-m_{1i} y_i - 1}{m_{1i}^2}\right)\right) \exp(-m_{1i} y_i) \end{aligned}$$

In order to determine the $f_i(y)$ coefficients A_{1i}, A_{2i}, A_{3i} and A_{4i} the boundary conditions must be considered, as well as the displacement and transverse stresses continuity.

Pagano assumes simply supported edges for the 2D beam:

$$\begin{aligned} \sigma_y(0, y) &= \sigma_y(l, y) = 0 \\ v(0, y) &= v(l, y) = 0 \end{aligned} \tag{25}$$

This is automatically satisfied by Eq. (8). Therefore, there is still a total of 4*m* unknowns to be determined for a *m* layered laminate. This is achieved solving the system given by the 4*m* equations from the remnant boundary conditions and continuity equations:

$$\sigma_y^{(1)}\left(x, \frac{h_1}{2}\right) = q_0 \sin px \; ; \; \sigma_y^{(m)}\left(x, -\frac{h_n}{2}\right) = 0 \tag{26}$$

$$\tau_{xy}^{(1)}\left(x,\frac{h_1}{2}\right)=0\ ;\ \tau_{xy}^{(m)}\left(x,-\frac{h_n}{2}\right)=0$$
$$\sigma_y^{(i)}\left(x,-\frac{h_i}{2}\right)=\sigma_y^{(i+1)}\left(x,\frac{h_{i+1}}{2}\right)$$
$$\tau_{xy}^{(i)}\left(x,-\frac{h_i}{2}\right)=\tau_{xy}^{(i+1)}\left(x,\frac{h_{i+1}}{2}\right)$$
$$u_i\left(x,-\frac{h_i}{2}\right)=u_{i+1}\left(x,\frac{h_{i+1}}{2}\right)$$
$$v_i\left(x,-\frac{h_i}{2}\right)=v_{i+1}\left(x,\frac{h_{i+1}}{2}\right)$$

3. NUMERICAL RESULTS

In order to assess the results of the proposed formulation, a thick 0º/90º/0º laminate under constant temperature field $\Delta T = \Delta T_0$ was evaluated. The beam dimensions are such that $l/h = 4$, where $l = 1$ m is the beam length and $h = 0.25$ m is the beam thickness. The results were compared to a commercial finite element solution using 2D plane stress four-noded bilinear elements using increasing number of elements per layer (ELPL). The 2 ELPL mesh used 120 elements (6 x 20), the 3 ELPL mesh used 288 elements (9 x 32), the 4 ELPL mesh used 480 elements (12 x 40), the 5 ELPL mesh used 780 elements (15 x 52) and the 30 ELPL mesh used 32400 elements (90 x 360).

In order to represent the constant temperature distribution, the Fourier expansion required is:

$$\Delta T\ (x)=\frac{4}{\pi}\sum_{n=1}^{\infty}\frac{1}{n}\Delta T_0\sin px \tag{27}$$

with $\Delta T_0 = 1\ K$.

As the representation is more accurate as more terms are considered, 3001 terms were considered. Also, as the sinusoidal expansion is problematic on the beam edges, the results were evaluated at $x = 0.25l$, where the boundary effects are not representative.

The mechanical properties of the unidirectional lamina are [7]:

$E_L = 150.0$ GPa; $E_T = 10.0$ GPa;

$\nu_{LT} = 0.3$; $\nu_{TT} = 0.48$;

$G_{LT} = 5.0$ GPa; $G_{TT} = 3.378$ GPa;

$\alpha_L = 0.139\ 10^{-6}\ K^{-1}$; $\alpha_T = 9.0\ 10^{-6}\ K^{-1}$;

where the superscript *l* denotes the longitudinal direction (fibre direction) and the *t* denotes the transverse direction.

The finite element convergence is attested as 30ELPL mesh meets perfectly the Pagano's solution.

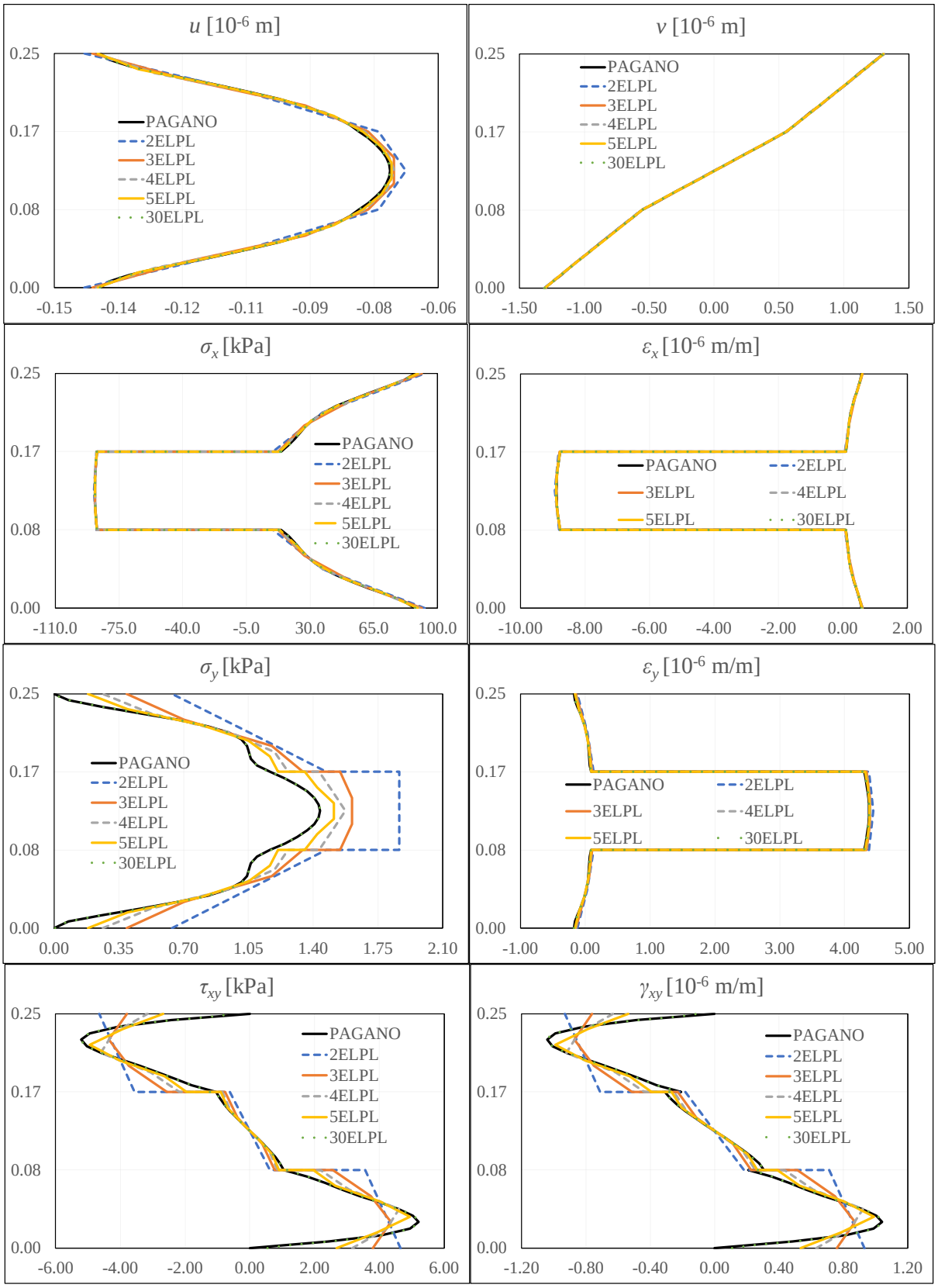

Figure 1: Analytical solution and finite element results.

It is common in composite problems to model structures using one element per layer [8], but by the results illustrated in Fig. 1 it is clear that, even for a simple problem such as the one evaluated, using few elements per layer is a poor approximation, especially considering transverse strains and stresses. One can see that even using five elements per layer the value of σ_y stress, critical to delamination problems, is overestimated.

4. CONCLUSIONS

The present work is a straightforward development of Pagano's solution for 2D solution of laminated composite beam under cylindrical bending including thermal-effects and is a reliable reference for the development of composite structure theories and models.

An important conclusion from the primary application of the model in contrast to traditional finite element modelling is that, in order to have accurate results concerning transverse strains and stresses, more than five elements per layer are required. Therefore, common strategies for modelling composite structures must be carefully studied.

ACKNOWLEDGEMENTS

The authors would like to acknowledge the Brazilian funding agencies CAPES and CNPQ for the grants CAPES 1642839 and CNPq 306193/2017-5 that supported this research.

REFERENCES

[1] A. S. Sayyad and Y. M. Ghugal, "On the free vibration analysis of laminated composite and sandwich plates: A review of recent literature with some numerical results," *Compos. Struct.*, vol. 129, pp. 177–201, 2015.

[2] A. S. Sayyad and Y. M. Ghugal, "Bending, buckling and free vibration of laminated composite and sandwich beams: A critical review of literature," *Compos. Struct.*, vol. 171, pp. 486–504, 2017.

[3] N. J. Pagano, "Exact Solutions for Composite Laminates in Cylindrical Bending," *J. Compos. Mater.*, vol. 3, no. 3, pp. 398–411, 1969.

[4] N. J. Pagano, "Exact Solutions for Rectangular Bidirectional Composites and Sandwich Plates," *J. Compos. Mater.*, vol. 4, no. 1, pp. 20–34, 1970.

[5] H. Qian, D. Zhou, W. Q. Liu, H. Fang, and W. D. Lu, "3-D elasticity solutions of layered rectangular plates subjected to thermo-loads," *J. Therm. Stress.*, vol. 38, no. 4, pp. 377–398, 2015.

[6] H. Qian, D. Zhou, W. Liu, H. Fang, and W. Lu, "Elasticity solutions of simply supported laminated cylindrical arches subjected to thermo-loads," *Compos. Struct.*, vol. 131, pp. 273–281, 2015.

[7] W. Zhen and T. Li, "C0-type global-local higher-order theory including transverse normal thermal strain for laminated composite plates under thermal loading," *Compos. Struct.*, vol. 101, pp. 157–167, Jul. 2013.

[8] T. Nyman, M. Rudlund, J. Bohlin, R. Berg, V. Engineering, and C. Sky, "Shape Distortion Analysis of a Complex Shaped Wing," no. July, pp. 19–24, 2015.

CRITICAL REVIEW OF DISPLACEMENT-BASED LAMINATE THEORIES AND MODELING TECHNIQUES

André S. de Lima (1), Alfredo R. de Faria (1) and José J. R. Faria (1)

(1) Department of Aeronautical and Mechanical Engineering, Instituto Tecnológico de Aeronáutica, Brazil

https://doi.org/doi/10.21452/bccm4.2018.01.02

Abstract

Composite materials present many particularities and challenges when it comes to structural modelling. These challenges come from the anisotropic and nonhomogeneous nature of these materials combined with the continuity requirements of displacement and transverse stresses through the thickness, commonly named C^0_z requirements. The different approaches developed to assess the structural behaviour of composites can be divided into two major branches: displacement-based theories and mixed-formulation theories. Among the displacement-based theories, the most common approaches are: Equivalent Single Layer (ESLT), that includes the Classical Laminate Theory (CLT); Layerwise Theories (LT), that includes the Zig-Zag Theories (ZZT); Quasi-Layerwise Theories (QLT); and Global-Local Superposition Theories (GLST). The present paper discusses how these different displacement-based models handle the particularities of structural composites, highlighting the main advantages and disadvantages of each formulation, as well as their applicability to common structural problems.

1. INTRODUCTION

The nonhomogeneous nature of composite materials pose a series of particularities regarding their structural behaviour, especially in the transverse (through-the-thickness) direction. This characteristic, combined with the principles of macro-mechanics, result in the inherited C^0 continuity requirements of transverse displacements and stresses. These are commonly named C^0_z continuity requirements [1], where the subscript *z* denotes the transverse direction. Moreover, because of the nonhomogeneous characteristic on that direction, in-plane displacements and transverse shear stresses usually present kinks (discontinuities on the first derivative) in the interfaces between laminas. Therefore, a robust composite theory must account for these effects.

Investigating the history of two-dimensional composite modelling techniques, one can conclude that there has been a gradual evolution of laminate theories, in order to account for the aforementioned particularities, which cannot be fully represented by classical plate and beam theories. The current study presents a critical review of the displacement-based theories in contrast

to those inherited requirements of composite structures. It is noteworthy to mention that the present work is of introductory nature. A number of authors have conducted extensive and comprehensive reviews on this topic, namely Liu and Li [2], Carrera [3,4] and more recently Sayyad and Ghugal [5,6].

2. DISPLACEMENT-BASED FORMULATIONS

The displacement-based theories receive this name because the primary variables are displacement-related and compose the displacement field assumed by the theory. Departing from their displacement field and assuming strain-displacement and constitutive relationships, the stresses and strains are determined.

The displacement field of most displacement-based formulations are a combination of one or more fields illustrated on Figure 1.

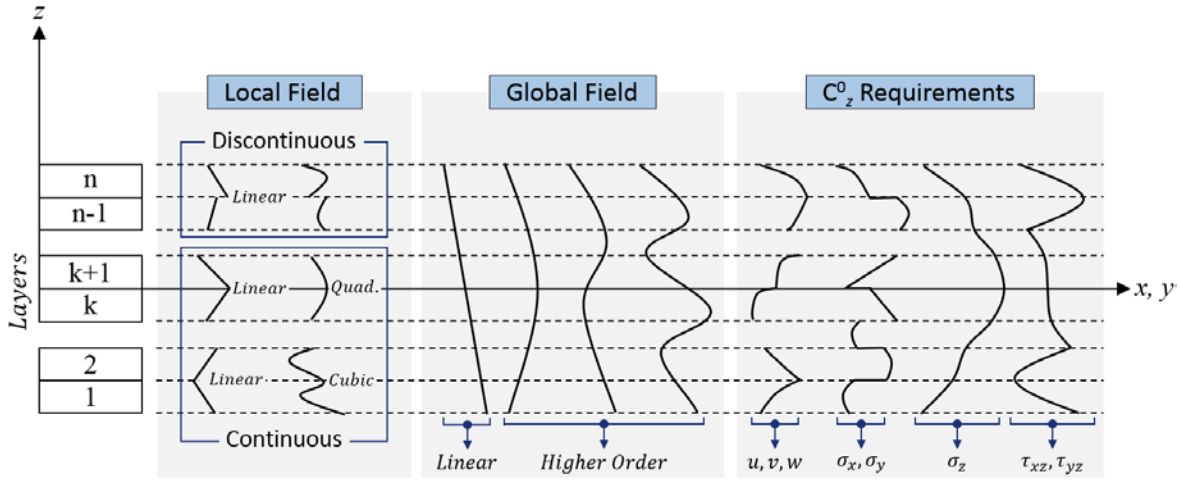

Figure 1: Comparison of assumed displacement fields (local and global) and C^0_z requirements.

In Figure 1, the displacement fields are represented by polynomial functions only; however, other types of functions, such as exponential, trigonometric and hyperbolic, were also used to develop displacement-based theories [5], [6].

The next sections present, in a very succinct and general form, an overview of the most common two-dimensional displacement-based formulations applied to composite laminates.

2.1 Equivalent Single Layer Theories

The first attempts to model composite structures used traditional plate theories, where the displacement field was assumed smoothly continuous along the thickness, implicating in a transverse global behaviour independent of the number of layers, thus treating the laminate as a single layer. Therefore, these theories are commonly classified as Equivalent Single Layer Theories (ESLT).

In this universe, the Classical Laminate Theory (CLT) is based on the straightforward application of Kirchhoff's plate theory [7] to laminates, whose displacement field is presented in Table 1**.** One outstanding deficiency of the CLT is the assumption of zero transverse shear. In order to overcome this serious limitation constant shear theories were developed applying Reissner [8] and Mindlin [9] formulations to laminated plates. Because the polynomials used in these theories are linear in the *z*-coordinate (through the thickness) and the predicted shear is constant, they are commonly referred to as first-order shear deformation theories.

Subsequently, several researches proposed theories where the displacement fields were described with higher-order polynomials, giving rise to Higher-Order Shear Deformation Theories (HSDT). A generic expression of the HSDT is also presented in Table 1.

Table 1: CLT and HSDT displacement fields

CLT	HSDT
$u(x,y,z) = u_0(x,y) - \frac{dw}{dx}z$	$u(x,y,z) = \sum_{i=0}^{m} u_i(x,y)z^i$
$v(x,y,z) = v_0(x,y) - \frac{dw}{dy}z$	$v(x,y,z) = \sum_{i=0}^{m} v_i(x,y)z^i$
$w(x,y,z) = w_0(x,y)$	$w(x,y,z) = \sum_{i=0}^{m} w_i(x,y)z^i$

Sayyad and Ghugal [4,5] recently conducted extensive reviews on beam and plate theories for composite plates with more than 800 references. From this extensive compilation, it is observed that not only polynomial functions were used to express displacement fields, but also exponential, hyperbolic and trigonometric functions, as previously mentioned. One can also observe that many theories consider transverse shear strains, but neglect the transverse normal strain, keeping the traditional homogeneous plate assumption that the transverse displacement *w* is constant through the thickness. This implicates in the inability to determine the transverse normal stress σ_z directly from the constitutive relationships, requiring its recovery via integration of the equilibrium equation (Eq. 1). In fact, only a small number of theories account for transverse normal deformation, which in many applications is important. Two examples of such applications are delamination prediction and thermo-mechanical analysis.

$$\sigma_{z,z} + \tau_{xz,x} + \tau_{yz,y} = 0 \quad (1)$$

The major benefit of this class of theories is the low computational burden. On the other hand, the major drawback~~s~~ ~~are~~ is the inability of describing zig-zag distribution (kinks) of in-plane displacements, as illustrated in Figure 1. This implies in continuous strains through-the-thickness and in double-valued transverse stresses on the lamina interfaces, regardless of the order of ESLT.

2.2 Layerwise Theories

In a broad sense, Layerwise Theories (LT) encompass all theories that assume a local displacement field expansion within each material layer. By doing so, these theories allow for the computation of zig-zag shaped displacements and continuous transverse stresses through-the-thickness, better predicting the overall behaviour of laminated composites. However, this is not achieved without penalties, as computational efficiency is sacrificed in exchange for numerical accuracy. Carrera [4] conducted a broad historical review of LTs (referred to by the author as Zig-Zag Theories), which highlights the importance of the early studies developed by Lekhnitskii [10], Ambartsumian [11] and Reissner [12]. According to Carrera, most of the subsequent developments of laminate LTs are somewhat refinements of these original studies, despite the lack of recognition in the open literature, particularly for Lekhnitskii's work.

Lee and Liu [13] proposed a full LT of third-order assigning a translational component and its first derivatives as variables for each layer surface and using Hermite cubics as interpolation functions in order to model the displacement field of a composite layer. According to Liu and Li [2], the results from Lee and Liu's full LT [13] are believed to be the most accurate among all the laminate theories available in the literature.

Following the approach of Liu and Li [2], a generalized form of the displacement field of the third-order LT can be written as follows:

$$\begin{aligned} u^k(x,y,z) &= u_0^k(x,y) + u_1^k(x,y)z + u_2^k(x,y)z^2 + u_3^k(x,y)z^3 \\ v^k(x,y,z) &= v_0^k(x,y) + v_1^k(x,y)z + v_3^k(x,y)z^2 + v_3^k(x,y)z^3 \\ w^k(x,y,z) &= w_0^k(x,y) + w_1^k(x,y)z + w_3^k(x,y)z^2 + w_3^k(x,y)z^3 \end{aligned} \quad (2)$$

Notice that the displacement fields presented in Eq. 2 possess four variables in each component, totalizing 12*n* variables for a laminate with *n* layers. The total number of variables can be reduced by imposing displacement (*u*,*v*,*w*) and transverse stresses (τ_{xz}, τ_{yz}, σ_z) continuity at every lamina interface, yielding 6(*n*+1) variables. This not only reduces the total number of variables, but significantly improves overall accuracy [13]. Additionally, by imposing transverse stress boundary conditions on the upper and lower surfaces of the laminate, the number of variables can be further reduced to 6*n*. It is possible to notice the resemblance of Eq. 2 with the HSDT formulation presented in Table 1. In fact, the HSDT can be seen as a simplified version of the LT.

2.2.1 Zig-Zag Theories

As one may anticipate, the term Zig-Zag Theory (ZZT) is granted due to the zig-zag distribution of in-plane displacements through-the-thickness attained by these formulations. They are a particular type of LT, in the sense that they make use of global and layer-dependent (local) displacement components. A number of early ZZTs were proposed assuming in-plane displacement continuity only [10–12]. These theories improved in-plane stress prediction, but transverse shear stresses were still constant through-the-thickness, due to the low order of the assumed displacement fields. Later developments also failed to predict transverse shear stresses by employing higher-order displacement terms, and it was not until Cho and Parmerter [17] that transverse stress continuity conditions were accounted for and correct transverse shear stresses were predicted directly from constitutive relations.

Liu and Li [2] unified the notations of the ZZTs by expressing the displacement fields as:

$$\begin{aligned} u^k(x,y,z) &= u_0^k(x,y) + u_1^k(x,y)z + u_2(x,y)z^2 + u_3(x,y)z^3 \\ v^k(x,y,z) &= v_0^k(x,y) + v_1^k(x,y)z + v_2(x,y)z^2 + v_3(x,y)z^3 \\ w^k(x,y,z) &= w_0(x,y) \end{aligned} \quad (3)$$

Other ZZTs were developed by changing the order of the layer-dependent terms (i.e. zeroth and second order, first and second order, etc.), but in all of them, there are only two layer-dependent terms. This is because using two layer-dependent terms, the number of layer-dependent variables (4*n*) is equal to the number of the displacement (*u*, *v*) and transverse stresses (τ_{xz}, τ_{yz}) continuity equations (4*n* - 4), plus the boundary conditions for the transverse stresses on the upper and lower surfaces (4). As a result, all layer dependent variables can be eliminated.

Because transverse deformation is neglected, the continuity equations related to *w* and σ_z are not available, as in the full LTs. These theories are also referred to as Quasi-Layerwise Theories (QLT) [2].

One drawback of this class of theories is that the predicted transverse shear stress is smooth through-the-thickness, failing to capture distinct kinks in lamina interfaces (See Figure 1) even when employing higher-order local displacement components. Moreover, the *w* displacement continues to be assumed constant through-the-thickness, meaning that the transverse normal strain is neglected, and the transverse normal stress can only be recovered from the integration of the equilibrium equations. Also, there is a dependency of the definition of the local coordinate system for the layers [2], reducing the robustness of such theories.

2.2.2. Superposition Theories

In the light of the improvements achieved by these so-called ZZTs, it became evident that an attractive strategy to develop an accurate and computationally efficient theory for laminated plates would be to combine the layer-independence of HSDTs with the capability of predicting layerwise behaviour, while also preserving the capability to determine transverse stresses directly from the constitutive equations, without the need of postprocessing. Liu and Li [18] proposed such an approach by introducing global and local displacement components based on a generalized coordinate system, named Superposition Theory (ST).

The displacement field of the *k*th layer of a laminated composite plate can be expressed in terms of global and local (layer-dependent) components as:

$$\begin{aligned} u^k &= u_G + u_L^k \\ v^k &= v_G + v_L^k \\ w^k &= w_G \end{aligned} \tag{4}$$

where k is the layer order and the subscripts L and G represent local and global components, respectively. Departing from Eq. 3 (also known as 0-1 QLT) and Eq. 4, the 0-1 ST can be written as:

$$\begin{aligned} u^k(x,y,z) &= u_0(x,y) + u_1(x,y)z + u_2(x,y)z^2 + u_3(x,y)z^3 + u_0^k + u_1^k\xi_k \\ v^k(x,y,z) &= v_0(x,y) + v_1(x,y)z + v_2(x,y)z^2 + v_3(x,y)z^3 + v_0^k + v_1^k\xi_k \\ w^k(x,y,z) &= w_0(x,y) \end{aligned} \tag{5}$$

Notice that for global displacement terms the z-coordinate is used, while for local description, a linear coordinate ξ_k for the kth layer is used. This is the fundamental difference between ZZTs, or QLTs, and STs, which renders the biggest advantages of STs: independence of the number of layers and of the definition of the local coordinate system.

As for the QLTs, STs can be classified by the order of the local terms (i.e. 0-1, 0-2, 0-3, 1-2, 1-3, 2-3). The 1-3 ST (local terms are of first and third-order) is considered the best among the other six investigated theories of this family, due to its excellent predictions of τ_{xz} and τ_{yz} [2]. This indicates that the first and third-order terms play an important role on the overall accuracy, both for displacement and stresses. According to Liu and Li [2] a possible interpretation is that the first-order layer dependent term is considered the most fundamental one (associated with rotational angle), while the third-order term is particularly important in order to predict the layerwise parabolic distribution of the shear stress. Nevertheless, with the exception of the zeroth-order terms, which can be accurately represented globally, all local terms have a distinct contribution to laminate performance.

2.2.3 Double-Superposition Theories

In view of a more accurate representation of the laminate behaviour, accounting for as many local terms as possible, Liu and Li [2] propose the Double Superposition Theory (DBST), which consists of applying the ST technique twice to three local terms. This is necessary since only two continuity conditions can be satisfied in composite layer assembly, limiting the number of variables associated to local behaviour to two, as noted in Section 2.2.1. The displacement field then assumes the following general form:

$$\begin{aligned} u^k &= u_{\mathrm{G}} + \bar{u}_{\mathrm{L}}^k + \tilde{u}_{\mathrm{L}}^k \\ v^k &= v_{\mathrm{G}} + \bar{v}_{\mathrm{L}}^k + \tilde{v}_{\mathrm{L}}^k \\ w^k &= w_{\mathrm{G}} \end{aligned} \tag{6}$$

The local terms can have different arrangements of first, second and third-order, giving rise to different theories, for example the 1,2-3 DBST:

$$\begin{aligned} &\bar{u}_{\mathrm{L}}^k(x,y,\xi_k) = u_1^k + u_2^k {\xi_k}^2 \;;\; \tilde{u}_{\mathrm{L}}^k(x,y,\xi_k) = u_3^k {\xi_k}^3 \\ &\bar{v}_{\mathrm{L}}^k(x,y,\xi_k) = v_1^k + v_2^k {\xi_k}^2 \;;\; \tilde{v}_{\mathrm{L}}^k(x,y,\xi_k) = v_3^k {\xi_k}^3 \end{aligned} \tag{7}$$

According to Liu and Li [2], the results of the different arrangements of DBST are equivalent. Although an excellent prediction of displacements and transverse stresses, there is still the need of post-processing to recover the transverse normal stress for ST and DBST. The reason for this is that the variation of *w* through-the-thickness is still neglected or assumed as a global distribution. This is a common aspect to most of the presented formulations, with the exception of full layerwise theories, which assume the general form of Eq. 2.

In an effort to overcome this drawback, Lima and Faria [19] proposed a 0-1 ST formulation for a two-dimensional beam finite element considering a local *w*-displacement distribution. There was a satisfactory response of the displacements, in-plane stress and transverse shear stress, but the predicted transverse normal strain and stresses obtained directly from constitutive relations did not possess the same level of accuracy, and post-processing was required to correct the results. Despite the deficient accuracy of the later quantities, the element meets all C^0_z requirements, with the exception of the kinks in transverse shear stress, handling non-homogeneous boundary conditions on the laminate surfaces and obtaining all stresses directly from the constitutive relations. Improved results are expected by increasing the order of the local terms, such as 1-3 ST, according to the observations of Liu and Li [2].

3. SUMMARY AND CONCLUSIONS

The previous sections gave an overview of the main displacement-based theories, presenting their displacement fields and capabilities to satisfy the so-called C^0_z continuity requirements, illustrated in Figure 1. In order to provide a clear comparison between the theories in a summarized manner, they were organized in a table form, and their main characteristics highlighted:

Table 2: Comparison of the different displacement theories

	CLT	HSDT	ZZT	GLT	LT
Displacement Continuity	Yes	Yes	Yes	Yes	Yes
Zig-zag shape of in-plane disp.	No	No	Yes	Yes	Yes
Transverse stresses continuity	No	No	Yes	Yes	Yes
τ_{xz} ; τ_{yz} accuracy	τ_{xz} ; τ_{yz} neglected	Low	Good above 5-th order. Dependent coordinate system definition. Smooth.	Good when first and third-order local terms are considered. Kinks are captured.	Excellent
σ_z accuracy	Neglects	Postprocessed	Postprocessed	Postprocessed	Excellent
Dependency on the number of layers	No	No	No	No	Yes

It becomes clear that laminated composite structures require a higher level of discretization when compared to homogeneous structures, since layerwise behaviour must be well represented. Therefore, there is a continuous effort in the academia to develop accurate and computational efficient theories capable of describing the behaviour of laminated composite structures. Among the discussed theories, the ones that present best compromise between numerical efficiency and accuracy are the ones based on the global-local superposition approach; however, there are still improvements to be done in the theories currently available in the open literature.

ACKNOWLEDGEMENTS

The authors would like to acknowledge the Brazilian funding agencies CAPES and CNPQ for the grants CAPES 1642839, CNPq 306193/2017-5 and 163101/2017-5 that supported this research.

REFERENCES

[1] E. Carrera, “A class of two-dimensional theories for anisotropic multilayered plates analysis,” *Atti della Accad. delle Sci. di Torino. Cl. di Sci. Fis. Mat. e Nat.*, vol. 19, pp. 49–87, 1995.

[2] D. Liu and X. Li, “An Overall View of Laminate Theories Based on Displacement Hypothesis,” *J. Compos. Mater.*, vol. 30, no. 14, pp. 1539–1561, 1996.

[3] E. Carrera, *Theories and finite elements for multilayered, anisotropic, composite plates and shells*, vol. 9, no. 2. 2002.

[4] E. Carrera, “Historical review of Zig-Zag theories for multilayered plates and shells,” *Appl. Mech. Rev.*, vol. 56, no. 3, p. 287, 2003.

[5] A. S. Sayyad and Y. M. Ghugal, "On the free vibration analysis of laminated composite and sandwich plates: A review of recent literature with some numerical results," *Compos. Struct.*, vol. 129, pp. 177–201, 2015.

[6] A. S. Sayyad and Y. M. Ghugal, "Bending, buckling and free vibration of laminated composite and sandwich beams: A critical review of literature," *Compos. Struct.*, vol. 171, pp. 486–504, 2017.

[7] G. Kirchhoff, "Ueber das Gleichgewicht und die Bewegung eines unendlich dünnen elastischen Stabes," *J. für die reine und Angew. Math.*, no. 56, pp. 285–313, 1859.

[8] E. Reissner, "On transverse bending of plates, including the effect of transverse shear deformation," *Int. J. Solids Struct.*, vol. 11, no. 5, pp. 569–573, 1975.

[9] R. D. Mindlin, "Influence of rotatory inertia and shear in flexural motions of isotropic elastic plates," *ASME J. Appl. Mech.*, vol. 18, pp. 1031–1036, 1951.

[10] S. G. Lekhnitskii, "Strength calculation of composite beams," *Vestn. inzhen i tekhnikov*, vol. 9, 1935.

[11] S. A. Ambartsumian, "On the theory of bending of anisotropic plates and shallow shells," *J. Appl. Math. Mech.*, vol. 24, no. 2, pp. 500–514, 1960.

[12] E. Reissner, "On a certain mixed variational theorem and a proposed application," *Int. J. Numer. Methods Eng.*, vol. 20, no. 7, pp. 1366–1368, 1984.

[13] C. Y. Lee and D. Liu, "An interlaminar stress continuity theory for laminated composite analysis," *Comput. Struct.*, vol. 42, no. 1, pp. 69–78, 1992.

[14] M. di Sciuva, "Bending, vibration and buckling of simply supported thick multilayered orthotropic plates: An evaluation of a new displacement model," *J. Sound Vib.*, vol. 105, no. 3, pp. 425–442, 1986.

[15] H. Murakami, "Laminated Composite Plate Theory With Improved In-Plane Responses," *J. Appl. Mech.*, vol. 53, no. 3, pp. 661–666, Sep. 1986.

[16] E. J. Barbero, J. N. Reddy, and J. Teply, "An accurate determination of stresses in thick laminates using a generalized plate theory," *Int. J. Numer. Methods Eng.*, vol. 29, no. 1, pp. 1–14, 1990.

[17] M. Cho and R. R. Parmerter, "An efficient higher order plate theory for laminated composites," *Compos. Struct.*, vol. 20, no. 2, pp. 113–123, 1992.

[18] X. Li and D. Liu, "A laminate theory based on global–local superposition," *Commun. Numer. Methods Eng.*, vol. 11, no. 8, pp. 633–641, 1995.

[19] A. Lima and A. Faria, "A composite beam element with through the thickness capabilities based on global-local superposition," no. Ic, pp. 1–26.

ELASTOPLASTIC RESIDUAL STRESSES IN COMPOSITE BEAMS - A SEMI-ANALYTICAL STUDY

Lucas L. Vignoli [1,2], **Paulo P. Kenedi** [3]

(1) Center for Nonlinear Mechanics, COPPE, Department of Mechanical Engineering, Universidade Federal do Rio de Janeiro, Brazil

(2) Mechanical Engineering, Universidade Federal do Rio de Janeiro - Campus Macaé, Brazil

(3) Programa de Pós-graduação em Engenharia Mecânica e Tecnologia de Materiais, CEFET/RJ, Brazil.

https://doi.org/10.21452/bccm4.2018.01.03

Abstract

Composite materials have been widely used due to their lightweight capability. For different industrial applications, hybrid beams have been designed to combine the potential advantage of each layer; for instace, for aeronautical structures it is usual to combine Glass Fiber Reinforced Plastic (GFRP) and aluminum layers. In this article a three layer beam is considered, a medial layer is made of GFRP and the other layers are made of aluminum. A detailed discusison about a semi-analytic procedure to evaluate the residual stress in such structure is presented, analising the influence of fiber volume fraction on the GFRP layer and the layers thickness. The results indicate the possibility of growing up plastic residual stresses in the aluminum layers.

1. INTRODUCTION

Combinations of unidirectional GFRP (Glass Fiber Reinforced Plastic) laminas and thin aluminum-alloy plies were used as the composite material in this article. The application of large bending moment loads, for instance, can yield the aluminum plies of a composite beam, generating a residual stresses distribution along its cross section. In this article a semi- analytical approach is proposed, based on Mechanics of Solids, to estimate the cross section elastoplastic residual stress distribution in composite beams submitted to large bending moments. The metallic layers were modelled considering isotropic elastic-perfectly plastic behavior, while GFRP plie was modelled as linear-elastic with transversally isotropy on the fibers plane. The Euler-Bernoulli hypotheses were utilized to develop the proposed analytical model as in Crandall [1] and Vinson and Sierakowski [2].

2. ANALYTICAL MODEL

Considering a symmetric composite beam lay-up with three layers, where the central layer was made of GFRP and the extremities ones were made of aluminum, submitted to pure bending moment, as illustrated in Fig. 1.

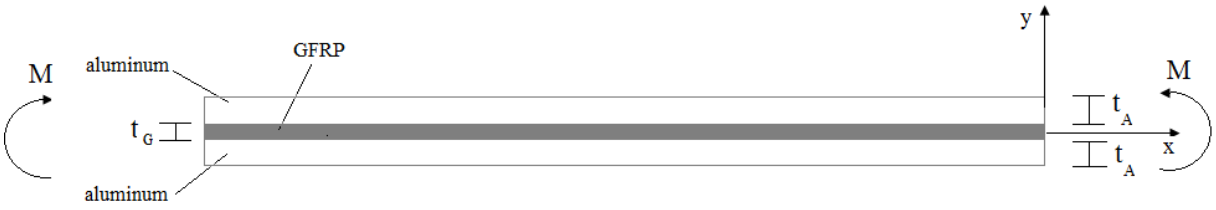

Figure 1: Three layers composite beam

The maximum bending moment applied in this beam is limited, by hyphotesis, to avoid the failure of the GFRP layer. Assuming that GFRP has a smaller strength in compression than in tension Barbero [3], the maximum allowable stress in this layer must be equal to its compressive strength, computed by the following equation as Lo & Chim [4]

$$S_{11}^{c} = \frac{G_G}{1.5 + 12(6/p)^2 (G_G / E_G)} \tag{1}$$

Where E_G and G_G are the longitudinal elastic modulus and the in-plane shear modulus of the GFRP layer, respectively, estimated by

$$E_G = E_f V_f + (1 - V_f) E_m \tag{2}$$

$$G_G = G_m \frac{G_f(1+V_f) + G_m(1-V_f)}{G_f(1-V_f) + G_m(1+V_f)} \tag{3}$$

where V_f is the fiber volume fraction, E_f and E_m are the fiber and matrix longitudinal elastic modulus; G_f and G_m are the fiber and matrix shear modulus.

If the bending moment is such as the whole aluminum layers yield, this bending moment is the maximum that can be applied to avoid the failure of the GFRP layer

$$M_{max}^{ult} = b\left[S_{11}^{c}\frac{t_G^2}{6} + S_y t_A (t_A + t_G)\right] \tag{4}$$

where b is the beam width, t_G and t_A are, respectively, the GFRP and aluminum layers thicknesses and S_y is the aluminum yield strength.

The cross section stress distribution in this limit situation is shown in (5.a)

$$\sigma_{load} = \begin{cases} -E_G \dfrac{M_{max}^{ult}}{EI_{load}} y & if \; -0.5t_G \le y \le 0.5t_G \\ -S_y sign(y) & otherwise \end{cases} \tag{5.a}$$

$$\sigma_{load} = \begin{cases} -E_G \dfrac{M_{max}}{EI_{load}} y & if \; -0.5t_G \le y \le 0.5t_G \\ -S_y sign(y) & otherwise \end{cases} \tag{5.b}$$

where $EI_{load} = E_G I_G$ is the equivalent bend stiffness during the load and $I_G = bt_G^{\,3} / 12$ is the second moment of inertia of the GFRP layer.

The unload, or springback, is mathematically equivalent to the application of a moment with the same magnitute and oposite direction. Thus, the residual stress is computed using the superposition principle.

In an intermediary situation where the aluminum thicknesses aren't totally yielded $t^* < t_A$ (see Fig. 2), the following equations must be satisfied

$$M_{max} = |k| EI_{unload} + 4S_y bt^* \frac{(h - t^*)}{2} \tag{6}$$

$$|k| = \frac{2S_y}{E_A(0.5h - t^*)} \tag{7}$$

where $EI_{unload} = E_A I_A + E_G I_G$ is the equivalent bend stiffness during the unload and $I_A = b[(h - 2t^*)^3 - t_G^{\,3}] / 12$ is the second moment of inertia of the aluminum layer. To obtain the magnitude of $|k|$ and t^*, a simple iterative procedure was implemented in MATLAB. Note that this is the unique numerical step of the present study.

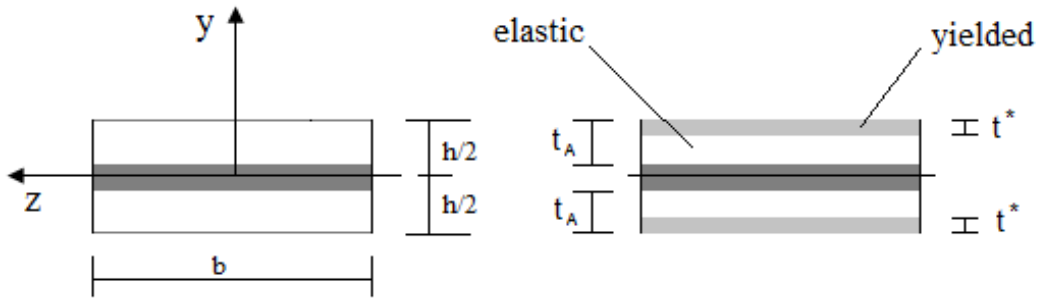

(a) (b)

Figure 2: Composite beam cross section, (a) before loading and (b) after unloading

Once the parameters $|k|$ and t^* are obtained, the stresses of the unload process is estimated:

$$\sigma_{unload} = \begin{cases} E_G \dfrac{M_{max}}{EI_{unload}} y & if \quad -0.5t_G \le y \le 0.5t_G \\ 2\, S_y sign(y) & if \quad -\left(\dfrac{h}{2} - t^*\right) \le y \le \left(\dfrac{h}{2} - t^*\right) \\ E_A \dfrac{M_{max}}{EI_{unload}} y & otherwise \end{cases} \tag{8}$$

Using Eq.(5.b) and Eq.(8), the residual stress cross section distribution can be estimated as

$$s_{residual} = s_{load} + s_{unload} \tag{9}$$

3. RESULTS AND DISCUSSION

In this analysis, the elastic and shear modulus of the glass fiber and of the epoxy matrix are, respectively: $E_f = 87GPa$ and $G_f = 36.25GPa$; $E_m = 3.2GPa$ and $G_m = 1.18GPa$ as in Kaddour and MJ Hinton [5]. The elastic modulus and the yield strength of the aluminum are $E_A = 72.4GPa$ and $S_y = 345MPa$ as in Abouhamzeh [6]. The beam cross section has the width $b = 10mm$ and height $h = 10mm$. Figure 3 shows the stress distribution along the beam height for different values of fiber volume fractions; each one of them represents a different ratio between the GFRP and aluminum thicknesses.

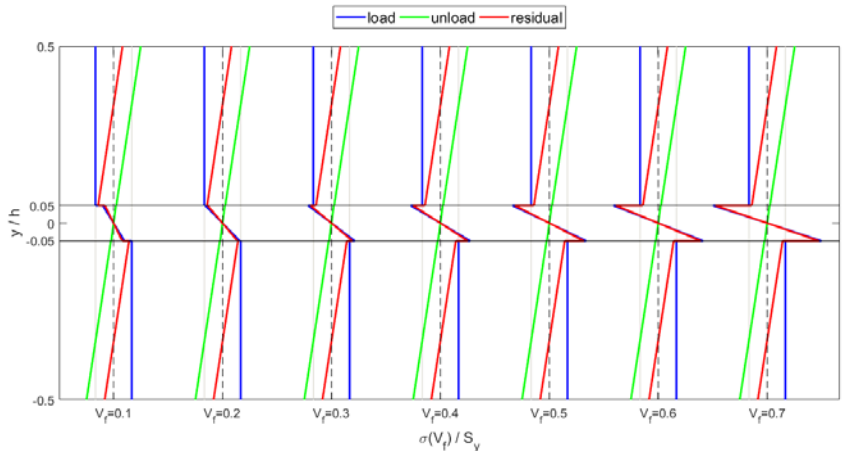

(a)

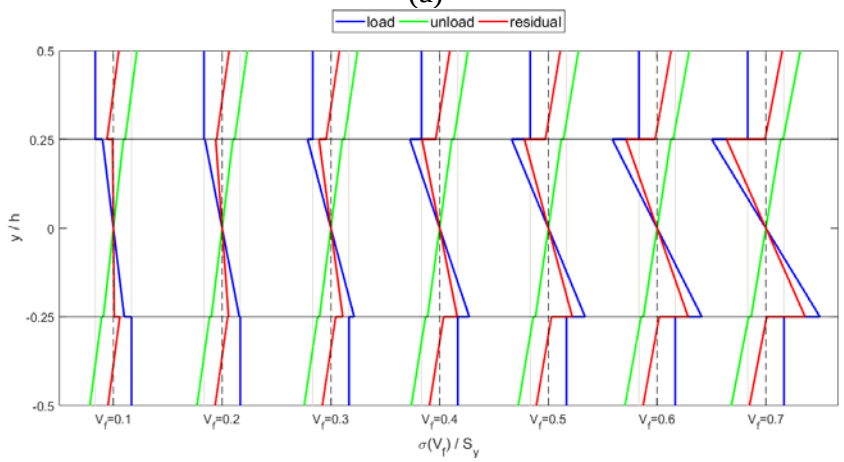

(b)

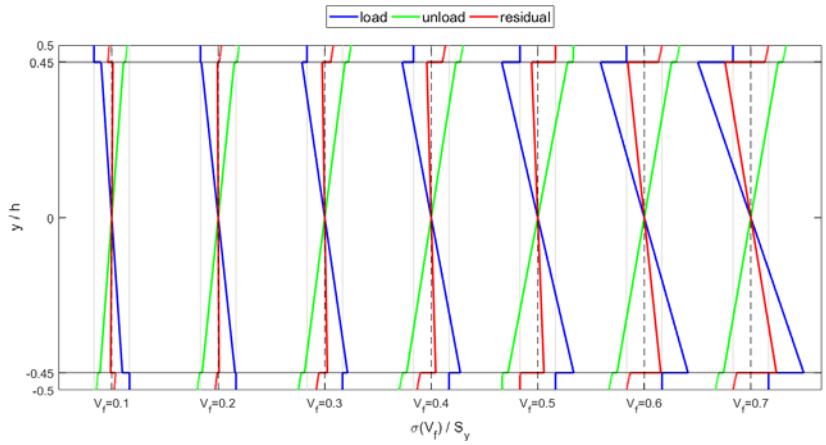

(c)

Figure 3: Stress distribution along the beam height (load, unload and residual) according to: (a) $t_G = 0.1h$, (b) $t_G = 0.5h$ and (c) $t_G = 0.9h$

Note in Fig.3.c the red lines indicate the possibility of residual plastic stress for laminates with thicker GFRP layer and higher fiber volume fraction.

A detailed analysis for the laminate with $t_G = 0.9h$ is presented in Fig.4. In Fig. 4.a shows the contour map of stress for the load application, Fig. 4.b shows the contour map of stress during unload, which is equivalent to a second load, with the same magnitude but with oposite direction and Fig. 4.c shows the contour map of residual stress distribution.

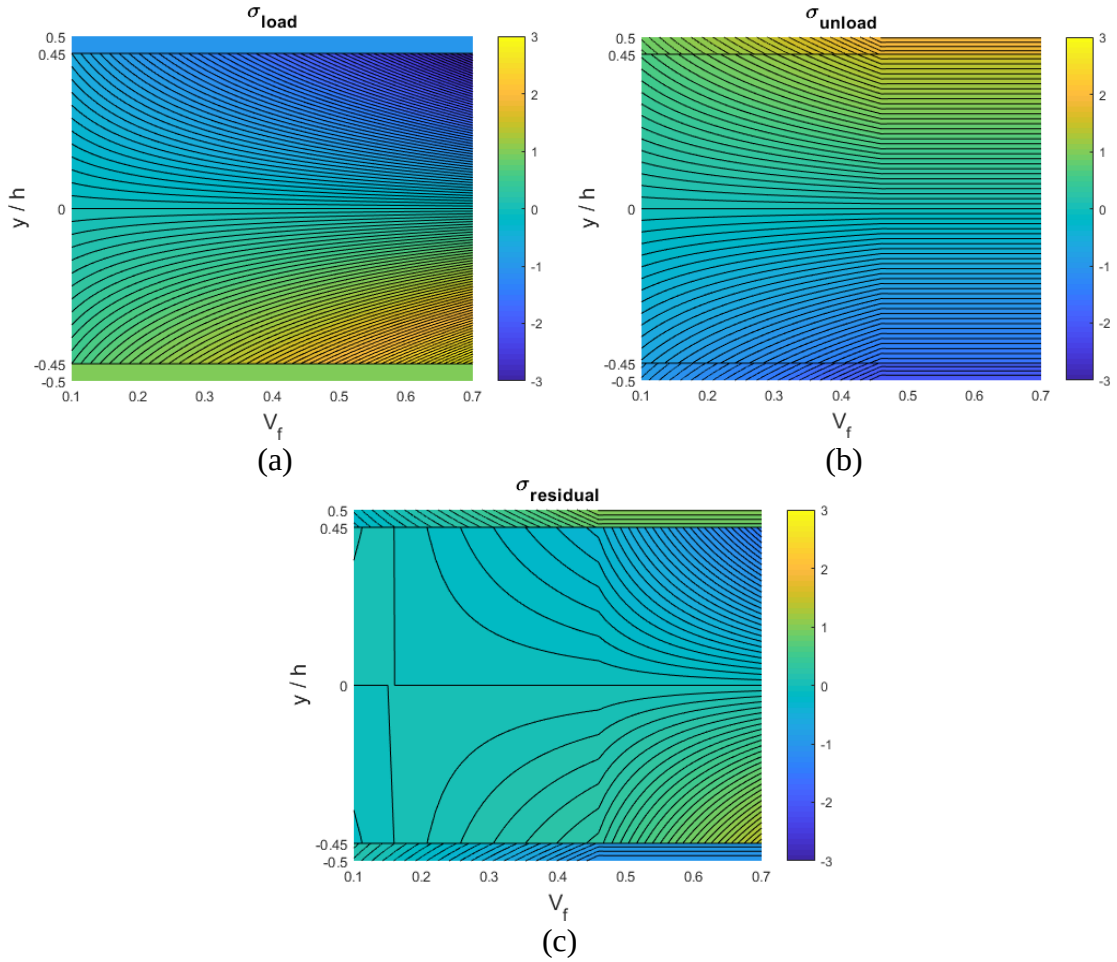

Figure 4: Contour map of the stress distibution ($t_G = 0.9h$): (a) load, (b) unload and (c) residual stresses

Note that the scale of collors was parameterized using σ/S_y and the whole aluminum layers yield during the load. The horizontal lines on the unload and on the residual maps indicate the yield during the unload step (note for $V_f > 0.45$). As Fig. 4 shows the possibility of plastic residual stress distribution, the main question to be answered is under which conditions the yield during unload could occur.

Figure 5 shows for various combinations of t_G and V_f which ones generate an elastoplastic residual stress distribution along the beam thickness.

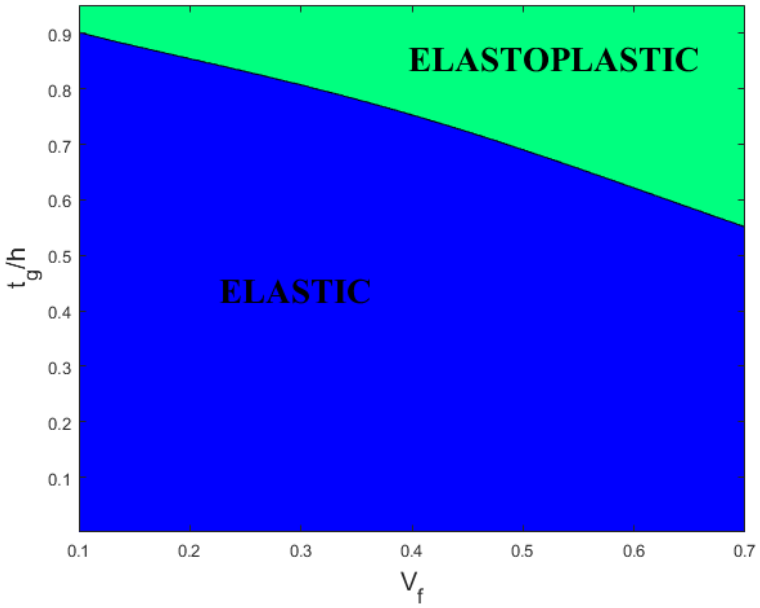

Figure 5: Map indicating for each combinations of V_f and t_G there exist plastic residual stress.

It is possible to recognize that even for very small values of fiber volume fraction it is possible to have a plastic residual stress for high values of GFRP thicknesses.

4. CONCLUSIONS

A semi-analytical model, based in mechanics of solids, was proposed to investigate the behavior of a composite beam, made of plies of aluminum and GFRP, submitted to large value of pure bending moment. Different plies thicknesses and different fiber volume fractions on the GFRP layer were implemented. It was concluded that both variables, fiber volume fraction on the GFRP layer and the layers thickness, can produces significative effects in the beam cross section residual stress distribution. Also, for high bending moments it was verified that the aluminum plies can yield even during unloading.

5. ACKNOWLEDGEMENTS

L.L. Vignoli is grateful for scholarship granted by CAPES.

6. REFERENCES

[1] Crandall, S.H., Dahl, N.C. and Lardner, T.J., ‘An Introduction to the Mechanics of Solids’, Second Edition with SI units (McGraw Hill International Editions, 1978).

[2] Vinson, R. and Sierakowski, R.L., 'The Behavior of Structures Composed of Composite Materials', Second Edition (Solid Mechanics and Its Applications, Volume 105, ISBN 978-94-009-5187-7, 1987).
[3] Barbero, E.J., 2018, Introduction to Composite Materials Design, 3 ed., CRC Press.
[4] Lo, K.H., Chim, E.S.M., 1992, "Compressive Strength of Unidirectional Composites", Journal of Reinforced Plastics and Composites, v. 11.
[5] Kaddour, A.S. and Hinton, M.J., 'Input data for test cases used in benchmarking triaxial failure theories of composites', *Journal of Composite Materials* **46** (19–20) (2012), 2295–2312.
[6] Abouhamzeh, M., Sinke, J., Jansen, K.M.B., Benedictus, R. 'Closed form expression for esidual stresses and warpage during cure of composite laminates', *Composite Structures*, **133** (902–910), 2015.

7. RESPONSIBILITY NOTICE

The authors are the only responsible for the printed material included in this paper.

HYBRID COMPOSITES: EXPERIMENTAL AND ANALYTICAL ASSESSMENT AIDED BY ONLINE SOFTWARE

Eduardo A. W. de Menezes [(1)], Mário J. Kunz Filho [(2)], Frederico Eggers [(3)] and Sandro C. Amico[(3)]

(1) PROMEC, Federal University of Rio Grande do Sul, Brazil

(2) Department of Computational Sciences, Federal University of Rio Grande do Sul, Brazil

(3) PPGEM, Federal University of Rio Grande do Sul, Brazil

https://doi.org/10.21452/bccm4.2018.01.04

Abstract

Hybrid composites are commonly applied to obtain tailor-made properties due to the additive or synergistic effect between matrix and fibers, offering a wide range of properties that could not be achieved with a single fiber. However, addition of more than one fiber makes the mechanical behavior of hybrid composites more complex, and classical approaches such as rule of mixtures must be reconsidered when evaluating their mechanical properties using micromechanical theories. The aim of this work is to present an online software tool for researchers and designers, where different models for evaluating mechanical and thermal properties of hybrid composites were incorporated, allowing the user to quickly assess them based on the fibers and matrix properties. The developed software is web-based and was programmed and designed with mark-up and programming languages such as Python, HTML, JavaScript and MySQL, and also enable analysis of single fiber composites (short and long fibers, aligned or random), particulate composites and nanocomposites. In order to verify the available models, an experimental study was carried out by producing an epoxy composite with glass and carbon fibers at different relative fiber volume fraction. The samples were submitted to longitudinal and transverse tensile and in-plane shear testing to produce experimental values for Elastic moduli, Poisson's ratio and shear modulus of the intraply hybrid composite. Good correlation was found between experimental and analytical approaches considering the adopted assumptions, especially for the Chamis and Chou models.

1. INTRODUCTION

Hybrid composites are commonly referred as a matrix reinforced by at least two distinct fibers, aiming to provide a synergistic effect between the multiple fibers [1]. According to Ashori and Nourbakhsh [2], for the hybrid effect to appear, fibers of different mechanical properties are

required, forming also interfaces with different properties. Hybridization may offer a more cost-effective way to meet design requirements compared to traditional engineering materials, since it allows composites to reach tailor-made properties [3], balanced thermal stability, strength and stiffness, better toughness, and fatigue and impact resistance [4]. In order to reach balanced properties, it is essential to accurately equalize the volume fraction of matrix and fibers and evaluate the composite mechanical properties or estimate them through micromechanics. However, hybrid effects may not be accurately modelled by the rule-of-mixtures (ROM) [5], increasing the complexity of closed-form solutions. Despite that, micromechanical equations for hybrid composites (HC) provide accurate solutions for predicting mechanical properties, yielding results quite close to the ones obtained through finite element modelling [6].

Unlike isotropic materials, experimental characterization of composite materials is expensive and time consuming due to many variables involved [7]. Aiming to provide an easy way to quickly compute hybrid composite properties from micromechanics, equations found in literature for these material classes were compiled and fed to the MECH-Gcomp software developed by the group. The program interface was built using html customized with CSS. Language JavaScript was used, allowing the scripts to be executed by the user without passing by the server, increasing the development speed. The calculations and server side of the web application used Python, a widely used language, with large online community, high abstraction level and easy programming for the interaction with other languages and libraries. Interaction between Python and framework Django was crucial for a robust web development, together with the program Mysql for MECH-Gcomp database management.

The software MECH-Gcomp already has many different micromechanical approaches, validated with experimental data for nanocomposites [8], particulate composites [9], short [10] and long [11] single fiber composites. The present work aims to compare micromechanical equations available in the literature with experimental results for hybrid glass+carbon/epoxy composites, at different relative fiber volume fractions, to verify their robustness in predicting the composite properties.

2. MATERIALS AND METHODS

2.1 Mathematical Models

Due to different simplifications and assumptions of different micromechanical models (no voids, neglection of interface, perfect alignment of fibers, etc.), MECH-Gcomp software presents all available options and lets the user decide which one will be chosen. It incorporates in its code several models to compute engineering constants, mechanical strengths and thermal properties of HC. Regarding longitudinal Young modulus (E_1) and Poisson ratio (ν_{12}), Rule of Mixture (ROM) is able to provide accurate results, even for hybrid composites [6, 12].

$$E_1 = E_{1,f1}V_{f1} + E_{1,f2}V_{f2} + E_mV_m \tag{1}$$

$$\nu_{12} = \nu_{13} = \nu_{12,f1}V_{f1} + \nu_{12,f2}V_{f2} + \nu_mV_m \tag{2}$$

For the other engineering constants, Banerjee (2014) [6] extended the semi-empirical models proposed by Halpin (1976) [13], applying the following set of equations:

$$E_2 = E_3 = E_m\left[\frac{1+\xi\left(\eta_{f1}V_{f1}+\eta_{f2}V_{f2}\right)}{1-\eta_{f1}V_{f1}-\eta_{f2}V_{f2}}\right];\ \eta_{f1}=\frac{\frac{E_{1,f1}}{E_m}-1}{\frac{E_{1,f1}}{E_m}+\xi};\ \eta_{f2}=\frac{\frac{E_{1,f2}}{E_m}-1}{\frac{E_{1,f2}}{E_m}+\xi} \tag{3}$$

$$G_{12} = G_{13} = G_m\left[\frac{1+\xi\left(\eta_{f1}V_{f1}+\eta_{f2}V_{f2}\right)}{1-\eta_{f1}V_{f1}-\eta_{f2}V_{f2}}\right];\ \eta_{f1}=\frac{\frac{G_{12,f1}}{G_m}-1}{\frac{G_{12,f1}}{G_m}+\xi};\ \eta_{f2}=\frac{\frac{G_{12,f2}}{G_m}-1}{\frac{G_{12,f2}}{G_m}+\xi} \tag{4}$$

where E_2 is the transverse Young Modulus, G_{12} is the in-plane shear modulus, V is the volume fraction, and ξ is a parameter associated with fiber geometry (for circular fibers its value is 1.165 in Equation (3) and 1.01 in Equation (4)). Subscripts *m*, *f*1 and *f*2 designate matrix, primary and secondary fiber, respectively.

Regarding longitudinal tensile strength, it is assumed that the composite will fail when its first constituent reaches its ultimate strain, as depicted in Equation (5), where σ_1^T is the longitudinal tensile strength and ε is the lower ultimate strain among the composite constituents.

$$\sigma_1^T = E_1\varepsilon \tag{5}$$

According to Chamis (1980) [12], HC properties can be achieved by splitting it on primary composite (PC) and secondary composite (SC), where the first is reinforced by *fiber 1* and the second by *fiber 2*, with the matrix proportionally distributed. The methodology applied to compute these composite properties is analogous to that applied for single-fiber composites, as depicted in Chamis (1989) [14]. Then, the HC engineering constants and strengths are evaluated according to a new ROM. Equation (6) shows how to obtain the transverse Young modulus and, by substituting E_2 for G_{12} in Equation (6), one can obtain the HC shear modulus.

$$E_{2,PC} = \frac{E_m}{1-\sqrt{V_{f,PC}}\left(1-\frac{E_m}{E_{2,f1}}\right)};\quad E_{2,SC} = \frac{E_m}{1-\sqrt{V_{f,SC}}\left(1-\frac{E_m}{E_{2,f2}}\right)} \tag{6}$$

$$E_2 = E_{2,PC}V_{PC} + E_{2,SC}V_{SC}$$

The model presented by Chou [15] splits the composite producing a high modulus (HM) and a low modulus (LM) composite. The equations proposed by Chamis [12] are used to compute their engineering constants, but the final properties are obtained by using the following equations:

$$E_1 = E_{1,HM}V_{HM} + E_{1,LM}V_{LM};\quad \nu_{12} = \nu_{12,HM}V_{HM} + \nu_{12,LM}V_{LM}; \tag{7}$$

$$E_2 = \frac{E_{2,HM}}{1+V_{LM}\left(\frac{E_{2,HM}}{E_{2,LM}}-1\right)};\quad G_{12} = \frac{G_{12,HM}}{1+V_{LM}\left(\frac{G_{12,HM}}{G_{12,LM}}-1\right)}$$

2.2 Experimental Tests

Hybrid and non-hybrid composite laminates were produced by using carbon/epoxy and glass/epoxy towpregs from TCR Composites, Toray T700-12K-50C and 158B-AB-450, respectively, both pre-impregnated with UF3369 epoxy resin system. The flat laminates were manufactured by dry filament winding using a KUKA 140 L100 robot integrated with peripheral control systems from MF TECH. The equipment delivery eye is able to process up to four towpregs simultaneously allowing the manufacturing of hybrid composites with different compositions. The composite design was performed in the CadWind software and the data containing all the winding parameters were entered. These parameters are converted into a simulated model for manufacture optimization. The simulation is then processed and converted into a robot programming language.

Hoop flat laminates were produced from the deposition of the fiber tows on top of a stainless-steel mandrel (327 × 228 × 12 mm³), as shown in Figure 1. Five laminates with different relative contents of reinforcing material were produced, with up to 4 simultaneous tows. Two of the five laminates are composed of a single fiber, glass or carbon. Table 1 shows the amount of tows used and the final thickness of the composite. The laminate ID designates the carbon and glass fiber volume fractions. After winding, the material was cured in a hot hydraulic press under six ton at 120 °C for 4 h. After that, the system was cooled to room temperature, and the mandrel unscrewed to extract the flat composite.

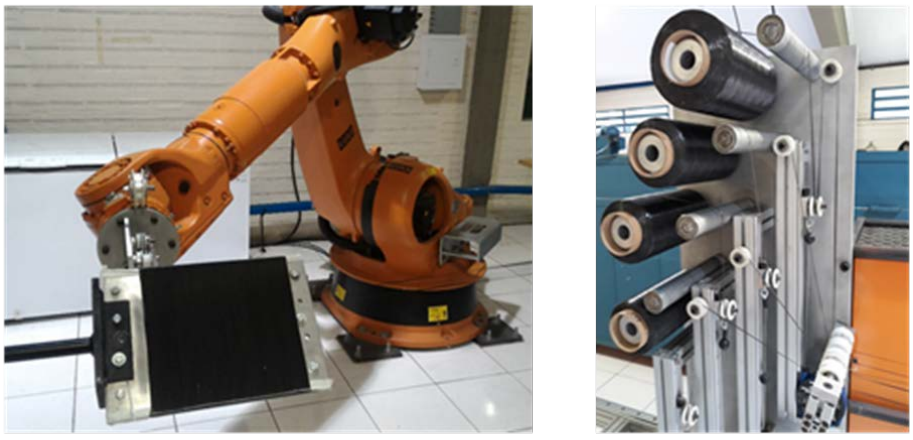

(a) (b)

Figure 1: (a) Manufacturing of a flat laminate by filament winding and (b) arrangement with four simultaneous tows.

Table 2: Specification of the manufactured laminates.

Laminate ID*	Tows		Layers	Mean thickness (mm)
	Carbon/epoxy	Glass/epoxy		
0C:64G	0	2	3	2.01
19C:44G	1	3	3	2.25
36C:30G	1	1	3	2.00
49C:13G	3	1	3	2.27
61C:0G	2	0	3	2.06

*C-carbon, G-glass

The unidirectional composites were cut using a CNC router machine, longitudinally and transversely to the fiber direction. The specimens were then sanded and the dimensions measured.

All the experiments were performed in an Instron Universal machine model 3382 with a 100 kN load cell. Tensile tests were performed according to ASTM D3039-17 at constant speed (2 mm/min) and using two analogical extensometers. Seven specimens for each composite were tested to obtain elastic moduli and Poisson's ratio. For transverse tensile tests, length of the samples was 27 mm shorter than suggested by the standard due to the limited dimensions of the plates. The shear properties were characterized using ASTM D7078-12, which is recommended for high-modulus fiber-reinforced composite materials. Four samples were tested at a speed rate of 2 mm/min. Strain gages of the rosette type KFG-5-120-D17-11 from KYOWA were used to enable calculation of the in-plane shear modulus, G_{12}.

Fibers and resin mechanical properties are compiled in Table 2, along with densities (ρ) and weight fraction in towpregs (W_f). Some of the data shown in this table were extracted from the literature [16] when not provided by the manufacturer.

Table 3: Properties of fibers and resin of the towpregs.

Property	**Glass fiber 158B-AB-450**	**Carbon fiber T700**	**Epoxy resin UF3369-100**
E_1 **(GPa)**	72.4	230	3.10
E_2 **(GPa)**	72.4	15.0	3.10
ν_{12}	0.200*	0.200*	0.350*
G_{12} **(GPa)**	3.08*	14.7*	1.24*
ρ **(kg/m³)**	2580	1800	1180
W_f **(%)**	75.1	70.3	-

**Extracted from [16]*

3. RESULTS AND DISCUSSION

Equations (1)-(7) were used to evaluate the five different composites depicted in Table 1. Figures 2 and 3 present the analytical results from the micromechanics models compared to the experimental data, and the relative deviations are depicted in Table 3.

ROM could accurately predict the E_1 value, including the HC. While the models from Banerjee [6] and Chamis [12] could predict with relative good accuracy E_2 and G_{12}, the Chou model [15] deviated significantly from the measured values.

Regarding ν_{12}, none of the models could adequately fit the measured values. This may have occurred due to incorrect input values adopted for fibers and resin, which refer to generic data. The models proposed by Banerjee [6] and Chamis [12] yield generally intermediate values between the composite with *fiber 1* and the composite with *fiber 2*, while Chou [15] model acts in a conservative way, applying ROM with "-1" exponent to compute the final HC properties, yielding final properties similar to the LM composite.

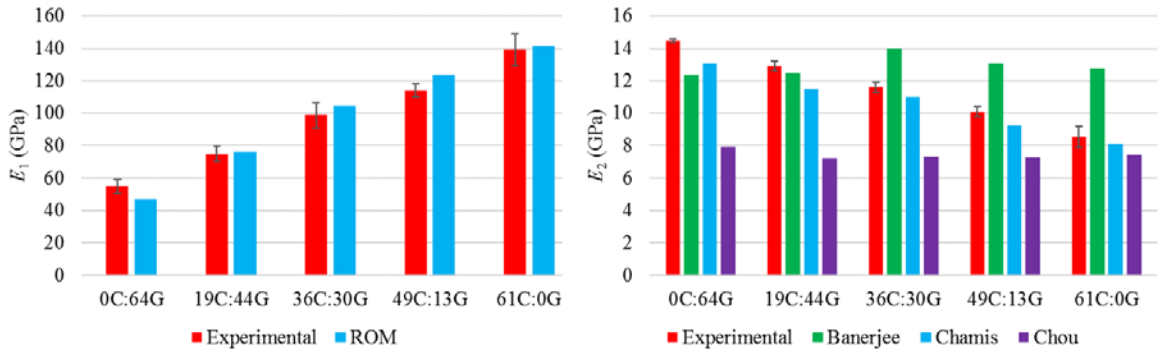

Figure 2: E_1 and E_2 for the five different composite configurations.

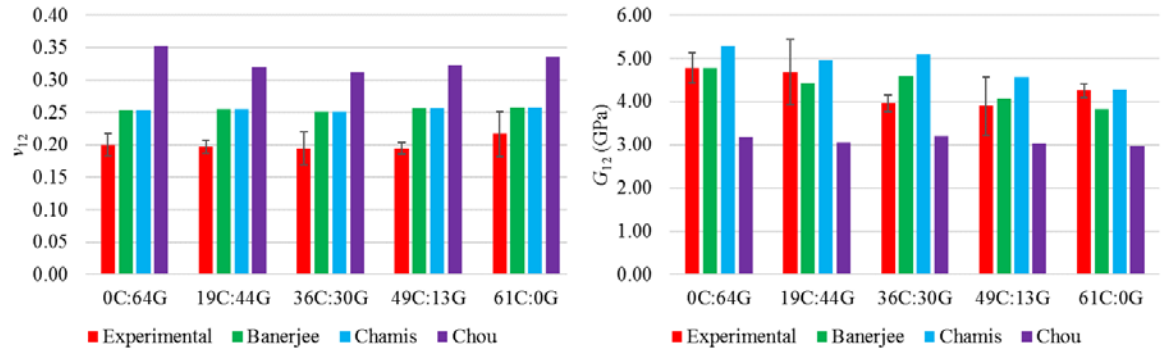

Figure 3: v_{12} and G_{12} for the five different composite configurations.

Table 4: Error between experimental data and micromechanics models.

Deviation	Composition	100G	25C:75G	50C:50G	75C:25G	100C
E_1 (%)	ROM	14.36	2.00	5.77	8.25	1.51
E_2 (%)	Banerjee	14.90	3.26	20.34	29.21	50.00
	Chamis	9.86	11.01	5.34	8.61	4.58
	Chou	45.45	44.11	36.72	27.92	12.91
G_{12} (%)	Banerjee	0.21	5.13	15.62	4.62	10.33
	Chamis	10.46	5.98	28.46	17.18	0.70
	Chou	33.47	34.83	19.14	22.05	30.05
v_{12}	Banerjee	27.00	29.44	28.42	31.79	18.89
	Chamis	27.00	29.44	28.42	31.79	18.89
	Chou	76.00	61.93	60.00	65.64	54.84

**Deviations below 15% have been highlighted for easier comparison.*

4. CONCLUSIONS

Micromechanical models for hybrid composite materials obtained in the relevant literature were implemented on an online software, allowing its users to quickly compute composite mechanical properties based on fiber and matrix types and volume fractions. In order to verify the model's accuracy, experimental tests were performed for five different configurations.

Considering the already mentioned assumptions and simplifications, and the difficulties in obtaining some materials properties, results were in good agreement with experimental data. Relative to E_1, E_2 and G_{12}, micromechanics models showed a deviation of about 10%, except for the Chou model. Poisson´s ratio could not be accurately predicted by any model. Thus, it is possible to conclude that two of the micromechanical models can be applied for predicting hybrid composites properties in a satisfactory level as first estimates.

ACKNOWLEDGEMENTS

The authors gratefully acknowledge the National Council for Scientific and Technological Development (CNPq) and UFRGS for the undergraduate scholarships.

REFERENCES

[1] Kalantari, M., Dong, C. and Davies, I.J., 'Multi-objective analysis for optimal and robust design of unidirectional glass/carbon fibre reinforced hybrid epoxy composites under flexural loading', *Comp. P. B: Eng*. **84** (2016) 130-139.

[2] Ashori, A., Nourbakhsh, A., 'Hybrid composites from waste materials', *J. of Pol. And Env*. **18** (1) (2010) 65-70.

[3] Thakur, V. K., Thakur, M. K. and Pappu, A. 'Hybrid Polymer Composite Materials – Properties and Characterization', 1st Edn (Woodhead Publishing, Duxford, 2017).

[4] Ferrante, L., Tirillò, J., Sarasini, F., et. al., 'Behaviour of woven hybrid basalt-carbon/epoxy composites subjected to laser shock wave testing: Preliminary results', *Comp. Part B: Eng.* **78** (2015) 162-173.

[5] Henry, J., Pimenta, S., 'Modelling hybrid effects on the stiffness of aligned discontinuous composites with hybrid fibre-types', *Comp. Sci. and Tech.* **152** (2017) 275-289.

[6] Banerjee, S., Sankar, B. V., 'Mechanical properties of hybrid composites using finite element method based micromechanics', *Comp. Part B: Eng.* **58** (2014) 318-327.

[7] Kaw, A. K., 'Mchanics of Composite Materials', 2nd Edn (CRC Press, Boca Raton, 2006).

[8] Rodrigues, G., Menezes, E. A. W., Angrizani, C. C., Amico, S. C., 'Evaluation of Nanocomposite properties assisted by software', in '3rd Brazilian Conference on Composite Materials', Gramado-RS, Brazil, 2016.

[9] Angrizani, C. C., Menezes, E. A. W., Muller, A. A., Luz, F. F., Amico, S. C., 'Uso de software acadêmico MECH-Gcomp para ensino de compósitos particulados', *Ver. De Ens. De Eng*. **36** (1) (2017) 13-23.

[10] Menezes, E. A. W., Angrizani, C. C., Smidt, R., Amico, S. C., 'Propriedades mecânicas de compósitos com fibras curtas aleatórias com auxílio de software online', in '13° Congresso Brasileiro de Polímeros', Natal-RN, Brazil, 2015.

[11] Luz, F. F., Angrizani, C. C., Muller, A. A., Sarti, A. C. G., Amico, S. C., 'Study of the Properties of unidirectional composites using a dedicated online software', in '2nd Brazilian Conference on Composite Materials', São José dos Campos-SP, Brazil, 2014.

[12] Chamis, C. C., Sinclair, J. H., 'Mechanics of Intraply Hybrid Composites – Properties, Analysis and Design', *Pol. Comp.* **1** (1) (1980) 7-13.

[13] Halpin, J. C., Kardos, J. L., 'The Halpin-Tsai equations: A review article', *Pol. Eng. And Sci.* **16** (1976) 344-352.

[14] Chamis, C. C., 'Mechanics of Composite Materials: Past, Present and Future', *J. of Comp. Tech. and Res.*, **11** (1) (1989) 3-14.

[15] Chou, T., 'Microstructural design of fiber composites', 1st Edn (Cambridge University Press, New York, 1992).

[16] Hinton, M. J., Kaddour, O. S., Sodden, P. D., 'Failure criteria in fibre reinforced polymer composites: the world-wide failure exercise'. 1st edn. (Elsevier, Oxford, 2004).

2. CEMENT-BASED COMPOSITES

FIBER REINFORCED CONCRETE: FIVE DECADES OF PROGRESS

Antoine E. Naaman

Professor Emeritus, Department of Civil and Environmental Engineering, University of Michigan, Ann Arbor, USA

https://doi.org/10.21452/bccm4.2018.02.01

Abstract

Cementitious matrices such as concrete have low tensile strength and fail in a brittle manner. Adding short needle-like fibers to such matrices enhances their mechanical properties, particularly their toughness, ductility and energy absorbing capacity. The past five decades mark the modern development and broad expansion of fiber reinforced concrete (FRC), which leads to today extensive applications and increased market penetration. Such a success is due in part to significant advances in the fiber reinforcement, the cementitious matrix, the interface bond between fiber and matrix, and fundamental understanding of the mechanics of the composite. Following a brief summary of: 1) the history of fibers in concrete, 3) the reasons why FRC failed during its first 100 years, 3) the underlying principles of fiber reinforcement in cement based composites, 4) the key causal parameters, and 5) related technical as well as practical limitations, this paper-presentation describes the rationale behind the modern developments of FRC composites leading to today's ultra-high performance fiber reinforced concretes, which exhibit tensile strengths of the same order as the compressive strength of normal concretes. It stresses in particular the importance of the transition in composite response from a strain-softening to a strain-hardening behavior in tension, and the resulting transition of the composite function from an engineering material to a structural material with potential stand-alone usage. Relevant examples of applications will be described in the presentation only.

1. INTRODUCTION

The content of this paper is essentially taken from a recently published book on FRC by the author [1]. While the oral presentation (as suggested by the title) offers a more detailed overall perspective, next only two important milestones leading to today classification of all FRC composites as either strain-softening or strain-hardening are documented.

1.1 Fiber Reinforced Cement and Concrete (FRC) Composites

For practical purposes and mechanical modeling, as defined in **[1],** fiber reinforced cement and/or concrete (FRC) composites are defined as composites with two main constituents, the fiber and the matrix (Fig.1). Generally the fiber is assumed to be discontinuous and, unless otherwise stated, randomly oriented and distributed within the volume of the composite. Both the fiber and the matrix are assumed to work together through bond, thus providing the synergism needed to make an effective composite. The matrix, whether it is a paste (cement mixed with water), mortar (paste with sand), or concrete (mortar with coarse aggregates) is assumed to contain all the aggregates and additives specified. A *concrete* matrix is supposed to contain large size aggregates, say with an equivalent diameter in excess of 8 mm (3/8 in). A *mortar* matrix generally contains sand (of mostly less than 3 mm (1/8 in)) but no large size aggregates. A cement *paste* may contain very fine sand, silica powder, fly ash, silica fume, and other fine additives. Air voids entrapped in the matrix during mixing are assumed to be also part of the matrix (Fig. 1). For simplicity, unless otherwise specifically noted, the term "concrete" will be generally used to represent a cementitious matrix whether it is a paste, a mortar or a concrete.

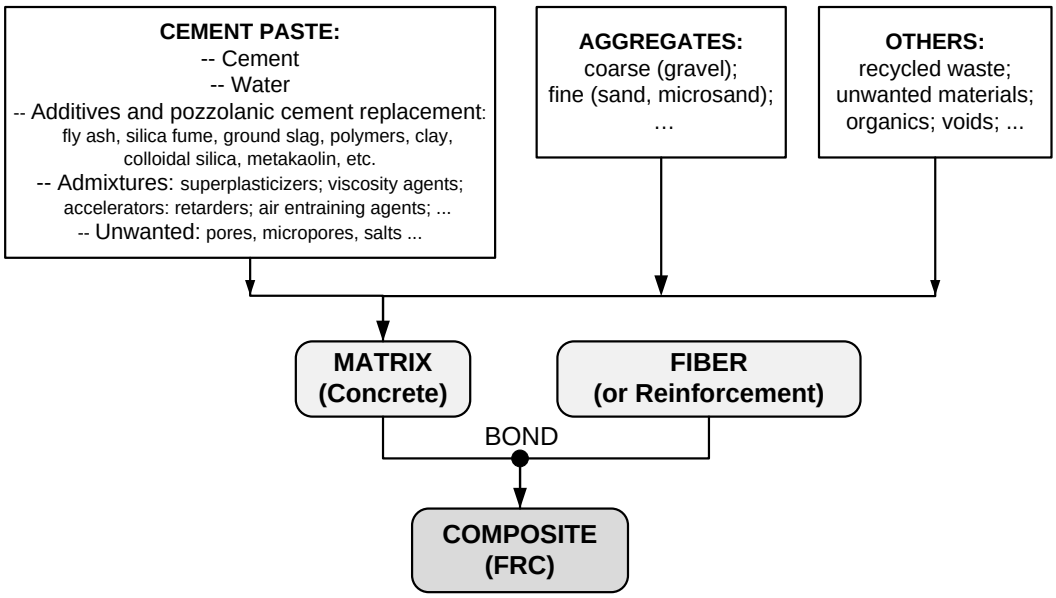

Figure 1 Composite model considered as a two-constituent system, namely fiber and matrix, as applied to fiber reinforced cements and concretes.

Thus from the broadest perspective, fiber reinforced concrete can be defined as follows:

Fiber reinforced concrete (FRC) is concrete with suitable discontinuous fibers added to it for the purpose of achieving a desired level of performance in a particular property (or properties).

If the fibers are continuous, a different terminology is used to describe the composite such as ferrocement, textile reinforced concrete (TRC), or laminate cementitious composites which use continuous reinforcements made out of continuous wires, textiles, or meshes. Reinforced and prestressed concrete (RC and PC) are also considered composites with continuous reinforcements mostly made out of steel rebars or prestressing strands, but other reinforcing materials (such as fiber reinforced polymer (FRP) reinforcements) are also used.

Figure 2 illustrates how the combination of a concrete matrix with reinforcement, be it continuous or discontinuous, leads to various structural composites developed since the mid nineteenth century; these include the most broadly used structural materials worldwide, namely reinforced and prestressed concrete.

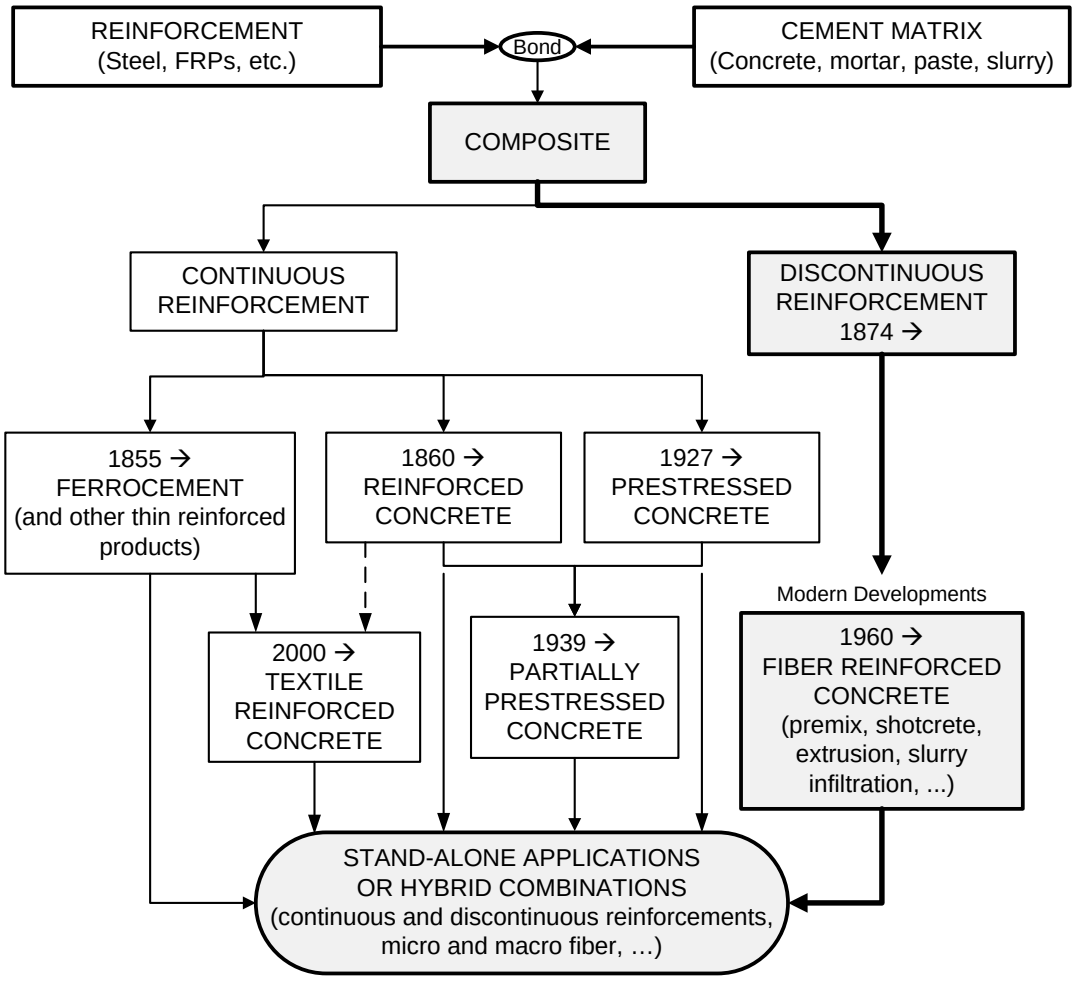

Figure 2 Common cement- and concrete-based composites and possible hybrid combinations.

As described in Section 3.2, modern fiber reinforced concrete started in the early 1960s; here, modern implies the use of a scientific approach to better understand the fundamental properties of the composite. At time of this writing, fiber reinforced concrete has gained a place of its own in the family of structural concrete materials. Figure 2 illustrates its position within that group. It can be observed that fiber reinforced concrete can be used on its own or in combination with reinforced concrete (RC), prestressed concrete (PC), or ferrocement, thus leading to a hybrid composite containing both discontinuous fibers and continuous reinforcements. Hybrid composites also include the use of fibers of different materials and/or different geometric and mechanical properties (not addressed in this paper).

2. FRC COMPOSITES: HISTORICAL BRIEF

The concept of using fibers to improve the behavior of building materials is old and intuitive. Examples include adding straw fibers to sun-dried mud bricks primarily made out of clay (adobe), horse hair to mud clay, and asbestos fibers to ceramic pottery, thus creating a composite with a better performance.

In the case of adobe for instance, as used in Mesopotamia in the Middle East, straw fibers may not have led to an increase in tensile strength. However, their real benefits (as we understand them today) were to limit fragmentation after cracking, keep cracks from opening wider, decrease the rate of degradation with repetitive cycles of temperature and humidity, and improve toughness. Thus, it is no surprise that when Portland cement concrete started evolving as a building material during the 19th century, attempts were made to add fibers to it to improve its behavior.

In 1855, the French patent of *Joseph Louis Lambot* advocated the combination of "iron wires (forming a continuous grid) and cement" leading to a material called in French "fer-ciment", known today as ferrocement [2]. Shortly thereafter reinforced concrete was born. Prestressed concrete followed in the first third of the 20th century (Fig. 2).

However, the use of continuous reinforcement, as in reinforced concrete, requires careful placement and higher technical labor skills, hence higher cost. It also leads to an anisotropic building material with which the average layman is not very comfortable.

The idea of using strong discontinuous fibers as reinforcement for concrete seems to have been both a seduction and a challenge to many practitioner and civil engineers. Adding the reinforcement to the concrete mixer in the form of fibers, simply like adding sand or admixtures, to create a homogeneous, isotropic, strong, tough, durable and moldable structural material is a dream that started toward the end of the 19th century and is still in the making today.

3. DEVELOPMENT OF FIBERS FOR CONCRETE AND FIBER REINFORCED CONCRETE

Two distinct time periods seem to characterize the pace of development of fibers specifically intended for concrete (Fig. 3). The first period, prior to the 1960's, corresponds to a slow pioneering phase with many ideas but almost no applications, while the second period, since the early 1960's corresponds to a phase of more rapid and modern developments paralleled by increasing applications.

The first period (1874-1960) can be considered a dormant period during which many patents were submitted on the subject but were not technically convincing since they claimed an increase in tensile or

bending resistance by addition of fibers, but only deflection softening behavior was observed from limited experimental tests (Fig. 3). The second time period termed modern development started with a scientifically based study by Romualdi et al. [3, 4] in the early 1960's; while it also claimed the increase in tensile strength of the composite by fiber addition, it mainly brought awareness of the increase in fracture resistance of the composite. This became a starting point for an intense number of fundamental analytical and experimental studies on the mechanics and behavior of the composite. This second phase was accompanied by the increasing use of modern scientific methods to better understand the reinforcing mechanisms of the fibers, the role of bond, and the contribution of the two main constituent materials. Eventually not only the significant increase in fracture toughness was discovered as the most important benefit of fiber addition, but also researchers were able to develop composites with tensile and bending strengths way higher than those of the matrix alone; thus in effect satisfying what early patents have claimed but could not achieve due to lack of fundamental research. The right side of Fig. 3 is to be correlated with Fig. 14 below where additional details (SS, SH, DS, DS) are explained.

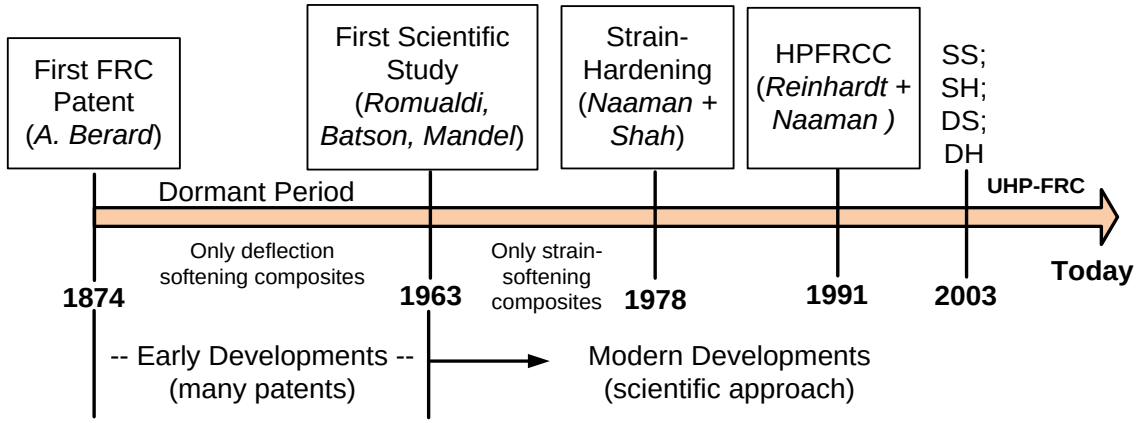

Figure 3 Milestones in the development of fiber reinforced concrete illustrating two distinct time periods.

Numerous patents on fiber reinforced concrete have been granted. They generally address one or a combination of the following: the fiber itself, the fiber reinforced concrete mix, the production process, and the application. A selective number [5 to 12] is reviewed in [1] and summarized next to illustrate the underlying idea behind each patent and the evolution of new ideas with time.

3.1 Pioneering Developments: 1874 – 1960

The first patent (1874) on fiber reinforced concrete seems to be due to *A. Berard* from California who suggested the use of granular waste iron in a concrete mix to create an artificial stone. A similar idea suggesting the use of steel shavings and metal scraps was patented by *J.C. Seailles* in France, in 1920. In 1911, *G.M. Graham* (US) suggested the use of steel fibers (short cut steel wires) in addition to conventional reinforcement to increase the strength and stability of reinforced concrete.

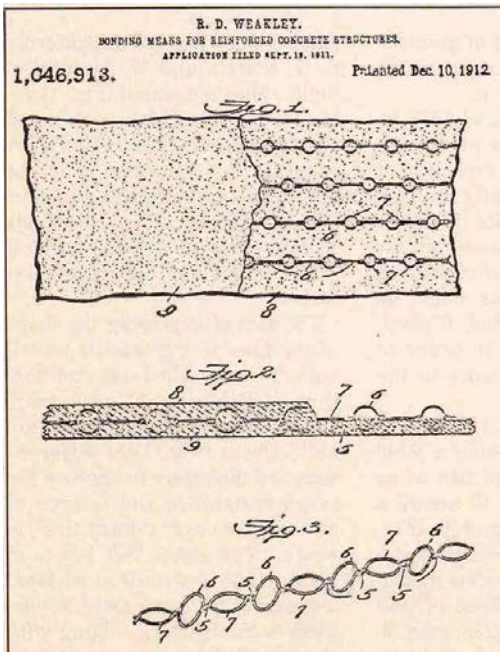

Figure 4 *Weakley*'s two-dimensional steel fiber made out of two wires (US Patent 1912).

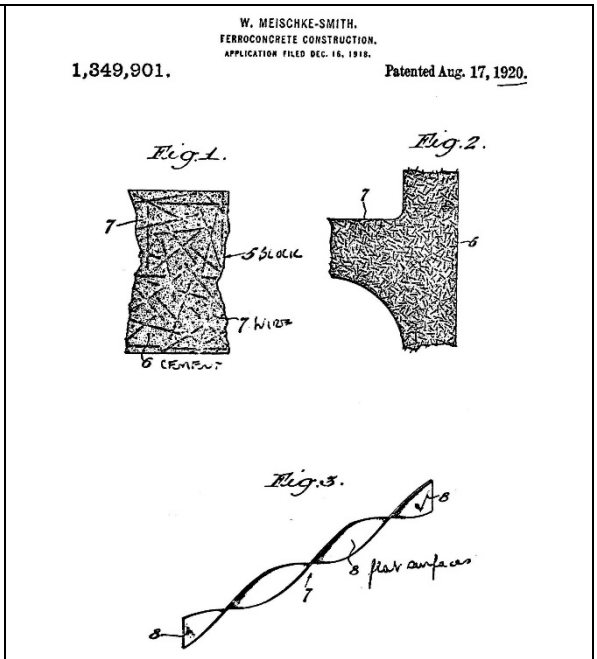

Figure 5 *Meischke-Smith* flat twisted steel fiber (US Patent 1920).

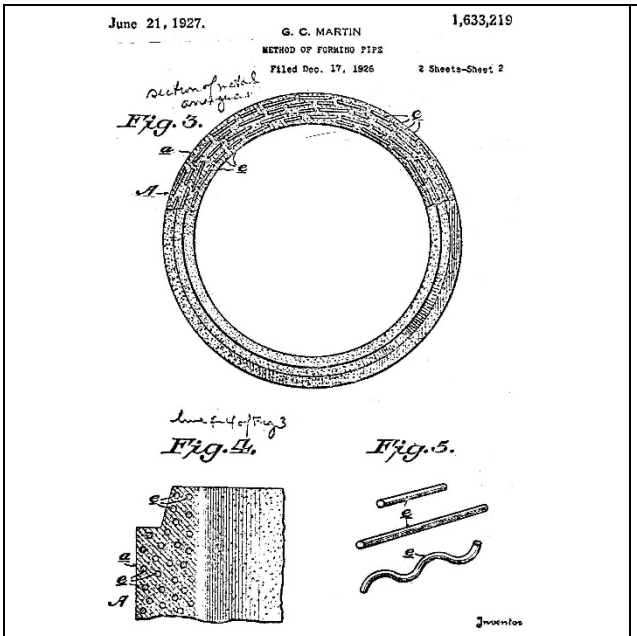

Figure 6 Martin's straight and crimped steel wire fiber (US Patent 1927).

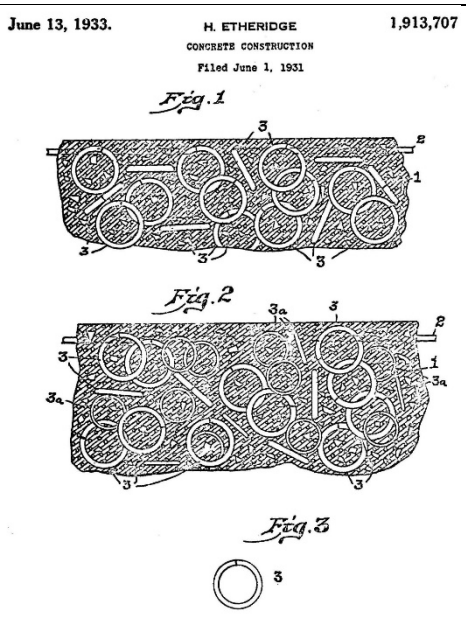

Figure 7 Etheridge's annuli fibers intended to stitch the cracks in concrete (US Patent 1933).

A French patent dated 1918 by *H. Alfsen* describes a process to improve the tensile strength of concrete by uniformly mixing small longitudinal bodies (fibers) of iron, wood or other materials. It also suggests

that the surface of these fiber elements must be rough or roughened and, if possible, their ends bent in order to provide better adherence to the concrete.

R. Weakly (Missouri) obtained a patent in 1912 for using steel fibers made out of two wires and containing loops to secure a durable bond with concrete (Fig. 4). *Weakly*'s fibers were two-dimensional; a tridimensional steel fiber is described farther below.

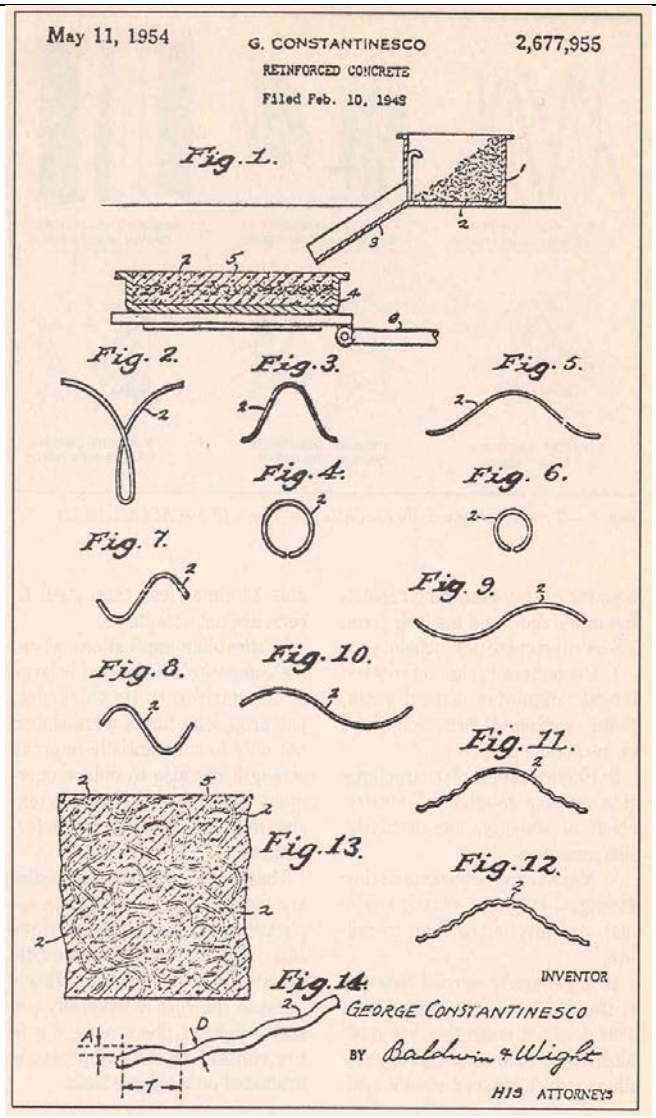

Figure 8 Constantinesco's patent (1943, 1954) for steel fibers: straight, crimped, coiled, helical shape.

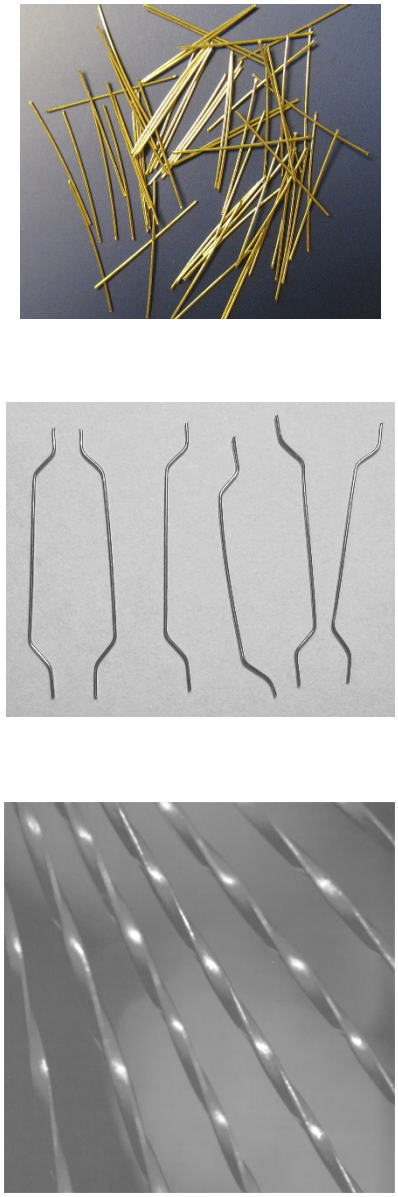

Figure 9 Modern fibers made out of steel wires: (from top) straight, hooked and twisted.

In 1920, *A. Kleinlogel* from Germany filed a patent for mixing a relatively large volume of iron particles (up to 50% of 2 mm long steel fibers) with concrete in order to produce a moldable mass capable of being chilled, turned, sawed, and filed similarly to an iron mass.

Two relevant patents were granted in California in the 1920's. *Meischke-Smith*'s patent (Fig. 5) describes the use of flat twisted pieces of wires as fiber reinforcement for concrete mixtures. *Martin*'s patent (Fig. 6) describes the use of plain or crimped pieces of steel wires mixed with concrete to strengthen concrete pipes.

The idea of improving the shape of the fiber to increase its contribution was pushed one step further by *H. Etheridge* (New Jersey, 1933) who proposed adding "annuli" fibers (Fig. 7) of different sizes and diameters to improve the crack resistance and fatigue of concrete for use in railway ties. He wrote: "*The object that I have in view is the prevention of local cracks and fractures and I accomplish such object by mixing with the plastic concrete a mass of metal annuli in sufficient quantity to effect coupling of what I may term the 'stitching' together of the adjacent masses of concrete...*".

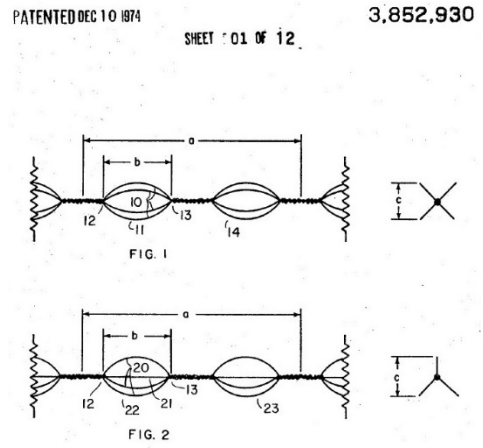

(US Patent 1974; see also Fig. 14.14).

Figure 10 Naaman's tridimentional steel fiber designed to enhance toughness and energy absorption capacity of concrete.

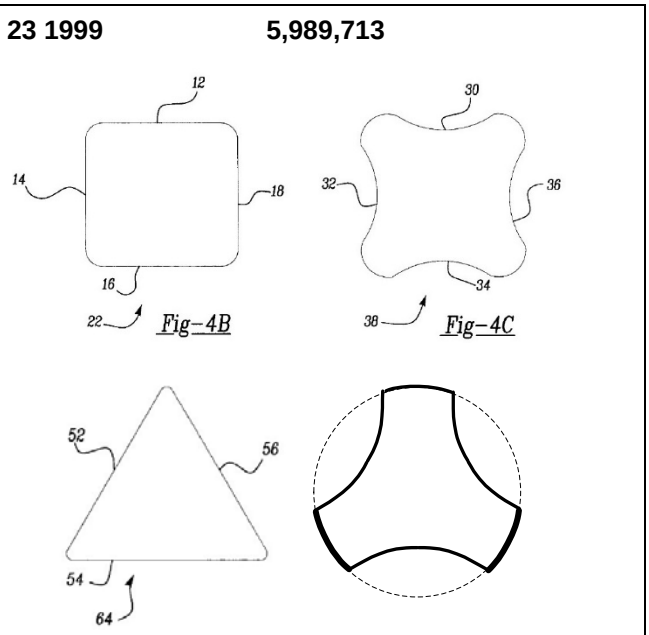

Figure 11 Naaman's twisted polygonal fibers with optimized geometry (US Patent 1999, 2000).

Numerous patents were granted in different countries in the following years. That of *G. Constantinesco* (England 1943, United States 1954) deserves a special mention since the fiber reinforcing parameters he recommended are quite similar to those of steel fiber reinforced concrete of today. The patent (Fig. 8) describes the use of coiled or helical type steel fibers in order to increase the crack resistance and energy absorption of concrete masses. Suggested applications included army tanks, air raid shelters, machinery foundations, and the like. For comparison, Figure 9 illustrates examples of modern steel fibers marketed since the 1960's.

A tridimensional steel fiber made with four wires forming a frame like two successive footballs was patented by *A.E. Naaman* [11] in 1974 (Fig. 10). It was shown experimentally to provide higher composite strength through an efficient anchorage, and higher toughness through extensive fiber elongation and matrix crushing inside the balls. However, it is not commercially available. The patent stated that the fibers could be premixed or placed in a mold and penetrated by the matrix. Later, *Lankard* [13, 14] developed the SIFCON process whereas straight steel fibers were placed in a mold and infiltrated by a cement-based slurry.

Another patent by *A.E. Naaman* [12] was granted in 1999 for straight steel fibers with optimized geometries (Fig. 11); the fiber cross-section is primarily square or triangular (offering a lateral surface for bond higher than that of a circular fiber of same cross-section) and by nature of its shape can be twisted along its length offering a higher mechanical bond than a smooth fiber.

3.2 Modern Developments: 1960 to Date

The modern developments of fiber reinforced concrete started in the early 1960's following the research work of *J.P. Romualdi, J.A. Mandel and G.P. Batson* in the US [3, 4], and *H. Krenchel,* in Denmark [15]. The US researchers hypothesized that the cracking tensile strength of concrete can be significantly increased by adding fibers, and that, in correlation with *Griffith*'s theory of fracture, the strength can be inversely proportional to the square root of the fiber spacing (for details, see [1]). They assumed that fibers play a critical role in arresting cracks and that fiber spacing is thus equal to the maximum crack size. This hypothesis generated considerable attention (and controversy) among researchers and practitioners because it offered a solution for increasing the tensile strength of concrete; indeed, the relatively weak tensile strength of concrete is considered its main drawback and is generally neglected in design. While several studies by different researchers including *S.P. Shah* [16], *A.E. Naaman* [17 to 19], *and N. Swamy* [20, 21] reported experimental observations significantly less optimistic than predicted by *Romualdi's* hypothesis, the spark has been lighted and the impetus to arrive at realistic models continued.

Since the 1960's, a multitude of fibers and fiber materials were introduced and are being continuously introduced in the market as new discoveries and new applications are identified. Many patents have been filed worldwide and can be best accessed through web searches and the US Patent and Trademark Office. The introduction of new fibers or fiber material is invariably preceded and accompanied by research studies providing experimental support and a better understanding of the mechanics of fiber reinforcement (mechanics of composite materials, fracture mechanics, damage mechanics). In turn, such studies point toward a better understanding and identification of desirable fiber and matrix characteristics for any particular application.

At the time of this writing, tens of thousands of technical papers, hundreds of symposia proceedings, numerous guidelines, reports, thesis, standards and books have been written to address fiber reinforced cements and concrete composites, and of course innumerable applications using these composites have been implemented. Several technical societies (ACI, ASTM, JCI, PCI, RILEM, ASCE, etc…) have committees addressing fiber reinforced concrete and have published many related documents on the subject. Several technical journals frequently publish technical papers on FRC composites.

No reference list, no matter how extensive, can be complete and give sufficient credit to all those individuals and organizations responsible for advancing the knowledge base on fiber reinforced concrete. In **[1]** the author lists in order: 1) books on fiber reinforced concrete known to the author at time of this writing; 2) special symposia proceedings series dealing with fiber reinforced concrete; 3) the address of

some web sites where technical information can be obtained; 4) some US Patents on fiber reinforced concrete; and 5) a large number of technical references which served as sources for figures and cited results.

4. WHY THE INITIAL LACK OF SUCCESS FOR ALMOST ONE CENTURY

It is important to understand why the pioneers, as described in Section 3.1, did not succeed in getting fiber reinforced concrete adopted enthusiastically by the profession early on. Most of the patents on fibers for concrete developed prior to the 1960's have claimed that the fibers play a role similar to reinforcing bars in reinforced concrete thus providing a reinforcing effect, namely by increasing the tensile strength of concrete (mixing-in the reinforcement).

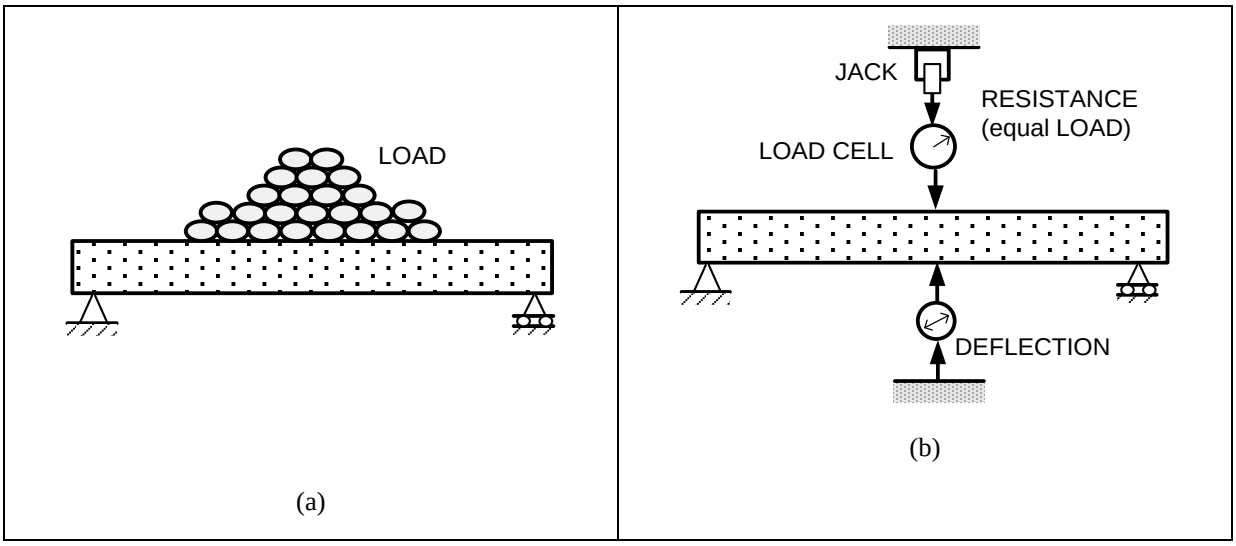

Figure 12 Bending test: (a) Load-type test. (b) Deflection- or deformation-type test.

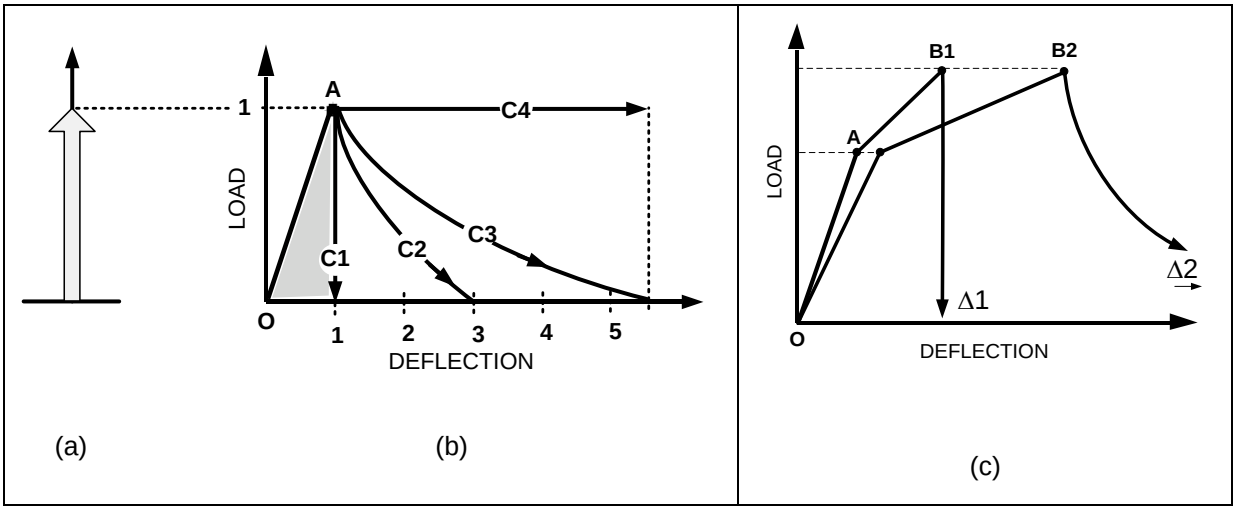

Figure 13 Schematic load-deflection curves illustrating: (a) Load controlled test. (b) Deflection controlled test with deflection-softening from elastic-brittle to elastic-plastic response. (c) Deflection controlled test with deflection-hardening response.

The proof was to carry out a typical bending test of a simply supported concrete beam and observe if the presence of fibers increased its bending resistance. Loading was carried out by piling up sand bags on top of the beam until failure (Fig. 12a). Such a test, called a load-controlled test, does not capture the resistance of the beam after its maximum load is attained. It is likely that fibers used at the time were not efficient and did not increase the tensile resistance of concrete (after cracking); however, their key hidden benefit (improved toughness) could not be identified by this type of test. The fiber reinforcing parameters and the mechanics of the composite were little understood at the time, and deformation-controlled testing was not available; in such testing, a slowly increasing deflection is applied to the beam and the resistance to the deflection is measured, thus, even after maximum load, the beam resistance, if any, up to very large deflections could be recorded (Fig. 12b). And this is exactly where the most important benefit of the fibers lies. The post peak response is indicative of toughness, energy absorption capacity, and ductility.

Figure 13a illustrates a "load" type test where only the load, up to its maximum value is recorded; while Fig. 13b illustrates a "deformation" or deflection type test. In the deflection type test, an incremental mid-span deflection is imposed while recording the resistance of the beam to that deflection through a load cell (Fig. 12b); the load (or beam resistance here) for each imposed deflection can thus be recorded throughout, even after the maximum or peak load, up to complete failure.

Consider Fig. 13b where four load-deflection curves are plotted for four different materials; these could be, for instance, concretes with different volume fractions of same fibers or concretes with different fibers. Assume all beams have the same initial response up to the maximum load at point A.

If one uses a load type test (Fig. 13a), the four beams would be considered to fail at A and their possible resistance after A is not recorded (Fig. 12a). One can conclude that the four materials are equivalent. Such was the conclusion in numerous early attempts to demonstrate the potential benefits of fiber reinforcement, leading to little interest from the users. However, a deformation type test would uncover the entire curves of Fig. 13b including the descending branch after point A. The area under each curve is a measure of toughness or energy absorption capacity. While the load type test with same maximum load A cannot differentiate between the four beams, the deflection type test clearly suggests that material C4 is better that C3 which is better than C2 which is better than C1. Figure 13c illustrates another example where deflection hardening is observed; here also, while the load-type test would suggest that B1 is equivalent to B2, the deflection-type test provides more information which can be important in design, such as B2 has a higher energy absorption capacity (area under the load-deflection curve) and higher deflection to failure (i.e. $\Delta 2 > \Delta 1$) but its material has a smaller elastic modulus.

4.1 Summary and Key Observation

During the first period of development of fiber reinforced concrete (Fig. 3), that is until about 1960, the civil engineering profession did not yet fully understand the importance of energy absorption or toughness as compared to strength. Thus two test beams leading to the same bending resistance, but with one exhibiting a toughness ten times larger than the other, would be considered equal (Fig. 13b). A more in-depth scientific and engineering knowledge was needed to better understand the role of the fiber, the matrix, the bond, the production process, and what type of testing and measurements may identify different properties. This has become the norm starting in the 1960's.

We can simply conclude that while the first patents on fibers for concrete contained excellent ideas at the time they were submitted, some not too different from today's fibers, scientific knowledge was insufficient to identify the most important benefit of fiber reinforcement, that is, an increase in toughness

translated into increases in energy absorption capacity, ductility and impact resistance. At the time and with the parameters tested, increases in tensile strength were not possible. The lack of initial success in experimental and field tests, and the added cost of fibers, did not encourage usage.

We know today that the paramount advantage of fiber reinforcement in concrete is the substantial increase in the toughness or energy absorption capacity of the composite. However, continuous efforts are being devoted and continuous progress is being achieved to increase the composite's tensile strength through improved fibers, fiber efficiency, fiber content, additives, and the like.

Another important benefit of fibers, being increasingly recognized today, is the improved performance of conventional reinforced and prestressed concrete structures using matrices with fibers. Benefits include increases in bond strength of reinforcing bars and prestressing strands, increases in resistance to shear, increases in resistance to seismic excitation under cyclic loading, reduced spalling, improvement in structural ductility and impact resistance, and an overall increase in damage tolerance and resilience of the structure [1].

5. EVOLUTION SUMMARY OF PARAMOUNT MECHANICAL RESPONSE

During the modern period of development (Fig. 3), and after about fifty years of research and progress, what was achieved is a simple classification of FRC composites that allows us to immediately anticipate what type of application can be used. That is, to distinguish an FRC composite strictly based on its tensile or bending behavior without prior knowledge of the hundreds of parameters (fiber, matrix, bond, etc.) which can affect such behavior.

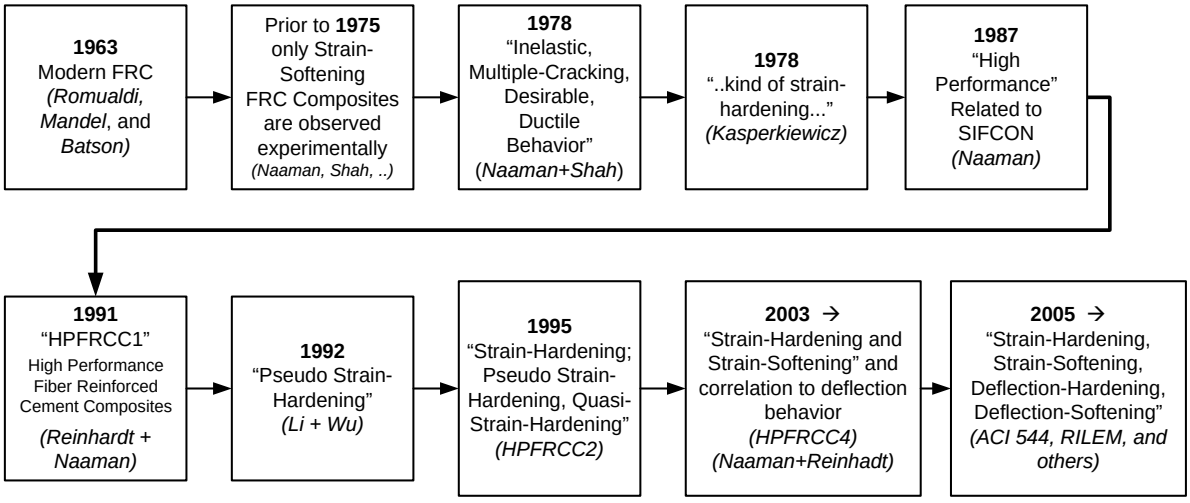

Figure 14 Evolution of terminology to describe strain-hardening behavior in tension, since modern theory of fiber reinforced concrete.

Without going into innumerable details, Fig. 14 summarizes the evolution of terminology and related progress over about four decades, of fiber reinforced cement composites in relation to their fundamental

behavior in tension, that is, either strain softening or strain hardening [1, 22]. The current terminology while very simple encompasses all possible behaviors. It allows a unifying platform and suggests a better discipline for reporting future research and developments. Some clarifications are given next.

5.1 General Classification: Strain-Softening and Strain-Hardening FRC Composites

Assuming a failure mode where pull-out (full or partial) prevails, practically all fiber reinforced cement composites currently available are covered by a simple and general classification according to their tensile behavior, as illustrated in Fig. 15, namely, either "strain-softening" or "strain-hardening" [1, 23 to 27]; of course the limit case of "elastic perfectly plastic" (curve 4 of Fig. 13b) is theoretically possible but should be mostly viewed as a conceptual boundary.

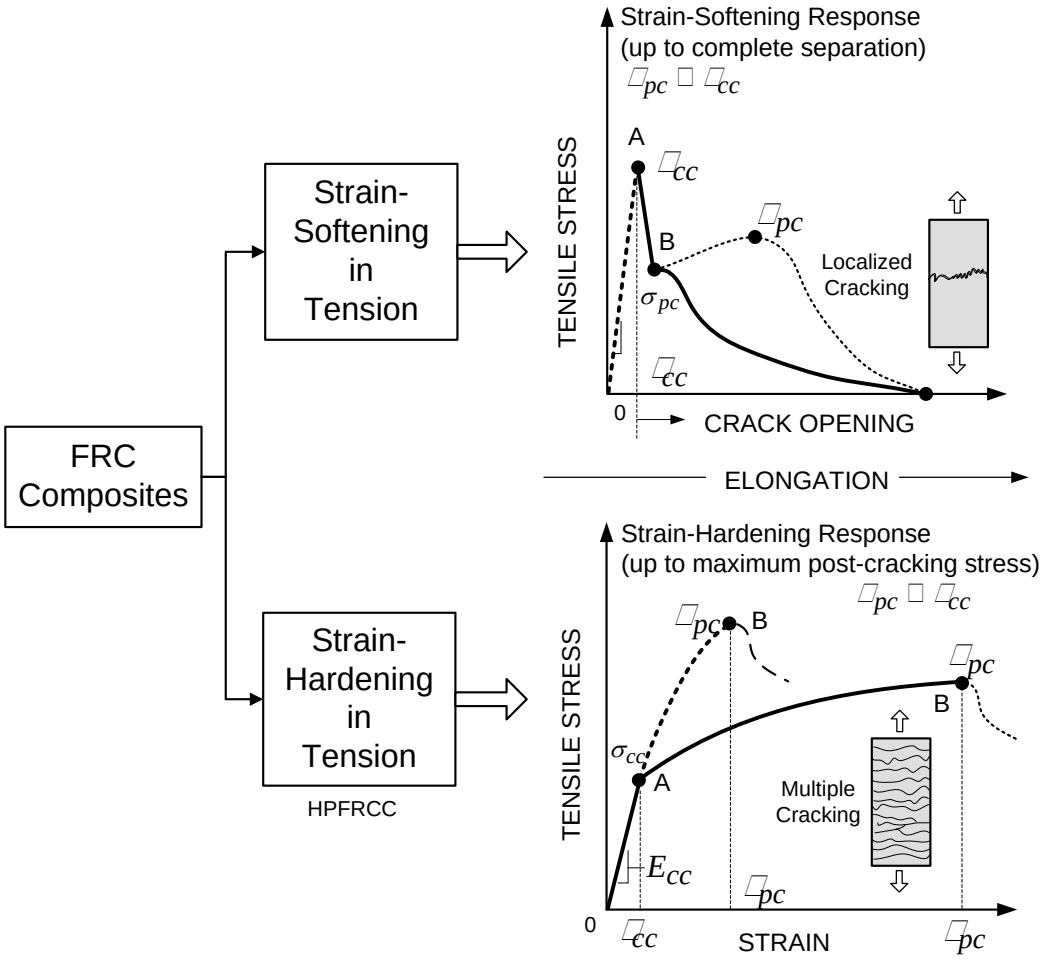

Figure 15 Simple classification of all FRC composites based on their tensile response.

Figure 15 shows for each case (strain-softening or strain hardening) a couple of representative curves. The inset in each figure shows one crack for the strain-softening case and multiple cracks for the strain-hardening case. The units of the *x* axis are also different. For a plain cement matrix, it is assumed that the

stress-strain response is linear elastic brittle such as curve C1 in Fig. 13b, although special closed-loop testing could identify some strain-softening behavior (after point A) especially when aggregates are used. However, here the matrix will be assumed simply elastic brittle. Figure 16 compares a tensile strain-softening versus a strain-hardening curve using the same vertical axis that separates strain from crack opening after localization of the failure crack.

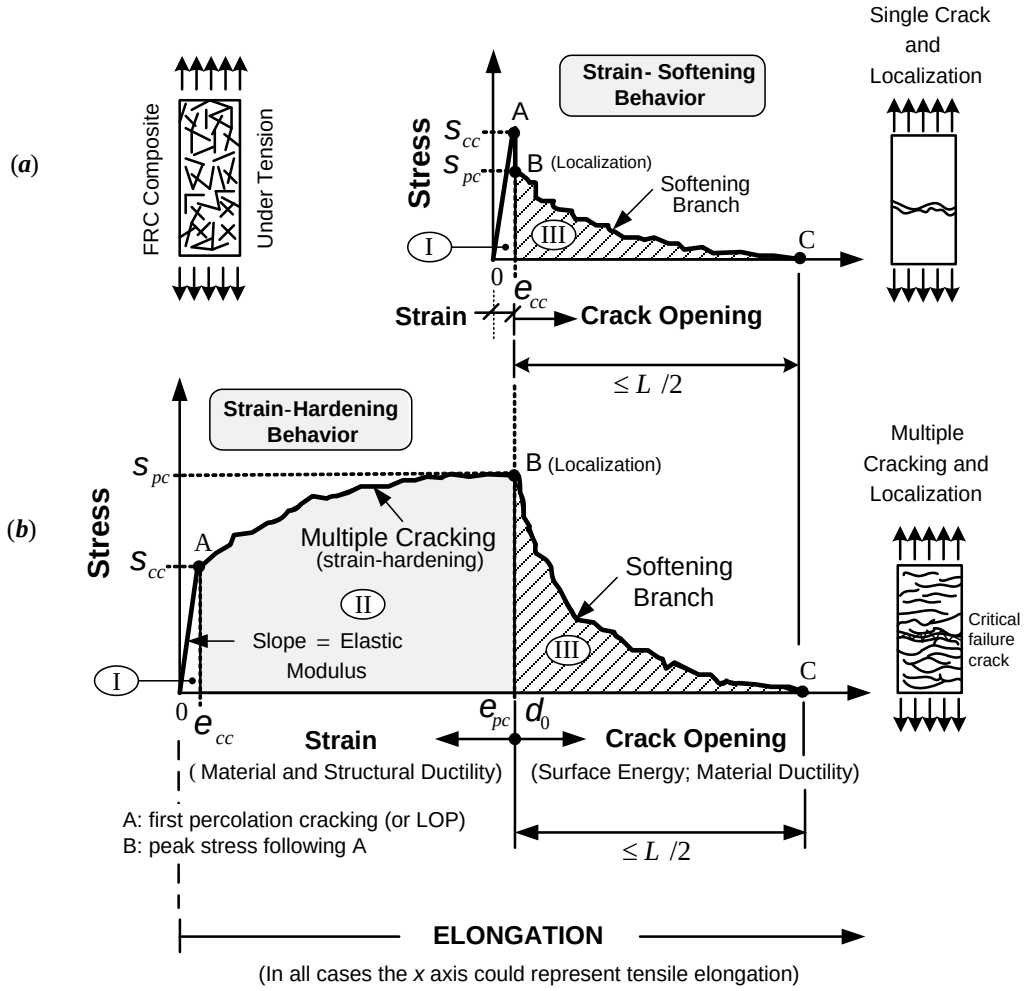

Figure 16 Typical stress-strain or stress-elongation curve in tension up to complete separation. *(a)* Conventional strain-softening FRC composite. *(b)* Strain-hardening FRC composite (also often termed HPFRC composite).

Typically the stress-strain (or stress-elongation) curve of a strain-softening FRC composite (Fig. 16*a*) starts with a steep initial ascending portion up to first percolation cracking (part I), which also corresponds to the maximum stress point as characterized by its stress and strain coordinates $(\sigma_{cc}, \varepsilon_{cc})$. Here the crack becomes immediately critical (failure crack) defining the onset of crack localization. The resistance drops thereafter. No more cracks can develop, and only the critical crack will open under increased deformation. There is generally a descending branch which corresponds mainly to the load versus opening of the critical crack (part III of Fig. 16*a*). The stress is always smaller than the stress at first percolation cracking (here the peak stress). Along that branch fibers can pull-out, fail, or a combination of these phenomena may occur

. Also, the cement matrix may contribute some resistance along that part of the curve up to a certain crack opening, but its contribution is generally assumed negligible.

In a strain-softening composite after first cracking (part III of Fig. 16a), the maximum post-cracking stress resistance of the composite, σ_{pc}, is lower than that recorded at first cracking, σ_{cc}. The elongation corresponding to σ_{pc} can be either about equal to that at σ_{cc} or substantially larger depending on the fiber reinforcing parameters such as bond strength, elastic modulus of the fiber, and the fiber content. Because only one crack develops, the elongation of the composite is mainly dictated by the opening of that crack. This elongation cannot be translated into strain for the entire prism, but only describes the opening or width of that crack.

Typically the stress-strain curve of a strain-hardening FRC composite (Fig. 15 and 16*b*) starts the same way as for a strain-softening composite (part I); however, unlike for the strain-softening case, it is immediately followed by a strain-hardening branch where multiple cracking develops and significant energy is absorbed (part II). Here the fibers bridging the first percolation crack resist the tensile load sufficiently, allowing multiple cracks to develop in the matrix at stresses equal or higher than the cracking strength of the composite. This process continues until multiple-cracking stabilizes (at a certain level of average crack spacing and width); with a further increase in elongation (or strain), one crack becomes critical (localization at maximum post-cracking strength, ($\sigma_{pc}, \varepsilon_{pc}$)), and the fibers bridging that crack start pulling out, or fail, or a combination of both leading to a decrease in composite resistance (Part III of Fib. 16b). After σ_{pc} the resistance drops continually and the width of the failure crack increases significantly while the widths of the other cracks decrease. The descending branch is similar in nature to that of a strain-softening composite (part III of Fig. 16*a*). The elongation of the composite up to critical crack localization (at σ_{pc}) can be translated into strain, while thereafter it translates into crack opening, crack width, or member elongation.

Whether strain-softening or a strain-hardening behavior occurs, the elongation of the composite before crack localization can be translated into tensile strain. However, after localization, the elongation is controlled by the opening of the critical crack. Note that the critical failure crack may not look like a single crack but could be a smeared crack with several branches and micro-cracks surrounding its main path.

In summary, for strain-hardening composites, $\sigma_{pc} \geq \sigma_{cc}$, while for strain-softening composites $\sigma_{pc} < \sigma_{cc}$ (Figs. 15 and 16). The analytical condition to achieve strain-hardening is covered in detail in [1, 24].

5.5.1 Important Summary: *As observed from the above discussion, the addition of fibers to concrete fundamentally changes the nature of its tensile response. In particular, whether the response is described as strain-softening or strain-hardening, the stress-elongation curves contain elements (Part II and Part III) that, for all practical purposes, either do not exist (Part II), or are considered negligible (Part III) in conventional concretes without fibers. Moreover, in comparing with plain concrete, there is a paramount element that now emerges as a material characteristic, that is some level of ductility or toughness or energy absorption capacity in contrast to extreme brittleness. Note finally that changes in tensile response significantly influence changes in other properties at the material and structural level (Section 2.10).*

5.2 Correlation Between Bending and Tensile Response

Figure **17a** describes schematically the bending response of all FRC composites. Numerous possible load-deflection curves are shown. The terminology "deflection-softening" and "deflection-hardening" describing the behavior under bending correlates with the description of the tensile response as shown in Figs. 15 and 16. The general relationship that ties tensile and bending behavior together is illustrated in Fig. 17b. Note that while the tensile response represents a fundamental property of the composite, the bending response (while not fundamental in nature) is related to the most common applications of fiber reinforced cement and concrete composites. Such a description can provide the basis for a performance specification for the composite and related structural applications. Details on the mechanical conditions leading to either state can be found in [1, 25]. Practically all fiber reinforced cement composites currently available are covered by the simple classification of Fig. 17.b (an extension of Fig. 15) [1, 22 to 27].

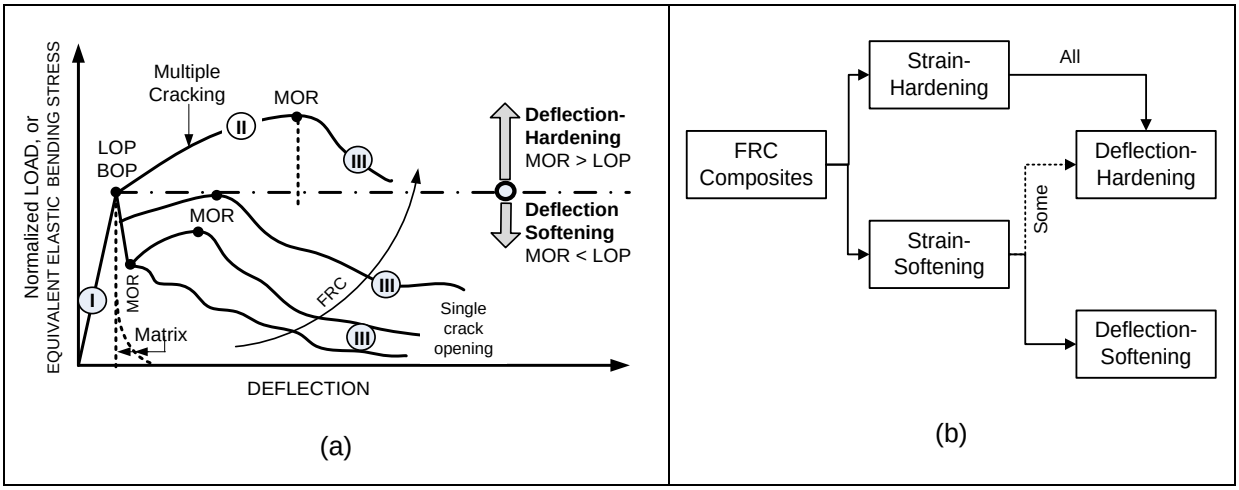

Figure 17 (a) Schematic bending response of all FRC composites [1]. (b) Classification of all FRC composites based on their tensile response and implication for bending response of structural elements [*Naaman* and *Reinhardt* [25, 26].

The terminology used in Fig. 17 clearly reflects the very similar qualitative behavior of FRC composites in tension and bending. The shapes of the stress deformation curves and the wording to describe them are very similar. Analytical modeling of bending response from the tensile response also suggests that all strain-hardening FRC composites in tension should lead to deflection-hardening behavior in bending, while strain-softening FRC composites in tension will lead to either deflection-hardening or deflection-softening behavior depending on the fiber reinforcing parameters. The mechanical condition for a tension strain-softening material to lead to a deflection-hardening behavior is expanded upon in [1]. In short, the bending resistance (MOR) after first cracking (LOP) can be shown to be in the range of 2.5 to 3 times the post-cracking strength in tension, σ_{pc} (Fig. 16); equivalently for deflection hardening to start occurring, σ_{pc} needs only to be in the range of $0.33\sigma_{cc}$ to $0.4\sigma_{cc}$. As a first approximation, one can thus estimate MOR from a tensile test, or vice-versa, σ_{pc} from a bending test using the following relation:

$$2.5\sigma_{pc} \leq MOR \leq 3\sigma_{pc} \quad (1)$$

Deflection-hardening behavior is useful in structural applications where bending prevails, while deflection-softening composites cover a wide range of practical applications starting at the lower end by the control of plastic shrinkage cracking of concrete, to the higher end where they are used in concrete pavements and slabs on grade. Note that, as with other materials, scale and size effects can be significant, and therefore, the response of very small specimens may not be indicative of the response of real scale structural elements in either tension or bending.

6. FIBER-MATRIX REINFORCING EFFECTIVENESS: BASIC APPROACH

In order to better understand the use of fibers in cement based matrices, it is important to keep in mind the key mechanical properties needed from the fibers. Some of the recommendations summarized next will become more easily understood once models to predict the tensile properties of the composite are explained [1].

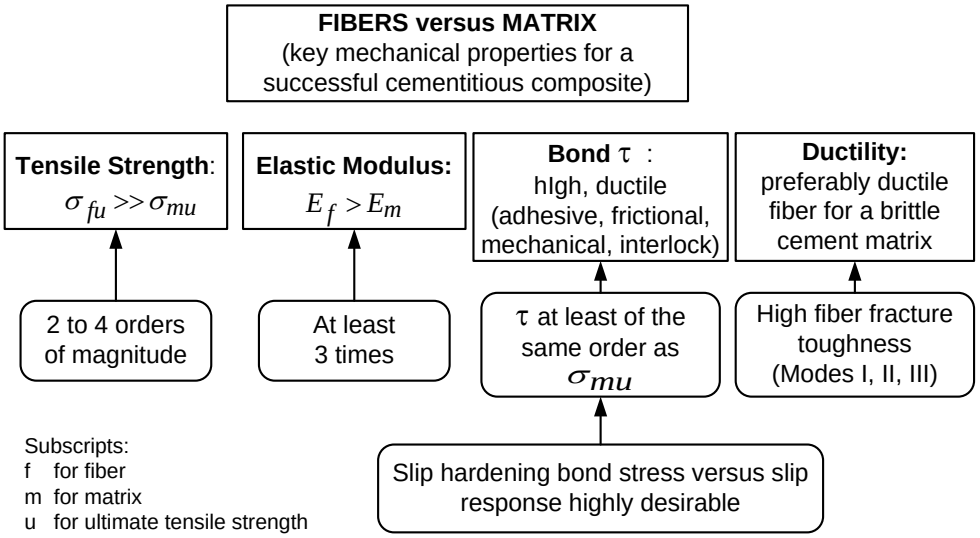

Figure 18 Desirable fiber versus matrix properties for successful cementitious composites.

By its very definition a reinforcement (i.e., the fiber) is supposed to induce an increase in strength in the material to be reinforced (i.e., the matrix). Both analysis and experimental test results suggest that, in order to be effective in concrete matrices, fibers must preferably have the following qualitative properties (Fig. 18): 1) a tensile strength significantly higher than that of concrete (two to three orders of magnitude); 2) a bond strength with the concrete matrix preferably of the same order as or higher than the tensile strength of the matrix; and 3) unless self-stressing is used through fiber reinforcement, an elastic modulus in tension significantly higher than that of the concrete matrix. Moreover, everything else being equal, a ductile fiber under tension is preferable to a brittle fiber, and a ductile or slip-hardening bond-stress versus slip response is preferable to a brittle or slip-softening one. The *Poisson'*s ratio and the coefficient of thermal expansion should preferably be of the same order for both the fiber and the matrix. Indeed if the *Poisson*'s ratio of the fiber is significantly larger than that of the matrix, detrimental debonding will occur under tensile load.

However, these drawbacks can be overcome by various methods such as inducing surface deformation to create mechanical anchorage.

Figure 18 assumes that the fiber and matrix are chemically compatible (compatibility issues need to be evaluated for each fiber material); steel fibers are likely to corrode due to environmental exposure should they be crossed by a crack in concrete; and glass fibers, unless properly treated, will react with the alkali of the cement matrix. Similar evaluation should be carried out if the FRC structure is to be operating under high temperatures in service.

Given that a normal weight concrete matrix has an elastic modulus in the range of 15 to 50 GPa depending on its compressive strength and numerous other parameters, synthetic fiber materials intended to act as reinforcement for concrete should have not only a high tensile strength but also a relatively high tensile elastic modulus. Thus high end synthetic fibers are more suitable for use in normal weight cement and concrete matrices. Low end fibers, with relatively low elastic modulus, are likely to be more effective in lightweight and very lightweight cement matrices which themselves are characterized by very low values of elastic modulus. Although many synthetic fibers have been used in numerous small scale applications, their large scale adoption (except for the case of plastic shrinkage cracking control) did not materialize so far. Mixing and dispersion difficulties, fire rating resistance, observed performance, and cost are the commonly cited drawbacks.

7. SIMPLE FRC MECHANICS FOR INITIAL DESIGN

In plain concrete a correlation exists between compressive strength (f'_c) and tensile, bending, and shear strength, {such as $3\sqrt{f'_c}$, $7.5\sqrt{f'_c}$, and $2\sqrt{f'_c}$ in psi units}, respectively; even the elastic modulus can be related to the compressive strength, f'_c .

The most evident observation to the addition of fiber to concrete subjected to tensile loading is the appearance of some ductility or post-cracking resistance after initial cracking.

It is shown in [1] that the tensile, compression, bending and shear response of an FRC composite are strongly correlated; in effect the tensile response sets the tone for the rest A key equation which predicts the post-cracking tensile strength of an FRC composite is reproduced in Fig. 19.

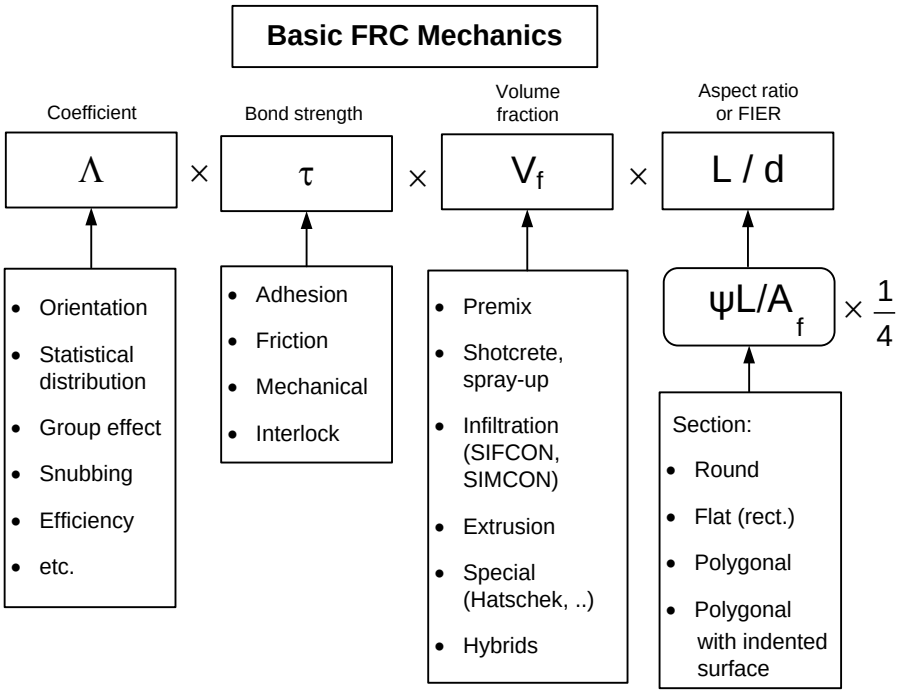

Figure 19 Simple relationship to consider when optimizing the performance of FRC in tension, bending, shear and compression.

The parameters of Fig. 19 allow for the pre-selection of a suitable fiber for a given concrete matrix, with the objective to improve the chances of success of the composite. These parameters are paramount in controlling the mechanical properties of the composite. They are the fiber aspect ratio, L/d, that is, the length of the fiber over its diameter or equivalent diameter; the fiber volume fraction, V_f, that is, the volume of fiber per unit volume of composite; the bond at the fiber matrix interface, τ; and their product. The aspect ratio is particularly useful for fibers of circular cross-section or substantially circular ones for which an equivalent diameter can be derived by setting the area of the actual fiber equal to that of an equivalent circular fiber. If the fiber is of significantly different shape, its lateral surface area is critical since it represents the bonded area between fiber and matrix; a shown in Fig. 19 the aspect ratio is then replaced by the quantity $0.25\times\psi L/A_f$, where ψ is the perimeter and A_f is the cross-sectional area of the fiber. The bond is a very complex property covered in more details in Chapter 13 of Ref. [1], and encompasses the effects of adhesion, friction, mechanical anchorage and fiber to fiber interlock. The product of the three parameters, $\tau\times V_f\times L/d$, is present in predicting the post-cracking tensile strength of the composite, its bending resistance, and its surface energy; and since both shear and compression response strongly correlate with tensile response, it can be easily said that most mechanical properties are likely to improve with an increase in the product $\tau\times V_f\times L/d$. In Fig. 19, Λ is a coefficient which is the product of several other coefficients detailed in [1].

Some other parameters also influence the key mechanical properties and relate to the number of fibers per unit volume of composite, the number of fibers crossing a unit area, and the specific surface of fiber reinforcement, but are related to the parameters of Fig. 19.

Since fibers are assumed to be randomly oriented and distributed, their contribution to the composite is also significantly influenced by the statistical nature of the variables involved and the size of the specimen. While all prediction equations are derived assuming deterministic models, real life situations involve random variables, and thus the designer must expect and account for the increased variability inherent in these systems.

8. FRC VERSUS OTHER FIBER REINFORCED COMPOSITES: FUNDAMENTAL DIFFERENCE

Fiber reinforced composites occupy a very important role in the field of engineering materials encompassing all areas of applications such as civil, mechanical, manufacturing, naval, aeronautics and aerospace engineering. Most widely used fiber reinforced composites are identified according to the matrix they use: polymer or plastic composites, metal composites, ceramic composites, and cementitious composites. Figure 2 illustrates how fiber reinforced concrete fits within the general family of reinforced cement-based composites. Figure 20 offers a visual flow chart of how FRC composites fit within the general family of fiber reinforced composites. It is observed that all fiber reinforced composites can be grouped according to their matrix's ductility, namely: 1) brittle matrix composites, or 2) ductile matrix composites. This last category is addressed broadly in the technical literature and its treatment can serve as an excellent background to, and extension for the treatment of brittle matrix composites.

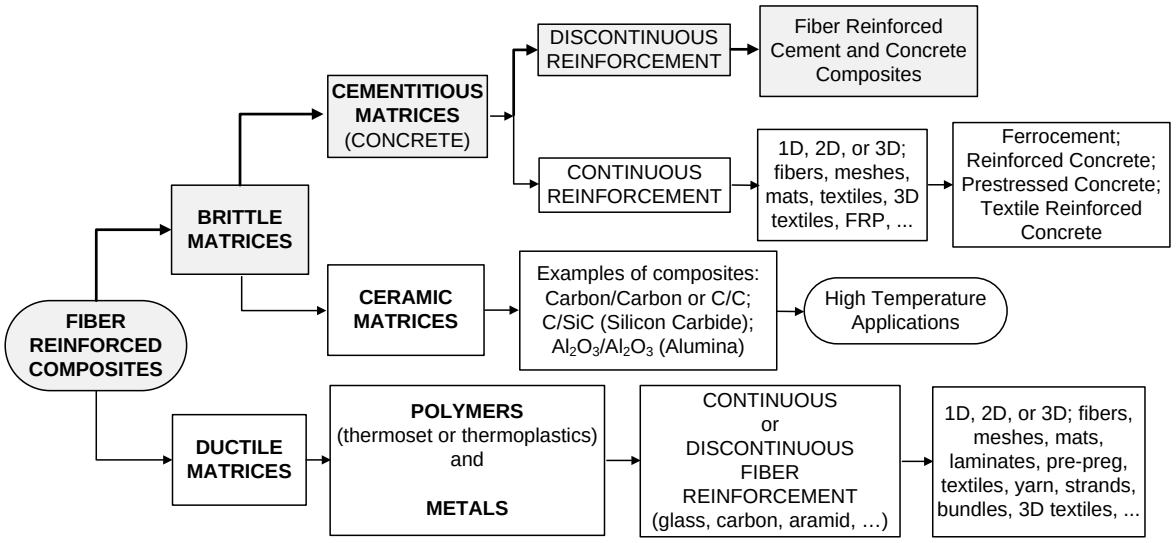

Figure 20 The two major classes of fiber reinforced composites for modeling purposes based on their matrices: brittle or ductile.

Fiber reinforced polymer and metallic composites typically use matrices with a tensile strain at failure much larger than that of the fiber and a tensile strength significantly smaller than that of the fiber. Examples of matrices include epoxy resins, bismaleimides (BMI), and polyesters; they are generally identified as either thermo-set or thermo-plastic polymers. Fibers used in industrial and aerospace applications are primarily made of manufactured fibers embedded in various polymeric matrices of epoxy, vinyl-ester and the like. The fibers are generally characterized by high tensile strength and a relatively high stiffness such as glass, carbon, aramid (Kevlar), or ultra-high molecular weight polyethylene (Spectra).

Hence, failure of the composite implies either failure of the fibers, or their complete debonding while the matrix may be in a yielding state.

Metallic matrix composites include aluminum, magnesium and titanium matrices with carbon, silicon-carbide, boron, and alumina whiskers. They are considered ductile matrix composites. Ceramic composites which are particularly designed for high temperature applications are considered to belong to brittle matrix composites; they often use the same basic material for fiber and matrix but in different forms, such as carbon and graphene or graphite whiskers.

9. CONCLUDING REMARK

Two time periods mark the history of fiber reinforced concrete. The pioneering period started in 1874 and claimed strengthening of concrete (in tension or bending) by addition of fibers; but that claim could not be confirmed by test results. Thus the first period saw little progress for almost a century and can be described as technically dormant. The modern period started in the 1960's whereas initial attention focused on the claim that fibers increase the fracture energy of the composite. This drew enormous interest from the technical profession. Fundamental studies and research led to a better understanding of the effect of fibers on energy absorption capacity and all other properties, eventually leading to the development of FRC composites with tensile and bending resistance higher than those of the matrix. It also led to a simple classification of all FRC composites based on their tensile response leading to the qualifiers: "strain-softening" or "strain-hardening", and consequently "deflection-softening" or "deflection-hardening." With the increasing penetration of ultra-high performance concrete (UHPC) and fiber reinforced concrete (UHP-FRC) and the introduction of enhanced fiber materials, progress will continue. "*The engineering dream and challenge that started in the 1870's, that is, to mix fibers into concrete like sand or aggregates to create an isotropic, homogeneous, moldable, strong, ductile and durable composite for construction applications with comparable strength and ductility as reinforced concrete, is today closer than ever" [1].*

10. SELECTED REFERENCES

[1] Naaman, A.E., "*Fiber Reinforced Cement and Concrete Composites,"* Techno Press 3000, Florida, www.technopress3000.com, 2017, 765 pages.

[2] Naaman, A.E., *Ferrocement and Laminated Cementitious Composites.* Techno Press 3000, Ann Arbor, Michigan, ISBN 0-9674939-0-0, 2000, 370 pages, (www.technopress3000.com).

[3] Romualdi, J.P., and Batson, G.B., "Mechanics of Crack Arrest in Concrete," *J. Engineering Mechanics, ASCE*. 89, 1963, 147–168.

[4] Romualdi, J.P., and Mandel, J.A., "Tensile Strength of Concrete Affected by Uniformly Distributed and Closely Spaced Short Lengths of Wire Reinforcement, *Journal of the American Concrete Institute*, Vol. 61, 1964, 657–670.

[5] US Patent No. 1,046,913 by Weakley, R.D., "Bonding Means for Reinforced Concrete Structure," Dec. 10, 1912.

[6] US Patent No. 1,349,901, by Meischke-Smith, W., "Ferroconcrete Construction," Aug. 17, 1920.

[7] US Patent No. 1,633,219, by Martin, G.C., "Method of Forming Pipe," June 21, 1927.

[8] US Patent No. 1,913,707, by Etheridge, H., "Concrete Construction," June 13, 1933.

[9] US Patent No. 2,677,955, by Constantinesco, G., "Reinforced Concrete," May 11, 1954.

[10] U.S. Patent No. 3,439,094, by Romualdi, J.P., "Two Phase Concrete and Steel Materials," Feb. 25, 1969.

[11] U.S. Patent No. 3852930, by Naaman, A.E., "Tridimensional Fiber Reinforcement of Portland Cement Concrete Matrices," December 10, 1974.
[12] U.S. Patent No. 5,989,713, by Naaman, A.E., "Optimized Geometries of Fiber Reinforcements of Cement, Ceramic and Polymeric Based Composites," November 23, 1999. Divisional: US Patent No. 6,060,163; May 9, 2000.
[13] Lankard, D., "Slurry Infiltrated Fiber Concrete (SIFCON)," Concrete International, Vol. 6, No. 12, Dec. 1984, pp. 44-47.
[14] Lankard, D., and Newell, J.K., "Preparation of Highly Reinforced Concrete Composites," American Concrete Institute, SP-81, Detroit, MI, 1984, pp. 286-306.
[15] Krenchel, H., "*Fibre Reinforcement*, "Akademick Forlag, Copenhagen, Denmark, English translation, 1964, 159 pages.
[16] Shah, S.P., and Rangan, V.B., "Fiber Reinforced Concrete Properties," *Journal of the American Concrete Institute*, Vo. 68, No. 2, 1971, pp. 126-135.
[17] Naaman, A.E., "A Statistical Theory of Strength for Fiber Reinforced Concrete," Thesis presented to the Massachusetts Institute of Technology, Civil Engineering Department in partial fulfillment for the degree of Doctor of Philosophy, Sept. 1972, 196 pp.
[18] Naaman, A.E., Argon A., and Moavenzadeh, F., "A Fracture Model for Fiber Reinforced Cementitious Materials," *Cement and Concrete Research*, Vol. 3(4) 1973, pp. 397-411.
[19] Naaman, A.E., Moavenzadeh, F., and McGarry, F.J., "Probabilistic Analysis of Fiber Reinforced Concrete," *Journal of the Engineering Mechanic's Division*, ASCE, Vol. 100, No. EM2, April 1974, pp. 397-413.
[20] Swamy, R.N., Mangat, P.S., and Rao, C.V.S.K., 'The Mechanics of Fibre Reinforcement of Cement Matrices," *Fiber Reinforced Concrete*, ACI SP-44, American Concrete Institute, Detroit, MI, 1974, pp. 1–28.
[21] Swamy R.N. and Stavrides, H. "Some Properties of High Workability Steel Fibre Concrete," in A. Neville (ed.) *Fibre-Reinforced Cement and Concrete*, RILEM Symp., The Construction Press, Lancaster, England, 1975, pp. 197–208.
[22] Naaman, A.E., "Development and evolution of tensile strain hardening FRC composites," in Fiber Reinforced Concrete: Design and Applications, Proceedings of International Symposium, BEFIB 2008, Edited by Ravindra Gettu, RILEM PRO 60, 2008, pp. 1-28.
[23] Naaman, A.E., and Reinhardt, H.W., "Setting the Stage: toward Performance Based Classification of FRC Composites," in High Performance Fiber Reinforced Cement Composites (HPFRCC-4), A.E. Naaman and H.W. Reinhardt, Editors, RILEM Publications, Pro. 30, June 2003, pp. 1-4.
[24] Naaman, A.E., "Strain Hardening and Deflection Hardening Fiber Reinforced Cement Composites," in High Performance Fiber Reinforced Cement Composites (HPFRCC-4), A.E. Naaman and H.W. Reinhardt, Editors, RILEM Publications, Pro. 30, June 2003, pp. 95-113.
[25] Naaman, A.E., and Reinhardt, H.W., "High Performance Fiber Reinforced Cement Composites (HPFRCC-4): International RILEM Report," Materials and Structures, Vol. 36, Dec. 2003, pp. 710-712. Also same in Cement and Concrete Composites, Vol. 26, 2004, pp. 757-759.
[26] Naaman, A.E., and Reinhardt, H.W., "Proposed Classification of FRC Composites Based on their Tensile Response " *Materials and Structures*, Vol. 39, page 547-555, 2006. Also, Proceedings of symposium honoring S. Mindess, N. Banthia, Editor, University of British Columbia, Canada, August 2005. Electronic proceedings, 13 pages.
[27] Naaman, A.E., "Deflection Softening and Deflection Hardening FRC Composites: Characterization and Modeling," in ACI special publication on Deflection and Stiffness Issues in FRC and Thin Structural Elements, P. Bischoff and R. Malhas, Editors, ACI SP-248, 2007, Electronic Proceedings, pp. 53-66.

A THERMAL CONDUCTIVITY MODEL FOR RUBBERISED MORTAR

S. Yang (1), N. Ukrainczyk (1) and E. A. B. Koenders (1)

(1) Institute of Construction and Building Materials, Technische Universität Darmstadt, Franziska-Braun-Straße 3, 64287 Darmstadt, Germany

https://doi.org/10.21452/bccm4.2018.02.02

Abstract

The study reported in this paper was done with the aim to investigate the effective thermal conductivity of crumb-rubber-modified mortar through a numerical way. Crumb rubber with the particle size (1-2 mm) was used to replace 5%, 7.5%, 10%, 12.5%, and 15% of the volume of quartz sand with the same size. A numerical simulation method for heat transfer at the meso-scale level of this composite material was applied to model the meso-structure of this composite material, with emphasis on the random packing of spherical particles, volume fractions, and particle size distributions (PSDs), for each component, i.e. rubber, quartz sand and air. A representative volume element (RVE model) was generated using an implicit finite difference method to solve the three-dimensional heat transport equation. In fact, the effective thermal conductivity was strongly depending on the thermal conductivities of all individual solid components. From this, a parameter estimation method was applied whereby the Levenberg-Marquardt algorithm was implemented in MatLab. Simulation results were validated by comparison with literature data. Using the estimated parameters, the effective thermal conductivity of mortar, including the effect of crumb rubber replacement, was presented. Comparison indicated that good agreement existed between the present simulations and the experimental results.

1. INTRODUCTION

In order to effectively reduce the environmental impact caused by the rapid increase of waste rubber tires, mixing its crumb rubber flacks into cementitious materials will immobilize these environmental pollutants and turning it into a green resource in a practical and sustainable way. Several previous studies proved that the addition of rubber particles may significantly reduce the effective thermal conductivity (ETC) of these cement-based composites [1][2][3][4][5]. However, numerical modelling results of this material are yet very scarce in the literature. Nevertheless, some numerical simulations in terms of heat transfer in composite and porous materials may serve as valuable reference for this study.

Coquard and Baillis [6] investigated the conductive heat transfer though heterogeneous cellular materials using a numerically finite volume method based on a meso-structure, which was obtained through X-ray tomography. Wang and Pan [7] solved a thermal energy transport equation for an

open-cell foam structure by using a highly-efficiency lattice Boltzmann method. She et al. [8] presented a random generation method to generate microstructures of foamed concretes, and used a finite volume method to simulate the heat transfer through porous structures. Hui et al. [9] determined ETCs of graded composites by means of a finite element method approach. Based on previous work, in this study a numerical model for determination of ETC of rubberised mortar was developed. Moreover, an inverse identification method for parameters estimation was proposed as well.

2. NUMERICAL APPROACH FOR DETERMINATION OF ETC

The starting point for the modelling is that spherical particles are randomly positioned inside a predefined volume representing an initial cement paste matrix, while following particles size distribution (PSD) for each component: rubber, quartz sand and air. The process began with stacking the larger particles, subsequently followed by smaller ones. Particle size distributions of crumb rubber and quartz sand are measured through Horiba LA-950 Laser Diffraction Particle Size Analyser, which is approximated by the following Rosin-Rammler function

$$G(x) = 1 - \exp(-b * x^n), \tag{1}$$

where G(x) is the particle cumulative weight (g) with diameter x (mm), and with b and n being constants representing the shape of the grading curve.

The basic principle of the developed conductivity model is Fourier's first law of heat conductivity, which can be expressed as:

$$Q_x = -\lambda A \frac{\partial T}{\partial x}, \tag{2}$$

where, Q_x (W) is the heat flow rate by a conductivity λ (W/mK), which is the thermal conductivity of a material, A (m²) is the cross-sectional area normal to the gradient $\partial T/\partial x$ (K/m), which is the derivative of temperature with respect to the x-direction. The negative sign in Fourier's equation indicates that the heat flows in the direction of a decreasing temperature. When Fourier's law is combined with the law of thermal energy conservation, a one dimensional heat conduction equation can be expressed as:

$$\frac{\partial^2 T}{\partial x^2} + \frac{g_0}{\alpha} = \frac{1}{\alpha}\frac{\partial T}{\partial t}, \tag{3}$$

where, $\alpha=\lambda/(\rho * C_p)$ (m²/s).

In case of a steady state heat conductivity problem, when the heat flow takes place in three dimensions, and there is no internal heat generation, equation (3) expands to the Laplace's equation:

$$\lambda_x \frac{\partial^2 T}{\partial x^2} + \lambda_y \frac{\partial^2 T}{\partial y^2} + \lambda_z \frac{\partial^2 T}{\partial z^2} = 0. \tag{4}$$

When considering heat transfer through a porous medium (in z-direction), this is only possible when the heat gradient goes from the warm surface to the colder surface, which also holds for a regular cement paste. When the other four sides of the representative volume are isolated (see Figure 1), a true one dimensional heat flow will occur in the sample. According to this, the boundary conditions are given as follows:

$$\left.\frac{\partial T}{\partial x}\right|_{x=0} = \left.\frac{\partial T}{\partial x}\right|_{x=L} = 0; \left.\frac{\partial T}{\partial y}\right|_{y=0} = \left.\frac{\partial T}{\partial y}\right|_{y=L} = 0, \tag{5}$$

$$T|_{z=0} = T_{hot}, T|_{z=L} = T_{cold}. \tag{6}$$

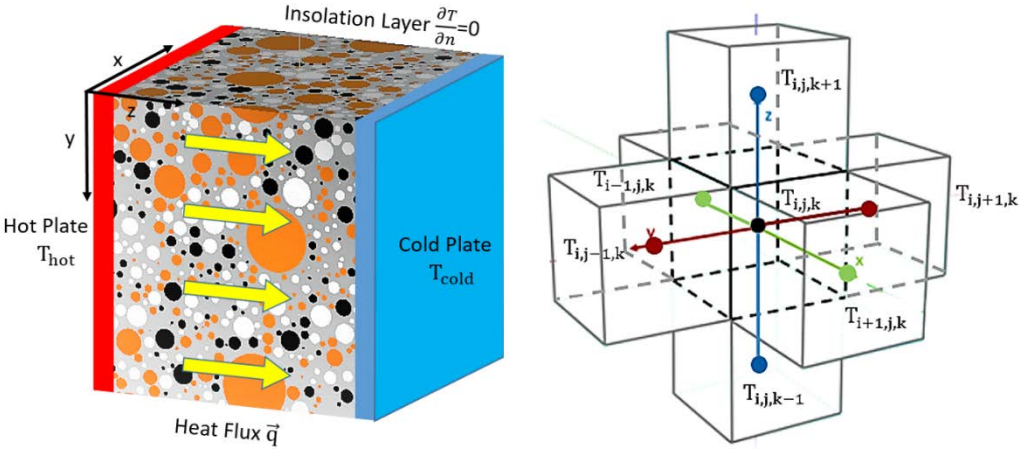

Figure 3: Illustration of the principle of the ETC modelling

The lattice points represent the each component with a different thermal conductivity. In order to establish the connection between two adjacent points, the thermal conductivity in the middle of two points can be expressed as:

$$\lambda_m = 2/(\frac{1}{\lambda_i} + \frac{1}{\lambda_{i+k}}), \tag{7}$$

where k=1 (in x-direction), L (in y-direction) or L^2 (in z-direction). L represents the number of voxels in a row.

Each lattice point exchanges heat with six neighbouring lattices points (see Figure 1, right). According to the energy balance principle, the sum of the heat that flows into the lattice should be equal to the heat that flows out of the lattice. The equation with all lattice points can be represented in a matrix form as follows:

$$A\mu = b, \tag{8}$$

where the matrix μ is a space-matrix vector and A is a sparse symmetrical matrix, which corresponds to the temperatures of all unknown lattice points, b is a vector, which represents the boundary conditions of the system.

The heat flow through each point along the z-axis can be calculated as:

$$q_{i,z} = \frac{1}{2}[(\mu_{i-L} - \mu_i)\lambda_{z,i-L} + (\mu_i - \mu_{i+L})\lambda_{z,i}]. \tag{9}$$

Owing to the microstructure of rubberised cement-based composite regarded as an equivalent continuous medium, the effective thermal conductivity λ_i of the composite is equal to the effective thermal conductivity $\lambda_{i,z}$ calculated in z-direction.

$$\lambda_i = \lambda_{i,z} = -\frac{Q_z}{L^3} * \left(\frac{L+1}{T_{hot}-T_{cold}}\right). \quad (10)$$

3. MATERIALS AND EXPERIMENTAL TESTING

Materials used in this study consist of the Portland cement CEM I 42.5R (HeidelbergCement company), crumb rubber (Genan A/S company), quartz sand (Euroquartz company), water and superplasticiser (Sika® ViscoCrete). Three particle sizes of sand were used: 0.1-0.5 mm, 0.5-1.0 mm and 1.0-2.0 mm. The crumb rubber with particles size of 0.8-2.0 mm was obtained through the ambient grinding process. Crumb rubber replacement levels were set to 5%, 7.5%, 10%, 12.5% and 15% by volume of quartz sand, respectively. As for the mix proportion, the water-cement ratio was set to 0.45. The detailed mix design of rubberized mortar and reference mortar are presented in Table 1.

Table 5: Mix design

No.	crumb rubber (vol.-%)	w/c	cement (kg/m³)	water (kg/m³)	crumb rubber (kg/m³)	quartz sand (kg/m³)			superplasti-ciser (kg/m³)
						0.1-0.5	0.5-1.0	1.0-2.0	
REF	0	0.45	550	245.7	0	563.52	290.62	440.49	1.93
CR_2.0a	5	0.45	550	245.7	59	563.52	290.62	309.74	1.93
	7.5				88.5			244.37	
	10				118			178.99	
	12.5				147.5			113.62	
	15				177			48.24	

For each mixture, three samples of 40x40x160 mm³ prisms were prepared and cured in water at 20±1 °C. The specimens were dried at the age of 28 days in an oven at 45 °C and weighed at 24 h intervals until the loss in weight did not exceed 0.2% in 24 hours. The TPS instrument (manufactured by Hot Disk AB) was used to measure the effective thermal conductivity of mortar specimens at 20 °C. For each specimen, three measurements were performed.

4. STATISTICAL EVALUATION OF REPRESENTATIVE ELEMENT VOLUME

4.1 Concept of REV

A cement-based material is a heterogeneous system, which consists of a solid matrix and a complex pore system. To describe a heterogeneous system, as suggested by Bear [10], this can be done by introducing the concept of representative elementary volume (REV). In this study, a REV was determined through a statistical analysis of simulations [11]. Several experiments of increasing sizes of the microstructure were conducted, and for each microstructure different particles' position and voxel resolution were considered. Then the chi-square statistic was applied for determining the size of the REV.

$$\chi^2 = \frac{\sum_{i=1}^{m}(\lambda_i-\lambda_a)^2}{\lambda_a}, \quad (11)$$

in this, λ_i is the investigated thermal conductivity of current microstructure, which is calculated from Equation (10). λ_a is the average of all λ_i and *m* is the number of realisations for the current rib size. This procedure demonstrates that the smaller the value of χ^2 is, the closer is the volume

of the respective sample to the expected REV. In spite of this, a sample with a smaller volume can be generally used when the value of χ^2 is acceptably low. In this study, 0.1 is used as an acceptable value, and the degree of freedom is 1 which is the random distribution of particles. This means that if χ^2 is lower than 0.1, there is at least a 95% chance probability confidence that the visual particle structure can be regard as REV.

4.2 Determination of REV and results analysis

The tests were conducted with several rib sizes from 30 mm to 200 mm. For each rib size, three voxel resolutions were analysed: 1 pixels/mm, 2 pixels/mm and 4 pixels/mm. For each rib size and each voxel resolution, five visual microstructures were generated. A total of 105

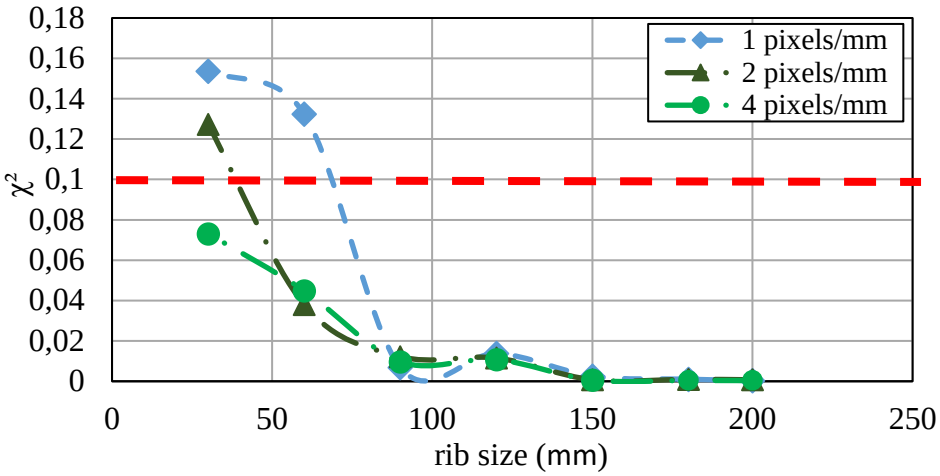

Figure 4: statistical analysis of REV

numerical tests were performed. The determination procedure was carried out with C++ language using GNU Compiler Collection (GCC 6.3.0) on a high-performance computer at TU-Darmstadt Lichtenberg (12 cores, 5900 TFlops/s, Intel Xeon E5-2670 Sandy Bridge). In order to improve the efficiency of used of computer memory and speed up the implementation of the procedure, a parallel computing scheme was achieved through Open Multi-Processing (OpenMP 2.0.1). The results of the REV size determination are presented in Figure 2. When a chi-squared value of 0.1 is acceptable with a probability of at least 95%, then the rib size of the microstructure of the mortar to establish the REV should be larger than 90 mm (1 pixels/mm), 60 mm (2 pixels/mm) and 30 mm (4 pixels/mm). The results of this analysis were applied for predicting the effective thermal conductivity and parameter estimation in the following sections.

5. INVERSE APPROACH FOR PARAMETER ESTIMATION

Based on an actual experimental investigation on a composite, the thermal conductivities of its components can be estimated by minimising the deviation between simulated and experimental data. The objective function is expressed as follows:

$$\min F(\lambda_i) = [\lambda_{sim}(\lambda_i) - \lambda_{exp}]^T [\lambda_{sim}(\lambda_i) - \lambda_{exp}], \quad (12)$$

where $F(\lambda_i)$ represents a non-linear function of the parameters, $\lambda_{sim}(\lambda_i)$ is the effective thermal conductivity of a composite, which is calculated based on the thermal conductivities of components and their spatial distributions. λ_{exp} is the experimental value. The unknown parameter

λ_i is obtained and can minimise the objective function. A Levenberg-Marquardt algorithm [12][13] of the MatLab Optimisation Toolbox was used to estimate the thermal conductivity of quartz sand and rubber. The step tolerance (TolX) and the function tolerance (TolFun) were set to the same value 1e-3. However, this method cannot guarantee to find the global minimum. Therefore, different initial points were test in order to achieve good coverage on optimal solutions. A cube with the side length of 90 mm and with the voxel resolution of 1 pixels/mm was chosen as the representative elementary volume (REV) of an agar- quartz sand/rubber structure (see Figure 3). In order to determine the air void content, a compress equalisation method was adopted, by which a TESTING air entrainment meter was used. During the measurement, agar was in liquid state.

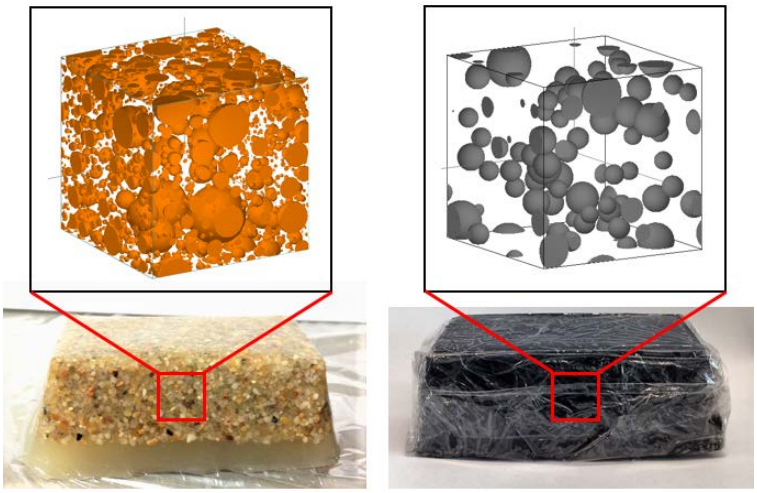

Figure 5: View of ETC of agar- quartz sand/rubber samples and numerical meso-structures.

6. SIMULATION RESULTS AND ANALYSIS

The results show that the effective thermal conductivity of agar- quartz sand and agar-rubber sample is 2.563 (W/mK) and 0.485 (W/mK) with the corresponding air void content 0.21 vol.-% and 3.0 vol.-%, respectively. The estimated thermal conductivity of quartz sand and rubber particle is 4.420 (W/mK) and 0.214 (W/mK), respectively.

Due to different chemical compositions, the estimated thermal conductivity of rubber is slightly higher than the value in literature (from 0.13 to 0.19 W/mK [2][22][23][24][25]). Furthermore, since the thermal conductivity of quartz sand is strongly depending on the quartz content and moisture content [14][15][16][21], and measurement approaches are various, the literature shows a wide range of variation. In the study of Côté & Konrad [16], the result was summarised from nearly 1000 test results in the literature. Kersten [15] performed an extensive series of tests on different types of quartz sand. The comparison of the parameter estimation results and the values from published literature is shown in Figure 4.

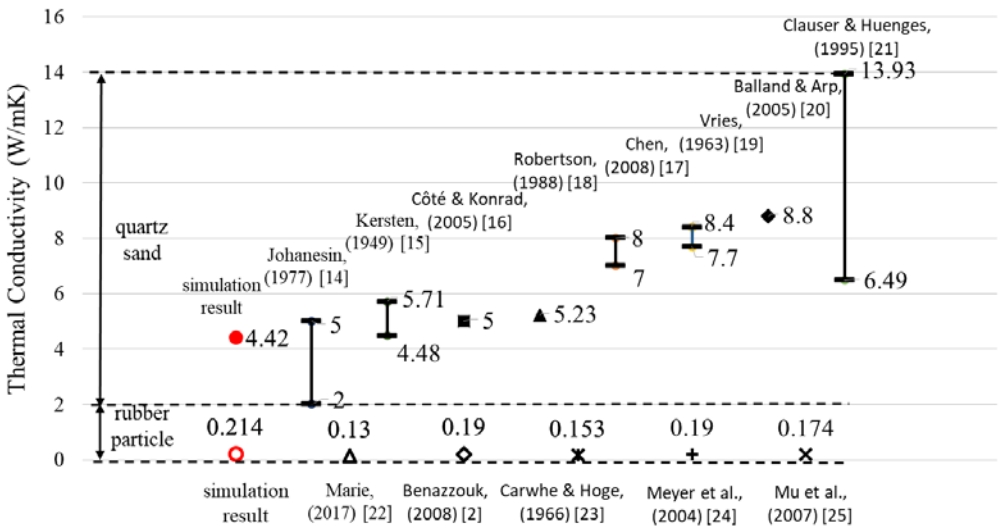

Figure 6: Parameter estimation results and literature survey of thermal conductivity of quartz sand and rubber

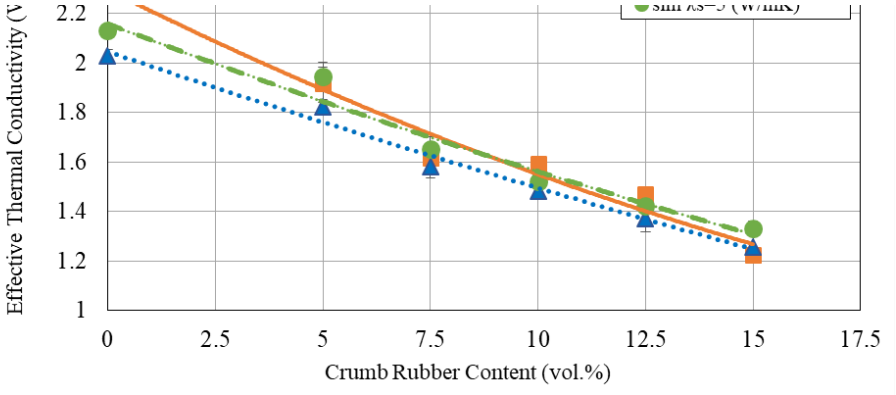

Figure 7: Effect of crumb rubber content on thermal conductivity of mortar

Notably, the thermal conductivity of quartz sand is much higher than that of rubber. Only a minor deviation of thermal conductivity of quartz sand can lead to a significant change of the ETC of mortar. Thus, it is very crucial to ensure a suitable accuracy of simulation results. In the following numerical experiment, two values of quartz sand (4.420 W/mK and 5 W/mK from the literature) were tested. The thermal conductivity of cement paste with a 0.45 w/c ratio at 28-days was measured through the hot disk method, its value is 0.685 (W/mK). The thermal conductivity of air 0.026 (W/mK) is taken from the literature [26][27]. For each sample, 6 simulation estimations were performed. The predicted parameter was produced by the average of all results. The comparisons of the simulation results with the experimental data in terms of the impact of crumb rubber content on the ETC of mortar are illustrated in Figure 5.

A decreasing tendency of the effective thermal conductivity of mortar with the increase in crumb rubber content and air void content was described using a second order polynomial, respectively. The experimental results show that by replacing quartz sand with crumb rubber at 5% to 15%, the effective thermal conductivity of mortar was reduced from 17% up to 47%. This

is not only due to increased air void content from 5% to 12%, but also because the thermal conductivity of crumb rubber is much lower than that of quartz sand. Moreover, it can be deduced from Figure 5 that when a tipping point of crumb rubber content is reached, the ETC of mortar will not decrease anymore. It is mainly because of a reduction in the workability with increasing crumb rubber content. Since the air bubbles are formed in the cement paste, a reduction of the workability of mortar makes it hard to entrain air in the cement past.

By using the estimated thermal conductivity of quartz sand (4.420 W/mK), the results are slightly lower than the experimental results. When the thermal conductivity of sand is increased to 5 (W/mK) and the other parameters stay constant, the results get much closer to the experimental results. The average differences of two ETC simulation results are 5.88% and 4.12 %, respectively.

The error originates mainly from the air void content of the agar- quartz sand sample in the liquid state measured through a compress equalisation method. This method is based on Boyle's law 0, which states that the volume occupied by a given mass of gas is proportional to the applied pressure. If the sample is entrained with a large amount of small air bubbles, they will not register a change in pressure. Therefore, the air void content of agar- quartz sand sample determined through this method is less than the actual value, which leads to the predicted thermal conductivity of quartz sand to be smaller than the values in the literature, lowering the simulated ETC of mortar. This trend is considerably more pronounced when the mortar contains more quartz sand, like the reference mortar. Therefore, a more accurate approach is required.

7. CONCLUSION

A meso-scale numerically modelling is developed for predicting the effective thermal conductivity of rubberised mortar. The effective thermal conductivity of heterogeneous material is described via the concept of representative volume elements. When a chi-squared value of 0.1 is regard as an acceptable value, the REV should be larger than 90 µm (1pixels/µm), 60 µm (2 pixels/µm) or 30 µm (4 pixels/µm).

A Levenberg-Marquardt algorithm was used to estimate the thermal conductivity of quartz sand and rubber particle based on measurement results of agar- quartz sand/rubber sample. The estimation results are within the range of values from the literature. Moreover, the simulated ETCs of rubberised mortars are in good agreement with the experimental results. When the thermal conductivity of quartz sand 5 (W/mK) instead of 4.420 (W/mK) was adopted, which proved a better approximation of experimental results.

ACKNOWLEDGEMENTS

The authors would like to thank the contributors of laboratory of the institute of Construction and Building Materials of the TU Darmstadt.

REFERENCES

[1] Herrero, S., et al., 'Influence of proportion and particle size gradation of rubber from end-of-life tires on mechanical, thermal and acoustic properties of plaster–rubber mortars', *Materials & Design*. **47** (2013) 633–642.

[2] Benazzouk, A., et al., 'Thermal conductivity of cement composites containing rubber waste particles', *Construction and Building Materials*. **22** (4) (2008) 573–579.

[3] Sukontasukkul, P., 'Use of rubber to improve thermal and sound properties of pre-cast concrete panel', *Construction and Building Materials*. **23** (2) (2009) 1084–1092.
[4] Najim, K. B. and Hall, M. R., 'Workability and mechanical properties of crumb-rubber concrete', *Construction Materials*. **166** (1) (2013) 7–17.
[5] Marie, I., 'Thermal conductivity of hybrid recycled aggregate – Rubberized concrete', *Construction and Building Materials*. **133** (2017) 516–524.
[6] Coquard, R. and Baillis, D., 'Numerical investigation of conductive heat transfer in high porosity foams', *Acta Materialia*. **57** (18) (2009) 5466–5479.
[7] Wang, M. and Pan, N., 'Modeling and prediction of the effective thermal conductivity of random open-cell porous foams', *Int. Journal of Heat and Mass Transfer*. **51** (5-6) (2008) 1325–1331.
[8] She, W., et al., 'Three-dimensional numerical modeling and simulation of the thermal properties of foamed concrete', *Construction and Building Materials*. **50** (2014) 421–431.
[9] Hui, P.M., Zhang, X., Markworth, A.J. et al., 'Thermal conductivity of graded composites: Numerical simulations and an effective medium approximation', *Journal of Materials Science*. **34** (1999) 5497-5503.
[10] Bear, J., 'Dynamics of Fluids in Porous Media', New York, Dover Publ. (1972).
[11] Gitman, M. B. and Askes, H., 'Quantification of stochastically stable representative volumes for random heterogeneous materials', *Archive of Applied Mechanics*. **75** (2006) 79-92.
[12] Moré, J. J., 'The Levenberg-Marquardt Algorithm: Implementation and Theory', Numerical Analysis, ed. G. A. Watson, Lecture Notes in Mathematics 630, Springer Verlag. (1977) 105–116.
[13] Henri, P. G., 'The Levenberg-Marquardt method for nonlinear least squares curve-fitting problems', North Carolina, USA. (2013).
[14] Johanesin, O., 'Thermal conductivity of soils', Ph. D. thesis, Trondheim, Norway. (1977).
[15] Kersten, M., S., 'Thermal properties of soils', Ph. D. thesis, University of Minnesota Engineering Experiment Station Bulletin. **28** (1949).
[16] Côté, J. and Konrad, J. M., 'A generalized thermal conductivity model for soils and construction materials', *Canadian Geotechnical Journal*. **42** (2) (2005) 443-458.
[17] Chen, S. X., 'Thermal conductivity of sands', *Heat Mass Transfer*. **44** (10) (2008) 1241–1246.
[18] Robertson, E., C., 'Thermal properties of rocks', *United States Department of the Interior Geological Survey*. (1988) 88–441.
[19] Vries, D. A. de, 'Thermal properties of soils', *Physics of Plant Environment*. (1963) 210–235.
[20] Balland, V. and Arp, P. A., 'Modeling soil thermal conductivities over a wide range of conditions', *Environmental Engineering & Science*. **4** (6) (2005). 549–558.
[21] Clauser, C. and Huenges, E., 'Thermal conductivity of rocks and minerals', *Rock Physics and Phase Relations*. (1995) 105–126.
[22] Marie, I., 'Thermal conductivity of hybrid recycled aggregate – Rubberized concrete', *Construction and Building Materials*. **133** (2017) 516–524.
[23] CarwHe, L. C. K. and Hoge, H. J., 'Thermal conductivity of soft vulcanized natural rubber: selected values'. (1966).
[24] Meyer, L., et al., 'Thermal conductivity of filled silicone rubber and its relationship to erosion resistance in the inclined plane test', *IEEE Transactions on Dielectrics and Electrical Insulation*. **11** (4) (2004) 620–630.
[25] Mu, Q. H., et al., 'Thermal conductivity of silicone rubber filled with ZnO', *Polymer Composites*. **28** (2) (2007) 125–130.
[26] Kadoya. K., Matsunaga. N., Nagashima, A., 'Viscosity and thermal-conductivity of dry air in the gaseous-phase', *J. Phys. Chem. Ref. Data.* **14** (4) (1985) 947-970.
[27] Montgomery, R. B., 'Viscosity and thermal conductivity of air and diffusivity of water vapour in air'. *J. Meteor*. **4** (1948) 193-196.
[28] Bonnor, W. B., 'Boyle's law and gravitational instability', *MNRAS.* **116** (351) (1956) 351-359.

EXPERIMENTAL ASSESSMENT OF THE EFFECT OF PLASTICIZING AND AIR-ENTRAINING ADDITIVES ON MECHANICAL PROPERTIES OF REFRACTORY CEMENT COMPOSITE

M. Jogl (1) and P. Reiterman (1)

(1) Experimental Centre, Faculty of Civil Engineering, Czech Technical University in Prague, Czech Republic

https://doi.org/10.21452/bccm4.2018.02.03

Abstract

This article is focusing on comparison of plasticizing and air-entraining additives and their effect on mechanical properties of composite based on aluminous cement. Achieved results supposed to help during the development of lightweight composite able to withstand temperatures over 1000 °C and reduce heat transfer from a high temperature source, either by direct contact (conduction/convection) or via radiation. Operation at high temperature is of fundamental importance to many major sectors of industry, including material production and processing, chemical engineering, power generation and more. Objective is to achieve competitive performance with competitive life cycle costs. Maximum material efficiency and minimum manufacturing and operating costs are key factors in meeting this objective. Selection of a materials with sufficient economic conditions for a particular application must take account of many factors. For the purpose of this experiment, specimens were created from cement paste and different dosage of chopped carbon fibres. Experimental investigation underwent two series of samples different in the type of used additives. First series contains plasticizing additive, second series contains air-entraining additive. The purpose was to determine the different effect on the workability of fresh mixture, bulk density and mechanical properties. The strength of samples was measured after exposure to high temperatures of 600 °C and 1000 °C. The residual properties were compared between each other and also to samples dried at the temperature of 105 °C. Obtained results revealed the level of influence of mentioned additives on the composition of studied refractory composite.

Keywords: Refractory composite, aluminous cement, high-thermal loading, superplasticizing additive, air-entraining additive.

1. INTRODUCTION

Refractory materials can be divided into several classes based on: chemical composition (acid, basic and special), method of implementation (shaped and unshaped), method of manufacture (fused and sintered), and porosity content (porous and dense) [1,2]. Refractories act as a thermal barrier between a hot medium and the wall of the containing vessel, they insure a strong physical protection, preventing the erosion of walls and they act as thermal insulation, insuring heat retention [3].

One of the most well-known techniques for the production of refractories and ceramics is the mixing of several components in the form of powder, formation of the mixture to the final shape and firing to the suitable temperature, where desired properties are attained [3]. For the formation of refractories can be used different bonding systems, such as ceramic bond, hydraulic bond and organic bond. Ceramic bond is a bond which comes into play typically at high temperatures through ceramization reactions, while hydraulic bond is ensured by the hydration of aluminous refractory cement added to the product [3].

Development of new composite materials is the worldwide extremely progressive branch of engineering activity. Composite materials are applied in many industries. Modern composites are often complicated system of selected binder modified by mineral additives and number of other chemical admixtures. Thanks today's technologies it is possible to reach required properties like high strength and good durability which is determined by extremely low level of water-cement ratio [4].

2. MATERIALS

The binder and its hydration products significantly control final properties, behavior and thermal resistance of composite [5] (SB). Silica composites based on Portland cement are not able to resist the effects of high temperatures, therefore a heat resistant mixtures in this experiment includes aluminous cement as binder of studied composites, allowing application for high temperatures more than 1000 °C. Resistance of aluminous cement is directly affected by the content of Al_2O_3. Chemical properties of used aluminous cement is given in Table 1. With those formulated cement is possible to reach satisfactory resistant to high temperature.

Table 1: Chemical composition of aluminous cement

Components	Al_2O_3	CaO	SiO_2	Fe_2O_3	Na_2O	MgO	K_2O	Specific surface
% weight	70.80	27.50	0.58	0.42	0.27	0.21	0.06	381 m^2/kg

The main interest of this study was the effect of plasticizing and air-entraining additives on mixture's workability while in a plastic state and as mentioned on durability and mechanical properties of refractory cement composite before and after high thermal loading. For the creation of test samples was used commercial superplasticizer STACHEMENT 2000 (FM), based on polycarboxylate polymers, and air-entraining agent MICROPORAN 2 (LP), surface-active substance which is creating micro-size air bubbles. Both additives were provided by the company STACHEMA CZ s.r.o. The amount of additives in mixture was chosen according to the manufacturer's recommendations, 1% by weight of the cement dose. Their actions are only physical in fluidizing the mixture, made even with low water ratio.

Part of the research was also application of chopped carbon fibres and to analyze their degree of influence on workability of fresh mixture and residual properties of high temperature loaded composites. Fibre reinforced composite allows better durability in service than composite without fibres because of volume changes limiting and increasing of final tensile strength [6]. The material properties of the carbon fibre are presented in Table 2.

Table 2: Physical properties of carbon fibre

Density (g/cm^3)	Length (mm)	Diameter (μm)	Tensile strength (GPa)	Tensile modulus (GPa)
1.80	6	7	4.0	240

3. SPECIMEN PREPARATION AND TEST PROCEDURE

For the experimental program were prepared prismatic specimens with the total dimensions of 40 mm × 40 mm × 160 mm. Compositions of mixtures are shown in Table 3.

Table 3: Composition of mixtures

Component [kg/m^3]	Mixtures						
	AC	LP_0.0	FM_0.0	LP_0.5	FM_0.5	LP_1.0	FM_1.0
Superplasticizer	0	0	9	0	9	0	9
Air-entrainer	0	9	0	9	0	9	0
Water	224	224	224	224	224	224	224
Aluminous cement	900	900	900	900	900	900	720
Carbon fibres	0	0	0	9	9	18	18

It is necessary to carry out a drying procedure and firing after cement composites maturity [7, 8]. All specimens were cured in humid environment for the 28 days, then dried at 105°C for 24 hours to eliminate initiating of cracks caused by the water vapor escaping. One third of specimens was tested immediately after the samples were dried out. Other two thirds were loaded by elevated high temperature.

The high-thermal loading was carried out in an electric kiln, which automatically increased the temperature by 10 °C/min from ambient temperature to the desired values of 600 °C or 1000 °C. Set temperature was then maintained automatically for 180 minutes and then the kiln cooled naturally.

The flexural and compressive strength of tested composites was investigated after the high-thermal loading was completed.

4. RESULTS AND DISCUSSION

Influence of composition changes was evaluated by the results of physical and mechanical testing. Flexural strength f_{tm} measurement was organized as a three point test with supports distance of 100 mm according and was calculated by help of the maximum reached force. The

compressive strength test f_{cm} was performed on two fragments left after flexural test. The area under compressive load (40 mm × 40 mm) has been demarcated by the loading device. Next to the mechanical properties, changes of bulk density ρ were studied, since they are related to structural transformation during heating. All tests of mechanical properties were carried out according to the methodology described in European standard EN 196-1:2005 Methods of testing cement – Part1: Determination of strength.

All values of compressive strength, flexural strength and bulk density are presented after drying at 105 °C and after exposure to 600 °C and 1000 °C. The summary results of the measured properties of the produced refractory composites are shown in Table 4. These values are means of three specimens (except of compressive strength f_{cm}, which is average from six performed tests). Table shows also an overview of the dependence of bulk density on temperature.

Table 4: Summarized characteristic of experimental specimens.

	Bulk Density ρ [kg/m^3]			Flexural Strength f_{tm} [MPa]			Compressive Strength f_{cm} [MPa]		
	105°C	600°C	1000°C	105°C	600°C	1000°C	105°C	600°C	1000°C
AC	2110	1721	1695	6.2	1.9	1.6	123.0	99.8	64.9
FM_0.0	2155	1787	1756	8.0	2.4	2.2	130.3	102.2	66.2
LP_0.0	2110	1646	1585	4.6	1.4	1.1	121.0	98.6	64.3
FM_0.5	2098	1747	1722	12.6	4.2	3.2	125.1	83.5	51.1
LP_0.5	1954	1573	1536	8.2	2.6	2.2	118.2	92.1	59.4
FM_1.0	2059	1679	1649	15.1	5.5	3.8	116.8	76.8	49.7
LP_1.0	1905	1540	1485	12.0	3.2	2.8	114.1	82.3	51.5

Flexural strength is predominantly affected by the dose of fibres. Reference set of specimens (without fibres) exhibits lower values of flexural strength than the specimens with added carbon fibres in doses of 0.5% and 1.0% by specimen's volume. Detailed results are shown in the Figure 1.

The results of compressive strength shown in Figure 2 are corresponding with the results of bulk density. There is obvious effect of fibres and air-entraining additive causing an increase of the air content in composites, which can have a negative impact on the adhesion of fibres and binding matrix. This fact can cause limits to their application and undesirable effects on mechanical properties. On the other side, fibers contribute to the limitation of volume changes during thermal loading and related crack formation [9]. This assumption is confirmed by the results of flexural strength.

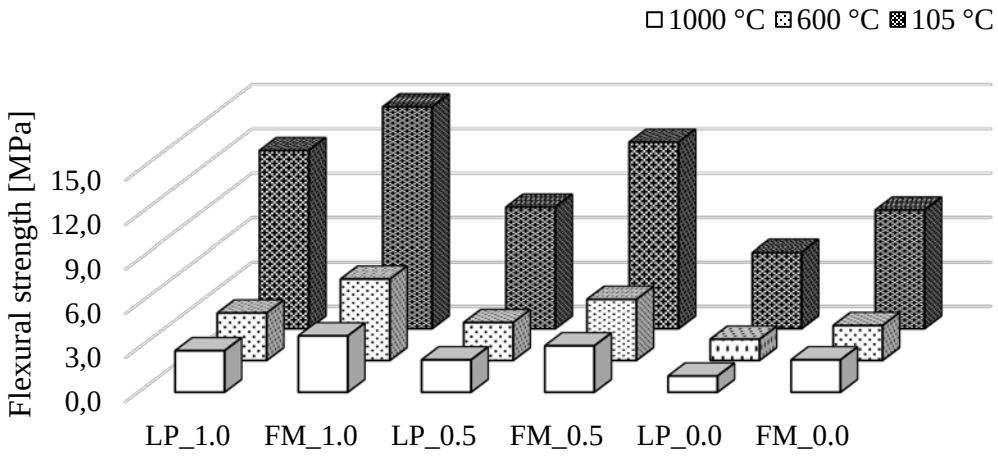

Figure 1: Relative values of flexural strength

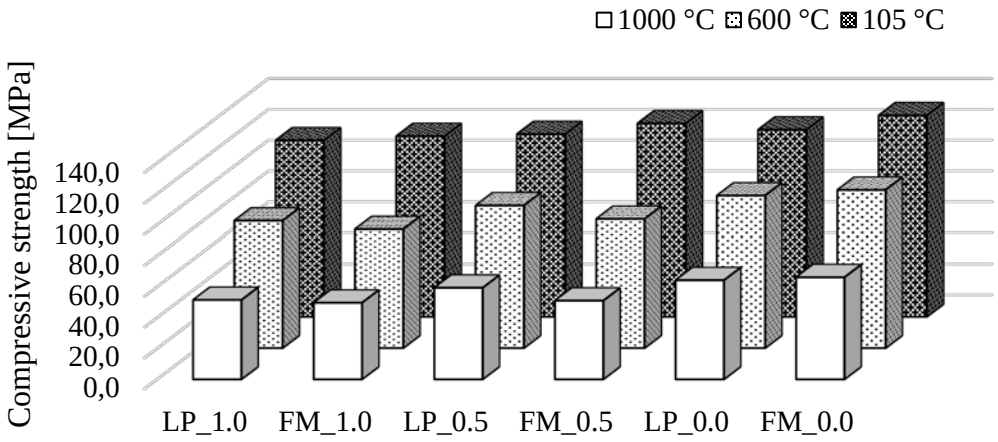

Figure 2: Relative values of compressive strength.

Figure 3 shows the values of bulk density of studied and thermally loaded composites. We can observe significant decline of the bulk density due to thermal loading which is caused by the mineralogical transformation and the loss of physically-bound water. Major role on the reduction of values of bulk density has the chemical decomposition of the hydration products and the content of siliceous components in the mixture. The bulk density values are also affected by the dosage of air-entraining additive. Thanks to the air-entrainer, micro-size air bubbles are created during mixing of the plastic composite and will stay as part of the hardened mixture.

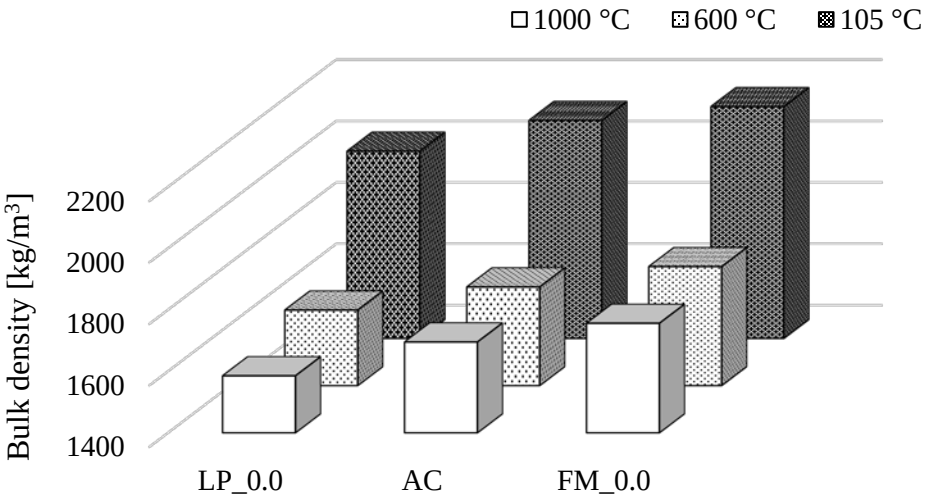

Figure 3: Relative values of bulk density.

5. CONCLUSIONS

Present paper contributes to the category of experimental research of special composites development. On the basis of performed experiments can be conclude that, in terms of mechanical properties, the most suitable values have been achieved by the composites with superplasticizing addtive. This fact arises in all cases of specimens, as in the case of fibre reinforced composites, as well in the case of composites without fibres. However, the amount of superplasticizer in designed mixture causes separation of water from cement mortar during the creation of specimens. Important is also evaluation of the bulk density results, where is evident the reduction of values due to air-entraining additive. But composites with air-entraining additive do not achieve such a level of workability as composites with the same amount of plasticizer.

The subsequent experiments will aim to increase the amount of the air-entraining additive and also to combine it with a reduced dose of superplasticizer, in order to improve the mixture's workability and further reduce the bulk density of hardened composites, while as much as possible preserve their properties after high temperature loading for the purpose of thermal barrier in an optional form between a hot medium and supporting structure.

ACKNOWLEDGEMENTS

The authors gratefully acknowledge the financial support provided by the project SGS16/199/OHK1/3T/11: Multicomponent binder systems for composite building materials.

REFERENCES

[1] Koňáková D., Hovorková V., Vejmelková E., Keppert M. and Černý R., 2014, 'Influence of Metashale as Cement Replacement on the Hygric Transport Properties of Concrete', *Advanced Materials Research* **1054** (2014) 188-193.

[2] Sadik Ch., Amrani I.-E. E., Albizane A., 'Recent advances in silica-alumina refractory: A review', *Journal of Asian Ceramic Societies* **2** (2006) 83-96.
[3] Katsavou I.D., Krokida M.K., Ziomas I. C., 'Determination of mechanical properties and thermal treatment behaviour of alumina-based refractories', *Ceramics International* **38** (2012) 5747-5756.
[4] Jogl M., Reiterman P., Holčapek O., Koťátková J., 'Proposal of Fire Resistant Composites with Application of Lightweight Aggregate Liaver', *Advanced Materials Research* **1054** (2014) 43-47.
[5] M. Bruncvik, P. Štemberk, 'Explosion-resistant reinforced-concrete construction kit for shelter in extreme situations', *Modelling, Measurement and Control* **81** (2012) 34-49.
[6] Banthia N., 'Durability enhancements in concrete with fibre reinforcement', in Kraus R. N., Naik T. R., Clasisse P., Sadeghi P., editors, *Proc. Int. Conf: Sustainable construction materials and technologies,* 'Conventry, special papers proceedings', Pub UW Milwaukee CBU (2007) 209-219.
[7] G.A. Khoury, 'Effect of fire on concrete and concrete structures', *Progress in Structural Engineering and Materials* **2** (4) (2000) 429-447.
[8] R. Boris et al., 'Effect of holding temperature on properties of different types of heat-resistant concrete', *Refractories and Industrial Ceramics* **54** (2014) 397–400.
[9] D. Koňáková, V. Špedlová, M. Čáchová, E. Vejmelková, R. Černý, 'Influence of Basalt Fibres and Aggregates on the Thermal Expansion of Cement-Based Composites', *Advanced Materials Research* **1054** (2014) 17-21.

BRAZILIAN SPLITTING TEST – EXPERIMENTAL AND NUMERICAL ANALYSIS

Marcelo De Simone (1) (2), **Lourdes M. S. Souza** (2) **and Deane Roehl** (1) (2)

(1) Department of Civil and Environmental Engineering, Pontifícia Universidade Católica do Rio de Janeiro, Brazil

(2) Instituto Tecgraf, Pontifícia Universidade Católica do Rio de Janeiro, Brazil

https://doi.org/10.21452/bccm4.2018.02.04

Abstract

The Brazilian splitting test is commonly used in order to estimate the tensile strength of brittle materials such as rocks and concretes. This test is performed by compressing a specimen disc in the direction of its diameter. Splitting tensile stresses are induced perpendicularly to the direction of the applied compressive load. Even though this test has been established for decades, standards, such as the ASTM D3967 – 16, still suggest numerous different test configurations, which may lead to different results.

In the present study, Brazilian Splitting Tests were conducted on Indiana Limestone discs of 54 mm diameter and 25 mm thickness. The discs were placed on flat platens. Digital Image Correlation (DIC) was used in order to obtain the strain fields developed during the tests. This technique allows the measurement of displacement/strain fields without contact.

The development of the stress fields and the crack formation were investigated by numerical models using the Finite Element Method (FEM). Two FEM models were carried out: Model I simulated a concentrated applied load (scenario I) while Model II considered a distributed load (scenario II). The model from scenario I resulted in a strain field on the sample surface similar to the one observed by DIC during the tests with flat platens. There was a higher tensile strain in the horizontal direction near the point of applied load. This indicates that, when flat platens are used, a concentrated load is applied, as expected.

Although this study is still a work in progress, the preliminary results indicate that, when load is applied using flat platens, the crack initiates at the load application point, while crack initiates in the center of the sample when load is distributed.

1. INTRODUCTION

Direct tensile tests are difficult to be performed on brittle materials, such as rocks and concretes. Alternatively, the Brazilian splitting test (BST), also known as indirect tensile test, is commonly used in order to estimate the tensile strength of such materials. The BST is performed by

compressing the sample in the direction of its diameter. Splitting tensile stresses are induced perpendicularly to the direction of the applied compressive load, inducing tensile fracture. Even though this test has been established for decades, various studies and standards, such as the ASTM D3967-16 [1], suggest numerous different test configurations, which may lead to different results. Li & Wong [2] presented a comprehensive review on the test, including the different loading configurations that have been used. Generally, it is assumed that the disc specimen is loaded uniformly and that the crack forms in the center of the specimen. However, this is not always observed in the laboratory and the validity of the test has been debated.

In order to improve the understanding of measurements from the laboratory tests, numerical and analytical solutions have been employed. Both Finite Element Method (FEM) and Discrete Element Method (DEM) have been used in the literature. Han et al. [3] presented a methodology to measure the elastic properties (E and ν) using the BST. In addition, the authors compared the results for stress and strain from a finite element model with an analytical solution. Using discrete element models, Xu et al. [4] and Ma & Huang [5] studied the sample behavior during the Brazilian Splitting Test.

In the present paper, the preliminary results for an experimental, analytical and numerical study on the Brazilian splitting test is presented. Indiana Limestone samples were submitted to the BST with digital image correlation (DIC) analysis to evaluate the strain development. The development of the stress fields was further investigated by FEM and analytical models.

2. EXPERIMENTAL PROCEDURE

In this study, Brazilian Splitting Tests were conducted on four discs of Indiana Limestone of 54 mm diameter and 25 mm thickness. The tests were conducted on a MTS testing machine, model 810 with load capacity of 250kN, under displacement control of the actuator at a rate of 0.02 mm/min. The discs were placed on flat platens. The splitting tensile strength was calculated by the equation ASTM D3967-16, , [1]:

$$\sigma_t = \frac{2\,P}{\pi\,t\,D} \tag{1}$$

where σ_t is the splitting tensile strength (in MPa), P is the maximum applied load (in N), t and D are the thickness and diameter of the specimen (in mm), respectively.

Digital Image Correlation (DIC) method was used in order to obtain the strain fields developed during the tests. This technique allows the measurement of displacement/strain fields without contact. Two CCD cameras with 5MP (Point Grey GRAS-50S5M) with resolution of 2448 x 2028 pixels and high resolution lenses type Tamron A031 (AF28-200mm F/3.8-5.6) were used and the pictures were taken at the rate of 1 fps. The software VIC SNAP and VIC-3D 2010, both from Correlated Solutions Inc., were used for image acquisition and processing. The test apparatus is shown in Figure 1. For the DIC method, the specimens were painted white with black speckles.

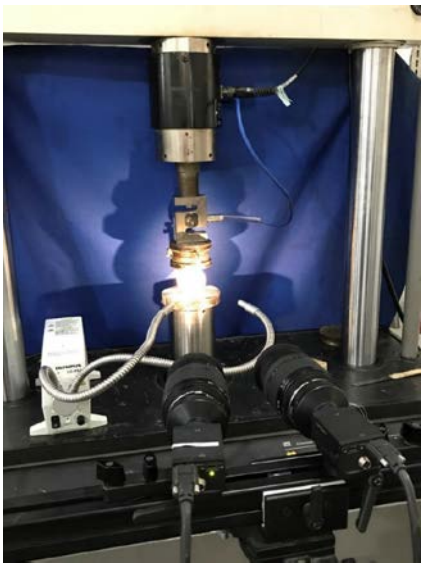

Figure 8: System used for the DIC in the Brazilian test

3. FINITE ELEMENT METHOD MODEL

The development of the stress fields and the crack formation were investigated by numerical models using the Finite Element Method (FEM). Two different models were carried out using the FEM software Abaqus. Model I simulated a concentrated applied load (scenario I) while Model II considered a distributed load (scenario II). In these models, the linear elastic assumption was adopted for simplicity. Based on Walton *et al.* [6], the Young's Modulus was considered to be 24.6 GPa while the Poisson's coefficient was assumed as 0.16.The load (P), the diameter (D) and the thickness (t) were obtained from the laboratory tests.

The models simulate a plane stress condition, with quadratic elements and reduced integration. The only difference between these two models is the applied load, as presented in Figure 2.

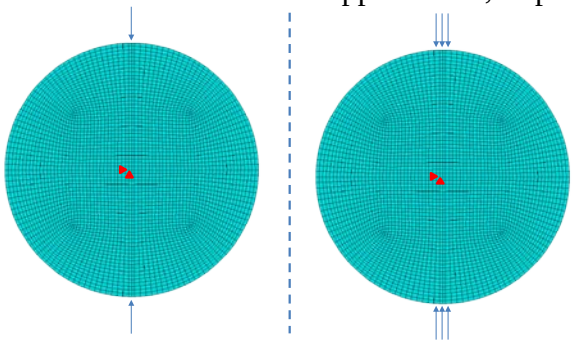

a) b)

Figure 9: a) Scenario 1 with concentrated load and b) Scenario2 with distributed load

These models are obviously simplified, as they are developed only to compare the results from the strain field from DIC with the finite element. Therefore, the main objective of the FEM modelling in the present paper is to observe the strain (horizontal (x) and vertical (y) directions) field around the sample.

4. ANALYTICAL SOLUTION

The strain and stress fields over the sample surface were also studied using two analytical solutions. The first (Analytical 1) was presented by Jianhong et al. [7] and considers a concentrated applied load (Figure 3a).

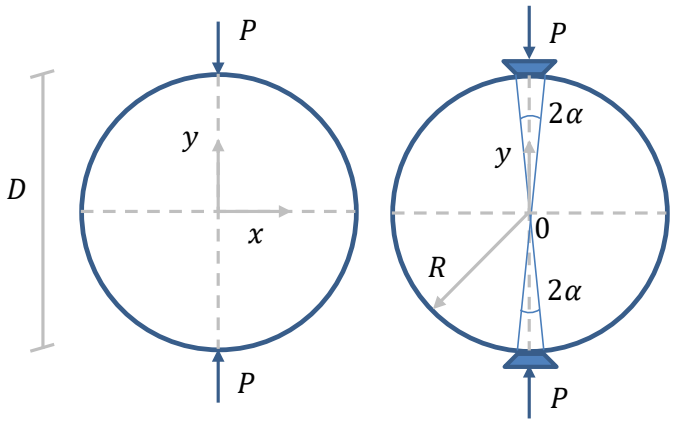

a) b)

Figure 10: Load application assumption for the analytical solution presented by a) Jianhong et al. [7] and b) Li & Wong [2].

In this solution, equation (1) presents the horizontal stress and equation (2) the vertical stress in any point of the model.

$$S_{xx}(x,y) = \frac{2P}{\pi t}\left\{\frac{\left[\left(\frac{D}{2}\right)-y\right]x^2}{\left[\left(\left(\frac{D}{2}\right)-y\right)^2+x^2\right]^2}+\frac{\left[\left(\frac{D}{2}\right)+y\right]x^2}{\left[\left(\left(\frac{D}{2}\right)+y\right)^2+x^2\right]^2}-\frac{1}{D}\right\} \quad \textbf{4} \quad (1)$$

$$S_{yy}(x,y) = \frac{2P}{\pi t}\left\{\frac{\left[\left(\frac{D}{2}\right)-y\right]^3}{\left[\left(\left(\frac{D}{2}\right)-y\right)^2+x^2\right]^2}+\frac{\left[\left(\frac{D}{2}\right)+y\right]^3}{\left[\left(\left(\frac{D}{2}\right)+y\right)^2+x^2\right]^2}-\frac{1}{D}\right\} \quad \textbf{5} \quad (2)$$

The second analytical equation (Analytical 2) considers a distributed load in a small arc length, 2α (Figure 3b). This solution was presented by Li & Wong [2], where the stresses in the horizontal and vertical directions are evaluated along the direction of the applied load. Those stresses are presented in equation (3) and (4) for the horizontal and vertical directions, respectively.

$$S_{xx}(y) = \frac{P}{\pi R t \alpha}\left\{\frac{\left[1-\left(\frac{y}{R}\right)^2\right]sin(2\alpha)}{1-2\left(\frac{y}{R}\right)^2 cos(2\alpha)+\left(\frac{y}{R}\right)^4}-tan^{-1}\left[\frac{1+\left(\frac{y}{R}\right)^2}{1-\left(\frac{y}{R}\right)^2}tan(\alpha)\right]\right\} \quad \textbf{6} \quad (3)$$

$$S_{yy}(y) = -\frac{P}{\pi R t \alpha}\left\{\frac{\left[1-\left(\frac{y}{R}\right)^2\right]sin(2\alpha)}{1-2\left(\frac{y}{R}\right)^2 cos(2\alpha)+\left(\frac{y}{R}\right)^4}+tan^{-1}\left[\frac{1+\left(\frac{y}{R}\right)^2}{1-\left(\frac{y}{R}\right)^2}tan(\alpha)\right]\right\} \quad \textbf{7} \quad (4)$$

5. RESULTS AND DISCUSSION

The Indiana Limestone specimens had average splitting strength of 1.43 ± 0.12 MPa, with average maximum applied load of 3.05 ± 0.20 kN. After the sample fails under tensile stress, a crack propagates in the middle of the sample in the same direction of the applied load. Using digital image correlation (DIC), the picture from the sample right before failure was used in order to get the strain field over the sample surface. Figure 4 presents the strain field in the horizontal and vertical directions of IL2 with 54 mm.

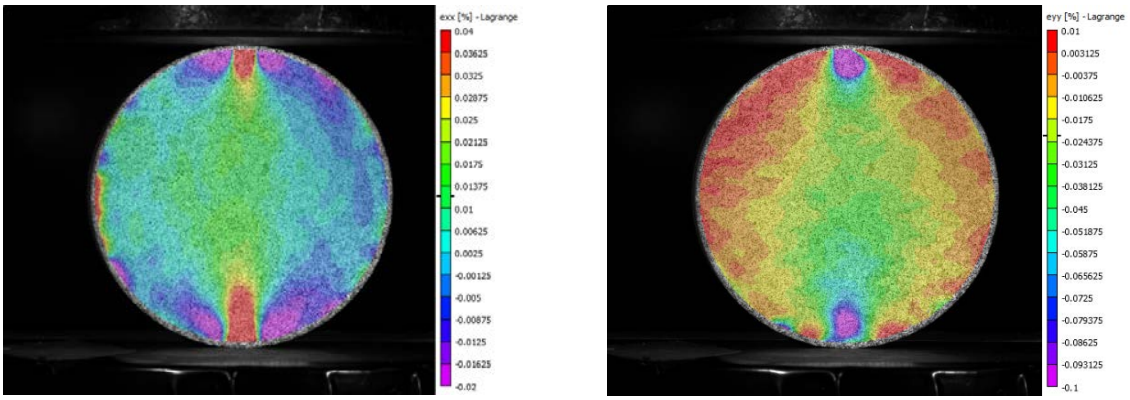

a) b)

Figure 11: Strain field in a) horizontal and b) vertical directions of sample IL2 with 54 mm in diameter.

From the DIC results, stress concentration is clear around the applied load points, both in horizontal stress (tensile) and in vertical stress (compressive). This observation is similar to the assumption from Model 1, presented in sections 3 and 4. For each sample, the DIC result showed a similar trend. This trend shows higher strains starting on the point of applied load and propagating to the center of the sample. This is expected as the plate is in direct contact with the sample. In order to avoid this stress concentration, some techniques are discussed in the ASTM D3967-16 [1].

Before comparing numerical, analytical and laboratory results, Model 1 and Model 2 are compared, considering both numerical and analytical solutions. The result for the vertical stress along the direction of the applied load is presented in Figure 5 for the numerical and analytical solutions, while the result for the horizontal direction is described in Figure 6.

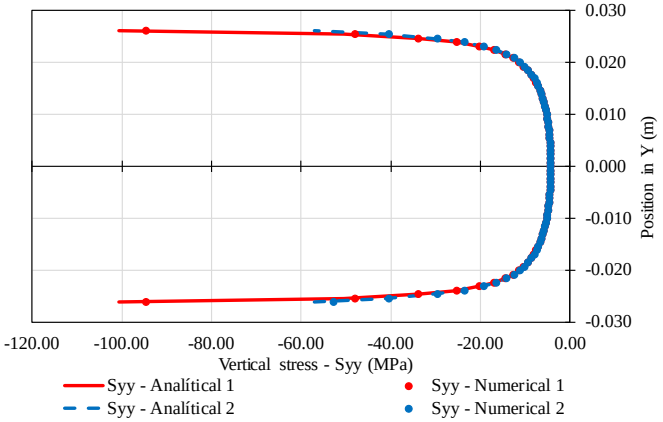

Figure 12: Vertical stress along the direction of the applied load

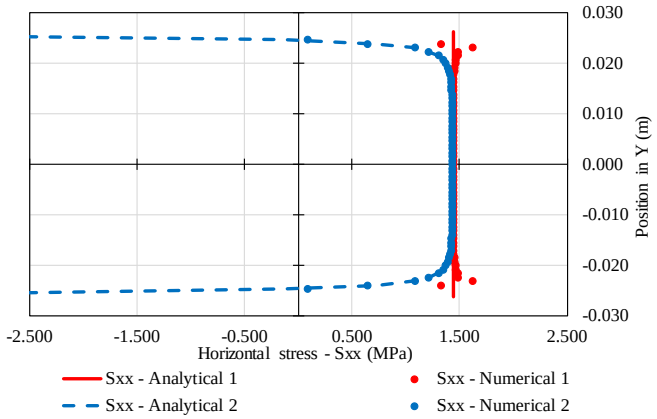

Figure 13: Vertical stress along the direction of the applied load

For the vertical stress, Model 1 and Model 2 are in agreement, as well as the numerical and analytical solutions. On the other hand, for the horizontal stress, Model 2 shows good agreement between analytical and numerical approaches while for Model 1 the results are quite different. In addition, the results from Model 1 and Model 2 are different in the horizontal stress.

The reason for the difference between the results from Analytical 1 and Numerical 1 is that the Analytical 1 considers a constant value in the horizontal stress along the direction of applied load. On the other hand, as Numerical 1 has a concentrated force, the stress field near the applied load changes because of stress concentration. From Figure 6, it is possible to conclude that when a concentrated load is applied to the sample, the maximum tensile stress is near the applied load, while for the distributed load the maximum tensile stress is in the middle of the sample.

To enhance the reliability of the DIC method, lab results are compared with the model with concentrated load (Model 1). Figure 7 displays the comparison between experimental (DIC), Analytical 1 and Numerical 1 results for the horizontal strain along the direction of applied load. Figure 8 exhibits the result for vertical strain.

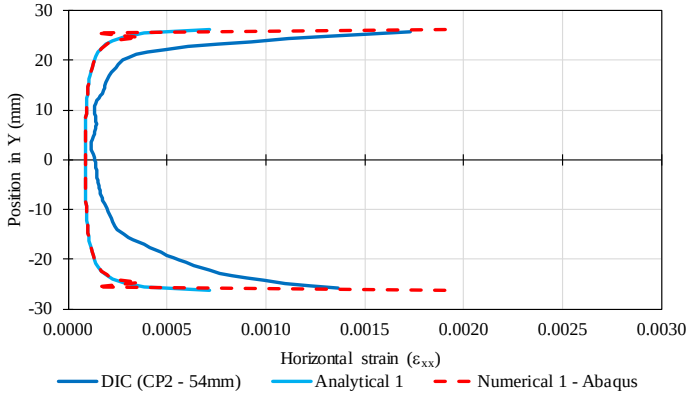

Figure 14: Horizontal strain along the direction of the applied load.

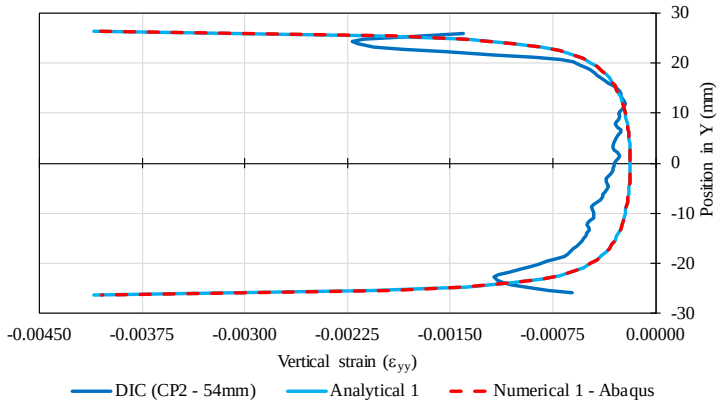

Figure 15: Vertical strain along the direction of the applied load.

It is observed from Figure 7 and Figure 8 that both Analytical 1 and Numerical 1 are in agreement with the laboratory results (DIC). This enhances the reliability of the DIC methodology applied in the Brazilian Splitting Test. In addition, it shows that the procedure used in the laboratory test is equivalent to applying a concentrated load in the sample, which would start the crack opening near the applied load.

6. CONCLUSION

The Brazilian Splitting Test was performed on four Indiana Limestone samples. DIC was adopted during the test to measure the development of displacement, and consequently, strain on these four samples. The stress and strain fields were also investigated by two numerical and two analytical solutions. By assessing the results from numerical and analytical models, good agreement was found. A difference is noticed when comparing the horizontal stresses near the point of applied load, as Model 1 considers a concentrated load, generating a stress concentration region, while Model 2 considers a distributed load.

When comparing Model 1 from analytical and numerical approaches with DIC, the results for the horizontal strain are very similar. This is due to the set-up used in the laboratory test. The piston was in direct contact with the sample, creating stress concentration near the point of applied load, as a concentrated load.

Another preliminary conclusion obtained from this work is regarding fracture initiation. When a concentrated load is applied on the sample, fracture tends to initiate near the point of applied load. This can be noticed by observing the high tensile strain near this point. On the other hand, fracture initiates close to the center of the sample when a distributed load is applied, as it presents a higher tensile strain around this point.

This study is currently under development, as it is important to confirm the numerical and analytical results by performing different laboratory tests, with set-ups capable of applying distributed load.

REFERENCES

[1] ASTM, “Standard Test Method for Splitting Tensile Strength of Intact Rock Core Specimens 1 D3967-08,” *ASTM Int. West Conshohocken, PA*, no. Reapproved, pp. 1–5, 2016.

[2] D. Li and L. N. Y. Wong, “The brazilian disc test for rock mechanics applications: Review and new insights,” *Rock Mech. Rock Eng.*, vol. 46, no. 2, pp. 269–287, 2013.

[3] Y. Han, B. Lai, H.-H. Liu, and H. Li, "Measurement of elastic properties in Brazilian disc test: solution derivation and numerical verification," *Geomech. Geophys. Geo-Energy Geo-Resources*, vol. 4, no. 1, pp. 63–77, 2018.

[4] X. Xu, S. Wu, Y. Gao, and M. Xu, "Effects of Micro-structure and Micro-parameters on Brazilian Tensile Strength Using Flat-Joint Model," *Rock Mech. Rock Eng.*, vol. 49, no. 9, pp. 3575–3595, 2016.

[5] Y. Ma and H. Huang, "Tensile strength calibration in DEM modeling," in *American Rock Mechanics Association*, 2017, p. 8.

[6] G. Walton, J. Arzúa, L. R. Alejano, and M. S. Diederichs, "A laboratory-testing-based study on the strength, deformability, and dilatancy of carbonate rocks at low confinement," *Rock Mech. Rock Eng.*, vol. 48, no. 3, pp. 941–958, 2015.

[7] Y. Jianhong, F. Q. Wu, and J. Z. Sun, "Estimation of the tensile elastic modulus using Brazilian disc by applying diametrically opposed concentrated loads," *Int. J. Rock Mech. Min. Sci.*, vol. 46, no. 3, pp. 568–576, 2009.

PROBABILISTIC ASSESSMENT OF THE LOAD CAPACITY OF FIBER REINFORCED CONCRETE

Marcello Congro [1] [2] , Cristian Mejía [2] and Deane Roehl [1] [2]

(1) Department of Civil and Environmental Engineering, Pontifical Catholic University of Rio de Janeiro, Brazil.

(2) Tecgraf Institute, Pontifical Catholic University of Rio de Janeiro, Brazil.

https://doi.org/10.21452/bccm4.2018.02.05

Abstract

Prediction and verification of material properties are essential to ensure the performance of most engineering structures. For those involving composite materials, as fiber reinforced concrete, the main target of probabilistic studies is not only related to the concepts of lifespan and durability, but also to how fiber distribution affects the macro material behavior. In practice, during the concrete mixing process, steel fibers are randomly distributed and dispersed under the cementitious matrix. According to fiber arrangement, orientation, and geometry, fractures can propagate along different paths. Computational simulations are employed to predict load capacity of a given structural system.

This paper presents the numerical modelling of direct tensile test for a fiber reinforced concrete. Cohesive interface elements are used to model the steel fiber behavior within the concrete matrix. These cohesive elements are placed at the edges of the solid elements, allowing fracture propagation. In order to reproduce the effect of the random distribution of steel fibers within the cementitious matrix, random values of elasticity modulus E and tensile strength σ_r are assigned to each solid and cohesive element, respectively. Marangon (2011) provides the mean and standard deviation values of the experimental data. Normal, lognormal and logistic distributions are considered for each parameter. Three distinct simulation sets are analyzed: (i) structured mesh with random elasticity modulus for each solid element, (ii) structured mesh with random tensile strength for each cohesive element, and (iii) unstructured mesh with random tensile strength for each cohesive element. For each set, the predicted fracture paths and load capacity present satisfactory results when compared to those obtained experimentally by Marangon (2011). All three-distribution functions lead to results in the expected experimental range. The results also show that the fiber dispersion and orientation contribute to the structural load capacity, increasing the structure durability.

1. INTRODUCTION

In recent years, engineers are creating and using software that perform numerical analysis and optimization techniques with high levels of accuracy. It is important to observe that, despite the robustness of the model, the predictions, assumptions or idealized conditions may or not reflect the real phenomena. Therefore, engineering decisions are typically analyzed considering some conditions of uncertainty and their respective associated risks.

For structures involving composite materials, as fiber reinforced concrete, the main goal of probabilistic studies is to determine how fiber distribution interferes in its properties. In practice, during the concrete mixing process, steel fibers are randomly distributed and dispersed under the cementitious matrix. According to fiber arrangement, orientation, and geometry, fractures can propagate along different paths. Therefore, computational simulations are employed to predict load capacity of a given structural system. In addition, the random layout can be modeled by considering the distinct probability distributions, such as normal, lognormal and logistic functions.

Through repeated simulations, it is possible to obtain a measure of sensitivity of system response to changes in the input parameters. Finally, after these simulations, it is determined which distribution best approximates the load-displacement curve obtained when mathematical models are employed in order to represent fracture propagation.

2. EXPERIMENTAL AND NUMERICAL PROCEDURES

The probabilistic analysis developed in this paper is based on the direct tensile test reported in the literature by Marangon (2011). Congro et al (2017) present a numerical analysis of this test by using numerical algorithms for fracture modeling, as the Interface Element Model and the Extended Finite Element Method (XFEM). Thus, the probabilistic analysis developed in this study gives continuity to the numerical simulation of a fiber reinforced concrete structure.

A rigid system with fixed ends was introduced in order to perform the direct tensile test. The apparatus for the experimental program comes down to the use of two accessories connected together by steel plates bonded to the specimen with an epoxy resin. Figure 1 indicates the schematic representation of the experimental test (Marangon, 2011).

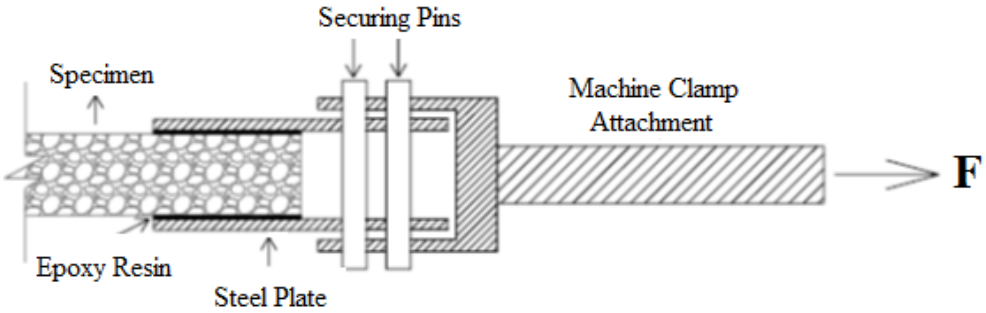

Figure 1. Schematic representation of the direct tensile test (Adapted from Marangon, 2011).

The direct tensile test reported by Marangon uses a prismatic specimen reinforced with steel fibers. This prismatic element is set at one of its edges and submitted to axial extension on the opposite side. The concrete matrix was discretized with quadrilateral elements (9.5 x 7.5 mm) under the assumption of linear elasticity. The numerical test was performed using arc-length control, with the adoption of an exponential softening model for the interface elements. Figure 2 presents the element mesh and the input parameters for the simulation.

Fiber Reinforced Concrete	
E (GPa)	35,77
v	0,2

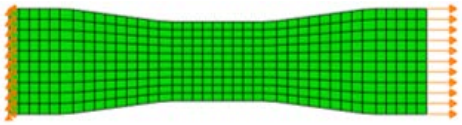

Fracture	
σ_r (MPa)	4,65
α	1,3
$\Delta\delta$ (mm)	4,62

Figure 2. Element mesh and input parameters for the numerical analysis (Congro et al, 2017).

All results from the numerical simulations considering the properties above are indicated in Congro et al (2017).

3. FIBER ARRANGEMENT IN REINFORCED CONCRETE

In recent decades, fiber reinforced composites have been widely used in engineering structures and in high technology areas, especially due to their excellent mechanical properties. The addition of ductile fibers in the brittle matrix can significantly improve the brittleness of the matrix material. The hardening stress is determined considering the effects of the individual fibers along the structure's rupture plan, according to the crack stress-aperture curve.

The mathematical formulations employed to compute the critical fiber volume in the reinforced concrete are not checked under practical conditions, since this formulation considers that fibers are continuous and perfectly aligned to the main stress axis. In practice, fibers are discontinuous and randomly distributed in the concrete matrix. Thus, their actual behavior in concrete is different from that predicted by the formulations of Aveston, Cooper and Kelly (1971).

The variability in the cross-section of the fibers, for example, will provide deviations in their area, and consequently the force that each fiber can withstand. The variations of the fiber stiffness in the concrete matrix also influence the strength properties of the material, providing different behaviors for the composite material according to the random dispersion of the fibers (Figure 4). The elasticity modulus is variable not only for steel fibers, but also can be extended to any other fiber type, in particular to natural fibers, such as sisal and bamboo.

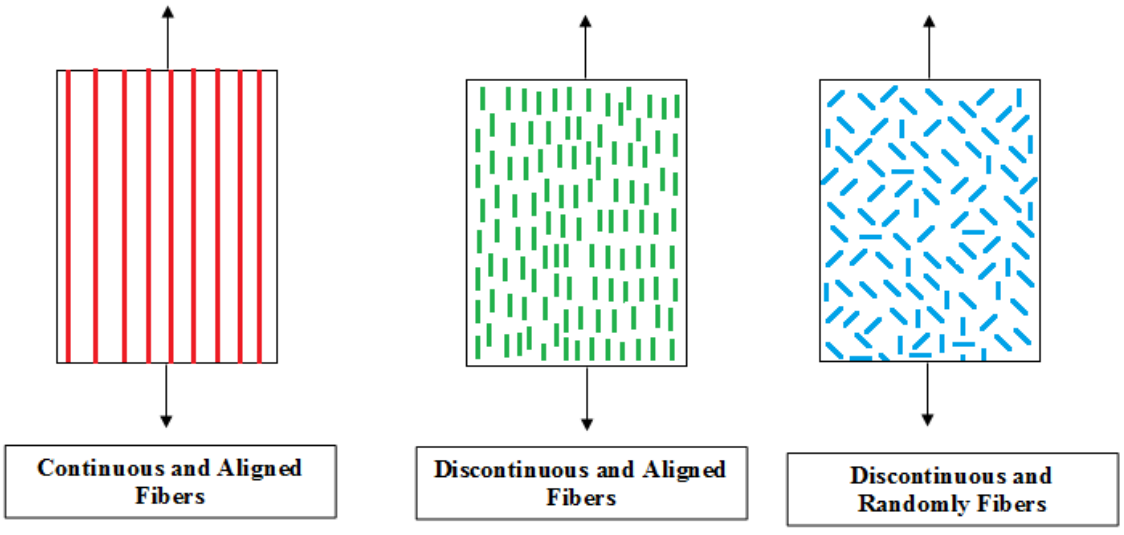

Figure 4. Representation of fibers and their respective arrangement.

In this way, the random values of stiffness and tensile strength used in the numerical simulations represent distinct values of fiber parameters in the concrete matrix. These

arrangements gather random variables with known or assumed probability distributions. It is possible, in this way, to carry out repeated simulations, using in each of them a particular set of values of the random variables, originated according to the respective functions of a probability distribution. Thus, the results of the simulations are statistically variable, converting response distribution rules into response variables, allowing predictions of the structural system behavior.

4. PROBABILISTIC ANALYSIS

For the analysis of the load capacity of the reinforced concrete specimen with fibers, three probability density functions that best fit numerical modeling were considered: normal distribution, lognormal distribution and logistic distribution. These probability functions were chosen because Marangon (2011) explicitly provides the mean and standard deviation values of the samples tested for the direct tensile test. In this sense, the random generation of the material parameters was easier and more intuitive.

The main idea of the probabilistic study of this paper is to reproduce the direct tensile test in a finite element analysis. Secondly, using a sub-routine developed in *MATLAB*, random values of elasticity modulus 'E' and tensile strength σ_r are generated, according to the probability function that governs the random distribution of these parameters. These values will be assigned to each of the elements in the central region of the mesh, given the expectation of fracture occurrence in this region. Figure 5 exhibits the computational model that replicates Marangon's direct tensile test.

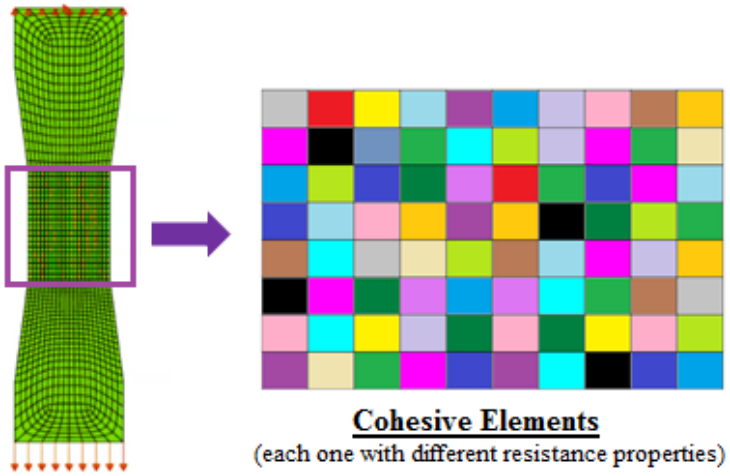

Figure 5. Computational model and detail of the central region of the specimen where the fiber properties are modified.

Two strength properties of the fiber reinforced concrete were modified: the elasticity modulus 'E' of the random fibers and, subsequently, the tensile strength σ_r. In this way, three distinct simulation sets were developed: (i) random generation of stiffness values for each element using a quadrangular structured mesh, (ii) random generation of tensile strength for each element using a quadrangular structured mesh and (iii) random generation of tensile strength for each element using unstructured mesh. The third simulation set was also included in the analyses since the fracture propagation path is better approximated through a non-structured mesh, representing accurately the structure behavior.

4.1. First Simulations Set

The first simulation sets used random values of elasticity modulus E, following normal, lognormal and logistic distributions. These numerical values were properly associated with the elements in the central region of the specimen. The analyses were repeated at least five times for each distribution. Table 1 summarizes the mechanical properties of the fiber reinforced concrete used throughout these simulations.

Table 1 – Fiber reinforced concrete mechanical properties for probabilistic simulations of Simulation Sets I.

Fiber Reinforced Concrete	
E (GPa)	Variable
v	0.2
σ_r (MPa)	4.65

Figure 6 presents the damage evolution variable for some simulation rounds, comparing the fracture propagation with the experimental results. This figure brings the best results for each distribution, although more rounds were performed during the analysis.

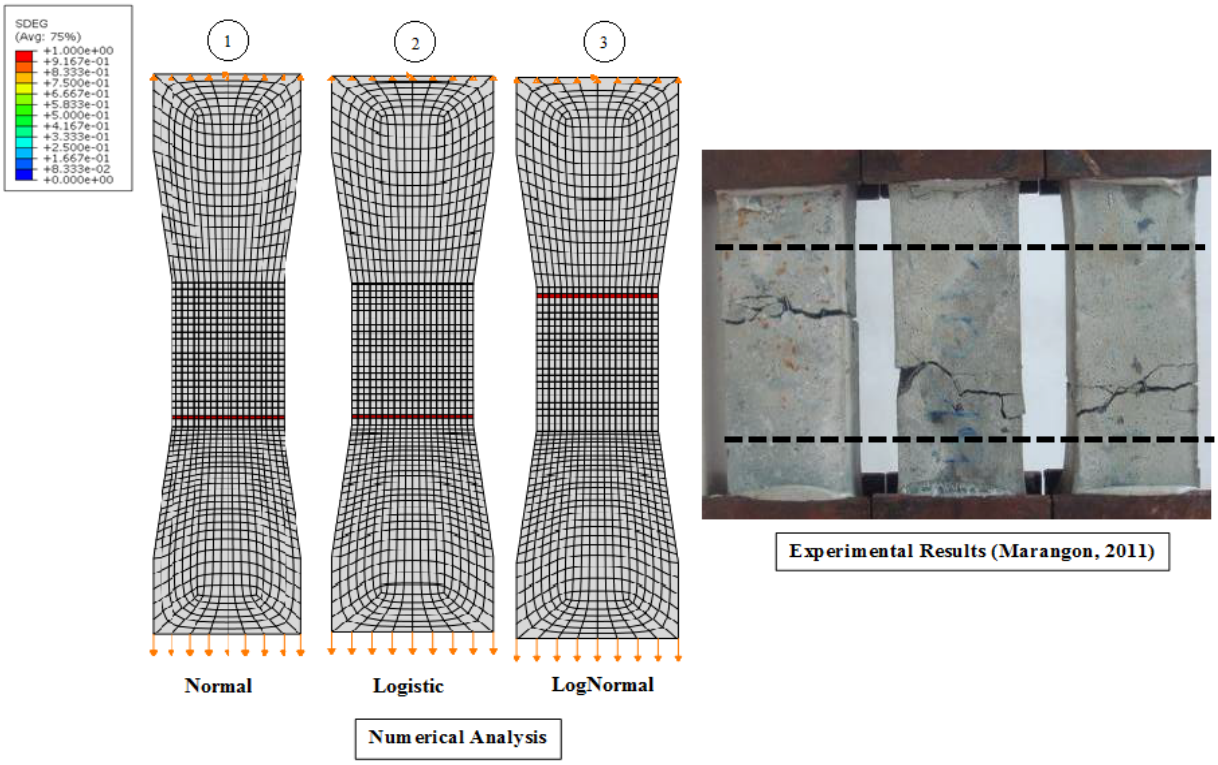

Figure 6. Comparative analysis of fracture propagation for the best simulation rounds in Simulation Sets 1.

4.2. Second Simulation Sets

The second simulation sets generated random values for the tensile strength σ_r, following normal, lognormal and logistic distributions. These numerical values were associated with the elements in the central region of the specimen. The analyses were repeated at least five times for each distribution. Table 2 summarizes the mechanical properties of the fiber reinforced concrete used throughout these simulations.

Table 2 – Fracture mechanical properties for probabilistic simulations of Set 2.

Fracture	
σ_r (MPa)	Variable
α	1.3
Δδ (mm)	4.62

Figure 7 presents the damage evolution variable for some simulation rounds, comparing the fracture propagation with the results obtained experimentally. These are the best matches for each distribution, although more rounds were performed.

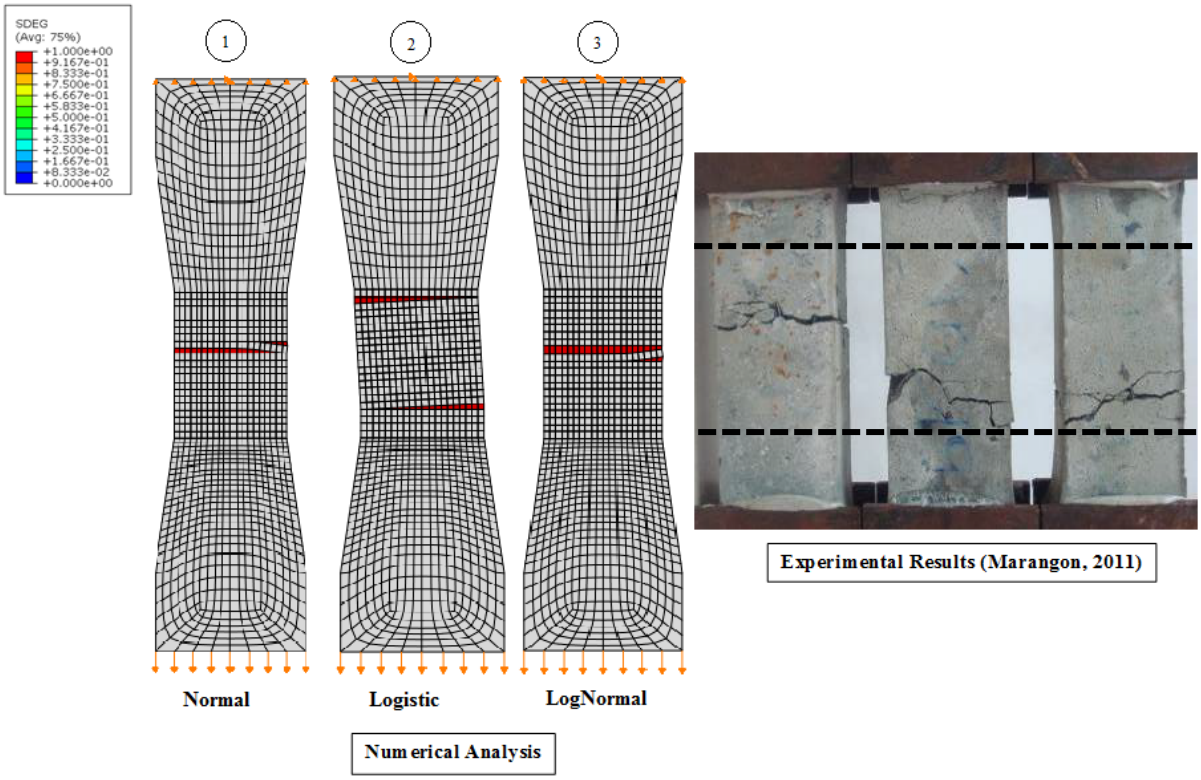

Figure 7. Comparative analysis of fracture propagation for the best matches to experimental data in Set 2.

4.2. Third Simulation Sets

The third simulation sets generated random values of tensile strength σ_r, following normal, lognormal and logistic distributions for a non-structured finite element mesh. These numerical values were associated with the elements in the central region of the specimen. The analyses were repeated at least five times for each distribution. The fracture mechanical properties are the same from the second simulation sets.

Figure 8 presents the damage evolution variable for some simulation rounds, comparing the fracture propagation with the results obtained experimentally in the central area. This figure shows the best results for each distribution, although more rounds were performed.

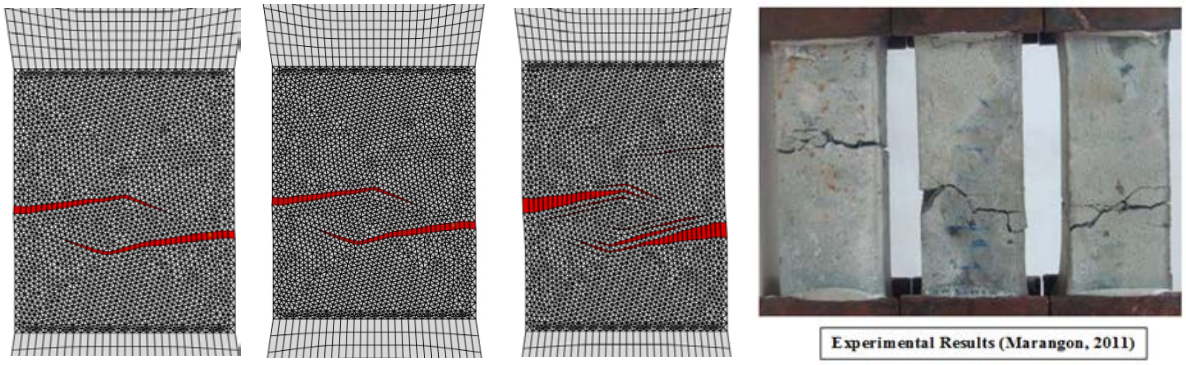

Figure 8. Fracture propagation for the best simulation rounds the third sets.

Finally, Figure 9 compares the load-displacement curves for all three-simulation sets analyzed during this paper. Each plot exhibits the probability distribution that best represents the structure behavior during the analysis.

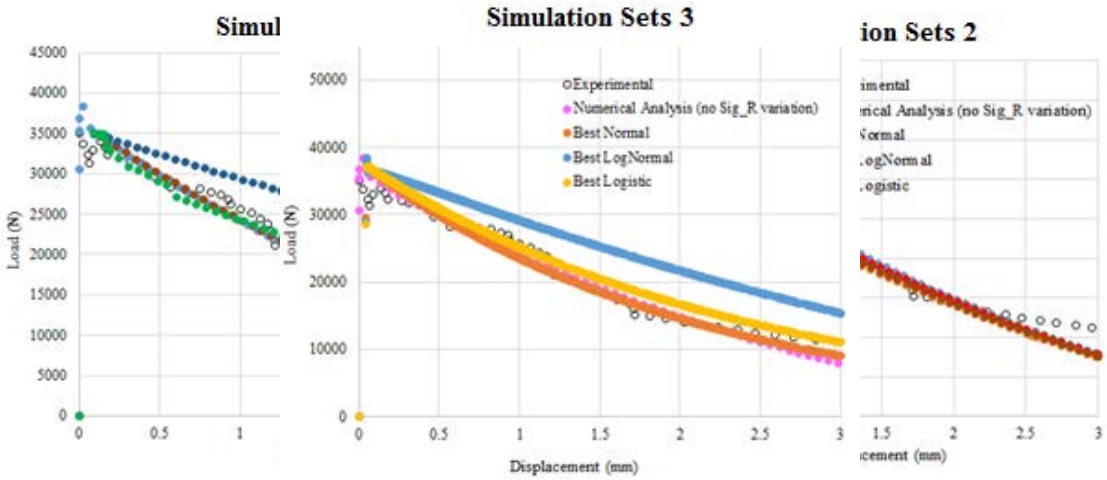

Figure 9. Load-displacement curves for each studied sets.

5. CONCLUSIONS

This probabilistic study was carried out in order to verify the influence of the dispersion and orientation of the steel fibers in the concrete matrix. It is important to emphasize that the addition of fibers in concrete structures reduces the effects of crack propagation in the material, due to the phenomenon of the shear stress transfer. The many possibilities of orientation of steel fibers produced some distinct behaviors in the load-displacement curves of the specimen. This effect is due to the arrangement of the fibers, which can take place in multiple directions, favorable or not to the applied load. Three distribution functions define the parameter values, randomly modifying each element of the central region of the part.

In a first simulation set, a structured mesh was used and the elasticity modulus E was modified for each of the elements of the central region of the specimen. This region has undergone a greater refinement, since it is where the fracture process occurs in this type of test. The second simulation set used a structured mesh, modifying the tensile strength σ_r . Finally, the third set of simulations maintained the same procedure of the second set, adopting a non-structured element mesh, aiming at allowing more generally the fracture paths.

All three-distribution functions lead to results in the expected experimental range. The results also show that the fiber dispersion and orientation contribute to increase the structural load capacity. The third numerical model reached good levels of accuracy, due to the adoption of an unstructured mesh capable of reproducing the crack propagation pattern in the reinforced concrete material, as reported by the experimental procedures. In addition, fibers constitute an efficient reinforcement for the concrete, and their inclusion reduces the appearance of cracks, increasing structure durability. In this sense, the numerical simulation using cohesive elements allied to probability functions becomes an attractive approach to predict fiber reinforced concrete behavior.

REFERENCES

[1] ABAQUS 2011. Abaqus Documentation 6.14. Dessault Systèmes, 2011.
[2] American Concrete Institute. ACI 544.1R-96 Report on Fiber Reinforced Concrete. ACI Committee 544 (Reapproved 2009), Detroit, United States, 2009.
[3] Ang, A.; Tang, W.H. 'Probability Concepts in Engineering Planning and Design – Decision, Risk and Reliability'. John Wiley & Sons, v. 2, United States, 1984.
[4] Callister, William D. 'Materials Science and Engineering: An Introduction'. John Willey & Sons, Inc. New York, United States, 2007.
[5] Congro, M.; Mejia, C.; Roehl, D. 'XFEM and Interface Element Models Applied to Fracture of Fiber Reinforced Concrete Beams'. XXXVIII CILAMCE – Ibero Latin-American Congress of Computational Methods in Engineering. Florianópolis, Brazil, 2017.
[6] Fischer, A. C. 'Introduction to contact mechanics'. Springer, 2nd edition, 2007.
[7] Kutschera, M & Breiner, T & Wiese, H & Leitl, M & Braeu, Michael. Nano-modification of Building Materials for Sustainable Construction, p. 275-280, 2009.
[8] Marangon, E. 'Caracterização material e estrutural de concretos autoadensáveis reforçados com fibras de aço'. PhD Thesis. Federal University of Rio de Janeiro, Rio de Janeiro, Brazil, 2011.
[9] Naaman A. E., Hammoud H. 'Fatigue characteristics of high performance concrete'. Cement and Concrete Composites, v.20: p. 353-363, 1998.

ACKNOWLEDGEMENTS

The authors would like to thank Tecgraf Institute and Pontifical Catholic University of Rio de Janeiro for all support and assistance during the execution of this project.

MECHANICAL BEHAVIOUR OF POLYPROPYLENE AND STEEL FIBER SELF-CONSOLIDATING CONCRETE

Vitor Moreira de Alencar Monteiro(1) and Flávio de Andrade Silva(1)

(1) Department of Civil and Environmental Engineering, Pontifícia Universidade Católica do Rio de Janeiro, Brazil

https://doi.org/10.21452/bccm4.2018.02.06

Abstract

This article presents the results of an experimental investigation on the mechanical behavior of a self-consolidating concrete reinforced with steel and polypropylene fibers. Hooked end steel fibers were used as reinforcement in fiber volume fractions of 0.25%, 0.50% and 1.00%. Polypropylene fibers were used as reinforcement in volume fractions of 0.33%, 0.66% and 1.10%.

Pre-notched concrete prims were tested under three point bending tests. The tests were controlled by the crack mouth opening displacement in order to have a better analysis of the post cracking regime. Although the use of steel fibers promoted higher values of flexural residual stress due to its geometrical and material properties, the addition of polypropylene fibers promoted higher residual resistance for higher values of CMOD.

The mechanical behavior of the addition of the fibers were explained by pullout tests. This significant difference is associated not only with the fiber type, but also with the fiber anchorage. While the polypropylene fiber in concrete matrix is associated only with the interfacial shear stress, the hooked end steel fiber presents another component associated with the anchorage of the hook, promoting higher values of pullout resistance.

1. INTRODUCTION

The addition of fibers to enhance the mechanical behavior of concrete has been widely used for many years, but its practical use in structural engineering applications still rely on the development of technical standards to guarantee its safety. While the use of fibers considerably improves mechanical properties such as ductility and crack-width control [1], it does not change the compressive strength and the modulus of elasticity [2] of the composite.

This improvement is associated with the difficulty of crack opening and propagation. The fibers act as a bridge mechanism across the crack surfaces, promoting a strain-hardening or a softening behavior after the appearance of the first crack. This effect is dependent on the fiber-matrix interface, fiber tensile strength and fiber geometry [1]. The bridging mechanism presents not only an improvement in toughness, but also promotes a long-term residual resistance [3].

FRC has been widely used in many engineering applications such as stabilization of rock excavations. Fiber reinforced shotcrete, in combination with other support elements, can provide effective ground support after blasting or excavation with the development of flexural strength and toughness [4]. The advantage of fiber reinforced shotcrete over shotcrete with wire mesh is associated with labor and time saving, material reduction and improved safety.

Steel fibers is the more conventional reinforcement used due to its high elasticity modulus, which promotes strength in high volume fractions and post-peak load carrying capacity [5]. The synthetic fibers also showed important improvements associated with strain capacity and crack control of fiber reinforced concrete despite its low elasticity modulus [6]. Hence, the use of polypropylene fibers can be an alternative to steel fibers when the post cracking residual strength is not the main objective of the objective of the fiber reinforcement.

Pajak and Ponikiewski [7] conducted a study on the flexural behavior of self-compacting concrete reinforced with straight and hooked end steel fibers. The post-peak behavior of the composite was analyzed through three point bending tests in accordance with RILEM TC 152-TDF [8] and EN14651 [9]. While the deflection-hardening response was observed the self-compacting concrete was reinforced with the hooked end fibers, the addition of straight fibers reported a softening response after reaching its peak. The increase of fiber volume ratio was responsible for increasing the flexural tensile strength with a higher increase of fracture energy for the hooked end steel fiber.

On the other hand, the addition of synthetic fiber in concrete reported distinct results when compared with steel fibers. Cifuentes et al. [6] showed that the presence o synthetic fiber in the concrete mix increased the mechanical properties and ductility. In lower strength concrete, the effect of the fiber is more remarkable due to lower stresses in the cohesive zone. Therefore, the bridge effect with presence of the fibers showed a greater influence.

The effect of steel and polypropylene fibers on the mechanical properties of the self-consolidating FRC are addressed in this work. Three fiber volume fractions were tested for each fiber type. All the compositions were analyzed by bending tests based on the European standard EN 14651 [9]. Finally, pullout tests were carried on both polypropylene and hooked end steel fibers with the aim to better understand the bond mechanism in the concrete matrix.

2. GENERAL SPECIFICATIONS

2.1 Materials

The cementitious materials used in the production of the self-compacting concrete were the Brazilian cement type CPV, fly ash and silica fume. Two classes of particle size of river sand were used: one ranging from 0.15 mm to 4.8 mm (S1) and the other ranging from 0.15 mm to 0.85 mm (S2). Coarse aggregate with maximum diameter of 9.5 mm, silica flour (ground quartz) and superplasticizer (Glenium® 51) were also mixed together with the other materials. The average compressive strength after 28 days was 73 MPa and the obtained slump spreading was 750 mm for a water/cement ratio of 0.5. For more information on the mix procedure and matrix mechanical behavior refer to Pereira [10] and Rambo [11].

2.2 Fiber Types

One steel fiber with hooked end (SF) and one polypropylene fiber (PPF) were used as reinforcement. The steel fiber (SF) presented a length of 30 mm with an aspect ratio of 45 (d = 0.62 mm) while the PPF presented a length of 40 mm and aspect ratio of 74 (d = 0.54). Other properties of the used fibers, according to their manufacturers, are presented in Table 1.

Table 1: Fiber Properties.

Properties	SF	PP
View		
Fiber Type	Dramix 3D 45/30	TUF Strand SF
Fiber Shape	Hooked end	Monofilament
Length (mm)	30	40
Diameter (mm)	0.62	0.54
Aspect Ratio	45	74
Tensile Strength (MPa)	1270 +/- 7.5%	600-650
Elastic Modulus (Gpa)	210	9.5
Density (g/cm³)	7.85	0.92

2.3 Mixing Procedure

To evaluate the effects of the fibers on the mechanical properties of the composite, seven different mixtures were produced. The first one associated with the matrix without fibers and three mixtures with steel fiber volume fractions of 0.25% (20 kg/m³), 0.50% (40 kg/m³) and 1.00% (80 kg/m³) named, respectively, as C0.25%SF, C0.50%SF and C1.00%SF. Moreover, other three mixtures were tested with polypropylene fiber volume fractions of 0.33% (3 kg/m³), 0.66% (6 kg/m³) and 1.10% (10 kg/m³) named as C0.33%PPF, C0.66%PPF and C1.10%PPF. The amount of water, sand, cement and the other supplies for the seven mixtures is presented at Tables 2 and 3. For pullout tests, the matrix composition was produced without the total amount of coarse aggregate.

The mixing procedure was conducted through five main stages. First, all the aggregates (sands S1, S2 and coarse aggregate) were mixed together with 70% of the water for 1 minute with the help of a concrete mixer (previously wet). All additives (silica fume, fly ash and silica flour) were also added to the mix and blended for 1 minute. Afterwards the total amount of cement was added and mixed for another minute. All the superplasticizer was added to the mix with the remaining water and then blended with the rest of the materials for 10 minutes. Finally, the total amount of fibers was mixed for another 5 minutes. The specimens were cured for 28 days at room temperature of 24.4 ºC and 65.7% of humidity before testing.

Table 2: Mix composition of the matrix and steel fiber reinforced concrete.

Constituent	Mixtures			
	Matrix	C0.25%SF	C0.5%SF	C1.00%SF
Coarse aggregate (G) (kg/m³)	492.04	485.29	478.54	465.04
Sand (S1) (kg/m³)	826.71	826.71	826.71	826.71
Sand (S2) (kg/m³)	99.60	99.60	99.60	99.60
Silica Mesh 325 (SM) (kg/m³)	70	70	70	70
Cement (C) (kg/m³)	360	360	360	360
Fly Ash (FA) (kg/m³)	168	168	168	168
Silica Fume (SF) (kg/m³)	45	45	45	45
Superplasticizer (SP) (%)	6.0%	6.0%	6.0%	6.0%
Water (W) (kg/m³)	155.65	155.65	155.65	155.65
SF (kg/m³)	0	20	40	80
PPF (kg/m³)	0	0	0	0
Water/Cement ratio	0.50	0.50	0.50	0.50

* Sand (S2): Sand (S1) with diameter less than 0.85 mm.

Table 3: Mix composition of polypropylene fiber reinforced concrete.

Constituent	Mixtures		
	C0.33%PPF	C0.66%PPF	C1.10%PPF
Coarse aggregate (G) (kg/m³)	483.24	474.43	462.69
Sand (S1) (kg/m³)	826.71	826.71	826.71
Sand (S2) (kg/m³)	99.60	99.60	99.60
Silica Mesh 325 (SM) (kg/m³)	70	70	70
Cement (C) (kg/m³)	360	360	360
Fly Ash (FA) (kg/m³)	168	168	168
Silica Fume (SF) (kg/m³)	45	45	45
Superplasticizer (SP) (%)	6.0%	6.0%	6.0%
Water (W) (kg/m³)	155.65	155.65	155.65
SF (kg/m³)	0	0	0
PPF (kg/m³)	3	6	10
Water/Cement ratio	0.50	0.50	0.50

* Sand (S2): Sand (S1) with diameter less than 0.85 mm.

3. TEST PROGRAM

3.1 Three Point Bending Test

For the three point bending test, three specimens with 150 mm x 150 mm x 550 mm were produced for each concrete mix in accordance with EN14651 [9]. The span between supports was 500 mm and the bottom side of each sample was notched with a 25 mm depth using a 3 mm diamond saw. These measurements and details are presented in Figures 1(a) and 1(b).

The tests were carried on using a MTS servo-controlled hydraulic testing machine with a closed loop type of control and a load cell of 100 kN. The tests were conducted at a constant rate of 0.10 mm/min and controlled by the CMOD (Crack Mouth Opening Displacement) using a clip-gauge and limited to 4 mm opening.

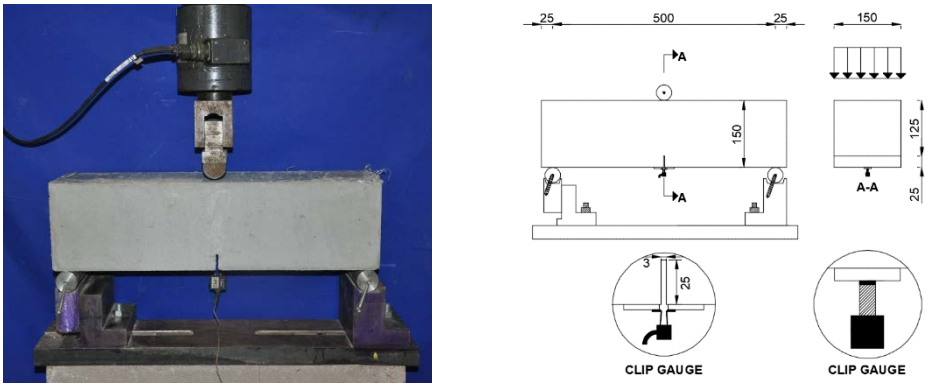

(a) (b)

Figure 1. (a) Three point bending test setup. (b) Setup details in accordance with EN14651 [9]. All dimensions in mm.

3.2 Pullout Tests

The pullout tests were performed using a MTS 810 servo-controlled hydraulic-system, with 250 kN capacity. With a 2.5 kN cell attached to the crosshead, the tests were controlled by the internal LVDT displacement at a rate of 1.5 mm/min. The tests were limited to a maximum displacement of 25 mm. Ten cylindrical specimens measuring 20 mm of diameter and 25 mm of embedment (Lf) were prepared for each tests series. The polypropylene fiber was pulled out with a rigid plate fixed with two bolts and the hooked-end steel fiber was clamped with a metal claw. The specimens were fixed at the bottom inside a metal cup. The complete test setup for both fibers is presented in Figures 2(a) and 2(b). For more information about the pullout tests refer to Castoldi [12].

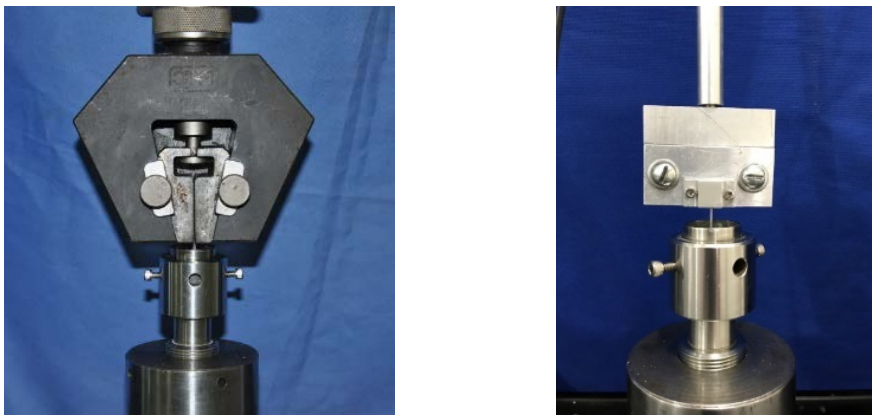

(a) (b)

Figure 3. Pullout test setup for (a) steel and (b) polypropylene fibers.

4. DISCUSSION AND ANALYSIS

The presented stress-CMOD curves at Figures 4(a), 4(b) and 4(c) report the flexural response obtained on plain prisms, specimens reinforced with 0.25%, 0.50% and 1.00% of volume fractions of hooked end steel fibers and prisms reinforced with 0.33%, 0.66% and 1.10% of polypropylene fiber. Each stress-CMOD curve is associated with the average result of three tested specimens. The mechanical behavior of plain self-compacting concrete (specified as 'Matrix' in Fig. 4) is associated with a brittle material with linear elastic zone before cracking followed by a fast stress decrease with the increase in CMOD.

The use of hooked end steel fibers significantly enhanced the mechanical behavior of the composite, especially the residual stress and tenacity. The use of 0.25% and 0.50% of SF presented a similar behavior with a strain-softening response after reaching its peak. However, the addition of 1.00% of steel fiber in concrete was responsible for a strain-hardening behavior before reaching the ultimate stress capacity.

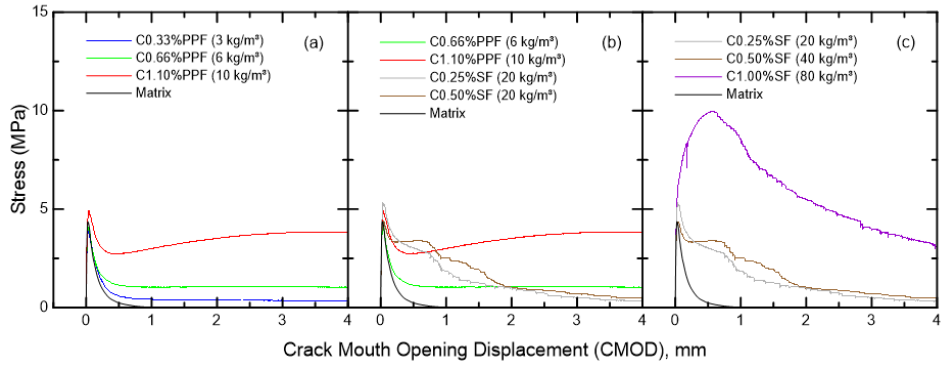

Figure 4. Results from three point bending tests: (a) SCC with different volume ratios of polypropylene fibers. (b) Comparison between polypropylene and steel fiber SCC. (c) SCC with different volume ratios of hooked end steel fibers.

As expected, the post-peak stage of the stress-CMOD curve differs much when comparing steel with polypropylene fibers. Although the addition of synthetic fibers indicated a sudden drop after the peak load, the residual strength remained almost constant after reaching CMOD levels of 0.5 mm. The 1.10% polypropylene fiber reinforcement indicated a slight increase in resistance when reaching higher CMOD levels.

It possible to see through Figure 4(b) that the use of high volume fractions of polypropylene can result in higher residual flexural stress when compared with the addition of steel fibers. Especially for CMOD values greater than 2 mm, the use of 0.66% and 1.10% PPF in concrete reports higher values of flexural resistance.

The mechanical behavior polypropylene and steel fiber reinforced concretes can be explained by the bond between of the fiber in the concrete matrix. Figure 5(a) presents the mean curve of the pullout tests for both SF and PPF. In the case of the PPF, the pullout load does not present a sudden drop of resistance after reaching the peak load, it exhibits an unstable growth until reaching its maximum value at 14 mm of slip. The almost constant pullout strength with increasing slip promotes the post-peak behavior of the PPF reinforced concrete.

The significant difference in the residual resistance is associated with the fiber anchorage. The anchorage effect provided by the hook plays the leading role in increasing the pullout load [1], improving the the post-peak resistance of the composite. Figure 5(b) illustrates the difference in the interfacial shear mechanism between the PPF and SF.

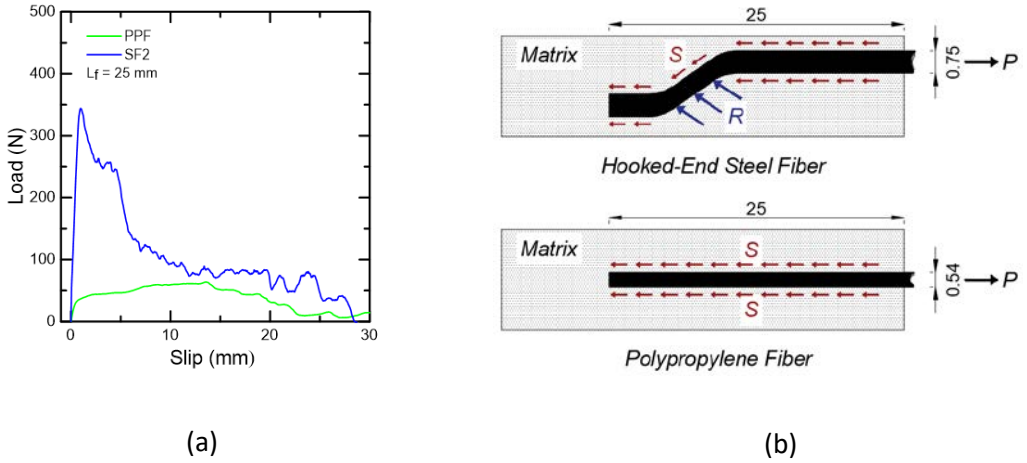

Figure 5. (a) Pullout results. (b) Bond of hooked-end steel and polypropylene fibers in the concrete matrix, where S is the interfacial shear stress, R is the normal component due to the mechanical anchorage of the hook and P is the pullout load. All dimensions in mm.

5. CONCLUSIONS

The following general conclusions can be drawn from the present work:

- The use of lower volume fractions (0.25% and 0.50%) of steel fibers in concrete promotes similar flexural resistance after peak when compared with the addition of 0.66% and 1.10% of polypropylene fiber. While the use of steel fibers presents a rapid decrease of strength after peak, the PPF reinforced concrete reported constant residual strength with increasing CMOD. Hence, the use of PPF in concrete promoted higher residual strength for higher values of CMOD.

- The main difference between polypropylene and hooked end steel fibers reinforcements can be explained through the bond of the fibers in concrete. The PPF presented almost constant strength with increasing slip, while the pullout tests with SF presented a gradual decrease in load after reaching peak. The higher pullout strength of the hooked end steel fiber is also associated with the presence of the hook, which promotes a stronger bond due to its mechanical anchorage.

REFERENCES

[1] A. Bentur, S. Mindess, “Fiber reinforced cementitious composites”. Second Ed: Taylor & Francis, London, 2007.
[2] A. Alsalman, C. N. Dang, G. S. Prinz, and W. M. Hale, “Evaluation of modulus of elasticity of ultra-high performance concrete,” Constr. Build. Mater., vol. 153, pp. 918–928, 2017.
[3] A. E. Naaman, “High Performance Fiber Reinforced Cement Composites,” High Perform. Constr. Mater. Sci. Appl., no. 5, pp. 91–153, 2008.
[4] J. M. Yang, J. K. Kim, and D. Y. Yoo, “Performance of shotcrete containing amorphous fibers for tunnel applications,” Tunn. Undergr. Sp. Technol., vol. 64, pp. 85–94, 2017.
[5] A. E. Naaman and H. W. Reinhardt, “Proposed classification of HPFRC composites based on their tensile response,” Mater. Struct. Constr., vol. 39, no. 289, pp. 547–555, 2006.
[6] H. Cifuentes, F. García, O. Maeso, and F. Medina, “Influence of the properties of polypropylene fibres on the fracture behaviour of low-, normal- and high-strength FRC,” Constr. Build. Mater., vol. 45, pp. 130–137, 2013.
[7] M. Pająk and T. Ponikiewski, “Flexural behavior of self-compacting concrete reinforced with different types of steel fibers,” Constr. Build. Mater., vol. 47, pp. 397–408, 2013.
[8] RILEM TC 162-TDF. Test and design methods for steel fiber reinforced concrete, final recommendations," Mater. Struct. Constr., vol. 36, pp. 579–582, 2002.
[9] BS EN 14651, “Test method for metallic fibred concrete — Measuring the flexural tensile strength (limit of proportionality (LOP), residual),” Br. Stand. Inst., vol. 3, pp. 1–17, 2005.
[10] E. Pereira, "Influência de fibras de aço no comportamento mecânico e nos mecanismos de fissuração de concretos autoadensáveis," MSc dissertation (2017), 170 p. Rio de Janeiro, Brazil: PUC-Rio.
[11] D.A.S. Rambo, “Concretos autoadensáveis reforçados com fibras de aço híbridas: aspectos materiais e estruturais,” MSc dissertation (2012), 185 p. Rio de Janeiro, Brazil: Universidade Federal do Rio de Janeiro (COPPE/UFRJ).
[12] R. Castoldi, “Propriedades mecânicas e durabilidade de concretos reforçados com fibras de polipropileno e sisal,” MSc dissertation (2018), 147 p. Rio de Janeiro, Brazil: PUC-Rio.

USE OF CACTUS WOOD *CEREUS JAMACARU* AS AGGREGATE IN LIGHTWEIGHT BIOCONCRETE PRODUCTION

Silveira, M. N. L. [(1)], Menali, L. O. [(1)], da Gloria, M. Y. R. [(2)], Toledo Filho, R. D. [(2)] and Ferreira, S. R. [(1)]

(1) Civil Engineering Department, Universidade Federal de Lavras, Brazil

(2) Civil Engineering Department, COPPE, Universidade Federal do Rio de Janeiro, Brazil

https://doi.org/10.21452/bccm4.2018.02.07

Abstract

It is constant, especially in the civil construction sector, the search for new material sources that meet the assumptions of sustainable development. In this way, the cacti are pointed as a good alternative. Therefore, the objective of the present research was to develop and characterize physically and mechanically lightweight bioconcretes produced with Cereus wood from this lignocellulosic source. *Cereus jamacaru* wood was used after washing in hot water (at 80° C). In the studied matrix, Portland Cement CP V-ARI was used and a water-to-cement ratio of 0.4. To accelerate the cement hydration reactions 3% (relative to the cement mass) of calcium chloride was added. Mixtures with two types of wood particles classified as green and brown were produced and for both cases varying the percentage of compensation water (100 and 200%), cement-to-wood ratio (3,4 and 7) and moulding method (compacting with metal rod or not). A flow table test was used to characterize the fresh mixtures. The mechanical characterization was performed through uniaxial compression test. The density of the composites with the brown particles varied from 892 to 1452 kg/m³ and the compressive strength from 3.38 to 10.51 MPa. The blends with green particles reached between 872 and 1347 kg/m³ of density and between 1.72 and 8.94 MPa of compressive strength. The mixtures with higher cement-to-wood proportions and lower amount of compensating water reached higher compressive strength. The results show that Cactus Wood can be used in the production of bioconcretes with good properties and varied applications in civil construction.

Keywords: Lightweight concrete; Bioconcrete; Cactus Wood; Sustainability; Construction.

1. INTRODUCTION

According to da Gloria [1], the construction industry is one of the great generators of waste and a major consumer of natural resources, and therefore, the search for new resources and technologies able to cause less aggression to the environment is urgent. In this context, the use of alternative lignocellulosic sources for the development of materials is necessary to cause less environmental impacts [2][3]. The main advantages of the lignocellulosic materials are carbon trapping, depending on the application, and the fact that they are renewable.

Cement composites of vegetable biomass are products basically composed of mineral binders combined with vegetal aggregates and other additives [4]. Beraldo [4], also states that the main advantages of using composites are the high availability of raw materials, which are renewable, the lightness of the final product, between 400 and 1500 kg/m³. Others advantages are the resistance to biodegradable agents, good dimensional stability the resistance to impact and the satisfactory mechanical, thermic and acoustic properties. According to Beraldo [5], in some applications, these materials can efficiently replace traditional materials in the construction.

A challenge in the production of cement composites with lignocellulosic materials, which may be called bioconcretes, is the chemical incompatibility between cement and vegetable biomass that can lead to retardation / inhibition of cement hydration reactions. According to Simantupang et al. [6], the extractives present in the wood are the main responsible for this impediment of cement solidification. Beraldo [4] explained that no vegetal species can be added in its natural state to the cement, since the chemical constituents of the plant are very sensitive to the alkaline environment of the cement matrix. The author also showed the importance and effectiveness of applying preliminary treatments in the biomass allied to the use of handle accelerators. In his studies he obtained satisfactory setting and hardening results by using the Brazilian Portland cement CPV-ARI, and 3% of calcium chloride, with biomass previously washed with hot water to reduce the extractives amount.

The water-to-cement ratio is a variable of extreme influence on the resistance of the bioconcrete and according to Andreola [7] the cement hydration will occur completely only if this ratio is greater than 0.38. Because of the high water absorption of the biomass, it is important to have enough water to keep the biomass saturated, to allow the cement hydration and also to guaranty the consistence of the bioconcrete. Another important factor to be analyzed in the production of bioconcrete is the granulometry of the lignocellulosic material that will be used as well as the particle format. Beraldo [5] verified the lack of adhesion between bamboo and cement paste when whole stems of large diameter bamboos, which do not present side shoots, were used. Latorraca [8] concluded that granulometry has a significant influence even in cement pickling and solidification time.

In view of the above, the present research aimed at the development and physical-mechanical characterization of lightweight bioconcretes produced through the use of cactus wood, an innovative lignocellulosic source, as bio-aggregate in order to verify the possibility of use as an alternative material in civil construction.

2. EXPERIMENTAL MATERIALS AND METHODS

2.1 Bio-aggregate

The cactus wood used was of the species *Cereus jamacaru* from Barueri - São Paulo, Brazil. The samples were obtained from the base of three years age tree. Manual cutting was performed to remove the samples. The aggregates presented different aspects depending on the stem position

which they were extracted. For this research these different woods were separated after extraction: dark green coloration (dark fragments with greater proximity to the leaves of cactus) and brownish coloration (clear fragments coming from a more internal region of the trunk).

The fragments were reduced to smaller size with a hammer mill and all the generated particles whose length exceeded three times the diameter value were discarded due to the possible adhesion damage that they can generate in the final composite. With the remaining particles, particle size analysis was performed.

Figure 1: Granulometric curves of greenish and brownish particles (on the right) and comparison between the light browns of the dark greenish fragments (on the left).

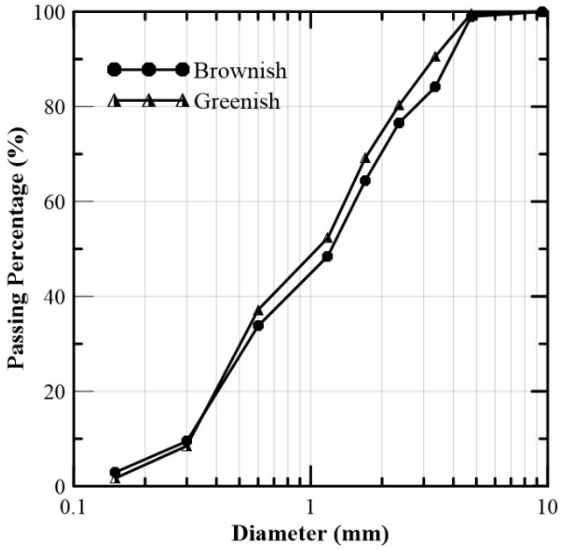

To determine the amount of washes required to reduce the extractives, a wash cycle experiment was performed with a Magnetic Stirrer, IKA brand, model C-MAG HS 7, an Electronic Contact Thermometer, also of the brand IKA, model ETS-D5 and two beakers with a capacity of 500 mL. Firt, 5 g of cactus particles and 300 ml of distilled water were added to the beaker. The water was kept at 80 °C for one hour, its final color was recorded and then a new cycle started. The cycles were repeated until it was noticed that the final water was clear.

In order to characterize physically the bio-aggregate, the test of basic density and water absorption of the wood (NBR 11941 / ABNT 2003) was performed pre-grinding and tests of apparent specific mass (NM 52/2009) and moisture content (NM 9939/2011) after milling. The results for the two types of particles (greenish and brownish) were close enough to be considered the same. The results are expressed in table 1.

Table 1: Physical characterization of the bioaggregate *Cereus Jamacaru*.

Basic density (kg/m³)	**Moisture content (%)**	**Water absorption (%)**	**Apparent Specific mass (kg/m³)**
340	6.30	199.00	250

2.2 Binder and additive

The Brazilian Portland Cement CP V - ARI (cement of high initial strength) was used as binder. The chemical composition and density of the cement can be verified in Andreola et al.[9]. To

accelerate the cement hydration, 3% (based on the cement mass) of calcium chloride ($CaCl_2$) was added to the blends.

2.3 Bioconcretes

Table 3 shows the relations cement mass: cactus wood used for the production of cactus bioconcretes (BC). The letters L and F indicate the type of particle used, where L is for brownish and F for greenish. For all mixtures the water -to-cement ratio (w/c) ratio was 0.4.

The composition of these bioconcretes was set as follows: for cement mixtures BCL 100, BCL 200 and BCF 200 the cement consumption and the volume of wood were set following Andreola [7]. The variation in compensating water had the objective to evaluate the necessity of its placement in front of the wood's absorption obtained (almost 200% based on wood mass) and the desired workability. For the mixtures BCL 3, BCF 3 and BCL 4 was fixed the cement: wood ratio following the results obtained by da Gloria [1]. Numbers 3 and 4 indicate the ratio cement mass: wood mass.

Table 2 : Blend Compositions

Blend	Cement comsumption (kg/m^3)	Wood volume (%)	Final trace mass				
			Cement	Wood	Water	Compensation water	$CaCl_2$
BCL 100	775.000	45.0	1.000	0.145	0.400	0.145	0.030
BCL200 /BCF 200	775.000	45.0	1.000	0.145	0.400	0.290	0.030
BCL3 /BCF 3	488.093	65.1	1.000	0.333	0.400	0.667	0.030
BCL 4	582.935	58.3	1.000	0.250	0.400	0.500	0.030

The cactus bioconcretes (BC) were produced in a planetary mortar, with a 5-liter capacity vat and stainless steel beater. The water was initially mixed with the calcium chloride in a reserved container forming a homogeneous solution. The cement and wood particles were also mixed separately and were placed first in the equipment. At low rotational speed (136 rpm), during the first minute the was added gradually to the dry materials. After the first minute of mixing the turning of the mortar was interrupted for manual release of the material that was attached to the vats. . Next the mix continued until reach 05 min of total time.

Cylindrical specimens of 5 x 10 cm (diameter x height) were produced. The molds were filled in three layers and the type of compaction was varied: manual with 15 strokes per layer (BCL / BCF 200 and BCL 100) and vibrating table (BCL 3, BCF 3 and BCL 4). The molds were protected against moisture loss until demolding, which happened 24 hours later. Finally, the specimens were placed in a humid chamber at 20 ° C (± 2 ° C) and 95% (± 2%) humidity until they reached the age of 28 days.

During the production of the composites it was observed that there was no segregation or exudation between the blends and that the adhesion between the wood and the other components was ideal.

At fresh state, the property evaluated was the spreading through the flow table test. The consistence index of each mixture was obtained from the average of the diameters reached. Based on the Brazilian standard NBR 5739 (ABNT 2007), the compressive test was performed after 28 days in a Shimadzu-1000 KN universal test machine, at a speed of 0.3 mm / min. The vertical displacements were obtained from the average reading of two Linear variable differential

transformers LVDTs. For each mixture, four cylindrical specimens were tested. . The modulus of elasticity was determined according to the requirements of standard NBR 8522 (ABNT 2008).

3. RESULTS

3.1 Extractive Reduction

A gradual variation of the water coloration is observed with washing in hot deionized water. The color change (Figures 7 and 8) is noticeable in each cycle and can be explained by the reduction of extractives of the biomass. It is also possible to observe that the removal of the extractives happens mainly during the first three washing cycles since the color difference between the third and the fourth waste water was not significant.

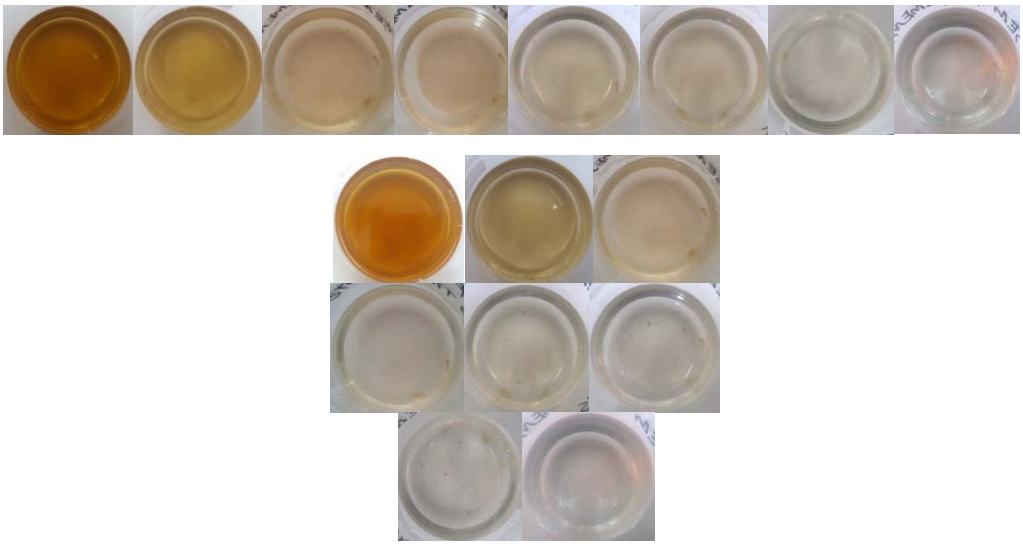

Figure 2 : Comparison of the water coloration at the end of each washing cycle for the greenish (top) and browned (botton) particles.

With the washing cycle experiment it was established that the particles would be submitted to 3 cycles of washes before being used for the bioconcrete production.

3.2 Properties at the fresh state

The pulps achieved good workability as can be seen by analyzing the results of Table 3.

Table 3: Result of the spreading test

Blend	BCL 100	BCL 200	BCF 200	BCL 4	BCF 4	BCF 3
Consistence index (mm)	225.0	282.5	298.5	287.5	257.5	212.5

3.3 Properties at the hardened state

After 24 hours of its production the specimens were demoulded and it was possible to perceive a good homogeneity of the particles in the cementitious matrix.

After 28 days of age the BC were then submitted to the uniaxial test and with the generated data it was possible to generate stress - axial strain graphs for the mixtures.

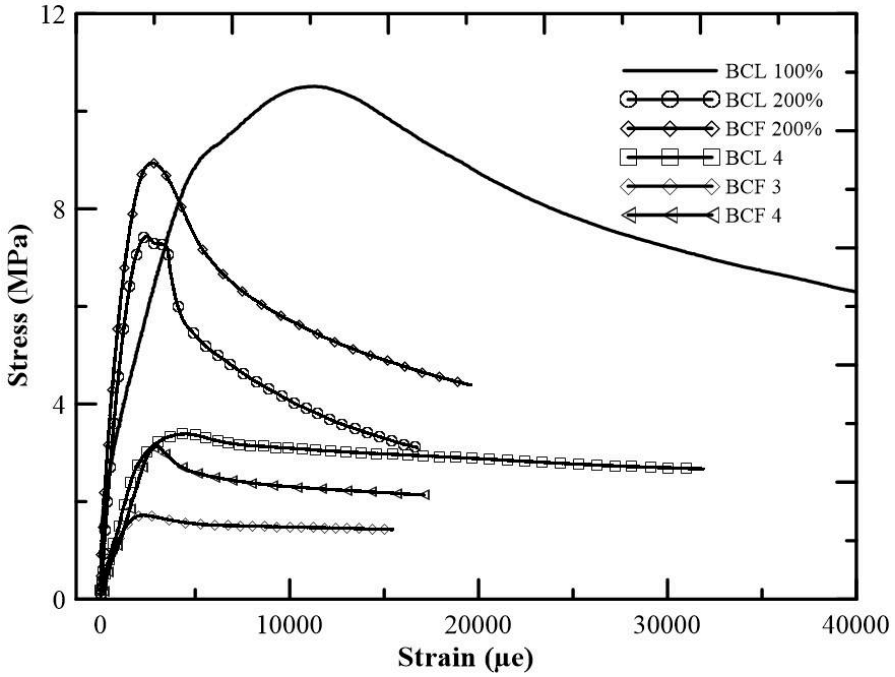

Figure 3: Typical stress-strain curves of BC.

The values of maximum strength as well as the modulus of elasticity and density of the bioconcretes studied are shown in Table 4.

Table 4: Properties of the bioconcretes in the hardened state

Blend	Resistance (MPa)	E (GPa)	Density (kg/m³)
BCL 100	10.512	11.525	1451.600
BCL 200	7.438	10.289	1284.000
BCF 200	8.936	11.978	1347.100
BCL 4	3.387	2.549	997.400
BCF 3	1.720	2.302	872.500
BCF 4	3.135	2.028	999.600

4. DISCUSSION

4.1 Fresh state

The composites with cactus wood and cement studied were demoulded with one day of age indicating that the treatment of washes used, as well as the addition of calcium chloride and the

use of cement CP V- ARI were effective in preventing delay / inhibition of cement hydration reactions.

The BCF 200 and BCL 200 with 200% of compensating water and fixed cement consumption and the BCL 4 achieved better workability; the spreading values were between 282.5 and 298.5 mm. This result indicates that the higher quantity of wood in the mixtures negatively influenced the workability.

4.2 Hardened state

The bioconcretes with greenish particles reached bulk density between 872.5 and 1347.1 kg / m³ while the density of the bioconcretes with the brown particles ranged from 997.4 to 1451.6 kg / m³. According to Rilem [10], they can be classified as lightweight materials, since they have a density of less than 1800 kg / m^3. The determinant variables on density were the amount of water and cactus wood (more water and more cactus wood resulted lower densities), and there are indications (analysis BCL 200 versus BCF 200; BCL 4 versus BCF 4) that for similar mixtures with different types of particles, bioconcretes with greenwish particles results in a composite with higher densities.

With the stress versus strain curve generated, it was possible to observe that the composites presented an initial elastic linear behavior, followed by a region of marked nonlinearity until reaching the maximum tension. The rounded aspect of the curve can be explained by microcracking pre-rupture of the bioconcrete that increases the deformations recorded by the LVTDs.

The blends with greenish particles (BCF-x) reached between 1.72 and 8.94 MPa of compressive strength and browned (BCL-x) between 3.38 and 10.51 MPa. There is no data showing any trend in relation to the maximum voltage reached varying only the type of particle.

The specimens with fixed consumption of 775 kg / m³ (BCL 100, BCL 200 and BCF 200) achieved better resistance / density ratio and higher stiffness, that is, lower deformations for a given request, which is a property of great interest in engineering civil. Analyzing the results of the BCL 100 and BCL 200 mixtures, it was observed that by reducing the compensating water in half the bioconcrete had a small gain of density, increase of the MOE, a significant gain of resistance and a great loss of workability.

For the same trace of BCF 3 - in which it was possible to obtain 1.72 MPa of resistance, 2.30 GPa of MOE and 872.5 kg / m³ of density, da Gloria [1] obtained, using wood sawdust, 15.97 MPa of resistance, 4.03 GPa of MOE and 1250 kg / m³. Andreola et. al.[7] studied bioconcrete with bamboo particles and obtained 12.01 MPa of resistance, 4.03 GPa and 1157 kg / m³ of density. These data show that for this trace calculation methodology the composites with cactus wood although less resistant have as main differential the low density that they can achieve and the fact of maintaining a relatively high stiffness. The comparison with the results of the study by Beraldo [5], which also deals with the production of a cementitious composite with bamboo particles, corroborates with the previous analysis.

The traces of the BCL 200 and BCF 200 mixtures - whose results are: 7.44 MPa for maximum strength, 10.29 GPa of MOE, density of 1284 kg / m³ and spreading 282.5 mm; 8.94 MPa for maximum strength, 11.98 GPa of MOE, density of 1347.100 kg / m³ and spreading 298.5 mm - are similar to those of Andreola [7] who working with bamboo particles obtained maximum resistance of 4.20 MPa, MOE of 2.35 GPa and 788.47 kg / m³ of density and 285 mm of scattering. These results show that in cement fixation the cactus bioconcrete obtained better properties than the bamboo, which is probably due to the large amount of fines present in the mixture, which

reduced the amount of voids, densified the mixture and consequently increased the other properties.

5. CONCLUSION

The objective of producing light bioconcretes was reached given the low final density of the products. In addition, good physical, mechanical and workability properties (properties of interest in construction) have been reached and it can be concluded that cactus wood can be used as an alternative lignocellulosic source in the production of bioconcretes for use in various purposes in the construction industry.

ACKNOWLEDGEMENTS

The authors are grateful to the Experimental Unit of Wood Panels and the Laboratory of Nanotechnology of the Federal University of Lavras and the Structures and Materials Laboratory Lobo Carneiro of the Federal University of Rio de Janeiro.

REFERENCES

[1] da GLORIA, M. Y. R.**. Desenvolvimento e caracterização de painéis sanduíches de Concreto com núcleo leve e faces em laminados reforçados com fibras longas de sisal**. 2015.133 f. Dissertação (Mestrado em Ciências em Engenharia Civil) – Universidade Federal do Rio de Janeiro, RJ, 2015.

[2] MESQUITA, R.G.A.; MENDES, L.M.; MENDES, R.F.; TONOLI, G.H.D.; MARCONCINI, J. M.; **Inclusão de feixes de sisal na produção de painéis MDP de eucalipto**. Scientia Forestalis (IPEF) v.43, p.1-8, 2015.

[3] SOLTAN, D.G.; das NEVES, P.; OLVERA, A.; SAVASTANO Junior, H.; LI, V.C.; **Introducing a Curauá fiber reinforced cement-based composite with strain-hardening behavior**. Industrial Crops and Products, v. 103, p.1-12, 2017.

[4] BERALDO, A. L. **Compuestos de biomasa vegetal y cemento. Aprovechamiento de residuos agro-industriales como fuente sostenible de materiales de construcción**, v. 1, pp. 301-326, 2011.

[5] BERALDO, A. L.. **Bambu-cimento: alternativa para construções rurais. Encontro Nacional sobre Edificações e Comunidades Sustentáveis**, v. 1, p. 145-50, 1997.

[6] SIMATUPANG, M. H.; SCHWARZ, G. H.; BROKER, F. W. Small scale plants for the manufacture of mineral-bonded wood composites. In: WORLD FORESTRY CONGRESS, 8., 1978, Indonésia. **Proceedings**, Indonésia, 1978.

[7] ANDREOLA, V.M. **Caracterização física, mecânica e ambiental de bio-concretos de bambu.** 2017.100 f. Dissertação (Mestrado em Ciências em Engenharia Civil) – Universidade Federal do Rio de Janeiro, RJ, 2017.

[8] LATORRACA, J. V. D. F. **Eucalyptus spp. na produção de painéis de cimento-madeira.** Tese de Doutorado, Departamento de Ciências Agrárias, Universidade Federal do Paraná, Curitiba, 2000.

[9] ANDREOLA, V.M.; da GLORIA, M. Y. R.; TOLEDO FILHO, R. D. ;.. **Desenvolvimento de biocompósitos contendo partículas de bambu.** In: II Congresso Luso-Brasileiro de Materiais de Construção Sustentáveis, 2016, João Pessoa. Desenvolvimento de biocompósitos contendo partículas de bambu, 2016.

[10] RILEM, L**. Functional classification of lightweight concrete**. Springer journal collection, v. 11, n. 64, pp. 281 – 283, 1978.

MECHANICAL AND BOND BEHAVIOR OF CARBON TEXTILE REINFORCED CONCRETES UNDER TENSILE LOADING

Rebecca Mansur de Castro Silva (1) and Flávio de Andrade Silva (1)

(1) Department of Civil and Environmental Engineering, Pontifícia Universidade Católica do Rio de Janeiro, Rio de Janeiro, Brazil

https://doi.org/10.21452/bccm4.2018.02.08

Abstract

In the last years the use of textile reinforced concrete (TRC) has grown considerably. Several types of fibers can be used in the form of textiles. Carbon fabrics have become an interesting reinforcement for TRC due to their excellent mechanical properties. However, the bond between carbon textile and cementitious matrix is not elevated. There are methods that can modify the textile-matrix bond, improving the mechanical behavior of the composite. In this paper the mechanical behavior of carbon textile reinforced concretes under tensile loading is discussed. Two types of carbon fabrics were studied: a flexible and a rigid one. The influence of the use of a coating made with an epoxy resin and sand in the response of the composite was investigated. Various stages of loading corresponding to initiation, propagation, distribution, opening, and localization of a crack system in the specimen were discussed. Pull-out tests were performed in textile's yarns to characterize and compare the interface between the two types of carbon reinforcement and the cementitious matrix. The results obtained showed that the TRC with rigid carbon fabric achieved superior mechanical response under tensile loading. The addition of the coating made with an epoxy resin and sand was able to improve the tensile mechanical response of these composites, suggesting an enhancement in the bond between the fabric and the matrix. This improvement was more significant in the TRC with the flexible carbon fabric.

1. INTRODUCTION

The research of new materials that allow the construction of thinner, lighter and less expensive structures has grown considerably in the last years. An interesting example of these materials is the cementitious matrix reinforced with fibers composites. The fibers control the matrix cracking, modifying the mechanical behavior of the composite after the first matrix crack and improving its ductility [1].

Textile reinforced concrete (TRC) is a cementitious matrix composite reinforced with multiple layers of 2D or 3D fabrics [2]. Several fibers can be used to fabricate this type of reinforcement, such as natural, glass, polypropylene and carbon. Among these materials, carbon fibers show elevated mechanical and durability properties [3,4,1,5].That poses as one of the reasons why the

use of carbon textile as reinforcement in cementitious matrices is becoming extremely attractive. Recent studies [6–9] show the elevated mechanical behavior of the carbon TRC under tensile loading and bending.

The mechanical behavior of TRC is influenced by the properties of the matrix, reinforcement, and mostly the interface between them. The bond between the reinforcement and the matrix is one of the main characteristics of the interface [10]. However, the bond between fabrics constituted of multifilament yarns, as carbon textiles, is not elevated [1]. Studies [6,8,11,12] show that there are methods to improve the bond between the fabric and the cementitious matrix, enhancing the mechanical behavior of the composite.

This work presents a study of the mechanical and bond behavior of carbon textile reinforced concretes under tensile loading. Direct tensile tests were performed in TRC with two types of carbon fabrics (flexible and rigid) to evaluate their mechanical behavior. The influence of the addition of a coating made with and epoxy resin and sand on the tensile mechanical response of the carbon TRC was also investigated. In order to analyze the interface between the reinforcement and the cementitious matrix, pull-out tests were performed in carbon yarns.

2. EXPERIMENTAL PROGRAM

2.1 Cementitious matrix

The matrix used in this research was a fine-grained concrete with compression behaviour shown in Figure 1. The mix proportion used was 1:1:0.3 (sand:cementitious material:water by weight). Portland cement CPII F-32, defined by the Brazilian standard [13], and river sand with maximum diameter of 1.18 mm were used. Glenium 51 (MS) with content of solids of 30% was used as superplasticizers. Table 1 presents the compositions of the fine-grained concrete matrix.

(a) (b)

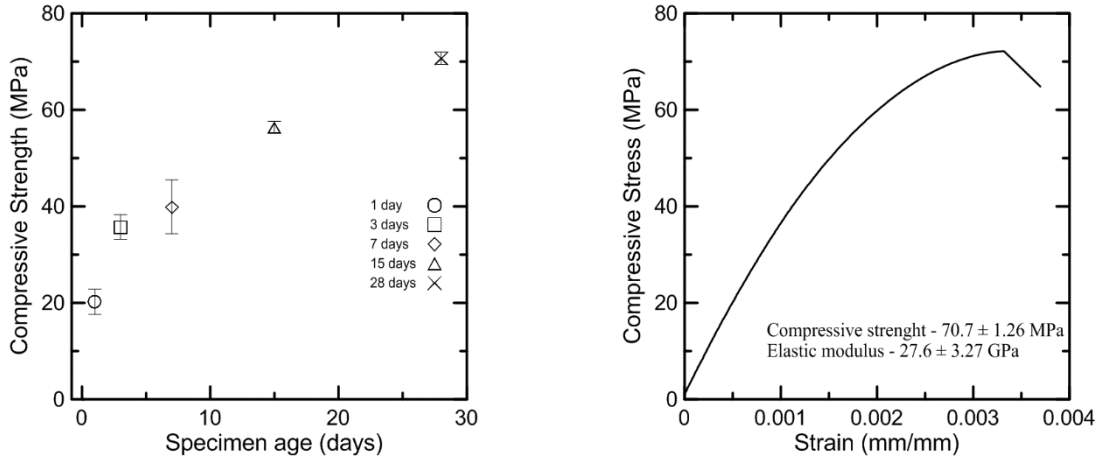

Figure 16: (a) Strength evolution and (b) compressive behavior of the cementitious matrix.

Table 6: Cementitious matrix composition.

Composition	
Sand (kg/m³)	947
Cement CPII F-32 (kg/m³)	750
Fly ash (kg/m³)	265
Silica fume (kg/m³)	50.5
Water (kg/m³)	279.7
Superplasticizer (kg/m³)	6.31

2.2 Carbon fabric

Two types of carbon fabric were used as reinforcement: a flexible, provided by V.Fraas GmbH, and a rigid one, provided by Solidian GmbH. Both fabrics present an open mesh layout, as shown in Figure 2, and were coated during their fabrication process. According to the suppliers, the rigid fabric has an epoxy resin coating and is tensile strength corresponds to 4000 MPa, and the flexible fabric, has a styrene butadiene resin (SBR) coating and tensile strength of 1700 MPa.

A coating made with epoxy resin, Sikadur®-32, and sand with the same grain size of the one used in the matrix were applied to the fabrics. The resin were spread on both sides of the textiles and then sand were sprinkled over it.

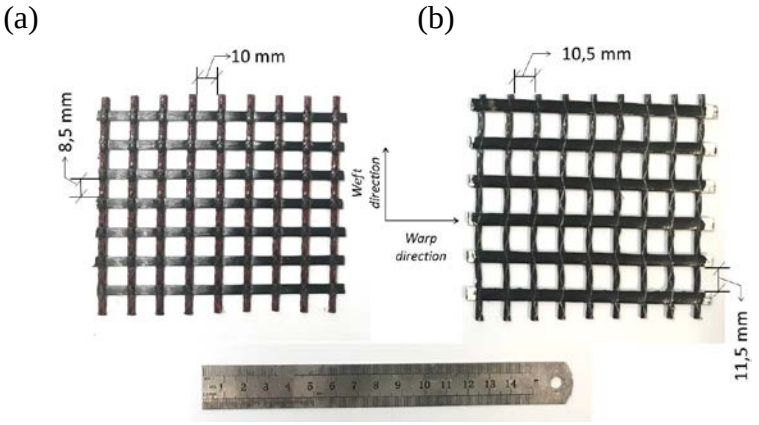

Figure 17: (a) Flexible and (b) rigid carbon fabrics.

2.3 Composite manufacturing

The matrix was produced using a bench-mounted mechanical mix of 20 L capacity. The cementitious materials and sand were dry mixed for 60 s. The water was added and the mix was homogenised for 4 min. Then, the superplasticizer was incorporated and the mix was blended for additional 5 min.

For the direct tensile tests, rectangular plates were casted in a steel mold measuring 1000 mm x 120 mm x 18 mm (length x width x thickness). Figure 3.a shows the specimens production using a lamination technique. A thin concrete layer was placed on the bottom of the mold and the carbon textile reinforcement was positioned over the fresh concrete. Another thin layer of concrete was placed over the fabric. To avoid bending and slippage during the casting, the fabrics layers were

attached into screws at the ends of the mold. In order to reduce the section of the specimen in the mid-span, two aluminum plates measuring 500 mm x 120 mm x 1,5 mm (length x width x thickness) were used, one at the bottom of the mold and the other at the top of the mold. The thickness of the samples varied according to the type of carbon fabric used and the presence or not of a coating made of epoxy resin and sand. The specimens were covered in their molds for 24 h. After that period they were wetted and involved in plastic film and stored in a room with controlled temperature (20ºC ± 2ºC) and humidity (55% ± 5%) for 28 days.

For the pull-out tests, cylinders were casted in PVC molds with 25 x 20 mm (diameter x high) supported on an acrylic plate (Figure 3.b). The matrix was put on the molds and a yarn of the carbon fabric, with embedded length of 20 mm, was positioned in the center of the cylinders (Figure 3.b). The specimens were removed from the molds after 24 h and stored in a wet chamber with 100% of humidity and temperature of 21ºC ± 2ºC for 7 days.

(a) (b)

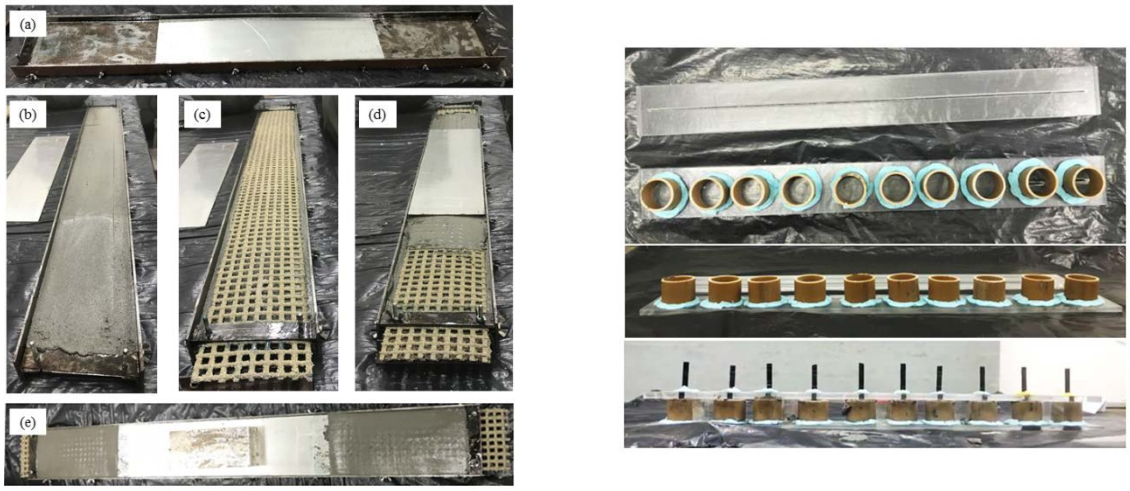

Figure 18: Fabrication of carbon TRC composites for (a) direct tensile and (b) pull-out tests.

2.4 Direct tensile tests

Direct tensile tests on the carbon TRC plates were performed in a MTS 311 universal testing machine with capacity of 1000 kN. The tests were controlled by the actuator displacement at a rate of 0.5 mm/min. The specimens were tested using a gage length of 500 mm with fixed-fixed boundary conditions. The specimens were fixed in steel plates at their ends with screws (Figure 4). The screws were tightened with a torque wrench and emery papers were glued at the surfaces of the specimens that were in contact with the steel plates, in order to avoid slippage between the specimens and the steel plates. The boundary conditions (number of screws, torque and contact surface between the specimen and the steel plate) varied according to the type of the composite (Table 2). To obtain the displacement of the specimens, two linear variable differential transducers (LVDTs) with reading capacity of 250 mm and a extensor made of aluminum attached to them were used. At least four specimens for each variation were tested.

The tensile stress was obtained dividing the load recorded from the load cell by the composite area (width x thickness). The strain was obtained by the division of the average displacement measure by the LVDTs and the gage length of the specimen (500 mm).

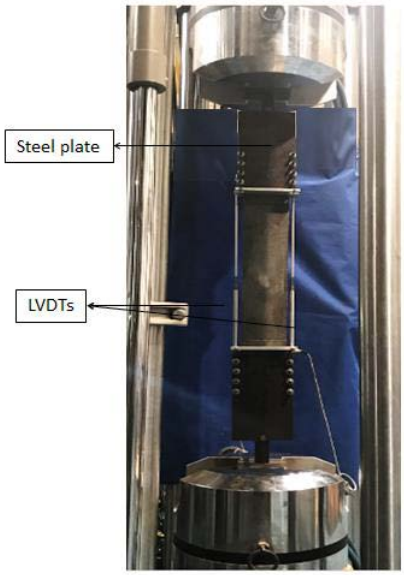

Figure 19: Direct tensile test setup.

Table 7: Boundary conditions for the carbon TRC submitted to direct tensile tests.

	Plain flexible fabric	Coated flexible fabric	Plain rigid fabric	Coated rigid fabric
Screws/steel plate	8	8	10	10
Torque (Nm)	18	19	18	29
Contact surface (mm^2)	18000	24000	24000	24000

2.5 Pull-out tests

Pull-out tests on the carbon yarns were performed in a MTS 810 universal testing machine with capacity of 250 kN. The tests were controlled by displacement at a rate of 1.5 mm/min. To obtain more accurate results, a load cell with 2.5 kN capacity was used. The specimens were attached to the machine through claws, in a fixed boundary conditions system (Figure 5). The yarns slip was obtained directly from the machine displacement [14]. At least eight specimens for each variation were tested.

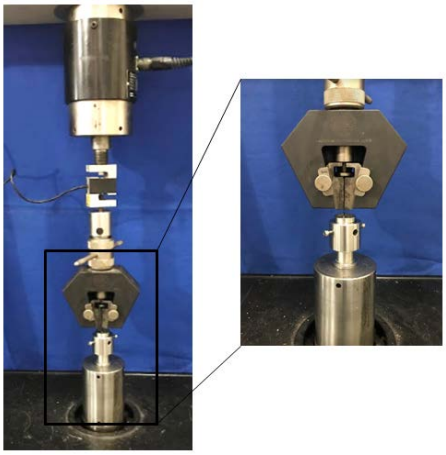

Figure 20: Pull-out test setup.

3. DISCUSSION AND ANALYSES

The carbon TRC with flexible and rigid fabric presented a strain hardening behavior in direct tensile tests. Figure 6 shows representative tensile stress-strain curves obtained from the tests, which present three distinct stages, identified with roman numerals. In Stage I both matrix and reinforcement behave linearly, corresponding to an elastic-linear region. The point where occurs the first matrix crack is known as bend over point (BOP) and represents the limit of State I. In

Stage II as the applied strain increases more cracks are formed culminating in a multiple cracking pattern along the composite. Since the fabric provides ways to transfer the stresses through the cracks, after the initiation of crack in the matrix the load-carrying capacity of TRC does not reduce. The Stage III is characterized by the widening of the existing cracks, with no formation of new cracks, leading to a stretching of the fabric, and posterior failure of the composite.

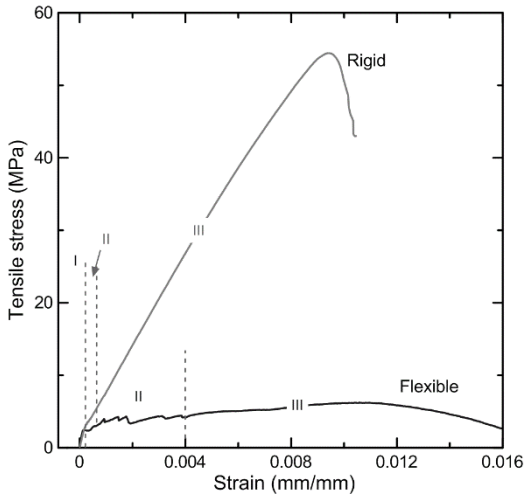

Figure 21: Influence of type of fabric on the tensile stress-strain relation for carbon TRC.

The TRC with rigid carbon fabric showed superior tensile mechanical performance than the TRC with flexible carbon fabric. This could indicate that the bond between the rigid fabric and the cementitious matrix is superior to the bond between the flexible fabric and the cementitious matrix. The difference between the bonds of the two reinforcements with the matrix may be related to the different polymeric coatings used in the fabrication of the textiles. The polymeric coating fills the spaces between the filaments of a yarn, guaranteeing that all the filaments are anchored in the matrix. Therefore, the interaction between the reinforcement and the matrix is improved [8,10,15]. Hence, the coating used in the fabrication of the rigid carbon fabric (epoxy resin) seems to be more efficient in filling the spaces between the filaments than the one used in the fabrication of the flexible carbon fabric (SBR).

Figure 7 shows the influence of the addition of a coating made of epoxy resin and sand on the tensile response of TRC with flexible and rigid carbon fabrics. For both types of composites the impregnation of the reinforcement with epoxy resin and sand improved the mechanical behavior of the material, indicating an improvement in the bond between the carbon textile and the cementitious matrix. Since the plain flexible fabric exhibited lower bond with the matrix than the plain rigid fabric, the effect of the coating with epoxy resin and sand was more significant to the tensile behavior of the TRC with flexible carbon fabric.

Pull-out tests were performed to analyze the reinforcement-matrix interface. The representative curves pull-out load *versus* slip obtained from the pull-out tests are showed in Figure 8. The TRC with rigid fabric presented higher pull-out loads of the yarn than the one with flexible fabric, indicating that the bond between this fabric and the cementitious matrix is superior. The addition of a coating made with an epoxy resin and sand raised the pull-out load of the carbon yarns. The difference between the pull-out loads of the plain and coated yarns was more pronounced for the flexible fabric. The results obtained from the pull-out tests justify and reinforce the carbon TRC behavior under direct tensile loading.

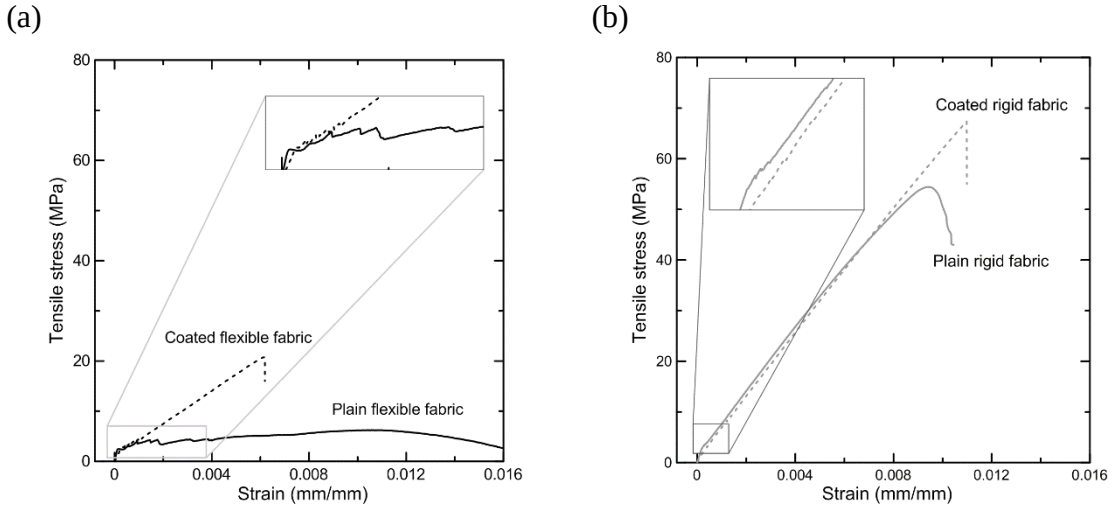

Figure 22: Influence of the coating made of epoxy resin and sand on the tensile response of TRC with (a) flexible and (b) rigid carbon fabrics.

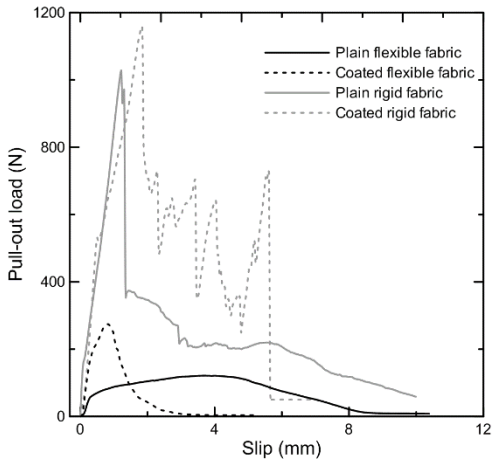

Figure 23: Representative curves obtained from pull-out tests.

4. CONCLUSIONS

A study on the mechanical and bond behavior of carbon textile reinforced concrete under tensile loading was presented. Two types of carbon fabrics, a flexible and a rigid one, were used and the influence of the addition of a coating made with an epoxy resin and sand was investigated through direct tensile and pull-out tests.

All the composites tested showed strain hardening behavior under direct tensile loading, as expected for this type of material. Three typical distinct zones could be observed in the tensile stress-strain curves. The TRC with rigid carbon fabric presented superior tensile performance, indicating that the bond of this textile with the cementitious matrix was higher than the bond of the flexible carbon fabric. The results from the pull-out tests seem to support this assumption.

The addition of a coating made with epoxy resin and sand improved the mechanical response of carbon TRC composites under tensile loading. This improvement was more significant in the TRC with flexible carbon fabric. Once more the results obtained from the pull-out tests confirm the response of the composite under direct tensile loading.

5. AKNOWLEDGMENTS

The authors gratefully acknowledge the CNPq and CAPES (Brazilian National Science Foundations) for partial financial support for this work and Solidian GmbH for the donation of the rigid carbon fabric.

6. REFERENCES

[1] Bentur, A., Mindess, S., 'Fiber Reinforced Cementitious Composites', 2nd Edn (CRC Press, 2006).
[2] Naaman, A. E., 'Textile reinforced cement composites: competitive status and research directions', International RILEM Conference on Materials Science (MatSci) I, 2010, 3–22.
[3] Chand, S., 'Review - carbon fibers for composites', *J. Mater. Sci.* **35** (6) (2000) 1303–13.
[4] Sauder, C., Lamon, J., Pailler, R., 'The tensile behavior of carbon fibers at high temperatures up to 2400 °C', *Carbon* **42** (4) (2004) 715–725.
[5] Arboleda, D., Babaeidarabad, S., Nanni, A., 'Durability of fabric reinforced cementitious matrix (FRCM) composites', 7th International Conference on FRP Composites in Civil Engineering, Vancouver, August, 2014 (International Institute for FRP in Construction).
[6] Dvorkin, D., Poursaee, A., Peled, A.,Weiss, W. J., 'Influence of bundle coating on the tensile behavior, bonding, cracking and fluid transport of fabric cement-based composites', *Cem. Concr. Compos*. **42** (2013) 9–19.
[7] Schuetze, E., Lorenz, E., Curbach, M., 'Static and dynamic fatigue strength of textile reinforced concrete', Proceedings of IABSE Symposium Report, 2015 (International Association for Bridge and Structural Engineering) 1–8.
[8] Donnini, J., Corinaldesi, V., Nanni, A., 'Mechanical properties of FRCM using carbon fabrics with different coating treatments', *Compos. Part B Eng.* **88** (2016) 220-228..
[9] Halvaei, M., Latifi, M., Jamshidi, M., 'Study of the microstructure and flexural behavior of cementitious composites reinforced by surface modified carbon textiles', *Constr. Build Mater*. **158** (2018) 243-256.
[10] RILEM, 'State of Art Report - Textile Reinforced Concrete', (Rilem publications, 2006).
[11] Xu, S., Krüger, M., Reinhardt, H. W., Ožbolt, J., 'Bond characteristics of carbon, alkali resistant glass, and aramid textiles in mortar', *J. Mater. Civ. Eng.* **16** (4) (2004) 356-364.
[12] Xu, S., Li, H., 'Bond properties and experimental methods of textile reinforced concrete', *J. Wuhan Univ. Technol. Mater. Sci*. **22** (3) (2007) 529-532.
[13] Brazilian Standard NBR 11578, 'Cimento Portland composto', *Associação Brasileira de Normas Técnicas (ABNT)* (1991). [in Portuguese]
[14] Trindade, A. C. C., 'Desenvolvimento e comportamento mecânico de compósitos geopoliméricos têxteis reforçados com fibra de juta', Master Thesis, Pontifícia Universidade Católica do Rio de Janeiro (Rio de Janeiro, 2017). [in Portuguese]
[15] Dvorkin, D., Peled, A., 'Effect of reinforcement with carbon fabrics impregnated with nanoparticles on the tensile behavior of cement-based composites', *Cem. Concr. Res.* **85** (2016) 28-38.

STUDY OF CRACKING PATTERN AND ITS EVOLUTION ON NATURAL TEXTILE REINFORCED CONCRETE BY IMAGE ANALYSIS

Letícia O. de Souza (1), Lourdes M.S. de Souza (2) and Flávio A. Silva(1)

(1) Department of Civil and Environmental Engineering, Pontifícia Universidade Católica do Rio de Janeiro, Brazil

(2) Institute Tecgraf, Pontifícia Universidade Católica do Rio de Janeiro (PUC-Rio), Brazil.

https://doi.org/10.21452/bccm4.2018.02.09

Abstract

Textile reinforced concrete (TRC) is an emergent class of material with great deformation capacity and multiple crack formation. Natural fibers are a more eco-friendly alternative to synthetic textile and they are gaining attention in the construction field. In the present study, a Brazilian natural fiber, called curauá, is used in the form of uni-directional textile as reinforcement of cementitious matrix. The composites were manufactured with a hand lay-up technique, varying its thickness and fiber volume fraction. Three types of laminates were investigated under direct tensile tests and its cracking patterns were evaluated by distinct two methodologies. An image processing software was used on photos taken during the tests and a digital image correlation (DIC) technique was also used. The differences between the methods and their limitations are addressed. Parameters as crack spacing and mean crack widths are estimated. The more cracks the composite presented, the more difficult was to perform the measurements due to overlapping of strain fields by DIC. The image analysis performed by the software was able to estimate the number of cracks and the crack spacing for all three types of composites. The mean crack width during the tests was estimated from DIC data.

Keywords: TRC, natural textile, curauá fiber, cement-based composite, image analysis, DIC.

1. INTRODUCTION

Textile reinforced composites (TRC) are a class of materials consist of a fine-grained cementitious matrix reinforced with uni or bi-directional textiles [1,2]. The textile may be of several types, such as carbon, basalt, glass and synthetic fibers [3–5]. Natural fibers are an environmental friendly alternative for textile as they present good strength properties and low cost. Previously works investigated the natural textile capacity of reinforce cementitious matrix, as uni and bi-directional forms [6–9]. An example of uni-directional natural textile reinforced composite is the one developed by Silva et al. [6]: besides the evaluation of the mechanical properties, they

investigated the number of cracks and crack spacing of the composites. The sisal TRC presented mean strength and elastic modulus of 12 and 25 MPa and 34 and 30 GPa, respectively. Image analysis was used and it was found that the crack spacing curve is approximated by an exponential decay function [6].

With improved tensile and ductile properties, TRC are presented as an alternative thin material and may be used for facades and for elements subjected to high strain levels and also for repair. These materials usually present multiple crack formation and their properties are enhanced after the first crack. With that in mind, it is important to understand how cracks behave during the composite loading.

In this work, three types of natural uni-directional TRC are developed and their mechanical responses are studied by means of direct tensile tests. Two distinct methods for investigate crack pattern of the composites during the tensile tests were used: image analysis by acquisition and process of images at regular intervals and digital image correlation (DIC) technique. All the composites presented strain-hardening behavior with multiple crack formation. Their crack pattern was characterized according with the method employed. Besides the parameters obtained with image analysis, DIC also allowed performing an estimation of the mean crack width. This could not be done for all the composites due to cracking characteristics and method's limitation.

2. EXPERIMENTAL PROGRAM

2.1 Materials and process

The curauá fibers used as reinforcement for the composites are obtained from an amazon plant, *Ananas erectifolius*. The strength of curauá is between 250 and 735 MPa [10–12], considered of high performance. Curauá fibers were provided by the CEAPAC organization, from state of Pará, Brazil. The fibers were first cleaned by submersion in hot (around 80ºC) tap water for 1 hour. They were dried in an open atmosphere for 48 hours protected from sunlight. Then, they were brushed to be separated into individual filaments. The long and aligned curauá fibers were used as uni-directional textile. They were cut into 500 mm length and assembled into layers of 6.6 g.

One of the main problems of the use of lignocellulosic fibers in cementitious matrix is the durability of the composite. The durability issues are usually caused by alkali attack, fiber mineralization and volume instability [13,14]. The approach used was to reduce the matrix alkalinity by replacing part of the Portland cement by pozzolanic materials. This strategy has proved to be a successful previously [15,16]. In this work, part of Portland cement was replaced by metakaolin and fly ash. The Portland cement used was the Brazilian type CPII F-32, metakaolin was obtained from Metacaulim do Brasil Industria e Comercio Ltda and the fly ash from an industry in Santa Catarina – Brazil. The sand used had a maximum diameter of 1.18 mm and density equals to 2.67g/cm³. In order to assure workability, superplasticizer (Glenium 51 (MS)) was used with proportion of 2.5% of the cementitious materials, in weight. The mortar matrix was based on a mix proportion of 1:1:0.4 (cementitious materials:sand:water). The cementitious materials included 50% of Portland cement, 40% of metakaolin and 10% of fly ash, in mass. The mortar was mixed in a 5 L capacity planetary mixer for 1.5 min at 136 rpm and for 4 min at 281 rpm. The resulting matrix presented compressive strength of 54.3 ± 0.5 MPa at 28 days.

The composites were manufactured in a steel mold, intercalating layers of mortar and curauá fibers, starting with a layer of mortar, until reaching the number of layers desired. The dimensions of the laminates were 500 mm (length) by 60 mm (width). The thickness varied with the numbers of layers. It was produced three types of composites with one, three and five fabric layers, resulting in thickness of 6 mm, 11 mm and 14 mm, respectively. The curauá volume fraction was of 4.5%,

7.0% and 8.5% for the composites with one, three and five layers, respectively. The specimens were covered in their molds for 48 h. Then, they were demolded and cured in water for 26 days.

2.2 Direct tensile test

The specimens were submitted to direct tensile tests. The tests were carried on a servo hydraulic MTS testing machine with closed loop control, model 311.11, with hydraulic wedge grips and load capacity of 1000 kN. Steel plates were added to decrease stress concentration. The tests were performed under displacement control at a rate of 0.1 mm/min. Six specimens with dimensions of 500 mm length were tested of each composite: five for image analysis and one for DIC. The set-up resulted in a fixed-fixed boundary condition. The composites deformations were measured by two LVDTs positioned on the sides of the specimens under a 190 mm gauge length.

2.3 Cracking pattern measurements

After the tests, the specimens were taken under a stereoscope model Nikon SMZ800N to characterize their cracking pattern: number of cracks, cracking space and mean crack width without load applied. The results are the basis for comparison.

2.3.1 Image analysis

During the tensile tests, a digital camera, model Nikon D90, was placed on a frame grabber directly to the arrangement, as shown in Figure 1-a. The Camera ControlPro2 software was used to capture images of 4200 x 2690 pixels at 10 second intervals. The images with new visible cracks were selected and the space between them was measure by using ImageJ software.

2.3.2 DIC

The DIC is a non-contact and high sensibility technique used in this work to strain field measurements. This method was developed by Sutton et al. [17] and consists of tracking the center of a subset from a reference image to a deformed one. Subsets are groups of pixels and come from a pre-defined area of interest divided into grids. The cross-correlation between the images was performed by the normalized squared differences (NSD) algorithm. The specimens' surfaces were characterized to assure the singularity of each subset, with a high contrast random pattern, as shown in Figure 1-b.

(a) (b)

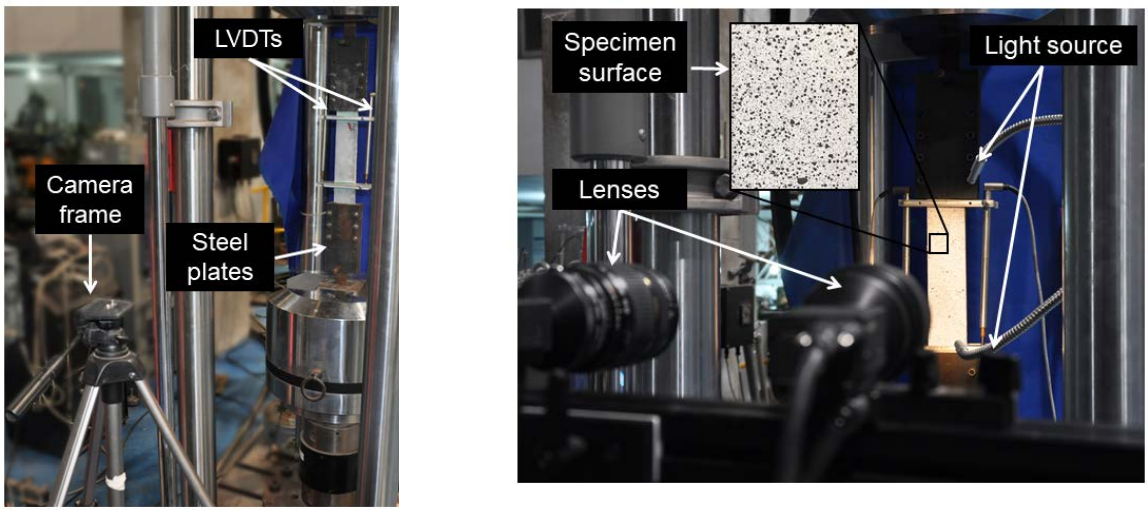

Figure 1: Direct tensile arrangement for (a) image analysis and (b) DIC.

The stereoscope system was formed by two CCD cameras (Point Grey GRAS-50S5M) with resolution of 2448 x 2048 pixels and Tamron A031 (AF28-200mm F/3.8-5.6) lenses. Light sources are used to decrease luminosity variations. The acquisition and processing of images were carried by the software VIC SNAP and VIC-3D 2010, both from Correlated Solutions Inc. The area of interest included 200 mm (form -100 to +100) of the specimens and was divided into 27 subsets. In order to investigate the crack formation, it was plotted strain values versus axial Y position for different test instants. With these information, it was possible to estimate the mean crack width during loading stage.

3. RESULTS AND DISCUSSION

3.1 Tensile response

Figure 2 shows the representative response of the three curauá TRC under direct tensile tests. All the composites presented strain-hardening behavior with multiple crack formation. This behavior is characterized by an elastic linear zone, mostly ruled by the matrix properties due to its major fraction on the composite volume [2]. The deviation of linearity occurs after the first crack and then there is the formation of multiple cracks. More cracks are formed and instead of composite failure, the load bearing capacity is increased due to the cracks bridging by the long curauá fibers. The system is stiff enough to keep the cracks tight until it reaches a steady state condition, marked by the saturation of cracking spacing. Then, there is the widening of the pre-existing cracks: in this zone, no new cracks are formed and it ends when one crack is localized leading to the composite failure. Three and five layered composites presented the above zones well distinguished although this did not occur for the one layered composite.

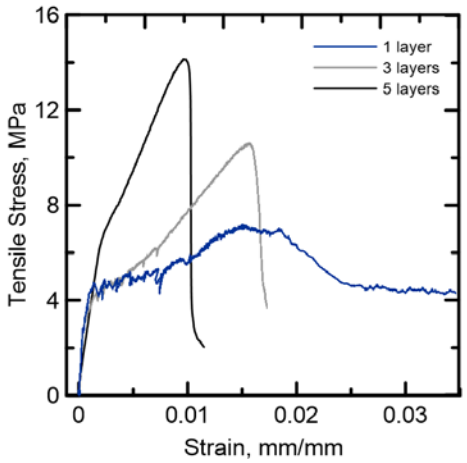

Figure 2: Tensile stress versus strain curves for curauá TRC.

It is possible to observe that the more fiber volume fraction of the composite, the more stiffness it presented as well as ultimate stress. The ultimate strain (correlated with the ultimate stress) decreases with the fiber volume fraction. Thus, the higher ultimate stress, the lower ultimate strain. The drops in the stress-strain response are an indicative of crack formation. The longer the system takes to recover the load bearing capacity, the wider the crack width may be. Thus, the curves in Figure 2 indicate that the mean crack width is decreasing with the higher fiber volume fraction (number of layers). This was confirmed after the tests, with the specimens analyzed under the

stereoscope. The resulting crack pattern for the three types of composites is presented on Table 1, as well as the mechanical parameters discussed.

Table 1: Curauá TRC tensile properties and their cracking pattern measured after the tests.

Composite	Mechanical Properties		Measured Cracking Pattern		
	Strength* (MPa)	Strain* (mm/mm)	Number of Cracks	Mean Width (μm)	Crack Spacing (mm)
1 layer	6.3±0.8	1.2±0.4	12	42	21.5
3 layers	9.7±1.4	1.4±0.1	17	39	13.9
5 layers	14.7±1.2	1.6±0.2	56	18	4.2

3.2 Cracking pattern

The image analysis allowed recognition of the number of cracks and the space between them. The DIC method, besides the parameters obtained from image analysis, also allowed an estimated mean crack width. Accuracy and limitations of each method are discussed as follows.

3.2.1 Image analysis

The cracks were time correlated to the strain of each test and the result is shown in Figure 3.

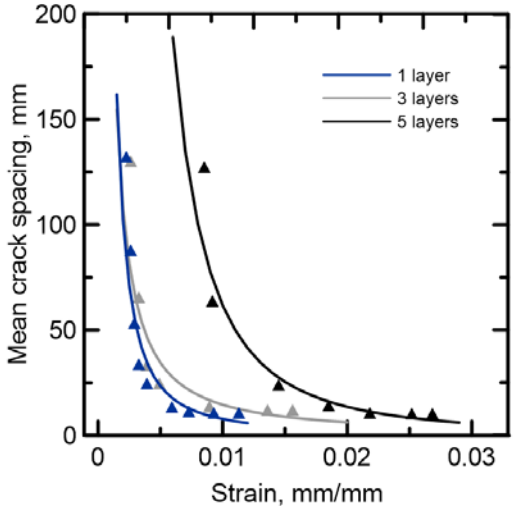

Figure 3: Mean crack spacing measured from image analysis.

It is possible to notice from Figure 3 that the crack evolution of composites reinforced with one and three layers of curauá fabric behave similarly. The mean crack spacing of the five layered composite is shifted around 0.005 mm/mm compared to the other two. This is a result of the difficulty in visualize the cracks initiation, related to its small width. From Table 1, by the end of the test, the mean crack width was of 18 μm, indicating that by the initialization, cracks may be even tighter.

3.2.2 DIC

Table 2 shows the results of the number of visible cracks and the space between them calculated from DIC strain data. The values related with stress level of 4.8 MPa, with correlation

of the images, not only strain data. The DIC method could not contemplate five layered composite analysis due to the crack overlapping (red rectangles in Figure 4). This lead to complications on separating cracks near to each other.

From Figure 4, it is possible to observe that each peak on strain curve is a reasonable approximation of one crack. The same did not happen to the five layered composite, since the cracks are closely spaced (see Table 1). Combining both DIC data and images from the test, it was possible to make an estimate of crack width evolution for different instants of the tests and correlate them with stress levels, as shown in Figure 5. Those values are an approximation due to limitations of the method, since the resolution is 60 microstrains.

Table 2: Crack pattern from DIC analysis.

Composite	Nº of cracks	Mean crack spacing (mm)	Mean crack width* (µm)
1 layer	7	22.5	337
3 layers	11	15.7	122
5 layers	26	5.8	19

* Values related to stress level of 4.8 MPa.

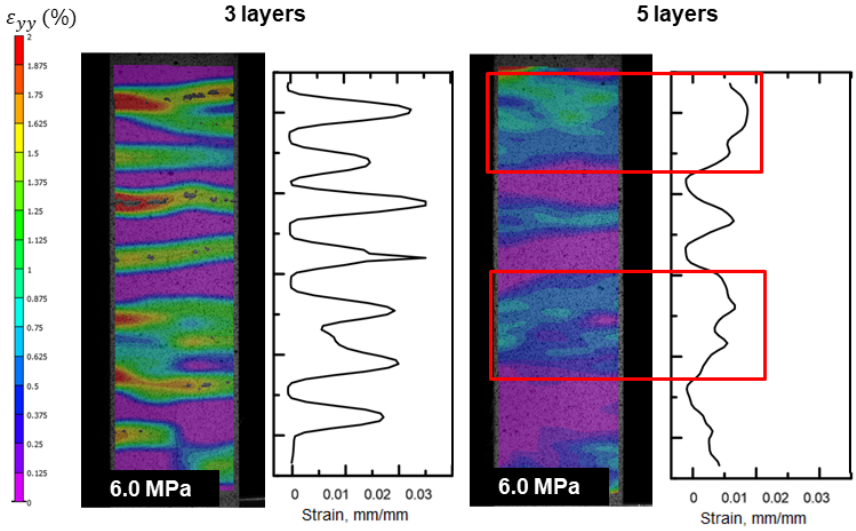

Figure 4: Comparison between DIC data for three and five layered composites. Red rectangles indicating overlapping in strain curve.

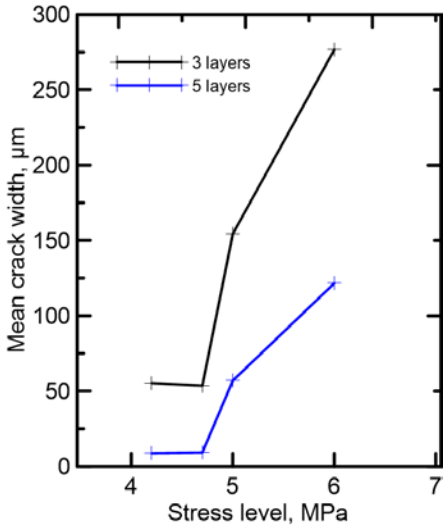

Figure 5: Mean crack width evolution during tensile test, for three and five layered composites.

4. CONCLUSIONS

Curauá uni-directional textile was able to reinforce cementitious composites and provide them of strain-hardening behavior even for the ones with fiber fraction of 4.5%.

The image analysis was able to estimate the number of cracks and the crack spacing and the results are in good agreement with the values measured with the stereoscope. The DIC analysis resulted in crack spacing measurements in good accordance with the real one for the one and three layers types of composites. The same did not happen with the five layered composite due to cracks overlapping since they are closely spaced, mostly for stress level above 5 MPa. The mean crack width during the tests was estimated by combining DIC data and images taken during the tests.

ACKNOWLEDGEMENTS

The authors gratefully acknowledge the CNPq and CAPES (Brazilian National Science Foundations) for partial financial support for this work.

REFERENCES

[1] Textile Reinforced Concrete, State-of-the-Art Report of RILEM Technical Committee 201-TRC., Bagneux, France, 2006.

[2] B. Mobasher, Mechanics of fiber and textile reinforced cement composites, 2012.

[3] F.D.A. Silva, M. Butler, S. Hempel, R.D. Toledo Filho, V. Mechtcherine, Effects of elevated temperatures on the interface properties of carbon textile-reinforced concrete, Cem. Concr. Compos. 48 (2014) 26–34. doi:10.1016/j.cemconcomp.2014.01.007.

[4] D. Alan, S. Rambo, F.D.A. Silva, R. Dias, T. Filho, P.O. Box, R. De Janeiro, Effect of high temperature on the behavior of basalt textile reinforced refractory concrete under uniaxial tensile loading, 1 (2014).

[5] F. de A. Silva, M. Butler, V. Mechtcherine, D. Zhu, B. Mobasher, Strain rate effect on the tensile behaviour of textile-reinforced concrete under static and dynamic loading, Mater. Sci. Eng. A. 528 (2011) 1727–1734. doi:10.1016/j.msea.2010.11.014.

[6] F. de A. Silva, B. Mobasher, R.D.T. Filho, Cracking mechanisms in durable sisal fiber reinforced cement composites, Cem. Concr. Compos. 31 (2009) 721–730. doi:10.1016/j.cemconcomp.2009.07.004.

[7] J. Claramunt, L.J. Fernández-carrasco, H. Ventura, M. Ardanuy, Natural fiber nonwoven reinforced cement composites as sustainable materials for building envelopes, 115 (2016) 230–239. doi:10.1016/j.conbuildmat.2016.04.044.

[8] A. Hakamy, F.U.A. Shaikh, I.M. Low, Characteristics of hemp fabric reinforced nanoclay – cement nanocomposites, Cem. Concr. Compos. 50 (2014) 27–35. doi:10.1016/j.cemconcomp.2014.03.002.

[9] M.E.A. Fidelis, F. de A. Silva, R.D.T. Filho, The Influence of Fiber Treatment on the Mechanical Behavior of Jute Textile Reinforced Concrete, Key Eng. Mater. 600 (2014) 469–474. doi:10.4028/www.scientific.net/KEM.600.469.

[10] M.A.S. Spinacé, C.S. Lambert, K.K.G. Fermoselli, M. De Paoli, Characterization of lignocellulosic curaua fibres, Carbohydr. Polym. 77 (2009) 47–53. doi:10.1016/j.carbpol.2008.12.005.

[11] F. Tomczak, K.G. Satyanarayana, T.H.D. Sydenstricker, Studies on lignocellulosic fibers of Brazil : Part III – Morphology and properties of Brazilian curauá fibers, Compos. Part A Appl. Sci. Manuf. 38 (2007) 2227–2236. doi:10.1016/j.compositesa.2007.06.005.

[12] D.G. Soltan, P. das Neves, A. Olvera, H. Savastano Junior, V.C. Li, Introducing a curauá fiber reinforced cement-based composite with strain-hardening behavior, Ind. Crops Prod. 103 (2017) 1–12. doi:10.1016/j.indcrop.2017.03.016.

[13] R.D.T. Filho, K. Scrivener, G.L. England, K. Ghavami, Durability of alkali-sensitive sisal and coconut fibres in cement mortar composites, Cem. Concr. Compos. 22 (2000) 127–143.

[14] R.D.T. Filho, F. de A. Silva, E.M.R. Fairbairn, J. de A.M. Filho, Durability of compression molded sisal fiber reinforced mortar laminates, Constr. Build. Mater. 23 (2009) 2409–2420. doi:10.1016/j.conbuildmat.2008.10.012.

[15] R.D.T. Filho, K. Ghavami, G.L. England, K. Scrivener, Development of vegetable fibre – mortar composites of improved durability, Cem. Concr. Compos. 25 (2003) 185–196.

[16] J. Wei, C. Meyer, Degradation mechanisms of natural fi ber in the matrix of cement composites, Cem. Concr. Res. 73 (2015) 1–16. doi:http://dx.doi.org/10.1016/j.cemconres.2015.02.019.

[17] M.A. Sutton, J.L. Turner, H.A. Bruck, T.A. Chae, Full . field Representation of Discretely Sampled Surface Deformation for Displacement and Strain Analysis, Exp. Mech. (1991) 168–177.

CYCLIC FLEXURAL BEHAVIOR OF POLYPROPYLENE AND SISAL FIBER REINFORCED CONCRETE

Raylane de Souza Castoldi [(1)], Lourdes Maria Silva de Souza [(1)] and Flávio de Andrade Silva[(1)]

(1) Department of Civil and Environmental Engineering, Pontifícia Universidade Católica do Rio de Janeiro, Brazil

https://doi.org/10.21452/bccm4.2018.02.10

Abstract

This experimental research investigation aims to compare the cyclic behavior of concrete reinforced with discrete polypropylene and sisal fibers. Prismatic concrete specimens having dimensions of 550 x 150 x 150 mm were produced with concrete containing low alkaline content. Both fibers used were 51 mm long and were incorporated into fractions of 6 kg/m^3 and 10 kg/m^3 of polypropylene and sisal fiber, respectively. A cyclic three-point flexural test was conducted in notched beams based on recommendations of RILEM TC 89-FMT. All the composites presented deflection softening behavior and both fibers provided the same level of residual loads. The loading and unloading cycles resulted in degradation of stiffness with increasing CMOD, being more evident for concretes reinforced with polypropylene fiber. Some fracture parameters obtained from the cyclic tests showed that both composites presented similar fracture properties.

1. INTRODUCTION

Concrete is one of the most widely used materials in construction mainly due to the various advantages of this material, which includes high mechanical strength, easy production and molding, with relatively low cost [1]. However, concrete presents some limitations, such as low deformation capacity and the rapid propagation of cracks when subjected to tensile stresses, being considered a fragile material [1,2]. An alternative to minimize this limitation is the use of dispersed fibers into the cementitious matrix. The incorporation of fibers results in higher flexural toughness, fatigue resistance and impact strength. In addition, fiber reinforced concretes become more efficient after the formation of the first crack [3]. Fibers act as a bridge to transfer the stress in the region of a crack, increasing the energy absorption capacity of the material and reducing the propagation and expansion of the existing cracks [2,3].

There are several types of fibers available, produced by different materials and shapes. Despite the possibility of use in the form of textiles, the use of randomly dispersed fibers in the matrix has been more evident for economic reasons [4]. Nowadays, the most used fibers as concrete reinforcement are the steel and polypropylene fibers. However, the polymeric fibers present some

advantages such as the chemical resistance and the higher durability in cementitious matrices [2]. Currently, they are widely used for floor and pavements applications, sprayed concrete and precast elements [2,5].

Some fibers from natural resources, such as sisal fiber, appear as an alternative to synthetic fibers. Natural fibers exist in abundance and have their use encouraged by being renewable, biodegradable and with high availability at low cost [2]. However, the low durability of this type of fiber in alkaline environment is still a barrier to its use in a large scale and the use of these fibers as discrete reinforcement in the concrete is still little studied [6]. Therefore, the evaluation of the application of this type of fiber is important to encourage their use and make them competitive in relation to synthetic fibers.

In order to evaluate the influence of the presence of dispersed fibers in the cementitous matrix, is common to use some method for measure the composite tensile stress-strain response. Although the uniaxial tensile test is the most appropriate, there are some complications due to the configuration of this test. There is the possibility of stress accumulation in the specimen clamping on the test arrangement and the specimen geometry can influence the results obtained. For these reasons, flexural tests have become an alternative to evaluate these composites [7].

Most studies of fiber reinforced concrete investigate the flexural behavior under monotonic loading instead evaluate under cyclic loading [8]. The RILEM TC 89-FMT [9] committee recommends flexural tests on notched prismatic specimens submitted to loading and unloading cycles. By the relation between load and crack mouth opening displacement (load-CMOD curve), some experimental parameters of the cycles can be obtained: the load at the beginning of each cycle, the residual CMOD value, the initial compliance (C_i) and the compliance at each cycle (C_u). From this procedure, it is possible to measure some fracture parameters that are sufficient to characterize the fracture resistance and energy dissipation of the composite [7,9]. Moreover, previous researches have shown that the compliance variation at each cycle performed represents the dissipation of energy with the development of crack the during loading [8,10,11].

The studies on determining the fracture parameters of cementitious materials initiated by Kaplan in 1961 [12,13]. At this time, he applied the principles of classical linear elastic fracture mechanism (LEFM) [14], in which a single fracture parameter is used to characterize the composite. In the 1970s, experimental investigations indicated that LEFM was no longer valid for quasi-brittle materials such as concrete [7,14–16]. Consequently, several models were proposed to describe the concrete failure, such as the fictitious crack model [17], the crack band model [18], the two-parameter model [19], the effective crack model [20], among others. In these cases it is necessary at least two fracture parameters to characterize the composite. The RILEM TC 89-FMT [9] recommendation is based on the two-parameter model, which two parameters may be determinate from three-point flexural tests on notched beams: the critical stress intensity factor K_{IC} and the critical crack tip opening displacement $CTOD_c$.

The main objective of this work is to investigate experimentally the flexural behavior of polypropylene and sisal fiber reinforced concrete under cyclic loading and compare the mechanical behavior of these composites. The test methodology adopted was similar to the recommendations of RILEM TC 89-FMT [9] conducting cyclic three-point flexural tests in notched beams.

2. MATERIALS AND SPECIMEN PREPARATION

2.1 Fibers

The sisal fibers were extracted from *Agave sisalana* plant by a decortication process. The fibers were obtained in a farm located in the city of Valente, state of Bahia, Brazil. After receiving the sisal fibers in bundles of long fibers, it was necessary a preliminary procedure to remove all the impurities. This procedure consisted in submerging the fibers in water at 70 ± 5ºC for approximately one hour. After, the fibers were air-dried for 48 hours and finally cut manually into segments of 51 mm length. On the other hand, the polypropylene fiber was received ready for use as reinforcement. These fibers presented twisted geometry, which result in improvement on the mechanical anchorage with the matrix. The main physical and mechanical characteristics of these fibers obtained in laboratory are shown in Table 1.

Table 1: Fibers properties. Standard deviation values are presented in parenthesis.

Properties	Polypropylene fiber	Sisal fiber
Length (mm)	51	51
Cross-sectional area (mm^2)	0.63 (0.13)	0.03 (0.01)
Aspect ratio	57.77 (6.07)	269.67 (39.26)
Tensile strength (MPa)	260.72 (13.15)	383.88 (49.88)
Elastic modulus (GPa)	2.29 (0.56)	8.77 (3.53)

2.2 Matrix

The concrete matrix was an adaptation of a mix ratio proposed by Marangon [21]. In order to obtain a low alkaline matrix to minimize the degradation process of sisal fibers, 50% by mass of Portland cement was replaced by 30% of metakaolin and 20% of fly ash. The cementitous materials used in the concrete production were Brazilian cement type CP II F-32, fly ash, metakaolin, silica fume and silica flour (quartz powder). Fine aggregates of two classes of particle size were used: one ranging from 0.15 to 0.85 mm (S1) and the other ranging from 0.85 mm to 4.8 mm (S2). Coarse aggregate with maximum diameter of 12.5 mm and superplasticizer were also included on the mix. The resulting water/cement ratio was 0.5. The concrete compressive strength after 28 days was 57.0 ± 21.05 MPa and the slump spreading was 479 ± 2 mm. The concrete composition is given in Table 2.

Table 2: Proportions on concrete composition. All values in kg/m^3.

Coarse Aggregate	Fine Aggregate		Cement	Fly Ash	Metakaolin	Silica Fume	Silica Flour	Water	Super-plasticizer
	S1	S2							
492.0	826.7	99.6	180.0	224.0	94.8	45.0	70.0	155.7	21.6

2.3 Preparation of samples

Two different composites were produced: the composite CPP6, which the reinforcement was 6 kg/m^3 of polypropylene fiber and the composite CSI10, with 10 kg/m^3 of sisal fiber as

reinforcement. For each mixture, three composites were made. The specimens for the flexural tests were prismatic, with dimensions of 550 x 150 x 150 mm. Notches with 25 mm long centered on the bottom side of the prisms were made using a 3 mm thick diamond saw. The specimens were cured for 28 days at room temperature of 24.4ºC and 65.7% of humidity before testing.

3. TESTING METHODS

The cyclic flexural tests were performed based on the recommendations of RILEM TC 89-FMT [9]. Three-point flexural tests were carried by using a MTS servo-controlled hydraulic testing machine with a closed loop type of control and a load cell of 100 kN. The span between the support rollers was 500 mm. The superior roller for load application was fixed on the specimen midspan. The three rollers had a diameter of 37 mm. One clip gage fixed on the notch was used for the measurement of the crack mouth opening displacement (CMOD). The details of the setup are presented in Figure 1.

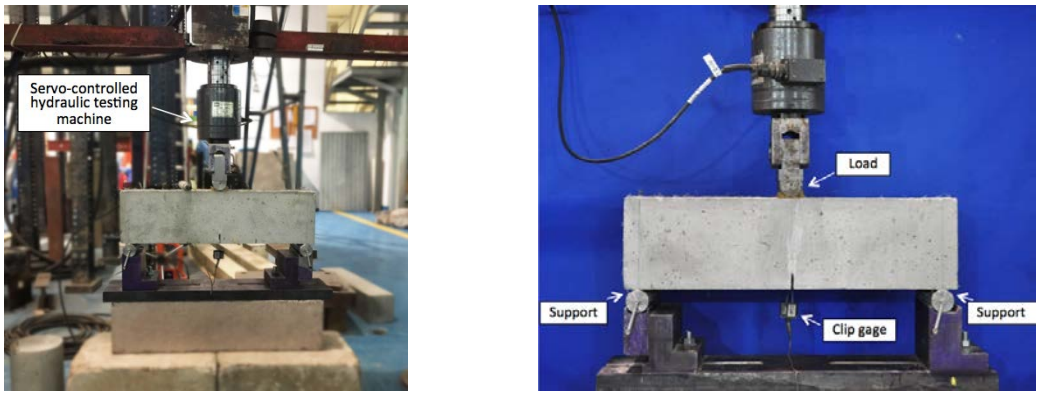

(a) (b)

Figure 1: (a) Servo-controlled hydraulic testing machine used in the test and (b) the three-point flexural test setup in detail.

The loading procedure was controlled by the CMOD. Up to CMOD equal to 0.18 mm, the loading rate was 0.05 mm/min. After 0.18 mm, the loading rate was 0.2 mm/min until reach CMOD equal to 1 mm, which was the end of the test. The unloading procedure was controlled by the load. The unloading was executed at pre-defined CMOD levels (0.02, 0.04, 0.06, 0.10, 0.14, 0.18, 0.30 and 0.50) with the load rate of 8kN/m for all unloading performed. The loading and unloading procedure and the specimen geometry is shown in Figures 2a and 2c, respectively.

The elastic modulus (E) is calculated from the Eq. 2, in which the parameter C_i is defined as the initial compliance shown in Figure 2.b. In addition, $V(\alpha)$ is obtained from the Eq. 3, where α_0 is the normalized notch length, defined as a_0/d.

$$E = \frac{6Sa_0V(\alpha_0)}{C_i d^2 t} \tag{2}$$

$$V(\alpha) = 0.76 - 2.28\alpha + 3.87\alpha^2 - 2.04\alpha^3 + \frac{0.66}{(1-\alpha)^2} \tag{3}$$

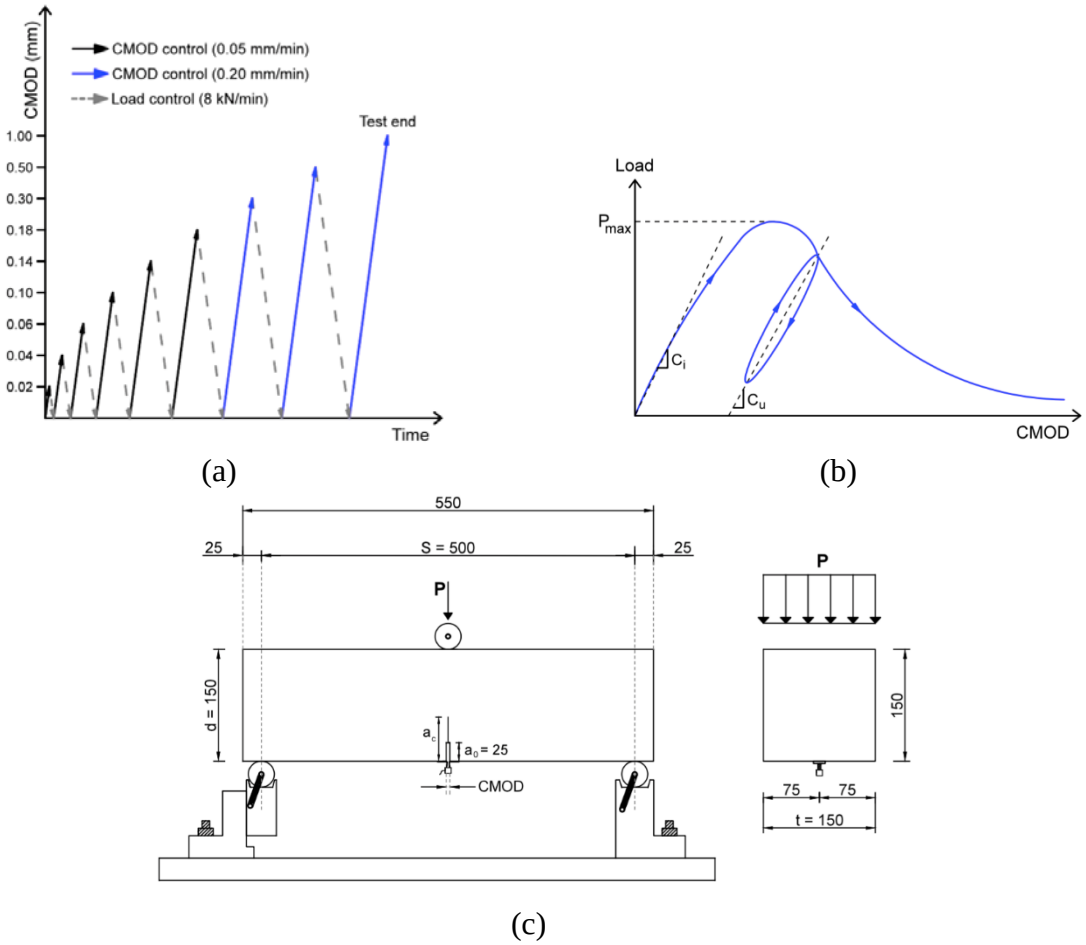

Figure 2: (a) Cyclic loading and unloading procedure, (b) a typical load-CMOD response with some experimental parameters and (c) the testing configuration and geometry of specimen. All dimensions in mm.

The critical crack length a_c is the crack length at which the crack becomes unstable [10]. This parameter is obtained by the Eq. 4 by an iterative process and can be used to determine the crack length at any cycle. The term C_u is the compliance corresponding to the unloading cycle and the normalized critical crack length α_c is defined as a_c/d. In addition, the critical stress intensity factor (K_{IC}) is obtained from Eq. 6. This parameter is defined as the stress intensity factor obtained at the critical effective crack tip, using the measured maximum load [9].

$$a_c = \frac{E C_u d^2 t}{6 S V(\alpha_c)} \tag{4}$$

$$K_{IC} = 3 P_{max} \frac{S\sqrt{(\pi a_c)} F(\alpha_c)}{2 d^2 t} \tag{5}$$

$$F(\alpha_c) = \frac{1.99 - \alpha_c(1-\alpha_c)(2.15 - 3.93\alpha_c + 2.7{\alpha_c}^2)}{\sqrt{\pi}(1+2\alpha_c)(1-\alpha_c)^{3/2}} \tag{6}$$

The critical crack tip opening displacement ($CTOD_c$), obtained from Eq. 7, is defined as the $CTOD$ calculated at the original notch tip of the specimen, using the measured maximum load and

the critical effective crack length [9]. The critical intrinsic fracture toughness (G_{IC}) is the critical level of toughness against crack initiation [7], and is obtained from Eq. 8. The term β_0 is equivalent to the relation a_c/a_0.

$$CTOD_c = \frac{6P_{max}Sa_cV(\alpha_c)}{Ed^2t}\sqrt{(1-\beta_0)^2 + (1.081 - 1.149\alpha_c)(\beta_0 - {\beta_0}^2)} \quad (7)$$

$$G_{IC} = \frac{{K_{IC}}^2}{E} \quad (8)$$

4. RESULTS AND DISCUSSION

The load-CMOD curves presented at Figures 3a and 3b report the flexural responses obtained for the composite CPP6 and CSI10, respectively. Each curve corresponds to one specimen tested, named S1, S2 and S3. Figure 3c shows the mean curves for the composites CPP6 and CSI10, for comparison. It was observed that all the composites presented linear behavior until the appearance of the first crack, followed by a decrease in load with the increase of the CMOD. This behavior is named deflection softening, and is characterized by the appearance of a single crack, common in composites reinforced with discrete fibers [22–24]. Although the pre-cracking behavior was similar for both composites, the post-cracking behavior varied according to the fiber type.

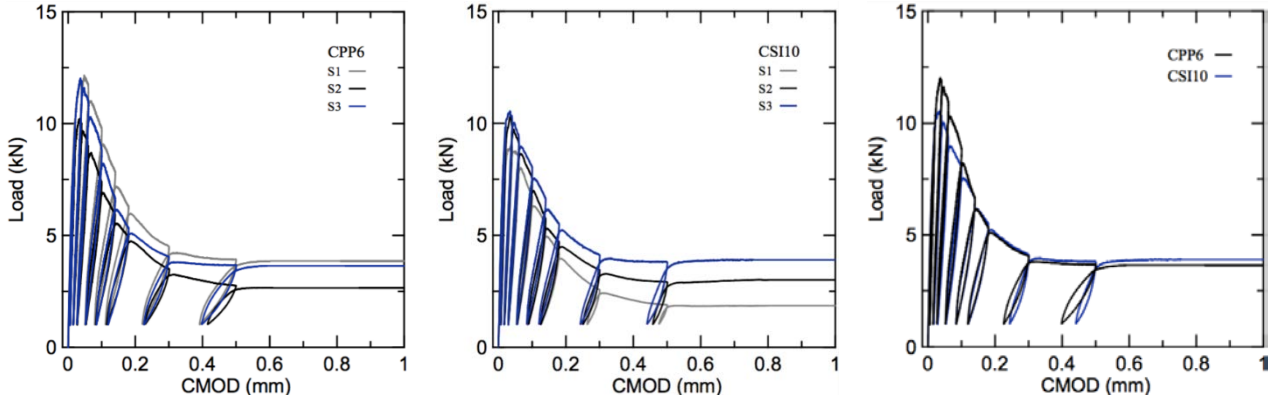

(a) (b) (c)

Figure 3: Results from cyclic three-point flexural tests for (a) CPP6 and (b) CSI10 composites. (c) Representative curve for each composite.

The loading and unloading curves of all concretes tested did not coincide and were not parallel to the initial slope. The slope was inversely proportional to the crack mouth opening displacement. The larger the CMOD, smaller the slope [7,8,10,11]. This fact indicates that there is a degradation of stiffness, which is related to energy dissipation during the loading and unloading process [8]. With the increasing of the load, the cracks develop and the damages are gradually accumulated, while the stiffness decreases. From Figure 3c it is possible to notice that the slope decrease was more evident for the composite CPP6. Even though loading levels were similar for both composites, the lower amount of polypropylene fibers resulted in higher loss of stiffness with the crack development, mainly for CMOD equal to 4 mm.

The change in compliance and inelastic deformation at each loading and unloading cycle are indicators of crack increase and were used to calculate parameters of fracture mechanics [9,10],

presented in Table 3. The similar values for modulus of rupture means that both composites presented the same tensile strength. Due to the low amount of fibers incorporated into the matrix, the tensile strength of the composite may be associated with the plain concrete tensile strength, and the fibers only act on the load absorption in the post-cracking region.

Other parameters such as modulus of elasticity, critical effective crack length, critical intensity factor and $CTOD_c$ did not presented considered discrepancy between the two evaluated composites. The difference observed in the critical strain energy release rate may be associated with the distribution of fibers on the cracked section, which can present variation due to the difficult in disperse the fibers on the mixture process of the samples.

Table 3: Summary of cyclic frature parameters. Standard deviation values are presented in parentheses.

Parameters	CPP6	CSI10
Number of cycles	8	8
Apparent MOR (MPa)	3.7 (0.3)	3.2 (0.3)
Elastic modulus (GPa)	19.6 (1.5)	20.2 (0.9)
Critical crack length a_c (mm)	41.3 (4.3)	41.0 (2.0)
Critical stress intensity factor K_{IC} (MPa.mm$^{0.5}$)	30.1 (3.9)	25.9 (0.9)
Critical *CTOD* (μm)	20.9 (5.1)	17.0 (0.9)
Critical strain energy release rate G_{IC} (N/mm)	46.7 (9.8)	33.2 (3.8)

5. CONCLUSIONS

After the cracking of the matrix, both fibers guaranteed the deflection softening behavior to the cementitious matrix. It was observed that sisal fiber could provide the same level of residual strength as the polypropylene fiber, considering superior dosage of sisal fiber. It was possible to verify from the load-CMOD curves that the concrete reinforced with polypropylene fiber presented higher degradation of the stiffness, evidenced by the higher reduction of the cycles slopes with the development of the crack. However, is important to highlight that this may have happened due to the less amount of polypropylene fiber in the cracked section and it is not necessary associated with the fiber properties used for reinforcement. The fracture parameters obtained for the three flexural tests show that both composites presented similar values for most of the parameters.

After evaluation of the cyclic behavior and fracture parameters obtained from the composites, it can be concluded that sisal fibers can successfully be used as concrete reinforcement, considering the need of higher dosage of sisal fiber than polypropylene fiber.

REFERENCES

[1] MEHTA, P. K.; MONTEIRO, P. J. M. Concrete: Microstructure, Properties and Materials. 3.ed. McGraw-Hill, 2006.

[2] BENTUR, A.; MINDESS, S. Fibre Reinforced Cementitious Composites. 2.ed. Taylor & Francis, 2007.

[3] NAAMAN, A. E.; REINHARDT, H. W. Proposed classification of HPFRC composites based on their tensile response. Mater Struct, vol. 39, no. 289, pp. 547–555, 2006.

[4] PEREIRA, E. V. Influência de Fibras de Aço no Comportamento Mecânico e nos Mecanismos de Fissuração de Concretos Autoadensáveis. Rio de Janeiro, 2017. Dissertação de Mestrado - Departamento de Engenharia Civil e Ambiental, Pontifícia Universidade Católica.

[5] FIGUEIREDO, A. D. Concreto Reforçado Com Fibras. São Paulo, 2011. Livre Docência - Escola Politécnica, Universidade de São Paulo.
[6] BERGSTROM, S. G.; GRAM, H. Durability of alkali-sensitive fibres in concrete. Int J Cem Comp Light Concr, vol. 6, no. 2, pp. 75– 80, 1984.
[7] MOBASHER, B.; BONAKDAR, A.; BAKHSHI, M. Back-calculation procedure for cyclic flexural fracture tests in fiber reinforced concrete. Fract Mech Appl Concr - ACI Technical Publication, SP-300. January, 2015.
[8] BOULEKBACHE, B.; HAMRAT, M.; CHEMROUK, M.; AMZIANE, S. Flexural behaviour of steel fibre-reinforced concrete under cyclic loading. Constr Build Mater, vol. 126, pp. 253–262, 2016.
[9] RILEM TECHNICAL COMMITTEES. RILEM TC 89-FMT: Fracture mechanics of concrete - Determination of fracture parameters of plain concrete using three-point bend tests. United States, 1991.
[10] DEY, V.; KACHALA, R.; BONAKDARR, A.; MOBASHER, B. Mechanical properties of micro and sub-micron wollastonite fibers in cementitious composites. Constr Build Mater, vol. 82, no. April, pp. 351–359, 2015.
[11] HAMAD, W. I.; OWEN, J. S.; HUSSEIN, M. F. M. An efficient approach of modelling the flexural cracking behaviour of un-notched plain concrete prisms subject to monotonic and cyclic loading. Eng Struct, vol. 51, pp. 36–50, 2013.
[12] OHTSU, M. Crack propagation in concrete: linear elastic fracture mechanics and boundary element method. Theor Appl Fract Mech, vol. 9, pp. 55–60, 1988.
[13] KAPLAN, M. Crack propagation and the fracture of concrete. ACI J Proc, vol. 58, pp. 591–610, 1961.
[14] INCE, R.; ALYAMAÇ, K. Determination of fracture parameters of concrete based on water-cement ratio. Indian J Eng Mater Sci, vol. 15, pp. 14–22, 2008.
[15] CHENGSHENG, O.; BARZIN, M.; SURENDRA, P. An r-curve approach for fracture of quasi-brittle materials. Eng Fract Mech, vol. 37, pp. 901–13, 1990.
[16] KARIHALOO, B.; NALLATHAMBI, P. Effective crack Model for the determination of fracture toughness of concrete. Eng Fract Mech, vol. 35, pp. 637–45, 1990.
[17] HILLERBORG, A.; MODÉER, M.; PETERSSON, P. Analysis of crack formation and crack growth in concrete by means of fracture mechanics and finite elements. Cem Concr Res, vol. 6, pp. 773–81, 1976.
[18] BAZANT, Z.; OH, B. Crack band theory of concrete. Mater and Struct, vol. 16, pp. 155–77, 1983.
[19] JENQ, B.; SHAH, S. Two Parameter Fracture Model for Concrete. J Eng Mech, vol. 111, pp. 1227–41, 1986.
[20] NALLATHAMBI, P.; KARIHALOO, B. Prediction of load deflection behavior of plain concrete from fracture energy. Cem Concr Res, vol. 16, pp. 373–82, 1986.
[21] MARANGON, E. Desenvolvimento e caracterização de concretos auto- adensáveis reforçados com fibras de aço. Rio de Janeiro, 2006. Dissertação de Mestrado - COPPE, Universidade Federal do Rio de Janeiro.
[22] CIFUENTES, H.; GARCÍA, F.; MAESO, O.; MEDINA, F. Influence of the properties of polypropylene fibres on the fracture behaviour of low-, normal- and high-strength FRC. Constr Build Mater, vol. 45, pp. 130–137, 2013.
[23] LEE, J. H.; CHO, B.; CHOI, E.; KIM, Y. H. Experimental study of the reinforcement effect of macro-type high strength polypropylene on the flexural capacity of concrete. Constr Build Mater, vol. 126, pp. 967–975, 2016
[24] SANTOS, F. M. R.; SOUZA, T. F.; BARQUETE, D. M.; AMADO, F. D. R. Comparative analysis of the sisal and piassava fibers as reinforcements in lightweight cementitious composites with EVA waste. Constr Build Mater, vol. 128, pp. 315–323, 2016.

USE OF LATEX IN CELLULOSE FIBERS AND REPLACEMENT WITH METACAULIM FOR APPLICATION IN COMPOSITES WITH CEMENT MATRIX

Rondinele Alberto dos Reis Ferreira [(1)], Lara Cristina Péres dos Santos [(1)], Leila Aparecida de Castro Motta [(1)] and Daniel Pasquini [(2)]

(1) Civil Engineering School, Federal University of Uberlandia, Uberlandia, MG, Brazil

(2) Institute of Chemistry, Federal University of Uberlandia, Uberlandia, MG, Brazil

https://doi.org/10.21452/bccm4.2018.02.11

Abstract

In this work, it was studied the addition of latex in cellulose pulps in cement matrices. It is known that the alkalinity of the matrix degrades the fiber. Therefore, in addition of latex in fiber, the alkalinity of the matrix was reduced by replacing part of the cement with metakaolin. The influence of the analyzed parameters (percentage of cellulose, the percentage of latex and percentage of metakaolin) on the mechanical and physical properties of the cement composites was evaluated through an experimental planning. From this planning, it was possible to develop a model of equations that optimized the results of the modulus of rupture and water absorption. Flexural strength and water absorption tests were made on composites at 28 days of age. It was observed that the best conditions analyzed to maximize the value of the rupture modulus was the combinations of the values of cellulose in 8.5%, of latex in the value of 0.249% and of metakaolin in the central point (19%), resulting in the value for rupture modulus of 14.5 MPa. Regarding the absorption, it was observed that only the cellulose variable was significant for this response. Higher concentrations of cellulose resulted in higher values for percentage of absorption, due to the hydrophilicity of the natural fiber.

Keywords: Cellulose fiber, latex, metakaolin, mechanical properties, absorption

1. INTRODUCTION

Sustainability is the ability to meet the needs of the present without compromising future generations. However, one of the main problems faced by the construction industry is the generation of waste, the scarcity of natural resources, the consumption of energy, the emission of gases, that is, the impact caused to the environment. In this sense, numerous searches are being carried out with the objective of guaranteeing environmental preservation with renewable materials or the reuse of industrial waste. The plant fibers are worthy of note observation because

they present interesting properties, such as good mechanical performance in fragile matrices, high availability, renewable source and low cost of production [1,2]. Several studies are focused on the treatment of fibers, or even the matrix, to enable their use in the long term. Among the treatments is the reduction of the alkalinity of the matrix by the replacement of part of the cement by pozzolanic materials [3] or by accelerated carbonation [4]. Chemical treatments of the fibers (alkaline treatment) [5] and acetylation [6]. Finally, physical treatments such as thermomechanical treatment [7] and hornification [8] can also be applied. The aim of the present study was to study the physical treatment of cellulose fibers with the addition of natural rubber latex, and the reduction of alkalinity of the cement matrix, with the replacement of part of the cement by metakaolin in the manufacture of cementitious composites.

2. MATERIALS AND METHODS

2.1 Characteristics of cellulose, cement, latex and metakaolin

The composites were molded using cellulose, with the specific mass of 1.5 g/cm^3, extracted from *Eucalyptus urograndis*, processed industrially by the Kraft method, and supplied by Suzano (Limeira/SP). The sheets of Kraft paper have a length, width and thickness of approximately 39.5 cm, 31 cm and 0.13 cm, respectively. The cement used was the Ultra Fast - CPV ARI, of the Holcim brand. The solids content of the latex was obtained according to the parameters determined in ASTM D 1076-02. Natural rubber latex with a solids content of 43.33% by weight was supplied by Fazenda Varginha, located in Araguari, Minas Gerais. The latex was extracted directly from the rubber tree (*Heveabrasilensis*). Metacaulim HP ULTRA, awarded by Metacaulim do Brasil (Jundiaí-SP). This product consists of SiO_2 and Al_2O_3 in the amorphous phase. Furthermore, the average particle diameter is 12.4 μm and a specific mass of approximately 2.65 kg/m^3 [9].

2.2 Preparation of the composites and design of experiments

The mixing and preparation of the composites were carried out using the principle of the Hatschek process, developed by Ludwing Hatschek [10]. Initially, the cellulose was incorporated into the water, followed by latex, cement and metakaolin. To each material added to the mixer, the mixture was stirred for 5 min until its complete homogenization. The mass solids concentration, for each composite, was 40.2%. The specimens had dimensions of 20 cm x 20 cm the side and 4 mm in thickness.

In order to carry out the experimental planning, cement composites with fixed volume were molded(160 cm^3). The planning was elaborated for α of orthogonality of 1.41421. The limits of the factors studied for percentage of cellulose in the mixture – X_1 (the largest additions of mechanical resistance in the pulp), latex (X_2) and metakaolin (X_3) (percentage used as an addition in cement composites cited in the literature) are shown in Table 1. The studied responses were the modulus of rupture and absorption. Flexural tests was performed at 28 days. The recommendations and parameters contained in [11] was adopted. An INSTRON universal test machine, model 5982 and a load cell of 5 kN were used. Water absorption tests were also carried out according to ASTM C 948-81 (2009).

3. RESULTS AND DISCUSSION

3.1 Statistical analysis - Effect of independent variables

Table 1 shows the experimental conditions studied in central composite design (CCD) matrix, with uncoded values of parameters and results obtained for modulus of rupture (MR) and

absorption (A). The equations obtained by multiple regression to represent the modulus of rupture and absorption as a function of the independent variables studied can be visualized in equations 1 and 2, respectively.

Table 1: The experimental conditions studied in CCD matrix, with coded and uncoded values of parameters

E	Cel[1] % (coded)	Lat[2] % (coded)	Mk[3] % (coded)	Modulus of rupture (MPa)	Absorption (%)
1	1.50 (-1)	0.02 (-1)	4 (-1)	9.11	10.28
2	1.50 (-1)	0.02 (-1)	34 (+1)	8 .85	10.76
3	1.50 (-1)	0.21 (+1)	4 (-1)	7.23	11.51
4	1.50 (-1)	0.21 (+1)	34 (+1)	8.78	13.17
5	8.50 (+1)	0.02 (-1)	4 (-1)	9.10	37.58
6	8.50 (+1)	0.02 (-1)	34 (+1)	7.29	39.42
7	8.50 (+1)	0.21 (+1)	4 (-1)	13.26	33.15
8	8.50 (+1)	0.21 (+1)	34 (+1)	14.42	28.58
9	0.05 (-1.41)	0.115 (0)	19 (0)	4.51	11.30
10	9.95 (+1.41)	0.115 (0)	19 (0)	4.54	66.42
11	5.00 (0)	0 (-1.41)	19 (0)	10.29	21.19
12	5.00 (0)	0.249 (+1.41)	19 (0)	13.73	18.13
13	5.00 (0)	0.115 (0)	0 (-1.41)	10 .91	16.54
14	5.00 (0)	0.115 (0)	40.2 (+1.41)	12.57	21.81
15 (C)	5.00 (0)	0.115 (0)	19(0)	11.42	19.34
16 (C)	5.00 (0)	0.115 (0)	19 (0)	12.47	24.03
17 (C)	5.00 (0)	0.115 (0)	19 (0)	9.03	21.00
18 (C)	5.00 (0)	0.115 (0)	19 (0)	10.93	25.23

[1]Cellulose; [2]Latex; [3]Metakaolin.

$$(MR) = 10.7+0.8(X_{cel})-2.9(X_{cel})^2+1.2(X_{Lat})+0.9(X_{Lat})^2+0.25(X_{Mk})+0.8(X_{Mk})^2+1.7(X_{cel})\ (X_{Lat})-0.24(X_{cel})(X_{Mk})+0.6(X_{Lat})(X_{Mk}) \quad (1)$$

It was observed that equation 1 significantly represented the modulus of rupture (MR) response, with a coefficient of variation (R^2) of 0.90, for a confidence level of 90%. In this way, it was possible to construct the response surfaces for the modulus rupture (Figure 1).

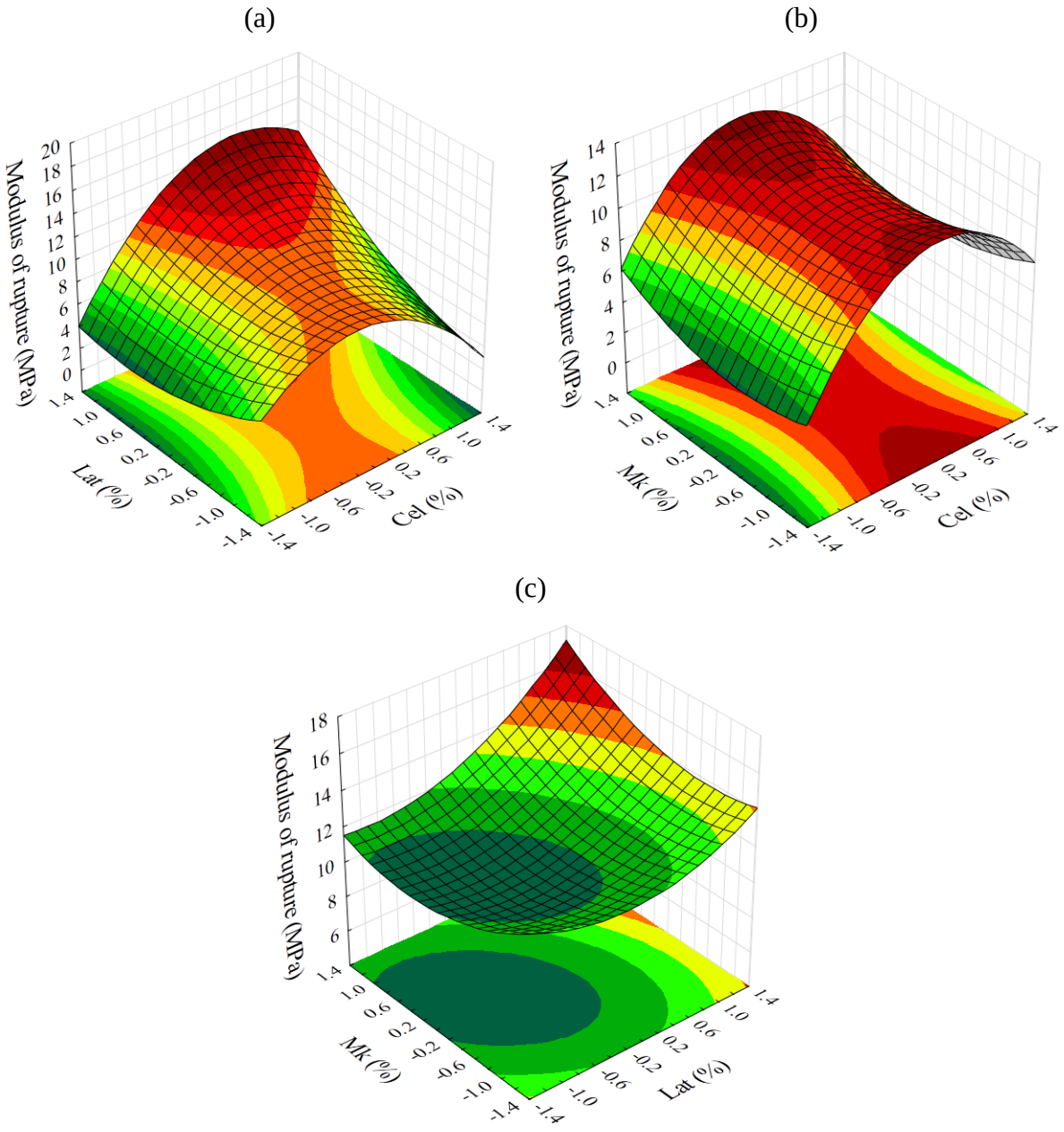

Figure 1: Surface response to the modulus of rupture - (a)% metakaolin in the central level (X_3 = 0); (b) % latex in the central level (X_2 = 0) ; (c) % cellulose in the central level (X_1=0)

According to Figure 1a it was possible to observe the influence of the variables X_1 (cellulose) and X_2 (latex) in the modulus of rupture of the composite. The figure presented five regions. Among these regions it is worth mentioning the maximum point located at the intersection of the maximum concentration of latex, in the coded value of 1.41, equivalent to the decoded value of 0.249%, and the coded value of cellulose around 1.0, equivalent to 8.5% (decoded) , resulting in a rupture modulus value of 14.5 MPa. This result can be justified by the rough surface of the fiber that conditions an appropriate anchorage and an adequate reinforcement [12]. In addition, possibly,

the presence of a greater amount of latex particles not only reduce the amount of water movement through the capillary blockage but also when cracking occurs, polymer latex film captures these channels and restricts their propagation. This results in increased flexural strength. The contact of the cellulosic fiber with the latex may have caused a certain hydrophobization of the same, protecting it from possible chemical attacks. However, there are minimum points at the intersection of the minimum concentration of latex (0%) and the maximum concentration of cellulose (10%) that can be attributed to the difficulty of molding the composite caused by the high content of cellulose, influencing its homogeneity and causing points of concentration of tensions [13].

However, with the reduction of the cellulose content, a decrease in the value of the rupture modulus was observed since the reinforcement was not enough. This same behavior was observed in the evaluation of the cellulose content and metakaolin content (Figure 1b). The maximum value for the modulus of rupture (around 12.6 MPa) was exactly in cellulose values around 5.7% and in the largest replacement of cement by metakaolin (40.2%, referring to the coded value of 1.41). Higher values of metakaolin probably resulted in a lower porosity of the matrix, resulting, possible, in higher values for the modulus of rupture [14]. In addition, due to the property of lowering the alkalinity in the matrix, possibly decreased cellulose degradation and improved the durability of the composites [15]. When the analysis was performed evaluating the % latex and metakaolin variables, with the cellulose value at the central point (5%) (Figure 1c), it was observed that there was a minimum area for the modulus of rupture response. This result can be explained by the lower reinforcement attributed to the lower quantity of cellulose, a smaller decrease in the number of pores, with the replacement of only 22% of metakaolin reducing its resistance and for the content 0.06% of latex, resulting in less modification of the cement matrix. Thus, it was observed that the best conditions analyzed to maximize the value of the rupture modulus were the combinations of the values of cellulose in 8.5%, of latex in the value of 0.249% and of metakaolin in the central point (19%).

For the absorption response, it was observed that equation 2 was significant, with a coefficient of variation (R^2) of 0.92, for a confidence level of 90%. In this way, it was possible to construct the response surfaces for the absorption (Figure 2).

$$(A) = 23.4+14.2(X_{cel})+6.7(X_{cel})^2-1.3(X_{Lat})-2.9(X_{Lat})^2+0.6(X_{Mk})-3.2(X_{Mk})^2- 2.3(X_{cel}) \quad (2)$$
$$(X_{Lat})-0.6(X_{cel})(X_{Mk})-0.7(X_{Lat})(X_{Mk})$$

According to Figures 2a,b, it was possible to observe the influence of the variables X_1 (cellulose), X_2 (latex) and X_3 (metakaolin) in the absorption value of the composite. It can be observed that, when analyzing only variable X_1, large amounts of cellulose in the composite results in higher values for absorption, with a maximum value of approximately 60%, independent of the concentrations used for latex and metakaolin. This fact, possibly, was due to the hydrophilic nature of cellulose, which absorbs water when in contact with moisture.

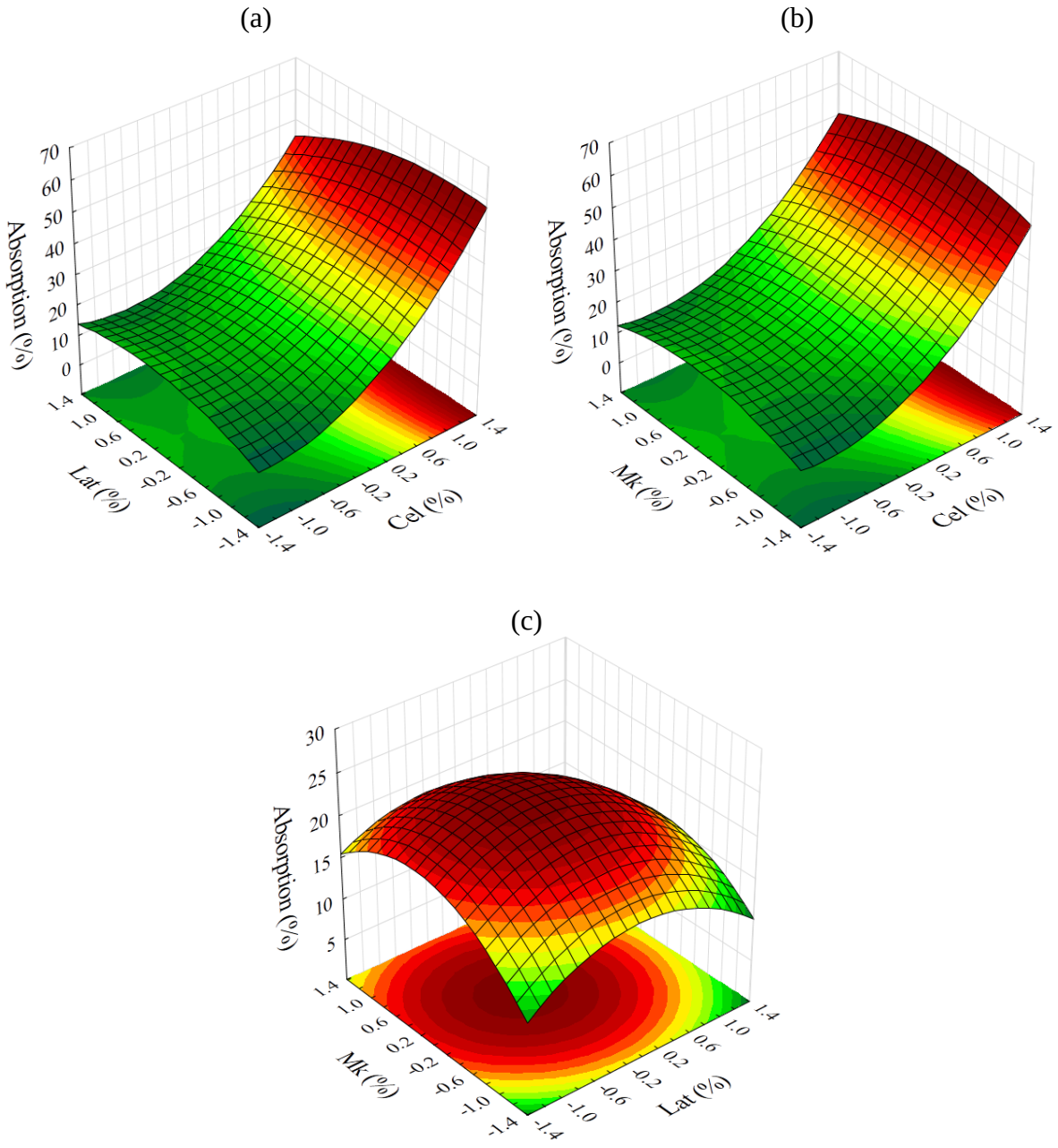

Figure 2: Surface response to the absorption - (a) % metakaolin in the central level ($X_3 = 0$); (b) % latex in the central level ($X_2 = 0$) ; (c) % cellulose in the central level ($X_1=0$)

According to [16] the absorption of water is one of the main problems that limit the application of materials based on cellulose, as this affects dimensional stability, mechanical properties and durability. However, there are minimum regions for the absorption value when working with combinations of variables. In the percentage of cellulose around point -1 (1.5%),% latex value at the maximum point of 1.41 (0.249%) and metakaolin at the central point equal to 0 (19%), a minimum absorption value was observed, around 11.54%.

When analyzing for the same value of cellulose, metakaolin at the maximum point of 1.41 (40.2%) and latex at the central point equal to 0 (0.115%) (Figure 2b), the absorption value was 11.23%. When the values found for the first combination and the second combination were compared, it was observed that the values for absorption were statistically the same. Thus, it was possible to affirm that only the cellulose variable (X1) is significant for the analysis of the absorption response. Possibly a better dispersion of the latex or a longer time of contact with the cellulose could result in a different behavior after the 28 days of cure, ensuring, possibly, not only the modification of the cementitious matrix, also increasing its resistance to chemical attacks and greater resistance, as decrease the hydrophilicity of the cellulose, resulting in lower values for absorption. After analyzing the response surfaces for the rupture modulus and the absorption, it was possible to understand the behavior of the composites against the variables chosen for the study (cellulose, latex and metakaolin), within the ranges used, showing the importance of this analysis for the possible utilization of natural fibers added of latex and replacement of part of cement by metakaolin in cement matrix.

4. CONCLUSIONS

- The use of natural fiber (cellulose) increased the strength of the composite.
- The highest percentage of latex used in the planning (0.249%) possibly caused a certain hydrophobization of cellulose fiber, resulting in greater resistance to rupture.
- Use of metakaolin as a substitute for cement possibly resulted in the lower porosity of the matrix, resulting in the increase of the modulus of rupture.
- The best condition analyzed to maximize the value of the rupture modulus was the combination of the values of cellulose in 8.5%, of latex in the value of 0.249% and of metakaolin in the central point (19%).
- Cellulose is the most significant variable in the analysis of the absorption of the composite due to its hydrophilicity.
- Thus, it was possible to observe that the modification of cellulose fiber with the use of latex, together with the replacement of part of cement by metakaolin, is a route that can be used in the civil construction since correctly studied the combination between these variables.

ACKNOWLEDGEMENTS

The authors would like to acknowledge CNPq, CAPES and FAPEMIG for supporting this work.

REFERENCES

[1] Silva, R., Haraguchi, S.K., Muniz, E.C., Rubira, A.F., ‘Aplicações de fibras lignocelulósicas na química de polímeros e em compósitos’, *Quim. Nova*. **32** (3) (2009) 661-671.

[2] Onuaguluchi, O. and Banthia, N., ‘Plant-based natural fibre reinforced cement composites: A review’, *Cem. Concr. Compos.* **68** (1) (2016) 96-108.

[3] Lima, P.R.L., Toledo-Filho, R., ‘Uso de metacaulinita para incremento da durabilidade de compósitos à base de cimento reforçados com fibras de sisal’, *Ambiente construído*. **8** (4) (2008) 7-19.

[4] Macvicar, R., Matuana, L. M., Balatinecz, J.J., ‘Aging mechanisms in cellulose fiber reinforced cement composites’. *Cem. Concr. Compos.* **21** (3) (1999) 189-196.

[5] Mohanta, N., Acharya, S.K., 'Fiber surface treatment: Its effect on structural, thermal, and mechanical properties of *Luffa cylindrical* fiber and its composite', *J. Compos. Mater.* **50** (22) (2015) 1-15.
[6] D'Almeida, A.L.F.S., Calado, V., Barreto, D.W., 'Acetilação da Fibra de Bucha (*Luffacylindrica*)', *Polímeros: Ciência e Tecnologia*. **15** (1) (2005) 59-62.
[7] Motta, L.A.C., John, V.M., Agopyan, V., 'Thermo-mechanical treatment to improve properties of sisal fibres for composites', *Mater. Sci. Forum*. **636-637** (2010) 253-259.
[8] Claramunt, J., Ardanuy, M., García-Hortal, J.A., 'Effect of drying and rewetting cycles on the structure and physicochemical characteristics of softwood fibres for reinforcement of cementitious composites'. *Carbohydr. Polym.* **79** (1) (2010) 200-205.
[9] Rabello, M. 'Estudo da influência do Metacaulim HP como adição de alta eficiência em concretos de cimento Portland', *Metacaulim do Brasil*. (2003) 1-65.
[10] Bentur, A. and Mindess S., 'Fibre reinforced cementitious composites', 2nd Edn (Grã-Bretanha, Taylor & Francis, 2007).
[11] Rilem. Technical Committee 49 TRF. 'Test for determination of modulus of rupture and limit of proporcionality of thin fibre reinforced cement section', *Matériaux et Constructions*. **17** (102) (1989) 441-443.
[12] Savastano Jr., H., 'Materiais à base de cimento reforçados com fibra vegetal: reciclagem de resíduos para a construção de baixo custo', *Tese (Livre-Docência)* - Escola Politécnica da Universidade de São Paulo, São Paulo.(2000).
[13] Pimentel, M.G., Borges, J.P.C., Picanço, M.S., Ghavami, K., 'Resposta à flexão e análise de tenacidade de argamassas reforçadas com fibra de Curauá', *Revista Matéria*. **21** (1) (2016) 18-26.
[14] Antoni, M., Rossen, J., Martirena, F., Scrivener, K., 'Cement substitution by a combination of metakaolin and limestone', *Cem. Concr. Res.***42** (12) (2012) 1579-1589.
[15] Wei, J., Ma, S., Thomas, D.G., 'Correlation between hydration of cement and durability of natural fiber-reinforced cement composites', *Corros. Sci.***106** (1) (2016) 1-15.
[16] Moon, R.J., Martini, A., Nairn, J., Simonsen, J., Youngblood, J., 'Cellulose nanomaterials review: structure, properties and nanocomposites', *Chem. Soc. Rev.***1** (7) (2011) 3941-3994.

STUDY ON MECHANICAL BEHAVIOR OF CEMENTITIOUS COMPOSITES PRODUCED WITH MINERAL ADDITIONS AND REINFORCED WITH JUTE FIBER MESH

Ficher Nadine M.[(1)], Eichholz Emanuele[(1)], Stefanello, Leonardo [(1)], Marangon, Ederli[(1)] Kosteski, Luis E. [(1)]

(1) Department of Civil Engineering, Federal University of Pampa. Alegrete, Brazil

https://doi.org/10.21452/bccm4.2018.02.12

Abstract

This work aims to study the behavior of cementitious composites reinforced with natural jute fibers mesh by means of mechanical tests. For this, samples were prepared with Brazilian Portland cement, and with replacement of 50% of the cement, on mass, by metakaolin, fly ash and rice husk silica. The study, 35x40x1,2cm size plates (LxCxE) were molded in which five layers of jute fiber mesh were embedded with a 5x5 mm opening. After 21 days of age the plates were cut with a diamond saw in 5x40x1,2cm (LxCxE) samples. For order to obtain the evaluation of the mechanical behavior of the composites bending tests were performed. The use of the fibers directly affected the decrease of the first crack stress when compared to composites without fibers. The reduction of this value, on average, to the reference matrix 69,36%, while the reduction for the substitutions of fly ash, metakaolin and silica of rice husk were, respectively, 57%, 38,32% and 15,89%. On the oder hand, the reduction of the first crack stresses, the addition of the jute fiber was able to overcome the fragile behavior of the cementitious matrix, presenting a strain-softening behavior.

1. INTRODUCTION

Civil construction has been seeking in recent times, along with the other branches of the construction industry, technological innovations that will provide improvements in its most varied areas. The science of materials, for example, is one of the fields that has undergone great evolution. Within this context of innovation in materials science, composites are elements that have gained an important focus, since they have a good resistance to compression, with this they have a wide applicability in the civil construction, like tiles, partitions and wall coverings, in the However they are brittle materials when subjected to traction and loads dynamicase that has small deformation at break. To overcome the brittle behavior and improve the properties of this material in terms of ductility, thus increasing its field of application, it is suggested the combination with another material that has properties capable of absorbing these deformations.

Many authors, such as [1][2[3], investigate the mechanical properties of very different plant fibers available in nature, such as coconut, bamboo, sisal, curauá and jute, mainly due to the fact that natural plant fibers have the advantages of being non-toxic , renewable, recyclable and biodegradable and have a relatively low cost (considered to be one of the greatest advantages over steel fibers, for example).

The use of pozzolanic materials - such as fly ash, metakaolin and rice husk silica - is a requirement when using vegetable fiber reinforcement in cementitious matrices, because they are responsible for consuming calcium hydroxide (CH) during the process of hydration of the Portland cement, the main cause of the degradation of the natural fibers[1][4].

[1] and [5], studied the ideal amount of layers of natural fibrous reinforcement, and the fibers used for the study were jute and sisal, respectively. The authors concluded that the higher the number of reinforcement layers, the greater the formation of fissures and the higher the values of ultimate stress, being 5 considered the ideal number by this study. Jute fiber reinforcement was associated with a partial substitution of Portland cement by 40% of metakaolin and 10% of volatile ash, other percentages of the same additions were studied, which was the one that provided the highest consumption of calcium hydroxide at 28 days . The sisal reinforcement was inserted into a matrix with partial replacement of Portland cement by 50% of calcined clays (metacaulinite and ground brick), which, through microscopy, were also efficient in calcium hydroxide consumption.

Thermogravimetric tests performed on composites reinforced with natural fibers that were submitted to a wetting and drying cycle, proved that the mass substitution of 30% of Portland cement by metakaolin is able to reduce the calcium hydroxide content to zero by controlling the pH of the solution and being effective for the mitigation of the degradation of the natural reinforcements, without damaging the mechanical behavior of the composite [1][6][7].

[4] studied the behavior of sisal fiber reinforced composites, produced with a matrix with 30% partial replacement of Portland cement by rice hull ash, this substitution content was able to mitigate alkaline deterioration and mineralization of sisal fiber, showing that rice hull ash has effects similar to fly ash and metacaulim found in the studies cited above.

2. EXPERIMENTAL PROGRAM

2.1 Materials and processing

In the production of the cementitious composites, was used jute fibers mesh, Brazilian Portland CP V-ARI cement, mineral additions (fly ash, metakaolin and rice husk silica), river sand with a maximum diameter of 1,18mm and superplasticizer in amounts adjusted according to each matrix to maintain the desired workability in the blends (between 250mm and 300mm). The concrete mixtures used for the different matrices were based on previous research [2].

Table 1 shows the proportions of cement (CT), fly ash (CV), metakaolin (MK) and rice husk silica (SL) ratios used in the fourth mixtures that were prepared, namely M1, M2, M3 and M4, respectively. For each matrix, laminates were molded without reinforcement and reinforced with 5 layers of jute fibers. The composites were molded into 35x40x1,2cm (LxCxE) dimensions that after 21 days of curing were cut by a diamond saw in the dimensions of 5x40x1,2cm.

Table 1: Composition of matrixes and composites

Composite	CT(%)	CV(%)	MK(%)	SL(%)	Layers
M1-0	100	0	0	0	0
M1-5	100	0	0	0	5
M2-0	50	50	0	0	0
M2-5	50	50	0	0	5
M3-0	50	0	50	0	0
M3-5	50	0	50	0	5
M4-0	50	0	0	50	0
M4-5	50	0	0	50	5

2.2 Mechanical test methods

After 180 days, the samples were submitted to a three-point flexural test to evaluate the mechanical behaviour of the composites. The tests were performed on the Shimadzu AGS-X mechanical test machine, Figure 1, which has a maximum capacity of 5 kN. The tests were run at a controlled speed of 0.2mm/min with capacity of 5kN.

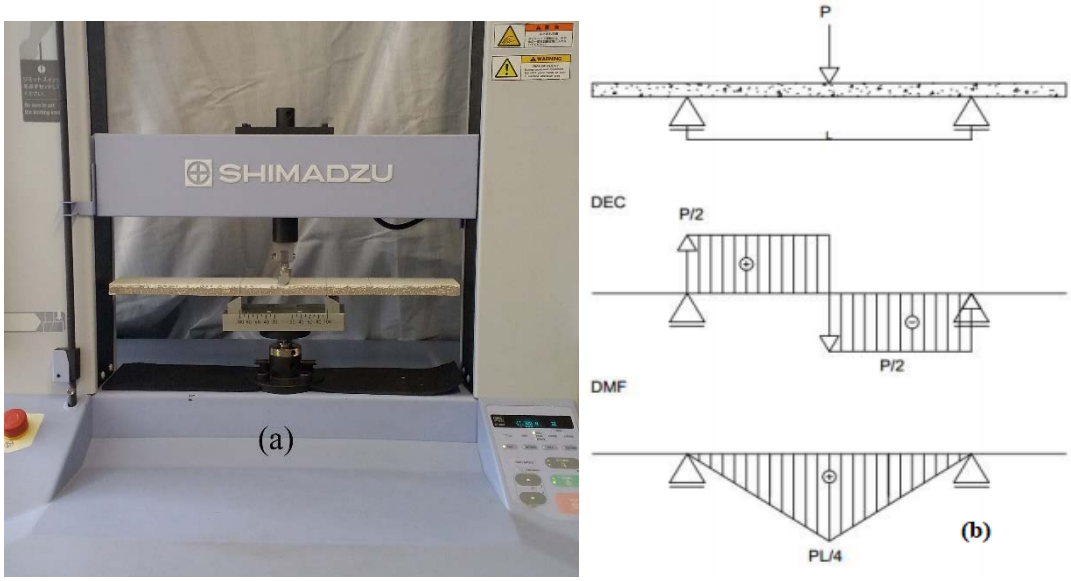

Figure 1: (a) Bending test in progress at Shimadzu (b) Configuration of the behavior of the sample under flexural tests.

3. RESULTS AND DISCUSSION

3.1 Compressive Stress

Compressive tests were performed on the matrices produced, the values of compressive strength, as well as standard deviation and coefficient of variation, are shown in Table 2.

Table 2: Compressive Strength of the matrices

Matrix	*fc(MPa)*
M1	72,68 (±14,8%)
M2	58,61 (±3,19%)
M3	58,44 (±11,96%)
M4	60,51 (±16,34%)

Analyzing the results it is possible to observe that the partial replacement of the Portland cement by mineral additions caused a decrease in the compressive strength of the cement matrix, being a reduction of 24% from M1 to M2, 24.36% for M3 and 20.11% compared with the matrix M4.

3.2 Bending behavior of the composites

In Figure 2 are the values of the average maximum stress reached for each composite produced. Through the analysis of the data, it is observed that the matrices M2-0, M3-0 and M4-0 had a maximum strain reduction around 35% in relation to the composite M1-0. In contrast, it is possible to observe that the composites M1-5 had a greater influence on the maximum peak resistances, suffering a reduction of 69,36% compared to the composite M1-0, while the composites M2-5, M3-5 and M4 -5 were reduced by 57%, 38.32% and 15.89%, respectively, compared to composite references (M2-0, M3-0 and M4-0).

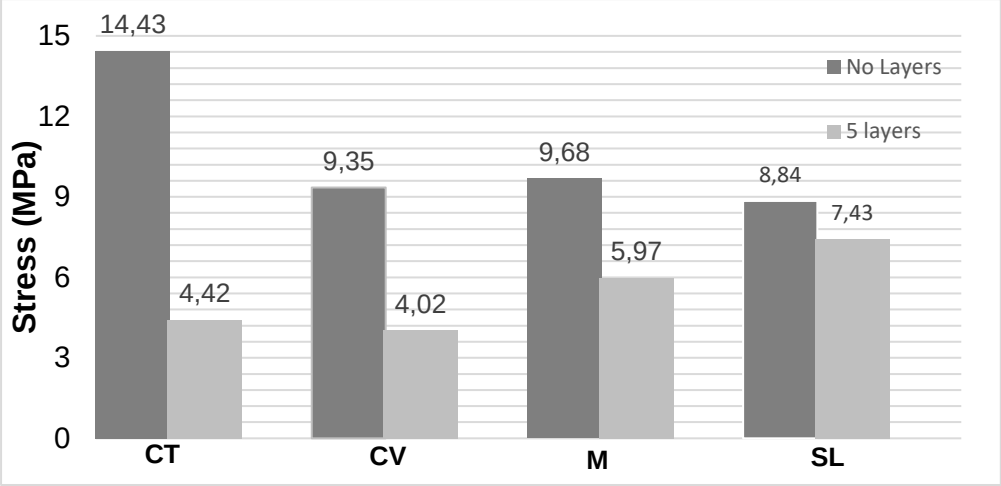

Figure 2: Maximum stresses of rupture of the composites

The typical Stress x Displacement curves of the composites M1-0, M2-0, M3-0 and M4-0 are shown in Figure 3, according to the expected behavior of these composites is fragile, breaking immediately when the sample reaches the maximum breaking strength.

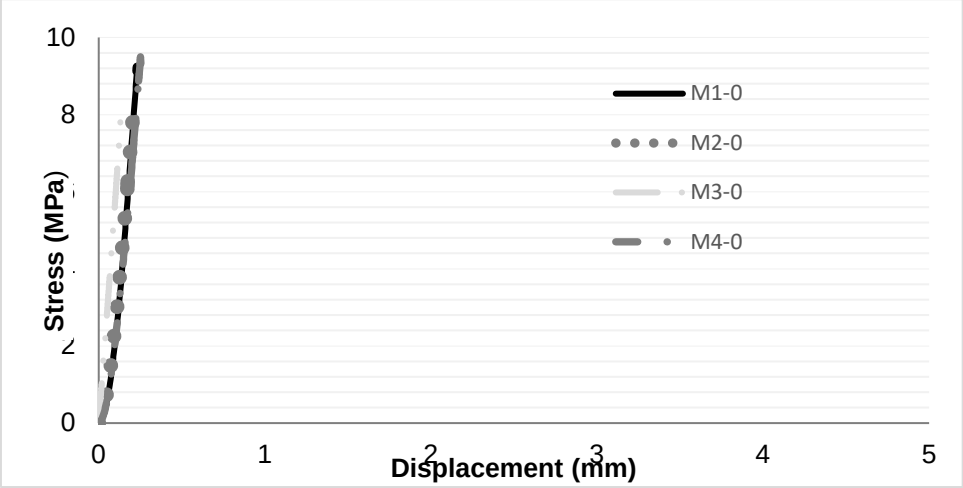

Figure 3: Typical curves of composite behavior without reinforcement

According to the typical Strain x Displacement curves of the composites M1-5, M2-5, M3-5 and M4-5 in Figure 4, the reinforced composites with 5 reinforcement layers when reaching their maximum peak tension suffer a large fall of resistance, but there is no abrupt rupture of the material, thus characterizing *strain softening* behavior. Thus, the mesh used as reinforcement was able to overcome the problem of composite fragility.

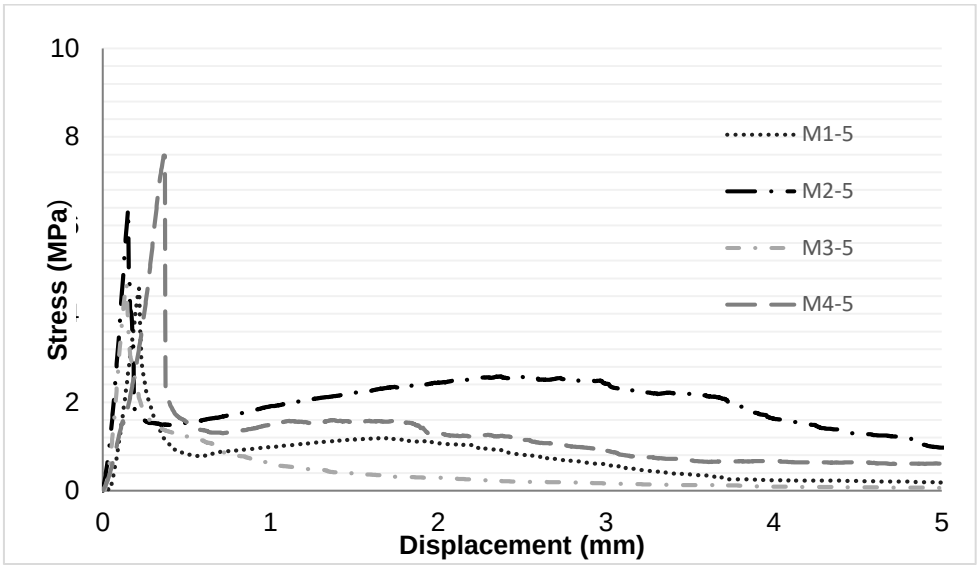

Figure 4: Typical composite behavior curves with 5 layers

4. CONCLUSIONS

- The partial substitution of Portland cement by mineral additions caused a reduction in the resistance of the cimenticeas matrices produced, in both the compressive strength and the maximum tensile strength. The compressive strength losses were 24% for the

replacement of fly ash and metakaolin and 20% for rice husk silica, while for tensile the reduction was approximately 55% for the three mineral additions.

- The use of the jute fiber fabric as a reinforcement of the composites decreased the maximum tensile strength of the composites, reaching a reduction of more than 50% in the case of the composites produced with the matrix M1 and M2. The composite M4-5 also presented reduction in the load capacity in relation to the composite M4-0, but in a relatively low value, only 15.89%, in comparison with the other composites.
- It is believed that the reduction of the performance of the composites is associated with the fluidity and viscosity of the matrix used. Possibly, the rheological properties were not adequate to fill the mesh of the jute, impairing the transfer of stresses.

REFERENCES

[1] SILVA, F. A. Durabilidade e propriedades mecânicas de compósitos cimentícios reforçados por fibras de sisal. 2009. 243 p. Tese (Doutorado em Engenharia Civil) – Universidade Federal do Rio de Janeiro, Rio de Janeiro, 2009.Sterman, S. and Marsden, J.G., 'Silane coupling agents', *Ind. Engng. Chem.* **58 (**3) (1966) 33-77.

[2] MELO FILHO, J. A. Durabilidade química e térmica e comportamento mecânico de compósitos de alto desempenho reforçados com fibra de sisal. 2012. 184 f. Tese (Doutorado em Engenharia Civil) – Universidade Federal do Rio de Janeiro, Rio de Janeiro, 2012.

[3] FIDELIS, M. E. A. Desenvolvimento e caracterização mecânica de compósitos cimentícios têxteis reforçados com fibras de juta. 2014. 266 f. Tese (Doutorado em Engenharia Civil) –Universidade Federal do Rio de Janeiro, Rio de Janeiro, 2014.

[4] WEI J. MEYER C. Utilization of rice husk ash in green natural fiber-reinforced cement composites: Mitigating degradation of sisal fiber. Cement and Concrete Research, v. 81, p.94-111, 2016.

[5] MELO FILHO, J. A. Desenvolvimento e caracterização de laminados cimentíceos reforçados com fibras longas de sisal. 2005. 124 f. Dissertação (Mestrado em Engenharia Civil) – Universidade Federal do Rio de Janeiro, Rio de Janeiro, 2005.

[6] LIMA, P. R. L. TOLEDO FILHO, R. D. Uso de metacaulinita para incremento da durabilidade de compósitos à base de cimento reforçados com fibras de sisal. Ambiente Construído, v. 8, p.7-19, 2008.

[7] WEI J. MEYER C. Degradation mechanisms of natural fiber in the matrix of cement composites. Cement and Concrete Research, v. 73, p.1-16, 2015.

DEVELOPMENT OF CEMENT- BASED MATRIX COMPOSITES REINFORCED WITH TREATED JUTE FABRICS USING THE POLYMER STYRENE-BUTADIENE

Bruno Marani Siciliano (1), Gabriel Furtado (1), Lucca de Campos Fontolan (1) and Saulo Rocha Ferreira (1)

(1) Department of Engineering, Universidade Federal de Lavras, Brazil

https://doi.org/10.21452/bccm4.2018.02.13

Abstract

The use of plant fibers for low impact and durable composites development has a well-known importance, since they are biodegradable and low cost. These fibers and their fabrics are used as reinforcement on cement based composites in order to improve their mechanical properties. However, it is important to consider the interface between the natural fibers and the matrix. In the present paper, jute fibers fabric were treated superficially using several styrene-butadiene polymers to promote durability and to increase bonding to a cement based system. A matrix free of calcium hydroxide was used. Jute fabrics were evaluated by mechanical and chemical analysis. Adhesion was evaluated by Pull-out tests.

Keywords: Natural vegetable fiber, Jute, Styrene-Butadiene, Polymer, Composite.

1. INTRODUCTION

Despite the benefits of the use of natural fibers as the ultimate green material option, such as minimizing the use of natural resources and overall lifetime impact, the use of such material is not that simple. In the line of development of materials reinforced with natural fibers, many researchers have been carried out on cementitious and polymeric matrix composites and promising results have been achieved.

Even with results showing an improvement in strength and ductility there still a lack of information about fiber and composite durability.

The impregnation treatment using the styrene-butadiene (SBR) polymer can be an alternative to improve adhesion and promote composite durability, considering that SBR polymer builds a physical and chemical bond to both cellulose and cement based matrix [5]. Therefore, both the partial replacement of cement by metakaulin can promote natural fibers protection mechanisms against alkaline degradation.

In summary, this research objective was to evaluate the mechanical and chemical behaviour of polymer treated jute fabrics regarding the interface with a cement-based matrix.

2. MATERIALS AND METHODS

2.1 Natural jute fabrics and polymer treatments

The Natural jute fabrics used in the present study were obtained from a Brazilian company, located in the city of São Paulo. The average diameter of natural jute fibers was 0.066 mm. Each jute string contained, in average, 12 fibers, and its average diameter was 0.785. Moreover, natural jute fabric contained, in average, 2.7 strings/cm and 3.5 strings/cm, transversely and longitudinally, respectively.

The polymer treatment used in the present study consisted in an impregnation by immersing a fabric of fibers in three different polymers: NTL-271 carboxilated styrene-butadiene polymer (SBR-X), NTL-350 (SBR-1) and L-2108 (SBR-2) its monomers emulsion where the continuous phase is water (See table 1). The jute fibers were placed in a container with the polymer emulsion for 50 minutes. The fibers were then dried in an oven during 24h at 40ºC.

Table 1: Polymers used to treat the Natural jute fabrics

	Styrene content (%)	**pH**	**Surface Tension (dynes/cm)**	**Brookfield Viscosity (cP)**	**Solid content (%)**
SBR-X (NTL-218)	50%	8.5 – 9.5	40 - 50	90 – 200	48 - 50
SBR-1 (NTL-350)	-	11-12	35-45	70	49-51
SBR-2 (L-2108)	21.5-25.5	10.7 – 11.7	55 – 60	43	38-41

2.2 Direct tensile tests (fabric)

Four samples for each treatment and for the natural fabric were crafted for these tests. The treated and natural fabrics were cut in 30 cm x 5 cm (length x width) tapes and a 4 cm silver-tape protection was set at the fabric edges in order to mitigate the fabric displacement during the test, so that, the effective dimensions of the fabric requested in the test were 22 cm x 5 cm (length x width).

The fabric tapes were tested in an Arotec machine with a load cell of 300 kN, at the Department of Engineering at UFLA, at a 1.25 mm/min speed.

2.3 Differential Scanning Calorimetry (fiber)

Fiber samples, extracted from the jute fabrics, weighing 10mg were subjected to a heating rate of 10°C/min until reaching 1000°C in a platinum crucible using 100 ml/min of nitrogen as the purge gas. The DSC tests took place at the Department of Chemistry at UFLA.

2.4 Developed matrix

The cement-based matrix that was used in this project was made using a 20L volume mixer. The design mix adopted was the following one: 1 (cement): 0.8 (metakaulin): 1.2 (fly ash): 1.52 (sand): 0.38 (water). Furthermore, 0.85% (bwc) of Glenium 51 super-plasticizer, acquired from BASF Brazil.

2.5 Pull-out test (string)

Thirteen samples for each treatment and for the natural string were crafted for these tests. Cylindrical samples with internal diameter of ¾ in and 25 mm high were made using the cement-based matrix established before and using PVC tubes with same dimensions as molds. The matrix was inserted in the molds, while the jute strings, extracted from the fabrics, were aligned uprightly at their centers. The pull-out tests were performed at the Department of Food Science at UFLA, using a Stable Micro System Lite Texturometer at 0.3 mm/min speed, after 7 days age.

3. RESULTS AND DISCUSSION

3.1 Direct tensile tests (fabric)

The average diameter of natural jute fibers was 0.066 mm. After polymer treatment the average value changed to 0.068, 0.070 and 0.068mm to polymer SBR-1, SBR-2 and SBR-X, respectively. Figure 1 shows the typical curves of raw and treated fabrics subjected to tensile test. According to Figure 1, it is notable that the treated fabrics reached a higher capacity of deformation while requested in the direct tensile test. It is possible to observe that the treatments improved strain capacity in 79.78, 92.22, 63.33 % to SBR-1 SBR-2 and SBR-X, respectively, in comparison to the raw jute.

Moreover, as shown in Figure 1, all treatments decreased stiffness values, in comparison to raw jute. The jute fabrics treated with Styrene and Butadiene achieved similar stiffness values. The Styrene treatment improved the maximum value of the material's strain in 10.70 %, while the others treatments reduced this maximum value, comparing to the natural fabrics (Figure 1).

Figure 1: Typical curves of raw and treated fabrics subjected to tensile test.

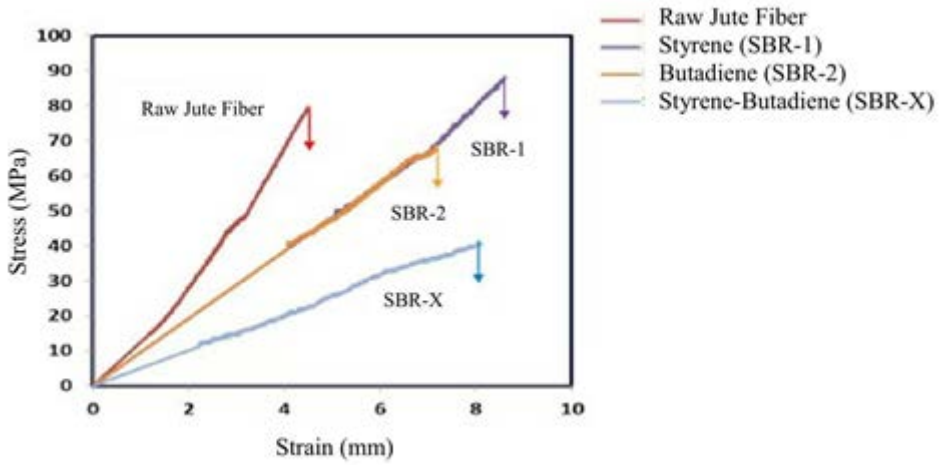

3.2 Differential Scanning Calorimetry tests (fiber)

Figure 2 indicates the thermal evolution of fibers substances degradation events with the temperature.

As shown in figure 2, for all the treatments, cellulose molecules were degraded for temperatures greater than 350 ºC, which is their typical degradation temperature. Thus, it can be deduced that all applied treatments intensified the interaction of cellulose molecules with each other.

Figure 2: Thermal evolution of fibers substances degradation event with the temperature.

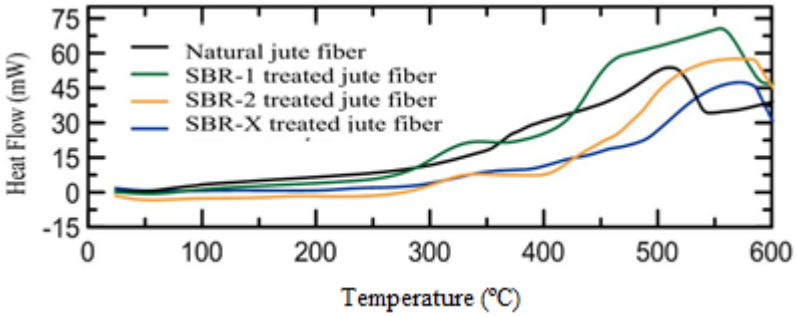

3.3 Pull-out tests (string)

Figure 3 indicates the typical curves of natural and treated jute strings when subjected to the pull-out test.

According to Figure 3, it is notable that the SBR-X treatment increased in 33.63 % the pull-out load of the string, comparing to the natural one. This result indicates that the Styrene-butadiene treatment increases the adhesion between the jute string and the matrix.

Figure 3: Typical curves of natural and treated jute strings subjected to the pull-out test.

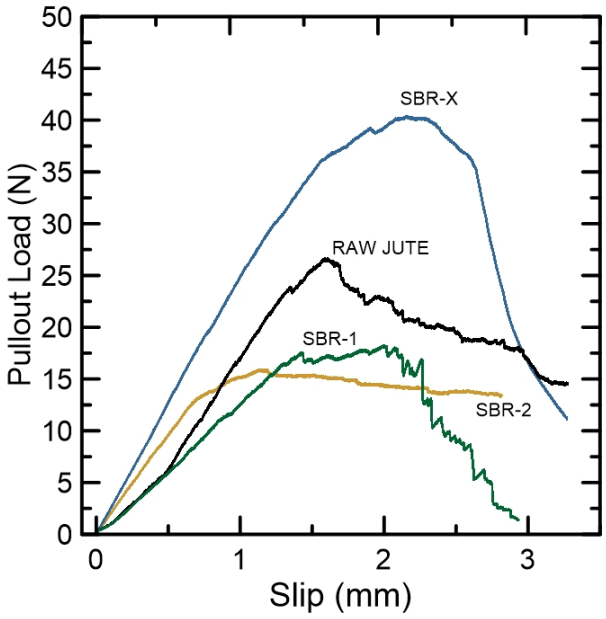

4. CONCLUSION

The work in hand investigated the effect of several polymers treatments on jute fibers mechanical and fiber-matrix interface properties. The following conclusions can be drawn from the present research:

- All applied treatments promoted an increase of thermic stability of cellulose;
- After treatment the jute fibers presented an increase of strain capacity;
- SBR-X polymer treatment was more effective on increasing fiber-matrix adhesion.

ACKNOWLEDGEMENTS

BASF S.A. Brasil;
Conselho Nacional de Desenvolvimento Científico e Tecnológico (CNPq);
Metaculim do Brasil Indústria e Comércio;
Nitriflex S.A. Indústria e Comércio.

REFERENCES

[1] SANTIAGO, M. O. *Aplicações do GCR – cimento reforçado com fibra de vidro em novos estádios de Sevilha.* In: Arquimacom'2002, 2002, São Paulo.
[2] HANNANT, D. J. *Fibre cements and fibre concrete*. Nova Iorque, EUA: John Wiley and Sons, 1978.
[3] HOLMER, S. J. *Materiais á base de cimento reforçados com fibra vegetal: reciclagem de resíduos para a construção de baixo custo*. 2000. 76 f. Tese – Escola Politécnica, Universidade de São Paulo, São Paulo.
[4] TOLEDO FILHO, R. D. et al. Development of vegetable fibre-mortar composites of improved durability. *Cement & Concrete Composites*, v. 25, pp. 185-196.
[5] FIDELIS, M.E.A. *Desenvolvimento e caracterização mecânica de compósitos cimentícios têxteis reforçados com fibras de juta.* 2014
[6] FERREIRA, S. R. *Effect of Sisal Fiber Hornification on the Fiber-Matrix Bonding Characteristics and Bending Behavior of Cement Based Composites*. Key Engineering Materials. 2014
[7] OHAMA Y. Handbook of polymer-modified concrete and mortars. *Properties and process technology,* 1 ed. New Jersey, Noyes Publications, 1995.
[8] GOMES, C.E.M., FERREIRA, O.P., *Influência das adições do copolímero VA/VEOVA e fibras sintéticas nas propriedades da pasta de cimento Portland*. Revista Iberoamericana de Polímeros v.7, n. 3, pp. 162-173, ago. 2006.

UTILIZATION OF CASTOR OIL TO PRODUCE AN AIR INCORPORATOR ADDITIVE FOR CONCRETES

Rodrigo M. S. Silva (1), Amanda L. M. S. Melo (1) and Filipe S. Duarte (1)

Federal Institute of Education, Science and Technology of Alagoas, Brazil

https://doi.org/10.21452/bccm4.2018.02.14

Abstract

The importance of developing efficient and sustainable alternatives to the high toxicity products in the civil construction market is one of the most relevant topics in Materials Science and Engineering worldwide. Within this reality are the additives for concrete and mortars, which despite being widely used products, are still produced without taking into consideration the environmental impacts that their substances cause to the environment. One type of additive that is increasingly in focus in the construction industry is the air incorporator to concretes additive type, used to produce the so-called "cellular concrete" that has the specific weight substantially reduced by the additive effect, generating great savings in works that use constructive systems with this type of concrete. The formulation used for the preparation of this type of additive by the industries present in the market is based on toxic materials that attack the environment, such as linear alkylbenzene and miscellaneous materials. Therefore, due to the high toxicity of these compositions, these products generate a high environmental impact when they come into contact with nature. From this reality, the present work proposes to elaborate a process for the development of a bioaddtive incorporating air based on castor oil (Ricinus communis L.), which was collected in the city of Arapiraca-AL, in northeastern Brazil. This process is described through the analysis of physical and chemical properties of the plant and experimental tests and dosages in order to analyze its quality in relation to the standards contained in the literature and thus contribute to the efficient, economical and sustainable evolution of civil construction.

1. INTRODUCTION

The chemical addition in the production of concrete and mortars modifies one or more properties of such mixtures. These chemical additives, being widely used in the construction industry, can be considered as the fourth component of concrete, in addition to water, cement and aggregates. It is possible to emphasize the importance of the additives and several additions, allowing significant changes in the mechanical properties and the durability of concretes [1].

The additive type IA (Air incorporators), has been increasingly used in Brazil and the world in the making of the so-called "cellular concrete". This additive aims to produce a microscopic bubble system that is stable and uniform, producing concretes with reduced specific gravity, with

excellent thermal, acoustic behavior and considerable concrete savings in the work. These bubbles substantially improve the durability of concrete subjected to freezing and thawing stages, allowing greater workability in the fresh state [2].

Air-entraining additives produced by the construction industry are mainly composed of linear alkylbenzene sulfonate, such as: alkyl-arylsulphonated. Anionic surfactant is a surfactant, which is considered to be toxic. Some of the main environmental impacts of this substance are the decreases in the concentration of elements necessary for aquatic life, for example: dissolved oxygen, due to the reduction of water / air surface tension; decrease the permeability of light by keeping the particles present in suspension; increase of the concentration of xenobiotics and mainly the formation of foam and consequent inhibition of autodepuration of the water courses and dissipation of impurities.

The reasons for provoking the incorporation of air in the concrete are many, being the main ones: the increase of resistance to the cycles of freezing and thawing and the increase of the workability of the mixture and economy of building materials. These improvements are due to the air bubbles incorporated during the mixing process [3].

As a result of the absence of references on manufacturing methods for this type of additive, the objective of this work was to elaborate a process for the development of a bioaddress incorporating air based on the oil of the castor bean plant, collected in the city of Arapiraca-AL, northeast of Brazil. In this procedure, they are presented from the phases of collection of the vegetable and checks of quality of the raw material, until the preparation of fact of the additive.

2. METHODOLOGY

2.1 Collection and reserve of the raw material.

It is important to look that the castor plant, although to be a excelent adaptable plant, the clusters of the castor plant, where the seeds are, do not develop at the same time in the plant, since the flowering of the castor bean is called the botanical sympodial, where the appearance of the inflorescence takes place sequentially, between 20 and 35 days between

The collected fruits were left in the sun to dry and hatch, and then the seeds were stored in plastic bags until the time of their use. The storage should always be done in a dry and ventilated place. Figure 1 shows the dry, ready-to-use seeds, witch is the raw material for this process.

Figure 1: The raw material

2.2 Analysis of the seed moisture

Characterizing the properties of the materials of organic origin is an unpredictable factor, since there can be great variation in these properties influenced by several factors.

For this research, the analyses were performed in 4 samples of 2 grams weighed in a scale of 0.0001 precision, in order to compare its results and to draw a mean between the values.

2.3 Extraction of oil from collected seeds.

An important point about the used vegetable is the yield of its oil. The castor bean plant produces oil-rich seeds. In this work solvent extraction was used, using ethanol as the solvent for this process. In this extraction method, a liquid solvent is used to dissolve a solid or liquid substance from a solid mixture containing less soluble substances. In this process the separation of the phases occurs and then it is possible to separate the crude oil from the other substances of the seed through simple procedures of chemical separation of mixtures.

To extract the oil of the collected seeds, 40g of seeds were ground in a mortar and homogenized with ethyl alcohol. The process of separating the oil and ethanol from the pie was done by filtration. The cake held in the filter was subjected to a simple filtration for 24 hours in order to obtain a more precise yield of the oil. Finally, to remove the alcohol from the oil, the mixture was heated to 80 ° C. For the calculation of the oil yield, a relation was made between the mass of the dried seeds used and the mass of the oil obtained.

2.4 Determination of the acid value of castor oil

It is defined as the amount in (mg) of some base needed to neutralize the free acids present in one gram of oil or fat. [4] Indicate that the state of conservation of the oil is closely related to the origin and quality of the raw material.

The acidity index is a very important analysis to know the oil, since high acidity can disrupt the result of reactions that use it. For its determination, titration was made, in which titration was a solution of sodium hydroxide (NaOH) and the indicator, phenolphthalein. The procedure consisted of weighing 7 grams of the oil in a 250 ml Erlenmeyer flask, then adding 75 ml of 95% ethanol and 3 drops of the 1% phenolphthalein indicator. For the calculation, the volume of NaOH spent in the titration per gram of the sample was used.

2.5 Development of bubbles produce mechanism

The next step of the process was the development of a bubbles produce mechanism. Soaps are produced from the oils by the saponification reactions, which is a neutralization reaction. The scientific name for the soap is sodium carboxylate, due to its forming reagents, which are esters and sodium hydroxide.

The stable and simple form of the compost was the purpose, then, for the production of the liquid detergent from the castor oil, the oil was mixed with ethyl alcohol, potassium hydroxide solution and water in a Becker.

2.6 Elaboration of the additive

The following phase was to improve the able of producing and retain bubbles. An acid-base reaction is a type of chemical reaction that occurs between an acid and a base and releases certain substrates. Several definitions exist regarding this type of reaction, which provide alternative concepts for the reaction mechanisms involved and their possible applications. The additive was produced from acid-base reactions in contact with the detergent produced, in order to retain the CO2 released by the reactions.

In this type of reaction in which the CO_2 is released, when the CO_2 is produced it causes a pressure and exits together with the solution, which results in a foam. This CO_2 foam when in contact with natural detergent made with castor oil, becomes larger and more stable, that is, the viscosity of the detergent causes the CO_2 released to be partially trapped.

2.7 Analysis of performance of the additive

To verify the performance of the air incorporator additive for concrete, 18 cylindrical specimens 10x20 cm were molded, of which 9 were filled with conventional concrete and 9 with the same concrete with the additive. The workability of the concrete were analyzed by the Slump Test, standardized in Brazil as cone trunk abatement test, according to [5]. The incorporation of air from the concretes were analyzed by the comparative weighing of the cylindical specimens of concrete molded with and without the additive.

3. RESULTS AND DISCUSSIONS

3.1 Analysis of the seed moisture

The percentage of moisture obtained in the samples is in agreement with the standards, close to the results found by [6]. See Figure 2.

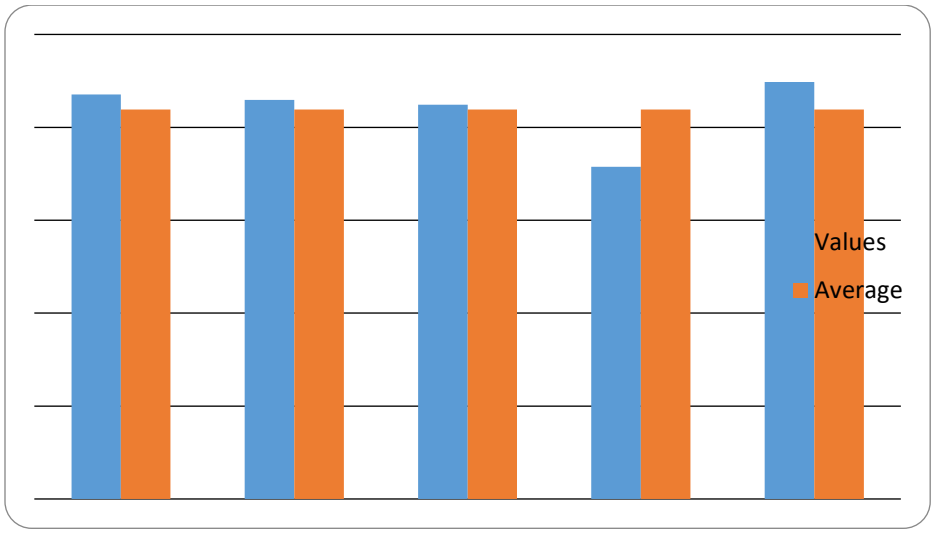

Figure 2: Seed moisture content.

3.2 Extraction of oil from collected seeds

The solvent extraction is a more modern procedure than pressing and is used to obtain higher yield than in other extraction processes. Processed seeds are immersed in the specific solvent and the separation is carried out chemically by distillation at special temperatures which causes only evaporation of the solvent, not the oil, followed by a filtration process to separate the oil from the solid part of the seed.

After extraction, a ratio was calculated between the mass of the dried seeds used and the mass of the oil obtained. The yield was 39.7%. The values were close to those found by [7], who reported values between 44%. The procedures for extraction were quite satisfactory, as the result presented a value close to those cited. See Figure 3.

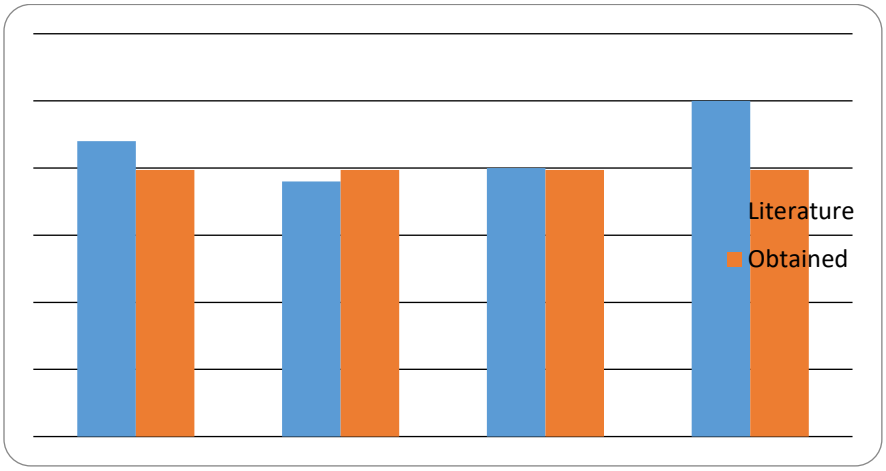

Figure 3: Average of the yeild of extraction.

3.3 Determination of the acid value of castor oil

If fatty acids form the oils and fats, a high amount of free fatty acids indicates that the product is in an advanced state of deterioration. A high acidity index indicates that the oil or fat is suffering breaks in its chain, releasing its main constituents.

The acid value is calculated by the volume equation of the titrate by the mass of the sample. The results of the test are presented in Table 1.

Table 1: Results of Acidity Index.

(mg) of KOH per gram of sample	0,73432
(%) of oleic acid	0,3932

3.4 Development of bubbles produce mechanism

The soaps are able to reduce the surface tension of the liquids that come in contact, reducing, in this way, the amount of interactions between the molecules that constitute it. A neutral liquid soap (detergent) was produced based on castor oil.

3.5 Elaboration of the additive

The produced additive was able to form a microbubble system with the CO_2 released in the acid - base reactions retained inside, in a partially stable way. See Figure 4.

Figure 4 : Additive

3.6 Analysis of performance of the addive

According to [2], there are several factors that can interfere with the incorporated air content and, although the incorporated air content is not the only parameter that should be taken into account, it is the mainly parameter that need to be measured in the fresh state of concrete by the comparative weighing of the cylindical specimens molded with and without the additive.

The concrete made with the additive obtained an incorporated air content of 8.12% and a improvement of the workability of 20 mm in the Slump Test. See tables 2 and 3.

Table 2: Incorporation of air

Dates	Concrete weight without additive	Concrete weight with additive	Incorporation of air
7 days	3779	3444	8,86%
14 days	3654	3321	9,11%
28 days	3675	3441	6,37%
Average	3702,7	3402	8,12%

Table 3: Workability improvement

Tests	Meansure of the concrete without additve (mm)	Meansure of the concrete with additive (mm)	Improvement of workability (mm)
A	100	122	22
B	89	115	26
C	93	105	12
Average	94	114,0	20,0

5. CONCLUSIONS

Based on the tests carried out for the determination of the moisture content of castor bean seeds, it was possible to verify that the samples had the necessary quality for the extraction of the oil. The oil obtained in the laboratory extraction process was adapted to the acid index indexes described in the literature. With this, it was possible to elaborate a method to develop an air incorporator additive for concrete, using as base raw material the vegetable oil of the castor bean plant, thus offering to the construction industry a new path for the development of products as alternatives to those currently on the market. Another important point was that it was possible to observe a significant increase in the concrete workability through the Slump Test procedure, in which it was verified that there was a 20 mm increase in the concrete abatement that used the additive. The incorporated air index, acquired with this additive, was on average 8,12% , which is quite satisfactory and meaning a great saving of materials.

REFERENCES

[1] Pereira, M.R., Study of the addition of expanded clay in the formulation of lightweight concretes. Dissertation of M.Sc., Federal University of Rio Grande do Norte, Natal, Brazil. 2008.

[2] Kosmatka, S. H ., Kerkhoff, B ., Paranaense, W. C. Design and control of concrete mixtures. 14th ed. Stokie: PCA. 2003.

[3] Dolch, W. L. Air-Entraining Admixtures. In: Ramachandran, V. S. (Ed.). Manual of Concrete Admixtures: Properties, Science and Technology. 2nd ed. New Jersey: Noyes Publications,. P. 518-557. 1996.

[4] Ribeiro, E. P ., Seravalli, E.A. G . Food chemistry. Instituto Mauá de Tecnologia, Editora Edgard Blücher LTDA, São Caetano do Sul - SP, p. 111-143 and p. 169-173. 2001.

[5] Brazilian Association of Technical Standards. NBR NM 67: Concrete - Determination of consistency by cone trunk abatement. Rio de Janeiro. 1998

[6] Souza L.A ., Tonetti O.A.O ., Davide A.C. Determination of water content in castor bean seeds (Ricinus Communis L.) By greenhouse methods and microwave oven. II Brazilian Congress of Oleaginous Plants, Oils, Fats and Biodiesel, Varginha-MG. 2005.

[7] Machado C.C., Garcia A.R., Silva E., Souza A.P. Technical-economic analysis of the use of castor oil (Ricinus communis, L.) and mineral oils as lubricants for the motorcycle cut set. Revista Árvore 1998, n. 22 (1), p.123-134. 1998.

AN OVERVIEW ON THE APPLICATION OF FRC AS A STRUCTURAL MATERIAL IN BRAZIL AND FUTURE TRENDS

Antonio D. de Figueiredo

Department of Civil Construction Engineering, University of São Paulo, Brazil

https://doi.org/10.21452/bccm4.2018.02.15

Abstract

The use of FRC as a structural material has gained a greater level of confidence in Brazil in recent years with the publication of technical standards, recommended practices and some emblematic applications. The main applications are still underground projects, such as the tunnels linings and the production of concrete pipes for sanitation works. This meets some of the main infrastructure demands attributed to the country's development stage. Although close to the European philosophy, Brazilian practices have specificities that deserve to be presented. In this sense, it should be emphasized the greater rigor in quality control programs and the differentiation of the requirements required for the material depending on the type of structure to be executed. In addition, there are also innovations in this subject that can guarantee greater reliability in the evaluation process of existing structures and that are being proposed for future publication as technical standard.

1. INTRODUCTION

The evolution of fibres reinforced concrete (FRC) in Brazil is something backward in relation to the observed in other countries. In Europe, FRC has been used for suspended slabs on buildings as the unique reinforcement system [1, 2] ten years ago. On the other hand, in Brazil the used of FRC was, basically, focused in applications of low level structural demand, such the case two industrial pavements and sprayed concrete in the same period [3]. One referential application of FRC in Brazil was the construction of São Paulo Subway Line 4 (Yellow Line) where the segments for TBM (Tunnel Boring Machine) were produced using only steel fibres as reinforcement [4]. Therefore, the main applications are underground projects, such as the tunnels linings and the production of concrete pipes for sanitation works. This meets some of the main infrastructure demands attributed to the country's development stage. In this period, a main problem is the fact that the standardization was restricted to steel fibres specifications of its use for concrete pipes reinforcement [5]. This condition starts to change in recent period with the publications of recommended practices as described in the next item.

2. BRAZILIAN RECOMMENDED PRACTICES

CT 303 is the Technical Committee created in 2011 to produce recommended practices for the use of fibre reinforced concrete for structural purposes. This committee involve the Brazilian Concrete Institute (IBRACON) and the Brazilian Association of Engineering and Structural Consulting (ABECE). Its main objectives were the elaboration of referential documents for the structural application of the FRC with the establishment of guidelines for the design of structures and technological control.

The committee used as reference main the fib Model Code 2010 [6, 7]. The main Brazilian document for design approach of FRC [8] for structural purposes follows completely the philosophy of the fib Model Code 2010 [7] for conventional structures such as buildings. The main difference occurs for structures such as pavements where the FRC residual strength parameters are required in terms of average values instead the characteristic ones.

The innovative contribution of the CT303 is more focused on the recommended practice for controlling the quality of the FRC [9]. In this guideline, it is recommended to carry out a previous homologation study of the FRC in order to certify its structural behavioural characteristics as in conformity with the ones specified in the design. The main parameterization of the FRC in terms of mechanical behaviour to verify its conformity with the design conditions is done through the EN14651 test [10]. However, this test method present difficulties to be performed in routine practice of quality control. In that sense, the CT303 allowed previous studies of correlation with the double punch test, also known as Barcelona test [11,12], to be used in this condition.

Another working front for the establishment of best practices for the use of fibres in structural concretes is starting in the Brazilian Committee of Tunnels (CBT). In this group it is wanted to parameterize the use of FRC designed for tunnel lining. The approach is very close to that adopted by EFNARC [13] but prioritizing the use of the double punch test to perform the quality control of the material and also allow the evaluation of the tunnel coating through extracted cores [14].

3. FUTURE PERSPECTIVES

One of the main current concerns is the analysis of the reliability of the FRC for the fire situation. This concern occurs both for its application in tunnels and for buildings. In the case of tunnels, the concern is in terms of preserving structural safety, avoiding collapse of the structure during and after the fire. This concern is emphasized in Brazil by the fact that there are large numbers of tunnels running on soft soils. For this reason, some researches are being developed in order to parameterize this behaviour [15]. This is particularly important because there are a large number of suppliers of synthetic macrofibres, which are more susceptible to the action of high temperatures. The concern is even greater in the case of use of FRC in building construction, especially in the particular situation of elevated slabs.

Other research and developments have been made aiming to verbalize the use of FRC in pre-cast elements. The concrete pipes are an established application of fibre reinforcement. Currently in Europe and Brazil, the evaluation of pipes made with FRC is more rigorous than the conventional reinforcement [16]. The specific standard, currently being revised, will seek to match the evaluation method and parameters of concrete pipes with different types or reinforcement: steel fibres and rebars. This idea makes the application more reliable in terms of durability and the fibres more competitive to ensure better control of cracking [17].

Another trend that has been studied in Brazil is the use of FRC in mixed structures of concrete and steel [18] as an alternative for conventional reinforcement. In this particular case, there will

be advances in terms of elements production which will be facilitated. Other studies are being carried out in order to evaluate the use of fibres to substitute conventional shear reinforcement in precast elements, even when recycled aggregates are used [19].

4. CONCLUDING REMARKS

Technological developments in Brazil tend to focus more on quality control models than on innovative products. This is due to the Brazilian technological tradition that emphasizes the control of concrete mechanical properties. In large part, this tradition is based on the fact that there are no earthquakes in Brazil, which makes the responsibility of concrete strength greater to guarantee the structural stability. Therefore, the great number of researches are aiming at simple tests developments, easy to reproduce and able to evaluate the structural behaviour of the material reliably.

The construction applications, although still very focused on conventional uses, are beginning to show innovation trends in terms of increasing the use of FRC in precast elements. This is because fibres turn out to be advantageous in more industrialized systems where there is greater control of production, reducing time production and costs.

REFERENCES

[1] DESTRÉE, X. Steel-fibre-only reinforced concrete in free suspended elevated slabs. Concrete Engineering International. Spring, 2009. pp 47-.9

[2] BARROS, J.A.O., SALEHIAN, H., PIRES, N.M.M.A., GONÇALVES, D.M.F. Design and testing elevated steel fibre reinforced self-compacting concrete slabs. In: Eighth RILEM International Symposium on Fibre Reinforced Concrete (BEFIB 2012), 2012, Guimarães. Fibre Reinforced Concrete: challenges and opportunities. Bagneux: RILEM Publications SARL, 2012.

[3] FIGUEIREDO, A. D. Concreto Reforçado com Fibras. São Paulo, 2011. 247p. Thesis (for Associate Professor examination). Escola Politécnica, University of São Paulo (in Portuguese). (http://www.teses.usp.br/teses/disponiveis/livredocencia/3/tde-18052012-112833/pt-br.php).

[4] TELLES, R. C. D.; FIGUEIREDO, A. D. Possibilidades de incorporação de novas tecnologias em anel de concreto pré-fabricado para túneis com tuneladora. Concreto & Construção, São Paulo, v. XXXIII, n.41, p. 30-35, 2006.

[5] FIGUEIREDO, A. D., CHAMA NETO, P. J., FARIA, H. M. A nova normalização brasileira sobre fibras de aço. Concreto e Construção. v. XXXVI. IBRACON. p.67 - 76, 2008.

[6] di PRISCO, M.; PLIZZARI, G.; VANDEWALLE, L. Fibre reinforced concrete: new design perspectives. Material and Structures, v. 42, p. 1261-1281, 2009.

[7] FÉDÉRATION INTERNATIONALE DU BÉTON – FIB. Fib Model Code for Concrete Structures 2010. Swtizerland, 2013. 402p.

[8] IBRACON/ABECE. Estruturas de concreto reforçado com fibras – Recomendações para projeto. Prática Recomendada, 2016.

[9] IBRACON/ABECE. Controle da qualidade do concreto reforçado com fibras: Práticas Recomendadas, São Paulo, 2017.

[10] EN 14651. Test method for metallic fibre concrete - Measuring the flexural tensile strength (limit of proportionality residual). European Standard. 2007.

[11] ASOCIACIÓN ESPAÑOLA DE NORMALIZACIÓN Y CERTIFICACIÓN. **UNE 83515**. Hormigones con fibras. Determinación de la resistencia a fisuración, tenacidad y resistencia residual a tracción. Método Barcelona. Barcelona, 2010. 10p.

[12]GALOBARDES, I.; FIGUEIREDO, A. D. Correlation between beam and Barcelona tests for FRC quality control for structural applications. In: 8th International Conference on Fibre Concrete, 2015, Prague. Fibre Concrete 2015. Prague: Czech Technical University in Prague, 2015.

[13]EFNARC. European Specification for Sprayed Concrete. European Federation of Producers and Applicators of Specialist Products for Structures (EFNARC), Hampshire, UK, 1996. 30p.

[14]ESTRADA, A. R. C.; SANTOS, F. P.; FIGUEIREDO, A. D. Parâmetros para especificação e controle do concreto projetado com fibras aplicado como revestimento de túneis. CONCRETO & CONTRUÇÃO, v. 88, p. 79-85, 2017.

[15]RAMBO, D. A. S.; BLANCO, A.; FIGUEIREDO, A. D.; SANTOS, E. R. F.; TOLEDO FILHO, R. D.; GOMES, O. F. M. Study of temperature effect on macro-synthetic fiber reinforced concretes by means of Barcelona tests: An approach focused on tunnels assessment. CONSTRUCTION AND BUILDING MATERIALS, v. 158, p. 443-453, 2018.

[16]FIGUEIREDO, A. D.; de la FUENTE, A.; MOLINS, C.; AGUADO, A. A new approach on crushing strength test for fibre reinforced concrete pipes. In: Eighth RILEM International Symposium on Fibre Reinforced Concrete (BEFIB 2012), 2012, Guimarães. Fibre Reinforced Concrete: challenges and opportunities. Bagneux: RILEM Publications SARL, 2012.

[17]FIGUEIREDO, A. D.; de la FUENTE, A.; AGUADO, A.; MOLINS, C.; CHAMA NETO, P. J. Steel fiber reinforced concrete pipes: part 1: technological analysis of the mechanical behavior. Revista IBRACON de Estruturas e Materiais, v. 5, p. 1-11, 2012.

[18]PEREIRA, M. F.; De NARDIN, S.; El DEBS, A. L. H. Uso de fibras de aço em pilares mistos parcialmente revestidos de concreto. REVISTA DA ESTRUTURA DE AÇO, v. 5, p. 99-115, 2016.

[19]GAO, D., ZHANG, L., NOKKEN, M. Mechanical behavior of recycled coarse aggregate concrete reinforced with steel fibers under direct shear. Cement and Concrete Composites 79 (2017). P. 1-8.

THE INFLUENCE OF CARBON NANOTUBES ON THE FRACTURE ENERGY, FLEXURAL AND TENSILE BEHAVIOUR OF CEMENT BASED COMPOSITES

Vanessa Vilela Rocha [(1)], Péter Ludvig [(1)], Flávio de Andrade Silva [(2)], Ana Carolina Constâncio Trindade [(2)]

(1) Department of Civil Engineering, Federal Centre for Technological Education of Minas Gerais, Belo Horizonte, Brazil

(2) Department of Civil and Environmental Engineering, Pontifícia Universidade Católica do Rio de Janeiro, Brazil

https://doi.org/10.21452/bccm4.2018.02.16

Abstract

Due to the necessity to improve the mechanical properties of cement-based materials, carbon nanotubes (CNTs) have been studied to prepare cement composites. Once they present high tensile strength, if well dispersed and well adhered to the cement hydration products, they can improve the mechanical properties of a cement paste system. Because of that, an effective dispersion process is crucial. Studies involving CNTs dispersion in cement particles in presence of a non-aqueous media of isopropanol resulted in improvements in mechanical properties suggesting a good dispersion and strong bond between CNTs and cement particles. Considering that, the present paper analysed a cement paste reinforced with 0%, 0.05% and 0.10% of CNTs dispersed in a non-aqueous media of isopropanol through three-point bending tests in notched specimens and direct tensile tests. The influence of CNTs on the material fracture energy, flexural strength, and tensile strength was addressed. The results pointed out an improvement of 90% of fracture energy in composites with 0.05% of CNTs. The results of direct tensile tests indicate an improvement of about 20% tensile strength in cement paste with 0.05% of CNTs and images by scanning electron microscopy indicate a better dispersion by this proportion. These results suggest not only an effective dispersion of CNTs in cement matrix by the used dispersion methodology at a dosage of 0.05% of CNTs, but also that the cement composites properties may be improved by the presence of them.

1. INTRODUCTION

Cement pastes usually present low fracture energy and low tensile strength, leading them to early cracking and making the cement matrix susceptible to penetration of deleterious agents. This

behaviour implies that the durability of cement-based materials is a concern; however, they can be improved by the presence of other materials forming composites with better mechanical properties.

Carbon nanotubes (CNTs) have been studied as reinforcement in ordinary Portland cement (OPC) due to their extraordinary mechanical properties [1]. CNTs dispersion, however, appears as the greatest challenge to the incorporation of them in cement composites. They are hydrophobic and tend to agglomerate in the presence of water, which can reduce the cement pastes mechanical performance [2]. Researches, however, by the proper dispersion process recorded improvements in mechanical properties of cement-based composites prepared with CNTs [1-6].

Wang and Liu (2013) [3] prepared cement pastes with the incorporation of up to 0.15% of multi-walled carbon nanotubes (MWCNTs) modified by anionic gum and dispersed by a surfactant-ultrasonic method. The results showed an increase of 57.5% in flexural strength and 501% in fracture energy in the presence of 0.08% MWCNTs when compared with the reference paste (0%). In general, research involving dispersion of carbon nanotubes in surfactants use rates ranging from 0.045% [4] to 0.50% [5].

The cement pastes prepared by ZOU et al. (2015) [1] had additions of 0.038% to 0.075% of MWCNTS that were previously functionalized in COOH and dispersed using a polycarboxylate plasticizer and ultrasonication energy in aqueous solution. The results pointed out an increase of 31.5% in Young's modulus, 49.9% in flexural strength and 62.6% in fracture energy with a paste incorporating 0.075% of CNTs.

HU et al. (2014) [6] dispersed MWCNTs in concentrations of 0.05% and 0.10% in COOH and SDS surfactant and ultrasonic frequency, separately. An improvement in the presence of 0.10% of CNTs was achieved, recording 26.9% of gain in fracture energy dispersed in SDS surfactant and 42.9% dispersed in COOH; 19.2% dispersed in COOH and 11.4% dispersed in SDS surfactant as results of fractural toughness. These results suggest that CNTs can be used as a reinforcement material by both dispersion processes researched by HU et al. (2014) [6] at a proportion of 0.10% of CNTs.

CNTs dispersed in cement particles in the presence of a non-aqueous media of isopropanol resulted in evidences of bond between the CNTs and cement matrix [7], CNTs acting as crack propagation controllers [7], densification of C-S-H [8] and compressive and splitting tensile strengths gains of approximately 50% [2]. The results obtained by Rocha and Ludvig (2017) [2] suggest that the optimum range for incorporation of MWCNTs by dispersion on cement particles in an aqueous media of isopropanol is close to the 0.05% ratio.

According to those results, the present work investigates the fracture energy under flexural loading and direct tensile behaviour of cement paste reinforced with MWCNTs at proportions of 0%, 0.05% and 0.10% (by cement weight) dispersed on the cement particles in a non-aqueous isopropanol media by sonication, and tested after 28 days of curing.

2. MATERIALS

The materials used are: (i) Brazilian Type CP-V Portland cement, due to its low percentage of mineral additions; (ii) multi-walled carbon nanotubes (MWCNTs), with estimated tube lengths between 5μm and 30μm, 99% of external diameter between 10nm and 50nm, and purity greater than 93%, produced in the Nanomaterials Laboratory of the Physics Department of the Federal University of Minas Gerais (UFMG); and (iii) isopropanol absolute grade.

3. METHODS

3.1. CNTs dispersion

The dispersion methodology adopted was based on process described by Rocha and Ludvig (2017) [2]: 10% of the total amount of cement was mixed with CNTs, stirred and sonicated in a solution of isopropanol for one hour at 42Hz. The CNTs were previously sonicated in isopropanol for 30 minutes. The isopropanol was later left to evaporate resulting in a dry powder of cement particles incorporated with CNTs. Rocha and Ludvig (2017) [2] suggest an effective dispersion at those proportions due to the gains in mechanical resistance achieved.

After the dispersion process, a small sample of cement with dispersed CNTs was analyzed by scanning electron microscopy. The images were obtained in a FEG - Quanta 200 FEI (Center of Microscopy, UFMG). A five nanometers carbon coating was used to ensure the sample conductivity.

3.2. Preparation of cement paste specimens

The obtained dry dispersion was mixed with the remaining quantity of cement. Water was added and three types of cement pastes were prepared in a mortar blender: (i) ISO-REF: without CNTs, (ii) ISO-0.05: with 0.05% of CNTs and (ii) ISO-0.10: with 0.10% of CNTs. The procedures to prepare and cure the cement pastes were the same as described by Rocha and Ludvig (2017) [2]. Figure 1 illustrates the dispersion process and cement paste preparation.

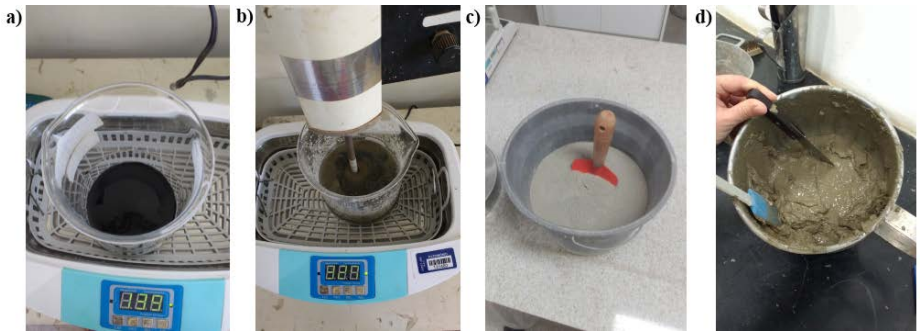

Figure 1: (a) Carbon nanotubes and isopropanol by sonication; (b) Carbon nanotubes, cement and isopropanol mixture being mechanically stirred and sonicated; (c) dry powder cement particles incorporated with CNTs mixed with the remaining quantity of cement; (d) cement paste with carbon nanotubes.

Nine specimens were prepared for each type of cement paste. Three of them were prismatic with 160 mm of length, 40 mm of width and 40 mm of height, used to three-point bending tests. Three of them were cylindrical with 5 cm of diameter and 10 cm height for splitting tensile tests. Tthe other three were used for direct tensile tests. The specimen geometry plan view is illustrated in Figure 2. The specimens had 40 mm of both height and width. The geometry adopted was defined according to the specimen specifications of Mechtcherine et al. (2011) [9] used to run direct tensile tests in cement based composites incorporated with short PVA fibers.

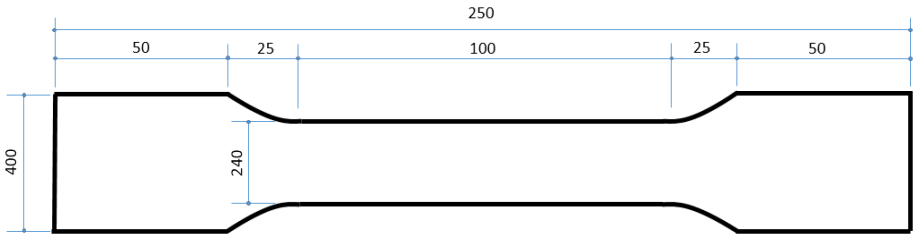

Figure 2: Specimen geometry used for tensile tests.

Three-point bending, splitting tensile test and direct tensile tests were performed after 28 days curing in a tank of lime-saturated water.

3.3. Three-point bending tests

The prismatic specimens were prepared with a notch in order to conduct the crack during the loading application. The cutting was performed using a specific apparatus developed for this purpose in order to ensure the alignment of the cut in the prismatic bars, and was executed in a depth of approximately 10 mm.

Close to the notch, two metal plates were attached, as indicated in Figure 3a. An MTS 632.02B-20 model extensometer was attached on the plates to measure crack mouth opening displacement, as showed in Figure 3b.

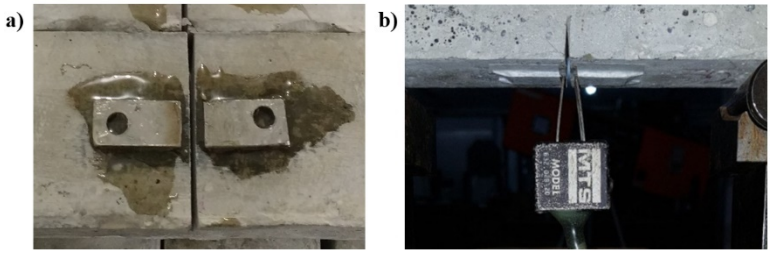

Figure 3: (a) Metal plates glued on the prismatic specimens; (b) extensometer placed on the prismatic specimens for three-point bending tests.

The three-point bending tests were carried on using a servo-hydraulic MTS testing system with closed loop control and a load cell of 2.5 kN. All specimens were tested at a constant crack mouth opening displacement (CMOD) rate of 0.008 mm/min, in order to keep the crack growth stable.

The maximum load applied divided by the effective cross section area was used to calculate the flexural strength. The area below the Stress x CMOD (Crack mouth opening displacement) graph, limited to 0.04 mm of displacement, was used to calculate the fracture energy. The results of flexural strength and the fracture energy were the mean values of the three results of each type of paste.

3.4. Splitting tensile tests

The splitting tensile strength tests were performed using an apparatus specially developed for this test, as showed in Figure 4. The tests were carried on using an EMIC brand test equipment with load cell of 20kN. The load increment used was equal to 1.0 mm/min.

Figure 4: Splitting tensile strength test

3.5. Direct tensile tests

At the age of 28 days, the specimens for tensile tests were placed between rubber papers, sandpapers and metal claws as showed in Figure 5a. The rubber paper and the sandpaper were used to create a friction between the specimen and the metal claws, and a torque of 5 N.m was applied at the screws. The metal claws were attached to the equipment, and a Linear Variable Differential Transformer (LVDT) was placed to record the linear displacement, as showed in Figure 5b.

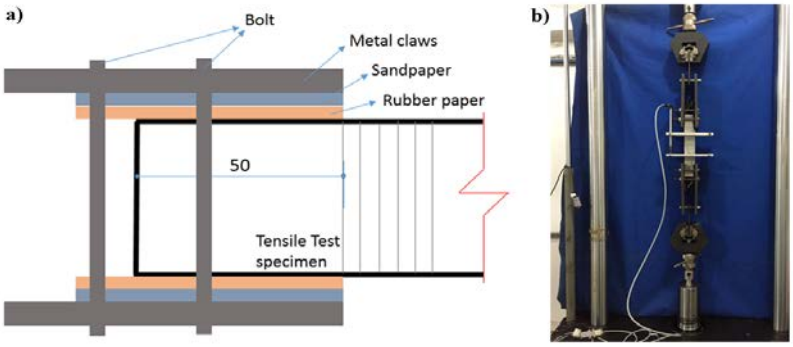

Figure 5: (a) Sketch showing the assembly and preparation of the specimens for tensile tests; (b) Specimens properly positioned in the equipment before testing

The tensile tests were carried on using a servo hydraulic MTS 810 load frame with closed loop control and a load cell of 250 kN. All specimens were tested under a displacement rate of 0.06 mm/min. The maximum load applied divided by the cross-section area (240 mm x 400 mm) was used to calculate the tensile stress.

4. RESULTS AND ANALYSIS

4.1. Three-point bending tests

The results obtained in the three-point tests are showed in Tables 1 and 2. The Figure 6 shows the graphs corresponding to the stress x CMOD behaviour of the specimens during the loading of the ISO-REF, ISO-0.05 and ISO-0.10.

According to the information presented on Tables 1 and 2 and Figure 6, it is possible to affirm that the presence of CNTs contributes to enhance both fracture energy and flexural strength. The flexural strength was improved in the presence of CNTs, suggesting an effective dispersion by the used methodology and a strong bond between cement hydration products and CNTs. The flexural

tests indicated a 31% of gain in flexural strength in the presence of 0.10% of CNTs while the cement paste with 0.05% indicated 26% of gain. This behaviour is showed at Figure 6 in which the cement pastes with 0.05% of CNTs were able to keep higher stresses even after the peak load. Differently, the ISO-REF and ISO-0.10 pastes show a more abrupt resistance drop after reaching the maximum load.

Table 1: Flexural Stress test results

	Flexural Stress (MPa)	Standard Deviation (MPa)
ISO-REF	1.21	0.18
ISO -0.05	1.63	0.12
ISO -0.10	1.76	0.07

Table 2: Fracture Energy test results

	Fracture Energy (N.mm)	Standard Deviation (N.mm)
ISO-REF	6.72	0.48
ISO -0.05	12.76	2.71
ISO -0.10	8.99	0.92

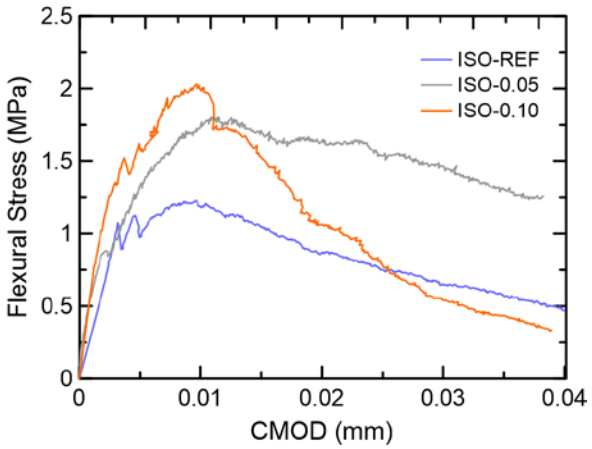

Figure 6: Influence of carbon nanotubes on the flexural behaviour of cement pastes.

According to the information presented on Table 1, Table 2 and Figure 6, it is possible to affirm that the presence of CNTs contributes to enhance both fracture energy and flexural strength. The flexural strength was improved in the presence of CNTs, suggesting an effective dispersion by the used methodology and a strong bond between cement hydration products and CNTs. The flexural tests indicated a 31% of gain in flexural strength in the presence of 0.10% of CNTs while the cement paste with 0.05% indicated 26% of gain. This behaviour is showed at Figure 6 in which the cement pastes with 0.05% of CNTs were able to keep higher stresses even after the peak load. Differently, the ISO-REF and ISO-0.10 pastes show a more abrupt resistance drop after reaching the maximum load.

The difference pointed out by the fracture energy is more expressive in the presence of 0.05% of CNTs: 90%. In presence of 0.10% of CNTs the gain in fracture was 34%. These results suggest that the dispersion in isopropanol is effective and allows CNTs to act as crack propagation controllers as the ISO-0.05 cement paste absorbed more energy when the cracks propagated.

These results are related to the effective dispersion by the method adopted, and the more expressive gain in fracture energy of 0.05% CNT content when compared to ISO-0.10 paste may be related to the optimum range at this proportion using this methodology.

4.2. Splitting tensile tests

The results of splitting tensile tests are showed in Table 3 and Figure 7. The cement paste with 0.05% of CNTs recorded a resistance gain of 37% in comparison with the reference material, while the cement paste with 0.10% of CNTs recorded 28%.

Both splitting tensile strength and three-point bending tests showed better performances of pastes prepared with CNTs, suggesting that the proportions of 0.05% and 0.10% of CNTs dispersed in isopropanol may act as adequate reinforcements to the cement pastes.

Table 3: Splitting tensile strength test results

	Splitting Tensile Strength Test (MPa)	Standard Deviation (MPa)
ISO-REF	1.87	0.25
ISO-0.05	2.56	0.26
ISO-0.10	2.38	0.24

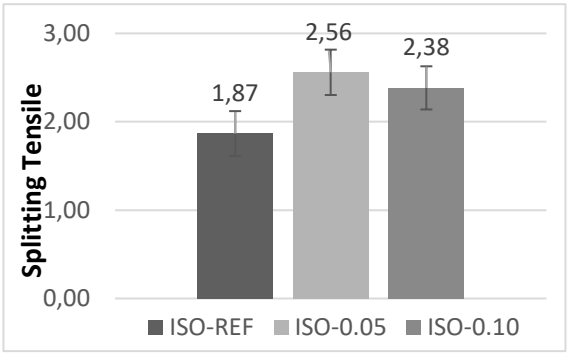

Figure 7: Splitting tensile test graph

4.3. Direct tensile tests

Three specimens of each type of cement paste were prepared. However, the fragility of the ceramic composites made it difficult to assembly the specimens to perform the direct tensile tests. During the test assembly, 67% of the specimens were lost due to the torque application or due to the eccentric positioning of the specimens in the equipment, which led to the realization of only one sample of each type of cement paste. It is noteworthy, however, that few results can be found in literature regarding direct tensile tests on CNT reinforced composites.

The obtained results in direct tensile tests are showed in Table 4. The Figure 8 shows the graphs corresponding to the stress x strain behaviour of the specimens during the loading of the ISO-REF, ISO-0.05 and ISO-0.10 pastes.

Despite the small number of specimens, the results of tensile tests are in accordance with the results presented by the splitting tensile and three-point bending tests, as they pointed out a better tensile performance of the cement paste with 0.05% of CNT. The ISO-0.05 achieved 19% of improvement in tensile.

The loss in tensile strength recorded for ISO-0.10 paste in comparison with ISO-0.05 may be attributed to the inefficiency of dispersion of CNTs at this proportion using this methodology. The maximum amount of CNTs that can be effectively dispersed on cement particles in isopropanol using sonication should be close to 0.05%. Only one sample was tested of each type of cement paste due to the difficulty of assembling and running the tensile tests, however these results are in accordance with the splitting tensile test results. Even though ISO-0.10 in both tensile and splitting tensile tests presents strength improvements in comparison to the reference material, ISO-0.05 recorded the higher tensile strength gain. It suggests that the effective dispersion limit of CNTs by this method has probably been achieved around 0.05% of CNTs, as affirmed by Rocha and Ludvig (2017) [2].

Table 4: Tensile tests results

	Tensile Strength (MPa)
ISO-REF	0.47
ISO -0.05	0.58
ISO -0.10	0.53

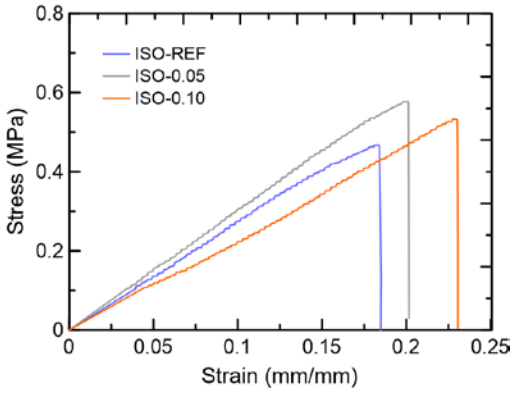

Figure 8: Influence of CNTs dosage on the tensile behavior of a cement paste

The values obtained by direct tensile tests were around 23% of the results of splitting tensile strength tests and around 35% of the results of splitting tensile strength tests. The difference recorded is natural due to the different specifications and methodologies used in each one of those tests. However, in all of them the presence of CNTs dispersed in isopropanol recorded an improvement in tensile strength of cement pastes, suggesting efficiency in the dispersion process carried out.

4.3. Scanning Electron Microscopy images

The scanning electron microscopy images of the cement anhydrous with the CNTs are seen in Figure 9 by enlargement of 50000x.

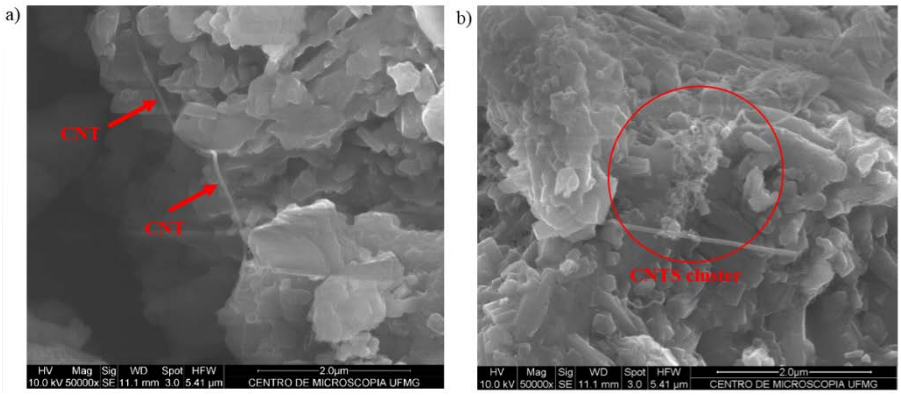

Figure 9: Scanning electron microscopy images of the anhydrous cement with (a) 0.05% of CNTs; (b) with 0.10% of CNTs

In presence of 0.05% of CNTs it was found a well dispersed CNTs filament among anhydrous cement particles and it was not possible to identify presence of CNTs clusters. In presence of 0.10%, however, the image suggests a small cluster, and the presence of clusters may be the cause of the lower tensile strength and fracture energy in comparison with ISO-0.05.

Those images are in agreement with the fracture energy and tensile strength results, in which the better mechanical behaviour of ISO-0.05 were due to an effective dispersion, also corroborating with Rocha and Ludvig (2017) [2] that the optimum range for incorporation of

MWCNTs by dispersion on cement particles in an aqueous media of isopropanol is close to the 0.05% content.

5. CONCLUSIONS

According to the results, CNTs dispersed in isopropanol are effective and appropriate to prepare cement composites with enhanced mechanical properties. The flexural strength and fracture energy were improved in presence of CNTs, confirming that they can be used as a reinforcement material. The 90% of gain in fracture energy of composites with 0.05% of CNTs in comparison with 34% of gain achieved by the cement paste with 0.10% suggests a better dispersion of CNTs in the proportion of 0.05%. These findings corroborate with Rocha and Ludvig (2017) [2] results, in which the optimum CNT content using this dispersion methodology was 0.05%. The tensile strength was also higher in the presence of 0.05% of CNTs and the scanning electron microscopy images are in accordance with the mechanical behaviour, suggesting a better dispersion in a non-aqueous media of isopropanol methodology in presence of 0.05% of CNTs.

ACKNOWLEDGEMENTS

The authors would like to thank to CAPES, CEFET-MG, PUC-RIO, CTNANO, Center of Microscopy of UFMG, CNPq, FAPEMIG and UFMG for the financial and technical support provided for this work.

REFERENCES

[1] ZOU, B. et al. Effect of ultrasonication energy on engineering properties of carbon nanotube reinforced cement pastes. Carbon, v. 85, p. 212-220, 2015. ISSN 0008-6223.

[2] ROCHA V. V., LUDVIG P. Nanocomposites prepared by a dispersion of CNTs on cement particles. Architecture Civil Engineering Environment, 02/2018, p.71-75, 2018. ISSN 1899-0142.

[3] WANG, B.; HAN, Y.; LIU, S. Effect of highly dispersed carbon nanotubes on the flexural toughness of cement-based composites. Construction and Building Materials, v. 46, p. 8-12, 2013. ISSN 0950-0618.

[4] CWIRZEN, A.; HABERMEHL-CWIRZEN, K.; PENTTALA, V. Surface decoration of carbon nanotubes and mechanical properties of cement/carbon nanotube composites. Advances in cement research, v. 20, n. 2, p. 65-74, 2008.

[5] ROCHA V. V., LUDVIG P. Preparação e caracterização de nanocompósitos com nanotubos de carbono dispersos em surfactantes. The Journal of Engineering and Extract Sciences – JCEC, v. 3, p. 1097-1105, n. 8, 2017.

[6] HU, Y. et al. Fracture toughness enhancement of cement paste with multi-walled carbon nanotubes. Construction and Building Materials, v. 70, p. 332-338, 2014. ISSN 0950-0618.

[7] MAKAR, J.; MARGESON, J.; LUH, J. Carbon nanotube/cement composites-early results and potential applications. Conference on Construction Materials, 2005.

[8] MAKAR, J. M.; CHAN, G. W. Growth of Cement Hydration Products on Single-Walled Carbon Nanotubes. The American Ceramic Society, 2009.

[9] MECHTCHERINE, V. et al. Behaviour of strain-hardening cement-based composites under high strain rates. Journal of Advanced Concrete Technology, Vol. 9, No. 1, 51-62, 2011.

EFFECT OF THE RESIDUAL FINE ELEMENTS AND CONTRIBUTION ON FRESH PROPERTIES OF SELF-LEVELING MORTARS

Henrique Duarte Sales Carvalho [(1)], Janaíde Cavalcante Rocha [(1)] and Malik Cheriaf [(1)]

(1) Department of Civil Engineering, Universidade Federal de Santa Catarina, UFSC, Brazil

https://doi.org/10.21452/bccm4.2018.02.17

ABSTRACT

The self-leveling mortar is a fluid product that has as a low viscosity and high fluidity. This building material that requires no vibration and leveling, having very low thickness (30 mm). The purpose of this study is to evaluate fresh properties of self-leveling SLU using three by-products: bottom-ashes, fine elements of quarry limestone and fine elements from recycled-concrete-waste. Portland Cement OPC was partially replaced by 0,10, 15 e 20% of fines. The water/binder was maintained constant at 0.50 and mix proportion 1:2 cement and sand (by weight) was used. Fresh properties were examined: plastic shrinkage, curling and heat measurements using a semi-adiabatic calorimeter. A superplasticizer (polycarboxylate) was used to assure a fluidity. During drying (HR=50%) a mass loss was monitored. To the same cement content fine from bottom-ash acted efficiently to reduce a shrinkage. The curling phenomenon is high, with more than 1.70 for mortars based on fine from recycled-concrete-waste. Higher early curling was obtained for mortars with quarry limestone. A good performance could be assured with ternary mixes with bottom ashes (curling less than 8mm). Self-leveling mortar systems with more than 20% of fine resulted negative effect on segregation and bleeding, so not recommended to self-leveling mortar purposes.

KEYWORDS: bottom ashes, fine from CDW aggregates, self-leveling mortars, fresh properties, shrinkage.

1. INTRODUCTION

Self-leveling mortars are characterized by their ability to spread quickly and self level, without the need of manual or mechanical intervention. The homogeneity of these compounds is necessary to ensure the endurance and durability characteristics of the final product, therefore, it is imperative that the mixture exhibits high stability [1]. The most important properties in a self-leveling mortar system, considering its viability and its final characteristics are: self leveling, low viscosity, fast hardening, fast setting time, fast rate of strength, dimensional stability, high final compressive

strength, surface durability and a strong adhesion to the substrate. To meet all these requirements, self-leveling mortars often contain a wide variety of organic and inorganic compounds [2].
The use of self-leveling mortar system offers environmental and economic advantages. Among these advantages, it is possible to highlight the use of residues from other processes, such as a source of admixtures to replace part of the Portland cement, and to improve the characteristics of the final product, mainly the rheological properties [3]. In Spain, natural coarse aggregates may be substituted by Recycled Concrete Waste (RCW) to concrete production in proportions of 20% to 100% [4, 5], however the fine fraction of RCW is not allowed. The greater difficulty in the use of fine RCW is related to its high absorption of water [6]. In order to ensure self-leveling behaviour, a greater amount of fine is required to achieve an effective fluidity [7]. Therefore, the use of the fine portion of this residue can be a sustainable solution to manufacture coarse recycled aggregate from recycling plants.
Mortar and concrete are porous materials, which are susceptible to volume variations due to shrinkage during hydration and drying. In particular, the development of cement based self-leveling mortars still limited because of problems such as cracking or warping of corners [8, 9]. These cracks are caused by shrinkage occurring from drying. The shrinkage in self-leveling systems is influenced by the high content of fine particles required to achieve effective fluidity [10, 11]. The fine particles demand more water, due to the greater specific surface area, increasing the tendency of greater volumetric variation during drying.
The Coal Bottom Ash (CBA) when used as a substitute for the natural fine aggregate can improve internal curing, and reduce capillary forces, hydration temperature and consequently the shrinkage in concretes [12]. Concrete mixtures which incorporate bottom ash as fine aggregates for partial or total replacement of natural sand exhibit better dimensional stability. The structure of porous particle in bottom ash was beneficial for decreasing shrinkage in concrete samples. At the age of 180 days, concrete mixtures with bottom ashes FBC 2 (50%), FBC 3 (75%) and FBC 4 (100%) presented 21.79%, 34.62% and 37.17%, respectively, demonstrating lower shrinkage values by drying compared to the control mixture [13].
In this context, the present study aims to produce self-leveling mortars using fines of residues (CBA and RCW) as partial substitutes for Portland cement and contribute to sustainable development.

2. MATERIALS

The materials used in the research were Portland Cement CP V - ARI (Hight initial strength), limestone powder (LP), recycled concrete waste (RCW) and coal bottom ash (CBA) fines. As natural aggregate, sand was used (Dmáx=2 mm) and a superplasticizer (SP) admixtures based on polycarboxylate.

3. METHOD

3.1 Material characterization

The material characterization tests were carried out according to the procedures established in Brazilian technical standards. The specific gravity of the fines and the sand was determined

according to the standard ABNT NBR NM 52/2009. The specific gravity of the Portland cement was determined according to the standard ABNT NBR NM 23/2001.
The specific area of the Portland cement and its fineness modulus were determined according to the standard ABNT NBR NM 76/1998.
The grain size distribution of the sand was determined according to the standard ABNT NBR NM 248/2003. Particle sizes were determined on the fines (LP, RCW and CBA) by laser granulometry using the Microtrac S3500 equipment. Chemical analysis of fine materials (CP, LP, RCW and CBA) were analysed by energy dispersive X-Ray Spectrometer 700 (EDX 700) Shimadzu equipment.

3.2 Mortar study

The fines (LP, RCW and CBA) were used as partial replacing of the Portland cement CP V ARI, in content of 10%, 15% and 20%, by volume, due to difference between the specific gravity of the fines. The sand and fines were added to the dry condition.
Initially, experiments were carried out to evaluate the consistency properties of the mortar in the fresh state. For this purpose, the mortar was dosed to determine the range of admixtures superplasticizer and the content of fines. All mixes were prepared with cement and sand ratio of 1:2 ratio (cement / aggregate) and a w/c (water / cement) constant at 0.5.
Once tests at the fresh state were conducted and mortars with satisfactory fluidity and cohesion properties for self-leveling systems were choosen, tests were carried out in the hardened state to evaluate the heat of hydration, drying shrinkage and curling, aiming to identify indicators of durability.

3.3 Flow value

The flowability was measure using a mini-cone flow. Chemical admixtures consumption was determined trough to flow test (spreading) fixed by 24 and 27 cm, to evaluate a flowability. The tests were performed shortly after preparation of the mixtures. After removal of a mini cone, the flow was evaluated over a glass suport marked with 20 cm, 25 cm and 30 cm diameters. The final value was considered as the mean between two perpendicular measurements of spreading.
The self-leveling mortars chosen were those behaving cohesively without signs of segregation or bleeding and with a good visual appearance. The selected mortars were identified according to the material used and the cement replacement content (Table 1).

Table 1: Identification of self-leveling mortars and mixes proportions.

Identification	Cement Consumption (m^3)	Cement Replacement Content	Fines Content (%)		
			LP	RCW	CBA
FC 10	536.4	10%	10		
FC + RCD 10	534.2		5	5	
FC + CBA 10	530.1		5		5
FC + RCD +CBA 10	529.4		5	2.5	2.5
FC 15	527.9	15%	15		
FC + RCD 15	517.9		7.5	7.5	
FC + CBA 15	528.4		7.5		7.5
FC + RCD + CBA 15	516.3		7.5	3.75	3.75

3.4 Temperature of hydration of mortars

A semi-adiabatic calorimeter was used to evaluate the temperature evolution of self-leveling mortars. The mortars were placed, still under the fresh state, in a cylindrical container of polystyrene. Thereafter, the container was placed in a thermal box. Temperature measurements from the samples were collected through thermocouples and processed into a Hewlett-Packard data logger, model 34970A, connected to a computer for data storage, with readings at every 20 seconds.

3.5 Drying shrinkage

In order to evaluate displacements of the corners (curling), an experiment on plates was carried out. Following the procedure adopted by other researchers [9, 14] that evaluated the drying shrinkage in self-leveling mortars.

Tests to measure curling and the linear shrinkage of self-leveling mortars were performed simultaneously with the same sample. The displacement values were verified by Linear Variable Differential Transformer (LVTDs) and processed automatically through a data acquisition equipment (Data Logger), which was connected to a computer for data storage (Figure 1). After the mortar had started to hardening (according to the results of evolution of hydration temperature of mortars), equipments for linear shrinkage and curling data collection were connected for a period of 5 consecutive days (Fig.1). The temperature (23 ± 2 ^{0}C) and relative humidity (60% ± 5%) were monitored during the test period.

Figure 1: Experimental set up for curling.

4. RESULTS AND ANALYSIS

4.1 Characterization

The physical and chemical properties of cement and fines materials are shown in Table 2.

Table 2: Chemical compositions and physical properties of materials.

Oxides	**Cement Portland CP V**	**Limestone Filer**	**Fines CBA**	**Fines RCW**
Chemical analysis (%)				
Oxides				
CaO	74.795	54.788	1.733	41.202
SiO_2	12.303	4.321	40.819	29.048
Al_2O_3			37.458	
Fe_2O_3	4.458	0.775	5.713	9.805
K_2O	2.071	0.472	5.197	3.905
SO_3	1.984			
TiO_2				1.447
CO_2	3.243		6.674	13.22
Physical properties				
Specific gravity (Kg/m^3)	3040	2680	1920	2460
Blaine Fineness (m^2/Kg)	505	228	218	502

Only the fines from bottom ash presented aluminum in a significant amount (37%), in contrast the CaO content (1.7%) was much lower than the other materials. The bottom ash, class F, showed the lowest specific gravity, probably due to its high internal porosity.
The results for granulometric analysis of the aggregate were: characteristic maximum dimension of 1.2 mm, characteristic minimum dimension of 0.075 mm and fineness modulus of 1.39. Approximately 13% of the natural sand showed grains inferior to 0.15 mm.
The results of laser granulometry showed that the finest addition was the LP, with all grains less than 50 μm. The addition with the largest grain sizes was CBA, with all grains less than 0.15 mm. All grain-sizes of FC and RCW were less than 0.075 mm, while approximately 30% of the grains of CBA were larger.

4.2 Flow value

The results of flowing tests in relation to SP additive, content for self-leveling mortars with 10% and 15% of substitution are presented in Figure 2 and 3, respectively.

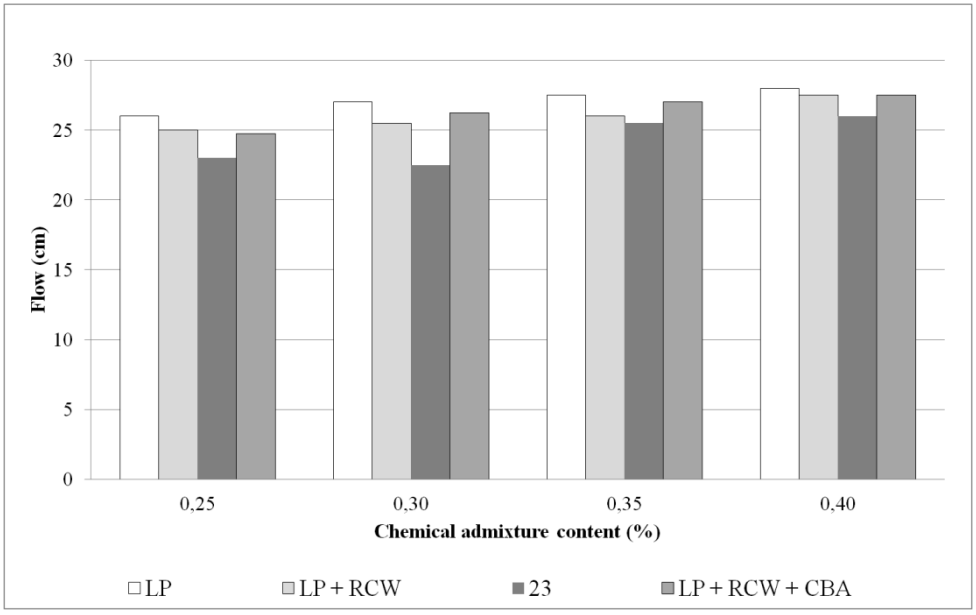

Figure 2: Self-leveling mortar flow values results - 10% of fine replacement.

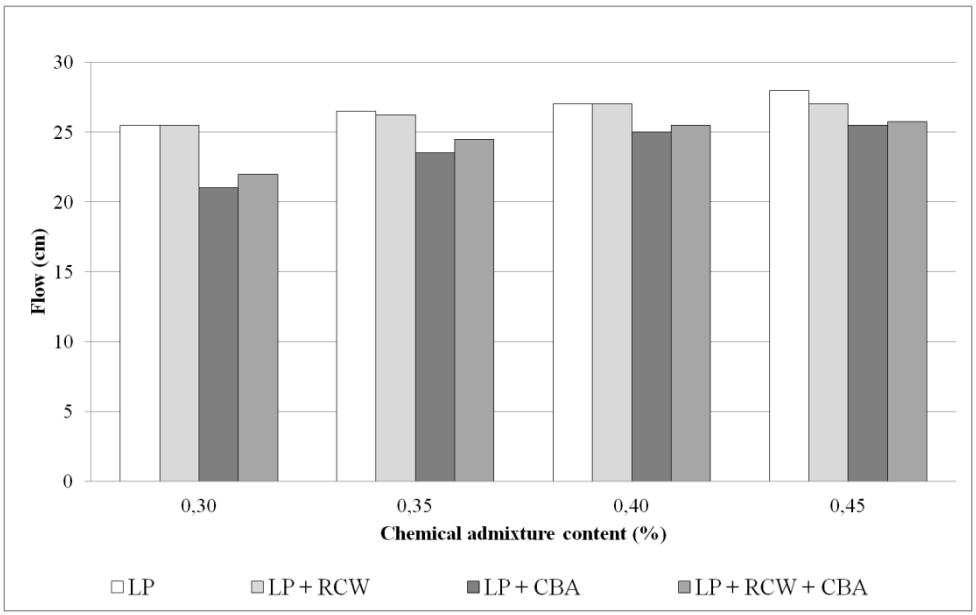

Figure 3: Self-leveling mortar flow values results- a15% of fine replacement.

The maximum content of the SP chemical admixture used was 0.40%, above which the flow of the mortars did not change significantly. In chemical admixtures, most of the mixtures with 0.45% and 0.50% showed signs of bleeding and /or segregation.

It was verified that the flow decreased with the increase of the content of fines, in all of the mixes analyzed. The same results were found by other researchers [10, 15]. The results can be explained by the increase of the fineness and the specific surface area of the fines, because with the increase of the fine content it becomes necessary more water to wet the surface of the particles and to maintain the same fluidity.

Mixes with 20% cement substitution (from cements to the fines) were also tested, in the same manner as mixtures with 10% and 15% substitution. However, samples composed with LP + CBA and LP + CBA + RCW presented segregation, in addition to providing lower scattering values. Thus, the scattering results for substitution contents of 20% were not considered satisfactory.

The scattering results of the selected mortars with the respective additives content are summarized in Table 3.

Table 3: Chosen Mortars.

Identification	**Additive Content (%)**	**Flow (cm)**	**Cement Replacement Content (%)**
FC 10	0.25	26.0	10%
FC + RCD 10	0.35	26.5	
FC + CBA 10	0.40	26.0	
FC + RCD + CBA 10	0.30	26.25	
FC 15	0.30	25.5	15%
FC + RCD 15	0.30	25.5	
FC + CBA 15	0.40	25.0	
FC + RCD + CBA 15	0.40	25.5	

4.3 Temperature of hydration of mortars

In order to determine the initial setting time of mortar the points of the curve were chosen where the gradual increase in temperature began. To determine the amount of time required to reach the maximum temperature, the points with the peak temperature were selected in the graph. The results are shown in Figures 4 and 5 for 10% and 15% substitution, respectively.

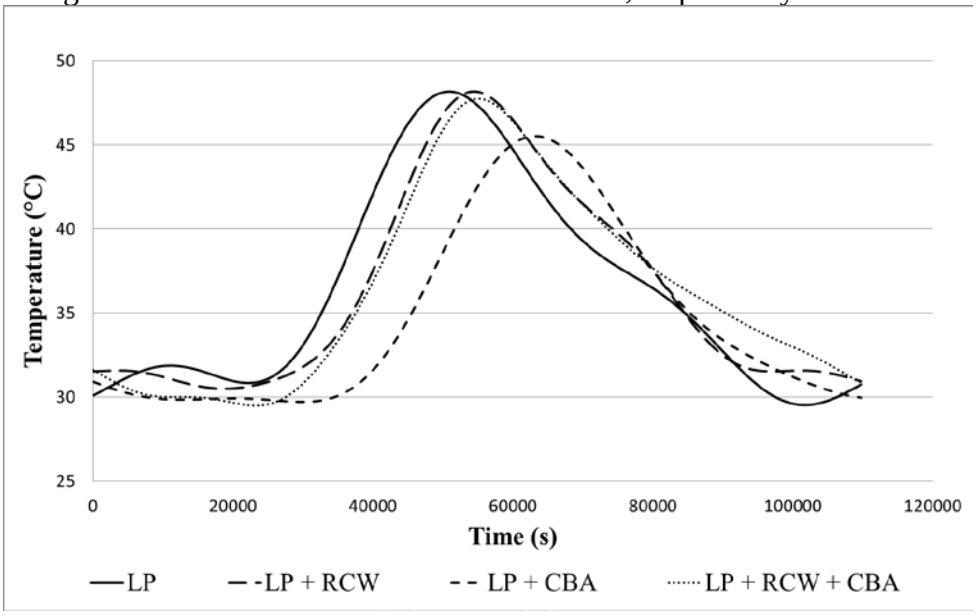

Figure 4: Evolution of the Temperature Versus Time for Mortar With 10% Replacement.

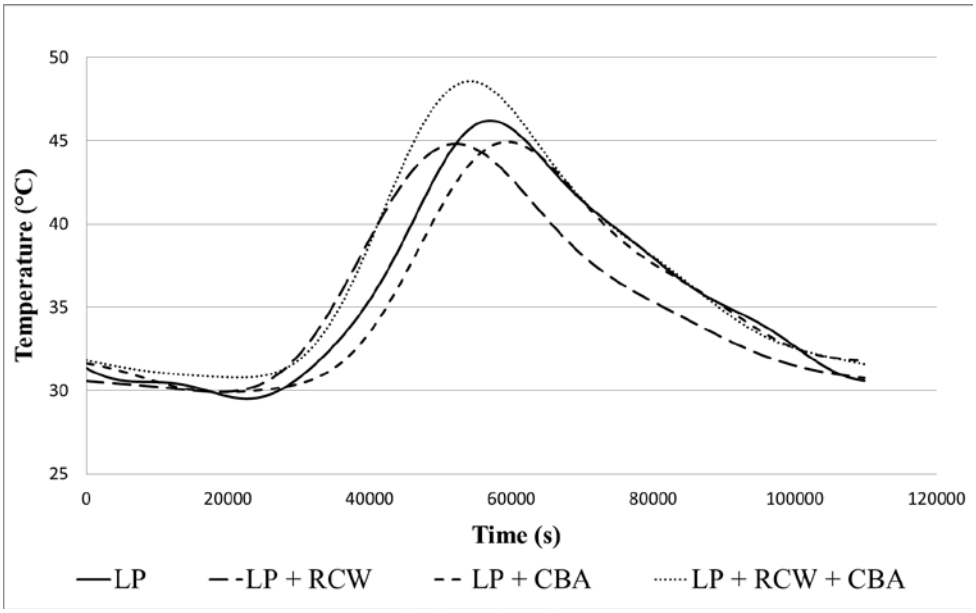

Figure 5: Evolution of the Temperature Versus Time for Mortar With 15% Replacement.

For 10% of substitution, the LP + CBA 10 mixes presented the highest time for initiation of acceleration of the hydration reactions (approximately 8 hours). This fact occurred due to the

higher content of SP chemical admixture used to achieve the required flow. The other mixes showed start times of setting of the mortar varying between 5 and 6 hours, approximately.
For mortars with a 15% substitution, all samples showed shorter initial setting times than the reference (FC 15). The mortars LP + CBA 15 and LP + RCW 15 presented the lowest maximum temperatures. Although the maximum temperature difference between all mixtures produced has been small (± 30 ° C), a mixture with the lowest maximum temperature may help reduce shrinkage in self-leveling mortars. Lower temperatures during the hydration process tend to reduce the amount of water that evaporates, and consequently the dimensional variation tends to decrease.

Dimensional variation (Linear shrinkage)

Results for linear shrinkage are shown on Figure 6.

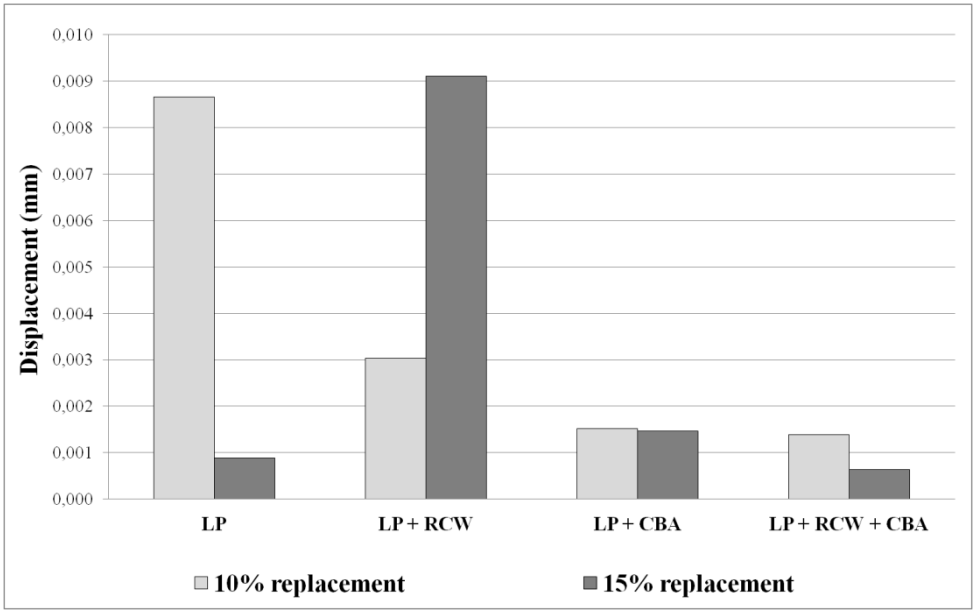

Figure 6: Linear shrinkage results.

For the mortars with 10% of substitution, all of the mixes with recycled fines were more efficient than the reference, since they presented smaller displacements. However for 15% of substitution, the mortar LP + RCW 15 presented the worst result of all samples tested. Furthermore, the mortar LP + RCW + CBA 15 presented the smallest linear shrinkage shifts (0.006 mm) of the eight mixtures analyzed. The LP + CBA mixtures did not present great displacement variations with the increase in the content of fines (10% to 15%). Based on the results, it was possible to conclude that the mixtures LP + CBA and LP + RCW + CBA presented good results for both percentages of substitutions tested (10 and 15%).

Dimensional stability (curling)

The average values of the final displacements due to the curling phenomenon generated in self-leveling mortars produced are summarized in the bar graph (Figure 7).

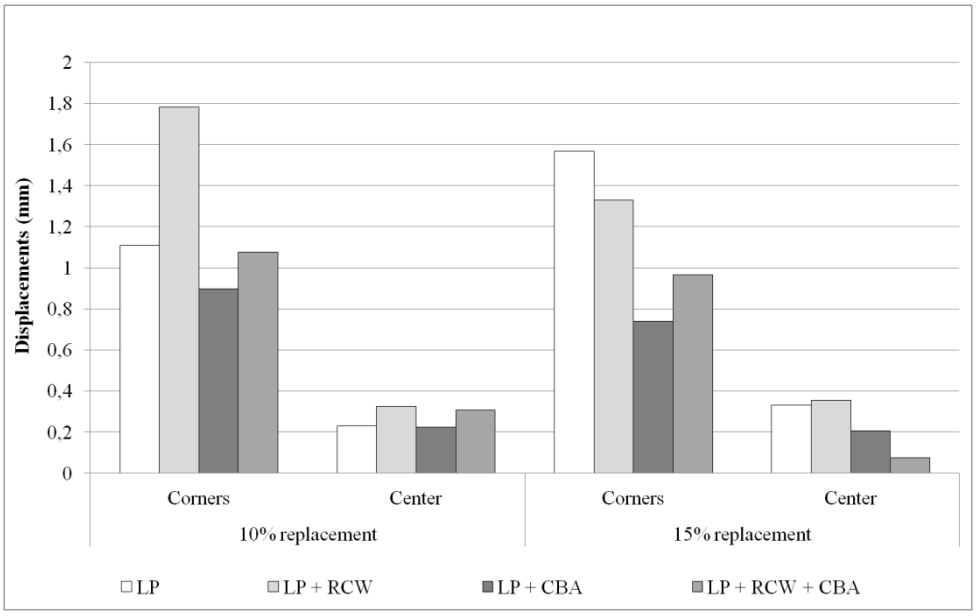

Figure 7: Average displacement in the corners and centers of the plates.

As can be observed, only the sample LP + RCW 10 (10% of replacement of OPC) presented values of median displacement of the corners, greater than the reference (FC). For 15% of substitution, all the self-leveling mortars were more efficient than the reference and the sample LP + CBA 15 presented the best result of all mortars produced. It was possible to identify a reduction in the displacement of corners results, with an increase of the fine content, except for the reference mortar.

The dimensional variations due to the drying process of the plates resulted in ascending curves, which are predominantly more pronounced over the corners (curling) [9]. The self-leveling mortar FC + CBA 15 achieved 0.74 mm of mean displacement at the corners for 130 hours of test (Figure 8).

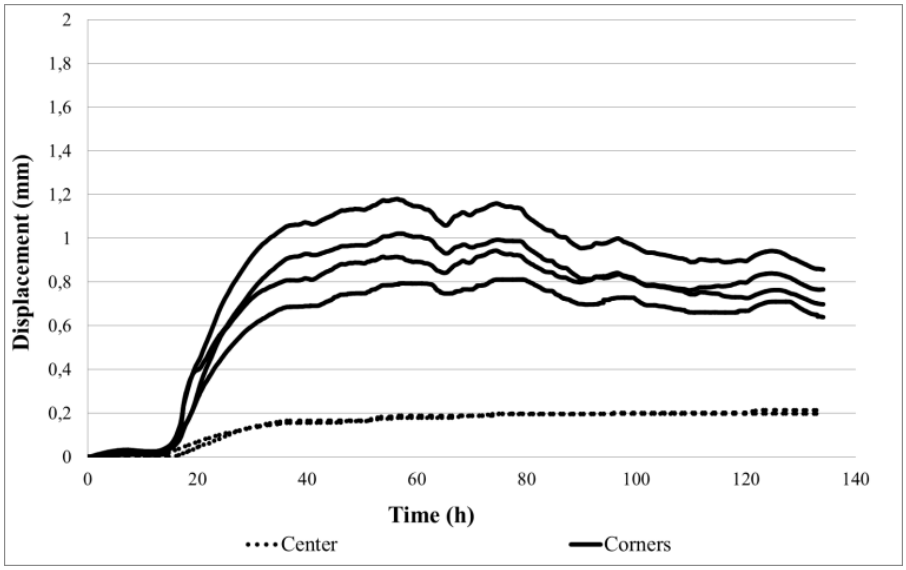

Figure 8: Curling results for self-leveling mortar LP + CBA 15 mixes .

The lowest values of shrinkage are related to the effect of internal curing as a function of the addition bottom ash. The physical characteristics of bottom ash (high porosity) confer a higher initial water absorption. As time proceeds the water absorbed initially is gradually released during the drying process of the mortar. Therefore, the internal relative humidity of the mortar undergoes minor variations and the drying shrinkage can be reduced [13, 16]. Furthermore, mixes with lower maximum hydration temperatures (LP + CBA 15) might reduce water evaporation and thus the shrinkage tends to be lower [12].
It was visually verified that none of the samples produced presented cracks. Higher shrinkage values can give rise to cracks and, consequently, contribute for penetration of external aggressive agents that degrades the material, such as salts, acids, microorganisms, water, among others. The influence of these external agents on the self-leveling mortar tends to reduce the durability of the material.

5. CONCLUSIONS

In the self - leveling mortars analyzed in this present study it was possible to verify the viability of application of the recycled fines (RCD and CBA) in replacement of 10 and 15% of cement substitution, and maximum SP chemical admixtures contents of 0.40% of the binder (wt%).

- Mortars based on RCW demonstrated scatter values similar to those of the reference mixture (LP), in addition to a adequate consistency and good visual appearance.
- Mortars composed of CBA as fine elements demonstrated more efficiency in combating bleeding, despite of reducing the flow in contrast to the reference. Therefore, the use of LP + CBA in binary binder compositions required higher amounts of SP chemical admixtures.
- Mortars formulated with CBA as fines were more prone to segregation for higher chemical admixtures contents ($\geq$ 0.45%) of the binder mass and for higher binder substitution contents ($\geq$ 20%);
- The ternary mixes (LP + RCW + CBA) exhibits similar flowability to the reference (LP).

The main goal of the present research was to evaluate the shrinkage, as it is considered one of the main problems generated in self-leveling mortars. Data from the curling effect and maximum hydration temperature indicated that the LP + CBA 15 mortar presented the most efficient results. The LP + CRW + CBA 15 sample was the most efficient for the linear shrinkage test. In this way, it was possible to conclude that the use of bottom ash fines (CBA) reduces the drying shrinkage. Finally, we can conclude that the mortars LP + CBA 15 and LP + RCW + CBA 15 were the most efficient mixes.

ACKNOWLEDGEMENTS

The authors gratefully acknowledge the National Council for Scientific and Technological Development (CNPq), CAPES, for financial support of this work.

REFERENCES

[1] Mehdipour, I.; Razzagui,M.S.; Amini, K.; Shekarchi, M. 'Effect of mineral admixtures on fluidity and stability of self-consolidating mortar subjected to prolonged mixing time'. *Construction and Building Materials*, **40**, p. 10. 29-1037, 2013.

[2] Seifert, S.; Neubauer, J.; Neunhoeffer, F.G. 'Spatially resolved quantitative in-situ phase analysis of a self-leveling compound'. *Cement and Concrete Research*, **42**, p. 919-927, 2012.
[3] Alrifai, A.; Aggoun, S.; Kadri, A.; Kenai, S.; Kadri, E.H. 'Paste and mortar studies on the influence of mix design parameters on autogenous shrinkage of self-compacting concrete'. *Construction and Building Materials*, **47**, p. 969-976, 2013.
[4] ACHE, 'Use of recycled aggregates for production of structural concrete'. Asociación Científica del Hormigón Estructural, Madrid, 2005 (in Spanish). AENOR, EHE-08 regulation of structural concrete, Spain, 2008 (in Spanish).
[5] Zhao, Z,; Remond, S.; Damidot, D.; Xu, W. 'Influence of fine recycled concrete aggregates on the properties of mortars. *Construction and Building Materials*', **81**, p.179-186, 2015.
[6] López, D.C.; Fonteboa B. G.; Brito J.; Abella, F. M.; Taboada, I.G.; Silva, S. 'Study of the rheology of self-compacting concrete with fine recycled concrete aggregates'. *Construction and Building Materials*, **96**, p. 491-501, 2015.
[7] Georgin, J.F.; Ambroise, J.; Péra, J.; Reynouard, J.M. 'Development of self-leveling screed based on calcium sulfoaluminate cement: modelling of curling due to drying'. *Cement & Concrete Composites*, **30**, p. 769–778, 2008.
[8] LE-Bihan, T.; Georgin, J.F.; Michel, M.; Ambroise, J.; Morestin, F. 'Measurements and modeling of cement base materials deformation at early age: The cause of sulfo-aluminous cement'. *Cement and Concrete Research*, **42**, p. 1055-1065, 2012.
[9] Benabed, B. Kadri, E. H. Azzouz, L. Kenai, S. 'Properties of self-compacting mortar made with various types of sand'. *Cement & Concrete Composites*, **34**, p.1167-1173, 2012.
[10] Onishi, K.; Bier, T. 'Investigation into relations among technological properties, hydration kinetics and early age hydration of self-leveling underlayments'. *Cement and Concrete Research*, **40**, p. 1034-1040, 2010.
[11] Andrade, L.B.; Rocha, J.C.; Cheriaf, M. 'Influence of coal bottom ash as fine aggregate on fresh properties of concrete'. *Construction and Building Materials*, v. 23, p. 609-614, 2009.
[12] Rafieizonooz, M.; Mirza, J.; Salim, M. R.; Hussin, M. W.; Khankhaje, E. 'Investigation of coal bottom ash and fly ash in concrete as replacement for sand and cement'. *Construction and Building Materials*, **116**, p. 15 - 24, 2016.
[13] Péra, J.; Ambroise, J. 'New applications of calcium sulfoaluminate cement'. *Cement and Concrete Research*, **34**, p. 671-676, 2004.
[14] Libre, N.A.; Khoshnazar, R.; Shekarchi, M. 'Relationship between fluidity and stability of self-consolidating mortar incorporating chemical and mineral admixtures'. *Construction and Building Materials*, **24**, p. 1262-1271, 2010.
[15] Wyrzykowski, M.; Ghourchian, S.; Sinthupinyo, S.; Chitvoranund, N.; Chintana, T.; Lura, P. 'Internal curing of high performance mortars with bottom ash'. Cement & Concrete Composites, **71**, p. 1 – 9, 2016.
[16] ABNT - Associação Brasileira de normas técnicas, NBR NM 52 'Agregado Miúdo – Determinação da massa específica e massa específica aparente. ' (2009).
[17] ABNT - NBR NM 23 'Cimento Portland e outros materiais em pó – Determinação da massa específica'. (2001).
[18] ABNT - NBR NM 248. 'Agregados – Determinação da composição granulométrica'. (2003)
[19] ABNT - NBR NM 76. 'Cimento Portland - Determinação da finura pelo método de permeabilidade ao ar (Método de Blaine) '. (1998).

EVALUATION OF INTERACTIONS BETWEEN RETARDING ADMIXTURES AND FINE MATERIALS IN LONG-TERM FLOWABILITY CEMENT PASTES

Eduardo Nobre Guindani[(1)]; Malik Cheriaf [(2)]; Janaíde Cavalcante Rocha [(3)]

(1) Federal University of Santa Catarina, Post-Graduate Program in Civil Engineering

(2) University Federal of Santa Catarina, Department of Civil Engineering

(3) University Federal of Santa Catarina, Department of Civil Engineering

https://doi.org/10.21452/bccm4.2018.02.18

Abstract

The retarding effects in the hydration of Portland cement caused by organic molecules such as gluconates, sucrose and organic acids are mainly used to setting control required for the production of ready-mix-mortars. Three commercial products, indicated for the control of hydration reactions of Portland cement, were evaluated regarding to maintain the flowability over time of cement pastes containing additions of fine materials (<75μm). The cement pastes were produced with replacement of the cement up to 50% (by weight) by fine materials (d<75μm): basalt filler; fly ash; quartz filler; perlite filler (perlite was replaced by volume). The organic admixtures were used by 0.5 to 1.0% (by weight of cement). Changes in the flowability of the cement pastes over time were evaluated through mini-flow tests and rheometer measurements. The results demonstrate an important reduction in the shear stress of the cement pastes under the effect of the organic molecules, as a consequence of the homogenization of the ionic charges on the surface of the particles. In addition, all organic admixtures at a dosage of 1.0% were able to maintain the flowability for more than 400 hours, however, with gradual reductions of the mini-flow scattering throughout this period, resulting from a probable partial hydration of the cement. The cement pastes with basalt filler showed a faster reduction of flowability over time, which may indicate reactivity between the mineral particles of the filler and the organic molecules. On the other hand, quartz filler contribute to the increase in initial flow. Calorimeter measurements were used to evaluate the interactions between the fine material and the organic molecules confirming that the basalt filler actually reduces the effect of the admixtures.

1. INTRODUCTION

The retarding effects on cement hydration caused by organic molecules, mainly gluconates and sucrose, are explored to control the hydration time of cementitious materials. Depending on the dosage used, these molecules can retard the setting time of cement for more than 72 hours and are used to prolong the fresh state of mortar and concrete [1][2].

In ready-mix mortar fine materials, either inert fillers or pozzolanic fines, are added to the cementitious materials to improve properties on fresh state, such as cohesion and flowability, as well as to improve mechanical properties, compressive strength, and specially to reduce porosity of system. These fine materials can change the hydration kinetics and interact with the organic molecules present in the mixes. In this sense, when retarding admixtures are used in conjunction with fine materials, significant changes in the retardation time can be observed, often reducing the efficiency of the chemical admixtures [3].

Researches have been carried out aiming to evaluate additions of fine materials with quite different physicochemical characteristics, under the effect of retard admixtures (designed for manufacture of ready-mix-mortar). It was known to evaluate mainly changes in the hydration kinetics wich can be associated to the interaction between the chemical admixtures and the fine materials. In addition, the research was supplemented by evaluation of the fluidity and rheological properties of cement pastes over time during the period that they remained on fresh state.

2. MATERIALS AND METHODS

2.1.Materials

Brazilian cement type CP II F-32 was used to produce the cement pastes. The fine materials were: Basalt filler (BF) - Residual; Fly ash (FA) - Pozzolanic; Quartz filler (QF) - Inert; Perlite (PT) - Lightweight. All the fines were sieved to obtain particles less than 75μm.

The main physico-chemical characteristics of these materials are presented in Table 1. The measurement of the particle size distribution was performed using Mastersizer 2000 equipment. The chemical composition of the total oxides present in the materials was carried out using Shimatzu EDX-7000 equipment. In addition, complementary characteristics such as specific surface (Blaine) and loss on ignition were determined.

Table 1 : Chemical and physical characteristics of materials.

Sample Notation	Density (g/cm^3)	Specific Surface (Blaine) (cm^2/g)	d_{50} (μm)	d_{10} (μm)	SiO_2 (%)	Al_2O_3 (%)	CaO (%)	Fe_2O_3 (%)	Loss on ignition (%)
FA	2.087	3594.2	32.15	9.92	70.18	12.75	5.24	5.82	1.06
BF	2.542	2599.4	34.13	4.71	76.55	14.33	0.82	1.13	1.57
QF	2.618	2687.6	38.91	3.43	(>99)	-	-	-	-
PT	1.110	8269.9	58.93	19.71	61.06	27.32	249	2.47	3.17
Cement	3.081	3267.0	21.18	4.73	18.48	4.19	60.47	2.97	5.12

Three different commercial retarding admixtures were used (indicated mainly for the manufacture of ready-mix-mortars). They were identified as POW; ETM; MR; and are composed

by organic molecules such as gluconates and sucrose. These products were evaluated at concentrations of 0.5 and 1.0% in the initial mini-flow studies, although the remainder of the research was used 0.5%.

The composition of the mixes is shown in Table 2. All samples were produced following the same mixing and storage procedure. After mixing the pastes in a standard mixer to mortars, the samples were stored in a hermetically sealed polyethylene container to prevent water evaporation and any contact with the environment, and kept at room temperature of 23 ± 1 ° C.

Table 2 : Mix proportion of sample (wt).

Sample Notations	*Cement (g)*	*BF (g)*	*FA (g)*	*QF (g)*	*PT (g)*	*Água (g)*	*POW (g)*	*ETM (g)*	*MR (g)*
Ref.100%C	400	0	0	0	0	180	0	0	0
Ref.50%BF	200	200	0	0	0	180	0	0	0
Ref.50%FA	200	0	200	0	0	180	0	0	0
Ref.50%QF	200	0	0	200	0	180	0	0	0
Ref.50%PT	200	0	0	0	72.1*	240*	0	0	0
100%C.0,5%POW	400	0	0	0	0	180	2.00	0	0
100%C.0,5%ETM	400	0	0	0	0	180	0	2.00	0
100%C.0,5%MR	400	0	0	0	0	180	0	0	2.00
50%BF.0,5%POW	200	200	0	0	0	180	1.00	0	0
50%FA.0,5%POW	200	0	200	0	0	180	1.00	0	0
50%QF.0,5%POW	200	0	0	200	0	180	1.00	0	0
50%PT.0,5%POW	200	0	0	0	72.1*	240*	1.00	0	0
50%BF.0,5%ETM	200	200	0	0	0	180	0	1.00	0
50%FA.0,5%ETM	200	0	200	0	0	180	0	1.00	0
50%QF.0,5%ETM	200	0	0	200		180	0	1.00	0
50%PT.0,5%ETM	200	0	0	0	72.1*	240*	0	1.00	0
50%BF.0,5%MR	200	200	0	0	0	180	0	0	1.00
50%FA.0,5%MR	200	0	200	0	0	180	0	0	1.00
50%QF.0,5%MR	200	0	0	200	0	180	0	0	1.00
50%PT.0,5%MR	200	0	0	0	72.1*	240*	0	0	1.00

* The mixes with perlite were calculated by volumetric substitution, due to their low bulk density. It was necessary to increase 60g of water in each sample in order to achieve the minimum flowability for the tests.

2.2.Flowability measurements

To determine the behavior of the cement pastes under the effect of the chemical admixtures, mini-slump test was used. The flow measurements were performed over time. To evaluate the results, the diameter of spreading the base of the mini-cone (40mm) was taken as reference for calculating the Flow Index accorAlsoding to Equation 1:

$$FI = \left(\frac{Flow_{(t)} - 40}{Flow_{(t0)} - 40}\right) * 100 \qquad \textit{Equation (1).}$$

FI = Flow Index (%); $Flow_{(t)}$ = flow on time "t" (mm); $Flow_{(t0)}$ = initial flow (mm).

The pastes with fines were evaluated in a Haake Mars Rheometer in order to determine the changes of the shear stress over time. The measurement methods was similar to that used by [4]. Measurements were made at 6-second steps, increasing the shear rate from 1^{-sec} to 60^{-sec} in 3 min. The geometry used was a smooth cylinder. A pre-shear of 30s was performed and the samples

were kept at constant temperature of 24° C. The pastes were evaluated at times: 0; 3h; 24h and 48 hours.

2.3.Reaction kinetic measurements

The evaluation of the hydration processes was performed in a 6-channel semi-adiabatic calorimeter. The retarding effect caused by chemical admixtures, as well as the interference caused by fines, could be evaluated through the temperature curves of the pastes temperature. The differential temperature of each sample (ΔT in °C) was used to generate the curves, which can be considered as the effective increase of heat caused by the cement hydration. 580g of cement paste was used. All samples were initially at 24°C.

3. RESULTS

The initial results obtained from mini-slump test were important for the characterization of the performance of the chemical admixtures over time. As can be seen in Figure 1, these chemical products are able of prolonging the fresh state of the pastes for more than 80 hours at a dosage of 0.5% and more than 340 hours at a dosage of 1.0%. In addition, distinct behaviors could be observed between them, which is most evident in samples made with 1.0%. The pastes with MR leading a more pronounced reduction in the flowability of pastes regardless of the dosage used. The POW and ETM showed a great reduction in the flowability in the first hours after the mixture, which can be demonstrated in both tests: mini-slump and rheological measurements. However, between 48 and 96 hours after, the flowability of pastes was partially recovered for both. Further, a smooth and constant reduction of flowability is a characteristic pertinent to both (POW and ETM), and which becomes more evident in the pastes at a dosage of 1.0%.

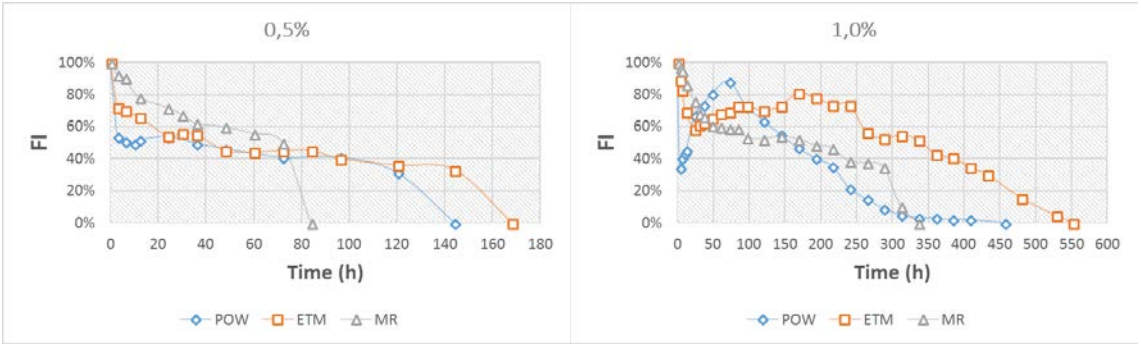

Figure 24 : Flow Index (FI) measurements over time

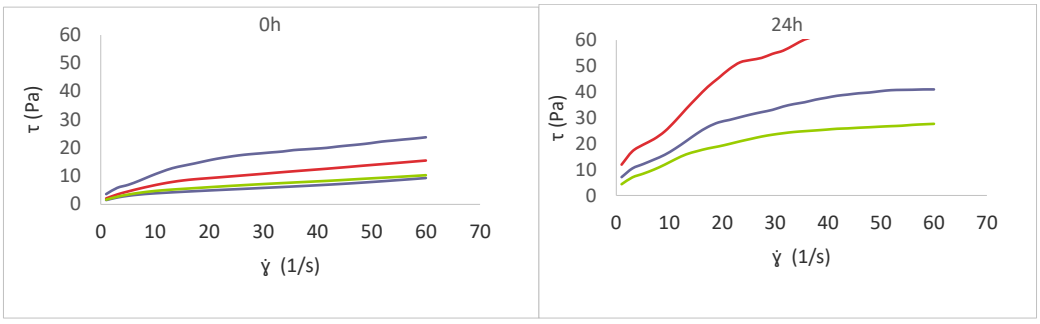

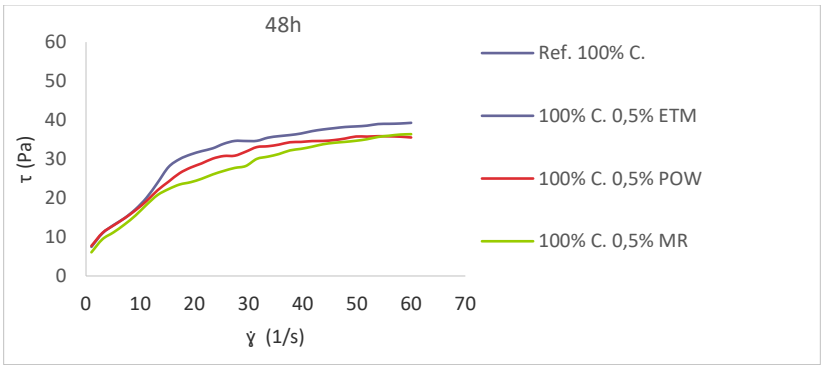

Figure 25 : Rheological measurements of pastes, 100% cement, over time.

A secondary effect that can be observed is the increase in the initial flowability of the pastes, which can be evidenced due the shear stress values of the samples with chemical admixtures were initially smaller than the reference paste, Figure 2. Comparing all the chemical products evaluated, the ETM presented lower initial shear stresses, as well as it kept the samples in the fresh state for longer, reaching 550 hours with 1.0% content (Figure 1).

Among the different fines evaluated, the lowest shear stress was observed in QF sample. The highest stress was observed in the sample with BF, which was always higher than the others during the whole period of measurements. It is important to observe that the samples with BF and MR additive do not have data from 24h because the sample hardened before the measurement could be performed.

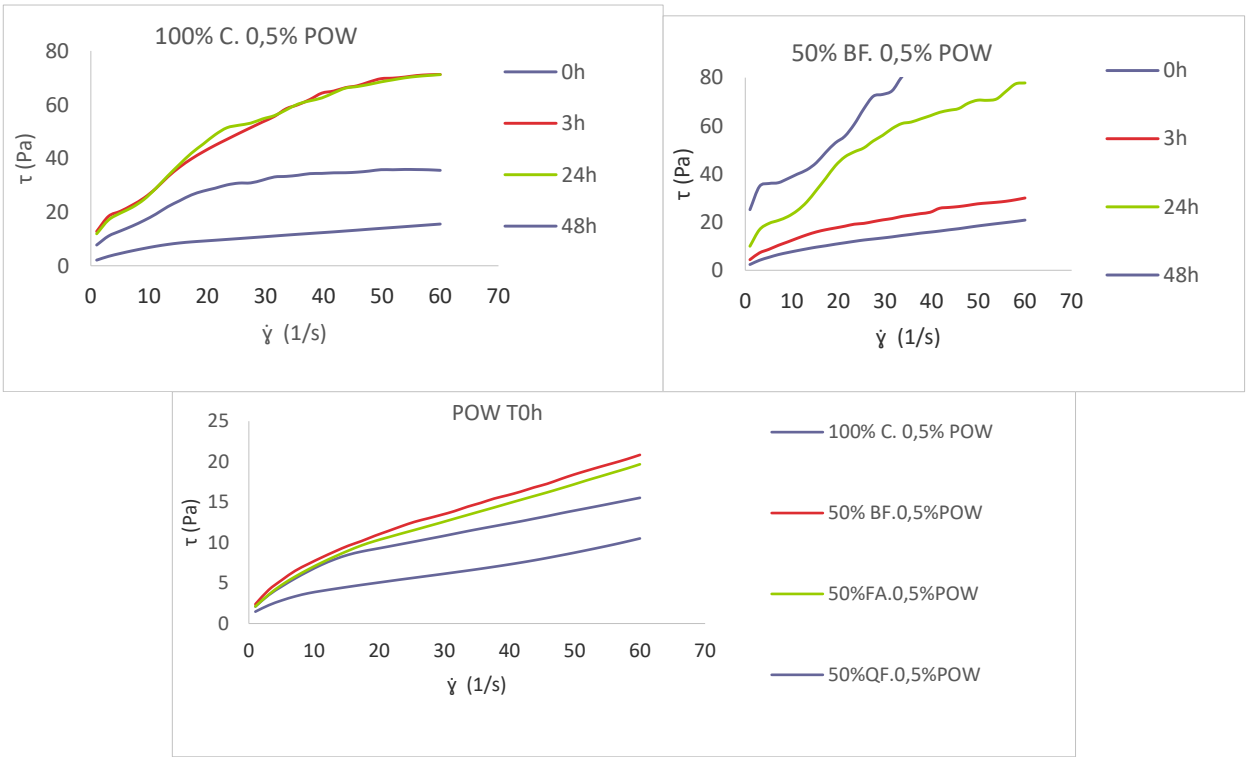

Figure 26 : Rheological measurements of POW pastes over time.

The results of the calorimetry are shown in Figure 4. The MR samples were that presented the earlier set time in all the comparatives, as could be observed in the evaluation of the fluidity over time. Even pastes with ETM was the samples that presented the peak of longer heat release.

The curve of temperature monitoring of the sample with ETM presented double peak of heat release. This phenomenon was observed exclusively for this sample. In addition, it is important to note that samples produced with fines and with ETM additive did not show temperature peaks up to 250 hours of testing when they were removed from the calorimeter.

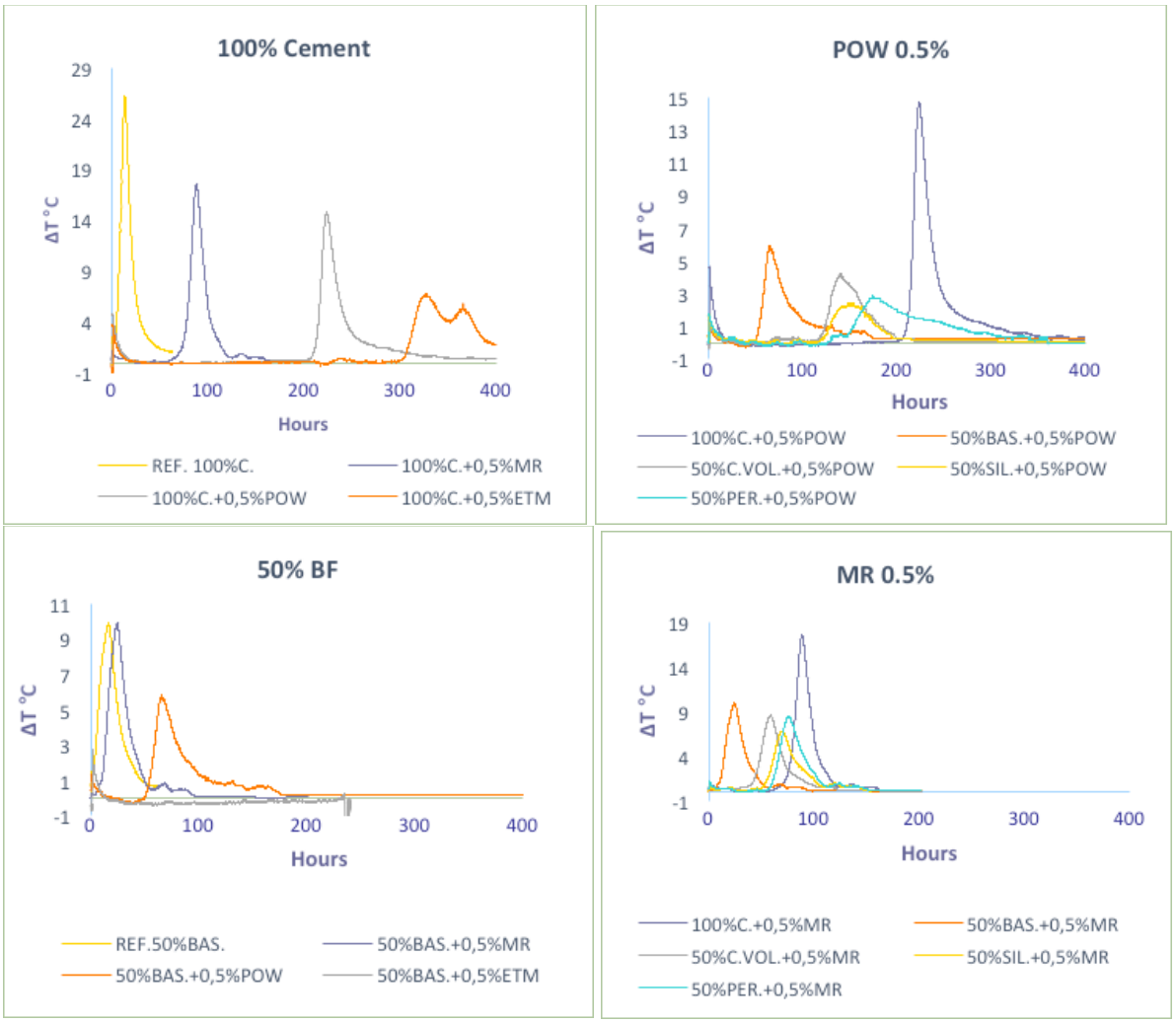

Figure 27 : Evaluation of temperature increase of cement pastes.

4. DISCUSSION

The flowability of the samples with POW in the mini-slump tests (100% C. + 1.0% POW) and in the rheological study (100% C. + 0.5% POW) can be interpreted as a " false-set-time ", a behavior commonly presented by organic admixtures whose composition has sucrose. When added to cement materials before the sulfate phase has been consumed, sucrose accelerates the formation of ettringite, drastically reducing the fluidity of the mixes [5].

The considerable increase in the initial fluidity caused by the retarding admixtures was also observed by the authors [2] and [6] when evaluating mortars with sodium gluconate (organic molecules used like raw material by retarding admixtures). This behavior probably occurs due to the homogenization of the ionic charges of the surface of the particles, caused by the action of the organic molecules.

The gradual reduction of flowability (Figure 1), reaffirmed by the shear stress increase over time (Figure 2), is an evidence that hydration reactions may be occurring slowly in pastes, generating internal interparticle set [1]. A slow formation of ettringite could be the explanation for this phenomenon, since it is the main hydrate responsible for the reduction of flowability in cementitious materials, besides being the first hydrate formed during the hydration process.

The shear stress values of the samples with QF were always the lowest when compared to the other samples. This indicates a plasticizing effect of this material, which was also observed by [7]. This effect also contributed to the prolongation of fluidity over time, since this same behavior was observed also in 48h.

The behaviors observed in the calorimetry, comparing the curves with fines, is very similar to what was observed by [3]. The samples that contained fines, despite the effects of dilution of the clinker, were the ones that presented set time earlier than samples with 100% cement. Moreover, another factor that contributes to this behavior is the fact that the dosage of the chemical admixtures is on the cement mass and not on the binder (cement + fines).

The temperature curve of the sample 100% C. + 0.5% ETM, presented double peak. This may have been a result of the sample segregation process during the time it remained in the calorimeter. Due to the high flowability of the material, formation of layers with different concentrations of cement may have occurred during the measurement period. Possibly the bottom layer with higher solids concentration reacted before the upper layer, with lower concentration of solid material.

The comparisons of calorimetry between the fines show that the samples with BF reacted sooner than the others. It is also important to note that the height of the temperature peaks of these samples is slightly higher than the other fines. In addition, the rheological tests point to a much larger shear stress increase over time for the BF samples. These facts indicate that BF considerably reduces the retarding effects of the organic molecules.

5. CONCLUSIONS

The retarding admixtures are able of promoting increased in initial flowability of the cementitious materials as well as maintaining the fresh state of cement pastes for more than 80 hours (0.5% dosage). The composition of different chemical bases, such as gluconates and sucrose, results in chemical admixtures with different behaviors, such as the POW, in which the effect of the “false-set-time” can be observed, followed by an increase in flowability in the following hours.

The BF considerably reduces the efficiency of the retarding admixtures, as evidenced by both the rheological study and the calorimetry study. On the other hand, the fine of QF flavors cause an increase in flowability and its maintenance over time.

Acknowledgements

We gratefully acknowledge financial support from the CNPq and CAPES.

REFERENCES

[1] CHEUNG, J., JEKNAVORIAN, A., ROBERTS, L., & SILVA, D. Impact of admixtures on the hydration kinetics of Portland cement. *Cement and Concrete Research*, 41(12), 1289-1309. 2011.

[2] MA, S., LI, W., ZHANG, S., GE, D., YU, J., & SHEN, X. Influence of sodium gluconate on the performance and hydration of Portland cement. *Construction and Building Materials*, 91, 138-144. 2015.

[3] ATAIE, F. F., JUENGER, M. C., TAYLOR-LANGE, S. C., & RIDING, K. A. Comparison of the retarding mechanisms of zinc oxide and sucrose on cement hydration and interactions with supplementary cementitious materials. *Cement and Concrete Research*, 72, 128-136. 2015.

[4] CEPURITIS, R., JACOBSEN, S., SMEPLASS, S., MØRTSELL, E., WIGUM, B. J., & NG, S. Influence of crushed aggregate fines with micro-proportioned particle size distributions on rheology of cement paste. *Cement and Concrete Composites*. 2017.
[5] RICKERT, J. Influence of Retarders on the Hydration of Clinker and Cement. *Concrete Technology Reports*, 2001.
[6] BESSAIES-BEY, H., BAUMANN, R., SCHMITZ, M., RADLER, M., & ROUSSEL, N. Organic admixtures and cement particles: Competitive adsorption and its macroscopic rheological consequences. *Cement and Concrete Research*, 80, 1-9. 2016.
[7] TALERO. R, PEDRAJAS. C, GONZÁLEZ. M, ARAMBURO. C, BLÁZQUEZ. A, RAHHAL.V. Role of the filler on Portland cement hydration at very early ages: Rheological behaviour of their fresh cement pastes. *Construction and Building Materials, 151, 939-949, 2017.*

COLD-PRESSED HYBRID COMPOSITES REINFORCED WITH COIR FIBRES AND CEMENT PARTICLES: A STATISTICAL APPROACH

Gabriela C. Coura(1), Lívia A. Oliveira(1,2), Bruna T. Ferreira(1), Júlio C. dos Santos(1,2), Rodrigo T. S. Freire(1), Túlio H. Panzera(1,2)

(1) Centre for Innovation and Technology in Composite Materials, Department of Mechanical Engineering, Federal University of São João del Rei, Brazil

(2) Department of Natural Sciences, Federal University of São João del Rei, Brazil

https://doi.org/10.21452/bccm4.2018.02.19

Abstract: The mechanical properties of polyester hybrid composites reinforced with treated and untreated coir fibres and 15 wt.% of cement microparticles at different locations were investigated in this work. A Full Factorial Design ($2^1 3^1$) was conducted to identify the effect of the chemical treatment of coir fibres and location of cement inclusions on the tensile (and flexural) strength and modulus. In general, the alkaline treatment led to increased tensile properties and flexural strength compared to untreated fibre composites. The inclusion of cement particles, especially added throughout the whole sample, increased the tensile and flexural strength and tensile modulus of untreated coir fibre composites. A significant increase in flexural modulus was observed only in composites made with treated coir fibres along with the incorporation of cement particles in the whole sample.

Keywords: hybrid composites, coir fibre, polyester, cement, chemical treatment, mechanical properties.

1. INTRODUCTION

Natural fibres such as flax, hemp, jute, sisal, coir, and henequen have been used since ancient times in a wide variety of products, ranging from clothing to house roofing [1-3]. The investigation of natural fibres as reinforcements in hybrid composite materials has recently risen as sustainability and environmental issues are considered, owing in particular to their renewability and biodegradability. [4-6].

Coir is a low cost, versatile, renewable and biodegradable lignocelullosic fibre obtained from the coconut palm (*Cocos nucifera*), which is very abundant in coastal areas of tropical countries and plays an important role in the economy of these regions [2, 7-8]. Apart from its conventional applications (e.g., cordage, cushions, sacking, floor-furnishing [7], mats, carpets and seat covers

[9]), coir has recently been used as a reinforcement in cement, concrete, particleboard and polymer composites due to their valuable properties such as renewability, resilience, rigidity, toughness, elongation at break and weather resistance [7]. These composite materials may potentially be used in the aeronautics, leisure, construction, sport, packaging and automotive industries [10-11].

An important issue, however, is fibre-matrix compatibility [12]. Natural fibres are in general of hydrophilic nature while the polymeric matrices are hydrophobic, resulting in low fibre-matrix adhesion, which plays an important role in the final mechanical performance [13]. Such compatibility may be substantially improved through the chemical modification of the fibre surface [14-16]. Alkaline treatments are currently considered the most economical and effective technique, removing impurities such as pectin, fats and lignin. This process increases the roughness of the fibre surface and consequently improves fibre-matrix mechanical interlocking [17].

In addition, the thermal stability and stiffness of fibre-reinforced composites improve upon the incorporation of a second rigid particulate phase, such as SiO_2 micro- or nanoparticles, glass, Al_2O_3, $Mg(OH)_2$, $CaCO_3$ and carbon nanotubes [18-20]. According to Silva *et al.* [21], when the composite material is under stress, the crack propagation is prevented across the locations where the particles are concentrated due to their high strength. Therefore, additional stress is required for the crack propagation through the fibre–particle or particle–matrix interfaces, which increases the mechanical strength of the composites. However, this increase strongly depends on particle size, particle content and interface adhesion [20].

This work investigates, via ANOVA and Design of Experiments (DoE), the effect of the treatment of coir fibres and the location of microparticles on the mechanical properties of hybrid short coir fibre composites with Portland cement particle inclusions. A preliminary experiment was conducted to identify the effect of particle type (silica or cement) and particle mass fraction (5, 10 or 15 wt%) on the mechanical properties of the matrix phase. The best experimental condition was used as a reinforced matrix phase for the fabrication of the hybrid composites.

2. MATERIALS AND METHODS

2.1 Materials

Polylite polyester resin 10316-10 and Methyl Ethyl Ketone Peroxide hardener were supplied by Reichhold (Brazil). Coir fibres were supplied by *Deflor Bioengenharia* (Brazil), being treated with sodium hydroxide (NaOH, 99%, sourced from Sulfal - Brazil). Portland cement (ASTM III) and silica microparticles were supplied by Holcim (Brazil) and *Moinhos Gerais* (Brazil), respectively. Both particles were classified by sieving process in a particle size range of 44 - 26 μm.

2.2 Coir fibre treatment

Coir fibres in pristine conditions were manually cleaned for the complete removal of plant debris (Figure 1a). The fibres were subsequently immersed in a 10 wt.% sodium hydroxide solution at room temperature for 15 h (Figure 1b) and then washed in water. Finally, the treated coir fibres were oven-dried at 60 ^{o}C for 72 h (Figure 1c).

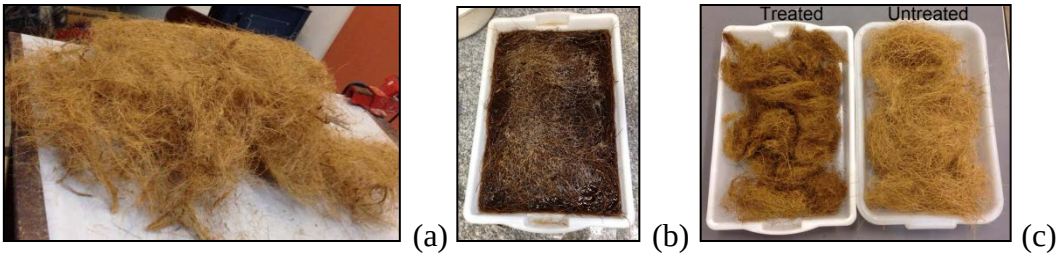

(a) (b) (c)

Figure 1. Coir fibres: (a) in pristine condition, (b) under sodium hydroxide treatment, (c) ready to be used as a reinforcing material.

2.3 Design of experiment

The factors and levels investigated in the experiment were set based on preliminary tests. A Full Factorial Design ($2^1 3^1$) was established to investigate the effect of the fibre chemical treatment (treated and untreated) and cement location (no particles; upper (under compression) beam side and whole sample) on the flexural and tensile strength and modulus of hybrid composites, resulting in 6 experimental conditions (E.C.), as shown in Table 1. Minitab v.17 software was used to perform the Design of Experiment (DoE) and Analysis of Variance (ANOVA) techniques.

Table 1. Full Factorial Design ($2^1 3^1$).

E.C.	Chemical Treatment	Cement Location	E.C.	Chemical Treatment	Cement Location
1	Untreated	No particles	4	Treated	No particles
2	Untreated	Upper side	5	Treated	Upper side
3	Untreated	Whole sample	6	Treated	Whole sample

The constant factors considered in this experiment were established based on a previous work [22]: type of matrix (polyester), fibre grammage (300 g/m^2), fibre volume fraction (30%), particle mass fraction (15 wt.%), number of fibre layers per composite plate (3 layers), cold-pressing time (22 h), compaction pressure (654 kPa) and curing time (28 days).

Ten specimens (five for tensile and five for flexural tests) were fabricated for each of the 6 experimental conditions. Two replicates were considered, running a total of 120 specimens.

2.4 Manufacturing process

The composite materials were fabricated using the hand lay-up technique followed by cold compaction. The treated/untreated short coir fibres (20 – 180 mm) were weighed according to the required grammage (300 g/m^2) and randomly distributed into a 300 x 300 mm metallic mould (Figure 2a). A preliminary uniaxial pressure of 654 kPa was applied for 2 min to obtain a randomly oriented coir fibre fabric (Figure 2b). An aluminium plate (Figure 2c), covered with a thin wax layer as a release agent, was placed into the mould to provide good surface finish. The polymer matrix was prepared by first mixing the resin and hardener according to the fabricant's orientation (2 wt%). The microparticles were subsequently added and hand-mixed for 5 min at room temperature (~23 ^{o}C). Three fabric layers were assembled into the mould and the polymer matrix (modified and non-modified, depending on the experimental condition considered) was uniformly spread over the coir fibre layers (Figure 2d). A lid was then placed on the mould and a pressure of 654 kPa was applied for 22 h (Figure 2e). The material was subsequently demoulded (Figure 2f)

and placed in a plastic container to prevent moisture absorption for curing (28 days). The composite plate was finally cut (Figure 2g) according to ASTM standards and tested.

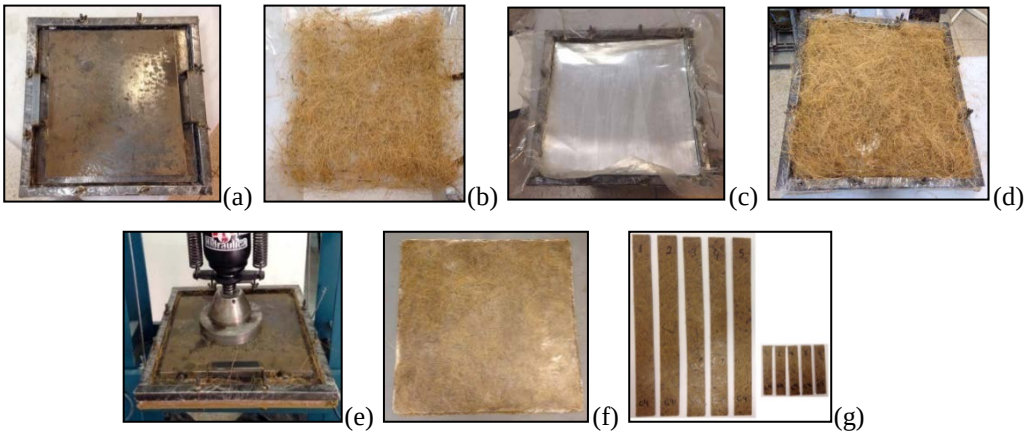

Figure 2. Fabrication process of the composites: (a) metallic mould, (b) fabric of random coir fibres, (c) aluminium plate, (d) fabric arranged inside the mould, (e) cold pressing, (f) composite plate and (g) specimens for testing.

2.5 Characterisation

The mechanical properties of the reinforced polymer matrix with 5, 10 and 15 wt.% Portland cement or silica particles was characterised via flexural, tensile and compressive tests, performed according to ASTM D790-15 [23], ASTM D638-14 [24] and ASTM D695-15 [25], respectively. Tensile and flexural tests were also conducted for the characterisation of the hybrid composites, following the recommendations of ASTM D3039-14 [26] and ASTM D790-15 [23], respectively. A Shimadzu AG-X Plus test machine equipped with a 100 kN and velocity of 2 mm/min load cell was used to perform the mechanical tests.

3. RESULTS AND DISCUSSION

3.1 Matrix phase characterisation

Table 2 presents the mean and standard deviation of the mechanical test results for the polyester polymer in pristine conditions and modified with silica and Portland cement particles.

The incorporation of microparticles decreased the tensile and flexural strength of the matrices, which can be attributed to the low particle-matrix interfacial adhesion and stress concentration at larger deformations. On the other hand, the compressive strength was increased due to the greater capacity of these microparticles to withstand stress under compressive loads. These results justify the choice of using microparticles in the upper beam side of the laminates, since the specimens will be under compressive stress when subjected to flexural loading, compensating for the low compressive strength of the fibres. In addition, the use of microparticles, especially at higher mass fractions, may contribute to the enhancement of the mechanical modulus of the composites, due to their inherent high stiffness.

In general, the inclusion of cement microparticles provided better results on the mechanical properties of modified matrices when compared to silica results. Similar findings have been reported by Torres *et al.* [27] and Martuscelli *et al.* [28], which evaluated the modified epoxy polymer matrix with silica and cement microparticles under compression. This mechanical

enhancement has been attributed to the presence of hydrated cement products, which stiffen the polymer [28].

It is also observed in Table 2 that the modified matrix containing 15 wt% of cement particles generally provided better results in comparison to the other amounts, which justifies the choice of this percentage as the reinforcement level used in the hybrid biocomposites.

Table 2. Mechanical properties of modified and non-modified matrices.

Type of Matrix (wt.%)		Tensile		Compressive		Flexural	
		Strength (MPa)	Modulus (GPa)	Strength (MPa)	Modulus (GPa)	Strength (MPa)	Modulus (GPa)
Ref.	0	36.89 (±3.55)	2.43 (±0.01)	60.30 (±1.41)	1.93 (±0.03)	54.45 (±1.94)	2.22 (±0.11)
Silica	5	30.42 (±2.86)	2.42 (±0.02)	63.09 (±2.36)	2.11 (±0.07)	42.84 (±3.11)	2.44 (±0.04)
	10	25.04 (±2.58)	2.36 (±0.03)	65.62 (±1.96)	2.30 (±0.01)	48.09 (±0.89)	2.58 (±0.02)
	15	21.19 (±0.22)	2.51 (±0.18)	69.87 (±2.77)	2.45 (±0.04)	33.22 (±1.62)	2.69 (±0.09)
Cement	5	31.33 (±0.02)	2.39 (±0.01)	98.08 (±0.88)	2.81 (±0.01)	33.07 (±2.37)	2.50 (±0.08)
	10	30.67 (±0.02)	2.59 (±0.12)	106.79 (±3.95)	3.15 (±0.22)	37.76 (±1.66)	2.70 (±0.08)
	15	32.32 (±0.40)	2.66 (±0.15)	107.18 (±5.49)	3.34 (±0.16)	45.31 (±0.19)	2.81 (±0.06)

3.2 Statistical results

Table 3 presents the mean and standard deviation of the two replicates considered for the mechanical tests of hybrid coir fibre-reinforced composites with 15 wt.% of cement inclusions. Table 4 shows the Analysis of Variance (ANOVA) results obtained through Design of Experiment (DoE). If the P-value is less than or equal to 0.05, this implies that the effect (or interaction of effects) is statistically significant within a 95% confidence level (underlined values in Table 4). Values in bold were interpreted via effect plots. The values of R^2-(adjusted), ranging from 73.81% to 96.88% (Table 4), imply a satisfactory predictability for the underlying statistical model used. ANOVA was validated by the Anderson-Darling normality test, exhibiting P-values greater than 0.05 (0.503 – 0.977), implying that the data follow a normal distribution.

Table 3. Mechanical properties of the composite materials.

Experimental Condition		Tensile		Flexural	
		Strength (MPa)	Modulus (GPa)	Strength (MPa)	Modulus (GPa)
Replicate 1	1	9.25 (±0.32)	2.25 (±0.08)	18.27 (±0.77)	2.55 (±0.41)
	2	9.71 (±1.28)	3.48 (±0.23)	20.56 (±1.71)	2.55 (±0.15)
	3	12.11 (±1.84)	3.98 (±0.25)	24.15 (±2.25)	2.66 (±0.15)
	4	10.82 (±0.16)	2.61 (±0.14)	29.65 (±4.85)	2.63 (±0.32)
	5	14.14 (±0.15)	4.58 (±0.45)	25.67 (±1.12)	2.57 (±0.11)
	6	10.63 (±1.50)	4.32 (±0.51)	25.48 (±1.60)	2.89 (±0.11)
Replicate 2	1	9.30 (±0.96)	2.20 (±0.22)	15.50 (±1.33)	2.55 (±0.30)
	2	9.47 (±0.81)	3.54 (±0.48)	19.01 (±2.81)	2.56 (±0.18)
	3	11.59 (±1.59)	3.53 (±0.30)	24.50 (±2.03)	2.55 (±0.30)
	4	10.98 (±1.36)	2.60 (±0.01)	30.60 (±5.32)	2.39 (±0.24)
	5	13.18 (±1.81)	4.36 (±0.40)	26.30 (±1.60)	2.61 (±0.13)
	6	10.61 (±0.50)	4.18 (±0.59)	26.91 (±1.89)	3.04 (±0.40)

Table 4. Analysis of Variance (ANOVA).

ANOVA		P-value ≤ 0.05			
	Experimental Factors	Tensile Strength (MPa)	Tensile Modulus (GPa)	Flexural Strength (MPa)	Flexural Modulus (GPa)
Main Factors	Chemical Treatment	0.000	**0.000**	0.000	0.060
	Cement Location	0.001	**0.000**	0.046	0.014
Interaction.	Chemical Treatment x Cement Location	**0.000**	0.076	**0.001**	**0.040**
	R^2 - adj	95.57%	96.88%	94.74%	73.81%
	P-value (Anderson Darling) ≥ 0.05	0.503	0.641	0.977	0.764

3.2.1 Tensile Test

Figure 3a presents the second-order interaction effect plot for the mean tensile strength. Letters stand for Tukey's comparison test, in which similar letters belong to the same group, i.e., equivalent means.

The chemical treatment provided an increase in tensile strength, when compared to composites manufactured with untreated fibres. This behaviour may be attributed to enhanced fibre bridging effects, since the alkaline treatment increases fibre roughness. In fact, Mulinari *et al.* [29], reports that the alkaline treatment enhances fibre roughness and fibre-matrix adhesion, owing to the removal of the superficial layer of coir fibres, increasing the exposure area of fibrils and surface pits (tyloses). Particles may also increase the composite strength, acting as barriers against crack propagation and enhancing fibre-matrix interlocking. It is worth noting a relevant increase (42.44%) observed for treated coir fibres with cement inclusions in the upper half of the laminate.

A significant drop in strength (22.5%), however, was observed for treated fibre composites with microparticle inclusions in the whole laminate. Such behaviour demands further investigations.

Figure 3b presents the main effect plots for mean tensile modulus. Figure 3b, item a, reveals that the tensile modulus of treated coir fibre composites are 19.34% higher relative to untreated ones, which is attributed to enhanced interlocking as well as an increase in fibre stiffness after the alkaline treatment, as reported by Oliveira *et al.* [22]. Figure 3b, item b, shows a substantial increase in stiffness (65.22%) when cement microparticles were incorporated into the upper beam side and in the whole composite, with no difference between means as shown by the same group A. These results are consistent with the matrix characterisation results (Table 2), which presents an increase in modulus after the incorporation of 15 wt.% of cement particles, attributed to the high stiffness of the microparticles. In addition, cement particles also enhances fibre-matrix interaction through the interlocking effect.

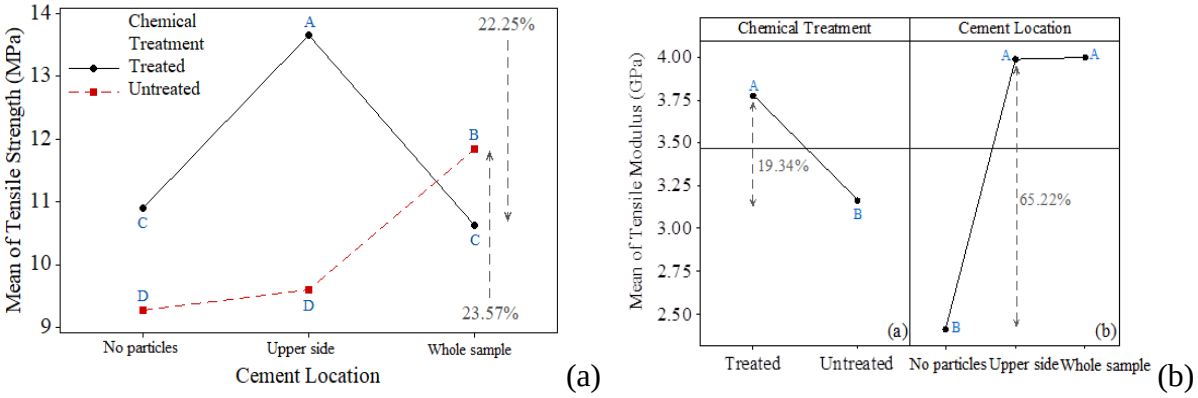

Figure 3. Effect plot for the mean: (a) tensile strength and (b) tensile modulus of the composites.

3.2.2 Flexural Test

Figure 4a presents the second-order interaction analysis for the mean flexural strength. A substantial increase in strength was observed when treated coir fibres were used, especially for those non-particulate composites (78.41%), attributed to enhanced fibre-matrix compatibility and bridging effects after the alkaline treatment. However, the inclusion of cement microparticles in the upper beam side and in the entire sample of treated composites led to a decrease in strength of 15.93%. An opposite behaviour was observed for untreated fibre composites, with an increase in flexural strength upon the inclusion of cement microparticles, which may act as barriers for crack propagation.

Figure 4b shows the plot of second-order interaction effects for the mean flexural modulus. Untreated and treated coir fibre composites present a similar behaviour at all levels (group B), except when the particles were added to the whole sample (group A). This increase of 13.82% is attributed to an increase in stiffness of post-treated fibres [22] as well as of the reinforced matrix phase. This also implies that the particles may play an important role even when added to the lower beam side (under tensile stress), which can be attributed to enhanced interlocking effects.

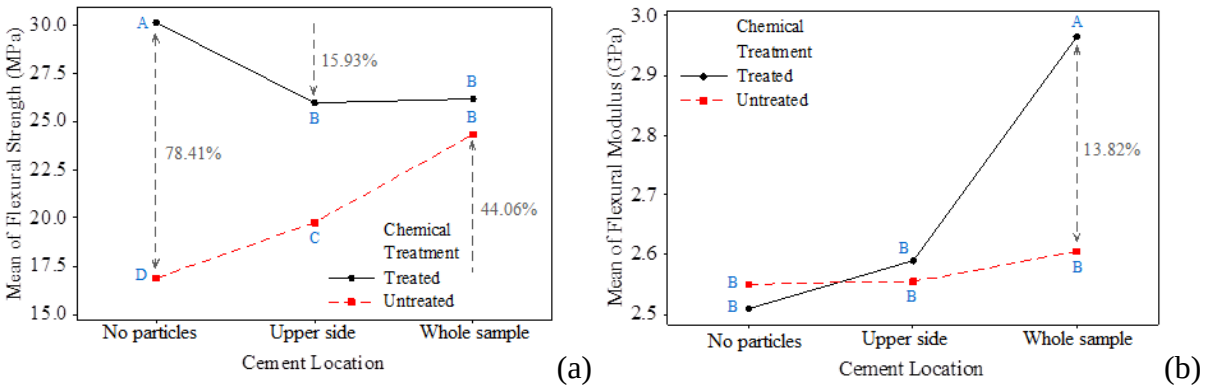

Figure 4. Effect plot for the mean responses: (a) flexural strength and (b) flexural modulus of the composites.

4. CONCLUSIONS

A Full Factorial Design was used to investigate the mechanical properties of hybrid composites reinforced with treated and untreated coir fibres and cement microparticles in different locations. The matrix phase was also characterized. The conclusions are described as follows:

- The incorporation of cement in the polyester matrix led to the increase of mechanical properties in relation to the silica particles, especially when it was considered 15 wt.%.
- The inclusion of particles reduced the tensile and flexural strength of the matrices, except for the compressive strength. In contrast, an increase in mechanical moduli was observed for all reinforced matrices.
- In general, the chemical treatment enhanced the tensile properties and flexural strength of the composites. However, a slight decrease in strength was obtained when the particles were incorporated throughout the treated fibre laminates.
- The cement particles promoted a substantial increase in tensile modulus for all laminates because of their high stiffness. A positive effect was also evidenced for the tensile and flexural strength of untreated coir fibre composites.
- A slight increase in flexural modulus was observed only in composites with treated coir fibres and cement added throughout the sample.

ACKNOWLEDGMENTS

The authors would like to thank CAPES (MSc scholarship), CNPq (PP-306767/2016-3) and FAPEMIG (PPM-00075-17) for the financial support provided.

REFERENCES

[1] Ramesh, M., Palanikumar, K. and Reddy, K. H., 'Plant fibre based bio-composites: sustainable and renewable green materials', *Renew. Sust. Energ. Rev*. **79** (2017) 558-584.

[2] Monteiro, S.N., Terrones, L.A.H. and D'almeida, J.R.M., 'Mechanical performance of coir fiber/polyester composites', *Polym. Test*. **27** (2008) 591-595.

[3] Abdul Khalil, H.P.S., Bhat, A.H. and Ireana Yusra, A. F., 'Green composites from sustainable cellulose nanofibrils: A review', *Carbohyd. Polym*. **87** (2012) 963-979.

[4] Satyanarayana, K.G., Sukumaran, K., Mukherjee, P.S., Pavithran, C. and Pillai, S.G.K., 'Natural fibre-polymer composites', *Cement Concrete Comp.* **12** (1990) 117-136.

[5] Defoirdt, N. *et al.*, 'Assessment of tensile properties of coir, bamboo and jute fibre', *Compos Part A.* **41** (2010) 588-595.
[6] Yan, L., Su, S. and Chouw, N., 'Microstructure, flexural properties and durability of coir fibre reinforced concrete beams externally strengthened with flax FRP composites', *Compos. Part. B.* **80** (2015) 343-354.
[7] Zhang, L. and Hu, Y., 'Novel lignocellulosic hybrid particleboard composites made from rice straws and coir fibers', *Mater. Design.* **55** (2014) 19-26.
[8] Lecompte, T., Perrot, A., Subrianto, A., Le Duigou, A. and Ausias, G., 'A novel pull-out device used to study the influence of pressure during processing of cement-based material reinforced with coir', *Constr. Build. Mater.* **78** (2015) 224-233.
[9] Silva, G.G., Souza, D.A., Machado, J.C. and Hourston, D.J., 'Mechanical and thermal characterization of native Brazilian coir fiber', *J. App. Polym. Sci.* **76** (2000) 1197-1206.
[10] Akil, H.M., Omar, M.F., Mazuki, A.A.M., Safiee, S., Ishak, Z.A.M. and Abu Bakar, A., 'Kenaf fiber reinforced composites: A review', *Mater. Design.* **32** (2011) 4107-4121.
[11] Thakur, V.K., Thakur, M.K. 'Processing and characterization of natural cellulose fibers/thermoset polymer composites', *Carbohyd. Polym.* **109** (2014) 102-117.
[12] Ezekiel, N., Ndazi, B., Nyahumwa, C. and Karlsson, S., 'Effect of temperature and durations of heating on coir fibers', *Ind. Crop. Prod.* **33** (2011) 638-643.
[13] Brahmakumar, M., Pavithran, C. and Pillai, R.M., 'Coconut fibre reinforced polyethylene composites: effect of natural waxy surface layer of the fibre on fibre/matrix interfacial bonding and strength of composites', *Compos. Sci Technol.* **65** (2005) 563-569.
[14] Suresh Kumar, S.M., Duraibadu, D. and Subramanian, K., 'Studies on mechanical, thermal and dynamic mechanical properties of untreated (raw) and treated coconut sheath fiber reinforced epoxy composites', *Mater. Design.* **59** (2014) 63-69.
[15] Mir, S.S., Nafsin, N., Hasan, M., Hasan, N. and Hassan, A., 'Improvement of physico-mechanical properties of coir-polypropylene biocomposites by fiber chemical treatment', *Mater. Design.* **52** (2013) 251-257.
[16] Nam, T.H., Ogihara, S., Tung, N.H. and Kobayashi, S., 'Effect of alkali treatment on interfacial and mechanical properties of coir fiber reinforced poly(butylene succinate) biodegradable composites', *Compos. Part. B.* **42** (2011) 1648-1656.
[17] Gu, K., 'Tensile behaviours of the coir fibre and related composites after NaOH treatment', *Mater. Design*', **30** (2009) 3931-3934.
[18] Abot, J.L., Song, Y., Schulz, M.J. and Shanov, V.N., 'Novel carbon nanotube array-reinforced laminated composite materials with higher interlaminar elastic properties', *Compos. Sci. Technol.* **68** (2008) 2755–2760.
[19] Chowdhury, F.H., Hosur, M.V. and Jeelani, S., 'Investigations on the thermal and flexural properties of plain weave carbon/epoxy-nanoclay composites by hand-layup technique', *J. Mater. Sci.* **42** (2007) 2690-2700.
[20] Fu, S.-Y, Feng, X.-Q., Lauke, B. and Mai, Y.-W., 'Effects of particle size, particle/matrix interface adhesion and particle loading on mechanical properties of particulate–polymer composites', *Compos. Part. B.* **39** (2008) 933-961.
[21] Silva, L.J., Panzera, T.H., Velloso, V.R., Rubio, J.C.C., Christoforo, A.L. and Scarpa, F., 'Statistical design of polymeric composites reinforced with banana fibres and silica microparticles', *J. Compos. Mater.* **47** (2012) 1199-1210.
[22] Oliveira, L.A., Santos, J.C., Panzera, T.H., Freire, R.T., Vieira, L.M.G. and Scarpa, F., 'Evaluation of Hybrid-Short-Coir-Fibre-Reinforced Composites via Full Factorial Design', *Compos. Struct.* (2018). doi.org/10.1016/j.compstruct.2018.01.088

[23] ASTM D790-15e2, Standard Test Methods for Flexural Properties of Unreinforced and Reinforced Plastics and Electrical Insulating Materials, ASTM International, West Conshohocken, PA, 2015, www.astm.org.
[24] ASTM D638-14, Standard Test Method for Tensile Properties of Plastics, ASTM International, West Conshohocken, PA, 2014, www.astm.org.
[25] ASTM D695-15, Standard Test Method for Compressive Properties of Rigid Plastics, ASTM International, West Conshohocken, PA, 2015, www.astm.org.
[26] ASTM D3039 / D3039M-14, Standard Test Method for Tensile Properties of Polymer Matrix Composite Materials, ASTM International, West Conshohocken, PA, 2014, www.astm.org.
[27] Torres, R.B., Santos, J.C., Panzera, T.H., Christoforo, A.L., Borges, P.H.R. and Scarpa, F., 'Hybrid glass fibre reinforced composites containing silica and cement microparticles based on a design of experiment', *Polym. Test.* **7** (2017) 87-93.
[28] Martuscelli, C.C., Santos, J.C., Oliveira, P.R., Panzera, T.H., Aguilar, M.T.P. and Garcia, C.T., 'Polymer-cementitious composites containing recycled rubber particles', *Constr. Build. Mater.* **170** (2018) 446-454.
[29] Mulinari, D.R., Baptista, C.A.R.P., Souza, J.V.C. and Voowald, H.J.C., 'Mechanical properties of coconut fibers reinforced polyester composites', *Procedia Eng.* **10** (2011) 2074-2079.

CORRELATIONS ON ULTRA PULSE VELOCITY AND PHYSICAL-MECHANICAL PROPERTIES OF CEMENT MORTAR CONTAINING QUARTZ AND RECYCLED-PP AGGREGATES

Kívia M. Nascimento[1,2], Túlio H. Panzera[1], Carlos E. S. da Silva[2], Paulo H. R. Borges[3], André L. dos Santos[1], Alexandre Einstein Vale[1]

(1) Centre for Innovation and Technology in Composite Materials - CIT^{e}C, Department of Mechanical Engineering, Federal University of São João del Rei - UFSJ, São João del Rei, Minas Gerais, Brazil

(2) Institute of Production and Management Engineering – IEPG, Federal University of Itajubá – UNIFEI, Itajubá, Minas Gerais, Brazil

(3) Department of Civil Engineering, Federal Centre for Technological Education of Minas Gerais – CEFET-MG, Belo Horizonte, Minas Gerais, Brazil

https://doi.org/10.21452/bccm4.2018.02.20

Abstract

The consumption of polymeric materials and their waste increases considerably throughout the world, leading to a constant concern with alternative recycling routes. Polypropylene (PP) is one of the most produced, but it is not recycled in an expressive way. A significant amount of research has been conducted to reuse discarded material into new composites, especially the cementitious ones, combining environmental, economic and technological issues. Non-destructive tests, such as ultra-pulse velocity, can be used to characterize and estimate the physical and mechanical properties of cement-based materials. This work investigates the effect of partial replacement of natural aggregates (NA) by recycled PP aggregates (PP-RPA) on pulse velocity and physical-mechanical properties of mortars and their correlations. Coarse particles of PP (at 4 -10 US-Tyler and 10 – 20 US-Tyler) provided better mechanical behaviour to composites made with fine particles (20–50 US Tyler), the latter being largely affected by the presence of pores. Ultra-pulse velocity can be used to predict the physical and mechanical properties of mortars containing PP aggregates.

Keywords: mortar, recycled plastic aggregate (RPA), polypropylene (PP), mechanical properties, ultra-pulse velocity (UPV)

1. INTRODUCTION

The reuse of solid waste has been a growing concern in today´s modern world. Several residues are disposed in the environment without proper control or treatment. A significant amount of

research in materials science has been conducted to find alternative routes for such waste, combining environmental, economic and technological issues [1–4].

In this context, there is a considerable increase in the production and consumption of polymeric materials, as well as the production of solid polymeric waste [3, 5]. This growth has occurred all over the world due to its friendly properties such as low cost, durability, strength and low density [6]. According to a survey carried out by Ferreira *et al.* [2], data from the Central Pollution Control Panel indicate that there is a consumption of about 150 million tons of polymers per year in the world, with a per capita production of 25kg/year. In addition, estimative indicates that every 10 years there is a doubling of the world production of polymer waste [2].

Among possible alternatives for the reuse of polymeric materials, an inexpensive and environmentally friendly way is their use in the production of cement products [2, 3]. The use of polymer fibres for concrete reinforcement was studied for the first time during the 90's. Subsequently, new studies have addressed the production of concrete with polymer admixtures and, more recently, with recycled plastic aggregates (RPAs) [2].

The replacement of natural aggregates (NAs) by RPAs directly affects the physical and mechanical properties of cement-based materials [3, 6–9]. A reduction in density, which is an interesting factor for some cement products, such as tiles, is obtained by the RPA inclusions, but the compressive strength and porosity are impaired. It is therefore necessary to develop experimental studies related to the incorporation of polypropylene – PP-RPA in cement products for their physical-mechanical characterisation [3, 10].

Ultra-pulse velocity is a simple, fast and inexpensive non-destructive test for the characterization of cement products. The UPV test has many advantages compared with the conventional non-destructives testing methods, because it is linked to elastic mechanical properties of the test material [11] and changes of ultrasonic pulses parameters can be used to determine the damage and defects in cement based materials [12, 13]. Some authors have developed theoretical models for the prediction of physical-mechanical properties of cementitious composites based on UPV measurements [11, 14–24].

This work investigates the effect of the partial replacement of the NAs with PP-RPA wastes on the physical-mechanical properties, such as compressive strength, ultra-pulse velocity (UPV), dynamic modulus of elasticity, bulk density, apparent porosity and water absorption, of mortars for concrete tiles. In addition, the relationships between the UPV and the physical-mechanical properties are evaluated.

2. EXPERIMENTAL

2.1. Composite preparation

The cementitious composites were fabricated with ordinary Portland Cement (OPC), quartz and polypropylene (PP) aggregates. The OPC was a Brazilian CP V ARI (ASTM Type III) sourced by Holcim®. The quartz aggregates were sourced by *Moinhos Gerais* Mining Company (Brazil). PP-RPAs were derived from the comminution of Coke® PET bottle caps. The bottle caps were initially washed in water to remove impurities and, subsequently, the polymer was granulated into small pieces using a knife mill.

The composite mix is based in an aggregate particle size distribution (PSD) used in the production of tiles. Table 1 shows the reference PSD as well as the particle size envelopes used in this study.

Table 8: Quartz particle size distribution for cementitious tiles and work setup

General particle size distribution for concrete tiles		Particle size envelope (wt%)
Sieve US-Tyler – (mm)	Retained (%)	
4 US-Tyler – (5mm)	0	4-10 US-Tyler (15wt%)
5 US- Tyler – (4 mm)	5	
7 US- Tyler – (2.8 mm)	11.4	
9 US- Tyler – (2 mm)	15.89	10-20 US-Tyler (40wt%)
16 US- Tyler – (1 mm)	27.08	
32 US- Tyler – (0.500 mm)	28.44	20-50 US-Tyler (30wt%)
60 US- Tyler – (0.250 mm)	10.91	50-100 US-Tyler (15wt%)
115 US- Tyler – (0.125 mm)	1.28	

Six different batches were prepared, including one reference batch and five batches containing PP-RPA as a partial replacement for the NAs, corresponding to the experimental treatments (C1 to C6) shown in Table 2. Four samples for each experimental condition were fabricated, in a total of 24 specimens.

Table 9: Experimental Treatments

Experimental Treatments	NA/RPA replacement particle size (amount)
C1-ref	---
C2-15	4-10 US-Tyler (15wt%)
C3-30	20-50 US-Tyler (30wt%)
C4-40	10-20 US-Tyler (40wt%)
C5-55	4-20 US-Tyler (55wt%)
C6-85	4-50 US-Tyler (85wt%)

A water/cement ratio (w/c) of 0.42 and an aggregate/cement (a/c) ratio of 3.75 were maintained constant for all composites. The w/c chosen in this study was sufficient to permit full hydration of the cement, as well as adequate compaction of the samples. A Marshall Hammer was used to produce the cylindrical specimens in order to reproduce the level of compaction of extruded concrete products in the laboratory (Figure 1). A constant volume and 6 hammed-blows were considered for each sample, resulting in cylinders with approximately 50 mm in height and 54.5 mm in diameter. The cylinders were demoulded immediately after the compaction. The samples were kept in a closed container for 28 days at room temperature for curing. The response variables investigated were the ultra-pulse velocity, bulk density, apparent density, apparent porosity and compressive strength.

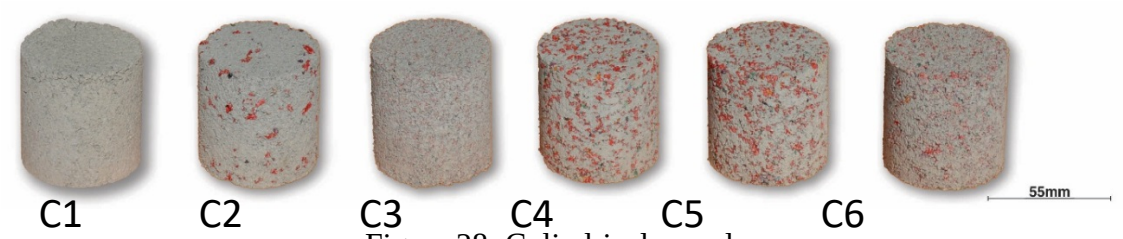

Figure 28: Cylindrical samples

2.2. Bulk density

The bulk density (ρ) of the composites was calculated by dividing the dry mass of the samples after 28 days of curing (m_1) by its volume (V). The bulk density and volume were calculated using the equations (1) and (2), respectively, where D is the diameter and L is the length of the sample:

$$\rho = \frac{m_1}{V} \quad (1)$$

$$V = \frac{\pi D^2}{4} \times L \quad (2)$$

2.3. Ultra-pulse velocity and dynamic modulus of elasticity

A pulse of longitudinal vibrations is produced by an electro-acoustic transducer which is held in contact with one surface of the concrete sample under test [25]. After traversing a known path length L in the concrete, the pulse of vibrations is converted into an electrical signal by a second transducer. Electronic timing circuits enable the measurement of the transit time T of the pulse to be measured. The ultrasonic measurement is conducted using a portable ultrasonic non-destructive digital indicating tester (Pundit Plus) with a 150 kHz transducer. The pulse velocity (in m/s) is given by equation (3):

$$v = \frac{L}{T} \quad (3)$$

The dynamic modulus of elasticity (E_d) is a measure that express the relationship between pulse velocity and elastic constants [25]. The dynamic modulus of elasticity is given by equation (4).

$$E_d = Bv^2 \frac{(1+\mu)(1-2\mu)}{(1-\mu)} \quad (4)$$

where μ is the dynamic Poisson's ratio which value for concrete varies generally in the range of 0.15-0.22 [26]. In this work the Poisson´s Ratio was considered at 0.15 which is recommended for mortars [27].

2.4. Apparent porosity

The apparent porosity (p) represents a percentage or fraction of the void spaces in a material, varying from 0 to 100% or 0 to 1. The apparent porosity was calculated according to British Standard 10545-3 [28]. The samples were weighted after 28 days of curing and the dry mass (m_1) was recorded. Subsequently, the samples were saturated with water under vacuum and the saturated mass (m_2) and the suspended saturated mass (m_3) were measured. The apparent porosity was calculated using the equation (5).

$$p = \frac{m_2 - m_1}{m_2 - m_3} \quad (5)$$

2.5. Water Absorption

The water absorption (E) is the percentage of water absorbed by the sample after being immersed in water under vacuum, as described for the determination of the apparent porosity, following the BS 10545-3 [28]. The equation (6) was used to calculate the water absorption.

$$E = \frac{m_2 - m_1}{m_1} \times 100 \quad (6)$$

2.6. Compressive strength

The British Standard 12390-3 [29] was used to measure the compressive strength of the samples. The compressive strength can be determined by dividing the maximum force applied to the sample (F_{max}) by its initial area (A_0), according to the equation (7).

$$f_c = \frac{F_{max}}{A_0} \quad (7)$$

The compression tests were carried out at 1mm/min using a AG-X Plus SHIMADZU testing machine equipped with a load cell of 100 kN.

3. RESULTS

Table 3 summarizes the mean and standard deviation of the investigated properties. It is noteworthy that the investigated factor depends on particle size and amount levels. In general, the physical-mechanical properties are substantially affected by the PP-replacement levels.

In general, the porosity and water absorption increased while the UPV, bulk density compressive strength and dynamic modulus decreased when a large amount of PP particles was incorporated as quartz replacement. It is noteworthy, C3 composite made with 30wt% of PP at 20-50US-Tyler particle range achieved lower elastic properties than C4 and C5 composites made with 40wt% and 55wt% of PP particles, respectively. This behaviour can be attributed to the presence of fine PP particles, with larger surface area, in C3 composites, affecting the packing of particles of the system.

Table 10: Experimental Results

Setup	Pulse Velocity (m/s)	Bulk Density (g/cm^3)	Apparent Porosity (%)	Water Absorption (%)	Compressive Strength (MPa)	Dynamic Modulus (GPa)
C1-ref	4182.78±252.34	2.11±0.07	7.04±2.41	3.25±1.23	29.87±6.60	42.77±6.34
C2-15	3670.20±168.92	1.94±0.07	8.91±2.67	4.47±1.49	20.76±5.71	30.21±3.74
C3-30	2800.71±124.81	1.66±0.05	14.01±1.20	8.09±0.84	7.88±1.52	15.04±1.74
C4-40	2666.40±120.05	1.66±0.06	11.35±2.09	6.63±1.43	11.84±2.26	13.58±1.61
C5-55	2385.62±117.58	1.52±0.02	11.38±1.78	7.22±1.27	8.64±2.00	9.99±0.99
C6-85	1872.84±179.61	1.22±0.12	14.12±1.74	11.54±1.72	5.16±1.14	4.92±0.670

Backscattering electron images were obtained at 30× (Figure 2) and 100× (Figure 3) of magnification to verify the microstructure of the composites and analyse the interface between the PP-RPA and the cement matrix. Higher NA/PP-RPA replacement led to increased amount of pores. Besides, larger pore sizes were observed when fine PP particles were incorporated, as revealed by C3 composites (Figure 3c). Fine low-density particles contribute to increase the volume of PP particles in the system, consequently, affecting the porosity and the elastic properties. The interfacial transition zone (ITZ) between the PP particles and cement was more porous when fine particles were used (Figure 3c), in contrast to coarse PP particles (Fig. 3a,b).

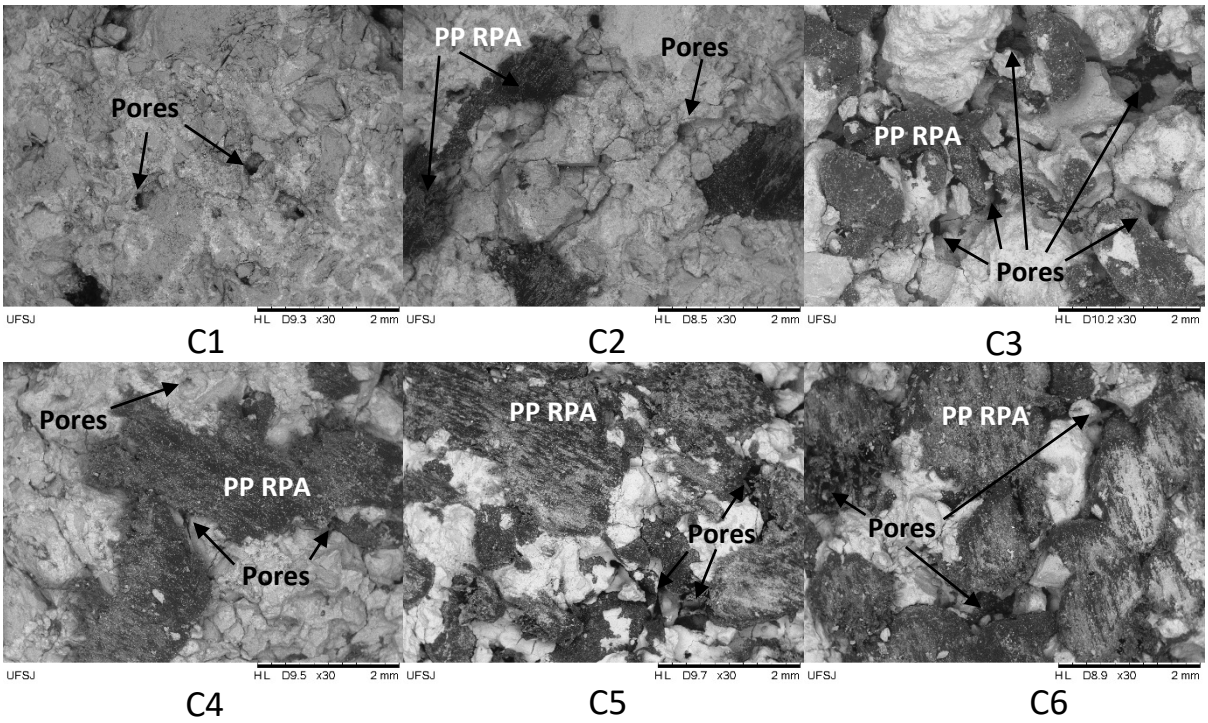

Figure 29: Backscattering electron images of the experimental treatments

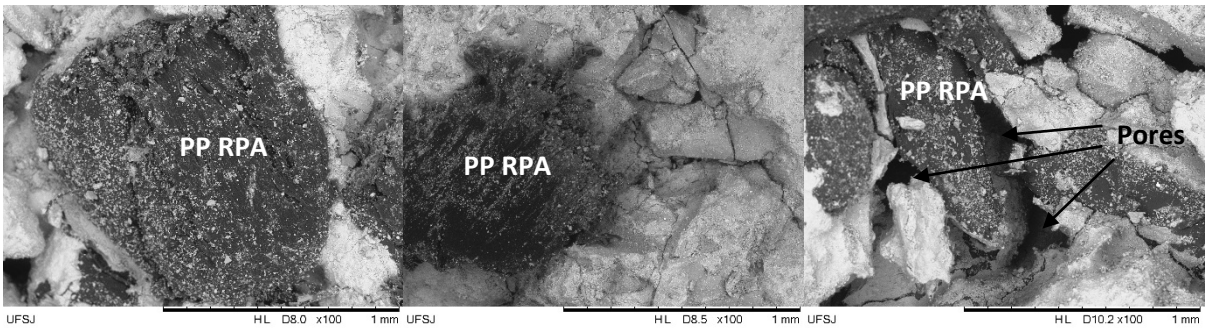

4-10 US-Tyler (a) 10-20 US-Tyler (b) 20-50 US-Tyler (c)

Figure 30: PP-RPA and matrix phase interface evaluation

1. 3.1. Statistical Analysis

The software Minitab17® was used to perform all the statistical analysis. A correlation analysis of the responses variables is shown in Table 4. The first and second rows for each response exhibit the Person Correlation (PC) and the P-value, respectively.

Table 11: Correlation Analysis

		Pulse Velocity	Bulk Density	Apparent Porosity	Water Absorption	Compressive Strength
Bulk Density	PC	0.960				
	P-value	0.000				
Apparent Porosity	PC	-0.794	-0.790			
	P-value	0.000	0.000			
Water Absorption	PC	-0.889	-0.926	0.921		
	P-value	0.000	0.000	0.000		
Compressive Strength	PC	0.929	0.899	-0.914	-0.884	
	P-value	0.000	0.000	0.000	0.000	
Dynamic Modulus of Elasticity	PC	0.983	0.938	-0.820	-0.859	0.966
	P-value	0.000	0.000	0.000	0.000	0.00

The PC ranges from -1 to 1, and the further away from 0, the greater the correlation between the variables. A significant correlation occurs when the P-value is less than or equal to 0.05, considering a confidence level of 95% (α=0.05). As shown in Table 5, the correlations between the analysed variables are significant (P-value < 0.05) and strong (PC > 0.600). Based on response correlations, a multivariate analysis of variance (MANOVA) [30] was performed and presented in Table 5. The MANOVA tests the equality of several means at the same time using the covariance structure among the variables, unlike the ANOVA that tests one by one. When the analysed variables are correlated, the MANOVA design is able to detect a smaller mean variation compared to ANOVAs. As successive ANOVAs are performed, the chances of incorrectly rejecting the null hypothesis increase, which does not occur in MANOVA, since the means are tested at the same time, maintaining the error at the alpha level. Significant effect factors are indicated by MANOVA when the P-value is lower than 0.05. Each treatment can be considered a specific composite and its physical-mechanical properties are affected by the size of the NA / RPA replacement particles.

Table 12: ANOVA and MANOVA

		P-value	R^2 (adj.) (%)
ANOVA	Pulse velocity	0.000	95.69
	Bulk Density	0.000	94.18
	Apparent Porosity	0.000	58.56
	Water absorption	0.000	79.03
	Compressive Strength	0.000	83.39
	Dynamic Modulus of Elasticity	0.000	94.46
MANOVA	Wilks' Test	0.000	

A Regression Analysis was performed to model a relationship between the responses (Figure 4). Table 6 shows the equations and the adjustments of the generated models (R^2).

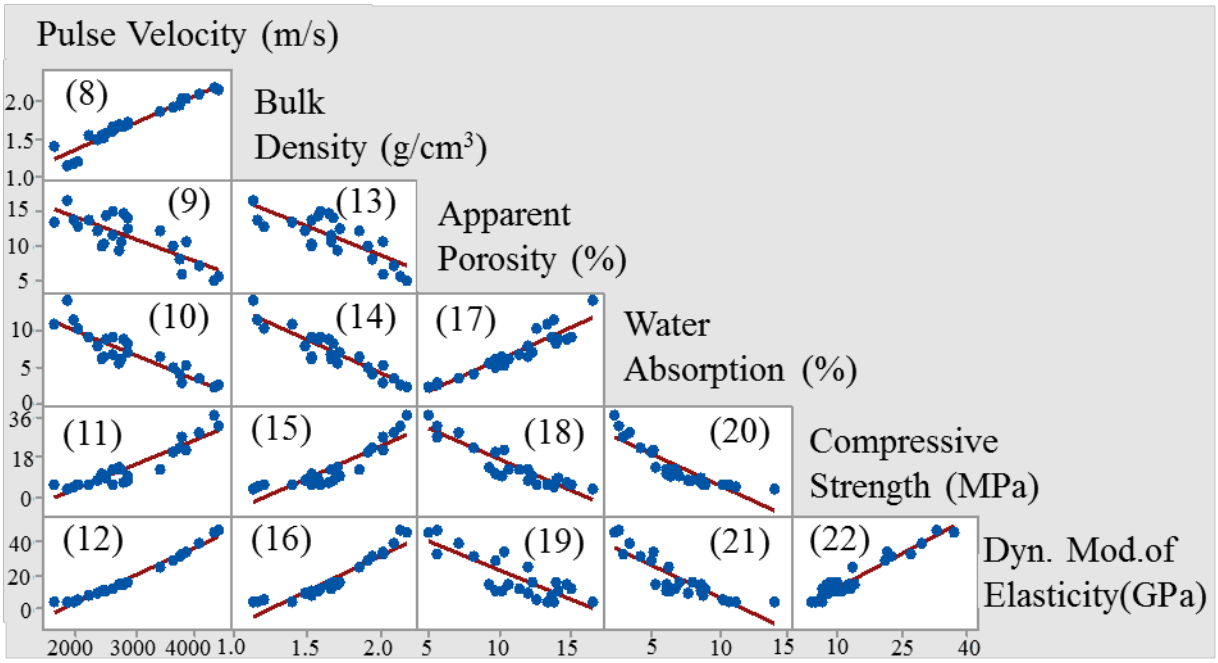

Figure 31: Correlation between the response variable

Table 13: Regression analysis

		Model	R^2 (%)
(8)	$B(v)$	$B = 0.6469 + 0.000355v$	91.74
(9)	$p(v)$	$p = 20.28 - 0.003120v$	61.40
(10)	$E(v)$	$E = 16.45 - 0.003272v$	78.08
(11)	$f_c(v)$	$f_c = -17.85 + 0{,}010879v$	85.75
(12)	$E_d(v)$	$E_d = -29.05 + 0.016544v$	96.55
(13)	$p(B)$	$p = 25.29 - 8.39B$	60.73
(14)	$E(B)$	$E = 22.41 - 9.210B$	85.08
(15)	$f_c(B)$	$f_c = -33.94 + 28.43B$	79.87
(16)	$E_d(B)$	$E_d = -52.55 + 42.66B$	87.47
(17)	$E(p)$	$E = -2.734 + 0.8624p$	84.05
(18)	$f_c(p)$	$f_c = 44.36 - 2.724p$	82.84
(19)	$E_d(p)$	$E_d = 58.51 - 3.511p$	65.74
(20)	$f_c(E)$	$f_c = 33.33 - 2.810E$	77.08
(21)	$E_d(E)$	$E_d = 46.39 - 3.927E$	72.60
(22)	$E_d(f_c)$	$E_d = -0.04 + 1.3878f_c$	92.95

A linear relation was identified among the variables. Based on the regression analysis, satisfactory adjustments of the models were evidenced, except for (9), (13) and (19), which exhibited R^2 values close to 60%. This fact can be attributed to the porosity (p) response variable involved, which is determined using three measures of dry mass (m_1), saturated mass (m_2) and suspended saturated mass (m_3). Suspended saturated mass measurements should be further affected because the PP particle density is lower than the water density. The water absorption response (E) is similar to the porosity, however its models have an adequate adjustment. The

calculation of water absorption does not consider m_3, which evidences the effect of the suspended mass previously commented.

As most models showed high R^2, it is possible to reliably estimate the physical-mechanical properties based on these models. It is worth mentioning that the models involving UPV (see Table 6 (8-12)) can be extremely useful, since they are obtained by means of a non-destructive test, being possible to estimate the other properties, impacting the cost, ease and speed of the characterization [14].

4. CONCLUSIONS

This paper investigated the effect of the partial replacement of NAs with PP-RPAs wastes on the physical-mechanical properties of sustainable mortar for tiles and the relationship between the ultra pulse velocity and the other responses. The conclusions are described as follows:

(a) MANOVA indicated that the NA/RPA replacement particle size affects the physical-mechanical properties of the mortars. In general, this replacement has a negative effect on pulse velocity, porosity, water absorption, compressive strength and dynamic modulus, however it reduces the bulk density, which is an interesting behaviour for concrete tiles.

(b) Coarse particles of PP (at 4 -10 US-Tyler and 10 – 20 US-Tyler) provided better mechanical behaviour to composites made with fine particles (20–50 US Tyler); the latter is largely affected by the presence of pores, especially in the interfacial transition zone and the packaging of the particles in the system.

(c) Good correlations were obtained between the response variables studied - pulse velocity, bulk density, apparent porosity, water porosity, compressive strength and dynamic modulus of elasticity - being possible to estimate the properties through a non-destructive parameter, like ultra-pulse velocity. The equations are related to the materials studied in this work, however, similar equations can be developed for other precast concrete materials.

ACKNOWLEDGEMENTS

The authors would like to thank CAPES, CNPq and FAPEMIG for the financial support provided.

REFERENCES

[1] S. Yang, X. Yue, X. Liu, and Y. Tong, “Properties of self-compacting lightweight concrete containing recycled plastic particles,” *Constr. Build. Mater.*, vol. 84, no. June, pp. 444–453, 2015.

[2] L. Ferreira, J. De Brito, and N. Saikia, “Influence of curing conditions on the mechanical performance of concrete containing recycled plastic aggregate,” *Constr. Build. Mater.*, vol. 36, pp. 196–204, 2012.

[3] T. Ozbakkaloglu, L. Gu, and A. Gholampour, “Short-Term Mechanical Properties of Concrete Containing Recycled Polypropylene Coarse Aggregates under Ambient and Elevated Temperature,” vol. 2013, no. Ceresana 2014, pp. 1–10, 2017.

[4] I. H. Alfahdawi, S. A. Osman, R. Hamid, and A. I. Al-Hadithi, “Utilizing waste plastic polypropylene and polyethylene terephthalate as alternative aggregates to produce lightweight concrete: A review,” *J. Eng. Sci. Technol.*, vol. 11, no. 8, pp. 1165–1173, 2016.

[5] M. Gürü, M. K. Çubuk, D. Arslan, S. A. Farzanian, and I. Bilici, “An approach to the usage of polyethylene terephthalate (PET) waste as roadway pavement material,” *J. Hazard. Mater.*, vol.

279, pp. 302–310, 2014.
[6] J. O. Akinyele, R. W. Salim, and G. Oyeti, "Use of Recycled Polypropylene Grains as Partial Replacement of Fine Aggregate in Reinforced Concrete Beams," *Eng. Struct. Technol.*, vol. 6, no. 4, pp. 184–190, 2014.
[7] N. Saikia and J. De Brito, "Use of plastic waste as aggregate in cement mortar and concrete preparation: A review," *Constr. Build. Mater.*, vol. 34, pp. 385–401, 2012.
[8] L. Gu and T. Ozbakkaloglu, "Use of recycled plastics in concrete: A critical review," *Waste Manag.*, vol. 51, pp. 19–42, 2016.
[9] R. Sharma and P. P. Bansal, "Use of different forms of waste plastic in concrete - A review," *J. Clean. Prod.*, vol. 112, pp. 473–482, 2016.
[10] S. Gavela *et al.*, "A study of concretes containig thermoplastic wastes as aggregates," *Gavela Stamatia*, no. 1, pp. 0–8, 2004.
[11] J. S. Popovics and K. V. L. Subramaniam, "Review of Ultrasonic Wave Reflection Applied to Early-Age Concrete and Cementitious Materials," *J. Nondestruct. Eval.*, vol. 34, no. 1, 2015.
[12] Y. Li, C. E. Sui, and Q. J. Ding, "Study on the cracking process of cement-based materials by AC impedance method and ultrasonic method," *J. Nondestruct. Eval.*, vol. 31, no. 3, pp. 284–291, 2012.
[13] D. Bui, S. A. Kodjo, P. Rivard, and B. Fournier, "Evaluation of concrete distributed cracks by ultrasonic travel time shift under an external mechanical perturbation: Study of indirect and semi-direct transmission configurations," *J. Nondestruct. Eval.*, vol. 32, no. 1, pp. 25–36, 2013.
[14] T. Panzera, A. Christoforo, and F. Cota, "Ultrasonic Pulse Velocity Evaluation of Cementitious Materials," in *Advances in Composite Materials - Analysis of Natural and Man-Made Materials*, no. September, 2011, pp. 411–436.
[15] S. K. Rao, P. Sravana, and T. C. Rao, "Experimental studies in Ultrasonic Pulse Velocity of roller compacted concrete pavement containing fly ash and M-sand Studies in Ultrasonic Pulse Velocity of Roller compacted concrete pavement," *Int. J. Pavement Res. Technol.*, vol. 9, pp. 289–301, 2016.
[16] J. Bogas, M. Gomes, and A. Gomes, "Compressive strength evaluation of structural lightweight concrete by non-destructive ultrasonic pulse velocity method," *Ultrasonics*, vol. 53, no. 5, pp. 962–972, 2013.
[17] C. C. Wang and H. Y. Wang, "Assessment of the compressive strength of recycled waste LCD glass concrete using the ultrasonic pulse velocity," *Constr. Build. Mater.*, vol. 137, pp. 345–353, 2017.
[18] K. Rashid and R. Waqas, "Compressive strength evaluation by non-destructive techniques: An automated approach in construction industry," *J. Build. Eng.*, vol. 12, no. May, pp. 147–154, 2017.
[19] T. Gehlot, D. S. S. Sankhla, D. S. S. Gehlot, and A. Gupta, "Study of Concrete Quality Assessment of Structural Elements Using Ultrasonic Pulse Velocity Test," *IOSR J. Mech. Civ. Eng.*, vol. 13, no. 5, pp. 15–22, 2016.
[20] C. Kurtulus and A. Bozkurt, "Determination of concrete compressive strength of the structures in Istanbul and Izmit Cities (Turkey) by combination of destructive and non-destructive methods," *Int. J. Phys. Sci.*, vol. 6, no. 16, pp. 3929–3932, 2011.
[21] R. Pucinotti, "Reinforced concrete structure: Non destructive in situ strength assessment of concrete," *Constr. Build. Mater.*, vol. 75, pp. 331–341, 2015.
[22] A. Sadrmomtazi and R. Z. Zanoosh, "Properties of Cement Composite Containing Waste Tire Rubber,Silica Fume and Polypropylene Fiber," *Sustain. Constr. Mater. Comput. Eng.*, vol. 346, pp. 12–17, 2012.
[23] T. H. Panzera, P. H. R. Borges, A. L. R. Sabariz, and F. P. Cota, "Recycled glass as potential aggregate for concrete tiles: a statistical analysis of the physical and engineering properties," *Int. J. Environ. Waste Manag.*, vol. 12, no. 3, p. 280, 2013.
[24] K. Ali-Benyahia, Z. M. Sbartaï, D. Breysse, S. Kenai, and M. Ghrici, "Analysis of the single and combined non-destructive test approaches for on-site concrete strength assessment: General statements based on a real case-study," *Case Stud. Constr. Mater.*, vol. 6, pp. 109–119, 2017.
[25] British Standards Institution BSI, "BS 1881: Part 203: 1986: Measurement of Velocity of Ultrasonic Pulses in Concrete," 1986.

[26] A. M. Neville, *Properties of Concrete*, 5th editio. London, England, 2011.
[27] A. M. Neville, *Properties of Concrete*. 2011.
[28] British Standards Institution BSI, "BS EN ISO 10545: Ceramic Tiles - Part 3: Determination of water absorption, apparent porosity, apparent relative density and bulk density," *Br. Stand.*, 1997.
[29] British Standards Institution BSI, "BS EN 12390: Testing hardened concrete - Part 3: Compressive strength of test specimens," *Br. Stand.*, 2009.
[30] D. W. Johnson, R. A, Wichern, *Applied Multivariate Statistical Anayisis*, 6th editio. Pearson Prentice Hall, 2007.

EFFECT OF RICE HUSK ASH INCORPORATION IN STEEL FIBER REINFORCED CONCRETES

Felipe S. B. Jorge (1) and Conrado S. Rodrigues (1)

(1) Department of Civil Engineering, Centro Federal de Educação Tecnológica de Minas Gerais, Brazil

https://doi.org/10.21452/bccm4.2018.02.21

Abstract

Steel fiber reinforcement aims to improve composites properties regarding to crack propagation. It is known that concrete has high compressive strength and durability, but its toughness is low, being considered a fragile material. The role of the fibers as a toughening strategy depends on several factors, including bond strength between the fiber and matrix. RHA has a high content of amorphous silica, which gives it high pozzolanic activity. This RHA characteristic may lead to the formation of new hydration products, especially C-S-H, giving a higher density to the cement matrix; thus, enhancing the bonding between fibers and the cementitious matrix. This research aims to evaluate if a highly reactive RHA incorporated as mineral admixture in steel fiber reinforced concrete improves its toughness. Concrete samples were produced with fiber volume fractions of 0.5, 0.75 and 1.0%. To investigate the RHA effect, the same reinforcement rates were used in concretes in which cement was partially replaced by 15% RHA. Four points bending tests were carried out in a servo controlled universal testing machine, with being controlled by the displacement transducer. The results indicate that RHA composites presented slightly higher values of toughness and residual stress than those without the mineral admixture. Therefore, RHA can be considered as viable approach to enhance fiber-matrix interactions and making the reinforcement more effective when in considering the whole composite behaviour.

Keywords: Rice Husk Ash; Flexural test, Steel Fiber

1. INTRODUCTION

The main approach to improve concrete performance regarding toughness is the incorporation of fibers to the matrix, which act as a stress bridge, promoting higher resistance to crack propagation. The fiber acts by transmitting the stresses from one side of fissure to the other, avoiding stress concentration and early material failure [1]; [2].

Steel fiber reinforced concretes can be produced using the same procedure adopted to make conventional concrete, with adaptations to promote homogeneity. Particular attention should be

given to the uniform dispersion of the fiber along the concrete mix in order to achieve performance improvements in concrete mechanical properties, also considering the workability required for a suitable mix, release and finishing of this composite. Even with the use of superplasticizers, this percentage of incorporation remains around 2% when adopting conventional concrete mixing practices [3]. To Johnston [4], this percentage is between 0.25 and 1.0% by volume.

Many factors influence the properties of fiber-reinforced concrete, mainly: the type and size of the fiber; their constituent material and aspect ratio; incorporated fiber volume and the quality of the cementitious matrix (characterized by interfacial transition zone between composite phases). All these variables influence the fiber / matrix adhesion stress, which is the property that will promote toughness to fiber reinforced concrete [3]; [5].

The interaction between the concrete matrix and fibers is one of the main challenges for reinforced concrete research. The region known as Interfacial Transition Zone (ITZ) is responsible for the adhesion between the materials. As this region becomes denser, the interaction becomes better and consequently increases composite strength [6].

Pozzolanic activity of materials consisting of large amounts of silica, such as rice husk ash (RHA), is of great importance to promote a more complete cement hydration, making the matrix denser and less subject to degradation by external agents. In the case of steel fiber reinforced concrete, it increases the adhesion strength between the materials [7]. In addition, because they have particles smaller than cement, they allow a better compaction of the cement paste [8].

The research objective was to evaluate the effect of cement substitution by RHA, aiming to densify the cement matrix to the point where the adhesion stress with the steel fiber was higher than in the conventional mixture. For this, control specimens and specimens with 15% of cement replaced by RHA were produced. In addition, steel fiber incorporation was evaluated in percentages of 0.5, 0.75 and 1.0% by volume. Using the four-point flexural test, it was possible to measure the toughness of each formulation. The results indicate an increase in toughness in comparisons with and without the addition of RHA, besides a gain of load capacity in the post-cracking phase.

2. MATERIALS AND METHODS

2.1 Materials

The materials used in this research were cement, sand, gravel # 0, steel fiber, water, superplasticizer and rice husk ash. The cement used was the Portland High Initial Strength Cement (CPV-ARI) from Holcim. Because it is a purer cement, it is ideal to evaluate the efficiency of RHA incorporation and its pozzolanic activity in the composite. The sand used was average river sand, with fineness modulus of 1.65 and maximum characteristic size of 1.2mm. Coarse aggregate was grade # 0 of gneiss with 12.5mm for maximum dimension and 1.11 fineness modulus. Industrialized highly reactive RHA presenting 92% of amorphous silica, average diameter of 7.7 μm, density and its specific surface area (S_{BET}) of, respectively, 2161 Kg/m^3 and 21150 m^2/Kg. As superplasticizer, Fluxer RMX 7000 from ERCA was used.

The steel fibers adopted in this research were DRAMIX type 80/60BG fibers manufactured by Belgo Bekaert in accordance with ASTM [9]. It is a smooth fiber with hooks. The fiber characterization is described in Table 1.

Table 1 – Steel fiber characterization

Steel fiber Dramix 80/60BG - Belgo Bekaert	
Type of fiber	SF01
Diameter (mm)	0,75
Length (mm)	60
Tensile strength (N/mm²)	1.100
Max. load (N)	485
Aspect ratio (l/d)	80

Source: Belgo Bekaert

2.2 Methods

Table 2 shows the proposed formulations. In all formulations, the amounts of the following materials were maintained: water/binder factor, sand, gravel and superplasticizer. The percentages of 0.5, 0.75 and 1.0% by volume of concrete were adopted as variables for the incorporated fiber volume. The formulations were also adopted without the addition of RHA and with the replacement of 15% of cement by RHA.

Table 2 – Quantitative materials for each formulation

Materials for 1m³ of concrete	Formulations						
	CPFL_00_0	CPFL_00_0.5	CPFL_00_0.75	CPFL_00_1.0	CPFL_15_0.5	CPFL_15_0.75	CPFL_15_1.0
Cement (Kg)	409,84	409,84	409,84	409,84	348,36	348,36	348,36
RHA (Kg)	0	0	0	0	61,48	61,48	61,48
Sand (Kg)	568,85	568,85	568,85	568,85	568,85	568,85	568,85
Grain #0 (Kg)	1292,62	1292,62	1292,62	1292,62	1292,62	1292,62	1292,62
Water (Kg)	179,51	179,51	179,51	179,51	179,51	179,51	179,51
Water / Cement factor	0,44	0,44	0,44	0,44	0,44	0,44	0,44
Steel fiber (Kg)	0	39,25	58,88	78,50	39,25	58,88	78,50
Superplasticizer (Kg)	2,61	2,61	2,61	2,61	2,61	2,61	2,61

Samples

Three prismatic specimens were produced for each proposed formulation, with 21 samples in total. Samples were produced in the dimensions of 100x100x350mm, according to the American standard ASTM [10] for flexural tests.

A conventional 200 litres mixer was used for the concrete production. The total mixing time was 10 minutes. The moulds were filled in two layers that were compacted using a metal rod with 75 strokes. Samples were removed from the moulds after 48hs and the curing method was by immersion in water saturated with calcium hydroxide for a minimum 28 days in order to protect the steel fiber from corrosion. After the curing period, the specimens were tested for flexural strength

Four-point flexural test

Four-point flexural tests followed the requirements of ASTM [10]. According to the norm mentioned, the toughness value obtained in the four point bending test is given by the area under the load X deflection curve up to limit of L/150. L corresponds to the span length (300mm). The test machine used has a MTS servo-hydraulic actuator with load capacity equal to 100KN, mounted under a rigid gantry with a vertical displacement controller monitored by an LVDT device with a measuring capacity of 4mm. The LVDT device HBM 20mm was attached to each sample using a Yoke type apparatus, shown in Picture1.

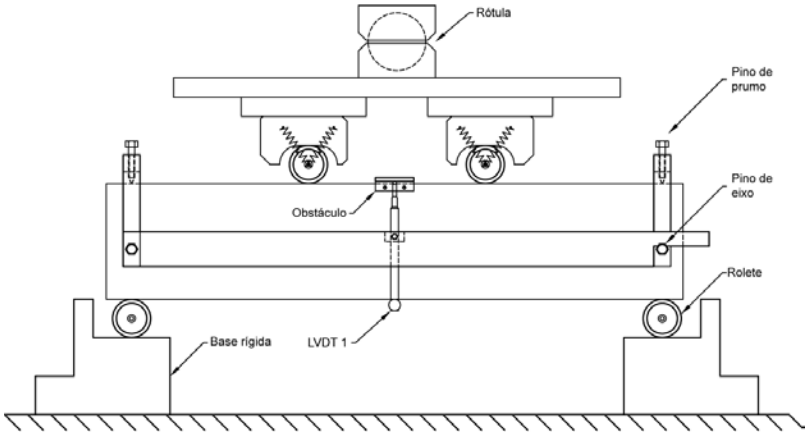

Picture 1 – Mounting detail for four-point flexural test [11]

The test parameter used an actuator displacement rate of 0.1mm/min, with data acquisition frequency of 5Hz. The deflection measured by the LVDT was used as the control of the test, being limited to 2mm (equivalent to L/150, as prescribed by the reference standard). The base of the gantry was aligned, followed by the positioning of the support rollers and the adjustment of the wheelbase. Support rollers were 300mm apart and 25mm from the ends of the samples. Load application rollers, in turn, were 100mm apart, placed in the middle third of the samples. In order to measure deflection during the test, a Yoke support device and the obstacle plate for data acquisition via LVDT were installed in each sample. Finally, the LVDT was connected to the QuantumX MX440B HBM data acquisition device (Picture 2).

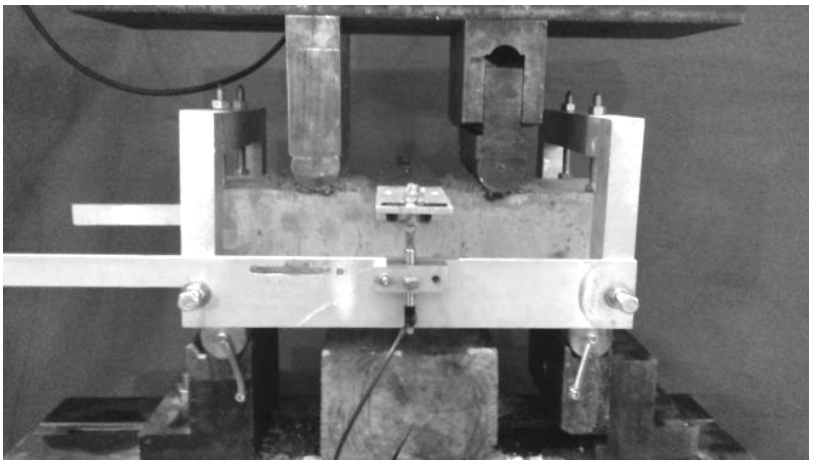

Picture 2 – Sample detail prepared for testing with LVDT device and Yoke support

3. RESULTS

The average results obtained in each of the seven series tested under flexion are in Table 3.

Table 3 – Flexural test results

Four-point flexural test results												
Formulations	cure	δp1	Cp1	*f*p1	δL/600	CL/600	*f*L/600	δL/150	CL/150	*fL/150*	T	dev. T
	(days)	(mm)	(KN)	(MPa)	(mm)	(KN)	(MPa)	(mm)	(KN)	(MPa)	(KN.mm)	(KN.mm)
CPFL_00_0	65	0,040	21,03	6,31	0,50	0,69	0,21	2,00	-	-	2,32	0,36
CPFL_00_0.5	36	0,043	26,92	8,08	0,50	16,86	5,06	2,00	14,73	4,42	33,05	3,88
CPFL_00_0.75	42	0,042	24,47	7,34	0,50	21,90	6,57	2,00	21,08	6,32	32,52	12,18
CPFL_00_1.0	44	0,067	28,02	8,41	0,50	33,56	10,07	2,00	27,02	8,11	60,53	3,28
CPFL_15_0.5	63	0,047	25,81	7,74	0,50	19,21	5,76	2,00	15,62	4,69	36,70	13,30
CPFL_15_0.75	50	0,042	28,26	8,48	0,50	22,91	6,87	2,00	22,08	6,62	45,82	7,32
CPFL_15_1.0	61	0,044	29,58	8,87	0,50	35,14	10,54	2,00	34,71	10,41	75,13	10,94

Where,

δp1 = deflection at peak load, or first cracking;
Cp1 = peak at the point of first cracking;
fp1 = tension in first crack;
δL/600 = deflection at point L/600 (0,5mm);
CL/600 = load at point L/600 (0.5mm);
fL/600 = tension at point L/600 (0.5mm);
δL/150 = deflection at point L/150 (2.0mm);
CL/150 = load at point L/150 (2.0mm);
fL/150 = tension at point L/150 (2.0mm);
T = toughness (by area under load X deflection curve);
dev. T = standard deviation for toughness calculation.

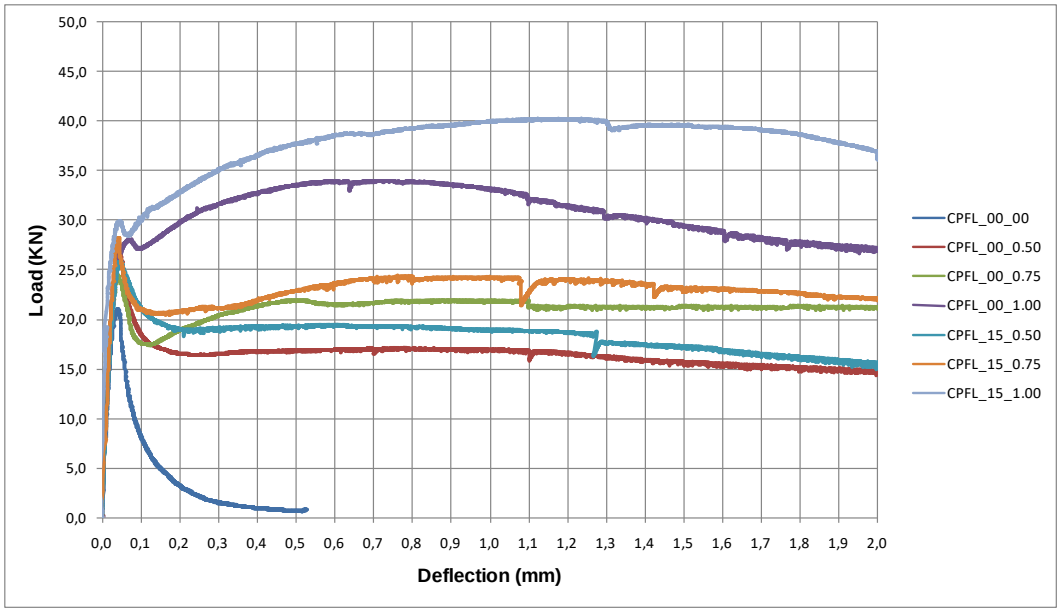

Picture 3 – Load X deflections graph

Regarding the post-cracking residual strength (Picture 3), the graph shows the strain-hardening behaviour for 1.0% fiber formulations. In formulations with 0.5 and 0.75% of fiber, the analysed behaviour is strain-softening.

According to Picture 4, formulations with 0.50% addition of steel fibers presented a toughness gain of 11%, comparing the propositions with and without RHA. In formulations with 0.75% addition, the gain was of 41%, and for the additions of 1.00%, an increase of 24.1% was observed.

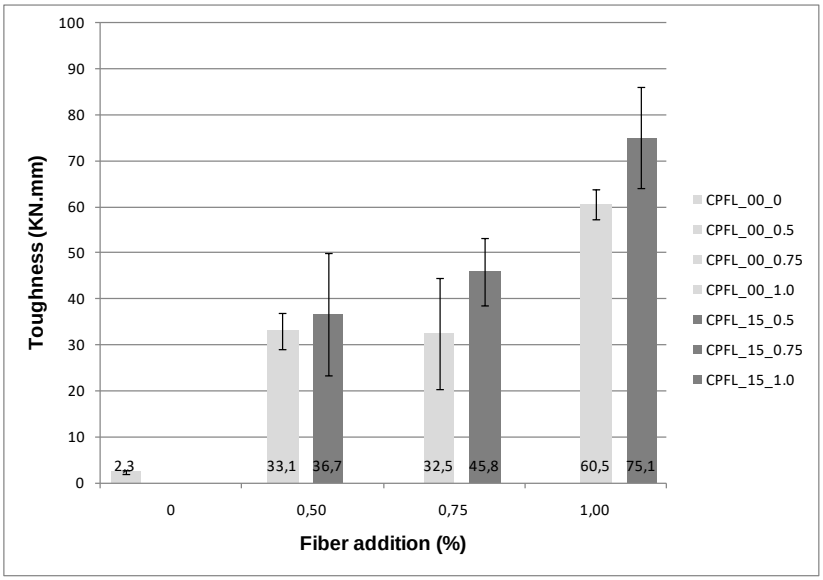

Picture 4 – Comparison of toughness between formulations

4. CONCLUSIONS

- For formulations with 0.5 and 0.75% of fibers, the post-cracking behaviour was strain-softening, which means there was little contribution of the residual strength for the load capacity.
- In composites with 1.0% of fibers, the profile of strain-hardening was observed with load peaks in the residual phase being higher than the first peaks. In flexure tests, it was also possible to verify that cracks always appeared in the intermediate region of the samples, which is a pure flexion zone;
- With regard to composites toughness, the increase in this characteristic becomes evident as the percentage of the addition rises. With the propositions studied, it was not possible to establish the limit of fiber addition that corresponds to maximum gain of toughness. Therefore, there is a need for complementary studies;
- The use of RHA in partial replacement of cement as a measure of densification of ITZ and consequently improvement of adhesion between materials showed promising results. Four-point flexural strength tests showed significant increases in toughness (in order of 24% for 1.0% fiber formulations). Therefore, it is correct to assert that, in general, RHA contributes for the increase in steel fiber reinforced concrete properties;

ACKNOWLEDGEMENTS

These results are part of a project involving PUC-Rio, CEFET-MG and Belgo Bekaert Arames S.A. The project is being financed by FAPERJ and FAPEMIG.

REFERENCES

[1] BRAZ, M. C. A.; NASCIMENTO, F. B. C. Concreto reforçado com fibras de aço. Ciências exatas e tecnológicas, v. 3, n. 1, p. 43-56, 2014. ISSN 2357-9919.
[2] BREITENBUCHER, R.; MESCHKE, G.; SONG, F.; ZHAN, Y. Experimental, analytical and numerical analysis of the pullout behaviour of steel fibres considering different fibre types, inclinations and concrete strengths. Structural Concrete, v. 15, n. 2, p. 126-135, 2014. DOI 10.1002/suco.201300058.
[3] BENTUR, A.; MINDESS, S. Fibre reinforced cementitious composites. 2. New York: Taylor & Francis Group, 2007. ISBN 978-0-415-25048-1.
[4] JOHNSTON, C. D. Fiber-reinforced cements and concretes. New York: Taylor & Francis Group, 2001. ISBN 90-5699-694-0.
[5] RANA, A. Some Studies on Steel Fiber Reinforced Concrete. International Journal of Emerging Technology and Advanced Engineering, v. 3, n. 1, p. 120-127, 2013. ISSN 2250-2459.
[6] LIAO, K. Y.; CHANG, P. K.; PENG, Y. N.; YANG, C. C. A study on characteristics of interfacial transition zone in concrete. Cement and Concrete Research, v. 34, p. 977-989, 2004. ISSN 0008-8846/$.
[7] KULKARNI, M. S.; MIRGAL, P. G.; BODHALE, P. P., TANDE, S. N. Effect of rice husk ash on properties of concrete. Journal of Civil Engineering and Environmental Technology, v. 1, n. 1, p. 26-29, 2014. ISSN 2349-8404.
[8] KAIKEA, A.; ACHOURA, D.; DUPLAN, F.; RIZZUTI, L. Effect of mineral admixtures and steel fiber volume contents on the behaviour of high performance fiber reinforced concrete. Materials and Design, v. 63, p. 493-499, 2014. ISSN 0261-3069.
[9] ASTM-A820. Standard Specification for Steel Fibers for Fiber-Reinforced Concrete. United States of America: American Society for testing and materials: 4 p. 2016.
[10] ASTM-C1609. Standard Test Method for Flexural Performance of Fiber-Reinforced Concrete (Using Beam With Third-Point Loading). United States of America: American Society for testing and materials: 9 p. 2012.
[11] PEREIRA, E. V. Influência de Fibras de Aço no Comportamento Mecânico e nos Mecanismos de Fissuração de Concretos Autoadensáveis. Dissertação de Mestrado. Departamento de Engenharia Civil, PUC-Rio, Brasil. 2017.

DEVELOPING REINFORCED FOAM CONCRETE AS A COMPOSITE MATERIAL FOR DURABLE STRUCTURAL APPLICATION

Gideon P.A.G. van Zijl and Algurnon S. van Rooyen

Department of Civil Engineering, Stellenbosch University, South Africa

https://doi.org/10.21452/bccm4.2018.02.22

Abstract

A research programme in Stellenbosch University was launched to develop and characterize lightweight foam concrete for structural application. A particular aim is to develop the material with sound mechanical and durability properties for structural application in load bearing walling systems of low to medium rise residential infrastructure. The benefits of thermal and sound insulation make it an ideal construction material for residences in hot or fluctuating climates. In particular, its low self-weight may be exploited in regions of seismic activity, leading to lower inertia forces in earthquake ground acceleration. Having been in use for nearly a century, its use has been dominantly for non-structural insulation and backfill for drainage. In the past decade it has received renewed attention as potential structural material. Significantly improved mechanical properties are reported in this contribution. Also, the closed pore structure, despite the high percentage of pores, is visualized. Results of carbonation-induced and chloride-induced corrosion of embedded steel in LWFC are presented. To illustrate the potential of a structural walling system, results of recent pull-over laboratory tests and modelling are presented on a R/LWFC walling system comprising a founding beam, two interconnected wall panels, and an upper beam simulating upper floor restraint. The modular construction method, foam concrete, and on-site connection systems are shown to present behavior viable for application in industry.

Keywords Foam concrete; steel reinforcement; carbonation; chloride-ingress; corrosion

1. INTRODUCTION

Lightweight foam concrete (LWFC) originates from early in the previous century. Applications are dominated by non-structural applications such as insulation and backfill for drainage [1, 2]. The base composition of this composite material comprises a cement paste prepared by mixing cement and water, and subsequent addition of pre-mixed foam to form the air voids. Aggregates can be added, and cement can be partially replaced by alternative binder or filler materials such as fly ash. It is characterized by a porous microstructure which is responsible for its superior thermal performance compared to normal weight concrete. At the same time, the voids are responsible for

its relatively low compressive strength, stiffness and fracture energy [3]. In order to exploit the light weight and insulation properties in structural application, advances have been made in developing and characterizing the mechanical properties and durability. While foam concrete can be produced in a wide density range, a density range of 1200 to 1600 kg/m^3 is believed to hold potential for structural use [2, 3]. Optimization of the paste, which forms the skeleton of LWFC, and improved foaming agents to form well-dispersed, small diameter air voids have led to significant advances in mechanical behavior. Micro-fiber reinforcement may be an additional ingredient to either control early age shrinkage and potential plastic shrinkage cracking, or to reinforce the composite in the hardened state. To advance structural applications of foamed concrete, the durability behavior of reinforced LWFC over time, as well as how to adequately reinforce a material with lower fracture energy must be understood. The following sections present an overview of recent results of mechanical and durability characterization.

2. DEVELOPMENT OF MECHANICAL PROPERTIES

Recent development has led to improved mechanical performance of LWFC [1-5]. Table 1 summarizes a subset of LWFC mixes developed and characterized by the authors at Stellenbosch University.

Mix design improvements have led to the ability to accurately design for desired densities in the range 1000 to 1600 kg/m^3. In this range, the air voids comprise a significant portion of the composite, up to 40-50% by volume. As expected, increased air content leads to reduced strength and stiffness in the hardened state. However, the skeleton composition, and control of the air voids to remain fine and well-dispersed, enable strengths to be achieved that suffice for structural application. Figure 1 shows LWFC compressive and tensile strength as function of density. Note that the strength values are normalized to that of a standard class 40 MPa concrete for the purpose of illustration. Error bars for 1400 kg/m^3 show the possible range in strength obtained by the authors for various paste compositions. Stiffness, here in terms of Young's Modulus E, is shown to be approximately proportionate to density, despite the disproportionate compressive and tensile strengths. Fracture energy has been found to be low, but improved by [5] as reflected by the G_f error bar for 1400 kg/m^3 LWFC by inclusion of 0.35% by volume of polypropylene fiber of length 12 mm and diameter 0.04 mm.

Bond of LWFC with ribbed steel reinforcement bars is also shown to be relatively low in Figure 1. Note that these bond values were determined by beam-end tests [3] for LWFC without fiber. This motivated the work to increase fracture energy [5], whereby it is believed the splitting cracking caused in steel bar bond failure is controlled, whereby the bond is significantly improved. Beam-end tests have not yet been repeated for fiber LWFC, but in Section 4 the tests on steel reinforced LWFC wall system did not exhibit debonding of steel, but rather expected crack patterns in the R/LWFC walls indicating proper composite action.

Table 1: Mix compositions

	Zvinokona et al. [6]							**Mabatapasango et al. [7]**			**Dunn et al. [5]**	
	A:C=0			**A:C=1**			**A:C=2**				**LWFC**	**NWC**
Target Casting Density [kg/m^3]	1600							1400			1550	2400
Dry density	1450							1250			1400	
Wet density	1600±25							1375±15			1550±25	
CEM II-52.5 [kg]	1110			593.3			404.4	511.7			371.8	378
Fly-ash, Class S [kg]	0			593.3			808.9	511.7			743.7	122.5
Coarse aggregate 6−9 mm [kg]	0			0			0	0			0	769.5
Polypropylene Fiber [kg]	5			5			5	0			4.1	0
Malmesbury Sand [kg]	0			0			0	0			0	972
Water [Litre]	475			403.3			375.6	358.2			479.7	180
Foam [kg]	12.8			10.4			9.5	18.4			4.819	N/A
Super Plasticizer [kg]	0			0			0	0			0	7.56
Compressive strength: age(d)	1	28	56		1	28	56	28d	56d	112d		
Reference (untreated)	18.5	30.5	34.5		3.5	18.5	25.5	22	25	20.3		
(MPa) Integral[1]								28.5	33.7	32.3		
Surface treated[2]								18.5	22.5	21.2		

[1] Integral water repellant agent Sikalite or Chryso Fuge B

[2] Surface treatment painted on, Sikagard 706 Thixo, 0.2% wt binder) 200-300 g/m^2

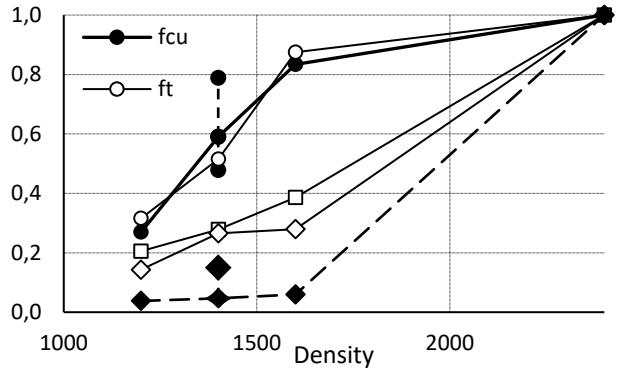

Figure 1: Normalized strength (f_{cu}, f_t), stiffness (E), fracture energy (G_f) and bond stress of LWFC, showing recent improvements for 1400 kg/m^3 in f_{cu} and G_f with error bars.

3. DURABILITY OF LWFC

Optimized LWFC has a porous, yet cellular, closed microstructure. Figure 1(a) shows the pore size distribution, and their interconnectivity is shown in Figure 2(b) through X-Ray computer tomography (CT) of a 1400 kg/m^3 LWFC included in Table 1, with A:C=1. For the particular LWFC the mean pore size was found to be 310 μm, and this was slightly reduced to 286 μm in the case of integral water repellence treatment of the same LWFC mix. Importantly, the pores are interconnected to only an insignificant degree, which is important for ingress of deleterious substances into LWFC.

Durability tests have been performed on LWFC, and a summary is given in Table 2. Reference, untreated LWFC, as well as specimens treated for water repellence through mixing the water

repellence agent into the matrix, denoted integral in Table 2, and others that were surface coated after curing were included in the experimental programs. Carbonation and chloride-induced corrosion were investigated. Cover depths of 20 mm and 35 mm to single 12 mm diameter steel reinforcement bars were used in chloride aqueous solution cyclic ponding tests for accelerated corrosion of R/LWFC. In the case of carbonation, only a 35 mm cover depth was used. See Figure 3 for full details of the durability tests, the reader is referred to [6] and [7].

Figures 3(a) and (b) show results of chloride profiling and carbonation depth from these tests. It must be noted that drying shrinkage restraint by the embedded reinforcement bars caused crack formation in the specimens, which are illustrated in Figure 4 on plan views of the 500 mm x 100 mm x 100 mm specimens used for chloride-induced corrosion, for all mix types (A:C = 0, 1, 2) and cover depths (20 mm, 35 mm). Chloride profiles were obtained by drilling into the specimens after 9 week of cyclic ponding with chloride aqueous solution [4], collecting the powder and performing X-Ray Fluorescence (XRF) to determine the total chloride content. This was done by drilling into cracks, and into uncracked parts respectively, denoted by cracked and uncrakced in the legend of Figure 3(a). It is clear that for surface treated LWFC, whether cracked or uncracked, the chloride penetration was limited. For integral water repellent LWFC, chloride did not penetrate deep into uncracked LWFC, but in the crack, significant amount of chloride penetrated to the surface of the reinforcing bar. This amount was only exceeded by the cracked, untreated LWFC. To prevent restrained shrinkage cracks, Grafe (2017) developed a fiber reinforced LWFC, which is included in the second last column of Tables 1 and 2, as used by [5] for large scale wall system testing. The fibers prevented restrained shrinkage cracks in those mixes, despite inclusion of reinforcing steel meshes, as reported in Section 3.

The carbonation depth did not reach the level of steel (Figure 3(b)), and no corrosion initiated in those specimens. Corrosion did initiate and propagate in the accelerated chloride-induced specimens, ascribed to the restrained shrinkage cracks. Figure 4 summarizes corrosion rates in the various R/LWFC specimens.

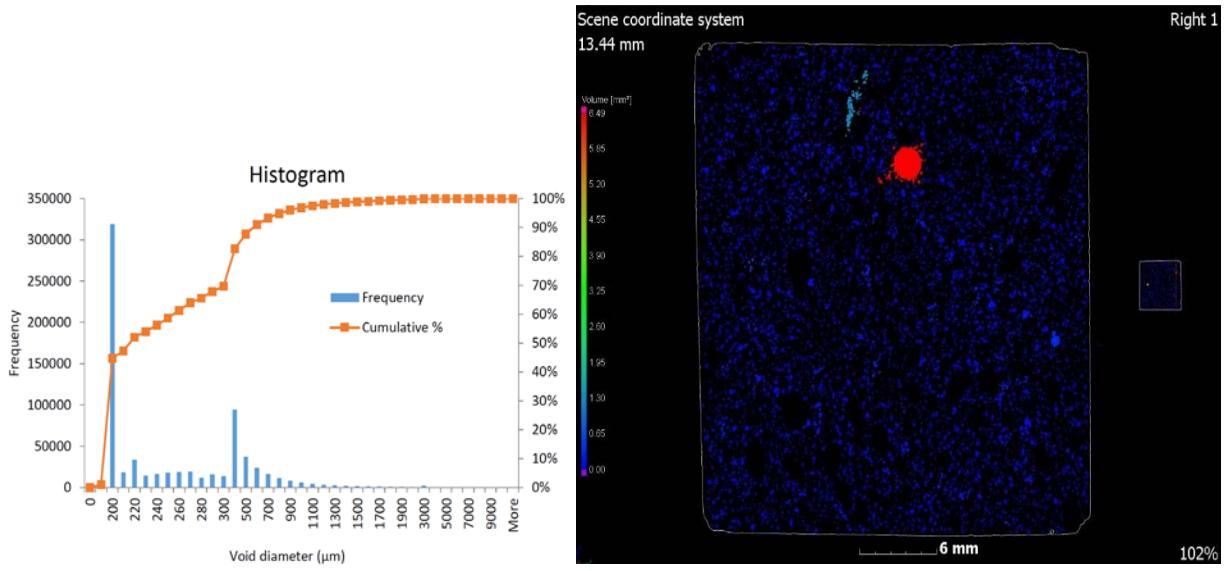

(a) (b)

Figure 2: LWFC of density 1400 kg/m^3 air void (a) diameter distribution and (b) connectivity.

Table 2: Durability properties of LWFC

	Zvinokona et al. [6]			**Mabatapasango et al. [7]**		
	A:C=0	**A:C=1**	**A:C=2**	**A:C=1**		
Target Casting Density [kg/m^3]	1600			1400		
Water penetration depth (mm)						
Reference (untreated)						
Integral						
Surface treated				4.5[3]		
Carbonation depth: weeks				4	8	12
Reference (untreated)				12	23	24.3
(mm) Integral				2.5	8	12
Surface treated				3.5	12.5	17
Chloride penetration depth :						
Reference (untreated)	11	12	34			
(mm) Integral[1]	9	12	19			
Surface treated[2]	5	5	6			

[1] Integral water repellant agent Sikalite or Chryso Fuge B
[2] Surface treatment painted on, Sikagard 706 Thixo, 0.2% wt binder) 200-300 g/m^2
[3] Water penetration depth test according to EN 1504-2:2004

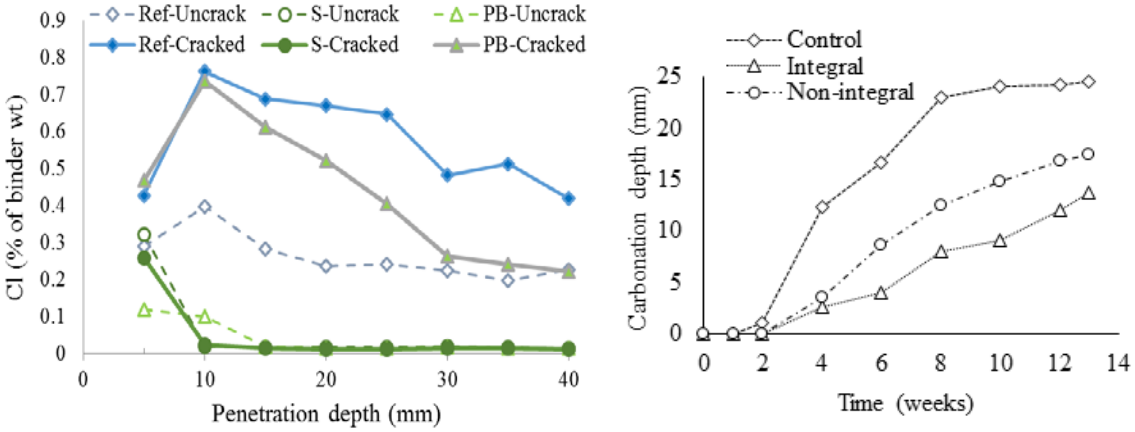

(a) (b)

Figure 3: (a) Chloride profiles in LWFC specimens after 9 weeks of cyclic ponding with Chloride aqueous solution, (b) carbonation depth [4].

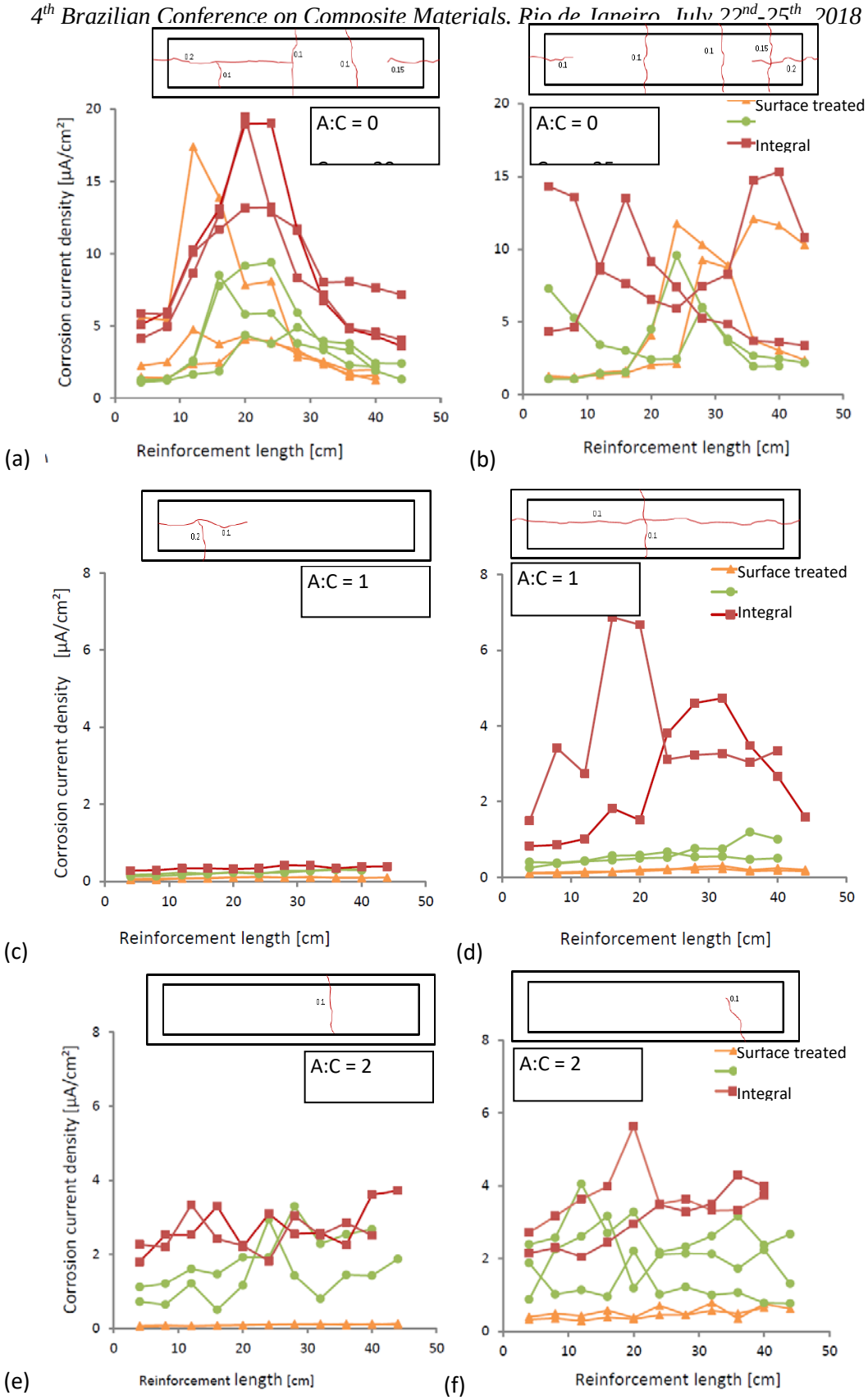

Figure 4: Corrosion rate in R/LWFC specimens with various Fly Ash to Cement ratios (0, 1, 2), and cover to steel (20 mm, 35 mm). Typical crack patterns and widths are also shown.

4. STRUCTURAL R/LWFC WALLING SYSTEM

A R/LWFC walling system is proposed that consists of connected precast reinforced LWFC panels. Current residential infrastructure in the Western Cape of South Africa comprise mainly of unreinforced, load bearing masonry (URM) and precast, hollow-core floors. These three and four storey buildings do not conform to the SANS 10160-4:2017 seismic design criteria and are susceptible to the low-moderate peak ground acceleration of $a_g = 0.15 \cdot g$ predicted for the area. As an alternative structural system, a LWFC walling system will take advantage of the thermal, acoustic and fire-resistant properties of LWFC, as well as light weight and associated low inertia forces. This structural system will also contribute to reduce the housing backlog through high quality, high output factory production, and sustained employment in industrialized construction.

To test the proposed walling system, a wall section of a prototype building shown in Figure 5(a) is modelled for laboratory testing as well as finite element analysis. The scaled test assembly (Figure 5b) comprise two wall panels, each of dimensions $1380x920x150$ (mm), and two reinforced concrete panels/beams to simulate a foundation and floor interaction. The concrete mix design for both the LWFC and NWC panels are given in Table 1. Each wall panel was reinforced with two layers of a local South African (Ref .193) steel mesh, comprising of 5.6 mm diameter, 520 MPa yield strength steel bar at a grid spacing of 200 mm x 200 mm, placed with 40 mm cover from each wall face. The walls were precast horizontally in wooden moulds, and after 14 days tilted up and transported from the Materials Laboratory to the Structures Laboratory for assembly. Heat curing can be employed and removal of the moulds can be done within days. The vertical dashed lines in Figure 5(b) indicate the locations of grouted dowels along the horizontal connections, each consisting of a 12 mm diameter, 520 MPa yield stress steel bar, encased in a 40 mm diameter PVC pipe and grouted with SikaGrout®212. Wall 1 had three dowels per panel per interface. The four horizontal connections (boxed in red) are the connections that were removed as a variable for the second pull-over test, in Wall 2. The vertical connection boxes between the two wall panels are shown in Figure 5(d). These horizontal connections follow the precast connection guidelines outlined in the New Zealand building codes [8, 9]. This guideline suggests that reinforcement across a connection be less than the reinforcement within the wall, to ensure failure at the connections where ductility can be confirmed.

The self-weight load of the structure above was applied to the wall system via springs to the top of the wall and distributed through a $254x254x89$ structural steel H-section. The walls were displaced through a $500\ kN$ Instron Mechanical Testing Machine (MTM) and transferred across the structural steel section by embedded shear bolts into the top NWC panel. Details of the experimental setup can be found in Dunn et al. (2017).

The results indicated sound responses of the two wall systems to quasi-static pull-over. Figure 6 shows the responses of Wall 1 and Wall 2, with distinct difference caused by the connection system. Recall that fewer dowel connectors were included in Wall 2 than Wall 1 (Figure 5b). This led to a separate rotation of the two wall parts (Figure 6a), due to balanced vertical and horizontal connection detail, and subsequent larger pull-over resistance and energy dissipation in Wall 1 than Wall 2 (Figure 6(a) versus Figure 6(b)). Moreover, well-developed patterns of, diagonal fine cracks were observed in Wall 1, but less in Wall 2, explaining the lower ductility of Wall 2 than that of Wall 1.

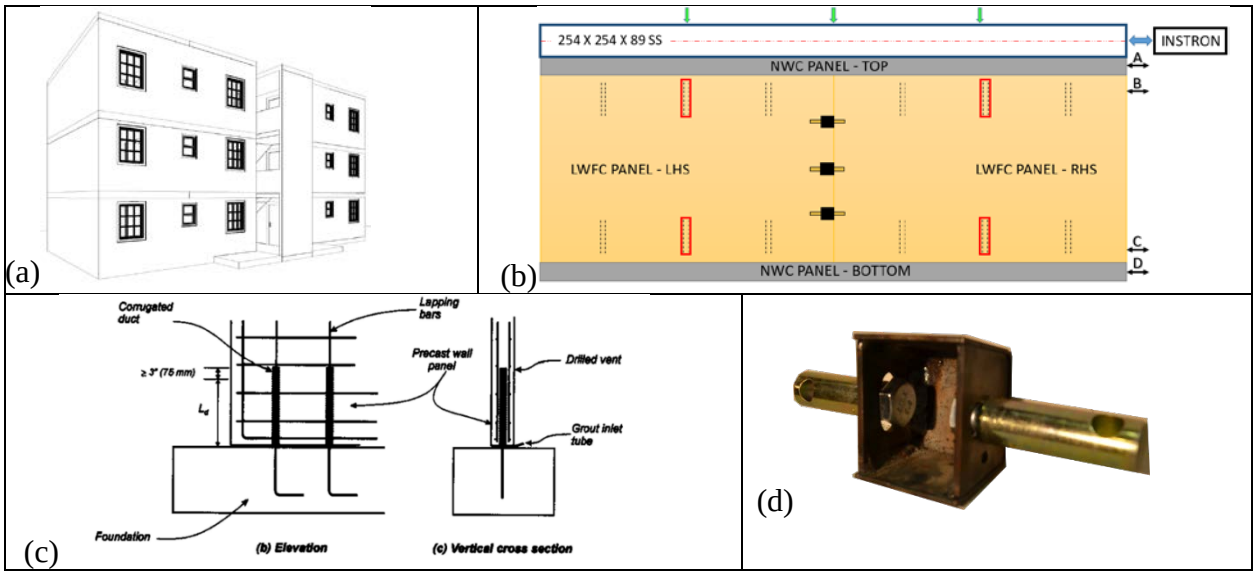

Figure 5: (a) Prototype residential building, (b) wall test section comprising two interconnected wall panels, a foundation and floor beams, (c) illustration of foundation-wall dowel connections and (d) photo of the wall panel connectors used in vertical joints.

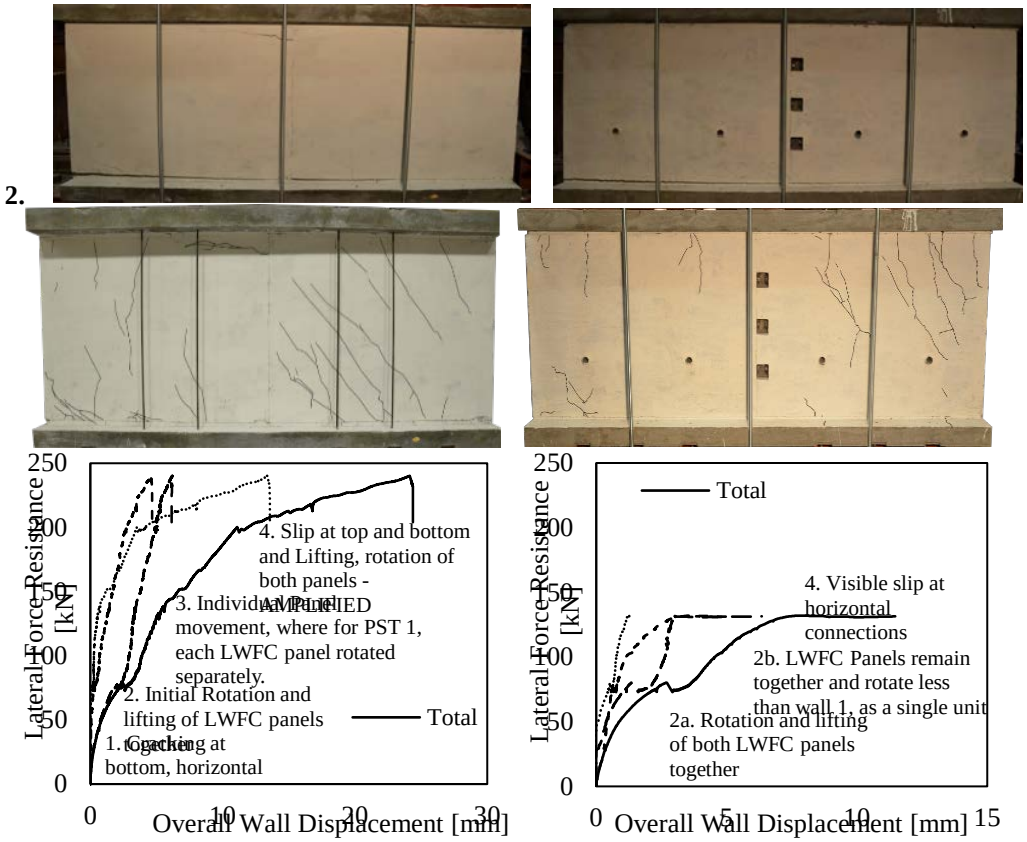

(a) Wall 1 response (b) Wall 2 response

Figure 6: (a) Separate wall panel rotation with 3 dowel connections per wall part and lower and upper beams, versus (b) wall panels rotating together as a single unit in two dowel connections per panel per interface.

5. CONCLUSIONS

Lightweight foam concrete can be used structurally, thanks to the development in materials technology to improve the strength and stiffness, as well as fracture energy. Inclusion of a small amount of micro fiber prevents the formation of restrained shrinkage cracks. In absence of cracks, carbonation and chloride penetration is restricted, even more so if integral, or preferably surface treatment is applied for water repellence. Yet, even without such treatment, the closed, fine, dispersed pore structure in foam concrete prevents significant ingress of deleterious materials. Thereby, deterioration processes like chloride-induced corrosion, are slow.

REFERENCES

[1] Kearsley, E. and Mostert, H. 2005. Designing mix composition of foamed concrete with high fly ash contents. In: Use of Foamed Concrete in Construction: Proceedings of the International Conference held at the University of Dundee, Scotland, UK on 5 July 2005, pp. 29–36. Thomas Telford Publishing.

[2] Jones, M.R., McCarthy, A. 2005. Preliminary views on the potential of foamed concrete as a structural material, Magazine of Concrete Research 2005 57(1)21-31.

[3] De Villiers, J.P., van Zijl, G.P.A.G., van Rooyen, A.S. 'Bond of deformed steel reinforcement in lightweight foamed concrete (LWFC)'. Structural Concrete, international journal of *fib*, June 2017, 18(3): 496-506.

[4] Van Rooyen, A.S., Van Zijl, G.P.A.G. 'Chloride profiling of integral and non-integral surface treated Lightweight foamed concrete'. Paper ID 120, 71st RILEM week and ICACMS, 3-8 September 2017, Chennai, India, pp. 11-16.

[5] Dunn T.P.A., Van Rooyen, A.S., Van Zijl, G.P.A.G. 'Reinforced Lightweight Foamed Concrete for Seismically Resistant Low-rise Residential Buildings', Paper ID 101, 71st RILEM week and ICACMS, 3-8 September 2017, Chennai, India, Volume 3, pp. 269-278.

[6] Zvinokona, A.R., Van Rooyen, A.S., Bezuidenhout, S.R., Van Zijl, G.P.A.G. 'Chloride-induced corrosion in structural lightweight foam concrete'. In: 9th International Symposium on Cement and Concrete (ISCC2017), 1-3 November 2017, Wuhan, China.

[7] Mubatapasango, M.S., Van Rooyen, A.S., Van Zijl, G.P.A.G. 'Effect of surface protection on carbonation induced corrosion in reinforced foam concrete'. Paper ID 114, 71st RILEM week and ICACMS, Proceedings International conference on Advances in Construction Materials and Systems 2017, 3-8 September 2017, Chennai, India, pp. 179-188.

[8] Seifi, P., Henry, R. & Ingham, J., 2016. Panel connection details in existing New Zealand precast concrete buildings. Bulletin of the New Zealand Society for Earthquake Engineering.

[9] New Zealand Concrete Society, 1999. Guidelines for the Use of Structural Precast Concrete in Buildings. Christchurch: University of Canterbury.

INCORPORATION OF REUSED SUGARCANE FIBRES APPLIED IN THE TREATMENT OF EFFLUENTS CONTAMINATED WITH ENGINE OIL AS REINFORCEMENT OF CEMENTITIOUS COMPOSITES

Viviane V. S. Guilarduci(1), Patrícia Benedini Martelli(2), Honória de Fátima Gorgulho(2) Pablo Resende Oliveira(3) and Túlio Hallak Panzera(3)

(1) Center for Environment, Health and Safety, IF Sudeste MG - Campus São João del-Rei, São João del-Rei, Brazil.
(2) Department of Natural Sciences – DCNAT, Federal University of São João Del-Rei - UFSJ, Brazil.
(3) Centre for Innovation and Technology in Composite Materials – CITeC, Department of Mechanical Engineering, Federal University of São João Del-Rei - UFSJ, Brazil.

https://doi.org/10.21452/bccm4.2018.02.23

Abstract

This work investigates the reutilisation of natural (SCB) and modified sugarcane bagasse fibres with aminopropyltriethoxysilane (MSCB) in cementitious composites. The modified fibres were used in the treatment of effluents contaminated with oil-engine. A full factorial design was used to identify the effects of fibre type (natural and modified sugarcane), fibre length (0.6 and 1.2 mm), fibre amount (1 and 2wt%), and fibre condition (before and after oil filtration) on apparent density, water absorption, apparent porosity, ultra-pulse velocity, dynamic modulus, flexural strength and modulus. SCB fibres led to increased apparent density compared to MSCB fibre reinforced composites. The MSCB fibres contributed to reduce the porosity of the composite, leading to higher mechanical properties. The reduced area of MSCB fibres increased the amount of cementitious phase per unit volume which increases the sample strength. Longer fibres (1.2 mm) have a higher surface area, leading to a higher concentration of fibres per unit volume, increasing water absorption by 17%. The amounts of fibres had no significant effect on the mechanical and physical responses. Samples made with 2wt% MSCB fibres of 0.6 mm in length achieved promising results for non-structural applications in civil engineering.

1. INTRODUCTION

The construction industry requires significant amounts of raw materials and energy for its development, generating a significant amount of pollution (CO2 emissions are an urgent risk) and waste. The search for sustainable solutions includes the correct use of industrial and agroindustry materials. New approaches to efficient projects are related to the development and use of natural building materials [6].

Gatto *et al.* [1] reported several advantages in composites with natural fibres, such as reduced apparent specific gravity, higher porosity, satisfactory tensile and impact strength, greater fracture control, and ductile failure. Further benefits are biodegradability of fibres, reduced costs and damages to manufacturing machinery when compared to synthetic fibres [2]. On the other hand, cement-based matrices are fragile and may present small cracks, even under small tensile loads or under deformation. The incorporation of fibres can reduce the propagation of the matrix crack, since the fibres can bind the sample parts between the cracks. As a result, fibre inclusions may increase sample toughness, tensile and impact strength [3-4]. Cementitious composites with reinforcement of natural fibres have been developed in several applications, such as in the automotive and building industries, as a substitute for conventional materials, with glass fibre being an example of fibre replacement [5].

A significant amount of natural fibres (hemp, straw, linen, bamboo, cork, etc.) has been applied as reinforcing phase to conventional matrices (cement, mortar, sand, plaster, concrete, etc.) for the design of composite materials. Many factors can affect the properties of fibre-reinforced composites, including fibre geometry, distribution, orientation, shape and length, as well as, the properties of individual phases (matrix and fibres), contact type, phase mixing ratio and manufacturing, etc. [7]. Most studies found in the literature investigated only a few significant parameters, such as fibre amount, length and type, to estimate composite performance [8].

Metha and Monteiro [9] reported an inverse relationship between porosity (volumetric fraction of pores) and mechanical strength in solids. In a multi-phase material, the porosity of each component or phase within its structure is a limiting factor for composite resistance. Although the water/cement ratio is the most important factor in determining matrix and transition zone porosities, in addition to the mechanical strength of cementitious composites, other factors such as densification, curing conditions (hydration degree of cement), aggregate dimensions and mineralogy, additives, sample geometry and moisture, and load type may have a significant effect on the mechanical properties.

Reis and Carneiro [5] highlighted the advantages of natural fibres, which include low cost, lightweight, high availability, easy recycling, good thermal and acoustic insulation, moderate mechanical properties and reduced CO_2 emissions. On average, the production of natural fibres as composite reinforcements require 60% less energy than the production of glass fibre. Besides reinforcing cementitious composites, natural fibres can also be used as absorbing material. Scarcity of water resources poses a challenge to the sustainable development of industrial and agricultural activities. The production of significant amounts of industrial effluents and the awareness of the impact of their effects on nature have forced the industry to adopt new environmental policies [10-11]. One method widely applied in last decades for the treatment of water contaminated with oil is the use of absorbent materials, which easily remove and recover the oil. Many materials can be used at this stage, being natural organic products of living organisms, also known as biosorbents, advantageous because of the high availability and low cost. Some examples are sawdust, cotton, peat, sugarcane bagasse, straw and corn cob. They are highly capable to float and are biodegradable.

Annunciado *et al.* [12] reported that natural fibres are example of low cost absorbents from renewable sources that may represent a sustainable alternative in reducing oil contamination. Sawdust, cellulose, rice husk, sugarcane bagasse, corn cob and straw, cotton, etc. are abundantly produced in Brazil. However, most of these fibres are discarded due to lack of suitable applications. They represent a suitable alternative for oil adsorption, due to its high absorption, low cost, no

need for regeneration, and the contribution of the cellulosic nature to the degradation the oil in aqueous systems [13].

Although natural fibres can be an alternative for oil absorption, they have limitations because these fibres also tend to absorb water. This side effect occurs due to the presence of hydroxyl groups in cellulose, hemicellulose, and lignin. These groups, in particular, are responsible for the hygroscopic properties of lignocellulosic materials. However, the hygroscopic properties of the samples can be reduced by superficial modifications [14]. One possible approach is to replace the hydroxy functional group with hydrophobic groups through chemical reactions.

This work investigates the use of sugarcane bagasse fibres in pristine (SCB) and modified fibre with aminopropyltriethoxysilane (MSCB) applied in the treatment of effluents contaminated with engine oil as reinforcement of cementitious composites. The use of natural fibres for effluents treatment has been described by Gatto *et al.* [1] and Guilharduci *et al.* [16].

2. MATERIALS AND METHODS

2.1. Materials

The cement used was the Portland cement (ASTM III) supplied by Cauê Company (Brazil). The sand particles were supplied by *Omega Mining Company (*Brazil). The sugarcane bagasse (SCB) fibres were sourced by *Cachaça Coqueiro* Stiller (Brazil). Aminopropyltriethoxysilane (APTS, 98%, $(H_2NCH_2CH_2CH_2)$-Si-$(OCH_2CH_3)_3$) was purchased from Dow Corning and was used without further purification. The other analytical grade reagents were obtained from Merck and were used as received.

2.2. Methods

The factors analysed were the type of fibre in pristine (SBC) and modified condition (MSCB), fibre length (0.6 and 1.2 mm), fibre amount (1 and 2%wt as a replacement of aggregates), and treatment conditions (before and after oil absorption), resulting in a Full Factorial Design 2^4 type, as shown in Table 1. The fibres with absorbed oil were prepared with the effluent collected at *Del-Rei Rectifier Company (*Brazil). One gram of fibres was immersed in 100 ml of effluent under stirring during 24h. Subsequently, the fibres were filtered and dried at room temperature [16]. Table 1 presents the factors investigated and their respective levels.

Table 1: Factors and experimental levels (2^4 = 16 conditions)

Factors	***Levels***	
Type	SCB	MSCB
Length	0.6 mm	1.2 mm
Amount	1%wt	2%wt
Condition	Before oil absorption	After oil absorption

The Design of Experiment (DoE) and Analysis of Variance (ANOVA) were performed via Minitab 18. The samples were prepared according to the standard NBR 7215 [17]. They were manufactured with mortar matrix composed of one part of cement and three parts of standard sand (20% of fine aggregate, 50% of medium aggregates and 30% of coarse aggregates) and water/cement ratio of 0.55. The mixture was inserted into prismatic moulds of 40 mm square cross-section area and 160 mm length. An electromagnetic vibrator was applied for 8 minutes to ensure a uniform batch. The samples were identified and covered by plastic film to prevent loss of moisture. As recommended by NBR 5738 [18], the samples were demoulded after 7 days and kept at room temperature. Samples were tested after 28-days cure under three-point bending load

according to ASTM C348-14 [20] at a cross-head speed of 0.5 mm/min to obtain flexural strength (σ_f). The flexural test was conducted in a universal testing machine Shimadzu AGX with 100 kN load using the integrated software Trapezium X. The static modulus of elasticity (E_s) was then calculated based on ASTM C580-02 [20]. The pulse velocity (v) was obtained using a portable ultrasonic non-destructive digital indicating test (PUNDIT) equipment in accordance with ASTM C597-09 [21]. The dynamic modulus of elasticity (E_d) was obtained based on ASTM C348-14 [19] standard. Physical properties, such as water absorption (W_{abs}) apparent porosity (P_a), and apparent density (ρ_a) were also determined using British standard BS 20545-3 [22].

3. RESULTS AND DISCUSSIONS

The statistical test investigated whether the factors analysed, such as type of fibre (SCB and MSCB), amount of fibre (1 and 2%wt), fibre length (0.6 and 1.2 mm), and fibre condition (with and without absorbed oil) could affect the results of evaluated responses. A statistical analysis was performed using the P-Values of ANOVA to verify if there is any interference of the factors analysed. The P-Values underlined in Table 2 indicate the significant factors within a 95% confidence level. The reported values of R^2 also indicate that the quality of model adjustment was satisfactory for all variables. The assumption of data normality is an additional requirement to validate the use of hypothesis tests and analysis of variance. The normality of the experimental data was verified using the Anderson-Darling test. This test indicate that the data follows the normal distribution if the P-Value is greater than 0.05. In this case, all data follow a normal distribution (see Table 2), validating ANOVA model.

Table 2: Analysis of Variance results – P-Values

	Factors	ρ_a	W_{abs}	P_a	v	E_d	σ_f	E_s
Main	**Type of Fibre (T)**	0.000	0.000	0.000	0.022	0.003	0.035	0.008
	Amount of Fibre (A)	0.009	0.000	0.000	0.530	0.172	0.126	0.100
	Length of Fibre (L)	0.279	0.000	0.000	0.101	0.032	0.002	0.267
	Condition of Fibre (C)	0.571	0.005	0.000	0.083	0.173	0.586	0.262
Interactions	**T*A**	0.000	0.000	0.762	0.000	0.000	0.188	0.000
	T*L	0.023	0.000	0.000	0.349	0.021	0.047	0.002
	T*C	0.000	0.000	0.000	0.846	0.834	0.009	0.884
	A*L	0.000	0.000	0.000	0.213	0.278	0.604	0.866
	A*C	0.000	0.000	0.000	0.866	0.787	0.868	0.000
	L*C	0.000	0.000	0.000	0.088	0.455	0.030	0.001
	T*A*L	0.000	0.000	0.000	0.526	0.142	0.016	0.335
	T*A*C	0.004	0.185	0.000	0.000	0.033	0.084	0.000
	T*L*C	0.000	0.001	0.000	0.161	0.113	0.209	0.000
	A*L*C	0.000	0.000	0.000	0.521	0.790	0.128	0.521
	T*A*L*C	0.000	0.000	0.000	0.001	0.020	0.072	0.695
R^2 (%)		99.03	99.89	99.89	82.48	81.17	79.52	93.12

Anderson Darling (P-value>0.05)	0.879	0.643	0.881	0.890	0.755	0.091	0.721

3.1 Physical Properties

The apparent density data ranged from 2.25 to 2.37 g/cm³. Benmansour *et al.* [6] investigated the use of palm fibres in different lengths (3 and 6 mm) and amounts (5, 10 and 15wt%) in mortar, obtaining values of density lower than 0.984 to 1.476 g/cm³. Aggarwal [24] used sugarcane bagasse fibres in mortar involving two fibre amounts (12 and 16wt%), obtaining a density variation between 1.55 and 1.65 g/cm³.

Table 2 reports that the type of fibre (treated and untreated) and fibre amount (0.6 and 1.2 mm) factors individually affect apparent density. They also influence the remaining factors, as noted in the interactions shown in Table 2. The individual plots are presented in Figure 1 to assess the effect of each parameter on the apparent density. The use of natural bagasse fibres increased composite apparent density when compared to treated fibre reinforced composites (MSCB – see Figure 1a). The substantial difference of 208% between the fibre densities (0.71 g/cm³ for SCB and 0.23 g/cm³ for MSCB) justifies this behaviour. Figure 1b reveals the increase in the amount of fibre from 1 to 2wt% led to reduced composite density, since the fibre density is smaller than the aggregate density.

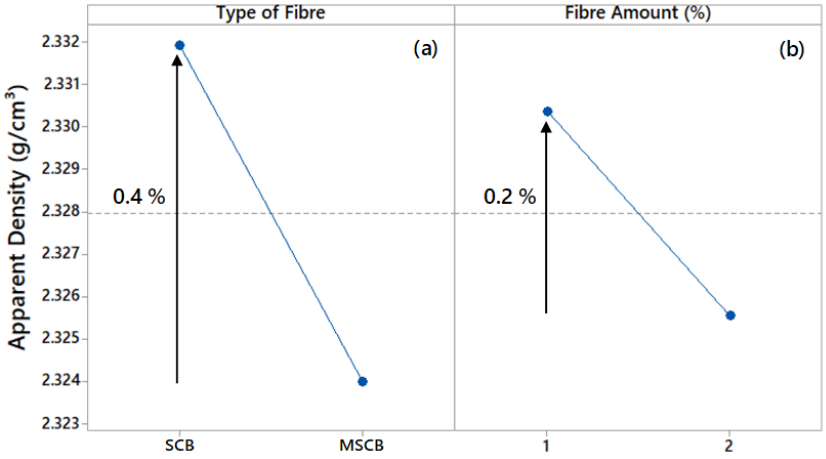

Figure 1: Main effect plots for mean apparent density.

The water absorption values ranged from 2.41 to 8.01%. Aggarwal [24] studied two amounts of sugarcane bagasse particles (12 and 16wt%) as reinforcement in cement composites, presenting a water absorption ratio between 12.5 and 14.5%. Filho [25] investigated sisal fibres reinforced composites at two lengths (25 and 50 mm) and three amount levels (2, 4, and 6%), reaching water absorption values of 7.73 to 11.47%. These findings indicate that the range of absorption found in this study is promising. The benefits of fibre inclusions are evident when the water absorption ratio for the reference condition (without fibres) is evaluated. A large absorption of 7.38% was obtained for the reference condition, being attributed to the excess water in the system. It is noteworthy that water can be absorbed when fibres are incorporated into the system. Table 2 indicates that four main factors were considered significant for the water absorption response. The influence of individual factors is shown in Figure 2.

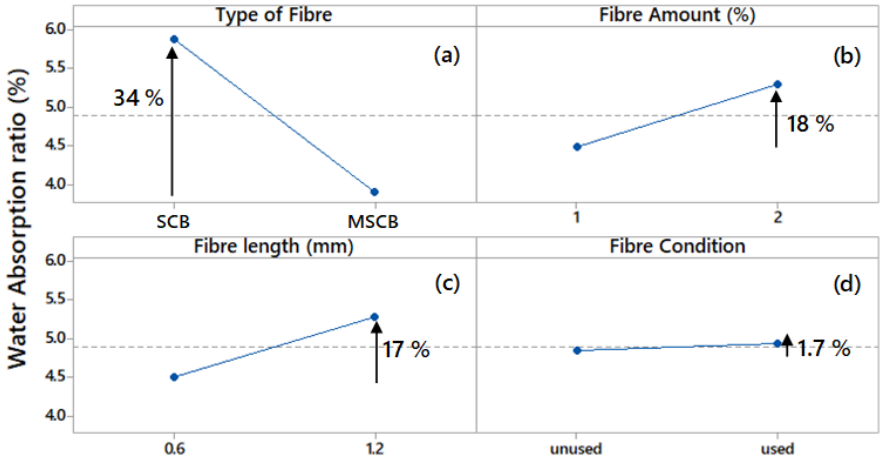

Figure 2: Main effect plots for mean water absorption ratio.

The apparent porosity varied from 5.21 to 15.95%. The findings reported by Filho [25] ranged from 14.87 and 21.48%. Teixeira [26] investigated composites reinforced with Curauá fibres of varying lengths (6 and 10 mm) and amounts (1 and 2%), with a resulting porosity between 28.16 and 31.90%. The results found in this work were significantly lower than those reported in the literature. The reference condition also presented higher apparent porosity (14.74%) than most of the conditions tested, similar to the results of water absorption. It is observed in Table 2 that all individual factors significantly affected the apparent porosity (Figure 3).

The treated fibres (MSBC) tended to absorb more water, which led to reduced pores within the cementitious sample and reduced water absorption and porosity levels (Figure 2a and 3a). In addition, MSBC fibres present lower porosity than untreated fibres (SCB). Fibre porosity directly affects the composite water absorption and porosity after cement-hydration process, increasing these properties when a larger amount of fibre is used (see Figure 2b and 3b). Longer fibres (1.2 mm in length) exhibit higher superficial area compared to fibres of 0.6 mm in length, which increases fibre concentration per unit volume. Therefore, longer fibres increase the water absorption ratio and sample porosity by 17% and 13%, respectively (see Figures 2c and 3c), due to the higher volume of fibres within the sample. Figures 2d and 3d show a reduced variation for the fibre condition (unused and used fibres), however this effect is important to identify the dominance of the cementitious matrix over resulting properties. MSBC fibres were able to absorb less water in the system, leading to excess water in the sample, consequently increasing the porosity and water absorption of the cured samples.

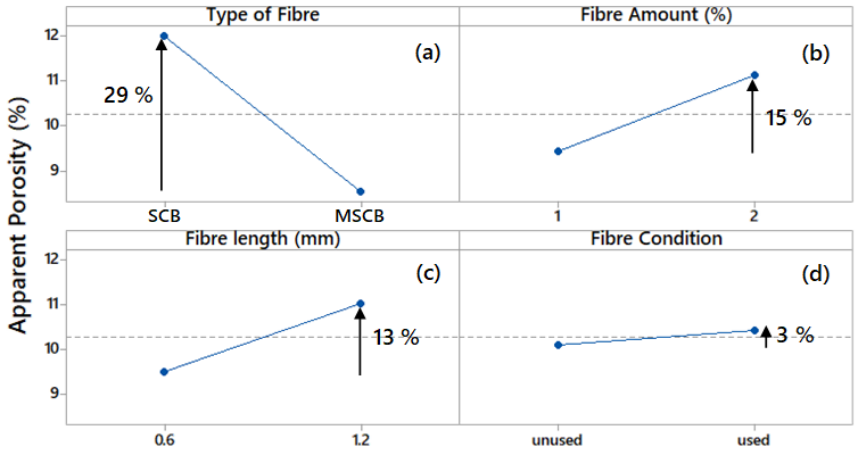

Figure 3: Main effect plots for mean apparent porosity.

3.2 Ultra-pulse velocity and Dynamic modulus

The pulse velocity data for composite samples varied from 352.97 to 393.17 m/sec. Valenciano [4] investigated cementitious composites with 2 wt% sugarcane bagasse fibres in varied lengths. The fibres were used untreated and with chemical treatment by immersion in 5% sodium silicate solution and in 30% aluminium sulphate. These samples presented pulse velocities between 1290 and 1880 m/s. The results found in the present work were significantly lower than the literature values, which can be attributed to different fibre lengths, amounts and chemical treatments, as well as the components ratio (cement:aggregates:fibre:water). The overall results, however, are reasonable when considering the result for reference condition without fibre inclusions (371.41 m/s). Table 2 indicates that only the main factor "Type of Fibre" significantly affects the response (see Figure 4). The ultra-pulse velocity of the composites increased when treated fibres (MSCB) were incorporated. This behaviour can be explained by the effect of the fibres on the matrix properties. The MSCB fibres exhibit higher water absorption, which consumes the water/cement ratio of the system, leading to a less porous cementitious sample, thus achieving a higher ultra-pulse velocity.

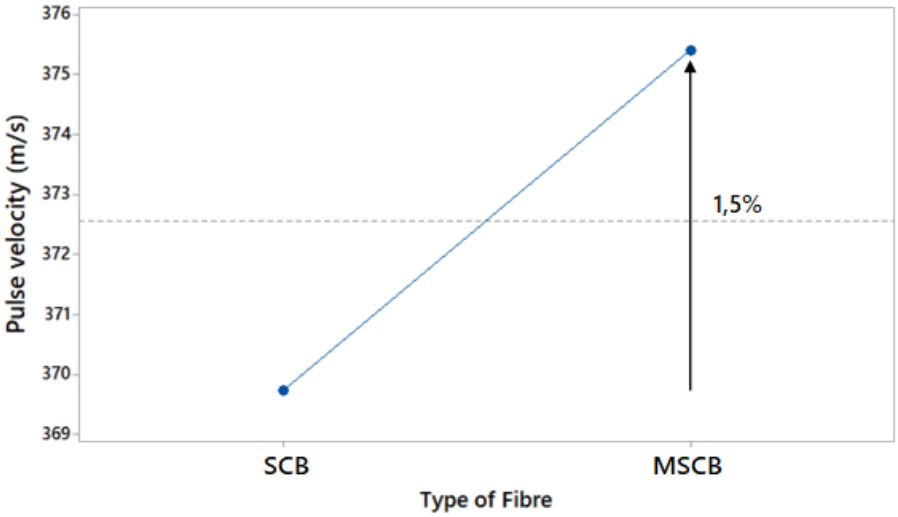

Figure 4: Main effect plot for mean ultra-pulse velocity.

The values of the dynamic elastic modulus ranged from 0.241 to 0.310 GPa. Valenciano [4] also reported the dynamic modulus of bagasse-reinforced cementitious composites, which ranged from 2.37 to 6.03 GPa. These values are again above the results obtained in the present work. It is noteworthy that the dynamic modulus of the reference condition was 0.27 GPa, which indicates an appropriate variation of the results. Table 2 shows that the factors "Type of fibre" and "Fibre length" significantly affect the dynamic modulus (Figure 5). As previously discussed, MSCB fibres tend to absorb more water in the sample, reducing the porosity of the cementitious specimens, which increases the ultra-pulse velocity. As a result, an increased dynamic modulus was reached when the composites were reinforced with MSBC fibres (see Figure 5a). The fibre length also affects the volume occupied by the matrix phase in the system. Shorter fibres led to larger amounts of matrix, leading to the increase of the dynamic modulus (Figure 5b).

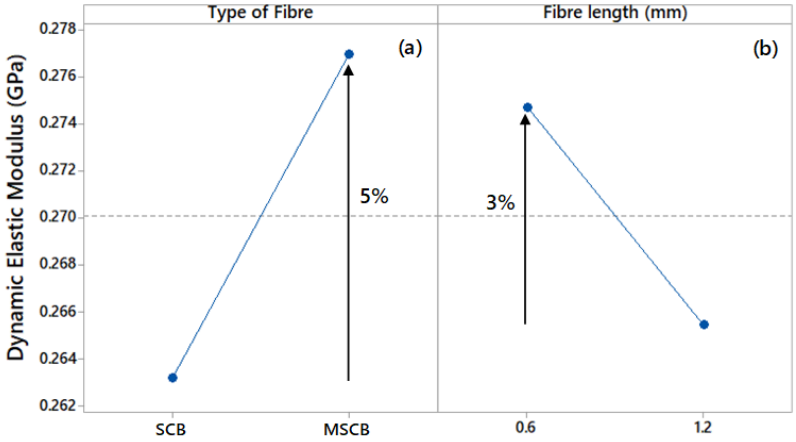

Figure 5: Main effect plots for mean dynamic elastic modulus.

3.3 Mechanical Properties

The flexural strength of cementitious composites varied from 4.56 to 7.78 MPa. These results are in agreement with the values reported by Sales [27], considering that the author has investigated reinforced composites with 8 and 12 wt% of bamboo pulp. The results of the flexural strength were reported as, respectively, 7.50 and 4.43 MPa. The type, amount, length and conditions of fibres have been reported as the main factors influencing flexural strength of reinforced cementitious samples. In this work, the fibre type and length were statistically significant (Figure 6), the fibre length being the factor that most influenced the flexural strength. The composites made with MSCB fibres provided reduced porosity (see Figure 3a) and thus achieving higher strength when compared to SCB composites (see Figure 6a). MSCB fibres have a lower superficial area than natural ones, which increases the amount of cementitious paste in the sample, leading to superior flexural strength. Shorter fibres (0.6 mm) also present lower superficial area, reaching higher composite strength (Figure 6b).

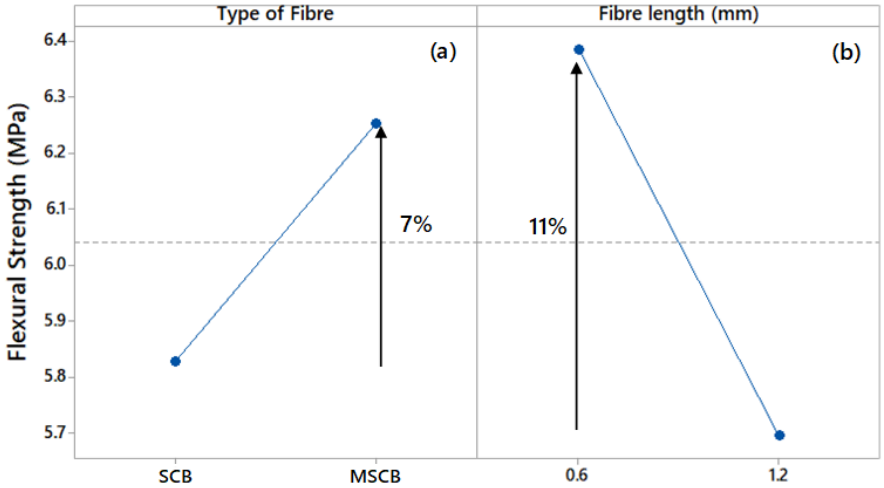

Figure 6: Main effect plot for mean flexural strength.

The flexural modulus ranged from 0.303 to 0.678 GPa. Picanço and Ghavami [28] investigated composites reinforced with *curauá*, jute and sisal fibres at 2 and 3wt% inclusions and lengths at 15, 25, and 45 mm. The authors found that the flexural modulus varied from 18.24 to 29.33 GPa. These findings are highly superior to those obtained in this work. It is noteworthy that many other factors, such as densification, curing conditions, fibre type, length and amount can also influence the mechanical properties of the composite. The results obtained in this research show satisfactory agreement with the reference condition (0.50 GPa). Table 2 reveals that the type of fibre factor significantly affects the flexural modulus (Figure 7). Figure 7 shows that the natural fibre reinforced composites (SCB) achieved 8% higher flexural modulus than MSCB composites, being attributed to the fibre-matrix adhesion condition. The natural fibres exhibit a rougher surface than the treated ones (MSCB), which contributes to enhance the modulus of elasticity of the composites.

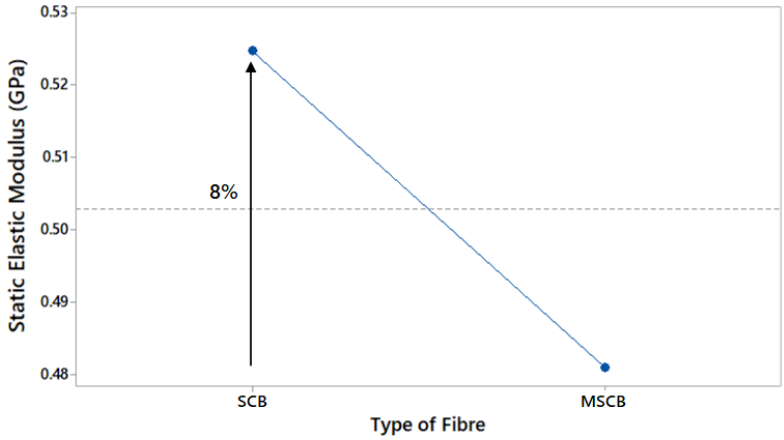

Figure 7: Main effect plot for mean flexural modulus.

4. CONCLUSIONS

This study investigated the reuse of natural fibres, after treatment with effluents contaminated with oil, as reinforcement of cementitious composites. A statistical analysis was conducted to

evaluate the influence of the fibre length, amount, treatment and condition on the mechanical and physical responses. The main conclusions are as follows:

- The presence of oil in the fibres was not significant to affect the mechanical properties of the composites. It indicates that the reuse of absorbing fibres into cementitious products is feasible;
- The amount of fibre (1 and 2wt%) did not affect the mechanical properties of the samples. However, higher amounts of fibres led to increased porosity and water absorption, which may reduce the durability of cementitious products in outdoor environments. Since natural fibres are only suitable for indoor applications, the 2wt% fibre amount level is adequate in a context of increasing need for natural fibres in the construction industry;
- The type of fibre (natural and treated fibres) had a significant influence on the responses, with higher strength for MSCB fibres and higher stiffness for natural fibres. Due to the high functionality of treated-fibres (MSCB) in the effluent treatment, it can be concluded that both types can be used in non-structural engineering applications.;
- Fibre length (0.6 and 1.2 mm) factor affected the physical and mechanical properties by reducing sample permeability and increasing the flexural strength of composites with 0.6 mm fibres by approximately 11%.

Cementitious composites fabricated with 2wt% MSCB fibres of 0.6 mm in length, used in effluent treatments, are then considered promising in non-structural applications for the construction industry.

ACKNOWLEDGEMENTS

The authors would like to acknowledge the Brazilian research funding agencies (CNPq, FAPEMIG, and CAPES) and the IF Sudeste MG campus São João del Rei.

REFERENCES

[1] GATTO, E. G.; KAWABATA, C. Y.; SAVASTANO JUNIOR, H. Polpas kraft de Agave sisalana e de Musa cavendishii para reforço de fibrocimento alternativo. Revista Engenharia Agrícola, v.23, n.2, 2003, p.211-220.

[2] D'ALMEIDA, A. L. F. S., CALADO, V., BARRETO, D. W., D'ALMEIDA, J. R. M. Acetilação da fibra de bucha (Luffa cylindrica). Polímeros: Ciência e Tecnologia, vol. 15, n.1, p. 59-62, 2005.

[3] LOPES F. F. M., ARAÚJO, G. T., LUNA S., NASCIMENTO J. W. B., SILVA V. R. Modificação das propriedades das fibras de curauá por acetilação. Revista Brasileira de Engenharia Agrícola e Ambiental. v.15, n.3, 2011, p.316–321.

[4] VALENCIANO M. D. C. M. Durabilidade de compósitos cimentícios com materiais lignocelulósicos. 2004. 186p. Tese de Doutorado. Universidade Estadual de Campinas – Campinas.

[5] REIS, J. M. L., CARNEIRO E. P. Effect of piassava lees in the fracture behavior of polymer mortars. Composite Structures. 2013, 95, 564–568.

[6] BENMANSOUR A. N., AGOUDJILA B., GHERABLIA A., KARECHEA A., BOUDENNEBA A. Thermal and mechanical performance of natural mortar reinforced with date palm fibers for use as insulating materials in building. Energy and Buildings. 2014, 81, 98–104.

[7] BENMANSOUR A. N., AGOUDJIL B., BOUDENNE A., GARNIER B. Numerical investigation of heat transfer of silver-coated glass particles dispersed in ethylene vinyl acetate matrix. International Journal of Thermophysics. 2013.

[8] LI, Z., WANG, X., WANG, L. Properties of hemp fibre reinforced concrete composites, Composites Part A. Applied Science and Manufacturing. 2006, 37, 497–505.

[9] MEHTA, P. K.; MONTEIRO, P. J. M. Concreto: Estrutura, Propriedades e Materiais. São Paulo: Pini, 1994.
[10] QUEIROS Y. G. C., CLARISSE M. D., OLIVEIRA R. S., REIS B. D., LUCAS E. F. LOUVISSE A. M. T. Materiais Poliméricos para Tratamento de Água Oleosa: Utilização, Saturação e Regeneração. Polímeros: Ciência e Tecnologia, vol. 16, n° 3, 2006, p. 224-229.
[11] BASHAT, H. Managing Waste in Exploration and Production Activities of the Petroleum Industry. Biotechnology and Bioprocess Engineering. 2009, v. 17, issue 6, 1300-1305.
[12] ANNUNCIADO, T. R.; SYDENSTRICKER, T. H. D; AMICO, S. C. Estudo da Chorisia speciosa e outras fibras vegetais como sorventes para o setor de petróleo. 2005. 90p. Dissertação de Mestrado. Universidade Federal do Paraná – Curitiba.
[13] FERREIRA, T.R. Sorção de petróleo em fibras vegetais. 2009. 65p. Dissertação de mestrado. Universidade Federal do Rio Grande do Norte – Natal.
[14] YUSOF N. A., MUKHAIR H., MALEK E. A., MOHAMMAD F. Esterified Coconut Coir by Fatty Acid Chloride as Biosorbent in Oil Spill Removal. BioResources. 2015, v.10, n.04. Pp.8025-8038.
[15] GUILARDUCI V. V. D. S, MARTELLI P.B., GORGULHO H. F., CORRÊA, W. G., SANTOS, V. S. Avaliação do bagaço de cana natural e modificado como potencial sorvente de óleo vegetal. Revista Verde de Agroecologia e Desenvolvimento Sustentável V.11, Nº 4, p. 129-134, 2016.
[16] GUILHARDUCI, V. V. D. S., GORGULHO, HONORIA FATIMA E MARTELLI, PATRICIA BENEDINI. Efficiency of sugarcane bagasse-based sorbents for oil removal from engine washing wastewater. *water science & techonology*. 2017, Vol. 75.1, p. 9.
[17] ASSOCIAÇÃO BRASILEIRA DE NORMAS TÉCNICAS. NBR 7215: Cimento Portland – Determinação da resistência à compressão. 1996.
[18] ASSOCIAÇÃO BRASILEIRA DE NORMAS TÉCNICAS. NBR 5738: Concreto: Procedimento para moldagem e cura de corpos-de-prova. 2008.
[19] AMERICAN SOCIETY FOR TESTING AND MATERIALS. ASTM C348-14: Standard Test Method for Flexural Strength of Hydraulic-Cement Mortars. 2014.
[20] AMERICAN SOCIETY FOR TESTING AND MATERIALS. ASTM C580-02: Standard Test Method for Flexural Strength and Modulus of Elasticity of Chemical-Resistant Mortars, Grouts, Monolithic Surfacings, and Polymer Concretes. 2012.
[21] AMERICAN SOCIETY FOR TESTING AND MATERIALS. ASTM C597-09: Standard Test Method for Pulse Velocity through Concrete. 2010.
[22] BRITISH STANDARD. BS EN ISO 10545-3: Ceramic Tiles - Part 3: Determination of water absorption, apparent porosity, apparent relative density and bulk density. 1997.
[23] LOPES, M. M.; CASTELO BRANCO, V. T. F.; SOARES, J. B. Utilização dos testes estatísticos de Kolmogorov-Smirnov e Shapiro-Wilk para verificação da normalidade para materiais de pavimentação. Transportes. v. 21, n. 01, 2013, p. 59-66.
[24] AGGARWAL, L. K. Bagasse-Reinforced Cement Composites. Cement & Concrete Composites. 1995, Vol. 17, n. 2, Elsevier Science, p. 107-112.
[25] FILHO, J. A. M. Durabilidade química e térmica e comportamento mecânico de compósitos de alto desempenho reforçados com fibras de sisal. 2012. 161p. Tese de doutorado. Universidade Federal do Rio de Janeiro. Instituto Alberto Luiz Coimbra de pós-graduação e pesquisa de engenharia (COPPE). Rio de Janeiro.
[26] TEIXEIRA, R. S. Efeito das fibras de curauá e de polipropileno no desempenho de compósitos cimentícios produzidos por extrusão. 2015. 149p. Tese de doutorado. Universidade de São Paulo. Escola de engenharia de São Carlos,
[27] SALES, A. T. C. Retração, fluência e fratura em compósitos cimentícios reforçados com polpa de bambu. 2006. 273p. Tese de Doutorado. Pontifícia Universidade Católica do Rio de Janeiro – Rio de Janeiro.
[28] PICANÇO M. S., GHAVAMI K. Comportamento à compressão de argamassas reforçadas com fibras vegetais da Amazônia. REM: R. Esc. Minas, Ouro Preto, 2008, 61(1): 13-18.

STEEL FIBERS ADDITION EFFECT ON TENSILE STRENGTH OF CONCRETE

Silva, Mayara D. T. [(1)], Cocco, Guilherme D. [(1)], Bandeira, Matthews V.V.[(2)], Kosteski, Luis E. [(2)] e Marangon, Ederli [(2)]

(1) Grupo MAEC, Engenharia Civil, Universidade Federal do Pampa – Campus Alegrete, RS, Brasil.

(2) Grupo MAEC, Programa de Pós-Graduação em Engenharia, Universidade Federal do Pampa – Campus Alegrete, RS, Brasil.

https://doi.org/10.21452/bccm4.2018.02.24

Abstract

This paper is an experimental study on a concrete class C50, reinforced with steel fibers (1,5% by volume) and assessment its properties in the resistance to direct and indirect traction. Uniaxial tensile, splitting and flexural tensile tests were performed with and without fiber reinforcement. The standard axial compression strength of the two concretes was found. To perform the direct tensile tests, prismatic specimens with a cross section of 25 x 100 mm and a length of 400 mm were made. Plates made of metal were glued to the ends of the concrete samples with epoxy adhesive to couple them to the press in order to obtain tensile forces. The Splitting Test and Flexural Tensile test were performed according to Brazilian standards. It was verified that the direct tensile strength is the lowest found for both concretes, and it varies around 20% in relation to the tensile tests by splitting and flexural traction in the simple concrete and 30% for the reinforced one. No significant differences were found in the strengths obtained between the Splitting test and the Flexural Tensile test for simple and reinforced concrete. As expected, the test results indicate the positive influence of the fibers on the tensile strength of the concrete. Gains of around 40%, 50% and 60% were obtained with steel reinforcement in uniaxial tensile, splitting and flexural tensile tests, respectively. Also as expected, it was observed that the fibers played their role in increasing the ductility and control of composite cracks.

INTRODUCTION

The concrete presents compressive strength as the main mechanical property from the structural point of view, however, when subjected to tensile stresses, it behaves in a fragile manner and with little deformation at rupture. An alternative to overcome this behavior is to add steel fibers to the

matrix, which modify this fragile material behavior, significantly improving properties such as impact strength, crack propagation, ductility and toughness [1-2- 3-4-5].

So, by reinforcing a concrete with steel fibers, it is possible to revert its brittle character due to the stress transfer bridge formed through the fiber, causing the concentration of stresses at the ends of the concrete to be minimized and the speed of crack propagation reduced [6]. However, it is common the occurrence of dispersions and significant differences in the results, which can be generated by variations in orientation, embedded volume, geometry and uniform distribution of fibers in the composite [7].

To the extent that the benefits in the use of fibers stand out through tensile tests, it should be emphasized that these have low reproducibility and are not standardized and because of this, and other methods are often used to acquire this data. Indirect results are achieved through the splitting test and flexural tensile test, but present great variability among them [8]. In order to correct this fact, since these results differ from the reference and traction value of the direct traction (fct), the conversion coefficients 0,9 and 0,7 are applied for the results of splitting test and flexural tensile test respectively [9]. According to the same source, if these tests cannot be performed, the results of uniaxial tensile can still be obtained through the compressive strength of the concrete (fck) by equation 1.

$$f_{ct,m} = 0{,}3fck^{2/3} \quad (1)$$

Therefore, the present study aims to evaluate mechanical behavior of concrete samples with and without addition of steel fibers in terms of tensile strength measured in three different ways, uniaxial tensile, splitting and flexural tensile tests. The correlation between these different test methods is conferred in comparison with standards and bibliography. Moreover, it is sought to quantify the effect of fiber addition on the results obtained by these three methods.

MATERIALS AND METHODS

2.1 Methods

Two mixtures of concrete were executed. The simple or reference concrete (SC) with the mixture proportion of: 43% gravel, 14% sand type 1, 17% sand type 2, 18% cement, 0.24% superplasticizer and 8% (water / cement ratio of 0.44). For the (CRFA) the previous trace was reinforced with 1.5% of steel fibers. The cement used was the Brazilian Portland Cement CP-V ARI. The gravel has a maximum aggregate diameter of 12.7 mm and a fineness modulus of 6.77. The sands used were of natural origin (sand 1 and sand 2), and their granulometry were classified as averages, which presented characteristic diameters and modulus of fineness respectively of 0.425 mm and 1.16 for sand 1 and 0.6 mm and 1.38 for sand 2. A superplasticizer additive (MC-PowerFlow, company MC-BAUCHEMIE) with a density of 1.05 g / cm was also added. The metal fibers have a length of 30 mm with hook at each end, and aspect ratio of 65.

2.2 Methods

2.2.1 Molding and curing of concrete

The molding and curing procedure followed the standard NBR 5738 [10], using cylindrical specimens with a diameter of 100mm and a height of 200mm, and prismatic with two cross sections of 25x100mm and 100x100mm, both with length of 400mm. These were left at room temperature for 24 hours for hardening and were subsequently cured in a humid chamber for 28 days.

The tests to characterize the axial compression strength were performed with cylindrical specimens following the procedures described by NBR 5739 [11]. Measurements of displacements through a strain gauge were still made, and these were fixed to the surface of the specimen. The test speed was performed at 0.08 mm / min, displacement of the traverse of the machine.

2.2.2 Uniaxial tensile test

The uniaxial tensile tests were performed on concrete prisms with cross section of 25x100mm and 400mm in length. As shown in Figure 1, steel slabs were glued on both sides at the two ends of the specimens through epoxy adhesive. The metal plates are used for the transfer of charge to the specimens through a rigid system composed of the labeled connection between the steel plates and the machine through a connecting pin.

It should be emphasized that during the process of fixing the plates to the prisms, it was necessary to ensure alignment, not only between plate and prism, but also between the central holes of the plates, which serve as the connection between the system and the machine. This process is taken to minimize or minimize eccentricities in performing the assay. The speed of the tests was 0.5 mm / min of the traverse of the machine.

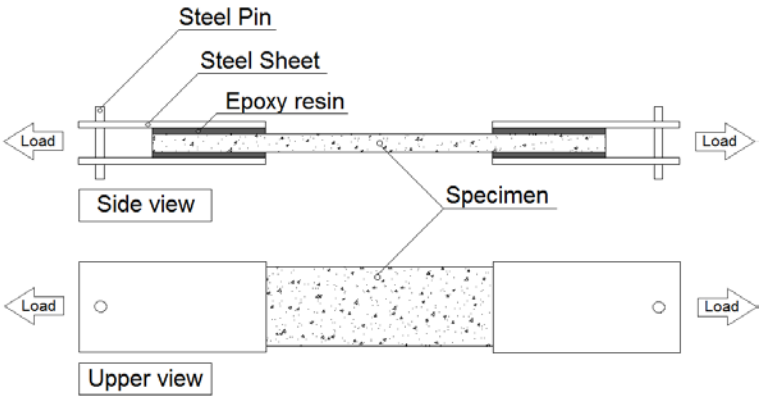

Figure 32: Detail of uniaxial tensile test

2.2.3 Splitting test

The tests were performed according to prescriptions and definitions of NBR 7222 [12]. The "Cumaru" (Dipteryx Odorata) wood, with an apparent density of 1090 kg/m³ and a compressive strength parallel to its fibers of 94,2 MPa [13], were used to perform the responsible wood stripe of the contact between the press and the test piece. The construction of the slabs was carried out according to the specifications of NBR 10024 [14] and the tests performed with a traverse displacement speed of 1.1mm/min.

2.2.4 Flexural tensile test

This test was performed according to NBR 12142 [15], thus imposing two concentrated loads, located at a distance of L/3 to the nearest support. The test was carried out at a speed of 0.5 mm / min of the displacement of the machine beam.

RESULTS AND DISCUSSION

The average compressive strength (fcj28) SC and SFRC, determined by the Uniaxial Compression test with three specimens for each trait, was 49.3MPa (CV = 3.2%) and 48.5MPa (CV = 3, 0%), respectively. Figure 2a shows the typical compressive stress x deformation curves found in the uniaxial compression test. It is observed in this figure that the addition of steel fibers to the concrete provides a relatively low improvement in its ductility and modulus of elasticity, on average 33 GPa.

The typical uniaxial tensile test curves are shown in Figure 2b. It was found that the SFRC obtained a performance in the order of 40% higher than SC against the ability to withstand the axial loads of traction. As mentioned by [6], this occurs due to the fact that the steel fibers arranged inside the matrix act as bridges between the fissures, controlling their propagation.

SFRC specimens also showed an increase in tensile strength obtained by the indirect tests normalized by NBR 7222 [12] and NBR 12142 [15], when compared to SC, 56% higher for the splitting test and 60% in the flexural tensile test. The typical force-displacement curves for the two analyzed traces found in the splitting test and in the flexural tensile test are presented in Figure 2c and Figure 2d respectively.

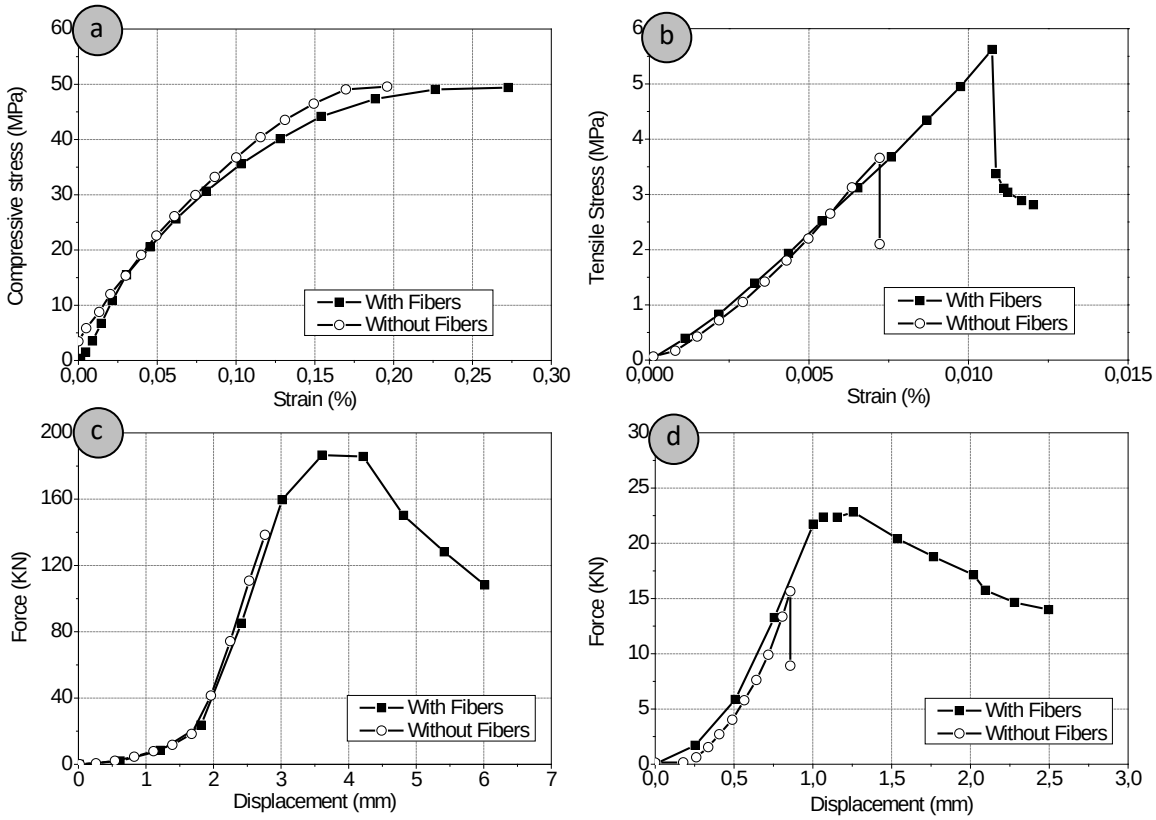

Figure 2: Typical stress-strain curves: a) Uniaxial Compression test and b) uniaxial tensile test and typical force displacement curve for c) splitting test and d) flexural test.

Figure 3 shows the results of the strengths obtained for each test performed on the concrete with and without fibers.

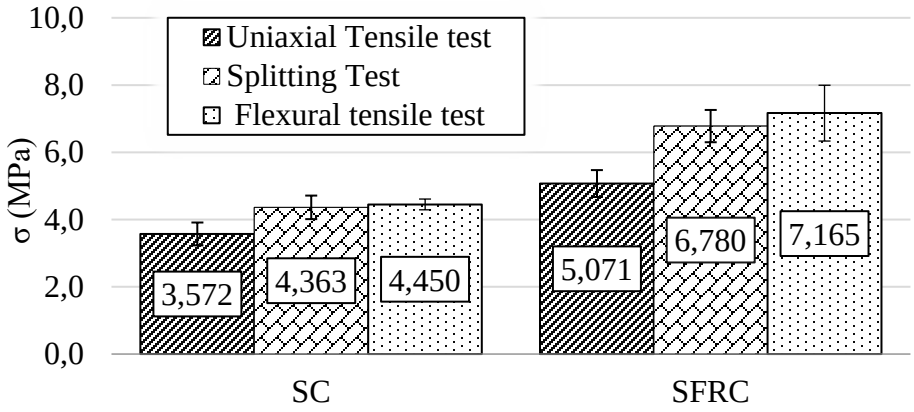

Figure 3: Tensile strength of SC and SFRC obtained with different methods. One standard deviation is plotted in the graphic.

Performing a variance analysis (ANOVA) of the results it was possible to verify that the interaction between the test methods and the use or not of fibers, are not statistically significant factors. However, both the test method performed and the addition or not of fibers modify the results. A comparison of means by the Fisher method [16] found that between the tensile and Brazilian test flexural tests there is no statistically significant variation for both SC and SFRC. These results are presented in Figure 3. Thus, according to the experimental tests carried out in this work, it can be inferred that the use of indirect methods to determine the tensile strength of concrete has an equivalence, independent of the addition or not of steel fibers.

This last observation is in agreement with NBR 6118 [9] which states that the uniaxial tensile test (fct) can be calculated from the uniaxial tensile tests found by the Splitting test (fct,sp) or flexural test (fct,f) applying corrective factors that are worth 0.9 and 0.7 respectively. In this work it was found that the correction factor should be of the order of 0.80 for the two indirect SC-related tests.

When the relationship between indirect and direct resistance to reinforced concrete was analyzed, it was possible to verify that the correction factor is between 0.7 and 0.75, regardless of the indirect method analyzed.

Two observations can be made here. First, the fibers increased the difference between the direct and indirect tensile strengths and, secondly, that the number of tests performed were not sufficient to find a statistically significant difference between the splitting test and the flexural test, but a difference in means was observed. In this way, further testing is necessary to ensure these results.

The analysis of the empirical relations for uniaxial tensile test from the compressive characteristic strength provided by NBR 6118 [9] (equation 1) for simple concrete are shown below (Table 1).

Table 1: Results submitted to stress relationship criteria according to NBR 6118 [9]

fck (MPa)	**f**ctm (MPa)		
	fctm	**f**tk,inf	**f**tk,sup
49,3	4,03	2,82	5,24

A compressive strength of 49.3MPa results in an average tensile strength of 4.03MPa. This value is 13% higher than the experimentally found average (3.57MPa). However, considering the intervals of lower and upper variation of 2.82MPa and 5.24MPa, respectively, all the results found in the direct and indirect tests concerning the simple concrete, would be within the limits of

variation imposed by reference to the norm. Also, according to NBR 6118 [9], the value to be used for the calculations that depend on the traction value is fct, inf, that is, before the values found the norm is very conservative, since the (3.57 MPa SC) the difference is 26%, whereas for concrete SFRC it is approximately 80% lower.

It is also emphasized the role of fibers in the control and development of multiple cracks [7], developed by the same ones through the better distribution of the tensions inside the composite [6]. Analyzing the typical curves of the tests (Figure 2), the addition of fibers in the cementitious matrix provides a product with a pseudo-ductile characteristic, with no brittle rupture and with significant increases in resistance to direct and indirect tensile stresses.

The type of rupture resulting from the different tensile tests studied is presented in Figure 4, where the images marked with a1, a2, a3 refer respectively to uniaxial tensile test, splitting test and flexural tensile of SC and the images marked with b1, b2, b3 are referring, respectively, to the same tests already mentioned, but for the SFRC. It is observed in the images of the concrete SC the appearance of practically a main fissure, whereas in the images of the concrete SFRC, multiple fissures appear, and in the surroundings of these main fissures a nucleation of small cracks, provoked by the pulling of the fibers.

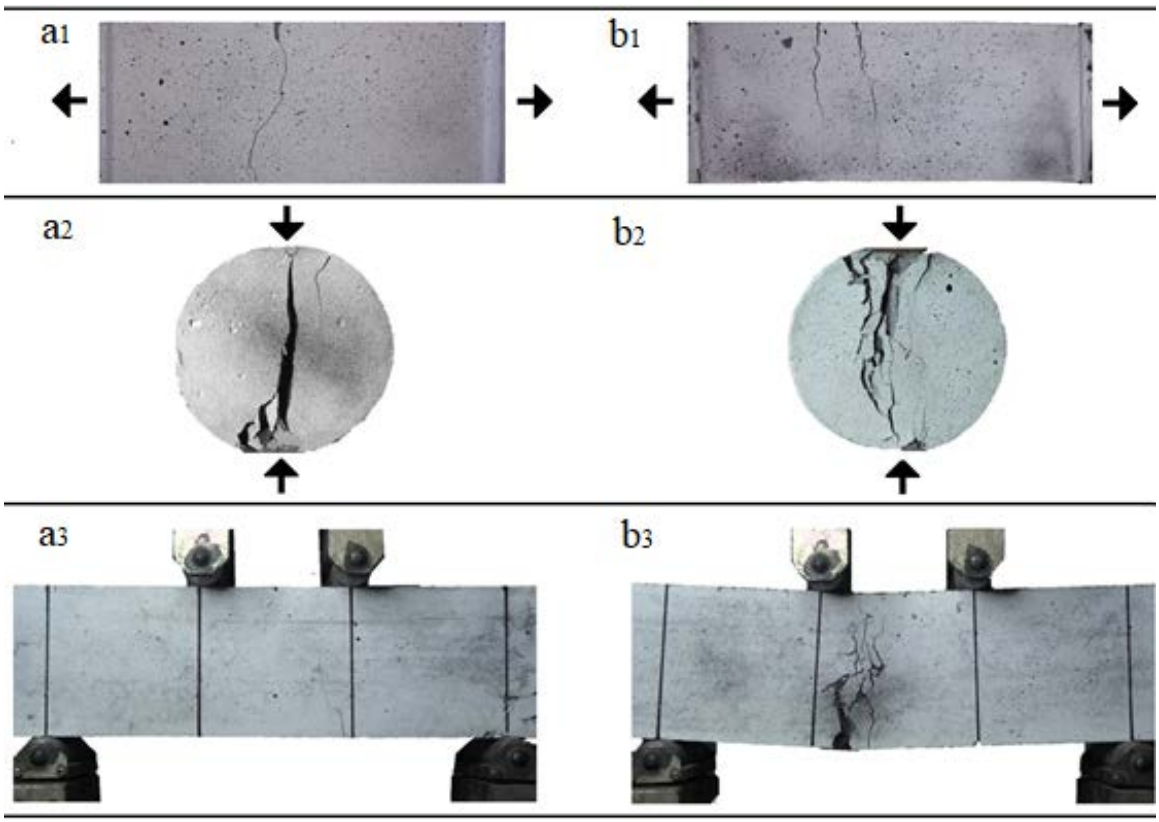

Figure 4: Comparison of (a) SC and (b) SFRC rupture versus (1) direct tensile test, (2) splitting test and (3) flexure tensile test.

4. CONCLUSIONS

In this paper an experimental study under the influence of fiber addition on the tensile strength of the concrete obtained by different methods is presented. The direct tensile strength of SC is 20%

lower than the resistance found in indirect tests. The SFRC concrete behaves in the same way, but with a difference of 25 to 30% lower than the other tests.

The addition of steel fiber to the simple concrete followed the expected and contributed to the increase of ductility and control of fissures. This addition also provided positive gains in increasing manner comparing the tests of uniaxial tensile, splitting and flexural tensile. In addition, it was possible to note that two types of indirect tests performed return values without significant variations. Finally, when compared to the values of tensile strength determined by NBR 6118 [9], it is observed that for the concrete containing fibers, the determined value is about 80% smaller, indicating that the standard is quite conservative.

ACKNOWLEDGEMENTS

The authors are grateful for the UNIPAMPA, FAPERGS and CNPQ support, who have made and did their best to carry out our research. they are especially grateful for the support of Pilecco Nobre, a constant partner in the MAEC research group.

REFERENCES

[1] Sirijaroonchai, K., El-Tawil, S., Parra-Montesinos, G., 'Behavior of high performance fiber reinforced cement composites under multi-axial compressive loading', United States, January, 2010 (Cement & Concrete Composites) 62-72.

[2] Domski, J., Katzer, J., Zakrzewski, M., Ponikiewski, T., 'Comparison of the mechanical characteristics of engineered and waste steel fiber used as reinforcement for concrete', Poland, August, 2017 (Journal of Cleaner Production) 18-28.

[3] Abbass, W., Khan, M. I., Mourad, S., 'Evaluation of mechanical properties of steel fiber reinforced concrete with different strengths of concrete', Saudi Arabia, April, 2018 (Construction and Building Materials) 556-569.

[4] Bencardino, F., Rizzuti, L., Spadea, G., Swamy, R. N., 'Fracture properties of steel fiber reinforced high strength concrete using work of fracture and size effect methods', Iran, July, 2017 (Composites: Part B) 17-24.

[5] Kazemi, M. T., Golsorkhtabar, H., Beygi, M. H. A., Gholamitabar, H., 'Experimental evaluation of fiber reinforced concrete fracture properties', Italy, January, 2010 (Construction and Building Materials) 482-489.

[6] Figueiredo, A. D., 'Concreto reforçado com fibras', Tese (Livre Docência em Materiais e Componentes de Construção Civil) - Escola Politécnica, University of São Paulo, São Paulo, 2011. Disponível em: <http://www.teses.usp.br/teses/disponiveis/livredocencia/3/tde-18052012-112833/>. Acesso em: 2018-04-17.

[7] Marangon, E., 'Caracterização material e estrutural de concretos autoadensáveis reforçados com fibras de aço', Tese (Doutorado) - COPPE/UFRJ, Rio de Janeiro, 2011.

[8] MEHTA, P.K., MONTEIRO, P. J. M., 'Concreto - microestrutura, propriedades e materiais', in 'IBRACON' 3rd Edn., São Paulo, 2008.

[9] NBR 6118, Projeto de estruturas de concreto — Procedimento. ABNT, 2014.

[10] NBR 5738, Concreto – Procedimento para moldagem e cura de corpos-de-prova. ABNT, 2003.

[11] NBR 5739, Concreto – Ensaio de Compressão de Corpos-de-prova Cilíndricos. ABNT, 1994.

[12] NBR 7222, Concreto e argamassa — Determinação da resistência à tração por compressão diametral de corpos de prova cilíndricos. ABNT, 2011.

[13] IPT - INSTITUTO DE PESQUISAS TECNOLÓGICAS. 'Catálogo de Madeiras Brasileiras para a Construção Civil', São Paulo, 2013.

[14] NBR 10024, Chapa dura de fibra de madeira — Requisitos e métodos de ensaio. ABNT, 2012.

[15] NBR 12142, Concreto - Determinação da resistência à tração na flexão de corpos de prova prismáticos. ABNT, 2010.

[16] William W.H., et al., 'Probabilidade e Estatística na Engenharia, 4ª ed. (Rio de Janeiro, Brasil, 2012).

PRODUCTION OF CEMENTITIOUS LAMINATES REINFORCED WITH FIBERS FROM AMAZONIA

Fernanda F. Oikava [(1)], João de Almeida M. Filho [(2)] and Gleicyanne O. de S. Portela [(3)]

(1) Master Student at Civil Engineering Postgraduate Program, Universidade Federal do Amazonas, Brazil.

(2) Doctoral Degree from Universidade Federal do Rio de Janeiro/COPPE, Brazil.

(3) Masters Degree from Universidade Federal do Amazonas, Brazil.

https://doi.org/10.21452/bccm4.2018.02.25

Abstract

This project's aim is to develop and characterize cementitious composites laminates reinforced with tissue of jute fibers. The laminates studied were reinforced with 2 layers of fiber, and some composites have treatment with polymer in their reinforcement, intending to improve the behavior of the fibers. Some cementitious compositions of laminates were changed with the desired objective of creating a free calcium hydroxide matrix, by partial replacement of cement by pozzolanic material, the metakaolinite. Bending tests were performed, allowing a comparison between the behavior of different types of laminates developed. The composites were submitted to mechanical tests after 180 days and the results make feasible the evaluation of fiber durability, indicating that the treatment is very effective.

Key-words: cementitious composites, pozzolanic material, flexural strength.

1. INTRODUCTION

Composite materials are made from two or more materials combined which stay distinct and identifiable, this combination result some final characteristics different from all the individual components.

The development of cementitious composites reinforced with natural textile fibers indicates a progress for society, because it is a material based on natural resources and still can achieve high resistance. It is a material with many applications in the civil construction. Reinforcements of structural elements, panels, partitions between environments and elements of cover are some examples.

The low production cost of the tissues of these fibers should be noted, which makes it feasible to work with this type of material and, especially, the encouragement generated to the numerous families of the varzea regions in the North of the country, who live from Jute fiber extraction, for example.

Jute fiber is found commercially in the fabric form and has good tensile behavior. When working with tissue-shaped fibres, for better uniformity in your distribution, when compared to the random fibers, in addition the better productivity. In addition it was realized that this fiber can show great performance as reinforcement of cimentícias arrays, increasing the resilience of the set.

The studies on this theme aim to enhance and develop a composite with the best conditions possible. Among various factors that can be considered, the present work emphasizes not only the mechanical strength of cementitious laminates but also the behavior of the set as the durability, since the cement hydration results in the calcium hydroxide, which tends to change the structure of the fibres [1].

Therefore, this research purpose the development and characterisation of cementitious composites reinforced with jute tissue. Being possible to carry out a brief performance comparison thereof, by means of tests of flexural strength, given some changes such as an matrix of free calcium hydroxide and the polymer tissue treatment.

2. MATERIAL AND METHOD

2.1 Methodology

It was considered different composites in their matrix, being composed mainly of sand, Portland cement and superplasticizer, changing the matrix took from the partial replacement of Portland cement by a Pozzolanic material, making it free calcium hydroxide. Mechanical characterization of plates produced from flexion tests.

With these data it is possible to draw up a comparative between the plates with different characteristics. The composites developed were manufactured with cementitious matrix and Jute fiber reinforcement in the form of fabric. As mentioned before, certain composites feature free matrix of calcium hydroxide, through the partial replacement of Portland cement by metacaulinita. As well as polymeric treatment performed in some composites reinforcement. The different types of laminates produced are described in Figure 1.

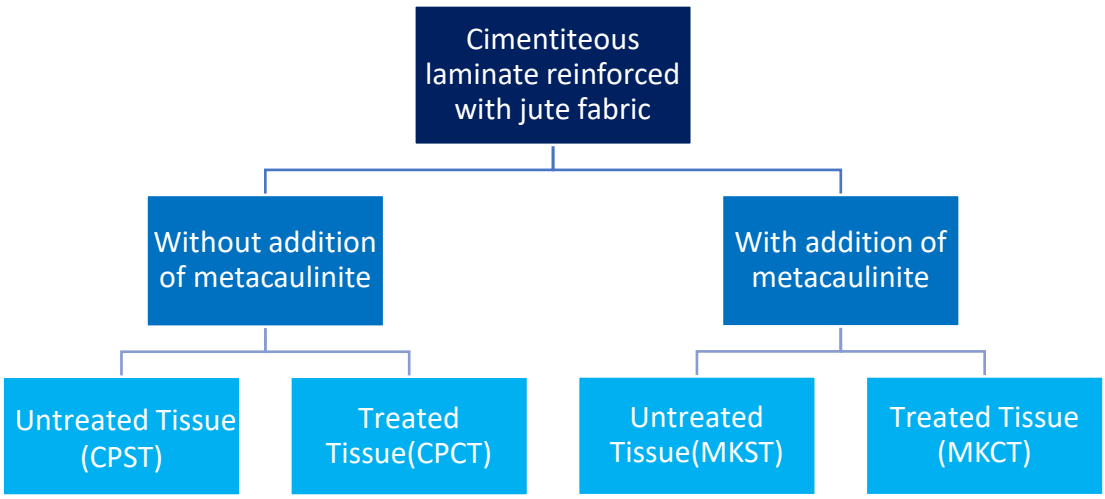

Figure 1 – Flow chart of composites produced.

2.2 Preparation and treatment of fabric fibers

The jute fiber fabric, Figure 2, is presented in the form of trade. The same was cut with 400x400mm measures and treatment of did by impregnation with varnish, Figure 3, since the polymer aims to form a physical barrier to protect the fiber from contact with the hydration products, improving the durability of composite [2]. We used a brush to spread the varnish on the fibers, then were extended in a line of ropes to dry for about 12 hours, an average temperature of 25ºc. After this process the tissue was maintained for a period of at least 24 hours in open container until the molding of composite.

Figure 2 – Jute fiber in the form of fabric.

Figure 3 – Preparation and treatment with varnish (Polymeric Treatment) of fibre tissue.

2.3 Preparation of mortar

Based on the data used by Melo Filho (2012) [3], to the mortar of the present work, 1 stroke: 1:0.4 (cementitious material: sand: water), and plasticizer content of 0.3%. For certain composites, made also an adaptation in the constituents used in the partial replacement of cement by replacing 50% of the mass of cement by 50% metacaulinite. The mass of materials for each dosage, with and without Pozzolanic material, is described in Table 1.

Table 1 – Dosages used

Dosage	Cement	Metacaulinite	Sand	Water	Superplasticizer
1	785,20g	-	785,20g	311,10g	5,30g
2	392,60g	392,60g	785,20g	311,10g	5,30g

The preparation of matrix follow these steps:

- Manually mixture of dry components (cement, metacaulinita and sand) for 1 minute;
- Addition of dry materials in mixer and mix for 1 minute on low speed;
- Dilution of superplasticizer on water and gradual release on mixer, until the mixture presents visually homogeneous;
- Remained the mixture for 2 minutes on low speed and 2 minutes on high speed.

2.4 Lamintates production process

The molding process of the laminates is done in a cast acrylic with dimensions 400 mm x 400 mm. The molding scheme, Figure 4 (a), is to put a layer of mortar and spread, Figure 4 (b), with the aid of a spatula. After the mortar is applied on a layer of fiber fabric and this process is repeated until conclude the third layer of mortar. At the end, there is a plate with 6 mm thick, and 2 layers of fabric and 3 layers of mortar, interspersed with each other.

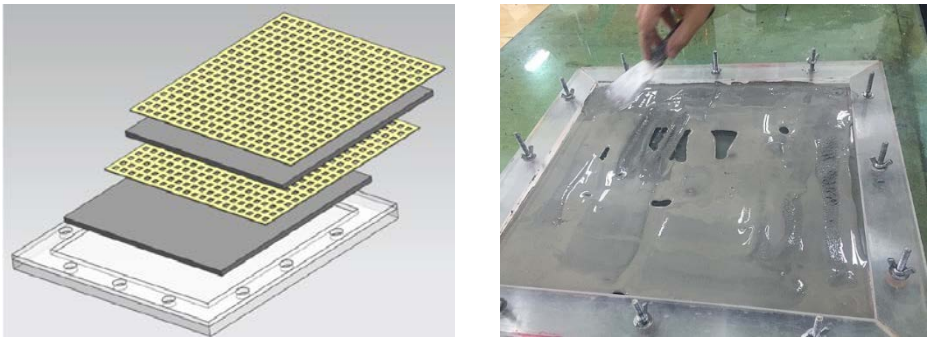

Figure 4 – Diagram of molding. Source: Portela, 2016 [4] (a) initial production process (b).

2.5 Pull test on bending of composites

The three-point bending test consists of applying a load in the center of the specimens supported by two points. The test was conducted on a universal testing machine Instron 5980. The speed used in the test was 0.5 mm/min, standardized for all bending tests. The gap between support was 250 mm

The results are expressed in flexion voltage, Equation 3, based on the resistance of materials, according to Equation 1 and Equation 2.

$$\sigma = \frac{M \,.\, y}{I_z} \tag{1}$$

$$I_z = \frac{b \,.\, d^3}{12} \tag{2}$$

$$\sigma_{máx} = \frac{3 \,.\, P \,.\, L}{2 \,.\, b \,.\, d^2} \tag{3}$$

Being that:

M = bending moment
y = distance to the neutral line
Iz = moment of inertia in relation to the neutral line
σ = flexion traction voltage;
P = load;
L = distance between the supports;
b = width of the sample;
d = thickness of the sample.

3. RESULTS AND DISCUSSION

The laminates produced weigh about 10 kg per square meter, and in Figure 5 are presented the typical stress-deflection curves obtained from flexion tests in 3 points, carried out in four different types of composites produced.

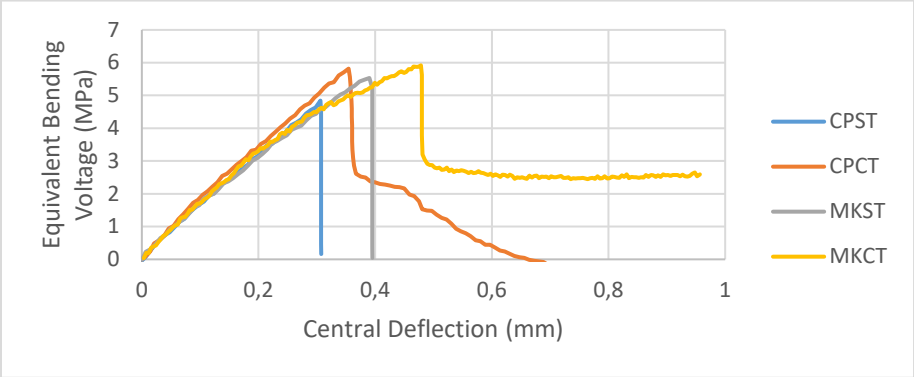

Figure 5 – Curves obtained from the bending test on 3 points

In Table 2 are expressed the results of first crack deflection, voltage of first cracking and stress cracking post.

Table 2 – Values of deformation and tension of the first fissure, post tension cracking and their coefficients of variation

Laminados	$d_{1f}\ (mm)$ CV (%)	$\sigma_{1f}\ (MPa)$ CV (%)	$\sigma_{pf}\ (MPa)$ CV (%)
CPST	0,31 (4,14)	4,84 (9,13)	0,00 (0,00)
CPCT	0,35 (23,25)	5,82 (22,25)	2,53 (0,00)
MKST	0,39 (0,00)	5,53 (0,00)	0,00 (0,00)
MKCT	0,47 (16,07)	5,92 (11,27)	2,91 (1,51)

The CPST laminates and MKST have brittle fracture mode. Comparing both free plates of calcium hydroxides, the PBX shows better results for deformation and breakdown voltage, which is 20% higher than in CPST, maintaining a post tension cracking.

MKST composites and MKCT were produced from the same array and not show difference of breakdown voltage very significant, so the 50% replacement of Portland cement by metacaulinite did not affect the resistance.

For the laminates that not show widespread rupture, has a residual voltage (σr), which can be associated with the polymer and fiber treatment compared with each other for analysis of array. The MKCT array has residual resistance almost uniform up to 1 mm of deflection, with an approximate value of 2.55 MPa, while the voltage a main post MKST cracking of 2.53 Mpa but that suffers constant decrease until it reaches 0 Mpa in 0,65 mm. It may be noted the difference of voltages of composites in 0,5 mm and 0,6 mm offset. Therefore, the laminate MKCT features far superior deformability when compared to other laminates produced.

4. CONCLUSIONS

- Treatment with polymer resin in natural fibre fabric shows an improvement in the mechanical behavior of the composite, as it raises both the tensile strength for bending as the deflection of the same, causing a break mode develop laminate less fragile.
- The use of metacaulinite provided a more durable matrix, since the composites with the partial replacement of cement showed best result of resistance to bending efforts.
- The use of natural fibre fabric has improved the features of the set, since the cementitious material by itself does not reach such resistance, and can be a promising material for construction.

REFERENCES

[1] GRAM, H. Durability of natural fibres in concrete. In: SWAMY, R. N. (Ed.) Natural fibre reinforced cement and concrete. London: Blackie and Son Ltd, 1988. v. 5.

[2] FIDELIS, Maria Ernestina Alves. Desenvolvimento e caracterização mecânica de compósitos cimentícios têxteis reforçados com fibras de juta. Rio de Janeiro: UFRJ/COPPE, 2014. 266p.

[3] MELO FILHO, J. Durabilidade química e térmica e comportamento mecânico de compósitos de alto desempenho reforçados com fibras de sisal. Universidade Federal do Rio de Janeiro, 2012.

[4] PORTELA, G. O. S.; Compósito Geopolimérico Reforçado com Tecido de Juta. Tese de Mestrado/UFAM. Manaus, Brasil. 2016.

INFLUENCE OF LOW CONTENT OF STEEL FIBRE ON CONCRETES PRODUCED WITH RECYCLED COARSE AGGREGATES WITH DIFFERENT LEVELS OF DENSITY

Antonio D. de Figueiredo [(1)], Ivie Pietra [(2)] and Luís A. G. Bitencourt Jr. [(3)]

(1) Department of Civil Construction Engineering, University of São Paulo, Brazil

(2) Joy Congero Constructions, Brazil

(3) Department of Structural and Geotechnical Engineering, University of São Paulo, Brazil

https://doi.org/10.21452/bccm4.2018.02.26

Abstract

When construction and demolition (C&D) waste is applied in concrete as aggregate, its porosity leads to a concrete with a reduced strength. Normally, this drawback induces to mix-designs with higher cement contents in order to compensate the strength reduction, which also increases the environmental impact of the material. The experimental study carried out in this work demonstrates that the flexural strength reduction is diminished with steel fibres reinforcement. This condition could compensate this drawback for some applications where the use of fibres is already forecasted. Recycled C&D aggregates with different density levels were produced to be added in concrete with different steel fibres contents. The experimental and numerical results demonstrate that the reduction of C&D aggregates oven-dry (OD) density will lead to a reduction on compressive strength without any influence of the fibres. Instead, the use of steel fibres could mitigate the flexural strength decrease. The performance of the concrete with recycled aggregates were approximated to the conventional concrete when the fibre content was increased on the first one. The behaviour was even closer when the w/c ratio was higher and the matrix strength was reduced for both types of concrete.

1. INTRODUCTION

Some of the essential aspects of sustainable development are the actions focusing the environment preservation and conservation of the rapidly diminishing ordinary resources. In that sense, efforts have been historically made, by trying to find out viable applications for construction and demolition (C&D) waste in order to avoid its disposal [1,2].

Normally, the use of C&D recycled aggregates will reduce the concrete strength proportionally to the aggregates density [3]. Normally, the decrease in the strength will be considered a problem that requires an increase in cement consumption or improve the aggregates through treatments. Both of them are responsible for increasing costs and environmental impacts. In that sense, some

recent studies have been carried out in order to turn viable the use of steel fibre reinforced recycled coarse aggregate concrete (SFRRCAC) [4]. Nevertheless, this research was not conclusive about the flexural strength due to some limitations of the experimental study.

The study of Gao & Zhang [5], focusing the analysis of SFRRCAC flexural performance, was also non-conclusive when low contents of steel fibre (less than 0.5%) were used, defining the behaviour of the material as non-obvious. In that sense, an experimental study was developed in order to better understand the behaviour of SFRRCAC varying the aggregate density. The main objective of the study is to establish relations between the matrix characteristics and the effect of steel fibre reinforcement on the flexural strength of the composite. In addition, numerical analyses are carried out in order to better understand the influence of the fibres on the composite behaviour for some mixtures considered in this research.

2. EXPERIMENTAL PROGRAM

2.1 Recycled aggregates preparation

The experimental study was performed based on the possibility of variation of the coarse aggregates density. The processing of recycled aggregates aimed the separation in different bands of density. This separation can be performed through heavy media separation, which is a process applied to the separation of minerals according to their densities by the use of organic liquids, solutions of inorganic salts or stable suspension of pre-determined density.

A sample of about one cubic meter of recycled aggregate was obtained from the Itaquera Recycling Plant located in the city of São Paulo, Brazil. The aggregates were produced by crushing C&D waste in a primary impact crusher. The retained 19.1 mm fraction was crushed again in a lab jaw crusher to fit the specified particle size distribution. The aggregates were sieved, and the fraction below 9.5 mm was discarded in order to provide similar mixture conditions to the ordinary crushed stone aggregate. Then, the coarse fraction (19.1–9.5 mm) was washed in order to remove any fine particles adhering to outer surfaces. The fraction was then dried on a ventilated oven at 110ºC for 24 h.

The C&D aggregates were prepared for the experimental program through a classification into 2 classes according to their porosity by sink–and–float procedure. The sink–float technique turns possible C&D aggregate particles separation into different OD density classes [3]. Therefore, this procedure turns possible to analyse the influence of the aggregates density in the composite behaviour. The equipment used in this experimental study is the same used by Angulo et al. [3]. The sink and float separation provided two ranges of specific weight: between 1.9 and 2.2 g/cm^3, and between 2.2 and 2.5 g/cm^3. The phase composition (cement based, ceramic, ordinary rocks) of each density class was determined by hand sorting and the result is presented in Table 1.

The characterization of the recycled aggregate is presented in Table 2 together with the ordinary coarse aggregate. The determination of the OD densities of coarse aggregates follow the Equation (1). The recycled aggregates were pre-saturated for 10 minutes in water to prevent the aggregate influence in concrete's water demand [6,7].

$$ODdensity = Md \div (MSSD - MW) \quad (1)$$

where,

ODdenstity is the density in kg/dm^3;

Md is the aggregate mass dried at 110ºC for 24 h (kg);

MSSD is the mass at saturated surface-dry (SSD) condition (kg), and

MW is the mass under water (kg).

Table 1: Characteristics of recycled aggregates used in the experimental program

Phase	1.9 < d < 2.2 (%)	2.2 < d < 2.5 (%)
Concrete and mortar	92.37	53.15
Red ceramic	2.43	0.18
White ceramic	2.81	0.17
Granite	0.48	44.91
Bitumen	1.73	1.59
Asbestos	0.18	0.00
Total	100.00	100.00

*d = density (g/cm³)

2.2 Ordinary materials

The ordinary crushed aggregate (granite), ordinary quartz river sand, Portland cement blended with roughly 35% blast furnace slag (CP II E type with a 28-day compressive strength of 32 MPa) and the dispersion admixture (Lignosulfonate) were obtained from the local market. The hooked end fibres used were produced from cutting steel sheet (fibre type A II according to Brazilian standard ABNT NBR 15530:2007), and also obtained in local market. The average yield strength of the fibres was 600 MPa with a length of 49 mm and rectangular cross section of 0.45 mm by 1.84 mm as informed by the producer.

Table 2: Composition of recycled aggregates used in the experimental program

Coarse Aggregate	Recycled 1.9 – 2.2 g/cm^3	Recycled 2.2 – 2.5 g/cm^3	Ordinary
Density (g/cm^3)	2.07	2.50	2.63
Water absorption (%)	6.75	2.16	0.03
Maximum size (mm)	19	19	19

2.3 Concrete mix proportions

The matrix mix-design was performed using the same method used by other Brazilian researchers [8] to evaluate the efficiency of recycled aggregate in plastic concretes with respect to its mechanical strength and durability, by maintaining the same workability conditions [9]. In this method, the optimum mortar proportion is determined in terms of dry materials (α) according to Equation (2). This determination was made for each range of density of recycled aggregate and for the ordinary aggregate. The α determination is normally done by visual evaluation. The optimum α is the minimum that provides to concrete a smooth aspect when the slump cone mould is removed. The α value is reported as the responsible for the concrete cohesive characteristics and could be related to the volume of mortar responsible to fill up the coarse aggregate voids.

Consequently, it will depend on aggregates characteristics. Once α value is determined, this value is kept constant for all mixtures in the study. A similar approach was adopted by other researchers as the equivalent mortar volume method [10] for recycled aggregate concretes. This approach allows keeping constant the relative volume proportion of mortar to coarse aggregates in concrete. In this particular case, the constant volume of coarse aggregates will avoid the influence of different aggregate densities in the mix-proportions. Table 3 presents the results of an optimum mortar obtained for each coarse aggregate.

$$\alpha = (1 + a) / (1 + a + b) \quad (2)$$

where,

α = mortar content in terms of dry materials;

a = fine aggregate mass proportion to cement;

b = coarse aggregate mass proportion to cement.

One of the fundaments of this method is to produce three concretes with the same workability conditions (fixed slump and mortar content), by varying the cement content. Therefore, three concrete mix proportions where produced adjusting the amount of water to obtain a consistency in the slump range of 80 ± 10 mm for all of them. Thus, it was defined families of concretes with constant consistency and mortar content, but with three different cement contents and w/c ratios. For each matrix obtained, it was used the following steel fibre contents: 0, 10, 20 and 40 kg/m^3. Where the addition of fibres has incurred loss of slump, water consumption was adjusted to yield a slump equal to 80 ± 10 mm. The slump was measured by the usual slump testing.

Table 3: Optimum mortar (α) for each coarse aggregate used

Coarse Aggregate	Recycled 2.07 g/cm^3	Recycled 2.50 g/cm^3	Ordinary 2.63 g/cm^3
α	54%	52%	48%

2.4 Specimens cast and testing

For each mixture, the specific gravity weight of the concrete was measured in fresh state using a recipient with a known volume. For each mixture five cylindrical specimens (10 x 20 cm) were produced from a single batch in order to measure compressive strength and water absorption. Compressive strengths tests were performed in a 2000 kN hydraulic Shimadzu® testing machine. For this test, three cylindrical specimens were tested for each mix composition. For each mixture, four prismatic specimens (10 x 10 x 40) cm³ were also produced in order to obtain the flexural strength values, using the same test machine. All the casted specimens remained in their moulds for 24 hours. The specimens were cured in a moist chamber with a temperature of 23 ± 2 ºC and relative humidity equal or greater than 95% for 28 days. Finally, the specimens were tested at the age of 28 days.

3. NUMERICAL ANALYSES

Numerical Analyses were performed to verify the contribution of the fibres on the flexural behavior of the composite with recycled coarse aggregates (2,07 g/cm³) and ordinary crushed aggregates (2,63g/cm³). Figure 1 illustrates the numerical model constructed using a discrete and explicit representation of the fibres, as proposed by Bitencourt Jr. [11], for steel fibre contents of 40kg/m³. It important to mention that the aggregates are homogenised in the matrix and the

effective mechanical properties are evaluated using the mixture theory in order to consider the porosity of these inclusions.

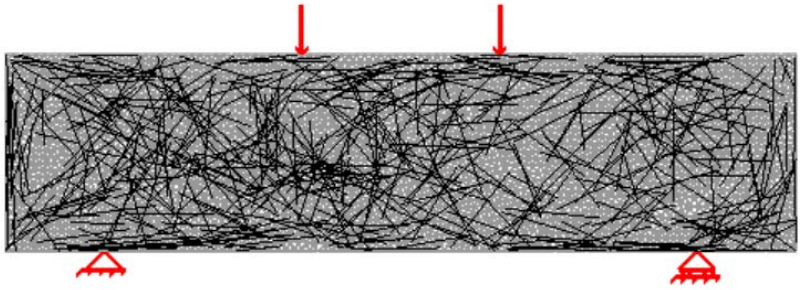

Figure 1: Numerical model to study the contribution of the fibres on the flexural behaviour of the composite

The steel fibres are modelled using two-node finite elements (truss elements) with an elastic perfectly plastic constitutive model with Young's modulus of 210GPa and yield stress of 1200MPa. They are positioned using an uniform isotropic random distribution, considering the wall effect of the mold.

A continuum damage model with two independent scalar damage variables is applied to describe the concrete behaviour under tension and compression. Three-node triangular finite element is used in the discretization of the concrete in finite elements. The material parameters adopted are listed in Table 4.

Table 4: Parameters adopted for the concrete in the numerical analyses

	Recycled 2.07 g/cm^3	Ordinary 2.63 g/cm^3
Young's modulus (MPa)	21000	35000
Poisson's ratio	0.2	0.2
Fracture energy (N/mm)	0.15	0.15
Tensile strength (MPa)	2.10	2.88
Compression stress damage threshold (MPa)	21.0	28.8
Compressive parameter A^-	0.89	0.89
Compressive parameter B^-	1.16	1.16

The concrete-fibre interaction is described by a non-rigid coupling scheme proposed by Bitencourt Jr. [11] by adopting an appropriate constitutive damage model to describe the relation between the shear stress (adherence stress) and the relative sliding between the concrete and each fibre individually. In Table 5 are listed the material parameters adopted.

Table 5: Parameters adopted for the concrete-fibre interaction in the numerical analyses

	Recycled 2.07 g/cm^3	Ordinary 2.63 g/cm^3
Maximum shear stress (MPa)	12.0	12.0
Residual shear stress (MPa)	4.5	4.5
Alpha	0.4	0.4
Slip s_1 (mm)	0.01	0.01
Slip s_2 (mm)	6.5	6.5
coupling constant (normal) (MPa/mm)	10^9	10^9
coupling constant (tangential) (MPa/mm)	10^3	10^3

More details about the numerical model employed can be found in Bitencourt Jr. [11].

4. RESULTS AND DISCUSSION

4.1 Compressive strength

The obtained results show that the compressive strength does not change with increasing content of steel fibres. Therefore, the fibre content will be ignored in the analysis of compressive strength. On the other hand, the w/c ratio is clearly a strong influence on compressive strength, as can be seen in Figure 2, where Abram´s Law curves obtained for each type of aggregates are presented. In this figure is possible to observe that the behaviour of the concretes with ordinary aggregates and recycled with 2.50 g/cm³ envelop density were very close. The mixtures produced with recycled aggregates with 2.07 g/cm³ presented a reduced level of strength for lower level of w/c ratio. When w/c ratio used was higher than 0.6, the performance of the mixtures became close. When the w/c ratio is higher, the porosity of the recycled aggregates ceases to be critical and the porous cement paste controls the fracture of the material.

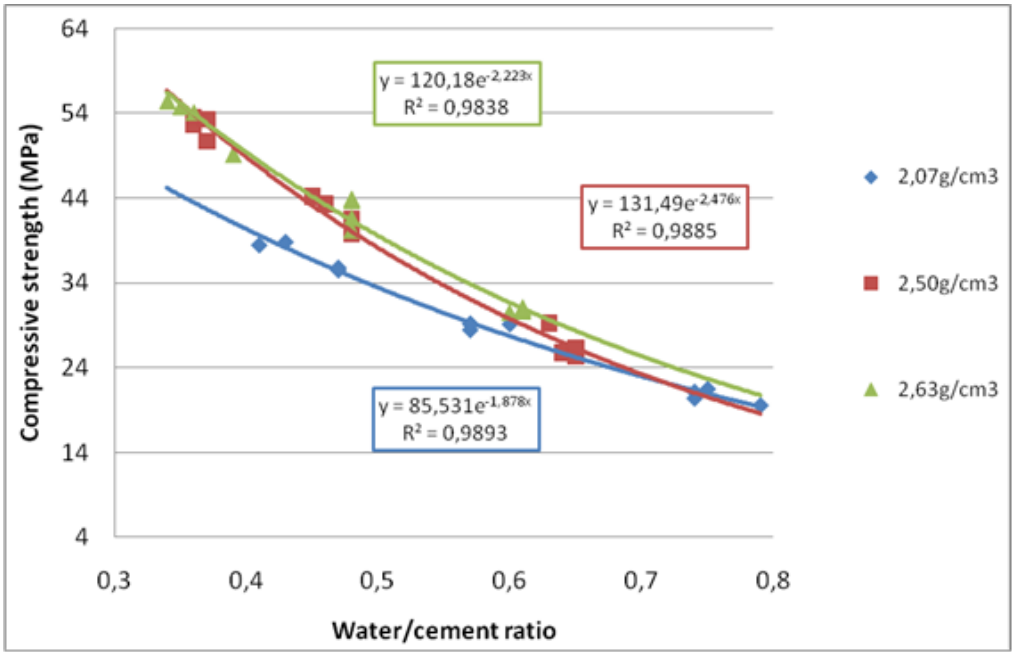

Figure 2: Correlation between the water absorption and w/c ratio for all types of coarse aggregates

4.2 Flexural strength and numerical simulation

In Figure 3, the correlation between the results of the flexural strength and the w/c ratio is presented for each coarse aggregate density class and each fibre consumption for an overall visualization of the behaviour. For flexural strength, the fibres showed an opposite behaviour to the compressive strength, and clearly demonstrate an effect in the results in combination with the coarse aggregate density class. For mix proportions with ordinary coarse aggregate (continuous lines), the increase in the steel fibre content did not influence the flexural strength. However, for mix proportions with recycled coarse aggregate, the flexural strength was increased proportionally to the fibre contents. This increase is more intense for the recycled aggregates with envelop density of 2.03 g/cm^3 (dotted lines) and low levels of w/c ratio. This pattern is the same observed in the study of KAYALI et al. [12] for lightweight concrete. The mixtures with envelop density of 2.50 g/cm³ presented an intermediate behaviour, but closer to the mixtures produced with ordinary aggregates.

The scatter of the results was greater when lower the w/c ratio used. In this case, the better adhesion of the fibre to the cement paste provided a greater ability to reinforce the system to inhibit the crack propagation. This condition brought the behaviour of the concrete with recycled aggregates closer of ordinary concrete as the fibre content was increased. On the other hand, for higher w/c ratios, the critical condition for defining the behaviour is the low paste strength. In this situation, the scatter of the results is smaller, similarly to the contribution of the fibre. This lower contribution of the fibre results from the decrease in its tensile transfer capacity due to the increase in the porosity of the paste. Contrary to the observed for compressive strength, it is possible to affirm that steel fibres help to minimize the reducing effect of flexural strength provided by the use of recycled aggregates.

The numerical simulation generated values of flexural strength very close to the experimental ones for the concretes of lower w/c ratio. In the case of ordinary aggregates, the simulation

provided flexural strengths of 6.5 and 6.6 MPa for concretes with 0 and 40 kg/m^3 of fibres, respectively. These values are very close to those obtained experimentally which corresponded to 6.5±0.7 MPa and 6.4±0.2 MPa. The simulation for concretes with aggregates with lower density produced flexural strengths of 4.6 MPa and 5.1 MPa for fibre consumption of 0 and 40 kg/m^3, respectively. These values were also very close to the average test results of 4.3±0.1 MPa and 4.9±0.5 MPa. The flexural strength gain obtained with the fibres was about 10% and 14% for the numerical simulation and experimental results, respectively, proving that the fibres contribute to minimize the strength reduction generated by the use of more porous recycled aggregates.

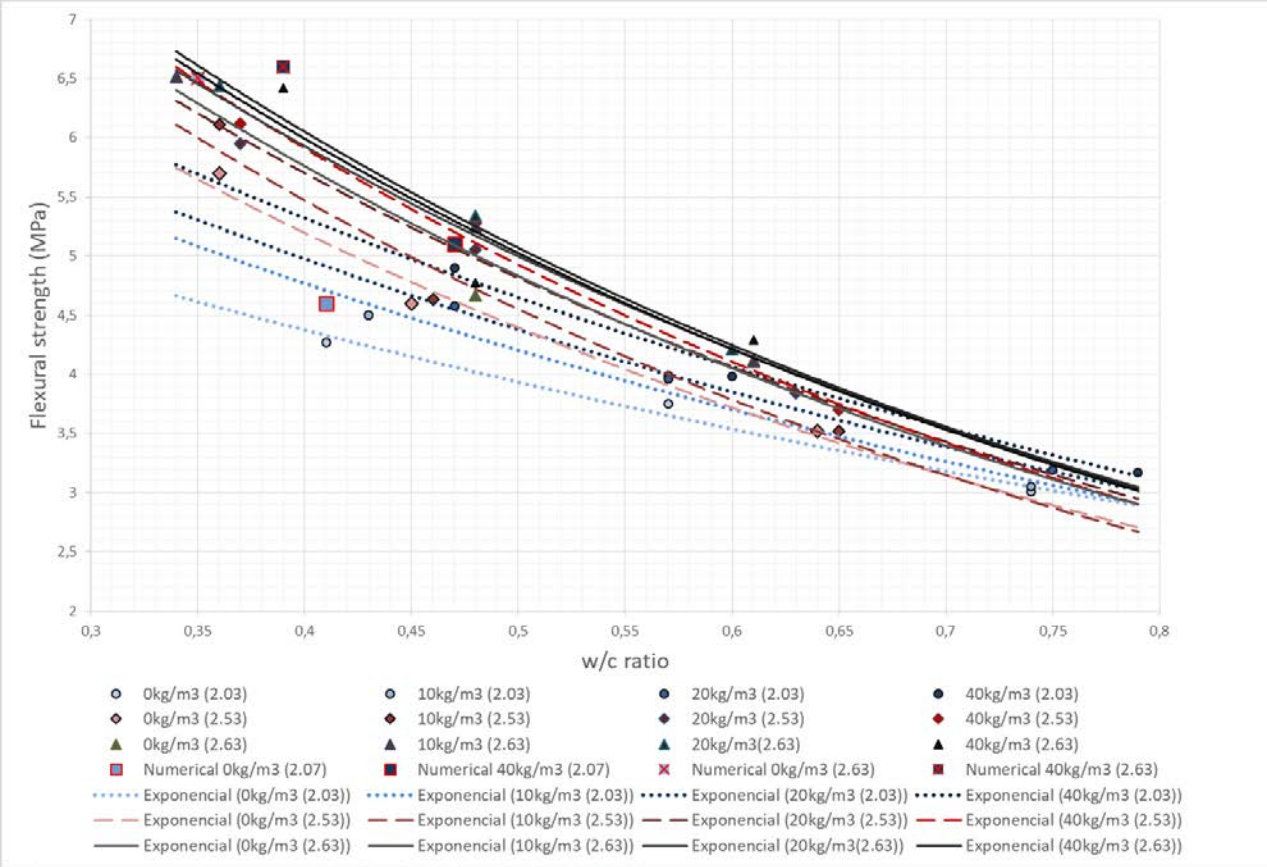

Figure 3: Flexural strength versus w/c ratio for all mix proportions with recycled and ordinary coarse aggregate

5. CONCLUDING REMARKS

The use of recycled C&D aggregates with envelope density closer to the ordinary aggregates bring minor reductions to the composite performance. The total replacement of ordinary aggregates by C&D recycled aggregate with envelope density of 2.50 g/cm^3 shows similar performance to the reference concrete. This finding is very similar to the results obtained by Choi & Yun [13] using a recycled aggregate with an envelope density of greater than 2.50 g/cm³. In this case, steel fibre contents higher than 20 kg/m^3 allow to SFRRCAC to present equivalent flexural behaviour to ordinary SFRC.

The reduction in flexural strength was more intense for the C&D aggregates with lower density (2.07 g/cm^3), which is more intense when the recycled aggregates present higher level of porosity and, also, when low levels of w/c ratio are used. In this case, the use of steel fibre provides an

approximation of the behaviour between ordinary SFRC and SFRRCAC. For w/c ratio higher than 0.6, the matrix flexural strength has no significant influence of the aggregates porosity and the fibre might not be effective because the cement paste is not dense enough to provide better conditions to stress transfer to the fibre. These findings where confirmed by numerical analysis and test results. The fibre contribution could be interesting in order to reduce the cement demand to enhance the strength of concretes made with C&D waste recycled aggregates in order to minimize the reduction in the flexural strength, a property usually found in applications such as pavements.

REFERENCES

[1] OIKONOMOU, N. D. Recycled concrete aggregates, Cement & Concrete Composites. 27 (2005), 315-318.
[2] RAO, A., JHA.K. N., MISRA, S. Use of aggregates from recycled construction and demolition waste in concrete. Resources, Conservation and Recycling 50 (2007) 71–81.
[3] ANGULO, S. C.; CARRIJO, P. M.; FIGUEIREDO, A. D.; CHAVES, A. P. JOHN, V. M. On the classification of mixed construction and demolition waste aggregate by porosity and its impact on the mechanical performance of concrete. Materials and Structures 43 (2010) 519–528.
[4] AHMADI, M.; FARZIN, S., HASSANI, A.; MOTAMEDI, M. Mechanical properties of the concrete containing recycled fibres and aggregates. Construction and Building Materials 144 (2017) 392–398;
[5] GAO, D., ZHANG, L. Flexural performance and evaluation method of steel fiber reinforced recycled coarse aggregate concrete. Construction and Building Materials 159 (2018) 126–136
[6] POON, C.S.; SHUI, Z.H.; LAM, L.; FOK, H.; KOU, S.C. Influence of moisture states of ordinary and recycled aggregates on the slump and compressive strength of concrete. Cement and Concrete Research 34 (2004) 31–36.
[7] GÓMEZ-SOBERÓN J. Porosity of recycled concrete with substitution of recycled concrete aggregate – an experimental study. Cement and Concrete Research 32 (2002) 1301– 1311.
[8] LEVY S. M, HELENE P. Durability of recycled aggregates concrete: a safeway to sustainable development. Cement Concrete Research. 34 (11) (2004) 175–180.
[9] FIGUEIREDO, A. D.; CECCATO, M. R. Workability Analysis of Steel Fibre Reinforced Concrete Using Slump and Ve-Be Test. Materials Research, 18 (2015), p. 1284-1290.
[10] ABBAS, A. et al. Durability of recycled aggregate concrete designed with equivalent mortar volume method. Cement & Concrete Composites. 31 (2009) 555–563
[11] BITENCOURT JR., L. A. G. (2015) Numerical modelling of failure processes in steel fiber reinforced cementitious materials. Ph.D. Thesis. Polytechnic School, University of São Paulo.
[12] KAYALI, O.; HAQUE, M.N.; ZHU, B. Some characteristics of high strength fibre reinforced lightweight aggregate concrete. Cement & Concrete Composites. 25 (2003) 207–213.
[13] CHOI, W., YUN, H., Long-term deflection and flexural behavior of reinforced concrete beams with recycled aggregate, Mater. Design. 51 (2013) 742–750.

MECHANICAL CHARACTERIZATION OF CONCRETE REINFORCED WITH COMPOSITE GLASS MACROFIBRE

Manzioni, Joelma P.(1); Real, Ligia V.(2); de Figueiredo, Antonio D.(3); Monte, Renata(4)

(1) Msc. Student. (2) Phd student. (3) Associate Professor. (4) Phd Researcher.

Department of Civil Engineering, Universidade de São Paulo, São Paulo, Brazil

https://doi.org/10.21452/bccm4.2018.02.27

Abstract

The introduction of fibre reinforced concrete (FRC) as a structural material in the fib Model Code 2010 represents an important advance for this technology. Nevertheless, it makes even more relevant the concern about the knowledge of parameters for quality control. In this context, the introduction of new fibres in the market should be followed with simple and reliable test methods to perform its evaluation. One of the major problems is the determination of fibres mechanical properties through tests that require the use of yarns, which are not easily available for the consumers. Other concern is related to difficulties associate to the execution of the FRC evaluation through the EN 14651 three-point bending test (3PBT) for regular quality control. This test was chosen by the fib Model Code to parameterize the FRC post-crack behaviour but requires more complex equipment and careful execution. This paper presents an experimental investigation using composite AR-glass macrofibre, performing the fibre characterization directly in the macrofibre and post-cracking behaviour measured with 3PBT test together with the double punch test (DPT). The tensile strength measured directly in the composite glass macrofibre showed good results, but the Young's modulus procedure needed further implementation to increase accuracy in deformation measurements. The results also indicate an excellent correlation between the 3PBT and DPT, what makes possible to perform regular quality control of FRC in a simpler mode, even when composite glass macrofibre was used.

1. INTRODUCTION

The adding of fibres to increase ductility in cementitious materials is a well stablished technology. Fibres can be considered as a randomly distributed reinforcement and they can provide an improvement in the crack distribution restraining the crack width. These fibres can be derived from materials with different characteristics, such as steel, glass or polymers, resulting in composites with different mechanical behaviour.

The new fib Model Code 2010 [1] introduces a parameterization which turns possible to consider the fibre reinforced concrete (FRC) as a structural material, providing a more assuredness condition to designers work. Fibres can be used as partial or total substitution of conventional reinforcement [2]. Nevertheless, fibre produced with materials with a Young´s modulus that are significantly affected by time and/or thermo-hygrometrical phenomena are not covered by this code. Consequently, polymeric macrofibres have been the subject of many studies focusing on creep behaviour [3]. These studies aim to produce subsidies for the specific parameterization of these fibres to be introduced in future revisions of the fib Model Code.

Alkali-resistant (AR) glass fibres have been successfully used as a reinforcement for very thin precast elements produced with cementitious materials, known as GRC (glass fibre reinforced concrete). The use of AR-glass macrofibre as main concrete reinforcement is already been studied, especially on structural applications characterized by a high degree of redundancy, as slabs on ground [4, 5] and concrete pipes [6]. More recently, a new glass macrofibre, composed of filaments grouped in bundle, was introduced in market. This new product was designed to provide post-cracking strength and increase toughness to concrete, improving impact and fatigue resistance. However, it is already known that the type of material with which the fibre is produced affects the FRC behaviour [7]. In this way, the characterization of the fibre is important because this will influence its capacity of reinforcement. The problem is the fact that the standard test methods prescribed for fibre characterization is based on tests performed with the yarn, which is normally inaccessible for users.

The three-point bending test (3PBT) carried out on a notched beam according to EN 14651 [8] is the method chosen by the fib Model Code 2010 to characterize FRC as a structural material. Nevertheless, alternative tests can be used if correlation factors with the EN 14651 are proven [1]. Alternatively, the double punch test (DPT) [9], also known as Barcelona test, has been indicated as a quality control test method for post-cracking evaluation. The DPT has a series of advantages over the traditional flexural beam tests, including (1) smaller and lighter specimens that can be more easily handled by a single technician; (2) specimens made in cylindrical moulds of Φ150 mm x 150 mm or that are cut from standardized cylinders of Φ150 mm x 300 mm normally used in compressive strength tests; and (3) tests can be carried out in a conventional testing machine without closed loop system. Several other advantages of the DPT were highlighted by researchers in comparison with bending tests, such as material and time saving, larger failure surface, lighter specimens and the possibility of testing cores extracted from structural elements [9, 10, 14]. Despite these advantages, the dissemination of DPT for characterization of FRC is limited by the lack of correlations with the 3PBT [9].

The objective of this paper is to present an experimental investigation using composed AR-glass macrofibre, performing the fibre characterization directly in the macrofibre and post-cracking behaviour measured with 3PBT and DPT. The paper also presents a correlation between the FRC post-cracking results obtained with both tests. This correlation is required by the fib Model Code 2010 to assume the DPT as an alternative method to the 3PBT.

2. METHODOLOGY

In order to characterize the FRC, initial tests were carried out to evaluate the geometric characteristics of the fibre, as well as its tensile strength and Young´s modulus. Then, the post-cracking behaviour was analysed by the 3PBT together with the DPT as described in more details in the following items.

– **2.1 Fibre characterization**

It is well known that the type of the fibre and its geometric characteristics directly affect the mechanical proprieties and the fibre-matrix interaction [7]. Therefore, these parameters and the tests used in this experimental program are presented in this section.

This study focused a macrofibre composed by AR-glass microfibres covered by a thermoset resin as shown in the Fig. 1.

Figure 33: Composite AR-glass macrofibre

To verify the geometric characteristics, thirty samples were analysed for length (L), diameter (d) and aspect ratio (length/diameter) determination. The length was measured with digital calliper with an accuracy of 0.1 mm. The density (ρ) of the macrofibres was evaluated using a helium gas pycnometer (Multipycnometer Quantachrome MVP 5DC) at 26 °C. The diameter (d) was obtained based on the Eq. (1). The mass (m) of the macrofibres were measured with a scale accuracy of 0.0001g.

$$d = \sqrt{\frac{4000.m}{\pi.\rho.L}} \quad (1)$$

–

Where,
d = diameter of the fibre (cm);
m = mass of the fibre (g);
ρ = density of the fibre (g/cm^3), and
L = length of the fibre (cm).

The ASTM D225 standard [11] describes the procedure to evaluate the tensile strength of many types of yarns, included the glass ones. As the method was developed for yarn testing, both sample length and fixing method cannot be adopted directed for macrofibres, which are shorter. However, the end consumer usually does not have access to yarn samples. Hence, the first need in evaluating the tensile strength directly on the macrofibre is to ensure its fixation, avoiding specimen slipping. In that sense, the macrofibre ends were embedded in epoxy resin, as showed in Fig. 2. Thus, it was possible to fix the samples in the claws, as it can be seen in Fig. 3. Fourteen samples were tested

in an Instron machine, Model 5569, with a load cell of 1 kN. The load was applied using the rate of displacement of 0.5 mm/min. The rupture of the fibres occurred in the centre of the sample and not in the epoxy resin, as shown in Fig. 4.

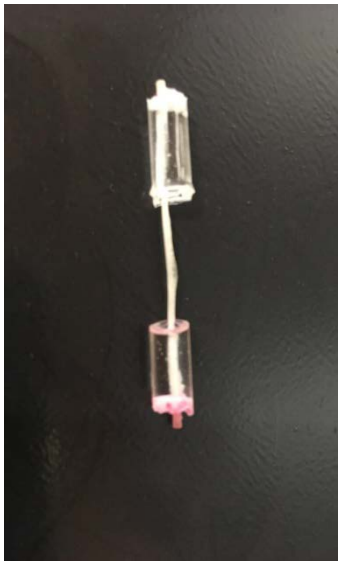

Figure 34: Microfibre embedded in epoxy resin before test

Figure 35: Macrofibre placed between the grips

Figure 36: Microfibre after test

The output of the tensile test was expressed by load (F) versus displacement (δ) curves, which are converted to stress (σ)versus strain (ε) curves. The tensile stress was calculated dividing the load (F) by the transversal section area calculated using the diameters previously obtained by Eq. (1).

The Young´s modulus was estimated as proposed by [12], considering the stresses related to the 10 and 30% of the macrofibres tensile strengths and their respective strains (ε), which were determined by dividing the value of the displacement (δ) by the distance between the grips (L).

– 2.2 FRC characterization

The concrete mix used in this study is presented in Table 1. The amount of superplasticizer was 0.05% by weight of cement. Three macrofibre contents were used in the experiment: 3.8, 7.6 and 11.5 kg/m³. A plain concrete was also tested as a reference.

Table 14: Mix design of the concrete

Cement [kg]	Fine sand [kg]	Coarse sand [kg]	Gravel 12.5 mm [kg]	Gravel 19 mm [kg]	Water [kg]	Superplasticizer [g]
394	134	536	532	532	193	394

The 3PBT followed the recommendations of the standard EN 14651 [8]. The samples were notched beams with dimensions equal to (150x150x550) mm³. The crack opening, measured as crack mouth opening displacement (CMOD), was evaluated with a clip gauge fixed at the notch (Fig. 5). The results are represented through a load-CMOD curve, as illustrated in Fig. 6.

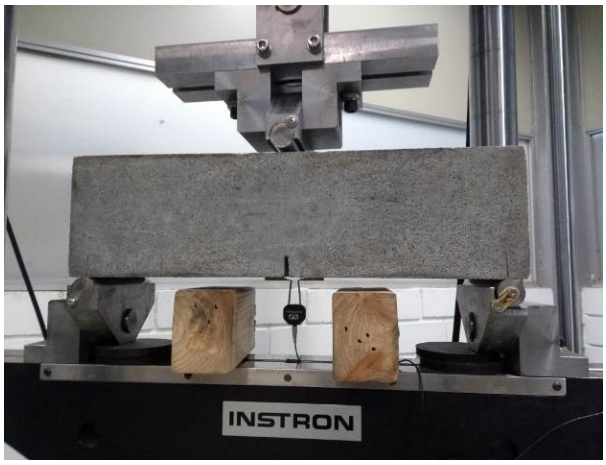

Figure 37: Three-point bending test (3PBT)

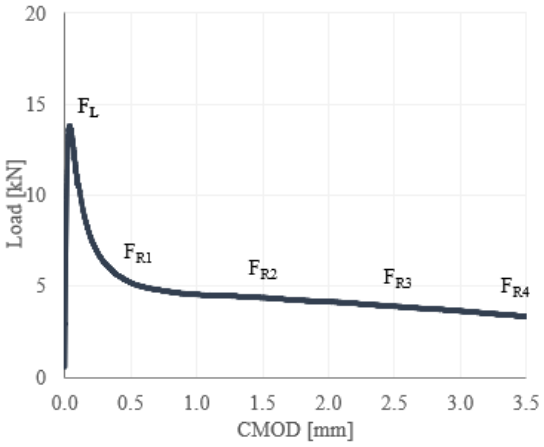

Figure 38: Schematic curve of 3PBT

The DPT was presented in [9] and standardized by UNE 88515 [13]. The initial configuration of the DPT involved measuring the circumferential displacement with a chain extensometer. Nevertheless, the use of this extensometer limits its applicability and an alternative setup controlling the axial displacement without the need of the extensometer was proposed [14] and used in this study. In this new test configuration, the cylindrical specimen is positioned between two steel cylindrical punches that receive the load applied by the plates of the press at a constant rate of displacement of 0.5 mm/min (Fig. 7). The test is characterized by the appearance of 2 to 4 radial cracks, as shown in Fig. 8. The cracking load (F_{cr}) is obtained when the stresses reach the tensile strength of the concrete matrix and, after that, the fibres bridge the crack resulting a residual strength. The results are represented through a load-axial displacement curve, as illustrated in Fig. 9.

Figure 39: Double punch test (DPT)

Figure 40: Cracking patterns observed

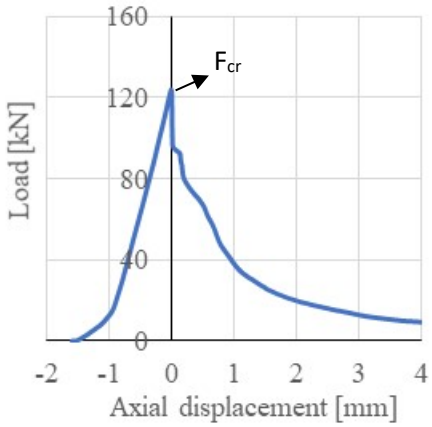

Figure 41: Schematic curve of DPT

The specimen used has a diameter and a height of 150 mm and was produced by cut from standardized cylinders of Φ150 mm x 300 mm. Six specimens were tested for each fibre content. The residual forces ($F_{R,i}$) were obtained from the curves for axial displacements of 0.5, 1.5, 2.5 and 3.5 mm. Also, the energy dissipated at these level of axial displacements ($E_{DPT,i}$) was determined in order to calculate the predicted residual 3PBT strength ($F_{3PBT,i}$), as proposed by [10] using the Eq. (2).

$$F_{3PBT,i} = \alpha . F_{DPT,i} + \beta . E_{DPT,i}^2 \quad (2)$$

The terms α and β are constants obtained in a regression considering both CMOD and axial displacements of *i* and are presented in [10].

3. RESULTS AND DISCUSSION

– 3.1 Physical and geometric characterization

The geometric characterization of AR-glass macrofibre is presented in Table 2. Standard features were obtained from product data sheet.

Table 15: Geometric characterization of composite AR-glass macrofibre

Characteristics	Product data sheet	Average	Standard deviation	CV (%)
Length [mm]	43 ± 2	43	0.93	2.2
Diameter [mm]	0.70	0.73	0.02	2.1
Density [g/dm³]	2.0 ± 0.1	1.96	0.03	1.5
Aspect ratio [length/diameter]	59 - 64	59	1.68	2.9

As presented in Table 2, the average of all the geometric features evaluated are in accordance with the product data sheet. The exception is determined diameter of glass macrofibre which was 4.3% larger than the declared dimension. The result is an average equivalent diameter. This difference could be justified by the fact that the diameter was calculated by the density method which is not affected by the pressure employed by the calliper load claws or the position of the fibre [15] as regularly used for this kind of determination.

The low coefficient of variation of all the features analysed must be noted because these parameters have an important influence in the AR-glass macrofibre mechanical properties determination.

– 3.2 Tensile strength and elastic modulus

The load-extension and stress-strain curves are shown in Fig. 10. The lighter colour curves represent the individual results and the darker one represents the average curves. The synthesis of the results is presented in Table 3, including the product data sheet provide by the manufacturer.

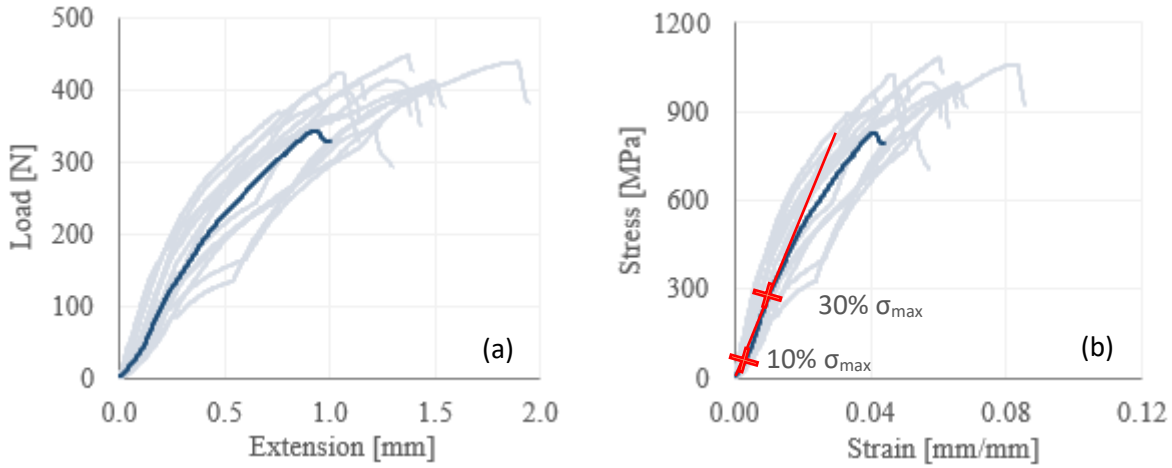

Figure 42: Curves of composite AR-glass macrofibre: (a) Load – Extension (b) Stress-Strain

Table 3: Mechanical characterization of composite AR-glass macrofibre

Parameter	Product data sheet	Number of samples	Average	Standard deviation	CV (%)
Load [N]	385		403	30	7
Tensile strength [MPa]	> 1000	14	973	72	7
Elastic modulus [GPa]	42		17	4	27

Considering the scatter of the results, the average value obtained for the maximum load was in accordance with the product data sheet. However, the average tensile strength was below the minimum value presented by the manufacturer. This condition could be explained by the fact that the fibre´s diameter presented by the producer is inferior the diameter measured in this study (Table 2), which was used to calculate the section area and the tensile stress consequently.

The average value obtained for the Young´s modulus was significantly less than the value informed by the manufacturer. Partially, this result can be explained by the previously observed reduction of the stress measured by this method in relation to the values presented by the producer. In addition, the measurement of the strain of the fibre considering the total displacement between claws is an approximation that tends to overestimate the strain. Therefore, the Young´s modulus measured here is underestimated in relation to the actual values. An alternative for future works is the use of a high-speed camera to measure fibre deformation in order to maximize the test precision.

3.3 FRC characterization

The basic mechanical characterization of the composites is presented in Table 4.

Table 4: Basic mechanical characterization of the composites

	Compressive strength [MPa]			Young´s modulus [GPa]		
Fibre content (kg/m³)	**3.8**	**7.6**	**11.5**	**3.8**	**7.6**	**11.5**
Average	47.4	47.8	47.2	27.7	29.2	28.1
Standard deviation	3.2	1.4	0.0	-	0.1	0.8
CV	7%	3%	0.0%	-	0.4%	2.7%

. The results showed very similar compressive strength and elastic modulus for the different macrofibre contents used. It is also notice that the scatter of the results is very low.

3.4 Three-point bending test

The results presented in Fig. 11 show the 3PBT load-CMOD curves obtained for all mixtures. The lighter colour curves represent individual results and the darker one represents the average curve.

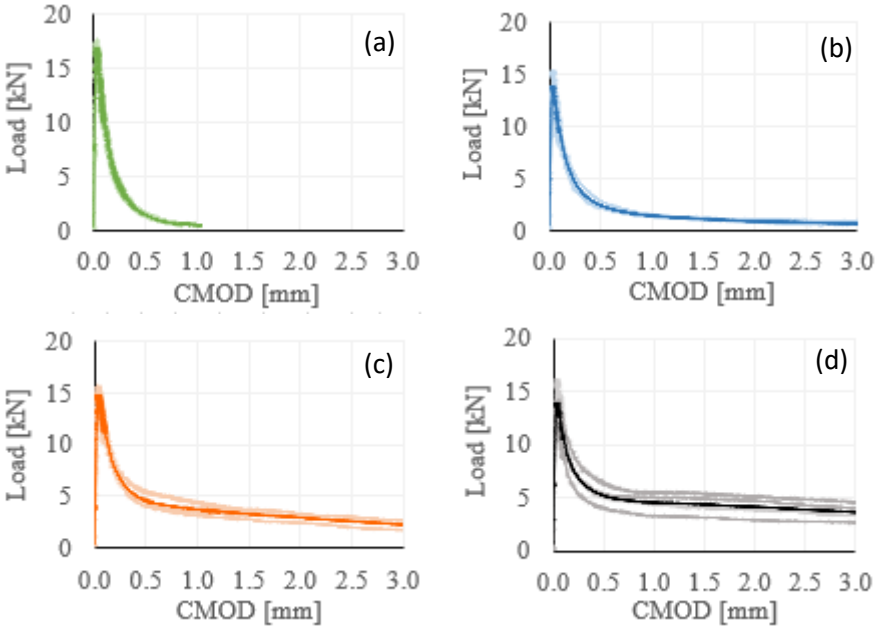

Figure 43: 3PBT load-CMOD curves: (a) Plain concrete (b) 3.8 kg/m³ (c) 7.6 kg/m³ (d) 11.5 kg/m³

The 3PBT results showed low variability, as can it be seen in Fig. 11. The three fibre contents tested exhibited the same tendency, reducing the load capacity with the development of the crack opening. In other words, the results showed a clear softening behaviour. For the plain concrete (Fig. 11a), the experiment was interrupted with a 1 mm crack opening in order to guarantee the safety of the equipment avoiding the collapse of the specimen over the clip gauge. It is also possible to notice that the limit of proportionality (F_L) was approximately 15 kN for all fibre contents and for the reference concrete. These results were considered statistically equal in the ANOVA test performed with 0.05 of significance (p-value of 0.214).

To classify the post-cracking strength of FRC, characteristic flexural residual strength values must be analysed for serviceability (F_{R1k}, CMOD = 0.5 mm) and ultimate (F_{R3k}, CMOD = 2.5 mm) conditions [1]. The characteristics flexural strength for crack opening, F_{R1k} and F_{R3k} and their respective variations are presented in Table 5.

Table 16 : Characteristics flexural strength of composite AR-glass macrofibre

Fibre content	**Parameter**	**Characteristic flexural strength**	**Standard Deviation**	**CV (%)**
Plain concrete	F_L	4.73	0.06	1
	F_{R1}	0.47	0.00	0
3.8 kg/m³	F_L	3.62	0.47	11
	F_{R1}	0.67	0.09	12
	F_{R3}	0.19	0.05	19
7.6 kg/m³	F_L	4.22	0.32	7
	F_{R1}	1.27	0.17	11
	F_{R3}	0.67	0.14	17
11.5 kg/m³	F_L	3.76	0.58	13
	F_{R1}	1.54	0.22	12
	F_{R3}	1.14	0.20	14

It is shown in Fig. 12 the linear correlation between the characteristic flexural strength measured at 0.5 and 2.5 mm crack openings with the fibre content. For both cases, the obtained coefficients of determination (R^2) were higher than 0.93. As can be seen in Fig. 11a, the plain concrete presented some residual strength for 0.5 mm crack opening (F_{R1k} = 0.47), but not at all for 2.5 mm. Consequently, the curve referring to f_{R3k} intercept the origin, while for f_{R1k} the value for plain concrete was included (Fig. 12). This consideration allows to estimate the residual strength for CMOD of 0.5 mm when fibre contents are under 3.8 kg/m³.

Furthermore, according to [1], the minimum requirement performance to consider a FRC as a structural material must to obey the following conditions: $F_{R1k}/F_{Lk} > 0.4$ and $F_{R3k}/F_{R1k} > 0.5$, where F_{Lk} is the characteristic value for the limit of proportionality. As can be seen in Fig. 13 and Fig. 14, linear trendlines were obtained when comparing the mentioned parameters with the tested fibre contents. Although, the contents of 7.6 and 11.5 kg/m³ presented F_{R3k}/F_{R1k} relations higher than 0.5, a fibre content of at least 12 kg/m³ was required to ensure $F_{R1k}/F_{Lk} > 0.4$. In order words, for the concrete matrix used in this study, it is necessary the minimum fibre content of 12 kg/m³ to substitute conventional reinforcement. This will ensure a FRC in 1.5b classification of *fib* Model Code 2010 [1].

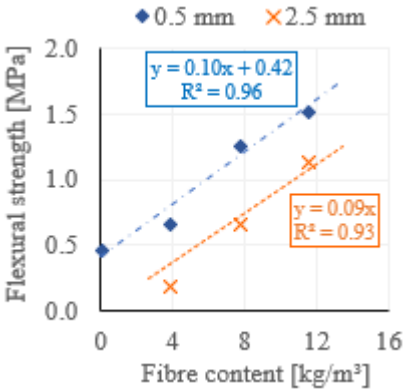

Figure 44: Characteristic flexural residual strength *versus* fibre content

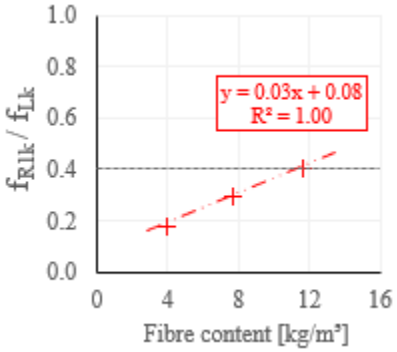

Figure 45: f_{R1k} / f_{Lk} *versus* fibre content

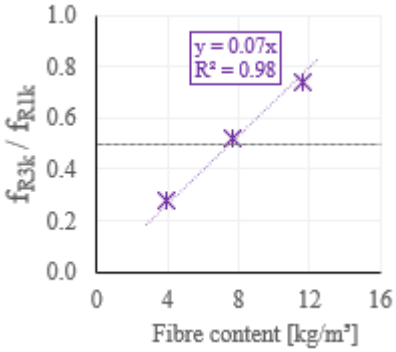

Figure 46: f_{R3k} / f_{R1k} *versus* fibre content

3.5 Double punch test

The results presented in Fig. 15 show the DPT residual load-axial displacement curves obtained for all FRC evaluated in this study. The lighter colour curves represent the individual results and the darker one represents the average curve. In order to better evaluate the results, the average relevant loads are presented in Table 6 together with standard deviation and coefficient of variation. The results permit to affirm that the cracking load (F_{cr}) is not influenced by the fibre content. The ANOVA test result a p-value of 0.827 for the effect of fibre content, greater than 0.05, indicating not significant influence of this parameter. On the opposite, the post-cracking behaviour increases proportionally to the fibre content, and the ANOVA test results a p-value of 0.001, lower than 0.05, indicating significant effect.

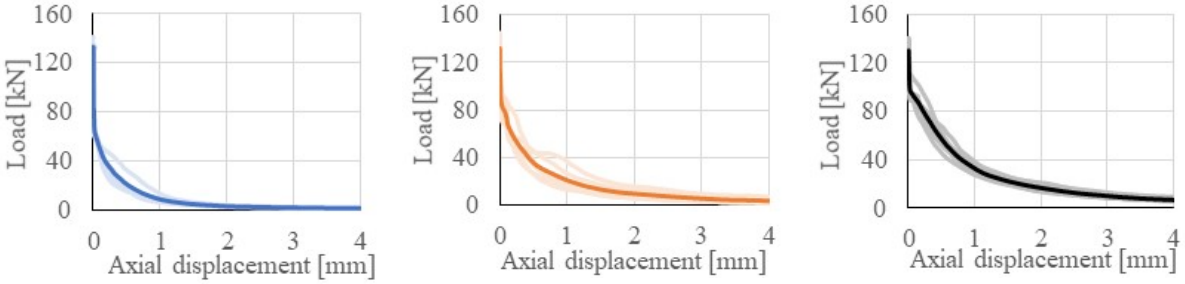

(a) (b) (c)

Figure 47: Residual load-axial displacement curves in DPT (a) 3.8 kg/m³, (b) 7.6 kg/m³ and (c) 11.5 kg/m³

Table 17 : Characteristics flexural strength of composite AR-glass macrofibre

Fibre content		**Relevant loads (kN)**				
		F_{cr}	**$F_{R,0.5}$**	**$F_{R,1.5}$**	**$F_{R,2.5}$**	**$F_{R,3.5}$**
3.8 kg/m³	Average	126.7	19.9	4.7	2.3	1.5
	Standard deviation	13.0	7.1	1.0	0.5	0.5
	CV	10%	36%	22%	21%	31%
7.6 kg/m³	Average	125.5	35.7	13.2	7.3	4.3
	Standard deviation	15.0	8.3	5.4	3.6	2.6
	CV	12%	23%	41%	49%	61%
11.5 kg/m³	Average	129.9	57.0	22.3	12.7	8.1
	Standard deviation	9.4	7.9	2.9	2.5	1.5
	CV	7%	14%	13%	20%	18%

Table 6 shows that lowest coefficients of variation (CV) were obtained for the F_{cr} results, between 7% and 12%. The residual loads present coefficient of variation between 13% and 61%, and the highest CV values are associated to higher crack openings ($f_{R,2.5}$ and $f_{R,3.5}$).

The correlation between the DPT and the 3PBT was determined in two ways. First, the experimental results of residual loads obtained from both tests were correlated, considering the axial displacement for DPT and CMOD for 3PBT (Fig. 16). The results presented in Fig. 16 express the excellent correlation between the experimental results of residual loads measured with the 3PBT and DPT. The coefficients of determination (R^2) are higher than 0.89, for values of *i* corresponding to 0.5 mm. This may be attributed to the differences in terms of crack formation in both tests, whose influence is evident for low displacements [9].

Fig. 17 shows a second correlation between the results obtained from 3PBT and the corresponding result estimated with Eq. (2) from the results of the DPT for the displacements *i* of 1.5, 2.5 and 3.5 mm. The predictions made with Eq. (2) really approaches the results from the 3PBT, with a R^2 of 0.97, confirming the potential of DPT use as an alternative test method to quality control of FRC.

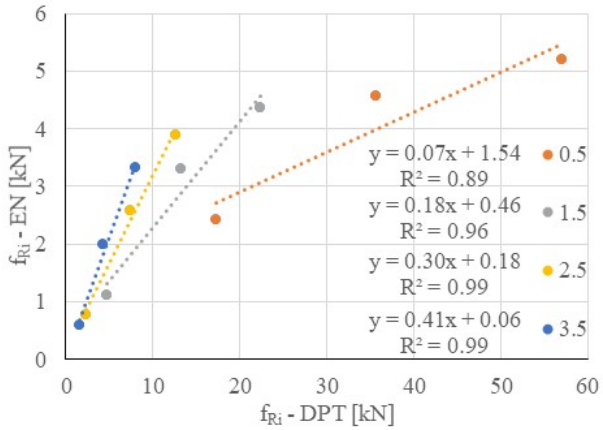

Figure 48: Correlation with experimental results of 3PBT and DPT

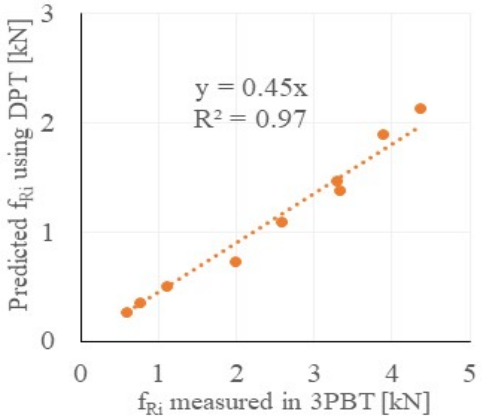

Figure 49: Correlation between experimental and predicted 3PBT loads

4. CONCLUSIONS

This paper proposes an experimental investigation using composed AR-glass macrofibre, performing the fibre characterization directly in the macrofibre and measuring the post-cracking behaviour with 3PBT and the DPT. The following conclusions may be derived from the results of this study.

- The geometric characterization presents very low coefficient of variation of the results, which indicates high-quality control in the production of these composed macrofibre. Only the diameter measurement presented a significant difference in relation to the producer declared dimension. However, the diameter measurement procedure used in this study was more reliable because is less susceptible to be underestimate due to the effect of the pressure of the calliper claws on the macrofibre.
- The tensile strength results demonstrate the feasibility of direct tensile testing method made directly in the composed AR-glass macrofibre. It is a meaningful contribution for this material consumers that do not have access to yarn samples. Conversely, the test method was not effective to the Young´s modulus determination because presented a tendency to underestimate the measured value. Nonetheless, a high-speed camera may be used to measure fibre deformation in future works in order to improve the accuracy of the test.
- The 3PBT results showed low variability and the three fibre contents tested exhibited a softening behaviour. The influence of the contents is depicted in the linear trendlines obtained in characteristic flexural strength versus fibre content for 0.5 and 2.5 mm CMOD. This kind of correlations could be a very useful tool for FRC mix-design.
- In the present study, the requirements of the fib Model Code for the definition of minimum FRC behavior as structural material were only fully met when the glass fibre content of 12kg/m^3 was used. This content ensured the classification of the material in the category 1.5b classification of fib Model Code 2010.
- The DPT results also exhibited a softening behaviour but presenting higher dispersion in comparison to 3PBT. The cracking load (F_{cr}) is not influenced by the fibre content and the post-cracking behaviour increases as the fibre content increases, as expected. The results of DPT and 3PBT were exceptionally well correlated. The coefficient of determination (R^2) is 0.89, for values of *i* corresponding to 0.5 mm, and higher than 0.96 for other values of *i*. Also, a very good correlation ($R^2 = 0.97$) was obtained between the experimental 3PBT results and the corresponding result estimated from the results of the DPT. This fact confirms the potential DPT use as an alternative test method to perform the regular quality control procedure of the FRC, even if composite AR-glass macrofibre was used.

ACKNOWLEDGEMENTS

This research was supported by the Escola Politécnica da Universidade de São Paulo. The opinions expressed in this paper are those of the writers and do not necessarily reflect the views of the sponsors.

REFERENCES

[1] Fédération Internationale du Béton - Fib. Model Code for Concrete Structures 2010. Switzerland, 2013. 402p.

[2] di Prisco, M., Plizzari, G., Vanderwalle, L. 'Fibre reinforced concrete: new design perspectives', Materials and structures, 42 (9) (2009) 1261-1281.
[3] Serna, P., Llano-Torre, A., Cavalaro, S., 'Creep Behaviour in Cracked Sections of Fibre Reinforced Concrete'. RILEM Bookseries, vol 14. Springer, Dordrecht.
[4] Barragan, B. et al. 'Design of Glass Fiber Reinforced Concrete floors according to the fib Model Code 2010'. In 'FRC 2014', Joint ACI-fib International Workshop, Montreal, 2014.
[5] Löber, P. et al. 'Glass fiber reinforced concrete for slabs on ground - Material characterization and application'. Proceedings of the International Conference FIBRE CONCRETE. (2015) 302-313.
[6] Peyvandi, A., Soroushian, P., Jahangirnejad, S. 'Enhancement of the structural efficiency and performance of concrete pipes through fiber reinforcement'. Construction and Building Materials, 45 (2013) 36-44.
[7] Bentur, A.; Mindess, S. Fibre reinforced cementitious composites, New York: Taylor & Francis, 2007.
[8] CEN (European Committee for Standardization). EN 14651. Test Method FOR Metallic Fiber Concrete – Measuring the Flexural Tensile Strength (Limit of Proportionality, Residual), 2007. 20p.
[9] Molins, C., Aguado, A., Saludes, S. 'Double Punch Test to control the tensile properties of FRC (Barcelona test)'. Materials and Structures, 42 (4) (2009) 415-425.
[10] Galeote, E. et al. 'Correlation between the Barcelona test and the bending test in fibre reinforced concrete'. Construction and Building Materials, 152 (2017) 529-538.
[11] ASTM (American Society for Testing Materials). ASTM D2256/D2256M: standard test method for tensile properties of yarns by the single-strand method Philadelphia, 2015. 13p.
[12] Cáceres, A. R. E., Galobardes, I., Figueiredo, A.D., 'Mechanical Characterization of Synthetic Macrofibres'. Materials Research, 19 (2016) 711-720.
[13] AENOR (Asociación Española de Normalización y Certificación). UNE 83515: hormigones con fibras - determinación de la resistencia a fisuración, tenacidad y resistencia residual a tracción - método Barcelona. España, 2010. 10p.
[14] Pujadas, P. et al. 'Multidirectional double punch test to assess the post-cracking behaviour and fibre orientation on FRC'. Construction and Building Materials, 58 (2014) 214–224.
[15] Cáceres, A. R. E., et al. 'Geometric characterization of polymeric macrofibers'. Rev IBRACON Estruturas E Materiais. 8 (2015) 644–655.

PERFORMANCE EVALUATION OF PRESTRESSED CONCRETE SLEEPERS REINFORCED WITH STEEL FIBERS

Paula Helene Toraldo Teixeira Silveira (1) and Flávio de Andrade Silva (1)

(1) Department of Civil and Environmental Engineering, Pontifícia Universidade Católica do Rio de Janeiro, Brazil

https://doi.org/10.21452/bccm4.2018.02.28

Abstract

The primary elements of railway superstructures are sleepers, which distribute the wheel loads of trains from rails to the ground. While wood was previously the dominant material used in sleeper construction, concrete is now becoming more common. Over time, a continuous increase of load, speed and traffic on railways have caused a rise in damage to prestressed concrete sleepers but have also stimulated efforts to improve them. This research investigates the performance of prestressed concrete sleepers reinforced with steel fibers, including their load-carrying capacity and energy absorption characteristics. Negative bending moment tests were conducted at mid-span of reinforced concrete sleepers with 0.5% of the 35 and 60 mm long fibers. The results of the research have indicated that the use of steel fibers in concrete leads to an increase in load-carrying capacity, energy absorption, and consequently, improvements in the service life of structures, including sleepers. The experimental results were verified by theoretical calculations. The increment ratio of the ultimate moment by the fiber addition was the same for the theoretical and experimental analyses.

Keywords: Prestressed concrete sleepers; steel fibers; mechanical property; structural behavior.

1. INTRODUCTION

Sleepers are one of the core elements of the permanent track, whose main functions are: to support and maintain the distance between the internal faces of the rails (gauge), the vertical, lateral and longitudinal stability of the track, to transmit to the ballast the loads coming from the rails and to partially cushion vibrations. The aforementioned characteristics make it necessary for the sleeper to have a high resistance, which in general leads to a high stiffness. At the same time, elasticity is also necessary, since it must be able to withstand very high impact forces and dynamic actions [1].

Wood was the first material to be used as a sleeper, when railroads were beginning to emerge in Europe and the United States. Wood is a suitable material for dynamic demands. It is a good electrical and acoustic insulator, however due to a limited supply of resources, the environmental

requirements, and difficulty of recycling due to the chemical treatment by which the sleepers pass, the use of this material is decreasing [2].

Prestressed concrete sleepers are the most used sleepers nowadays due to their technical superiority, considering: long-term durability, rails stability, larger self-weight, ideal for high speed and high loads, lower life cycle cost and it is sustainable, considering the fact that it does not need chemical treatments and it can be recycled [3].

Despite the good performance, the prestressed concrete sleepers also present failures. In some of the studies [4–6], the perceived damages in concrete sleepers were largely related to cracking. When cracking occurs, the deterioration of concrete is accelerated, creating pathways for the deterioration of steel. The concrete matrix loses the ability to transfer tension through the crack causing a concentration of stress in the possibly deteriorated prestressing wires, thus leading to rupture of the structure.

Considering the high costs related to the interruption of a track, it is of great interest for the railway industry that its elements have a high lifespan. Cracking on concrete sleepers causes its service life to be reduced. Fiber reinforced concrete controls crack propagation, the use of this reinforcement also allows tensions to be transferred through the cracks, reducing the demand for the prestressing wires. For these reasons, steel fiber reinforcement have been researched as good option to be used on the sleeper industry [7–10].

2. MATERIALS AND MIXING PROCEDURE

The concrete composition is presented on table 1. The values are in mass for the volume of 1 m^3 of material.

Table 1. Concrete composition

Fiber volume ratio		**0%**	**0.25%**	**0.50%**	**1.00%**
Cement CPV	1	410 kg	410 kg	410 kg	410 kg
Sand	1.39	569 kg	569 kg	569 kg	569 kg
Coarse aggregate	3.15	1293 kg	1286 kg	1279 kg	1266 kg
Water		180 kg	180 kg	180 kg	180 kg
Superplasticizer		2.6 kg	2.6 kg	2.6 kg	2.6 kg
Steel fiber			19.6 kg	39.3 kg	78.5 kg
Water/Cement ratio 0.44					

2.1 Materials

The cementitious material used in the production of the concrete was the Brazilian cement type CPV. The sand had the maximum diameter of 4.76 mm and the coarse aggregate 19.1 mm. Superplasticizer (Grace ADVA™ CAST 525) was also mixed together with the other materials. The water/cement ratio of the mix was 0.44 and the average compressive strength after 28 days was 60 MPa

2.2 Fiber type

Two different types of steel fibers were used, all of which had hooked ends and are supplied glued. The first is 35 mm long and it has 0.55 mm diameter, it is named by the manufacturer as RC 65/35. The second is 60 mm long and it has 0.75 mm diameter, it is named as RC 60/80 as shown in Figure 2.

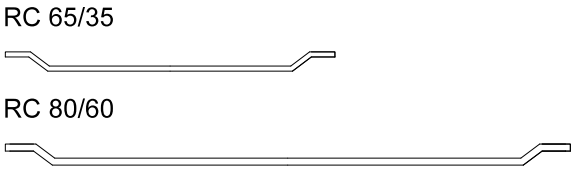

Figure 2. Geometry of the steel fibers used

2.3 Mixing procedure

The mixing procedure was carried out in three stages:

1st stage - the sand and coarse aggregate were mixed together with about 70% of the water for moistening and homogenization for one minute;

2nd stage - the cement was added and mixed for approximately one minute;

3rd stage - the remaining water and the superplasticizer were.

The manufacturing process was terminated after uninterrupted mixing for five minutes. When steel fibers were used, the additions were made gradually, using about two additional minutes of mixing, until it obtained a homogeneous appearance.

3. TEST PROGRAM

Three specimens were produced in total. In order to evaluate the benefits of fiber addition, one of the manufactured sleepers had no fibrous reinforcement, while the other two were reinforced with a 0.5% volume ratio of hooked end steel fiber, being one of the specimens casted with a fiber provided with aspect ratio of 65 and 35 mm long, and the other with fibers with aspect ratio of 80 and 60 mm long, the sleeper geometry is presented in Table 2. In order to compare the bending strength capacity of the different sleepers, negative bending moment test was performed at mid-span on all of the constructed sleepers in accordance with AREMA [11] and Brazilian standards [12]. The test setup is presented in Figure 3. The test machine consists in a hydraulic actuator with 500 kN capacity, controlled by a MTS® central station. The actuator displacement was controlled on a rate of 1 mm/min. The cross-section of the sleeper as well as the prestressing wires distribution is presented in Figure 4.

Table 2. Sleeper geometry

Depth*	28,5 cm
Height*	23 cm
Length*	245 cm
Height at mid-span	24.5 cm
*Maximum dimensions	

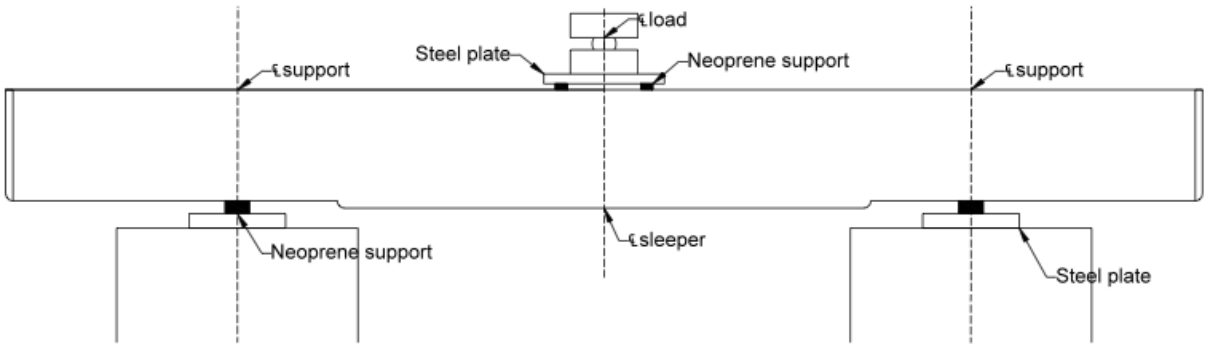

Figure 3. Test setup

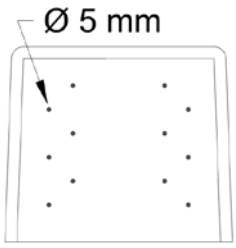

Figure 4. Sleeper cross-section

4. DISCUSSION AND ANALYSES

The Load-Displacement as well as the Load-Strain curves for the three sleepers tested are shown in Figure 5. The point that the lower layer of prestressing wires ruptures is indicated in the graph.

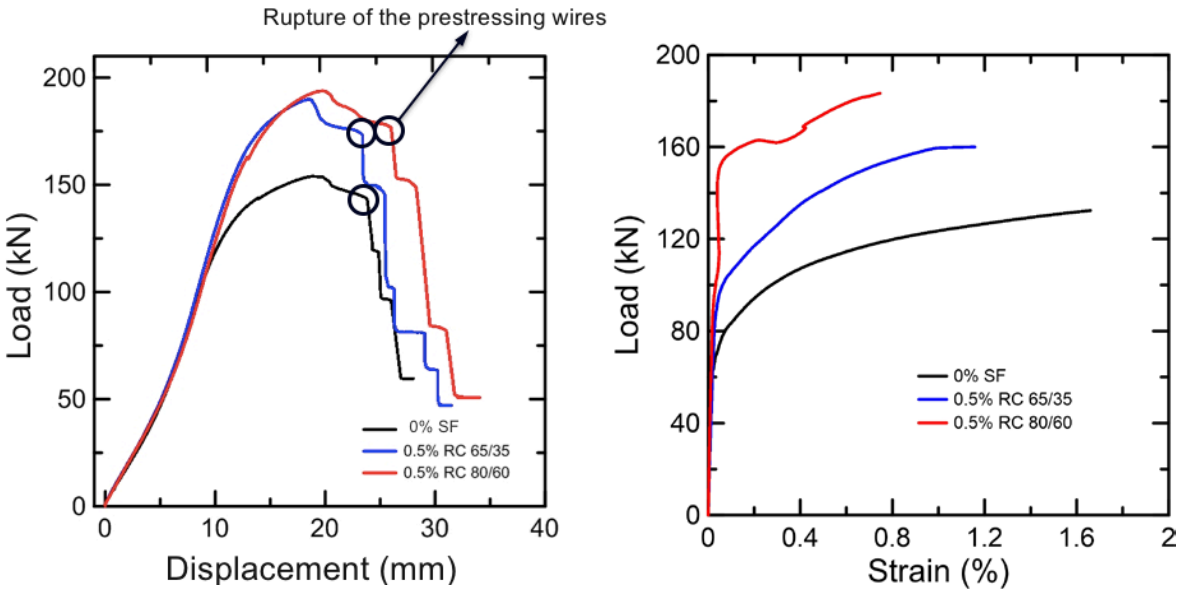

Figure 5. Load-Displacement and Load-Strain curves for each concrete mixture

The sleeper without fiber reinforcement withstood an ultimate load (P_u) of 153.9 kN and had its first crack (P_c) opened with a load of 61.5 kN (Table 4).

The ultimate load capacity of the sleeper reinforced with 0.5% volume ratio of hooked end fibers, with aspect ratio of 65 and 35 mm length was 189.8 kN and its first crack opened with a 83 kN load, resulting in a increment in resistance of 23% for the ultimate load and 35% for the first crack opening.

The ultimate load capacity of the sleeper reinforced with 0.5% volume ratio of hooked end fibers, with aspect ratio of 80 and 60 mm length was 193.7 kN and its first crack opened with a 85 kN load, resulting in a increment in resistance of 26% for the ultimate load and 38% for the first crack opening.

From the graph shown in Figure 5 is possible to conclude that the addition of fibers contributes to the increase of the concrete resistance and improves its post-cracking behavior, resulting in higher residual loads. The fiber contribution in transfer stress can be observed by the delay of the rupture of the prestressing wires. Similar results were obtained by Bastos [10].

The first crack opening point was identified by the change in curvature of the Load-Strain curves obtained by strain gauges positioned in the lower part of the specimen.

Table 4. Values for load at first crack, ultimate load and ultimate moment for each concrete mixture

Mixture	**P_c**	**P_u**	**M_u**
0% SF	61.5 kN	153.9 kN	52.63 kN.m
0.5% RC 65/35	83.0 kN	189.8 kN	64.91 kN.m
0.5% RC 80/60	85.0 kN	193.7 kN	66.26 kN.m

The energy absorbing capacity of the sleepers tested is represented by the Toughness-Displacement curve shown in Figure 6, it was obtained from the calculated area under the Load-Displacement curve for each specimen.

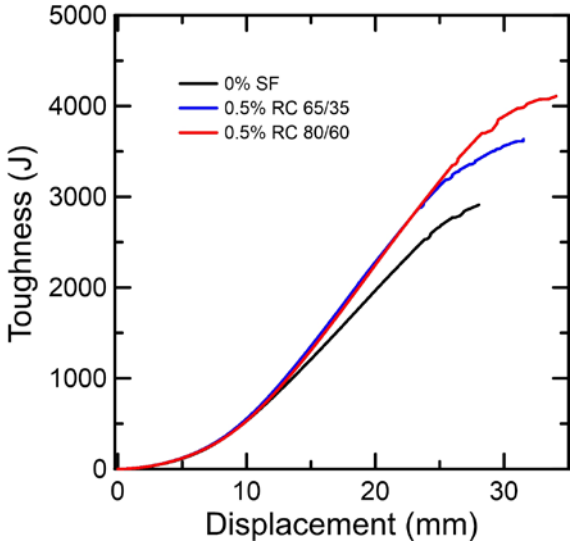

Figure 6. Toughness-Displacement curves for each concrete mixture

It can be seen from the graph shown in Figure 6 that the addition of fibers contributes to the increase in the energy absorbing capacity of the material.

5. THEORETICAL CALCULATIONS

For the purpose of checking the experimental results obtained, the theoretical calculation of the resistant moment of the sleepers tested was performed according to Brazilian code [13]. It was considered in the calculation the losses in prestress such as: elastic shortening, shrinkage of concrete, creep of concrete and relaxation of steel. The steel rupture strain was defined as 10‰ for the bottom layer, that value summed with the strain imposed on the steel to prestress was used to obtain the stress in the wire at that point through a stress-strain curve of the prestressing wire. Since the neutral axis was unknown (x), the software Mathcad® was used to do an iterative calculation so the position of the neutral axis was obtained by force balancing.

By triangle similarity it was possible to obtain the strain in every layer and consequently the stress and force in function of x. The compression component was obtained in function of x, by a simplification of the parabolic stress distribution. A force diagram is presented in Figure 7.

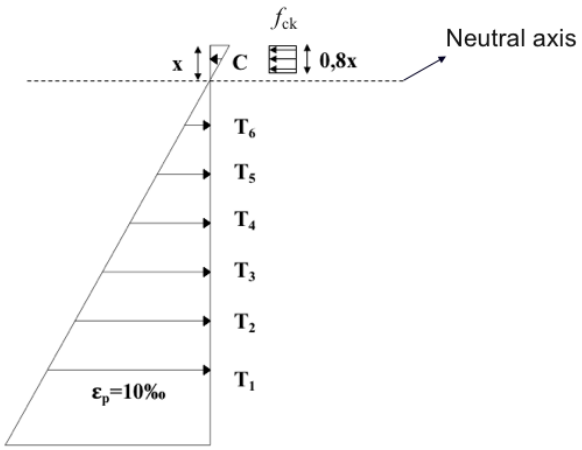

Figure 7. Force diagram for the sleeper without fibrous reinforcement

The neutral axis position of 2.76 cm was obtained, there being no prestressing wires in the compressed zone. The moment was then calculated by multiplying the tensile components by their distance from the compression component. The theoretical resistant moment of the sleeper without fibrous reinforcement was 43.5 kN.m, equivalent to 83% of the experimental value.

The theoretical calculation of the fiber reinforced sleeper was made using the same methodology of the sleeper without the fibrous reinforcement. These differ, since in addition to the tensile components of the prestressing wires, there is also a tensile component from the addition of fibers, as shown in Figure 8.

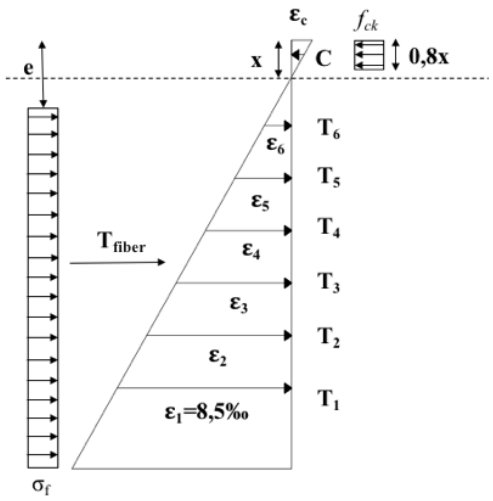

Figure 8. Force diagram for the sleepers with fibrous reinforcement

The calculation of the ultimate moment was done according to ACI 544.4R [14]. The distance between the fiber collaborative area and the top of section (e) was evaluated as a function of fiber strain and neutral axis position. In this case the strain of the prestressing wire is at most 8.5 ‰ as recommended by the ACI [14]. The fiber contribution stress (σ_f) is defined by the ACI as a function of the aspect ratio, volume ratio and fiber efficiency factor, not taking into account its specific geometry and matrix. For this reason, the value of σ_f used in this calculation was obtained experimentally through direct tensile tests in dog bone shaped specimens.

The resulting force of fiber collaboration (T_{fiber}) was calculated as a function of the neutral axis (x), and as was done for the first sleeper, the value of x was calculated per balance of forces. Neutral line position values of 3.25 and 3.30 cm were obtained for reinforced sleepers with RC 65/35 and RC 80/60 fibers, respectively, with no prestressing wires in the compressed zone for both cases. The moment was then calculated by multiplying the tensile components by their distance from the compression component.

The theoretical resistant moment of the sleeper reinforced with 35 mm long fibers (RC 65/35) was 52.3 kN.m, equivalent to 81% of the experimental value and to 120% of the theoretical value of the sleeper without fibrous reinforcement.

The theoretical resistant moment of the sleeper reinforced with 60 mm long fibers (RC 80/60) was 53 kN.m, equivalent to 80% of the experimental value and to 122% of the theoretical value of the sleeper without fibrous reinforcement.

The different moment values obtained experimentally and theoretically are presented in Figure 9.

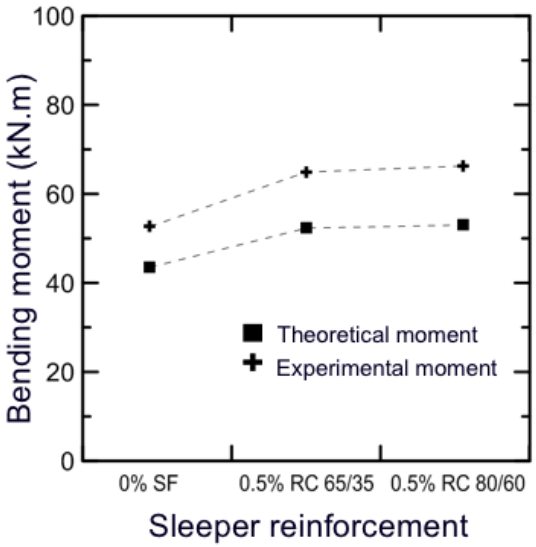

Figure 9. Comparative chart of bending moment values obtained by experimental test and theoretical calculations

It is possible to observe from Figure 9 that the calculated moments follow the same pattern of the values obtained experimentally, being the method used ideal for the analysis of the reinforced concrete with fibers.

6. CONCLUSION

Negative moment tests were performed on concrete sleepers with static loading applied on its mid-span. Concretes mixtures were evaluated with and without reinforcement of 0.5% of steel fibers of 35 and 60 mm length, totaling three specimens. It has been observed that the addition of fibers delays the opening of a macro crack, increases the ultimate load and delays the rupture of prestressing wires. It was obtained the increase of 23 and 26% of the ultimate moment resisted by the structure, promoted by the addition of the fiber of 35 and 60 mm, respectively. In order to verify the results obtained by the experimental tests, theoretical calculations were made based on the recommendations of Brazilian standards and ACI 544.4R. The calculated ultimate moments were 20% lower than the experimentally obtained ones. However, the increase of resistance promoted by the use of fibers was similar to the experimental, being the increase of 20 and 22% in the ultimate moment, promoted by the addition of 35 and 60 mm fibers, respectively. It can be concluded that the theoretical method used was ideal for the evaluation of the structure.

REFERENCES

[1] H. L. Brina, 'Estradas de Ferro'. (Rio de Janeiro, 1979).

[2] E. Röthlisberger, 'History and development of the wooden sleeper'. Available at: http://www.corbat-holding.ch/Timber-railway-sleepers/Sleepers/Track-sleepers.

[3] Fédération Internacional du Béton, 'FIB bulletin 37: Precast Concrete Railway Track Systems', 2006.

[4] H. Thun, 'Assessment of Fatigue Resistance and Strength in Existing Concrete Structures'. Luleå, 2006. 59p. Doctoral thesis. Luleå University of Technology.

[5] W. Ferdous e A. Manalo, 'Failures of mainline railway sleepers and suggested remedies - Review of current practice', *Eng. Fail. Anal.*,**44** (2014) 17–35.

[6] B. J. Van Dyk, M. S. Dersch, e J. R. Edwards, 'International Concrete Crosstie and Fastening System Survey – Final Results', Urbana. 2012. 38p. University of Illinois at Urbana-Champaign.

[7] N. Wang, 'Resistance of Concrete Railroad Ties to Impact Loading', Vancouver, 1996. 268p. Doctoral thesis. The University of British Columbia.

[8] J. Sadeghi, A. Reza, T. Kian, e A. S. Khabbazi, 'Improvement of Mechanical Properties of Railway Track Concrete Sleepers Using Steel Fibers', *J. Mater. Civ. Eng.*, **28** (11) (2016) .

[9] J.-M. Yang, H.-O. Shin, Y.-S. Yoon, e D. Mitchell, 'Benefits of blast furnace slag and steel fibers on the static and fatigue performance of prestressed concrete sleepers', *Eng. Struct.*, **34** (2017) 317–333.

[10] P. S. dos S. Bastos, 'Análise experimental de dormentes de concreto protendido reforçados com fibras de aço'. São Carlos, 1999. 270p. Doctoral thesis. Universidade de São Paulo.

[11] American Railway Engineering and Manutenance Association. 'Manual for Railway Engineering - Concrete Ties'. AREMA, v.2, cap.10, 54 p. 2010.

[12] Associação Brasileira de Normas Técnicas. 'NBR 11709: Dormente de concreto — Projeto, materiais e componentes'. Rio de Janeiro: ABNT, 2015.

[13] Associação Brasileira de Normas Técnicas. 'NBR 6118: Projeto de estruturas de concreto – Procedimento'. Rio de Janeiro: ABNT, 2014.

[14] American Concrete Institute. 'ACI 544.4R-88: Design Considerations for Steel Fiber Reinforced Concrete', 1999.

EFFECT OF VISCOSITY MODIFIER ADMIXTURE ON PORTLAND CEMENT HYDRATION

Stefan Chaves Figueiredo [(1)], Oğuzhan Çopuroğlu [(1)] and Erik Schlangen [(1)]

(1) Microlab, Faculty of Civil Engineering and Geosciences, Delft University of Technology, The Netherlands.

https://doi.org/10.21452/bccm4.2018.02.29

Abstract

Significant attention has been given to the development of materials and techniques employed on the additive manufacturing process or also called 3-dimensional printing (3D printing) applied on the construction market. This building technique extrudes cementitious composites to form the contour of the desired geometry. Together with a robotic arm and linked to the blueprints the material is extruded exactly as digitally designed. Therefore, making this building technique a progress on the automation process on the construction industry. In order to have the exact contour as designed for the building, the material used on this application must be developed respecting rigorous rheology parameters. To achieve such high viscosity in cementitious materials, usually viscosity modifiers admixtures (VMA) are employed. One of the commonly used chemical admixtures for this purpose is the hydroxypropyl methylcellulose. However, the consequences of using high content of this admixture in cementitious matrices is still not fully understood. This study characterized the influence of different VMA content on Portland cement paste, by means of a microstructure analysis. The hydration development was assessed, and the influence of the admixture was measured for different curing ages. Important negative side effects were found such as: VMA increasing the cement setting time, different distribution of hydration products on the bulk or increasing the void content. On the other hand, positive effects were also found such as: evidences of internal curing, higher degree of hydration and the lack of undesired hydration products.

1. INTRODUCTION

A promising construction technique which has drawn notable attention in the past few years was the additive manufacturing (AM). This revolutionary technique is likely to open a new era on the construction industry, optimizing process and materials [1]. AM is a general classification for technologies which fabricates objects with the help of automated equipment, directly from a digital design technology [2], [3]. There are several different techniques to manufacture the objects developed based on AM, such as the powder bedding with an inkjet head [4] or the laser melting [5], and the counter craft technology which employs extrusion techniques to fabricate objects [6].

Both AM technologies builds the object through a layer by layer deposition process. The counter craft AM has drawn a lot of attention in the construction market as its implementation looks feasible to be applied in large scale for this industry. It should be noted that materials with unique properties need to be developed to meet the mechanical and durability-related demands of a long-lasting and safe structure.

Recent investigations have shown the development of cementitious composites with different aggregate particle sizes. Concrete and mortars have been developed with printable characteristics. In some studies fibres have been incorporated to stabilize the mixture at fresh state or to minimize the occurrence of cracks due to shrinkage. However, the materials and printing methods have not yet delivered solutions to improve the composites hardened performance when loaded in tension [7], [8].

Moreover, researchers have addressed this problem developing a technique to produce mortar filaments through AM reinforced by a steel wire. Higher ductility was achieved with samples reinforced by the steel wire. Further, more research is needed to enhance the interface bond between the wire and the mortar [9].

Another strategy to increase the ductility of printed brittle materials is the incorporation of fibres. Great plastic deformations can be achieved on cementitious composites reinforced by fibres namely, strain hardening cementitious composites (SHCC), for instance. This type of composite can deliver high tensile strain, strength, higher frequency but smaller multiples cracks during tensile loads [10].

SHCCs are cementitious composites reinforced by high volume of fibres. Usually the reinforcement level is around 2% of the total composite's volume, which brings challenges regarding the flowability of such mix designs. An alternative often approached to enhance the fibre dispersion and even thought keep a high flowability is the employment of viscosity modifier admixtures (VMA) [11]. These admixtures are usually composed by a long organic chain with -OH ramifications, that "arrest" the free water on the mixture through hydrogen intermolecular bridge. One of the most used VMA is composed by Hydroxypropyl methylcellulose (HPMC) [12]. In addition, the use of VMA is also a key factor while developing a printable cementitious composite. The right tune of the amount of the chemical admixture, coupled with a good distribution of the grain size of the particles employed on the matrix, and optimum water-to-solid ratio may lead towards a material with the needed viscosity for printing.

Besides the fact that VMA can help on the controlling of the rheology properties of a solid suspension, the consequences on the microstructure of hydrated Portland cement is not yet fully understood. The influence of some water-soluble polymers on the microstructure development of Portland cement was investigated by [13]. They have shown a delay on the hydration process, formation of unusual minerals at early ages, a slightly lower $Ca(OH)_2$ content and a higher amount of chemically bound water. Furthermore, the cement hydration delay was explained with the influence that HPMC has on the precipitation of calcium hydroxide, the polymer's absorption capacity [14]–[16], and the methyl content [17]. Moreover, a study have also reported the influence of molecular weight on the rheology of cement paste modified by HPMC admixture and its potential to combine via intermolecular and intramolecular crosslinks with Ca^{+2} ions [18].

The present research aims to build a better understanding to the consequences of HPMC use in cement paste. This information together with the literature already available, contributes to a better understanding to the new generation of construction materials which are under development to be applied on 3D printing.

2. EXPERIMENTAL METHODS

Microstructure characterization of cement paste for different curing ages and VMA content were studied. Chemical composition of the Ordinary Portland Cement (OPC) CEM I 42,5N and its loss on ignition (LOI) can be found on Table 1. They were assessed by X-ray fluorescence analysis (XRF) and thermogravimetric analysis (TGA) performed at 10°C/min under Argon atmosphere. The LOI was calculated using the loss of mass between 45 and 1000°C.

Table 18: Chemical composition of Portland Cement.

Compound	CaO	SiO_2	Fe_2O_3	Al_2O_3	SO_3	MgO	K_2O	TiO_2	P_2O_5	Rest	LOI
CEM I 42,5 N [wt. %]	69.53	15.6	3.84	3.09	2.6	1.67	0.55	0.31	0.14	0.53	2.14

VMA is composed by HPMC with viscosity 201000mPa.s was provided by Shanghai Ying Jia Industrial Development Co., Ltd. The samples were cast mixing a volume of 0.5 litres in a planetary mixer (HOBART) according to the following procedure:

- All dry materials were mixed for two minutes at speed 1;
- While mixing at speed 1, during approximately one minute, the water was added;
- The wet powders were steered for the next two minutes at speed 1. In this phase it is possible to observe a significant change in the mixture's viscosity. A dough like consistence is achieved;
- At speed 2, the dough like mixture is further mixed. At this phase the dough opens on the mixing bowl.

A reference cement paste with a water-to-cement ratio of 0.3 (REF) and three levels of VMA, 0.1, 0.3 and 1% of the cement weight, named 1M, 3M and 10M respectively were evaluated. The mixed paste was cast on plastic containers and sealed with the help of paraffin paper. Right after moulding they were left for 24 hours rotating around their own axis to ensure a homogenous material avoiding any segregation. With the exception of 10M samples, afterwards, they were demoulded and cut in slices of approximately 5mm and the followed curing time was done in a curing room at (20 ± 2)°C and relative humidity of (98 ± 2)%. 10M samples could be demoulded and cut only after 48 hours after the casting.

To stop cement hydration the cut slices were manually crushed in small particles and partially submerged on liquid nitrogen for 3 minutes and completely submerged for 5 minutes. Immediately after, crushed particles were conditioned on plastic bags with holes to allow the release of moisture from the samples and stored in a freeze drier for further drying. Those samples were used on the TGA tests. Stopping hydration employing liquid nitrogen was chosen for TGA tests, as [19] reported formation of carbonate like minerals at high temperatures in samples where solvent exchange technique was used. The small cut slices destined to electron microscopy observations, X-ray diffraction (XRD) and Fourier Transform Infrared Spectroscopy (FTIR) had their hydration arrested by solvent exchange procedure, employing ethanol.

3. RESULTS

Before the description of all results found for evaluated specimens it is important to show that the VMA employed was investigated under electron microscope, TGA and XRD. The results from these tests have demonstrated that the chemical admixture suffers of a small volume of sodium chloride impurity.

3.1 Isothermal calorimetry test

On Figure 1 the result from the isothermal calorimetry test is reported. The increasing volume of viscosity modifier on the cement paste, lead towards delaying Portland cement hydration. The greatest consequences were measured on pastes with 1% of VMA, where the dormant stage was prolonged up to 9 hours of hydration.

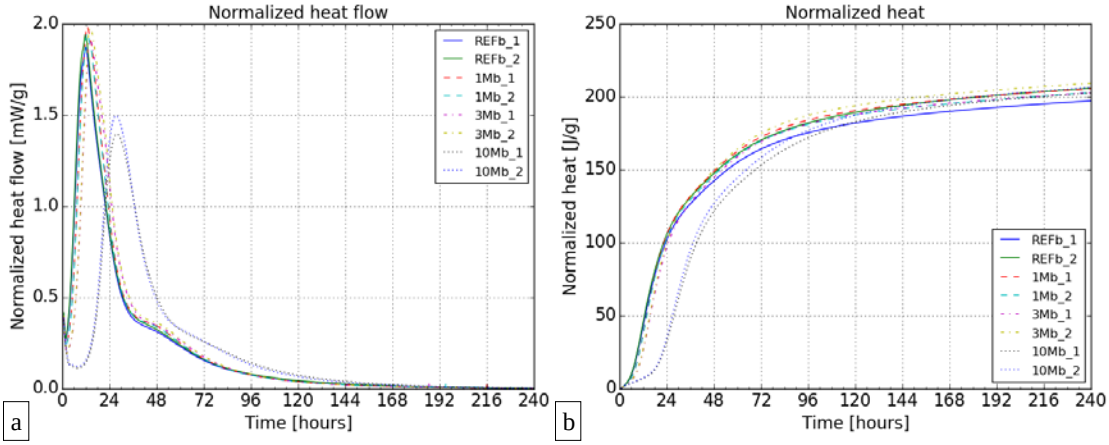

Figure 50: (a) normalized heat flow and normalized total heat released (b) results from isothermal calorimetry tests.

Specimens 1M and 3M had also their early age properties changed. Both had a slightly longer dormant period, then reference. However, the C_3S peak obtained for both were also slightly higher than reference samples, meaning that the hydration reactions were significantly accelerated. Other fact that shows this acceleration is the overlapping of the peak of heat generated by the hydration of C_3S and the renewed formation of ettringite [20]. On reference samples after about 10 hours the slope of the heat released decreases, followed by a reacceleration after some minutes. 1M samples the different slopes can also be noticed however, the second slope was shown only during the descending part of the curve, after approximately 10.5 hours. Specimens with 0.3% of VMA do not show these two slopes. The heat released by these clinker components overlay creating a wider peak.

On Figure 1b the total heat generated during the measurement period is plotted. Besides the fact that the employment of VMA delays the Portland cement hydration, after approximately 30 hours of hydration samples 1M and 3M had already a slightly higher total heat released. In general, samples with HPMC have released a higher amount of energy during the first 10 days of curing.

3.2 Thermogravimetry analysis

Thermogravimetry results were especially important to quantify the results found on this study. A summary with all results obtained with the test is give on Table 2. The influence of 1% VMA on the hydration delay of cement paste could also be noticed on the TGA results. Degree of hydration was calculated for all samples and the results show a significant loss on 1 day cured samples for 10M specimens. Moreover, a significant increase in α since the 1st day of hydration for 1M and 3M specimens was noticed. 10M specimens only develop higher degree of hydration after the 3rd day.

Table 19: Summary of properties measured using TGA technique.

	Age [days]	α	H_2O from 105 to 450°C [%]	Portlandite [%]	Calcium carbonate [%]
REF	1	0.2853	3.97	8.86	5.64
	2	0.3693	5.33	9.40	7.10
	3	0.4062	5.84	10.46	5.73
	29	0.6475	8.96	14.52	6.56
1M	1	0.3584	4.90	9.64	7.14
	2	0.4073	5.43	10.69	7.28
	3	0.4281	5.78	9.72	10.44
	7	0.5686	7.56	13.70	9.18
	29	0.7424	9.45	14.69	11.77
3M	1	0.3377	4.62	7.94	8.48
	2	0.4286	5.71	10.20	8.82
	3	0.4917	6.55	11.32	8.60
	7	0.6097	7.97	13.44	8.95
	29	0.8050	10.14	16.70	9.22
10M	1	0.1423	2.16	2.65	5.73
	2	0.3181	4.43	7.54	9.36
	3	0.4391	5.98	9.45	12.46
	7	0.5438	7.19	11.03	17.11
	29	0.7652	9.52	14.57	15.86

To explain the higher values found for samples with HPMC an understanding of how this chemical admixture changes the viscosity of solid solutions must be approached. The HPMC molecules can “arrest” water through hydrogen intermolecular interactions. These interactions decrease the availability of water during the first hours of cement hydration increasing significantly the viscosity of the water which surrounds OPC particles. As soon as pH values rise, the increasing availability of OH^- ions decreases the capabilities of VMA in change the viscosity’s solution. Gradually this phenomenon happens on the paste, and therefore gradually the water “arrested” on HPMC molecules are released to become available for hydration. This description is also found to explain the phenomena known as internal curing. Therefore, it is believed that the VMA does not

only contributes for the viscosity modifying of the solid suspension, the chemical admixture can also contribute to improve OPC hydration.

The total loss of water from ettringite and CSH, as well as the total amount of calcium hydroxide is smaller for 10M samples only until the 3rd day of hydration. Nevertheless, with exception of 3M specimen, all 29 days cured samples have close values of calcium hydroxide content. As it was measured, the higher degree of hydration found on samples with VMA is coming mainly from the water lost from 105 until 450°C, corresponding to hydration products like ettringite, and C-S-H.

Another important characteristic from samples where the viscosity modifier was employed is the total amount of calcium carbonate. The proportions from this mineral rise with the increasing employment of the admixture. This phenomenon might be correlated with the large amount of entrapped air voids found on samples with HPMC. The high void content would increase the paste exposure therefore, perhaps increasing the carbonation speed.

3.3 X-ray diffraction

The delay of hydration caused using VMA, and the lack of distinguish of ettringite and C_3S heat release peaks might lead to a lack on the availability of some intermediate minerals for the cement hydration. Therefore, an investigation of the mineralogical properties was conducted to verify if the formation of the main crystals on samples with admixture followed the same trend as the reference. Besides the fact that formation of non-conventional minerals were reported by [21], the XRD patterns from all evaluated ages and different VMA content did not present formation or lack of mineral. Therefore, the employment of rheology modifier does not generate any hazardous minerals which could lead to a decrease on the durability or reliability of printed cementitious composites.

3.4 Fourier transform infrared spectroscopy

The band corresponding with presence of $Ca(OH)_2$ is found at $3645cm^{-1}$ and from 1635 to $3445cm^{-1}$ are bands due to the presence of calcium sulphate in the form of ettringite [21]. FTIR results corresponding the first 3 days of hydration emphasizes the bands corresponding to ettringite. Moreover, the bands measured during the test were also in accordance with the calorimetry tests, demonstrating that the employment of VMA delays hydration of Portland cement. 3M samples show higher transmittance bands, until the 3rd day of hydration. However, from the 7th hydration day 10M samples take over, as the reactions for those samples were significantly delayed, as reported with the calorimetry results. The FTIR results followed the same trend observed on TGA and calorimetry test results.

3.5 Electron scanning microscopy

The microstructure of 29 days samples was observed under scanning electron microscope and are exemplified on Figure 2. One of the first noticed differences was the number of voids on samples where the chemical admixture was employed. This might be caused due to the high viscosity achieved while mixing the paste, when air can be entrapped.

Besides that, around the voids found on samples with VMA a darker region is always found, leading to the conclusion that these are less dense than the bulk paste. This means that the voids found on these samples were perhaps filled or at least highly concentrated with water. This is an important result that is connected to the fact that the HPMC molecules can “arrest” part of the

mixing water through its -OH ramifications. Progressing the hydration reactions this water is released, locally rising the water-to-cement ratio on these regions.

One other important observation is the location where portlandite is found. Usually, $Ca(OH)_2$ grows spread on the paste's bulk and eventually on the void or pore walls. However, samples with the chemical admixture had their voids progressively filled with portlandite, from 0.1 to 1 wt.% of VMA. Remarkably, voids from 10M samples were almost totally filled with portlandite.

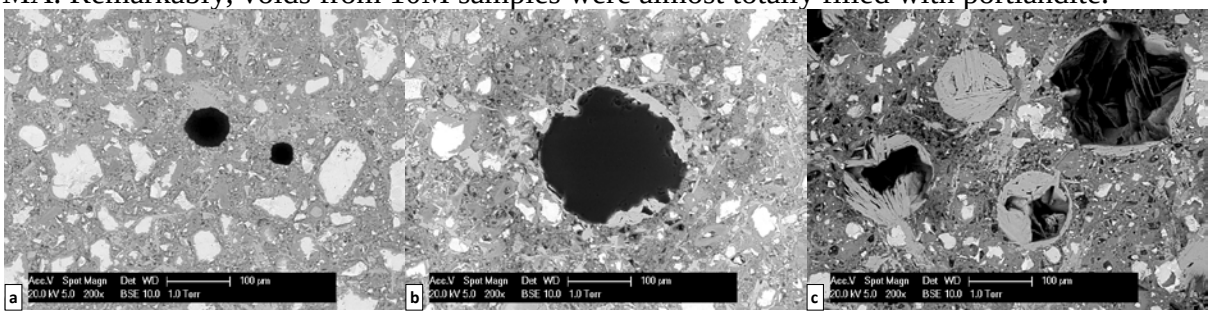

Figure 51: SEM pictures from REF samples (a), 1M (b) and 10M (c).

4. CONCLUSIONS

The results obtained during this study are of fundamental importance for the understanding of the chemical admixture employed on the extrusion and nowadays additive manufacturing industries. Summarizing the main conclusions are:

- VMA concentration is of high importance on OPC hydration. Even small concentrations of the admixture lead to retardation of the initial hydration. 1 wt.% already leads to a large latent time of the Portland cement;
- The rheology modifier admixture "arrest" the available water with hydrogen bonds. The admixture only loses its preference for the water when the pH of the solution increases, making stronger connections with other ions;
- As demonstrated with the degree of hydration and the total heat released VMA can also be employed for internal curing purposes.
- Under electron microscope, it was possible to observe that air voids formed during mixing works also as water reservoir. As soon as the pH of the paste rises, the water released from VMA develops a region around theses voids with a higher water/cement ratio, in comparison with the rest of the matrix.
- To modify the rheology parameters of solid suspensions, the grain size distribution or the employment of viscosity modifier admixtures are usually employed. However, according with the manufacture specifications sheet the VMA employed on this study works within pH values 4 to 8. Therefore, solid suspensions which have high pH from the beginning of the mixing, like alkali activated materials, will be challenged to decrease the solution's pH or provide a well distributed particles grain size.

ACKNOWLEDGEMENTS

The authors would like to acknowledge the funding from Science Without Borders from the National Council for Scientific and Technological Development of Brazil (201620/2014-6).

REFERENCES

[1] P. Wu, J. Wang, and X. Wang, 'A critical review of the use of 3-D printing in the construction

industry', *Autom. Constr.*, vol. 68, pp. 21–31, 2016.
[2] H. Kodama, 'Automatic method for fabricating a three-dimensional plastic model with photo-hardening polymer', *Rev. Sci. Instrum.*, vol. 52, no. 11, pp. 1770–1773, 1981.
[3] E. Sachs *et al.*, 'Three-Dimensional Printing: The Physics and Implications of Additive Manufacturing', *CIRP Ann. - Manuf. Technol.*, vol. 42, no. 1, pp. 257–260, 1993.
[4] R. A. Buswell, R. C. Soar, A. G. F. Gibb, and A. Thorpe, 'Freeform Construction: Mega-scale Rapid Manufacturing for construction', *Autom. Constr.*, vol. 16, no. 2, pp. 224–231, 2007.
[5] J. Wilkes, Y. Hagedorn, W. Meiners, and K. Wissenbach, 'Additive manufacturing of ZrO_2-Al_2O_3 ceramic components by selective laser melting', *Rapid Prototyp. J.*, vol. 19, no. 1, pp. 51–57, 2013.
[6] B. Khoshnevis, 'Automated construction by contour crafting - Related robotics and information technologies', *Autom. Constr.*, vol. 13, no. 1, pp. 5–19, 2004.
[7] F. Bos, R. Wolfs, Z. Ahmed, and T. Salet, 'Additive manufacturing of concrete in construction: potentials and challenges of 3D concrete printing', *Virtual Phys. Prototyp.*, vol. 11, no. 3, pp. 209–225, 2016.
[8] A. Kazemian, X. Yuan, E. Cochran, and B. Khoshnevis, 'Cementitious materials for construction-scale 3D printing : Laboratory testing of fresh printing mixture', *Constr. Build. Mater.*, vol. 145, pp. 639–647, 2017.
[9] F. P. Bos, Z. Y. Ahmed, E. R. Jutinov, and T. A. M. Salet, 'Experimental exploration of metal cable as reinforcement in 3D printed concrete', *Materials (Basel).*, vol. 10, no. 11, 2017.
[10] V. C. Li, H. Horii, P. Kabele, T. Kanda, and Y. M. Lim, 'Repair and retrofit with engineered cementitious composites', *Eng. Fract. Mech.*, vol. 65, no. 2–3, pp. 317–334, 2000.
[11] T. Kamada and V. C. Li, 'Effects of surface preparation on the fracture behavior of ECC/concrete repair system', *Cem. Concr. Compos.*, vol. 22, no. 6, pp. 423–431, 2000.
[12] S. Srinivasan, D. Deford, and P. S. Shah, 'The use of extrusion rheometry in the development of extrudate fibre-reinforced cement composites', *Concr. Sci. Eng.*, vol. 1, no. 11, pp. 26–36, 1999.
[13] E. Knapen and D. Van Gemert, 'Cement hydration and microstructure formation in the presence of water-soluble polymers', *Cem. Concr. Res.*, vol. 39, no. 1, pp. 6–13, 2009.
[14] J. Pourchez, A. Peschard, P. Grosseau, R. Guyonnet, B. Guilhot, and F. Vallée, 'HPMC and HEMC influence on cement hydration', *Cem. Concr. Res.*, vol. 36, no. 2, pp. 288–294, 2006.
[15] J. Pourchez, P. Grosseau, and B. Ruot, 'Changes in C3S hydration in the presence of cellulose ethers', *Cem. Concr. Res.*, vol. 40, no. 2, pp. 179–188, 2010.
[16] J. Pourchez, P. Grosseau, and B. Ruot, 'Current understanding of cellulose ethers impact on the hydration of C3A and C3A-sulphate systems', *Cem. Concr. Res.*, vol. 39, no. 8, pp. 664–669, 2009.
[17] Z. H. Ou, B. G. Ma, and S. W. Jian, 'Influence of cellulose ethers molecular parameters on hydration kinetics of Portland cement at early ages', *Constr. Build. Mater.*, vol. 33, pp. 78–83, 2012.
[18] B. Ma *et al.*, 'Effect of hydroxypropyl-methyl cellulose ether on rheology of cement paste plasticized by polycarboxylate superplasticizer', *Constr. Build. Mater.*, vol. 160, pp. 341–350, 2018.
[19] J. Zhang and G. W. Scherer, 'Comparison of methods for arresting hydration of cement', *Cem. Concr. Res.*, vol. 41, no. 10, pp. 1024–1036, 2011.
[20] H. F. W. Taylor, *Cement Chemistry*. Academic Press, 1990.
[21] N. K. Singh, P. C. Mishra, V. K. Singh, and K. K. Narang, 'Effects of hydroxyethyl cellulose and oxalic acid on the properties of cement', *Cem. Concr. Res.*, vol. 33, no. 9, pp. 1319–1329, 2003.

FLEXURAL BEHAVIOR OF UNDER-REINFORCED STEEL FIBER CONCRETE (R/SFRC) BEAMS

Daniel C. T. Cardoso [(1)], Gabriel B. S. Pereira [(1)], Julio J. S. Holtz Filho [(1)], Flávio A. Silva [(1)], Eric V. Pereira [(1)]

(1) Department of Civil and Environmental Engineering, Pontifícia Universidade Católica do Rio de Janeiro, Brazil

https://doi.org/10.21452/bccm4.2018.02.30

Abstract

This paper reports the findings of an experimental program aiming to investigate the influence of steel fibers in the flexural behavior of under-reinforced reinforced concrete beams (S/SFRC). Hooked end steel fibers with aspect ratios of 48 or 60 were used to produce matrices with fiber content ranging from 0 to 2%, in volume. A full mechanical characterization was carried for each matrix studied, as well as for the reinforcing steel used. Reduced scale beams with reinforcing ratios of 0.28, 0.44 and 0.70% were instrumented with strain gages and displacement transducers. Digital image correlation (DIC) was also used to monitor strain field and crack formation and growth throughout the constant moment region during loading. Experimental load-deflection and moment-curvature relationships are reported, showing gains of capacity ranging from 21 to 109% with respect to conventional reinforced concrete (RC) beams. Increases in cracked stiffness were also observed and all beams presented ductility within desired limits. The results obtained using analytical models are compared to the experimental results and excellent agreement achieved shows that models can be successfully adopted to predict the actual behavior of R/SFRC beams in flexure. Finally, crack formation and growth are reported, showing that the use of steel fibers leads to a pattern characterized by multiple small cracks and a critical wider crack, but with opening much smaller than that obtained for RC.

1. INTRODUCTION

Introduced during the 1960's, fibrous concrete – or fiber-reinforced concrete (FRC) – is defined as a concrete containing dispersed randomly oriented fibers and its advantages over plain concrete include post-crack tensile residual strength and enhanced toughness. FRC has gained acceptance among civil engineers and has been widely adopted in applications such as slabs on ground, precast pipes and façade panels, retaining walls and tunnel linings as an alternative to conventional reinforced concrete [1, 2]. On the other hand, the use of conventional flexural reinforcement combined with FRC in load-carrying members has been very limited [3, 4], despite the advantages

with respect to conventional RC, including: i) improve in shear strength, leading to the possibility to fully or partially substitute stirrups by fibers; ii) increased flexural stiffness and strength; and iii) improvement of adherence between concrete and steel, leading to multiple crack formation and a better crack width control at serviceability limit states [1, 5].

The flexural behavior of reinforced steel fiber concrete (R/SFRC) beams has been investigated by several authors, but Henager and Doherty [6] were the first to propose an analytical approach to the strength of R/SFRC beams. In the method, the bending strength is determined assuming the rectangular stress blocks for concrete in tension and compression zones. In their study, Henager and Doherty [6] observed an increase up to 25% in strength with respect to conventional RC and good agreement was achieved between proposed approach and experimental results for beams containing 1.22 to 1.51% of straight fibers in volume (aspect ratios l_f/d_f = 38 and 57) and low yield strength steel. The method was also successfully used by other authors in comparison with experiments considering different material properties and cross-section configurations [7-10], showing that, apparently, the design strategy can be adopted regardless reinforcing steel, fiber volume fraction, type of fiber and concrete compressive strength. This approach is currently recommended by fib Model Code 2010 [11] for the design of S/SFRC beams. A different approach to strength was recently proposed by Van Zijl and Mbewe [12], assuming that failure may occur before concrete reaches the strain corresponding to the stress peak in compression. Linear and non-linear stress distributions were considered in the study and a parametric study was carried on. To validate the method, five beams having 1.0 and 1.5% by volume of hooked end fibers (l_f/d_f = 60) and high tensile yield strength bars were tested in bending. The authors concluded that Henager and Doherty's approach underpredicted the experimental results, while better agreement was achieved for their proposed approach. It was also acknowledged that strain-hardening of steel bars may increase significantly the bending capacity.

To investigate the influence of reinforcing ratio in failure modes, capacity and ductility of R/SFRC beams, Mertol *et al.* [13] tested 20 beams having V_f = 0 or 1% (hooked end fibers with l_f/d_f = 60) and ρ_s ranging from 0.2 to 2.5%. Classification of sections in over- and under-reinforced groups were made based on the balanced ratio calculated (1.6%) for conventional RC. Trends in behavior were reported by the authors, such as the slight increase in capacity and in stiffness for R/SFRC specimens and the significant improve in toughness for specimens having ρ_s > 0.4%. Results from load-deflection curves were finally compared with predictions made using different assumed stress-strain models for concrete in compression. From tables reported by authors, a large deviation can be observed between theory and experiments, which can be explained by the following reasons: i) a full material characterization has not been carried out by authors; ii) the conversion of moment-curvature relationships obtained from theoretical models in load-deflection response used in the work and proposed by other authors [14, 15] is not straightforward due to the contribution of uncracked concrete in tension zone (tension-stiffening effect).

In the present work, the results from an experimental program carried out on R/SFRC beams subject to 4-point bending are reported. For a comprehensive study, the testing program included the use hooked end steel fibers with l_f/d_f = 45 and 80, with contents in volume ranging from 0 to 2% and different reinforcing ratios. To allow a better comparison with theory, a full material characterization was conducted to obtain representative stress-strain models and curvatures and neutral axis depths were measured in the constant moment region using digital image correlation (DIC). From the validated models, it is possible to clearly determine the contributions of conventional reinforcement and fibers to the behavior. Crack growth and patterns are also reported.

2. EXPERIMENTAL PROGRAM

The experimental program consisted in flexural tests of R/SFRC beams having different fiber types and contents and reinforcing ratios. A full material characterization was also performed.

2.1 Materials

The materials used in the production of the concrete matrix used in the self-compacting SFRC were: natural river sand, gravel, high early strength cement, fly ash, active silica, Silica 325, hook-ended steel fiber and superplasticizer. Two different types Dramix® fiber were considered in the study: 45/30 and 80/60 ("aspect ratio/fiber length"). Table 1 shows the mix proportions adopted in the study.

Table 1: Concrete mixture proportions per m3.

Materials	Quantity (kg)
Cement (Type III)	360
Gravel (9.5 mm)	494
Natural sand #.85	830
Natural sand #.15	100
Silica 325	70
Fly Ash	168
Active silica	45
Superplasticizer	45
Water	150
Steel fiber	0, 39.3, 78.5 and 157*

* respectively for 0, 0.5, 1 and 2% of fiber content in volume

2.2 Mechanical Characterization

To obtain the relevant mechanical properties of materials used in the study, the following tests were carried out: cylinder compression and direct tension of SFRC matrix; and tensile test for reinforcing steel. At least three specimens for each matrix and bar diameter considered in the study were tested (except for 6.3 mm rebar, not tested). In Figure 1, representative stress-strain relationships are presented. It is important to note that, for the tensile test, term 'strain' refers to the bar elongation divided by the gage length. Properties obtained for concrete matrix and reinforcing steel are summarized in Tables 2 and 3, respectively.

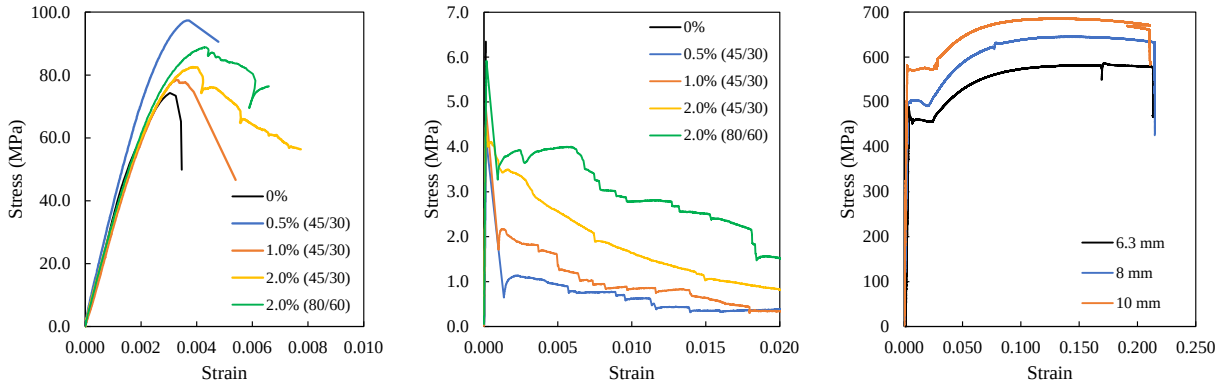

Figure 1 : Representative stress-strain relationships: a) cylinder compression; b) direct tension of matrix; and c) rebar tension.

Table 2: Summary of mechanical properties for concrete matrix.

Property	V_f (%)				
	0	**0.5**	**1.0**	**2.0(45/30)**	**2.0 (80/60)**
Compressive strength f_c' (MPa)	76.3 ± 1.8	95.2 ± 1.4	80.2 ± 2.5	81.3 ± 2.3	84.9 ± 3.8
Compressive strain at peak ε_{c0} (‰)	3.03 ± 0.01	3.65 ± 0.11	3.29 ± 0.52	3.30 ± 0.82	3.99 ± 0.36
Tensile strength f_{ct} (MPa)	6.04 ± 0.89	4.96 ± 0.69	5.12 ± 0.23	4.54 ± 0.31	5.15 ± 0.55
Tensile strain at peak ε_{t0} (‰)	0.13 ± 0.01	0.16 ± 0.01	0.16 ± 0.02	0.13 ± 0.02	0.15 ± 0.02
Tensile modulus E_c (GPa)	46.5	31.0	32.0	34.9	34.3
Tensile stress for 'strain' 10‰ $f_{ctr,10}$ (MPa)	-	0.67 ± 0.39	1.13 ± 0.25	1.75 ± 0.46	2.70 ± 0.46
Tensile stress for 'strain' 5‰ $f_{ctr,5}$ (MPa)	-	1.27 ± 0.50	1.83 ± 0.35	2.53 ± 0.49	3.68 ± 0.37

Table 3: Summary of mechanical properties for reinforcing steel.

	Rebar diameter ϕ (mm)	
	8	**10**
Yielding strength f_y (MPa)	497 ± 18	553 ± 18
Strain at yielding ε_y (‰)	2.28 ± 0.13	2.75 ± 0.20
Elastic modulus E_s (GPa)	218 ± 8	203 ± 20

2.3 Beam Tests

To study the behavior of beams reinforced with conventional steel and discrete fibers, nine 15x15x120 cm beams with 2-cm cover were fabricated in laboratory and tested in four-point bending over a span of 110 cm with a constant moment region length of 37 cm. Testing matrix is presented in Table 3 and it can be noted that three control specimens without fibers and with different reinforcing ratios were produced to allow comparison with results for R/SFRC beams. To induce first crack at midspan, a triangular-shaped notch 1.5-cm-wide x 1.0-cm-tall was introduced at the middle of the bottom face of each specimen. To avoid shear rupture, 5-mm-diameter stirrups were adopted along shear spans. To measure crack kinematics and to obtain curvature at cracked section with load, 2D digital image correlation analysis (DIC-2D) was carried out to obtain the displacement field at the constant moment region. Data were calculated from a sequence of high resolution images obtained during the test and compared with a reference image. Alternatively, to monitor the strains during loading, strain gages were used in three different positions of each rebar and other two positioned at the beam top face. Beam deflections at midspan were measured with a displacement transducer. Tests were conducted up to failure with displacement control at a rate of 2 mm/min using an MTS actuator with 500 kN capacity. Figure 2 shows an overview of test setup.

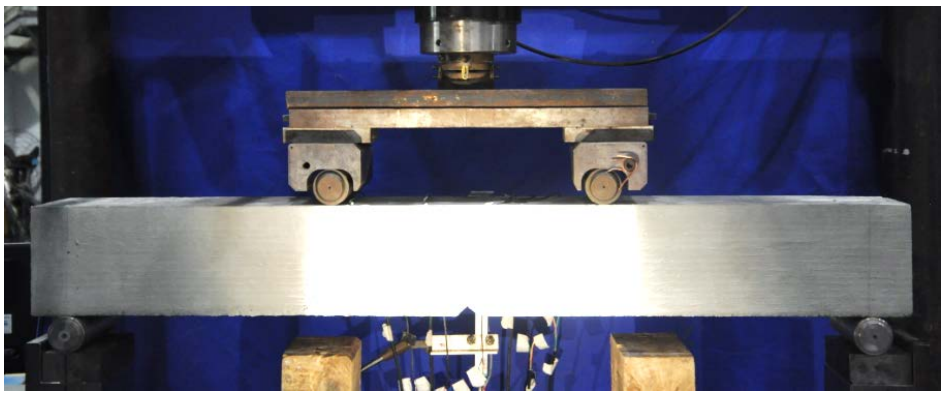

Figure 2: Overview of setup for 4-point bending tests.

Table 3: Beam testing matrix.

Specimen	V_f (%)	Fiber type	Bar diameter (mm)	Number of bars	Reinforcing ratio (%)
B1-0-6	0	HE 45/30	6.3	2	0.28
B2-0-8	0	HE 45/30	8	2	0.44
B3-0-10	0	HE 45/30	10	2	0.70
B4-0.5/S-10	0.5	HE 45/30	10	2	0.70
B5-1/S-10	1	HE 45/30	10	2	0.70
B6-2/S-6	2	HE 45/30	6.3	2	0.28
B7-2/S-8	2	HE 45/30	8	2	0.44
B8-2/S-10	2	HE 45/30	10	2	0.70
B9-2/L-10	2	HE 80/60	10	2	0.70

3. DISCUSSION OF RESULTS

All tested beams exhibited significant crack opening prior to failure and, based on strain gage readings, yielding of reinforcing steel occurred in all cases. Typical failure modes observed for RC and R/SFRC beams are presented in Figure 3. For RC beams, wide cracks regularly spaced formed along the constant moment region and failure mode was characterized by excessive deformation of reinforcement. For R/SFRC beams, one or two wider cracks could be clearly identified and failure was governed by fiber pull-out followed by concrete crushing. For beams B8-2/S-10 and B9-2/L-10, compressive strain at the top of the beam was greater than 0.004.

DIC strains were obtained dividing the relative displacement between two points located the same vertical position by their distance (approximately 200 mm). In general, good agreement was achieved between strain gage readings and those obtained using DIC, validating the image correlation analysis. Moment-curvature relationships obtained using DIC are presented in Figure 4a. It can be seen that all beams reached curvatures greater than 0.1 m^{-1}. For the cross-section studied, this value corresponds approximately to a steel strain of 0.01 and concrete strain close to 0.003, which is acceptable in terms of required ductility. RC beams exhibited gain of capacity after yielding, which is associated to the strain hardening behavior of reinforcing steel. On the other hand, peak moments for R/SFRC beams occurred for a curvature coinciding with the beginning of yielding of steel rebars, Φ_y, followed by a gradual reduction of moment with increasing curvature, which is associated to the tensile stress decay. In Figure 4b, load-deflection curves are also presented, showing a similar behavior and confirmed that use of fibers resulted in loss of ductility.

(a) (b)

Figure 3: Failure modes observed for RC and R/SFRC beams: a) B3-0-10; b) B9-2/L-10.

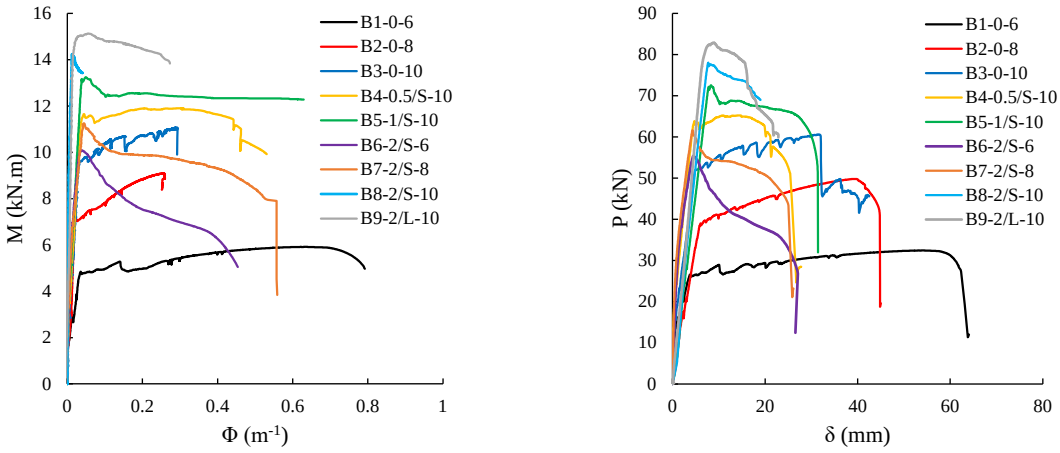

(a) (b)

Figure 4: Beams response: a) moment-curvature; and b) load-deflection.

A summary of the main results obtained from moment-curvature relationships is presented in Table 4. Significantly increase in the moment at yielding, M_y, was achieved with the use of fibers, with ratios between R/SFRC and RC beams ($M_{R/SFRC}/M_{RC}$) ranging from 1.21 to 2.09. Increases in cracked stiffness, $(EI)_{cracked}$, were also obtained with increasing fiber content. Finally, moment capacities for a curvature of 0.1 m^{-1}, $M_{0.1}$, were compared to those computed with Henager and Doherty's approach, M_{HD}, leading to a good agreement, especially for beams containing 10-mm diameter rebars. Differences with respect to other rebars may be explained by deviations in mechanical properties of rebars used.

Table 4: Summary of results for beam tests.

Specimen	**M_y (kN.m)**	**$M_{0.1}$ (kN.m)**	**Φ_y (m^{-1})**	**$(EI)_{cracked}$ ($kN.m^2$)**	**$M_{R/SFRC}/M_{RC}$**	**$M_{0,1}/M_{HD}$**
B1-0-6	4.84	4.97	0.045	108	-	0.86
B2-0-8	7.05	7.82	0.039(SG)	181	-	0.77
B3-0-10	9.60	10.4	0.036	267	-	1.01
B4-0.5/S-10	11.6	11.5	0.046	252	1.21	1.01
B5-1/S-10	13.2	12.5	0.039	338	1.38	0.97
B6-2/S-6	10.1	8.73	0.037	273	2.09	0.76
B7-2/S-8	11.2	10.2	0.043	260	1.59	0.85
B8-2/S-10	14.2	*	0.032(SG)	444	1.48	*
B9-2/L-10	15.0	14.9	0.031	484	1.56	0.97

(SG) data obtained using strain gage
* malfunction

With the constitutive relationships for the materials, it is also possible to develop non-linear cross-section analysis to obtain a full theoretical moment-curvature relationship. A comparison between predicted and experimental moment-curvature for beams B3-0-10, B5-1/S-10 and B9-2/L-10 are presented in Figures 5a, 5b and 5c, respectively. Excellent agreement was achieved between models and experiments and the contributions of reinforcing steel and concrete in tension to the bending capacity can be obtained from the model.

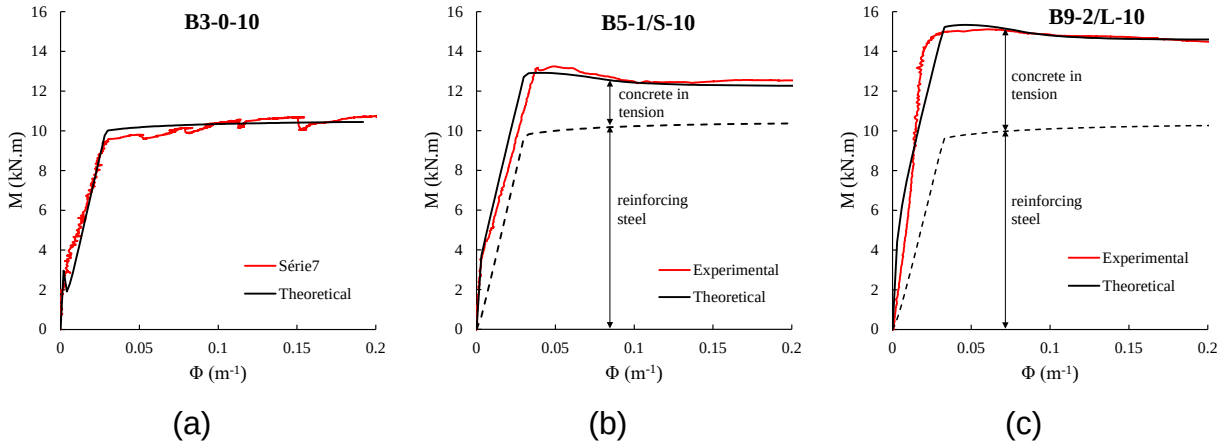

Figure 5: Comparison between theory and experiment and contributions of fiber in tension and reinforcing steel: a) B3-0-10; b) B5-1/S-10; c) B9-2/L-10.

Regarding crack formation and growth, a comparison between beams B2-0-8 and B7-2/S-8 is presented in Figure 6. It can be seen that cracks for R/SFRC beams are thinner even for greater bending moments. For example, crack openings smaller than 0.3 mm were obtained for a bending moment M = 11.1 kN.m applied to B8, whereas openings close to 0.9 mm were measured for M = 7.3 kN.m applied to B2. In general, a critical section with a wider crack clearly distinguishable from the others could be identified. This is likely associated with a lesser fiber content in that section, leading to a considerable fiber pullout when compared to other sections. This may also explain the fact that, in some cases, cracks other than the critical cannot be seen with naked eye. However, as shown in Figure 6, these 'invisible' cracks can be captured using DIC.

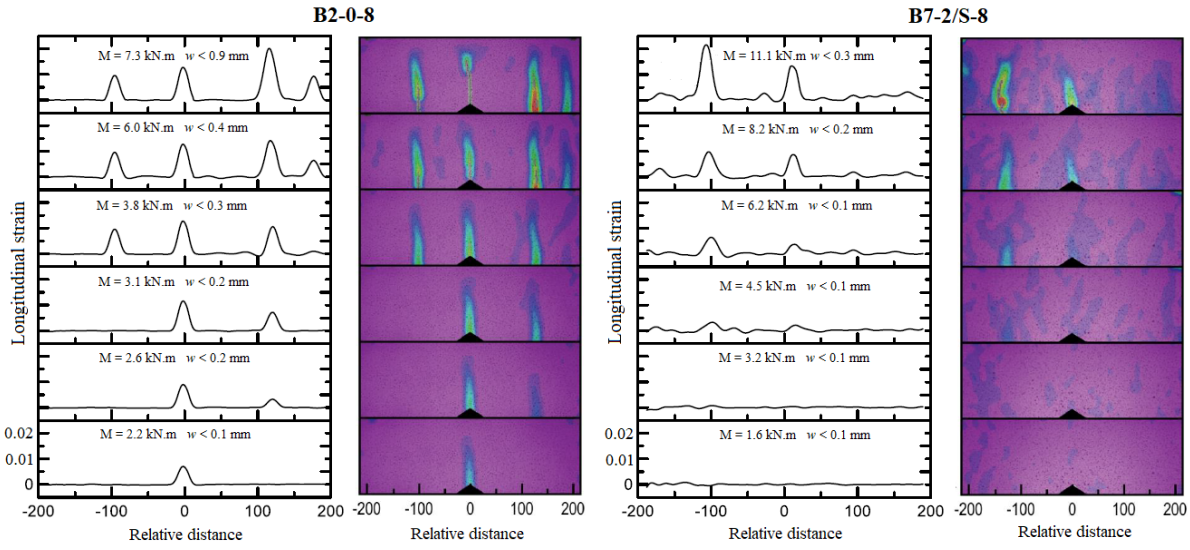

Figure 6: Crack pattern and growth: a) B2-0-8; b) B7-2/S-8.

4. CONCLUSIONS

In this work, behavior of R/SFRC beams subject to flexure was studied. Full material characterization was carried out and under-reinforced beams having different fiber contents and reinforcing ratios were tested under 4-point bending and monitored using DIC. The following conclusions can be drawn from the study:

- DIC proved to be suitable non-contact method to monitor curvature and crack formation and growth in reinforced concrete structures;
- Increases in moment capacity ranging from 21 to 109% were achieved with the use of fiber reinforced concrete matrix with respect to plain concrete. Cracked stiffness was also improved with increasing fiber contents;
- Theoretical predictions with cross-section analysis using actual non-linear constitutive relationships proved to be useful to predict behavior and can be extended to other cross-section configurations and material properties;
- Thinner cracks were obtained for R/SFRC beams even for greater loads. Crack pattern of R/SFRC crack was also different from RC, characterized by a critical wider crack and multiple thin cracks, sometime imperceptible.

ACKNOWLEDGMENTS

The authors acknowledge Brazilian research agencies (CAPES, CNPq and FAPERJ) for financial support and Lafarge-Holcim and Ibrata for supplying the material for the research. Authors would like to express their gratitude to Dr. Giancarlo Gonzáles and Prof. José Roberto Freire for the valuable support with DIC analysis.

REFERENCES

[1] Di Prisco, M., Plizzari, G., & Vandewalle, L. (2009). Fibre reinforced concrete: new design perspectives. Materials and Structures, 42(9), 1261-1281.

[2] Sorelli, L. G., Meda, A., & Plizzari, G. A. (2006). Steel fiber concrete slabs on ground: a structural matter. ACI Structural Journal, 103(4), 551.

[3] Chiaia, B., Fantilli, A. P., & Vallini, P. (2009). Combining fiber-reinforced concrete with traditional reinforcement in tunnel linings. Engineering Structures, 31(7), 1600-1606.

[4] Carter W. (1971). Wire-reinforced precast concrete decking panels, Precast Concrete (UK), pp. 703-708.

[5] Dinh, H. H., Parra-Montesinos, G. J., & Wight, J. K. (2010). Shear strength model for steel fiber reinforced concrete beams without stirrup reinforcement. Journal of Structural Engineering, 137(10), 1039-1051.

[6] Henager, C. H., & Doherty, T. J. (1976). Analysis of reinforced fibrous concrete beams. Journal of the Structural Division, 102.

[7] Swamy, R. N., and Al-Ta'an, S. A. (1981). Deformation and ultimate strength in flexure of reinforced concrete beams made with steel fiber concrete. ACI Journal, 395-405.

[8] Oh, B. H. (1992). Flexural analysis of reinforced concrete beams containing steel fibers. Journal of Structural Engineering, 118(10), 2821-2835.

[9] Bentur, A., & Mindess, S. (1983). Concrete beams reinforced with conventional steel bars and steel fibres: properties in static loading. International Journal of Cement Composites and Lightweight Concrete, 5(3), 199-202.

[10] Abdul-Ahad, R. B., & Aziz, O. Q. (1999). Flexural strength of reinforced concrete T-beams with steel fibers. Cement and Concrete Composites, 21(4), 263-268.

[11] Fib, Fédération Internationale du Béton (2010). fib model code for concrete structures 2010, October 2013. Berlin: Ernst&Sohn.

[12] van Zijl, G. P. A. G., & Mbewe, P. B. K. (2013). Flexural modelling of steel fibre-reinforced concrete beams with and without steel bars. Engineering Structures, 53, 52-62.

[13] Mertol, H. C., Baran, E., & Bello, H. J. (2015). Flexural behavior of lightly and heavily reinforced steel fiber concrete beams. Construction and Building Materials, 98, 185-193.

[14] Lim, T. Y., Paramasivam, P., & Lee, S. L. (1987). Behavior of reinforced steel-fiber-concrete beams in flexure. Journal of Structural Engineering, 113(12), 2439-2458.

[15] Mobasher, B., Yao, Y., & Soranakom, C. (2015). Analytical solutions for flexural design of hybrid steel fiber reinforced concrete beams. Engineering Structures, 100, 164-177.

FUTHER ANALYSES ON HORNIFICATION PROMOTION BY WASHING CYCLES ON NATURAL VEGETABLE FIBERS

Sophia Mendes(1), Lisiane Nunes Hugen (2), Renata Daniel dos Santos(3), Romildo Dias Toledo Filho(3) and Saulo Ferreira Rocha (1)

(1) Department of Engineering, Universidade Federal de Lavras, Minas Gerais-MG, Brazil

(2) Department of Forest Science, Universidade Federal de Lavras, Minas Gerais-MG, Brazil

(3) Department of Civil Engineering, COPPE, Universidade Federal do Rio de Janeiro, Rio de Janeiro-RJ, Brazil

https://doi.org/10.21452/bccm4.2018.02.31

Abstract

Several treatments on natural fibers are presented by literature as effective process to mitigate the high water absorption and reduce dimensional variation. The wetting and drying cycles treatment is pointed as an efficient treatment since they promote the stiffening of the polymer structure of the fiber cells, known as hornification. One of the main characteristics of this process is the greater dimensional stability of the fibers. In this context, the objective of the present research is to investigate the influence of wetting time, fiber/water ratio and number of wetting and drying cycles on the treatment and its effect on sisal fibers chemical and mechanical properties. The treatment of the fibers was performed in water at room temperature (T = 22 °C), varying wetting time (1h and 3h) and fiber/water ratio (1:10 and 1:40), drying process 80°C during 15 hours. Direct tensile tests, thermogravimetry analysis (TG) and infrared spectroscopy (FTIR) were performed on raw, pre-washed and treated fibers. The results revealed that lower fiber/water ratios are better to hornification promotion. Immersion times of 3 hours were efficient to increase stiffness in all studied cases.

Keywords: Natural fibres, Fiber treatments, Hornification, Mechanical properties.

1. INTRODUCTION

Composites reinforced with vegetable fibers have the potential to become the final choice of green material, since it is a material of renewable origin, has wide availability and low relative cost [1]. However, it has disadvantages, such as low chemical adhesion, high water absorption capacity. The increase of the composite moisture causes the variation in fiber volume, which

results in a weaker physical interaction between the materials [2]. In this way, several studies involving physical and chemical treatments in natural fibers have been developed to solve this problem. These treatments seek to promote the increase of surface roughness, the cleaning of the surface of the fiber and decrease the absorption of moisture [3].

The hornification reduces the water absorption capacity of the fibers and improves fiber-matrix bonding, that is because it causes structural changes in the cellulosic fibers from the wetting and drying cycles in the fibers [4,5,6]. In addition to simple and low energy consumption, this procedure increases the degree of crosslinking in the fiber microstructure, reduces the volumetric changes of natural fibers as well as promotes changes in their mechanical properties [1].

According to Ferreira et al. [5], the hornification in sisal fibers provides improvement in interfacial adhesion to the matrix. The treatment applied consisted of immersion in water for three hours followed by a slow drying, of 16 hours, at 80 ° C. In another research, Ferreira et al. [1] applied the same treatment to different fibers, subjected to 5 and 10 washing cycles. The results indicated a variation in treatment efficiency. The author attributed these differences to the nature of the fibers, such as morphology and its chemical composition. However, the variables of the treatment itself was approached by the author as a critical point for the effectiveness of drying and wetting cycles.

However, there are still several bottlenecks on the effect of this treatment on the fiber, and to what extent it can improve the fiber / matrix interface. In this context, the objective of the present research is to investigate the influence of wetting time variation, fiber / water ratio and number of wetting and drying cycles on the property of the fibers (chemical and mechanical).

2. MATERIALS AND METHODS

2.1 Materials

Sisal fibers were obtained from the Municipality of Valente-BA provided by the Association of Sustainable Development and Solidarity of the Region Sisaleira (APAEB), former Association of Small Farmers, with length ranging from 90 cm to 100 cm. These fibers were the same studied by Ferreira et al. [1,5]. According to Silva et al. [7], the microstructure of the sisal fiber is formed by numerous individual fibers (fiber-cell) with a diameter of 6 to 30 μm and a chemical composition of 54 to 66% of cellulose, 12 to 17% of hemicellulose, 7 to 14% lignin, 1% to 7% ash.

The sisal fibers were washed in hot water at 80 ° C for one hour to remove the surface residues from the extraction process, at the end of this process the fibers were dried at 40 ° C. This process was named "prewash". This procedure was executed according Ferreira et al. [5]

2.2 The fiber hornification treatment

The hornification treatment was applied to the prewashed fibers. The treatment of the fibers was performed using water at room temperature (T = 22 °C ± 2°C), varying the wetting time, and the fiber/water ratio. The drying process was performed in a muffle-type oven Quimis, at a temperature of 80 °C.

The oven was programmed to reach 80 °C at a heating rate of 1 °C/min and maintain this temperature for 15 h. After this drying time, the oven was natural air cooled to 22 °C in order to avoid possible thermal shocks in the fibers. This procedure was repeated 1 and 5 times. The treatments are best described in Table 1.

Table 1 : Description of treatments.

Treatment code	Wetting Time	Temperature	Fiber/Water Ratio	Cycles
1.A.10.1	1h	22 °C	1:10	1
1.A.10.5	1h	22 °C	1:10	5
1.A.40.1	1h	22 °C	1:40	1
1.A.40.5	1h	22 °C	1:40	5
3.A.10.1	3h	22 °C	1:10	1
3.A.10.5	3h	22 °C	1:10	5
3.A.40.1	3h	22 °C	1:40	1
3.A.40.5	3h	22 °C	1:40	5

2.3 Thermogravimetrical analyses (TGA)

TGA analyses were performed in a DGA-60H Shimadzu, getting simultaneous TGA/ DTA. Samples with 4 mg weight were subjected to a heating rate of 10 °C/min until reaching 500 °C in an open platinum crucible using 60 mL/min of nitrogen as the purge gas.

2.4 Fourier transform infrared (FTIR) spectroscopy

FT-IR analyses were performed in an IRAffinity-1 Spectrometer Shimadzu, through the attenuated total reflection technique (ATR), with resolution of 4 cm^{-1} in the range of 4000 to 600 cm^{-1}. Stored results were averages of 24 scans.

2.5 Wettability analysis

The contact angle was performed according to ASTM D-7334 [8] using the Krüss goniometer DSA25 (Krüss, Germany) by the sessile drop method at room temperature (22 ± 2°C). The contact angle measurements were performed with the deposition of deionized water droplets, with a volume of 100 μL, using a 0.507 mm diameter needle. ImageJ software was used for data processing.

2.6 Direct tensile tests

For the tensile tests, the MTS Tytron 250 electromechanical test machine was used with a 50 kN load cell, with a displacement rate of 0.3 mm / min, according to ASTM C1557 [9]. Where each fiber had a length of 40 mm and a average diamenter of 0.023 mm^2 [1, 10], fixed in paper mold for better alignment in the machine and adhering the grips of the equipment. Fifteen repetitions were used for each treatment.

3. RESULTS AND DISCUSSION

3.1 Thermogravimetrical analysis (TGA)

Figure 1 shows the thermogravimetric analysis (TGA) performed in the natural and treated sisal fibers.

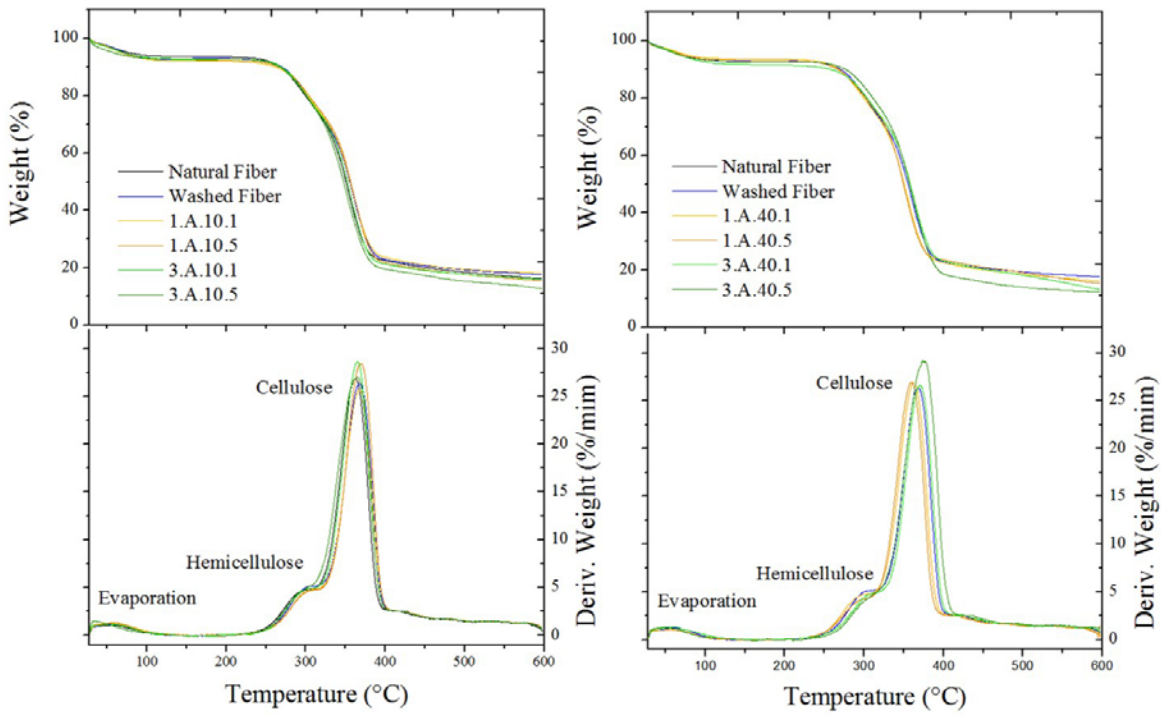

Figure 1: Thermogravimetry analysis (TG/DTG) of the sisal fibers before and after the different treatments.

According Figure 1 three decomposition intervals for all the fibers studied can be observed. The first step being water loss (about 100 ° C). The second stage occurs between 250 and 350 ° C, which corresponds to the simultaneous decomposition of cellulose, hemicelluloses, lignin and pectins [11].

At intervals between 350 and 400 ° C the third step occurs which is characteristic of cellulose degradation. At the end of the third peak there is a "shoulder" in relation to the slow degradation of lignin, which occurs between 250 and 600 ° C [1].

The results indicate that no significant difference in the thermoanalysis was observed, indicating no significant removal of soluble lignin and hemicelluloses.

3.2 Fourier transform infrared (FTIR) spectroscopy

The FTIR spectra of sisal fibers are show in Figure 2. The spectra obtained in the present study for natural and treated fibers present vibration modes according to the literature [12] and [13], observing characteristics of the lignocellulosic fibers. Sisal fibers have cellulose, hemicellulose and lignin as the most important components, and these elements present peaks in the largest region between 800 and 2000 cm^{-1} [1]. The majority of them are related to lignin, correlated with the aromatic ring groups of the groups Metoxil ($-OCH_3$), C-O-C and C = C [14,15].

An increase in peak intensity at 3400 cm^{-1} was observed to treated fibers. The increase in this peak was higher for treated fibers with longer immersion time and longer treatment cycles. This modification may be attributed to hydroxyl groups (-OH). According to Ferreira et al. [1], hornification provides increased structural hydrogen bonds due to the high energy utilized by the treatment that blocks these bonds.

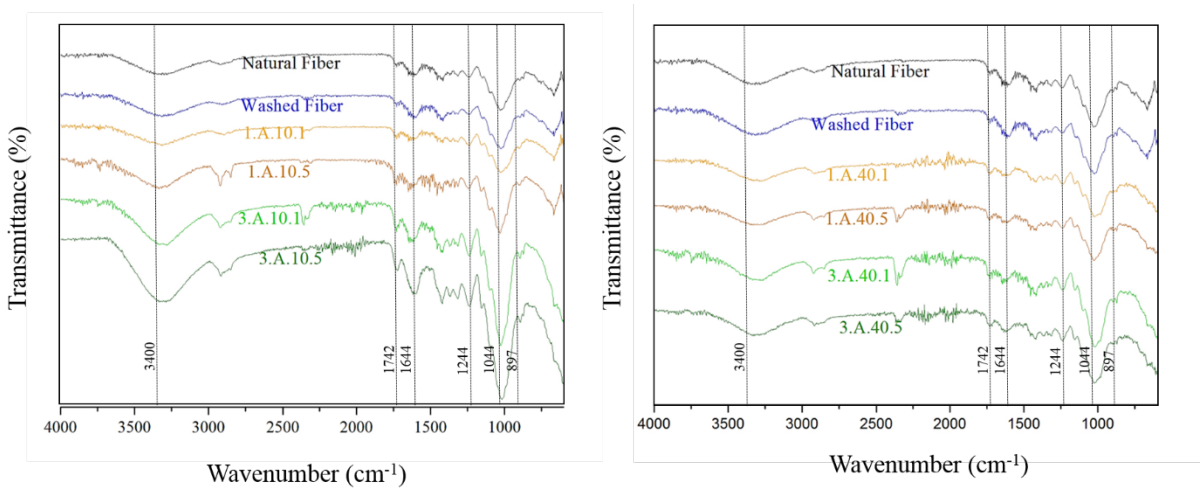

Figure 2: Infrared spectroscopy of sisal fiber before and after the different treatments.

The C = O elongation attributed to the 1742 cm^{-1} range corresponds to the carboxylic acid and ester components of the hemicelluloses [16]. The carboxylic groups are able to connect to another functional group through hydrogen bonds, which may result in an increase in the network of lignin macromolecules [17].

This mechanism promotes a better interaction between lignin, cellulose and hemicellulose, resulting in a more resistant material and in greater crystallinity, stiffness and deformation capacity [5]. Studies have also suggested that the covalent bonds between lignin and hemicelluloses exist in native wood [18]. In addition to the covalent bond between lignin and hemicellulose, there is also hydrogen bonding between hemicellulose and cellulose [5].

The peak at 1044 cm-1 is attributed to the stretching of CO and to the cellulose group vibration [15]. The peak 1644 cm^{-1} is attributed to the C = C elongation of lignin and 1244 cm^{-1} is attributed to the axial asymmetry of link =COC both to ether, esther and phenol groups [1]. According Morán et al. [19] these modifications may be correlated to absorbed water on cellulose. This water can be presented in -OH linkages, difficulting the interaction between fiber and water, resulting in a lower water absorption.

3.3 Wettability analysis

The results of contact angle measurement on all fibers are shown in Figure 3. Values and standard deviation of measurements are presented in Table 2.

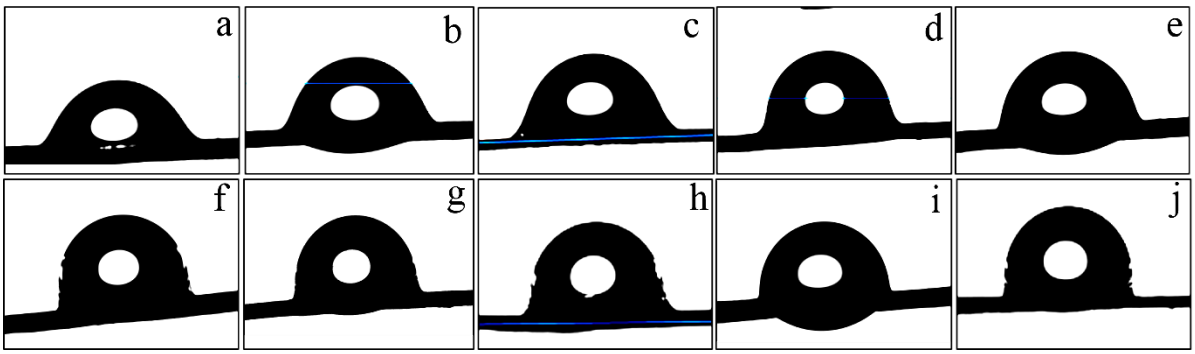

Figure 3: Images of the angle formed on the sisal fiber : a) Natural Fiber, b) Washed Fiber, c) 1.A.10.1, d) 1.A10.5, e) 1.A.40.1, f) 1.A.40.5, g) 3.A.10.1, h) 3.A.10.5, i) 3.A40.1, j) 3.A 40.5.

It is possible to observe that after treatment application the drop above the fiber present a uniform and circular shape. This significant difference between raw and treated fibers is not only present on probe geometries but in the contact angles (Table 2).

Table 2: Mean values and standard deviations for initial and final contact angles measured for water on natural fibers.

	Contact angle (deg)	
Treatment	T Initial	T Last
Natural Fiber	27.09 (10.42)	24.81 (10.93)
Washed Fiber	37.95 (17.85)	36.33 (11.09)
1.A.10.1	34.78 (20.60)	29.43 (17.52)
1.A.10.5	53.30 (9.97)	48.22 (14.57)
1.A.40.1	77.12 (20.11)	75.99 (24.52)
1.A.40.5	72.08 (12.35)	69.62 (11.78)
3.A.10.1	60.01 (12.51)	59.47 (11.55)
3.A.10.5	66.32 (9.54)	60.62 (22.34)
3.A.40.1	58.89 (15.45)	57.20 (19.89)
3.A.40.5	75.60 (8.25)	74.71 (16.39)

Treatments with lower number os cycles present a higher contact angle. The same result was obsreved to treatments with lower fiber/water ratio. This results corroborate with FTIR data. The increase in the OH groups may difficult water sorption, promoting a more hydrophobic surface.

3.4 Direct tensile tests

Typical stress-strain curves of untreated and treated sisal fibers are shown in Figure 4. The tensile strength and stiffness of sisal fiber increased after mostly treatments. It is possible to observe that one hour immersion was more effective in comparison to 3 hours in all studied ratios.

.

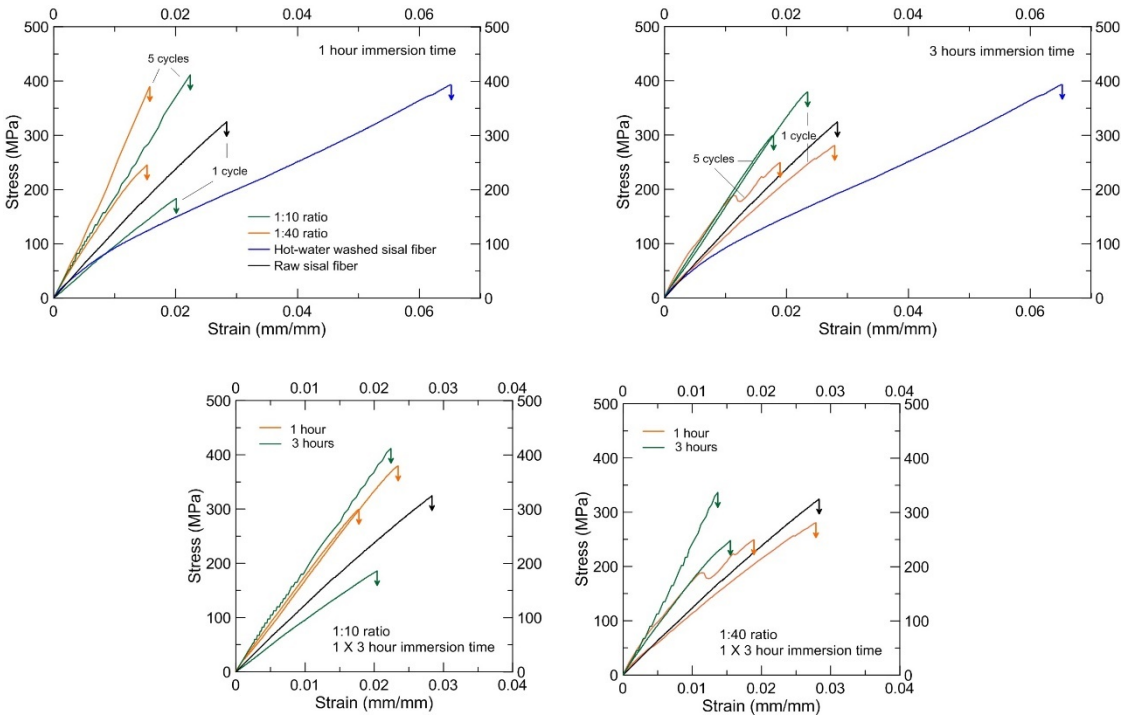

Figure 4: typical tensile curves of raw and treated fibres.

Results indicate that 5 cycles treatment was more effective in hornification promotion, even with no control of fiber/water ratio. Cycles of wetting and drying change the microstructure of vegetable fibers, which modifies the polymeric structure of the fiber-cells resulting in higher tensile strength and strain [1].

4. CONCLUSIONS

The work in hand investigated the effect treatments on sisal fibers properties. The following conclusions can be drawn from the present research. In evaluating the effect of the hornification cycles on sisal fibers, it is noted that the treatment did not cause changes in the thermal degradation of the fiber. After the treatments, the sisal fibers showed alterations in their chemical bonds, especially the acetyl group and promoted a reduction in the water absorption capacity of the fibers, allowing greater dimensional stability. When correlating the obtained results, it is emphasized that 3.A.10.5 of hornification improves characteristics of sisal fibers that reinforce its use as reinforcement in composites.

ACKNOWLEDGEMENTS

Authors thank to Universidade Federal de Lavras (UFLA), the Núcleo de Ensino e Pesquisa em Materiais e Tecnologias de Baixo Impacto, à Ambiental na Construção Sustentável (NUMATS-UFRJ), for supporting the experimental work, and also thank the financial support granted by Coordenação de Aperfeiçoamento de Pessoal de Nível Superior (CAPES), Conselho Nacional de Desenvolvimento Científico e Tecnológico (CNPq) and Fundação de Amparo à Pesquisa do Estado de Minas Gerais (FAPEMIG).

REFERENCES

[1] Ferreira, S. R.; Silva, F. A.; Lima, P. R. L.; Toledo Filho, R. Dias. Effect of hornification on the structure, tensile behavior and fiber matrix bond of sisal, jute and curauá fiber cement based composite systems. Construction and Building Materials, v. 139, p. 551–561, 2017.

[2] Li, Y.; Hu, C.; Yu, Y. Interfacial studies of sisal fiber reinforced high density polyethylene (HDPE) composites. Composites Part A: Applied Science and Manufacturing, v. 39, n. 4, pp. 570- 578, 2008

[3] Abou-Yousef, H.; El-Sakhawy, M.; Kamel, S. Multistage pulping by using alkali/cairo's acid treatment. Ind. Crops Prod. v. 21, n. 3, p. 337–341, 2004.

[4] Ferreira, S. R.; Lima, P. R. L.; Silva, F. A.; Toledo Filho, R. D. Effect of sisal fiber hornification on the adhesion with Portland cement matrices. Revista Materia. v. 17, p. 1024–1034, 2012.

[5] Ferreira, S. R.; Silva, F. A.; Lima, P. R. L.; Toledo Filho, R. D. Effect of fiber treatments on the sisal fiber properties and fiber–matrix bond in cement based systems. Construction and Building Materials, v. 101, p. 730–740, 2015.

[6] Claramunt, J.; Ardanuy, M.; García-Hortal, J. A.; Tolêdo Filho, R. D. The hornification of vegetable fibers to improve the durability of cement mortar composites. Cem. Concr. Compos. v. 33, p. 586–595, 2011.

[7] Silva, F. A.; Chawla, N.; Toledo Filho, R. D. Tensile behavior of high performance natural (sisal) fibers. Compos. Sci. Technol. v. 68, p. 3438–3443, 2008.

[8] AMERICAN SOCIETY FOR TESTING AND MATERIALS - ASTM D-7334, Standard Practice for Surface Wettability of Coatings, Substrates and Pigments by Advancing Contact Angle Measurement, West Conshohocken, 2008.

[9] AMERICAN SOCIETY FOR TESTING AND MATERIALS - ASTM C1557, Standard Test Method for Tensile Strength and Young's Modulus of Fibers, West Conshohocken, PA, 2013.

[10] Ferreira, S. R.; Pepe, M.; Martinelli, E.; de Andrade Silva, F.; Toledo Filho, R. D. Influence of natural fibers characteristics on the interface mechanics with cement based matrices. Composites Part B: Engineering, v. 140, p. 183-196, 2018.

[11] Arbelaiz, A.; Fernández, B.; Ramos, J.A.; Mondragon, I. Thermal and crystallization studies of short flax fibre reinforced polypropylene matrix composites: effect of treatments. Thermochim. Acta, v. 440, p. 111–121, 2006.

[12] Barreto, A.C.H.; Rosa, D.S.; Fechine, P.B.A.; Mazzetto, S.E. Properties of sisal fibers treated by alkali solution and their application into cardanol-based biocomposites. Compos. A. v. 42, p. 492–500, 2011.

[13] Herrera-Franco PJ, Valadez-González A. A study of the mechanical properties of short natural-fiber reinforced composites. Composites Part B. v. 8, p. 597–608, 2005.

[14] Yang, H.; Yan, R.; Chen, H.; Lee, D. H.; Zheng, C. Characteristics of hemicellulose, cellulose and lignin pyrolysis, Fuel. v. 86, n. 12–13, pp. 1781–1788, 2007.

[15] Sarkanen, K.V., Lignins: occurrence, formation, structure and reactions. 1987, university of washington: seattle, washington.

[16] Zugernmaier P. Crystalline cellulose and derivatives: characterization and structures. Springer series in wood science. Springer, 2008.

[17] Derkacheva, O., Studying the structure of native, residual and dissolved lignins by FTIR spectroscopy method. Proceedings of first international workshop on physicochemical properties of lignins, p.255 – 257, 2005.

[18] Bjorkman, A. Studies o finley divided wood part 3. extraction of lignin-carbohydrate complexes with neural solvents. svensk papperstidning, v. 60, n. 7, p. 243-251, 1957.

[19] Morán, J. I.; Alvarez, V. A.; Cyras, V. P.; Vázquez, A. Extraction of cellulose and preparation of nanocellulose from sisal fibers. Cellulose, v. 15, n. 1, p. 149-

TOUGHNESS ANALYSIS OF STEEL FIBER REINFORCED CONCRETE BY PULLOUT TEST

Felipe S. B. Jorge (1) and Conrado S. Rodrigues (1)

(1) Department of Civil Engineering, Centro Federal de Educação Tecnológica de Minas Gerais, Brazil

https://doi.org/10.21452/bccm4.2018.02.32

Abstract

Use of steel fibers in cement-based composites has become popular due to possibility of using that material as total or partial replacement of conventional reinforcement, as in floor slabs or tunnel cover. This reinforcement aims at improving composites properties with regard, mainly, to cracks propagation. It's known that concrete has high compressive strength and durability, but its toughness is low, being considered a fragile material. The performance of the fiber as stress bridge depends on several factors, among them bond strength between fiber and matrix. Interfacial Transition Zone (ITZ) is one in which first cracks that lead to material failure appear. Some researches with mineral additives, such as rice husk ash (RHA), are aimed at ITZ densification. RHA has a high content of amorphous silica, which gives it high potential for its pozzolanic activity. That RHA characteristic is able to potentiate new hydration products formation, especially C-S-H, giving a higher density to cement matrix and pores and voids reduction. Research's objective was to evaluate the effect of cement substitution by RHA, aiming to densify cement matrix to point where the adhesion tension with steel fiber was higher than in conventional mixture. For this, control specimens were produced and 15% of the cement replaced by RHA. Through the single fiber pullout test it was possible to measure the adhesion tension between steel fiber and cement matrix. Results indicate an increase in the adhesion strength with a long curing time, indicating that the RHA hydration occurs late in relation to cement.

Keywords: Rice Husk Ash; Bond Strength, Steel Fiber

1. INTRODUCTION

In order to improve the concrete performance, with respect to toughness, studies have been developed through incorporation of fibers to the matrix, which act as a bridge of stress, promoting to the composite a better fissure response. The fiber acts by transmitting tensions from one side to other of fissure, avoiding the stress concentration, which avoids the early material failure [1]; [2].

Steel fiber reinforced concretes can be produced using the same practice of producing a conventional concrete, with adaptations to promote homogeneity. Particular attention should be given to the uniform fiber dispersion along the concrete mixing in order to achieve performance improvements in concrete mechanical properties, also considering the workability required for a suitable mixing, release and finishing of this composite. Even with use of superplasticizers, this percentage of incorporation remains around 2% when turning into conventional concrete mixing practices [3]. To Johnston [4], this percentage is between 0.25 and 1.0% by volume.

Although the increase in fiber-reinforced concrete properties is known, it is not yet possible to quantify this gain, since fibers are randomly distributed in the matrix. Other factors influencing this relationship are type and size fiber, their constituent material, aspect ratio, incorporated fiber volume and the quality of the cementitious matrix (characterized by interfacial transition zone between composite phases). All these variables influence the fiber / matrix adhesion stress, which is property that will promote toughness to fiber reinforced concrete [3]; [5].

The interaction of concrete matrix and fibers is one of main challenges of reinforced concrete research. This region known as Interfacial Transition Zone (ITZ) is responsible for the adhesion between that materials and as this region becomes denser, the interaction will be better and consequently increases composite strength [6].

Pozzolanic activity of materials consisting of large amounts of silica, such as rice husk ash (RHA), is of great importance to promote a more complete cement hydration, making the matrix more dense and less subject to degradation by external agents and, in case of steel fiber reinforced concrete reinforced, increase the adhesion strength between the materials [7]. In addition, because they have particles smaller than cement, they allow a better compaction of the cement paste [8].

Research's objective was to evaluate the effect of cement substitution by RHA, aiming to densify cement matrix to point where the adhesion tension with steel fiber was higher than in conventional mixture. For this, control specimens were produced and 15% of the cement replaced by RHA. Through the single fiber pullout test it was possible to measure the adhesion tension between steel fiber and cement matrix. Results indicate an increase in the adhesion strength with a long curing time, which confirms that the RHA hydration occurs late in relation to cement.

2. MATERIALS AND METHODS

2.1 Materials

The materials used in this research were cement, sand, gravel # 0, steel fiber, water, superplasticizer and rice husk ash. The cement used was the Portland High Initial Strength Cement (CPV-ARI) from Holcim. Because it is a purer cement, it is ideal to evaluate the efficiency of RHA incorporation and its pozzolanic activity in the composite. The sand used was average river sand, with fineness modulus of 1.65 and maximum characteristic size of 1.2mm. Coarse aggregate was grade # 0 of gneiss with 12.5mm for maximum dimension and 1.11 fineness modulus. Industrialized highly reactive RHA presenting 92% of amorphous silica, average diameter of 7.7 μm, density and its specific surface area (S_{BET}) of, respectively, 2161 Kg/m^3 and 21150 m^2/Kg. As superplasticizer, Fluxer RMX 7000 from ERCA was used.

The steel fibers adopted in this research were DRAMIX type 80/60BG fibers manufactured by Belgo Bekaert in accordance with ASTM A820 [10]. It is a smooth fiber with hooks. The fiber characterization is described in Table 1.

Table 1 – Steel fiber characterization

Steel fiber Dramix 80/60BG - Belgo Bekaert	
Type of fiber	SF01
Diameter (mm)	0,75
Length (mm)	60
Tensile strength (N/mm²)	1.100
Max. load (N)	485
Aspect ratio (l/d)	80

Source: Belgo Bekaert

2.2 Methods

Table with proposed formulations is presented in Table 2. For the formulations water / binder factor, sand, gravel and superplasticizer were maintained. As variables were adopted formulations without RHA and with replacement of 15% of cement by RHA.

Table 2 – Quantitative materials for each formulation

Materials for 1m³ of concrete	**Control**	**15% RHA**
Cement (Kg)	409,84	348,36
RHA (Kg)	0,00	61,48
Sand (Kg)	568,85	568,85
Gravel (Kg)*	1292,62	1292,62
Water (Kg)	179,51	179,51
Water / binder factor	0,44	0,44
Superplasticizer (Kg)	2,61	2,61
* removal after mixing in concrete mixer		

Samples

Five cylindrical specimens of ø50mm per 100mm height were produced for each proposed formulation. It was adopted as a mixing procedure of the materials the launch in conventional concrete mixer of 200 litres, first of half of the water, followed by aggregates. Mixture was blended for one minute for humidification of these components. Afterwards, the remainder of water, binders and superplasticizer were added. For 5 minutes these materials were homogenized. Total mixing time was 10 minutes. After homogenization, the material was sieved in a # 4.8mm mesh to remove the gravel, leaving only the paste and small aggregate. Moulds were filled in four layers and each one was compacted with a metal socket with 30 strokes. In each proof body (PB) a ø6.3mm steel bar 90mm long was introduced in the lower face, with half of this bar being kept external to the specimen. In the upper face was introduced a single steel fiber, which had the hooks subtracted, with anchorage length fixed at 20mm. Hooks were subtracted in order to measure only

the adhesion strength between matrix and fiber, without mechanical action generated by hooks. A device adapted to vibrate the mixture was used. Figure 1 shows details of the mould produced in acrylic, according to Abbas and Khan [9]. The PB's were demoulded with 24hs and curing method was by immersion in water saturated with calcium hydroxide in order to protect steel fiber against corrosion during minimum period of 28 days. After the curing period, the specimens were submitted to pullout test.

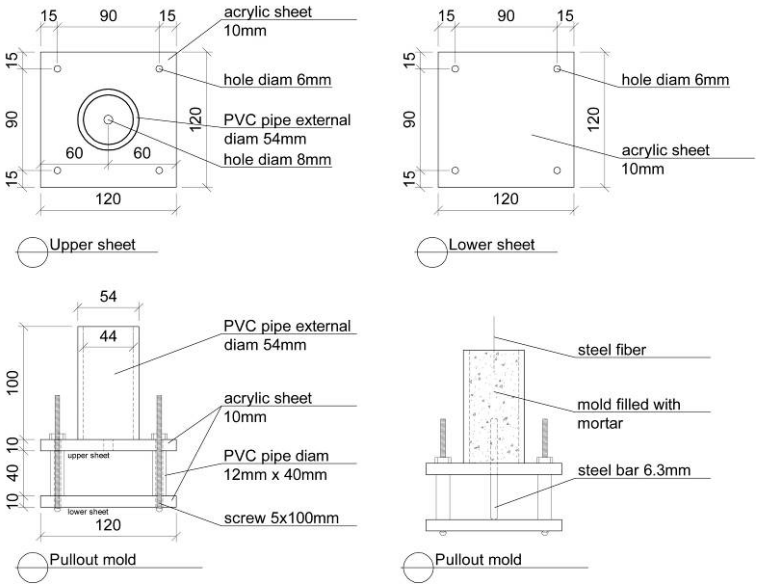

Figure 1 – Detail of acrylic mould for pullout testing [9]

Pullout test

Pullout tests were carried out using a universal EMIC / Instron 23-300 test machine, in which the appropriate claws for traction tests were installed. Lower clamp was used to fix the ø6.3mm rod, while upper clamp fixed steel fiber, as shown in Figure 2. Actuator displacement rate was defined as 0.2 mm/min and the cell load factor was 20KN. The software used to capture data was Bluehill 3, from Instron.

Figure 2 – Pullout test

3. RESULTS

In the analyses, first load peak (1), which configures adhesion tension zone and displacement limit point (2), was considered as key points, which for that research was 5mm. This point is located in frictional tension area, which extends from peak of load until complete pulling of fiber (in case of fibers without hook).

For the formulations with RHA, the linear phase is observed until the peak of load (adhesion tension) and then phase of frictional tension. For PB's without RHA results are dispersed and it is not possible to identify in some with clarity phase changes throughout the test, according to graphs shown in Figures 3a and 3b. It is also possible to notice a less diverse behaviour among PB's during trials, with lower variability of results and a more uniform pattern of results in those using RHA.

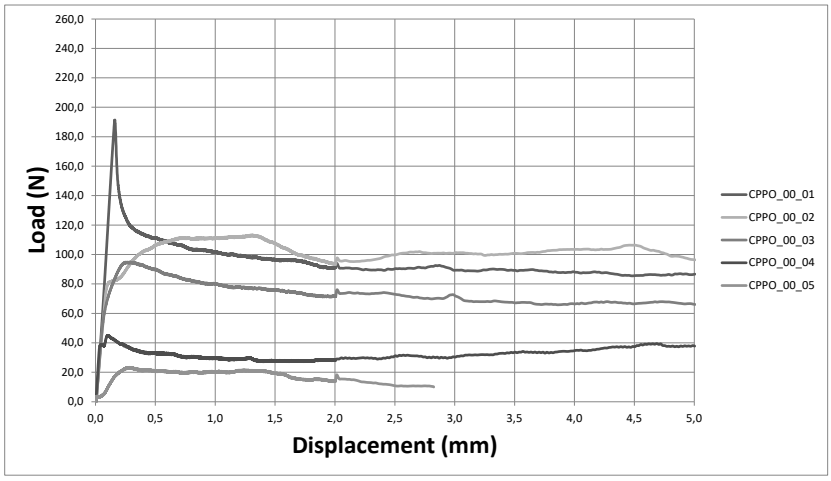

(a)

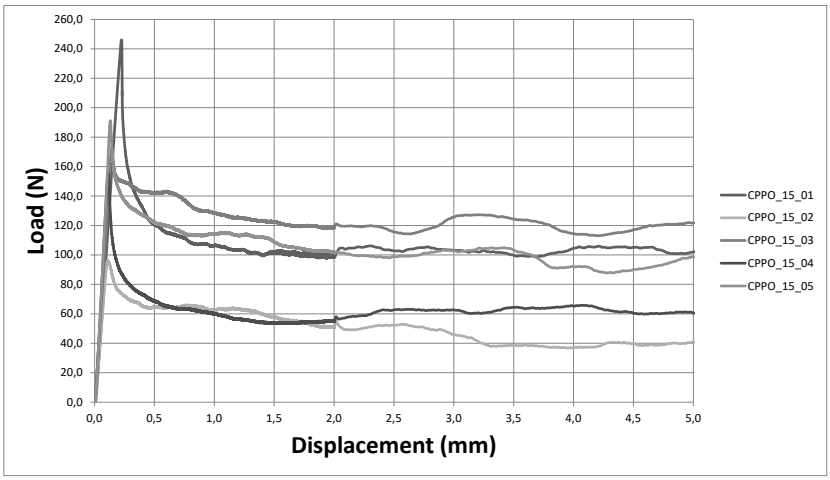

(b)

Figure 3a and 3b – Pullout results

Table 3 summarizes test results.

Table 3 – Pullout results

Pullout results									
Formulations	curing (days)	δp1 (mm)	Cp1 (N)	*f* p1 (MPa)	δp2 (mm)	Cp2 (N)	*f* p2 (MPa)	T (N.mm)	dev. T (N.mm)
CPPO_00_01	90	0,161	191,37	4,06	5,00	86,67	1,84	472,3	
CPPO_00_02	90	1,300	113,26	2,40	5,00	96,38	2,05	505,1	
CPPO_00_03	90	0,288	94,93	2,01	5,00	66,06	1,40	364,5	
CPPO_00_04	90	0,103	45,10	0,96	5,00	37,77	0,80	162,1	
CPPO_00_05	90	0,283	23,41	0,50	5,00	-	-	47,0	
Average_00			**93,6**	**1,987**		**71,7**	**1,522**	**310,2**	**199,0**
CPPO_15_01	90	0,224	245,99	5,22	5,00	102,13	2,17	534,3	
CPPO_15_02	90	0,113	96,20	2,04	5,00	40,87	0,87	252,6	
CPPO_15_03	90	0,145	172,56	3,66	5,00	121,73	2,58	615,2	
CPPO_15_04	90	0,116	155,11	3,29	5,00	60,36	1,28	314,6	
CPPO_15_05	90	0,132	191,31	4,06	5,00	98,81	2,10	521,4	
Average_15			**172,2**	**3,655**		**84,8**	**1,799**	**447,6**	**155,5**

Regarding post-crack friction strength, it was verified that mean tension at 5mm displacement point is of order of 18% higher in RHA formulations. It is also possible to note that the average peak load in formulations with RHA is 84% higher. Regarding the composites toughness, a gain of 44% was verified in formulations with RHA.

Standard deviation of composite toughness without RHA addition is significantly higher than in RHA formulations, suggesting that matrix is more heterogeneous with regions of different strengths in its composition.

Bond stiffness obtained for each pull-out curve is reported in Table 4. Results obtained for formulations with RHA are on the order of 36% higher than those without that mineral addition. In addition, the variation in results is lower (60%) for RHA formulations.

Table 4 – Bond stiffness

Bond stiffness		
Formulations	E (MPa)	dev. E (MPa)
Average_00%	408,1	172,0
Average_15%	554,3	104,5

4. CONCLUSIONS

- In pullout tests dispersed results were obtained, which did not follow a pattern of behaviour. This variability is due to the fact that cement matrix and, especially, the ITZ have regions of different resistances in its interior, besides the position, geometry and surface of constituent aggregates, as reported by ISLA et al. [11];
- With regard to bond stiffness, RHA had a good contribution in increasing modulus of elasticity, increasing the values obtained, as well as reducing variability of that results. This suggests a densification and homogenization of the ITZ, which contributes to improved performance of fiber reinforced composites;
- The strength gains at the initial load peak (84%), residual strength (18%) and toughness (44%) were also relevant. Therefore, it is correct to state, even with the great variability in the results, that in general, RHA contributes to the increase of steel fiber reinforced concrete properties, especially, toughness;
- It should be emphasized that a greater sampling is necessary to increase representativeness of results and dispersions. Pullout tests typically have a number of discarded specimens.

ACKNOWLEDGEMENTS

These results are part of a project involving PUC-Rio, CEFET-MG and Belgo Bekaert Arames S.A. The project is being financed by FAPERJ and FAPEMIG.

REFERENCES

[1] BRAZ, M. C. A.; NASCIMENTO, F. B. C. Concreto reforçado com fibras de aço. Ciências exatas e tecnológicas, v. 3, n. 1, p. 43-56, 2014. ISSN 2357-9919.

[2] BREITENBUCHER, R.; MESCHKE, G.; SONG, F.; ZHAN, Y. Experimental, analytical and numerical analysis of the pullout behaviour of steel fibres considering different fibre types, inclinations and concrete strengths. Structural Concrete, v. 15, n. 2, p. 126-135, 2014. DOI 10.1002/suco.201300058.

[3] BENTUR, A.; MINDESS, S. Fibre reinforced cementitious composites. 2. New York: Taylor & Francis Group, 2007. ISBN 978-0-415-25048-1.

[4] JOHNSTON, C. D. Fiber-reinforced cements and concretes. New York: Taylor & Francis Group, 2001. ISBN 90-5699-694-0.

[5] RANA, A. Some Studies on Steel Fiber Reinforced Concrete. International Journal of Emerging Technology and Advanced Engineering, v. 3, n. 1, p. 120-127, 2013. ISSN 2250-2459.

[6] LIAO, K. Y.; CHANG, P. K.; PENG, Y. N.; YANG, C. C. A study on characteristics of interfacial transition zone in concrete. Cement and Concrete Research, v. 34, p. 977-989, 2004. ISSN 0008-8846/$.

[7] KULKARNI, M. S.; MIRGAL, P. G.; BODHALE, P. P., TANDE, S. N. Effect of rice husk ash on properties of concrete. Journal of Civil Engineering and Environmental Technology, v. 1, n. 1, p. 26-29, 2014. ISSN 2349-8404.

[8] KAIKEA, A.; ACHOURA, D.; DUPLAN, F.; RIZZUTI, L. Effect of mineral admixtures and steel fiber volume contents on the behavior of high performance fiber reinforced concrete. Materials and Design, v. 63, p. 493-499, 2014. ISSN 0261-3069.

[9] ABBAS, M. Y.; KHAN, M. I. Fiber-Matrix Interfacial Behavior of Hooked-End Steel Fiber-Reinforced Concrete. Journal of Materials in Civil Engineering, v. 28, n. 11, 2016. DOI 10.1061/(ASCE)MT.1943-5533.0001626.

[10] ASTM-A820. Standard Specification for Steel Fibers for Fiber-Reinforced Concrete. United States of America: American Society for testing and materials: 4 p. 2016.

[11] ISLA, F.; RUANO, G; LUCCIONI, B. Analysis of steel fibers pull-out. Experimental study. Construction and Building Materials, v. 100, p. 183-193. 2015. ISSN 0950-0618.

COMPRESSIVE STRESS-STRAIN BEHAVIOUR OF R-PET FIBRE REINFORCED MORTARS

Matheus S. V. Fernandes(1), Margareth S. Magalhães(1) and Rodrigo B. Burgos(1)

(1) Postgraduate Program in Civil Engineering, Rio de Janeiro State University (UERJ), Rio de Janeiro, RJ, Brazil.

https://doi.org/10.21452/bccm4.2018.02.33

Abstract

This paper deals with an experimental and analytical study on the influence of recycled polyethylene terephthalate (R-PET) fibres as reinforcement of mortars. The mixtures were produced using Portland cement, fly ash, silica sand, superplasticizer and different amounts of R-PET fibres (0%, 1.0% and 2.0%). Dry density, total porosity and compressive tests were carried out. The results indicated that the incorporation of R-PET fibres significantly improves the post-cracking behaviour of mortars with a major improvement in mortar toughness. However, the addition of R-PET had no beneficial effect on the compressive strength and elastic modulus of the composite mixtures with 1% and 2%. A reduction of strength (up to 54%) and elastic modulus (up to 28%) was observed for composite mixtures due to increased porosity caused by fibre addition. Analytical models found in the literature for stress-strain behaviour were used along with curve fitting algorithms.

Keywords: Cement based composites, R-PET fibres, stress-strain behaviour.

1. INTRODUCTION

Polyethylene terephthalate (PET) is one of the most important and extensively used plastics in the world, especially for manufacturing beverage containers. In 2016, the worldwide annual consumption represented 480 billion PET bottles. However, most PET used as beverage bottles are thrown away after a single usage and disposed bottles are managed by landfill or incineration, which is causing serious environmental problems. Plastic materials are non-biodegradable in nature and burning is not a solution to consume such waste because this process releases dangerous chemical gases into the air. According to ABIPET [1], in 2015 only 51% of terephthalate bottles were recycled in Brazil.

Considerable research has been undertaken on the potential use of recycled PET (R-PET) in replacing natural aggregates of plain concrete [2,3], reinforced concrete beams [4] or as

reinforcement of cementitious matrices [5, 6, 7, 8, 9, 10], since fibres can overcome some disadvantages of concrete, such as low energy absorption and low ductility [11].

In general, addition of R-PET fibre in cement-based materials improves the splitting tensile strength [12], flexural strength and ductility [5, 13] of plain concrete or mortar. R-PET fibres also provide excellent impact resistance [14] and demonstrate excellent characteristics in suppressing early-age crack generation [6] of cement-based materials.

Ochi et al. [5] and Kim et al. [6] investigated the bond behaviour of R-PET fibres with a concrete matrix, discussing the effects of the fibre surface characteristics. Embossed fibres provided the highest bond strength, followed by crimped and straight ones.

Regarding the influence of R-PET fibres on the compressive strength of R-PET composites, contradictory results have been found in the literature. Ochi et al. [5] reported a moderate increase of the compressive strength (from 6% to 13%) for fibre volume fractions up to 1%; however, for higher fibre content, this increase diminished or even turned into a decrease. On the other hand, Kim et al. [13] reported a moderate decrease of up to 9% for fibre contents of 0.5-1% and Borg et al [15] reported that the addition of R-PET fibres leads to a reduction between 0.5% and 8.5% in compressive strength when compared to the reference mixture. All studies agree that R-PET composites feature a lower elastic modulus than the plain matrix, decreasing with the increase in fibre content.

In this work, experimental results regarding compressive properties of an eco-friendly mortar reinforced with R-PET fibre are presented. The main objective of this study is, therefore, to investigate the influence of the addition of R-PET fibre on the compressive stress-strain behaviour of mortar. Compressive tests are used to analyse and characterize composites with different fibre volume contents (1.0% and 2.0%). Several analytical models found in the literature were tested against experimental data.

2. EXPERIMENTAL PROGRAM

3. 2.1 Raw materials and composite manufacturing

The mixtures were produced using CPII F-32 Portland cement (6% calcareous filler), with 32 MPa compressive strength at 28 days and density of 3.08 g/cm³; fly ash with density of 2.35 g/cm³; silica sand with maximum diameter of 212 μm and density of 2.60 g/cm³; a superplasticizer, Glenium 51 (manufactured by MBT Brazil) based on modified polycarboxylic ether with 32.5% solid content and density of 1.20 g/cm³ and R-PET fibre.

The R-PET fibre used in this study is produced by M&G Fibras Brazil LTDA with a length of 32 mm, a 14 μm diameter and density of 1.43 g/cm³. The fibres were produced by means of an extrusion of plastic filaments from flakes of recycled polyethylene terephthalate.

Unreinforced mortar (matrix) and R-PET fibre reinforced composite specimens were prepared to study the influence of different R-PET reinforcement volume fractions (1.0% and 2.0%) on the compressive properties of the final material.

In all composites, the water/cementitious material ratio and superplasticizer content were dosed such that all mixtures would have similar fresh properties measured by the flow table test (between 160-190 mm). A slight adjustment in the superplasticizer content in each mixture was made to achieve consistent rheological properties for better fibre distribution and workability. The mixture proportions are given in Table 1.

To produce the mixtures, all dry raw materials were mixed for 3 minutes in a mechanical mixer with a 20-litre capacity. Water and superplasticizer were added to form the basic matrix and the

mixture was stirred for another 8 minutes. Fibres were then dispersed carefully by hand into the mortar mixture and it was stirred for 5 minutes more. The specimens were cast in steel moulds, demoulded 24 hours after and, then, cured for 28 days in a curing chamber with 100% relative humidity and 21 ± 1ºC temperature.

Table 1. Materials composition in the mixture.

Ingredients	M01	M02	M03
Water / (cement + fly ash)	0.36	0.36	0.36
Cement (Kg/m³)	505.00	505.00	505.00
Fly ash (Kg/m³)	605.00	605.00	605.00
Sand (Kg/m³)	404.00	404.00	404.00
Water (Kg/m³)	404.00	404.00	404.00
Superplasticizer (Kg/m³)	6.05	6.05	6.81
Fibre (Kg/m³)	-	14.33	28.66
Fibre content (%)	-	1.00	2.00

4. 2.2 Testing procedure

Dry density and total porosity of hardened composites were determined according to NBR 9778 [16], after 28 days of curing. A compressive test was performed at the age of 28 days in a Shimadzu universal testing machine (UH- FI-1000KN) controlled by computer under strain control and a loading rate of 0.2%FS/min. The load and corresponding displacement were continuously recorded. Three 50 x 100 mm (diameter x height) cylindrical specimens were tested per composite mixture.

3. RESULTS AND DISCUSSION

5. 3.1 Porosity and dry density of composites

The total porosity of the composites was found between 18.81% and 27.86%, higher than the total porosity of the matrix (18.59%). The volume of voids created by the addition of fibre is strongly linked to their characteristics (shape, thickness, length, and dosage added). The higher the amount of fibres, the higher will be the porosity induced.

Due to the low density of the R-PET fibre and the high pore volume induced by its addition, all the R-PET mixtures develop a lower dry density with respect to the matrix. Measured dry density of composite mixtures was in the range of 1440 to 1664 kg/m^3, while the matrix dry density was 1780 kg/m^3.

6. 3.1 Compressive behaviour

Figure 1 shows the stress–strain curves obtained from the compressive tests. The results indicate that addition of PET fibres had little effect on the pre-cracking behaviour but had great effect on the post-peak behaviour of specimens.

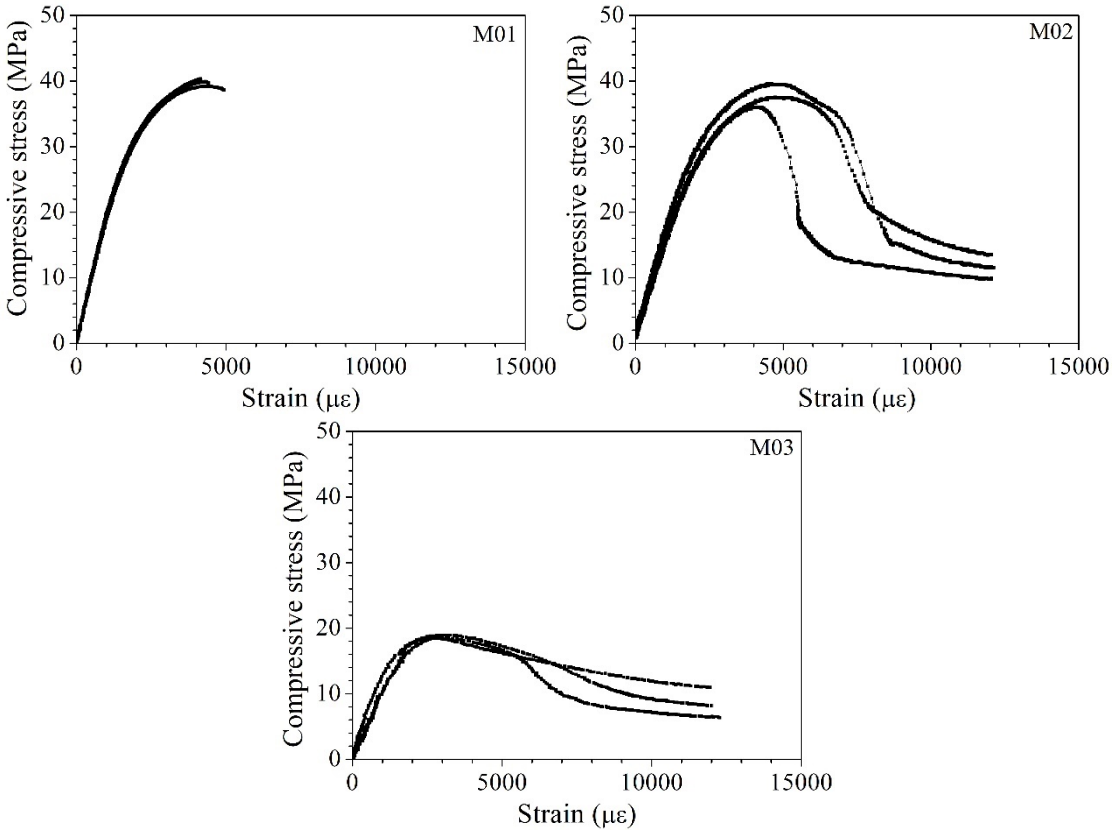

Figure 1. Compressive stress-strain curves of the matrix and fibre- reinforced composites.

For each specimen, the curve could be divided into four stages, i.e., linear elastic ascending stage, nonlinear ascending stage, cracking stage and residual softening stage [17]. After the applied loading reached approximately 48-52% of the compressive strength, the curves deviated from linear elastic behaviour and showed nonlinear behaviour up to the peak stress. This is attributed to the emergence and development of internal defects and micro cracks during the loading process. These two stages were similar for matrix and PET fibre reinforced composites. After the peak stress, the curves dropped with different slopes to a certain stress level. In the post-peak stage, the fibres in the matrix played an important role in bridging the cracks. For mixture with 1% fibre (M02), when the stress decreased to about 47% of the ultimate strength, an apparent inflection point appeared in the stress-strain curves. The curves after the inflection point were defined as residual softening stage, in which the stress decreased stably with the strain until final failure occurred. For the other mixture (M03, 2%), the stress, in the post-peak stage, decreased stably with the strain until final failure occurred.

The mechanical properties of cement-based materials are important for structural analysis, and the main parameters include the peak stress (compressive strength), the strain corresponding to the peak load, the elastic modulus, and the toughness index. The compressive strength was calculated by dividing the peak load by the cross-section area of the specimen. The strain corresponding to the peak strength was obtained by dividing the displacement at the peak load by the gauge length of 50mm. The elastic modulus was calculated based on the method in NBR 8522 [18]. The compressive toughness was calculated as the ratio of area under the stress-strain curve up to strain of 120000με and the equivalent area of the elastoplastic material with the same elastic modulus

and compressive strength. The mean values and standard deviations (in parenthesis) are summarized in Table 2.

Table 2. Summary of physical and compressive tests of the mixtures at 28 days

Mixture	Elastic modulus, GPa	Compressive strength, MPa	Strain at peak stress, με	Toughness
M01	19.40 (0.61)	39.83 (0.58)	4227.88 (74.33)	0.30 (0.04)
M02	14.43 (1.11)	37.73 (1.76)	4288.77 (457.10)	0.67 (0.09)
M03	13.95 (1.48)	18.34 (0.45)	2969.41 (92.33)	0.78 (0.04)

As seen from the results, the addition of R-PET had no beneficial effect on the compressive strength of the composite mixtures. A reduction of strength ranging from 5.3% to 54% was observed for M02 and M03 mixtures when compared to the unreinforced mortar (M01). Similar effect was also observed in the elastic modulus. The elastic modulus of M02, and M03 were reduced by respectively 25.6% and 28.1%. Results are coherent with ones from previous investigations [13, 15, 19].

Figure 2 shows the relationship between the average porosity and compressive strength of the specimens. The increased porosity caused by fibre addition decreases the compressive strength and stiffness of the specimens (see Table 2).

The strain at peak stress indicates the deformability of the specimen at the ultimate strength. The results indicate that the average strain at peak load is between 2970 and 4290 με for specimens with different R-PET fibre content. Results demonstrate that addition of R-PET fibre reduced the strain at peak stress under compression. However, it is more evident when 2% of PET fibre was added.

Regarding post-peak behaviour, the results presented in Table 2 and Figure 1 indicate that the matrix without fibre is characterized by post-peak fragility; however, when R-PET fibre is added, the compressive toughness index of the composite was increased up to 217%, indicating that the ductility was increased.

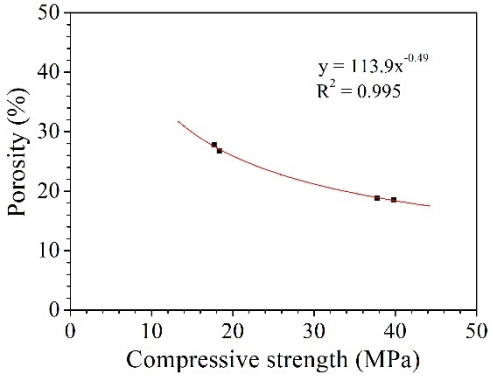

Figure 2. Relationship of porosity with the compressive strength.

7. 3.2 Analytical modelling of PET composites in compression

There are many stress-strain relations for the modelling of concrete and fibre reinforced concrete in the literature. For the matrix without reinforcement, typical models present good

agreement. Models by Desayi and Krishan [20] and Saenz [21] were used as shown in Fig. 3. Equations (1) and (2) show, respectively, the expressions for these models:

$$\sigma = \frac{E\varepsilon}{1+\left(\varepsilon/\varepsilon_0\right)^2} \tag{1}$$

$$\sigma = \frac{E\varepsilon}{1+\left(E/E_S - 2\right)\left(\varepsilon/\varepsilon_0\right)+\left(\varepsilon/\varepsilon_0\right)^2} \tag{2}$$

where σ and ε are compressive stress and strain, E is tangent Young's modulus, E_S is secant Young's modulus (calculated at peak stress) and ε_0 is strain at peak stress. If the ratio E/E_S is equal to 2, both models are identical, which is not the case as shown in Fig. 3.

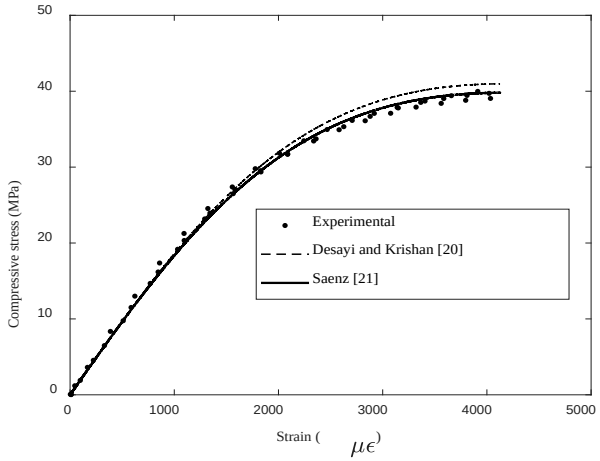

Figure 3. Stress-strain relation for the matrix

In the case of fibre-reinforced samples, Xu and Cai [22] proposed a model that presents 2 different expressions for the ascending ($0 \le \varepsilon \le \varepsilon_0$) and descending ($\varepsilon > \varepsilon_0$) branches, shown in Eq. (3). Based on the expressions proposed by Ezeldin and Balaguru [23], the descending branch was also modelled according to Eq. (4).

$$\frac{\sigma}{f_c} = \frac{A\left(\varepsilon/\varepsilon_0\right)+B\left(\varepsilon/\varepsilon_0\right)^2}{1+C\left(\varepsilon/\varepsilon_0\right)+D\left(\varepsilon/\varepsilon_0\right)^2}, \quad \left(0 \le \varepsilon \le \varepsilon_0\right) \qquad \frac{\sigma}{f_c} = \frac{\left(\varepsilon/\varepsilon_0\right)}{\left(\varepsilon/\varepsilon_0\right)+b_0\left(\varepsilon/\varepsilon_0 - 1\right)^2}, \quad \left(\varepsilon \ge \varepsilon_0\right) \tag{3}$$

$$\frac{\sigma}{f_c} = \frac{\beta\left(\varepsilon/\varepsilon_0\right)}{\beta - 1+\left(\varepsilon/\varepsilon_0\right)^{\beta}}, \quad \left(\varepsilon \ge \varepsilon_0\right) \tag{4}$$

In Eqs. (3) and (4), f_c is the peak stress and coefficients A, B, C, D, b_0 and β are determined by curve fitting algorithm using MATLAB software [24]. Fig. 4 shows experimental and analytical

curves in terms of nondimensionalized stress and strain and Table 3 shows the values obtained for each coefficient in the expressions.

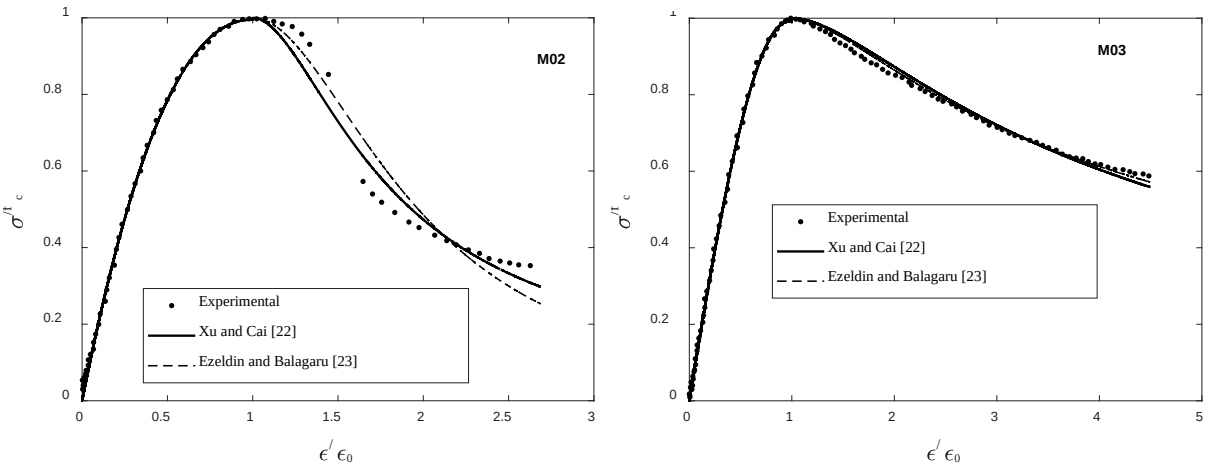

Figure 4. Experimental and analytical results

Table 3. Summary of coefficients obtained by curve fitting algorithm

Mixture	*A*	*B*	*C*	*D*	b_0	β
M02	2.252	-0.8505	0.2489	0.1597	2.227	3.620
M03	1.665	-0.8797	-0.3785	0.1716	0.2907	1.683

4. CONCLUSIONS

Based on the results obtained in the present work it can be concluded that the use of recycled PET (R-PET) fibres as reinforcement of mortars is a promising technique for developing sustainable materials to be applied in the civil construction industry.

The main effects of the addition of R-PET fibres to mortars are:

- reduction of the compressive strength and elastic modulus of composite mixtures;
- reduction of the strain at peak stress under compression;
- increase in the compressive toughness index indicating increase in ductility.

A good agreement between experimental and analytical results was found. However, there is no physical meaning for the coefficients found by the curve fitting algorithm. Future works will focus on finding relationships between those coefficients and mechanical properties of specimens.

ACKNOWLEDGEMENTS

The authors acknowledge the Brazilian Agency FAPERJ for the financial support and M&G Fibras Brazil LTDA for donation of the fibre.

REFERENCES

[1] ABIPET - Associação Brasileira da Indústria do PET. Décimo censo da reciclagem do PET no Brasil 2016. In: http://www.abipet.org.br/index.html?method=mostrarDownloads&categoria.id=3. Accessed on April 21, 2018.

[2] Choi Y.W., Moon D.J., Chung J.S. and Cho S.K., 'Effects of waste PET bottles aggregate on the properties of concrete', Cem Concr Res, **35** (4) (2005) 776–781.

[3] Frigione M., 'Recycling of PET bottles as fine aggregate in concrete', Waste Manage **30** (2010) 1101–1106.
[4] Azad A. M., 'Flexural behavior and analysis of reinforced concrete beams made of recycled PET waste concrete', Construction and Building Materials, **155 (**2017) 593-604.
[5] Ochi T., Okubo S. and Fukui K., 'Development of recycled PET fiber and its application as concrete-reinforcing fiber', Cem Concr Compos, **29** (2007) 448–455.
[6] Kim J.J., Park C.G, Lee S.W., Lee S.W. and Won J.P., 'Effects of the geometry of recycled PET fiber reinforcement on shrinkage cracking of cement-based composites', Compos Part B: Eng **39** (2008) 442–450.
[7] Siddique R., Khatib J. and Kaur I., 'Use of recycled plastic in concrete: a review', Waste Manage **28 (**2008) 1835–1852.
[8] Oliveira L.A.P. and Gomes J.P.C., 'Physical and mechanical behaviour of recycled PET fibre reinforced mortar', Constr Build Mater, **25** (2011) 1712–1717.
[9] Fraternali F., Farina I., Polzone C., Pagliuca E. and Feo L., 'On the use of R-PET strips for the reinforcement of cement mortars', Compos Part B: Eng, **46** (2013) 207–210.
[10] Magalhães M.S, Fernandes M.S.V., 'Bending Behaviour of Recycled PET Fiber Reinforced Cement-Based Composite', Int J Eng and Tech **7** (2015) 282-285.
[11] Bentur A. and Mindess S., 'Fibre Reinforced Cementitious Composites, 2nd ed., Modern Concrete Technology, (CRC Press, 2006).
[12] Khalid, F.S., Irwan, J.M., Wan Ibrahim, M.H., Othman, N., Shahidan, S., 'Splitting tensile and pullout behavior of synthetic wastes as fiber-reinforced concrete', Construc and Build Mater, **171** (2018) 54-64.
[13] Kim S.B., Yi N.H, Kim H.Y., Kim J. and Song Y., 'Material and structural performance evaluation of recycled PET fiber reinforced concrete', Cem Concr Compos, **32** (2010) 232–240.
[14] Lu, C., Yu, J., Leung, C.K.Y., 'Tensile performance and impact resistance of Strain Hardening Cementitious Composites (SHCC) with recycled fibers', Construc and Build Mater **171**, (2018) 566-576.
[15] Borg, R.P., Baldacchino, O., Ferrara, L., 'Early age performance and mechanical characteristics of recycled PET fibre reinforced concrete', Construc and Build Mater **108** (2016) 29-47.
[16] ABNT, NBR 9778: Argamassa e concreto endurecidos - Determinação da absorção de água por imersão - Índice de vazios e massa específica, (Brazil, 2005).
[17] Zhou J, Pan J, Leung C. K. Y., 'Mechanical Behavior of Fiber-Reinforced Engineered Cementitious Composites in Uniaxial Compression', J of Mater Civil Eng. **27** (1) (2015) 1-10.
[18] ABNT, NBR 8522: Concreto - Determinação dos módulos estáticos de elasticidade e de deformação à compressão, (Brazil, 2017).
[19] Pelisser, F., Montedo, O., Gleize, P., Roman, H., 'Mechanical properties of recycled PET fibers in concrete', Mater. Res. **15** (2012), 679-686.
[20] Desayi, P. and Krishnan, S., 'Equation for the stress-strain curve of concrete', ACI J. **61** (1964) 345-350.
[21] Saenz, L.P., 'Discussion of "Equation for the stress-strain curve of concrete" by Desayi and Krishnan', ACI. J. Proc. **61** (1964) 1229-1235.
[22] Xu, S. L., and Cai, X. R., 'Experimental study and theoretical models on compressive properties of ultrahigh toughness cementitious composites', J. Mater. Civ. Eng. **22** (10) (2010) 1067–1077.
[23] Ezeldin, S., Balaguru, N., 'Normal and high-strength fiber-reinforced concrete under compression', J Mater Civ Eng **4** (4) (1993) 415-429.
[24] [24] MathWorks, 'Curve Fitting Toolbox: for Use with MATLAB®: User's Guide', (MA, 2018).

3. DAMAGE AND FRACTURE

QUASI-STATIC INDENTATION AND LOW-VELOCITY IMPACT RESPONSE OF ARAMID/EPOXY COMPOSITES

Stephanie G. Nunes[(1)], Luís Guilherme G. Reichwald[(1)], Wanderley F. A. Júnior[(2)], Andrea Manes[(3)] and Sandro C. Amico[(1)]

(1) Department of Material Engineering, Federal University of Rio Grande do Sul, Porto Alegre/RS, Brazil

(2) Department of Materials and Metallurgy, Federal University of Campina Grande, Campina Grande/PB, Brazil

(3) Department of Mechanical Engineering, Politecnico di Milano, Milan, Italy

https://doi.org/10.21452/bccm4.2018.03.01

Abstract

In applications that require impact loading, polymeric matrix composites reinforced with aramid fibers stand out, especially in relation to metals, due to characteristics such as high specific strength and stiffness, which give rise to light high-performance systems. However, such structures can fail through various modes, requiring comprehensive studies. Under low-velocity impact, the contact time between the impactor and the target is relatively large, and the effects of deformation rate and wave propagation are generally insignificant, allowing association of the damage caused in the composites via drop-weight (DW) to those of quasi-static indentation (QSI) tests, optimizing the overall material understanding. Thus, this work aims to comparatively analyze force × displacement curves and resulting damage from drop-weight and QSI tests. For that, laminates (2.5, 4.5 and 7.0 mm thick) were tested using variable impact energies (15, 30, 45 and 60 J) and displacement (11, 12 and 15 mm). Similarities in force × displacement curves and damage mechanisms between QSI and DW results were observed at the perforating threshold. However, to compare the response of the material and the damage mechanism generated by QSI and Drop-weight tests in composites, care must be taken, since there are many variables involved and the response of the composites to these tests will depend on such variables.

1. INTRODUCTION

Polymeric matrix composite materials, especially those reinforced with aramid fibers, are widely used since they offer attractive potential to reduce weight of high performance structures (e.g. metals) due to their high specific strength and stiffness. According to Aslan et al. [1] and Agrawal et al. [2], composite structures are more susceptible to impact damage than similar metal structures because they can fail through various failure modes and contain impact damages invisible to the naked eye, severely reducing the structural durability of the component. Therefore,

such loads, as well as the effect they cause on these structures, are a major concern and therefore require full understanding.

Impact at low speed considerably decreases strength and stability of composite structures. Even at very low impact energy, residual damage may not be visible, especially for fiber reinforced composites of low shear stiffness. Different approaches are used to investigate the response of laminates to impact at low speed, being the drop-weight test largely used [3].

In the drop-weight impact test, a mass is raised to a known height and released, impacting the sample. In general, such event does not promote complete destruction on the target, thereby allowing residual energy to be determined by rebounding of the impactor, if necessary. The main advantage of such test over other low speed tests (e.g. Charpy and Izod) is that it allows a variety of simple and complex geometries to be tested and actual impact conditions to be simulated [4,5].

In fact, a series of physical phenomena occur upon impact, such as shock and wave propagation, fracture and fragmentation, perforation and shattering [6]. In composite materials, the damage caused by low speed impact is mostly due to matrix rupture (fiber fracture is nearly non-existent) and there is a relationship between matrix rupture in the layers and delamination [7]. Low velocity impacts produce multiple delaminations in-between layers that drastically reduce their durability, strength and stiffness, even with no visible damage to the impacted surface. In fact, the energy can be absorbed at any point throughout the structure and far from the point of impact, so understanding of these damage mechanisms is very important [8,9].

As the effects of the rate of deformation and wave propagation are generally negligible for low velocity impacts, quasi-static indentation test (QSI) can also be used to study the impact response of a composite material [10]. According to Nettles and Douglas [11], the QSI damage can be more easily detected, deflection of the material can be directly measured with great accuracy and the maximum transverse force can be better controlled.

In this context, this work focuses on the behavior of aramid/epoxy laminates with different thicknesses (2.5, 4.5 and 7.0 mm) subjected to quasi-static indentation and drop-weight impact tests aiming at investigating similarities in the resulting damage.

2. MATERIALS AND METHODS

Laminate plates of variable thicknesses (≈ 2.5, 4.5 and 7.0 mm) were manufactured by vacuum infusion processing, which consisted in stacking 5, 8 or 13 layers of plain-weave Kevlar® 29 fabrics (aerial weight: 440 g/m^2) on a rigid mold with a flow media partly covering the reinforcement and a vacuum bag film. After sealing the bag to the rigid mold using a sealing tape, the vacuum of 1 bar was applied into the cavity for preform compaction. Then, the epoxy system (AR 260 + AH 260 hardener) was able to flow through the porous fabric preform, taking approximately 15 min to complete that. After 24 h of curing at room temperature, the composites were demolded and post-cured in an oven for 12 h at 60 ^{o}C.

The quasi-static indentation (QSI) test was performed on the laminates according to ASTM D6264, with an edge support configuration using the Instron machine, at a speed of 1.25 mm/min (also for the return). The indenter had a hemisphere shaped tip approximately 13 mm in diameter and indentation was interrupted when the sample was at the perforation threshold, to obtain failure by penetration only, not perforation. The absorbed energy (E_a) was calculated by the integral (i.e. area) of each load/unload curve using OriginPro software.

Low velocity impact tests were performed according to ASTM D7136 standard using a conventional drop-weight impact tester. Composite samples (dimensions: 100 × 150 mm^2) were placed between two 20-mm thick steel plates and impacted by an impactor (hardness: 60 HRC,

mass: 4.4 kg) with a smooth hemispherical tip approximately 16 mm in diameter. The impactor was instrumented with a Kistler Quartz Force Link Type 9331B (±20 kN) so that the impact load history could be recorded. The impact velocity, hence the energy, was measured by means of a ‘‘speed trap” comprised of two Mikroelektronik M5L/20 lasers 41 mm apart, which recorded the impactor crossing time. Acquisition of the signals of load cell and lasers was synchronous with a sampling frequency set to 51.2 kHz. Impact energy was varied by altering the initial velocity of the impactor (3.7-5.2 m/s), producing energy levels within 15-60 J. Only one impact event was allowed in each sample (i.e. no rebound).

Analysis of the damages generated by the QSI and drop-weight tests in the composites was performed with the help of a Sony professional camera, model Cyber-shot GPs HD, with 20.4 MPixels of resolution and optical zoom of 50×.

3. RESULTS

Figure 1 shows typical force-displacement curves generated by the QSI and Drop-weight tests. The calculated values of maximum load (F_{max}), maximum displacement (δ_{max}) and absorbed energy (E_a) are presented in Table 1. Figure 1(a) shows a second peak for the 5L-30J(DW) sample due to a faulty experimental condition in which the sample was also impacted by the support of the indenter. That second peak was not used in the calculations.

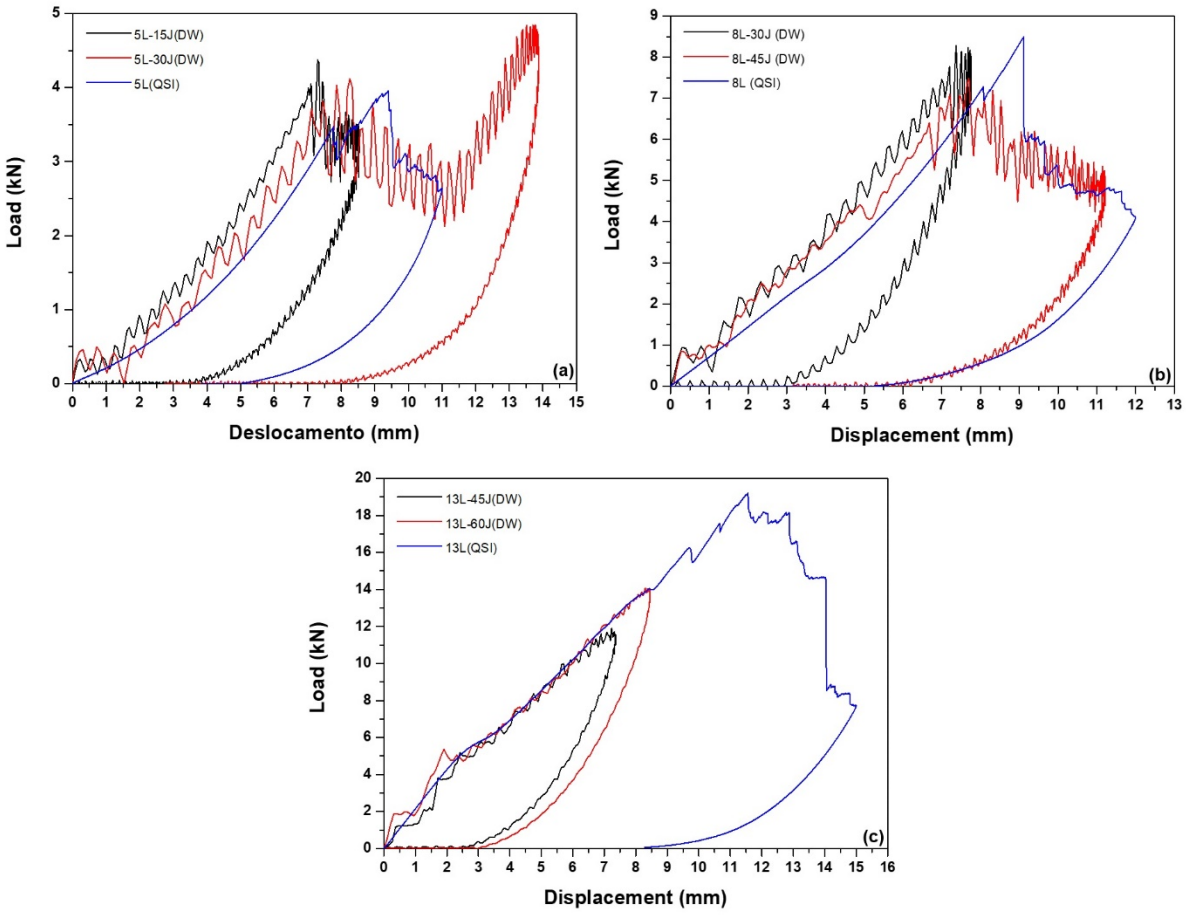

Figure 1: Force-displacement curves obtained in the drop-weight (DW) and QSI tests for the 5L (a), 8L (b) and 13L (c) composites.

In Figure 1, it is possible to observe a similarity in the behavior of the curves, with composites with 5 layers (for 15 J and 30 J) and 8 layers (for 30 J and 45 J) showed similar load peaks (4.4, 4.1, 8.3 and 7.5 kN, respectively), when impacted by drop-weight to those obtained by the QSI test for 5L(QSI) samples and 8L(QSI) (4.0 and 8.4 kN, respectively).

In Figure 1(a, b), it is possible to observe that the 5L-30J(DW) and 5L(QSI) curves practically overlap, which also happens for the 8L-45J(DW) and 8L(QSI) samples. The greater distance between loading & unloading phases in the curves and the high frequencies of oscillations of these curves indicate that the 5L-30J(DW) and 8L-45J(DW) samples absorbed a greater amount of energy.

In all cases, the force versus displacement graphs show closed curves, indicating that the laminates were not perforated in any of the cases and that all samples rebounded the impactor. The13L-45J(DW) sample showed he least deformation and probably the smallest damage. This is related to its stiffness, which affects the magnitude of the contact force, interfering in the extension of the damage due to the significant thickness of the composite for this impact level [2]. Also, as the 13L-60J(DW) composite was impacted with higher energy, both displacement and load (maximum peak) increased compared to the 13L-45J(DW) sample. Indeed, the limited energy available in the drop-weight test was not able to cause great damage to the 7.0 mm thick composite, with maximum peaks (11.9 and 14.1 kN for 7.0-45J(DW) and 13L-60J(DW), respectively) lower than those for the QSI (18.9 kN). Nevertheless, the loading curve generated by QSI presents the same behavior and follows the same trend as that of the drop-weight.

Table 1: QSI and drop-weight tests results for the various laminates and energies used.

Samples	**F_{max} (kN)**	**δ_{max} (mm)**	**E_a (J)**
5L-15J(DW)	4.4	8.5	12.01
5L-30J(DW)	4.1	11.4	22.86
5L(QSI)	4.0	11.0	15.93
8L-30J(DW)	8.3	7.8	18.06
8L-45J(DW)	7.5	11.2	39.30
8L(QSI)	8.4	12.0	39.17
13L-45J(DW)	11.9	7.36	28.19
13L-60J(DW)	14.1	8.45	40.50
13L(QSI)	18.9	15.0	135.78

Figures 2 and 3 present the damage occurring in the 5L (DW and QSI) and 8L (DW and QSI) composites, whose curves are more similar. The damage in the drop-weight and QSI events also showed similarity. In the rear view of the composites, an indenter cavity of similar depth is observed in Figure 2. This also happens in Figure 3 and refers to the deflection of the composites during testing, which was 11.4 and 11.0 mm, for the 5L-30J(DW) and 5L(QSI), respectively, and 11.2 and 12.0 mm for composites 8L-45J(DW) and 8L(QSI), respectively.

In the cross-section view of the composites (Figure 4), samples of the same thickness showed similar mechanisms of damage, including fiber and matrix fracture, and delamination. It is also possible to observe similar sinking at the contact faces of the indenters for composites of the same thickness, and all composites are at the perforation threshold.

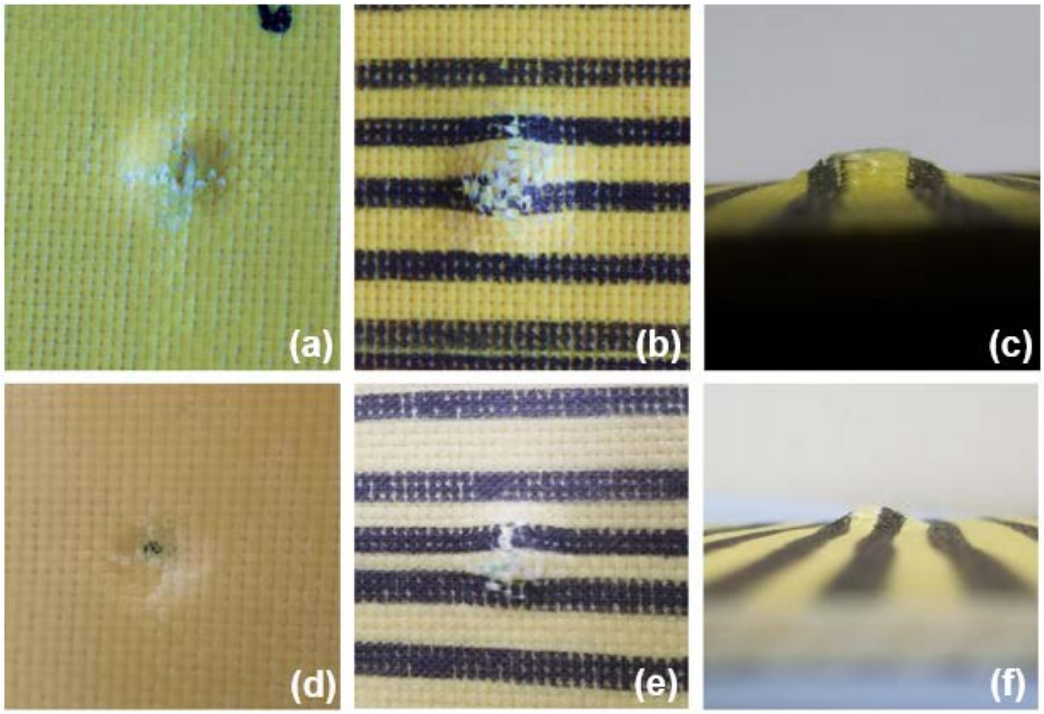

Figure 2: Front, back and side views of the damage zone for: 5L-30J(DW) (a, b, c, respectively) and 5L(QSI) (d, e, f, respectively).

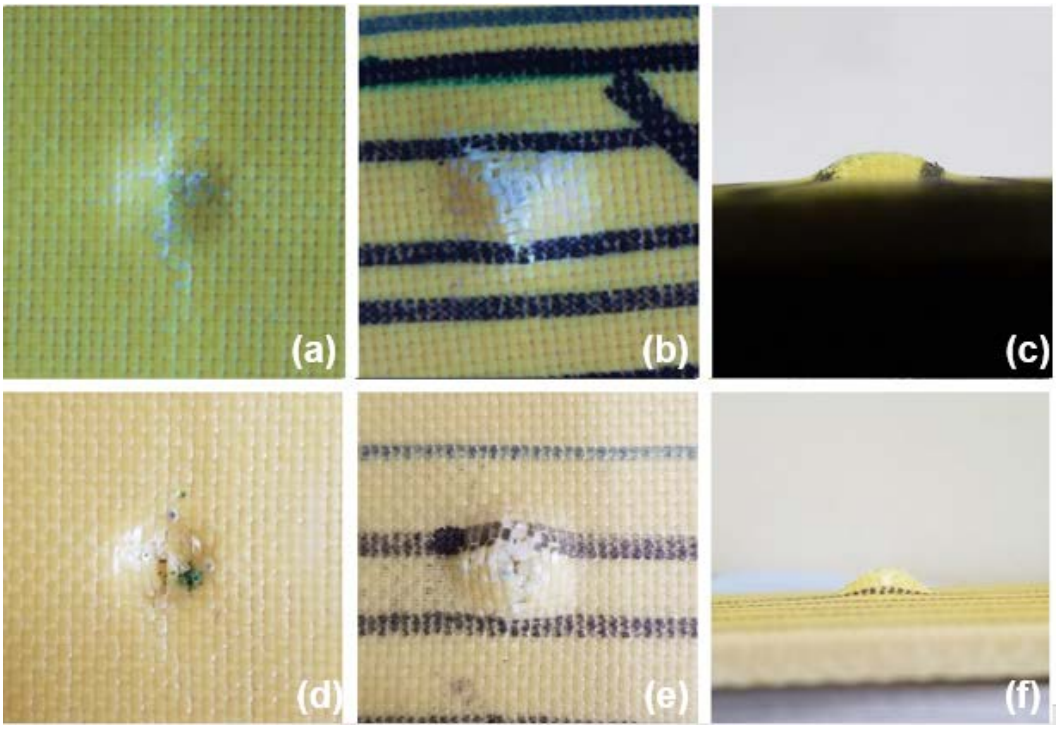

Figure 3: Front, back and side views of the damage zone for: 8L-45J(DW) (a, b, c, respectively) and 8L(QSI) (d, e, f, respectively).

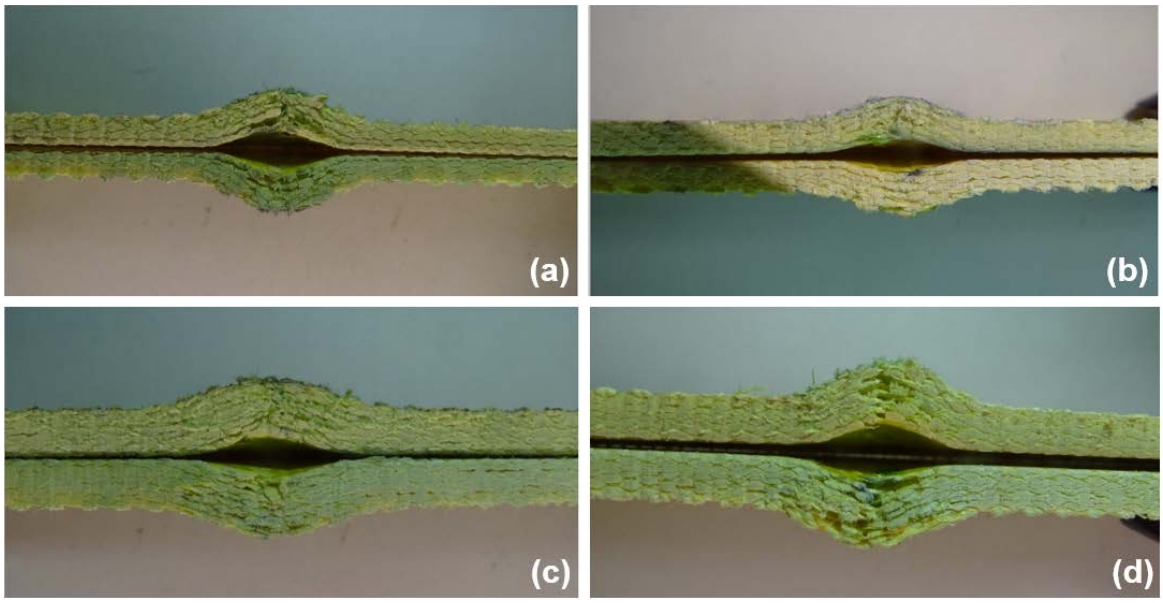

Figure 4: Cross-section view of the damage zones for: (a) 5L-30J(DW), (b) 5L(QSI), (c) 8L-45J(DW) and (d) 8L(QSI) (plates were cut in half to allow this view).

In his research comparing damage in carbon/epoxy composites submitted to QSI and drop-weight tests, Guan et al. [12] reported similarity between peak loads. Regarding damage, they reported that, in general, when impact energy is low, the composite presents smaller delaminated area after drop-weight. However, at high impact energy, the delaminated area in the composite is very similar for both tests, allowing them to conclude that QSI can be used to represent a drop-weight impact event, but with some restrictions. Nettles and Douglas [11] and Lee and Zahuta [13] also state that these two tests induce similar failure mechanism, with very similar damages and force × displacement curves, for carbon/epoxy composites. On the contrary, Lawrence et al. [14] and Spronk et al. [15] reported different damages and curves from QSI and drop-weight tests for glass-S2/epoxy, carbon/epoxy and glass/polyamide composites.

4. CONCLUSIONS

By comparing the response of aramid/epoxy composites under QSI and drop-weight tests, it was possible to conclude that there are similarities in the force × displacement curve and damages for the samples that are at the perforating threshold (5L-30J(DW) and 5L(QSI), and 8L-45J(DW) and 8L(QSI)). This indicates that these tests can be used comparatively as long as the thicknesses is small (2.5 and 4.5 mm), the impact energy levels are low (30 and 45 J) and the samples are not perforated. However, comparison of the response and the damage mechanism generated by QSI and drop-weight tests in composites must be done with care, since there are many influencing parameters involved in these tests, such as materials (matrix and reinforcement), thicknesses, sample sizes, impactor sizes and impact energies.

ACKNOWLEDGEMENTS

The authors would like to thank DuPont® for the fiber supply and CAPES for the financial support.

REFERENCES

[1] Aslan, Z., Karakuzu, R., Okutan, B., 'The response of laminated composite plates under low-velocity impact loading'. *Composite Structures*, 59 (2003) 119–127.

[2] Agrawal, S., Singh, K. K., Sarkar, P. K., 'Impact damage on fibre-reinforced polymer matrix composite – A review', *Journal of Composite Materials*, 48 (3) (2014) 317–332.

[3] Duell J.M., 'Impact testing of advanced composites. Advanced Topics in Characterization of Composites' (Michael Kessler, Canada, 2006).

[4] Cantwell, W. J.; Morton, J., 'The Impact Resistance of Composite Materials – A Review', *Composites*, 22 (5) (1991) 347 – 362.

[5] Safri, S. N. A.; Sultan, M. T. H.; Yidris, N.; Mustapha, F., 'Low Velocity and High Velocity Impact Test on Composite Materials – A review', *The International Journal of Engineering and Science*, 3 (9) (2014) 50 – 60.

[6] Razali, N.; Sultan, M. T. H., Mustapha, F.; Yidris, N.; Ishak, M. R., 'Impact Damage on Composite Structures – A Review', *The International Journal of Engineering and Science*, 3 (7) (2014) 08 – 20.

[7] Abrate, S. 'Impact on Composite Structures' (Cambridge University Press, New York, 1998).

[8] Shyr, T; Pan, Y., 'Impact Resistance and Damage Characteristics of Composite Laminates', *Composite Structures*, 62 (2003) 193 – 203.

[9] Evci, C; Gulgeç, M., 'An Experimental Investigation on the Impact Response of Composite Materials', *International Journal of Impact Engineering*, 43 (2012) 40 – 51.

[10] Ahmed, A.; Wei, L., 'The Low-Velocity Impact Damage Resistance of the Composite Structures - A Review', *Reviews on Advanced Materials Science*, 40 (2015) 127 – 145.

[11] Nettles, A. T.; Douglas, M. J., 'A Comparison of Quasi-Static Indentation to Low-Velocity Impact', National Aeronautics Scape Administration (NASA), Technical Report, NASA/TP – 2000 – 210481, 2000.

[12] Guan, Z.; Guo, Y.; Meng, Q.; Liu, D., 'Comparision of Damage Characterization of Composite Laminates Under Quasi-Static Indentation and Low-Velocity Impact', 17th International Conference on Composite Materials (ICCM17), 2009.

[13] Lee, S. M.; Zahuta, P, 'Instrumented Impact and Static Indentation of Composites', *Journal of Composite Materials*, 25 (1991), 204 – 222.

[14] Lawrence, B. D.; Emerson, R. P., 'A Comparison of Low-Velocity Impact and Quasi-Static Indentation', Army Research Laboratory Technical report, ARL-TR-6272, 2012.

[15] Spronk, S. W. F.; Kersemans, M.; De Baerdemaeker, J. C. A.; Gilabert, F. A.; Sevenois, R. D. B.; Garoz, D.; Kassapoglou, C.; Van Paepegem, W., 'Comparing Damage from Low-Velocity Impact and Quasi-Static Indentation in Automotive Carbon/Epoxy and Glass/Polyamide-6 Laminates', *Polymer Testing*, 65 (2018) 231 – 241.

MICROMECHANICAL MODELS FOR TRANSVERSAL ELASTIC MODULUS IN UNIDIRECTIONAL LAMINATES

Lucas L. Vignoli [1,2], **Marcelo M. Savi** [1]

(1) Center for Nonlinear Mechanics, COPPE, Department of Mechanical Engineering, Universidade Federal do Rio de Janeiro, Brazil

(2) Department of Mechanical Engineering, Universidade Federal do Rio de Janeiro - Campus Macaé, Brazil

https://doi.org/10.21452/bccm4.2018.03.02

Abstract

This paper deals with the first step required for composite design: the equivalent macromechanical properties according to the constituents. Assuming a transversally isotropic lamina, the material has five independent properties, namely longitudinal and transversal elastic modulus, in-plane and out-of-plane shear modulus and in-plane Poisson ratio. The longitudinal elastic modulus has a very reasonable prediction by the well-known Rule of Mixtures. On the other hand, the transversal elastic modulus estimative by the same model is poor compared with experimental data. There exist many additional proposed models, therefore all of them are based in hypotheses that usually are not true for real composites, as unit cell symmetry. Due to this fact, the predictions of the following nine models are evaluated: Asymptotic Homogenization with hexagonal unit cell, Asymptotic Homogenization with square unit cell, Bridging, Chamis, Generalized Self Consistent, Halpin-Tsai, modified Halpin-Tsai, Mori-Tanaka and Rule of Mixture. To stablish a comparison, a set of 65 experimental data are compiled from the literature. A semi-empirical modification of the Rule of Mixture is proposed based in a statistical adjust of the experimental data.

1. INTRODUCTION

The capability to estimate macromechancal properties of a unidirectional composite using the constituent data is a fundamental tool for composite design advance. Despite the recent advance of failure modelling due to the World Wide Failure Exercise [1-3], there is still a considerable lack of knowledge about the estimation of different micromechanical models, mainly for transversal elastic properties and strengths. The present paper is intended to provide a comparison between 10 models, 5 semi-empirical and 5 elasticity-based, and 65 experimental data for the transversal elastic modulus (E_2).

It is evident that the elasticity-based models have a physical basis much more consistent than the semi-empirical ones. Nevertheless, the goal of this comparative study is to evaluate which models, and consequently, which assumptions are more representative of the real structure. Figure 1 shows a microscopy image of a unidirectional lamina. The fiber distribution indicates an asymmetric pattern. Additionally, if a square unit cell is defined, the fiber volume fraction is dependent of where this square is located. Hence, the adjustable factors of semi-empirical model may represent a reasonable approximation for general laminae.

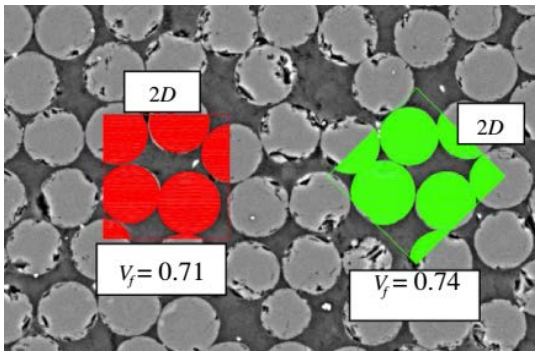

Figure 1: Microscopy of a real unidirectional lamina without simmetric arrangement [4].

2. ANALYTICAL MODELS

The analytical models presented in the literature are usually separated in two different approaches: semi-empirical and elasticity-based. In this study, the Rule of Misture, Chamis and Halpin-Tsai are semi-empirical, while Asymptotic Homogenization, Bridging, Generalized Self Consistent and Mori-Tanaka are elasticity-based. For simplicity, just the equations for semi-empirical models are completely defined and a brief explanation about the main idea of the elasticity-based models is presented.

The Rule of Mixture (ROM) is the simplest model and it is based on the idea of considering fibers and matrix as springs in series or in parallel, according to the applied load. For the longitudinal elastic modulus, this assumption works very well, since there is not abrupt perturbation on the stress and strain fields when a longitudinal load is applied (on the elastic range), and the lamina behaviour is similar to springs in parallel. For transversal load, the stress and strain fields are highly perturbed by the fibers distribution. Therefore, even with this limitation in mind, transversal elastic modulus is estimated using a simplified 2D geometry as [5]

$$E_2 = \frac{E_2^f E^m}{E_2^f (1 - V_f) + E^m V_f} \tag{1}$$

where E^m is the matrix elastic modulus, E_2^f is the fiber transversal elastic modulus and V_f is the fiber volume fraction.

The Chamis model (Ch) [6] proposes consider the nonlinear effect of the fiber and void volume fraction replacing V_f by its square root $\sqrt{(1-V_v)V_f}$. Hence, the Chamis model uses the following equation

$$E_2 = \frac{E^m}{1-\sqrt{(1-V_v)V_f}[1-(E^m / E_2^f)]} \tag{2}$$

For this study, it is considered two different void contents: $V_v = 0$ and $V_v = 2.5\%$.

The Halpin-Tsai model (HT) [7] includes an adjustable parameter, ζ_{E_2}, fitted according to experimental data. The transversal elastic model is estimated by

$$E_2 = E^m \left(\frac{1+\zeta_{E_2}\eta_{E_2}V_f}{1-\eta_{E_2}V_f} \right) \tag{3}$$

where

$$\eta_{E_2} = \frac{(E_2^f / E^m)-1}{(E_2^f / E^m)+\zeta_{E_2}} \tag{4}$$

Halpin & Kardos [8] suggest that in absence of experimental data for proper calibration, this parameter may be computed by

$$\zeta_{E_2} = 2 + 40V_f^{10} \tag{5}$$

Recently, Ginet *et al*.[9] carried out a numerical study with nonperiodic fiber distribution and callibrated this parameter using the following equation

$$\zeta_{E_2} = \begin{cases} 4.924 - 35.888V_f + 125.118V_f^2 - 145.121V_f^3 & if \quad V_f < 0.3 \\ 1.5 + 5500V_f^{18} & if \quad V_f \geq 0.3 \end{cases} \tag{6}$$

In the present study, the use of Halpin-Tsai model with Eq.(6) is named modified Halpin-Tsai (HTm).

The proposed semi-empirical model is based in a modification of the Rule of Mixture and on the Halpin-Tsai idea to add a calibration parameter. The following equation is proposed

$$E_2 = E^m \left(\frac{1}{1+\xi_{E_2}[(E^m / E_2^f)-1]V_f} \right) \tag{7}$$

where ξ_{E_2} is the calibrated term. Note that $\xi_{E_2} = 1$ reproduces the Rule of Mixture. Unlike the Halpin-Tsai model, which consider just the influence of V_f on the calibration, the present model

also consider the ratio E^m / E_2^f. Using the Levenberg-Marquardt [10] to calibrate this term, it is suggest using

$$\xi_{E_2} = \left[0.6897 + 0.4185 V_f - 0.0036 (E_2^f / E^m) \right]^{-2} \tag{8}$$

The main ideas of the elasticity-based models are:

(i) Asymptotic Homogenization (AH): using an asymptotic expansion of the displacement field and satisfy the boundary condition, according to the unit cell geometry, square (Ahs) [11] or hexagonal (Ahs) [12]; despite the need of infinity series to compute the proprieties, just the first two terms are necessary to convergence [13].

(ii) Bridging (Br): there exist two different approaches, one is based on the Generalized Self Consistent and the other on the Mori-Tanaka, therefore its main advance is the capability to implement nonlinear effects, like damage, using the bridging tensor [14].

(iii) Generalized Self Consistent (GSCM): this model assumes that fiber and matrix are approximately represented by concentric cylinder; by this hypothesis, a geometrically compatible displacement is proposed for each load and at last the average stress and strain fields are computed [15].

(iv) Mori-Tanaka (MT): the key point of this model is the eigenstrain concept and the Eshelby inclusion theory [16] and the definition of forth order tensors to relate the strain fields on the constituents [17].

3. RESULTS AND DISCUSSION

A set of 65 experimental data of E_2 was compiled from the literature [18-32] for the following comparison. Two different approaches are used for evaluation: the average error considering all the data available and the ranges of error, defining smaller than 10%, between 10% and 20%; between 20% and 30%, between 30% and 40%, between 40% and 50% and higher than 50%. The first one gives a value easier to compare, while the second offer a useful measure which is able to check if the average error is representative or not. For instance, if one data has a discrepant error, the average value is highly influenced, while the ranges allow a better representation. The results with both methodologies are presented in Figure 2 and Figure 3. The following conclusions are highlighted from these figures:

i) The semi-empirical model, namely *est(ROM)* on the graphics, is the unique model able to estimate more than 50% of the cases with an error smaller than 10% and to obtain an average error smaller than 15%.

ii) The void content does not result in a representative alteration on the Chamis model prediction.

iii) The modified Halpin-Tsai obtained a considerable amount of cases with errors higher than 50%, increasing the average error. Comparing with the classical Halpin-Tsai model, there is no advantage in this new equation for ζ_{E_2}.

iv) All the elasticity-based models had a similar prediction, but the semi-empirical models (except the Rule of Mixture) obtained a smaller error. This result indicates the capability of application of this simplified approaches.

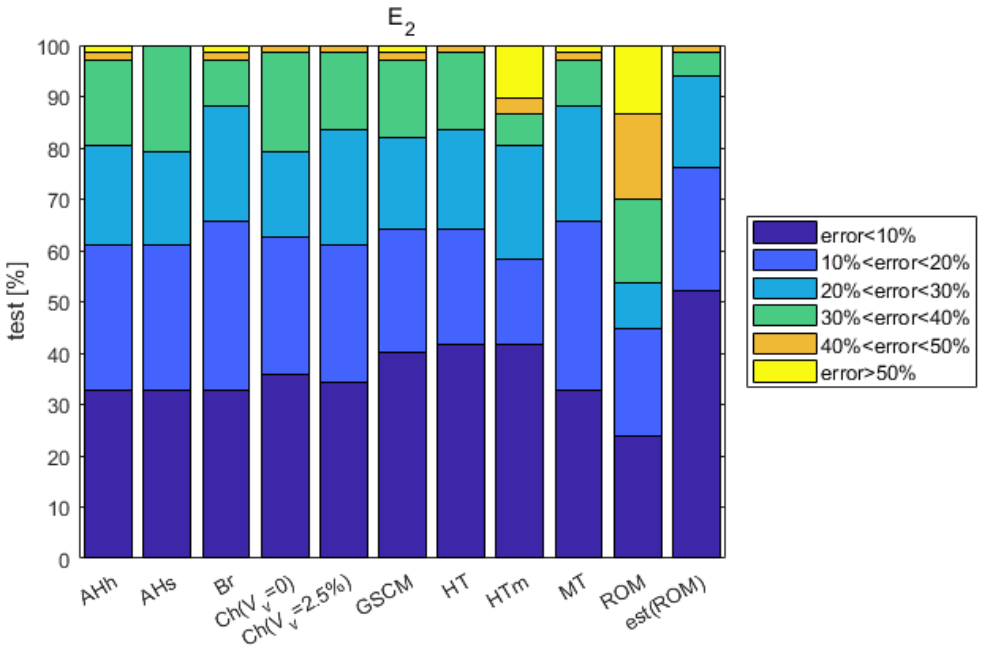

Figure 2: Ranges of error of the models estimations

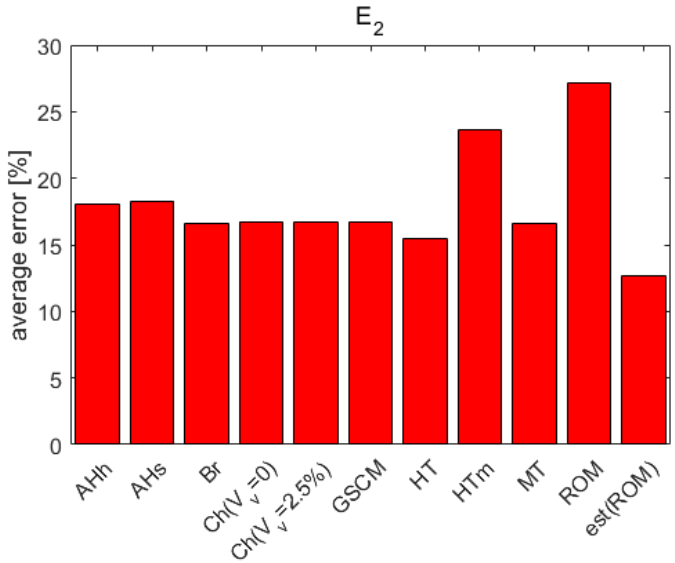

Figure 3: Average error of the models estimations

Several different manufacture processes were adopted for the compiled data. By this fact, a wide array of defects probably exists. For advanced manufactures, it is expected that the elasticity-based models become closer to the measured property, since none of them considers defects influence and the adjustable semi-empirical model considers this effect implicitly with calibrated terms.

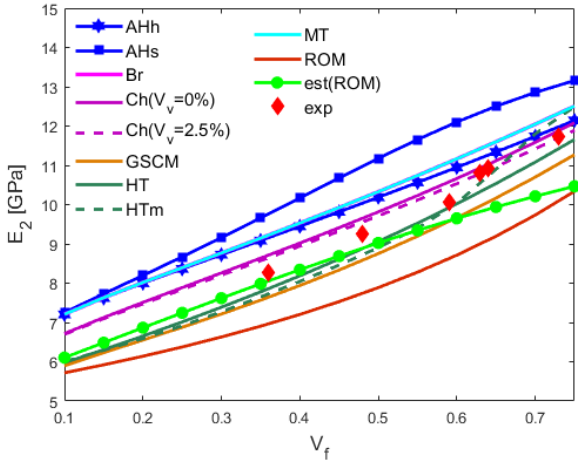

Figure 4: Comparision between models predictions and experimental data for carbon fiber [20,25].

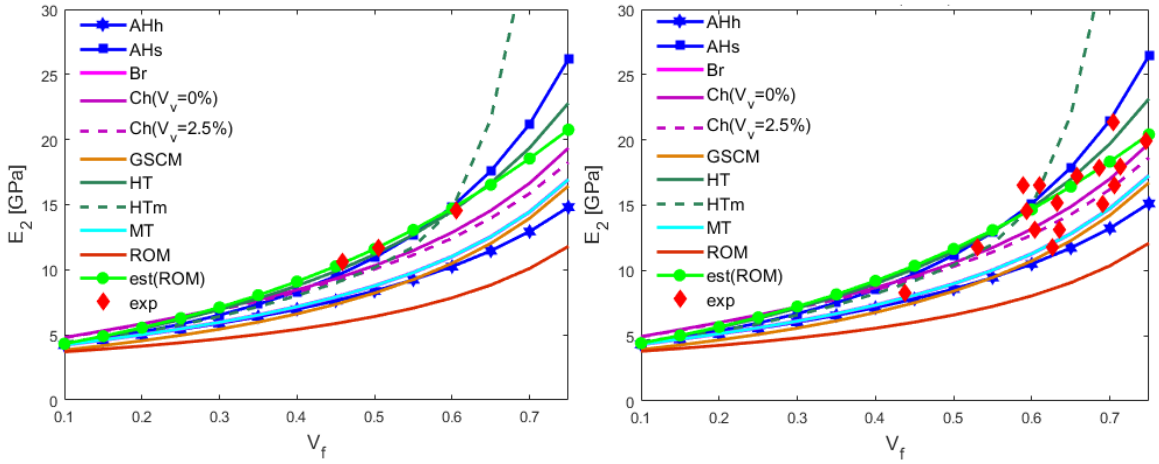

Figure 5: Comparision between models predictions and experimental data for glass fiber [21,30].

To evaluate how E_2 varies according V_f, the models estimations are plotted together with the set of data presented by Kris & Stinchcom [20] and Huang [25], Xin et al. [32] and Tsai & Huhn [21] in Figures 4-5. The reference and the fiber type are quoted over the figures. The main conclusions are:

i) The modified Halpin-Tsai model has a good representation of the experimental data for carbon fibers, while for glass fibers this model tends to overestimate the transversal elastic modulus.

ii) The Bridging and Mori-Tanaka models have an estimation between the Asymptotic Homogenization with square and hexagonal symmetry.

iii) Based on the results of the Asymptotic Homogenization, the square symmetry results in a higher transversal modulus than the hexagonal.

iv) The proposed semi-empirical model is able to reproduce the experimental data with good precision.

3. CONCLUSIONS

This paper presents a comparative analysis of 10 different micromechanical models to estimate the transversal elastic modulus. The models predictions are compared with a set of 65 experimental data compiled from literature. A semi-empirical model is proposed and a good correlation with experimental data is realized. This model obtained the smallest average error as well as the highest amount of case with error smaller than 10% (more than 50% of the cases).

ACKNOWLEDGEMENTS

The authors would like to acknowledge the support of the Brazilian Research Agencies CNPq, CAPES and FAPERJ. The Air Force Office of Scientific Research (AFOSR) is also acknowledged.

REFERENCES

[1] Soden, P.D., Kaddour, A.S., Hinton, M.J., 2004, "Recommendations for designers and researchers resulting from the world-wide failure exercise", Compos. Sci. Technol., v. 64, pp. 589-604.

[2] Kaddour, A.S., Hinton, M.J., 2013, "Evaluation of theories for predicting failure in polymer composite laminates under 3-D states of stress", J Compos Mater, v. 47, pp. 6-7.

[3] Kaddour, A.S., Hinton, M.J., Smith, P.A., Li, S., 2013, "The background to the third world-wide failure exercise", Journal of Composite Materials, v. 47, pp. 2417-2426.

[4] Selvadurai, A.P.S., Nikopour, H., 2012, "Transverse elasticity of a unidirectionally reinforced composite with an irregular fibre arrangement: Experiments, theory and computations", Composite Structures, v. 94, pp. 1973-1981.

[5] Barbero, E.J., 2018, Introduction to Composite Materials Design, 3 ed., CRC Press.

[6] Chamis, C.C., Abdi, F., Garg, M., Minnetyan, L., Baid, H., Huang, D., Housner, J., Talagani, F., 2013, "Micromechanics-based progressive failure analysis prediction for WWFE-III composite coupon test cases", *Journal of Composite Materials*, v. 47, pp. 2695-2712.

[7] Halpin, J.C., Tsai, S.W., 1969, Effects of Environmental Factors on Composite Materials, AFML-TR-67-423.

[8] Halpin, J. C.; Kardos, J. L., 1976, "The Halpin-Tsai Equations: A Review", Polymer Engineering and Science, v. 16, pp. 344-352.

[9] Ginet, E., Vercher, A., Marco, M., Arango, C., 2015, "Estimation of the reinforcement factor n for calculating the transverse stiffness E2 with the Halpin-Tsai equations using the finite element method". Composite Structures, v. 124, pp. 402-408.

[10] Nocedal, J., Wright, S.J., 1999, Numerical Optimization, Springer.

[11] Rodríguez-Ramos, R., Sabina, F.J., Guinovart-Díaz, R., Bravo-Castillero, J., 2001, "Closed-form expressions for the effective coefficients of a fiber-reinforced composite with transversely isotropic constituents - I. Elastic and square symmetry", Mechanics of Materials, v. 33, pp. 223-235

[12] Guinovart-Díaz, R., Bravo-Castillero, J., Rodríguez-Ramos, R., Sabina, F.J., 2001, "Closed-form expressions for the effective coefficients of fibre-reinforced composite with transversely isotropic constituents. I: Elastic and hexagonal symmetry", Journal of the Mechanics and Physics of Solids, v. 49, pp. 1445-1462.

[13] Bravo-Castillero, J., Guinovart-Díaz, J., Rodríguez-Ramos, R., Sabina, F.J., Brenner, R., 2012, "Unified analytical formulae for the effective properties of periodic fibrous composites", Materials Letters, v. 73, pp. 68-71.

[14] Wang, Y.C., Huang, Z.M., 2015, "A new approach to a bridging tensor". Polym. Compos., v. 36, pp. 1417-1431.

[15] Christensen, R., Miyano, Y., Nakada, M., 2015, "The size dependence of tensile strength for brittle isotropic materials and carbon fiber composite materials", *Composites Science and Technology*, v. 106, pp. 9-14.

[16] Mura, T., 1987, Micromechanics of defects in solids. Martinus Nijhoff.

[17] Benveniste, Y., 1987, "A new approach to the application of Mori-Tanaka's theory in composite materials", *Mechanics of Materials*, v. 6, pp. 147-57.

[18] Goggin, P.R., 1973, "The elastic constants of carbon-fibre composites", Journal of Materials Science, v. 8, pp. 233-244.

[19] Holmes, M., Al-khayatt, Q.J., 1975, "Structural properties of grp", Composites, v. 6, pp. 157-165.

[20] Kriz, R.D., Stinchcomb, W.W., 1979, "Elastic Moduli of Transversely Isotropic Graphite Fibers and Their Composites", Experimental Mechanics, v. 19, pp. 41-49.

[21] Tsai, S.W., Hahn, H.T., 1980, Introduction to Composite Materials, Technomic.

[22] Wilczynsky, A.P., Lewinski, J., 1995, "Predicting the Properties of Unidirectional Fibrous Composites with Monotropic Reinforcement", Composites Science and Technology, v. 55, pp. 139-143.

[23] Soden, P.D., Hinton, M.J., Kaddour, A.S., 1998, "Lamina Properties, Lay-up Configurations and Loading Conditions for a Range of Fibre-Reinforced Composite Laminates", Composites Science and Technology, v. 58, pp. 1011-1022.

[24] Bledzki, A.K., Kessler, A., Rikard, R., Chate, A., 1999, "Determination of elastic constants of glass/epoxy unidirectional laminates by the vibration testing of plates", *Composites Science and Technology*, v. 59, pp. 2015-2024.

[25] Huang, H., Talreja, R., 2005, "Effects of void geometry on elastic properties of unidirectional fiber reinforced composites", Composites Science and Technology, v. 65, pp. 1964-1981.

[26] Camanho, P.P., Miamí, P., Dávila, C.G., 2007, "Prediction of size effects in notched laminates using continuum damage mechanics", *Composites Science and Technology*, v. 67, pp. 2715-2727.

[27] Kaddour, A.S., Hinton, M.J., 2012, "Input data for test cases used in benchmarking triaxial failure theories of composites", Journal of Composite Materials, v. 46, pp. 2295-2312.

[28] Kaddour, A.S., Hinton, M.J., Smith, P.A., Li, S., 2013, "Benchmarking of matrix cracking, damage and failure models for composites: comparison between theories". J Compos Mater 2013, v. 47, pp. 20-21.

[29] Schaefer, J.D., Werner, B.T., Daniel, I.M., 2014, "Strain-Rate-Dependent Failure of a Toughened Matrix Composite", Experimental Mechanics, v. 54, pp. 1111-1120.

[30] Li, W., Cai, H., Zheng, J., 2014, "Characterization of Strength of Carbon Fiber Reinforced Polymer Composite Based on Micromechanics", Polymers and Polymer Composites, v. 22, pp. 105-116.

[31] Xin, H., Liu, Y., Mosallam, A.S., He, J., Du, A., 2017, "Evaluation on material behaviors of pultruded glass fiber reinforced polymer (GFRP) laminates", Composite Structures, v. 182, pp. 283-300.

NOTCHED STRENGTH OF SYMMETRIC ANGLE-PLY LAMINATES

Lucas L. Vignoli [1,2], **Jaime T.P. de Castro** [3]

(1) Center for Nonlinear Mechanics, COPPE, Department of Mechanical Engineering, Universidade Federal do Rio de Janeiro, Brazil

(2) Department of Mechanical Engineering, Universidade Federal do Rio de Janeiro - Campus Macaé, Brazil

(3) Department of Mechanical Engineering, Pontifícia Universidade Católica do Rio de Janeiro, Brazil

https://doi.org/10.21452/bccm4.2018.03.03

Abstract

Even though composite materials are ever more used in structural applications, mainly due to their excellent strength/weight ratio, this material class is also intrinsically anisotropic, a condition that must be properly considered in theirs macroscopic analyses. It is well known that angle-plies instead of unidirectional laminates are preferable for practical applications, but it is demonstrated here that in addition damage initiation around notch borders in angle-plies requires smaller nominal stresses than in unidirectional laminates, due to the uncoupling of normal/shear effects. To do so, the Stroh formalism and the Classical Laminate Theory are applied toghether with Tsai-Wu, Puck, and LaRC05 resistance criteria to analytically evaluate stress concentration effects introduced by circular holes in large anisotropic plates, and to estimate damage initiation around the hole border.

1. INTRODUCTION

Composite materials are widely used in various industrial areas for demanding structural applications, mainly because they have low specific weight and high strength. However, this material class is intrinsically anisotropic, especially unidirectional laminates that are the focus of this study. Since most real structures must contain notches for functional and/or assembly purposes, which induce stress/strain concentration effects that are the major cause for damage initiation, they must be properly analysed by suitable design procedures. This paper aims to discuss the analytical evaluation of such effects.

2. FUNDAMENTAL ELASTICITY SOLUTIONS

Considering a linear and elastic angle-ply laminate, the constitutive relation for its *P-th* ply in global coordinates is defined by [1]

$$[s_{ij}^{(g)}]_P = [s_{ijkl}^{(g)}]_P [e_{kl}^{(g)}]_P \tag{1}$$

where $s_{ij}^{(g)}$, $s_{ijkl}^{(g)}$ and $e_{kl}^{(g)}$ are the stress, stiffness and strain tensors defined in global coordinates.

Using the Kirchhoff-Love kinematical assumption, the strain tensor can be defined as

$$e_{ij}^{(g)} = \bar{e}_{ij}^{(g)} + x_3^{(g)} k_{ij}^{(g)} \tag{2}$$

where $\bar{e}_{ij}^{(g)}$ is the midplane strain tensor and $k_{ij}^{(g)}$ is the curvature.

According to the Classical Laminate Theory (CLT), the forces and moments per unit of lengths are computed by the following equations

$$N_{ij}^{(g)} = A_{ijkl}^{(g)} \bar{e}_{kl}^{(g)} + B_{ijkl}^{(g)} k_{kl}^{(g)} \tag{3}$$

$$M_{ij}^{(g)} = B_{ijkl}^{(g)} \bar{e}_{kl}^{(g)} + D_{ijkl}^{(g)} k_{kl}^{(g)} \tag{4}$$

where $N_{ij}^{(g)} = \int [s_{ij}^{(g)}]_P dx_3^{(g)}$, $M_{ij}^{(g)} = \int [s_{ij}^{(g)}]_P x_3^{(g)} dx_3^{(g)}$, $A_{ijkl}^{(g)} = \int s_{ijkl}^{(g)} dx_3^{(g)}$, $B_{ijkl}^{(g)} = \int s_{ijkl}^{(g)} x_3^{(g)} dx_3^{(g)}$ and $D_{ijkl}^{(g)} = \int s_{ijkl}^{(g)} (x_3^{(g)})^2 dx_3^{(g)}$. Restricting this study to symmetric laminates subjected to in-plane forces, $B_{ijkl}^{(g)} = 0$ and $M_{ij}^{(g)} = 0$. Hence, the laminate constitutive equation is

$$N_{ij}^{(g)} = A_{ijkl}^{(g)} \bar{e}_{kl}^{(g)} \tag{5}$$

Considering the average stress through the plate thickness, the average stiffness tensor is computed as

$$\tilde{s}_{ijkl}^{(g)} = A_{ijkl}^{(g)} / t \tag{6}$$

where t is the plate thickness.

Once the equivalent elastic properties of the laminate are obtained by the CLT, to analyze stress concentration effects induced by a circular hole, it is necessary to evaluate the stress distribution along the hole border. Using the Stroh formalism, a very useul tool for the theory elasticity of anisotropic materials, the hoop stress along the hole border is written as [2]

$$s_{11}^{(l)} = \mathbf{i}_1 \left(\mathbf{G}_1^{(l)} \mathbf{t}_2 + \mathbf{G}_3^{(l)} \mathbf{t}_1 \right) - \mathbf{i}_2 \left(\mathbf{G}_1^{(l)} \mathbf{t}_1 - \mathbf{G}_3^{(l)} \mathbf{t}_2 \right) \tag{7}$$

where $\mathbf{i}_1 = \begin{bmatrix} 1 & 0 & 0 \end{bmatrix}$, $\mathbf{i}_2 = \begin{bmatrix} 0 & 1 & 0 \end{bmatrix}$, $t_1 = \begin{bmatrix} s_{11}^{(g)} & s_{12}^{(g)} & 0 \end{bmatrix}^T$, $t_2 = \begin{bmatrix} s_{21}^{(g)} & s_{22}^{(g)} & 0 \end{bmatrix}^T$, $\mathbf{G}_1^{(l)} = \begin{bmatrix} \mathbf{N}_1^{(l)} \end{bmatrix}^T - \mathbf{N}_3^{(l)} \mathbf{S} \mathbf{L}^{-1}$, and $\mathbf{G}_3^{(l)} = -\mathbf{N}_3^{(l)} \mathbf{L}^{-1}$. $\mathbf{N}_1^{(l)}$ and $\mathbf{N}_3^{(l)}$ are known as the fundamental elasticity matrices, and $\mathbf{S}$ and $\mathbf{L}$ are the Barnet-Lothe tensors. These quantities are defined as

$$\mathbf{N}_1^{(l)} = -\left[\mathbf{T}^{(l)}\right]^{-1} \left[\mathbf{R}^{(l)}\right]^T \tag{8}$$

$$\mathbf{N}_3^{(l)} = -\mathbf{R}^{(l)} \left[\mathbf{T}^{(l)}\right]^{-1} \left[\mathbf{R}^{(l)}\right]^T - \mathbf{Q}^{(l)} \tag{9}$$

$$\mathbf{S} = \frac{1}{\pi} \int_0^{\pi} \mathbf{N}_1^{(l)} d\theta \tag{10}$$

$$L = \frac{1}{\pi} \int_0^{\pi} \mathbf{N}_3^{(l)} d\theta \tag{11}$$

where $Q_{ik} = s_{i1k1}^{(g)}$, $R_{ik} = s_{i1k2}^{(g)}$, $T_{ik} = s_{i2k2}^{(g)}$ and

$$\mathbf{Q}^{(l)} = \mathbf{Q}\cos^2\theta + (\mathbf{R} + \mathbf{R}^T)\sin\theta\cos\theta + \mathbf{T}\sin^2\theta \tag{12}$$

$$\mathbf{R}^{(l)} = \mathbf{R}\cos^2\theta + (\mathbf{T} - \mathbf{Q})\sin\theta\cos\theta + \mathbf{R}^T\sin^2\theta \tag{13}$$

$$\mathbf{T}^{(l)} = \mathbf{T}\cos^2\theta - (\mathbf{R} + \mathbf{R}^T)\sin\theta\cos\theta + \mathbf{Q}\sin^2\theta \tag{14}$$

3. FAILURE CRITERIA

According to Soden *et al*. [3], the models that better matched with experimental results from the worldwide failure exercise known as WWFE-1 (a round-robin to experimentally evaluate the modeling of composite failures) were Tsai-Wu, Puck, and Cuntze. Among these, Cuntze's model does not need to be discussed here because for damage initiation, this paper aim, it is quite similar to Puck's model. Kaddour and Hinton [4] pointed out that Carrere's and the LaRC05 models generated the better predictions for the data obtained in the following WWFE-II. However, just the LaRC05 is studied here, because Carrere's model includes micromechanics approaches, which are not within this paper scope. Thus, Tsai-Wu, Puck, and LaRC05 failure criteria are presented next, to be later used to estimate the strength of unnotched and notched laminated plates. Note that despite Puck and LaRC05 are able to indicate which constituint fails, they do not consider any explicit micromechanical approach.

3.1 Tsai-Wu Criterion

Tsai and Wu [5] proposed a well known and widely used generic failure criterion for anisotropic materials based on a polynomial function which is simple to implement and compute, albeit it does not distinguish failure mechanisms. For plane stress conditions, their damage function is described by

$$f_{TW} = \frac{s_{11}^2}{S_{11}^t S_{11}^c} + \frac{s_{22}^2}{S_{22}^t S_{22}^c} + \left(\frac{s_{12}}{S_{12}}\right)^2 + a_{1122}^* \frac{s_{11} s_{22}}{\sqrt{S_{11}^t S_{11}^c S_{22}^t S_{22}^c}} + \left(\frac{1}{S_{11}^t}\right) - \left(\frac{1}{S_{11}^c}\right) s_{11} + \left(\frac{1}{S_{22}^t}\right) - \left(\frac{1}{S_{22}^c}\right) s_{22} \tag{15}$$

where $a^{*}_{1122} = -1$ is recommended in absence of experimental data for proper calibration. For Eq.(15) and for all the other models, failure is assumed to take place when their damage functions equal 1.

3.2 Puck Criterion

The Puck criterion [6] use different approaches to model different failure mechanisms in composite materials, recognizing the difference between fiber and matrix failures, as well as different tension and compression effects. For fibers under tensile loads, using the maximum normal stress theory as a basis, his damage function is given by

$$f_P^{(f,t)} = \frac{1}{S_{11}^t}\left|s_{11} + \left(\frac{E_1}{E_1^{(f)}} n_{12}^{(f)} m_f - n_{12}\right) s_{22}\right| \tag{16}$$

where $m_f = 1.3$ is recommended for glass fibers.

Considering the shear influence on the fibers instability when they are compressed, the function to describe fiber damage under compression is

$$f_P^{(f,c)} = \frac{1}{S_{11}^c}\left|s_{11} + \left(\frac{E_1}{E_1^{(f)}} n_{12}^{(f)} m_f - n_{12}\right) s_{22}\right| + \left(10\frac{s_{12}}{G_{12}}\right)^2 \tag{17}$$

For modeling matrix failures, the key-point of Puck's model is to identify and to evaluate damage on a critical plane, similar to the Coulomb-Mohr criterion. For plane stress, three different failure modes are modelled: mode A, when the matrix is in tension and the critical plane is parallel to the fibers; mode B, that has the same critical plane than mode A but the matrix is compressed; and mode C, where the matrix is also in compression, however the critical plane inclination is $\gamma_C = a\cos\{[(1/2(1+p_{12}^c))((S_{23}^{(23)} s_{12}/S_{12} s_{22})^2 + 1)]^{1/2}\}$, where for glass fibers $p_{12}^c = 0.25$ and $S_{23}^{(23)} = S_{12}/2p_{12}^c[(1+2p_{12}^c S_{22}^c/S_{12})^{1/2} - 1]$. The damage functions for theses modes are

$$f_P^{(m,A)} = \left(\frac{s_{12}}{S_{12}}\right)^2 + \left(\frac{s_{22}}{S_{22}^t}\right)^2 + 2\frac{p_{12}^t}{S_{12}} s_{22}\left(1 - \frac{s_{22}}{S_{22}^t}\right) + \left(\frac{s_{11}}{X_{11}}\right) \tag{18}$$

$$f_P^{(m,B)} = \left(\frac{s_{12}}{S_{12}}\right)^2 + 2\frac{p_{12}^c}{S_{12}} s_{22} + \left(\frac{s_{11}}{X_{11}}\right) \tag{19}$$

$$f_P^{(m,C)} = \left(\frac{s_{12}\cos\gamma_c}{S_{12}}\right)^2 + \left(\frac{s_{22}\sin\gamma_c\cos\gamma_c}{S_{23}^{(23)}}\right)^2 + 2\frac{p_{12}^c}{S_{12}} s_{22}\cos^2\gamma_c + \left(\frac{s_{11}}{X_{11}}\right) \tag{20}$$

where $p_{12}^t = 0.30$ is recommended for glass fiber, $6 < n < 8$ ($n = 8$ is adopted here) and $X_{11} = 1.1S_{11}^t$ if $s_{11} \geq 0$ or $X_{11} = -1.1S_{11}^c$ otherwise.

3.3 LaRC05 Criterion

This failure criterion has been developed since 2000's and has been proven to be able to generate quite accurate predictions. Despite Pinho *et al*. [7] data indicates a nonlinear behavior of the transverse elastic and of the shear moduli, both are assumed linear here, since just initial damage is analyzed and these properties becomes nonlinear for higher strain levels.

For the matrix failure, the Puck model is used as a basis, mainly because of its use of a critical plane concept. Therefore, just one damage equation is used, but it requires a critical plane search. The matrix damage function is

$$f_L^{(m)} = \left(\frac{s_{12}\cos\gamma}{S_{12} - b_L s_{22}\cos^2\gamma}\right)^2 + \left(\frac{s_{22}\sin\gamma\cos\gamma}{S_{23}^{(23)} - b_T s_{22}\cos^2\gamma}\right)^2 + \left(\frac{\max\left\{0, s_{22}\cos^2\gamma\right\}}{S_{22}^t}\right)^2 \tag{21}$$

where b_L and b_T are parameters that can be experimentally calibrated, γ is the critical plane angle, and $S_{23}^{(23)}$ is the shear strength on this plane. According to Dávila *et al*. [8], $b_L = 0.082$ and $\theta_0 = 53°$, used in $b_T = -1/\tan 2\theta_0$ and $S_{23}^{(23)} = S_{22}^c \cos\theta_0 \left(\sin\theta_0 + \cos\theta_0/\tan 2\theta_0\right)$, are good approximations if no experimental data is available.

For modeling the failure of fibers under tensile loads, the maximum normal stress theory is assumed valid, resulting on the following damage function

$$f_L^{(f,t)} = s_{11}/S_{11}^t \tag{22}$$

The main advantage of this model when compared to the Puck's one is the modelling of fibers failure when these are compressed, because it considers in a more sophisticated way the fibers instability. If all the fibers are initially aligned, a rotation ϕ along the plane $x_2 - x_3$ is necessary to search the critical plane. Once this procedures is finished, the stress components in this plane are computed as $s_{ij}^{(f)} = l_{ik} l_{jl} s_{kl}$. Nevertheless, an initial misalignment of the fibers is an intrinsic issue for real manufacturing processes, and must be considered in failure analyses, because it may have a major contribution for instability failures due to the fibers initial deflection. Hence, in the presence of an initial misalignment angle φ_0, the total misalignment is computed considering the initial value induces the shear contribution:

$$\varphi = \mathrm{sign}(s_{12}^{(f)})\varphi_0 + 2\varepsilon_{12}^{(mis)} \tag{23}$$

where

$$\varphi_0 \cong \left(1 - S_{11}^c/G_{12}\right)\tan\left(\frac{1 - \sqrt{1 - 4\left(S_{12}/S_{11}^c + b_L\right)S_{12}/S_{11}^c}}{\left(2\left(S_{12}/S_{11}^c + b_L\right)\right)}\right) \tag{24}$$

Once the misalignment direction is obtained, the stress components in this planes are computed with the transformation $s_{ij}^{(mis)} = l_{ik} l_{jl} s_{kl}^{(f)}$. At last, the damage function of the fibers in compression is defined by

$$f_L^{(f,c)} = \left\langle \frac{s_{12}^{(mis)}}{S_{12} - b_L s_{22}^{(mis)}} \right\rangle^2 + \left\langle \frac{s_{23}^{(mis)}}{S_{23}^{(23)} - b_T s_{22}^{(mis)}} \right\rangle^2 + \left\langle \frac{\max\left\{0, s_{22}^{(mis)}\right\}}{S_{22}^t} \right\rangle^2 \qquad (25)$$

4. RESULTS AND DISCUSSION

Considering the unidirectional $[\alpha]_n$ and angle-ply $[\pm\alpha]_{ns}$ laminates, their tensile ($S_{FPF}^t(\alpha)$) and compressive ($S_{FPF}^c(\alpha)$) strength variations according to the fiber-to-load angles predicted by Tsai-Wu, Puck, and LaRC05 criteria are plotted in Fig. 1 for an unnotched plate. Notice the very high effect of the fiber angle with respect to the load direction on the laminate strength predicted by all criteria, a major issue when dealing with laminates. This is the main reason for their peculiar stress concentration behavior, studied next. Figure 1 illustrates how matrix failure usually is the dominant mechanism. For the single layered laminate, the tensile strength decrease more than 80% when the fibers angle α changes from 0º to 15º, a major effect that highlights well how directional such composite materials are.

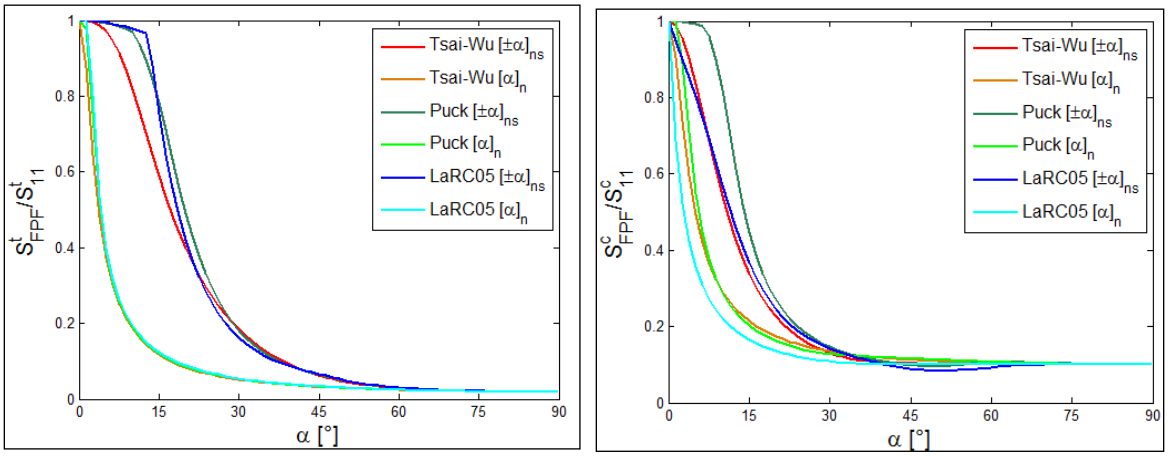

Figure 1. Variation of the unnotched laminate plate FPF strength prediction as function of the fiber orientation angle α with respect to the uniaxial load direction, $S_{FPF}^t(\alpha)/S_{11}^t$ and $S_{FPF}^c(\alpha)/S_{11}^c$, where S_{11}^t and S_{11}^c are the reference tensile and compressive strengths measured when the fibers are aligned with the load, i.e. when $\alpha = 0$.

This simple analysis, still without considering any stress concentration effects, helps to understand the results presented next. In particular, those that show that the critical point along a circular hole border in anisotropic plates in general is ***not*** the point where the stress concentration peaks occur. Instead, it is the point that maximizes the ratio between the local stress and the smallest (anisotropic) material strength along the notch border. This usually is a major issue when

designing notched components made of anisotropic materials, since their behaviour can be very different from the well-known behaviour of notched isotropic materials.

Additionally, the LaRC05 model indicated that the strength of angle-ply laminates may be smaller than that of unidirectional laminates with the same angle α. This conclusion applies for fiber-to-load angle α between 45º and 60º, and it is a consequence of the shear influence in the longitudinal compression resistance modelled by the LaRCO05 criterion.

First, using the CLT, it is possible to conclude that angle-ply laminates do not couple shear and normal stress and strains, because the elements responsible for this physical coupling on the equivalent stiffness and equivalent compliance tensors are null, unlike what happens for $[\alpha]_n$ if $\alpha \neq 0°, \pm 90°$, a result that is valid for any angle-ply laminate. Notice that $[+\alpha]_n$ and $[-\alpha]_n$ are two different laminates, and that $[\pm\alpha]_{ns}$ is one laminate that contains laminas with both angles, $+\alpha$ and $-\alpha$.

First ply failure (FPF) notched strength predictions for single-layered and angle-ply laminates are presented in Fig. 2. Clearly, the $[0]_n$ and $[90]_n$ laminates must be equivalent to $[\pm 0]_{ns}$ and $[\pm 90]_{ns}$, respectively, but their strength variation according to the fiber-to-load angle α have a significantly different behavior. For tension or for compression, the strength curves have a smoother shape for single layered laminates, unlike what happens for un-notched plates. Figure 1 shows that in notch-free laminates, the angle-plies strength variations are smoother. These results are justified by the vanishing effect of the normal-shear coupling in equivalent homogeneous materials, where the stress concentration is maximized, e.g. for $[\alpha]_n$ where the stress concentration is maximized if $\alpha = 0°, \pm 90°$.

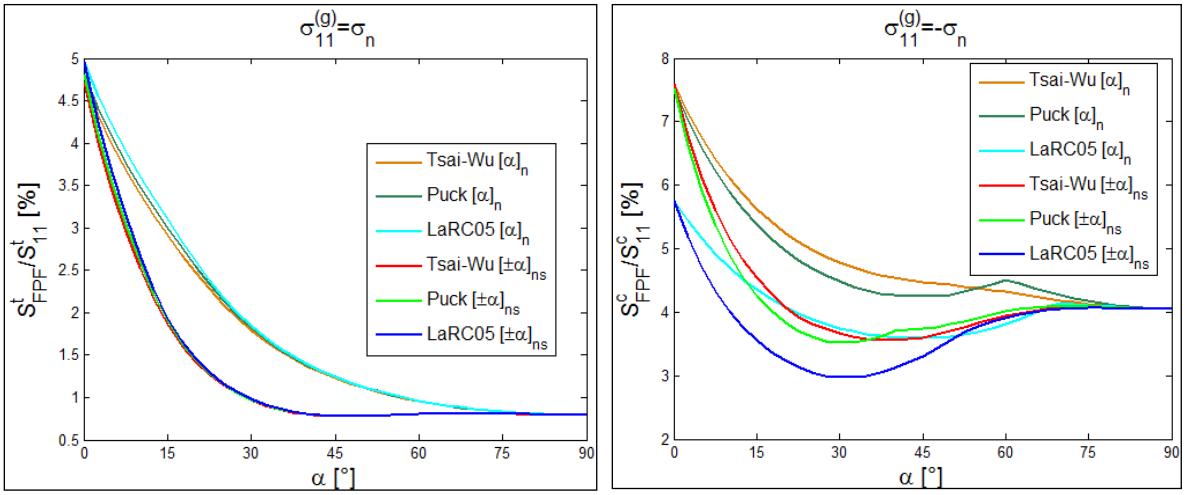

Figure 2. Prediction of S^t_{FPF}/S^t_{11} and S^c_{FPF}/S^c_{11} for the holed orthotropic plate FPF strength under tension and under compression loads by the 3 failure criteria, for angle-ply laminates, as a function of the fibers-to-load angle α.

While the stress concentration around the border of a circular hole in isotropic plates with uniaxial load ranges between -1 and 3 for isotropic materials, for the single-layered laminate studied it ranges between -4 and 7 [9]. For angle-ply laminates the stress concentration effect is even more pronounced. By this fact, the ration between notched and unnotched strengths presented in Fig. 2 is smaller than 10% for all cases.

5. CONCLUSIONS

This paper presented a brief review of some theoretical approaches for stress analyses of anisotropic materials, in particular laminated composites (Stroh Formalism and CLT). Three failure theories are studied here, using as basis the WWFE results and their recommendations: Tsai-Wu, Puck, and LaRC05. Then these techniques are used to predict the behaviour of simple notched plates. Large plates made by single layered unidirectional laminates with circular holes had a FPF strength decrease estimation of more than 95% and 90% for uniaxial tension and compression, respectively. These results, which differ significantly from the behaviour of isotropic plates, become even more pronounced depending of the fiber orientation. Notched angle-ply laminates have a smaller FPF strength for most of the cases analyzed, on the contrary of unnotched plates. For notched plates, the strength of symmetric angle-ply laminates is usually smaller than for unidirectional laminate due to the increase of stress concentration effects, what is the opposite of the observed for unnotched plates.

ACKNOWLEDGEMENTS

L.L. Vignoli would like to acknowledge the support of the Brazilian Research Agencies CNPq and CAPES, and ffrom PUC-Rio.

REFERENCES

[1] Jones, R.M., “Mechanics of Composite Materials”. 2nd Edition. Taylor & Francis Editions, 1998.
[2] Hwu, C., “Anisotropic Elastic Plates”. Springer, 2009.
[3] Soden, P.D., Kaddour, A.S., Hinton, M.J., Recommendations for designers and researchers resulting from the world-wide failure exercise. Compos. Sci. Technol. 2004;64:589–604.
[4] Kaddour, A.S., Hinton, M.J., Maturity of 3D failure criteria for fibre reinforced composites: Comparison between theories and experiments: Part B of WWFE-II. J. Compos. Mater. 2013;47:925–966.
[5] Tsai, S.W., Wu, E.M., A general theory of strength for anisotropic materials. J. Compos. Mater. 1971;5:58–80.
[6] Puck, A., Schürmann, H., Failure analysis of FRP laminates by means of physically based phenomenological models. Compos. Sci. Technol. 1998;58:1045–1067.
[7] Pinho, S.T., Darvizeh, R., Robinson, P., Schuecker, C., Camanho, P.P., Material and structural response of polymer-matrix fibre-reinforced composites. J. Compos. Mater. 2012;46:2313–2341.
[8] Pinho, S.T., Dávila, C.G., Camanho, P.P., Iannucci, L., Robinson, P., Failure Models and Criteria for FRP Under In-Plane or Three-Dimensional Stress States Including Shear Non-Linearity. NASA/TM-2005-213530, 2005.
[9] Vignoli, L.L., Castro, J.T.P., Meggiolaro, M.A., Stress Concentration Issues in Unidirectional Laminates, submitted to Composite Structures.

4. DURABILITY, AGEING AND AGGRESSIVE ENVIRONMENT

THE EFFECT OF ACCELERATED AGEING ON THE MECHANICAL AND PHYSICAL PROPERTIES OF THERMOSET POLYMERS

Francisco M. Dos Santos [(1)], Tulio H. Panzera [(1)], Alysson H. S. Bueno [(1)] , Alberto L. Santos [(2)] and Edson C. Botelho [(2)]

(1) Centre for Innovation and Technology in Composite Materials – CIT^{e}C, Department of Mechanical Engineering, Federal University of São João Del-Rei - UFSJ, Brazil.

(2) Departamento de Materiais e Tecnologia da Universidade Estadual Paulista (UNESP), Guaratinguetá, Brazil.

https://doi.org/10.21452/bccm4.2018.04.01

Abstract

Structural adhesives and composite materials are generally exposed to harsh environmental conditions that lead to their degradation. Saline and moisture environment at high temperatures are some of the common conditions that degrade polymers. A full factorial design was conducted to analyse the effects of accelerated ageing in salt-spray and 100% relative humidity (RH) chambers on the mechanical and physical properties of epoxy and unsaturated polyester (UP) polymers. In saline environment, the epoxy and UP polymers presented 42% and 38% less moisture absorption, respectively, than in 100% RH chamber. The epoxy polymer achieved 99% higher tensile strength than the UP in the condition without ageing, however the overall compressive properties of the UP were slightly higher than the epoxy.

Keywords: Thermoset polymers, epoxy properties, unsaturated polyester properties, harsh environment.

1. INTRODUCTION

Thermoset polymers can be used as structural adhesives or matrix of composite materials for application in several industries such as automotive and aeronautical. An adhesive may be defined as a material that can join components together and resist separation [1]. Epoxy polymers are the most widely accepted and used as structural adhesives, due to their good mechanical and thermal properties. On the other hand, unsaturated polyester (UP) is the most used polymer as composite matrix, particularly in the marine industry. UP possess low cost compared to the epoxy, good processing characteristics, specific physical properties and the ability to cure under room temperatures and pressures. Thus UP are widely used in materials such as glass fibre reinforced polyester composites [2, 3]. The composite matrix has several important functions, such as: it binds

the reinforcements together, maintains the shape of a component and transfers the applied load to the reinforcing fibres, and also protects the fibres from environmental attack [4].

Structural adhesives and composite materials are generally exposed to harsh environmental conditions that lead to their degradation. Saline and moisture environment at high temperatures are some of the common conditions that degrades polymers. Water molecules diffuse into adhesively-bonded joints and degrade both the interface and the adhesive itself [5]. Some authors [6 – 9] have found that water decreases the tensile strength and elastic modulus of epoxy polymers due to plasticization effect. When the time exposed in ageing is prolonged, an anomaly can occur due to more complex interactions between water molecules and epoxy cross chains forming hydrogen bonds. This effect can led to increased elastic modulus [10].

Quino *et al.* [11] have assessed the changes in the fracture and toughness properties of epoxy polymer when it is exposed to a wet environment. The toughness was affected locally varying moisture absorption over the cracking path. Arrieta *et al.* [12] have studied the thermal oxidative ageing of unsaturated polyester and vinyl ester plates at high temperatures of 120°C to 160°C. The findings revealed the vinyl ester was more oxidisable than the unsaturated polyester. Sugiman *et al.* [10] have analysed the water absorption and tensile properties of epoxy polymers after ageing in distilled and salt water in steady and fluctuating conditions at 50°C. The results showed that in steady and fluctuating conditions, the equilibrium water absorption of epoxy aged in the brine is lower than that of distilled water. The tensile properties of the epoxy polymer were not affected by the ageing conditions.

This paper investigates the effects of artificial ageing in high humidity, temperature and salt-spray fog on the tensile and compressive properties and moisture absorption of epoxy and polyester polymers. A design of experiments (DoE) was conduct in order to verify the effects of individual factors and interactions on the variable responses.

2. MATERIALS AND METHODS

2.1 Materials

The epoxy polymer used in this study was the low-viscosity Araldite® LY 5052 based on diglycidyl ether of bisphenol-A (DGEBA) with the hardener Aradur® 5052 which is a mixture of polyamines. This epoxy system is indicated for aeronautical applications and it is qualified by the Luftfahrtbundesamt (German Aircraft Authority) for the production of gliders. Both the epoxy resin and hardener were fabricated by Huntsman®. The unsaturated polyester resin used was the orthophthalic Polylite® 10316-10 pre-accelerated with cobalt octoate and the hardener was the methyl ethyl ketone peroxide (MEK-P), both fabricated by Reichhold®.

2.2 Fabrication and ageing of the specimens

The concentrations of hardeners considered were 38wt.% and 2wt.% for the epoxy and polyester system, respectively according to the manufacturer's recommendations. The resins and hardeners were hand mixed for 5 minutes. The fabrication and mechanical tests of the specimens followed the recommendations of the standards ASTM D638 [13] and ASTM D695 [14] for tensile and compressive properties respectively.

After the mixture, the polymers were poured into silicon moulds. The epoxy samples were left at room temperature for 7 days and the polyester samples for 12 h at room temperature (~22°C and 55% of relative humidity), with additional time of 48 h at 60°C in an oven. After the curing, the specimens were removed from the moulds, as shown in Figure 1. A set of specimens was left for more 7 (168 h) days at room temperature. Another set of specimens was left for 7 days in an

accelerated ageing chamber to simulate 100% of relative humidity (RH) at 40°C according to recommendations of ASTM D2247 [15], and other set was left for 7 days in a salt-spray chamber with 5wt.% of NaCl at 35°C following the recommendations of ASTM B117 [16].

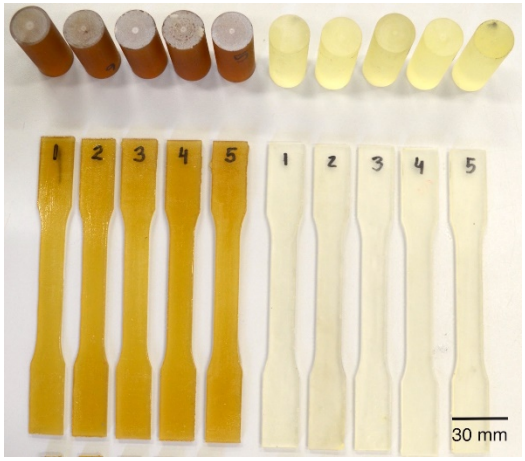

Figure 1: A set of specimens

A full factorial design was considered to analyse the effect of individual factors and their interactions. The design of experiments is shown in Table 1. Five repetitions were performed for each condition and two replicates were evaluated in order to estimate the experimental error of the individual response [17] resulting in a total of 60 specimens for tensile and 60 for compressive tests.

Table 1: Design of experiments $2^1 3^1$

Condition	**Factors**	
	Type of Polymer	**Environmental conditioning**
1	Epoxy	No degradation
2	Epoxy	100% R. humidity
3	Epoxy	Salt-spray
4	Polyester	No degradation
5	Polyester	100% R. humidity
6	Polyester	Salt-spray

2.3 Mechanical and physical evaluations of the specimens

After the environmental conditioning, the specimens were dried using a blow drier. The mechanical tests were performed using a Shimadzu AG-X Plus testing machine of 100 KN capacity with a testing speed of 2 mm/min. The moisture absorption was calculated considering the mass of the compressive specimens before and after the environmental ageing for 7 days in both harsh environments of 100% of relative humidity at 40°C and salt-spray chamber with 5wt.% of NaCl at 35°C according to the standard ASTM D5229 [18].

3. RESULTS AND DISCUSSION

3.1 Moisture absorption

After 7 days in the chambers of 100% RH and salt-spray fog, the epoxy specimens showed mean moisture absorption values of 0.49% and 0.34%, respectively. The polyester specimens presented mean values for moisture absorption of 0.30% in 100% RH and 0.21% in salt-spray fog. The moisture absorption was 42% and 38% lower in the 100% RH than in the salt-spray chambers for the epoxy and polyester polymers, respectively. According to Tan *et al.* [19], this reduction in moisture absorption at saline environment is probably due to the change in the driving force as the chemical potential of water is decreased in salt solution. This phenomenon would effectively generate an osmotic pressure that inhibits the moisture absorption by the polymer. Moreover, Prolongo *et al.* [20] have attributed this effect to the sodium chloride presence, which increases the density of the aqueous solution, consequently decreasing the diffusion coefficient of the solution in the polymer.

3.2 Mechanical testing

Table 2 shows the analyses of variance (ANOVA) for the mean response variables. The statistical software Minitab® v. 17 was used to manipulate the data. P-values lower or equal to 0.05 mean the effect was significant considering a confident interval of 95% [21]. The underlined P-values shown in Table 2 indicate the significant factors identified in this work. F-values evaluate which one of the factors provided a greater influence in the responses. The higher the F-value, the greater the effect of this factor on the response, i.e., the tensile modulus was more affected by the environmental conditioning factor (F-value = 140.46) than by the type of polymer (F-value = 35.88). When one or more interaction effects are significant, the factors that interact can be considered jointly. All interactions were significant and their P and F values are highlighted in bold letters in Table 2. The adjusted R^2 value indicates whether the model behaved properly. R^2 values closer to 1 (100%) indicate a more significant predictive ability of the model. R^2 values varied from 84.17% to 99.01%, indicating acceptable correlations obtained for the response variables analysed. A normality test via Anderson-Darling technique was used to validate the ANOVA. In this case, P-values must be equal or superior to 0.05 to follow a normal distribution configuration. As shown in Table 2, all data followed a normal distribution exhibiting P-values (And. Darling) higher than 0.05.

Figure 2 shows the interaction effect plots between "type of polymer" and "environmental conditioning" factors for the mean tensile modulus (a) and strength (b). The tensile modulus data varied from 2.92 GPa to 3.96 GPa. The letters in the graphs represent the results for the Tukey comparison test; similar letters belong to the same group indicating there is no significant variation between the means. For the condition with no degradation, the polyester presented 25% higher tensile modulus than the epoxy. The ageing decreased the polyester tensile modulus in 40% and 35% at 100% RH and salt-spray levels, respectively. According to Sugiman *et al.* [10], the modulus decreases as moisture content increases due to plasticisation; however, an anomaly might occur, such as the recovery of the tensile properties. Small variations were noted between environmental conditioning levels for the epoxy polymer. Tukey test revealed these means are equivalents, then, the conditioning did not provide any significant change in tensile modulus. The tensile strength data varied from 19.82 MPa to 54.50 MPa. The epoxy achieved 99% higher tensile strength than the UP in the condition without degradation as shown in the interaction plot (Figure 3b). Tukey's comparative test showed that the small variations between all levels of conditioning for the UP and between the level without degradation and chamber of 100% RH for the epoxy did not

significantly affect the tensile strength. However, sodium chloride caused a 20% increase in the tensile strength of the epoxy. This was probably due to the positive post-cure effect of the epoxy leading to an increase in the number of cross-reactions and thus increasing its resistance [22].

Table 2: Analyses of variance for the mechanical tests

		P and F values							
	Experimental factors	**Tensile modulus**		**Tensile strength**		**Compressive modulus**		**Compressive strength**	
		P	F	P	F	P	F	P	F
Main factors	Type of Polymer (Pol)	0.001	35.88	0.000	1044.08	0.002	29.99	0.000	118.98
	E. conditioning (E)	0.000	140.46	0.000	12.04	0.060	4.66	0.078	4.03
Interactions	Pol * E	**0.000**	**182.37**	**0.003**	**18.09**	**0.008**	**12.09**	**0.003**	**18.23**
	R^2 - adjusted	98.40%		99.01%		84.17%		93.51%	
	P-value (And. Darling)	0.158		0.167		0.875		0.709	

The compressive modulus (Figure 2c) for the polymers varied from 2.95 GPa to 3.14 GPa. The epoxy presented a modulus of 6.1% lower than the UP in a 100% RH chamber, probably due to the plasticisation effect [10, 22]. The formation of complementary crosslinks between the polyester chains is activated by raising the temperature through a suitable post cure and may lead to increased mechanical properties as observed for the 100% moisture and salt spray conditions [23]. However, the epoxy had the effect of plastification when conditioned in high humidity and temperature leading to a decrease of its modulus. The compressive strength (Figure 2d) for the polymers ranged from 110.07 MPa to 127.72 MPa. The UP achieved a slight increase of 9.2% in the compressive modulus for the specimens aged at 100% RH, being 13.9% higher than the epoxy at saline environment. This is probably due to the anomaly explained by Sugiman *et al.* [10] which could be due to competition between the plasticisation effect and the effect of additional crosslinking caused by the extended time at elevated temperatures and humidity, wherein the positive effect of an additional crosslinking is more dominant in polyester than the negative effect of plasticisation.

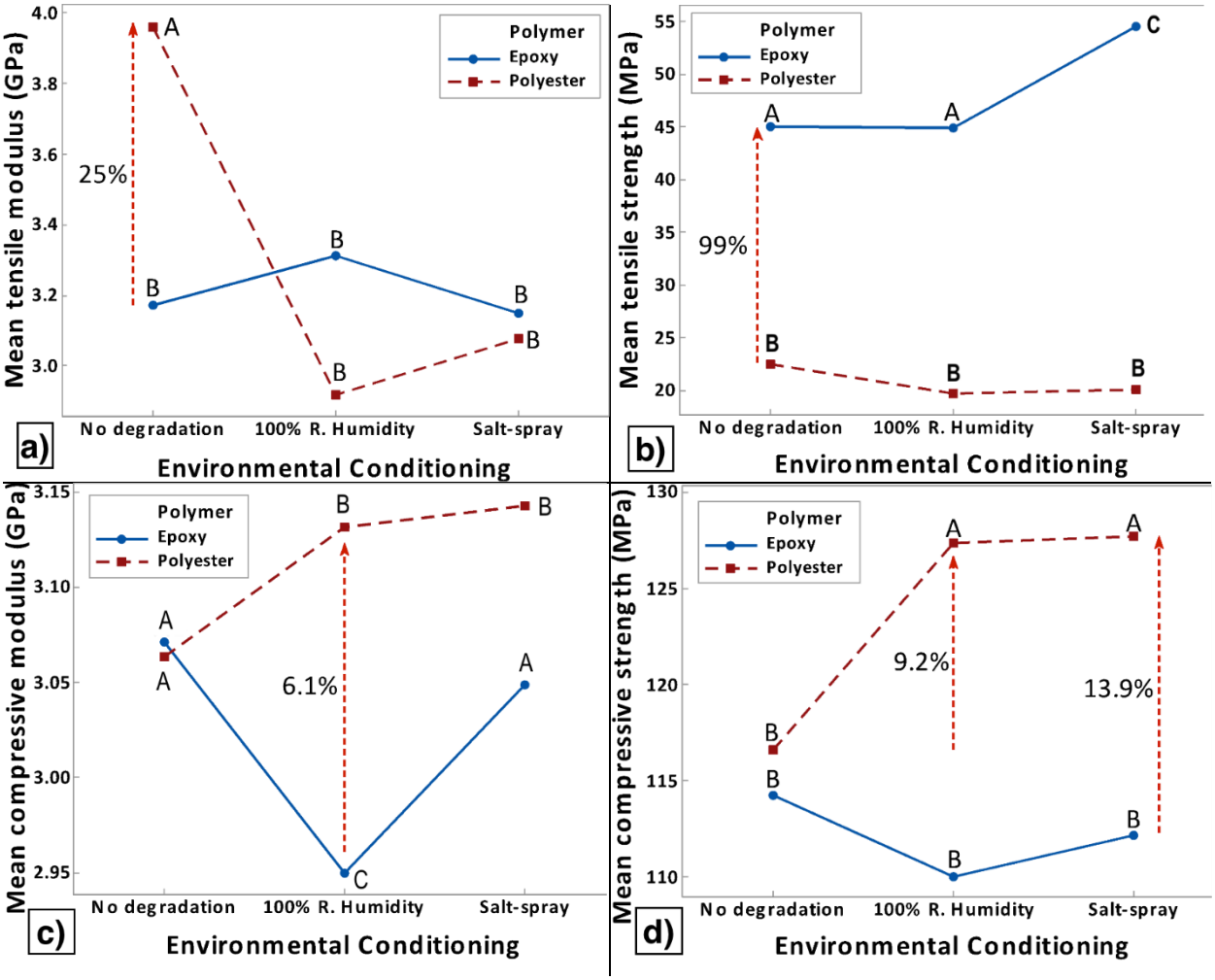

Figure 2: Interaction effect plots for the mean (a) tensile modulus, (b) tensile strength, (c) compressive modulus, (d) compressive strength.

4. CONCLUSION

This paper investigated the effects of environmental ageing in 100% RH and salt-spray chambers on the mechanical and physical properties of epoxy and unsaturated polyester polymers. The moisture absorption in salt-spray chamber was 42% and 38% lower than in 100% RH chamber for epoxy and UP, respectively. The tensile modulus of UP was 25% higher than the epoxy in condition without ageing. After ageing in both high humidity and salt-spray environments, the tensile modulus of UP dropped about 30%, being attributed to the negative effect of plasticisation. The tensile strength of the epoxy polymer was 99% higher than UP for the condition without ageing. The overall compressive properties of UP were slightly higher than epoxy.

ACKNOWLEDGEMENTS

The authors would like to thank CAPES, CNPq and FAPEMIG for the financial support provided.

REFERENCES

[1] R. Oosting, “Towards a New Durable and Environmentally compliant Adhesive Bonding Process

for Aluminium Alloys," Delft University of Technology, 1995.
[2] R. Raja, P. Kuppusamy, and S. Neogi, "Influence of curing agents on gelation and exotherm behaviour of an unsaturated polyester resin," vol. 36, no. 7, pp. 1217–1224, 2013.
[3] G. M. Shafiur Rahman, H. Aftab, M. Shariful Islam, M. Z. Bin Mukhlish, and F. Ali, "Enhanced physico-mechanical properties of polyester resin film using CaCO3 filler," *Fibers Polym.*, vol. 17, no. 1, pp. 59–65, 2016.
[4] M. Davallo, H. Pasdar, and M. Mohseni, "Mechanical Properties of Unsaturated Polyester Resin," *Chemtech*, vol. 2, no. 4, pp. 2113–2117, 2010.
[5] M. Savvilotidou, T. Keller, and A. P. Vassilopoulos, "Fatigue performance of a cold-curing structural epoxy adhesive subjected to moist environments," *Int. J. Fatigue*, vol. 103, pp. 405–414, 2017.
[6] I. A. Ashcroft, M. M. A. Wahab, A. D. Crocombe, D. J. Hughes, and S. J. Shaw, "Effect of environment on the fatigue of bonded composite joints. Part 1: Testing and fractography," *Compos. Part A Appl. Sci. Manuf.*, vol. 32, no. 1, pp. 45–58, 2001.
[7] S. Liu, X. Cheng, Q. Zhang, J. Zhang, J. Bao, and X. Guo, "An investigation of hygrothermal effects on adhesive materials and double lap shear joints of CFRP composite laminates," *Compos. Part B Eng.*, vol. 91, pp. 431–440, Apr. 2016.
[8] P. Fernandes, G. Viana, R. J. C. Carbas, M. Costa, L. F. M. da Silva, and M. D. Banea, "The influence of water on the fracture envelope of an adhesive joint," *Theor. Appl. Fract. Mech.*, vol. 89, pp. 1–15, Jun. 2017.
[9] M. P. Zanni-Deffarges and M. E. R. Shanahan, "Diffusion of water into an epoxy adhesive: comparison between bulk behaviour and adhesive joints," *Int. J. Adhes. Adhes.*, vol. 15, no. 3, pp. 137–142, Jul. 1995.
[10] S. Sugiman, I. K. P. Putra, and P. D. Setyawan, "Effects of the media and ageing condition on the tensile properties and fracture toughness of epoxy resin," *Polym. Degrad. Stab.*, vol. 134, pp. 311–321, 2016.
[11] G. Quino, J. El Yagoubi, and G. Lubineau, "Characterizing the toughness of an epoxy resin after wet aging using compact tension specimens with non-uniform moisture content," *Polym. Degrad. Stab.*, vol. 109, pp. 319–326, 2014.
[12] J. S. Arrieta, E. Richaud, B. Fayolle, and F. Nizeyimana, "Thermal oxidation of vinyl ester and unsaturated polyester resins," vol. 129, pp. 142–155, 2016.
[13] ASTM D638 -14, "Standard Test Method for Tensile Properties of Plastics," 2014.
[14] ASTM D695 - 15, "Standard Test Method for Compressive Properties of Rigid Plastics," 2015.
[15] ASTM D2247-15, "Standard Practice for Testing Water Resistance of Coatings in 100 % Relative Humidity," 2015.
[16] ASTM B117-16, "Standard Practice for Operating Salt Spray (FOG) Apparatus," 2016.
[17] M. C. C. Werkema and S. Aguiar, *Planejamento e Análise de Experimentos: Como identificar as principais variáveis influentes em um processo*. Belo Horizonte: Fundação Christiano Ottoni, 1996.
[18] ASTM D5229 - 92, "Standard Test Method for Moisture Absorption Properties and Equilibrium Conditioning of Polymer Matrix Composite Materials," 2010.
[19] K. T. Tan *et al.*, "Role of salt on adhesion of an epoxy/aluminum (oxide) interface in aqueous environments," *Polym. Eng. Sci.*, vol. 56, no. 1, pp. 18–26, Jan. 2016.
[20] S. G. Prolongo, K. F. Horcajo, G. Del Rosario, and A. Ureña, "Strength and Durability of Epoxy-Aluminum Joints," *J. Adhes.*, vol. 86, no. 4, pp. 409–429, Apr. 2010.
[21] D. C. Montgomery, *Design and Analysis of Experiments*, Eighth Edi. John Wiley & Sons, Inc., 2013.
[22] H. Chiu, R. Jeng, and J. Chung, "Thermal Cure Behavior of Unsaturated Polyester / Phenol Blends," *J. Appl. Polym. Sci.*, vol. Vol. 91, pp. 1041–1058, 2003.
[23] C. A. C. C. Rebelo, "Caracterização do comportamento à fratura de resinas poliéster insaturadas," Universidade de Porto, 1987.

DIFFERENT APPROCHES TO KINETICS DEGRADATION OF POLYESTER RESIN FROM RENEWABLE RESOURCES

Vinicius Moraes Kieling da Rocha [(1)], Heitor Luis Ornaghi Júnior [(1)], Sandro Campos Amico [(1)], Daniel Magalhães de Oliveira [(2)] and Kelly Cristina Coelho Benini [(2)]

(1) PPGE3M, Federal University of Rio Grande do Sul, Brazil

(2) Department of Materials and Technology, São Paulo State University (UNESP), Scholl of Engineering, Guaratinguetá, São Paulo, Brazil (12156-410)

https://doi.org/10.21452/bccm4.2018.04.02

Abstract

Different approaches to the kinetic analysis of the thermal degradation of polyester resins, one traditional and its green alternative from renewable sources, were studied. The first step to determine the degradation mechanism was to find the following kinetic parameters: activation energy (E_a) and the pre-exponential factor (A). For the study it was used four distinct methods: the Flynn-Wall-Ozawa (FWO), the Friedman, the Kissinger and the modified Coats-Redfern methods. The second step was to find the most probable degradation mechanism based on the kinetic parameters obtained so far. In this study was used master plots proposed by Criado's. The mean activation energy values, named E_{ISO}, and the pre-exponential factor ($\ln(A)$) for the traditional polyester resin were 189.79 ± 37.82 kJ and 24.62 ± 6.11 min^{-1}, respectively. For the resin from renewable resources, the values of E_a and $\ln(A)$ were 161.85 ± 14.35 kJ and 18.42 ± 2.36 min^{-1}, respectively. For both resins, the most probable degradation mechanism in all conversion range was nucleation and growth type mechanism. The methodology used in this study indicates that the kinetic parameters can be obtained in a reliable way, since combined.

1. INTRODUCTION

Concerts over the future availability of natural resources and the amount of produced waste have driven the need for the efficient use of these resources, aiming at sustainable development. The requirement for ecomaterials increased [1], and they are defined as materials manufactured from renewable resources and/or from the reuse of accumulated wastes in the environment, and that are also atoxic, among other characteristics [2].

Conventional thermoset polymers can be replaced by their green alternatives, as long as they maintain satisfactory properties. Thermal degradation, for instance, is an important characteristic for processing as well as in the definition of their applications. Its reliable prediction is an important tool to identify potential use of the material.

In this present work, different approaches to the kinetic analysis of the thermal degradation of a traditional polyester resin and its green alternative from renewable resources were studied.

2. TEORETICAL APPROACH

2.1 Degradation Kinetics

Thermogravimetric analysis can be used to determine the degradation kinetics and to obtain reliable values of factor frequency, activation energy and general reaction order, i.e. the kinetic triplet [3]. Kinetic parameters were calculated according to ICTAC recommendations [4].

The main equation for kinetics is:

$$\frac{d\alpha}{dt} = k(T)f(\alpha) \tag{1}$$

where $k(T) = Aexp(-E_a/RT)$, $f(\alpha) = (1-\alpha)^n$, A is the pre-exponential factor, E_a is the activation energy, R is the gas constant (8.314 J.kmol^{-1}), T is the absolute temperature and n is the reaction order.

Including the β term, i.e. heating rate, Equation (2) is obtained:

$$\frac{d\alpha}{dt} = \frac{A}{\beta} e^{\left(-\frac{E_a}{RT}\right)} f(\alpha) \tag{2}$$

The activation energy can be determined using distinct methods, including isoconversional Flynn-Wall-Ozawa (FWO), Friedman and Kissinger methods.

In the Kissinger method, the maximum of the reaction happens at the peak of the differential thermal analysis (DTA). This peak happens when the derivative of Equation (3) is zero. The activation energy for Kissinger can be determined plotting $ln\left(\beta/{T_m}^2\right)$ versus $1/{T_m}^2$.

$$\frac{d\alpha}{(1-\alpha)^n} = \left[\frac{Ae^{\left(-\frac{E_a}{RT}\right)}}{\beta}\right] dT \tag{3}$$

FWO is a conversional method, defined by Equation (4). Plotting $log(\beta)$ versus $1/T$ and applying a linear fit the factor frequency and the activation energy can be obtained. The slope gives E_a and the intercept gives A.

$$log(\beta) = log(A\,E_a/Rg(\alpha)) - 2.315 - 0.4567(E_a/RT) \tag{4}$$

The Friedman method is defined by Equation (5). By plotting $ln(d\alpha/dt)$ versus $1/T$ and applying a linear fit the factor frequency and the activation energy can be obtained. The slope gives E_a and the intercept gives A.

$$ln\left(\frac{d\alpha}{dt}\right) = ln[Af(\alpha)] - \frac{E_a}{RT} \tag{5}$$

2.2 Degradation Mechanism

The activation energy of one solid-state reaction can be determined without knowing the mechanism of degradation. So, E_a can be determined by isothermal or dynamics processes. After determination of the mean E_a (by isothermal methods), the most probable degradation can be estimated by comparing master plots using the method proposed by Criado [5] Equation (6).

$$Z(\alpha) = \frac{(d\alpha/dt)}{\beta}\pi(X)T \quad (6)$$

Peterson [6], proposed a relationship between $\pi(X)$ and the rotational equation $P(x)$, defined in Equation (7).

$$\pi(x) = xe^{x}P(x) \quad (7)$$

Senum and Yang [7], proposed a forth degree rational equation for $P(x)$. This was one of the equations used to estimate the precision of the Arrhenius integral and allowed a controlled margin of error. For the forth degree ration, the error is lower than 10^{-5}% for x>20.

Combination of Equations (1), (6) and (7) yields, Equation (8).

$$\pi(x) = f(\alpha)g(\alpha) \quad (8)$$

With Equation (8), it is possible to obtain theoretical thermogravimetric equations. The equations for $f(\alpha)$ and $g(\alpha)$ are determine according to the appropriate mechanism, as described in Table 1.

Table 1: The solid-state reaction mods and mechanisms of degradation.

Mechanism – Solid-state reaction	$f(\alpha)$ – Reaction mode	$g(\alpha)$ – Reaction mode
A_2(Avrami-Erofeev) – nucleation and growth	$2(1-\alpha)[-ln(1-\alpha)]^{1/2}$	$[-ln(1-\alpha)]^{1/2}$
A_3(Avrami-Erofeev) – nucleation and growth	$3(1-\alpha)[-ln(1-\alpha)]^{2/3}$	$[-ln(1-\alpha)]^{1/3}$
A_4(Avrami-Erofeev) – nucleation and growth	$4(1-\alpha)[-ln(1-\alpha)]^{3/4}$	$[-ln(1-\alpha)]^{1/4}$
R_1 – Controlled reaction in the phase contour (one-way movement)	1	α
R_2 – Controlled reaction in the phase contour (contracted area)	$(1-\alpha)^{1/2}$	$2\left[1-(1-\alpha)^{1/2}\right]$
R_3 – Controlled reaction in the phase contour (contracted volume)	$(1-\alpha)^{2/3}$	$3\left[1-(1-\alpha)^{1/3}\right]$
D_1 – Diffusion in one dimension	$1/2\,\alpha^{-1}$	$3\left[1-(1-\alpha)^{1/3}\right]$
D_2 – Diffusion in two dimensions (Valensi equation)	$[-ln(1-\alpha)]^{-1}$	α^2
D_3 – Diffusion in three dimensions (Jander equation)	$(3/2)\left[1-(1-\alpha)^{1/3}\right](1-\alpha)^{2/3}$	$(1-\alpha)ln(1-\alpha)+\alpha$
D_4 – Diffusion in three dimensions (Ginstling-Brounshtein equation)	$(3/2)\left[1-(1-\alpha)^{-1/3}\right]^{-1}$	$\left[1-(1-\alpha)^{1/3}\right]^2$

F_1 – Random nucleation with an individual particle core	$1-\alpha$	$[1-(2/3)\alpha]-(1-\alpha)^{2/3}$
F_2 – Random nucleation with two nuclei of individual particles	$(1-\alpha)^2$	$-ln(1-\alpha)$
F_3 – Random nucleation with three nuclei of individual particles	$(1/2)(1-\alpha)^3$	$1/(1-\alpha)$

To determine the reaction mechanism, theoretical and the experimental curves must be compared. The theoretical curves can be obtained using Equation (8) and the $P(x)$ value is obtained by Equation (9).

$$P(x)=\frac{e^{-x}}{x}\cdot\frac{x^3+18x^2+86x+96}{x^4+20x^3+120x^2+240x+120} \quad (9)$$

2.3 Modified Coats-Redfern method

The Modified Coats-Redfern method is also used to determine the activation energy and is defined by Equation (11).

$$\ln\left[\frac{\beta}{T^2\left(1-\frac{2RT}{E_a}\right)}\right]=ln\left[-\frac{AR}{E_a ln(1-\alpha)}\right]-\frac{E_a}{RT} \quad (11)$$

Plotting $ln(\beta/T^2)\ versus\ 1/T$ and applying a linear fit the factor frequency (A) and the activation energy (E_a) can be obtained. The slope gives $E_a$and the intercept gives A.

3. MATERIALS AND METHODS

Commercial unsaturated polyester resin BP5788 and its green alternative from renewable resources were provided by Elekeiroz and used for thermal degradation studies.

Thermogravimetric analysis was used to determine the kinetic parameters. Samples (10 mg) were analysed in an SII Nanotechnology INC equipment, Exstar 6000 model, TG/DTA 6200 series, operating under nitrogen flow of 100 mL.min^{-1}, in the 25 – 800°C temperature range.

4. RESULTS AND DISCUSSIONS

4.1 Kinetics parameters

Figure 1 illustrates all fitting using the four distinct kinetic models proposed. The obtained R^2 values (from linear fitting) for all methods were higher than 0.88 for the traditional resin, and higher than 0.97 for the resin from renewable sources.

The activation energy (E_a) values according to FWO, Friedman, and Coats-Redfern as function of the conversion degree are displayed Figure 2. The E_a for Kissinger, also shows in Figure 1, not was included because this method use the peak of derivative of mass loss only, representing a limited conversion degree range.

According to the results of Figure 2, The activation energy seems to be dependent on the conversion degree (α=0.1 – 0.9) for both resins. This variation suggests that the degradation process of this polymer is complex, possibly with multiple reaction step mechanisms (parallel, consecutive, overlapping, reversible or their combination). This could be justified by the heterogeneity of the polymer nature [8].

For the traditional resin, the curves have similar shapes, and linear correlations between E_a and α are found for α within 0.1 – 0.5 and 0.7 – 0.9. A maximum in E_a was found around α=0.6. And for the Friedman method, a more pronounced decrease occurred above α=0.7. For the resin from renewable resources, a linear correlation between E_a and α is found for α within 0.1 -0.4 and another one for α within 0.4 – 0.9. And for Friedman method, an abrupt decrease in E_a was observed when α goes from 0.4 from 0.5 and an abrupt increase was observed when α goes from 0.7 to 0.8.

The difference in the trend in Figure 2 for Friedman method compared to the other two methods (FWO and modified Coats-Redfern) is justified considering that in the Friedman method, the derivative of the conversion ($d\alpha/dt$) is used in the calculation, whereas in the others two methods the temperature is used.

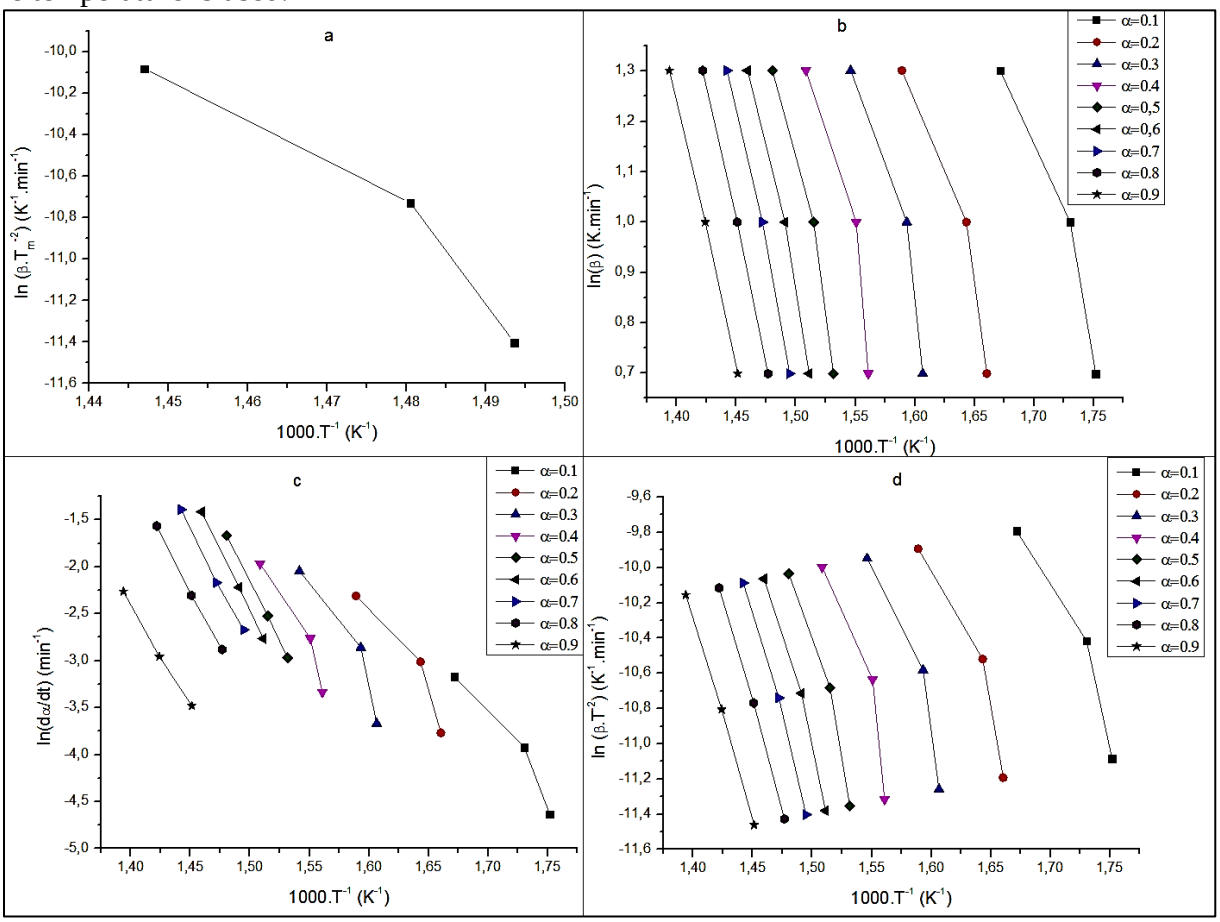

Figure 9 – Graphs used to determine the activation energy following Kissinger (a), FWO (b), Friedman (c) and Modified Coats-Redfern (d) methods.

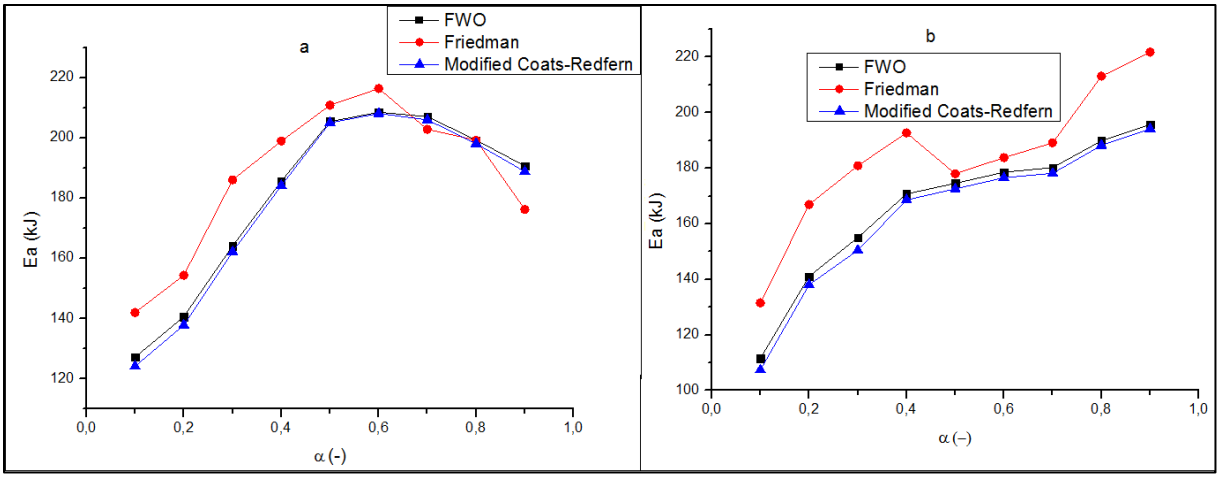

Figure 10 – The calculated activation energy as a function of the conversion degree for the traditional resin (a) and for the polyester from renewable resources (b).

By calculating the mean of all E_a values from the four methods, E_{ISO} was obtained. For the traditional resin was 189.79 ± 37.82 kJ, and the pre-exponential ($ln(A)$) factor was 24.62 ± 6.11 min^{-1}. For the resin from renewable resources the values were 161.85 ± 14.35 kJ and 18.42 ± 2.36 min^{-1}, respectively. And these values of E_{ISO} were used to calculate the value of $Z(\alpha)$ for the two resins.

4.2 Degradation mechanisms

Figure 3 illustrates the graphs used to determine the most probable the degradation mechanism. The most probable reaction degradation mechanism is compared considering the similarities in the curves. So, the resin can present different degradation mechanisms in different degrees.

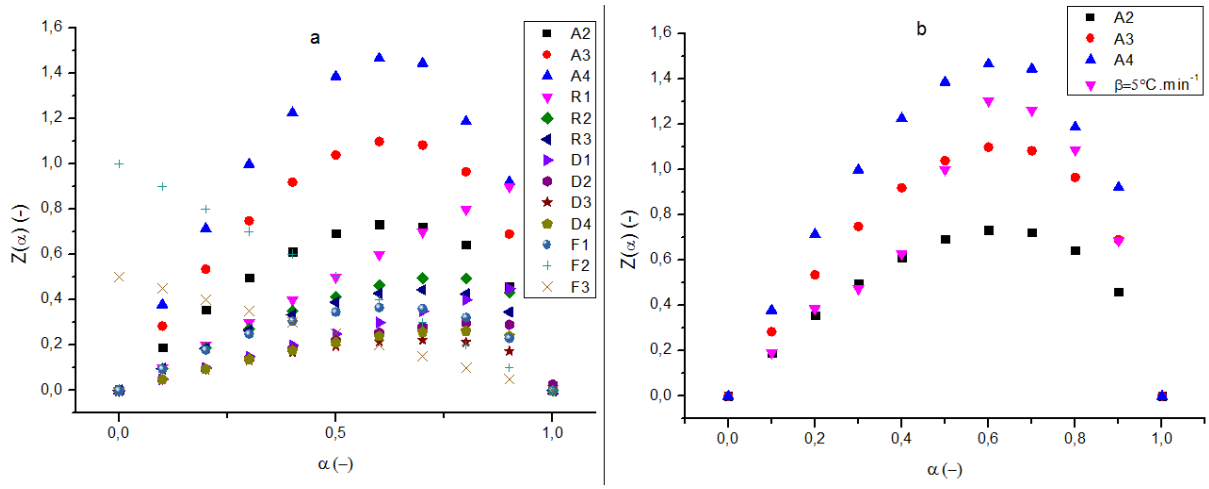

Figure 11 – Theoretical curves of the Criado degradation mechanism (a) and the graph obtained for the resin from renewable resource resin used in this work (b).

For the traditional resin, the shape of the curves did not follow a specific theoretical model for any heating rate, but *A* type mechanism could be considered for the sample. In this case, all mechanisms were defined by proximity of $Z(\alpha)$. For α within 0.1 – 0.4 (mechanism *A2*), α=0.5

(mechanism *A3*), α=0.6 (mechanism *A3*), for α within 0.7 – 0.8 (mechanism *A4*) and for α=0.9 (mechanism *A3*).

The same behaviour occurred for the resin from renewable resources, and, *A* type mechanism could be considered. For α within 0.1 – 0.4 (mechanism *A2*), α=0.5 (mechanism *A3*) and for α=0.9 (mechanism *A3*). However, were cases that the mechanism was defined by the curve shape. It happened for α within 0.6 – 0.8 (mechanism *A4*).

For the two resins, similarities in the mechanism from group *D* (*D1, D2, D3, D4*), related to diffusion, from group *F* (*F1, F2, F3*), related to random nucleation, or from group *R* (*R1, R2, R3*), related to controlled reactions in the phase contour, could not be found.

Analysing all results, the overall difference between the two resins is small, i.e. the degradation mechanisms were similar. There were differences at some conversion values, e.g. the mechanism at α=0.6 was *A3* for the traditional resin and *A4* for the other resin. Nevertheless, they were in the same group of mechanisms.

5. CONCLUSIONS

Analysing the activation energy results, the thermoset resins behaved as expected, and the E_a values varied as a function of the conversion degree.

The degradation mechanisms for the traditional unsaturated polyester resin and for that from renewable resources were similar. Using the method described by Criado, the degradation mechanisms at different conversions were found to be of the group *A* (*A2*, *A3* and *A4*), suggesting a single group of degradation mechanisms, related to nucleation and growth, independently of the source of the resin. Also, by comparing different kinetic approaches, a more reliable estimate of the kinetic parameters can be obtained.

REFERENCES

[1] Ferreira, O. P., Alves, O. L., Macedo, J. D. S., Gimenez, I. D. F. and Barreto, L. S. (2007). Ecomateriais: desenvolvimento e aplicação de materiais porosos funcionais para proteção ambiental. *Química Nova.*

[2] Rühle, M., Dosch, H., Mittemeijer, E. J. and Van de Voorde, M. H. (Eds.). (2001). European White Book on Fundamental Research in Materials Science. Stuttgart: Max-Planck-Institut für Metallforschung.

[3] Badia, J. D., Santonja-Blasco, L., Moriana, R. and Ribes-Greus, A. (2010). Thermal analysis applied to the characterization of degradation in soil of polylactide: II. On the thermal stability and thermal decomposition kinetics. *Polymer Degradation and Stability*, *95*(11), 2192-2199.

[4] Vyazovkin, S., Burnham, A. K., Criado, J. M., Pérez-Maqueda, L. A., Popescu, C. and Sbirrazzuoli, N. (2011). ICTAC Kinetics Committee recommendations for performing kinetic computations on thermal analysis data. *Thermochimica acta*, *520*(1-2), 1-19.

[5] Criado, J. M., Malek, J. and Ortega, A. (1989). Applicability of the master plots in kinetic analysis of non-isothermal data. *Thermochimica Acta*, *147*(2), 377-385.

[6] Paterson, W. L. (1971). Computation of the exponential trap population integral of glow curve theory. *Journal of Computational Physics*, *7*(1), 187-190.

[7] Pérez-Maqueda, L. and Criado, J. (2000). The accuracy of Senum and Yang's approximations to the Arrhenius integral. *Journal of thermal analysis and calorimetry*, *60*(3), 909-915.

[8] Poletto, M., Júnior, H. L. O. and Zattera, A. J. (2015). Thermal decomposition of natural fibers: kinetics and degradation mechanisms. *Reactions and Mechanisms in Thermal Analysis of Advanced Materials*, 515-545.

EFFECT OF GAMMA-RADIATION ON THERMAL AGEING OF BUTYL RUBBER COMPOUNDS

Sandra R. Scagliusi[1], Elizabeth C. L. Cardoso[1] and Ademar B. Lugão[1]

(1) Instituto de Pesquisas Energéticas e Nucleares – IPEN-CNEN-SP – Av. Lineu Prestes 2242 – CEP 05508-900 – Cidade Universitária, São Paulo, Brasil.

https://doi.org/10.21452/bccm4.2018.04.03

Abstract

Butyl rubber has a comprehensive use in sealing systems, especially in tires inner tubes, due to their low permeability to gases. So, it is required that butyl rubber compounds show a better performance, more and more. Butyl rubber is provided with excellent mechanical properties and oxidation resistance. Besides showing these properties, radiation exposures impart modifications in physical-chemical and morphological properties on butyl rubber materials. When exposed to gamma-radiation, rubbers suffer changes in their mechanical and physical properties, caused by material degradation. The major radiation effect in butyl rubbers is chain- scission; besides, ageing promotes too the same effect with further build-up of free radicals. This work aims to the study of gamma-radiation in physical-chemical properties of butyl rubber subjected to thermal ageing. Doses used herein were: 25 kGy, 50 kGy, 100 kGy, 150 kGy and 200 KGy. Samples were evaluated before and after ageing according to traditional essays, such as: hardness, tensile strength and elongation at break. From accomplished assessments it is possible to affirm that at doses higher than 50 kGy it was observed a sharp decreasing in butyl rubber physical-chemical properties, before and after exposure to ageing.

1. INTRODUCTION

Ageing effect study in rubber artifacts is relevant especially due to cost and quality, providing to the material resistance or not to exposure under more severe environmental conditions. Ageing degree depends on various factors as polymer type, formulation, product geometry and environmental conditions [1].

Accelerated ageing essays aim to reproduce within a relatively shorter time interval ageing effects due to air action, radiation and temperature from larger exposures. For this, an adequate combination is accomplished between exposure periods and temperatures. Thermal ageing in rubber compounds present their physical and mechanical properties changed in function of modifications in structure or in morphology.

Ageing expression for rubber compositions is related to molecular scission that provokes the appearing of smaller chains and a higher number of chain terminals and/or crosslinking favoring a network structure strongly connected [2].

Both of two basic reactions yield to elastomer chemical structure changes and are able to be exemplified according to mechanism shown in Figure 1, for simplified radical [3].Free radicals can be built up by decomposition of small amounts of hydro-peroxides, present in rubber after the processing. Depending on rubber type, these reactions lead to either a chain-scission or to a raise in crossing bonds [4].

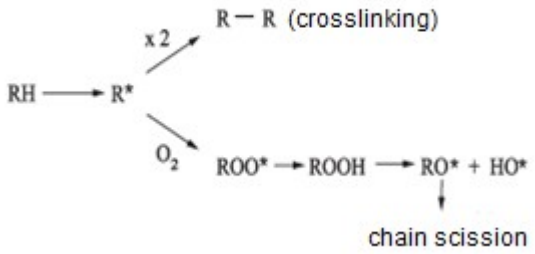

Figure 1**:** Elastomers reaction mechanism after ageing

It should be considered that chain-scission provokes a decreasing in viscosity, but, in case of crosslinking, the material becomes more rigid. Combination between scission and crosslinking results in creation of micro-cracks; presence of oxygenated products was detected even before the occurrence of chain-scission [3].

Butyl rubber is an isobutylene copolymer (98%) and isoprene (2%). In its hydrocarbon chain, unsaturation level is very low fostering an excellent resistance to ageing [5]. Butyl rubber when subjected to ionizing radiation exhibits two chemical effects: crosslinking and chain-scission with further degradation; nevertheless, chain-scission is predominant [6]. Various authors concluded that the major and practically unique effect due to ionizing radiations in butyl rubber is chain-scission with a significant reduction in molar mass, prejudicing physical and mechanical properties of the rubber. [7].

Rubber ageing is a structural chemical phenomenon that affects directly material mechanical properties. Thermo-oxidative ageing and radiation modify compound molecular structure imparting changes in rubber properties. According to Farmer [8] and collaborators, oxidation in polymers occurs with settlement of molecular oxygen in double bond to yield oxidized peroxide.

This work aims to the study of accelerated ageing in vulcanize compositions of butyl rubber before and after gamma-radiation, within 0 to 200 kGy. Behavior of studied materials for different doses applied was assessed as per mechanical properties.

2. MATERIALS

The elastomer used in this study was butyl rubber manufactured by Exxon Mobil Chemical, butyl 268 as commercial name, zinc oxide, stearic acid, sulphur, 2,2- dithiocarbaptobenzotiazol (MBTS) and tetrametiltiuram disulfide (TMTD), all of them commercial grade and used as such. Compositions were prepared according to a formulation normally used in tires and auto-parts industry (Table 1). Referred composition was irradiated and further subjected to accelerated ageing process.

Table 1. Formulation of Butyl Rubber.

Ingredients	**Quantities (phr)**
Butyl rubber	100
Zinc oxide	5
Stearic acid	1
Naphthenic oil	25
Carbon black N 330	70
Sulfur	2
TMTD	1
MBTS	0.5

2.1. Mixture and vulcanization process

Samples were prepared in an open cylinder (Copê), with two rolls, 40 kg capacity, according to ASTM D-3182 [9], at approximately 60 ºC; just after, the compound was vulcanized in a HIDRAUL-MAQ hydraulic press,5 MPa pressure and prepared according to ASTM D-3182 [9], at 180 ºC, for 4 min, packed in plastic bags and sent to irradiation.

2.2. Ageing

Butyl rubber composition after irradiation was subjected to accelerated ageing in an air-forced oven, at 70 ºC, for 72 h, in accordance with ASTM D 573 [10]. Aged mixtures were assessed for tensile strength, elongation at break and hardness. Specimens thickness used in ageing essays were: 0.6 cm for hardness and 0.2 cm for other tests.

2.3. Irradiation

Samples were irradiated in CBE/EMBRARAD and subjected to gamma radiation, in oxygen environment, at 25, 50, 100, 150 and 200 kGy doses, in Nordion Canadian irradiator, Cobalt 60 source, Model JS 7500, 5 kGy h^{-1} dose ratio.

3. METHODS

3.1 Compounding Characterization

Analyses were accomplished according with ASTM rules, in triplicate, for obtaining results average. Specimens were cut in accordance with specified methods of each essay. There were performed following tests:

3.2 Hardness

Hardness numerical indexes represent the deepness of penetration or adequate arbitrary values, derived from ASTM D 2240 [11]. Hardness is one of the properties the most evaluated in rubbers, being the Shore A, Instrutemp, portable digital model Dp-100 the durometer used herein. This instrument is provided with a conical needle emerging from the apparatus, kept at zero level by means of a spring.

3.3 Tensile strength and elongation at break

Tensile strength and elongation at break values were determined according to ASTM D-412 [12], by using a model C specimen, in an universal essay machine (EMIC), model DL 300, 300 kN maximum capacity and 500 mm/min grips speed, at room temperature.

4. RESULTS AND DISCUSSION

In Figure 2 (a e b) are shown results for Tensile Strength (a) and results for Elongation at Break (b) accomplished in butyl rubber irradiated and non-irradiated, before and after thermal ageing.

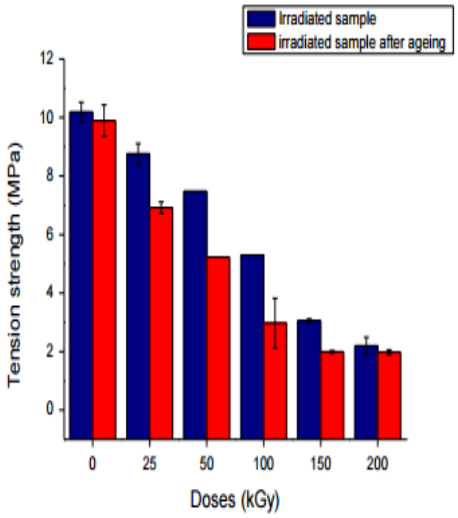

Figure 2 (a) -Ageing effect in strengthin in butyl rubber compounds, irradiated and non irradiated, subject to ageing

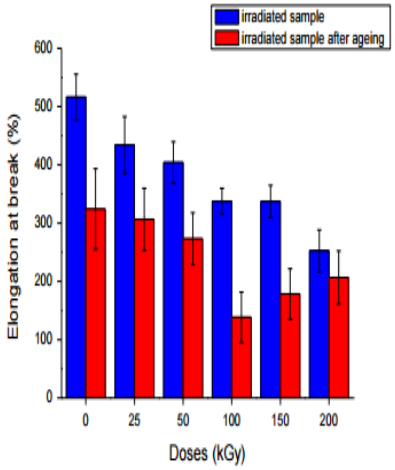

Figure 2 (b) -Ageing effect in elongation at break in butyl rubber compounds, irradiated and non irradiated, subject to ageing

Tensile strength and elongation at break results for butyl rubber samples showed that for low doses up to 25 kGy there is equivalence among tensile and elongation values after ageing, pointing that degradative effects were not enough to change these properties. For doses within 25 kGy and 50 kGy it is observed a decreasing in tensile and a balance in elongation results, probably due to a competition between scission and crosslinking, with number of crosslinking compensating chain scission. For doses within 100 kGy and 200 kGy it was observed a predominance of chain scission: smaller molecular chains have weaker intermolecular forces that do not resist to tensile strength.

Hardness is directly associated to rubber crosslinking degree: the more vulcanized the higher compound hardness. In Figure 3 are shown results for accelerated ageing of irradiated butyl rubber samples.

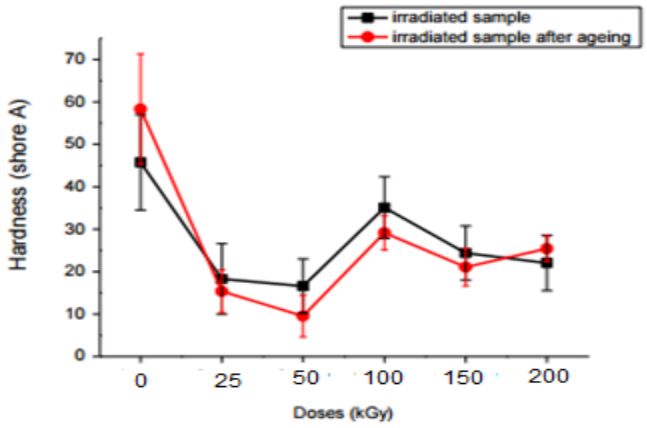

Figure 3: - Effect of ageing in hardness of butyl rubber compounds, irradiated and non-irradiated subjected to ageing.

According previously explained, hardness increases in function of a raise in crossing bonds [13]. Results showed that for non-irradiated sample (0 kGy) occurs an increase in hardness after ageing pointing toward a raise in build-up of crossing bonds imparting a higher stability to the compound. After irradiation and thermal ageing the hardness diminishes with further reduction in density of crossing bonds. For higher doses (above 50 kGy) occurs a slight raise without proportionality to dose, probably caused by oxidative degradation of polymeric chain.

The results of accelerated aging tests on butyl rubber compounds showed that the initial composition, even after irradiation, has a lower crosslinking index, therefore it will be possible to make blends with 25 kGy irradiated butyl rubber compositions after aging. . In future work, a mixture of 5 parts of aged butyl rubber will be performed replacing virgin butyl rubber parts in the original formulation that was used in this work, as shown in table 2.

Table 2. Formulation of Butyl Rubber.

Ingredients	**Quantities (phr)**
Butyl rubber	95
Ageing butyl rubber	5
Zinc oxide	5
Stearic acid	1
Naphthenic oil	25
Carbon black N 330	70
Sulfur	2
TMTD	1
MBTS	0.5

4. CONCLUSIONS

Processing using gamma rays in butyl rubbers proved a tendency toward chain scission with further free radicals build-up. Obtained results showed that gamma rays processing followed by thermal ageing caused a higher degradation in this type of rubber. Tensile strength tests showed gel build-up and consequently a more rigid and less elastic rubber.

Based in given results it can be concluded that aged butyl rubber compounds show a higher crosslinking density and exhibit a higher vulcanization degree when compared to non- irradiated compound, and consequently, best properties. Gamma rays are a powerful degradation agent for rubbers; together with thermal agent imparts to rubber a low crosslinking density even at low doses. Increasing of the dose imparts chain scission with molar mass reduction with further degradation and a few crosslinking sites.

It can be concluded that the aging mechanisms in the butyl rubber may also be acting to weaken the elastomeric matrix due to a main chain scission that contributes to the reduction of the analyzed properties, which allows its mixture in butyl rubber compounds, replacing parts of virgin butyl rubber for recycling purposes.

ACKNOWLEDGMENTS

The authors wish to thank CBE Embrarad for the irradiation process, Pirelli for the elastomers, Basile Chemistry for the raw materials, IPEN/CNEN-SP and CAPES agencies for their financial support**.**

REFERENCES

[1] R. P. Brown, M. J. Forrest, G. Soulagnet, - Rapra, 10, 3, 1999.

[2] M.Garbarczyk, W. Kuhn, J. Klinowski, S. Jurga, "Characterization of aged nitrile rubber elastomers by NMR spectroscopy and microimaging". *Polymer*, **43**, (2002), 3169–3172.

[3] P. Lucas, M. Baba, J. Lacoste, J. L. Gardette, "Crosslinking of dienic elastomers resulting from ageing: X-ray diffraction and refractometry measurements".*Polym. Degr. Stab.*,**76**, (2002), 449 - 453.

[4] E. Somers, T. J. Bastow, M. I. Burgar, M. Forsyth, A. J.Hill, "Quantifying rubber degradation using NMR" - *Polym. Degr. Stab.*, **70,** (2000) 31 -37.

[5] M. J. Caetano, Borracha Butílica: Poliisobitileno isopreno (IIR). http://ctborracha.com/?page_id=4330.

[6] A.Chapiro, Radiation Chemistry of Polymeric Systems, Nova York: (Interscience Publishier, 1962).

[7] T. Zaharescu, C. Postolache, M. Giurginca, "The structural changes in butyl and halogenated butyl elastomers during gamma irradiation*", J. of Appl.Polym.Sci*.,**59** (1996) 969- 974.

[8] E. H. Farmer, H. P. Koch, D. A. Sutton, "The Course of Autoxidation Reactions in Polyisoprenes and Allied Compounds. VII. Rearrangement of Double Bonds During Autoxidation". *J. Chem. Soc*.,**3** (1943) 541-547.

[9] Annual Book of Astm Standards. Standard Practice for Rubber- Materials, Equipment, and Procedures for Mixing Standart Compounds and Preparing Standard Vulcanized Sheets .**v. 09.01**, 2008 (ASTM D-3182).

[10] Annual Book of Astm Standards. Standard Test Method for Rubber – Deterioration in Air Oven, **v. 09.01**, 1996 (ASTM D-573).

[11] Annual Book of Astm Standards. Standard Test Method for Rubber Property – Durometer Hardness. **v. 09.01**, 2008 (ASTM D-2240).

[12] Annual Book of Astm Standards.Standard Test Methods for Vulcanized Rubber and Thermoplastic Rubber and Thermoplastic Elastomers – Tension.**v. 09.01**, 2008 (ASTM D- 412).

[13] R. JOSEPH, K. E. GEORGE, D. J. FRANCIS, "Studies on the cure characteristics and vulcanizate properties of 50/50 NR/SBR blend*". J. Appl. Polym. Sci.*, **35** (1988) 1003–1017.

5. EXPERIMENTAL TECHNIQUES

COMPARISON OF COMPLEX MODULUS PROVIDED BY THREE DIFFERENT DYNAMIC MECHANICAL ANALYZERS

I.R. Henriques [(1)], L.A. Borges [(1)], D.A. Castello [(1)], M.F. Costa [(2)] and B.G. Soares [(3)]

(1) Mechanical Engineering Department, Universidade Federal do Rio de Janeiro, Brazil

(2) Metallurgy and Materials Engineering Department, Universidade Federal do Rio de Janeiro, Brazil

(3) Instituto de Macromoléculas, Universidade Federal do Rio de Janeiro, Rio de Janeiro, Brazil

https://doi.org/ 10.21452/bccm4.2018.05.01

Abstract

Polymer matrix composites have been used in several applications of engineering and applied sciences. This wide range of applications is due to their distinguished properties. Therefore, the great understanding of their physical and mechanical properties is required to make an efficient use of these materials. Among the experimental techniques, Dynamic mechanical analysis (DMA) is one of the most common methods employed to study the materials' composition and properties. This work presents an investigation on the mathematical formulation for complex modulus determined by this technique and how it is evaluated. Measurements of temperature-dependent complex modulus were performed by three different dynamic mechanical analyzers using three-point bending mode. Test conditions were basically the same in these different machines. Comparisons of the results were made in order to observe the effects of testing equipment and test parameters.

1. INTRODUCTION

Polymer matrix composites (PMCs) have been widely used in many applications of engineering and applied sciences, such as civil engineering structures, aerospace, wind energy and super sport cars [1,2]. This great range of applications is due to their outstanding properties[2]. As the fields of applications have been continuously growing, many efforts have been done to characterize and model these materials in order to predict their mechanical behavior, optimize designs and minimize project risks.

Recently, the time and temperature dependences of PMCs have been pointed out to be related to the matrix properties. Etaati et al. [26] investigated the influence of fiber content in short hemp polypropylene composites. Results showed that the influence of temperature is independent of the

fiber, i.e., that the temperature dependence of this composite is related to the matrix properties. Liu et al. [27] reported that the effects of time and temperature on composites are concerned with the properties of the matrix. If one wants to characterize the thermal and temporal behavior of PMCs, it is essential to characterize their matrix properties.

One of the most common methods used to experimentally characterize materials' properties is the Dynamic Mechanical Analysis, also known as DMA. This technique has become a powerful one in the field of rheology by enabling one to identify and characterize the material's behavior especially as a function of temperature and frequency. It enables more information about the material's properties than techniques involving static tests [4].

Generally speaking, DMA is in some sense versatile. Depending on the operational mode and the parameters chosen, one can study about the composition, physical and viscoelastic properties of the material. It is possible to have information about the temperature- and time-dependent behavior, transitions, extent of phase mixing in blends, degree of crosslinking, crystallinity, interfacial adhesion, ageing, degradation, among others [5].

On this regard, DMA is becoming widely used in several areas to study the various aspects of a material. The traditional applications are concerned with the identification of thermal transitions [6–8] and how some parameters affect the material's properties [9–13]. Recently, the use of DMA as a characterization technique has been expanded to other studies such as crack healing [14], spatial distribution of material's properties [15] and mechanical properties of heterogeneous materials [16].

Despite the great range of DMA applications and its potential, literature indicates that there are some discrepancies in DMA results. The absolute values of the modulus and temperatures related to phase transitions are well-known to show divergences between samples and loading clamps even when the test conditions were essentially the same. Even though the property measured should be the same, regardless the DMA equipment [5,17–25]. However, few researches can be found on the mathematical formulation of the modulus and on the comparative data obtained by different machines.

The purpose of this work is to investigate how the complex modulus is mathematically formulated and measured by three DMA machines in three-point bending tests. Experimental tests were carried out in temperature scans to also evaluate how the temperature dependence of the material is identified by different machines. These tests were performed on an epoxy system which is a common matrix used in several applications [28]. Finally, the measurement results were compared to study the influence of testing equipment.

This work is organized as follows. Section 2 gives the principal aspects of DMA principles and how the complex modulus is formulated. Section 3 explains the experimental set-up. Section 4 presents the experimental results obtained, followed by our conclusions.

2. FUNDAMENTALS

2.1 DMA principles

Basically, DMA consists of applying a sinusoidal force to a sample and measuring the sample's deformation, or applying a sinusoidal deformation and measuring the sample's reaction force, or even as applying a constant force/deformation and measuring the sample's creep/relaxation modulus [19]. This material's response can be characterized as a function of temperature, frequency, time, stress or a combination of these control parameters, depending on the intended use of the material. Based on these measurements, DMA can determine the material's properties, like modulus and viscosity.

In particular, the material's modulus is reported over the test as a complex quantity that enables one to better analyze the material's behavior. The real part is usually called as storage modulus and corresponds to the material's ability to return or store energy. It may represent shear, tensile or flexural modulus, depending on the operational mode. On the other hand, the imaginary part is commonly known as loss modulus and corresponds to material's ability to dissipate energy. Further, the ratio between the real and imaginary parts is called tan δ or damping or even loss factor, and represents how quickly the material loses energy.

2.2 Mathematical formulation for complex modulus

Let consider the use of a dynamic stress to deform a sample, i.e., DMA is applying a sinusoidal stress to a sample and measuring its deformation. This oscillatory stress is expressed as

$$\sigma(t) = \sigma_0 \sin \omega t \tag{1}$$

with σ_0 as the amplitude, *t* as the time and ω as angular frequency. The strain history ε(t) can be given by

$$\varepsilon(t) = \varepsilon_0 \sin(\omega t + \delta) \tag{2}$$

with ε_0 as the amplitude of the strain history and δ as the phase angle between the applied stress and the response.

The one-dimensional stress-strain relation in the frequency domain [29] is expressed as

$$\sigma(t) = E^*(\omega)\,\varepsilon(t) = [E'(\omega) + jE''(\omega)]\,\varepsilon(t) = E'(\omega)\,[1 + j\,\eta(\omega)]\,\varepsilon(t), \tag{3}$$

where $E^*(\omega)$ is the complex modulus, $E'(\omega)$ is the storage modulus, $E''(\omega)$ is the loss modulus, and $\eta(\omega)$ is the loss factor given by

$$\eta(\omega) = \frac{E''(\omega)}{E'(\omega)} = \tan\delta. \tag{4}$$

From the measurements of the force, the displacement and the phase angle, DMA determines each component of complex modulus. This estimate also depends on sample geometry, operational mode and boundary conditions.

In this work, we performed three-point bending tests in three DMA machines, namely Netzsch 242 E Artemis, PerkinElmer 8000 and TA Q800. The mechanism of this test and the mathematical formulation provided by each DMA performed in this work are described below.

Three-point (3PT) bending mode consists of a sample being only supported on both ends by stationary clamps. The controlled force is applied in the middle through the moveable clamp. In this mode, the sample is free to move and there is no clamping effect, being considered as a pure mode of deformation.

As for the mathematical formulation of this mode, each DMA has its own considerations. Equations (5), (6) and (7) show how the absolute value of complex modulus is calculated, respectively, in PerkinElmer 8000, TA Q800 and Netzsch 242 E Artemis.

$$|E^*_{3PT}(\omega)|_{PerkinElmer} = \frac{F}{a}\frac{L^3}{48I}\left[1 + 2.9\left(\frac{t}{L}\right)^2\right] \tag{5}$$

$$|E^*_{3PT}(\omega)|_{TA} = \frac{F}{a}\frac{L^3}{6I}\left[1 + 0.6(1+\nu)\left(\frac{t}{L}\right)^2\right] \tag{6}$$

$$|E^*_{3PT}(\omega)|_{Netzsch} = \frac{F}{a}\frac{L^3}{48I} \quad (7)$$

where F is the force applied, a is the displacement amplitude, L is the span between the two supports, t is the sample's thickness, I is the inertia moment and ν is the Poisson's ratio.

Note that both PerkinElmer and TA assume small shear deformation as they both consider the influence of Poisson's ratio on the modulus formulation. PerkinElmer's assumption is based on a constant Poisson's ratio of 0.33 for glassy polymers and 0.5 for rubbers, namely 0.35. On the other hand, TA's assumption depends on the material.

3. EXPERIMENTAL SET-UP

3.1 Description of the testing equipments

Three different DMA machines from different manufacturers were used to perform dynamic tests to measure the complex modulus: DMA Netzsch 242 E Artemis, DMA PerkinElmer 8000 and DMA TA Q800.

These DMA machines are all made of four basic components: force motor, displacement sensor, sample holder and furnace. Force motor provides the control of all forces required to the sample. It has low compliance and is thermostatic. Displacement sensor is the detection system and it tracks any changes in the sample. Sample holders, in turn, enable one to perform different modes of operation. The clamps have a high stiffness to minimize the compliance and they also have low mass for a fast temperature equilibration. Finally, furnace provides a temperature control during the tests.

3.2 Test conditions

Dynamics tests were performed in three-point bending (3PT) mode in different DMA machines using similar conditions in order to obtain reliable results. Temperature scans were performed after an isotherm of 30 minutes at 25°C. Temperature varied from 25°C to 90°C with a heating rate of 2°C/min at a constant frequency of 1Hz. For all tests, strain mode was used and so, the amplitude was set to 50㎜. Furthermore, a force track was set to 120%, which means that the static force is 120% of the dynamic force.

3.3 Material and Samples' Manufacture

The material used in this work was an epoxy system which the epoxy resin was Araldite LY 1564 and the hardener, Aradur 2963. Specimens were prepared by casting at room temperature for 24h in silicone rubber molds with appropriate dimensions and then post-curing at 60°C for 8h.

Samples dimensions varied a little according to DMA machine. For Netzsch 242 E Artemis, samples were machined to approximately 60 mm x 10 mm x 3.2 mm. For TA Q800, they were approximately 60 mm x 12.7 mm x 3.2 mm. Finally, for PerkinElmer800, since it was possible to vary the span, two sets of samples were studied. In Set 1, they were 50 mm x 7 mm x 2 mm. In Set 2, on the other hand, they were 52.5 mm x 10 mm x 3.2 mm.

4. RESULTS AND DISCUSSION

Three-point bending mode was performed in three DMA machines, PerkinElmer 8000, TA Q800 and Netzsch 242 E Artemis using the same test conditions. In PerkinElmer 8000, tests were carried out for two sets of samples. The measurement results for storage and loss moduli are shown in Figure 1.

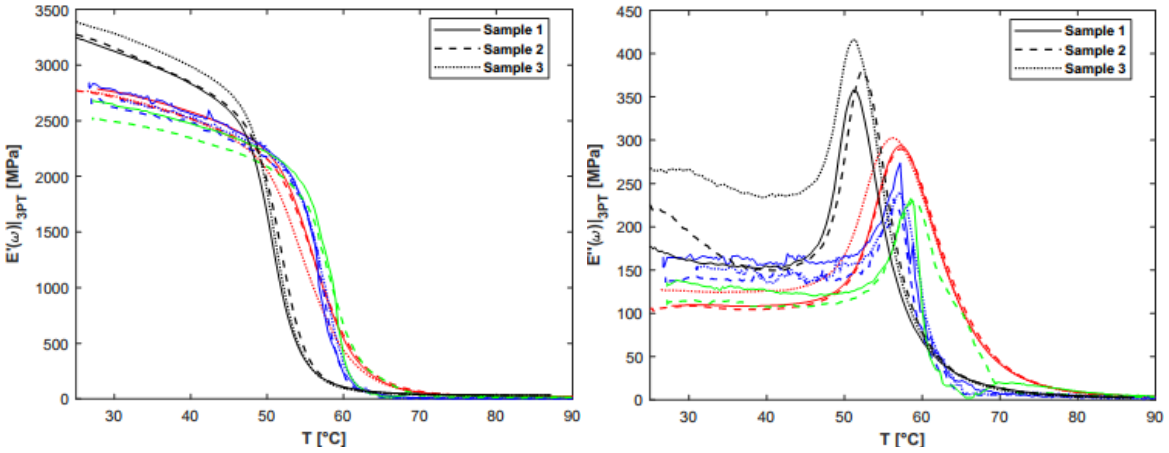

Figure 52 : Three-point bending results. (a) Storage modulus, (b) loss modulus. (Black lines: Netzsch 242 E Artemis, red lines: TA Q800, blue lines: PerkinElmer 8000 Set 1, and green lines: PerkinElmer 8000 Set 2)

The classical behavior of polymers [30] can be observed in all DMAs results. Storage modulus decreased with temperature. This decrease was even more rapid as the material approached its glass transition due to its morphological softening. Loss modulus increased slightly up to a certain temperature and from there, it suddenly decreased with temperature.

It can be observed that, when one performs tests using the same test conditions and testing parameters, all DMA provide good results. In other words, the repeatability and reproducibility is quite good. There is no great variability between the three samples from the same set.

However, Netzsch 242 E Artemis provided a higher storage and loss moduli in the glassy state than the other DMAs. The onset point of storage modulus and the peak point of loss modulus were identified in a lower temperature, indicating that the glass transition happened first in this DMA machine. While Netzsch identified this event in a temperature approximately 50°C, both PerkinElmer and TA measured it at around 60°C. This discrepancy in temperature may be correlated to the position of the sensor in relation to the sample, heat radiation in the furnace and a consequently thermal lag in the sample.

Nonetheless, it was surprising that the results of PerkinElmer 8000 and TA Q800 showed a good agreement, especially for storage modulus, regardless of the sample's dimensions. Although literature [19,23] suggested that instrumentation compliance, sample's stiffness and dimensions, and span-to-thickness ratio may influence DMA results, it is possible to observe that when performing tests in different machines, they can be correlated if the test conditions are the same.

When comparing DMA results from different machines, one should keep in mind that each DMA has its own mathematical formulation for complex modulus as explained earlier. Therefore, small variations in the measurements from different DMAs are quite expected to happen.

It is interesting to investigate how the parameters related to the modulus formulation, force and the displacement amplitude, were measured along each test by each machine. Figure 2 shows the results as function of temperature.

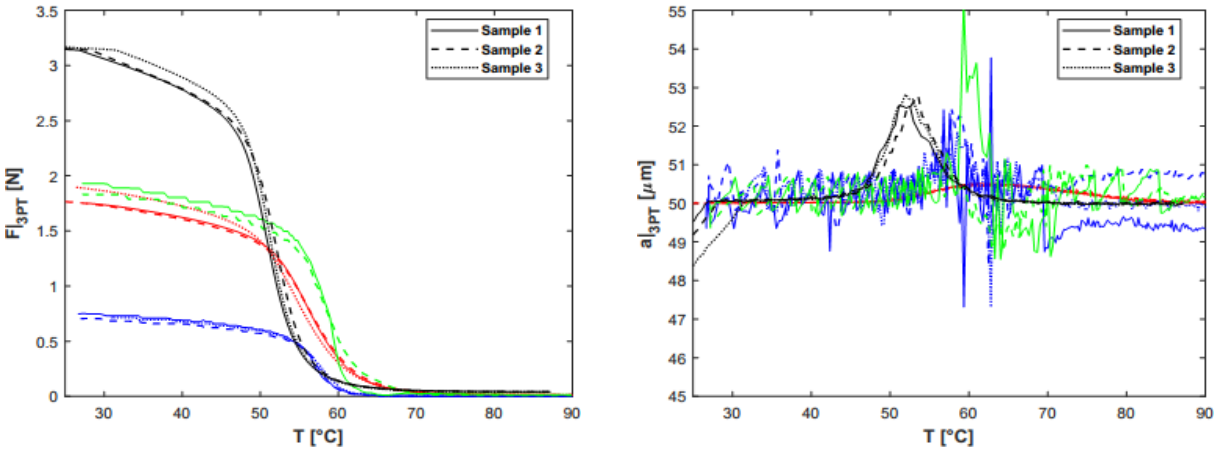

Figure 53: Three-point bending parameters. (a) Force, (b) displacement amplitude. (Black lines: Netzsch 242 E Artemis, red lines: TA Q800, blue lines: PerkinElmer 8000 Set 1, and green lines: PerkinElmer 8000 Set 2)

Note that, for each set of samples in each DMA machine, it was necessary the application of a specific force due to the sample's stiffness and the machine compliance. This applied force decreased with temperature because of the material's softening. It can also be noted that Netzsch applied a greater force than the others. In addition, TA applied almost the same force as PerkinElmer did for the second set of samples. It is worthwhile remind that the second set of samples of PerkinElmer had dimensions close to the ones of the samples of TA.

5. CONCLUSION

To summarize, it was found that each DMA has its own mathematical formulation for the same operational mode and as a consequence, some discrepancies between the measurement results from different DMA machines are somewhat expected to be observed even if the test conditions and testing parameters are the same. Nonetheless, it was possible to find some good agreement in the results, especially for storage modulus. In addition, it was shown that the effects of sample's geometry are not noticeable in this mode. A natural progression is to verify how DMA formulates the complex modulus in other operational modes and compare the measurements from different machines to observe both the effects of testing equipment and the effects of testing parameters into the results.

ACKNOWLEDGEMENTS

The authors would like to acknowledge the support of the Brazilian Research Agency CAPES.

REFERENCES

[1] A. Erber, S. Spitko, Expanded role for thermoplastic composites, Reinf. Plast. 58 (2014) 29–33. doi:10.1016/S0034-3617(14)70178-X.

[2] L. Van Den Einde, L. Zhao, F. Seible, Use of FRP composites in civil structural applications, Constr. Build. Mater. 17 (2003) 389–403. doi:10.1016/S0950-0618Ž03.00040-0.

[3] R.S. Lakes, Viscoelastic measurement techniques, 75 (2004) 797. doi:10.1063/1.1651639.

[4] K.P. Menard, Dynamic mechanical analysis : a practical introduction, CRC Press, Boca Raton, 1999.

[5] I. Lacík, I. Krupa, M. Stach, A. Kučma, J. Jurčiová, I. Chodák, Thermal lag and its practical

consequence in the dynamic mechanical analysis of polymers, Polym. Test. 19 (2000) 755–771. doi:10.1016/S0142-9418(99)00046-X.

[6] D.D. Shepard, B. Twombly, Simultaneous dynamic mechanical analysis and dielectric analysis of polymers, Thermochim. Acta. 272 (1996) 125–129. doi:10.1016/0040-6031(95)02622-3.

[7] A. Haque, M. Shamsuzzoha, F. Hussain, D. Dean, S2-glass/epoxy polymer nanocomposites: Manufacturing, structures, thermal and mechanical properties, J. Compos. Mater. 37 (2003) 1821–1838. doi:10.1177/002199803035186.

[8] S.R. Khimi, K.L. Pickering, A new method to predict optimum cure time of rubber compound using dynamic mechanical analysis, J. Appl. Polym. Sci. 131 (2014) 1–6. doi:10.1002/app.40008.

[9] O. Martin, L. Averous, Plasticization and properties of biodegradable multiphase systems polymer, Polymer (Guildf). 42 (2001) 6209–6219.

[10] W. Luo, X. Hu, C. Wang, Q. Li, Frequency- and strain-amplitude-dependent dynamical mechanical properties and hysteresis loss of CB-filled vulcanized natural rubber, Int. J. Mech. Sci. 52 (2010) 168–174. doi:10.1016/j.ijmecsci.2009.09.001.

[11] L. Rouleau, R. Pirk, B. Pluymers, W. Desmet, Characterization and Modeling of the Viscoelastic Behavior of a Self-Adhesive Rubber Using Dynamic Mechanical Analysis Tests, J. Aerosp. Technol. Manag. 7 (2015) 200–208. doi:10.5028/jatm.v7i2.474.

[12] S.E. Zeltmann, K.A. Prakash, M. Doddamani, N. Gupta, Prediction of modulus at various strain rates from dynamic mechanical analysis data for polymer matrix composites, Compos. Part B Eng. 120 (2017) 27–34. doi:10.1016/j.compositesb.2017.03.062.

[13] A.G. Leal, C. Marques, A. Frizera, M.J. Pontes, Dynamic Mechanical Analysis on a PolyMethyl Methacrylate (PMMA) Polymer Optical Fiber, IEEE Sens. J. 1748 (2018) 1–1. doi:10.1109/JSEN.2018.2797086.

[14] C. Nielsen, S. Nemat-nasser, Crack healing in cross-ply composites observed by dynamic mechanical analysis, J. Mech. Phys. Solids. 76 (2015) 193–207. doi:10.1016/j.jmps.2014.11.006.

[15] P. Kostka, K. Holeczek, A. Filippatos, N. Modler, Extension and application of dynamic mechanical analysis for the estimation of spatial distribution of material properties, Polym. Test. 52 (2016) 184–191. doi:10.1016/j.polymertesting.2016.04.019.

[16] Z. Jia, A. V Amirkhizi, W. Nantasetphong, S. Nemat-nasser, Experimentally-based relaxation modulus of polyurea and its composites, Mech Time-Depend Mater. (2016). doi:10.1007/s11043-015-9289-1.

[17] A.R. Wedgewood, J.C. Seferis, Error analysis and modelling of non-linear stress strain behaviour in measuring dynamic mechanical properties of polymers with the Rehovibron, Polymer (Guildf). 22 (1981) 966–991.

[18] N.M. Alves, J.F. Mano, J.L. Gómez Ribelles, Analysis of the thermal environment inside the furnace of a dynamic mechanical analyser, Polym. Test. 22 (2003) 471–481. doi:10.1016/S0142-9418(02)00134-4.

[19] S. Deng, M. Hou, L. Ye, Temperature-dependent elastic moduli of epoxies measured by DMA and their correlations to mechanical testing data, Polym. Test. 26 (2007) 803–813. doi:10.1016/j.polymertesting.2007.05.003.

[20] G. Swaminathan, K. Shivakumar, A Re-examination of DMA Testing of Polymer Matrix Composites, J. Reinf. Plast. Compos. 28 (2008) 979–994. doi:10.1177/0731684407087740.

[21] R. Kazakeviciute-Makovska, S. Mogharebi, H. Steeb, G. Eggeler, K. Neuking, A Critical Assessment of Experimental Methods for Determining the Dynamic Mechanical Characteristics of Shape Memory Polymers, Adv. Eng. Mater. 15 (2013) 732–739. doi:10.1002/adem.201200341.

[22] W. Sun, A.P. Vassilopoulos, T. Keller, Effect of thermal lag on glass transition temperature of polymers measured by DMA, Int. J. Adhes. Adhes. 52 (2014) 31–39. doi:10.1016/j.ijadhadh.2014.03.009.

[23] I.M. McAninch, G.R. Palmese, J.L. Lenhart, J.J. La Salsa, DMA Testing of Epoxy resins: the importance of dimensions, Polym. Eng. Sci. 55 (2015) 2761–2774. doi:10.1002/pen.24167.

[24] D. Ionita, M. Cristea, D. Banabic, Viscoelastic behavior of PMMA in relation to deformation mode,

J. Therm. Anal. Calorim. 120 (2015) 1775–1783. doi:10.1007/s10973-015-4558-4.
[25] J. Feng, Z. Guo, Temperature-frequency-dependent mechanical properties model of epoxy resin and its composites, Compos. Part B. 85 (2016) 161–169.
[26] A. Etaati, S. Pather, Z. Fang, H. Wang, The study of fiber/matrix bond strength hemp polypropylene composites from dynamical mechanical analysis, Compos. Part B. 62 (2014) 19–28.
[27] Z. Liu, Z. Guan, F. Liu, Time-temperature Dependent Mechanical Properties of Cured Epoxy Resin and Unidirectional CFRP, in: 8th Int. Conf. Mech. Aerosp. Eng., 2017: pp. 113–117.
[28] F.-L. Jin, X. Li, S.-J. Park, Synthesis and application of epoxy resins: A review, J. Ind. Eng. Chem. 29 (2015) 1–11. doi:10.1016/j.jiec.2015.03.026.
[29] R.M. Christensen, Theory of viscoelasticity: an introduction, 2nd ed., Academic Press, New York, 1982.
[30] M.T. Shaw, W.J. MacKnight, Introduction to polymer viscoelasticity, 3rd ed, Wiley-Interscience, Hoboken, N.J, 2005.

APPLICATIONS AND ADVANCES OF THE ACTIVE THERMOGRAPHY FOR THE INSPECTION OF COMPOSITE MATERIALS USED IN INDUSTRY

Marcella Grosso [(1)], Sergio D. Soares [(2)], Isabel C. P. Margarit-Mattos and Gabriela R. Pereira [(1)]

(1) Laboratory of Non Destrutive Testing, Corrosion and Welding (LNDC), Department of Metallurgical and Materials Engineering, Federal University of Rio de Janeiro (UFRJ), Rio de Janeiro, Brazil

(2) Petrobras Research Center (CENPES), Rio de Janeiro, Brazil

https://doi.org/10.21452/bccm4.2018.05.02

Abstract

In this paper, the ability of the active thermography technique (Pulsed, Pulsed Phase and Lockin) was evaluated for the inspection of structures made of composite materials that are used in the petroleum and petrochemical industry. Two types of GFRP joints (adhesive-bonded and laminated) and one sample with anticorrosive composite coating were studied, with controlled defects being inserted to evaluate the capacity of the technique for the defect detection. In addition, a computational simulation model was developed to optimize the results obtained experimentally and also be a tool to estimate the limit of detection of the technique in these materials. According to the results obtained, the use of the Active Thermography technique for the inspection of these composite materials showed the potential of the technique for detection of defects that are common to occur in these materials and are not detectable by visual inspection. The computational simulation model created proved to be reliable and useful for the reproduction of the physical phenomena involved in the experiments and thus becomes an important complementary tool to optimize the results to be obtained in the inspection of these materials.

1. INTRODUCTION

The critical structures made of composite materials, particularly in the petrochemical industry, have been continuously employed often on platforms, especially in pipes for water or oil transportation, and in industrial plants, such as anticorrosive composite coatings for storage tanks and heat exchangers. However, the integrity of these materials is compromised by the presence of defects, which can lead to risks of failure and severe damages to the environment. Therefore, the

application of nondestructive techniques becomes very important for detecting, locating, sizing defective regions during the manufacturing, installation and service life of composite materials.

Among the nondestructive techniques, thermography has been considered a powerful technique for the inspection of composite materials due to its main advantages: no contact with the surface, fast inspection, easy interpretation of thermograms and successfully used in the inspection of high emissivity materials, such as composite materials. The thermographic technique consists of analyzing the temperature distribution on the surface of the material (illustrated in the form of thermograms). The presence of subsurface defects in the inspected materials alters both the diffusion rate and the heat flow, so, in the thermograms obtained from the inspection by an infrared camera, these defects appears as areas of different in relation to the rest of the material (where there is no presence of defects). This is the principal mechanism to detect defective regions in thermograms obtained by thermography [1-4].

According to the thermal pulse type ad data analysis method, the active thermography can be classified as: Pulsed, Pulsed Phase, Lockin, Step Heating, Pulsed Eddy Current Thermography and Vibrothermography. For the present paper, Pulsed, Phase Pulsed and Lockin modalities will be evaluated. The Pulsed Thermography consists of briefly heating the sample surface and, then, the surface temperature decay is recorded. The result of the inspection using this modality is presented as a sequence of thermograms. In Pulsed Phase Thermography, the temperature evolution over time obtained in Pulsed modality is converted to the frequency domain through the Fourier Transform (FFT) and the result is expressed in two images, one referring to the values of angle of phase and the other concerning the amplitude (Fourier module) for each pixel at the chosen frequency analysis. The Lockin mode consists of the periodic heating of the surface of the material through modulated lamps and simultaneously the temperature evolution is monitored along the heating cycles. For each test, it is necessary to choose a single frequency of modulation and the choice of this is depends on the depth of penetration of the thermal wave desired in the material. The result of the Lockin modality is presented in the form of two images, one referring to the phase angle and the other referring to the amplitude, both generated by Fourier transform [1,5,6].

The use of computational simulation model associated with non destructive techniques has become an increasingly present task both in research and in industry. These tools allow the study of the best configuration of parameters to be used in inspection (experimental procedure), thus optimizing the results, both from the point of view of time and resources and also brings the knowledge of the limits of detection of the technique. In this paper, we will present the creation of a computational simulation model through finite elements for numerical reproduction of the physical phenomena present in the pulsed active thermography test and the preliminary results already obtained with the samples of the study experiments after the validation of the model.

In this paper, the ability of Active Thermography will be evaluated for the inspection of two types of GFRP (Glass Fiber Reinforced Polymer) joints (adhesive-bonded and laminated) used in pipelines and for inspection of some types of composite coatings that are used in storage tanks. Both experimental and simulation studies will be developed in order to evaluate the technique on the detection of defects that are found in these structures.

2. MATERIALS AND METHODS

The first sample (S1) used in this study is a concentric adhesive bonded joint of GFRP. The sample is formed by two pipes, with a diameter of 101.6 mm, thickness of 5 mm, joined trough a collar of 12 mm thickness. An epoxy adhesive, with a thickness of 1 mm, was applied both over the collar's inner surface and over a surface of the pipes which was introduced into the collar. On

the adhesive layer, two defects of lack of adhesive were inserted. Figure 1 shows a representative scheme of the geometry and positioning of the defects inserted in the adhesive layer.

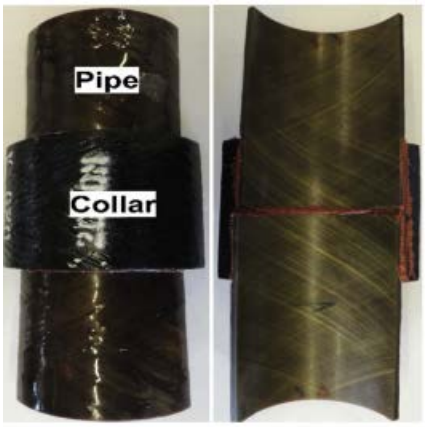

(a) (b)

Figure 1 – Photography of the ashesive joint (sample 1) viewed from: (a) outside and (b) inside [7].

The second sample (S2) evaluated in this study is a laminated joint of GFRP. This sample consists of two pipes, with a diameter of 152.4 mm, produced by filament winding and joined by the application of successive composite layers on the surface of the pipes, through a lamination process. The thickness of the joint varies from 10 to 25 mm. During the assembly of the joints, artificial defects were inserted between the composite layers and on the pipe surface to simulate, respectively, delamination and debonding defects. Figure 2 shows a photograph of the laminated joint sample.

Figure 2 – Photography of the laminated joint (S2) evaluated in this study.

The third sample (S3) is made of carbon steel substrate with dimensions of 150 mm x 100 mm x 4.7 mm with anti-corrosive composite coating (epoxy resin based). Before applying the coating, some notches were machined with different thicknesses and fulfilled with iron oxide on the substrate in order to simulate localized corrosion with the presence of undercoating solid corrosion products. The coating was applied over the acetate tape positioned on the substrate and then, this tape was removed and the coating film was applied on coating layer. In this way, a star-shaped

region was created on the surface of the substrate, where there is no presence of the coating layer, simulating adhesion failure in this region. Figure 3 shows the photography of this sample.

Figure 3 – Photography of the front side of the sample S3.

For the inspection of these samples, the Flir SC5600 thermographic camera was used simultaneously with the IR-Box system for the thermal excitation of the samples, both positioned in the reflection mode. This thermal stimulation system is controlled through IR-NDT software, which is responsible for the control of the lamps, the storage of thermographic images and the choice of data processing algorithms according to the modality of thermography to be applied.

The computational simulation model to be used in this paper was created in COMSOL Multiphysics software, versions 4.4 and 5.1. In this model was used the heat transfer module in solids, whose physical phenomena are applied in 3 dimensions (3D) and the evolution of temperature was time dependent, according to the principle of Pulsed Thermography technique. In addition to the equations describing the heat transfer in the three forms (conduction, convection and radiation), a heat flux was also added in the model in order to simulate the heating generated by the lamps on the surface of the sample.

3. RESULTS AND DISCUSSION

In order to evaluate the ability of the thermography technique to detect defects in composite adhesive joints, inspections by the Pulsed Thermography (PT) in sample S1 were performed both inside the joint and also from the outside the joint. The result of the inspection is presented in the form of a sequence of thermograms and the thermogram that produced the highest thermal contrast for each side of the sample is presented in Figure 4 (b). In addition, it was also evaluated the Pulsed Phase Thermography (PPT) on the inspection inside of the joint, as shown in Figure 4 (b). Analyzing these results, it is possible to observe that the PT was able to detect the defects of lack of adhesive when the inspection was carried out inside the joint even with a low thermal contrast, but the application of the PPT was able to highlight the two defective regions due to the greater contrast of the phase obtained.

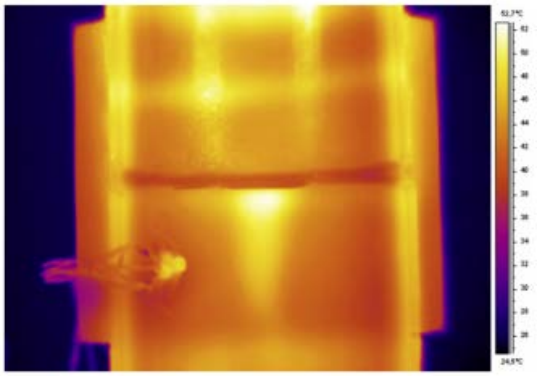

Figure 4 – Thermographic image at the time of highest contrast obtained by Pulsed Thermography performed on the inner side of the adhesive joint (sample 1).

The sample S2 was inspected by the three thermography modalities (PT, PPT and LT), in this region of the sample being inserted a delamination defect between the composite layers in the joint. The results obtained by each modality of thermography are presented in Figure 5 and these show that even in the simplest modality of thermography (PT), the defect could already be detected, however, the PPT and LT modalities presented a higher contrast in the region of the defect, allowing a better visualization of the contour and positioning of the same.

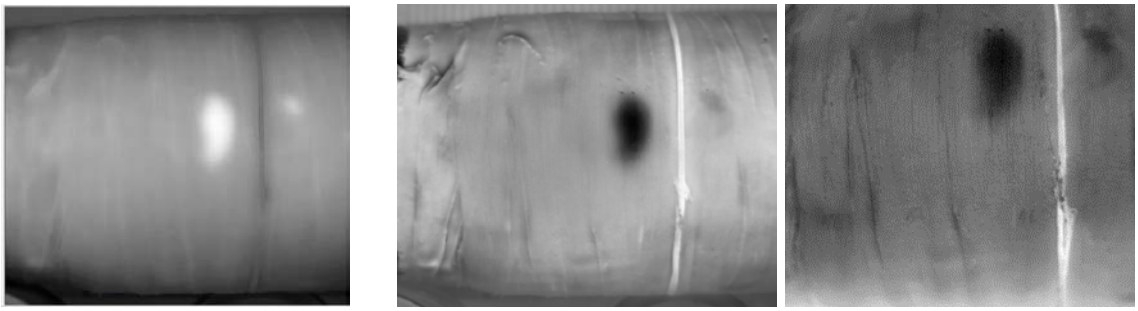

Figure 5 – (a) Thermographic image obtained by Pulsed Thermography, (b) phase image obtained by Pulsed Phase Thermography and (c) phase image obtained for Lockin Thermography with frequency of 0.01 Hz.

The higher contrast thermogram obtained for the sample S3 shows that the Pulsed Thermography was able to detect the two notches defects simulating the loss of thickness in the substrate and also the defect (star shape) simulating the adhesion failure. In addition to the defect type, this result shows that both the geometry of the defects and their thickness did not influence the detection when the inspection is performed on the front side of the sample. The presence of iron oxide filling the defects also did not generate any influence on the detection of defects by the thermography technique.

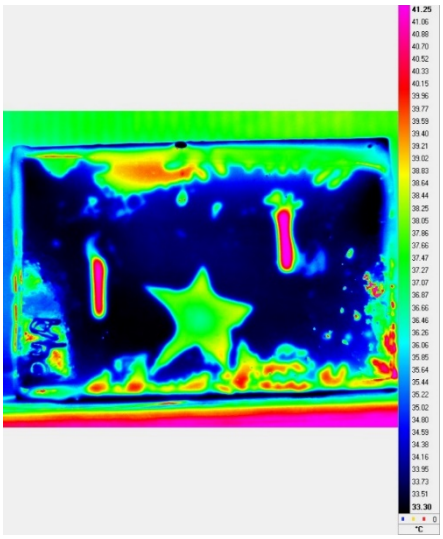

Figure 6 – Thermographic image at the time of the highest contrast obtained by Pulsed Thermography for the sample 3.

In Figure 7, the higher thermal contrast images obtained by the computational simulation of samples S1 and S3 are presented. According to the images, it is possible to observe that there is a behavior regarding the detection of defects very similar between the results obtained experimentally (Figure 4(a) and Figure 6) with the simulated ones. In addition, the thermal behavior, analyzed through the evolution of temperature in the two samples for each of the methodologies (experimental x simulation) also presented a great coherence.

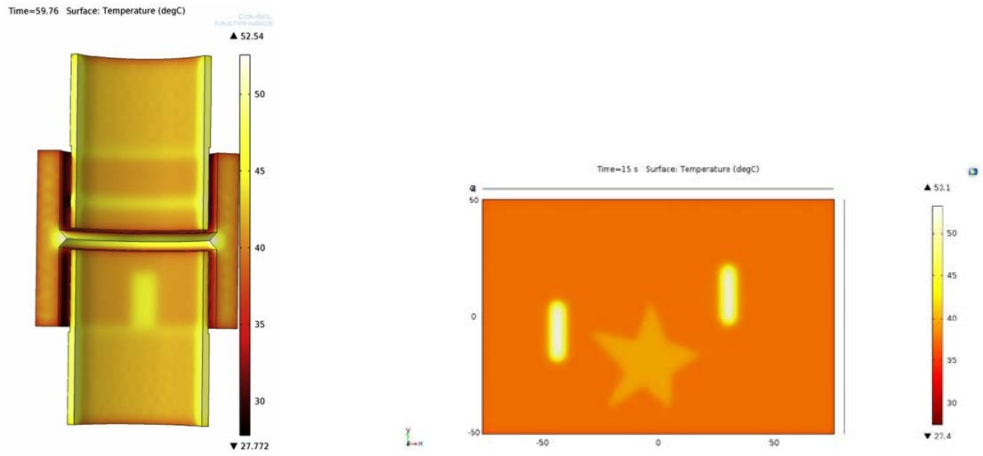

(a) (b)

Figure 7 – Image obtained by the computational simulation of the pulsed thermography showing the temperature distribution on the surface of the: (a) sample S1 and (b) sample S3.

4. CONCLUSIONS

According to the results obtained, the use of the Active Thermography technique for the inspection of adhesive and laminated composite joints showed the potential of the technique for the inspection of composite materials of high thicknesses (above 5 mm). This study becomes promising because most of the works published in the literature are restricted to the evaluation of

the technique in low thickness composites (below 5 mm), which demonstrates the challenge of this study. Another application of the technique studied in this paper was the inspection of composite coatings that are commonly used in storage tanks. Although visual inspection is the most used for inspection of these materials, the active thermography inspection has proved to be a powerful tool to detect defects that are common to occur (adhesion failure and localized corrosion on the substrate) and are not detectable by visual inspection.

By comparing the results for the two methodologies evaluated in this study (experimental and simulation), they showed a great similarity both in relation to the thermal behavior and in relation to the detection of the defects, thus allowing the validation of the model developed in this study. With this, the model created proved to be reliable and useful in to the reproduction of physical phenomena involved in the experiments. These results become interesting since the creation of a model by computational simulation able to reproduce the experimental test becomes a powerful tool for both in industry and in research since it allows the study of the best parameters to be used in the inspection, thus optimizing the results, both from the point of view of time and resources.

ACKNOWLEDGEMENTS

Authors would like to acknowledge the sponsorship of PETROBRAS, the Brazilian research agencies CNPq (Brazilian National Council for Scientific and Technological Development) and CAPES (Coordination for the Improvement of Higher Education).

REFERENCES

[1] Maldague, X.P.V., 'Infrared and Thermal Testing – non destructive testing', ASNT; 2001.
[2] Maldague, X., et al. 'Infrared image processing and data analysis', *Infrared Physics & Technology*, **46** (2004) 75-83.
[3] Maldague, X., Galmiche, F. and Ziadi, A., 'Advances in Pulsed Phase Thermography', *Infrared Physics & Technology*, **43** (2002) 175-181.
[4] Brown, J.R. and Hamilton, H.R., 'Quantitative infrared thermography inspection for FRP applied to concrete using single pixel analysis', *Constructing and Building Material*s **38** (2013) 1292-1302.
[5] Almnd, D. and Pickering, S. 'Matched excitation energy comparison of the pulse and lock-in thermography NDE techniques', *NDE&E International*, **41** (2008) 501-509.
[6] Busse, G. and Wu, D. 'Lock-in thermography for nondestructive evaluation of materials', Revue Generale de Thermique, 37 (2008) 501-509.
[7] Grosso, M. et al., 'Pulsed thermography inspection of adhesive of adhesive composite joints: computational simulation model and experimental validation', Composites Part B, **106** (2016), 1-6.

EXPERIMENTAL EVALUATION OF TEMPERATURE EFFECT ON THE TRANSVERSE PERMEABILITY OF A FIBROUS PREFORM

Rafael S. Trindade[(1)], Fernando Rodrigues[(1)], Eduardo Kerche[(1)], Affonso C. Ribeiro[(1)], Jeferson A. Souza[(2)], and Sandro C. Amico[(1)]

[(1)]Federal University of Rio Grande do Sul, Porto Alegre/RS, Brazil

[(2)]Federal University of Rio Grande, Rio Grande/RS, Brazil

https://doi.org/10.21452/bccm4.2018.05.03

Abstract

Study of the transverse permeability of fibrous reinforcements became increasingly important when liquid molding processes started being more widely employed to obtain more complex-shaped or thicker parts. In this paper, a system specially built to measure transverse permeability of fabrics based on the correlation between pressure difference and flow rate was used to evaluate the effect of temperature on the measurements of the transverse permeability of a E-glass fiber fabric. Three fiber volume fractions (38-61%) and three temperatures were studied (20-63ºC). The results have shown that the effect of the temperature on the transverse permeability was limited.

Keywords: Transverse permeability, Fibrous preform, Temperature effect.

1. INTRODUCTION

Efficient fiber impregnation is essential for the production of good quality polymer composite materials via any technique in the liquid molding processing family. The properties of the final products are dependent on how the resin advances inside the mold cavity forcing out the air within the preform, which is based on parameters like injection pressure, fluid velocity and reinforcement permeability [1].

Indeed, permeability of the fibrous reinforcement is a key parameter governing mold filling and preform impregnation. It is a measure of the resistance to flow of the fluid imposed by the reinforced medium. Permeability of a fabric may vary in the various directions, and precise characterization of all principal permeabilities (K_{xx}, K_{yy} and K_{zz}) of a preform is of uttermost importance, especially for more complex-shaped or thicker parts [2].

Past research on experimental permeability mostly focus on in-plane (K_{xx} and K_{yy}) measurements, in detriment of the through-the-thickness permeability. This is partly justified by the relative importance between them for a particular set of flowing parameters.

Previous studies on transverse viscous flow through square arrangements have concluded that the overall permeability of a fabric with porous tows is 25% greater than the permeability of solid tows [3]. Despite that, intra-tow porosity appears to have little effect on overall permeability [4].

The inter-tow porosity, on the other hand, has a prominent influence on the overall permeability and when it is increased the permeability does not increase uniformly and becomes more isotropic. Also, fiber nesting and non-uniform compaction of the layers change inter-tow spaces for different numbers of stacked layers, leading to variation in permeability values [5].

Depending on the type and architecture of the fabrics, the nesting degree may change the flow path and significantly contribute to permeability variations. Also, as the angle between successive plies increases, permeability in the transverse direction increases in a non-linear fashion due to the creation of empty spaces, i.e. low resistance pathways between layers [6]. In [7] and [8], the transverse permeability of fibrous preforms at various fiber contents was evaluated and low flow-rate was found crucial for continuous and discrete permeability measurements to avoid non-uniform flow.

The flow paths in the fabric transverse direction are mainly through meso-pores distributed through-the-thickness and they may be aligned or not (non-nested and fully nested, respectively). For large V_f (over 50%), the degree of nesting increases, leading to greater flow through the fiber tows (intra-tow flow) which is governed by micro-scale tow permeability [9]. Indeed, size of the inter-layer gap, inter-yarn spacing, yarns aspect ratio and intra-tow porosity were all reported to influence transverse flow for quasi-unidirectional non-crimp fabrics. And for high fiber content (from 48% to 60%), the influence of microscopic intra-yarn on in-plane and transverse permeabilities becomes greater [10].

In this article, a system developed to measure transverse permeability of reinforcements was used to evaluate the influence of temperature and fiber volume fraction on transverse permeability of a fibrous preform.

2. EXPERIMENTAL

2.1. Materials

The fabric chosen for the tests was an E-glass fiber fabric with a plain weave pattern (areal density of 303 g/m^2 and 405 tex) (Figure 1) supplied by Owens Corning. The fabric was cut manually using scissors and handled with care before they were placed within the mold cavity, as will be described later.

The working fluid was soy oil and its viscosity was measured using a Brookfield viscometer (Figure 2) with spindle configuration. Viscosity was evaluated in a range of temperature within 10-70 °C, based on the temperatures used in the permeability tests.

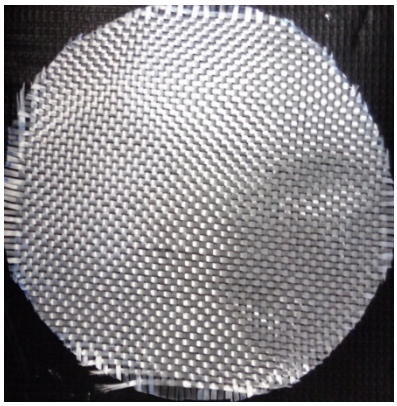

Figure 1: Plain-weave E-glass fiber used.

Figure 2: Viscosity evaluation of the soy oil used.

2.2. Permeability measurements

An apparatus specifically built for measuring transverse permeability (Figure 3) was used in this work. It consists of a lower cavity (entrance chamber) containing an opening for a pressure transducer and an inlet gate (8.4 mm diameter) for the fluid. This cavity is filled before the fluid reaches the first perforated plate and the preform. The other perforated plate limits the final thickness of the fibrous reinforcement and this height may be varied using spacers (3-22 mm), as needed.

The design of these perforated plates was chosen based on the findings of [11], being built with 68 holes of 8 mm diameter, which are positioned aligned in the set-up. These plates compact the reinforcement and prevent movement during testing, also allow a more uniform transverse flow through the reinforcement. On top, there is a conical chamber that converges the flow towards the outlet, which is coupled to a second pressure transducer. In this work, the height of the mold cavity was kept at 16.35 mm, and the final fiber volume fraction was varied (38%, 50% and 61%).

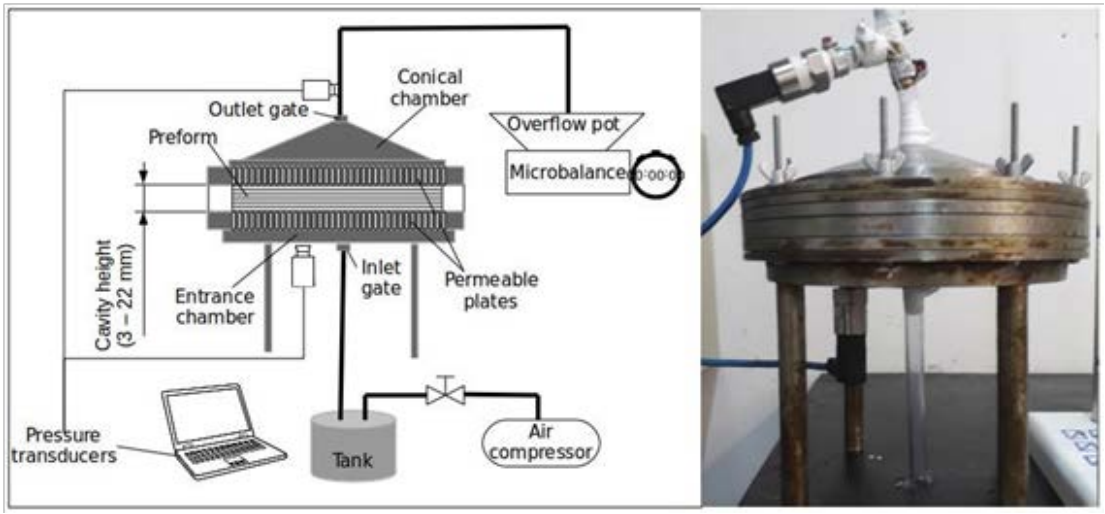

Figure 3: (a) Experimental set-up; (b) actual transverse permeability system.

After the mold is fully assembled, pressure is applied to a pressure pot containing the working fluid which is then forced through the mold. The fluid leaves the mold and is discharged into a

beaker placed on top of a balance. Flow rate measurements, i.e. the weight of collected fluid as a function of time, started only after total impregnation of the fabrics by the fluid and when the flow became stationary.

The applied pressure was varied six times in each test in order to obtain different flow rates. The pressure at the entrance was varied from 10 until 100 kPa. A linear relationship between pressure drop and flow rate (ΔP *vs*. Q) was obtained allowing calculation of the transverse permeability (K_{ZZ}, in [m²]) using 1-D Darcy's law.

(1)

where: Q is the volumetric flow rate [m³/s] calculated according to Equation 2, ΔP is the pressure drop [Pa], μ is the fluid viscosity [Pa.s], h is the preform thickness [m] and A is the cavity cross-section area [m²].

(2)

where ρ is fluid density [kg/m³], m is mass [kg] and t is time [s].

Before actual testing of the preforms, a series of tests were carried out with an empty mold, to determine the pressure drop as a result of the mold geometry. Then, a corrected correlation between flow rate and pressure drop was established for each experimental condition.

Considering the interest in this work to evaluate the effect of temperature on flow, the working fluid was heated in an oven up to a determined temperature, slightly higher than the desired temperature. This was necessary due to the delay between taking the fluid from the oven and starting the actual measurement. In addition, the metallic device was heated using domestic heaters close to it. A thermocouple was placed at the exit of the device (close to the second pressure transducer) and the temperature measured by it was identified as the test temperature. This temperature was used to correct the fluid's viscosity.

3. RESULTS AND DISCUSSION

Figure 4 presents the results of dynamic viscosity for the soy oil, which varied within 104-14 cP in that temperatures range (10-70 ºC). An exponential relationship between viscosity and temperature was fitted to allow a suitable viscosity reading according to the actual temperature in each experiment. The coefficient of determination of the best fitting equation was higher than 0.98.

Soy oil is a Newtonian fluid, which is important since the experimentally obtained dynamic viscosity is used directly into the Equation 1 that governs fluid flow and used to calculate permeability.

Therefore, soy oil was applied in every measurement of transverse permeability performed in this paper. This is justified taking into account that it is considerably less expensive, less dangerous and easier to handle than most other options. Another important advantage in using soy oil is the shorter time to achieve steady-flow conditions due to its lower viscosity.

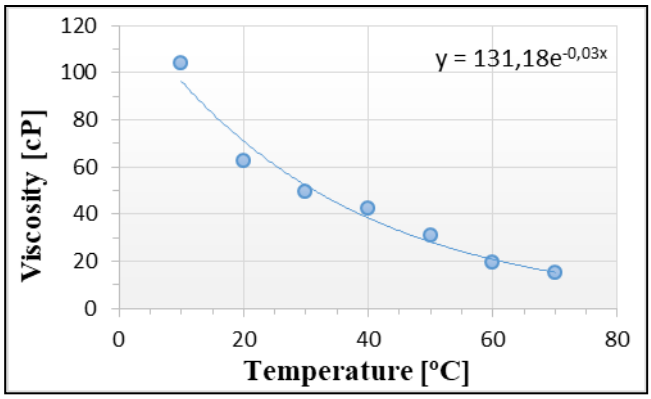

Figure 4: Working fluid viscosity results.

Transverse permeability results are presented in Figure 5a-b. As expected, the fiber volume fraction showed a remarkable effect on permeability. As one can see in Figure 5a, a change in V_f of 10% can alter the K_{zz} three-fold. Lower V_f values means less fibers (more pores) and lower level of preform compaction. When the V_f is higher, the resistance to the flow imposed by the fabrics is increased due to greater difficulty imposed to the flow in transverse direction.

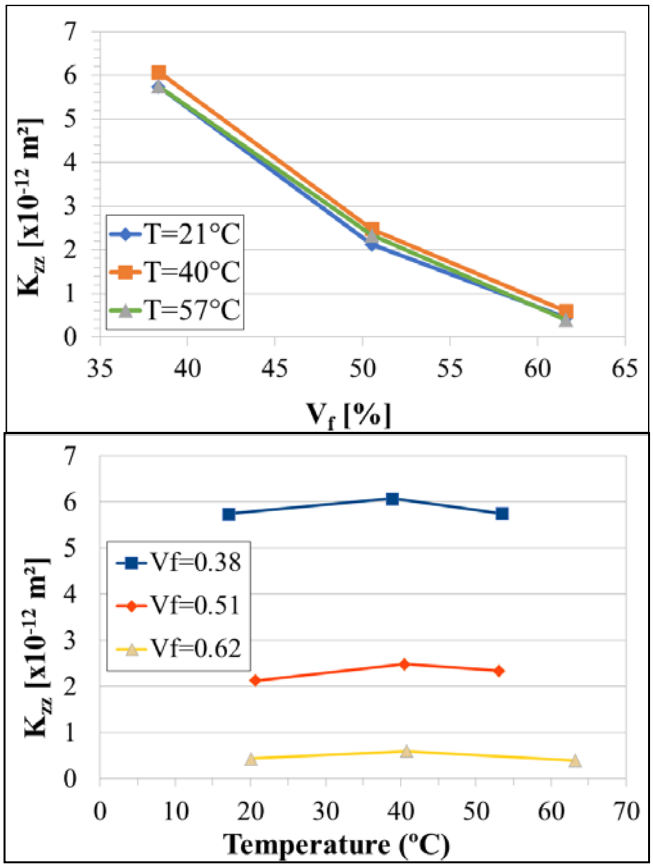

Figure 5: Transverse permeability results.

For the transverse flow through the meso-pores, large yarns (high tex) force the fluid to follow tortuous paths, and the tortuosity of the reinforcement has a more pronounced effect on the flow. Reinforcements with meso-pores structure will present higher macro-transverse permeability at

higher V_f. For lower values of V_f, the transverse flow goes through a meso-pore until it reaches the next layer and, thus, the transverse permeability is related with the space between layers and the resistance to flow of the empty spaces (in this case, a meso-pore) that depends on the dimensions of the hole

Considering now the effect of temperature, Figure 5b, there is no clear trend in the variation of values from 21 °C to 63 °C. Thus, the temperature is not influencing the measurement of transverse permeability, even though it greatly alters the working fluid viscosity. Also, this implies that general experiments can be carried out freely, at any room temperature for a particular test, when measuring transverse permeability of reinforcements.

The decrease in viscosity did not alter the K_{zz} values because the pressure gradient necessary to generate a similar flow rate also reduces accordingly, confirming the assumptions from the Darcy's Law.

4. CONCLUSIONS

Determination of transport characteristics of a fluid through a porous medium is not an easy task because it may depend on parameters such as pressure gradient, flow front velocity, viscosity and fluid compressibility. The device designed and constructed to measure the transverse permeability of preforms was tested and successfully obtained the desired results.

An E-glass plain-weave fabric was evaluated at three fiber volume fractions (38, 50 and 61%) and, as expected, transverse permeability decreased for higher fiber content, i.e. lower porosity between yarns. This is also related to the level of fabric compression at each V_f.

The temperature showed no significant effect on transverse permeability of the tested fabric, even though it greatly alters the working fluid viscosity. This implies that general experiments can be carried out freely, at any room temperature for a particular test, when measuring transverse permeability of reinforcements, as long as the viscosity is corrected. This is due to the balance between fluid viscosity and pressure difference applied to the system to generate a similar flow rate.

ACKNOWLEDGEMENTS

The authors would like to thank CAPES and CNPq for the financial support.

REFERENCES

[1] K. Okonkwo, P. Simacek, S.G. Advani, R.S. Parnas, Characterization of 3D fiber preform permeability tensor in radial flow using an inverse algorithm based on sensors and simulation, Compos. Part Appl. Sci. Manuf. 42 (2011) 1283–1292. doi:10.1016/j.compositesa.2011.05.010.

[2] L. Fang, J. Jiang, J. Wang, C. Deng, Effect of Nesting on the Out-of-Plane Permeability of Unidirectional Fabrics in Resin Transfer Molding, Appl. Compos. Mater. 22 (2014) 231–249. doi:10.1007/s10443-014-9403-6.

[3] T.A.K. Sadiq, S.G. Advani, R.S. Parnas, Experimental investigation of transverse flow through aligned cylinders, Int. J. Multiph. Flow. 21 (1995) 755–774. doi:10.1016/0301-9322(95)00026-T.

[4] M.W. Tahir, F. Stig, M. Åkermo, S. Hallström, A numerical study of the influence from architecture on the permeability of 3D-woven fibre reinforcement, Compos. Part Appl. Sci. Manuf. 74 (2015) 18–25. doi:10.1016/j.compositesa.2015.02.019.

[5] N. Vernet, E. Ruiz, S. Advani, J.B. Alms, M. Aubert, M. Barburski, B. Barari, J.M. Beraud, D.C. Berg, N. Correia, M. Danzi, T. Delavière, M. Dickert, C. Di Fratta, A. Endruweit, P. Ermanni, G. Francucci, J.A. Garcia, A. George, C. Hahn, F. Klunker, S.V. Lomov, A. Long, B. Louis, J. Maldonado, R. Meier, V. Michaud, H. Perrin, K. Pillai, E. Rodriguez, F. Trochu, S. Verheyden, M. Wietgrefe, W. Xiong, S. Zaremba, G. Ziegmann, Experimental determination of the permeability of engineering textiles: Benchmark II, Compos. Part Appl. Sci. Manuf. 61 (2014) 172–184. doi:10.1016/j.compositesa.2014.02.010.

[6] H.S. Sas, E.B. Wurtzel, P. Simacek, S.G. Advani, Effect of relative ply orientation on the through-thickness permeability of unidirectional fabrics, Compos. Sci. Technol. 96 (2014) 116–121. doi:10.1016/j.compscitech.2014.03.007.

[7] P. Ouagne, J. Bréard, Continuous transverse permeability of fibrous media, Compos. Part Appl. Sci. Manuf. 41 (2010) 22–28. doi:10.1016/j.compositesa.2009.07.008.

[8] P. Ouagne, T. Ouahbi, C.H. Park, J. Bréard, A. Saouab, Continuous measurement of fiber reinforcement permeability in the thickness direction: Experimental technique and validation, Compos. Part B Eng. 45 (2013) 609–618. doi:10.1016/j.compositesb.2012.06.007.

[9] M. Yun, T. Carella, P. Simacek, S. Advani, Stochastic modeling of through the thickness permeability variation in a fabric and its effect on void formation during Vacuum Assisted Resin Transfer Molding, Compos. Sci. Technol. 149 (2017) 100–107. doi:10.1016/j.compscitech.2017.06.016.

[10] E. Syerko, C. Binetruy, S. Comas-Cardona, A. Leygue, A numerical approach to design dual-scale porosity composite reinforcements with enhanced permeability, Mater. Des. 131 (2017) 307–322. doi:10.1016/j.matdes.2017.06.035.

[11] H.-S. Chae, Y.-S. Song, J.-R. Youn, Transverse permeability measurement of a circular braided preform in liquid composite molding, Korea-Aust. Rheol. J. 19 (2007) 17–25.

MECHANICAL ANALISYS OF POLYMERIC WEBBING TESTS WITH AND WITHOUT PRELOADS

Andrés Heemann Pereira Neto (1), Filipe Paixão Geiger (1), Tales de Vargas Lisbôa (1), Rogério José Marczak(1)

(1) Department of Mechanical Engineering, Universidade Federal do Rio Grande do Sul, Brazil

https://doi.org/10.21452/bccm4.2018.05.04

Abstract

The paper aim is the characterization of the mechanical behavior of webbings when exposed to multiple preloads and the comparison with the Mullins Effect. Since the webbings presents a non-linear behavior difficult to predict, the tests themselves are important to specify its mechanical response. The webbings are combinations of Polyester, Nylon, UHMWPE and other composites. The experiments were performed based on ASTM D6775 and WSTDA-TM-1, however it is highlighted the lack of standardization considering the type of material, therefore a methodology was proposed to perform the tests. The results showed that after an application of 3 preloads of 70% of the rupture load the webbing behavior remains unchanged as well as the rupture load. Two limits are noticeable, the lower (without preload) and the upper (with 10 preloads) limits.

Keywords: Webbing, Polymer, non-linear, experimental.

1. INTRODUCTION

The webbing, considering its material and geometry (shown in Figure 1), presents a nonlinear mechanical response in the traction test. Its manufacture results in voids and non-homogeneities that make it difficult to determine the real area to be used in strains and stresses, besides influencing the test. These webbings have combinations of materials, such as: Polyester, Nylon, UHMWPE and other polymeric fibers. Consequently, the final composite behaves differently from the original constituent by itself ([3] and [4]).

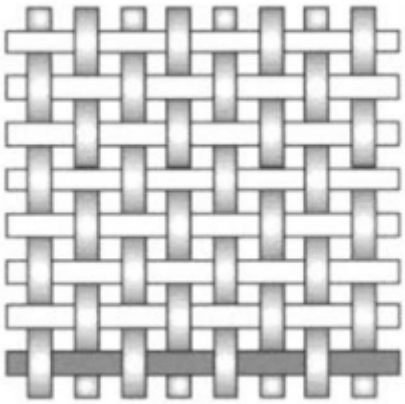

Figure 54 - Webbing pattern configuration [5]

Since the webbing have a complex mechanical behavior, the tests parameters must be studied beforehand. The length, speed and preload were some of the data determined before the experiments. Thus, a methodology was developed based on the existing standards ASTMD6775 [6] and WSTDA-TM-1 [7] applied in studies with elastomers [8] and composite fabrics [9]. Therefore, uncertainties and influences of the input parameters were discarded allowing the correct analysis of the samples.

The tests were performed using an universal testing machine together with a locking equipment for fastening the webbing. The data acquired from the machine were: force, displacement (or elongation of the tape) and duration of the test, since stresses and strains, commonly obtained in these tests with different materials, are difficult to be studied at this stage of the research.

The use of webbing in mooring, safety equipments and even sports practice is commonly observed today. However, during its application, several important factors like rupture load and preload (PL) that alter its behavior are disregarded. The main objective of the research is to determine how the application of PLs modifies the behavior of the webbing and the bursting loads through tests. Since elastomers and polymeric materials undergo changes in their behavior when subjected to cyclic loading [1] and [2], the present work seeks the mechanical characterization of this component.

2. METHODOLOGY

In order to perform the experiments, the universal machine Shimadzu AUTOGRAPH AG-X plus (displayed in Figure 2 (c)), whit a 250kN load cell, was used based on the standards (split drum presented in Figure 2 (a)) and works aforementioned (similarly to a stripe). Prior to the tests, the input parameters were determined to eliminate its influence in the mechanical response. The standards indicate a wide range of values for the parameters testing as well as a variation in the response when modifying the input parameters.

Several tests were performed in order to establish the test parameters. The values that best fit the proposed methodology were:

- Loading speed: 75mm / min;
- Sample length: 500mm;
- Preload: three preloads of 70% of the sample bursting load.

The data acquisition indicated by the standard was very rudimentary and inaccurate for this type of work. According to the standard [1]: "The equipment will be stopped and the distance between the two fine ink marks or pins measured with calipers or other suitable measuring device at the load level specified". Therefore, the procedure was changed, obtaining the values of displacement directly from the machine.

Tests were performed using 26 different webbings, each one with 5 samples, manufactured from companies in Brazil, Germany, USA and France. The webbing, shown in Figure 2 (b), composition and materials used are only known by the manufactures and are kept as a secret. NYLON, Poliester and UHMWPE are materials commonly applied in this component

(a) (b) (c)

Figure 2 – (a) Sample fixation, (b) Sample itself and (c) Sample in the machine

3. RESULTS

3.1 Initial Experiments

Initially the webbings were tested, without preload, to determine the rupture load. This result can be seen in Figure 3, showing a rupture load of approximately 27kN. A nonlinear behavior in the test, characteristic of this type of material and its construction (Figure 1), is observed. Since the tape is composed of several filaments organized in a pattern, the slippage of these wires until the alignment with the applied load increases the stiffness of the component to the as far as the local fiber rupture, causing overall webbing failure.

Since this type of material changes its behavior with the change of applied forces [10], a test with different preloads was performed. Figure 3 shows the curves of five cycles (1, 2, 3, 5, 10) of preloads of 70% of the rupture load (PL70) and the test until failure of cycles 3 and 10. It was verified that this parameter altered the shape of the curve, however, the rupture load was not altered

with the use of the PL. In addition, it has been observed that the non-linear effects of the webbing are reduced.

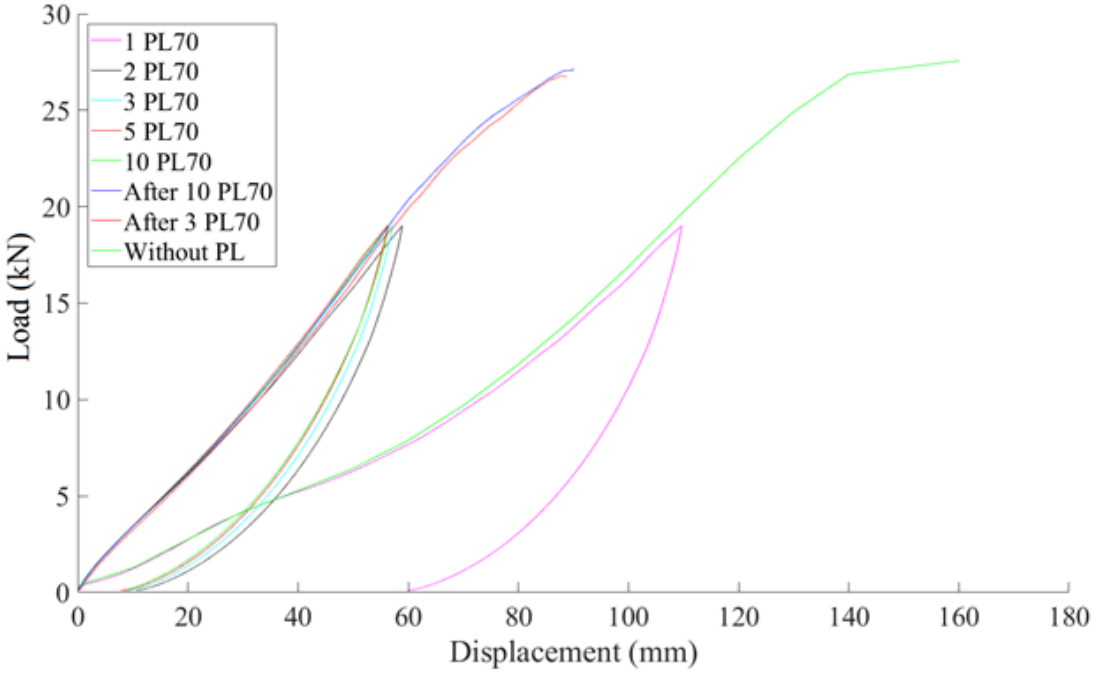

Figure 3 – Comparison between the test without preload and after five cycles of preload.

The change in the slope of the curve indicates the stiffening of the tape. This mechanism is a consequence of the fibers alignment in the loading direction. By the action of the remaining internal friction between fibers and fibers, and fibers and pattern, after discharging, these fibers remain aligned, which causes the increase of stiffness.

It is observed in Figure 3 that the first preload is responsible for most of the fiber alignment and removal of any geometric imperfection presented in the sample. Subsequent PLs have little, if any, effect on the mechanical response of the component. After applying three PL70 there was a stabilization of the tape behavior, i.e., from the 4th PC70 the influence on the final response is insignificant, consequently it was defined that three PC70s were sufficient to prepare the sample for tests and, even, real field use, like sports practice, load transportation and fixing.

3.2 Webbing Stiffning and Mullins Effect

After verifying the behavior change of the webbing when applied high preloads, an experiment was carried out to compare this phenomenon with the Mullins Effect (ME) [11]. This effect, represented in Figure 4, is characterized by energy conservation (having little hysteresis during cycles). However, the effect of the tapes has a significant hysteresis, according to Figure 5, due to the friction between the fibers. Another difference between the hypothesis is that in ME the loading and unloading cycles break the molecular chains, however, in the components tested these

cycles pre-align the fibers in the loading direction and remove any defect or slack between the fibers.

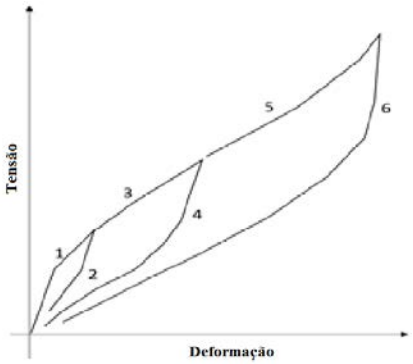

Figure 4 – Mullins effect representation [12].

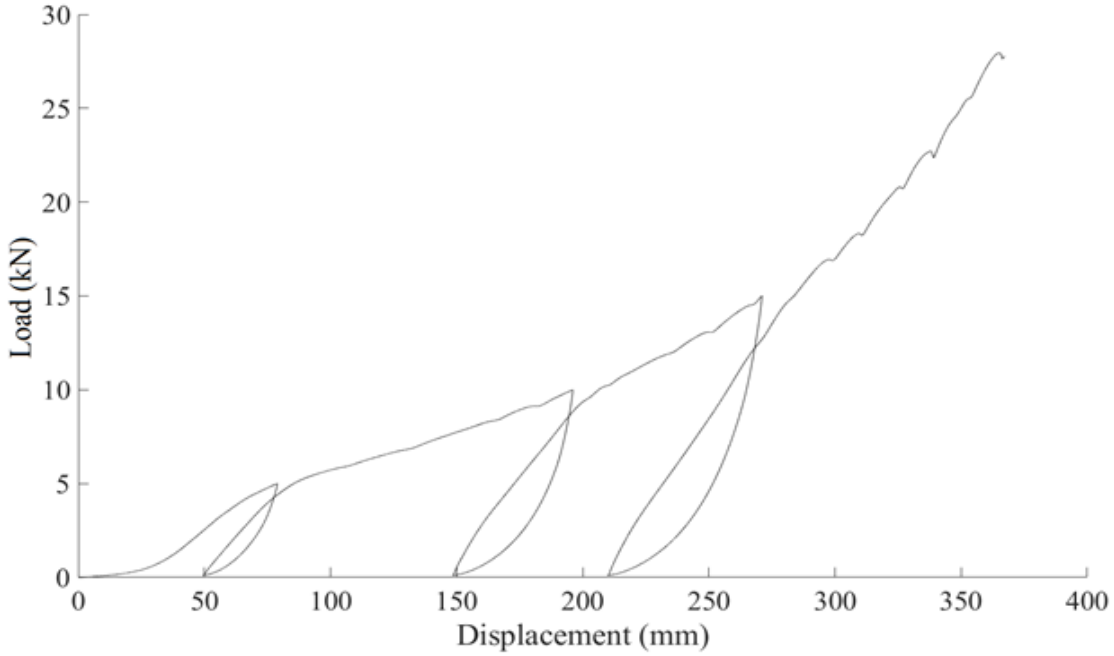

Figure 5 – Webbing test considering the preload cycle.

The experiment was performed using a PL of 0,1kN to eliminate any gap from the webbing and the test machine. Figure 5 shows three loading cycles increasing 5kN after every discharging. The new path, considering the new cycle, is different from the initial curve, a consequence from the pattern friction. Once again, no change in the rupture load is observed.

3.3 Low preload experiments

Since the product is used in the field in a different manner from that tested, it was necessary to perform an experiment with PL close to the loads used in field. Considering loads of 10kN during use (less than 50% of the rupture), the test is important to verify whether there would be alignment during use at the same ratio as with PL70. Therefore, a test was carried out in with 10 preloads of 7kN (PL7), corresponding to loads used in sports (slackline) and applied in cargo transport.

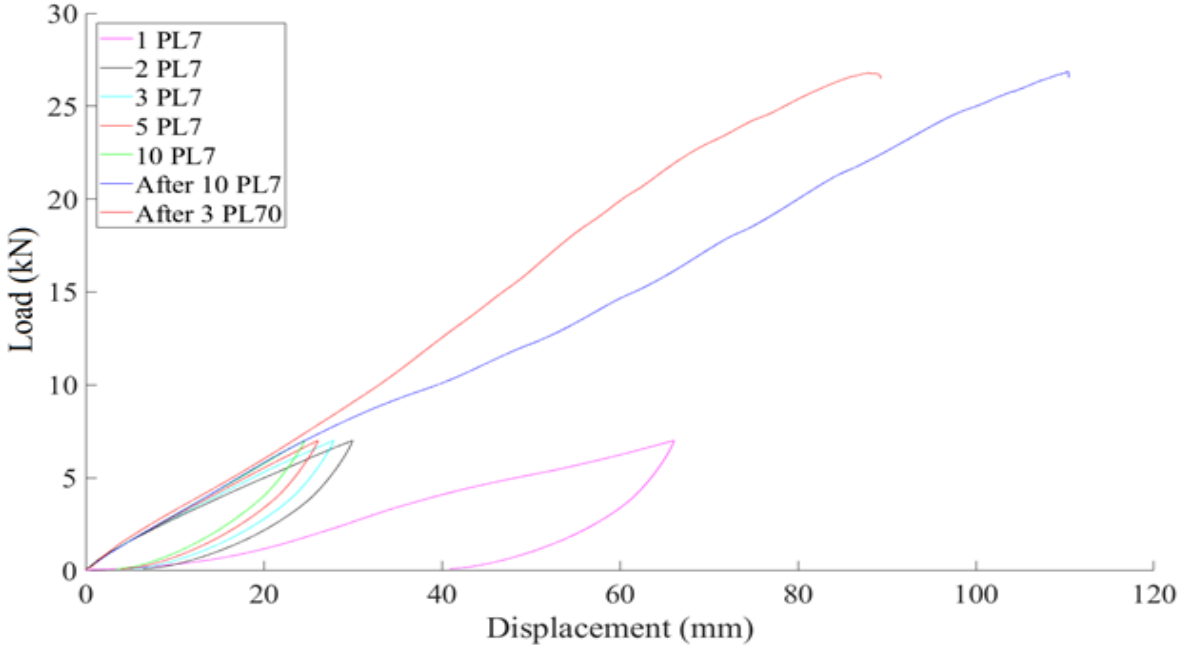

Figure 6 – Comparison from the experiment with preloads of 7kN and 70% of the rupture load.

The PL7 mechanical response was compared with 3 PL70. This comparison is shown in Figure 6, demonstrating that the load used in the field is not sufficient to completely align the fibers. Even after the application of 10 PC7, the behavior was not stabilized, that is, more repetitions would be necessary to possibly reproduce the PC70 result. The PL7 sample stiffness was initially similar to PC70, but the lack of complete alignment of the fibers resulted in a different behavior after 20mm of displacement. It is also observed that the breaking load remained the same.

3.4 Tests comparison

After all the tests were completed, the mechanical responses obtained from the different input parameters were compared in order to highlight the effects previously mentioned. This comparison is shown in Figure 7. The mean curve and every other result were obtained from five samples. Two limits are noticeable: The lower limit (without PL) represents the webbing minimum stiffness while the upper limit (10 PL70) indicates the maximum slope of the curve. Consequently, every result from PL applied will be contained between these limits.

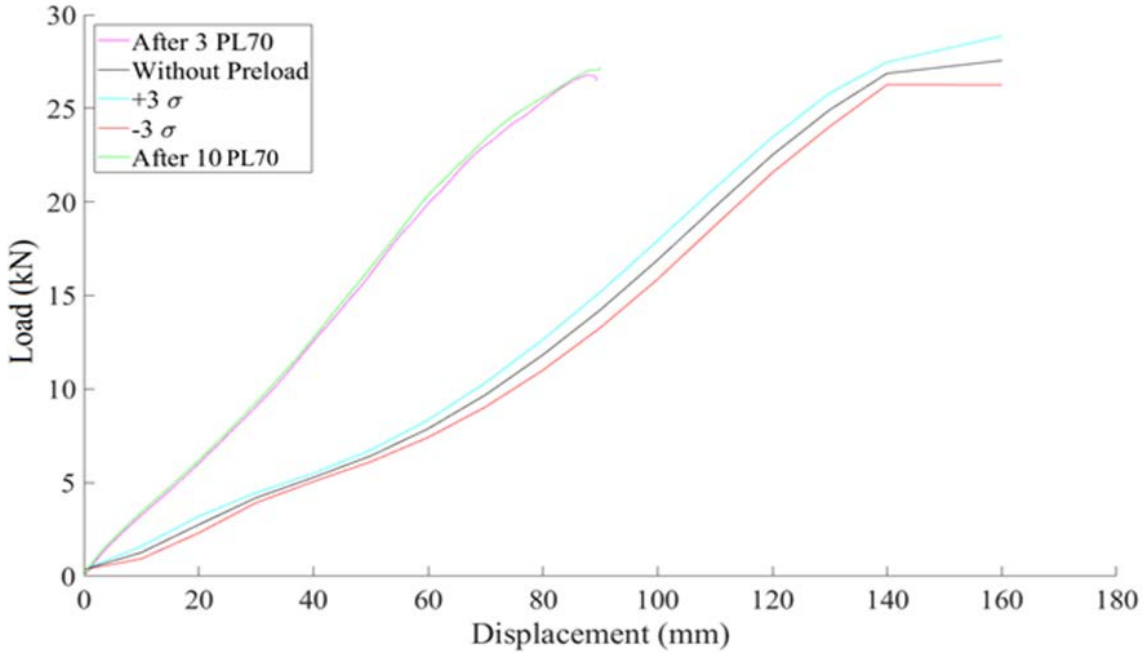

Figure 7 – All experiments rupture curve comparison.

4. CONCLUSIONS

An experimental methodology was proposed for polymeric webbing testing based on standards adaptations. The definition of the input parameters proved to be efficient and capable of capturing the effects necessary for the evaluation of the samples mechanical behavior.

After the initial tests, it was observed that with the use of preloads there was a change in the webbing behavior (increase of stiffness). The Mullins effect was compared to the webbing response considering the preload cycle and was shown to be efficient only to analogy purposes. Also, it was evaluated that low preloads do not generate complete fiber alignment nor stabilize the preload cycle. None of the studied cases changed the rupture load, remaining close to the initial test.

REFERENCES

[1] Mullins, L., Tobin. N. R., 'Stress softening in rubber vulcanizates. Part I. Use of a strain amplification factor to describe the elastic behavior of filler-reinforced vulcanized rubber' 1965.

[2] Roque, R. M., 'Análise teórica e experimental de elastômeros', Dissertação, (Mestrado em Engenharia Mecânica) - Instituto Superior Técnicc, Universidade Tecnica de Lisboa. Lisboa, Portugal. 2007.

[3] Takashi Ishikawa and Tsu-Wei Chou, 'Nonlinear Behavior of Woven Fabric Composites', Mechanical and Aerospace Engineering Department University of Delaware Newark, Delaware, (Journal of Composite Materials 1983) 17: 399 - American Society for Composites.

[4] C.Z. Paiva Júnior, L.H. de Carvalho, V.M. Fonseca, S.N. Monteiro, J.R.Md'Almeida, 'Analysis of the tensile strength of polyester/hybrid ramie–cotton fabric composites' - Polymer Testing - Volume 23, Issue 2, April 2004, Pages 131-135.

[5] Campbell, F. C., 'Manufacturing Processes for Advanced Composites' .Elsevier Ltd, U.K., 2004. Pg.52

[6] ASTM D6775 - 13. Standard Test Method for Breaking Strength and Elongation of Textile Webbing, Webbing and Braided Material, American Society for Testing and Materials, 2017.
[7] Strength & Elongation Recommended Test Method for Sling & Tie Down Webbing, Web Sling and Tie Down Association, Inc., Standard Specification WSTDA-TM-1.
[8] Constitutive modeling of the large strain time-dependent behavior of elastomers - J.S.BergströmM.C.Boyce - Volume 46, Issue 5, May 1998 - Journal of the Mechanics and Physics of Solids – J.S.Bergström, M.C.Boyce.
[9] K. Buet-Gautier and P. Boisse. 'Experimental Analysis and Modeling of Biaxial Mechanical Behavior of Woven Composite Reinforcements'. Setembro 2001 Experimental Mechanics (2001) 41: 260.
[10] Iemura. H., 'Structural Stability and Nonlinear Behavior, Vol. I', Department of Civil Engineering Systems, Kyoto University, Kyoto, Japan.
[11] Mullins. L., ' Softening of Rubber by Deformation. Rubber Chemistry and Technology'. March 1969, Vol. 42, No. 1, pp. 339-362.
[12] Dorfmann, A., Ogden, R. W., 'A constitutive model for the Mullins effect with permanent set in particle-reinforced rubber". International Journal of Solids and Structures. 41: 1855–1878.

TRIDIMENSIONAL CHARACTERIZATION OF EPOXY MATRIX GLASS-FIBER REINFORCED COMPOSITES

Lorenleyn De La Hoz Alford[a]; Sidnei Paciornik[a], José Roberto Moraes d'Almeida[a]; Haimon Diniz Lopes Alves[b]; Marcos H. de PinhoMauricio[a]

[a] Dept. of Chemical and Materials Engineering, PUC-Rio, Rua Marquês de São Vicente, 225, Gávea, 22451-900 Rio de Janeiro - RJ, Brazil.

[b] University of the State of Rio de Janeiro (UERJ), Rua São Francisco Xavier, 524 - 1°andar - Sala 1006 A - Maracanã, 20550-900, Rio de Janeiro – RJ, Brazil.

https://doi.org/10.21452/bccm4.2018.05.05

ABSTRACT

Composite materials are typically heterogeneous and non-isotropic. Failure mechanisms are affected by the spatial distribution of reinforcements and the quality of the adhesion at the reinforcement-matrix interface. The traditional techniques of microscopic characterization are quite limited to study this type of material, since two-dimensional sections or projections may not fully reveal the complex three-dimensional microstructure of a composite. When seeking to understand the origin of failure mechanisms, these limitations are even more important. In this work, a three-dimensional characterization methodology was developed based on x-ray microtomography (microCT). The material evaluated was a glass fiber/epoxy matrix composite reinforced by unidirectional fibers. Test specimens were tomographed before and after flexural tests. The 3D images were analysed to visualize and quantify voids and cracks, both originated in the manufacturing process and created by mechanical loading. Evaluation of the uncertainty of the procedure was performed by tomographing more than once each sample, aligning and comparing the 3D images. The analysis allowed to quantify the increase in defect volume after material failure.

Keywords
Fiber reinforced composites; failure mechanisms; microtomography; 3D visualization.

1. INTRODUCTION

Composite materials are generally formed by a continuous matrix phase and a discontinuous reinforcement phase. Traditionally, the characterization of these materials is performed by microscopy techniques, generating two-dimensional information of the material structure [1]. However, the microstructure and defects in composites are fundamentally three-dimensional.

Thus, it is important to have techniques that allow this kind of analysis.

X-ray Microtomography (microCT) serves this purpose. This is a technique that offers poorer resolution than optical microscopy (OM) and scanning electron microscopy (SEM), but it is widely used in the characterization of the internal morphology of materials, creating three-dimensional representations. MicroCT is non-destructive and does not require a previous step of sample preparation, as is the case with microscopy. MicroCT can be used in materials that have a sufficiently large density difference between their constituents or in the atomic composition in order to generate x-ray absorption contrast [2,3].

There are several results that demonstrate the feasibility of using microCT in the evaluation of the internal geometry of materials, and in the study of cracks and defects, including delamination and microcracks [4-6]. These results show that microCT images allow the visualization of defects and the analysis of the morphological characteristics of the samples, especially in the study of complex structures.

In this work, glass-fiber reinforced epoxy matrix composites were evaluated before and after bending tests by microCT. The presence of defects was visualized and quantified. A calibration procedure allowed to estimate the uncertainty of these measurements.

2. MATERIALS AND METHODS

2.1. Samples

The samples were manufactured by vacuum bagging of prepregs laminas. The epoxy matrix used was formulated by mixing the appropriated amounts of epoxy monomer, based on diglycidyl ether of bisphenol A (DGEBA), and triethylenetetramine (TETA) hardener. E-glass fibers were used as reinforcement, with a nominal volume fraction of 50%.

The analysis of cracks and defects was performed in two samples, having different geometric characteristics. Figure 1 shows the two specimens used (CP1 and CP2). CP2 has a notch, reducing its width from 12.7mm to 7mm in its central region (Figure 1b). The idea was to create a region of stress concentration to evaluate its impact on the formation/propagation of defects. Both specimens were cut in the dimensions shown in Figure 1 to allow higher spatial resolution during the analysis, which is inversely proportional to the sample thickness.

2.2. Flexural Tests

The specimens were submitted to a three-point flexural test according to ASTM D 790-10.

The tests were performed in the AME-2kN equipment with a capacity of 2kN.

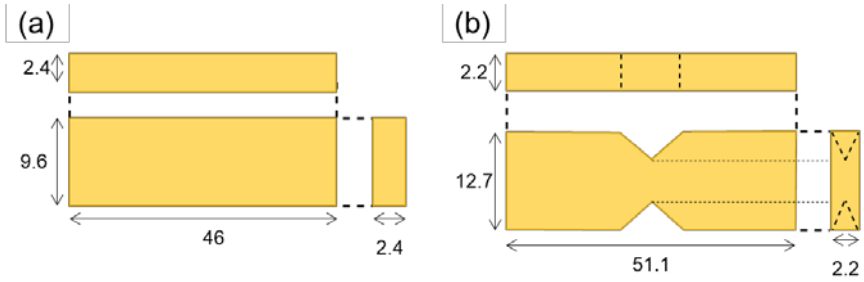

Figure 1: Schematic drawing of the specimens. (a) CP1. (b) CP2. Dimensions in mm.

2.3. MicroCT

MicroCT scans were obtained with the Zeiss Xradia 510 Versa microtomograph. This equipment combines the simple geometric magnification, dependent on source-sample-detector

distances, to optical magnification obtained with an optical microscope. Each optical lens is fitted with a scintillator that converts X-rays to light.

For this analysis a resolution around 13.75 μm given by the 0.4X lens was used, allowing a complete scan of the sample in a reasonable time. In order to minimize the total time of analysis, reconstructions were tested with 800, 1600 and 3201 projections, and the intermediate value of 1600 projections was chosen. The exposure time was 0.5s, leading to a total scan time of approximately two hours. Then the layers were reconstructed with the XMReconstructor V Cone Beam-11 software.

For a better understanding of the experimental methodology, it is necessary to understand the sequence of evaluation of the uncertainty of the procedure. As defects previously present in the sample and those created by the mechanical test appear in low fraction, uncertainties caused by the conditions of acquisition and/or processing of the images could lead to non-representative results. Thus, not only the operating conditions of the CT scanner were kept constant (x-ray energy, source-sample-detector geometry, lens, exposure time, number of projections, spatial resolution), but variations in the images caused by acquisition of the images were also evaluated, without influence of the flexure tests.

The methodology was divided into 2 stages as summarized in Table 1:

1) In the first step, the sensitivity of the procedure was determined by tomographing CP1 3 times before the flexure test. The first two scans were performed in sequence, without removing the sample from the scanner. The specimen was then removed and replaced in the tomograph, and a third scan was performed. The 3 images were processed and analyzed, as described below, and the volumetric fraction of defects quantified. Any variations in this step would only be caused by uncertainties in the acquisition of the images and served as a margin of error for the results obtained in the second step.
2) In the second step, the samples were submitted to two bending tests and were scanned after each one. In the first test, the samples were tested within the elastic regime, in the assumption that the mechanical stress would not cause damages. In the second test, the samples were taken to rupture.

Table 1: Image capture steps.

Stage	Sequence	Code
1	Tomography and initial reconstruction.	I1
	Tomography without removing the sample from the tomograph.	I2
	Tomography after removing and repositioning the sample.	Ret
2	Tomography of the test material 1 time.	E1
	Tomography of the test material 2 times.	E2

2.4. Image Processing and Analysis

Once the reconstructed images were obtained, an image processing sequence was performed. This stage is usually constituted by preprocessing steps for noise reduction, segmentation for object discrimination and post-processing for filtering objects and eliminating artifacts [7]. At the end, 3D visualization and orthogonal planes of the specimens are generated. For this analysis, 3D software Dragonfly v3.5 (Object Research Systems, Canada) was used.

2.4.1. Image Registration

To monitor the impact of the mechanical stress on generation of defects, it is important to evaluate equivalent regions in the sample, before and after the bending tests. For this, a 3D

alignment between the tomographic images obtained before and after the test was performed with the DataViewer program (Bruker Inc., UK).

This alignment was only possible because, even after the test, the external dimensions of the sample showed nearly no change. In fact, the alignment did not seek to correct for size and/or shape distortions generated by the mechanical test. The objective was only to correct the x-y-z displacement caused by the removal of the sample from the tomograph. Figure 2 shows two views of CP1 images I1 and E2 before and after alignment.

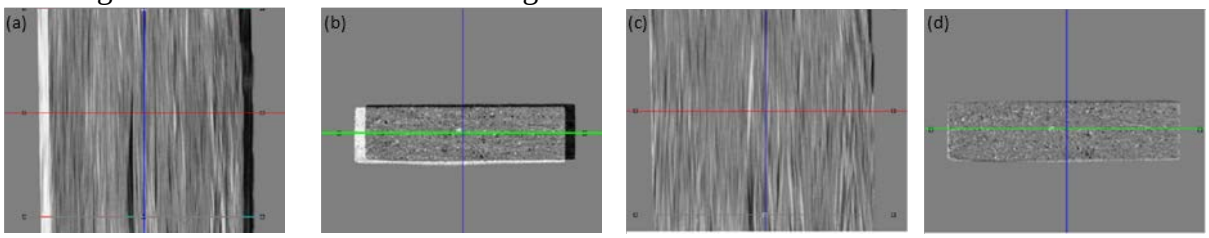

Figure 2: Images I1 and E2 of CP1 before (a, b) and after (c, d) of the 3D registration. The light and dark edges indicate the initial misalignment, corrected after the procedure.

2.4.2. Segmentation of defects and cracks

Defects and cracks appeared as darker regions within the composite matrix. The direct segmentation of these regions by tonal range was not viable, since regions external to the sample showed similar x-ray absorption and tone. Thus, the procedure involved segmenting the solid matrix, filling in the defects and subtracting, generating an image only of the defects.

The defects were filled in two stages. First, a 3D morphological closing operation with a neighborhood of 13 pixels was used to close the defects that touched the edges of the sample. Then, a hole-filling operator was applied along the x, y and z directions, successively [7,8].

The tonal threshold to segment the matrix was chosen from the 2D projections in the 3 orthogonal directions and from the 3D image. The critical point was to select the matrix without including regions corresponding to defects. To avoid introducing uncertainty, the tonal range used was kept constant for all CT scans (I1, I2, Ret, E1, E2).

Then, the matrix volumes (v_M), filled matrix (v_{MP}), which corresponds to the total volume of the specimen, and the defects $v_D = v_{MP} - v_M$, were measured. From these values, the volume fraction of defects % $V_D = v_D / v_{MP}$ was obtained.

3. RESULTS AND DISCUSSION

3.1. Flexural test

Analysis of the stress-strain behavior during the flexure test allowed the samples to be kept within the elastic limit in the first test and to bring them to rupture in the second test. Figure 3 shows the stress-strain curves for the second test of both samples. Note that CP2 has a higher flexural strength than CP1.

As both specimens were cut from the same composite plate, the differences in the flexural test could in principle be associated with the presence of the notch in CP2. However, this should contribute to reduce flexural strength and not to increase it, as shown in Figure 3. The explanation is probably associated with the defect concentration, as explained below.

3.2. Image analysis and observation of defects and cracks

Figures 4 and 5 show images of the two samples, after the flexure test. Defects appear as dark

regions against the gray background of the material.

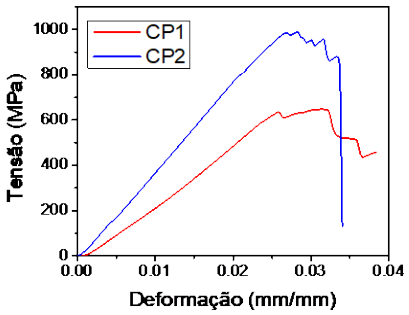

Figure 3: Comparison of stress-strain curves after the second mechanical test (E2, Table 1).

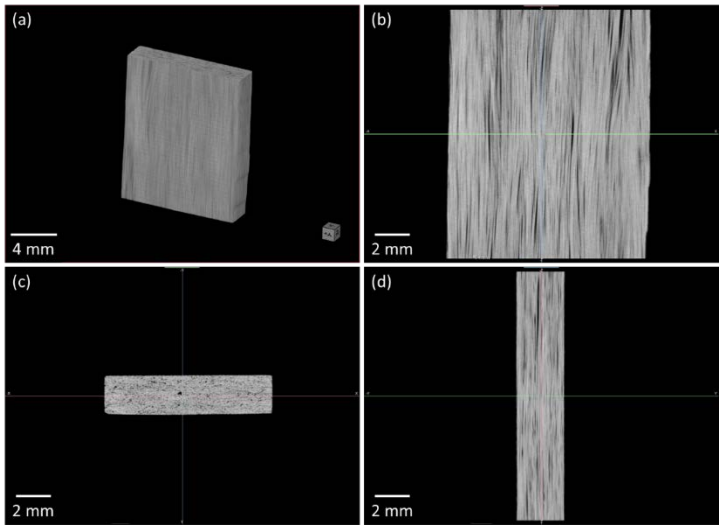

Figure 4: MicroCT image (CP1, condition E2). (a) 3D view; and planes (b) xz; (c) xy; (d) yz.

Figure 6 shows the results of defect segmentation for CP1, condition E2. The defects appear colored against the gray background formed by the material. In the 3D image, part of the sample was made transparent to show only the defects. It is worth mentioning that the 3D visualization gives the impression that the concentration of defects is much greater than in the 2D projections. This is a typical effect and depends heavily on the orientation in which the 3D image is presented. This visual effect will be criticized in the light of the quantitative analysis of defects, as described below.

Table 2 presents the volume fraction of defects (V_D) of CP1 at conditions I1, I2 and Ret (before the mechanical test), E1 (after the test at the elastic region), and E2 (after test to failure). The percentage changes, $\Delta(\%)$, with respect to the initial value, I1, are also presented.

The values for I1 and I2 are identical, indicating the stability of the image acquisition process. The values are also almost equal to Ret, indicating that errors caused by mechanical instabilities are small, ≈1% of the initial value. The value for E1 indicates a small increase of ≈6% in the defect fraction when the sample is tested within the elastic region. Finally, when the sample is taken to failure, the defect fraction increases almost 80% but does not reach 15%. This is not such a large value, which should be contrasted with the impression of high defect concentration brought by Figure 6a.

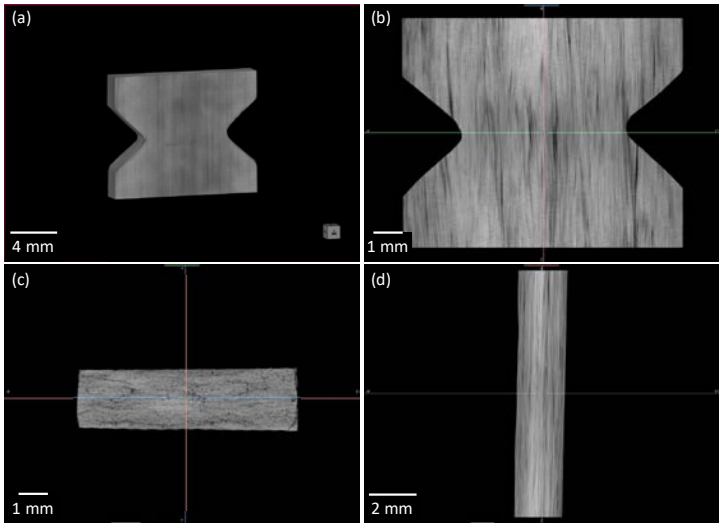

Figura 5: MicroCT image (CP2, condition E2). (a) 3D view; and planes (b) xz; (c) xy; (d) yz.

Table 2: Volumetric Defect Fraction

	CP1		CP2	
Tomographic Stage	V_D (%)	Δ (%)	V_D (%)	Δ (%)
I1	7.8	–	1.0	–
I2	7.8	0		
Ret	7.9	1.3		
E1	8.3	6.4		
E2	14.0	79.5	3.0	200

Figure 7 presents the defect analysis for CP2 in the E2 condition. In this case, the defect fraction is apparently smaller, which is confirmed by the quantitative analysis. The values for the defect fraction of CP2 are presented in Table 2 for the original condition (I1) and after the test until the rupture (E2). The initial volume fraction is much lower than that of CP1, but grows 200% after the test. Its maximum value reaches 3%, about 5 times less than in CP1. This large difference may explain the results of the bending test. Despite the notch, CP2 has a higher flexural strength, probably because it contains less defects than CP1.

Despite the smaller fraction of defects in CP2, a comparative visual analysis between states I1 and E2 brings relevant information. Figure 8 shows the presence of preexisting defects in the sample (pink rectangles) and defects generated during the flexure test (red rectangles).

To make the comparison more representative, the images of conditions I1 and E2 were aligned (section 2.4.1), the defects were segmented and overlapped (Figure 9). The appearance of cracks during the test, especially in the notch region, is evident. It can be observed that the upper right crack does not change after the test, but several new cracks appear. In polymer composites there are several failure modes, which can occur in the fiber, matrix or fiber-matrix interface. However, with the resolution employed in this work it was not possible to identify the main failure mode for this composite [11].

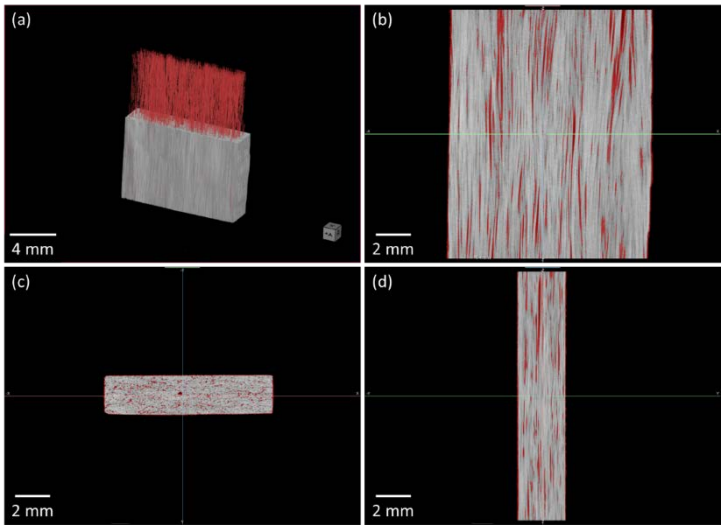

Figure 6: Defect detection - CP1 (condition E2). (a) 3D view; and planes (b) xz; (c) xy; (d) yz.

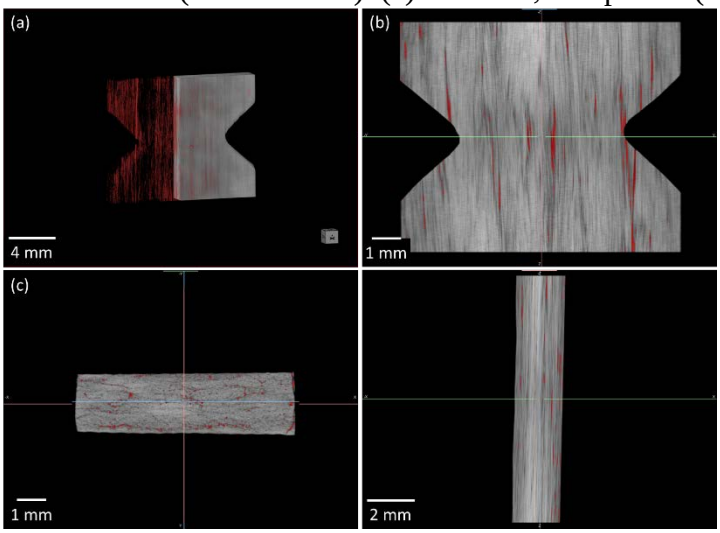

Figure 7: Defect detection - CP2 (condition E2). (a) 3D view; and planes (b) xz; (c) xy; (d) yz.

4. CONCLUSIONS

This work presented a methodology for the characterization of glass-fiber reinforced epoxy matrix composites from the 3D image analysis of microCT images.

From the qualitative point of view, the methodology allowed 3D visualization of defects formed as a function of the application of mechanical stress in the material. It was possible to compare the same specimen before and after a bending test, discriminating pre-existing cracking defects caused by mechanical stress.

The quantitative analysis, preceded by a sensitivity evaluation step, allowed to directly measuring the volumetric fraction of defects as a function of the applied stress level. As expected, the defect fraction remained approximately constant in the elastic regime and increased substantially upon reaching the material rupture stress.

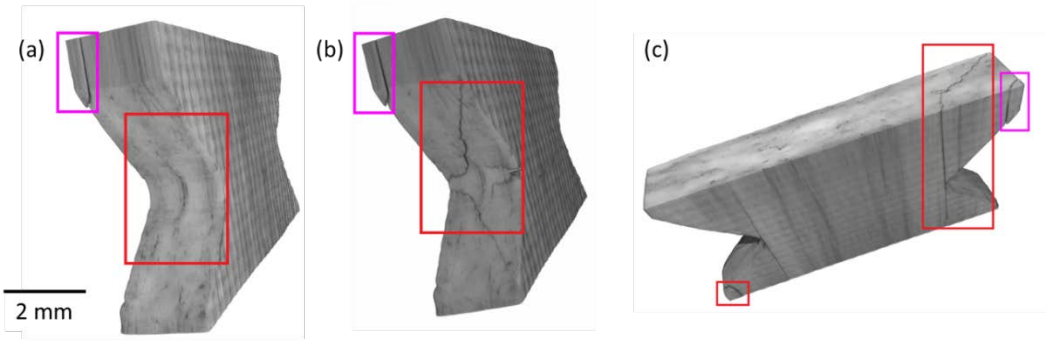

Figure 8: 3D visualization of defects and cracks in CP2. (a) Before the test (I1); b) and c) After the test (E2). Pre-existing crack (pink). Cracks generated by the test (red).

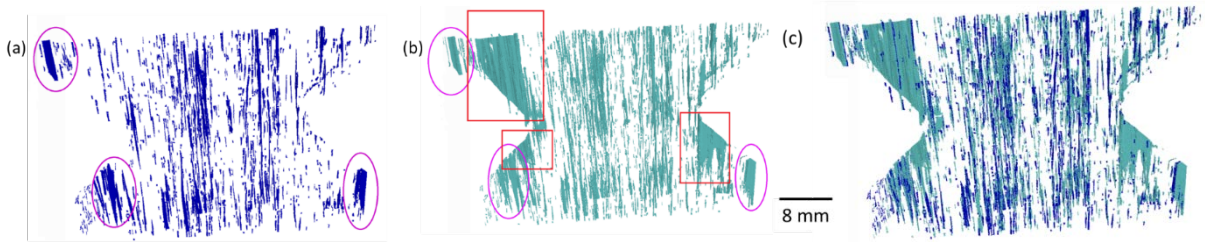

Figure 9: Comparative visualization of defects in CP2. (a) Condition I1; (b) Condition E2. Pre-existing defects (pink ellipses) and generated during the test (red rectangles). (c) Overlap of (a) and (b).

6. REFERENCES

[1] Evolution in the Characterization of Composite Materials through Digital Microscopy. Materials Science Research Journal 1(3/4) (2008) 331-383.

[2] ALVES H, LIMA I, LOPES RT. Methodology for attainment of density and effective atomic number through dual energy technique using microtomographic images. Applied Radiation and Isotopes **89**, 6-12, 2014.

[3] MEES, F; SWNNER, R.; VAN GEET, M.; AND JACOBS (EDS), P. Applications of x-ray computed tomography in the geosciences. Geological Society, Special Publications 215, 1-6, 2003.

[4] BUFFIÈREÁ J.-Y; MAIRE E.; CLOETENSB P.; LORMANDA G. AND FOUGÈRESÁ R. Characterization of internal damage in a MMCp using x-ray synchrotron phase contrast microtomography. Acta Materialia, **47**, 5, 1613-1625, 1999.

[5] SHILLING, P.; KAREDLA, B.; TATIPARTHI, A.; VERGES, M. & HERRINGTON, P. X-ray computed microtomography of internal damage in fiber reinforced polymer matrix composites. Composites science and technology, **65**, 14, 2071-2078, 2005.

[6] FIDAN, S.; SINMAZÇELIK, T.; AVCU, E. Internal damage investigation of the impacted glass/glass + aramid fiber reinforced composites by microcomputerized tomography. NDT&E International, **51**, 1-7, 2012.

[7] PACIORNIK, S. and MAURÍCIO, M H P. Digital Imaging, in: *ASM Handbook Volume 9: Metallography and Microstructures* (ed: G F Vander-Voort), pp 368-402 (ASM International: Materials Park), 2004

[8] SERRA, J. Image Analysis and Mathematical Morphology, Academic Press: London, 1982.

[9] AMBUR D. R.; STARNES J. H.; PRASAD, C. B. Low-speed Impact Damage-Initiation Characteristics of Selected Laminated Composite Plates. AIAA Journal, **33**, 10, 1919-1925, 1995.

ELECTROMAGNETIC CHARACTERIZATION OF PSU/CARBON BLACK MULTIFUNCTIONAL COMPOSITES

Tiago T. S. Braga[(1)], Daniel C. Silveira[(1)], Newton A. S. Gomes[(2)], Mirabel C. Rezende[(2,3)] and Edson C. Botelho[(1)]

(1) Department of Materials and Technology, São Paulo State University (UNESP), School of Engineering of Guaratinguetá, Brazil

(2) Electronic Warfare Laboratory, Technological Institute of Aeronautics (ITA), Brazil

(3) Institute of Science and Technology, Federal University of São Paulo (UNIFESP), Brazil

https://doi.org/10.21452/bccm4.2018.05.06

Abstract

Multifunctional composites are materials capable of combining structural properties with other properties, such as electrical or thermal conductivity, electromagnetic shielding capacity, among others. With the exponential increase in the use of electrical and electronic devices, a specific type of environmental pollution, electromagnetic interference (EMI), has arisen due to the spurious radiation emitted by such devices. Thus, this work proposes the development of a multifunctional composite material based on polysulfone (PSU) and carbon black (CB) and its electromagnetic characterization in the X-band frequency, between 8.2 and 12.4 GHz, widely used in communication and navigation system. The composite materials were produced with high-performance engineering thermoplastic polymer PSU, organic solvent Dichloromethane and two varieties of additive CB. The composite was processed through hot compression molding of films prepared from PSU polymer solutions with the dispersion of the CB additive by means of an ultrasonic tip. The composite processing cycle was obtained through the thermal characterization of the films by differential scanning calorimetry (DSC) and the electromagnetic characterization was conducted with a vector network analyzer (VNA) and rectangular waveguide. With the determination of the scattering parameters (Transmission and Reflection) it was possible to evaluate the interaction of the electromagnetic waves with the composites and quantify the portions of energy reflected, transmitted and absorbed. The composite presented a favorable behavior for electromagnetic shielding, with average reflection values greater than 65%, absorption greater than 21% and transmission lower than 11%.

Keywords: Carbon Black, Electromagnetic Characterization, EMI Shielding, Polysulfone, Scattering Parameters.

1. INTRODUCTION

The extensive development of communications equipment and electronic systems has been increasing electromagnetic pollution to new heights, which can lead to the malfunctioning of several types of systems, such as commercial antennas and electronic scientific instruments. Electromagnetic interference can be understood as the disturbance to electronic equipment due to spurious radiation emitted by other electric circuits [1].

Given the need to protect certain components against such pollution, electromagnetic shielding becomes necessary. The shielding is the reduction or attenuation of the waves to prevent interference. There are three mechanisms that can contribute to the effectiveness of electromagnetic shielding: reflection, absorption and multiple reflection inside the material [2-4].

A wide variety of materials can be used in electromagnetic shielding, with different properties of electrical conductivity, magnetic permeability and geometries [2]. Polymeric matrices are, generally, materials that doesn't have this property, most polymers are transparent to electromagnetic waves. However, to enjoy its excellent properties, such as low specific mass, low cost and ease of use, the dispersion of particles or fibers materials can be used to promote interaction with the waves [3,5], dissipating them through absorption or reflection, according to the additive and concentration [1].

The multifunctional composite class seeks to join structural functions of composites such as strength, stiffness, fracture toughness and damping to non-structural functions, such as electromagnetic shielding [6]. By joining a high-performance engineering polymer such as polysulfone, which, among other properties, has high hardness, impact strength and high temperature resistance, [7] with the carbon black load, a material widely used in electromagnetic shielding research [8-11], multifunctional composites with great potential may be obtained.

The objective of this work is process and characterize multifunctional polymer matrix composite with the dispersion of carbon black particles and verify its effect as EMI shielding material in frequency range between 8.2 and 12.4 GHz, most common in communication and navigation systems.

2. EXPERIMENTAL

2.1 Materials

The polymer matrix used was the amorphous polymer polysulfone, with a specific mass of 1.24 g/cm³, tensile strength of 70.3 MPa, tensile modulus of 2482 MPa, flexural strength of 106.2 MPa, flexural modulus of 2689 MPa and glass transition temperature of 185 °C.

To prepare the polymer solution, the solvent used was the organic solvent Dichloromethane in liquid form with clear appearance and ether characteristic odor, with chemical formula CH_2Cl_2, specific mass of 1.34 g/cm³, molecular weight of 84,9 g/mol, boiling point of 39.8 °C, solidification point of -96.7 °C and flash point of 640.5 °C.

To obtain the composite, carbon black additive in powder form was dispersed into the polymer solution. Materials from two different manufacturers was used, XE2B from Degussa, with 35 nm average particle size, 1,7-1,9 g/cm³ density at 20 °C and 1000 m²/g specific surface area, and XC72R from Cabot, with 50 nm average particle size, 1,7-1,9 g/cm³ density at 20 °C and 1000 m²/g specific surface area.

2.2 Film production

The films were produced through the preparation of polymer solutions of PSU and Dichloromethane, using 10 and 90 %m/m content, respectively. The solutions were prepared in fume hood at room temperature and with constant stirring.

Then, the CB additive were dispersed in the proportion of 15 %m/m of additive to 85 %m/m of polymer used in the preparation of the polymer solution, using a Sonic & Materials VC 750 ultrasonic tip, setup with 20% of maximum amplitude of the equipment for 5 minutes, intercalating 10 seconds in operation and 5 seconds in standby, to avoid overheating and solvent losses.

The preparation of the film was carried out in an oven with temperature control, for 2 hours at 40 °C, to promote the solvent evaporation.

2.3 Thermal characterization

The thermal characterization was performed by means of differential scanning calorimetry, in the dynamic mode, of the polymer films, determining the start, peak and end of melt temperatures (T_m). A differential calorimeter model Q20 from TA Instruments was used. Hermetic aluminum sample holder and heating rate of 7.6 °C/min were used up to 350 °C, to match the heating rate of the hydraulic press used in the processing, followed by cooling down to 25 °C.

2.4 Composite processing

The processing of the composite materials, by means of manual lay-up of PSU films with and without carbon black, was performed in a hydraulic press, model CMV100H-15-X, Monarch series from Carver and steel mold of 70 mm x 70 mm. Heating was performed up to 190 °C, due to limitations of sealing of the mold used, with 10 minutes of isotherm, followed by cooling down to room temperature. The entire process was performed with applied pressure of 2 MPa.

2.5 Electromagnetic characterization

The determination of the scattering parameters of the composite samples was performed using a four-port vector network analyzer (VNA) model PNA-L N5230C from Agilent Technologies, using ports 2 and 4, frequency generator between 300 kHz and 20 GHz, rectangular waveguide with adapter model 00281-60016 OPTION 006 also from Agilent Technologies. The transmitted and reflected energy plots were calculated using equation 1 [12].

$$\text{Attenuation (\%)} = 100 \,.\, [1 - 10^{\left(\frac{-dB}{10}\right)}] \quad (1)$$

From the calculation of the transmitted and reflected energy portions it is possible to determine the percentage of energy absorbed by the composite through equation 2 [13].

$$\text{Absorption (\%)} = 100 - (\text{Reflection} + \text{Transmission}) \quad (2)$$

3. RESULTS AND DISCUSSION

3.1 Thermal characterization and processing cycle

From the DSC of the PSU films, the temperature range at which the material melts was determined. Figure 1 presents the melting heat flow *vs* temperature graph.

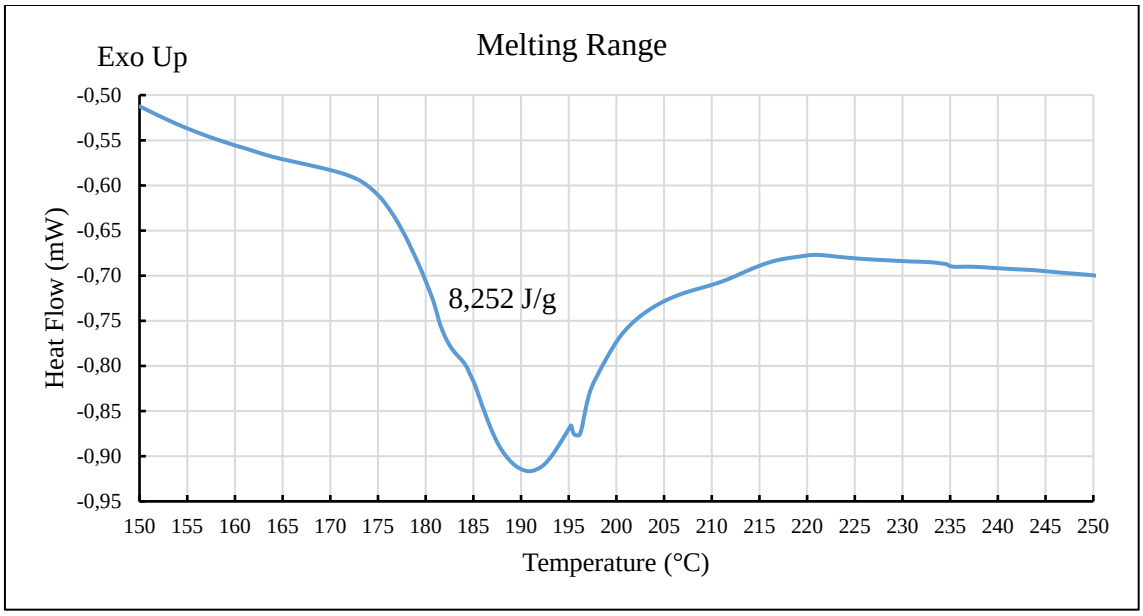

Figure 1: Melting range.

Based on the DSC characterization, the hot compression molding cycle was designed. Figure 2 presents the processing cycle, with constant applied pressure of 2 MPa.

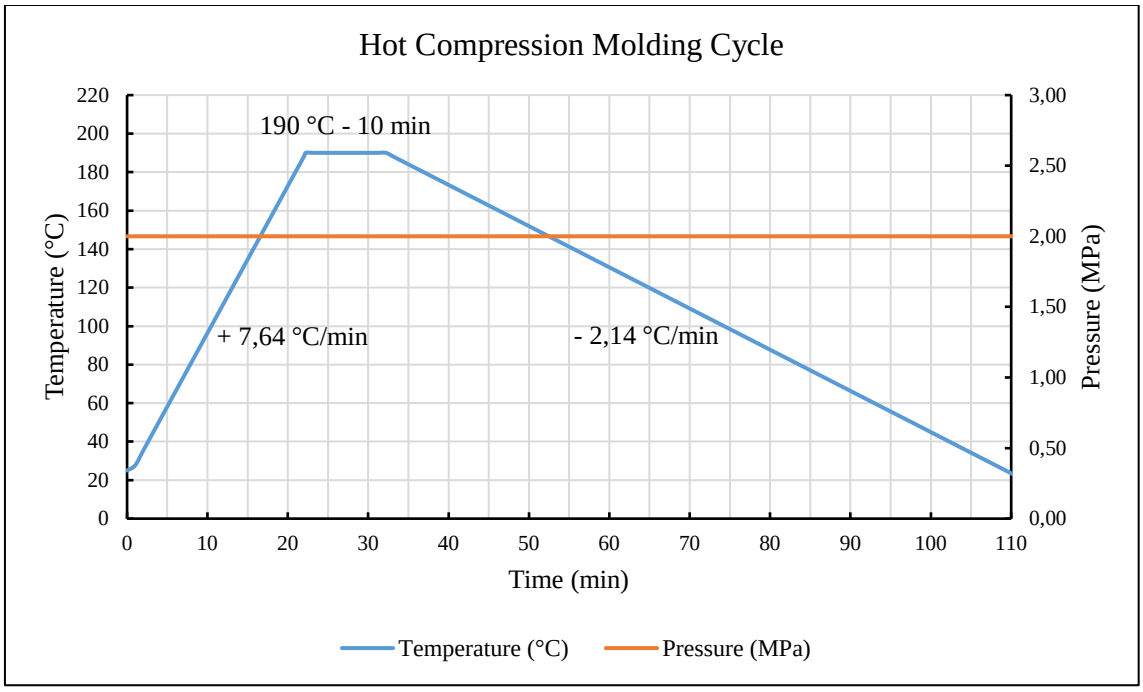

Figure 2: Hot compression molding cycle.

Through the thermal analyzes and the processing of the films, a composite in the form of a plate with 70 mm x 70 mm dimensions and thickness between 1.1 and 1.3 mm was obtained. From the qualitative evaluation of the plaques obtained, as union of the layers and rigidity of the plate, the

parameters used were considered adequate to proceed to the electromagnetic characterization of the composite samples.

3.2 Electromagnetic characterization

The electromagnetic characterization of the materials provided the scattering parameters for each sample: PSU films and composites, 85 %m/m PSU + 15 %m/m Degussa CB and 85 %m/m PSU + 15 %m/m Cabot CB.

With the attenuation data regarding transmission and reflection in the composite, and with equations 1 and 2, it is possible to generate graphs relating the transmission, reflection and absorption at each frequency in the studied range.

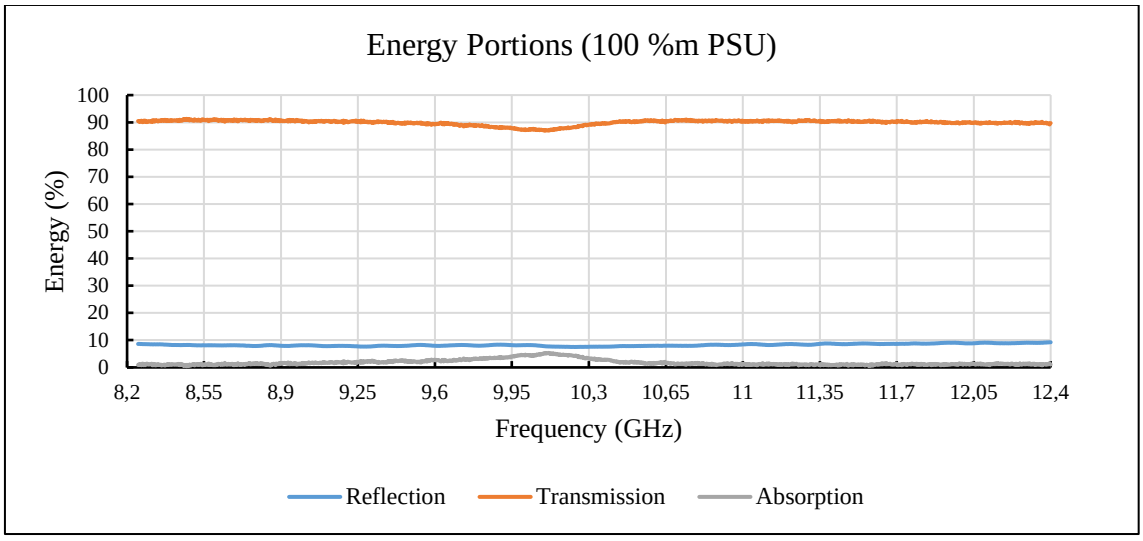

Figure 3: Energy portions (100 %m PSU).

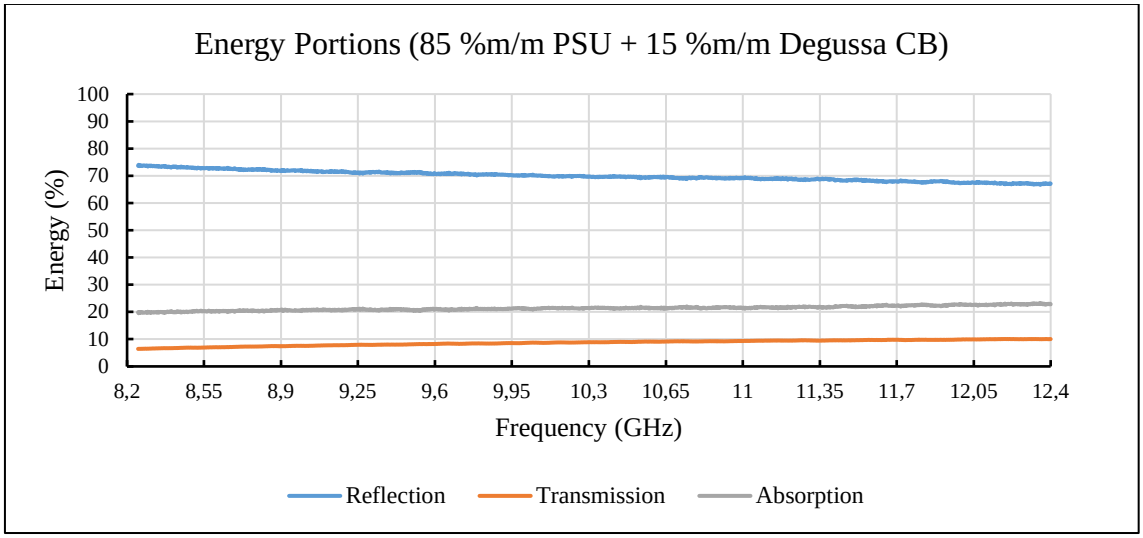

Figure 4: Energy portions (85 %m/m PSU + 15 %m/m Degussa CB).

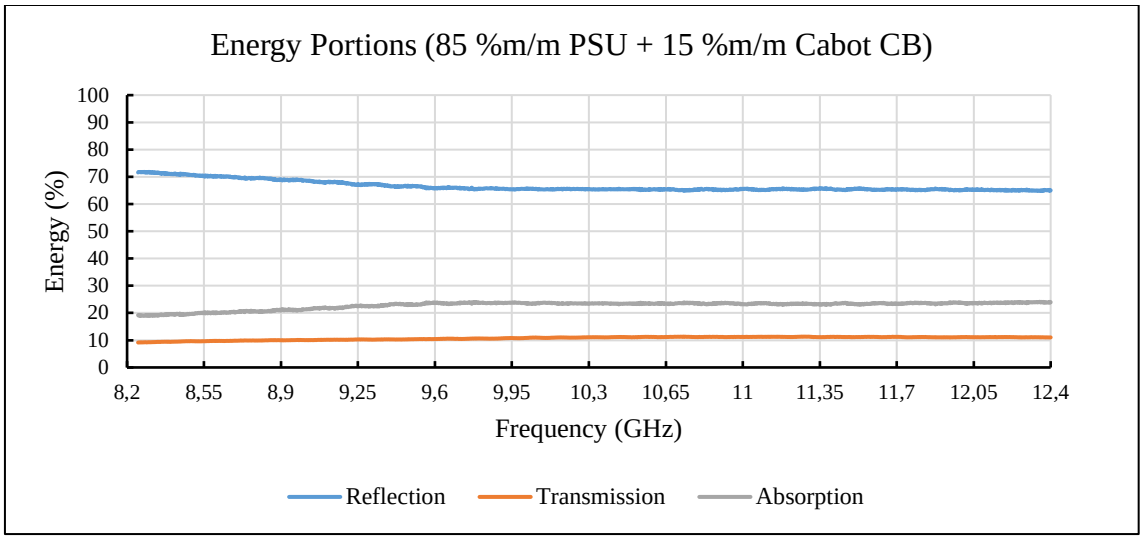

Figure 5: Energy portions (85 %m/m PSU + 15 %m/m Cabot CB).

It is observed that in all cases the transmitted, reflected and absorbed energy portions remained practically constant throughout the studied frequency range.

From the analysis of the graphs it is possible to obtain the average values of each energy portion for each sample, as shown in table 1.

Table 1: Mean values of energy portions for each sample.

Sample	Transmitted Energy (%)	Reflected Energy (%)	Absorbed Energy (%)
100 %m PSU	89,94	8,26	1,80
85 %m/m PSU + 15 %m/m Degussa CB	8,68	69,95	21,37
85 %m/m PSU + 15 %m/m Cabot CB	10,70	66,52	22,78

Despite the dimensional difference between the two varieties of CB used, the results obtained showed similar behavior, however the Degussa sample shows slightly higher reflection while the Cabot sample shows slightly higher transmission and absorption of the electromagnetic energy.

Therefore, it is observed that the composites present main behavior of high reflection, low transmission and intermediate absorption, characterizing their potential use for electromagnetic shielding.

4. CONCLUSIONS

Multifunctional composites based on polysulfone and carbon black were produced by hot compression molding of films prepared from the dissolution of the polymer with dichloromethane, followed by the dispersion via ultrasonic tip of carbon black additives.

Through the thermal characterization of the films by differential scanning calorimetry, it was possible to determine the start, peak and final melting temperatures of the polymer, which along

with information obtained from the literature, provided the designed hot compression molding cycle.

With the electromagnetic characterization, through a vector network analyzer and rectangular waveguide, it was possible to measure the scattering parameters of the composite when it was affected by electromagnetic waves in the X-band, between 8.2 and 12.4 GHz.

The composite material presents potential for EMI shielding, exhibiting highly reflective behavior, combined with intermediate absorption of microwaves. Promoting the shielding to approximately 90% of the electromagnetic radiation in all amplitude analyzed.

ACKNOWLEDGEMENTS

The authors are grateful to CNPq, São Paulo State University (UNESP) and Electronic Warfare Lab. in Technological Institute of Aeronautics (ITA).

REFERENCES

[1] Thomassin, J-M., Jérôme, C., Pardoen, T., Bailly, C., Huynen, I., Detrembleur, C., 'Polymer/carbon based composites as electromagnetic interference (EMI) shielding materials', *Materials Science and Engineering* R **74** (2013) 211-232.

[2] Tong, X.C., 'Advanced Materials and Design for Electromagnetic Interference Shielding', 1st Edn (Boca Raton, Florida, 2008).

[3] Chung D.D.L. 'Electromagnetic interference shielding effectiveness of carbon materials', *Carbon* **39** (2001) 279-285.

[4] Sudha, J.D., Sivakala, S., Prasanth, R., Reena V.L., Radhakrishnan Nair, P., 'Development of electromagnetic shielding materials from the conductive blends of polyaniline and polyaniline-clay nanocomposite-EVA: Preparation and properties', *Composites Science and Technology* **69** (2009) 358-364.

[5] Dhawan, S.K., Singh, N., Rodrigues, D., 'Electromagnetic shielding behavior of conducting polyaniline composites', *Science and Technology of Advanced Materials* **4** (2003) 105-113.

[6] Gibson R.F., 'A review of recent research on mechanics of multifunctional composite materials and structures', Composite Structures **92(12)** (2010) 2793-2810.

[7] Ebewele, R.O., 'Polymer science and technology' (Boca Raton, Florida, 1996).

[8] Mondal, S., Ganguly, S., Rahaman, M., Aldalbahi, A., Chaki, T.K., Khastgir, D., Das, N.Ch., 'A strategy to achieve enhanced electromagnetic interference shielding at low concentration with a new generation of conductive carbon black in a chlorinated polyethylene elastomeric matrix', *Physical Chemistry Chemical Physics* **18(35)** (2016) 24591-24599.

[9] Wen, Y., Song, J., Chen, J., Sun, Y., Yang, W., 'Synergistic Conductivity and Electromagnetic Interference Shielding Effectiveness of Epoxy/Carbon Fiber and Epoxy/Carbon Black Composites via Mixing with Bamboo Charcoal', *BioResources* **12(1)** (2017) 1288-1299.

[10] Song, J., Yuan, Q. Zhang, H., Huang, B., Fu, F., 'Elevated conductivity and electromagnetic interference shielding effectiveness of PVDF/PETG/carbon fiber composites through incorporating carbon black', *Journal of Polymer Research* **22** (2015) 158.

[11] Kuester, S., Merlini, C., Barra, G.M.O., Ferreira Jr., J.C., Lucas, A., Souza, A.C., Soares, B.G., 'Processing and characterization of conductive composites based on poly(styrene-b-ethylene-ran-butylene-b-styrene) (SEBS) and carbon additives: A comparative study of expanded graphite and carbon black', *Composites Part B* **84** (2016) 236-247.

[12] Lee, S.M., 'International encyclopedia of composites', (New York, New York, 1991).

[13] Gupta, K.K., Abbas, S.M., Goswami, T.H., Abhyankar, A.C., 'Microwave absorption in X and Ku band frequency of cotton fabric coated with Ni–Zn ferrite and carbon formulation in polyurethane matrix', *Journal of Magnetism and Magnetic Materials* **362** (2014) 216-225.

6. FRP FOR CIVIL ENGINEERING APPLICATIONS

IMPACT DAMAGED PIER STRENGTHENING USING CFRP FABRIC

Abheetha Peiris (1), Sahar Y. Ghanem (2) and Issam E. Harik (3)

(1) Kentucky Transportation Center, University of Kentucky, Lexington KY USA

(2) Department of Engineering & Technology Management, Morehead State University, Morehead, KY, USA

(3) Department of Civil Engineering, University of Kentucky, Lexington KY USA

https://doi.org/10.21452/bccm4.2018.06.01

Abstract

On October 21, 2015, a semi-trailer truck traveling south on the W.H. Natcher Parkway, near Bowling Green, Kentucky collided with the north pier supporting the Elrod road overpass. The impacted bridge is a four-span, 67 m (220 ft) long, reinforced concrete deck girder bridge. Large diagonal cracks propagated up the entire height of the column from the impact point. Horizontal cracking also appeared around the entire circumference near the point of impact. Large cracks occurred on the top face of the pier cap, between the girder pedestals, extending in the transverse direction. Because winter weather was approaching, the Kentucky Transportation Cabinet (KYTC) deemed a rapid retrofit necessary to maintain the bridge's structural integrity. Two types of uniaxial Carbon Fiber Reinforced Polymer (CFRP) fabric and one braided triaxial CFRP fabric were utilized in the retrofit design. A heavy uniaxial CFRP fabric was utilized as the primary strengthening material for the impacted column. A finite element model was utilized to analyse the effectiveness of the column retrofit. The retrofit construction work was completed in five workdays spread over an eight day period. The CFRP fabric-strengthened pier column is expected to be stronger than the original column.

1. INTRODUCTION

The use of composite material to strengthen reinforced concrete (RC) piers and columns has become well-established over the last few decades. Compared to traditional methods like steel jacketing, the use of Fiber Reinforced Polymer (FRP) material for column confinement can be cost effective due to their high strength and light weight properties promoting faster retrofits. Due to their inherent corrosion resistance this can also lead to lower life-cycle costs. Previous studies have shown that RC columns that are fully wrapped with FRP has increased ductility, moment and ultimate compressive load capacity, ultimate deformability and energy absorption compared to unconfined columns [1,2]. This can be advantageous when retrofitting damaged and/or

deteriorated RC piers and columns. Design guides by the American Concrete Institute [3], American Association of State Highway and Transportation Officials [4], and International Federation for Structural Concrete [5] are available on the use of FRP for confinement of RC concrete columns. Numerous field applications of FRP for retrofit of RC columns for axial loads and confinement, corrosion damage, and seismic loads have been reported [6].

Another method of bridge pier damage is due to accidental heavy vehicle collision, sometimes leading to loss of life and complete destruction of the bridge [7]. While certain code provisions such as AASHTO [8] exist for the design and placement of bridge piers next to roadways, these typically do not address vehicle characteristics and travel speeds [7]. The present paper details bridge pier damage due to an accidental truck impact, and the subsequent retrofit design and construction using Carbon Fiber Reinforced Polymer (CFRP) fabric. On October 21, 2015, a semi-trailer truck traveling south on the W.H. Natcher Parkway, near Bowling Green, Kentucky collided with the north pier supporting the Elrod road overpass. While a guardrail existed between the roadway and the pier, the semi-trailer truck had overrun the guardrail prior to impacting the pier column as shown in Figure 1.

Figure 1: Semi-trailer truck impact on Elrod road bridge

2. BRIDGE AND DAMAGE DETAILS

The Elrod road impacted bridge is a four-span, 67 m (220 ft) long, reinforced concrete deck girder bridge. The two center spans of the overpass are over the northbound and southbound lanes of W. H. Natcher Parkway in Kentucky. Each pier of the bridge is comprised of two reinforced concrete pier columns supporting the pier cap. The four cast-in-place reinforced concrete girders are continuous across the length of the bridge. While the girders were fixed over the center pier (pier 2), at all other locations including the impacted pier (pier 3) the girders rested on roller supports which allowed translational movement. The 0.76 m (2.5 ft) diameter RC pier column is reinforced by 8 No.32 (#10) rebars with a nominal diameter of 32.26 mm (1.27 inch). A general layout of the bridge and cross section of a pier identifying the impact area is shown in Figure 2.

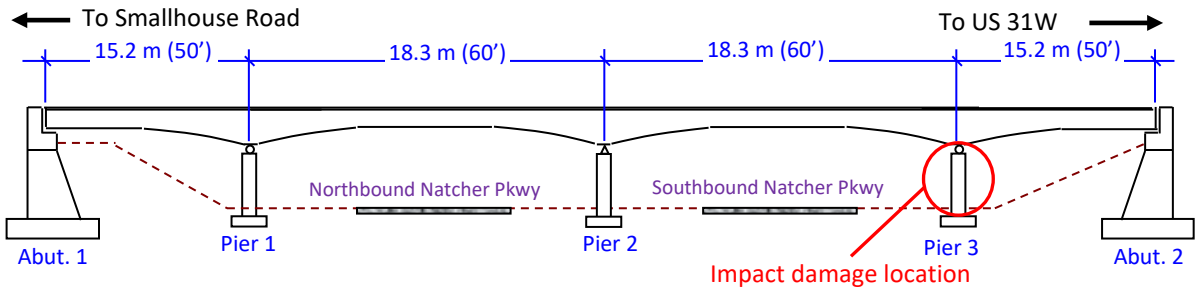

(a) General layout of the bridge

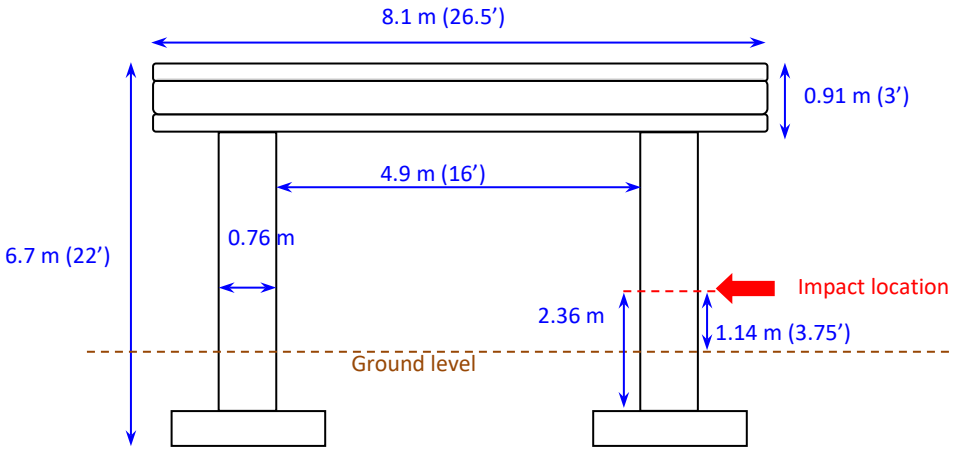

(b) Cross section of the Pier

Figure 2: Layout of the Elrod Road bridge with impact damage location

The semi-trailer truck collided with the north pier column of pier 3. Possibly due to a low impact speed and the guardrail potentially reducing the force of impact, the structural damage to the pier did not cause immediate failure of the bridge. The impact force had caused sufficient lateral movement between the pier and the beams that the rocker socket ends on each of the four RC beams were sheared. Concrete was damaged at the impact location, approximately 1.14 m (3.75 ft) above ground elevation, producing cracks on the impacted pier column as well as the pier cap above. Figure 3 highlights the damage at the impact location and the cracking in the column and pier cap.

Large diagonal cracks propagated up the entire height of the column from the impact point (Figure 3(b)). Horizontal cracks appeared around the column's entire circumference near the point of impact. Diagonal cracking occurred at the top of the column, where it intersects the pier cap (Figure 3(a)). Large transverse cracks appeared on the top face of the pier cap, between the girder pedestals (Figure 3(d)). Some transverse cracks spanned the entire width of the pier cap, with others extending down along the two vertical side faces. The cracks on the impacted column and pier cap affected the structural integrity of the bridge and raised concerns over whether they would accelerate corrosion of the reinforcing steel and lead to the deterioration of concrete. The objective of the retrofit was to repair and strengthen the impacted pier column and pier cap. Due to approaching winter weather, the Kentucky Transportation Cabinet (KYTC) required that the retrofit be designed and constructed rapidly.

(a) Impacted area of column

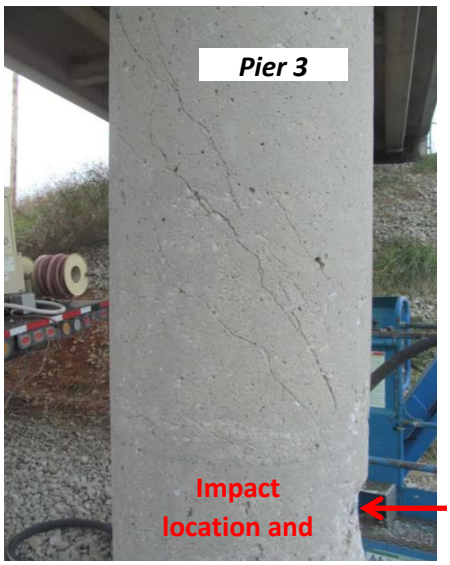

(b) Impacted column east face

(c) Top of impacted column

(d) Cracking on top of pier cap

Figure 3: Damage details and cracking in the pier column and pier cap

3. RETROFIT DESIGN

The axial capacity of the impacted column was of concern due to cracking. The structural integrity of the pier cap was concerning due to the cracks on the top of the pier cap. CFRP fabric was selected as the retrofit material for the damaged pier column and pier cap due to its high strength-to-weight ratio, which makes it an ideal material for quick and efficient repairs. Along with providing strength, the repair scheme was selected to protect the steel reinforcement, as corrosive agents could potentially penetrate the widening cracks. Several different types of CFRP fabric, including two uniaxial CFRP fabrics and a braided triaxial CFRP fabric, were used for the retrofit. The fabric selected depended on the type of strengthening being carried out. Table 1 lists the physical and mechanical properties of the CFRP fabric.

Table 1: Physical and mechanical properties of CFRP fabric

CFRP fabric type	Fabric width (mm)	Laminate thickness at 55% fiber volume (mm)	Fabric weight (g/m^2)	Tensile strength (MPa)	Elastic modulus (MPa)
UCF 120	305	0.76	757	2,848	139×10^3
UCF 055	305	0.36	305	2,848	139×10^3
TCF 012*	508	0.28	272	800	44×10^3

* The mechanical properties are the minimum for both longitudinal and transverse directions

3.1 Retrofit of pier cap

All three types of CFRP fabric were utilized for the pier cap retrofit. The UCF 120 uniaxial fabric, which can carry 535 kN of tensile force per 305 mm (120 kips of per 1-ft) width of fabric, was the first CFRP fabric used. To strengthen the top of the pier cap with cracked concrete, a layer of the UCF 120 fabric was placed on the top horizontal face of the pier cap, along both sides of the girder pedestals as well as in between the pedestals, parallel to the pier cap's longitudinal direction. The uniaxial UCF 055 CFRP fabric has a tensile capacity of 245 kN per 305 mm (55 kips per 1-ft) width of fabric. It was placed in continuous horizontal strips around the perimeter of the pier cap. To anchor the retrofit, a layer of the braided triaxial TCF 012 CFRP fabric was wrapped perpendicular to the previous two layers within the spaces along the pier cap between the pedestals. The triaxial fabric is a quasi-isotropic CFRP fabric with braided fibers running in 0°, and ±60° directions. The primary advantage of this fabric is that it provides approximately the same tensile capacity along any direction in the plane of the fabric. The triaxial CFRP fabric used in the present design has a tensile capacity of 53 kN per 305 mm (12 kips per 1-ft) width of fabric in all directions.

3.2 Retrofit of pier column

Two types of CFRP fabrics were used for the pier column retrofit. The first layer utilized the UCF 120 CFRP fabric. Fabric was placed in 305 mm (12-inch) wide strips around the circumference of the pier column. The second layer of fabric used on the column was the triaxial TCF 012 CFRP fabric. This fabric was placed in 508 mm (20-inch) wide strips around the circumference of the pier column, with a 100 mm (4-inch) vertical overlap between each strip. The purpose of the wrapping is to confine the concrete and increase the column's load carrying capacity. The FE model was used to model the impacted column, where the triaxial CFRP fabric is modeled as a linear orthotropic material where material properties are logged in the longitudinal and transverse directions. The loads applied on the column are calculated using the bridge plans to identify the attributed concentric axial load (P) and bending moment (M).The analysis found that the axial capacity of the column, at a load eccentricity of 276 mm (10.86 inch), increased by 260% [9]. Figure 4 presents the general retrofit design for both the pier cap and the impacted pier column.

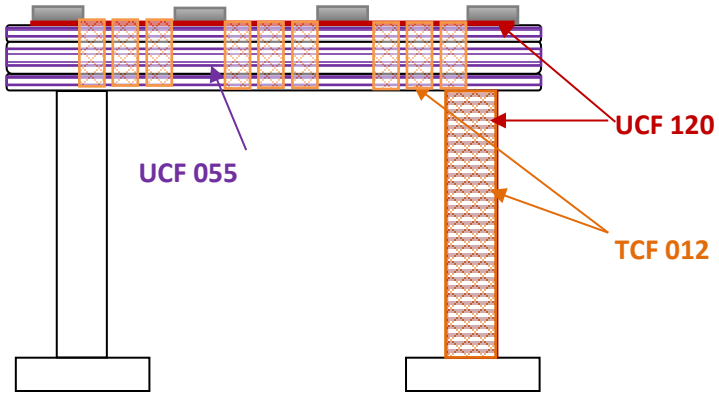

Figure 4: General retrofit scheme for impact damaged pier cap and column

4. RETROFIT CONSTRUCTION

After removing all loose material around the impact area, crews sandblasted the entire retrofit area to remove all loose material and to provide a roughened surface for CFRP fabric application. The sandblasting exposed previously unseen cracks while also cleaning the rebar steel exposed during the impact. After the placement of wooden formwork around the two repair sections, a rapid set repair mortar was applied to damaged areas on the pier column. After the mortar cured for a day, formwork was removed and the mortar ground down to remove surface variations with the pre-existing concrete column surface.

CFRP fabric was placed according to the design details provided in Section 2. Before applying the CFRP fabric, a primer coat was applied to the surface of the concrete. Laminating rollers were used to smooth out air pockets, voids, and irregularities in the fabric during its placement. Pier cap strengthening was carried out first. Initially the top of the pier cap was strengthened by placing strips of the UCF 120 fabric between the concrete pedestals as well as on either side of the pedestals. The pier cap was then wrapped with a layer of UCF 055. Due to a rustication detail on the pier cap, UCF 055 strips of two different widths were used to wrap the pier cap, as seen in Figure 5(a). Finally, a layer of TCF 012 CFRP fabric was placed, confining and anchoring the previous layers of CFRP fabric (Figure 5(b)).

(a) UCF 055 application (b) TCF 012 application

Figure 5: CFRP fabric application on pier cap

The UCF 120 CFRP fabric was wrapped on the impacted pier column without any vertical overlap between strips. Figure 6(a) depicts the application of UCF 120 at the top of the pier. The second layer of fabric, the TCF 012, was placed (Figure 6(b)) over the first layer of UCF 120. The joints for the TCF 012 layer were placed on the opposite side of the column from the joints of the UCF 120 CFRP fabric. Three days after the CFRP fabric application, a protective coating was applied over the retrofit area in order to protect against UV degradation. For aesthetic reasons, the entire pier, including the column that was not strengthened was coated. Repair and strengthening work was completed over four consecutive days, with the final day spent on the CFRP fabric wrapping. Including the day spent coating the pier, the project was completed in five work days spread over an eight-day period. Figure 7 captures the pier following the completion of the retrofit and application of the UV protective coating.

(a) UCF 120 application (b) TCF 012 application

Figure 6: CFRP fabric application on pier column

(a) Pier after CFRP wrapping (b) Following application of protective coating

Figure 7: Completed retrofit

5. SUMMARY AND CONCLUSIONS

The pier cap and pier column on an overpass over W.H. Natcher Parkway, near Bowling Green, Kentucky was damaged when a semi-trailer truck collided with the pier. Large diagonal cracks propagated up the entire height of the column from the impact point. Horizontal cracking also appeared around the entire circumference near the point of impact. Large cracks occurred on the top face of the pier cap, between the girder pedestals, extending in the transverse direction. Two types of uniaxial Carbon Fiber Reinforced Polymer (CFRP) fabric and one braided triaxial CFRP fabric were utilized in the retrofit design. A heavy uniaxial CFRP fabric was utilized as the primary strengthening material for the impacted column. A finite element model was utilized to analyse the effectiveness of the column retrofit.

The use of CFRP fabric enabled the retrofit construction work to be completed in five workdays spread over an eight day period. Excluding the final protective coating, all work was also completed within one month of the impact. Periodic inspections were conducted over a period of two and a half years, during which time no signs deterioration of the retrofit were observed. The CFRP fabric-strengthened pier column is expected to be stronger than the original column.

ACKNOWLEDGEMENTS

Funding for the project was provided by the Kentucky Transportation Cabinet (KYTC). The retrofit construction and traffic control was carried out by personnel from KYTC District 03.

REFERENCES

[1] Mirmiran, A., and Shahawy, M., 'Behavior of Concrete Columns Confined by Fiber Composites' *Journal of Structural Engineering*, 123(5), (1997) 583–590.

[2] Toutanji, H., 'Stress-Strain Characteristics of Concrete Columns Externally Confined with Advanced Fiber Composite Sheets' *ACI Material Journal*, 96(3) (1999) 397–404.

[3] American Association of State Highway and Transportation Officials, Design of Bonded FRP Systems for Repair and Strengthening of Concrete Bridge Elements—1st Edition (2012), AASHTO, Washington, D.C.

[4] American Concrete Institute, Guide to the Design and Construction of Externally Bonded FRP Systems for Strengthening Concrete Structures, ACI 440.2R-08 (2008), ACI Committee 440, Farmington Hills, MI.

[5] International federation for Structural Concrete (fib), Externally bonded FRP reinforcement for RC structures, fib Bulletin 14 (2001), fib Task Group 9.3, Lausanne, Switzerland.

[6] Parvin, A., and Brighton, D., 'FRP Composites Strengthening of Concrete Columns under Various Loading Conditions' *Polymers*, 6 (2014) 1040-1056. doi:10.3390/polym6041040

[7] El-Tawil, S., Severino, E., and Fonseca, P. 'Vehicle collision with bridge piers' *J. Bridg. Eng.*, 10(3) (2005), 345–353.

[8] American Association of State Highway and Transportation Officials, LRFD Bridge Design Specifications—Seventh Edition (2014), AASHTO, Washington, D.C.

[9] Ghanem S.Y., 'Circular RC columns partially confined with FRP' Theses and Dissertations—Civil Engineering (2016), University of Kentucky, Lexington, KY USA.

FIVE-ELEMENT MODELS FOR LONG-TERM RESPONSE OF PGFRP MEMBERS

Daniel C. T. Cardoso [(1)] **and Kent A. Harries** [(2, 3)]

(1) Department of Civil and Environmental Engineering, Pontifícia Universidade Católica do Rio de Janeiro, Brazil

(2) Department of Civil Engineering, University of Pittsburgh, United States

(3) Department of Architecture and Civil Engineering, University of Bath, United Kingdom

https://doi.org/10.21452/bccm4.2018.06.02

Abstract

Pultruded glass-fiber reinforced polymers (pGFRP) exhibit significant viscoelastic behavior even at room temperature, which may result in long-term loss of stability or excessive deflection. Several works in the literature have investigated creep of pGFRP, intending to characterize time-dependent behavior and to develop safe provisions for structural design of pGFRP members. The three-parameter Findley Power Law has been widely used by researchers and is usually calibrated to creep experiments conducted at constant stress and temperature. However, this empiricism and its lack of correlation with a mechanical model result in little predictive capacity for different resin types and fiber content. In this work, innovative linear viscoelastic models combining essentially elastic behavior of fiber and viscoelastic nature of matrix is proposed to represent the long-term behavior of pGFRP subject to stresses parallel or perpendicular to fiber direction. The model can also be used to assess long-term composite behavior for complex load history and for other viscoelastic phenomena such as recovery and relaxation, usually not addressed by Findley's law. The experimental results from a short and long-term mechanical characterization of a vinylester-based pGFRP are reported and compared with the proposed approach, showing that the model satisfactorily predicts creep and recovery of such composites for a given time span. It is also shown that the presence of fibers parallel to load direction result in much lower relative compliance and quicker recovery.

1. INTRODUCTION

Pultruded glass-fiber reinforced polymers (pGFRP) are gaining acceptance in civil engineering applications particularly due to their high strength, lightweight and non-corrosive nature. However, some aspects of pGFRP material behavior are not fully understood, including long-term performance. The limited knowledge has led to conservative design considerations in current and

in-development design standards, potentially increasing the cost of structures made with the pGFRP [1].

The pronounced creep behavior of pGFRP is usually attributed to the viscoelastic nature of the polymer resin, which is highly dependent on the curing and post-curing conditions [2, 3]. In the pultrusion process, pGFRP are pulled with speeds typically ranging from 300 to 500 mm/min through 500 to 1500 mm long dies heated to temperatures between 100 and 150 ºC, This process is likely to result in incomplete cure [3].Glass fibers may also exhibit a viscoelastic response, but usual at relatively greater stress levels, typically beyond those anticipated in structural service.

Findley's three-parameter empirical power law, described in Eq. 1, has been widely used to describe primary and secondary creep of polymers with good accuracy over a wide range of time, t [4].

$$\frac{\varepsilon(t)}{\sigma_0} = J(t) = \frac{1}{E_0} + \frac{1}{E_m} t^n \quad (1)$$

In which $\varepsilon(t)$ is the long-term strain, σ_0 is the constant applied stress, $J(t)$ is the creep compliance and E_0, E_m and n are stress-independent parameters. This equation is usually adequate for low stress levels and its popularity is based on its simplicity and excellent agreement with experiments.

In a seminal study, Bradley *et al.* [2] adopted flexural creep tests to characterize neat vinylester and polyester resins having different curing and post-curing conditions using Findley's power law. The authors observed that i) polyester-based specimens exhibited greater compliance than vinylester for the same curing condition; ii) temperature-cured specimens resulted in much lower creep exponent, n, than those cured at room temperatures; and iii) important reduction in creep compliances were observed with post-curing time. Differences are associated to the type of chemical structure of each resin and to the time-temperature relation for cross-linking completion. Finally, the authors tested vinylester specimens reinforced with woven E-glass fabric and showed that creep compliances are significantly reduced by the presence of fibers.

Findley's equation has also been successfully used by several authors for pGFRP, treating the composite as a single viscoelastic bulk material [1, 5–7]. One of the drawbacks is the large dispersion of values for the parameters reported in literature, which is certainly associated to differences of resin properties and fiber volume ratios, V_f, in each study. For example, creep exponents ranging from $n = 0.14$ to $n = 0.36$ have been reported in literature for pGFRP [1]. It can be noted that parameters are also dependent on the loading type and direction. Harries *et al.* [1] and Sá *et al.* [7] summarized some previous works intending to investigate the long-term behavior of pGFRP, and it can be seen that most creep data have been obtained for tension, compression or flexure of specimens loaded parallel to the pultrusion direction (i.e., in the longitudinal direction). To date, limited data has been reported about shear creep [8] and, to the best of authors' knowledge, there are no works addressing specimens subject to stresses perpendicular to the pultrusion direction (transverse). These two cases correspond to conditions where behavior is usually strongly dependent on resin properties. Moreover, information regarding relaxation, recovery and behavior under complex loading history are very limited. Sá *et al.* [7], for example, reported large immediate recovery in full scale pGFRP beams.

Findley's law is empirical and its parameters are usually determined to fit experimental results obtained under conditions of constant stress. The lack of correlation with a mechanical model may

result in little predictive capacity for a complex load history and for relevant phenomena for viscoelastic materials such as relaxation and immediate and delayed recovery. Linear models combining basic units – springs and dashpots – may be used along with superposition for full mathematical representation of general viscoelastic behavior. Usually, models using fewer basic units are easier for characterization and allow for better interpretation of mechanical behavior, but few viscoelastic materials have creep characteristics that can be described by such simple models. On the other hand, these simple models can be used to study long term behavior over a given time span [4]. Sá *et al.* [9], for example, reported good agreement with experimental creep results when using Dirichlet-Prony or Burgers-Kelvin models, whereas a poorer agreement was reported for simpler four-element Burgers' model. A Burgers' model for FRP laminates starting from properties of single phases was also proposed by Ascione *et al.* [10] and validated with experiments.

The present study aims to propose simple five-element models combining fiber and matrix individual mechanical properties, in a viscoelastic extension of the so-called rule-of-mixtures (RoM). The proposed approach accounts for different matrix properties and fiber contents, as well as for loading direction. The influence of fiber architecture on long-term behavior is discussed. Creep, recovery and relaxation phenomena are studied and contributions of matrix and fiber to behavior are discussed for loading parallel and perpendicular to the pultrusion direction. The partial results from an ongoing experimental program are compared to those predicted using the proposed method.

2. MECHANICAL MODELS

The proposed mechanical models are based on the following assumptions: i) fibers can be described by a linear elastic model, with negligible viscous deformation, as reported by Ascione *et al.* [10]; ii) the matrix is represented by a Burgers' viscoelastic model; iii) fibers are unidirectional and homogeneously distributed throughout matrix; and iv) perfect adhesion between constituents is assumed. In Figures 1a and 1b, models for loading applied parallel and perpendicular to the fiber direction are presented, respectively. In the former case, applied force is shared between reinforcement and matrix and the same strain is experienced by both constituents (association in parallel); for the latter case, applied force is the same for both reinforcement and matrix and the final strain is the sum of the strains obtained for each constituent (association in series). Similarly to the rule-of-mixtures, the properties for springs and dashpots (k_i and η_i) for each model are defined according to constituent properties and their corresponding volume fraction, as follows:

- load parallel to fiber direction (Fig. 1a): stiffnesses are obtained multiplying constituent stiffnesses by their corresponding volume fraction (e.g. $k_f = E_f V_f$, where E_f is the fiber modulus; $\eta_1 = c_1 V_m$ where c_1 is the matrix primary dashpot and $V_m = 1\text{-}V_f$ is the matrix content in volume);
- load perpendicular to fiber direction (Fig. 1b): stiffnesses are obtained dividing constituent stiffnesses by their corresponding volume fraction (e.g. $k_f = E_f/V_f$ and $\eta_1 = c_1/V_m$);

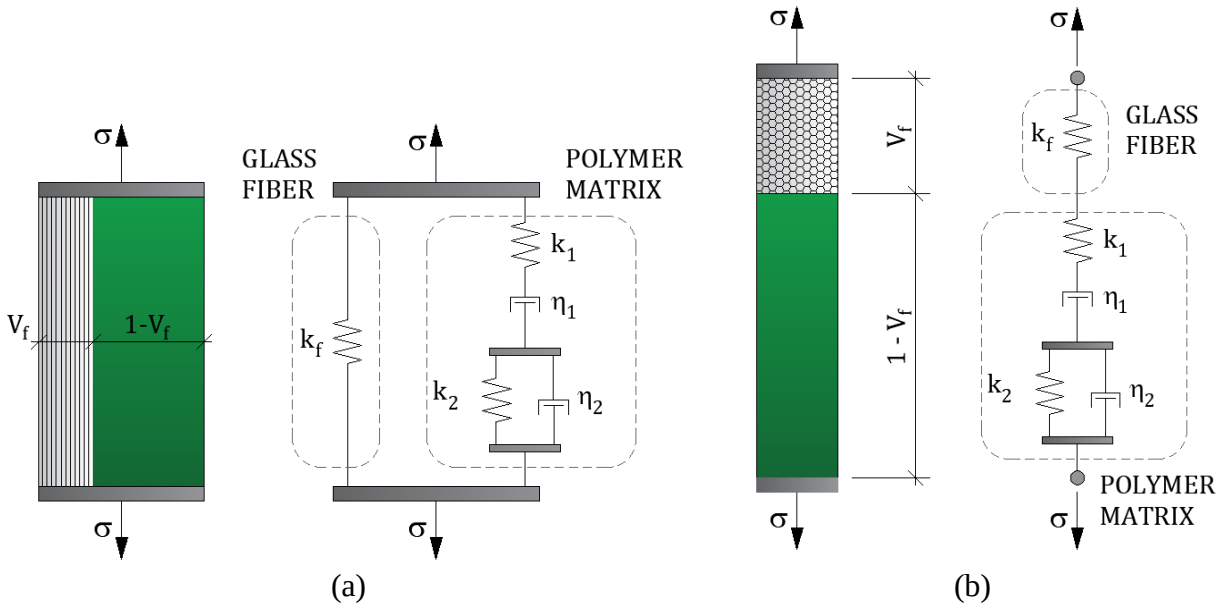

Figure 1 : Proposed mechanical models: a) load parallel to fiber direction (association in parallel); and b) load perpendicular to fiber direction (association in series).

In Figure 2a, relative creep compliances obtained for specimens loaded parallel to the fiber direction are presented for different fiber contents (V_f). Graphs in Figure 2 were obtained considering vinylester resin post-cured at 93 ºC for one week, as given in Table 1 [2]. For $V_f = 0$, the proposed model reduces to Burgers' model and a good agreement is obtained with experimental data for the time span considered. For $V_f > 0$, significant reductions in compliance are predicted. In general, as the matrix dashpots 'release strain', the overall matrix stiffness falls, affecting the stress distribution between matrix and fiber: the load carried by the fibers increases and the force transferred through the matrix decreases. This change in load distribution also leads to a reduction in the strain mobilized in matrix spring k_1.

Table 1 : Burgers' model parameters for vinylester with different post-curing conditions [2].

Property	**Post-curing condition**	
	RT – 1 month	**93 ºC – 1 week**
Primary modulus of vinylester resin (E_1)	3.5 GPa*	3.5 GPa*
Secondary modulus of vinylester resin (E_2)	9.0 GPa	17 GPa
Primary dashpot of vinylester resin (c_1)	1.0×10^6 GPa.s	4.0×10^6 GPa.s
Secondary dashpot of vinylester resin (c_2)	5.0×10^4 GPa.s	7.5×10^4 GPa.s

* average estimated
RT = room temperature

When loaded in the perpendicular to the fiber direction, in-series springs k_f and k_1 are subject to the same force. Therefore, they can be treated as a single equivalent spring with $k_{eq} = k_f k_1/(k_f+k_1)$ and the model reduces to a simple Burgers' model. As can be seen in Figure 2b, for loading perpendicular, relative creep compliances decrease with increasing fiber contents, but to a much significant degree as compared to the case where fibers are parallel to load direction (Figure 2a). The proposed models can also be used to predict relaxation and recovery phenomena and the strong

influence of fiber content and loading direction can be observed. A much quicker recovery and reduced relaxation is predicted when loads are applied parallel to fiber direction.

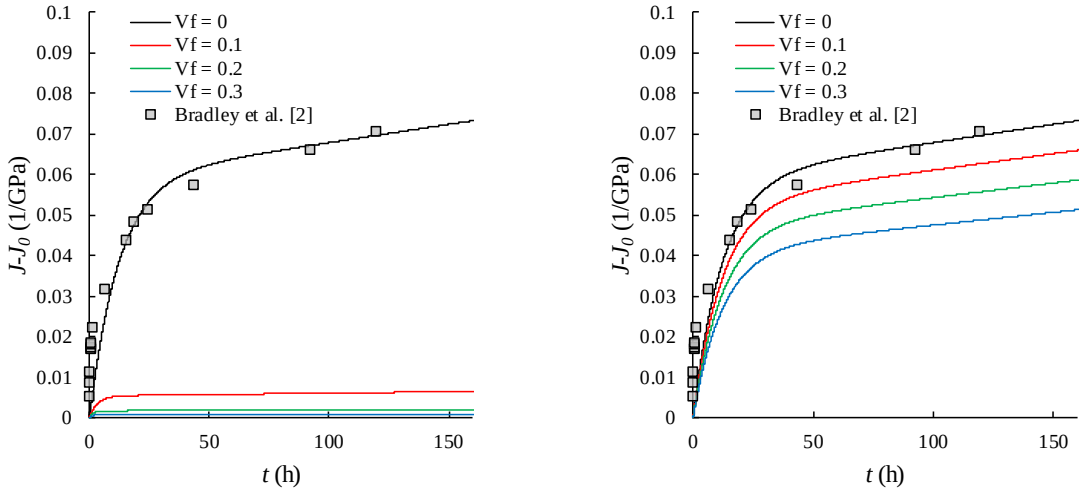

(a) (b)

Figure 2 : Predicted creep behavior for members with different fiber contents: a) loads applied parallel to fiber direction; b) loads applied perpendicular to fiber direction.

In real pGFRP, fiber volume content ranges from V_f = 0.20 to V_f = 0.50. This volume is composed of i) continuous strand mat (CSM), comprising about 10-20% of V_f, (thicker pultruded plates have lower proportions of CSM); and ii) roving layers, comprising the remaining 80 to 90% of V_f. Surface veils made of polyester are also used at the outer faces. Whereas roving layers are orthotropic due to the unidirectional contribution of fibers in the direction of pultrusion, CSM layers are usually assumed to be isotropic due to approximately equal contribution of randomly oriented fibers in both directions [11]. In Figure 3a, an idealized cross-section of thickness *h* is presented and, in Figure 3b, the corresponding distributions of flexural strains and stresses are shown, from which it can be highlighted that each layer contributes differently to resisting the applied moment, as in a laminate. Therefore, the effectiveness of fibers is reduced with respect to the case of pure axial load and is strongly dependent on the fiber architecture [12]. In the present work, for simplicity, the concept of effective volume fraction, $V_{f,eff}$, is introduced to represent the fiber content parallel to the loading direction homogeneously distributed throughout matrix for a linear stress distribution. Finally, it can be noted that, due to the presence of CSM in typical pGFRP, there will be always a certain proportion of fibers parallel to the direction of load. The presence of fillers may also affect the behavior, but is not considered in the present study.

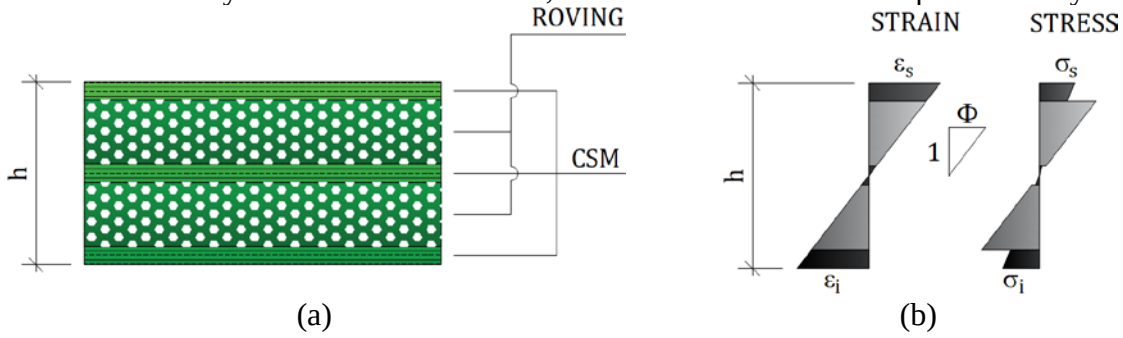

(a) (b)

Figure 3 : Behavior of idealized pGFRP: a) fiber architecture; b) flexural strain and stress.

3. EXPERIMENTAL PROGRAM

The experimental program consisted of short and long-term flexural characterization of a pGFRP composite plates loaded both parallel and perpendicular to the pultrusion direction. Specimens used in this study were extracted from a 152x6.3 mm vinylester-based pGFRP plates, an example of which is shown in Figure 4a. According to the manufacturer, the plates were produced using Dion® Impact 9102 GP resin or equivalent and E-glass fibers. The plates were fabricated with a pull speed of 280 mm/min through a 500 mm long mold having a temperature of approximately 150ºC.

3.1 Fiber Content and Architecture

To determine the fiber content, burnout tests were carried out according to ASTM D3171. A fiber volume fraction of approximately V_f = 0.30 was calculated; 15% of this volume corresponded to CSM. An optical microscope was also used to analyze the typical fiber architecture, which was found to be quite uniform as seen in Figure 4b.

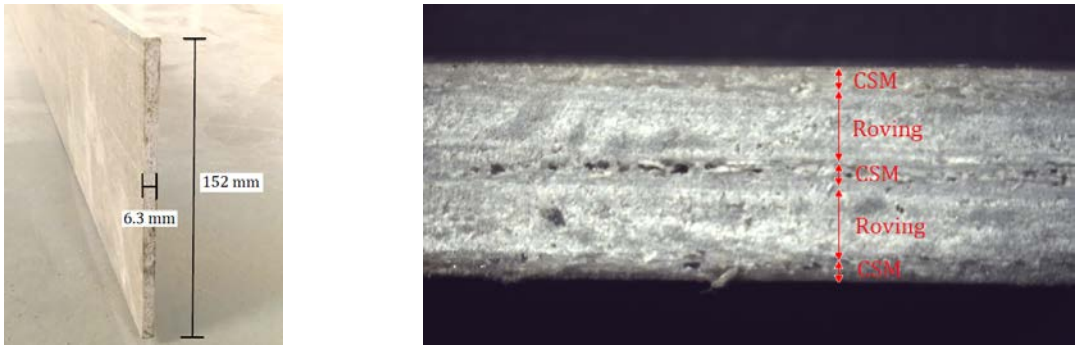

(a) (b)

Figure 4 : pGFRP material studied: a) original plate; b) fiber architecture.

3.2 Short and Long-Term Mechanical Characterization

To obtain short and long-term mechanical properties in the longitudinal direction, three 30x300 mm specimens were extracted from the plates and tested in a four-point bending configuration with total and shear spans of 250 and 100 mm, respectively (Figure 5a). It is important to note that the shear span-to-depth ratio exceeds 10, resulting in negligible contribution of shear deformation to the total deflection. A displacement transducer was used at the top of the rigid loading beam and strain gages were positioned on both top and bottom faces of the specimens at the constant moment region, as shown in Figure 5a. For short-term characterization, loads were applied in increments of 50 N up to 250 N (free weights), in less than one minute, and the unloaded in the same way. The procedure was repeated three times and a consistency in the results was observed. Following this initial loading, specimens were unloaded and remained in this condition at least for one week before being reloaded using similar increments for the long-term testing sequence. For long-term characterization, specimens were loaded with 200 or 250 N (see Table 2) for approximately 170 h, when they were unloaded. Recovery data were recorded for an additional 50 h period of time.

For the transverse direction, three 25x152 mm specimens were used and tested in three-point bending over a 140 mm span (Figure 5b). A displacement transducer was used at mid-span. The same procedure – although with different applied loads – as described for longitudinal specimens

was used. For short-term characterization, loads were applied in 10 N increments up to 80 N and for long-term characterization, specimens were loaded with 50 or 80 N (see Table 2).

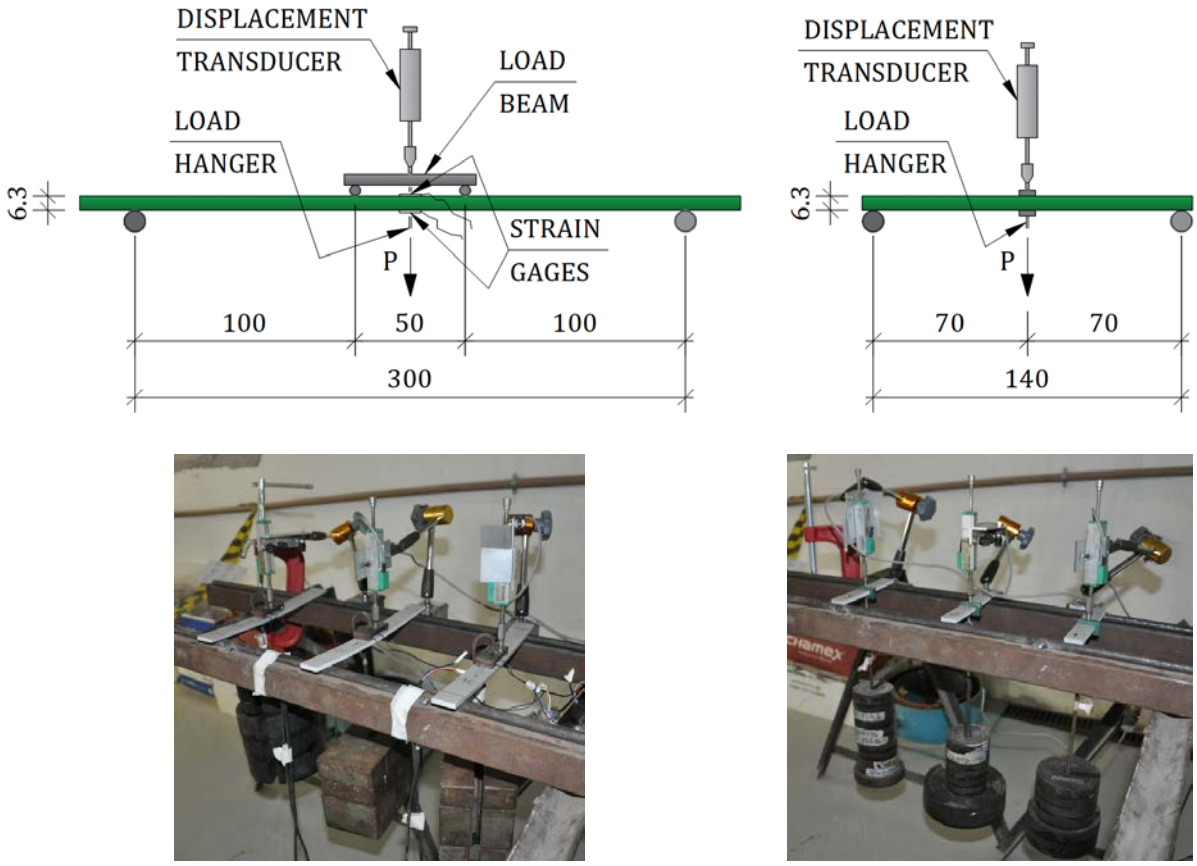

(a) (b)

Figure 5 : Scheme and view of characterization tests: a) longitudinal direction; b) transverse direction (dimensions in mm).

4. DISCUSSION OF RESULTS

In Table 2, measured dimensions (width *b* and thickness *h*) of specimens are reported, as well as the elastic flexural moduli obtained from short-term characterization, E_b, and effective fiber volume fractions. $V_{f,eff}$ was back-calculated from the rule-of-mixtures, assuming moduli of elasticity of fiber and matrix E_f = 72 GPa and E_1 = 3.5 GPa, respectively.

Table 2 :Measured dimensions, elastic moduli and effective volume fraction.

Specimen	b (mm)	h (mm)	E_b (GPa)	$V_{f,eff}$	Long-term load (N)
1 Longitudinal	30.2	6.12	21.9	0.27	250
2 Longitudinal	28.8	6.15	23.4	0.29	200
3 Longitudinal	31.4	6.10	22.6	0.28	200
1 Transverse	25.0	6.12	5.6	0.01	80
2 Transverse	23.2	6.18	5.5	0.01	80
3 Transverse	23.7	6.14	5.6	0.01	50

In Figure 6a, creep and recovery compliances for longitudinal specimens are presented. Results are relatively consistent for the three specimens, with differences only in initial compliance (associated to initial modulus). A large elastic recovery can be observed for the specimens. In Figure 6b, relative creep compliance obtained experimentally are presented. Results obtained with the proposed model using resin properties for different post-curing conditions given in Table 1: room temperature (RT) for 1 month and 93ºC for 1 week (cross-linking completion). An important difference between the model and experiments was observed immediately following loading, with the model predicting an initially greater creep rate. It can be seen that actual behavior corresponds to an intermediate case, but can satisfactorily be represented by the proposed model considering vinylester properties for 93ºC post-curing. In Figures 6c and 6d, similar graphs are presented for the specimens loaded in the transverse direction. Much greater compliances and relative compliances can be observed with respect to the longitudinal direction, as well as a less significant (greater residual compliance) recovery. The proposed model once again showed good agreement with experiments. Similar conclusions were obtained with strain gage data from the longitudinal specimens.

5. CONCLUSION

In this work, innovative mechanical models intending to represent orthotropic pGFRP composite viscoelastic behavior was proposed. The proposed models account for fiber content and for the properties of each phase of the composite and can be used to predict long-term behavior of such composites under complex loading history. Predictions obtained using the proposed models showed satisfactory agreement with creep-recovery experiments performed for longitudinal and transverse specimens. It is demonstrated that behavior is strongly affected by the presence of fibers parallel to the load direction, reducing relative compliance and promoting a greater elastic recovery. Mechanical characterization of glass fibers and resin for both short and long-term behavior are underway, as well as relaxation and shear creep-recovery tests.

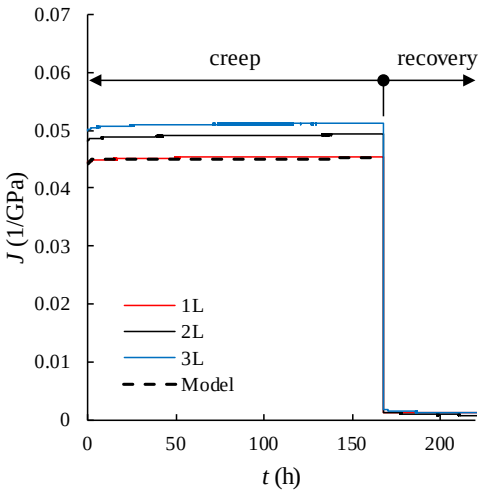

(a)

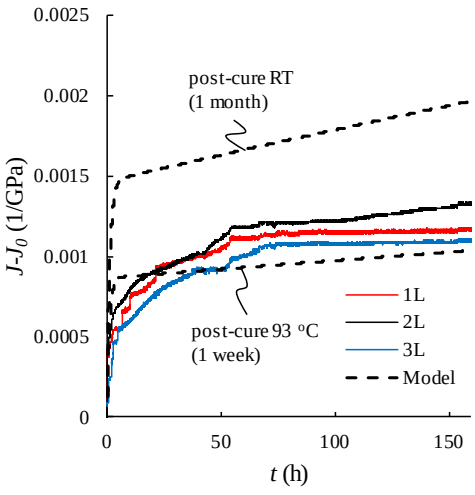

(b)

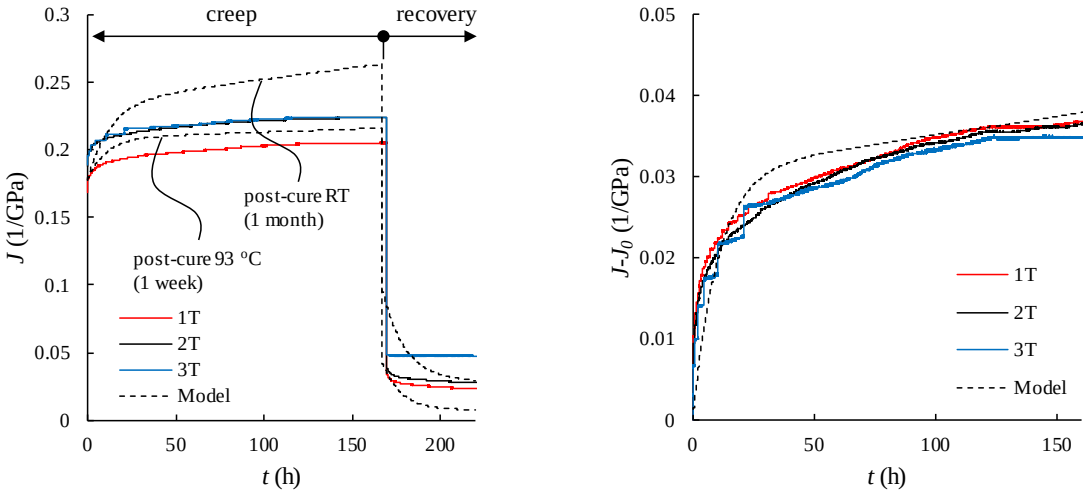

(c) (d)

Figure 6 : Creep and recovery results: a) creep and recovery (longitudinal); b) relative compliance (longitudinal); c) creep and recovery (transverse); d) relative compliance (transverse);

ACKNOWLEDGEMENTS

The authors would like to acknowledge Cogumelo for supplying the material used in this research. The first author acknowledges CNPq for financial support through process 402026/2016-0.

REFERENCES

[1] Harries, K. A., Guo, Q., & Cardoso, D. (2017). Creep and creep buckling of pultruded glass-reinforced polymer members. *Composite Structures*, **181**, 315-324.

[2] Bradley, S. W., Puckett, P. M., Bradley, W. L., & Sue, H. J. (1998). Viscoelastic creep characteristics of neat thermosets and thermosets reinforced with E-glass. *Journal of Composites, Technology and Research*, **20**(1), 51-58.

[3] Batch, G. L., & Macosko, C. W. (1993). Heat transfer and cure in pultrusion: model and experimental verification. *AIChE Journal*, **39**(7), 1228-1241.

[4] Findley, W. N., Lai, J. S. & Onaran, K. (1976). 'Creep and relaxation on nonlinear viscoelastic materials'. Dover Publications.

[5] Bank, L. C., & Mosallam, A. S. (1992). Creep and failure of a full-size fiber-reinforced plastic pultruded frame. *Composites Engineering*, 2(3), 213-227.

[6] Scott, D. W., & Zureick, A. H. (1998). Compression creep of a pultruded E-glass/vinylester composite. *Composites Science and Technology*, **58**(8), 1361-1369.

[7] Sá, M. F., Gomes, A. M., Correia, J. R., & Silvestre, N. (2011). Creep behavior of pultruded GFRP elements–Part 1: Literature review and experimental study. *Composite Structures*, **93**(10), 2450-2459.

[8] Bottoni, M., Mazzotti, C., & Savoia, M. (2014). Creep tests on GFRP pultruded specimens subjected to traction or shear. *Composite Structures*, **108**, 514-523.

[9] Sá, M. F., Gomes, A. M., Correia, J. R., & Silvestre, N. (2011). Creep behavior of pultruded GFRP elements–Part 2: Analytical study. *Composite structures*, **93**(9), 2409-2418.

[10] Ascione, L., Berardi, V. P., & D'Aponte, A. (2012). Creep phenomena in FRP materials. *Mechanics Research Communications*, **43**, 15-21.

[11] Naughton, B. P., Panhuizen, F., & Vermeulen, A. C. (1985). The elastic properties of chopped strand mat and woven roving in GR laminae. *Journal of reinforced plastics and composites*, **4**(2), 195-204.

[12] Liu, T., Harries, K.A. and Guo, Q. (2018) Effects of Fiber Architecture on Flexure Properties of Pultruded GFRP Plates and Sections, *Proceedings of the 9th International Conference on Fibre-Reinforced Polymer Composites in Construction (CICE 2018)*, Paris, July 2018.

CURVED PULTRUDED UNIDIRECTIONAL CARBON FIBER COMPOSITE UNDER INTERLAMINAR SHEAR FATIGUE LOADING

Maikson L. P. Tonatto (1), Rafaela G. Rodackievicz(2) and Sandro C. Amico (2)

(1) Department of Mechanical Engineering, Federal University of São João Del Rey/MG, Brazil

(2) Department of Materials Engineering, Federal University of Rio Grande do Sul/RS, Brazil

https://doi.org/10.21452/bccm4.2018.06.03

Abstract

Curved pultrusion is a new variation of traditional pultrusion and it has been recently used to produce curved composite components. Due to their excellent mechanical properties, curved composites may be used in aerospace, automotive and naval sectors. However, little is known about their fatigue behavior. In the present work, a short beam shear test (SBS) set up has been used to evaluate fatigue strength of curved pultruded carbon fiber composite samples. A servo-hydraulic machine was used to apply a frequency of 5 Hz, and at 80, 70, 60 and 50% of the quasi-static strength. The tests were carried out for a stress ratio R of 0.1, and additional tests were performed for ratio R of 0.5. Damage evolution has been observed using the apparent stiffness method. S-N curves have been normalized and the experimental data has been fitted using Basquins' Law. Observed failure and limitations of the SBS test to characterize the interlaminar shear fatigue behavior for curved composites are described and discussed.

Keywords: Curved composite, carbon fiber, pultruded, fatigue, short beam test.

1. INTRODUCTION

Manufacturing techniques for composite pultrusion materials are commonly used due to factors such as high precision in fiber positioning, high fiber volume fraction, low void content and process automatization. Pultrusion is known to produce flat profiles in varied cross sections [1]. Jansen [2] described that until recently pultrusion was the only high-scale production process for fiber-reinforced profiles and only allowed the manufacture of flat profiles. However, a new method called curved pultrusion has been developed to obtain curved profiles based on new concept of matrix format and matrix motion mechanism. In traditional pultrusion, the matrix is stationery and the fibers are drawn into a resin bath and pulled in order to produced a flat profile. In the curved pultrusion, the die is no longer stationary, but moves back and forth along the profile.

Curved composite structures are currently used in applications where dynamic loading occurs. Most studies treat fatigue life as a two-phase process that includes damage initiation and damage growth. It is not usual to find literature studies dedicated to analyzing fatigue behavior in composite structures subjected to loading that predominantly leads to delamination. This can lead to either

underestimated or conservative designs. Besides, it is very difficult to find any work on fatigue of curved composite structures.

Bureau and Denault [3] characterized the effect of consolidation on the fatigue strength of continuous glass fiber/polypropylene (CGF/PP) composites. Flexural fatigue tests were performed under three-point bending using traditional flat composite samples and failure was predominantly caused by tensile and compressive stresses in the fiber and the matrix.

Delamination is a very important factor in the design of composite structures subjected to fatigue loading. Its behavior is very particular and depends on the individual components (materials). Some authors have performed specific fatigue studies to understand the behavior of these structures. For instance, Kotik and Ipina [4] studied quasi-static and fatigue (R = 0.1; 5 Hz) interlaminar shear behavior of flat commercial FML (Glare 1 3/2) employing the short-beam shear (SBS) test in longitudinal and transverse orientations. Ju et al. [5] described that in laminated curved samples, delamination occurs more easily owing to the high peel stress in the curved region. And the reinforcement effect of grooved Z-pins is investigated for preventing delamination of curved beams.

The present study focuses on the evaluation of curved pultruded carbon fiber composites under interlaminar shear fatigue load. A real scale composite coil was used to obtain the fatigue samples. Experimental tests were carried out at two different stress ratios (R=0.1 and 0.5), and at 80, 70, 60 and 50% of the quasi-static strength.

2. EXPERIMENTAL TESTS

2.1 Materials and specimen preparation

The material used in this study was unidirectional carbon fiber/epoxy. A coil of circular cross section with diameter 12.7 mm and pitch 36 mm was manufactured by curved pultrusion. All unidirectional fibers were aligned along to the coil shape. The specimens for testing were cut and polished to the dimensions specified in ASTM D2344 using a manual saw. The specimens were cut to 76.2 mm long samples as shown in Figure 1 [6].

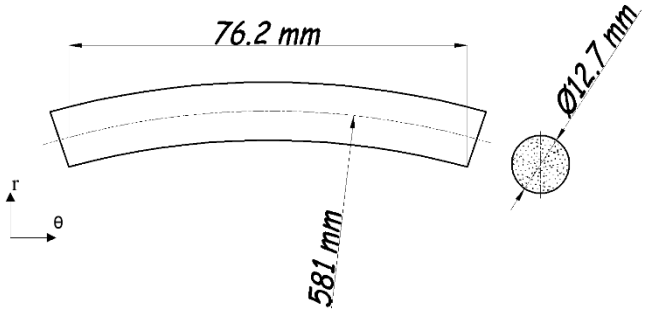

Figure 1: Curved pultruded composite sample and dimensions.

2.2 Quasi-static short beam test

A short beam shear test set-up was mounted in an INSTRON 3382 test machine. The test was performed according ASTM D2344. The samples were supported on a flat plate, using as span the length of the samples. Load was controlled with a 100 kN load cell and a loading roller (6 mm in diameter) was used. The test speed rate was 1 mm/min and each test was interrupted at the first major load drop.

The short-beam strength recommended for circular cross-section samples was determined according to $F^{sbs} = (2/3)\times P_b/A$, where P_b is the maximum load found and A is the circular cross-section of the sample. The test was performed in five specimens and the mean maximum load found was used as the reference value for fatigue loading.

2.3 Fatigue short beam test

Fatigue short beam tests were performed under sinusoidal load control. The same device used in the static tests was mounted in a MTS Landmark servo hydraulic machine equipped with a 100 kN load cell. Figure 2 shows a curved sample during the fatigue short beam test. The tests were carried out at a frequency of 5 Hz and for severities of 80%, 70%, 60% and 50% relative to the static short beam strength (F^{sbs}). The tests were run until a catastrophic failure was identified, until the maximum displacement had reached 20% in relation to that observed at the first load cycle, or for a maximum of 10^6 cycles. Two different ratios of minimum to maximum stress per load cycles, R=0.1 and R=0.5, were adopted.

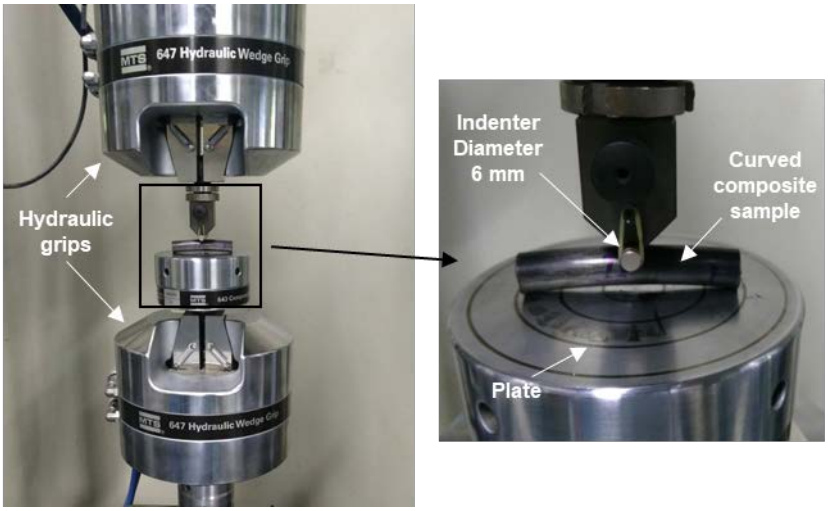

Figure 2: Fatigue short beam test experimental test setup.

3. RESULTS AND DISCUSSIONS

Under static load, the specimens were submitted to a increasing load until catastrophic failure occurred close to the mid-plane. The mean maximum load found was 10.9 kN, with a coefficient of variation of 5.8%. The mean short beam strength was 60.2 MPa with a coefficient of variation of 5.5%. The strength values found in these curved pultruded composites was high compared to traditional composite laminates. For instance, Tonatto et al. [7] reported a strength of 22.6 MPa for carbon/PPS curved laminate composite manufactured by filament winding (FW).

Figure 3a shows the normalized stiffness *vs*. normalized cycle of a sample submitted to R=0.1 and severity 80%. The change in stiffness is a good indicative of sample damage. It is possible to evaluate the normalized stiffness using the “apparent stiffness” parameter, defined as the inverse of displacement. In this case, maximum displacement in each cycle was used to evaluate stiffness change. Three main stages of fatigue are seen in this figure. According to Kotik and Ipina [4], the first stage is a transient in which the rate of maximum displacement decreases. In the second stage,

which lasts for most of the life of the sample, a constant rate is observed. In the last stage, the rate of growth of the maximum displacement considerably increases and material failure occurs.

May and Hallett [8] mentions that the change in maximum displacement may be caused by several factors: roller settling-in on the specimen or due to wear, machine compliance, internal damage and consequent reduction in stiffness. To eliminate machine compliance and settling-in of the roller, the apparent stiffness, E_{app}, was calculated using the variation of displacement in each cycle, as shown in Eq. 1:

$$E_{app} \approx \frac{1}{d_{max} - d_{min}} \tag{1}$$

Figure 3b shows the normalized apparent stiffness *vs* cycles for R=0.1 and severity 80%. A initial increase in apparent stiffness is seen, which is attributed to fiber straightening and redistribution of load in the early stages of fatigue loading [8]. Nevertheless, considering that predominant failure under interlaminar shear loading is in the resin, not in the fiber, local compressive load caused from the indenter combined with interlaminar shear stress has contributed to this phenomenon. Because of that, some authors do not use this data to precisely quantify the change in stiffness. Even so, delamination easily occurs in curved composite samples submitted to beam loads, causing catastrophic rupture, as easily evidenced in these tests (Figure 3a).

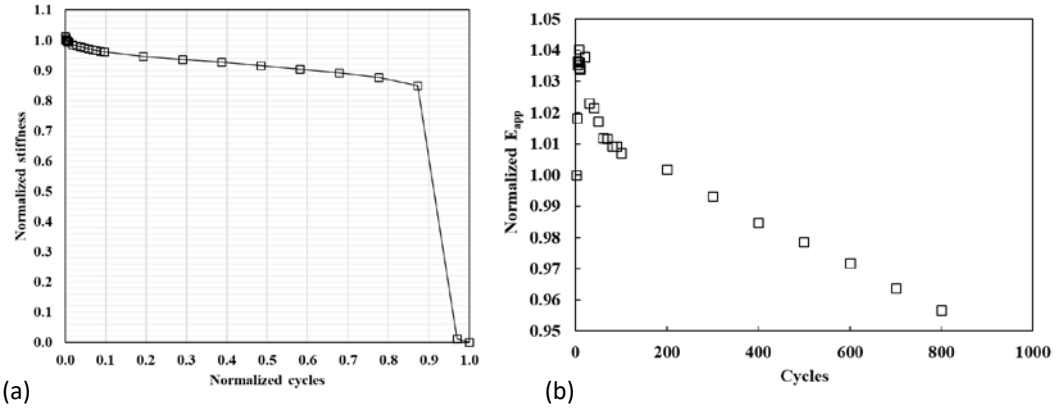

Figure 3: Normalized stiffness *vs*. normalized cycles (a) and normalized apparent stiffness *vs*. cycles (b) for R=0.1 and severity 80%.

All results of the interlaminar short beam fatigue tests are presented in Table 1 and in a severity-log graph (Figure 4). The cycles at failure were obtained as presented before. Three samples were tested at each load condition and the resulting scatter in cycles at failure is can be found in the table. This magnitude in scatter is typical of composite fatigue tests.

Basquins' law was used to fit the fatigue results. This law uses the least squares fit as described in Eq. 2:

$$\tau = \tau_{max} \cdot N^{\frac{-1}{b}} \tag{2}$$

where: τ is the maximum stress at each load cycle, τ_{max} is the quasi-static interlaminar shear strength, N is the number of cycles and b is a constant obtained from experiments [8].

Table 1: Number of cycles at failure for each studied condition.

R-ratio	*Severity (%)*	*Cycles*	*R-ratio*	*Severity (%)*	*Cycles*
0.1	80	900	0.5	80	4196
		300			6000
		200			1412
	70	1764		70	70000
		1400			1000000
		9000			1000000
		62717			548150
	60	94062		60	1000000
		54924			500000
		550000			1000000
	50	600000		50	1000000
		712805			1000000

Figure 4 shows the experimental results and Basquins' law for all severities tested (50, 60, 70 and 80%). The curve for R=0.5 is much flatter than for R=0.1 due to the greater load amplitude of the latter in each load cycle. The tests in which the samples reached 10^6 cycles were stopped and this was very common for the samples with R=0.5. In future work, residual strength of these samples will be evaluated.

Kotik and Ipiña [4] mentioned that curved samples submitted to beam loads are more susceptible to delamination. Similar behavior of fatigue curves of curved samples can be observed comparing with flat unidirectional carbon fiber/epoxy prepreg from Hexcel (IM7/8552) available in the literature [8]. Flat samples curves show higher fatigue strength when compared to curved samples due the increase of interlaminar shear stress in curved samples.

Composite laminates generally have well-defined resin rich regions in-between the layers which facilitates delamination, as described by Tonatto et al.[7] . Nevertheless, the decrease in fatigue strength of the curved samples was not as high as it could be because of the typically scattered areas rich in resin of the samples manufactured by curved pultrusion. This characteristic hinders the propagation of delamination.

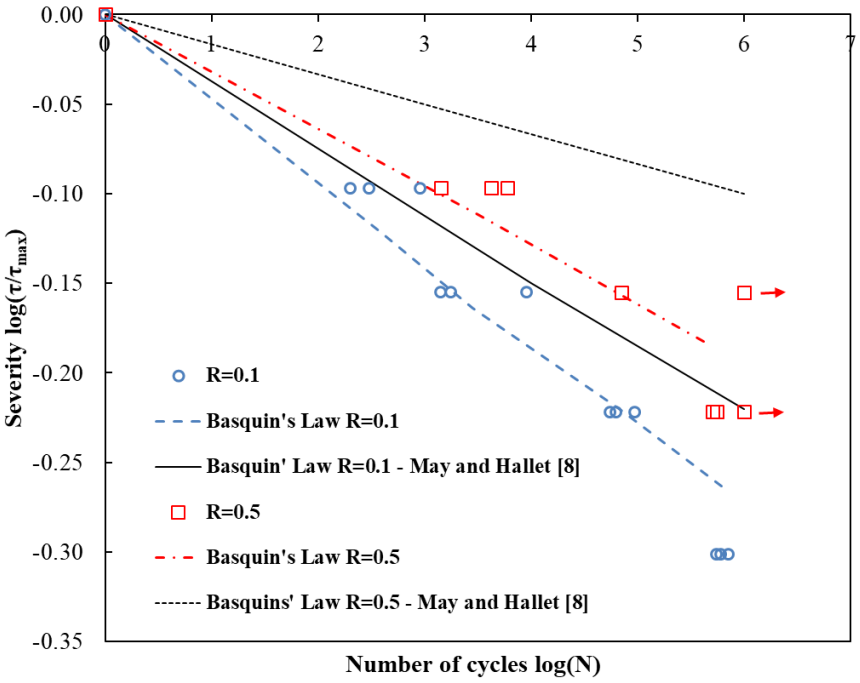

Figure 4: S-N curve (severity log *vs*. number of cycles log) for curved and flat composite submitted to interlaminar short beam test.

4. CONCLUSIONS

The short beam shear test set-up has been used to evaluate fatigue strength of curved composite samples. Different ratios of load cycle (R=0.1 and 0.5) and different severities (50, 60, 70 and 80% of the quasi-static short beam strength) were studied and apparent stiffness was used to evaluate failure. The curved samples showed catastrophic failure, damage onset was easily detected and delamination was evidenced in the samples after cycling. Also, curved samples have been demonstrated slightly lower fatigue strength compared to flat composite laminates.

Some limitations were found in this study. It is difficult to identify damage initiation with precision. Although curved samples exhibited catastrophic failure, damage can occur immediately before global failure. However, this can only be identified through imaging techniques. Another limitation is the identification of failure for higher stress ratio, e.g. R=0.5, and lower severities, e.g. 50%, because these samples reached 10^6 cycles and therefore may be submitted to more cycles or may be characterized to obtain residual strength.

ACKNOWLEDGEMENTS

The authors gratefully acknowledge Petrobras for the financial support of this work. Also, CNPq for research support.

REFERENCES

[1] Neto, F.L. and Pardini, L.C. 'Compósitos estruturais: Ciência e tecnologia', 1st Edn (São Paulo, Edgard Blucher, 2006).

[2] Jansen, K., 'Mass production of curved profiles for car bodies - Process and machines', in 'Automotive Composite Conference and Exhibition', Proceedings of an International Conference, Novi, September, 2016 (SPE Automotive and Composites Divisions, Novi, 2001) 1-13.

[3] Bureau, M.N. and Denault, J., 'Fatigue resistance of continuous glass fiber/polypropylene composites: consolidation dependence. Compos', *Sci. Technol.* **64** (2004) 1785–1794.

[4] Kotik, H.G. and Ipiña J.E.P., 'Short-beam shear fatigue behavior of fiber metal laminate (Glare)', *Int J Fatigue*. **110** (2017) 429-441.

[5] Ju H., Nguyen K., Chae S. and Kweon J., 'Delamination strength of composite curved beams reinforced by grooved stainless-steel Z-pins' *Compos. Struct.* **180** (2017) 497–506.

[6] Standard Test Method for Short-Beam Strength of Polymer Matrix Composite Materials and Their Laminates. ASTM International. West Conshohocken, p. 8. 2013. (ASTM D2344/D2344M).

[7] Tonatto M.L.P, Forte M.M.C., Tita V. and Amico S.C., 'Progressive damage modeling of spiral and ring composite structures for offloading hoses' *Mater Design* **108** (2015) 374–382.

[8] May M. and Hallett S.R., 'An assessment of through-thickness shear tests for initiation of fatigue failure' *Composites: Part A* **41** (2010) 1570–1578.

PROBABILISTIC FATIGUE LIFE MODELLING OF FRP COMPOSITES

Martin Noël (1)

(1) Department of Civil Engineering, University of Ottawa, Canada

https://doi.org/10.21452/bccm4.2018.06.04

Abstract

Fiber reinforced polymer (FRP) composites have been used in industries such as aerospace, marine transportation, and wind energy for several decades prior to attracting widespread attention for applications in civil engineering. While limited data is available on the long term fatigue performance of FRP materials for construction projects, it is worthwhile to review the extensive work done in other engineering disciplines and consider the lessons learned. In particular, the probabilistic nature of the fatigue life of composite materials under cyclic stresses has been captured by various models presented in literature; although the contextual parameters may differ, their use may extend to other applications. In this work, the Sendeckyj wear-out model based on the strength-life-equal-rank assumption is applied to fatigue data from a variety of material types and configurations intended for building projects. The results presented show that the model is versatile and can be calibrated to describe the probabilistic nature of both the static and fatigue response of FRP composite materials for various applications.

1. INTRODUCTION

Fiber reinforced polymer (FRP) composite materials are growing in popularity for a wide range of applications as a result of their unique properties which include light weight, versatility, high strength, and corrosion resistance. Whereas FRP composites have been used for many decades in industries such as aerospace, marine and automobile manufacturing, and wind turbines, their extension to civil engineering applications, particularly construction projects, has by comparison been more recent. As a result, data on long-term field performance, including damage accumulation due to cyclic loading, is lacking.

A relatively small number of research studies have focused on the fatigue life of FRP composites for civil engineering structures [1-9]. Conversely, the fatigue characteristics and failure mechanisms of FRP composites have been well-documented by researchers in mechanical engineering and other disciplines, and a variety of probabilistic and phenomenological models have been developed to explain their behavior [10-20]. While there are generally significant differences in the magnitude of deformations involved, the expected number of loading cycles over the service life of the component, the environment in which the materials are used, and the

manufacturing processes employed, there are nevertheless several lessons to be gained from a review of this work and some of the general findings are transferable and provide a basis for further study.

The fatigue behavior of FRP materials depends on many parameters, including the fiber and resin types, as well as the configuration and geometry of the test specimens [21]. Unlike metals and other homogeneous materials, fatigue failures in FRP are generally the result of damage accumulation rather than damage propagation in a single mode [22]. The predominant mechanisms leading to failure depend on the range of applied strain, dividing typical FRP fatigue life curves into three distinct stages (Figure 1) [12]. At high strain ranges, failure is dominated by fiber breakage and interfacial debonding resulting in a nearly horizontal band representing the non-progressive nature of random fiber ruptures. The second stage can generally be described by a power law function, where damage accumulation is dominated by progressive matrix cracking and interfacial shear failures. Finally, in the third stage, the slope tends to flatten out at low strain levels as the fatigue limit is approached; for low stiffness composites, such as glass FRP (GFRP), the strain limit is usually much less than the strain capacity of the composite and is therefore ignored for most practical applications.

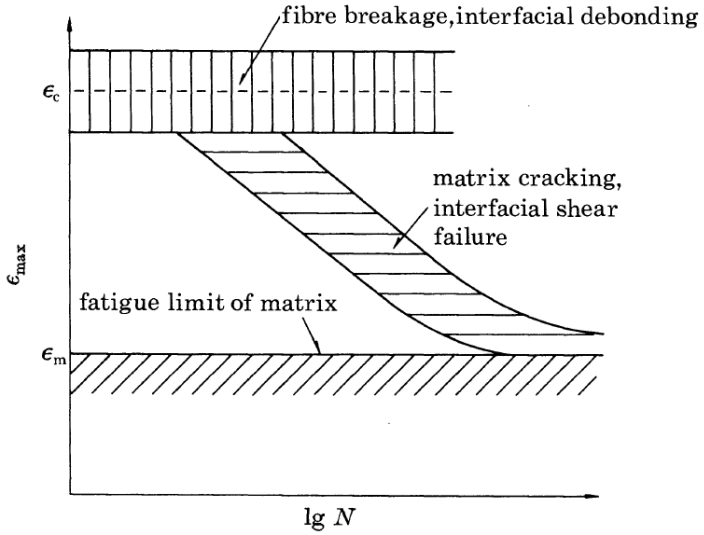

Figure 1: Fatigue life diagram for unidirectional composites [12]

The stochastic nature of fatigue in FRP composites has been widely observed [13, 16]. The scatter in fatigue life can exceed an order of magnitude for a given set of parametric values; this may be partially attributed to the high anisotropy of the material, density of defects, and distribution and alignment of fibers [11], as well as competing damage and failure mechanisms [19], and large variation in strength of individual fibers [20, 23].

2. MODELLING APPROACH

Fatigue life models for composite materials are often empirical in nature; the difficulty in developing rational models is linked to the various complex fatigue damage mechanisms, and the limited applicability of the fatigue and fracture mechanics concepts developed for metals [24]. It has also been argued that macroscopic phenomenological damage models are more practical than microscopic physical models since they require less data, are easier to measure, and the interaction of different damage types can often be neglected [25].

Chou & Croman [26] introduced a strength-life-equal-rank (SLER) assumption to relate the fatigue lives and static strengths of composites assuming that both followed 2-parameter Weibull distributions. SLER assumes that the static strengths are uniquely related to the fatigue lives and residual strengths of fatigue specimens at runout; i.e. the specimen with the highest static strength is also assumed to have the longest fatigue life and/or the highest residual strength following a fatigue test. This assumption is both simple and intuitive, although it is worth noting that it cannot be proven experimentally and may not necessarily be valid if competing failure modes are observed during fatigue tests.

Sendeckyj [27] used the SLER assumption to develop a method for fitting probabilistic fatigue life models to experimental data for composite materials. This method simultaneously determines the fatigue model parameters and the Weibull distribution parameters by converting fatigue data to equivalent static strength values using the maximum likelihood estimate method. The procedure is optimized by maximizing the Weibull shape parameter for the equivalent static strength data. The equivalent static strength of specimens tested under fatigue loading according to the so-called wear-out model is presented in Equation 1. The probability that a sample's static strength is higher than the equivalent static strength is given by Equation 2.

$$\sigma_e = \sigma_a[\left(\frac{\sigma_r}{\sigma_a}\right)^{1/S} + (n-1)C]^S \tag{1}$$

$$P(\sigma_e) = \exp[-(\frac{\sigma_e}{\beta})^{\alpha}] \tag{2}$$

Where, σ_e, σ_a, and σ_r are the equivalent static strength, applied stress level, and residual strength of the fatigue specimens, respectively, n is the number of applied cycles, C and S are model calibration coefficients, $P(\sigma_e)$ is the probability that the static strength is greater than the equivalent static strength, and α and β are Weibull distribution parameters.

For fatigue failure, the residual strength is equal to the applied stress level and the number of applied cycles is equal to the fatigue life, N. Equation 1 can therefore be simplified to give Equation 3:

$$\sigma_e = \sigma_a[1 - C + CN]^S \tag{3}$$

For $C = 1$, Equation 3 reduces to the classical power law fatigue failure criterion, whereas $C < 1$ results in an S-N curve that flattens out at low cycles on a log-log plot. Values of $C > 1$ result in a curve which steepens at low cycles.

The applied stress range corresponding to a specified fatigue life and probability of failure is given by Equations 4 and 5:

$$\sigma_a = \beta\left(\{-\ln[P(N)]\}^{\frac{1}{\alpha}}\right)[(N-A)C]^{-S} \tag{4}$$

$$A = -\frac{1-C}{C} \tag{5}$$

Where, $P(N)$ is the probability of survival after N cycles, and A is a model parameter.

3. ANALYSIS

The Sendeckyj model was used by [8] to analyse the fatigue life of GFRP reinforcing bars under axial tension and in beams, and by [9] for the fatigue behavior of GFRP-reinforced concrete slabs with CFRP post-tensioned tendons. A comparison with other fatigue models is discussed elsewhere [28]. The applicability of this approach to other research works with various material properties, configurations, and damage conditions is explored in this section.

3.1 GFRP reinforcing bars

Experimental fatigue testing of GFRP reinforcing bars were conducted by [8, 9]. The bars had a nominal diameter of 16 mm and the surface had a sand-coating layer to improve bond with concrete. The average tensile strength and modulus of elasticity were 784 MPa and 55.9 GPa, respectively. The bars were tested under cyclic loading in three configurations: axial tension-tension cycles using a novel anchor system and modified bar profile to control the location of the fatigue failure; beam-hinge specimens to investigate the effect of surrounding concrete on the fatigue performance; and as reinforcement in large concrete slabs with a length of 5 m and post-tensioned with CFRP tendons.

The results showed that the concrete had an adverse effect on the fatigue response, and that the fatigue behavior was also influenced by the stress ratio. An "effective" stress range was proposed to account for these effects as given by Equation 6:

$$\sigma_{eff} = K_{te}\sigma_n(1 + R) \tag{6}$$

Where, σ_{eff} and σ_n are the effective and nominal stress ranges, respectively, K_{te} is a factor to account for the abrasion at the FRP-concrete interface, and R is the stress ratio between the minimum and maximum stress values.

The static and fatigue data from the three test setups were used to calibrate the Sendeckyj model (Figure 2a). The failure band limits shown in Figure 2 correspond to 5% and 95% probabilities of failure. The approach was found to describe the data set well, including both static and fatigue results, while capturing the non-deterministic nature of fatigue behavior. A horizontal band is observed in the low-cycle fatigue region, while a steeper slope characterizes the intermediate-cycle fatigue range.

3.2 CFRP reinforcing bars

Few researchers have studied the fatigue life of FRP reinforcing bars in detail. Bare 9.4 mm diameter CFRP bars were tested by [4], while tests on 7.8 mm diameter CFRP bars in concrete were reported by [3]. The reported results and corresponding calibrated Sendeckyj models are shown in Figure 2b. It is worth noting that while [3] reported a lower fatigue life for bars in concrete, the bare bar results were not provided. Therefore, the factor K_{te} presented in Equation 6 was taken as unity for both studies; however, the applied stress ranges were multiplied by the factor $(1 + R)$ to account for the effect of the stress ratio.

It can be observed from Figure 2b that the slope and scatter of the S-N curves varied between the two different CFRP bars; nevertheless, the Sendeckyj model was able to capture the experimental results satisfactorily. It can also be observed that, unlike the GFRP bars in Figure 2a, there is no horizontal band in the low cycle region; hence, fatigue life data for CFRP composites are more likely to be well-described by a classical power law function.

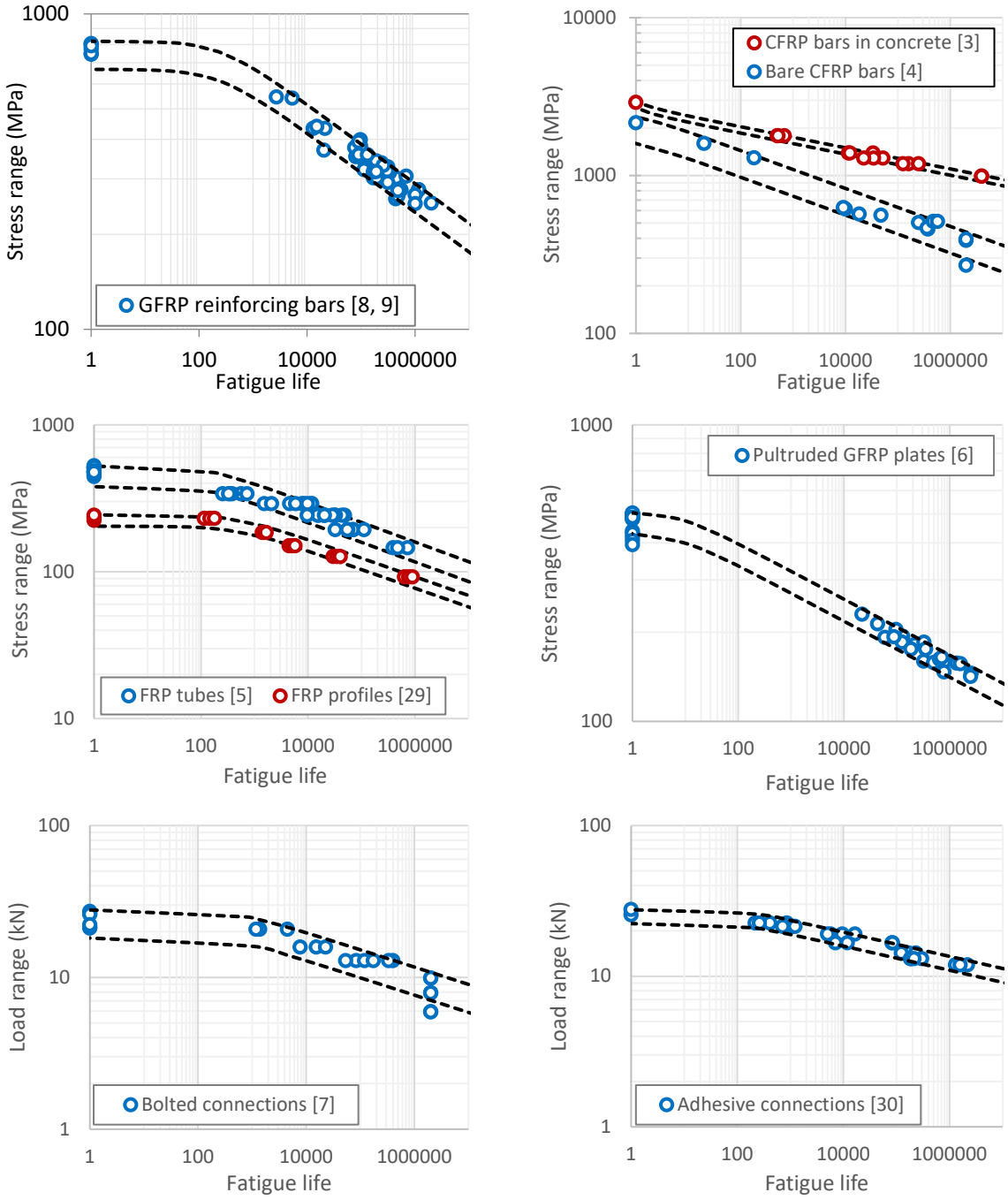

Figure 2: From top: calibrated models for a) GFRP reinforcing bars, b) CFRP reinforcing bars, c) GFRP coupons, d) pultruded GFRP plates, e) bolted connections, and f) adhesive connections

3.3 FRP coupons

Unlike FRP reinforcing bars, which have unidirectional fibers and are produced through pultrusion, many FRP applications make use of composites with different fiber orientations and manufacturing processes. [5] conducted a large number of fatigue tests on coupons cut from GFRP tubes with a thickness of 5.7 mm produced using a continuous filament winding process. The stacking sequence of different layers in the tube were [-87° / +10° / -87° / +10° / -87° / +10° / -87°

/ +10° / -87°]. The manufacturer reported properties include a tensile strength in the longitudinal direction of 402 MPa and an elastic modulus of 23.1 GPa.

The coupons were cut in various orientations; only the coupons in the direction parallel to the fibers are shown here (Figure 2c). Similarly, specimens tested under compression-compression cycles, or combined tension-compression are not included; while the Sendeckyj model can be used for such cases, the $(1 + R)$ modifier does not seem applicable.

Also shown are the fatigue results from FRP coupons cut from pultruded structural profiles [29]. The profiles had a nominal thickness of 8.0 mm and an average tensile strength of 233 MPa. The calibrated models and experimental results in Figure 2c show a similar trend to that of the pultruded GFRP bars in Figure 2a. A shallow band is observed in the low-cycle region followed by a steeper slope in the intermediate-life region.

3.4 FRP plates and connections

Fatigue testing has also been conducted on GFRP pultruded plates [6], bolted connections [7], and adhesively bonded connections [30]. The applicability of the Sendeckyj approach for these cases is demonstrated in Figure 2d, e, and f. It can be observed that while the slope and scatter of the results vary in each case, as well as the length of the horizontal low-cycle fatigue band, the experimental results are well-captured in each case.

3.5 Summary

The normalized predictions as a ratio of the ultimate static strength corresponding to a 50% probability of failure are presented in Figure 3. Conversely to the GFRP samples, the CFRP bars did not show a change in slope in the low-cycle region.

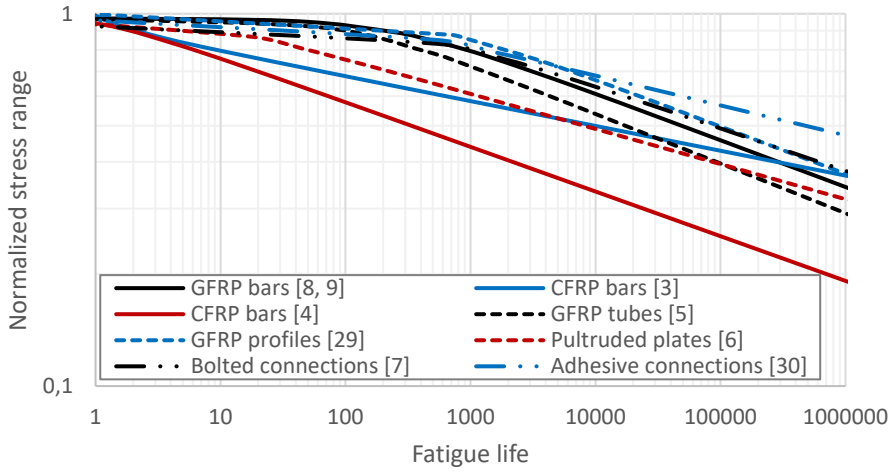

Figure 3: Summary of normalized fatigue results

The ratio of predicted fatigue life for a given stress range corresponding to a 5% reliability, P5, to a 95% reliability, P95, is approximately constant within the linear sloped region of each S-N curve, and may be considered as an indication of the scatter in the experimental results. As seen in Table 1, this ratio varied from approximately 4.0 to 42 for the studies considered in this work. The highest variability in results was observed in the bolted connections, whereas the lowest variability was observed in CFRP bars tested in concrete. Of course, it is important to note that many factors influence fatigue behavior, and no attempt is made here to draw general conclusions from this comparison.

Table 1 also shows the normalized stress range providing a 95% reliability for fatigue lives of 1 million and 10 million cycles. From a design perspective, this gives an indication of allowable stress ranges depending on the estimated number of load cycles applied throughout the expected service life. For 10 million cycles, the critical stress range varies from 11-34% of the ultimate static strength for the materials and configurations considered.

Table 1: Summary of fatigue life data

Source	Specimen type	P5/P95	P95 for 1 million cycles	P95 for 10 million cycles
[8, 9]	GFRP reinforcing bars	5.3	0.30	0.22
[3]	CFRP reinforcing bars	4.0	0.35	0.30
[4]	CFRP reinforcing bars	25.6	0.15	0.11
[35]	GFRP coupons	10.3	0.24	0.18
[36]	GFRP coupons	4.1	0.33	0.25
[6]	Pultruded GFRP plates	6.1	0.28	0.23
[7]	Bolted connections	42	0.29	0.22
[37]	Adhesive connections	14	0.41	0.34

4. CONCLUSIONS

The Sendeckyj model was used to fit experimental fatigue data for FRP composites with a range of material properties and configurations. The approach was able to satisfactorily capture the scatter of the experimental results under both static and fatigue loading.

The critical stress range for the FRP materials considered in this study for a fatigue life of 10 million cycles ranged from 11 to 34% of the ultimate static strength.

Many factors affect fatigue behavior, and no attempt is made here to draw general conclusions from the limited available data. Nevertheless, the proposed probabilistic approach is versatile and can be used to estimate fatigue lives of FRP components if sufficient experimental data is available for calibration.

REFERENCES

[1] Rahman, A.H., Adimi, M.R. and Benmokrane, B. 'Fatigue Behaviour of FRP Reinforcements Encased in Concrete.' *Proc. 2nd International Conference on Advanced Composite Materials in Bridges and Structures*, Montreal, Quebec, August 11-14 1996, 691-698.

[2] Nagaraj, V. and Gangarao, H. 'Fatigue behavior and connection efficiency of pultruded GFRP beams', *J. Composites for Construction* **2**(1), (1998) 57-65.

[3] Adimi, M.R., Rahman, A.H., and Benmokrane, B. 'New Method for Testing Fiber-Reinforced Polymer Rods under Fatigue', *J. Composites for Construction* **4**(4) (2000) 206-213.

[4] Elrefai, A., West, J. S. and Soudki, K. 'Performance of CFRP Tendon–Anchor Assembly Under Fatigue Loading', *Composite Structures* **80** (2007) 352-360.

[5] Helmi, K., Fam, A., and Mufti, A. 'Fatigue life assessment and static testing of structural GFRP tubes based on coupon tests', *J. Composites for Construction* **12**(2) (2008) 212-223.

[6] Tanaka, Y., Murakoshi, J., Nagaya, Y., and Watanabe, T. 'Static and fatigue behavior of thick pultruded GFRP plates with surface damage', *J. Bridge Engineering* **14**(2) (2009) 102-111.

[7] Wu, C., Feng, P., and Bai, Y. 'Comparative study on static and fatigue performances of pultruded GFRP joints using ordinary and blind bolts', *J. Comp. Construction* **19**(4) (2015) 04014065-1-10.

[8] Noel, M. and Soudki, K. 'Fatigue behavior of GFRP reinforcing bars in air and in concrete', *J. Composites for Construction* **04014006** (2014) 1-10.
[9] Noel, M. and Soudki, K. 'Fatigue behavior of full-scale slab bridge strips with FRP reinforcement', *J. Composites for Construction* **04014047** (2015) 1-10.
[10] Kim, H.C. and Ebert, L.J. 'Axial Fatigue Failure Sequence and Mechanisms in Unidirectional Fiberglass Composites', *J. Composite Materials* **12** (1978) 139-152.
[11] Kim, H.C. and Ebert, L.J. 'Fatigue Life-Limiting Parameters in Fibreglass Composites', *J. Materials Science* **14** (1979) 2616-2624.
[12] Talreja, R. 'Estimation of Weibull Parameters for Composite Material Strength and Fatigue Life Data' *ASTM STP 723* (1981) 291-311.
[13] Talreja, R. 'Statistical Considerations' *Fatigue of Composite Materials*, Ed. Reifsnider, K.L., Elsevier Science Publishing Company, New York, United States, (1991) 485-501.
[14] Curtis, P.T. 'The Fatigue Behaviour of Fibrous Composite Materials', *J. Strain Analysis* **24**(4) (1989) 235-244.
[15] Brondsted, P., Lilholt, H. and Anderson, S.I. 'Fatigue Damage Prediction by Measurements of the Stiffness Degradation in Polymer Matrix Composites' *Proc. Int. Conf. on Fatigue of Composites Eight International Spring Meeting*, Paris, June 3-5 1997.
[16] Demers, C.E. 'Fatigue Strength Degradation of E-glass FRP Composites and Carbon FRP Composites', *Const. Build. Materials* **12** (1998) 311-318.
[17] Van Paepegem, W. and Degrieck, J. 'A New Coupled Approach of Residual Stiffness and Strength For Fatigue of Fibre-Reinforced Composites', *Int. J. Fatigue* **24** (2002) 747-762.
[18] Zhou, Y. and Mallick, P.K. 'Fatigue Strength Characterization of E-Glass Fibers Using Fiber Bundle Test', *J. Comp. Mat.* **38**(22) (2004) 2025-2035.
[19] Nijssen, R.P.L 'Phenomenological Fatigue Analysis and Life Modelling', *Fatigue Life Prediction of Composites and Composite Structures*, Ed. Vassilopoulos, A.P. Woodhead Publishing Limited, Cambridge, United Kingdom (2010) 47-78.
[20] Mallick, P.K. 'Testing the Fatigue Strength of Fibers Used in Fiber-Reinforced Composites Using Fiber Bundle Tests', *Creep and Fatigue in Polymer Matrix Composites*, Ed. Guedes, R.M., Woodhead Publishing Limited, Cambridge, United Kingdom (2011) 409-423.
[21] Konur, O. And Matthews, F.L. 'Effect of the Properties of the Constituents on the Fatigue Performance of Composites: A Review', *Composites* **20**(4) (1989) 317-328.
[22] Reifsnider, K.L. 'Damage and Damage Mechanics', *Fatigue of Composite Materials*, Ed. Reifsnider, K.L., Elsevier Science Publishing Company, New York, United States (1991) 11-78.
[23] Curtis, P.T. 'Tensile Fatigue Mechanisms in Unidirectional Polymer Matrix Composite Materials' *Int. J. Fatigue* **13**(5) (1991) 377-382.
[24] Talreja, R. 'Damage Mechanics and Fatigue Life Assessment of Composite Materials', *Int. J. Damage Mechanics* **8** (1999) 339-354.
[25] Yao, W.X. and Himmel, N. 'A New Cumulative Fatigue Damage Model for Fibre-Reinforced Plastics', *Composites Science and Technology* **60** (2000) 59-64.
[26] Chou, P.C., and Croman, R. 'Residual Strength in Fatigue Based on the Strength-Life Equal Rank Assumption', *J. Composite Materials* **12** (1978) 177-194.
[27] Sendeckyj, G.P. 'Fitting Models to Composite Materials Fatigue Data', *ASTM STP 734* (1981) 245-260.
[28] Noel, M. 'Behaviour of post-tensioned slab bridges with FRP reinforcement under monotonic and fatigue loading', PhD thesis, University of Waterloo, Waterloo, Canada (2013).
[29] Vieira, P. R., Carvalho, E.M.L., Vieira, J.D., Filho, R.D.T. 'Experimental fatigue behavior of pultruded glass fibre reinforced polymer composite materials', *Comp. Part B* **146** (2018) 69-75.
[30] Sarfaraz, R., Vassilopoulos, A.P., Keller, T. 'Experimental investigation of the fatigue behavior of adhesively-bonded pultruded GFRP joints under different load ratios', *Int. J. Fatigue* **33** (2011) 1451-1460.

LOCAL BUCKLING OF PULTRUDED GFRP I-SECTION SUBJECT TO BENDING

Everton de S. Vieira (1), Janine D.Vieira (2) and Daniel C. T. Cardoso (1)

(1) Department of Civil and Environmental Engineering, Pontifícia Universidade Católica do Rio de Janeiro, Brazil

(2) Department of Civil Engineering, Universidade Federal Fluminense, Niteroi, Brazil

https://doi.org/10.21452/bccm4.2018.06.05

Abstract

The use of pultruded glass fiber reinforced polymer (pGFRP) has increased significantly in the last few years, especially in aggressive environments. The structural performance of pGFRP members is strongly dependent on their buckling behavior, because of the association of low elastic properties and relatively thin-walled sections adopted. The aim of this study is to present the results of an ongoing experimental work focused on evaluating the local buckling behavior of GFRP I-beams subject to 4-point bending tests. Lateral deflections were measured with displacement transducers and the curvature at compression flange during loading was measured with back-to-back strain gages. A finite element model using actual material properties and bracing conditions was adopted to ensure behavior governed by local buckling and to determine critical bending moment. The influence of web-to-flange rotational stiffness on the behaviour is discussed and, finally, experimental critical loads obtained using Southwell and Koiter techniques are compared to those obtained using analytical expressions recently proposed in literature and to computational analysis

1. INTRODUCTION

Pultruded glass fiber-reinforced polymer (pGFRP) members had their first applications in aerospace industry followed by oil and automotive industries. In the last years, the use of pGFRP increased in structural engineering because of its good performance in aggressive environments and high tensile and compressive strengths (parallel to fiber direction), comparable with steel. However, the association of the low modulus of elasticity in the longitudinal direction - about 1/8 that of steel – to the relatively thin-walled sections adopted and high material anisotropy makes pGRFP members susceptible to instability problems and significant interaction between local and global buckling modes [1].

Several authors have dedicated efforts to study local buckling behavior of pGFRP members subject to compression with different cross-sections (e.g. [2,3,1]). However, only a few have been exclusively dedicated to experimentally the local buckling in bending. In the early 1990's, Barbero et al. [4] conducted a series of tests in pGFRP beams subject to bending. Specimens were laterally braced at mid-span and the authors observed that failure by local buckling governed the behavior. Bank et al. [5] performed four-point bending tests in beams designed to fail in local buckling and reported typical failure mode by tearing along the web-flange junction at the constant-moment region. Later, Bank et al. [6] reviewed experimental data of three beams and proposed an appropriate technique to determine the critical load accounting for the non-linear behavior and avoiding overestimated results. Finite element method (FEM) analyses were also carried out to show that anisotropy and inhomogeneity of pultruded material may affect significantly local buckling behavior. Recently, Vieira et al. [7] reported the results of an experimental study aiming to investigate the flexural behavior of GFRP beams for a variety of section geometries and spans. The work showed different buckling modes and the experimental results were compared with those obtained using design methods available in standard under development (ASCE [8], EUR27666 [9]) as well as to the equation proposed by Kollar [10] and to Finite Strip Method (FSM). According to the authors, the design methods were found to be conservative. It is also worth reporting the interesting study carried out by Kubiak et al. [11] in non-pultruded composite channel sections. To ensure local buckling due to 'pure' flexure, i.e. avoiding influence of shear in the buckling mode, rigid blocks were adopted at the shear spans and, to account for the non-hyperbolic load-deflection behavior, experimental critical loads were obtained using Koiter's technique.

Several closed form equations to calculate the critical load for different loading conditions are available in literature [10, 12, 13, 14]. Kollar [10], for instance, presented explicit expressions considering the cross-section comprised of orthotropic plates with rotationally restrained edges. The method allows considering different cross-sections and loading conditions and has been validated for I-sections, resulting in its inclusion in the latest versions of standards under development. Closed form equations for I-section beams subject to pure bending are also presented by Ascione et al. [13] and Cardoso and Vieira [14]. In these works, equations were obtained using energy methods along with assumed approximate buckled shapes and good results were obtained when compared to numerical methods. Approaches considering interaction between flange and web lead to superior agreement and will soon prevail over the simple but old-fashioned approach where web-to-flange junction is assumed as hinged. Another important parameter is the flexibility of the flange-to-web junction, [15]. To date, there is no explicit equation accounting for this flexibility, although significant reduction in critical loads has been reported in literature [16].

The flexural performance of pGFRP is dependent on its buckling behavior. Due to its orthotropic properties, formulations proposed for isotropic materials on instability studies give unreliable results. The aim of this paper is to present results of an ongoing research on flexural behavior of pultruded GFRP I-sections. Results from tests on I-sections having flange-to-web width ratio equal to 1.0 are reported and compared to those obtained using finite element method (FEM) and analytical expressions proposed Cardoso and Vieira [15], as well as by EUR 27666 [9] and ASCE [8]. The influence of the flexibility of the web-to-flange junction is also discussed

2. EXPERIMENTAL PROGRAM

2.1 Material Characterization

The wide flange pultruded profiles with section depth, d, equal to flange width, bf, used in this study were made with vinyl ester resin and E-glass fiber. In order to obtain the relevant properties

of the material, specimens were extracted from flanges and web and mechanical characterization was carried out. The average values (and COV in parentheses) of the experimental mechanical properties as well as those reported by the manufacturer are presented in Table 1. It is important to mention that all moduli in flexure are related to the bending of constituent walls and that the transverse modulus, $E_{T,f}$, was determined with a non-standard test since the geometry of the pultruded profile did not allow extraction of specimens with standards dimensions. Figure 1 shows the tests performed for mechanical characterization of the pultruded material.

Table 1: Mechanical properties of GFRP profiles, in MPa.

Mechanical properties	Test method	Experimental values (COV)		Manufacturer reported
		Flange	Web	
Longitudinal modulus in tension, $E_{L,t}$	ISO 527-4	32653 (0.11)	26350 (0.03)	17260
Longitudinal modulus in compression, $E_{L,c}$	ASTM D6641	30401 (0.17)	28328 (0.09)	-
Longitudinal modulus in flexure, $E_{L,f}$	ISO 14125	19854 (0.25)	17425 (0.01)	10984
Transverse modulus in flexure, $E_{T,f}$	non-standard	7867 (0.05)	-	5492
Shear modulus, G_{LT}	ASTM D5379	2298 (0.42)	2374 (0.11)	-
Longitudinal strength in tension, $F_{L,t}$	ISO 527-4	425 (0.04)	330 (0.15)	287
Longitudinal strength in compression, $F_{L,c}$	ASTM D6641	275 (0.05)	370 (0.15)	287
Longitudinal strength in flexure, $F_{L,f}$	ISO 14125	470 (0.09)	477 (0.04)	287

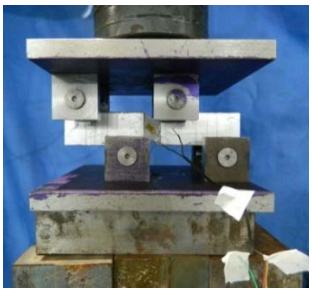

(a) Isosipescu test

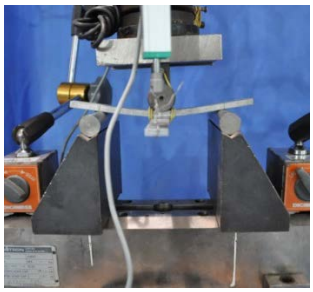

(b) Three point flexure test

(c) Tensile test

(d) Compression test

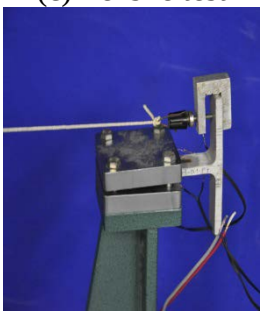

(e) and (f) Transverse flexure test

Figure 1: Mechanical characterizations tests

2.2 Rotational spring constant (kθ)

It has been shown in literature that the rotational stiffness of the web-to-flange junction may affect significantly the critical load and buckling mode [15,16]. In this work, an experimental characterization of the rotational spring constant was carried out. Three ‘tee’ specimens 85-mm

wide extracted from the pultruded profiles were used. The flange of the specimen was clamped at a test frame using rigid aluminum bars to ensure no displacement and steel plates were attached to the web to assure negligible plate bending during the tests. To measure the lateral displacement, a displacement transducer was placed at the free end of the 'tee' stem, in the direction of applied load. The load was applied using dead weights and was incremented manually. Figure 2 shows the set-up adopted for the experimental test. The average value for kθ obtained was 10085 N.mm/mm/rad.

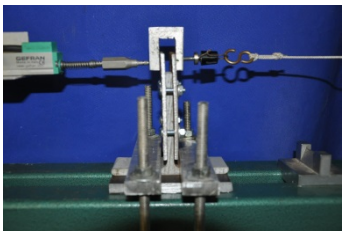

(a)Lateral view

(b) Overview

2.3 Flange Local Buckling (FLB) – Four-point bending test

For the flange local buckling (FLB) investigation, three I-sections with nominal dimensions 102 x 102 x 6 mm (d x bf x t, where t is the uniform thickness) with a flange slenderness, bf/2t, of 8.5 were tested. Four-point bending tests over a span of 1100 mm consisting of two 310-mm shear spans and a 480-mm constant moment region were carried out. In all tests, lateral supports were provided near supports and loading points to prevent lateral torsional buckling (LTB) and distortion. For this purpose, steel plates coated with teflon to avoid the friction between the profile and the plates were used. A narrow neoprene layer was used at the loading points to concentrate loads over web, i.e. without introducing transverse flexure on flanges. To monitor the onset and development of FLB, back-to-back strain gages were applied to both tips of the compression flange, at the middle of the constant moment region. Draw-wire transducers were used to measure the vertical deflection and the lateral displacement of the beam at mid-span.

All the tests were carried out using a 1000 kN capacity servo-hidraulic MTS actuator with a displacement control of 0.6 mm/min up to failure. Figure 3 shows the setup for the flexural tests.

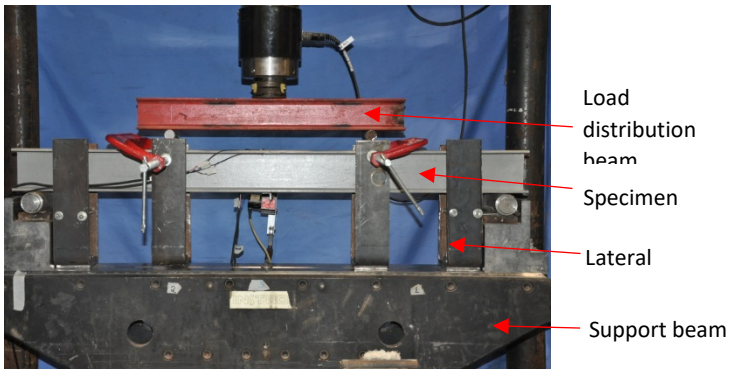

(a) front-view

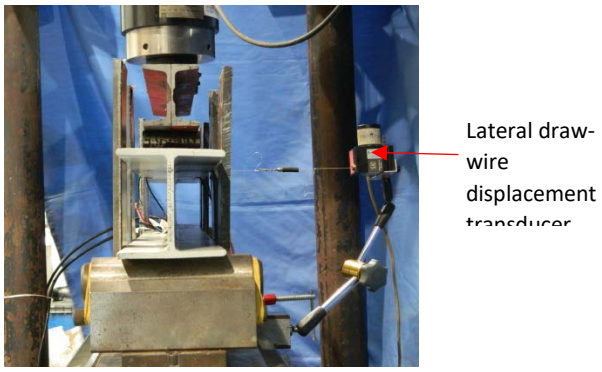

(b) lateral view

Figure 3: Set-up for pGRFP flexural tests.

2.4 Finite Element Method (FEM)

In order to predict the local buckling critical moment, linear eigenvalue FEM analysis was carried out using Abaqus 6.13.1 [17] software. The model was discretized with shell elements S8R5 and average experimental mechanical properties were used. To represent the rotational stiffness at the junction, flange and web were joined using connector-type elements with rotational spring about axis Z defined according to the experiments. To simulate the lateral supports, the displacements in X direction were restrained at both flanges. Translations in vertical direction (Y) were restrained at both ends whereas translation at Z direction was included in one of the ends. Figure 4 shows the model of the beam with their boundary conditions. Figure 5 illustrates the first buckling mode obtained from FEM analysis.

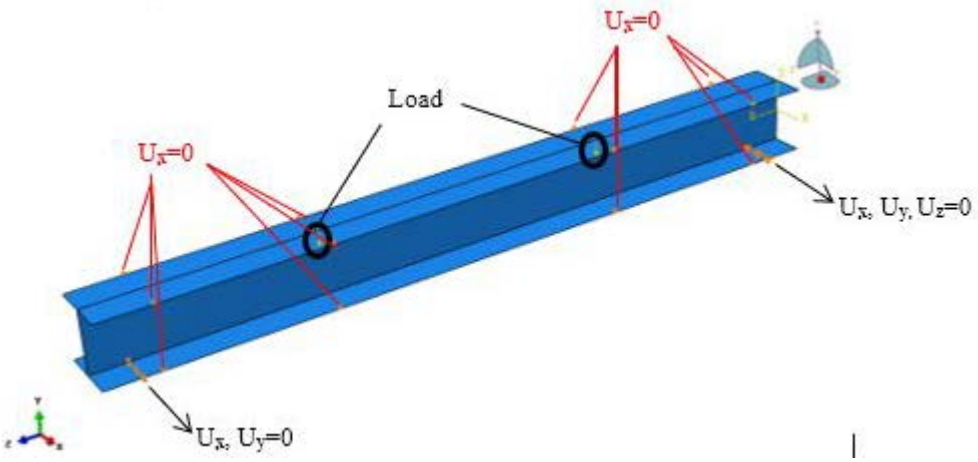

Figure 4: Boundary conditions of the beam implemented in FEM

3. RESULTS ANS DISCUSSIONS

Representative experimental moment vs vertical and moment vs lateral deflections are reproduced in Figure 6a and 6b, respectively. All the tests exhibited negligible lateral motions prior to local buckling. After the formation of local buckling waves, lateral deflections resulting from loss of stiffness can be observed. Failure finally results from an interaction between FLB and LTB, leading to premature failure and unnoticeable post-buckling reserve of strength. This phenomenon can be clearly observed from moment-lateral deflection shown in Figure 6b as well as from the differences in non-dimensional curvature, Φ (equal to strain at top minus strain at bottom of flange), obtained for the pairs of strain-gages for each side of the flange presented in moment vs non-dimensional curvature shown in Figure 6c, which suggests a greater compression stress in one side of the flange and a relief on the opposite side. Larger amplitude on the more compressed side could also be observed during tests, as shown in the typical buckling mode illustrated in Figure 7. All beams tested exhibited flange-to-web tearing failure.

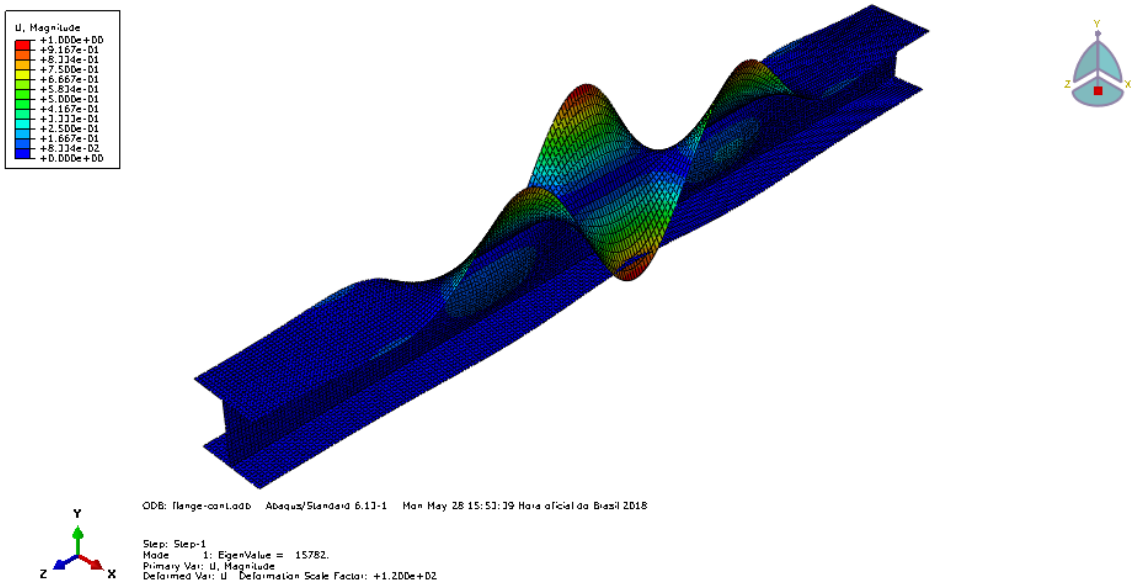

Figure 5: buckling mode of four-point bending FE model

The experimental critical FLB moments obtained using Southwell and Koiter techniques and the results obtained from analytical and computational analyses (FEM) are present in Table 2. In all analyses, nominal section dimensions were used. It is important to mention that Koiter's approach take into account the post-buckling behavior whereas Southwell is usually valid for columns with hyperbolic buckling behavior. A good agreement was achieved between experimental results and those obtained with ASCE Pre-standard [8], Cardoso and Vieira [14] and with Finite Element Method (FEM), whereas significant lower critical stress was obtained using EUR 27666 [9]. It is important to note that a closer prediction was expected using FEM model and differences may be explained by a low rotational stiffness and/or shear modulus adopted in the model, suggesting that more characterization tests are necessary to obtain reliable properties. It can also be highlighted that the method proposed by Cardoso and Vieira [14] is based on energy approach and assumes full compatibility of rotation between flange and web, therefore resulting in greatest prediction among all methods, although relatively close to the experimental results.

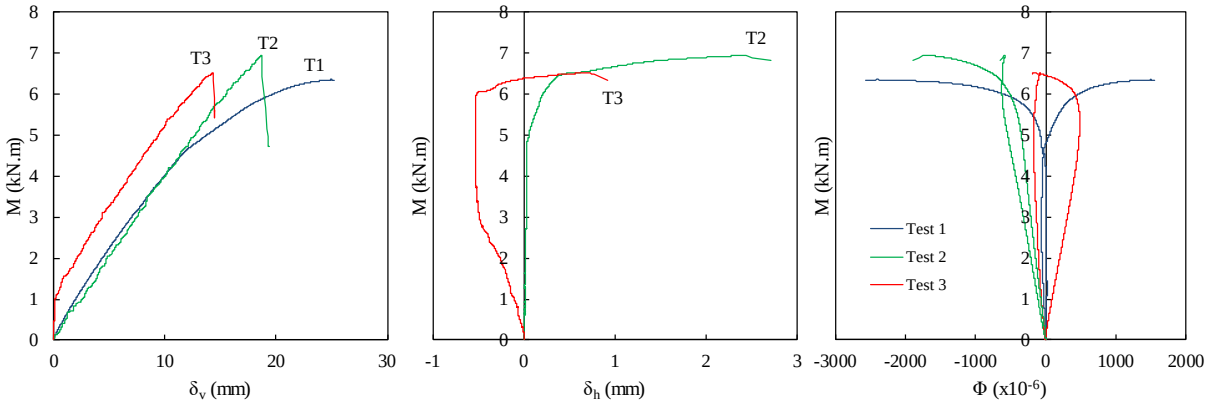

a) moment vs vertical deflection

b) moment vs horizontal deflection

c) moment vs non-dimensional curvature

Figure 6: Experimental results.

Table 2: Critical moments in N.m for various analyses.

Experimental (COV)		FEM		Cardoso and Vieira (2017)		EUR 27666 (2016)		ASCE (2010)	
Southwell	Koiter	M_{cr}	pred./exp.	M_{cr}	pred./exp.	M_{cr}	pred./exp.	M_{cr}	pred./exp.
5502 (0.069)	5509 (0.12)	4894	0.81-0.96	5754	0.96-1.13	4424	0.74-0.87	5523	0.92-1.09

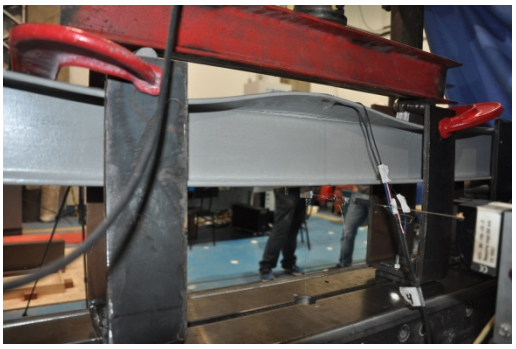

a) Flange local buckling at constant region moment

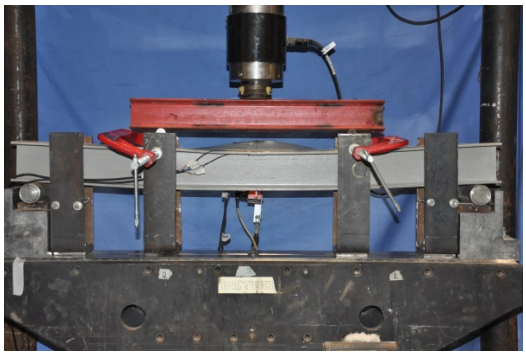

b) Differences in the amplitude of half-waves for both sides of compression flange.

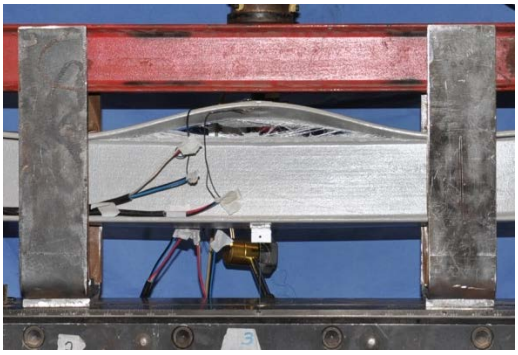

c) Web-junction tearing failure

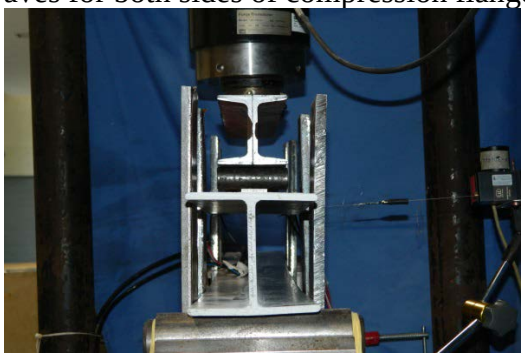

d) Compression flange rotation

Figure 7: Local flange buckling observed in the experimental tests

4. CONCLUSIONS

- This paper presented the results of an ongoing experimental work with the objective to evaluate the local buckling behaviour of GFRP I-beams subject to four-point bending tests. The experimental program included mechanical characterization tests and a simple nonstandard test to obtain the rotational spring constant was proposed.
- The beam tests showed that the rotational stiffness of web-to-flange junction influences critical moment and buckling behaviour. A FEM model of the beam was implemented with the rotational spring constant and a good correlation was observed, although FEM results in lower critical stress, which may be attributed to inherent variations of material properties. More characterization tests must be carried out to obtain reliable properties and, therefore, a closer agreement between FEM and experiments.
- The equations proposed by ASCE [8] and by Cardoso and Vieira [14] presented good agreement with the experimental results. On the other hand, the critical stress obtained

using the equation proposed in the EUR 27666 [9] underestimates significantly the experimental results. It is important to mention that all theoretical approaches studied neglect the rotational stiffness of the web-to-flange junction and more tests are necessary to validate the methods for general conditions.

- The failure modes were similar in all tests with rupture in web-flange junction. This type of failure is expected since it can be affected by presence of the resin-rich zone which interfere in the arrangements of the fibers and local imperfections due to the pultrusion process.

ACKNOWLEDGEMENTS

The first author thanks to CAPES (Coordenação de Aperfeiçoamento de Pessoal de Nivel Superior) for financial support. All authors wish to thanks Stratus Compostos Estruturais Ltda for supplying the GFRP profiles used in this work.

REFERENCES

[1] Cardoso D., Harries K. and Batista E. "Compressive local buckling of pultruded GFRP I-sections: development and numerical/experimental evaluation of an explicit equation". *ASCE Journal of Composites for Construction*, **19**(2), (2015)

[2] Tomblin, J. and Barbero, E. "Local buckling experiments on FRP columns". Thin-walled structures, **18**(2), (1994) 97-116.

[3] Turvey, G. and Zhang, Y. "A computational and experimental analysis of the buckling, postbucking and initial failure of pultruded GRP columns". *Computers and Structures*, **84**(22), (2006a) 1527-1537.

[4] Barbero, E., Fu, S., and Raftoyiannis, I. "Ultimate bending strength of composite beams". *Journal of Materials in Civil Engineering*, **3**(4), (1991) 292-306.

[5] Bank, L., Nadipelli, M., Gentry, T.. "Local buckling and failure of pultruded fiber-reinforced plastic beams". *Journal of Engineering Materials and Technology*, **116**(2), (1994) 233-237.

[6] Bank, L., Yin, J., and Nadipelli, M.. "Local buckling of pultruded beams—Nonlinearity, anisotropy and inhomogeneity". *Construction and Building Materials*, **9**(6), (1995) 325-331.

[7] Vieira, J., Liu, T., and Harries, K.. "Flexural stability of pultruded glass fibre-reinforced polymer I-sections". Proceedings of the Institution of Civil Engineers - Structures and Buildings, (2017) 1-12.

[8] ASCE – American Society of Civil Engineers (2010). "Pre-standard for load and resistance factor design (LRFD) of pultruded fiber reinforced polymer (FRP) structures". ASCE, Reston, VA, USA.

[9] Ascione, L. et al.. "Prospect for new guidance in the design of FRP: Support to the implementation and further development of the eurocode". Publications Office of the European Union, Brussels, Belgium, Report EUR 27666, (2016).

[10] Kollár, L. P.. "Local buckling of fiber reinforced plastic composite structural members with open and closed cross sections". *Journal of Structural Engineering*, **129**(11), (2003) 1503-1513.

[11] Kubiak, T., Kolakowski, Z., Swiniarski, J., Urbaniak, M., and Gliszczynski, A.. "Local buckling and post-buckling of composite channel-section beams–Numerical and experimental investigations". *Composites Part B: Engineering*, **91**, (2016) 176-188.

[12] Mottram, J. T.. "Determination of critical load for flange buckling in concentrically loaded pultruded columns". *Composites Part B: Engineering*, **35**(1), (2004) 35-47.

[13] Ascione, F., Feo, L., Lamberti, M., Minghini, F., and Tullini, N.. "A closed-form equation for the local buckling moment of pultruded FRP I-beams in major-axis bending". *Composites Part B: Engineering*, **97**, (2016) 292-299.

[14] Cardoso, D. C., and Vieira, J. D.. "Comprehensive local buckling equations for FRP I-sections in pure bending or compression". *Composite Structures*, **182**, (2017) 301-310.
[15] Turvey, G., and Zhang, Y.. "Characterization of the rotational stiffness and strength of web-flange junctions of pultruded GRP WF-sections via web bending tests". *Composites Part A: applied science and manufacturing*, **37**(2), (2006b) 152-164.
[16] Ascione, L., Berardi, V. P., Giordano, A., and Spadea, S.. "Local buckling behavior of FRP thin-walled beams: a mechanical model". *Composite Structures*, **98**, (2013) 111-120.
[17] ABAQUS. Software Documentation. Version 6.13.1 by SIMULIA, (2013).

7. GLARE AND FIBER-METAL LAMINATES

THERMAL BEHAVIOR OF POLYMER METAL HYBRIDS OF HOT STAMPED STEEL AND FIBER-REINFORCED THERMOPLASTICS

Michael Demes (1), Markus Kühn (1), Tobias Gebken (1) and Klaus Dröder (1)

(1) Institute of Machine Tools and Production Technology (IWF), Technische Universität Braunschweig, Germany

https://doi.org/10.21452/bccm4.2018.07.01

Abstract

Hot stamping constitutes a manufacturing process for both high strength and lightweight automotive structural components and is used to produce some 40 % of today's structural components in car bodies. Lightweight approaches aim at weight reduction by reducing steel thickness and applying fiber-reinforced plastics (FRP) to regain structural stiffness and strength. Inherent thermal metal processing renders hot stamping an adequate process chain for the manufacturing of hybrid metal polymer composites. Thereby, residual heat in metal parts is used to enhance adhesion between polymer and metal. In fact, the temperature of the parts after hot stamping is in the range of the processing temperatures of several technical polymers, thus providing process conditions suitable for thermal direct joining or activation of adhesion promoters. The temperature specification of the realized metal polymer composites equal specifications for vehicle bodies in the temperature range from - 40 °C to + 80 °C.

In this paper, the thermal behavior of polymer metal hybrids of hot stamped steel and FRP in means of deflection is investigated. Also the influence of mechanical interlocked and adhesively bonded hybrid specimens are investigated. Therefore, hybrid specimens are manufactured under realistic industrial conditions, varying the manufacturing process parameters. The specimens are tested with respect to temperature load investigating thermal expansion using optical measuring techniques.

1. INTRODUCTION

Production volumes of passenger vehicles are expected to increase from 89 million units in 2015 to 113 million units in 2025 [1]. While the production volumes are increasing, a reduction of greenhouse gases emitted by combustion engines is in contrast to achieving targets of global climate conventions [2,3]. Lightweight design is an approach to reduce the mass of vehicles resulting in a decreased need of fuel and emitted greenhouse gases [4]. Reducing masses in vehicle structures offers the opportunity to enhance the effect of lightweight design by decreasing also additional components mass [1,5].

Typical vehicle structures are made of steel or aluminum alloys. Lightweight design in the area of steel is primarily aiming at a reduction of material thickness by using other new high strength steel alloys [6,7]. Hot stamped steels reach very high strengths and opportunity to reduce material thicknesses. Steel sheets are heated in a roll furnace to approximately 950 °C to transform the microstructure to austenite. The heated steel sheet is then rapidly transferred and hot stamped thus creating strengths between 1,500 MPa to 2,000 MPa, reaching similar behaving parts compared to non-hot stamped parts with reduced masses [8-11]. Another approach to reduce vehicle structure mass is the use of high performance FRP [12-14]. The use of a multimaterial design consisting of a metal- and a FRP-component can realize advanced lightweight body parts able to be processed in state of the art body shops realizing economically advantageous lightweight design for large-scale production [15].

Inherent thermal metal processing renders hot stamping an adequate process chain for the manufacturing of hybrid metal polymer composites. Thereby, residual heat in metal parts can be used to enhance adhesion [16] and mechanical interlocking [17] between polymer and metal. In fact, the temperature of the parts after hot stamping is in the range of the processing temperatures of several technical polymers, thus providing process conditions suitable for thermal direct joining or activation of adhesion promoters. The temperature specification of the realized metal polymer composites equal specifications for vehicle bodies in the temperature range from -40 °C to +80 °C [18].

In this paper, the thermal behavior of adhesively bonded and textured polymer metal hybrids of hot stamped steel and FRP are investigated. Therefore, hybrid specimens are manufactured under realistic industrial conditions, varying the manufacturing process parameters. The specimens are tested with respect to thermal expansion using optical measuring techniques.

2. EXPERIMENTAL SETUP

2.1 Realizing hot stamped plastic metal hybrids

Figure 1 shows the schematic experimental setup based on hot stamping industry applications. First, a boron-manganese steel blank is cut to specimen dimensions and eventually austenitized at a temperature of approximately 950 °C. After allowing a sufficient heating time of at least 10 minutes, the flat specimen is rapidly transferred into a press where it is hot stamped. After hot stamping in a flat die, the specimen is quenched and kept in its flat dimension, finishing the quenching process when the specimen's surface temperature reaches 250 °C. The semi-finished part leaves the press at a temperature range which offers the potential to melt adhesion promoters and polymer surfaces, and to integrate an adhesive bonding process of thermoplastic FRP. In a final step, FRP adherends and metal adherends are joined to hybrid specimens using a hot press and eventually are tested with respect to thermal expansion using optical measuring techniques.

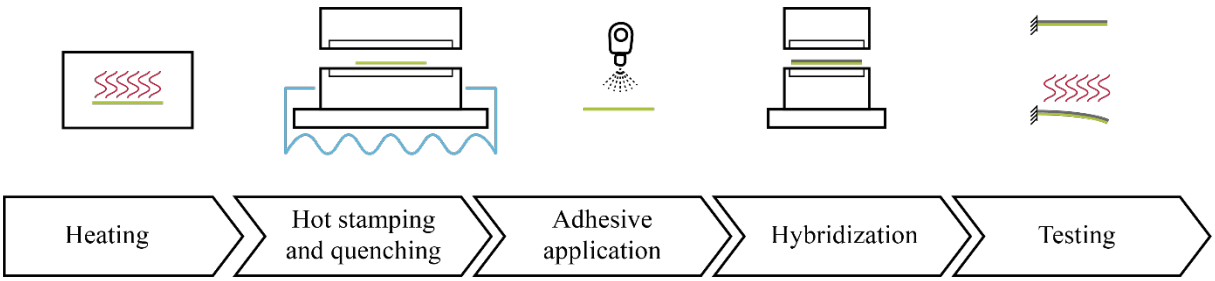

Figure 1: Experimental Setup

2.2 Hot stamping

Figure 2 shows a schematic of the temperature profile and condition of microstructure of a hot stamping process. In the as-delivered condition and at room temperature (RT) the boron-manganese steel specimen is showing ferrite and pearlite microstructure. After austenitization in a furnace at 950 °C, the temperature is kept to ensure fully austenitization of the specimen [2,19]. In a subsequent step the specimen is rapidly transferred into a flat press where it is kept in flat form and quenched until it reaches 250 °C [20]. After successful hot stamping the specimen microstructure developed a fully martensite microstructure.

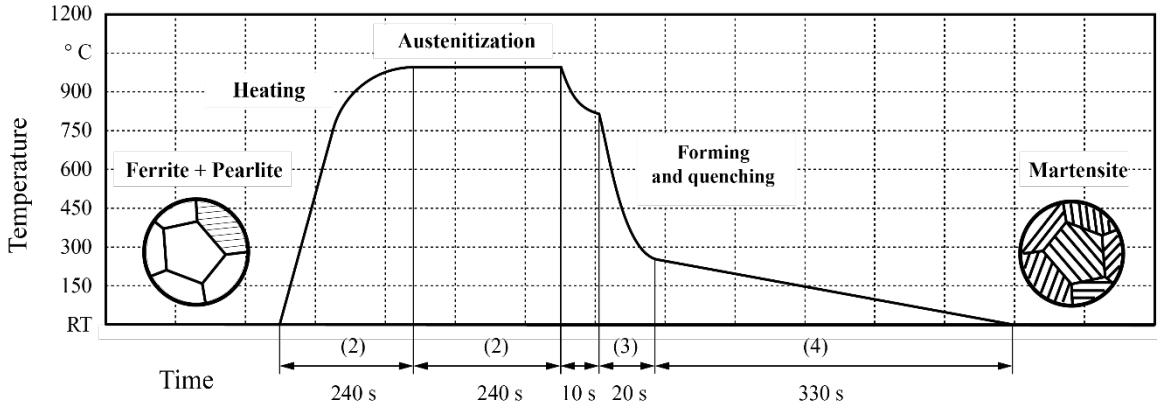

Figure 2: Hot Stamping

2.3 Materials and structures and combinations

To bond the metal component to the FRP adherend, an adhesion promoter in combination with a structured surface and type of steel´s microstructure are investigated. The adhesion promoter is a cross-linkable powder-based agent which is based on a reactive co-polyamide (Vestamelt X1333, Table 1).

Table 1: Adhesion promoter material properties [21]

				Temperatures	
Brand name	**Adhesive**	**Chemical base**	**Initial condition**	**Precoating**	**Activation**
Vestamelt®	X1333	reactive co-polyamid	powder	150 °C	> 165 °C

As FRP a consolidated composite laminate (CCL/organic sheet) consisting of multiple layers of continuous reinforcement glass fibers embedded in a polyamide 6 (PA 6) matrix is used. The metal component is a boron-manganese steel (22MnB5) with an aluminum-silicon coating (150 gm^{-2}). The tensile strength in as-received condition is 532 MPa. In Table 2, the material properties of the applied materials are shown.

Table 2: Adherend's material properties

	FRP materials	Metal materials	
	CCL	22MnB5 (as-delivered)	22MnB5 (hot stamped)
Fiber	glass	-	-
Density [g·cm^{-3}]	1.8	7.9	7.9
Polymer	PA 6	-	-
Melt temperature [°C]	220	-	-
Glass Content [vol. %]	47	-	-
Thickness [mm]	2.5	1.5	1.5
Tensile Strength [MPa]	404	532	1518
Coefficient of thermal expansion 10^{-6} [1/K]	17.3	11.7	11.7
Young's Modulus [MPa]	22,400	210,000	210,000

The setup of adhesive and structures on metal specimens is shown in Figure 3. In total six combinations of adhesive and structure application are inspected. To investigate the influence of the steel´s microstructure specimens in as-delivered condition (ferrite + pearlite) and after hot stamping (martensite), quenched in water, are used. Flat specimens without structured surfaces are investigated with only adhesive application. Structured specimens are investigated, structured with 0.08 structures/ 1 mm² and a structure height of 1.0 mm, with and without application of additional adhesive.

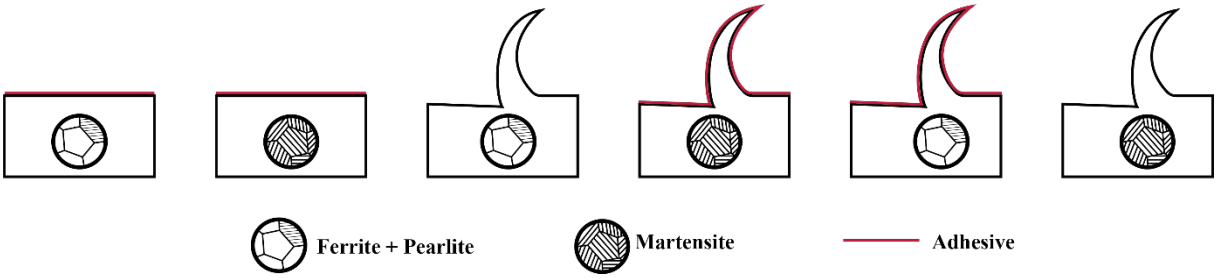

Figure 3: Combination of adhesive and structures on metal specimen

2.4 Hybridization

The metal and FRP adherends are joined using a hot press (Vogt LaboPress 400). Both adherends are heated up to 250 °C in the die of the hot press and joined with a press pressure of 3.0 MPa and a press duration of 20 s creating each five specimens per setup. After joining the specimen is cooled to 150 °C before being unmolded.

2.5 Thermal expansion

By using a theoretical approach, the thermal deflection is calculated for the hybrid beam structure. With the theoretical approach, an estimation of the expected deflection can be given. It is reliable for two homogenous materials with a stiff bond without a transition thickness. The equation for the thermal deflection can be written as follows [22]:

$$d = \frac{12 \cdot E_{Steel} E_{FRP} \cdot (\alpha_{FRP} - \alpha_{Steel}) \cdot \Delta T}{\frac{t_{Steel} + t_{FRP}}{2} \cdot (E_{Steel}^2 + 14 \cdot E_{Steel} E_{FRP} + E_{FRP}^2)} \cdot \frac{l^2}{2}$$

The result of the equation is the thermal deviation d. Moreover, E is the elastic modulus, α the thermal expansion coefficient, ΔT the temperature difference, l the specimen length and t the material thickness.

By inserting the value of table 2 the deflection d is calculated to:

$$d = 1{,}71\ mm$$

The calculated thermal deflection gives an orientation for the following experimental work and is validated by a homogenous hybrid structure without the structuring on the metal part.

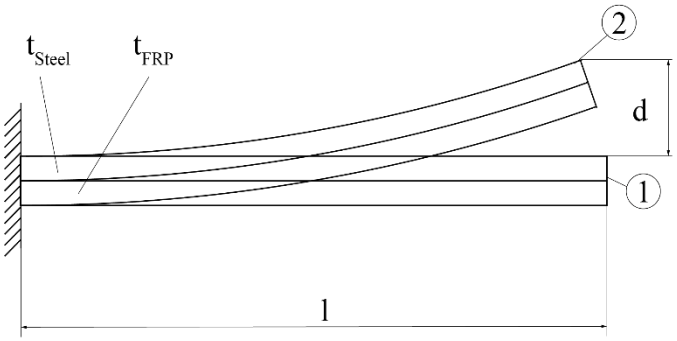

Specifications

Temperature:	t_1 = 21 °C	t_2 = 80 °C
Length:	l = 180 mm	
Width:	w = 25 mm	
Thickness:	t_{Steel} = 1.2 mm	
	t_{FRP} = 2.0 mm	
Steel:	22MnB5 (Ferrite + Pearlite)	
	22MnB5 (Martensite)	
FRP:	Polyamide 6 47 (fibre vol.) %	

Figure 4: Homogenous hybrid structure without structuring under temperature load (2)

3. RESULTS AND DISCUSSION

To investigate the thermal behavior in means of deflection of the specimens, GOM ARAMIS®, an optical measuring technique is used. Each five specimens per setup are fixed in a furnace with room temperature (21 °C) showing a free length of 180 mm. In the next step the furnace is heated up to 80 °C simulating one of the highest assumed temperatures for automotive structure components. When the furnace reaches 80 °C the temperature is kept for 10 minutes to ensure fully heated specimens. In the lowest area of the specimen a virtual measuring point is set detecting total deflection of hybrid specimens. Figure 5 shows the specimens installed in the furnace at a temperature load of 80 °C. The value in the yellow boxes is indicating the maximum measured deflection at the determined point (yellow point).

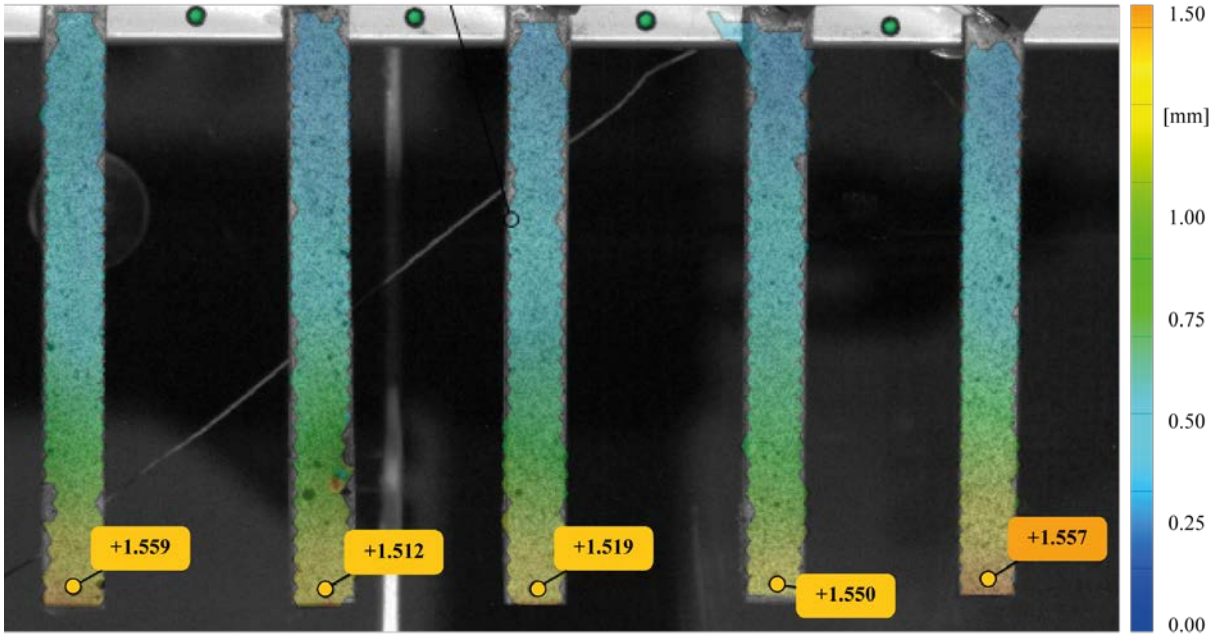

Figure 5: Specimens (no adhesive, structured) at temperature load (5 equal specimens, 80 °C)

The mean value of the maximum deflection in the lowest of each five specimens is determined and shown in figure 6. The maximum average deflection of 1.75 mm is occurring at adhesive-only bonded specimens. The lowest average deflection of 1.57 mm is shown at structured specimens without adhesive. The deflection of as-delivered steel specimens (ferrite and pearlite microstructure) and hot stamped steel (martensite microstructure) are in the range of the mean variation and are not showing an influence on deflection. Structured specimens with an applied layer of adhesive are showing a maximum deflection of 1.64 mm.

Comparing the results: Maximum deflection can be reduced by using structured metal components. The application of an additional adhesive smoothens the load transition between the two adherends but is resulting in a larger deflection. The larger resulting adhesive layer and FRP adherend are resulting in a larger total FRP component and larger deflection. The theoretical approach for a deflection determination is only suitable for the bonded materials. In case of inhomogeneous surface structure a numerical simulation of the deflection have to be performed.

Discussing the results: All structured specimens showing lower deflection at 80 °C compared to adhesive only bonded. This can be caused due to changed characterisicts of the boundary layer resulting of the clamped materials. The larger deflection of adhesive bonded specimens is caused by a larger total thicknesses of the specimens.

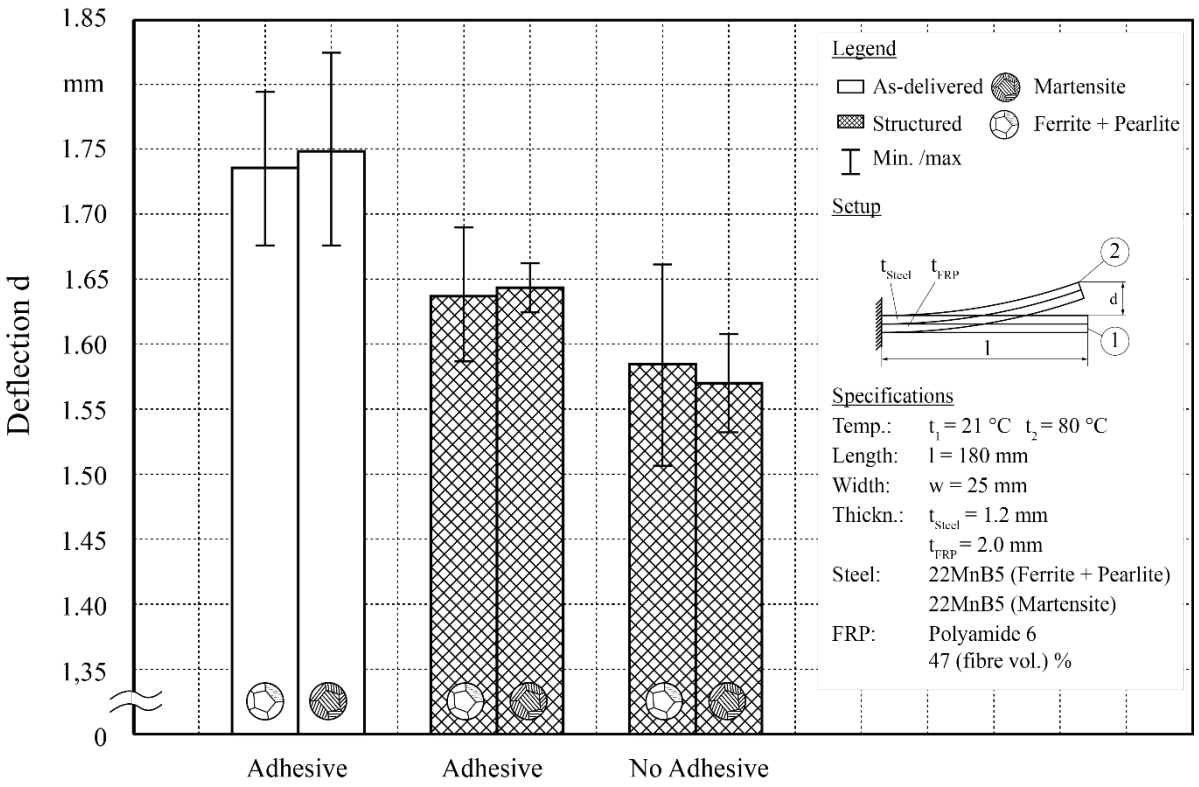

Figure 6: Deflection of specimens

4. SUMMARY AND OUTLOOK

The thermal behavior of hybrid components consisting of metal und FRP with different temperature expansion coefficient can be influenced by different joining methods. In this paper, the thermal behaviour in means of deflection of adhesive and structured bonded polymer metal hybrids of hot stamped steel and FRP was investigated by realizing flat hybrid specimens. With GOM ARAMIS optical measurement technology maximum deflection of free lowest area was detected and analyzed according to bonding mechanism.

Hybrid specimens with adhesive-only bonding are showing maximum deflection. A reduction of deflection can be achieved by structuring metal component and applying adhesive. A minimum deflection is realized by structured-only specimens. An influence on microstructure whether hot stamped or in as-delivered condition of boron-manganese steel is not observed.

In further investigations, the ageing influence after some temperature cycles will be investigated. The structure density can be improved in further studies by optimization of amount and geometry of structures to realize a smoother force transfer. Moreover, a numerical simulation of the deflection by respecting the surface structures for the hybrid design will be set up.

5. REFERENCES

[1] Thaden, G., Mogge, F., Riederle, S., (2017) *Automotive metal components for car bodies and chassis: Global market study*, Roland Berger, München, p. 11.
[2] International Energy Agency, (2015) *World Energy Outlook*, Paris: OECD/IEA, p. 36.
[3] European Union, (2009) *Regulation (EC) No 443/2009 of the European Parliament and the Council*.

[4] Markiewicz, M., (2017) *Reduction of CO2 Emissions from Road Transport in Cities: Impact of Dynamic Route Guidance System on Greenhouse Gas Emission*, Springer, Wiesbaden.
[5] Dlugosch, M., Lukaszewicz, D., Fritsch, J., Hiermaier, S., (19-24th July 2015) *Mechanical Characterization of Hybrid Material Systems Consisting of Sheet Metal and Advanced Composites*, 20th International Conference on Composite Materials, Copenhagen, p. 2.
[6] Eickenbusch, H., Krauss, O., (2014) *Werkstoffinnovationen für nachhaltige Mobilität und Energieversorgung* (VDI-GME-Studie), Verein Deutscher Ingenieure e.V., VDI-Gesellschaft Materials Engineering, Düsseldorf, p. 33.
[7] Howe, C., (2012) *Motor vehicle structure, and method of making a motor vehicle structure*, Patent US20120193939 A1, p. 1.
[8] Mori, K.; Bariani, P. F.; Behrens, B.-A.; Brosius, A.; Bruschi, S.; Maeno, T.; Merklein, M.; Yanagimoto, J. (2017) *Hot stamping of ultra-high strength steel parts*, CIRP Annals - Manufacturing Technology 66, p. 756.
[9] Eller, T. K., (2016) *Modeling of tailor hardened boron steel: for crash simulation*, Dissertation, University of Twente, Enschede, p. 1.
[10] Neugebauer, R.; Schieck, F.; Polster, S.; Mosel, A.; Rautenstrauch, A.; Schönherr, J.; Pierschel, N.., (2012) *Press hardening — An innovative and challenging technology*, Archives of Civil and Mechanical Engineering, vol. 12, no. 2, p. 113–118.
[11] Venturato, Giulia; Novella, Michele; Bruschi, Stefania; Ghiotti, Andrea; Shivpuri, Rajiv., (2017) *Effects of Phase Transformation in Hot Stamping of 22MnB5 High Strength Steel*, Procedia Engineering, vol. 183, pp. 316–321.
[12] Beier, U. (2010) *High-performance fibre-reinforced composites prepared by a novel preform manufacturing routine*, Dissertation, Universität Bayreuth.
[13] Starke, J., (2016) *Carbon Composites in Automotive Structuralapplikations*, Presentation Brussels, p. 14.
[14] Jakobi, R., Geiger, O., (2017) *Structural Composites for Automotive Industry*, Presentation, Pfinztal, p. 2.
[15] Lauter, C., (2014) *Entwicklung und Herstellung von Hybridbauteilen aus Metallen und Faserverbundkunststoffen für den Leichtbau im Automobil*, Dissertation, Universität Paderborn, p. 24.
[16] Demes, M., Weimer, J., Kühn, M., Kreling, S., Dröder, K., Dilger, K., (2017) *Creating Polymer Metal Hybrids Of Hot Stamped Steel And Fiber-Reinforced Thermoplastic Using Residual Process Heat*, SAMPE Conference Proceedings, Seattle, WA.
[17] Dröder, K., Brand, M., Kühn, M. (2016) *"Numerical and Experimental Analyses on the Influence of Array Patterns in Hybrid Metal-FRP Materials Interlocked by Mechanical Undercuts"*, 10th CIRP Conference on Intelligent Computation in Manufacturing Engineering, Ischia, Italy, p. 1.
[18] Forschungsvereinigung Automobiltechnik e.V. (FAT), (2012) *Beitrag zum Fortschritt im Automobilleichtbau durch belastungsgerechte Gestaltung und innovative Lösungen für lokale Verstärkungen von Fahrzeugstrukturen in Mischbauweise*, p. 147.
[19] Andreiev, A., Grydin, O., Schaper, M., (2016) *Evolution of Microstructure and Properties of Steel 22MnB5 due to Short Austenitization with Subsequent Quenching*, steel research international, vol. 87, no. 12, pp. 1733–1741, p. 1735.
[20] Brosius, A., (2015) *Spezielle Fertigungsverfahren und Mikrofertigungstechnik: Presshärten*, Presentation, Dresden, p. 11.
[21] Behrens, B.-A., Dilger, K., (2011) *Erweiterung von Prozessgrenzen der Bonded Blank Technologie durch hydromechanische Umformung*, Forschungsvereinigung Automobiltechnik e. V. (FAT), Berlin, p. 58.
[22] Gross, D., Ehlers, W., Wriggers, P., Schröder, J., Müller, R. (2017*) Formeln und Aufgaben zur Technischen Mechanik 2*, 12. Auflage, Springer Verlag, p. 110

INTEGRAL MANUFACTURING OF PLASTIC-METAL HYBRIDS CONSISTING OF ENDLESS FIBER REINFORCEMENT USING INJECTION MOLDING

Tobias Gebken[(1)], Markus Kühn[(1)], Michael Demes[(1)], Anke Müller[(1)] and Klaus Dröder[(1)]

(1) Technische Universität Braunschweig, Institute of Machine Tools and Production Technology, Braunschweig, Germany

https://doi.org/10.21452/bccm4.2018.07.02

Abstract

Injection molding is an economically attractive manufacturing process of short and long fiber-reinforced thermoplastic (TFRP) parts. The benefits in contrast to thermoset resin transfer molding (RTM) processes are the manufacturing of complex geometries in short cycle times. In the automotive sector, injection molding is one of the most common manufacturing processes for semi structural parts e.g. for the frontend, door coverings or functional joining parts.

In structural applications, the fiber specifications, volume content, length, material and orientation are influencing the characteristics of strength, stiffness and brittleness. Due to a nearly isotropic material behaviour of short TFRP parts, directional long or endless TFRP are suitable for a load path-oriented design. The load path oriented fibers lead to an anisotropic higher stiffness and strength. The integration of positioned long or endless fibers in the injection molding process and the realization of load transfer between metal and plastic are challenging tasks in present research works.

This paper deals with the integration of endless fibers in the injection molding process, focussing on the reinforced interface between metal and thermoplastic parts. The hybridization process and a calculation of the fiber infiltration time are presented. Furthermore, the performance of fiber-reinforced interfaces between metal and thermoplastic parts is characterized in tensile tests.

1. INTRODUCTION

Due to political restrictions of CO_2 emissions, the automotive industry is required to manufacture fuel efficient vehicles [1]. A major factor is the vehicle mass, e.g. in car body structures [2]. By reducing the vehicle mass, the fuel consumption decreases and thus CO_2 emissions are reduced as well. Therefore, new lightweight materials like fiber-reinforced plastics (FRP) and material combinations can be used to reduce vehicle's weight. However, integration of these new lightweight materials require highly efficient and economically advantageous manufacturing processes, compensating materials cost disadvantages. Current mid volume RTM processes, e.g. BMW's i3 with 17,000 vehicles per year (2014) [3], require long cycle times compared to manufacturing of conventional steel structures. Regarding FRP parts consisting of thermoset matrix, preforming, infiltration and curing take a significant amount of time. On the other hand, TFRP provide short cycle times suitable for automotive manufacturing processes as well as better recyclability.

Well-established manufacturing processes for thermoplastics and fiber-reinforced thermoplastics are thermoforming and injection molding technology. Thermoforming processes allow the manufacturing of large structures with long or endless fiber reinforcements but are restricted to flat geometries. In contrast, injection molding is qualified for large and geometrically complex parts with short and long fiber reinforcements while fiber lengths are limited to 3 mm due to polymer processing [4]. For structural or semi-structural parts, the fiber reinforcement is needed for higher strength, stiffness and impact strength [5]. Towards load path and lightweight designed FRP, it is necessary to integrate endless fiber reinforcements in load path orientation. The density of glass fibers (~2.5 g/cm³) is higher by a factor of > 2 compared to polyamide 6 (~1.1 g/cm³). Therefore, a local fiber reinforcement is a promising approach to avoid a high fiber volume content in part areas, where fibers are not needed [6, 7].

This paper deals with the integration of endless fibers in the interface of a metal and plastic structure. For fiber integration, an interface design is presented as well as a simulation to calculate the infiltration time subjected to the melt pressure and viscosity. The manufactured specimens with a fiber-reinforced interface are characterized in a tensile test. The overall bond strength is benchmarked with a conventional short fiber-reinforced thermoplast.

2. EXPERIMENTAL SETUP

2.1 Design

In vehicle structures, multimaterial design methods are increasingly pursued to create functional integration as well as weight reduction. In plastic-metal hybrid car structures, plastic-metal interface is a highly stressed transition zone where failures often occur by early cracks. For the design of high performance interfaces, mechanical interlocking and adhesive bonding are used. Therefore, mechanical undercuts [8] or a laser structuring on metal surfaces [9] are common processes. For the material bond adhesive promoters are used [10].

To improve the material interface strength and avoid an early crack in the interface area by a flank tensile crack, a fiber loop reinforcement in load path direction is pursued. The fiber loops are integrated in the injection molding die and embedded in the thermoplastic part. By using the flow direction of the melt, the fibers are positioned. The fiber loop reinforcements introduce the load directly from the metal into the thermoplastic material. Thereby, the interface zone is not limited to the metal surface area.

2.2 Process setup and test specimen

Figure 1 shows the experimental process chain for the manufacturing of hybrid TFRP with an endless fiber reinforcement in the interface zone. The process contains a pre-coating step for the application of an adhesive promoter. For a homogeneous thickness of the adhesive promoter, its application is performed with an electrical potential between adhesive promoter and metal part. The second step is the draping and fixation of the fibers around the metal as a loop. This process is performed at a minimum temperature of 165 °C to activate the adhesive promoter [11] and fixate the fiber. Injection molding is used for integral joining and forming.

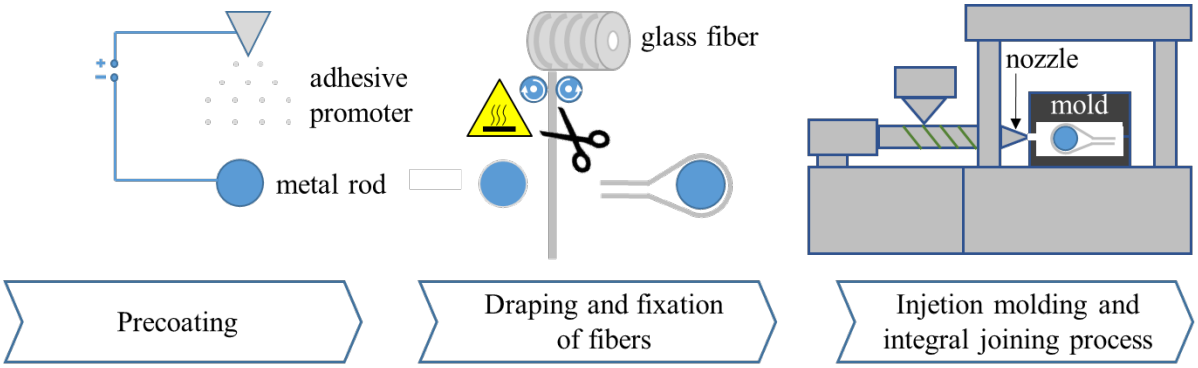

Figure 55: Process chain with endless fiber reinforcement in TFRP

In this paper, an injection mold is set up to manufacture an endless fiber-reinforced material interface between metal and thermoplastic material. The geometry of the specimens is shown in Figure 2. A metal rod with a diameter of 6 mm and a polymeric form with thicknesses between 4.0 mm and 7.2 mm are designed. The specimen depth is 20.0 mm.

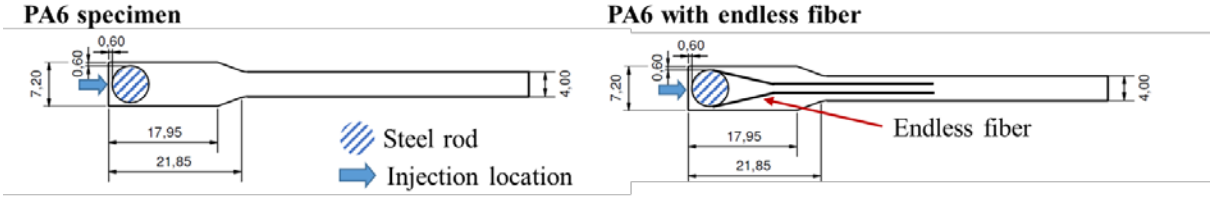

Figure 56: Geometry of the test specimen: Metal-PA6 (left), Metal-PA6 with fiber reinforcement (right)

2.3 Materials

The experiments are performed with the materials shown in Table 1. The inserts consist of a steel rod of 11SMn30+C and an electric glass fiber with 1,200 tex per roving. The fiber filaments have a diameter of approximately 16 µm. An easy flowing polyamide 6 (PA 6) is used without filling fibers as well as with a glass fiber volume content of 30 %. The short fiber-reinforced PA 6 is used during the experiments for benchmark reasons.

Table 20: Materials

	Type	Fiber content
Fiber	E-glass	1,200 tex
Polymer	PA 6	0 vol.% / 30 vol.%
Steel	11SMn30+C	-

3. PROCESS SIMULATION

3.1 Theoretical approach

The infiltration and consolidation of endless fibers in an injection molding process is an important step for a good matrix-fiber load transmission. Therefore, many efforts deal with the theoretical and numerical calculation of the degree of infiltration. In this work, the degree of infiltration is calculated with a theoretical approach, whereas the major variables are simulated. The degree of infiltration is shown in dependence of the number of fiber layers as well as the melt pressure in the mold.

The analytical approach towards the fiber bundle infiltration with one flow front [12, 13] is shown in equation 1. Here, t_{micro} represents the micro-infiltration time, η the viscosity, p the infiltration pressure. The ratio of the eccentricity x is calculated with $x = \frac{2 \cdot \lambda}{\lambda^2 + 1}$ $with\ \lambda = \frac{a}{b}$. The fiber bundle radius r_{fb} is calculated with equation 2.

$$\boldsymbol{t_{micro} = \frac{1}{4} \cdot \frac{\eta \cdot (1 - \varphi_{micro}) \cdot {r_{fb}}^2 \cdot x}{S \cdot p}} \quad (1) \quad \text{with} \quad \boldsymbol{r_{fb} = \sqrt{\frac{tex}{\pi \cdot \rho_{fil} \cdot \varphi_{micro}}} = 0.47\ mm} \quad (2)$$

Table 21: Fiber textile parameter

Parameter	Value
Fiber volume content φ_{micro}	0.7 $[-]$
Permeability S	$9.2 \cdot 10^{-14}$ $[m^2]$
Fiber bundle spread a	5 $[mm]$
Fiber bundle thickness b	0.25 and 1 $[mm]$
Fiber tex	1,200 $[\frac{g}{km}]$
Filament density ρ_{fil}	2.5 $[\frac{g}{cm^3}]$

The presented parameters in Table 2 are specific characteristics of the fiber textile. The process dependent parameters are the pressure p and the melt viscosity η. These parameters can be evaluated in experiments or can be simulated in an injection molding simulation. In this work, a study with a parameter variation is performed to investigate the influence of varying pressure profiles on the infiltration behavior. Furthermore, two different numbers of fiber layers are taken into account.

3.2 Injection molding

The injection molding simulation is performed by using the software Moldflow®. In Figure **3** the temperature distribution is shown for three different time steps. In the first time step at 0.4906 s, the compression phase is completed, whereas the second time step at 2.491 s is during the holding pressure. At the last time step at 5.485 s, the holding pressure is finished and the cooling phase starts. The core temperature of the melt during the compression and holding pressure phase balances around 261 °C. This value is validated by experiments with 258 °C melt temperature in the core. Heat transfer in the gating system can explain the temperature deviation of 3 °C. Furthermore, the decreasing temperature from the tool surface to the core is shown in Figure 3. A

fiber placement with respect to the fiber infiltration is only suitable in the high temperature core. The resultant viscosity and pressure profile at the point of measuring is shown in Figure 4.

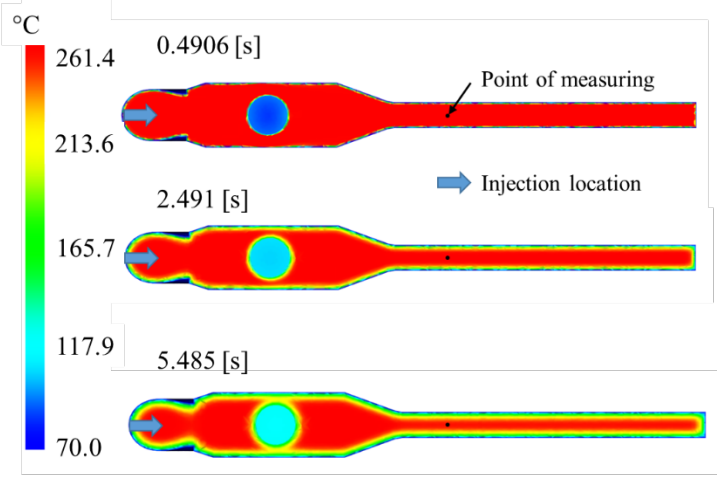

Figure 57: Simulation of specimen temperature during the injection molding process for a low pressure profile

3.3 Study of process parameters

The following study contains a time dependent simulation of the melt pressure and the melt viscosity. Therefore, three different pressure profiles are taken into account. For the pressure profiles an injection step, a compression step, a holding pressure step and a cooling step are characteristic. In Figure 4 a low, middle and high pressure profile is taken into account. In addition, the viscosity profiles are shown up for the different pressure profiles. The results show that the viscosity is nearly non-affected by the pressure. However, the results in Figure 3 and Figure 4 show an increasing viscosity with increasing time. During the cooling phase (> 6 s) the thermoplastic viscosity increases into solidification. With the time dependent pressure and viscosity, it is possible to calculate the total micro infiltration time t_{micro} with equation 1. Therefore, a total equation is needed to calculate the "degree of infiltration" considering I_{fil} the micro infiltration time as a function of the simulated time steps. The total equation is shown in equation 3.

$$I_{fil} = \sum_{i=1}^{t_n} \frac{t_{step,i} - t_{step,i-1}}{t_{micro,i}} \tag{3}$$

In Figure 4, the degree of infiltration I_{fil} is diagramed as a function of fiber textile layers (1 layer and 4 layers) as well as three different pressure profiles (low, middle, high). The results are calculated for a one-side fiber infiltration and a non-varying textile temperature.

The results show that the infiltration of the 1 layer and 4 layers textiles with a high and middle pressure profile is completed during the compression phase. The infiltration degree of the 1 layer with low pressure is completed during the holding pressure phase, whereas the 4 layer textile with the low pressure profile could not be completely infiltrated during the holding pressure phase (Figure 4). This textile only reaches an infiltration value of 50 %.

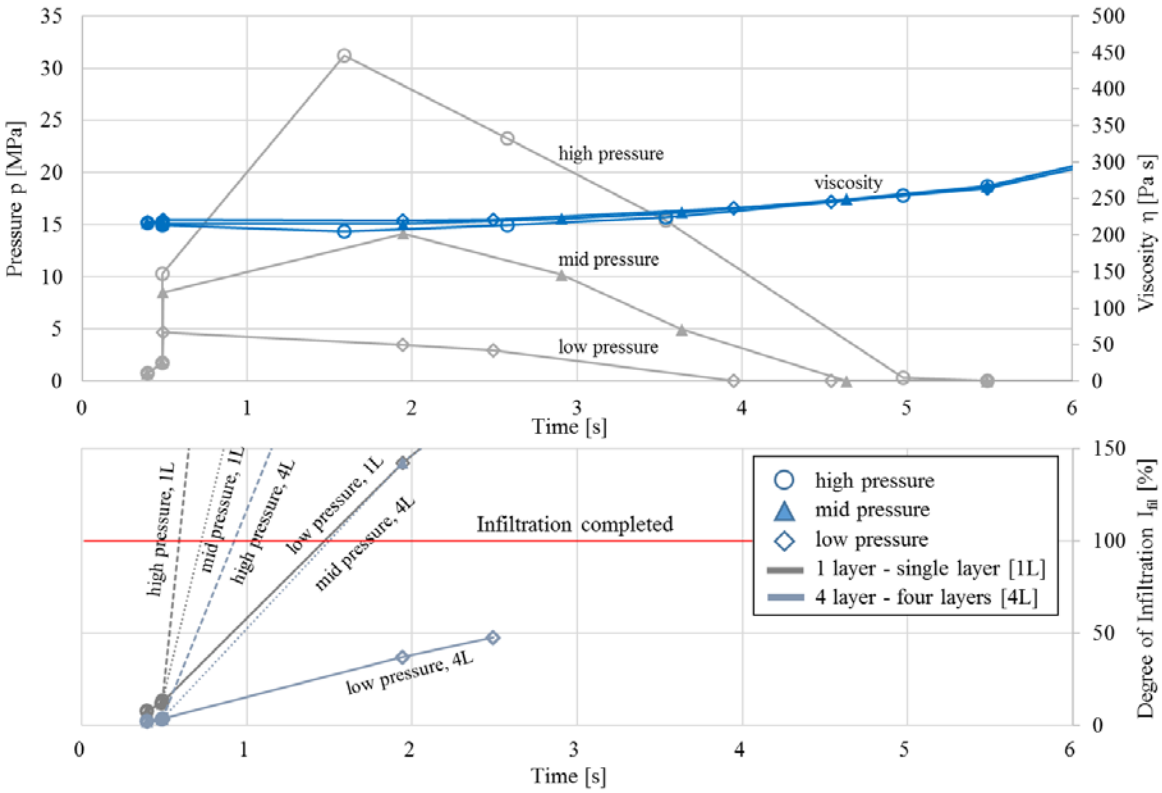

Figure 58: Calculated parameters; process pressure and viscosity (top); degree of infiltration calculated with equation (3) (bottom)

By using this co-calculation strategy between the analytical and numerical approach, it is possible to take varying process parameters for the calculation of infiltration degrees into account. Thus, a time and cost efficient process for the design of fiber reinforcements in the injection molding process can be performed.

5. TESTING

To investigate the bond strengths of plastic-metal interfaces using continous fiber loops for reinforcement, test specimens (Figure 2) are manufactured through injection molding. The benchmark is performed with a short glass fiber reinforced specimen. The parameter variation consists of a PA 6 specimen with no fiber reinforcement as well as a 1- and 2-fiber loop reinforcement. The metal inserts are placed into the mold at ambient temperature of 20 °C and a pre-heated mold temperature of 270 °C. During insert preparation and the dwell time in the mold, the mold temperature of 70 °C affects the metal rod temperature. Thereby, the temperature of the metal rod is increased from 20 °C to 50 °C and decreased from 270 °C to 200 °C. The manufactured specimens are tested with a testing speed of 5 mm/min in a tensile test with a predicted crack at the specimen flank.

The results of the investigation are shown in Figure 5. A non-reinforced PA 6 reaches a tensile load of 2.1 kN. The load can be increased to 2.9 kN with 1 fiber loop and to 3.9 kN with 2 fiber loops. The benchmark was performed with a 30 vol.% glass-fiber reinforced PA 6, which reaches a tensile load of 3.7 kN. The fiber volume contents of the single fiber loop and double fiber loop reinforced material flank can be calculate to 10 vol.% and 20 vol.%.

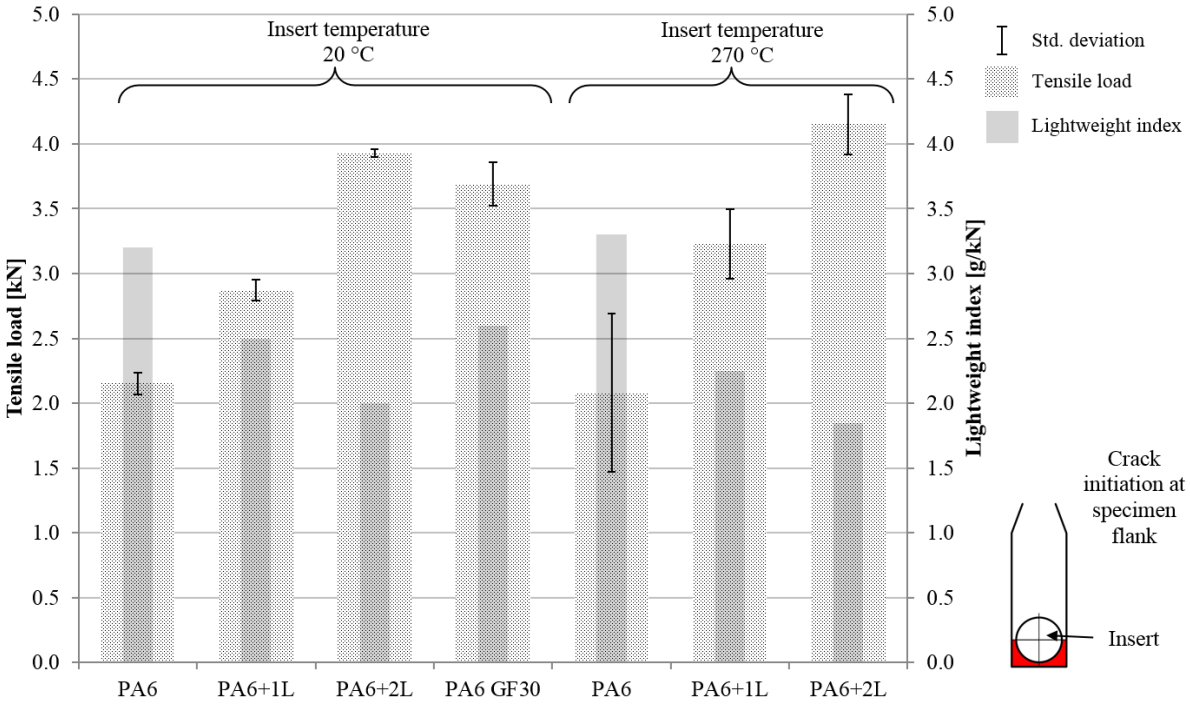

Figure 59: Results of tensile testing and failure behavior

In Figure 5 the relation between weight and tensile load is considered in the lightweight index. The results show, that the lightweight index for the fiber loop reinforced material interface is 2.5 g/kN and 2.0 g/kN, whereas the benchmark (PA6 GF30) reaches 2.6 g/kN. Furthermore, the preheated metal rods (270 °C) result in higher tensile loads, especially for the specimens with a fiber textile loop reinforcement. However, the results of the pre-heated metal rod inserts show a higher standard deviation, which can be caused in a temperature deviation of the metal inserts. Due to the higher metal insert temperature the infiltration of the textile is favored. Thus, a higher fiber matrix infiltration can be reached and lead to higher tensile loads.

6. SUMMARY AND OUTLOOK

In this work, a concept for a material interface between metal and a thermoplastic with higher performance is demonstrated. The performance improvement is reached through an endless fiber loop reinforcement. The process compatibility of fibers in the injection molding process is verified. By using the direction of the melt flow, a directional fiber orientation is achieved. Furthermore, a numerical approach to evaluate time dependent process parameters from the injection molding process is performed. The parameters are used for the analytical calculation of the fiber infiltration. The improvement of the fiber loops in the material interface are shown by the results of the tensile tests. Moreover, heated metal inserts are improving the fiber infiltration with thermoplastic melt, which leads to higher possible tensile loads. In further investigations, a parameter study by varying the metal insert temperature will be on focus. As well, an experimental validation of the infiltration calculation will be performed by using graphical microsection analysis.

REFERENCES

[1] Goede, M., (2007) *Karosserieleichtbau als Baustein einer CO2-Reduzierungsstrategie*, 16. Aachener Kolloquium Fahrzeug und Motorentechnik, Aachen

[2] Davies, G., (2012) *Materials for Automobile Bodies*, Second Edition, Butterworth-Heinemann, Oxford

[3] Pandow, G., (2016) *IHS-Prognose: BMW-i3-Absatz wird sich verdoppeln*, Automobil Produktion, Landsberg

[4] Faruk, O., (2012) *Biocomposites reinforced with natural fibers: 2000-2010*, Journal Progress in Polymer Science 37, Toronto, p. 1552-1596

[5] Thomason, J.L., (2002) *The influence of fibre length and concentration on the properties of glass fibre reinforced polypropylene: 5. Injection moulded long and short fibre PP*. In: Composites: Part A 33, p. 1641 - 1652

[6] Tröltzsch, J., (2011) *Entwicklungen zur partiellen Verstärkung von thermoplastischen Spritzgießbauteilen*, Abschlussseminar PAFATHERM, TU Chemnitz

[7] Gebken, T., Seemann, T., (2016) *Prozessentwicklung für den hybriden Leichtbau am Beispiel einer endlosfaserverstärkten Aluminium-FVK-Struktur*, Symposium Hybrider Leichtbau, its automotive nord, Braunschweig

[8] Dröder, K., Brand, M., Gebken, T., Kühn, M., Böl, M., (2016) *Increasing the interlocking effect between metal and FRP by mechanical undercuts*, Int. J. Automotive Composites, Vol. 2, Nos. 3/4

[9] Kahmann, M., Quentin, U., Kirchhoff, M., Brockmann, R., Löffler, K., (2015) *Laser based surface structuring for lightweight design*, Lasers in Manufacturing Conference

[10] Aßmann, K., Locher, A., (2014) *elements 48*, Quarterly Science Newsletter, Issue 3, Evonik Industries AG, Essen, pp. 6-11.

[11] Demes, M., Weimer, J., Kühn, M., Kreling, S., Dröder, K.; Dilger, K., (2017) *Creating polymer metal hybrids of hot stamped steel and fiber-reinforced thermoplastics using residual process heat*, SAMPE Conference Proceedings. Seattle, WA

[12] Ehleben, M., (2002) *Herstellung von endlosfaserverstärkten Rohren mit thermoplastischer Matrix im Schleuderverfahren*, Dissertation, Shaker Verlag, Aachen

[13] Gebken, T., Kühn, M., Dröder, K., (2017) *Integration of endless fibres in the injection moulding process*, SAMPE Europe Conference, Stuttgart, Germany

EXPERIMENTAL STUDY OF THE TENSILE STRENGTH OF OPEN-HOLE FIBER-METAL LAMINATES

Thays A. Barreto (1) and Rafael C. Santiago (2)

(1) Center of Engineering, Modelling and Social Sciences, Federal University of ABC, São Bernardo do Campo, SP, Brazil.

(2) Center of Engineering, Modelling and Social Sciences, Federal University of ABC, São Bernardo do Campo, SP, Brazil.

https://doi.org/10.21452/bccm4.2018.07.03

Abstract

Fiber-metal laminates are alternative materials for aeronautical applications because of their lightweight and high strength. However, deep study of material behaviour under field conditions is need. One of those cases is under the presence of holes, which mark positions of rivets and fittings in a laminate plate. This work aims to define the behaviour of fiber-metal laminates with open-holes through experimental tensile tests and the use of innovative technique for measuring deformation using image correlation (DIC, Digital Image Correlation).

1. INTRODUCTION

Lots of time and efforts have been invested in the development of new materials and techniques for aircraft structural design. The goal is to find the perfect balance between strength, weight and profitability.

Result of those efforts, the fiber-metal laminates are hybrid materials, composed of thin metal layers bonded with layers of composite material [1], like Glare™ (Glass Reinforced Laminate), a combination of aluminium alloy, glass fiber and epoxy [2]. Besides being lightweight and having good fatigue resistance, the processes and techniques related to the fabrication and maintenance of Glare are very similar to those of metals [3], reducing production costs with training and new processes. Sundi and Choi [4] also highlight the material's good fire resistance, reducing the number of emergency doors needed, and good damage tolerance, reducing the number of structural components need, the weight and the production cost of the aircraft.

Thin plates are essential elements in the aircraft structural design, not only providing covering to the structures, but also having important function in load bearing [5]. The fixation of the plates through rivets, on the other hand, implies in the presence of open-holes in the plate, which are

well-known stress concentrator factors [6], reducing the mechanical strength of the material [7] and possibly causing mechanical failure of the structure.

The open-hole tension test helps us understand the mechanical limitations of a plate containing holes like the ones described, it consists in the application of uniaxial strain to a plate containing a central hole. Because of the discontinuity represented by the hole, a region of stress concentration is formed close its edges, especially on the transversal section that cross the centre of the hole [8], the tension in these regions can get so high it may cause fractures, that's what makes this test so important.

Combining the test to the Digital Image Correlation method makes possible to document the deformation means of the material under such conditions. This technique use images captured during the whole test to measure the material local strain, defining the strain fields on the surface of an object [9]. Using the non-deformed image as reference and the Speckle Pattern technique of random painting, an algorithm divides the reference image into pre-defined areas and maps the displacement of those in the next images by looking for specific pixels.

Using both tools, this paper evaluated the behaviour of the fiber-metal laminate composed of aluminium, glass fiber and epoxy under tensile strain when containing an open-hole.

2. MATERIALS AND METHODOLOGY

The material used was FML 3/2 configuration composed of three layers of aluminium 2024-T3 and two layers of glass fiber composite at 0°/90° with epoxy, presented in Figure 1. This FML composition presents itself as a good option for aeronautical application since it has damage tolerance greater than the aluminium and the glass fiber/epoxy composite, better behaviour under fatigue, specific weight 10% smaller than the aluminium, better fire resistance and since it can be conformed and repaired using the same processes as the aluminium [2].

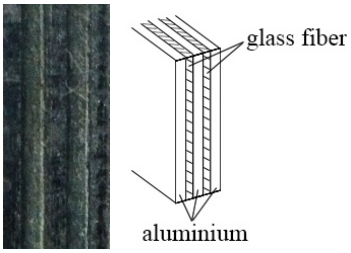

Figure 1: FML configuration tested.

Six specimens were selected for the behaviour analysis of the material plate with open-hole under tensile load, being one for characterization of the material and one as a backup, both un-notched. All the specimens tested had standard values of width (w) and thickness (t), varying only the diameter of the hole (d). It was defined a test length (L) of 100 mm to each specimen so that the stress implied in the clamping of the specimen would not interfere on the open-hole region. Table 1 presents measurements details of the specimens.

Table 1: Specimens Measurements.

Sample	1	2	3	4	5	6
d (mm)	0	2	4	6	8	0
t (mm)	3.1	3.1	3.1	3.1	3.1	3.1
w (mm)	22.5	22.5	22.5	22.5	22.5	22.5
L (mm)	100	100	100	100	100	100

The experimental tests were performed by subjecting each of the specimens to unidirectional tensile test in an Instron 3369 universal testing machine, programmed to collect data of load and displacement at the rate of 5 Hz. During the tests, a camera captured images of the specimens at the rate of 1 picture/s. These images were processed in the software VIC-2D, from Correlated Solutions, providing local strain fields for each image of the tests.

2.1 Material's Characterization

Through the data collected from the un-notched specimens tests, 1 and 6, and the equations (1) to (3), it was possible to develop the Stress x Strain curve of the material and its strain field for the ultimate strength (σ_N). Appling the theoretical approach to homogeneous material to those results makes it possible to extract the mechanical properties of the material: Tensile Strength (σ_0), from the maximum value of tension during the test; Elastic Modulus (E), from the Stress x Strain curve, considering ($\mathrm{E_x} = \mathrm{E_y} = E$); Poisson's Ratio ($\nu_{xy}$), from strain data in the principal directions (x and y) and Shear Modulus ($\mathrm{G_{xy}}$), estimated from equation (4).

$$A = w * t \tag{1}$$

$$\sigma_\infty = \frac{C}{A} \tag{2}$$

$$\varepsilon_\mathrm{G} = \frac{\Delta L}{L} \tag{3}$$

$$\mathrm{G_{xy}} = \frac{E}{2\,(1 + \nu_{xy})} \tag{4}$$

where A is the cross-sectional area of the specimen, σ_∞ is the applied stress, C is the applied load, ε_G is the global strain, ΔL is the displacement of the load cell.

2.2 Influence of the Hole in the Material's Strength

The influence of the presence of the hole and its diameter in the strength of the material was analysed using the data collected directly from the tension tests, generating graphics of Load x Displacement. To analyse the influence in tension terms, the equation (5) was applied in the generation of Notched Tensile Strength x Diameter graphics.

$$\sigma_\mathrm{N} = \frac{C_{max}}{A} \tag{5}$$

To evaluate the reliability of the data collected from the tests, they were compared to the the models proposed by Martins *et al.*, based on the analytical predictions made by Whitney-Nuismer and Mar-Lin [10].

Whitney and Nuismer proposed two methods: the Point Stress Criterion, equation (6), and the Average Stress Criterion, equation (7). The first one proposes that the failure of the material occurs when the stress at a distance d_0 ahead of the hole edge reaches the un-notched material strength (σ_0); the second one, proposes that the failure occur when the average stress over a distance a_0 ahead of the hole edge reaches the un-notched material strength (σ_0) [11].

$$\frac{\sigma_N}{\sigma_0} = \frac{2}{2 + \varphi^2 + 3\varphi^4 - (k_\sigma - 3)(5\varphi^6 - 7\varphi^8)} \tag{6}$$

$$\frac{\sigma_N}{\sigma_0} = \frac{2(1-\phi)}{2 - \varphi^2 - \varphi^4 + (k_\sigma - 3)(\varphi^6 - \varphi^8)} \tag{7}$$

where k_σ is the stress concentration factor for an anisotropic infinite plate with a hole, given by equation (8), and φ and ϕ, given by equations (9) and (10) respectively, are defined for simplification of calculus as functions of the hole radius (R).

$$k_\sigma = 1 + \sqrt{2\left[\frac{E_x}{E_y} - \upsilon_{xy}\right] + \frac{E_x}{G_{xy}}} \tag{8}$$

$$\varphi = \frac{R}{R + a_0} \tag{9}$$

$$\phi = \frac{R}{R + d_0} \tag{10}$$

The characteristics lengths a_0 and d_0 represent distances ahead of the hole edge and are determined through the best fit of the curves with the experimental results.

While these Whitney-Nuismer criterions consider the composite as a homogeneous material, Mar-Lin's consider the application and the behaviour of all the composing materials. This criterion propose that the failure occur after a cracking in the interface between the resin and the fibers [10]. Using properties like the hole diameter (d), the laminate fracture toughness (H_C) and the power of singularity (m), it defines:

$$\frac{\sigma_N}{\sigma_0} = \frac{H_C(d)^{-m}}{\sigma_0} \tag{11}$$

where H_C and m are properties of the material, defined through the best fit of the curves with the experimental results in a $log(^{\sigma_N}/_{\sigma_0})$ x $log(d)$ domain.

2.3 Influence of the Hole in the Material's Local Strain Profile

The influence of the hole presence and diameter in the local strain was obtained through analysis of the data collected using the DIC method. It was possible to calculate data of local strain in the direction of the applied load (ε_{yy}) over the crack axis in notched strength condition. Figure 2a shows the profile expected for the deformation field.

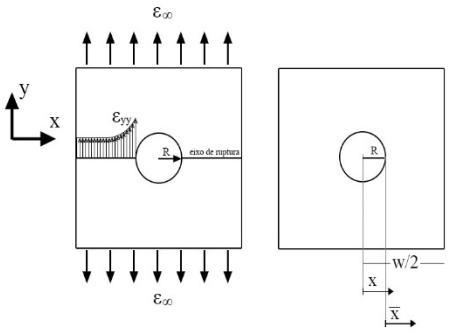

(a) (b)

Figure 2: (a) Expected deformation field and (b) Dimentions of the specimen used as reference to equation (12).

To analyse the deformation along the half-width of each specimen in increasing load, data of ($\varepsilon/\varepsilon_\infty$), from the deformation fields, was crossed with a dimensionless length ($\overline{x}$), defined by equation (12) and Figure 2b.

$$\overline{x} = \frac{x - R}{w/2 - R} \tag{12}$$

3. RESULTS AND DISCUSSION

Data collected from the un-notched specimens tests could not be used on the failure analysis, since their failure occurred in the clamp region, out of the camera's field of capture, but their load and strain data were very useful in the characterization of the material. On the other hand, the failure of the notched specimens occurred at the expected region: over x axis, crossing the center of the hole. Pictures of the specimens before and after the tests are presented in Figure 3.

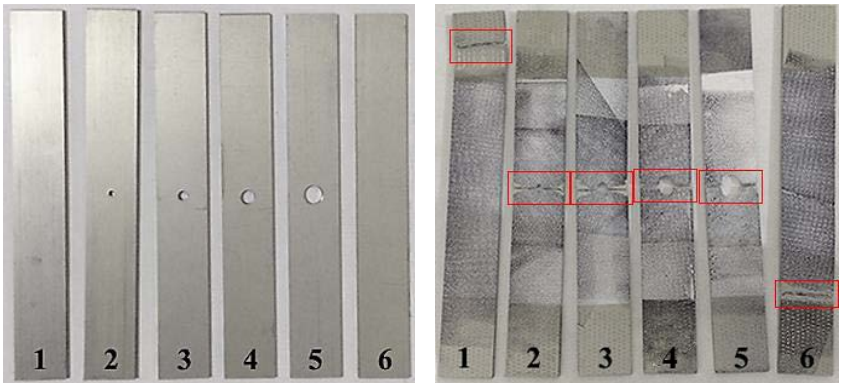

Figure 3: Specimens before and after the tests with fracture regions highlighted.

3.1 Material's Characterization

The material's properties, defined using data from the un-notched specimens tests are presented in Table 2.

Table 2 : Material Properties Values.

σ_0 (Mpa)	E (MPa)	ν_{xy}	G_{xy} (MPa)
448.80	12333.55	0.1982	5146.71

3.2 Influence of the Hole in the Material's Strength

Through the Load x Displacement curves, Figure 4, we can note that the hole diameter significantly affects the mechanical capacity of the material under tension. This reduction in its capacity is highlighted in Figure 5, in which it is possible to note that the Ultimate Strength exponentially decreases with the increasing of the hole diameter.

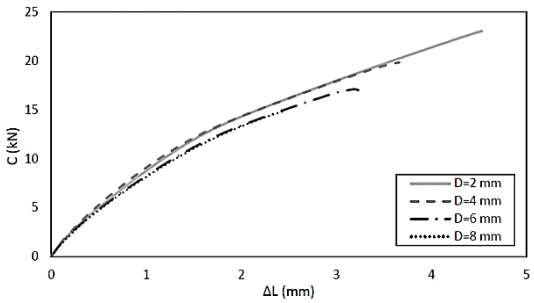

Figure 4: Relation between Load and Displacement for each hole diameter.

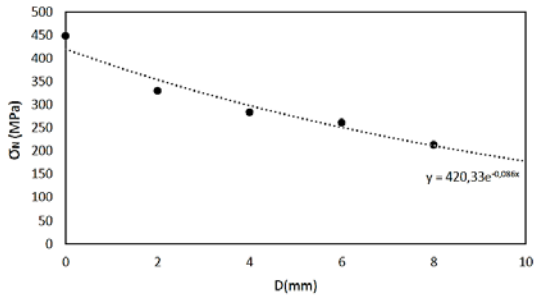

Figure 5: Ultimate Strength for each diameter tested and tendency curve.

The verification of the data reliability, made through comparison to Whitney-Nuismer and Mar-Lin criterions, provided great results. Figure 6 shows that the experimental results fit the curves with small disturbance, especially to the one related to Mar-Lin's criterion, probably because this is the one that take in account the non-homogenous character of the material. The only point that haven't corresponded to the theoretical prediction was the one of greatest diameter, in this case two stress concentration factors, the hole's edges and the specimen edges, were too close to each other, compromising the deformation capacity of the material to higher loads.

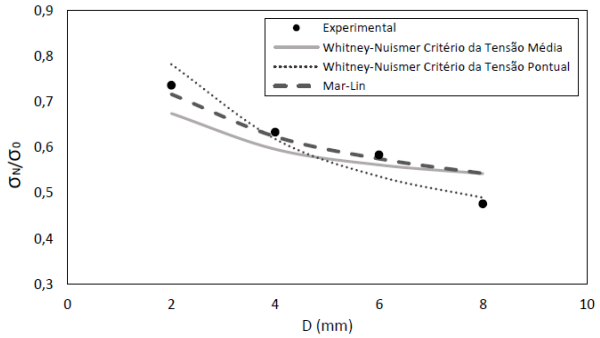

Figure 6: Comparison of the experimental tension rations to the theoretical ones.

3.3 Influence of the Hole in the Material's Local Strain Profile

The local strain (ε_{yy}) analysed over the failure axis for notched tensile strength conditions, presented in Figure 7, indicates greater strain closer to the holes edges, as expected. The local strain of the specimen of 8 mm diameter deformed less than the others specimens, because of the proximity between the hole's edges and the specimen's edges.

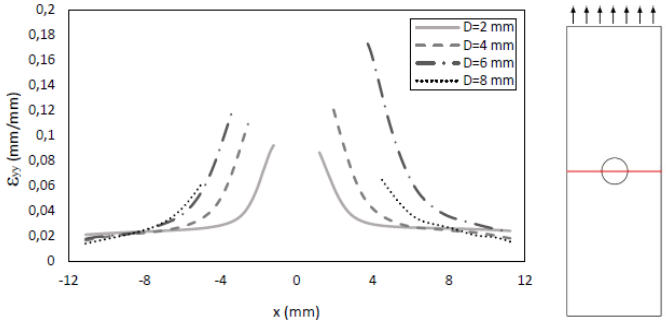

Figure 7: Maximum local strain over the failure axis.

The strain fields (Figure 8) show regions of greater strains, indication of tension (in red), and regions of smaller strains, indication of compression (in blue and pink). It is also possible to note that those tension regions develop in "X" form, indicating good stress transference by the fibers at 0°/90°.

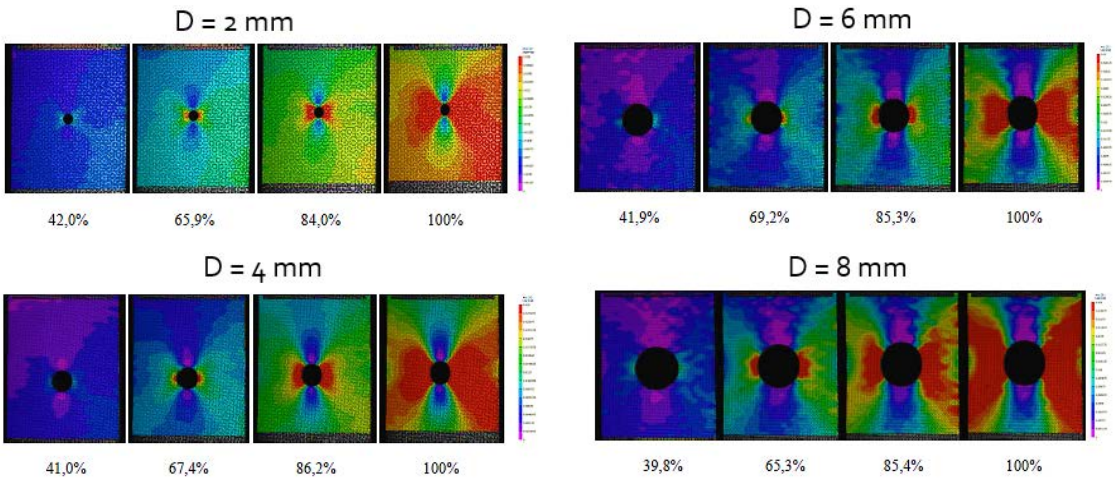

Figure 8: Strain fields presented in porcentage of Notched Tensile Strength ($\%\sigma_N$).

Analysing the tension regions in terms of $\overline{x}$ length under some conditions of tension, Figure 9, it is possible to verify that: before the failure the curves tend to ratio 1 in the specimen width; the curves that refer to the Notched Tensile Strength indicate lack of width length for the stress condition to normalize. It leads us to conclude that the ideal situation is that the ratio $\varepsilon/\varepsilon_\infty \rightarrow 1$ in $\overline{x} < 1$ for the maximum operation load of the plate.

The specimen with 8 mm of diameter is, again, an exception, since the stress concentrated in the hole's edges and in the specimen's edges interact with each other, causing the concentration of even greater stresses and resulting in earlier failure.

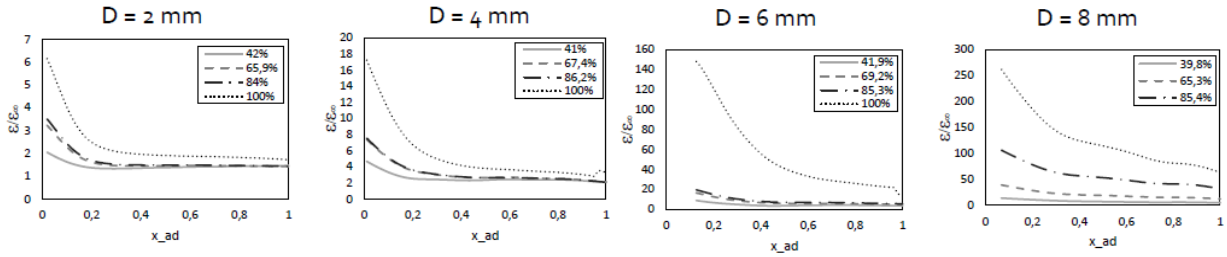

Figure 9: Relation between the strain ratio and the dimensionless length $\overline{x}$ in $\%\sigma_N$.

4. CONCLUSIONS

- The tests complied with theoretical methodologies and generated reliable characterization of the material's mechanical properties;
- The Digital Image Correlation technique has proven to be a simple and quick way to calculate the local strain of the specimens;
- Open-holes significantly reduce the material's plate strength and strain;
- The dimensions of the plate with holes must be defined to ensure that the edges of the holes are distant to other stress concentrator factors;
- Grater displacements in the region of the hole occur in the direction of the fibers and the tension region surrounding the hole in the strain fields develops in the form of "X", both phenomena are indications of the influence of the composite's fibers orientation and tensile transference.

REFERENCES

[1] Vlot, A., 'Glare: history of the development of a new aircraft material', (Kluwer Academic Publishers, Dordrecht, 2004).
[2] Vlot, A., Gunnink, J. W., 'Fiber Metal Laminates: An Introduction' (Springer Science+Business Media, Dordrecht, 2001).
[3] Hwang, W. J., Park, Y. T., Hwang, W., 'Fiber Reinforced Metal Laminates with a Circular Hole' in Metals and Materials International, v. 11 (2005), p. 197-204.
[4] Sundi, A., Choi, A. Y. N., 'Fiber Metal Laminates: An Advanced Material for Future Aircraft' in Journal of Materials Processing Technology, v. 63 (1997), p. 384-394.
[5] Megson, T. H. G., 'Aircraft Structures for Engineering Students', 4th edition (Butterworth-Heinemann, Oxford, 2007).
[6] Carlsson, L. A., Adams, D. F., Piper, R. B., 'Experimental Characterization of Advanced Composite Materials', 4th edition (CRC Press, 2014).
[7] Dowling, N. E., 'Mechanical Behaviour of Materials – Engineering Methods for Deformation Fracture and Fatigue', 4th edition (PEARSON, 2013).
[8] Gere, J. M., Goodno, B. J., 'Mechanics of Material', 8th edition (Cengage Learning, 2013).
[9] Rodi, R., Alderliesten, R. C., Benedictus, R., 'Crack-Tip Behaviour in Fiber/Metal Laminates by Means of Digital-Image Correlation' in Journal of Aircraft, v. 47 (2010), p. 1636-1646.
[10] Martins, R. D., Donadon, M. V., Almeida, S. F. M. D., 'The Effects of Curvature and Internal Pressure on the Compression-After-Impact Strength of Composite Laminates' in Journal of Composite Materials (2015).
[11] Whitney, J. M., Nuismer, R. J., 'Stress Fracture Criteria for Laminated Composites Containing Stress Concentrations' in Journal of Composite Materials (1974).

EVALUATION OF MECHANICAL PROPERTIES OF LOW COST FMLs FABRICATED WITH COIR FIBRE-REINFORCED COMPOSITES

Júlio C. dos Santos[1], Luciano M. G. Vieira[2], Rodrigo T. S. Freire[1,3], André L. Christoforo[4], Juan C. C. Rubio[2], Túlio H. Panzera[1].

[1] Centre for Innovation and Technology in Composite Materials, Department of Mechanical Engineering, Federal University of São João del Rei, Brazil.

[2] Department of Production Engineering, Federal University of Minas Gerais, Brazil.

[3] Department of Natural Sciences, Federal University of São João del Rei, Brazil.

[4] Federal University of São Carlos (UFSCar), Department of Civil Engineering, São Carlos, Brazil.

https://doi.org/10.21452/bccm4.2018.07.04

ABSTRACT: Fibre Metal Laminates (FMLs) are composite structures that comprise alternating metal layers and fibre-reinforced polymer composites (FRCs) combining their distinct physical-mechanical properties. Traditional FMLs are based on synthetic (carbon, glass and aramid) fibres. However, alternative FMLs based on natural fibre-reinforced composites have been developed to take advantage of available natural resources. A new eco-friendly FML sandwich based on random coir fibre-reinforced epoxy and polyester resin was developed in this research. Mechanical tests revealed that the tensile properties were fully dominated by the aluminium sheets, which were treated with alkali for degreasing and wash primer in order to enhance interfacial bonding. Such treatment efficiently reduced delamination and increased the flexural modulus (~67%). A similar increase in flexural (~22.94%) and impact strength (~99.16%) as well as in skin stress (~20.89%) of the new FMLs proposed was observed owing to the flexural and impact strength of composite cores and better core-layer stress transfer upon the aluminium treatment.

keywords: FML-sandwich composites, epoxy, polyester, coir fibre, mechanical properties.

1. INTRODUCTION

Fibre Metal Laminates (FMLs) are composite structures that comprise alternating metal layers and fibre-reinforced polymer composites (FRCs) combining their distinct physical and mechanical properties. As a result, the new structures have advantages over conventional fibre-reinforced composites, e.g. sustainability, resistance to fatigue, corrosion and impact [1]. ARALL, GLARE and CARAAL are traditional FMLs with synthetic fibre-based cores (carbon, glass and aramid fibres) [2]. However, alternative cores based on natural fibre-reinforced composites [3][4][5][6] have been developed due to increasing environmental concerns in order to take

advantage of the available natural resources FMLs may be manufactured with metallic faces composed of magnesium [1], titanium [7] , and a variety of aluminum alloys such as 2024-T3[6][8], 7075-O[9], 6061-O and T3[9] and aluminum-lithium[10]. The mechanical properties and thence the final applications of the FML depend on the selected metallic face and core. Vieira *et al*. [6] investigated the mechanical properties of a sisal fibre composite core FML with aluminium 2024-T3 faces and obtained ~23 GPa and 205 Mpa for flexural modulus and strength, respectively. These figures rank Vieira's material a promising FML for structural engineering applications.

FMLs can also be recognized as sandwich structures. In all FML applications, face-core bond strength is a fundamental property [11]. The mechanical efficiency of FMLs is indeed determined by the ability of this interfacial region to transfer mechanical loads through the constituents materials [4][5][6][12][10][3]. Thus, pre-treatments of aluminum faces are important to improve the inherently weak interlaminar bond strength between the aluminum alloy and the polymeric core [11][12][6].

The purpose of this work is to study an FML sandwich made of coir fibre-reinforced epoxy (CFREP) and polyester (CFRPO) composite cores, sandwiched to aluminium alloy ISO 1200 faces. A simple treatment method was used for aluminium faces in order to increase their consolidation with polymeric resins but an additional wash primer treatment was performed on the metallic sheets when polyester resin was used. The new eco-friendly FML sandwiched structure named CoRAL (Coir fibre-Reinforced ALuminium sheets) was evaluated under tensile, flexural and impact tests and its density was also determined.

2. EXPERIMENTAL PROCEDURES

2.1 Materials

CoRAL FML consists of two 0.5 mm-thick aluminium faces adhered to a coir-reinforced epoxy (or polyester) composite cores. The epoxy resin (Renlam M) and the amine-based hardener (Aradur HY 956) were provided by Huntsman (Brazil). The unsaturated polyester resin and Metil Ethil Ketone (2 wt%) were supplied by Reichhold (Brazil). Wash primer, (Sherwin Williams Automotive Finishes), was used as a coat sealant for aluminium. The raw coir fibre mat and aluminium sheets 1200-H14 (type ISO 1200) were obtained from Deflor Bioengenharia and Belmetal (Brazil), respectively.

2.2 Fabrication

CoRALs and their cores were produced were produced by hand lay-up with uniaxial cold compression. The fabrication was a two-step process, basically as described by [13].

1st step: Aluminium treatment

Coir fibre-reinforced polymer composites (CFRPCs) were manufactured by treating the surface of the aluminium moulding plates with *Tec Glaze-N* mould release agent to ensure eficient demoulding of the composite samples.

For CoRAL, the surface treatment of aluminium alloy faces was performed as follows: 1) washing with a surfactant; 2) mechanical abrasion with 150 sandpaper grit so as to produce a pattern of mutually perpendicular slots oriented at ± 45°; 3) alkaline degreasing with 5 wt% NaOH solution to promote the *"Bridging effect"* [11]; 4) priming - wash primer was applied by a compressed air spray gun. Two layers were successively applied with a 10 min interval.

It is worth noting that water molecules do not uniformly cover the surface of aluminium sheets washed only with surfactant (an effect known as "water breaking") (Figure 1a), due to remaining oil and other hydrophobic contaminants. These are subsequently removed by the alkaline-degreasing process, which results in the uniform film of water shown in Figure 1b. The alkaline treatment prepares the surface for the wash primer application (Figure 1c).

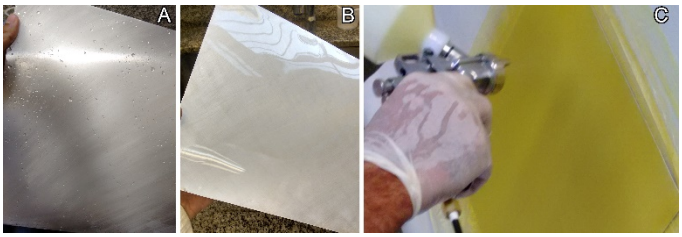

Figure 60. Aluminium treatment: a) water break after washing with surfactant and b) uniform film of water formed after mechanical abrasion with alkaline degreasing; c) wash primer application.

2nd step: Hand Lay-up manufacturing

After the first aluminium plate has been laid on the metallic mould (300 x 300 x 4 mm), the coir fibre mat (900 g/cm^2) along with the polymeric mixture (30/70 fibre-matrix volume fraction) was added (Figure 2a). The second aluminium face was then laid and the metallic mould was closed, as schematically shown in Figure 2b. The laminates were pressed in a hydraulic press under 645 KPa. To ensure the desired sample thickness, two steel bars (1 inch) were bolted over the top mould, Figure 2c, and the compaction load was released. After 60 hours, the FML was removed from the mould and cured for 14 days, period after which the laminates were cut (Figure 2d) and tested.

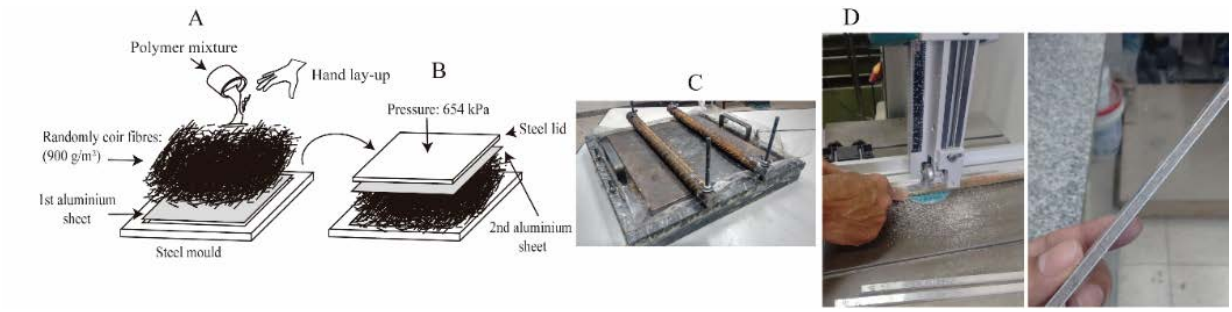

Figure 61. Manufacturing process.

2.3 Statistical analysis

Six (6) experimental conditions were considered for CoRALs based on the treatments decribed in Table 1. The sample code attributed to epoxy and polyester-based CoRALs is presented in Table 1.

Table 22. Experimental conditions investigated for CoRAL.

Aluminium treatment	Epoxy	Polyester
Untreated	E1	P1
Sandpapered-NaOH	E2	P2

Sandpapered-NaOH/wash primer	E3	P3

The analysis of variance (ANOVA) was conducted to investigate the main effects of the selected factors on the mechanical response variables considered. ANOVA is essentially a hypothesis test that considers the equivalence among mean values as the null hypothesis. The P-value, which is the risk of rejecting the null hypotheses (no effect from the main factor or interaction) when the null hypothesis is in fact true, is then calculated. In this work, the effect is considered statistically significant for $P \leq 0.05$. The Anderson–Darling test was used to verify the normality of the data distribution and validate the ANOVA. Though ANOVA identifies that means are statistically different, it does not determine which means are statistically different. Tukey's multiple comparison test was used for this task, so that means that do not share the same letter coding are significantly different, as will be shown below.

2.4 Mechanical and physical tests

Composite core (CFRPCs) as well as CoRALs were evaluated under tensile tests (TT) with rectangular specimens (250 x 25 mm) according to ASTM D3039[14]. Flexural tests (FT) of CFRPCs were performed in accordance to ASTM D790 (2015)[15]. CoRAL samples were tested under three-point bending tests according to ASTM D7249 (2012) recommendations [16]. These tests were performed on a Shimadzu AGX-Plus universal testing machine equipped with a 100 kN load cell. Edgewise Charpy Impact Strength tests (CIS) were performed in an XJJ- series impact testing machine with a 15 J hammer following ISO 179-1 (2010)[17], with samples of dimensions 80 x 10 x 4 mm. Tests were performed at 23 C and humidity level of 55%.

Equations 1 and 2 presented below represent a simple and consistent approach to determine the tensile normal stress to which each element (core or faces) are submitted. Assuming linear elasticity, the tensile yield load (in N) was divided by the cross-sectional area of the individual element to determine the average normal stress (σ), given by Equation 1 (aluminium face normal stress) and Equation 2 (composite core normal stress). The load at yield point was measured considering 2% deformation/strain.

$$\sigma_{al} = \frac{E_{al} \cdot F}{E_{al} \cdot S_{al} + E_c \cdot S_c} \quad (1)$$

$$\sigma_c = \frac{E_c \cdot F}{E_{al} \cdot S_{al} + E_c \cdot S_c} \quad (2)$$

In these equations, E_{al} stands for the aluminium tensile modulus and E_c for the composite tensile modulus. The parameter F is the tensile load at yield point and S_c and S_{al} are the cross-sectional areas of composite and aluminium faces, respectively.

According to the theory of laminated beams [18], the effective flexural modulus of the laminate composite (E_f) can be expressed as shown in Equation 3, where E_x is the composite modulus (GPa) and the coordinates $Z_j - Z_{j-1}$ define a generic layer (Figure 3). Once the effective flexural modulus has been calculated, the normal stress through the FML thickness may determined by Equation 4. This theory assumes the "*pure flexure*" or, in other words, the linear elastic state. Equation 4 considers the flexural yield load (N), based on 2% deformation/strain.

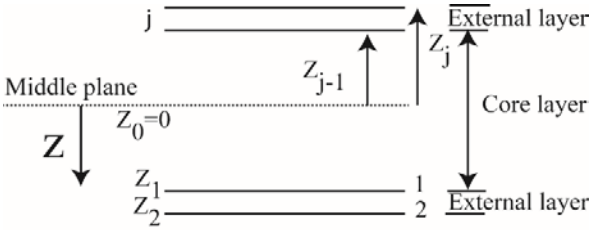

Figure 62. Distribution of generic layers of a 3 layers composites.

$$E_f = \frac{8}{t^3}\sum_{j=1}^{N/2}(E_x)_j\left(z_j^3 - z_{j-1}^3\right) \quad (3)$$

$$(\sigma_x)_j = \frac{MF.z}{I_{yy}}\left|\frac{(E_x)_j}{E_f}\right| \quad (4)$$

Fractographic analysis of the laminates was performed using an optical microscope. The density of CoRALs was also calculated by dividing the mass of the samples by the measured volume of the specimens. FMLs were also characterized by their metal volume fraction (MVF), defined as (Vlot and Gunnink, 2001) [6], [19]:

$$MVF = \frac{\sum_1^n t_{\text{metal (the thickness of total aluminium layer)}}}{t_{\text{laminated(thickness of total fml)}}} \quad (3)$$

3 RESULTS AND DISCUSSION

3.1 Physical and mechanical properties of cores and face

The results of the physical and mechanical properties of the core (CFREP and CRFPO) and face (1200 aluminium sheets) are listed in Table 2. The bases for the differences in the mechanical properties between the two coir-derived composites have been explored in another investigation, published elsewhere [20], and, therefore, are not described here.

Table 23. Physical and mechanical properties of CFRPCs and aluminium faces.

Material (isolated elements)		Tensile		Flexural		Impact	Density
		Mod.	Str.	Mod.	Str.	Str.	
		GPa	MPa	GPa	MPa	kJ/m²	g/cm³
Core	CFREP	2.33 (0.14)	17.48 (0.74)	2.27 (0.09)	34.90 (5.16)	6.04 (0.74)	1.03 (0.01)
	CFRPO	2.50 (0.07)	12.50 (1.11)	2.38 (0.13)	24.73 (3.61)	18.03 (2.37)	1.07 (0.03)
Face	AL. 1200	44-60	115-136	-	-	-	2.70

3.2 Demoulding and cutting process

CoRAL samples P1 and P2 presented delamination upon demoulding and/or cutting process. Due to poor consolidation with the polyester resin, mechanical tests for these conditions were not performed.

3.3 Physical properties of CoRAL: density and MVF

The density of CoRAL samples varied from 1.27 to 1.37 g/cm³. The density of epoxy based CoRALs increased 30% if compared to CFREP (1.03 g/cm³) and, 28.97% (CoRAL P3) compared to CFRPO (1.07 g/cm³).

Table 24. Physical properties of CoRAL.

Properties	*Coral E1*	*Coral E2*	*Coral E3*	*Coral P3*
Density (g/cm³)	1.37(0.08)	1.37(0.08)	1.28(0.05)	1.38(0.03)
Metal volume fraction (MVF)	24.11%	25.15%	23.00%	24.50%

With 23% of aluminium volume fraction, CoRAL E3 tended to present the lowest density value due to low aluminium volume fraction. The metal volume fraction shows that the addition of aluminium plates (2.7 g/cm³) contributed to an increase in density compared to coir-derived composites. Similar results were obtained in [6].

3.4 Tensile tests

Table 4 presents the mean tensile properties for CoRALs. No statistical significance was found for maximum tensile strength, since a p-value of 0.301 was obtained, indicating that the means of tensile strength are equal for all the conditions considered.

The post-yield linear part of tensile stress-strain curves for FMLs only depends on the stiffness of the core [21]. After yield point the aluminium face stress (extremely higher than CFREP and CFRPO – see Table 4), is suddenly transferred to the core resulting in catastrophic failure. No significant improvement was therefore obtained for maximum tensile strength of CoRAL samples.

Table 25. Mean of tensile properties of CoRAL samples.

Properties	*Coral E1*	*Coral E2*	*Coral E3*	*Coral P3*
Max. tensile strength (MPa)	36.88(1.93)	37.71 (2.00)	37.11(0.61)	36.08(1.90)
Core tensile yield strength (MPa)	5.83(0.09)	5.93(0.44)	6.02(0.41)	6.54(0.35)
Face tensile yield strength (MPa)	108.77(1.67)	110.74(8.24)	112.38(7.70)	111.17(6.07)

Typical stress-strain curves and fractographic analyses and failure modes observed after the tensile tests are presented in Figure 4. After unloading CoRAL E1 (see Figure 4 item CoRAL E1) presented delamination and plastic deformations of both faces between the CFREP and aluminium

layers, resulting of shear stresses in the interfacial plane and the energy dissipated at the moment of failure, caused by poor interface [21], [22]. Once maximum stress is achieved, a brittle fracture mode in the composite layers was observed, as well as fibre pull-out.

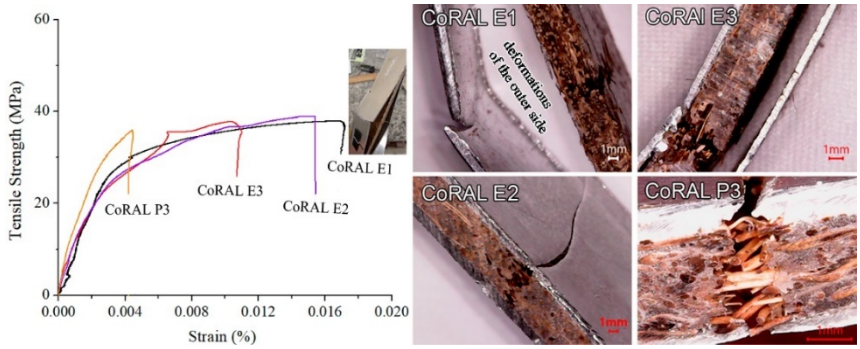

Figure 63. Tensile test: left) stress/strain curves right) morphologies of failure.

3.5 Three-point bending tests

3.5.1 Flexural modulus and strength

The flexural modulus ranged from 18.18 to 30.44 GPa (Table 5). The p-value for ANOVA was 0.024, indicating that the mean values for flexural modulus are significantly different. According to Tukey's test (see Table 5), the lowest flexural modulus value is attributed to CoRAL E1 samples. The increase of MVF contributes to improve flexural modulus. However, the appropriate surface preparation is essential to provide higher stiffness to FMLs [23]. Poor consolidation, due to chemical differences between inorganic aluminium faces and the organic polymer matrix core, resulted in a weak interface (see Figure 5 item CoRAL E1) and may explain the reduction in flexural properties.

The flexural strength of CoRALs varied from 83.92 to 103.17 MPa. CoRAL E2 presented the highest value for flexural strength (Table 5). The strength of CoRALs is strongly affected by the aluminium-core interaction, which is sensitively improved by the surface treatment used for CoRAL E2 samples. The specific flexural strength was also higher for CoRAL E2 (75.30 MPa).

Table 26. Mean of three-point bending test of CoRAL samples.

Properties	Flexural modulus (GPa)		Flexural strength (MPa)		Specific flexural strength ($MPa/g.cm^{-3}$)
	Mean	Tukey	Mean	Tukey	
CoRAL E1	18.18 (2.17)	C	83.92 (10.83)	C	61.25
CoRAL E2	30.44 (2.07)	A	103.17 (3.30)	A	75.30
CoRAL E3	24.07 (1.60)	B	90.55 (3.39)	B	70.74
CoRAL P3	27.13 (3.62)	A	89.25 (5.05)	B	64.67
ANOVA	*0.024*		*0.000*		-

Figure 5 (right side) depicts the interface evolution after aluminum treatment. After the linear state, the flexural behaviour of CoRALs shows the plasticity region due to the plastic deformation of the aluminium sheets – see Figure 5 (left side)[24]. When the CoRAL beam side submitted to tensile stress reaches failure, cracks initiate in the coir composite core which fails with a sudden load drop. Delamination in the aluminium-core interface was observed in CoRAL E1 (both sides) and E3 (side under tensile stress). Cracks in the aluminium face under tensile stress and through the core were the predominant failure modes in CoRAL E2 and P3. The failure of lower layers (submitted to tensile stress) greatly influences the flexural behaviour over other failures modes[24]. This effect is induced by the interfacial adhesion with the aluminium faces.

The comparison between CoRAL E2 and E3 (Table 5 and Figure 5) implies that the "*bridging effect*" (for more detail see ref. [11]) is more important than the wash primer treatment for epoxy based CoRALs. However, for polyester based CoRALs, the wash primer treatment was the only one able to provide an effective face-core consolidation. The reactions of wash primer bonding and curing are complex and many different reactions take place being unique for this chemistry[25].

An increase in the interfacial bonding with aluminium improves the maximum flexural load transfer, see Figure 5 (left side) [3][4][5][6][12][10]. Even with an effective aluminium-core bonding, the flexural strength of CoRAL P3 was only ~86% of CoRAL E2 and similar to CoRAL E3. However, experimental results showed that the flexural strength of composite cores also contributed to increase face-core load transfer. Such behaviour will be discussed in the following section.

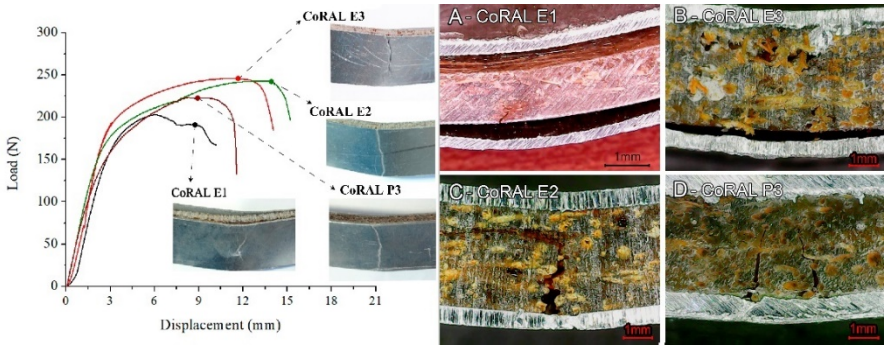

Figure 64. Flexural behaviour and failure mode for the CoRAL.

3.5.2 Normal stress distribution

The predicted stress distribution along the thickness of the CoRAL samples is presented in Figure 6. One can observed that the maximum normal stress occurs on the aluminium surface, Figure 5. The maximum stress occurs in the element with the higher modulus (aluminium faces - Table 2)[18].

As presented in Table 2, the flexural strength of CFREP (34.90 MPa) is ~41% higher than CFRPO (24.73 MPa). This explains why CoRAL P3 presented the lowest normal stress value at the Z_1(core) region (Table 6). However, the normal stress at Z_1(face) of the CoRAL E1 was the lowest of all other epoxy conditions. As previously reported, without treatment, a weak interfacial bonding takes place between aluminium sheets and the epoxy composite core. The load transferred between aluminium layers was reduced affecting the core stress. Owing to these effects, at Z_2(face) the stress of CoRAL E2 and E3 was superior than CoRAL E1 and P3.

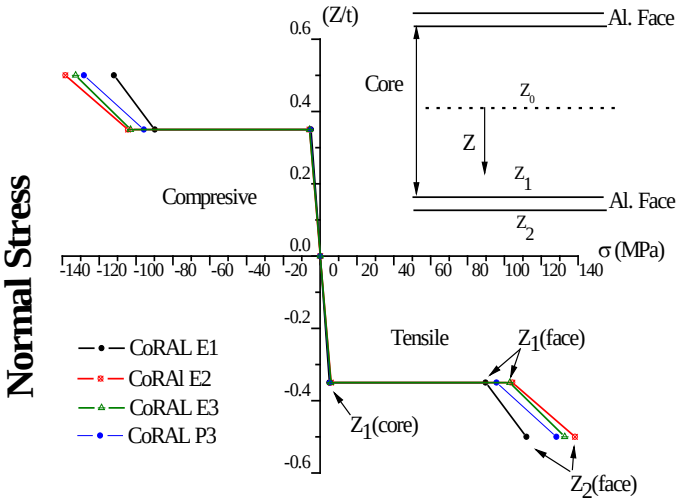

Figure 65. Normal stress distribution along the thickness of FML.

Table 27. Mean of normal stress (MPa) distribution along the thickness of CoRAL

Condition	Yield load						Max. load	
	Z_1(core)		Z_1(face)		Z_2(face)		Skin stress	
	Mean	Tukey	Mean	Tukey	Mean	Tukey	Mean	Tukey
CoRAL E1	5.24 (0.58)	AB	89.14 (5.02)	B	114.22 (7.99)	B	128.59 (14.54)	B
CoRAL E2	5.83 (0.19)	A	104.16 (3.43)	A	135.55 (2.77)	A	155.45 (7.76)	A
CoRAL E3	5.66 (0.18)	AB	101.17 (3.22)	A	134.96 (4.09)	A	146.44 (3.40)	AB
CoRAL P3	5.16 (0.29)	B	93.08 (4.04)	B	123.61 (5.57)	B	135.83 (9.29)	AB
ANOVA	*0.028*		*0.002*		*0.004*		*0.021*	

The superior skin stress for the experimental conditions was obtained for CoRAL E2. Experimental evidences based on the theory of laminated beams, imply the increase of CoRAL flexural behaviour is been induced by two factors: 1) interfacial bonding between aluminum and cores and 2) flexural strength of composite cores, which contributed to increase the load transfer.

3.6 Charpy impact test

The impact strength (Table 7) ranged from 32.33 to 64.39 kJ/m² for CoRAL E2 and CoRAL P3, respectively. The obtained p-value (0.001) reveals that the considered conditions significantly affected the impact strength and Tukey's test shows that the superior impact strength is attributed to CoRAL P3.

Table 28. Mean of impact test of CoRAL samples and Tukey's test.

Conditions	Impact Strength (kJ/m²)	
	mean	Tukey
CoRAL E1	a.d.c	-
CoRAL E2	32.33 (3.83)	B
CoRAL E3	36.40 (2.32)	B
CoRAL P3	64.39 (7.82)	A
ANOVA	*0.001*	
a.d.c* - aluminium debonding on cut.		

For FML sandwiches, crack propagation in the skin-core interface and through the core was responsible for the material failure [1]. In the epoxy and polyester CoRALs, fibre fracture and both aluminium and matrix fractures were observed (see Figure 7). The energy released with crack initiation or fracturing needs to be dissipated via various mechanisms. Fibre bridging and pull-out is one of the dominant methods of post-impact energy dissipation [1].

The loads from the cracking metal layers were transmitted via the adhesive to the fibres, thus unloading the metal layers and slowing down crack growth in these layers. The adhesive bonding between metal and composite core also plays an important role in the impact response of CoRAL. The impact strength of CFRPO (18.03 kJ/m³) was 198.51% higher than CFREP (6.04 kJ/m³). As a result, CoRAL P3 sandwich structure was found to have more efficient energy absorbing properties compared to CoRAL E1 and E2 under impact loading, because the coir fibre reinforced polyester core can dissipate more energy under impact load [20].

Figure 66. Post-impact fracture.

4 CONCLUSIONS

In this paper, the physical and mechanical properties of CoRALs were discussed. The tensile tests revealed that the metal layers control the tensile strength properties. No increase in tensile strength was obtained since the maximum tensile strength of composites cores was far below the maximum strength of aluminium. Different characteristic failure modes due to adhesive interface for the sandwich composites were found. The improvement of the interfacial adhesion between aluminium sheets and the composites cores was the major factor to increase the flexural load transfer and impact strength behaviour. The flexural behaviour can be described by two behaviours involving core flexural strength and interfacial aluminium/core shear transfer improved by aluminium treatment. With a good interface CoRAL-E showed superior flexural strength than CoRAL-P due to coir epoxy composites cores exhibiting greater flexural strength than polyester

composites. However, CoRAL-P has superior impact behaviour than other currently available CoRALs, once coir polyester composites core has superior impact strength than coir epoxy ones.

ACKNOWLEDGMENTS

The authors would like to thank the Brazilian Research Agencies, CNPq, Fapemig and CAPES, for the financial support provided.

REFERENCES

[1] R. Das, A. Chanda, J. Brechou, and A. Banerjee, *17 – Impact behaviour of fibre–metal laminates*, no. February. Elsevier, 2016.

[2] T. Sinmazçelik, E. Avcu, M. Ö. Bora, and O. Çoban, "A review: Fibre metal laminates, background, bonding types and applied test methods," *Mater. Des.*, vol. 32, no. 7, pp. 3671–3685, 2011.

[3] H. T. N. Kuan, W. J. Cantwell, M. a. Hazizan, and C. Santulli, "The fracture properties of environmental-friendly fiber metal laminates," *J. Reinf. Plast. Compos.*, vol. 30, no. 6, pp. 499–508, 2011.

[4] J. Y. Zhang, T. X. Yu, J. K. Kim, and G. X. Sui, "Static indentation and impact behaviour of reformed bamboo/aluminium laminated composites," *Compos. Struct.*, vol. 50, no. 2, pp. 207–216, 2000.

[5] C. Santulli, H. T. Kuan, F. Sarasini, I. De Rosa, and W. J. Cantwell, "Damage characterisation on PP-hemp/aluminium fibre–metal laminates using acoustic emission," *J. Compos. Mater.*, vol. 47, no. 18, pp. 2265–2274, 2013.

[6] L. M. G. Vieira, J. C. dos Santos, T. H. Panzera, J. C. C. Rubio, and F. Scarpa, "Novel fibre metal laminate sandwich composite structure with sisal woven core," *Ind. Crops Prod.*, vol. 99, pp. 189–195, 2017.

[7] H. Li, Y. Hu, C. Liu, X. Zheng, H. Liu, and J. Tao, "The effect of thermal fatigue on the mechanical properties of the novel fiber metal laminates based on aluminum-lithium alloy," *Compos. Part A Appl. Sci. Manuf.*, vol. 84, pp. 36–42, 2016.

[8] H. Ahmadi, G. H. Liaghat, H. Sabouri, and E. Bidkhouri, "Investigation on the high velocity impact properties of glass-reinforced fiber metal laminates," *J. Compos. Mater.*, vol. 47, no. 13, pp. 1605–1615, 2013.

[9] J. Zhou, Z. W. Guan, and W. J. Cantwell, "The influence of strain-rate on the perforation resistance of fiber metal laminates," *Compos. Struct.*, vol. 125, pp. 247–255, 2015.

[10] B. Yu, P. He, Z. Jiang, and J. Yang, "Interlaminar fracture properties of surface treated Ti-CFRP hybrid composites under long-term hygrothermal conditions," *Compos. Part A Appl. Sci. Manuf.*, vol. 96, pp. 9–17, 2017.

[11] W. Wu, D. Abliz, B. Jiang, G. Ziegmann, and D. Meiners, "A novel process for cost effective manufacturing of fiber metal laminate with textile reinforced pCBT composites and aluminum alloy," *Compos. Struct.*, vol. 108, no. 1, pp. 172–180, 2014.

[12] P. R. Oliveira, A. M. S. Bonaccorsi, T. H. Panzera, A. L. Christoforo, and F. Scarpa, "Sustainable sandwich composite structures made from aluminium sheets and disposed bottle caps," *Thin-Walled Struct.*, vol. 120, no. April, pp. 38–45, 2017.

[13] L. A. . OLIVEIRA, J. C. . SANTOS, T. H. . PANZERA, R. T. . FREIRE, L. M. G. . VIEIRA, and SCARPA, "Evaluation of Hybrid-Short-Coir-Fibre-Reinforced Composites via Full Factorial Design. Composite Structure," *Compos. Struct.*, 2018.

[14] ASTM D3039/D3039M − 14 and Standard, "Standard Test Method for Tensile Properties of Polymer Matrix Composite Materials1," pp. 1–13, 2014.
[15] ASTM D790-15, "Standard Test Methods for Flexural Properties of Unreinforced and Reinforced Plastics and Electrical Insulating Materials. D790," pp. 1–12, 2015.
[16] ASTM International, "ASTM D7249/D 7249M - 12 Standard Test Method for Facing Properties of Sandwich Constructions by Long Beam Flexure," *Annu. B. ASTM Stand.*, vol. i, pp. 1–9, 2012.
[17] P. M. Materials, "Standard Test Method for Determining the Charpy Impact Resistance of Notched Specimens of Plastics 1," pp. 1–17, 2010.
[18] R. F. Gibson, "Principles of Composite Material Mechanics," *Isbn0070234515 9780070234512*, no. 205, p. xxvii, 579 p., 1994.
[19] G. B. Chai and P. Manikandan, "Low velocity impact response of fibre-metal laminates - A review," *Compos. Struct.*, vol. 107, pp. 363–381, 2014.
[20] J. C. Santos, R. L. Siqueira, L. M. G. Vieira, R. T. S. Freire, V. Mano, and T. H. Panzera, "Effects of sodium carbonate on the performance of epoxy and polyester coir-reinforced composites," *Polym. Test.*, vol. 67, no. January, pp. 533–544, 2018.
[21] J. Bieniaś, K. Majerski, B. Surowska, and P. Jakubczak, "THE MECHANICAL PROPERTIES AND FAILURE ANALYSIS," *Compos. Theory Pract.*, vol. 3, pp. 220–224, 2013.
[22] L. M. G. Vieira, J. Cesar, T. Hallak, J. Carlos, C. Rubio, and F. Scarpa, "Novel fibre metal laminate sandwich composite structure with sisal woven core," *Ind. Crop. Prod.*, vol. 99, pp. 189–195, 2017.
[23] F. D. Morinière, R. C. Alderliesten, and R. Benedictus, "Modelling of impact damage and dynamics in fibre-metal laminates - A review," *Int. J. Impact Eng.*, vol. 67, pp. 27–38, 2014.
[24] G. S. Dhaliwal and G. M. Newaz, "Experimental and numerical investigation of flexural behavior of carbon fiber reinforced aluminum laminates," *J. Reinf. Plast. Compos.*, vol. 35, no. 12, pp. 945–956, 2016.
[25] A. E. Hughes, J. M. C. Mol, and R. G. B. Editors, *Springer Series in Materials Science 233 Active Protective Coatings*. .

IMPACT BEHAVIOR OF GLARE™ HYBRID LAMINATE UNDER EXTREME THERMAL CONDITIONS

Francisco J. Goyo-Brito, Matheus Vogler, Richard F. Silva, Alessandra C. Soares-Pozzi, José R. Tarpani*

Sao Carlos School of Engineering (EESC-USP), 13.566-590, Sao Carlos-SP, Brazil

*Corresponding author: jrpan@sc.usp.br

https://doi.org/10.21452/bccm4.2018.07.05

Abstract: Artificial bodies intentionally placed into low orbit around the earth (LEO) are exposed to critical thermal and mechanical in-service conditions, e.g. severe thermal cycling and micrometeoroid impact. To better understand the response of Glare™-5 2/1 fiber-metal laminate under such conditions, pristine test coupons were subjected to low-energy ballistic impact (21 J) at the temperatures of -196 and 100 °C. Another set of test pieces went through the same experimental conditions, except that they were first submitted to 1,200 thermal shock cycles from -196 to 100 °C. Thermally conditioned specimens exhibited higher resistance to externally visible damage in both test temperatures. On the other hand, internal failure mechanisms characterized via microscopy and X-ray CT inspection techniques have shown that specimens submitted to cryogenic impact after repeated thermal cycling presented the best impact resistance, being age hardening of outer 2024-T3 Al-alloy sheets a possible enhancing factor; besides, residual thermal stresses in the core glass fiber-reinforced epoxy matrix, associated to the post-cure of the latter may have led to higher interlaminar strength.

Keywords: Glare™ fiber metal-laminate; LEO extreme temperatures; low-energy ballistic impact, repeated thermal shock.

1. INTRODUCTION

Composites materials has increased their popularity in several application fields, especially in the construction of aeronautic and astronautic structures. They are preferred structural materials over traditional metallic alloys since they exhibit extraordinary structural efficiency, which means outstanding weight savings potential.

Fiber metal laminates (FML) are an especial class of composite materials, where alternating metal sheets and fiber-reinforced polymer (FRP) layers are bonded together, thus combining the great impact toughness of the former and the high fatigue resistance of the latter [1,2]. Glass

Reinforced-Fiber Metal Laminate (Glare™), comprising glass fiber-reinforced epoxy resin layers and high strength 2024-T3 Al-alloy sheets, is the greatest exponent of FML to date [3]. E.g., it has been chosen to serve as skin material in fuselage sections (500 m^2) of the Airbus A380, which means approximately 1 ton. of weight saving, corresponding to approximately 4 additional passengers [4].

The excellent performance of Glare™ in the aeronautical sector naturally led to expectations about its use in astronautic structures.

Satellites and spacecrafts orbiting around the earth are exposed to quite extreme temperature changes as they pass from earth shadow to direct sun radiation, leading to variations ranging from -190 to +120 °C, not to mention micrometeoroid particles' hyper-velocity impacts [5-8].

So far, to the best of our knowledge, there is no information regarding the impact behavior of Glare™ after withstanding extreme thermal cycles (i.e., repeated thermal shock conditions), as to simulate low orbit environment conditions.

In this work, the effect of multiple thermal shocks on the impact behavior of Glare™ laminate tested at extreme temperatures has been assessed. Internal failure mechanisms were characterized via optical and scanning electron microscopies and X-ray CT inspection, while thermal analysis, infrared spectroscopy, transmission electron microscopy, and nano- and micro-hardness techniques, besides three-point bend testing were employed to disclose the root causes of the observed performances of Glare™ under different pre-conditioning treatments and impact testing temperatures.

2. MATERIAL AND PROCEDURES

2.1 Material

1.6 mm-thick Glare™ 5 2/1 FML, consisting of two outer sheets of 2024-T3 Al-alloy and one inner S2 glass fibers/epoxy matrix laminate built according to the stacking sequence $[0/90]_s$, was used. Full-thickness samples and test pieces were cut from a 200 x 300 mm^2 plate supplied by Comtek Advances Structures™ - Canada. A bench saw using a water-cooled diamond disc was utilized for this purpose.

2.2 Thermal shock cycling (TSC)

Samples and test specimens were previously exposed to TSC treatment (1,200 cycles in total) between extreme temperatures, namely -196 and +100 °C. The lowest temperature was achieved in liquid nitrogen (L_2N), whereas the highest one in boiling water. Soaking time was 15 minutes for both liquid media.

2.3 Thermogravimetry analysis (TG)

Thermal stability of the glass fiber-reinforced epoxy resin (FRP – fiber-reinforce polymer) core of Glare™ in the as-received and TSC conditions was determined via Perkin Elmer™ analyzer model Pyris 1. TG scans were performed at 10 °C/min in the temperature range from 30 °C to 700 °C. N_2 atmosphere was used.

2.4 Fourier-transform infrared spectroscopy (FTIR)

FTIR spectra of Glare´s epoxy resin matrix in both pristine and TSC conditions were acquired in Perkin-Elmer™ model Spectrum 100 spectrophotometer. Wavelength range from 4000 to 600

cm^{-1} was swept at a resolution of 4 cm^{-1}. Attenuated total reflectance method (ATR) technique was employed.

2.5 Dynamic mechanical analysis (DMA)

DMA of Glare™ hybrid composite in the as-manufactured and TSC conditions were performed in Perkim Elmer™ model DMA 8000 to determine thermomechanical properties, namely, storage modulus (E'), loss modulus (E"), damping factor (tan δ) and glass transition temperature (T_g). The experiments were carried out in specimens with in-plane dimensions of 50 x 10 mm^2 tested in dual cantilever loading mode at a frequency of 1 Hz. Temperature ramp was 2 °C/min for a swept temperature range from 30 to 300 °C. T_g was determined from the peak of the tan δ curve.

2.6 Low-energy ballistic impact testing (LBT)

Square specimens with in-plane dimensions of 50 x 50 mm^2 were firmly clamped in a stainless-steel frame with a 45 x 45 mm^2 window, which was tightly fastened to a thin 2024 Al-alloy panel (2 x 1,75 x 1.6 mm^3) to simulate a repaired aircraft skin-substructure. LBT of as-fabricated and TSC conditions was performed with 5.5 caliber air-gun shooting cast lead bullets weighting 1.6 g. All specimens were centrally impacted at a bullet speed of 230 m/s. Considering the gun tip-to-specimen target distance of 15 cm and an impact angle of 45°, 21 J was estimated as the energy apportion to the FML test pieces. Test temperatures were -196 and +100 °C, respectively, which were achieved by, respectively, injecting L_2N and blowing hot air directly over the specimen faces for 15 minutes.

2.7 Permanent indentation height (PIH)

PIH corresponds to the maximum permanent deformation of the specimen after impact. Its determination was carried out by measuring the indentation height with the help of Digimess™ vernier caliper with precision of 0.01 mm.

2.8 Micro X-ray computed tomography (mXCT)

Impacted test pieces were scanned in a Brukker™ CT Scanner model Skyscan 1272. X-rays were generated by a Mo target, using voltage and current of, respectively, 100 kV and 100 µA. Image acquisition was performed with an effective voxel size of 10 µm for an exposure time of 4.6 seconds. 1 mm-thick Cu filter was used to collect a series of 1,012 projections in each case. Data visualization and processing was performed with PerGeos™ software. The segmentation strategy was based on manual seeding, by selecting the internal region of the sample through the Interactive Overlay Threshold (IOT) tool. First, a median filter was applied to the greyscale images to remove the noise from the data, followed by the application of the Marker-Based Watershed (MBW) and Separate Objects (SO) procedures to segment the region inside the sample from the outside.

2.9 Cross-section microscopy (CSM)

Following mXCT examination, Glare™ specimens were cross-sectioned at the impacted region and examined using AxionCam™ Model ICc 5 reflected light microscope (RLM) and Inspect™ F50 scanning electron microscope (SEM) to characterize internal damage and failure modes. The surfaces were platinum-coated previously to SEM inspection.

2.10 Transmission electron microscopy (TEM)

Thin 2024-T3 Al-alloy laminae were prepared by manual grinding the samples to a thickness of approximately 60 μm, followed by polishing them in Gatan™ Model 691 precision ion polishing system (PIPS). The microstructure was characterized by analyzing the distribution, morphology and chemical composition (EDS technique) of second phases in the grain interior and boundary. TEM images were obtained via Tecnai™ G2 F20 microscope operating at a voltage of 200 KV.

2.11 Nanohardness (NHAR)

Using the same specimens inspected by RLM and SEM, NHAR measurements were performed via Nanovea™ Model Pb1000 nanohardness equipment operating with Berkovich´s geometry indentator. 20 mN load was employed during indentation, each one lasting 6 minutes.

2.12 Three-point flexural testing (3PF)

Full-thickness rectangular specimens with in-plane dimensions of 50 x 50 mm^2 were subjected to quasi-static bending displacement-control test conditions to determining initial stiffness and ultimate strength in L_2N environment. Loading/unloading cycles were applied in Instron-EMIC universal testing machine with 1 kN full scale load cell. Load-train speed was 1 mm/min., and an adapted clip-gage was attached to the moving loading roller and a steady point in the test fixture between the bottom spans, so that load-line displacement could be accurately measured.

3. RESULTS AND DISCUSSION

3.1 TSC damage

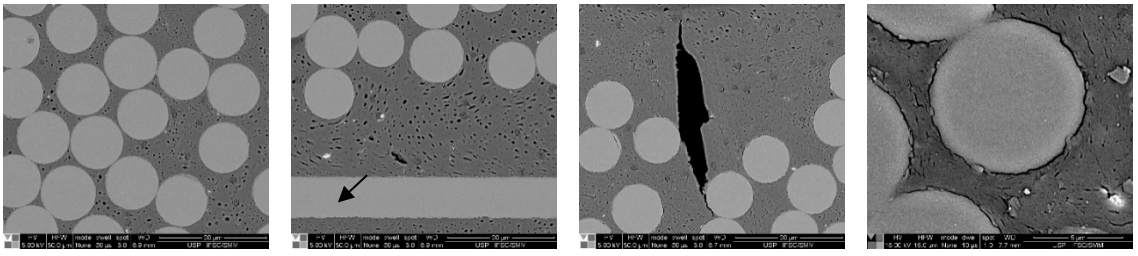

(a) (b) (c) (d)

Figure 1. SEM micrographs of Glare: virgin (a,b), and TSC (c,d) conditions.

Figure 1 displays SEM micrographs related to Glare™ in both pristine and after TSC treatment. While the first condition presents numerous, though very small resin matrix microvoids (Fig. 1a,b), the TSC sample exhibits very large matrix cracks (Fig. 1c) besides extensive fiber / matrix debonding (Fig. 1d). Transversal matrix cracking seems to originate in the fiber / matrix interphase (arrowed) by thermal fatigue, since the inorganic and organic phases have substantially different thermal expansion/contraction coefficients.

3.2 TG and FTIR

According to Figure 2a the beginning of thermal degradation is higher for the TSC glass fiber-reinforced epoxy resin composite core as compared to the pristine condition. This strongly indicates that resin crosslinking took place during the aging treatment, much probably a post-cure effect due to the +100 °C reversals.

Figure 2b shows less intense peaks associated to epoxy groups (bands between 950 and 860 cm^{-1}) for TSC condition when compared to the pristine one. This signalizes the consumption of epoxy groups during the post-cure conditioning (section 3.1 above) and/or the result from water (boiling water during TSC) reaction with epoxy. The first hypothesis is more reliable, not only due to the results provided in item 3.1, but also owing to the decrease of transmittance signal related to hydroxyl (OH^-) groups for the TSC treatment (peaks between 3600 and 3400 cm^{-1}).

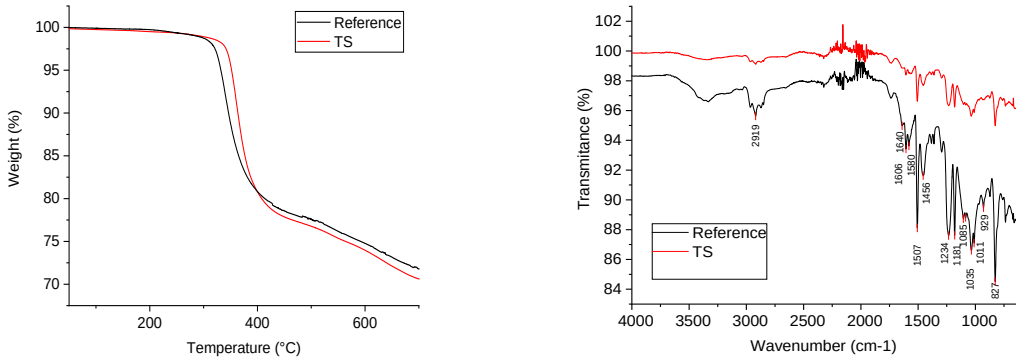

(a) (b)

Figure. 2: TG (a) and FTIR (b) analyses of Glare´s core composite.

3.3 DMA

DMA results plotted in Figure 3 show a significant increase of elastic modulus (E´) for TSC laminate when compared to the virgin material. The augment of crosslinking density during the thermal conditioning (sections 3.1 and 3.2 above) is likely to have incremented this property [9]. Thermal hardening of 2024-T3 Al-alloy of Glare laminate due to TSC pre-conditioning cannot though be discarded [10].

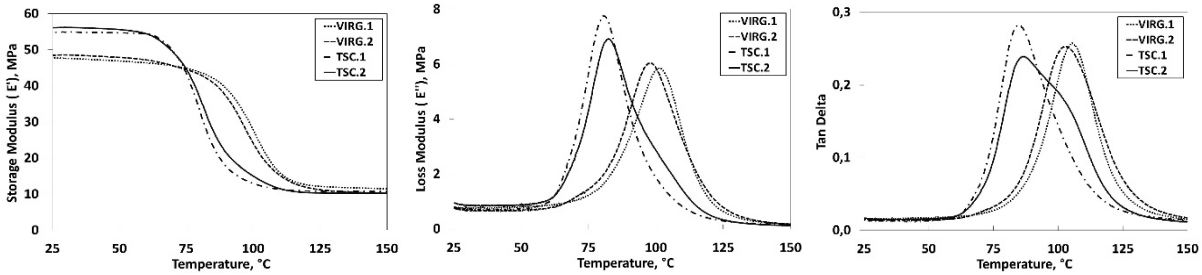

(a) (b) (c)

Figure 3. DMA analysis of Glare´s core composite: (a) E´, (b) E´´, (c) Tan δ.

It is also remarkable the decrease in the glass transition temperature (T_g) due to TSC treatment. Furthermore, an increase in the loss factor (tan δ) peak is noted. It is well-known that, in polymers, this effect is related to plasticity and mobility of macromolecule chains; however, according to [11] in FRP this outcome may result from stress relaxation caused by physical-chemical degradation of fiber / matrix interface. It is worth emphasizing that the lack of OH^- groups in the FTIR analysis in principle excludes the possibility of resin plasticization by water [12].

3.4 PIH and mXCT

The absorbed energy during ballistic impact is assumed to be proportional to the deformation of Glare beyond its global elastic regime, when, besides the outer Al-alloy sheets the FRP core can also be damaged (e.g., delamination, fiber breakage, matrix cracking, and so on). PIH values reflect this energy absorption capacity and are plotted in Figure 4(a). As expected, pristine test pieces impacted at +100 °C (HOT condition) exhibit higher indentation heights when compared to coupons tested at -196 °C. Moreover, TSC decreases substantially the ability of Glare to deform permanently for both HOT and COLD impact conditions.

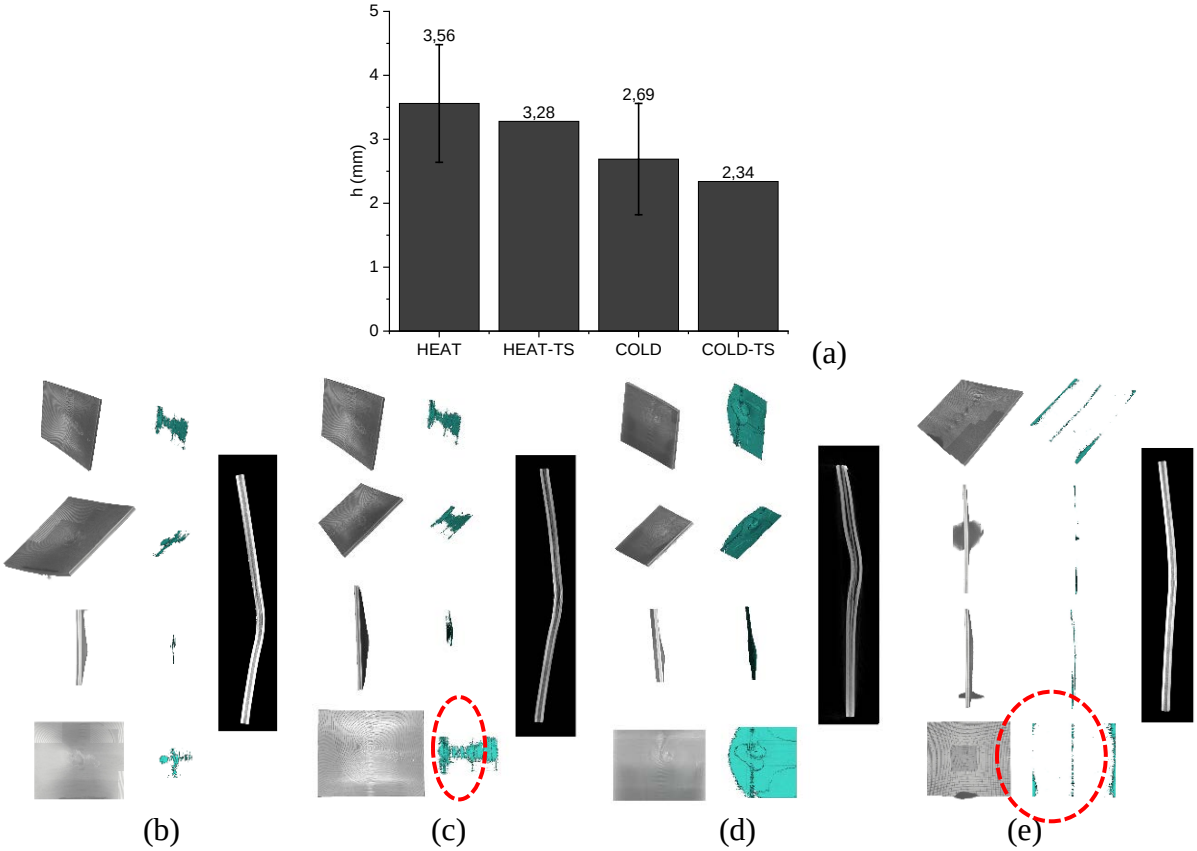

Figure 4. (a) PIH values for Glare™ hybrid laminate in four different combinations of thermal conditioning treatments and ballistic impact testing. Internal and external impact damages developed in Glare, according five mXCT views: (b) Virgin HOT, (c) TSC HOT, (d) Virgin COLD, (e) TSC COLD.

Regarding to mXCT results in Figure 4(b-e), TSC treatment does not seem to increase delamination growth substantially when the material is impacted at 100 °C. It is worth mentioning that dashed red ellipses in Figures 4(c,e) include solely noise signals, which are indeed X-R imaging artifacts. This behavior is likely to result from energy absorption essentially taken place in the outer 2024-T3 Al-alloy sheets of Glare, probably favored by matrix cracking and fiber-matrix debonding, as observed in TSC micrographs (later in this text).

On the other hand, virgin test pieces impacted under cryogenic conditions exhibit outstanding volume of voids (i.e. delaminations) extending almost all over the specimen´s internal interfacial planes, whereas the TSC test coupon is surprisingly virtually absent of this kind of damage. This behavior may be explained by simultaneous phenomena like cryogenic hardening of polymer

matrix, which is further enhanced by post-curing the laminate, better fiber / matrix interaction and, consequently, higher debonding resistance resulting from compressive residual strength in cryogenically treated composites, Al-alloy hardening due to precipitation aging at the time of TSC treatment. Besides, the thermal coefficient of shrinkage / expansion of the three phases present in Glare (ceramic fibers, epoxy resin and metal sheets) are determinant to establish the improvement of resin / fibers interplay. In this regard, since the resin matrix shrink more than the glass fibers, fiber compression and corresponding increase on fiber / matrix friction imply in improved toughening / strengthening mechanisms (e.g., fiber pull-out), not to mention the enhancement of the resin matrix resistance to cracking [9,10,13-20]. During impact at -196 °C (COLD condition) these effects are apparently improved, while at +100 °C (HOT) stress relaxation can take place overriding this, in principle, beneficial effect. Nevertheless, the TSC effect in the 2024-T3 Al-alloy sheets of Glare (items 3.3 and 3.4 above) and the consequences of ballistic impact temperature (HOT and COLD) in this material cannot be overlooked. This point will be returned later in this text.

3.5 CSM

Figure 5 presents optical microscopy views of impacted Glare laminate. Delamination at the metal / composite and composite laminae interfaces is the main damage mechanism detected. The extraordinary delamination resistance of TSC test coupon impacted under cryogenic temperature becomes evident as firstly detected via mXCT technique (section 3.4 above).

3.6 TEM

Figure 6 shows TEM microstructures of 2024 Al-alloy before (Fig. 6a) and after (6b) 1,200 thermal shock cycles. In the former condition it is possible to observe evenly distributed rod-like precipitates or T phases ($Al_{20}Cu_2Mn_3$) [21] in the grain interior, with no occurrence in the grain boundaries, whereas in the latter one needle like precipitates or S' phases (Al_2CuMg) are also noted in both grain interior and boundaries, which the authors inferred to enhance Al-alloys´ hardness [22].

3.7 NHAR

Figure 7 presents nanohardness results of virgin and TSC conditions of Glare™ laminate. One can notice that TSC treatment gave rise to a harder microstructure as compared to the pristine condition, thus confirming previous results provided in [22].

3.8 3PF

Figure 8 displays some results obtained in three-point flexural testing, where is possible to conclude that the elastic modulus (stiffness) and ultimate strength of Glare™ in TSC condition are substantially higher than the pristine hybrid laminate. These figures confirm previous inference based on sections 3.6 and 3.7.

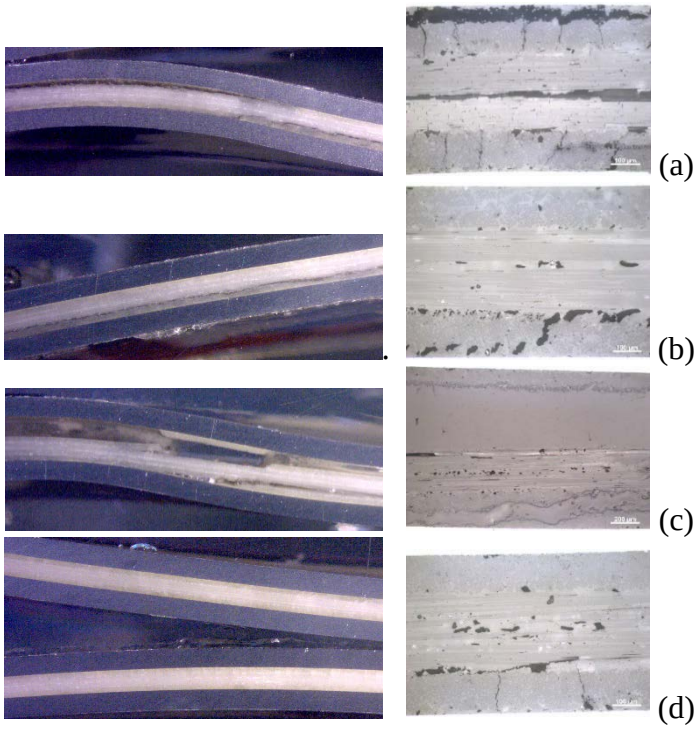

Figure 5. Optical micrographs of impact damaged Glare specimens: (a) Virgin HOT, (b) TSC HOT, (c) Virgin COLD, (d) TSC COLD.

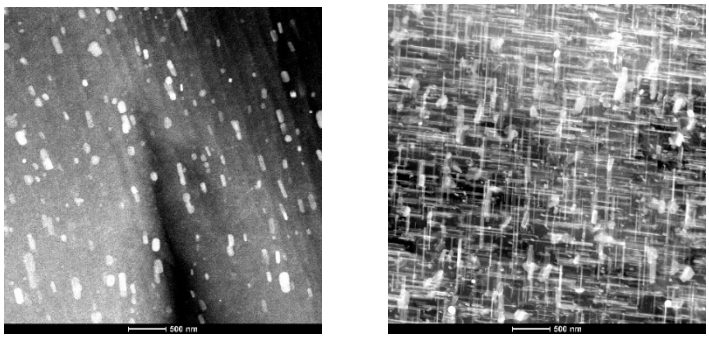

(a) (b)

Figure 6. TEM images of virgin (a) and TSC (b) Glare™ hybrid laminate (Dark Field).

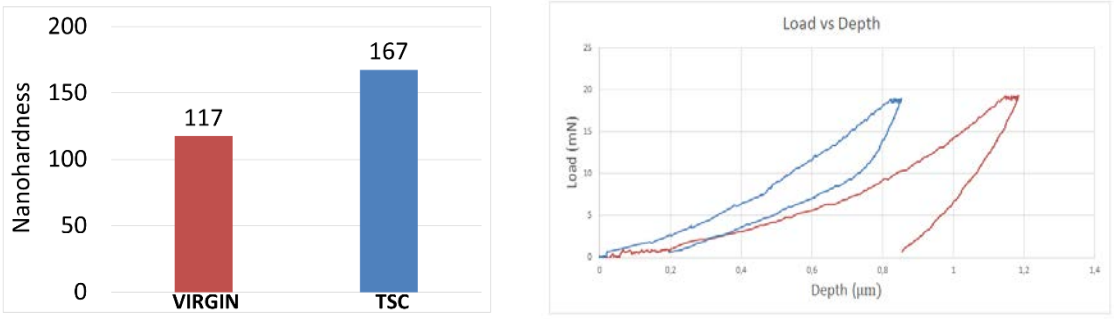

(a) (b)

Figure 7. Nanohardness results of Glare™ in pristine and TSC conditions: (a) Bar plot; (b) Corresponding load-depth curves.

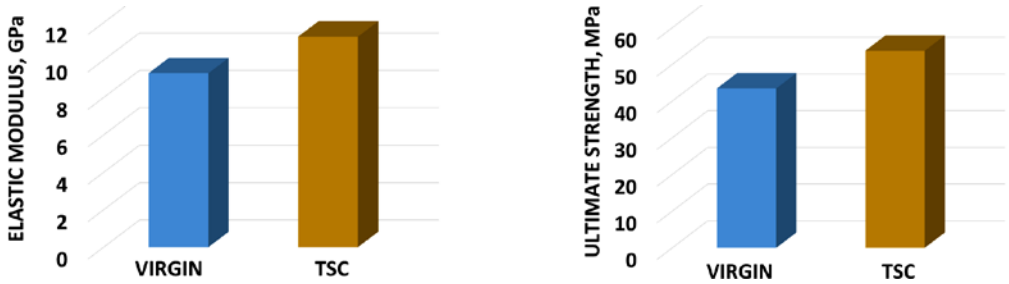

(a) (b)

Figure 8. Stiffness (a) and ultimate strength (b) of Glare™ in pristine and TSc conditions.

4. CONCLUSIONS

Despite thermal shock cycling under extreme temperatures (from -196 to +100 °C) led to higher resistance to externally visible damage after ballistic impact of Glare™ fiber-metal laminate, as compared to the pristine hybrid material, in very high and very low temperature test, internal failure mechanisms have shown that specimens submitted to cryogenic impact after repeated thermal shock cycling presented the best impact resistance.Age hardening of outer 2024-T3 Al-alloy sheets, besides residual thermal stresses in the core glass fiber-reinforced epoxy matrix, as well as post-cure of the latter were identified as the major responsible for the observe results.

Acknowlegments: To Ferreira A., Andreeta M., Bonagamba T. from Instituto de Física de Sao Carlos (IFSC), Brazil.

5. REFERENCES

[1] Sinke J. Development of fibre metal laminates: concurrent multi-scale modeling and testing. Journal of Materials Science, v.41, p.6777–6788, 2006. DOI: 10.1007/s10853-006-0206-5

[2] Vlot A., Gunnink J.W. Fibre metal laminatesKluwer Academic Publishers, Dordrecht, The Netherlands, 2001. ISBN 978-94-010-0995-9

[3] Vlot A. Glare: history of the development of a new aircraft material. Kluwer Academic Publishers, Dordrecht, The Netherlands, 2001. ISBN: 978-1-4020-0124-6, DOI: 10.1007/0-306-48398-X

[4] Alderliesten R.C. Fatigue and fracture of fibre metal laminates. Springer, Dordrecht, 2017. ISBN: 978-3-319-56227-8

[5] George P.E., Dursch H.W. Low-earth orbit effects on organic composite materials flown on LDEF. NASA - Marshall Space Flight Center, Document Identification: 19940026531, p. 335–354, 1993.

[6] Han J-H., Kim C-G. Low earth orbit space environment simulation and its effects on graphite/epoxy composites. Composite Structures, v.72, p.218–226, 2006. DOI: 10.1016/j.compstruct.2004.11.007

[7] Katz S., Grossman E. Space environment effects on polymer matrix composites, John Wiley & Sons, New Jersey, 2012. DOI: 10.1002/9781118097298.weoc228

[8] Yang B., Yue Z., Geng X. Effects of space environment temperature on the mechanical properties of carbon fiber/bismaleimide composites laminates. Proceedings of the Institution of Mechanical Engineers - Part G: Journal of Aerospace Engineering, v.232, p.3–16. DOI: 10.1177/0954410017740382

[9] Gao Y., Yang D., He S., Li Z. Effect of vacuum thermocycling on properties of unidirectional m40j/ag-80 composites. In: Kleiman J.I. (eds). Protection of materials and structures from the

space environment. space technology proceedings, vol 6, p.209–215. Springer, Dordrecht, 2006. DOI: 10.1007/1-4020-4319-8_19
[10] Pavan K.M, Sachin L.S. Mayur S., Chandrashekar A., Ajaykumar B.S. Effect of cryogenic treatment on the mechanical and microstructural properties of aluminium alloys - a brief study. International Journal of Mechanical and Production Engineering, v.2, p.95–99, 2014.
[11] Harris B., Braddell O., Almond D. Study of carbon fibre surface treatments by dynamic mechanical analysis. Journal of Materials Science, v.28, p.3353–3366, 1993. DOI: 10.1007/BF00354259
[12] Moy P., Karasz F.E. The interactions of water with epoxy resins. In: ACS Symposium Series, Chapter 30 Water in Polymers, v.127, p.505–513, 1980. DOI: 10.1021/bk-1980-0127.ch030
[13] Souza, c. S. R. De et al. Estudo do comportamento térmico de laminados carbono/epóxi submetidos a múltiplos ciclos térmicos. Polímeros, v.26, p.8–15, 2016. DOI: 10.1590/0104-1428.1769
[14] Ma H.L., Jia Z., Lau K., Leng J. Impact properties of glass fiber/epoxy composites at cryogenic environment. Composites Part B: Engineering, v.92, p.210–217, 2016.
[15] Park S.Y., Choi H.S., Choi W.J., Kwon H. Effect of vacuum thermal cyclic exposures on unidirectional carbon fiber/epoxy composites for low earth orbit space applications. Composites Part B: Engineering, v.43, p.726–738, 2012. 10.1016/j.compositesb.2011.03.007
[16] Wang J., Xue X., Yang Z., Zhang H., Zhou Y. Effect of cryogenic treatments on mechanical properties of 2A11 aluminum alloy. Advanced Materials Research, v.146–147, p.1646-1650, 2010. DOI: 10.4028/www.scientific.net/AMR.146-147.1646
[17] Kumar M.S., Sharma N., Ray B.C. Mechanical behavior of glass/epoxy composites at liquid nitrogen temperature. Journal of Reinforced Plastics and Composites, v.27, p.937–944, 2008. DOI: 10.1177/0731684407085877
[18] Indumathi J., Bijwe J., Ghosh A.K., Fahim M., Krishnaraj N. Wear of cryo-treated engineering polymers and composites. Wear, v.225229, p.343–353, 1999. DOI: 10.1016/S0043-1648(99)00063-0
[19] Anashkin O.P., Keilin V.E., Patrikeev V.M. Cryogenic vacuum tight adhesive. Cryogenics, v.39, p.795–798, 1999. DOI: 10.1016/S0011-2275(99)00089-2
[20] Kasen M.B. Mechanical and thermal properties of filamentary-reinforced structural composites at cryogenic temperatures 1: glass-reinforced composites. Cryogenics, v.15, p.327–349, 1975. DOI**:** 10.1016/0011-2275(75)90079-X
[21] Lv P., Zhang Z., Wang X., Ji L., Hou X., Guan Q. Microstructure evolution of 2024 and 7A09 aluminium alloys subjected to thermal cycling in simulated LEO space environment. Materials Research Innovations, v.18, p.169–175, 2014. DOI: 10.1179/1433075X13Y.0000000182
[22] Garay-Reyes C.G., González-Rodelas L., Cuadros-Lugo E., Martínez-Franco E., Aguilar-Santillan J., Estrada-Guel I., Maldonado-Orozco M.C., Martínez-Sánchez R. Evaluation of hardness and precipitation in Zn-modified Al2024alloy after plastic deformation and heat treatments. Journal of Alloys and Compounds, v.705, p.1–8, 2017. DOI: 10.1016/j.jallcom.2017.02.111

8. GEOPOLYMER COMPOSITES

MECHANICAL RESPONSE OF GEOPOLYMER COMPOSITES REINFORCED WITH DISTINCT TYPES OF FIBERS

Ana Carolina Constâncio Trindade [(1)], Paulo Henrique Ribeiro Borges [(2)] and Flávio de Andrade Silva [(1)]

(1) Department of Civil and Environmental Engineering, Pontifícia Universidade Católica do Rio de Janeiro, Brazil

(2) Department of Civil Engineering, Centro Federal de Educação Tecnológica de Minas Gerais, Brazil

https://doi.org/10.21452/bccm4.2018.08.01

Abstract

Ceramic materials, such as geopolymers, have been increasingly used in civil construction as a compatible, green-friendly, and even more efficient alternative. They are obtained through the mixture of an aluminosilicate source, with an alkali solution, and its mechanical properties may vary according to its molar ratios, curing regimes and processing conditions. Geopolymers present compatible mechanical and durable responses, despite their characteristic brittle behaviour. Fiber reinforcement appear as an interesting solution to overcome this vulnerability. Particulate, discrete and textile forms of distinct fibers can be used as reinforcements, resulting in sustainable solutions (natural fibers) and even ultra-ductility performance (synthetic fibers). This study presents an experimental evaluation of distinct geopolymer composites reinforced with natural (sisal, jute and curauá) and synthetic fibers (PVA). The geopolymer mixture was produced with metakaolin in a sodium based solution. Compression, tensile and pull-out tests were performed. Scanning electron microscopy (SEM) was used to investigate the hardened geopolymer microstructure. Despite presenting distinct quantitative responses, all composites exhibited strain-hardening behaviour with multiple cracking formation.

1. INTRODUCTION

The lack of an adequate variability of construction materials, and the consequences caused by the exponential production of non-renewable cementitious sources, leads to a demand for compatible alternatives. One of these alternatives are the so-called geopolymers, firstly developed by Davidovits in early 70s in France, in a successful attempt to manufacture a material capable of withstanding elevated temperatures [1]. However, with the knowledge dissemination and further investigations performed by several research groups around the globe, additional features appear

as advantages in the use of this technology, such as: high resistance in early ages [1]; improved durability behaviour [2]; and great adhesion performance with distinct types of fibers.

Geopolymers can be produced through the mixing of an aluminosilicate source, such as metakaolin or fly ash, with an alkaline solution (K, Na, or Cs based) [3]. The result is a polymeric inorganic network, with SiO_4 and AlO^-_4 linked by oxygen molecules [1,3]. Geopolymers, as well as any other ceramic materials, present fragile failure modes with low deformation capacity. Its mechanical response can be tailored with particulate (such as chamotte and sand) and/or fiber reinforcements [3]. These modifications can result in gains in tensile strength, ductility, toughness and even durability.

Recent studies demonstrate great improvements in the mechanical behavior of geopolymers with the use of reinforcements, such as: fique [4]; glass [5]; jute [2]; and steel fibers [6]. It is interesting, however, to notice that despite presenting distinct microstructural properties, it is possible to correlate the adhesion and stress transfer mechanisms of geopolymer and cementitious materials.

This work presents the results of an experimental investigation of a metakaolin-based geopolymer reinforced with distinct types of fibers: natural (jute, sisal and curauá), and synthetic (PVA) ones. The strength of the mixture is evaluated through compression tests. Its microstructure is investigated with the use SEM observations. The composites responses were studied through direct tensile tests. Additionally, pull-out tests were performed to try to demystify the fiber-matrix mechanisms.

2. EXPERIMENTAL PROGRAM

2.1 Materials and processing

The geopolymer mixture was manufactured through the combination of metakaolin ($Al_2O_3{\cdot}2SiO_2$), from Metacaulim do Brasil, and an alkaline solution based on sodium hydroxide and silicate, from Quimesp, resulting in a final composition of $Na_2O{\cdot}Al_2O_3{\cdot}3SiO_2{\cdot}11H_2O$. The latter was stablished following the results obtained in previous studies [7,8]. Sodium silicate and hydroxide solutions were mixed in appropriate proportions, and the final blend was cooled in a water bath for 10 min, before being added to the aluminosilicate source. A 5L capacity planetary mixer was used as follows: (i) 5 min at 136 rpm; (ii) removal of trapped solids on the walls of the container; (iii) final homogenization for 3 min at 281 rpm. River sand was incorporated as a natural aggregate, with density of 2.68 g/cm³ and maximum diameter of 1.18 mm.

Cylindrical specimens with 100 x 50 mm (height x diameter) were produced for compression tests. After the mixing process, the mixture was poured into steel molds protected by plastic papers (to avoid unwanted adhesion), alternating with medium vibration (to reduce voids content). The molds were sealed at room temperature for 24h to prevent crack formation due to dehydration during the curing process. After this period, the samples were withdrawn from the molds and stored in plastic bags for 6 more days, until mass constancy was obtained.

Geopolymer composites were produced with distinct types of reinforcements: natural (jute, sisal and curauá) and synthetic ones (PVA). Jute fibers are extracted from the stem of the plant *Corchorus capsularis*, while sisal and curauá fibers are extracted from the leafs of the plants *Agave sisalanais* and *Ananas erectfolius*, respectively. Jute was incorporated in a geopolymer material as a plain weave fabric (as received), while sisal and curauá were positioned in aligned unidirectional forms. All the natural reinforcements were used with 10% in weight content. Synthetic PVA fibers, with 12 mm in length, from Kuraray Co. (REC 15), were used as disperse reinforcement in a volume fraction of 2%. All fibers properties are presented in Table 1.

Table 1: Mechanical and physical properties of jute, sisal, curauá [9] and PVA fibers [10].

Properties	Jute	Sisal	Curauá	PVA
Tensile Strength (MPa)	104	447.2	632.1	1600
Strain-to-failure (mm/mm)	0.01	0.03	0.02	0.06
Young's modulus (GPa)	5.7	20.16	38.1	41
Average diameter (mm)	0.483	0.023	0.008	0.040

Plate specimens of geopolymer material reinforced with the four types of fibers mentioned before, with 450 x 60 x 12 mm (length x width x thickness), were produced for tensile tests. Cylindrical specimens with 25 x 20 mm (height x diameter) were produced for pull-out tests, where filaments of each fiber were embedded in 25 mm (natural fibers) and 4 mm (PVA) lengths into the geopolymer material. All specimens were prepared and cured following the indications previously mentioned for the cylindrical specimens.

3. TESTING METHODS

The flow table test was carried out with the fresh geopolymer mixture following the instructions presented in ASTM C143 [11]. Compression tests were performed on a MTS universal testing machine, model 810, using a load cell with maximum capacity of 500 kN, following the indications on ASTM C39 [12]. Three cylindrical specimens were tested using a displacement controlled rate of 0.5 mm/min. The upper and lower surfaces of the samples were regularized, in order to obtain an adequate mechanical response. The axial displacement was measured through the readings of two LVDTs, with 70 mm of length, coupled to acrylic rings positioned around the specimens.

A scanning electron microscope (SEM), model FEI Quanta 400, operated at 20 kV, was used to evaluate the microstructure of the hardened geopolymer. The samples were polished and thinned using a semiautomatic Struers equipment (Tegramin). For a better resolution (result of the amount of conductivity inside the equipment) a gold layer was applied on the sample for 20 seconds in a vacuum media.

Pull-out and tensile tests were carried out on a MTS testing equipment, model 810, with a load cell of 250 kN. For the pull-out tests, a load cell with maximum capacity of 1 kN was adapted for a better measurement. The displacement rate used was equal to 0.1 mm/min. For the pull-out tests, one LVDT (70 mm) was placed between the upper and lower grips, and 10 specimens were tested for each variation. However, for the tensile tests, two LVDTs were positioned on the sides of the specimens with 250 mm of gauge length. The tensile tests were performed following the recomendations described on ASTM 1275 [13], in 3 specimens for each reinforcement. The specimens were fixed in steel plates, and a 10 N.m torque was applied to each screw. Figure 1 presents the tests setups.

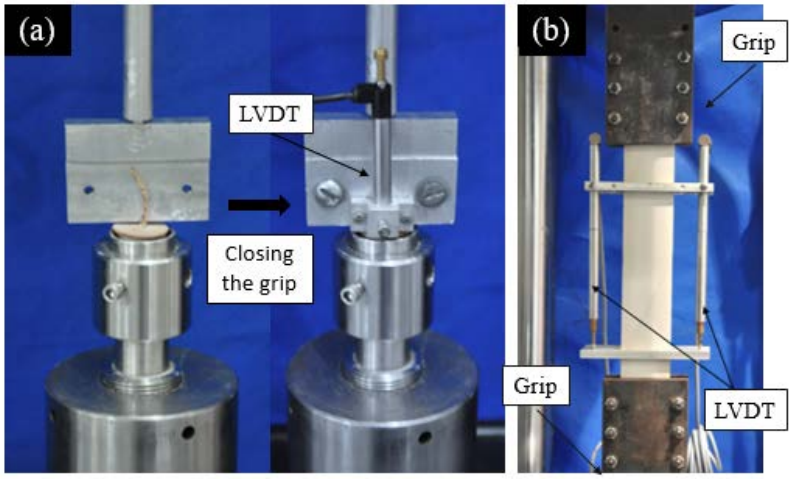

Figure 1: (a) Pull-out; and (b) tensile tests setups.

4. RESULTS AND DISCUSSION

The flow table tests results presented an average value of 127.5 mm for standard consistency, evidencing an intermediate fluidity for fresh geopolymer mixtures, according to the parameters proposed by previous studies [14]. This result is justified by the great H_2O absorption capacity of metakaolin based materials.

The compressions tests resulted in an average strength of 72.7 MPa and 14.26 GPa of Young's Modulus, with a fragile failure mode. The micrograph of the cured sample is presented in Figure 3. It is possible to distinguish unreacted MK particles and aggregates (distinct grey scales). It is, however, important to notice a significant presence of large pores interconnected by microcracks through the surface. Those are direct results from the dehydration occurring during the first hours of curing, where the water restrained inside the material looks for a way out, creating undesired internal pressures, resulting in microstructural defects (cracks and pores). The presence of aggregates is very important, since it creates difficulties during the crack formation process, resulting in strengthening mechanisms. Another method to improve the mechanical performance of fragile materials is the incorporation of fibers, which will be discussed below.

The tensile tests average responses for the geopolymer composites are presented in Figure 3 and Table 2. Weibull statistics was used for the ultimate stress values, mostly to determine the reliability of the results. Following the indications presented in previous studies [5,16], the parameters were obtained by plotting the following relation:

$$\ln\left[\ln\left[\frac{N+1}{N+1-i}\right]\right] = m\ln\left(\frac{\sigma}{\sigma_0}\right)$$

where N corresponds to the number of tested samples; i corresponds to the order of the stress (σ) related to each sample (from lowest to highest); m represents the Weibull modulus; and σ_0 is the characteristic strength in a scale parameter. The higher the Weibull modulus the lower is the dispersion of failure stresses.

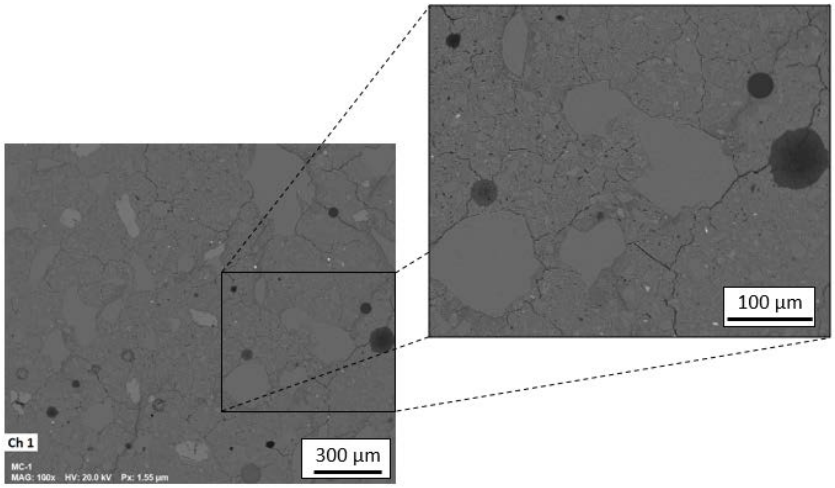

Figure 2: SEM micrograph of the hardened sodium based geopolymer.

It is possible to affirm that all composites (natural or synthetic fiber reinforced) exhibited a strain-hardening behaviour with multiple cracking formation during the tests. They all reached similar low responses in first cracking stresses (σ_{1f}), with greater results in ultimate average tensile stresses for curauá and sisal fiber reinforced ones, reaching 14.33 and 11.53 MPa, respectivelly. The latter, despite showing a small reduction in strength, exhibited a more ductile response than the previous one. A very distinct behaviour, regarding cracking formation, was observed for jute and PVA fibers reinforced geopolymers, with greater deformation capacities and lower crack formation, possibly due to insufficient fiber-matrix adhesion. Jute and PVA geopolymer composites reached ultimate stresses of 6.31 and 5.56 MPa, respectively. All composites exhibited great reliability, with a lower Weibull modulus, equal to 6.8, for PVA reinforced geopolymers. It is important to notice, however, that the content of PVA fibers was equal to 2% in mass, against 10% for the other fibers, resulting in an interesting mechanical behaviour due to its greater strength (1600 MPa) and Young's modulus (41 GPa).

Table 2: Results of direct tensile tests with geopolymer composites reinforced with: curauá, sisal, jute and PVA fibers.

Composite	σ_{1f} (MPa)	m	σ_0 (MPa)	σ_u (MPa)	S.D. (MPa)	95% C.I. (MPa)
Curauá GC	4.83	13.1	14.89	14.33	1.25	(13.9, 14.8)
Sisal GC	4.37	15.3	11.92	11.53	0.86	(11.2, 11.8)
Jute GC	4.13	9.2	6.65	6.31	0.78	(6.0, 6.6)
PVA GC	3.58	6.8	5.94	5.56	0.94	(5.2, 5.9)

σ_{1f} = first crack stress; m = Weibull modulus; σ_0 = ultimate stress (scale parameter); σ_u = ultimate stress (average); S.D. = standard deviation; 95% C.I. = 95% confidence interval.

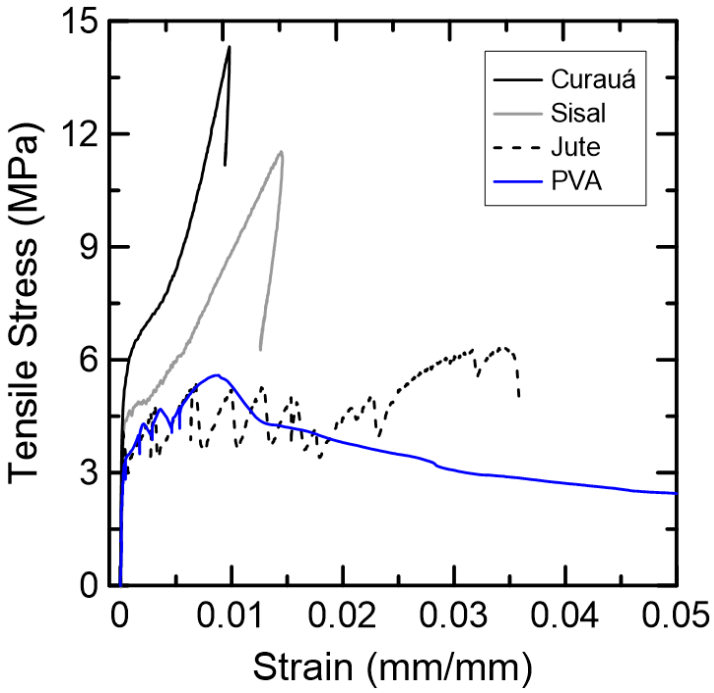

Figure 3: Tensile Stress x Strain curves for geopolymer composites reinforced with: curauá, sisal, jute and PVA fibers.

An additional evaluation of the fiber-matrix interface is presented in Figure 4, and Table 3, through the pull-out tests results. Its efficiency depends mainly on its chemical-physical bond, frictional adhesion and mechanical anchoring [17]. Among all fibers, it can be stated that sisal and curauá present the better adhesion (justifying its improved mechanical behaviour in the composite), followed by jute and PVA. This analysis indicates that the higher the fiber matrix adhesion, the greater it is the composite strength and the lower it is its deformation capacity. The amount of fibers incorporated in the geopolymer material also present significant changes in its mechanical capacities.

Table 3: Pull-out tests results for: curauá, sisal, jute and PVA fibers embedded in a geopolymer material.

Fiber	Embedded length (mm)	P_a (N)	D_a (mm)	Stiffness (N/mm)
Curauá	25	7.14	1.55	4.61
Sisal	25	8.47	2.12	3.99
Jute	25	4.84	1.83	2.64
PVA	4	0.65	0.74	2.91

P_a = adhesional force; D_a = adhesional displacement.

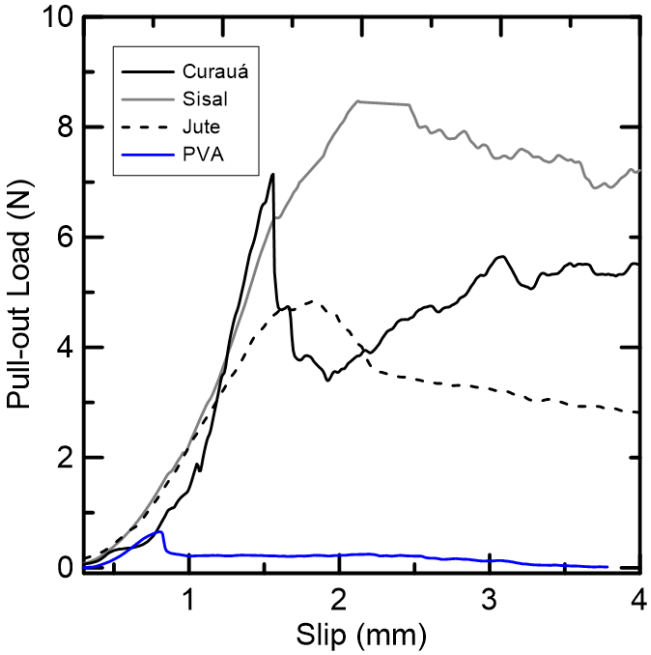

Figure 4: Pull-out load x Slip curves for: curauá, sisal, jute and PVA fibers embedded in a geopolymer material.

5. CONCLUSIONS

The geopolymer material, when incorporated with the natural aggregate sand, achieved 72.7 MPa in compression strength. All composites, reinforced with distinct types of fibers (natural and synthetic ones), achieved multiple cracking formation in a strain hardening behaviour. The curauá and sisal fibers presented the higher stresses when compared to the lower results obtained for jute and PVA fibers. The latter, despite being used in smaller contents (2% in weight), was still capable to present interesting mechanical responses and an improved deformation capacity (>5% in strain). It was possible to notice an increase in stress in a better fiber-matrix adhesion environment (evidenced by the pull-out tests), while weak adhesions presented greater deformation capacities.

ACKNOWLEDGEMENTS

The authors would like to thank Metacaulim do Brasil for the metakaolin donation. They are also grateful for the availability of the SEM equipment in CETEM laboratory. This work was funded by CNPQ and CAPES.

REFERENCES

[1] Davidovits, J., 'Geopolymers: inorganic polymeric new materials', *J. Thermal Analysis and Calor*. **37**(8) (1991) 1633-1656.

[2] Trindade, A.C.C., Alcamand, H.A., Borges, P.H.R. and Silva, F.A., 'On the durability behavior of natural fiber reinforced geopolymers', *Ceramic and Science Proceedings* **38**(3) (2017) 215-228.

[3] Kriven, W.M., 'Geopolymer-based composites', *Ceramics and Carbon Matrix Composites* **5** (2017), Elsevier.
[4] Sankar, K. and Kriven, W.M, 'Potassium geopolymer reinforced alkali-treated fique', *Cer. Engr. Sci. Proc.* **38**(10) (2015) 61-78.
[5] Sankar, K. and Kriven, W.M., 'Geopolymer reinforced with E-glass leno weaves', *J. American Cer. Soc*., **100**(6) (2017) 2492-2501.
[6] Castel, A. and Foster, S.J., "Bond strength between blended slag and class F fly ash geopolymer concrete with steel reinforcement", *Cem. And Concr. Res.* **72** (2015) 48-53.
[7] Borges, P.H.R., Banthia, N., Alcamand. H.A., Vasconcelos, W.L. and Nunes, E.H., 'Performance of blended metakaolin/blast furnace slag alkali-activated mortars', *Cem. Concr. Compos*. **71** (2016) 42-52.
[8] Trindade, A.C.C., Alcamand, H.A., Borges, P.H.R. and Silva, F.A., 'Influence of elevated temperatures on the mechanical behavior of jute-textile-reinforced geopolymers', *J. of Cer. Sci. and Tech.* **8**(3) (2017) 389-398.
[9] Fidelis, M.E.A., Pereira, T.V.C., Gomes, O.D.F.M, Silva, F.A. and Toledo Filho, R.D., 'The effect of fiber morphology on the tensile strength of natural fibers', *J. Mater. Res. Technol.* **2** (2013) 149-157.
[10] Nematollahi, B., Sanjayan, J., and Shaikh, F.U.A., 'Tensile strain hardening behavior of PVA fiber-reinforced engineered geopolymer composite', *J. Mater. Civ. Eng.,* **27**(10) (2015) 4015001-1–12.
[11] ASTM (American Society of Testing and Material): Standard test method for slump of hydraulic-cement concrete, C143/C143 M-09. *ASTM International*, West Conshohocken (2009).
[12] ASTM (American Society of Testing and Material): Standard test method for compressive strength of cylindrical concrete specimens, C39/C39 M-15a. *ASTM International*, West Conshohocken (2015).
[13] ASTM (American Society of Testing and Material): Standard test method for monotonic tensile behavior of continuous fiber-reinforced advanced ceramics with solid rectangular cross-section test specimens at ambient temperature. *ASTM International*, West Conshohocken (2015).
[14] Bhowmick, A. and Ghosh, S., 'Effect of synthesizing parameters on workability and compressive strength of fly ash based geopolymer mortar', *Int. J. Civ. Struct. Eng.* **3** (2012) 168-177.
[15] Silva, F.A., Chawla, N., and Toledo Filho, R.D., 'Tensile behavior of high performance natural (sisal) fibers', *Compos. Sci. Tech*. **68** (2008) 3438-3443.
[16] Ferreira, S.R., Silva, F.A. and Toledo Filho, R.D., 'Effect of hornification on the structure, tensile behavior and fiber matrix bon of sisal, jute and curauá fiber cement based composite systems', *Constr. Build. Mater.,* **139** (2017) 551-561.

RESISTANCE TO COMPRESSION AND ANALYSIS OF THE MICROSTRUCTURE OF METACAULINITE-BASED GEOPOLMERIC MORTAR

Gleicyanne O. S. Portela(1), Wanison Gil Pessoa Junior(2), Lizandro Manzato(2) and João de Almeida Melo Filho(3)

(1) Department of Civil and Environmental Engineering, Universidade Federal do Amazonas, Brazil

(2) Department of Materials, Instituto Federal do Amazonas, Brazil

https://doi.org/10.21452/bccm4.2018.08.02

Abstract

Geopolymer binders have been seen as an alternative material for reducing the use of Portland cement due to its excellent mechanical properties and low environmental impact. This article presents geopolymer mortars produced from metacaulinite, from kaolin calcination at 750 ° C for 6 hours. The developed geopolymers were synthesized with potassium hydroxide and potassium hydroxide silicate as activators mixed with metakaolin, cement and sand. The compressive strength tests were performed at the ages of 7, 14 and 28 days. The geopolymer microstructure was observed by scanning electron microscopy (SEM). Samples presented maximum performance of compressive strength of 58 Mpa, with a dense and homogeneous microstructure.

1. INTRODUCTION

The reduction of energy consumption and pollution generated during the production of cement became a concern in industrial processes of global manufacture. The search for alternative materials that could reduce energy demand and pollutants gases increased in recent years [1]. In this context, the development of geopolymers, formed through the activation of aluminosilicates in strongly alkaline environment, has great potential to replace conventional concrete [2]. The term "geopolymer" was created by J. Davidovits [3] to describe the chemical properties of inorganic polymers based on aluminosilicates.

Geopolymers have cementitious properties and can be composed from natural raw materials or residues from various sources, provided that these residues are rich in amorphous or semi-crystalline aluminosilicates, which through heat treatment become more reactive and alkaline [1]. Studies about the functions and behavior of raw materials involving kaolinite and other clays were initially used in 1974 and 1975. Davidovits [4] mainly used kaolin and calcined kaolin (metacaulinite) as the source of aluminosilicate oxides, in order to synthesize geopolymers. Many

other researchers have also focused on the manufacture of geopolymeric products and their industrial applications using a kaolinite or metakaolinite as the main reactant [5-7].

Metacaulinite as base of the geopolymer may have mechanical properties comparable or superior to Portland cement [8]. In general, the product obtained depends on the chemical and mineralogical composition of metacaulinite, which may have a greater or lesser degree of fineness, a greater or lesser specific surface, and present a white, creamy or slightly pinkish color. In essence metacaulinite consists of alternating layers of silicate, aluminum and silicon [9].

Another important factor are the grains, which the finer the better the gel dissolution and formation rates favor. However, the larger the particle diameter, the greater the occurrence of pores and specific mass [10,11]. The combination of fine particles, less than 5μm, and better dissolution, similar results are obtained with lower amounts of precursor materials [12].

This new technology contributes greatly to the reduction of environmental impact, since there is an 80% reduction in the emission of carbon dioxide to the atmosphere [13]. Another relevant feature, although it is water-based, the reaction products are not calcium hydrates as in conventional cements. This results in the formation of an amorphous matrix, but chemically stable. Thus, it has excellent durability, not suffering the intense degradation processes that are observed in the structures realized with conventional cement. It has higher bending and tensile strength than conventional ones [14].

This study develops a geopolymer mortar containing metacaulinite as a precursor, characterizing properties of resistance, microstructure and other tests, in order to present new alternatives in civil construction.

2. MATERIALS AND METHODS

2.1 Materials

In this work, cement of type CPIII 40RS was used. The silica used in the blends is industrial. The river sand, with granulometry passed through the 0.979mm sieve. The alkaline activator was potassium hydroxide (KOH).

The kaolin in natura was macerated with the aid of a rod, in a porcelain bowl. After the procedure, was placed in a greenhouse of brand De Leo for a period of 24 hours at a temperature of 100 ° C to remove moisture. The material was calcined in a muffle furnace of the manufacturer GP Scientific at a temperature of 750 ° C for a period of 6 hours to obtain metakaolin. Finally, it was placed in a ball mill for a period of 6 hours and sifted in the 200 mesh sieve.

2.2 Geopolymer synthesis

The mixing ratio of geopolymer mortar was determined by attempting blends so that the mortar gets good mechanical properties, moderate hardening time and suitable rheology. Table 1 shows the proportion of the materials used to make the matrix.

Table 1. Dosing of the mortar

Material	Proporção
Metacaulinita	0,228
Cimento	0,134
Areia	0,142
Silica	0,128
NaOH	0,193
Àgua	0,172

According to Palomo and Glasser [15], the mixing order of the reactants is a critical point that can significantly affect the phase development of the final product. From the chemical and physical point of view, there are compelling reasons to justify a particular order of mixing the components. According to the same authors, it would be interesting in a first step to mix and allow the soluble components to mature and then, in a later dispersed phase, add the products which are normally insoluble. Thus, the preparation of the mixtures was carried out in the following sequence:

- Production of potassium hydroxide silicate with the mixture of silica, water and potassium hydroxide;
- After 24 hours, mixing the powders: metacaulinite, cement and sand for 3 min manually;
- Addition in silicate mixer;
- Launch, little by little of powders;
- Mixing for 3 minutes;
- 1 minute stop for removal of material retained in the mortar;
- Mixing for 1 minute.

Figure 1 illustrates the molding process, in figure 1 (a) the mold is filled and Figure 1 (b) shows the compaction of the mortar. The demolding occurred 24 hours later, the specimens were placed in bags for complete cure, in order to avoid the appearance of microcracks.

Figure 1. Molding of specimens

2.3 FRX

To obtain a chemical measure of the materials an X-ray dispersive energy spectrometer (EDS), model EDX-720 from Shimadzu was used. An important mass was determined in a helium gas pycnometer, Micromeritics, model AccuPyc 1340. In order to determine the chemical composition of the materials, a ray dispersive energy spectrometer X (EDS), model EDX-720 Shimadzu. The specific mass was determined in a helium gas pycnometer, Micromeritics, model AccuPyc 1340. For the performance of the test, the sample was oven dried at 60 ° C for 24 hours.

Table 2. Chemical composition of materials

Composition	Metacaulinite	Cement CP-IV	Silica
Al2O3	42,1973%	8,348%	2,371%
SiO2	53,9093%	21,504%	85,449%
K2O	0,3353%	0,843%	2,479%
CaO	0,0833%	61,879%	0,755%
MnO	0,0020%	0,224%	0,112%
Fe2O3	1,3417%	2,621%	3,673%
TiO2	1,6093%	0,451%	
SO3		3,992%	2,439%
SrO		0,120%	0,007%
ZnO		0,019%	0,554%
MgO			2,021%
Especific mass	3,0522	3,1264	2,4679

2.4 MEV

The interface was observed by microscopy, the samples were removed from the test specimens after the compression test, where cubes with a maximum dimension of 1cm were extracted from sections that had undergone the most influence and rupture during the test. To prepare the sample, it was necessary to dip the cube in resin and let it dry for 24 hours. The analysis was performed using a scanning microscope, Hitachi, tm 3000.

2.5 Compressive strength testing

The compression test was performed on an Emic universal test machine, with a load capacity of 300 kN, at the ages of 7, 14 and 28 days. For each age, three cylindrical specimens of 50 mm diameter and 100 mm height were molded. The assay was performed at a rate of 0.2 mm / min.

3. RESULTS AND DISCUSSION

3.1 Compressive strength testing

In Fig. 2 shows the compression graph of the geopolymer matrix at the ages of 7, 14 and 28 days.

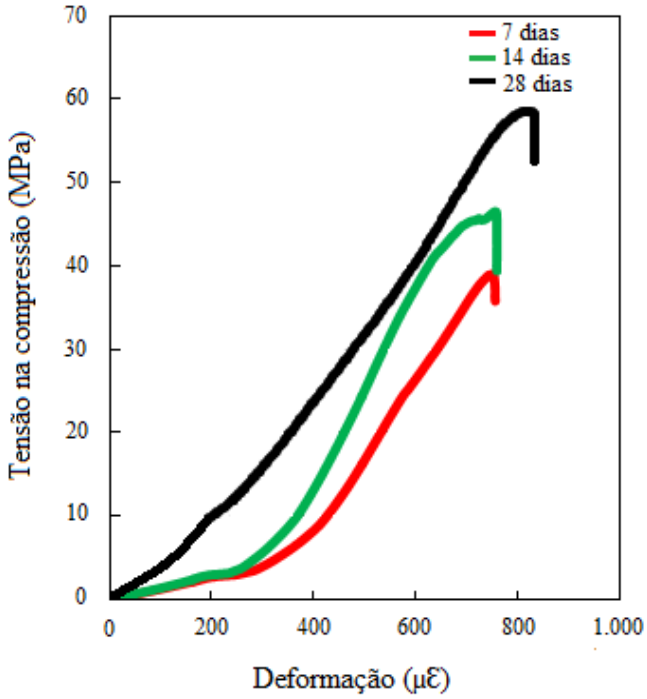

Figure 2. Stress curve in compression x deformation

From Stress x Strain curves, average values of maximum compression stress ($^{\delta}$max) and axial strain of maximum stress ($^{\varepsilon}$máx).The results are presented in table 3.

Table 3. Mean values of compressive strength, strain at tensile and modulus of elasticity

Age	Tensão máxima (MPa)	$^{\varepsilon}$máx (μ^{ε})
7	38,99 MPa	754,53
14	46,51MPa	758,05
28	58,29 MPa	832,00

From the obtained data, it is verified that the compressive strength increased according to curing time. At the 28th day it presented maximum tension of 58.29 MPa, and when compared with Arioz and Kockar's results [16], on what it obtained in its samples 33.07 MPa and 34.7 MPa at 7 and 28 days respectively, we noticed that the use of potassium hydroxide increases the resistance. Rodrigues [17] found very similar values for the 28 day trial, presenting the maximum value of 57 MPa. In the study of Demie, Nuruddin and Shafiq [18], obtained a compressive strength of 53.8 MPa, while Soutsos [19] obtained a maximum value of compression resistance of 60.9 MPa, this is due to the fact its precursor has high iron value, once in the conventional cement iron contributes to the high resistance according to the curing time, it is believed that the same can happen with the geopolymer, but there are no studies analyzing this influence.

The experimental results were close to those obtained by other authors. However, there are several activators and different precursors that can be used in the synthesis of geopolymers, so there will be in the literature divergent values of resistance to compression due to the different geopolymer types studied. It was necessary to analyze the matrix to determine the ideal time to test the plates. It was observed that on 14th day it supported 46.51 MPa, thus, it was chosen to carry out the tensile and flexion tests at 14 days, once the matrix showed a good resistance.

4.3 MEV

In most cementitious materials the weakest point is the appearance of microcracks [20]. When making the geopolymer numerous microcracks appeared, in order to eliminate them the sand was added to the mixture. This made the matrix a denser structure, as shown in Fig. 3, besides increasing the strength and durability of the geopolymer paste. We can emphasize the role of the soluble silica for the alkaline activation, it was responsible for developing the microstructure of the material.

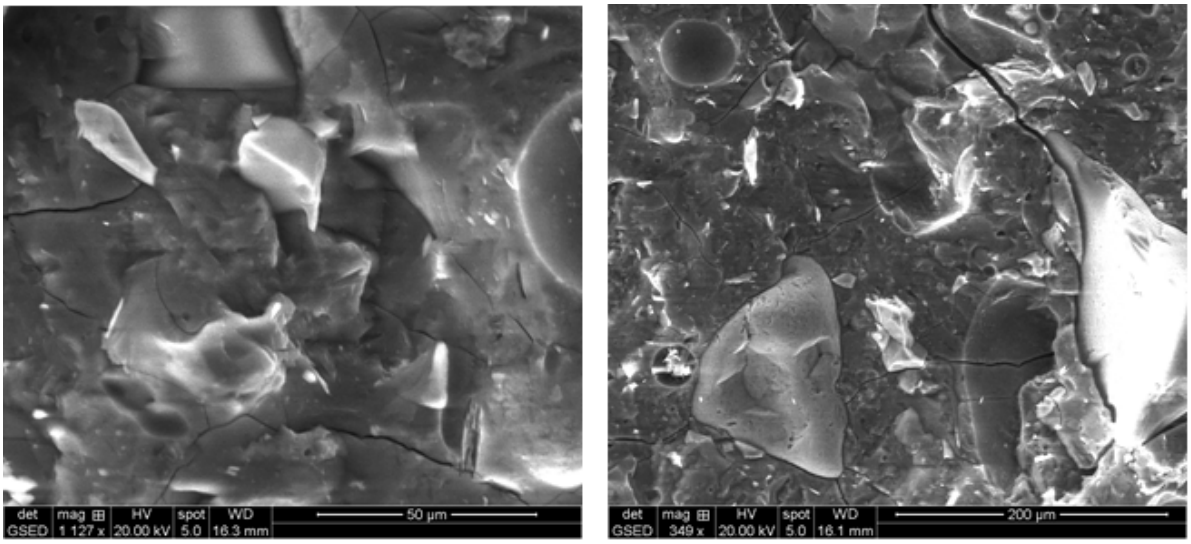

Figure 3. (a) Micrograph of the geopolymer matrix at 14 days (b) approximation of the sample

The use of metacaulinite as a source of aluminosilicate may alleviate this problem by providing a less impure starting material easier to characterize, facilitate the understanding of the microstructure that can be obtained by the analysis of the final products. Geopolymers based on metakaolinite are considered a model, without the complexities introduced by the use of fly ash, slag and other alternative raw materials due to the various amorphous and difficult characterization phases. Fly ash, for example, is not derived from a well-defined material, and consists of several crystalline phases [21]. Silva e Sagoe-Crenstil [22] reported that calcium-free metakaolinite-based geopolymers with higher compressive strengths were formed by a dense and homogeneous microstructure, according to SEM analyzes (figure 3).

5. CONCLUSIONS

It was observed the appearance of micro-cracks in the production of the specimens, and to eliminate them, sand was added to the mixture. This procedure provided a better grain spreading and increased mechanical properties. The tensile strength in the compression of the geopolymer mortar was found a value of 58.29 Mpa at the 28th day. This result was obtained by curing at room temperature.

ACKNOWLEDGEMENTS

The authors would like to thank the laboratory for the synthesis and characterization of nanomaterials (LSCN/ IFAM).

REFERENCES

[1] ZHANG, Hai Yan et al. Development of metakaolin–fly ash based geopolymers for fire resistance applications. Construction and Building Materials, v. 55, p. 38-45, 2014.

[2] SANTA, Rozineide A. Antunes Boca et al. Geopolymer synthetized from bottom coal ash and calcined paper sludge. Journal of Cleaner Production, v. 57, p. 302-307, 2013.

[3] DAVIDOVITS, Joseph. Synthesis of new high temperature geo-polymers for reinforced plastics/composites. SPE PACTEC, v. 79, p. 151-154, 1979.

[4] DAVIDOVITS, Joseph. Synthetic mineral polymer compound of the silicoaluminates family and preparation process. U.S. Patent n. 4,472,199, 18 set. 1984.

[5] XU, H.; DEVENTER, J. S. V. Geopolymerisation of multiple minerals. Minerals Engineering, Elsevier, v. 15, n. 12, p. 1131–1139, 2002.

[6] BARBOSA, V. F.; MACKENZIE, K. J. Synthesis and thermal behaviour of potassium sialate geopolymers. Materials Letters, Elsevier, v. 57, n. 9, p. 1477–1482, 2003.

[7] ANDINI, S.; CIOFFI, R.; COLANGELO, F.; GRIECO, T.; MONTAGNARO, F.; SANTORO, L. Coal fly ash as raw material for the manufacture of geopolymer-based products. Waste management, Elsevier, v. 28, n. 2, p. 416–423, 2008.

[8] DAVIDOVITS, J. Properties of geopolymer cements. In: First international conference on alkaline cements and concretes. [S.l.: s.n.], 1994. v. 1, p. 131–149.

[9] DAVIDOVITS, J. Geopolymer Chemistry and Applications. Institut Géopolymère (Geopolymer Institute): Saint-Quentin, France, 2008. [S.l.], 2008.

[10] HARDJITO, D.; SUMAJOUW, D. M.; WALLAH, S.; RANGAN, B. et al. Fly ash-based geopolymer concrete. Australian Journal of Structural Engineering, v. 6, n. 1, p. 77, 2005.

[11] JAARSVELD, J. V.; DEVENTER, J. V.; LORENZEN, L. The potential use of geopolymeric materials to immobilise toxic metals: Part i. theory and applications. Minerals Engineering, Elsevier, v. 10, n. 7, p. 659–669, 1997.

[12] XU, H.; DEVENTER, J. V. The geopolymerisation of alumino-silicate minerals. International Journal of Mineral Processing, Elsevier, v. 59, n. 3, p. 247–266, 2000.

[13] Wang Y, Qinghua Z, Yong G. Trajectory and driving factors for GHG emissions in the Chinese cement industry. J Clean Prod 2013;53:252–60.

[14] GEOPOLYMER. Out. 2015. http://www.geopolymer.com.br. Julho 22, 2015. Disponível em: <http://www.geopolymere.com.br>.

[15] PALOMO, A.; GLASSER, F. Chemically-bonded cementitious materials based on metakaolin. British ceramic. Transactions and journal, Institute of Materials, v. 91, n. 4, p. 107–112,1992.

[16] ARIOZ, O.; KOCKAR, O. M. An experimental study on the mechanical and microstructural properties of geopolymers. Procedia Engineering, Elsevier, v. 42, p. 100–105, 2012.

[17] RODRIGUES, T. M. C. G. Argamassas e betões geopoliméricos: estado da arte e potencial de industrialização em Portugal. Tese (Doutorado) — INSTITUTO SUPERIOR DE ENGENHARIA DE LISBOA, 2014.

[18] DEMIE, S.; NURUDDIN, M. F.; SHAFIQ, N. Effects of micro-structure characteristics of interfacial transition zone on the compressive strength of self-compacting geopolymer concrete. Construction and Building Materials, Elsevier, v. 41, p. 91–98, 2013.

[19] SOUTSOS, M.; BOYLE, A. P.; VINAI, R.; HADJIERAKLEOUS, A.; BARNETT, S. J. Factors influencing the compressive strength of fly ash based geopolymers. Construction and Building Materials, 2015.

[20] MONTEIRO, P. Concrete: Microstructure, Properties, and Materials. [S.l.]: McGraw-Hill Publishing, 2006.

[21] DUXSON, P.; PROVIS, J. L.; LUKEY, G. C.; MALLICOAT, S.W.; KRIVEN,W. M.; DEVENTER, J. S. V. Understanding the relationship between geopolymer composition, microstructure and mechanical properties. Colloids and Surfaces A: Physicochemical and Engineering Aspects, Elsevier, v. 269, n. 1, p. 47–58, 2005.

9. INDUSTRIAL APPLICATIONS

EFFECT OF THE ATMOSPHERE IN THE ABLATION OF CARBON-PHENOLIC COMPOSITES USED IN THERMAL PROTECTION SYSTEMS

Edison Bittencourt (1), Homero de Paula e Silva (1,2), Humberto AraújoMachado (2,4), Pedro Guilherme Silva Pesci (2), Cristian Clay Paterniani (3), Felipe Rocha Caliari (3)

(1) Departament of Chemical Engineering , Universidade Estadual de Campinas,São Paulo, Brazil

(2) Instituto de Aeronáutica e Espaço, São José dos Campos, São Paulo, Brazil

(3) Center for Science and Technology of Plasmas and Materials , Instituto Tecnológico da Aeronautica, São José dos Campos, São Paulo, Brazil

(4) Technology Departament, Universidade Estadual do Rio de Janeiro, Brazil

https://doi.org/10.21452/bccm4.2018.09.01

Abstract

Ablatives composite materials are vastly employed in rocket nozzle components and as thermal protection shields in aerospace industry. In this work, an experimental study on the influence of atmospheric pressure on the ablation of carbon-phenolic composites is performed. The composite is produced by wrapping process and used in the manufacture of thermal re-entry protections. Samples were tested in the following thermal fluxes: 0.626; 0.903; 1,376 and 1,725 MW/m^2 in the 30, 50, 70 and 90 sec exposure times in a plasma tunnel simulating the pressure of 400 Pa and compared to the results obtained in the same thermal fluxes and exposure times at atmospheric pressure. Results were also compared with a computational simulation and a simple and reliable model is proposed to express the influence of environment pressure, presenting good agreement and physical coherence. The specific mass loss rate at rarefied pressure was lower than obtained at dense atmospheric pressure but this difference decreases with the increase of the exposure time due to the process of densification of the carbonized layer. The low concentration of oxygen existing in the rarefied air pressure contributes to slow pyrolysis reaction during the ablation process

Keywords: ablation, carbon-phenolic composites, thermal protection.

1. INTRODUCTION

The launching and sounding vehicles are important devices for research and to practical and commercial use of space. They represent the transport system by which satellites, human beings

and inhabited stations are placed into Earth orbit. Additionally, microgravity experiments are conducted inside and outside the Earth's atmosphere and missions to space exploration [1].

Many components and integrated systems of launching vehicles are manufactured in composites in order to meet two basic design requirements for space vehicles that are stiffness and mechanical strength combined with low weight and heat resistance. Besides, mass reduction for components such as fairing, fins and motor cases is critical since they represents an increased in payload [2].

Some of these items made of composites for launching vehicles are exposed during a certain period of time under extreme temperature excursions (above 1000°C) and to high speed gas flow (Mach 3), as is the case of the thermal protections of fairings and of the reentry capsules when they return from their missions. Usually, these parts are exposed to temperatures which the working service limit and even the melting point of conventional alloys [3].

The heat absorbed by the composite structure (carbon fiber/phenolic resin) causes endothermic processes because the area in contact with the gas flow undergoing a pyrolisis process. This phenomenon is given the name of ablation [2].

The composites used as thermal protection systems have to present high heat capacity to dissipate heat per unit mass [2]. Among the composites that meet these requirements carbon fiber/phenolic resin composites plays their role. The choice of phenolic resin as matrix structure is because it has high carbon yield content when subjected to pyrolysis. The porous carbon residue structure obtained during the ablation process is a result of absorbed heat and protects the structural elements [3]

Ablation is a process involving phase change and chemical reactions suffered by the material, where the heat produced by the conversion of kinetic energy is eliminated by mass loss. Among the several factors that affect the physical phenomena during ablation of a composite, is the presence of the surrounding atmosphere and its composition. Since various chemical reactions are involved during the pyrolysis of the virgin material, resulting in the exit of the gases through the porous carbonized layer formed on the outer surface. Thus, it is necessary to evaluate the influence of the surrounding medium on the ablative properties of the material, so that it can be dimensioned accurately.

In the reentry phase, the vehicle starts from 120 km altitude with a speed of 7.6 km/s and decelerates by atmospheric friction to values of 2.0 km/s to 30 km altitude. Much of the kinetic energy of the vehicle is dissipated by braking in the atmosphere, generating thermal flows in the order of five to ten MW/m^2 and, consequently, heating at high temperatures, between 2000 K and 6000 K, due to the interaction of the gas with the surface of the vehicle characterizing this plasma of reentry as a thermal plasma.

Under these conditions, the gas is partially ionized consisting of neutral molecules, atomic and molecular radicals, electrons, positive ions, negative ions and photons. This ablative reentry environment [4][5] can be simulated in part by the use of thermal plasma torches, which are essential tools to reproduce the intense thermal flows in steady state (2 MW/m^2), to which these specimens were submitted.

In this work, a plasma tunnel consisting of a vacuum chamber with a volume of $3m^3$, which generates Mach 5 plasma jets, with a diameter of around 25 centimeters was used. The specific enthalpy levels reach 10 MJ/kg and plasma jet temperatures of the order of 3000 K.

The erosion rate of the samples was studied by varying their mass before and after the plasma torch ablation test. The experimental results allow to evaluate the properties and behavior of the ablative carbon-phenolic composites produced by wrapping process and also check the accuracy

of these with the theoretical results obtained by computer simulation using a numerical method previously validated.

2. EXPERIMENTAL PROCEDURE

2.1 Materials

The specimens were extracted from a carbon-phenolic preform made by biased tape wrapping process. The carbon fiber cloth used is T22R-ECHO with thickness 0.45 mm, weave pattern 2x2 Twill, areal weight 350 g/m^2 ± 35 g/m^2 and density 1.55 g/cm^3. A phenolic resin resol type matrix with viscosity of 1000 cPs at 20°C (manufactured by Plastiflow) has been used. The prepreg process was carried out on the Plastflow facilities. After wetting, the volume of fiber reached 55-60%.

These pre-pregs were cut in tapes with 110 mm width and wound on reels mounted on a winding machine. In this machine, a metal mandrel adapted with a support was set up to obtain the wrapping angle of 20° relative to the main axis of the winding mandrel direction. This process consists of compacting the pre-impregnated tape by means of a roller which compresses it against the surface of the mandrel. This roller shall exert a force resulting in a surface compression at the roller/tape contact area of approximately 7 MPa. Immediately before reaching the mandrel/roller contact point, where the compression occurs, the tape is heated with a heating turbine at a temperature of 80°C so that the resin becomes more fluid and the prepreg more malleable. The process then develops continuously throughout the mandrel as shown in Figure 1.

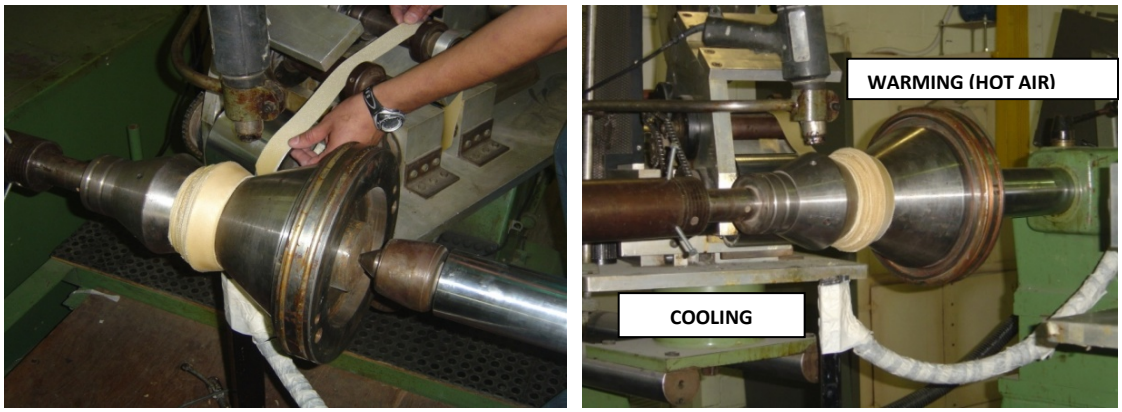

Figure 1: Biased tape wrapping process

After wrapping process, the workpiece was polymerized in a hydroclave following a cycle of 1h at 100°C and 3 hours at 165°C at a pressure of 7.0 MPa, with vacuum applied throughout the process to extract the volatiles from the phenolic reaction. After the curing cycle, the blank is demolded and undergoes a machining process to provide regular surface finish.

A cup saw was used to remove small cylinders with a diameter of 12.5 mm in the position indicated in Figure 2a. After cutting, the samples were machined with a diameter of 10.0 ± 0.3 mm with a length of 8 mm. these were identified and weighed on a precision scale (± 0.0001g). A new weighing of the specimens was also done after exposure to the thermal flow, to determine the rate of mass removed per unit area and time of exposure to the plasma jet (kg/m^{2}s), known as specific mass loss rate.

Sixteen (16) carbon/phenolic test specimens were machined and weighed, as shown in Figure 2b. Quartz/phenolic rings were machined and adjusted to the specimens in order to serve as a thermal insulation and in the sample holder assembly.

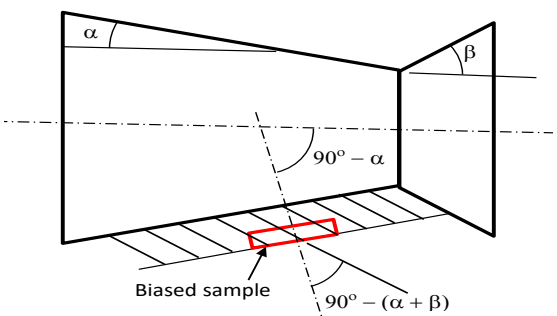

(a)

(b)

Figure 2:(a) Extraction position of the specimen in the blank; (b) Sample ready to tests

2.2 Ablation tests

The ablation tests were performed in the plasma wind tunnel of the Center of Science and Technology of Plasmas and Materials (Figure 3a), which contains an arc-jet plasma torch, according to Figure 3b. The plasma torch used in this work is a linear type with self-stabilized non-transferred electric arc. The supersonic nozzle in which the torch is coupled is known as Laval nozzle, used to accelerate the plasma jet, increasing the enthalpy of the torch. The assembly is coupled to the vacuum chamber (tunnel) by adaptation in one of the inspection windows of the rear chamber door [6].

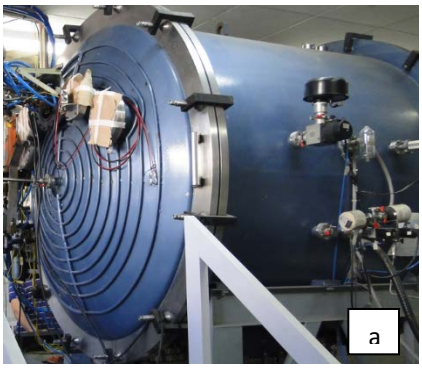

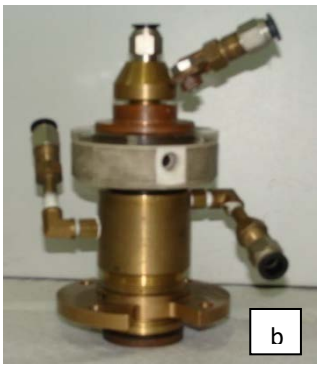

Figure 3: (a) Arc plasma facility; (b) Plasma torch

This vacuum chamber has a 3.2 m³ volume, built in stainless steel. It has a cylindrical shape of 1.5 m diameter and 1.8 m length and two doors with inspection windows. The side of the tunnel has flanges for insertion of accessories such as thermocouples, water hoses and electrical cables. There is a rotating structure, internal to the vacuum chamber, which has eight arms that supports the samples (sample holders), according to Figure 4a. These arms are cooled with water throughout the test, as are the torch and nozzle, and the sample is mounted at the tip of the arm to receive the plasma torch in the test, as shown in Figure 4b. The arms can be rotated and exposed to the plasma

by the axis shown in Figure 4a, which pass through a hole to the external side of the chamber, and can be manipuled by a kind of steering wheel that guarantees the sample position.

Figure 4: (a) Sample holder set ; (b) Sample holder 3D design

The test conditions were defined by relating the best enthalpy increase with the best thermal efficiency, obtaining an inlet gas flow value of 190 L/min.

The heat flux was measured along the axial line of the jet at several distances measured from the nozzle, to determine a relation between the thermal flux and the distance from the nozzle. It's used a copper disk calorimeter connected to a thermocouple at 3 mm from the exposed end of the calorimeter. The thermal flux curve was obtained as a function of the distance from the nozzle as shown in Figure 5. From this curve, the distances were calculated to perform the tests in varied determined heat flows.

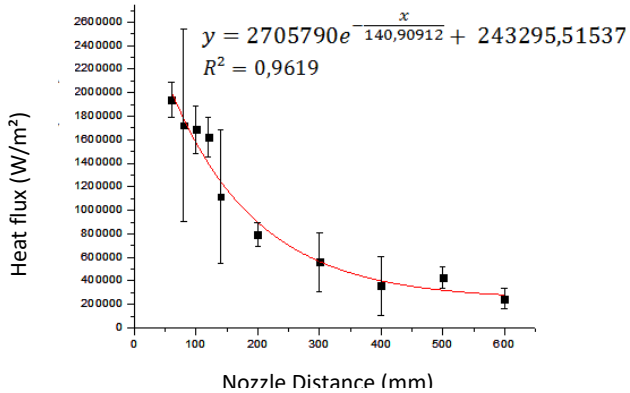

Figure 5: Thermal flux curve

Eight (8) sample holders containing the samples are first mounted on the rotating structure internally connected to the tunnel. They are positioned at the calculated distances for the desired heat flux and connected to the refrigeration system. Subsequently, the thermocouples are connected and the sample holders are aligned to the plasma jet axis using a laser system. The thermocouples collect the temperature of the unexposed surface of the sample, while exposed surface temperature is collected by an optical pyrometer connected to a computer.

The samples were exposed to the plasma jet heat fluxes: 0.636, 0.903 and 1.376 MW/m² at 30, 50, 70 and 90 sec.

2.3 Numerical Simulation

The mathematic model developed by Machado [7] was used for comparison between the experimental data and the simulation. The selected parameter was the specific mass loss rate, evaluated instantaneously by the model from the integration in each step of time. Also, the temperatures and the interfaces evolution were calculated and compared to the measured ones. The model used properties taken from literature, in Table 1.

Table 1 – Carbon/phenolic properties used on the mathematical model [8] [9] [10] [11]

Material	Property	Value
Virgin Material	Specific heat	1197 J/kg°C
	Thermal conductivity	0.867 W/m°C
	Specific mass	1398 kg/m^3
	Pyrolisis heat	1.40 MJ/kg
	Pyrolisis temperature	450 °C
	Emissivity	0.78
Char	Specific heat	1587 J/kg°C
	Thermal conductivity	1.58 W/m°C
	Specific mass	1135 kg/m^3
	Sublimation temperature	1666 °C
	Ablation heat (char)	26.48 MJ/kg
	Emissivity	0.70

The discrepancy between the experimental results for the tests performed at atmospheric pressure and low pressure must be explained by one or more physical phenomena. Due to the dependence of atmospheric pressure, these physical phenomena must occur on the external surface of the specimens. Thus, the mathematical model used must be modified taking account this effect.

One of the possibilities analyzed was the consideration of the convection between the external surface of the specimens and the environment air. A source term based on Newton's cooling law was added to the external contour condition, where the convective coefficient was estimated by empirical correlations where the environment pressure was inserted. No significant change was obtained in relation to the results obtained from the original model, which did not consider the effect of the pressure.

The gases resulting from the pyrolysis that percolate through the carbonized layer, degrade with temperature through complex reactions [12]. The modeling of these reactions goes beyond the scope of this work. However, it is possible to propose a simplified model based on the degradation and oxidation of these gases to account for their effect on surface heat flux, as a function of the environment pressure.

Assuming that the degradation reactions are approximately represented by a single carbon combustion reaction on the outer surface:

$$C + O_2 \rightarrow CO_2 + q_g$$

q_{CO20} – Combustion heat of CO_2, 8.95 MJ/kg for the resulting product at 300 K [13].
Cp_{CO2} – Specific heat of CO_2, 871 J/kgK at 300 K [13].

In this case, the surface heat flux in W/m^2 will be given by :

$$\dot{q_g} = q_g \dot{m_g} \quad (1)$$

Where: $\dot{m_g}$ is the rate of product formation of the reaction per unit area of the surface, in kg/m^{2}s . Assuming that the degradation reactions due to oxygen of the environment air occur according to the Arrhenius model, the reaction rate will be given by:

$$\frac{\partial \dot{C_{CO2}}}{\partial t} = K e^{-Ea/RT} C_C C_{O2} \quad (2)$$

Where: *C* is the concentration of reactants and product. The parameters *K*, *Ea* e *R* are respectively the reaction constant, the activation energy and the CO_2 constant. To construct an empirical model, the previous equation will be related term to term with the rate of formation of the product.

The concentration of the reactant carbon is linked to the gases formed by the pyrolysis. Thus, it is assumed that it is proportional to the rate of pyrolysis, that is, to the velocity of recession of the pyrolysis front:

$$C_C \propto V_p$$

The concentration of O_2 on the surface depends on the partial pressure thereof. As the percentage of O_2 in environment air is constant, it must be directly proportional to the environment pressure from the ideal gas equation (Amagat model):

$$C_{O2} \propto \frac{P}{RT}$$

Where: *R* is the air constant, 287 J/kgK.

Finally, the rate of formation of the products will be considered proportional to the rate of change of the CO_2 concentration generated by the reactions:

$$\dot{m_g} \propto \frac{\partial \dot{C_{CO2}}}{\partial t}$$

Combining the three proportions with the Arrhenius formulation, we can consider:

$$\dot{m_g} \propto \frac{P}{RT} V_{\boldsymbol{p}} = C_g \frac{P}{RT} V_{\boldsymbol{p}}$$

Where: *Cg* is a dimensionless proportionality constant unknown a priori, which must be evaluated empirically, from experimental results. Thus, the term source to be added to the heat flux imposed on the external surface will be:

$$\dot{q_g} = [q_{CO20} + Cp_{CO2}(T - 300)] C_g \frac{P}{RT} V_{\boldsymbol{p}} \quad (3)$$

This empirical equation correlates the effects of pressure, temperature and pyrolisis rate with the generation of an additional heat flux on the external surface where the ablation of the carbonized layer occurs, related to the degradation of percolated gases from the decomposition of the polymer resin.

3. RESULTS AND DISCUSSION

Figures 6a, 6b, 6c and 6d show the mass loss rate graphs obtained in dense atmospheric environment, taken from Silva [3], together with the rates obtained in this work. It is observed that the rates are lower for the tests performed in rarefied atmosphere, but the differences in these rates decrease according as the exposure time increases. This behavior is explained by the low pressure of the rarefied environment and its lower concentration of oxygen, which generates lower rates of

chemical reactions and consequently less heat addition to the system, leading to a reduction of the pyrolisis process speed and consequent *char* formation. This tendency of convergence between the curves according as the exposure time increases can be attributed to the phenomenon of cracking, which is the reduction of gases from pyrolisis to others of lower molecular mass. In this phenomenon occurs the pyrolitic deposition of carbon in the pore contours in the carbonized region generating densification of the carbonized structure and the consequent improvement in the thermal protection characteristics. At low pressure, this densification, although slower, with increasing exposure time has a tendency to equilibrate with the densification of the structure at atmospheric pressure, equating thermophysical properties and their effects.

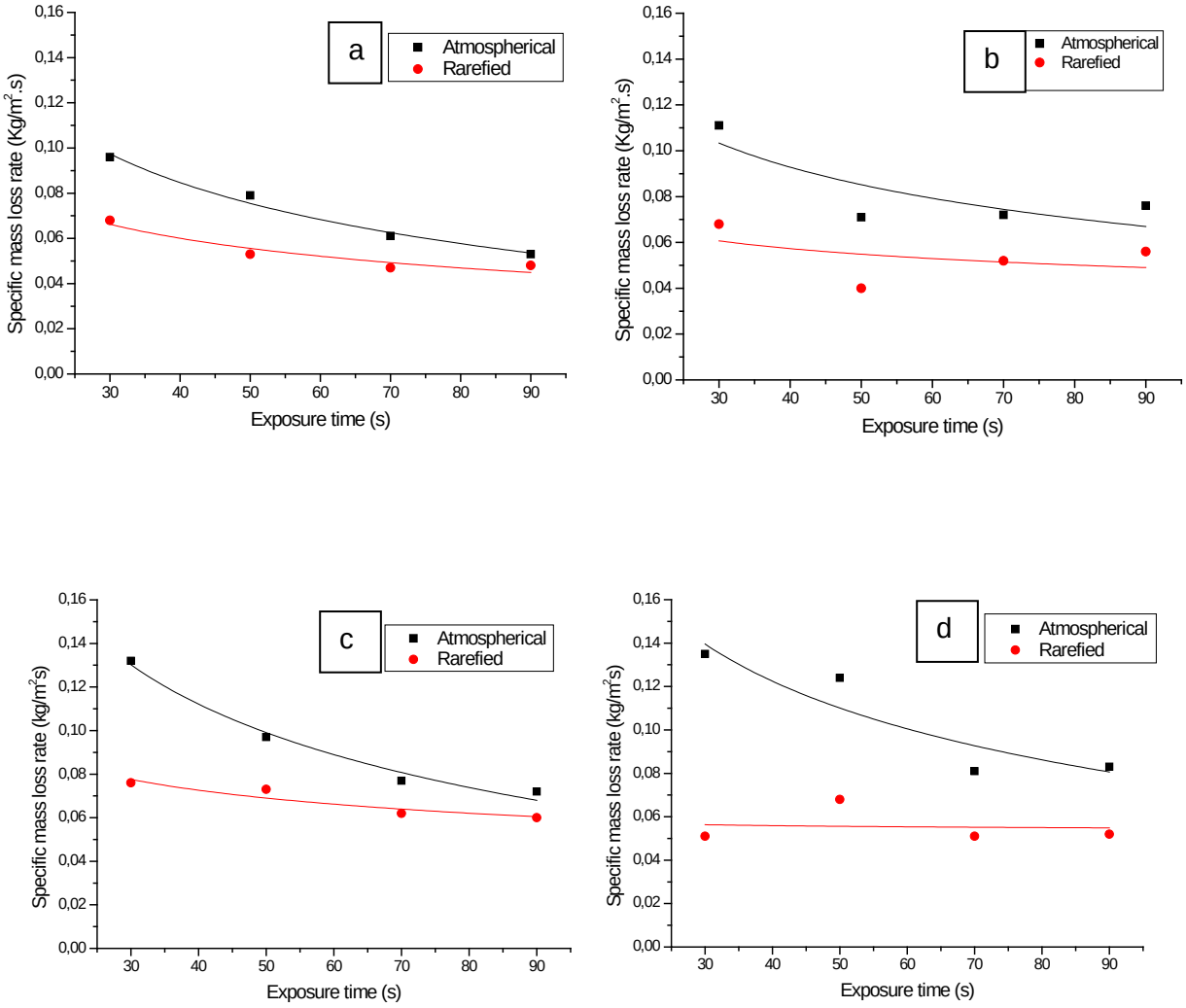

Figure 6: Mass loss rate versus exposure time to the fluxes:(a) 0.626 MW/m^2;(b) 0.903 MW/m^2;(c)1.376 MW/m^2;(d)1.725 MW/m^2

A computational model was used to simulate a one-dimensional process of ablation. This model has now been corrected considering the influence of the atmospheric pressure and its results compared with the data obtained experimentally. For this model, the data used in the simulation were presented in Table 1.

Figures 7a and 7b, 8a and 8b show the mass loss rate curves as a function of the exposure time for the analyzed thermal flows. Due to several processes occurring on the external surface exposed to the plasma torch, it was not possible to reproduce the temperatures measured in the experiments. However, this is not a parameter of interest for the model but rather the internal surface temperatures and the rate of mass loss, which effectively report on the performance of the material as thermal protection.

Initially, the experimental data obtained from Silva [3] were plotted considering the average atmospheric pressure of the city of São José dos Campos, 95 kPa identified in blue in the graphs. The constant C was obtained by trial and error in case of lower heat flux. A minimum, average and maximum value of 1500, 2000 and 2500, respectively, were tested. According to Figure 8a, where the results for the mass loss rate are presented, the best result was obtained for the mean value of 2000 because its curve is consistent with the corrected physical values within the error bar, which is then assumed for the other cases, shown in Figure 7b, 8a and 8b. The experimental data, in rarefied environment, are identified in red. It is observed that the curve corrected for this pressure of 400 Pa also involves the experimental points within the respective error bars. It is possible to observe the physical coherence of the modified model, which although it does not obtain a perfect agreement, reproduces the behavior of the experimental data. It should be considered that the properties used in the simulation were extracted from literature sources for generic carbon-phenolic composites and not measured from the composite used in the experiments.

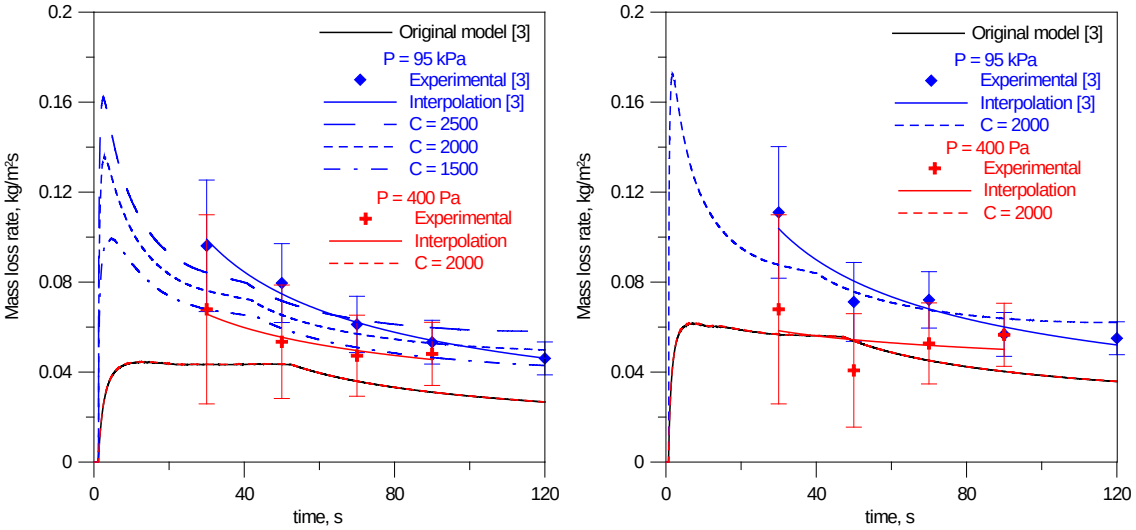

Figure 7: (a) Curves of mass loss rate with time between simulations and experimental data, q= 0.626 MW/m^2; (b) Curves of the mass loss rate with time between the simulations and experimental data, q= 0.903 MW/m^2.

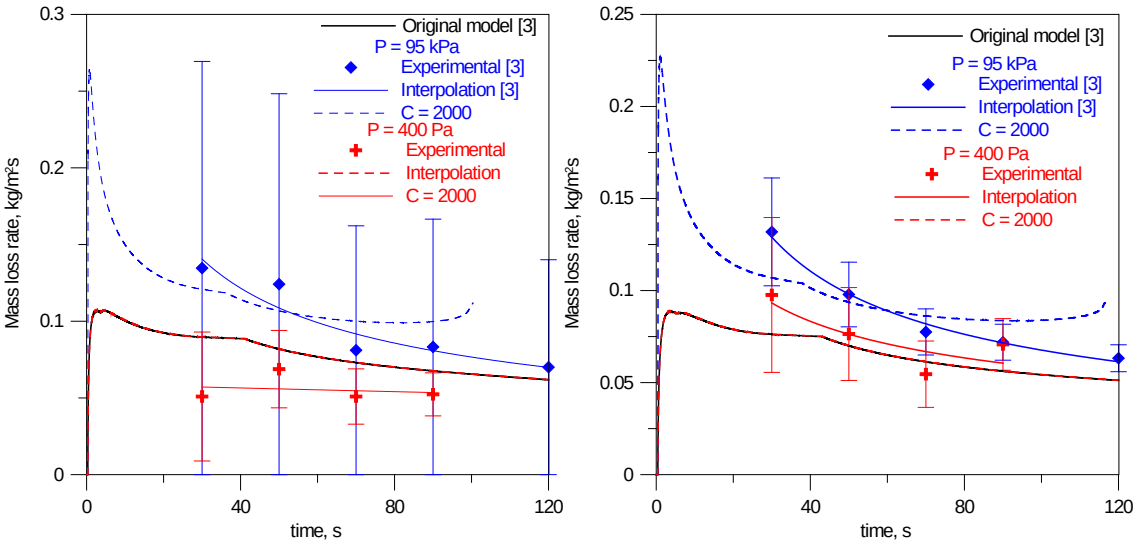

Figure 8: (a) Mass loss rate curves with time between simulations and experimental data, q = 1.376 MW/m^2, (b) Mass loss rate curve with time between simulations and experimental data , q = 1.725 MW/m^2.

4. CONCLUSIONS

- The rates of mass loss as a function of the exposure time obtained in this study are lower than atmospheric pressure but the differences in these rates decrease according as the exposure time increases. This behavior is explained by the low pressure of the rarefied environment and its lower oxygen concentration. According to the qualitative correction proposed for the physical model, the reactions between the gases resulting from the pyrolisis and the oxygen of the atmosphere generate an increase in the heat flux imposed on the external surface. The lower oxygen concentration implies lower reaction rates and consequently less heat addition to the system, causing a reduction of the pyrolysis process velocity and consequent char formation. The reduction of the difference between the rates of mass loss according as the exposure time increases can be attributed to the cracking phenomenon, which is the reduction of gases from the pyrolysis in others of lower molecular mass. In this phenomenon occurs the pyrolytic deposition of carbon in the pore contours in the carbonized region generating densification of the carbonized structure and the consequent improvement in the thermal protection characteristics. At low pressure, this densification, although slower, with increasing exposure time has a tendency to equilibrate with the densification of the structure at atmospheric pressure, equating the thermophysical properties and their effects.
- The ablation of carbon-phenolic composite used in thermal protection systems was studied experimentally and numerically. A plasma torch was used to produce ablation in the samples at two different pressures, and the mass loss rates was measured. The results were compared with the numerical data obtained from a modified form of a previous model to account the effect of pressure.
- The numerical computational simulation was validated with respect its modification considering the low test pressure when used in carbon/phenolic composites. To simulate the mass loss rate, the results were close to those obtained experimentally, so that the

results of the error bars cross the simulation curve. The pyrolysis and ablation profiles show a great proximity to the profiles obtained experimentally.

- The difference between the numerical and experimental results shows coherence with respect to the order of magnitude and evolutionary behavior of the investigated parameters, considering the limits of the proposed theoretical model, due to the simplification of the physical and chemical processes involved in the ablation process.

REFERENCES

[1] Gonçalves,A., 'Caracterização de Materiais Termoestruturais a base de Compósitos reforçados com Fibras de Carbono (CRFC) e Carbono Reforçado com Fibras de Silício (SiC)',Tese de Doutorado, Instituto Tecnológico da Aeronáutica - DCTA-ITA, São José dos Campos,2008

[2] Barbosa, C.A.L., 'Obtenção e Caracterização de Materiais Ablativos a Base de Compósitos de Fibra de Carbono/Resina Fenólica'. Dissertação de Mestrado – DCTA/ ITA - São José dos Campos, 2004. 142 110.

[3] Silva, S.F.C., 'Tecnologia de Plasma para Estudo das Propriedades Ablativas em Compósitos obtidos por Bobinagem para uso Aeroespacial', Tese de Doutorado, Universidade Estadual de Campinas-UNICAMP,Campinas,2015.

[4] Auweter Kurtz, M.,'Plasma source development for the qualification of thermal protection materials for atmospheric entry vehicles at IRS', Vacuum,Volume 65, Issues 3-4, 27 May 2002, Pages 247-261.

[5] Silva, W. G. Da, 'Qualificação de materiais utilizados em sistemas de proteção térmica para veículos espaciais'. 2009. Tese (Mestrado em Física dos Plasmas) - Instituto Tecnológico de Aeronáutica - São José dos Campos

[6] Charakhovski, L. et al., 'Hypersonic and Subsonic Plasma Setups for Testing Heat Shielding Materials'. In: Brazilian Congress of Thermal Engineering and Sciences, 12, 2008, Belo Horizonte, Brazil

[7] Machado, H. A., 'Two-Dimensional Simulation of Multi-Layer Ablation-Conduction Problem in a Rocket TPS via an Interface Tracking Method'. In: Thermophysics Conference, 41, San Antonio, 2009.

[8] Pesci, P.G.S., 'Avaliação do desempenho de compósitos ablativos em sistemas de proteção térmica'- Dissertação de Mestrado-Universidade Estadual Paulista -UNESP-Guaratinguetá, 2017 .

[9] Williams, S. D., Curry, D. M., 'Thermal Protection Materials', Thermophysical Property Data (Nasa Reference Publication 1289). Washington: NASA, dez. 1992. 234 p.

[10] Sutton, K., Nasa Technical Note, Nasa tn d-5930, 19960610 093 , 'An experimental study of a carbon-phenolic ablation material', Langley Research Center Hampton, Va. 23365- National Aeronautics and Space Administration- Washington, D. C.- September 1970.

[11] Sykes Jr., G. F., Nasa Technical Note, NASA tn d-3810, 'Decomposition characteristics oe a char-forming phenolic polymer used for ablative composites', Langley Research Center Langley Station, Hampton, Va.19960503 090 - National Aeronautics and Space Administration - Washington, D. C.- February 1967.

[12] Natali, M., Puri I., Rallini, M., Kenny, J., Torre, L. et al, 'Ablation modeling of state of the art EPDM based elastomeric heat shielding materials for solid rocket motors', Computational Materials Science 111 (2016) 460–480.

[13] Kuo, K.K.., 'Principles of Combustion', John Wiley & Sons, 1986.

STRUCTURAL BEHAVIOR OF FILAMENT WINDING TANKS

Jorge Nasseh (1), Jeniffer Kopetski (2) and Bárbara Vital (2)

(1) Barracuda Advanced Composites

(2) Marine Composites

https://doi.org/10.21452/bccm4.2018.09.02

Abstract

As communities, businesses and industries are increasingly being held accountable for meeting environmental requirements for liquids that require safe and design-proven storage, wastewater composite tanks have become the solution for a wide range of issues. Filament winding tanks built with fiberglass, by virtue of its materials and design, is naturally the superior choice for safe, structurally reliable, cost-effective option for long-term storage and treatment of wastewater. A numerical analysis using the finite element method was developed to predict stress, strain and safety factors of the composite structure as well as comparative structural performance regarding the change of winding angle. Internal workloads and external environmental loads were both applied to the model. This work aims to evaluate the structural behavior of a vertical and horizontal 100m^3 wastewater tank.

Keywords: Wastewater Tank. Filament Winding. FEA.

1. INTRODUCTION

Large wastewater treatment tanks are subjected to relevant stresses. Thus, their structural design must account for the effects of both internal and external loads, in order to enable the selection of appropriate materials and manufacturing processes.

The composites industry is in constant development of new technologies that aim to offer high-quality, low-maintenance products, driving itself to create innovative solutions that increase productivity and reduce manufacturing costs. It is in this context that filament winding process is presented as an engineering solution to the issues arising from the construction of fiberglass wastewater treatment tanks.

During the past years, the use of filament winding process has greatly contributed to the large-scale production of wastewater tanks, as well as to the development of more efficient effluent treatment plants (ETP). This has enabled cost-effective solutions for the construction of lighter, stronger tanks, with superior durability.

Considering that fiber reinforcement direction significantly affects the structural strength of the laminate, a case study was developed to evaluate stresses and strains variation according to the winding angle of the tank. This case study analyzes a 100m^3 tank using the Finite Element Method.

1.1 Filament winding process

Filament Winding is a fully automated manufacturing process, used in the production of pipes, cylinders, tanks and pressure vessels. During this process, continuous fibers are impregnated with resin and wrapped around a cylindrical mold (mandrel), until the latter's surface is covered up to the required thickness.

The horizontal movement of the carriage and the rotation of the mandrel create a helical pattern of the reinforcements. These combined movements enable the manufacturing of parts with chosen angle patterns that are controlled by the pitch, creating a $+\theta$ angle on the first ply and returning on a $-\theta$ angle in the second ply. The components of the filament winding process are shown in Figure 1.

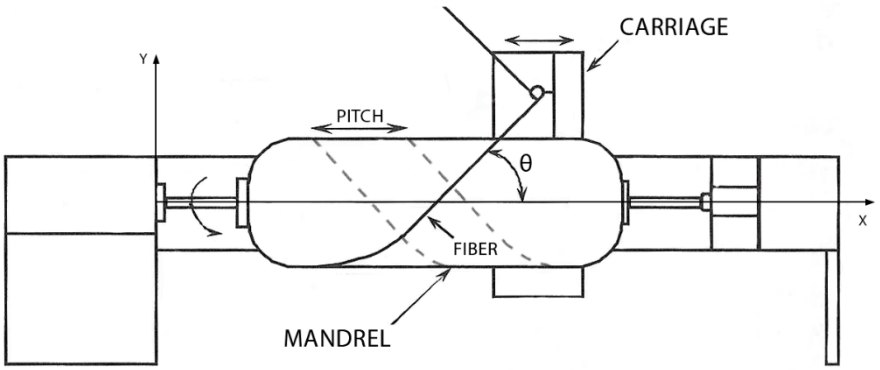

Figure 1: Winding angle

Some of the main advantages of filament winding process are the reduction of production time and the increase of fiber content, which enable the construction of extremely resistant tubular structures.

In order to meet the chemical and structural requirements of the wastewater treatment tank, the laminate is divided into three different parts: (a) the liner, (b) the chemical barrier, and (c) the structural layers. The parts are identified in Figure 2.

a. The liner is a very thin layer with high resin content that avoids liquid absorption and possible chemical attacks. The liner also provides a smooth internal surface and good cosmetics. The use of the surface veil is recommended to ensure the uniform thickness of the liner, to increase wear resistance and to minimize the propagation of surface cracks.
b. The chemical barrier is produced with chopped glass fibers with an average of 30% of fiber content. The chemical barrier aims to reinforce the liner, protecting the structural layers of possible chemical attacks. Usually, the amount of chopped strand mat ranges from 900g/m² to 1500g/m².

c. The structural layers are built by the continuous roving laid in the direction of the chosen angle, with high fiber content. The structural layers must support the structure weight and withstand the internal and external loads.

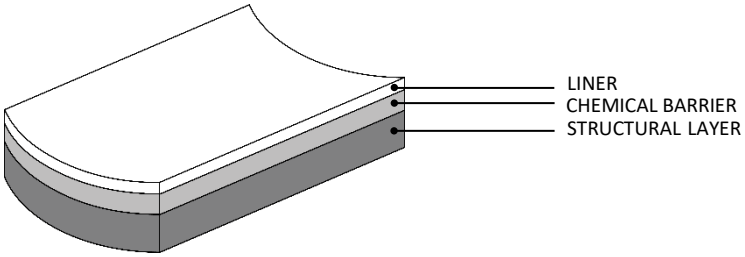

Figure 2: Plies

2. MATERIALS

The following table shows the typical mechanical properties of the composites stack used in most of filament winding tanks [4].

Table 1: Typical Ply Mechanical Properties

Components	Young's modulus, E (MPa)		Poisson's ratio, υ	Shear modulus, G (MPa)
	Ex	Ey		
Fiberglass roving	40.000	10.000	0.25	4500
Fiberglass Fabric	20.000	20.000	0.25	4500
Chopped Mat	7.000	7.000	0.30	3500
Surfacing Veil	7.000	7.000	0.30	3500

3. FAILURE CRITERION

The Tsai-Wu criterion is a failure indicator widely applied to orthotropic composite material shells. Since it analyzes tensile and compression strengths independently, it provides more reliable results. However, the Tsai-Wu criterion cannot predict different failure modes, such as matrix failure, and fibre-matrix interface failure.

The following equation demonstrates the calculation of the safety factor according to the properties of the material. SF is the coefficient by which all the stress components of the laminate must be multiplied to achieve the failure according to the Tsai-Wu criterion.

$$SF^2 (F_{11} \sigma_1^2 + F_{22} \sigma_2^2 + F_{66} \tau_{12}^2 + 2F_{12} \sigma_1 \sigma_2) + SF (F_1 \sigma_1 + F_2 \sigma_2 + F_6 \tau_{12}) = 1{,}00 \quad (1)$$

The equation (1), elaborated by Tsai and Wu [1], represents the general resistance theory for anisotropic materials. The coefficients Fij, are determined from the resistance properties of the lamina in the directions 1 and 2, which represent the direction of the orientation of the layer and the direction transverse to the orientation of the layer, respectively.

The complex part of the criterion is to obtain F_{12}, since it is necessary to perform a biaxial test [1], while the other coefficients are obtained from standardized uniaxial tests. Thus, Tsai and Hahn [2] proposed a direct and approximate formula for this value, based on existing experimental data:

$$F_{12} = 0{,}5\ (F_{11}\ F_{12})^{0{,}5} \quad (2)$$

4. LOAD STUDY

Simplified theoretical calculation procedures were applied in order to define the loads acting on the tanks during their operation, while the wind pressure was determined according to ABNT –Brazilian Standards [3] and the structure weight was determined by the composite laminate stack.

The loading conditions to which the tank is subjected during operation were estimated by the following formulation.

4.1 Hydrostatic pressure

$$p_h = (rho)gh \quad (3)$$

$p_{h\,-}$ Hydrostatic pressure (Pa);
ρ – Fluid density in kg/m³;
h – Liquid height in meters.

The liquid heights considered for the vertical tank 9.7m and for the horizontal was 2.8m.

4.2 Wind loads

The wind load was estimated according to ABNT-Brazilian Standards NBR 6123 and the characteristic speed was determined by the following formula:

$$V_k = S_1 S_2 S_3 V_0 \quad (4)$$

V_k – Characteristic wind speed in m/s;
S_1 – Topographic Factor;
S_2 - Factor that considers the influence of the terrain roughness, the dimensions of the tank, and its height on the ground;
V_o – Basic wind speed: which was based on the basic speed isopleths in Brazil.

Using the characteristic wind speed, it is possible to determine the dynamic pressure, by the expression:

$$q_{wind} = 0{,}613 V_k^2 \quad (5)$$

q_{vento} – Dynamic wind pressure, corresponding to the characteristic speed V_k, under normal conditions of pressure and temperature;
Vk - Characteristic wind speed in m/s.

The wind load

4.3 Load combinations

Some conditions where different loads are combined should be analyzed such as superposition of the tank weight and hydrostatic pressure and superposition of the tank weight, hydrostatic pressure and wind loads.

The load cases must consider the least favourable loads to which the tank will be subjected. For this study, the loads were applied as follows and listed in Table 2.

- Vertical Tank: subjected to the pressure of the liquid, wind load and its own weight.
- Horizontal Tank: subjected to the pressure of the liquid and its own weight;

Table 2: Load cases

Load Case	Loads[a] (kPa)	
	Hydrostatic Pressure	Wind Load
1 (Vertical Tank)	114	1,5
2 (Horizontal Tank)	33	-

[a] All analyzes have considered the acceleration of gravity

The hydrostatic pressure was applied in the tank length and it is proportional to the tank height, according to Equation 3. Wind pressure was applied to the vertical tank in the transverse direction of the surface.

5. FINITE ELEMENT ANALYSIS

Computational methods to predict stress and strain can be efficiently applied to a vast range of problems. Elasticity relations can be used to generate a complex system of equilibrium equations in order to obtain displacements and stresses of the structure.

As we move away from simple situations, such as a plain rectangular plate, the equations system become increasingly complicated to solve using classical methods, requiring sophisticated mathematical techniques to analyze structures with complex geometries.

The Finite Element Method (FEM) is an alternative approach to produce an approximated solution of a system of complex equations in a structural problem. Hence, if correctly applied, both methods, FEM and classical methods, should produce similar results for the same problem.

The Finite Element Method consists of discretizing the structure by subdividing its domain into a finite number of elements connected to each other by nodes, such a way as to represent the distortion of the structure under the specified loads.

This subdivision is the Finite Element Mesh and the solution is presented through the values of displacements at the mesh nodes. The method was initially developed for isotropic materials and the majority of elements available and to apply the technique to composite materials it requires different element formulations that adequately represent their orthotropic stiffness and strength nature.

After the mesh generation using forms that best represent the phenomena and geometry, it is necessary to inform the characteristics of the material, the boundary conditions and the loads which the model is subjected.

5.1 Model

Two different 3D models were developed to run the analysis: the vertical tank with a 7.5mm thick structural layer and the horizontal tank with a 5mm thick structural layer. The laminate is balanced so, for each ply with $+\theta$ angle there should be another one with $-\theta$ angle.

The horizontal tank beds were considered simple supported as well the bottom of the vertical tank. The vertical tank brackets were considered fixed. The mesh uses 6 degree of freedom orthotropic shell elements on the SolidWorks package.

5.2 Stress analysis

Structural analysis focus on the tank body. Below the results for both load cases and graphics showing results variations due to winding angle.

Table 3: Results of load case 1 (Vertical Tank)

Parameters	55°	70°	90°
Stress (MPa)	29.5	26.4	24.4
Displacement (mm)	18.6	23.1	26.0
Strain	0.0014	0.0013	0.0013
Safety Factor	3.6	4.7	6.0

Table 4: Results of load case 2 (Horizontal Tank)

Parameters	55°	70°	90°
Stress (MPa)	15.0	16.5	18.0
Displacement (mm)	25.0	25.5	26.4
Strain	0.0056	0.0053	0.0052
Safety Factor	1.6	1.8	1.6

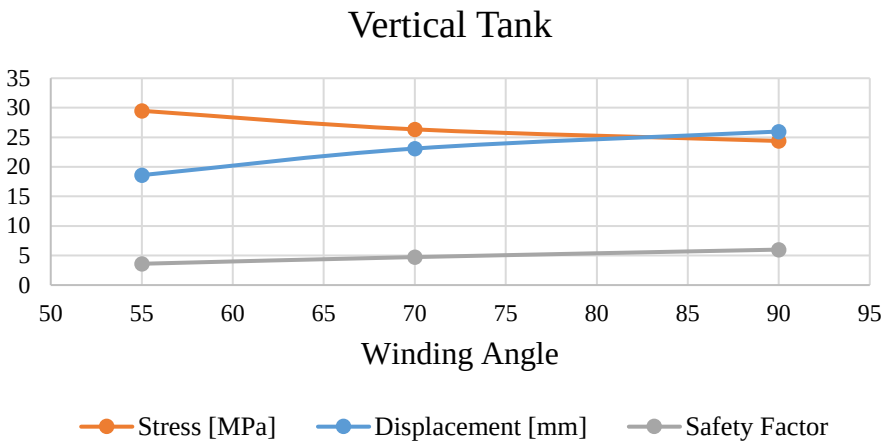

Figure 3: Vertical Tank Results

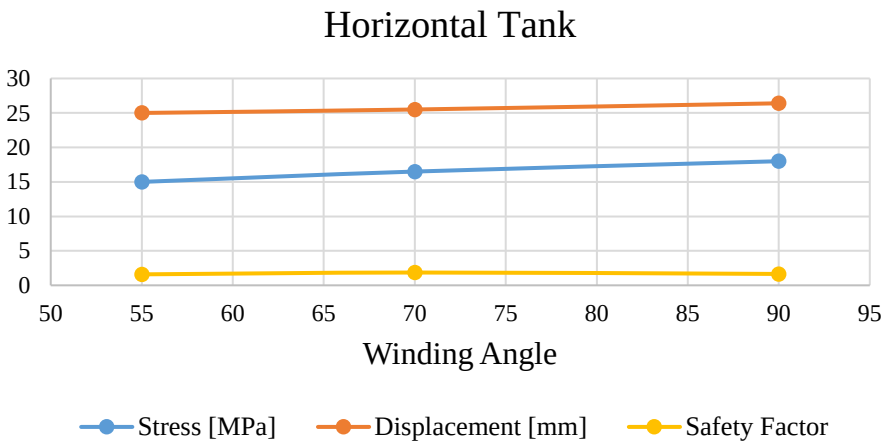

Figure 4: Horizontal Tank Results

The winding angle should be determined according to the required elastic modulus, considering that lower angles provide higher elastic modulus on x direction.

If a cylindrical structure is subjected only to circumferential loads, the axial stress is zero and the optimum winding angle is 90 degrees. In practice, the laminate should have some axial stiffness to resist handling, wind and seismic loads, therefore 70 degrees is often used.

6. RESULT COMMENTS

The following figures demonstrate the stress and displacement distribution of the evaluated structures.

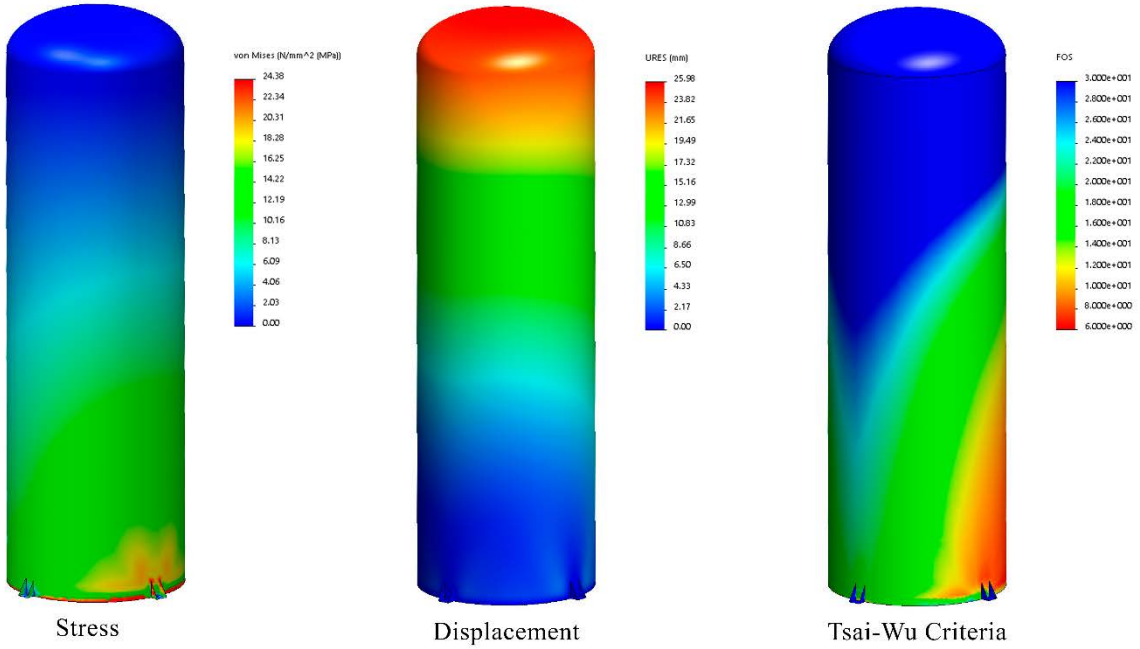

Figure 5: Vertical Tank Results

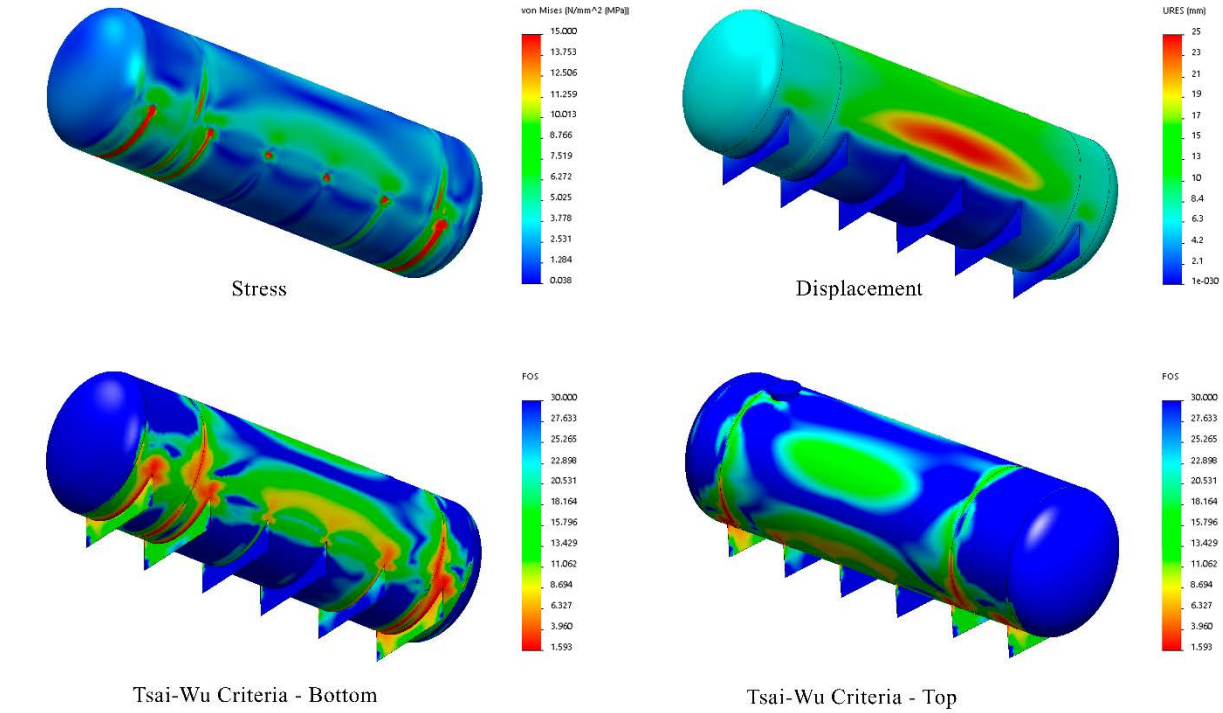

Figure 6: Horizontal Tank Results

The analysis of the vertical tank demonstrated that its stress decreased and its displacement increased with the use of higher winding angles. If a cylindrical structure is subjected only to circumferential loads, the axial stress is zero and the optimum winding angle would be near 90 degrees, however wind and handling loads may suggest that the winding angle can reach lower stress values at 70 degrees. Due to the nature of the Finite Element analysis, where an intermediate chemical layer made with quasi isotropic reinforcements is added, the result of lower stress at 90 degree wind angle is expected.

It could be noticed from the Finite Element analysis that both the stress and displacement of the horizontal tank tend to decrease with lower winding angles, reaching the same value calculated by trigonometric functions at 55 degrees winding angle. The lower winding angle also indicates the need of axial strength due to the tank ends pressure and the supports inducing flexural stress on the tank wall. This winding angle also proves to be more efficient by the Tsai-Wu failure criterion.

REFERENCES

[1] TSAI, S. W.; WU, E. M. A general theory of strength for anisotropic materials. Journal of Composite Materials, n. 1, v.5, p.58-80. Jan, 1971.
[2] TSAI, S. W.; HAHN, H. T. Introduction to composite materials. Technomic publishing, 1980.
[3] ABNT. NBR 6123: Forças devidas ao vento em edificações. Jun, 1988.
[4] CARVALHO, A. Compósitos para uso industrial. Minas Gerais: dez, 2012

A FAST METHOD FOR PRELIMINARY EVALUATION OF CHEMICAL EROSION ON A COMPOSITE NOZZLE

Flávia O.Untem(1), Fábio L. Calciolari(1), Luiz E. N. de Almeida(1), Gustavo H. Murari(1) and Wagner K. A. Silva(1)

(1) Avibras Indústria Aeroespacial S/A, Brazil

https://doi.org/10.21452/bccm4.2018.09.03

Abstract

Most solid rocket motors (SRM) make use of polymeric composites as ablative thermal protection system (TPS). One of the main advantages of this type of cooling is its simplicity and cost; however, the mechanism of erosion on the composite surface is very complex and tricky to model. In the present work, an ablation model was developed considering the reaction of H_2O and CO_2 molecules, present in the combustion gases, with the ablative material. This approach is valuable for a preliminary assessment of the behaviour of ablative layers. The investigation was based on a particular case of a SRM ablative nozzle since it is a critical setup for this type of thermal protection system. The bisection method was used for 02 particular propellant formulations in order to predict the mass consumption rate of the ablative material in function of the nozzle diameter and the mass fraction of aluminium.

Keywords: ablation model, SRM, nozzle, chemical erosion.

1. INTRODUCTION

Solid rocket motors nozzles operate in severe conditions of pressure and temperature, so that dimensioning the insulation protection is necessary in order to assure its integrity during the operation time [1]. The use of composite and ablative materials for this type of application is consecrated and it has been used since the 1970s in the aerospace industry [2].

The ablation is a complex phenomenon that may comprehends physical and chemical processes, including heat conduction, pyrolysis, carbonization, thermochemical reactions, mechanical erosion, and others [3]. Figure 1presents a scheme of the ablation process.

When using charring materials, the thermochemical ablation comprehends the degradation of the material and subsequent formation of a carbonaceous char layer due to the exposure of its surface to high temperature gas flow, and particles at high speed [1].

As the local temperature exceeds the pyrolysis temperature of the material, the degradation starts and the pyrolysis gases are released by diffusion. The endothermic reaction provides the

transformation of thermal energy into chemical energy, leading to cleavage of molecular bounds and formation of the char layer, which leads to the reduction of heat flow on the surface [2].

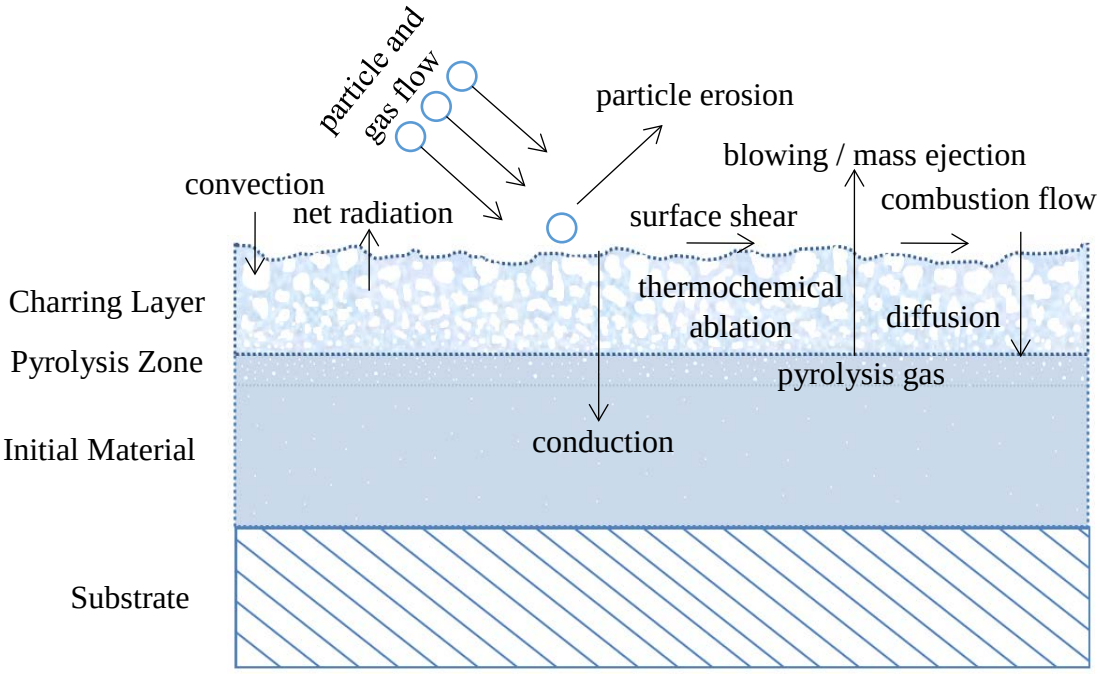

Figure 67: Scheme of ablation process based on [1].

In this context, it is of great interest to predict the efficacy of insulation protection system on a SRM and its behavior during operating time. Several ablation models and computational tools have been developed in order to study the ablation mechanism, with several levels of complexity [3, 4, 5].

Some models consider the ablation as a consequence strictly related to the interaction of combustion gases species with the ablative material surface. This approach disregards other events that contribute to a more intensive recession rate, once it is known that the presence of solid particles contributes to mechanical and thermal erosion of ablative material [6].

Although this kind of model is relatively simple, it can be used for preliminary selection of ablative materials for insulation protection systems, since it is a fast and low cost method [7], being a first step for a subsequent more complex ablation model adoption.

The objective of this work was to propose a fast method to predict the chemical erosion of ablative materials used in thermal protection systems of SRM, relating the material mass consumption rate as function of propellant formulation and project dimensions of the nozzle, assuming that the charred residue is composed only by carbon.

2. METHODOLOGY

2.1. Thermochemical Ablation Model

The equilibrium composition of the combustion products and their mass fraction were obtained from the computer program NASA –CEA [8]. Among all gases species resulting from the combustion, just CO_2 and H_2O were considered in the thermochemical ablation model, as they

represent the most significant portion of the phenomenon concerned. Thus, the main heterogeneous chemical reactions are represented in Equations (1) and (2):

$$C_{(s)} + CO_2 \rightarrow 2CO \quad (1)$$

$$C_{(s)} + H_2O \rightarrow CO + H_2 \quad (2)$$

The thermochemical ablation rate is defined by Equation 3[1][5]:

$$\dot{r} = k_i P_i^n \quad (3)$$

where $\dot{r}$ is the mass consumption rate of CO_2 and H_2O in kg/(m^2.s); k_i is the reaction rate constant (s/m); P_i is the partial pressure (Pa) of the reagent, and n is the pressure exponent.

The reaction rate constant (k_i) is expressed by the Arrhenius equation defined by:

$$k_i = A_i e^{(-E_i/RT_w)} \quad (4)$$

Where A_i is the pre exponential factor of the reaction rate (s/m), E_i is the reaction activation energy (J/mol), R is the universal gas constant (8.3144 J/mol.K), and T_w is the wall temperature (K).

The pre exponential factor, the pressure exponent and the activation energies of the chemical reactions described by Equations (1) and (2) were obtained from [1] and [9] and can be seen in Table 1.

Table 29: Pre exponential factor, activation energy and pressure exponent for chemical reactions described by Equations 1 and 2.

Reaction	A_i (kg.m^{-2}.s^{-1}.Pa^{-n})	E_i (J.kg^{-1})	n
$C + CO_2 \rightarrow 2CO$	9.0 x 103	284,658	0.5
$C + H_2O \rightarrow H_2 + CO$	4.8 x 105	287,584	0.5

The mass consumption rate of CO_2 and H_2O were calculated as Equations 5 and 6:

$$\dot{m}_{CO2} = 9{,}000 P_{CO2}^{0.5} e^{(-284{,}658/RT_w)} \quad (5)$$

$$\dot{m}_{H2O} = 480{,}000 P_{H2O}^{0.5} e^{(-287{,}584/RT_w)} \quad (6)$$

Finally, Equation 7 expresses the carbon mass consumption rate by thermochemical ablation:

$$\dot{m}_C = \left(\frac{M_C}{M_{CO2}}\right)\dot{m}_{CO2} + \left(\frac{M_C}{M_{H2O}}\right)\dot{m}_{H2O} \quad (7)$$

where $\dot{m}_C$ is the carbon mass consumption rate, and M_C, M_{CO2} and M_{H2O} are the molecular mass of C, CO_2, and H_2O (12.017 g/mol, 44.01 g/mol, and 18.015 g/mol, respectively).

2.2.Evaluation of the nozzle inner wall temperature

To evaluate the inner wall temperature of the nozzle the thermal resistance approach was used. This strategy is justified because despite the outer wall has a very long transient the inner wall rapidly reach the steady state condition [5]. Since the inner surface of the tube suffers a continuous regression, the energy balance in the internal boundary can be expressed as:

$$h_g(T_g - T_w) = -k_s \left.\frac{\partial T}{\partial r}\right|_{r=r_i} + \rho_s \dot{r} \Delta H_r \quad (8)$$

where h_g is the convective coefficient of the hot gases [W/(m².K)], T_g is the combustion products static temperature [K], T_w is the inner wall temperature [K], k_s is the conductive coefficient of the first layer [W/(m.K)], ρ_s is the density of the first layer [kg/m³], $\dot{r}$ is the surface progression rate due to chemical erosion [m/s], and ΔH_r is the net enthalpy of the reaction of interest [J/kg].

Since steady state conditions are being considered Equation (8) becomes:

$$h_g(T_g - T_w) = -k\frac{\partial T}{\partial r} + \rho_s \dot{r} \Delta H \tag{9}$$

Equation 10 represents the heat flux inside the tube:

$$q_r'' = -k\frac{\partial T}{\partial r} = U(T_w - T_O) \tag{10}$$

where T_O is the outer wall temperature and:

$$U = \frac{1}{r_1 \sum_{i=1}^{N} \frac{1}{k_i} ln\left(\frac{r_{i+1}}{r_i}\right)} \tag{11}$$

The heat flux of the wall can also be expressed as the amount of heat lost to the environment due to natural convection and radiation, so:

$$q_r'' = h_\infty(T_O - T_\infty) + \epsilon\sigma(T_0^4 - T_\infty^4) \tag{12}$$

where $h_\infty$is the natural convection coefficient and T_∞ is the reference temperature. The convective coefficient of the combustion gases passing through the nozzle can be determined by the following [10]:

$$h_g = 0.026k\left(\frac{\rho v}{\mu}\right)^{\frac{4}{5}}\left(\frac{1}{D}\right)^{\frac{1}{5}}\left(\frac{C_P \mu}{k}\right)^{\frac{2}{5}} \tag{13}$$

The convective coefficient on the cold side can be determined with the expression [11]

$$h_\infty = \left(\frac{k}{D}\right) C Ra^n \tag{14}$$

where R_a is the Rayleigh number and the parameters C and n are the ones presented in Table 2 [11]:

Table 30: Rayleigh number and the parameters C and n.

Ra	C	n
$10^{-10} - 10^{-2}$	0.675	0.058
$10^{-2} - 10^{2}$	1.020	0.148
$10^{2} - 10^{4}$	0.850	0.188
$10^{4} - 10^{7}$	0.480	0.250
$10^{7} - 10^{12}$	0.125	0.333

Using equations (9) - (14) and knowing that $T_\infty < T_O < T_g$ the problem can be easily solved by a bisection scheme.

In this work it was considered 2 propellants formulations based on AP/Al/HTPB, named as P1 and P2.The AP content was fixed at 70% and 80% for propellant P1 and P2, respectively, and mass consumption rates were evaluated in function of fraction of aluminium and nozzle diameter for each case.

3. RESULTS AND DISCUSSION

The method allowed the estimation of mass consumption rate of ablative materials for a wide range of propellant formulations and nozzle diameter. Figures 2 and 4 present contour plots for propellant P1 and P2, respectively, wherein each color line corresponds to a specific mass consumption rate

It is possible to notice from Figures 2 and 4 that mass consumption rate of ablative material is directly proportional to mass fraction of Al present in propellant formulation and inversely proportional to nozzle diameter, as expected.

However, when trying to achieve a desired recession rate one must not be restricted by the adjustment of these two parameters only, but the propulsive performance has to be taken into account as well. Figures 3 and 5 present the specific impulse as a function of the mass fraction of Al for propellant P1 and P2, respectively.

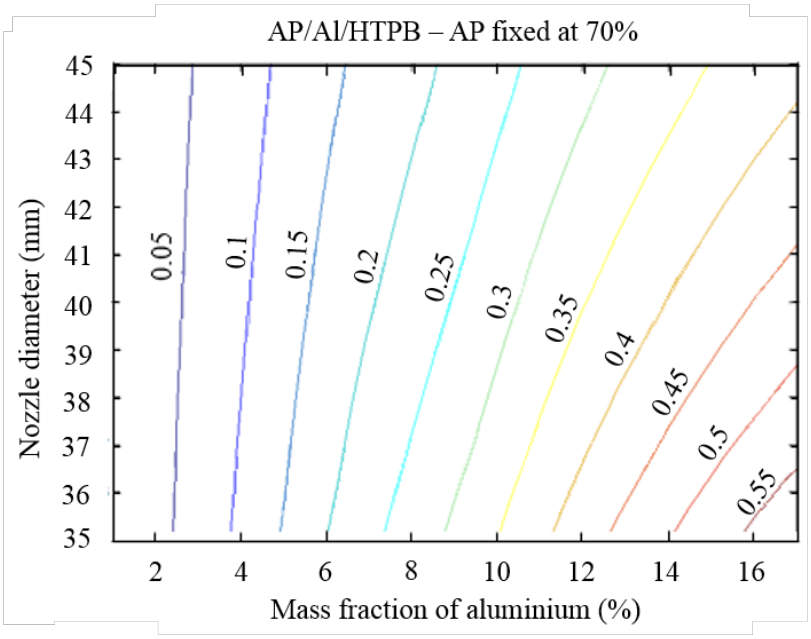

Figure 68: Contour plot for propellant P1

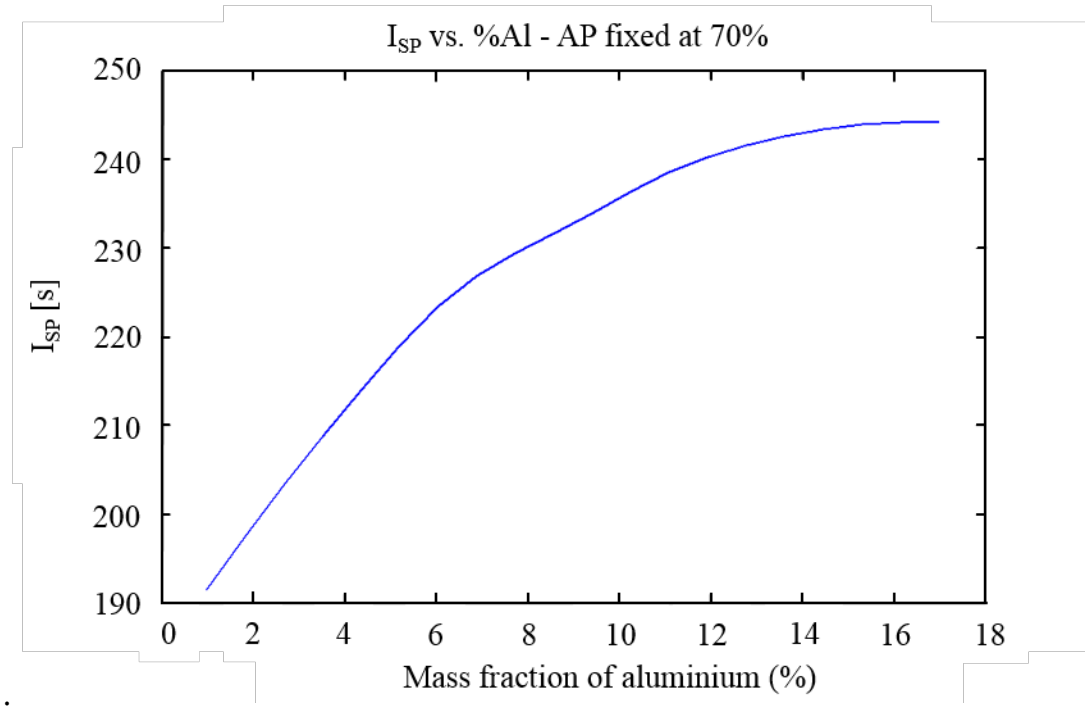

Figure 69: Specific impulse (s) as a function of mass fraction of Aluminium (%) for propellant P1.

From the contour plots, Figures 2 and 4, it can be seen that a design setup with propellant P1 the erosion rate is less sensitive to variations of nozzle diameter compared to one with propellant P2. As a contrast, the setup with propellant P2 is way less sensitive to Al mass fraction variations. The contour plots with the performance plots constitute, thus, a complex map to be used jointly for design decision making.

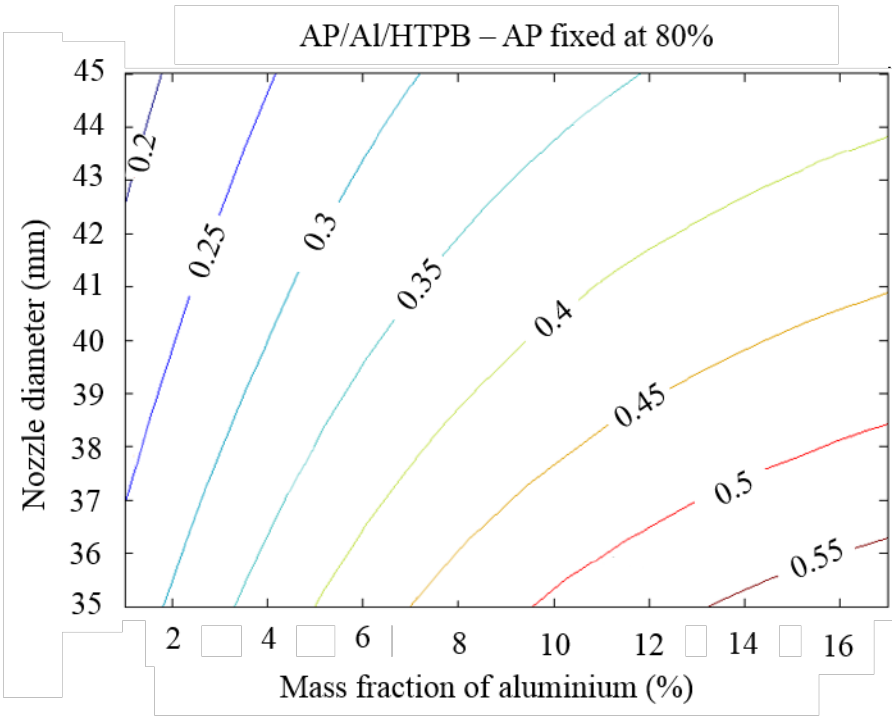

Figure 70: Contour plot for propellant P2.

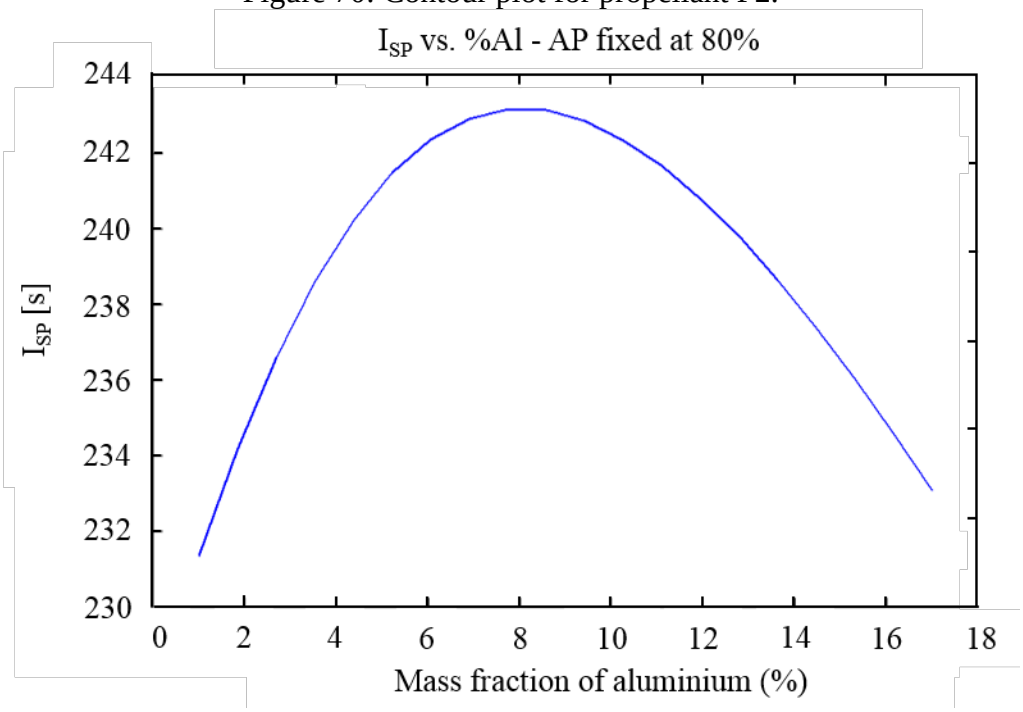

Figure 71: Specific impulse (s) as a function of mass fraction of Aluminium (%) for propellant P2.

5. CONCLUSIONS

The proposed method allows quick evaluation of the material behavior in relation to its chemical erosion, making it possible to verify the adequacy of material for such application in a preliminary basis. The contour plot is a valuable tool to comprehend the influence of both nozzle diameter and propellant chemical composition on the erosion rate and can be used along with the SRM propulsive performance plot to make project decisions. Neither the direct correlation among these 3 parameters, nor a methodology to evaluate preliminarily the material selection of TPS are usual in the literature. The selection and dimensioning of TPS materials in early design phase is often based on experience. In this context, one can consider the proposed method as a useful tool in the initial stages of TPS definition, that may be used in a step prior to the use of a more complex ablation model. As a future work, we suggest to perform functional tests that may support the validation of this method as a tool to define thermal protection solutions on early stages of development of SRMs.

ACKNOWLEGMENTS

The authors are thankful to AVIBRAS Indústria Aeroespacial for providing the materials used in this study and for allowing partial divulgation of test results.

REFERENCES

[1] Xu, Y. H., Hu, X., Yang, Y.X., Zeng, Z.X. and Hu, C.B., 'Dynamic Simulation of Insulation Material Ablation Process in Solid Propellant Rocket Motor',*Journal of Aerospace Engineering*, **28**, (5) (2015).

[2] Rossi R. C. and Wong, W. C. 'Availability of Aerospace Rayon for SRM Nozzle Insulators', *American Institute of Aeronautics and Astronautics*(1996).

[3] Liu, Y., Yang, S., He, G. and Li, J. 'An Overall Ablation Model of Ethyliene-Propylene-Diene Monomer Based on Porous Characteristcs in Char Layer',*Advances in Mechanical Engineering*, **8**(2) (2016) 2-10.

[4] Machado, H. A. 'Simulation of Ablation in a Composite Thermal Protection System via an Interface Tracking Method',*J. Aerosp. Technol. Manag.* (2012).

[5] Bianchi, D., Turchi, A., Nasuti, F. and Onofri,M. 'Chemical Erosion of Carbon-Phenolic Rocket Nozzles with Finite-Rate Surface Geometry',*Journal of Propulsion and Power*.**29**(5)(2013).

[6] Wirzberger H., and Yaniv, S. 'Prediction of Erosion in a Solid Rocket Motor by Alumina Particles',*41st AIAA/ASME/SAE/ASEE Joint Propulsion Conference & Exhibit*.(2005). 9.

[7] Li,J., Zhang, M. and Zhang, J. 'Numerical Simulation of Insulation Layer Ablation in Solid Rocket Motor Based on Fluent',*Applied Mechanics and Material*.(574) (2014) 224-22

[8] Gordon S., and McBride B. J. 'Computer Program for Calculation of Complex Chemical Equilibrium Compositions and Applications', *National Aeronautics and Space Administration, Office of Management, Scientific and Technical Information Program*. (1994).

[9] Chelliah, H. K., Makino, A., Kato, I., Araki, N. and Law, C. K. 'Modeling of Graphite Oxidation in a Stagnation-Point Flow Field using Detailed Homogeneous and Semiglobal Heterogeneous Mechanisms With Comparisons to Experiments',*Combust. Flame,***104** (1996) 469-480

[10]Humble, R. W., Henry, G. N. and Larson, W. J. 'Space Propulsion Analysis and Design, McGraw-Hill'.(1995).

[11]Bergman, T. L., Lavine, A. S., Incropera, F. P. and Dewitt,D. P. 'Fundamentals of Heat and Mass Transfer', 7th Edn (John Wiley & Sons, 2011).

DEVELOPMENT OF KEVLAR COMPOSITES FOR BALLISTIC APPLICATION

Viviane M Fonseca (1), Erick J.P. A Oliveira (1), Pedro T Lima(1), Laura H Carvalho (2)

(1) Department of Textil Engineering, Universidade Federal do Rio Grande do Norte, Brazil

(2) Department of Material Engineering, Universidade Federal de Campina Grande, Brazil

https://doi.org/10.21452/bccm4.2018.09.04

Abstract

Laminated ballistic composite panels are an important part of hard-plate protective body armour and may be subjected to a wide variety of impact conditions depending on the projectile, impact velocity and armour construction. Kevlar fiber is the type of reinforcement most widely applied in these materials. Within the composites industry, woven, knitted and nonwoven reinforcements made of glass fiber, carbon fiber and aramid fibers are now widely accepted as being technical textile products. The applied of textile fabrics has generally provided a lower composite manufacturing cost and a higher damage tolerance. The high-strength, high-modulus Kevlar 49 fiber is widely used today because of its superior properties. Aramid fibers are known for their large hardness and resistance to penetration. Due to their toughness aramid fibers are used where high impenetrability is required, e.g. bulletproof vests, bike tyres, airplanes wings, and sport equipment. In this work, Kevlar nonwoven, obtained by cutting apart of the bulletproof, as used for reinforced polyester composites and kevlar fabrics manufacturing using handcraft process reinforced polyester will be tested using .38 weapons in close range in order to simulate a real situation (confrontation). The impact properties of the reinforcements will also be determined in the same situations and their behavior after tests are compared. The preliminary results after the gunshot test demonstrated the efficiency of the reinforcements in the ballistic for bulletproof vest and the developed fabrics. This fact evidences the feasibility of using the fabric as a ballistic application. The performance of the composite under gunshot test for polyester reinforced kevlar fabrics of the composite was performed in a 3 different sample. The results showed the effective action of the composites developed for application in shields. Independently of the reinforcement contents, all the composites presented resistance to shooting using caliber, 38 and 40. For the use of the caliber; 40 the material presented a very satisfactory result, considering the level of damage of this type of ammunition This result is indicative that the material developed can be used in shields.

Keywords: aramid fabric; polyester, ballistic, kevlar, bulletproof

1. INTRODUCTION

Laminated ballistic composite panels are an important part of hard-plate protective body armour and may be subjected to a wide variety of impact conditions depending on the projectile, impact velocity and armour construction. kevlar is the type of reinforcement most widely applied in these materials.

Within the composites industry, woven, knitted and nonwoven reinforcements made of glass fiber, carbon fiber and aramid fibers are now widely accepted as being technical textile products. Traditionally the use of textile fibers is associated with clothing and household textiles. However, with the increasing technological evolution verified in recent years its use in other areas of engineering has been gaining prominence, mainly when it is necessary high performance. Thus many researchers around the world have been searching to innovate and maximize the potential of different fibrous materials in combination with polymer matrices, creating products with unique properties called composites [1-3].

The chemical and structural combination of different polymers produced a new class of textile products called high performance fibers with unique properties to be used in a wide variety of engineering fields [4,5]. For the development of these materials, a wide range of synthetic, artificial or natural fibers may be used. However, with the high technology domain, high performance fibers have superior characteristics for general specific applications due to compared then mechanical properties. These fibers present superior resistance and modulus of elasticity to the conventional synthetic fibers, becoming an important field to be explored in technological applications [6]. Aramid, UHMWPE and carbon fibers are examples of high performance fibers.

High specific strength, high specific module and excellent chemical resistance are attractive properties that polymer composites offer when compared to metallic materials. However, due to the anisotropic characteristic of the material, the mechanical strength is closely related to the orientation of the reinforcement provided by high-performance fibers where the mechanical strength is given in the same building material and the distribution and interaction between fiber and polymer matrix.[7,8]

Mechanical strength and stiffness can be changed depending on the type and orientation of the building structure and also the proportions of the constituent materials. When a fabric is considered, the properties of the fibers and the yarns essentially govern the fabric properties, but in addition to the geometric criteria such as the fabric weave structure, or the knitted or non-woven construction, cover factor, and the yarn crimp in woven fabrics must also be taken into account [1,4].

The applied of textile fabrics has generally provided a lower composite manufacturing cost and a higher damage tolerance. Plain weaves fabrics are the most commonly used basic reinforcements for woven fabric composites. Woven fabric composites containing into structure holes or cut-outs are often found in structural applications, because in composites will create stress or strain concentrations and hence will reduce the mechanical properties [1,2]. The prediction of reduction in the mechanical properties originating by holes is important for the composite designers. In order, to obtain further new properties, several researchers have applied the technique of hybridization, where besides the structure of the fabric, thread type and composition come into play as part of research [1-4]. Nowadays, a common way to produce hybrids is by laminating reinforced by using different fibers. The aerospace industry applied many hybrid laminates of this kind in very different applications, such as on helicopter blades and flaps [2]. Hybrid woven fabrics with interwoven glass, carbon and aramide such as Kevlar fibers are also a fine way to combine the best characteristics of those fibers in an unique material [1-3].

The high-strength, high-modulus Kevlar 49 fiber is widely used today because of its superior properties. Aramid fibers are known for their large hardness and resistance to penetration. Due to their toughness aramid fibers are used where high impenetrability is required, e.g. bulletproof vests, bike tyres, airplanes wings, and sport equipment. Aramid fibers are a very important reinforcement for advanced composites, which were developed during the 1960s and first introduced commercially by DuPont in the 1970s under the trade name Kevlar_. Their high degree of toughness, associated with the failure mechanism of aramids, and damage tolerance promotes good impact/ballistic performance. When aramid fibers break, they do not fail by brittle cracking, as do glass or carbon fibers. Instead, the aramid fibers fail by a series of small fibril failures, where the fibrils are molecular strands that make up each aramid fiber and are oriented in the same direction as the fiber itself. These many small failures absorb much energy and, therefore, result in very high toughness.[8]

The conventional textile structures are produced by weaving or knitting techniques, and weaving is the oldest technique for production of textile structures. This technique is based on the orthogonal interweaving of two yarn systems warp and weft. In order to allow a wide variety of structures, which differ according to the programming and properties of the yarns that make them. However, most derived from three fundamental structures: taffeta, twill and satin. These structures are being distinguished by the frequency of interlacing and / or degree of sequence in the arrangement of the yarns in the formation of the fabric.

The efficiency of a fibrous reinforcement depends on the type, length, volumetric fraction and orientation of the fibers during the mechanical test. The ideal choice of these parameters significantly influences one or more of the following characteristics of composite materials such as: density, tensile strength, compressive strength, compressive strength modulus, fracture and fatigue performance, impact load response, cost and properties thermal and electrical [7]

In this work, Kevlar nonwoven, obtained by cutting apart of the bulletproof, as used for reinforced polyester composites and kevlar fabrics manufacturing using handcraft process reinforced polyester will be tested using .38 weapons in close range in order to simulate a real situation (confrontation). The impact properties of the reinforcements will also be determined in the same situations and their behavior after tests are compared.

2. EXPERIMENTAL

In this study, two composites were produced: kevlar nonwoven reinforced polyester resin (CKNW) and kevlar fabrics reinforced polyester resin (CKF). Nonwoven fabric is obtained by dismantling a bulletproof vest used for military police and their material as supplied for BPChoque/RN (Figure 1). The fabrics were developed in laboratory scale using handloom machine for producing of aramid plain woven fabrics using twill structure (Figure 2).

The composite was produced using compression molding. Laminate made of layers of biaxial fabrics produced using Kevlar 49 fibers supplied for Dupont and development in laboratorial scale using handloom machine. The structure of the fabrics is twill. Layers of fabrics and nonwoven fabrics are cutup with the mold dimensions (200x150 mm) and disposed in the mold. The polyester resin is catalyzed using Butanox M50 at 1% was poured over the fabrics. The mold closed and the system pressed less than 5 ton for 12h at room temperature.

The ballistic test was performed in order to simulate a real confrontation situation. In this case, the samples were fixed in a metal support, Figure 3, using a adhesive tape and the distance of the shot was of 5 meters. This test was conducted at BPchoque / RN and the commander of the Squad unit was responsible for the shots. The weapon used was a .38 gun and .40 gun with exclusive

police ammunition, with a high explosion factor. In this test 3 samples of the reinforcements and composites were evaluated. Composite C1 – bulletfrof reinforced polyester, 46%; Composite T3 – fabric twill reinforced polyester, 30,5%; Composite T3 – fabric and nonwoven kevlar reinforced polyester, 17%

Figure 1- nonwoven fabrics for bulletproof

Figure 2- Fabric manufactured using handloom machine

Figure 3- Sample fixed for gunshot test

3. RESULTS AND DISCUSSION

The results after the gunshot test demonstrated the efficiency of the reinforcements in the ballistic for bulletproof vest and the developed fabrics. However it is necessary to consider that the sample of the bulletproof vest is composed of 32 unidirectional kevlar layers in a 90º / -90º configuration, while the woven sample consists of 4 layers in the same configuration. After the test, it was observed that the projectile, Figures 4 and 5 did not perforate the samples. This fact

evidences the feasibility of using the fabric as a ballistic application. Although an evaluation of the transmission of impact energy in the human body is required.

Figure 4- Bulletproof vest after gunshot test

Figure 5- Fabric bulletprof sample after gunshot test

The performance of the composite under gunshot test for polyester reinforced kevlar fabrics of the composite was performed in a 3 different samples. The target is composed of a ballistic plate, a vest structure and a polyurethane foam. After gun shot test all parts were evaluated in relation to the degree of perforation and damage. For all composites the ballistic plates acting after the shooting test, all the ballistic plates acted to support the bullet and even after different calibers did not present a critical fracture. These results are indicative that the developed composites are efficient for use as a ballistic plate (figures 6 a 8). The profile of damage after visual analysis as possible observed delamination under hight impact, but not broken. This result is indicative that the material developed can be used in shields, if the dissipation impact energy of the projectile's is taken into account. Although perforation in the plate occurs the projectiles were housed in the structure of the bulletprof.

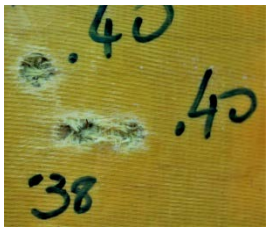

Figure 6 – Composite T3 after shotting test

Figure 7 – Composite C1 after shotting test

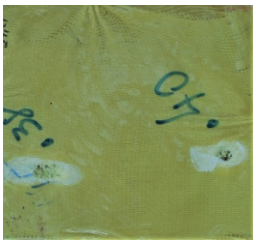

Figure 8 – Composite H1 after shotting test

4. CONCLUSIONS

The results showed the effective action of the composites developed for application in shields. Independently of the reinforcement contents, all the composites presented resistance to shooting using caliber, 38 and 40. For the use of the caliber; 40 the material presented a very satisfactory result, considering the level of damage of this type of ammunition.

ACKNOWLEDGEMENTS

We are indebted to T.C. Rodrigo Trigueiro BP Choque/RN for support and performance of the shooting tests.

REFERENCES

[1] Holme; Adhesion to textile fibres and fabrics *International Journal of Adhesion & Adhesives* 19 (1999) 455}463

[2] Manohar G. Kollegal and Srinivasan Sridharan; Strength Prediction of Plain Woven Fabrics; *Journal of Composite Materials*, V34 – 3, 2000, 240-257

[3] Horrocks, A.R and Anand, S.C – *Handbook of Technical Textiles*; CRC Press 2000.

[4] Reinhart,T.J.; "Introduction to Composites, in *Engineered Materials Handbook, Composites*", vol.1 - ASM International, Metals Park, EUA, 1987

[5] Hufenbach, W.; Böhm, R.; Kroll, L.; Langkamp, A- "Theoretical and experimental investigation of anisotropic damage in textile reinforced composite structures*"*. *Mechanics of Composites* Vol. 40 (6), 519-532; 2004.

[6] H.L.Gower; D.S.Cronin; A.Plumtree - Ballistic impact response of laminated composite panels; International Journal of Impact Engineering; V35, Issue 9,2008, 1000-1008

[7] Jang-Kyo Kim; Man LungSham; Impact and delamination failure of woven-fabric composites; Composites Science and Technology; V 60, Issue 5, 2000, 745-761

[8] Bryan A.Cheeseman andTravis A.Bogetti; Ballistic impact into fabric and compliant composite laminates; Composite Structures; V61, Issues 1–2, 2003, 161-173

EFFECT OF THE FILAMENT WINDING PATTERN MODELING ON THE AXIAL COMPRESSION OF CYLINDRICAL SHELLS

Cristiano B. de Azevedo(1), Frederico Eggers(1), José H. S. Almeida Jr.(2) and Sandro C. Amico (1)

(1) PPGE3M, Federal University of Rio Grande do Sul, Brazil

(2) Leibniz-Institut für Polymerforschung (IPF) e.V., Dresden, Germany

https://doi.org/10.21452/bccm4.2018.09.05

Abstract

Manufacturing characteristics of the filament winding process, such as the formation of a winding pattern, are usually disregarded in conventional numerical models. However, they could significantly affect stress and strain fields in thin-walled composite shells. This work presents an efficient way to realistically model the filament winding mosaic pattern in composite cylindrical shells under axial compression. The study comprises the linear finite element (FE) Eigenvalue and Eigenvector buckling model of thin-walled composite cylindrical shells using commercial software. A conventional model was developed and an optimization algorithm was used to find the highest Eigenvalue. After the optimum fiber angle was found, it was used for winding pattern drawing and modeling. Three winding patterns were modeled: 1/1, 3/1 and 5/1, where the numerator means the number of diamonds around the number of circumferences indicated by the denominator. The optimum angle-ply fiber layout found was [±30], which reached the highest critical buckling load. The winding pattern influenced the critical buckling load, and the 1/1, 3/1 and 5/1 patterns showed critical buckling loads of 11.237, 11.173 and 11.194 kN, respectively, whereas the conventional modeling approach indicates a critical load of 8.574 kN.

1. INTRODUCTION

Among the manufacturing processes available for polymer composites, filament winding (FW) stands out due to high accuracy in fiber positioning, high fiber volume fraction, low void content and process automation. Cylindrical structures, such as tubes and pressure vessels made by FW are being increasingly used in aeronautical, marine and automotive sectors. The high design freedom and the intrinsic orthotropy of long-fiber-reinforced composites provide numerous possibilities to decrease weight while fulfilling the load requirements [1]. Key parameters in FW process include winding angle, wall thickness and filament winding pattern [2].

Among the FW process parameters, the winding pattern number is usually disregarded in conventional numerical models since it requires complex and work-intensive modelling to accurately simulate the fiber path. This pattern is the main intrinsic parameter that controls fiber inter-crossing, and is typically determined as an X/Y fraction, where X represents the winding cycle and Y the bandwidth, i.e. for each X cycles, there is a Y band advance.

One cycle is characterized as a complete movement from beginning to end and the returning to the initial point on the mandrel. The winding process occurs through regular and repetitive movements of a pay-out eye that deposits the tow onto the mandrel. The first pass of the cycle has a positive winding angle, and the returning follows the same winding angle but negative. This way, the mandrel is covered twice and only an even number of layers are possible, forming an angle-ply $\pm\alpha$ layer. The number of cycles depends on the degree of covering and the tow width [3]. Due to the repetitive movements, the layout of the layer is characterized by the distinctive regular mosaic pattern consisting of triangular-shaped, repeating in chess-board fashion, two-ply units. The units are arranged in regular geometric pattern around the circumference and along the axis of rotation [4].

Several studies were carried out in order to determine the influence of FW parameters on the mechanical behavior of structures. For instance, Krishnan et al. [5] evaluated the influence of the winding angle in composite tubes subjected to multiaxial cyclic pressure loadings. Failure envelopes showed a strong dependence on stress ratio and winding angle, with $[\pm 45]_4$, tending to be axially dominant, and $[\pm 63]_4$ performing better under high hoop-dominant loading. Almeida Jr. et al. [6] developed an optimization procedure based on a genetic algorithm to determine the best stacking sequence in composite tubes under internal pressure loading. They found that asymmetrical and unconventional angles increase the burst strength for internally pressurized tubes. Other studies in the literature have reported the influence of the winding angle in composite tubes under compression loading [7,8] and composite rings under tensile loading [9,10].

Among the very few works in the literature dealing with winding pattern modeling, Morozov [4] numerically evaluated the influence of the winding pattern on tubes subjected to internal pressure. The stress fields were sensitive to the winding pattern and conventional models using nominal angle underestimated the stresses. Other studies reported the influence of the winding pattern on the mechanical behavior of composite tubes [11], pressure vessels [12] and flywheel disk [13].

This work aims at proposing a novel and efficient methodology to model the winding pattern in composite cylindrical shells. The influence of the winding pattern is evaluated with respect to the cylindrical shells under axial compressive load.

2. FINITE ELEMENT MODELING

2.1 Winding pattern generation

A numerical model that incorporates the winding pattern has been developed on Python language due to its excellent compatibility with the FE software herein used, Abaqus 6.14™. Another advantage is related to the use of trigonometric ratios to define the exact positioning of the lines that will form the winding pattern. The essence of model development consists on creating lines in datum planes and projecting them onto the surface of the cylinder to produce the winding pattern. Since the script uses functions common to other CAD platforms, the script can be easily adapted to other languages (e.g. C# or VBA).

The first step is to model a cylinder with radius *r* and length *l*, axially coincident with the z-axis (Fig. 1a). Then, the first datum plane is created where the lines that make the pattern are inserted

(Fig. 1b, and detailed in Fig. 2). The lines are projected onto the tube surface (Fig. 1c). In order to avoid distortions, the process is done in four planes of reference around the tube, changing only the positioning of the lines. Finally, a datum plane is used for the insertion of vertical lines (Fig. 1d), which will delimitate the hoop-wound reinforcement regions, and the lines that divide the diamonds into triangular regions (Fig. 1e).

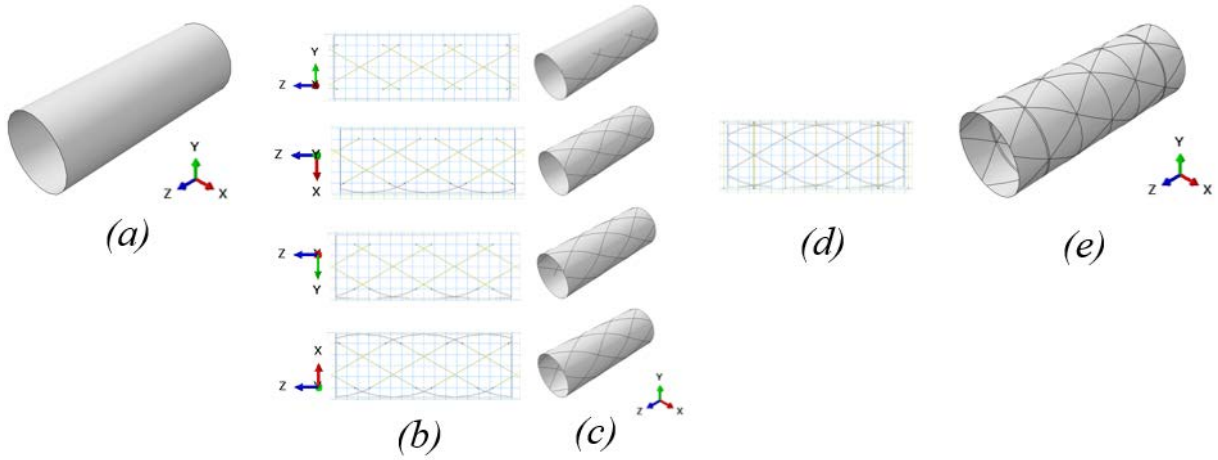

Figure 1 - Development stages of a particular winding pattern modeling: (a) cylinder modeling, (b) datum plane creation, (c) projection onto the tube surface, (d) insertion of vertical lines and (e) complete tube modeling.

The lines that make the winding pattern (Fig. 1b) start from a reference line between the points (x_0, y_0) and (x_1, y_1), with coordinates $(-\Delta x, -\Delta y)$ and $(+\Delta x, +\Delta y)$, respectively (Fig. 2), where Δy and Δx are determined by Eqs. 1 and 2, respectively.

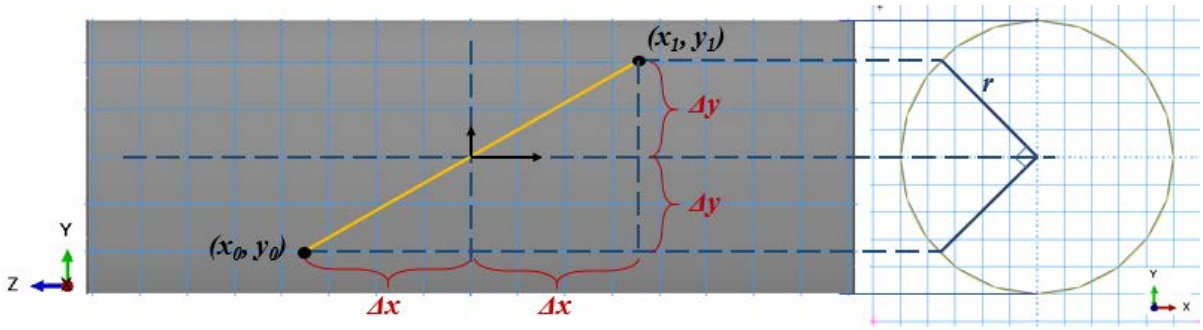

Figure 2 - Modeling of the first reference line that makes the pattern.

$$\Delta y = r.\cos 45° \tag{1}$$

$$\Delta x = \Delta y / \tan \alpha \tag{2}$$

The reference line is repeated along the axial direction of the tube with an offset defined by Eq. 3 (Fig. 3a), and then a new reference line is inserted with coordinates $(-\Delta x, +\Delta y)$ and $(+\Delta x, -\Delta y)$ and new offsets are generated (Fig. 3b).

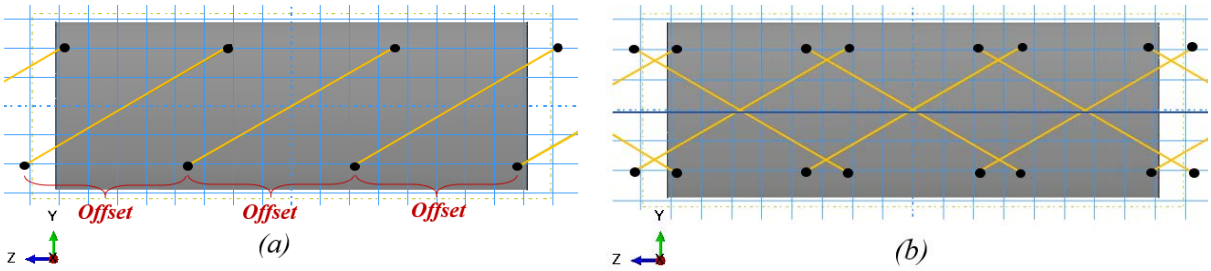

Figure 3 - Drawing of the other lines to compose the desired pattern: (a) offset from reference line, (b) process repeated with a new reference line with other coordinates.

$$\text{Offset} = 8\Delta x/p \tag{3}$$

The process of development in datum planes is performed in the other planes, however, in order to continue the helical shape of the winding pattern, the (x_0,y_0) point must coincide with the (x_1,y_1) point of the previous plane.

2.2 Winding angle optimization

A conventional FE model was first developed to determine the optimum winding angle with respect to critical buckling load. The outcome of this model was used as comparison for the results from the models in which the winding pattern was included. The cylindrical shell was modeled as an orthotropic homogeneous angle-ply, and the dimensions of the cylinders were ϕ = 50 mm and l = 140. A previous work carried out by the group [14] reported that thin-walled cylindrical shells fail due to crushing instead of buckling or material failure, which is not the scope of the current study. Similarly, a hoop reinforcement (20 mm long and 0.21 mm thick) was wound at the specimen ends to prevent crushing.

The material system used is a carbon/epoxy laminate (Toray T700-12K-50C carbon fiber and UF3369 epoxy resin), and its elastic properties were previously experimentally determined in [15] and used as input in the numerical models (Table 1). The cylinders were modeled using an equivalent single layer (ESL) formulation, with a three-node reduced integration shell element (S4R) with hourglass control. This element is suitable for thin-walled shells and was chosen to reduce simulation time and avoid numerical issues. As boundary conditions, the tube was axially clamped at one end, and a buckling perturbation load in the axial direction was applied on top of the cylinder (Fig. 4).

The linear buckling FE model shown in Fig. 4 is based on Eigenvalue analysis, which demands low computational time. It yields the theoretical buckling strength (bifurcation point) of the structure as output.

Table 1: Elastic constants used in the computational analysis [14].

Symbol	***Description***	***Value***
E_1 (GPa)	Longitudinal elastic modulus	129.3
$E_2 = E_3$ (GPa)	Transverse elastic modulus	9.11
$\nu_{12} = \nu_{13}$	Poisson's ratio in plane 1-2 or 1-3	0.32
ν_{23}	Poisson's ratio in plane 2-3	0.35
$G_{12} = G_{13}$ (GPa)	In-plane shear modulus	5.44
G_{23} (GPa)	Transverse shear modulus in plane 2-3	2.10

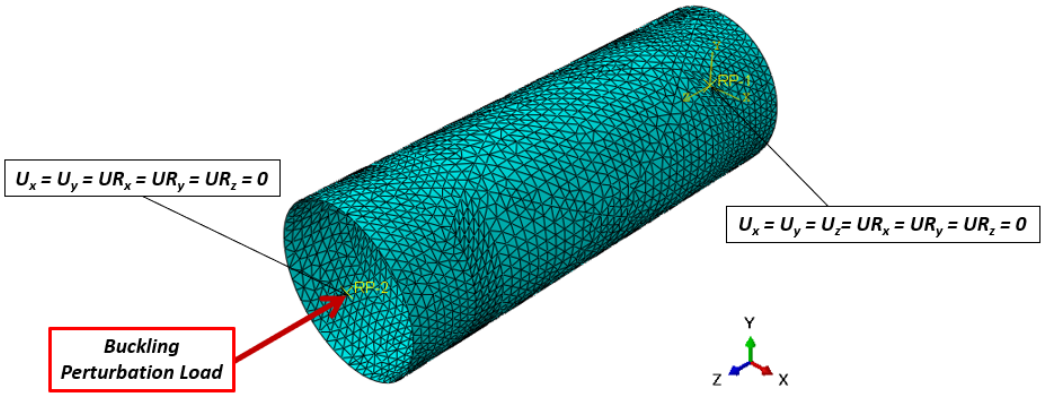

Figure 4 – Tube modeling, boundary conditions and mesh used.

Using the conventional modeling approach (Fig. 1a), the critical buckling load was determined for the winding angle in the 5° to 85° range. A Python script was used to perform this, running simulations in the 5° to 85° range. Winding angles at 0° and 90° were not considered since no winding pattern is formed during manufacturing of these angles, i.e. the band-width is just placed side-by-side.

2.3 Influence of the Winding pattern FE modeling

All patterns herein modeled have the same winding angle, which is assumed to be the optimum angle obtained from the procedure described in Section 2.2. Employing the modeling routine described in Section 2.1, the following winding patterns were modeled: 1/1, 3/1 and 5/1. The mesh differs from the conventional model due to the triangular elements, which are more consistent with the format of the partitions (triangular shapes as well). The models with 1/1, 3/1 and 5/1 patterns have 39,728, 44,712 and 41,260 elements, respectively, which were defined after a preliminary convergence analysis (see Fig. 7). Fig. 5 shows the models and the manufactured specimens for the various winding patterns.

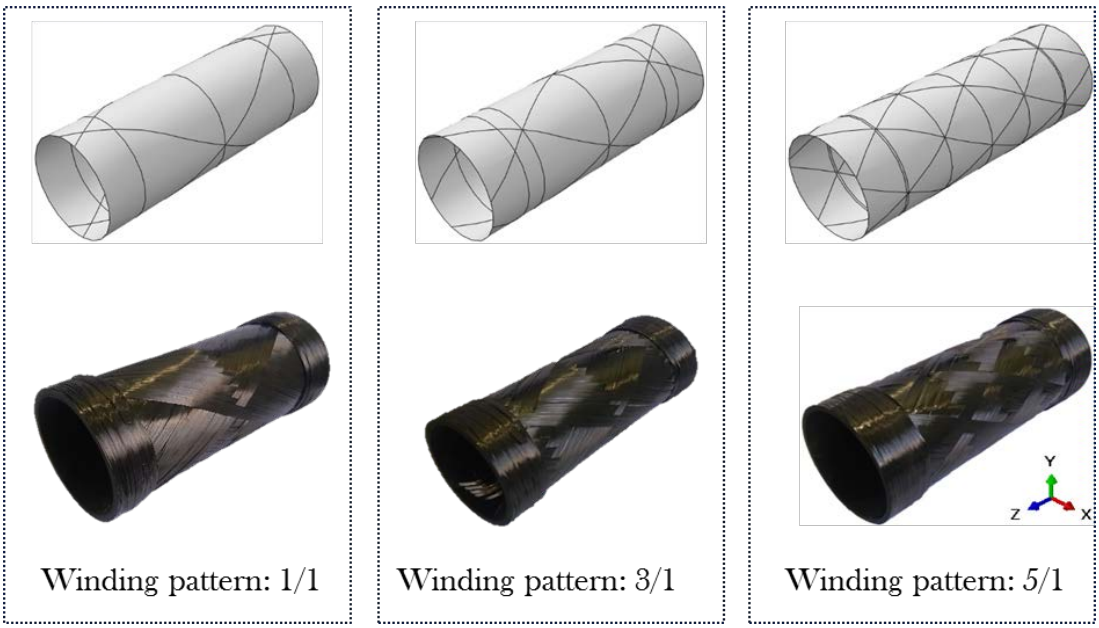

Figure 5 – Modeled and manufactured cylinders with distinct winding patterns.

4. RESULTS AND DISCUSSION

Fig. 6 shows that, for the boundary conditions used, the optimized configuration angle for buckling perturbation load is equal to [±30], where the critical load is 8.57 kN.

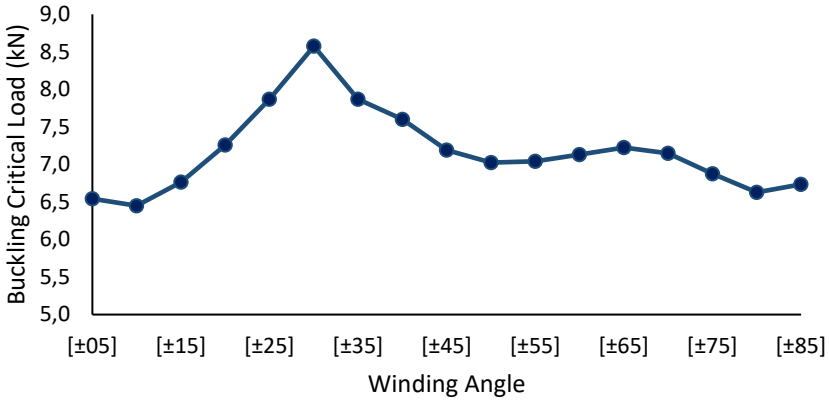

Figure 6 – Buckling load as a function of the winding angle using the conventional modeling approach.

Using the [±30] configuration, four models were developed: one reference model that does not consider the winding pattern and three models considering different winding patterns. Critical buckling load is very sensitive to mesh density, since buckling is a local phenomenon and may happen suddenly at any point of the structure. In all models, the load converged very well for an element size of 1 mm. The mesh sensitivity analysis is shown in Fig. 7 and the buckled deformed shapes are shown in Fig. 8. As can be seen, the deformations produced in the shells mimic the corresponding mosaic texture.

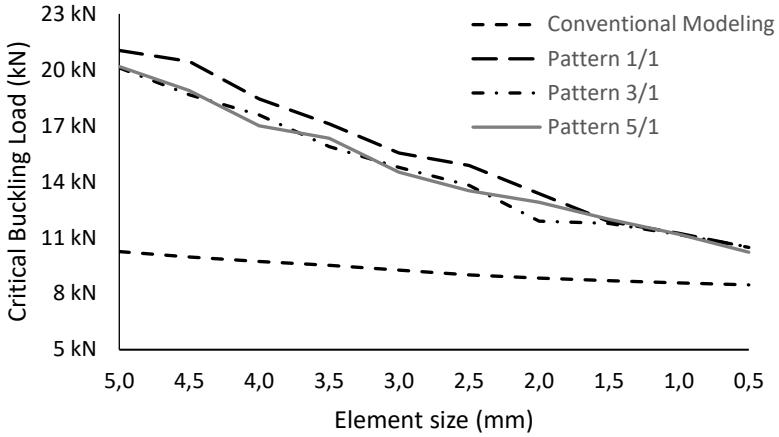

Figure 7 – Mesh convergence analysis.

The overall results for the select meshes are presented in Table 2. Taking into account the winding pattern leads to an increase in critical buckling load of about 30%. However, the variations due to the winding pattern are very small. This may be justified considering that buckling is mostly

influenced by the stiffness of the structure and not by the geometrical characteristic of the shell. In that case, non-linear geometrical buckling analysis would be more suitable to achieve more accurate predictions.

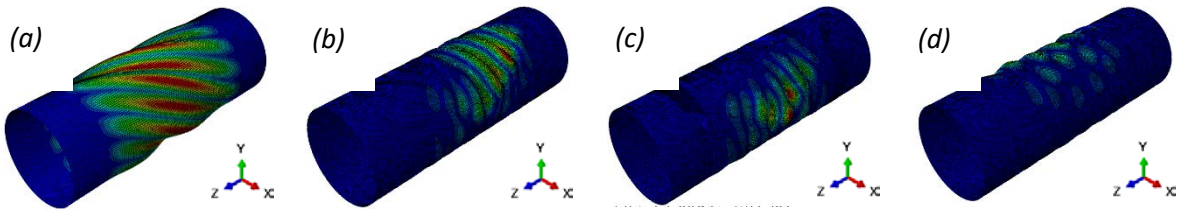

Figure 8 – Buckling shapes of the tubes: (a) No winding pattern modeled, (b) Pattern 1/1, (c) Pattern 3/1, (d) Pattern 5/1 (deformation scale factor: 3×).

Table 2: Predicted critical buckling loads for variable winding pattern.

Modeling	***Critical buckling load (kN)***	***Variation***
Conventional	8.574	----
1/1 pattern	11.237	31.059%
3/1 pattern	11.173	30.313%
5/1 pattern	11.194	30.557%

4. CONCLUSIONS

This work presented a methodology to realistically model the filament winding pattern and how those sketches are exported to a FE package. A conventional model considering a nominal angle in the whole structure was built and the optimum winding angle was found and used to model the various patterns studied, 1/1, 3/1 and 5/1. A case-study of cylinders under axial compression was evaluated considering linear eigenvalue analysis.

From the linear buckling analysis, an optimum winding angle of [±30°] was found. It was verified that the critical buckling load was sensitive to the modelling of the winding pattern. The conventional model provided underestimated results, but the variation observed for the various patterns were small for the type of loading considered. Next steps of this work include development of a nonlinear post buckling model and experimental validation.

REFERENCES

[1] Almeida Jr., J. H. S., Faria, H., Marques, A. T., Amico, S. C., 'Load sharing ability of the liner in type III composite pressure vessels under internal pressure', *Journal of Reinforced Plastics and Composites*, v. 33(24) (2014) 2274-2286.

[2] Koussios, S., 'Filament Winding: a Unified Approach', PhD Thesis Report, Design & Production of Composite structures, Faculty of Aerospace Engineering, Delft University of Technology. Delft University Press; 2004.

[3] Dalibor, I. H., Almeida Jr., J. H. S., Costamilan, E., Shynkarenko, O., Amico, S. C., 'Design of a composite nozzle manufactured by filament winding', in 'Aeronautical Composite Materials and Structures - MACMS', Proceedings of a National Conference, São Carlos, Brazil, 2015, 1-10.

[4] Morozov, E. 'The effect of filament-winding mosaic patterns on the strength of thin-walled composite shells'. *Composite Structures* 76, (2006) 123-129.
[5] P. Krishnan, M.S.A. Majida, M. Afendi, A.G. Gibson and H.F.A. Marzuki. 'Effects of winding angle on the behavior of glass/epoxy pipes under multiaxial cyclic loading', *Materials and Design* 88, (2015) 196–206.
[6] Almeida Jr., J.H.S., Ribeiro, M.L., Tita, V. and Amico, S.C., 'Stacking sequence optimization in composite tubes under internal pressure based on genetic algorithm accounting for progressive damage', *Composite Structures* 178 (2017) 20-26.
[7] Filho, P.S., 'Comportamento mecânico de cilindros de carbono/epóxi processados por enrolamento filamentar para semieixos de transmissão'. Masters Thesis, Programa de Pós-Graduação em Engenharia de Minas, Metalúrgica e de Materiais, Universidade Federal do Rio Grande do Sul, Porto Alegre, (2016).
[8] Gonçalves, A., Almeida, S.F.M. and Neto, F.L., 'Comportamento de cilindros de carbono/epóxi submetidos a cargas compressivas axiais', *Polímeros: Ciência e Tecnologia* 11, (2011) 94-101.
[9] Kaynak, C., Erdiller, E.S., Parnas, L. and Senel, F., 'Use of split-disk tests for the process parameters of filament wound epoxy composite tubes', *Polymer Testing* 24, (2005) 648-655.
[10] Almeida Jr., J.H.S., Tonatto, M.L.P., Gabbardo, F.R.S. and Amico, S.C. 'Resistência à tração circunferencial de anéis de carbono/epóxi produzidos por filamento winding – parte II: análise experimental'. 21º CBECIMAT - Congresso Brasileiro de Engenharia e Ciência dos Materiais, Cuiabá, (2014).
[11] Rousseau, J., Perreux, D., Verdière, N. 'The influence of winding patterns on the damage behaviour of filament-wound pipes'. *Composites Science and Technology* 59, (1999) 1439-1449.
[12] Mian, H., Rahman, H., 'Influence of mosaic patterns on the structural integrity of filament wound composite pressure vessels'. *International Journal of Structural Integrity* 02, (2011) 345-356.
[13] Uddin, Md.S., Morozov, E.V., Shankar, K. 'The effect of filament winding mosaic pattern on the stress state of filament wound composite flywheel disk' *Composite Structures* 107, (2014) 260-275.
[14] Almeida Jr., J. H. S., Tonatto, M. L. P., Ribeiro, M. L., Tita, V., Amico, S. C., 'Buckling and post-buckling of filament wound composite tubes under axial compression: linear, nonlinear, damage and experimental analyses'. *Composites Part B-Engineering*. 159, (2018) 227-239.
[15] Almeida Jr., J.H.S., Souza, S.D.B., Botelho, E.C. and Amico, S.C., 'Carbon fiber-reinforced epoxy filament-wound composite laminates exposed to hygrothermal conditioning'. *Journal of Materials Science* 51(9), (2016) 4697–708

DESIGN AND MANUFACTURING PROCESS OF A UAV COMPOSITE WING SPAR

Pablo M. N. Araujo [1, 3], Thiago R. Costa [1, 3] and Eduardo C. Silva [2, 3]

(1) Department of Mechanical Engineering, Pontifícia Universidade Católica do Rio de Janeiro, Brazil

(2) Department of Electrical Engineering, Pontifícia Universidade Católica do Rio de Janeiro, Brazil

(3) AeroRio, Pontifícia Universidade Católica do Rio de Janeiro, Brazil

https://doi.org/10.21452/bccm4.2018.09.06

Abstract

This paper presents the design and manufacturing process of a lightweight UAV composite wing spar, aiming at achieving a high structural efficiency. The study introduces a real UAV wing geometry, designed to the 2016 SAE Brazil Aero Design competition, and evaluates its aerodynamic loads. Different possibilities of feasible cross-sections are compared aiming to maximize the moment of inertia per area. The mechanical properties of traditional aluminum alloy for aerospace applications are compared with those of polymer matrix composite materials. An analytical dimensioning procedure is presented for structural sizing and the Tsai-Wu failure criterion is used to calculate structural margins of safety for the composite parts. The manufacturing process of the spar is detailed, which uses the vacuum bagging lay-up technique, unlike the traditional method. The mold is a high-density foam used as the structure core. The adopted methodology lead to a reliable wing spar with optimized mechanical properties, having a high strength-to-density ratio. The AeroRio's team reached the second place in the 2016 SAE Brazil Aero Design competition.

1. INTRODUCTION

The recent advances of new computational technologies, software development, telemetry links and small autopilots have contributed to the popularization of UAVs (Unmanned Aerial Vehicles) for end users and enterprise applications. A UAV can be classified into three groups: autonomous, semi-autonomous and remotely controlled aircrafts. That includes all types of multi-rotors, fixed wing, and VTOL (Vertical Take-off and Landing) drones that do not require a pilot inside of them. A recent market research pointed out that the global drones market revenue was worth US$ 6.8 billion in 2016 and is expected to grow up to US$ 36.9 billion by 2022. These vehicles can have several applications for different industries, they can carry special camera sensors capable of

taking pictures in order to build relevant mapping models of a specific land, helping farmers, agronomists and geographers in making decisions [1-2]. They also can carry payloads as delivery boxes [3] or even engineering sensors for high risk offshore inspection of oil and gas constructions [4].

Many of today's engineers' tasks are associated with designing and manufacturing new products with low cost and in short periods of time. Such tasks are possible due to modern computational systems, that are capable of assisting in the design process and evaluation of new composite materials characteristics. Polymer matrix composites are commonly used in modern industry due to their low manufacturing cost and satisfactory mechanical properties and are usually produced in the form of symmetrical and asymmetrical laminates. In turn, these materials, when reinforced by continuous fibers, show: low weight, high strength, high stiffness, corrosion resistance and damping capacity of vibrations. Thanks to their high strength/weight and stiffness/weight ratios, they are used in the automotive, sports and aerospace industries; in order to allow the construction of lightweight structures.

This paper presents the design and manufacturing process of a lightweight UAV composite wing spar, aiming at achieving a high structural efficiency. The wing spar was optimized in order to maximize the team's score in the SAE Brazil 2016 Aero Design competition. The most suitable materials were selected and combined in order to produce composite material with optimized structural performance. The wing spar sizing process is carefully described and the mechanical properties are meticulously evaluated, by analytical analysis.

These studies were conducted at the AeroRio Laboratory, which works on the design and development of unmanned aerial vehicles, such as fixed wing aircrafts and multi-rotors. The group develops multidisciplinary research projects, counting on the collaboration of professors from several engineering departments and with the participation of about 25 undergraduate and graduate engineering students. The team participates in national and international competitions, being three-time champion of SAE Aerodesign Brazil in the Advanced class (2012, 2013 and 2017), and recently, in 2018, the team reached the second place in the SAE Aerodesign East, one of the most important worldwide Aerodesign competitions.

2. DESIGN PROCESS

The wing design presented in this paper was optimized for the SAE Brazil 2016 Aero Design competition. This competition has encouraged students to design and build lightweight UAVs to carry heavy payloads. The competition score leads teams to design high efficiency structures. For instance, the MTOW (Maximum take-off weight) is limited to 30 kg and the flight score increases with payload, so the competitors try to reduce the aircraft empty weight to increase payload capability.

2.1 Wing Geometry

The wing design begins with the selection of the best airfoil for the UAV propose. Then, it is important to define the wing type (elliptical, rectangular, delta) and main dimensions, such as: wingspan, root and tip chords, taper ratio, sweep and twist angle, dihedral, etc. The XFLR5 software was used to design and estimate airfoil performance, which uses the Xfoil code to calculate lift, drag and moment curves of the selected airfoil. Figure 1 shows some of the main wing components, highlighting the ribs and the wing spar.

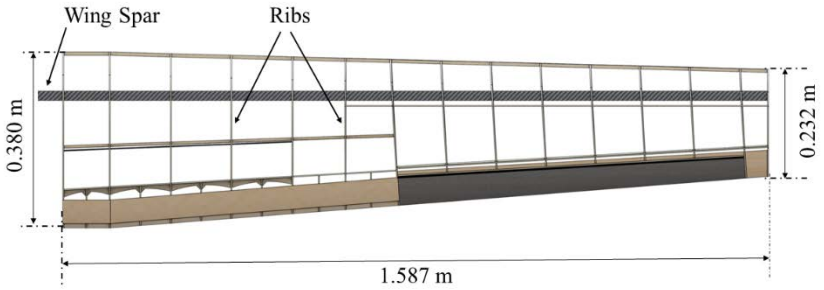

Figure 1: Wing layout

In order to relieve weight, the wing is made of thin plywood and balsa ribs covered with a tape skin. Ribs are just secondary structures, responsible for transferring load to the spar, which should be designed to withstand the aerodynamic loads.

2.2 Aerodynamic Loads

Aerodynamic forces should be estimated before wing design. XFLR5 was used to simulate important data of the 3D wing, as well as, lift and twisting moment loads along the wingspan. Distributed loads are calculated using the MTOW, however, during a maneuver those forces should be exceeded by a limited load factor n_{lim}, which represents the ratio between the aerodynamic force and the weight of the airplane. Miranda [5] recommends a maximum positive n_{lim} factor of 2.5 and a minimum negative of -1.0, for unmanned aircrafts. For design and analysis, the ultimate load factor n_{ult} is considered with a safety factor of 1.5.

$$n_{ult} = 1.5 \times n_{lim} \tag{1}$$

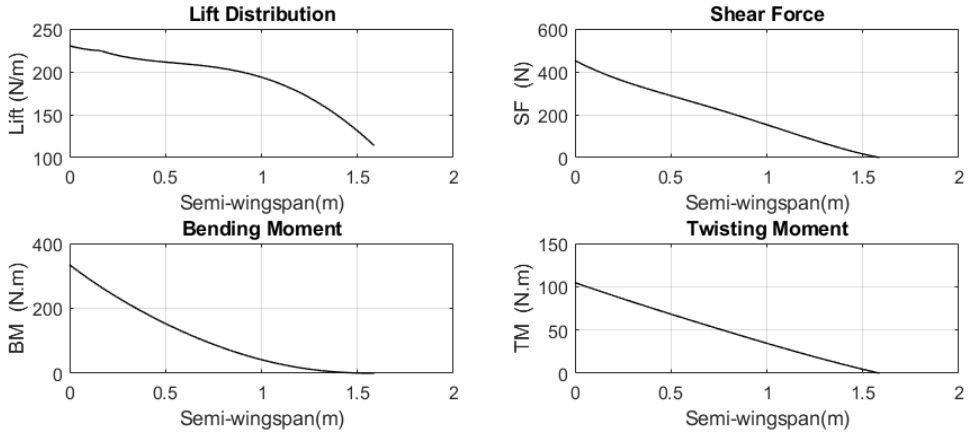

Figure 2: Wing Loads

2.3 Cross-section Design

The lift distribution along the wingspan is the most relevant load causing a large bending moment on the spar. To design an efficient spar, the cross-section should be chosen carefully, to maximize its moment of inertia. Because of the lay-up technology available in the laboratory, a cross-section geometry that could be manufactured using vacuum bagging technique was selected. Figure 3 shows a wing rib and the space available to the spar.

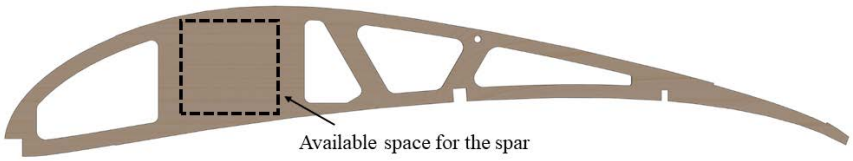

Figure 3: Wing rib

Aiming at maximizing spar strength, three feasible thin-wall cross-section geometries, depicted in Figure 4, are compared: circular, rectangular and I-shaped. For comparison purposes, all of the analyzed geometries have a unitary area (A = 1 a.u.^{2}), the same thickness (t = 0.0806 a.u.) and height (h = 4.0299 a.u.). The height of the circular cross-section is equal to its diameter, so d = 4.0299 a.u.. For maintaining the area equal to 1 a.u.^{2}, the width of the rectangular and I-shaped cross-sections were defined as b_r = 2.3349 a.u. and b_t = 4.2692 a.u., respectively. Table 1 presents the comparison between the torsion constants and moments of inertia of the cross-section geometries highlighted in Figure 4.

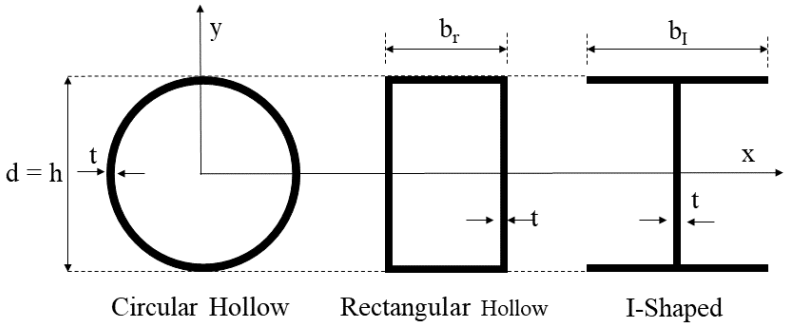

Figure 4: Cross-section shapes

Table 1: Cross-section comparison

	Symbol	Circular	Rectangular	I-shaped
Torsion Constant	K	3.9009	2.2423	0.0022
Moment of Inertia	I_{xx}	1.9505	24.000	23.284

Table 1 shows that the circular hollow cross-section is better to withstand twisting moments, because of its higher torsion constant. However, the rectangular thin-wall cross-section has a higher moment of inertia along the X-direction, almost 12 times larger than the circular section. Considering that the spar should resist bending moments rather than torsion moments, the rectangular thin-wall cross-section is chosen.

3. MATERIAL SELECTION

A high strength lightweight material should be chosen to the wing spar, considering the aerodynamic loads, calculated in section 2.2, and the cross-section geometry selected in section 2.3. Table 2 shows the comparison between an aerospace isotropic aluminum alloy, 7075-T7451

[6], with three polymer matrix composite materials: CFRP (Carbon Fiber Reinforced Polymer), GFRP (Glass Fiber Reinforced Polymer) and KFRP (Kevlar Fiber Reinforced Polymer) [7]. As carbon, glass and kevlar reinforced polymers are used in thin-wall structures, their properties are evaluated for plane stress state [8]. These materials are orthotropic and woven in orthogonal directions, which implies equal mechanical properties along the fibers directions.

Table 2: Mechanical properties of the analyzed materials

	Symbol	Unit	CFRP	GFRP	KFRP	7075-T7451
Ult. Tensile Strength 0°/90°	X_t/ Y_t	MPa	600	440	480	524
Ult. Comp. Strength 0°/90°	X_c/ Y_c	MPa	570	425	190	524
Young's Modulus 0°/90°	E_1/E_2	GPa	70	25	30	71.7
Ult. In-Plane Shear Stren.	S	MPa	90	40	50	303
In-Plane shear modulus	G_{12}	GPa	5	4	5	26.9
Major Poisson's Ratio	ν_{12}		0.10	0.20	0.20	0.33
Density	ρ	kg/m^3	1600	1900	1400	2830
Comp. Strength/Density	r	MNm/kg	0.356	0.224	0.136	0.185

An interesting parameter to choose a material for high structural efficiency is the ratio between strength and density. As shown in Table 2, CFRP has the largest ratio, besides, it has almost the same Young's Modulus of the aluminum alloy. These aspects lead to the selection of the CFRP to compose the UAV spar. To prevent the laminate from bucking, a high-density foam is used as a core. It also facilitates the manufacturing process, because the laminate can be laid-up directly on the core. Divinycell H45 foam is chosen due to its machinability, mechanical properties and low weight. Table 3 shows its main mechanical properties.

Table 3: Mechanical properties of the core material

	Symbol	Unit	H45
Ult. Tensile Strength	X_t	MPa	1.4
Ult. Comp. Strength	X_c	MPa	0.6
Young's Modulus	E	MPa	50
Ult. In-Plane Shear Stren.	S	MPa	0.56
In-Plane shear modulus	G_{12}	MPa	15
Density	ρ	kg/m^3	1600

4. STRUCTURAL SIZING

As the lift forces generate a bending moment on the wing, it is important to minimize bending stress. Consequently, the cross-section height should be as high as possible, without compromising each rib strength, maximizing the moment of inertia. As rib maximum thickness varies along the

wingspan, the cross-section height of the spar should also be variable. Figure 5 represents the typical cross-section of the composite spar, made of two materials: CFRP, and a high-density foam, H45, as described in section 3. The wing spar flanges are made of *2n* CFRP layers, while webs have only *n* layers, it designedly occurs because of the lay-up method that will be detailed later section 6.

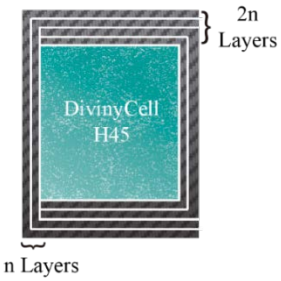

Figure 5: CFRP layers and core

A methodology was created in order to determine the number of layers *n*. All aerodynamic loads considered are used as inputs, the spar is discretized into various sections, and bending and torsional moments are calculated for each correspondent section. Initially, the algorithm considers *n* equal to one ply, then, tensile, compressive and shear stress are evaluated for both materials. Next, the Tsai-Wu criterion is used in each critical zone to evaluate laminate failure [8-9]. In case of failure in one of the materials, another ply is added and *n* increases in one unit. Then, all stresses are calculated again and the failure reevaluated. The process continues until it converges in all of the analyzed wing sections. The result is a file containing the number of plies required for each section, and the length of each ply along the spar to be used in the lay-up. The number of plies varies from 1 to 3, along the webs of the designed wing spar. The first ply has 3.176 m length, the second 1.700 m and the third 0.186 m. Consequently, it should be noted that the number of plies varies from 2 to 6 along the flanges, since there are two plies in the flanges for each ply in the webs. Some assumptions are: composites are macroscopically homogeneous and orthotropic, linearly elastic, initially stress free, free of voids and complete bonding at interfaces. Loads of each material are calculated assuming the same deflection, for bending and twisting, according to (2) and (3), respectively. Analytical formulas and equations for bending stress, shear stress and torsion constant are used [10-11]. Figure 6 shows the compressive and shear stress in CFRP and H45, along the semi-wing span.

$$BM_{CFRP} = \frac{BM\ E_{CFRP}\ I_{CFRP}}{(E_{CFRP}I_{CFRP} + E_{H45}I_{H45})} \tag{2}$$

$$TM_{CFRP} = \frac{TM\ G_{CFRP}\ K_{CFRP}}{(G_{CFRP}K_{CFRP} + G_{H45}K_{H45})} \tag{3}$$

where: BM is the bending moment, TM is the twisting moment, E is the Young's modulus, I is the moment of inertia, G is the shear modulus and K is the torsion constant.

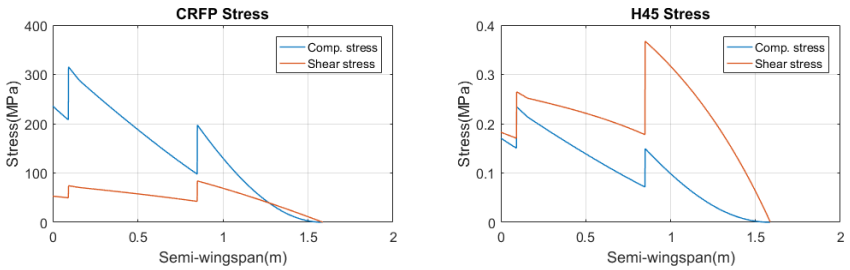

Figure 6: CFRP and H45 critical zone stress

5. MANUFACTURING

A vacuum bagging lay-up technique is used to manufacture CFRP. The propose process aims at maximizing the moment of inertia, by increasing the number of layers in the flanges, which is possible by splitting the process into two parts. Fist, the lay-up is made on one side of the core, resulting in a C-shaped CFRP laminate with *n* layers. After trimming, the core is rotated and the carbon woven is laid-up on the other side, producing another C-shaped laminate with an overlap of *2n* layers in the flanges, and only *n* layers in the web.

Since the wing spar is manufactured for a unique UAV, the lay-up is made directly on the core, because this procedure eliminates the machining of hard material molds. The core is machined from a 20 mm wide plate, since it has more machinability than MDF or aluminum, saving CNC (Computer Numerical Control) machine usage time. A mold overhang of 3 mm is cut on a laser CNC machine, preventing the carbon fabric fillet from removing material from flanges area, as depicted in Figure 7.

During the lay-up, an epoxy resin of the same weight of carbon fiber is mixed to wet the fabric. Besides, a breather and a release film are used between the vacuum bag and the fabric to absorb excess of epoxy. The result of this process is a 0.25 mm ply with approximately 35% of epoxy resin and 65% of carbon fiber in weight, at a vacuum of -600 mmHg. Figure 7 shows the first step of the lay-up procedure.

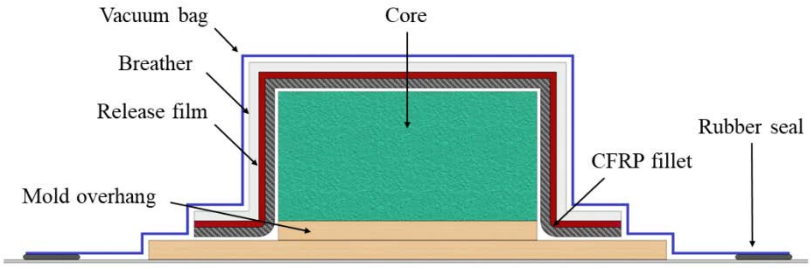

Figure 7: Vacuum bagging draft

6. CONCLUSIONS

Polymer matrix composites are widely used in modern aviation industry due to their high strength-to-weight and stiffness-to-weight ratios. In this paper, authors present the procedure to obtain a wing spar for a fixed wing UAV, with optimized mechanical properties. The proposed technique allowed the fabrication of a lightweight composite wing spar based on a high-density foam core reinforced with carbon fiber layers.

The wing design process was performed taking into account the optimization of the flight score, according to the rules established in the SAE Brazil 2016 Aero Design competition. The process involves the airfoil selection, the definition of the wing type and of its main dimensions. Besides, the aerodynamic loads were calculated along the wing span, such as: lift distribution, shear force, bending and torsional moments. A rectangular cross-section geometry was chosen for the wing spar aiming at maximizing spar strength, because it provides the highest moment of inertia among the analyzed cross sections.

The selection of the materials used in the wing spar lead to the comparison of the mechanical properties of an aerospace aluminum alloy, 7075-T7451, and three polymer matrix composite materials: CFRP, GFRP and KFRP. CFRP was selected due to its high strength-to-density ratio. Besides, a high-density foam was used as core to prevent the laminate from bucking.

The proposed methodology used to determine the optimal number of CFRP layers considers the aerodynamic loads and the Tsai-Wu criterion to evaluate laminate failure. The analytical calculations of the CFRP an H45 stress are presented along the wing span. The manufacturing process of the wing spar is also described.

The wing spar described in this work was used in the AeroRio's aircraft during the SAE Brazil 2016 Aero Design competition, where the team reached the second place of the Advanced Class.

ACKNOWLEDGEMENTS

Authors thank CNPQ and FAPERJ for financial support to the development of this work.

REFERENCES

[1] Jin-Ki, P., Amrita, D. and Jong-Hwa, P., 'Application trend of unmanned aerial vehicle (UAV) image in agricultural sector: Review and proposal', *Korean Journal of Agricultural Science* **42** (3) (2015) 269-276.

[2] Zhang, C. and Kovacs, J.M., 'The application of small unmanned aerial systems for precision agriculture: a review', *Precision Agriculture* **13** (6) (2012) 693-712.

[3] Gatteschi, V., Lamberti, F., Paravati, G., Sanna, A., Demartini, C., Lisanti, A. and Venezia, G., 'New frontiers of delivery services using drones; A prototype system exploiting a quadcopter for autonomous drug shipments', Proceedings of the 39th IEEE Annual Computer Software and Applications Conference (COMPSAC), 2015, vol. 2, 920-927.

[4] Shukla, A. and Karki, H. 'Application of robotics in offshore oil and gas industry— A review Part II', *Robotics and Autonomous Systems* **75** (2016) 508–524.

[5] Rodrigues, L.E.M.J., 'Fundamentos da Engenharia Aeronáutica – Aplicações ao Projeto SAE-AeroDesign', 1st Edn (Salto, São Paulo, 2014).

[6] Prasad, N.E. and Wanhill, R.J.H., 'Aerospace Materials and Material Technologies', 1st Edn (Springer, Singapore, 2017).

[7] Performance Composites. (Accessed on May, 2018) Available from http://www.performance-composites.com/carbonfibre/mechanicalproperties_2.asp .

[8] Christos, K., 'Design and analysis of composite structures: With applications to aerospace structures', 2nd Edn (Wiley, United Kingdom, 2013).

[9] Gdoutos, E. E., Daniel, I.M., 'Failure Mechanisms of Composite Sandwich Structures', *Proceedings of the Academy of Athens* **84** (2009).

[10] Gere, J.M. and Goodno, B.J., 'Mechanics of Materials' 9th Edn (Cengage Learning, USA, 2017).

[11] Young, W.C., Budynas, R.G. and Sadegh A., 'Roark's formulas for stress and strain.' 8th Edn (McGraw-Hill, New York, 2011).

10. LIGNOCELULOSIC AND GREEN COMPOSITES

MECHANICAL CHARACTERIZATION OF PINEAPPLE LEAF FIBER REINFORCED EPOXY COMPOSITES FILLED WITH CORN HUSK POWDER

M.Omkumar (1) and K. Selvakumar (2)

(1) Associate Professor, Department of Manufacturing Engineering, College of Engineering Guindy, Anna University, Chennai, Tamilnadu, India – 600 025. omkumar2000@gmail.com

(2) Research Scholar, Department of Manufacturing Engineering, College of Engineering Guindy, Anna University, Chennai, Tamilnadu, India – 600 025. selvaanr@gmail.com

https://doi.org/10.21452/bccm4.2018.10.01

Abstract

Composites are lightweight, fatigue resistant, easily moldable materials that are attractive alternative to metals in various engineering applications. Composites have the ability to meet diverse design requirements with significant weight reduction of parts yet offering high strength to weight ratio as compared to conventional materials. The need of new materials for applications demanding lighter construction materials, automobile parts and seismic resistant structures has motivated the use of advanced composite materials that can not only be an advantage in decreasing the dead weight but also in absorbing the impact load and vibration. Further, the reduction in weight of vehicle results in decrease in dead weight of the engine ensuring less power requirement and thereby lowering the fuel consumption. Natural fiber based composites are under intensive study due to their light weight, eco friendly nature and unique properties. Due to the continuous supply, ease of handling, safety and biodegradability, natural fibers are considered as better alternatives in replacing many structural and non structural components. Although natural fibers exhibit admirable physical and mechanical properties, the composites fabricated using natural fibers are found to vary in their properties with respect to the plant source, species, geography, and henceforth. Corn Husk Powder (CHP) and Pineapple Leaf Fiber (PALF) can be a new source of raw material to the industries and can be potential replacement of the expensive and nonrenewable synthetic fiber. In the present work, three different composites were fabricated with bidirectional PALF mat as the reinforcement material, corn husk powder as the filler material and epoxy as the matrix material by changing weight fraction of reinforcement and filler (10:20, 15:15 and 20:10 % of PALF and CHP respectively). PALF were subjected to alkali treatment for improving adhesion properties with matrix material. Composites were prepared using hand layup technique by maintaining constant fiber and matrix volume fraction. The samples of the composites thus fabricated were subjected to tensile, flexural and impact tests for finding the effect of corn husk powder in different concentrations. Tensile fractured surfaces of composites were analyzed for

determining bonding ability of fiber with matrix using Video Measuring System (VMS). The test results showed that the Tensile properties of composite B (15%PALF & 15% CHP) and Composite C (20%PALF & 10% CHP) reached the maximum tensile strength than composite A (10%PALF & 20% CHP). Composite C is found to have a maximum flexural strength of 76.26 MPa. The maximum impact strength of 1.96 joules is obtained for the sample C composite material. From the results, composite with more PALF showed maximum mechanical properties than composite with more corn husk powder. Microstructural image from VMS showed fiber pull out and internal cracks in the broken surface of the tensile test specimen of composite A.

Keywords: Pineapple Leaf Fiber (PALF), Corn Husk Powder (CHP), Epoxy, Mechanical Properties. Natural composites

1. INTRODUCTION

For the past few decades, Fiber Reinforced Composites (FRC) have found wide usage in advanced applications with its market growing continuously. It is known that the addition of fibers to polymers has several advantages, especially in increasing the mechanical properties of the composites. Synthetic fibers such as carbon/glass are reinforced in polymers to be used in high performance applications such as automobiles and aircraft industries. The performance of these composites has been improved continuously through rigorous research, often through mixing of two or more reinforcements/polymers or fillers. However, these high-performance composites are mostly of non bio-degradable nature posing serious threat to the environment[1]. It is interesting to note that natural fibers are abundantly available in developing countries like India, Malaysia, Philippines, Korea and Indonesia but is not optimally utilized. Plant fibers are nowadays exploited as reinforcement materials owing to their low cost, fairly good mechanical properties, high specific strength, non-abrasiveness, availability, eco-friendly and bio-degradability characteristics [2, 3]. Hybrid composites provide combination of material properties of those individual fibers and the reinforcement used. Carlos et al. [4] described the chemical composition, physical characteristics, thermal resistance, mechanical properties, crystallinity index and morphology of corn husk residue. As per the results, corn husk has low lignin content and equivalent amount of hemi cellulose and α-cellulose to those of the other fibers considered. In addition, the corn husk biomass showed better tensile property than piassava palm fiber and coir. The crystallinity index of corn husk is 21-26% and a large number of micro fibrils are present in its structure [4]. This increases the transfer of stress between the fiber and the matrix interface region. Nazire et al. [5] evaluated the effects of extraction process parameters on the physical properties, mechanical properties and thermal durability of corn husk fiber. The samples provided good tensile Strength that were obtained from 5-10g/L NaOH treatment for 60-90 min. Alkalization under harsher conditions results in higher thermal durability up to 320ºC with higher cellulose fraction, but lower durability above this temperature. The Fourier transform infrared spectrum analysis proves the presence of higher cellulose content but lower hemicelluloses and lignin with harsher treatment conditions. Yaning et al. [6] determined the physical properties (moisture content, particle size, bulk density and porosity) of corn cobs, leaves and stalks and analyzed the suitability for reinforcement. A positive relationship between the average particle size and porosity was observed for the corn residues. From this study it was concluded that the corn residues (cobs, leaves and stalks) observed to be suitable as reinforcement in composite. Nasmi Sari et al. [7] developed composites with 1%, 2%, 5%, and 8% NaOH treated corn husk fiber and found that the tensile properties of the treated composite panels were better than those of raw fiber composite panels. Khwanthi et al. [8] analyzed suitability of corn husk fiber and fiber glass for insulation material considering cost and

performance. Results indicated that corn husk was found to be technically and financially more suitable insulating material than fiber glass.

Kloykam et al. [9] investigated the compatibility and composite properties of alkaline and silane treated pineapple leaf fiber and polyamide 6 composites. Effect of fiber surface treatment and fiber loading on the properties of the composites was investigated. The thermal characteristics of the composites have not been affected by PALF types. From the results, it was found that alkali treatment is sufficient to improve compatibility and properties of the PALF/polyamide 6 composites at fiber loading of 30% wt. Madhukiran et al. [10] carried out an investigation on the flexural properties of banana and pineapple fiber reinforced composites (0/40, 15/25, 20/20, 25/15, and 40/0 Weight fraction ratios of banana and pineapple respectively). The hybridization of the reinforcement in the composite shows greater flexural strength, when compared to individual type of natural fibers reinforced composites. Epoxy resins are being widely used in many of the advanced composites due to their excellent adhesion to wide variety of fibers, and high performance at elevated temperatures [111]. Abdul et al. [12] fabricated the composites with bamboo fiber reinforced with the different polymeric resins, such as, polyester, epoxy, phenolic, polypropylene, Poly Vinyl Chloride and polystyrene. Tensile and flexural properties showed a maximum for composite with epoxy resin when compared to the other polymeric resins. Pickering et al. [13] reported that the tensile strength and young's modulus of the flax fiber reinforced epoxy composites to be 136 MPa and 10.5 GPa respectively. This Shows the effect of the epoxy resin on the fiber involved. Arunkumar et al. [14] fabricated the composite with glass fiber, filled with rice husk in epoxy matrix and investigated the mechanical properties and erosion wear response of these composites and made a comparison between the unfilled and filled samples. Results found to be better in rice husk filled composite due to increased bonding ability between fiber and matrix was achieved during fabrication. Haameem et al. [15] characterized the mechanical properties of NaOH treated Napier grass fiber reinforced composites. 10% alkali-treated Napier grass fibers yielded the highest tensile strength than other concentrations. The maximum tensile and flexural strengths of the composites were obtained at 25% fiber loading. In general, up to a certain value of volume fraction, the mechanical properties of the composites increased as the fiber volume fractions increases, following which, there was a reduction in properties.

The present work focuses on fabricating composite with pineapple leaf fiber and corn husk powder as the reinforcement and epoxy as the matrix material. Pineapple leaf fibers treated with 2 5 NaOH and corn husk powder with a size of approximately 75 microns were used at a fiber percentage of 10:20, 15:15 and 20:10 % by volume. Characterizing the fabricated cellulose fiber reinforced polymer composite has been attempted by testing tensile, flexural and Impact strength to determine the effect of corn husk powder when increasing filler percentage.

2. MATERIALS AND METHODS

The materials used for fabricating the composites and the methodology involved are discussed in detail as follows.

2.1 Raw Materials Used

Pineapple leaf fibers (PALF) in mat form and Corn husk in powder form were used as the reinforcement material. Corn husk (outer leaf) was collected from local market. Pineapple leaf fiber (PALF) was purchased in the length of 20 – 30 mm. The Matrix material used for the present work, Epoxy Ly 556 and corresponding hardener HY951 were purchased from Javanthee

Enterprises, Chennai, India. The physical properties of the raw materials used for the present work is shown in Table 1.

Table.1 : Physical Properties of Epoxy Resin [10, 16]

Sl. No	Properties	Epoxy	PALF	Corn Husk
1	Density, g/cm³	1.1-.14	1.44	1.12 – 1.32
2	Tensile Strength, Mpa	35-100	413-1627	140-450
3	Elastic Modulus, Gpa	3-6	60-82	45-70
4	Elongation , %	1-6	1.6-4	1.1-3
5	Water Absorption (24 Hrs in %)	0.1-0.4	11-12	12-14

2.2 Composite Fabrication

Corn husk was dried in sunlight for three days and then manually chopped into short fibers. Alkali treatment (NaOH) of corn husk fibers was carried for an hour with 2g/l of NaOH in distilled water. The treated fibers were dried in sunlight for two days, hammered and sieved in 75 micron sieve to get fine powder of corn husk. Pineapple leaf fiber (PALF) procured in the form of strands was made into a bidirectional mat of size 300 x 300 x 5mm. Hand lay-up technique was used for fabrication of composites. Composite were fabricated using the mould made of silicon rubber. The cast of each composite was cured under a load of about 50 kg for 24 hours before it was removed from the mould. Three different composites were fabricated by maintaining constant fiber matrix weight fraction (30:70 % of fiber and matrix respectively). The weight fraction and fiber composition used are shown in Table 2.

Table.2 : Weight Fraction of PALF and CHP in Each Composite

S.No	Composite Designation	Weight Fraction Distribution (%)			Total Weight of composite (g)	Weight of PALF mat (g)	Weight of corn husk powder (g)
		PALF	CHP	Epoxy			
1.	A	10	20	70	589.5	88	88
2.	B	15	15	70	595.8	59	118
3.	C	20	10	70	588.08	118	59

2.3 Mechanical Testing of composites

Test Samples were prepared according to ASTM standard using vertical zigzag cutting machine. For average values three samples per composite were prepared. Experiments to find the mechanical properties such as tensile, flexural and double shear strength were found by tensile test (ASTM D638), and Flexural test (ASTM D790) conducted on universal testing machine. Impact energy was determined by performing Izod impact test (ASTM D256). Finally Video Measuring

System (VMS) was used for analyzing the internal bonding between fiber and matrix and the microstructure of fractured surfaces.

3. RESULTS AND DISCUSSION

3.1. Tensile Strength

The results indicated that the sample C (20% PALF and 10% CHP) specimen gives better tensile strength than the other two composite A (10% PALF and 20% CHP) and composite B (15% PALF and 15% CHP). The addition of more amount of CHP shows comparatively low tensile strength than the other composites considered. The addition of corn husk powder (amorphous in nature) reduced the tensile strength which continuously decreased with increasing filler content (Figure 1). The reduction in tensile strength could be due to filler-filler interaction, which becomes more pronounced than that of the filler-matrix interactions [17].

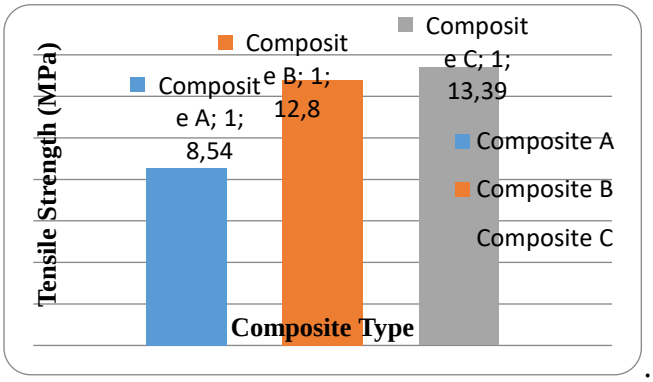

Figure 1: Average Tensile strengths of PALF - CHP/Epoxy composite

It is evident from the table 3 that the elongation at breaking strength decreases with increasing filler loading. Reduction of elongation at breaking point is common since, weak interfacial bonds due to poor filler/Epoxy interaction facilitated crack propagation and thus composites fracture at lower value of elongation was observed with increasing filler content [18].

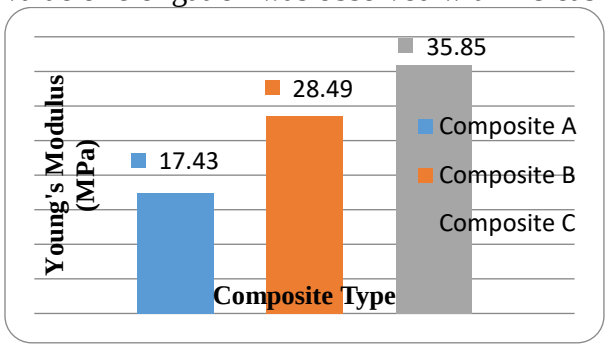

Figure 2: Average Young's Modulus of PALF - CHP /Epoxy composite

The Young's modulus of composites increase with increase in filler content (shown in figure 2).The presence of fillers hindered the polymer chain mobility of epoxy matrix, in addition to the stiffness of the composite [19]. The rigidity of the composite could also be linked to the cellulose contents of the peanut husk fillers. The increase in Young's modulus with filler content was in agreement with other reported works [20, 21].

3.2. Flexural Strength

The maximum average flexural strength (76.26MPa) was observed in Composite C (20% PALF -10%CHP). The result indicated that the displacement increases with the increase in applied load up to around 302.6 N, after which it tends to decrease and break. The maximum average displacement observed was 2.25 mm. Flexural strength of composite A

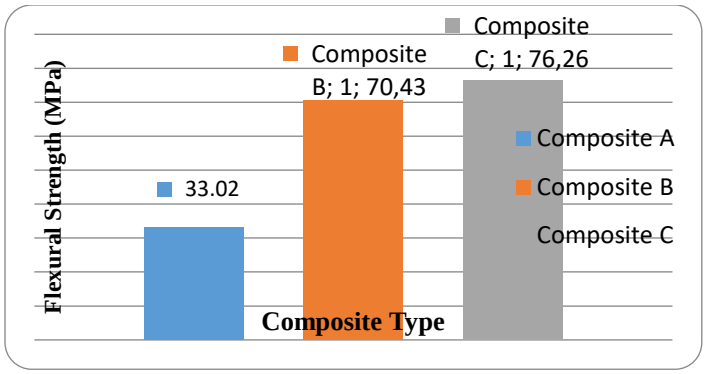

Figure 3: Average Flexural of PALF - CHP /Epoxy composite

and composite B was 33.04 MPa and 70.43 MPa respectively. When increasing corn husk powder to 20% by volume, flexural strength was decreased up to 130%. This result agrees with the findings of many researchers who have used natural fillers with polymers; Henry [17] observed an appreciable increase in the flexural strength of the composite when increasing fiber content with low filler material. This is because of well formed interface that allows better stress transfer from the matrix to the fiber [22].

Table.3 : Average Values of mechanical properties of each composites

Properties	Composite A	Composite B	Composite C
Tensile properties(MPa)	8.54	12.80	13.39
Elongation at Max (%)	49	44.92	37.35
Young's Modulus (MPa)	17.43	28.49	35.85
Flexural Strength (MPa)	33.02	70.43	76.26
Impact Energy (J)	1.86	2.53	2.97

3.3. Impact Energy

The mean of the maximum of the tensile, flexural and impact strengths of different specimen tested are tabulated in the table 3. The results indicated that the maximum impact strength was obtained for the composite C (shown in the Figure 4). Impact strength was decreased when corn husk filler content in composite increases. The decrease in impact strength indicates that the amount of matrix is probably not sufficient to transfer the stress effectively during a sudden

impact in combination with the lower absorption characteristic of the filler [23]. It has been observed that high filler content increases the chances of fiber agglomeration, which results in regions of stress concentration requiring less energy for crack propagation [24]. The impact strength of fiber filled polymer composites depends on the nature of the filler, the polymer, and fiber matrix interfacial bonding [3, 17 and 19].

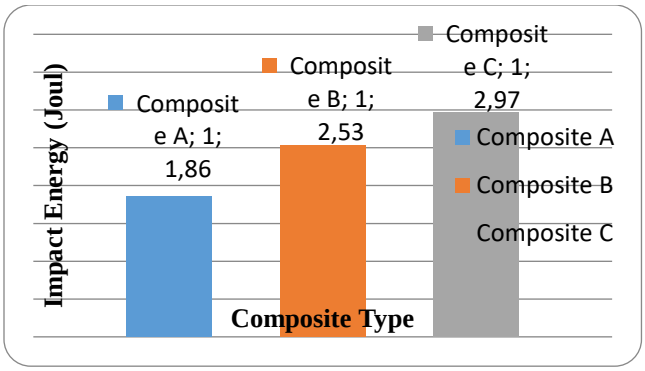

Figure 4: Average Impact Energy of PALF - CHP /Epoxy composite

3.4. Microstructure Analysis

In order to determine the factors affecting the tensile properties of PALF-CHP/epoxy composites, tensile fractured surfaces were analyzed using Video Measuring System (VMS). Figure 5 shows fractured surface of the composite B which depicts the breakage of pineapple leaf fiber at certain points due to tension but not pull out indicating good bonding nature with the matrix. The formation of grooves roughens the fiber surface, thus increasing the interfacial bonding between fiber and matrix by interlocking mechanism. Similar mechanisms

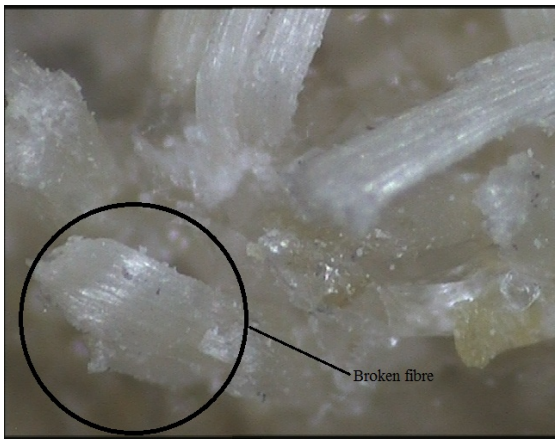

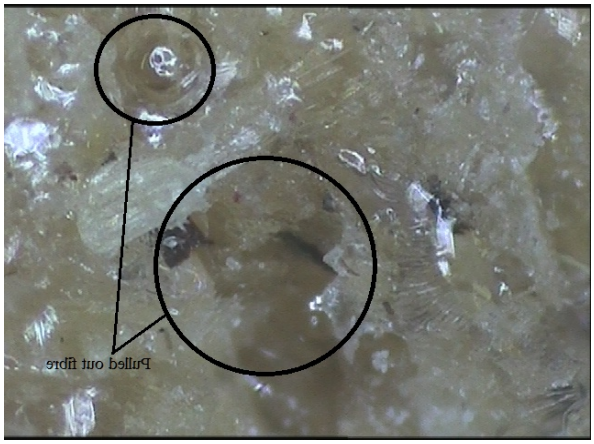

Figure 5 : Fractured surface of sample B **Figure 6: Fractured surface of sample A**

were due to interlocking as observed in our previous research works [25-28]. Figure 6 shows fractured surface of the composite A which is due to fiber pull indicating the weak bonding of fiber with the matrix. Poor interfacial adhesion results because of relatively ineffective force transfer between the matrix and the fiber. This results in poor mechanical properties that are inferred from the tensile and flexural test results.

4. CONCLUSION

This work has shown the fabrication of the pineapple leaf fiber reinforced epoxy composites filled with corn husk powder using hand lay-up technique. Composites were fabricated with three different fiber and filler volume fraction (10:20, 15:15, and 20:70 ratio of PALF/CHP respectively). Mechanical properties such as the tensile, flexural and Impact strength were determined. The results indicated that the composite B (15% PALF and 15% CHP) showed the maximum tensile strength and can hold the strength up to 13.29 MPa. The results indicate that the composite C (20% PALF and 10% CHP) gives better tensile strength than the other two composite samples . Adding corn husk powder with fiber reduces the tensile strength which continuously decreased with increasing filler content. The elongation at breaking strength decreases with increase in the filler content in the composite . At higher filler content, a drastic reduction of elongation at breaking strength was observed due to poor filler/Epoxy interaction facilitated crack propagation and thus composites fracture at lower value of elongation was obtained with increasing filler content. The maximum average flexural strength (76.26MPa) was observed in Composite C (20% PALF and10%CHP). When increasing corn husk powder to 20%, flexural strength was decreased up to 130%. Increase in the flexural strength of the composite with higher fiber content and low filler material is because of well formed interfacing that allows better stress transfer from the matrix to the fiber. From impact test results, the maximum impact strength was obtained for the composite C. The impact strength was found to decrease when corn husk filler content in composite increases. The decrease in impact strength indicates that the amount of matrix is probably not sufficient to transfer the stress effectively during sudden impact. This is also attributed in combination with the lower absorption characteristic of the filler. From the results, composite with higher fiber content and lower filler content showed better mechanical properties. Presence of more fiber content in composite ensures the stress transfer at the interface between the fiber and the matrix thus providing better mechanical properties of the composites.

REFERENCES

[1] Wambua P, Ivens J and Verpoest I,. “Natural fibres: can they replace glass in fibre reinforced plastics?” Composite Sciene and Technology., Volume 63, Issue 9, 2003, pp.1259-1264.

[2] Furqan Ahmad, Heung Soap Choi and Myung Kyun Park, “A Review: Natural Fiber Composites Selection in View of Mechanical, Light Weight, and Economic Properties” Macromolecular Materials and Engineering, Vol 300, Issue 1, 2015, pp. 10–24.

[3] Hoi-yan Cheung, Mei-po Ho, Kin-tak Lau, Francisco Cardona and David Hui, “Natural fibre-reinforced composites for bioengineering and environmental engineering applications”, Composites: Part B, Vol 40, 2009, pp 655–663.

[4] Carlos Augusto De Carvalho Mendes, Fernando Antônio De Oliveira Adnet, Márcia Christina Amorim Moreira Leite,Cristina RussiGuimarães Furtado and Ana Maria Furtado De Sousa, “Chemical, Physical, Mechanical, Thermal And Morphological Characterization Of Corn Husk Residue”.

[5] NazireDenizYilmaz,“Effect of chemical extraction parameters on corn husk fibers characteristics”, International Journal of Renewable Energy, January – June 2015, Volume – 10, No. 1.

[6] Yaning Zhang, A. E. Ghaly and Bingxi Li, “Physical Properties of Corn Residues”, American Journal of Biochemistry and Biotechnology, (2012), Volume – 8 (2), pp. 44 – 53, ISSN: 1553.

[7] NasmiHerlina Sari, I. N. G. Wardana, Yudy Surya Irawan and EkoSiswanto, "Physical and Acoustical Properties of Corn Husk Fiber Panels",Hindawi Publishing Corporation, Advances in Acoustics and Vibration, Volume – 2016, Article ID – 5971814, 8 pages.

[8] KhwanthiphaPandecha, Anan Pongtornkulpanich, SukrudeeSukchai and TawatSuriwong, "Thermal properties of corn husk fiber as insulation forflat plate solar collector", International Journal of Renewable Energy, January - June 2015, Volume – 10, No. 1

[9] KloykamolPanyasarta, NattawutChaiyuta, TaweechaiAmornsakchaib and OnumaSantawiteec,11th Eco – Energy and Materials Science and Engineering, (11th EMSES), "Effect of surface treatment on the properties of pine apple leaf fibers reinforced polyamide 6 composites",Energy Procedia, (2014), Volume – 56, pp. 406 – 413.

[10] Madhukiran. J, Dr. S. Srinivasa Rao and Madhusudan. S, "Fabrication and Testing of Natural Fiber Reinforced Hybrid Composites Banana / Pine Apple", International Journal of Modern Engineering Research (IJMER), July – August. 2013, Volume – 3, Issue. 4, pp. 2239 – 2243 ISSN: 2249 – 6645.

[11] NabiSaheb D and Jog J.P, "Natural Fiber Polymer Composites: A Review", Polymer Engineering Group, Chemical Engineering Division, National Chemical Laboratory, Pune, India 1999.

[12] Abdul Khalil H. P. S., Bhat I. U. H., Jawaid M., Zaidon A., Hermawan D. and Hadi Y. S., "Bamboo Fiber Reinforced Bio – Composites: A Review", Materials and Design, (2012), Volume – 42, pp. 353 – 368.

[13] Pickering K. L. and Tan Minh Le, "High Performance Aligned Short Natural Fiber – Epoxy Composites", Composites Part – B, (2016), Volume – 85, pp. 123 – 129.

[14] Arun Kumar Rout and AlokSatapathy, "Study on mechanical and tribo – performance of rice – husk filled glass–epoxyhybrid composites",Materials and Design, (2012), Volume – 41, pp. 131 – 141.

[15] M. Haameem J.A., M. S. Abdul Majid, M. Afendi, H. F. A. Marzuki, I. Fahmi, and A. G. Gibson, "Mechanical properties of Napier grass fibre/polyester composites",Composite Structures, (2016), Volume – 136, pp. 1–10.

[16] Nasmi Herlina Sari, I. N. G. Wardana, Yudy Surya Irawan and Eko Siswanto, "Physical and Acoustical Properties of Corn Husk Fiber Panels", Advances in Acoustics and Vibration, 2016, pp 1- 8. http://dx.doi.org/10.1155/2016/5971814

[17] Henry C. Obasi "Peanut Husk Filled Polyethylene Composites: Effects of Filler Content and Compatibilizer on Properties", Hindawi Publishing Corporation, Journal of Polymers, 2015, http://dx.doi.org/10.1155/2015/189289.

[18] Akshay N Baria and Sagar Choksi, "Wear and Friction Behaviour of Corn Husk Fiber Reinforced Polyester Composites", International Journal for Scientific Research & Development| Vol. 4, Issue 05, 2016, pp 803-806.

[19] Sudeep Deshpande and T Rangaswamy. "Effect of Fillers on E-Glass/Jute Fiber Reinforced Epoxy Composites" Int. Journal of Engineering Research and Applications, Vol. 4, Issue 8(Version 5), August 2014, pp.118-123 .

[20] K. Ajay Kumar, M.A. Mateen, N. Srinivasa and Rajneesh, "A Study on Effect of Filler on Mechanical Properties of GFRP Composites", International Journal of Innovative Research in Science, Engineering and Technology: Vol. 4, Issue 11, November 2015, pp 10669-10674.

[21] Sandhyarani Biswas, Alok Satapathy and Amar Patnaik, "Effect of Ceramic Fillers on Mechanical Properties of Bamboo Fiber Reinforced Epoxy Composites: A Comparative Study", Advanced Materials Research Vols. 123-125 (2010) pp 1031-1034

[22] AKINDAPO Jacob Olaitan, AGOV Emmanuel Terhemen, GARBA Danladi King and OGABI Rapheal Oluwatoyin, "Comparative Assessment of Mechanical Properties of Groundnut Shell and Rice Husk Reinforced Epoxy Composites, American Journal of Mechanical Engineering, 2017, Vol. 5, No. 3, 76-86.

[23] Dani. Jagadeesh, P. Sudhakara, D.W. Lee, H.S. Kim, B.S. Kim and J. I. Song, "Mechanical Properties of Corn Husk Flour/PP Bio-composites", Composite Research, Vol. 26, No. 4, 213-217 (2013) DOI: http://dx.doi.org/10.7234/composres.2013.26.4.213

[24] Vikas Dhawan, Sehijpal Singh, and Inderdeep Singh, "Effect of Natural Fillers on Mechanical Properties of GFRP Composites, Journal of Composites, 2013, http://dx.doi.org/10.1155/2013/792620.

[25] Selakumar K and Omkumar M, "Characterization of Human Hair Fiber Reinforced Polymer Composites", Proceedings of an International Conference on Recent Trends in Production Engineering (RIPE 2017): MIT, Anna University, pp 83-84, 2017.

[26] V.P.Vignesh , M. Omkumar , S. Anandakumar and K. Selvakumar, "Scope Of Sterculia Foetida in Composites", Proceedings of an International Conference on Recent Trends in Production Engineering(RIPE 2017): MIT, Anna University, pp 85-86, 2017.

[27] Selakumar K and Omkumar M, "Fabrication and Characterization of Animal Fiber Reinforced Polymer Composites", Proceedings of an International Conference on Contemporary Design and Analysis of Manufacturing and Industrial Engineering Systems (CDAMIES2018): NIT-Trichy, 2018.

[28] Selakumar K and Omkumar M, "Mechanical and Dynamic Mechanical Analysis of Jute and Human Hair Reinforced Polymer Composites", Polymer Composites: (2018), http://onlinelibrary.wiley.com/journal/10.1002/(ISSN)1548-0569. DOI:10.1002/pc.24818.

INFLUENCE OF ENVIRONMENTAL DEGRADATION IN MECHANICAL AND MICROSTRUCTURAL PERFORMANCE IN POLYMERIC COMPOSITES INCREASED BY LICURI FIBERS

Alexandre S. Moraes [(1)], Ana C. R. da Conceição [(2)], Pedro A. P. Almeida [(1)], Helen F. Sousa [(1)], Olímpio B. C. V. Neto [(1)], Mirtânia A. Leão [(1)]

(1) IFBA – Federal Institute of Education Science and Technology of Bahia, Bahia, Brazil

(2) Department of Civil Engineering, Federal University of Bahia, Brazil

https://doi.org/10.21452/bccm4.2018.10.02

Abstract

The search for new composites that use natural fibers as reinforcement has driven the study of the vegetal fibers they are renewable, biodegradable, low cost and cause low environmental impact. Licuri fiber is obtained from the leaves of the *Syagrus Coronata* palm tree and possesses sufficient malleability to be woven. However, this type of material is subject to changes in mechanical behavior as a consequence of the natural degradation, mainly to those due to moisture absorption that can cause irreversible structural damage. In this sense, the present work sought to make an analysis of the influence of moisture on the mechanical performance of a unidirectional composite laminate of polyester matrix reinforced with licuri fibers. The composite laminates were manufactured by the by hand lay-up process. Water absorption, Uniaxial tensile and Three-point bending tests were perfomed according to ASTM D 570-98, ASTM D 3039-08 and ASTM D 790-07 standards, respectively. The results obtained on tests with composite in saturated state when compared to the tests with composite in the dry state (literature data) have shown that the polyester matrix composite reinforced with natural licuri fibers has its mechanical properties reduced by around 27% when exposed to moisture, as a confirmation of the hydrophilic nature of plant fibers.

Key words: Licuri fibers, Laminate composite, Mechanical properties, Moisture absorption.

1. INTRODUCTION

The use of composites reinforced with natural fibers has increased in the last decades, due to the perspective of energy saving by reducing the weight of the components, as well as the aspects related to the recovery of the raw materials and the reuse of the materials at the end of the product life cycle [1,2].

Thus, natural fiber reinforced polymer composites have received special attention due to the

advantages of natural fibers when compared to synthetic fibers, since they are from renewable sources, have low density and low cost, are non-toxic, can be incinerated, biodegradable and mainly because they are considered sustainable [3,4].

The automobile industry has been developing research on the greater use of natural fibers in place of synthetic inputs. These fibers are already used in the manufacture of automotive parts, providing quality and well-being to the user, such as filling seats and headrests, side and door panels, instrument panel, air channel, roof coating, carton wheels and others. Among the fibers used are: sugarcane bagasse, sisal, jute, curauá and coconut fiber [5,6].

The vegetable fibers can undergo degradation due to biological agents, acidic and alkaline media, moisture absorption, ultraviolet radiation and temperature.

In the case of aging by moisture absorption the fibers reinforced by vegetable fibers, the water molecules absorbed by these fibers due to their hydrophilic nature act as plasticizers interfering in the fibers, the matrix and the interface simultaneously. Displacement at the fiber/resin interface may occur due to the development of osmotic pressure pockets on the fiber surface due to the leaching of water soluble substances from the fiber surface. In this way, the degradation of the composite occurs not only by the degradation of the individual constituents, matrix and fiber, but also due to the loss of the interaction between them [7].

The licuri fiber, originating from the *Syagrus Coronata* (Martius) Beccari palm, can be found in the vegetation of the Brazilian Caatinga. Endemic to South America and widely present in the states of Bahia and Minas Gerais [8], the licuri palm has its fruit widely used in the food and cosmetics sectors, while its fiber has more restricted application for craft purposes. More recently, the licuri fiber was studied as an alternative proposal for the reinforcement of polymer composites [9].

2. MATERIAL AND METHODS

The study material was a laminate composite with two layers of licuri unidirectional manufactured in manual loom.

The licuri fibers were passed on rolling rollers and treated with the solvent Hexano PA for a minimum period of 24 hours for removal of the natural wax fibers, in order to improve the process of impregnating the polyester resin.

The hand lay-up process was used to manufacture the composites laminates. The orthophthalic polyester resin (Novapol L120) as matrix. As a catalyst for curing the resin at room temperature, the methyl ethyl ketone solvent (MEKP) was used in the proportion of 1% of the resin volume, the curing process being at room temperature (25 °C). The weight obtained in the licuri tissue used in this work was 418.27 g/m².

The composite laminate (LCL) in its final design had the following dimensions (400x500x 4) mm, which corresponds to width, length and thickness respectively.

2.1 Water Absorption Test

To study the behaviour of water absorption of LCL laminates, water absorption test were carried out according ASTM D570-98. Composites samples were immersed in distilled water maintained at room temperature(25 °C) and at a time interval 24 hours, the samples were removed from water, dried and weighed. The weight measurement was taken periodicall for 336 hours which was after saturation in all the composites had been noticed.

Lastly, the weighings started to have intervals of two weeks, that is, of 14 days, until the difference of the increase of mass, and relation to the previous weighing was less than 1%.

2.2 Uniaxial tensile test

The uniaxial tensile test was performed according to ASTM D 3039-08 standard. Tests were performed for eight specimens fractured and five values recorded (required by standard) of the valid tests considdered. Uniaxial tensile test was conducted in the Universal Mechanical Testing Machine (DL 300 kN EMIC), with a loading speed of 1.0 mm/min and the average ambient temperature during the (25 ± 2) °C. The dimensions of LCL laminate specimens were (250x25x4) mm, respectively for length, width and thickness. The dimensions have tolerances of ±1%. The gauge length (span/greyhound) of all test specimens was 127 mm.

2.3 Three-point bending test

The three-point bending test after moisture absorption test was performed according to ASTM D 790-10 standard, being obtained for laminates proposed, the flexural strenght and flexural elastic modulus. The three-point bending test using a Universal Mechanical Testing Machine (DL 300 kN EMIC), and the loading speed of 2.0 mm/min and dimensions of the LCL laminate specimens were (100x13x4) mm and span of 80 mm. The dimensions correspond to lenght, width, and thickness, respectively. The average ambient temperature during the test was (25 ± 2) °C.

2.4 Analysis of fractures.

In order to analyze the real influence of the moisture degradation will be performed a qualitative analysis of mechanical fracture through of microscopic analysis. Optical microscopy was used the microscope Olimpus MG. For scanning electron microscopy (SEM), the microscope TECSAN, model Vega 3 LMU it was used.

3. RESULTS

3.1 Morphological evaluation

Figure 1 (a) and (b) shows the chromatic variation (photoxidation) of the surface of the specimens, before and after the moisture absorption test respectively, which is usually a first indication of the loss of the mechanical integrity of the material.

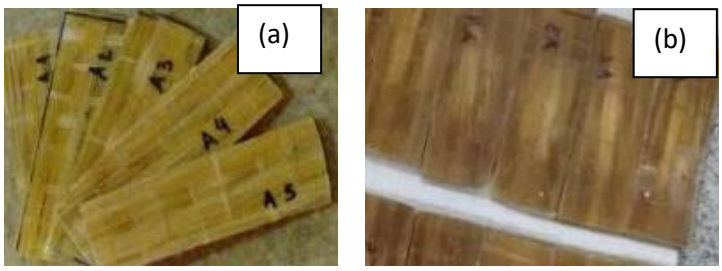

Figure 1: Chromatic variation of specimens surface. (a) before the moisture absorption test (dry); b) After the moisture absorption test.

3.2 Moisture absorption test

The mean values for mass gain of the composite due to the moisture absorption is shown graphically (Figure 2). The onset of saturation occurred at the 15th week of the test and the saturation condition at the 19th week was reached, according to ASTM D570-98 for the water absorption test for polymers. The material reached a mean mass increment of 4.97% after 336 hours of the moisture (saturation) test. According to previous studies, composites reinforced with

only natural fibers generally absorb a higher percentage than those reinforced with synthetic fibers and hybrid composites.

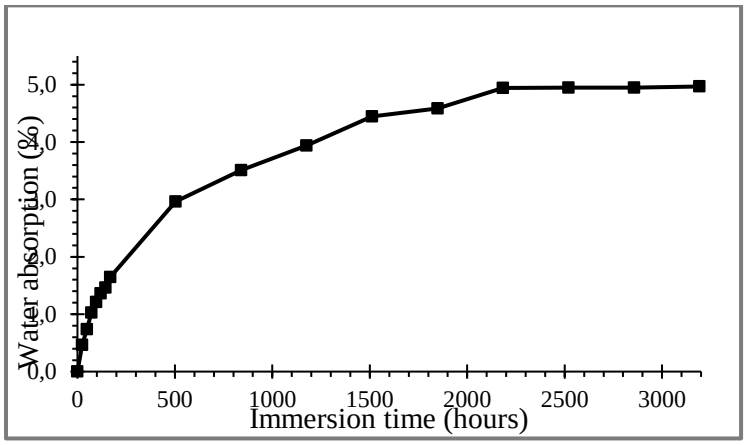

Figure 2: Water absorption *versus* Immersion time graph.

3.3 Mechanical Properties - uniaxial tensile

Mechanical behavior related to the uniaxial tensile test of LCL laminate are presented from the strees-strain diagram see Figure 3. LCL laminate has a linealy elastic behavior between the tension and the deform beginning from damage (approximately 40 % of tensile strengt) to fracture.

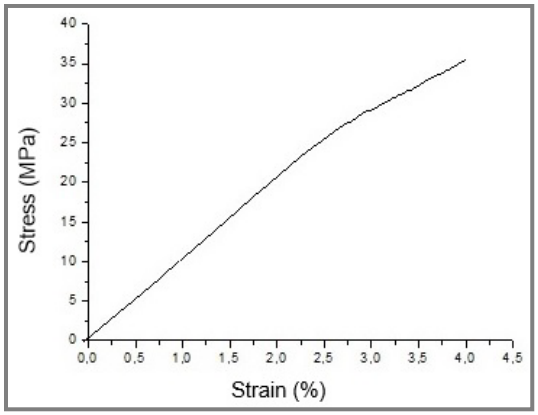

Figure 3: Stress x strain diagram – uniaxial tensile test.

Table 1 show the result of the mechanical properties (average values) and standard deviation obtained for uniaxial tensile test of LCL laminate. With respect to the modulus of elasticity value, it was calculated before the initial damage was started, in order to avoid the influence on the stiffness of the material.

Table 1: Mechanical properties – laminate LCL – uniaxial tensile.

Mechanical properties	Average
Tensile Strength (MPa)	31,39±4,3
Elastic Modulus (GPa)	0,95±0,1
Elongation (%)	3,39±0,2

3.4 Mechanical Properties of LCL Laminate – Three-Point BendingTest

Figure 4 shows the performance of the mechanical properties obtained from three-point bending test for both laminates, from the stress-flexural strain diagram. The LCL laminate has a linearly elastic behavior until the final fracture of the material.

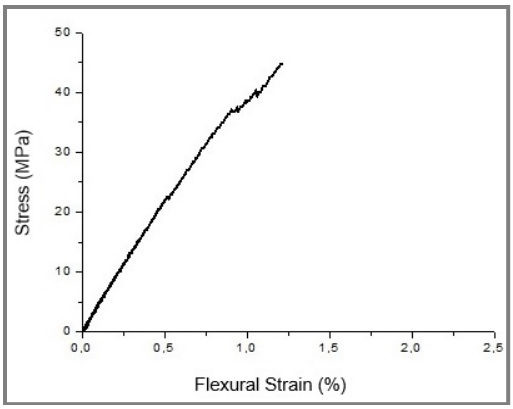

Figure 4 : Stress x Flexural Strain – three-point bending.

Table 3 it is possible to observe the synthesis of results of the mechanical properties (average values) determined at the three-point bending test as well as the values of the respective standard deviations.

Table 3: Mechanical properties – laminate LCL – Three-point bending.

Mechanical properties	Average
Flexural strength (MPa)	41,15±1,03
Flexural modulus (GPa)	3,94±0,33
Flexural strain (%)	1,31±0,04

3.5 Global Comparative diagram – Influence of moisture degradation

Figure 5 show a global view of uniaxial tensile test behavior for dry LCL laminate and wet LCL laminate. The wet LCL laminate exhibited a loss of tensile strength and a gain in elongation.

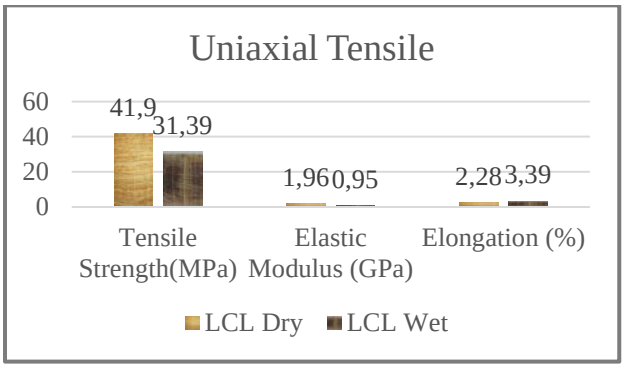

Figure 5: Global comparation – uniaxial tensile test.

Figure 6 show a global view of three-point bending test behavior for dry LCL laminate and wet LCL laminate. In relation to the moisture degradation process, the wet LCL laminate exhibited a loss of flexural strength and a gain in flexural modulus.

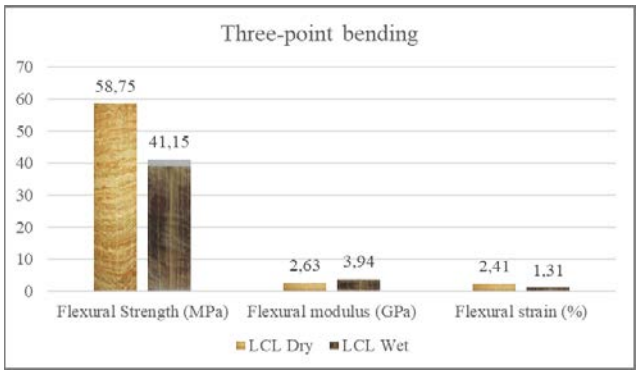

Figure 6: Global comparation – three-point bending test.

3.6 Fracture Analysis – uniaxial tensile test

The analysis of optical microscopy occurs in the fractured region (along the specimens thickness) of the LCL laminate, as shown in Figure 7. It is possible to observe cohesive fracture in the fibers, as well as, adhesive fracture in the fiber/matrix interface.

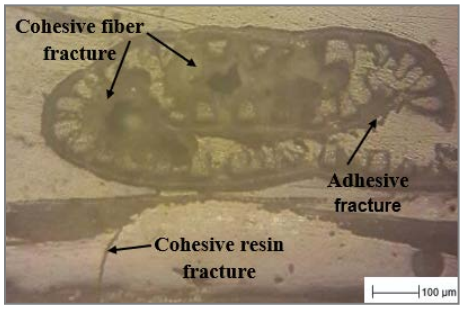

Figure 7: Fracture characteristics - LCL laminate.

By scanning electron microscopy (SEM), as shown in Figure 8, it is observed in the fracture region of the LCL laminate, the presence of cohesive fracture in the licuri fiber this type of damage tends to break the fiber longitudinally.

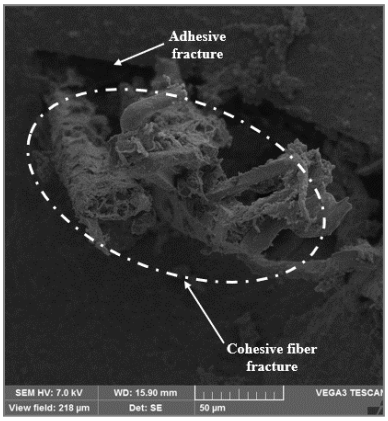

Figure 8: Fracture characteristics - LCL laminate.

3.7 Fracture Analysis – three-point bending test

Analyzing the optical microscopy of the transverse face of the sample, figure 9. It is possible to observe the presence of cohesive fracture in the matrix, where the propagation of the microcracks causes a demolding of the fiber/matrix (adhesive fracture).

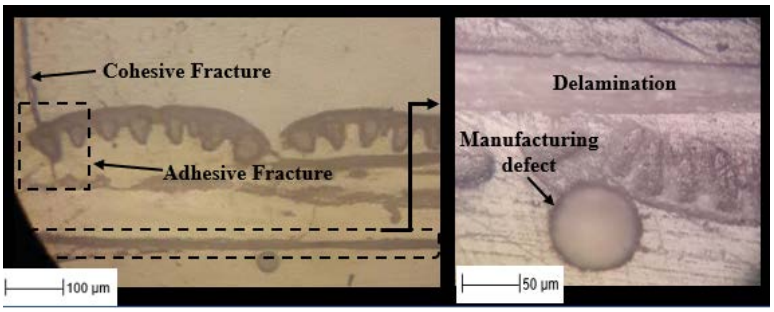

Figure 9: Fracture characteristics - LCL laminate.

In Figure 10 microscopy by SEM can be observed to delaminate, in addition to the formation of grooves in the matrix.

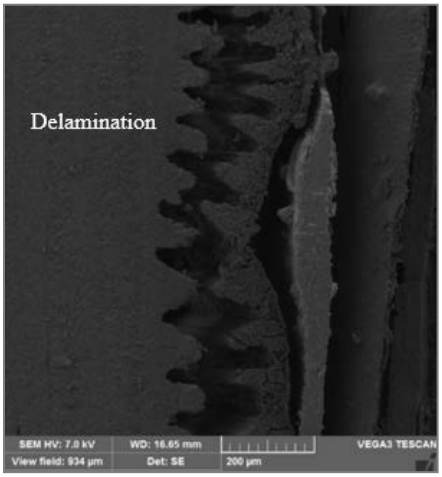

Figure 10: Fracture characteristics - LCL laminate..

4. CONCLUSIONS

- The moisture interferes in the fiber matrix adhesion and weakens the matrix, affirming the hydrophilic nature of the fibers.
- With respect to the last tensile strength property, the LCL laminate in the dry state presented superiority with respect to the LCL laminate in the saturated wet state, presenting a traction loss of approximately 25.08%, while for the Longitudinal Elasticity Modulus LCL laminate in the saturated wet state was superior, resulting in a gain of 48.68%.
- With respect to the property of Ultimate Flexural Strength and Modulus of Flexural Elasticity, the LCL laminate in the wet state presented reduction of approximately 29.96% and a gain of 49.81% respectively.
- Regarding the fractures of the LCL laminate after being submitted to the uniaxial tensile test, the fracture occurred perpendicular to the application of the load and within the useful area of the specimen.

- For the three-point bending test, it is observed that the fractures in the LCL laminate occurred on both the traction face.

REFERENCES

[1] Alves, C.; Ferrão, P. M. C.; Silva, A. J.; Reis, L. G.; Freitas, M.; Rodrigues, L. B.; Alves, D. E. Ecodesign of automotive components making use of natural jute fiber composites. *Journal of Cleaner Production*, v.18, p.313-327, 2010.

[2] Cerqueira E.F.; Baptista C. A. R. P.; Mulinari D. R. Mechanical behaviour of polyproplene reinforced sugarcane bagasse fibers composites**.** *ICM11* (*ScienceDirect)*, v.10, 2046-2051, 2011.

[3] Guimarães, J. L.; Frollini E.; Da Silva, C. G.; Wypych, F.; Satyanarayana, K. G. Characterization of banana, sugarcane bagasse and sponge gourd fibers of Brazil. *Industrial Crops Production*, v.30, p.407-415, 2009.

[4] Zah, R.; Hischier, R.; Leão, A. L.; Braun, I. Curauá fibers in the automobile industry – a sustainability assessment. *Journal of Clear Production*, v.15, p.1032-1040, 2007.

[5] Ramires, E. C.; Megiatto Junior, J. D.; Gardrat, C.; Castellan, A.; Frollini, E. Biobased composites from glyoxal-phenolic resins and sisal fibers. ***Bioresource Technology***, v. 101, p. 1998- 2006, 2010.

[6] Ibrahim, M. M.; Dufresne, A.; El-Zawawy, W. K.; Agblevor, F. A. Banana fibers and microfibrils as lignocellulosic reinforcements in polymer composites**.** ***Carbohydrate Polymers***, v.81, p.811-819, 2010.

[7] Leão, M. A.; Tinô S. R. L.; Aquino E. M. F. Accelerated environmental aging effects in structural integrity of licuri fiber reinforced plastics**.** ***Journal of Reinforced Plastics and Composites***, v.34(5) 351-363, 2015.

[8] Rufino, M. U. L.; Costa, J. T. M.; Silva, V. A.; Andrade, L. H. C. Conhecimento e uso do ouricuri (Sagrus coronata) e do babaçu (orbignya phalerata) em Buíque, PE, Brasil. ***Acta bot. bras***., v. 22, n. 4, p. 1141-1149, 2008.

[9] Leão, M. A. et al.; Licuri fibers: alternative reinforcement to polymeric composites. ***Journal of Reinforced Plastics and Composites***, v. 30(6), p. 516-523, 2011.

EVALUATION OF THE THERMAL PERFORMANCE OF GYPSUM COMPOSITES REINFORCED WITH SISAL FIBERS

Carolina Del P.C. Pinto [(1)], Alana S. Cunha[(2)] and Ricardo F. Carvalho[(3)]

(1) Postgraduate Program in Civil Engineering. Department of Construction and Structure. Federal University of Bahia, Salvador, Bahia, Brazil.

(2) Graduating Program in Civil Engineering. Department of Construction and Structure. Federal University of Bahia, Salvador, Bahia, Brazil.

(3) Full Professor. Department of Construction and Structure. Federal University of Bahia, Department of Construction and Structure. Federal University of Bahia, Salvador, Bahia, Brazil.

https://doi.org/10.21452/bccm4.2018.10.03

Abstract

New housing needs and constructive demands required new constructive solutions based on the use of innovative materials, aiming at energy efficiency of solutions, reducing waste, maintains of buildings and pollutants such as CO_2. The composites materials with a ceramic matrix and fibres as reinforcement originate materials widely used in building industry. However, the study of the thermal properties of these composites materials with ceramic matrix contributes to the determination of the conditions of use as thermal insulation providing the distribution of temperatures and thermal comfort of the built space. This study describes the experiments performed to characterize a thermal insulation material to determine the specific heat, resistance, transmittance and thermal delay of the gypsum composite reinforced with sisal nonwoven. The objective of this work is to make a comparative evaluation of the thermal performance, using gypsum (highly porous and without reinforcement) and a gypsum matrix composite material and sisal nonwoven ("*in natura*") as reinforcement phase. Among the composites used in this study are the following conformations: gypsum-sisal-gypsum (GMG), gypsum-sisal-sisal-gypsum (GMMG), gypsum-sisal-gypsum-sisal-gypsum (GMGMG). Specific heat, resistance, transmittance, and thermal delay tests are performed. The results shows that sisal fibres increase the thermal performance of the standard gypsum, increasing the specific heat of the material, the resistance and the thermal delay, reducing thermal transmittance and improving the thermal insulation function of the material.

1. INTRODUCTION

Currently, the construction industry faces an environmental crisis of various dimensions, since buildings are considered a cause of contamination. Conventional materials used as thermal insulation in civil construction are characterized by the high generation of waste, high energy consumption, and the generation of CO2, making it fundamental to reduce it [1]

It is fundamental to create new solutions for construction that achieve energy efficiency and environmentally friendly, from innovative materials such as composites that contribute to advances in civil construction, helping the evolution of conventional insulating materials.

The composite materials allow combining the properties of two or more materials in order to improve the physical, mechanical, thermal and acoustic properties. Conformed by a matrix phase and the reinforcing phase, the matrix acts as an envelope that will protect the reinforcement. Contrarily, the reinforcement will provide the matrix with greater resistance.

Currently there is an interest in the development of composites reinforced by natural fibers, presenting advantages such as lightness, renewable font, esthetics, ease handling, maintenance and versatility, which generate different investigations on the use and behavior of fibres as reinforcement for composites, in order to replace the synthetic fibres used in construction.

Sisal fibres are used as a component for the insulation material, benefiting from their flexibility, tensile strength, elasticity, density and high porosity in order to improve the thermal behaviour of the composite.

The matrix chosen was gypsum plaster. This plaster has been used in the building sector due to its physical and chemical properties, as well as for the acoustic and thermal performance, including the fire resistance. Its use has increased in building applications as panels, boards, furniture and ceiling, always as coating obviating its structural characteristic. Therefore, the blend of sisal and gypsum plaster fiber allows obtaining a light composite for use in social housing as a low cost solution, reducing the energy consumption of buildings [2]

The insulating materials must maintain the internal quality of the environment built, therefore it´s crucial to analyse the thermal properties of the composite material that will the influence on its behavior, in order to meet the technical criteria for this implementation in building.

Several studies have addressed thermal behavior to demonstrate the impact of the use of fiber in gypsum matrix to achieve thermal comfort in buildings. Firstly, Li, Mai and Ye (2000) analyzed the characteristics of sisal fibers and the composites conformed by a reinforcing phase with sisal fiber and with several matrix phases such as thermoplastics, thermosets, rubber, gypsum and cement. For sisal fiber-reinforced gypsum matrices for civil construction, the importance of interfacial bonding from the spacing of the composite cracks is presented as a material for the use of lining walls and linings with good resistance to the combustion of the composite, presenting a shrinkage of the plaster with the loss of water by the high temperatures that generate cracks in the surface of the plaster, emphasizing that these cracks decrease with the use of sisal fiber.

Ornaghi [3] evaluated the thermal and kinetic degradation of plant fiber decomposition, including sisal fiber. It concludes that there are two types of fibre degradation: diffusion and random nucleation, so the thermal stability is not related to the crystallinity content but to the lignocellulosic components of the sisal fibers. Consequently, sisal fiber loses properties with increasing temperature but the higher the amount of fibers, the less the loss of their properties.

Xu et al. [4] concluded that the thermal conductivity of a low density binderless composite is similar as the conventional material used for insulation. As well as gypsum composite with cocoanut coir mixture fibre and composite reinforces with wood shavings and barley straw [2]

Walker and Pavia [5] analyses the performance of brick walls with seven internal solutions including cork lime and hemp lime. These seven types of wall were compared to a traditional lime plaster finish. The results presented a lower thermal transmittance of the seven types of wall, between 34-61% and raising the external temperature of the wall provoking interstitial condensation of the wall. With the lime cork and hemp lime provide and 45% and 36,9%, respectively, improvement on the thermal transmittance. On the other hand, these types of walls present the best results for specific heat of the materials, allowing them to control the temperatures in the wall. So the thermal transmittance and the specific heat of the material need to be balanced, according to the density and thickness of the architectural solution.

Chikhi, Agoudjil, Boudense and Gherabli [2] subsequently develop a bio composite material with date palm fibers to be used as thermal insulation in buildings. The results showed that the thermal conductivity of the material decreases with the increasing of the fiber, decreasing the thermal transmittance with values close to the conventional insulating materials used in construction. Therefore the quantity of fiber used in the composition of the composite will improve not only the thermal performance also the mechanical properties.

The objective of this work is to make a comparative evaluation of the thermal performance, using gypsum (highly porous and without reinforcement) and a gypsum matrix composite material and sisal nonwoven "in nature" as reinforcement phase, setting a total of three composites.

2 Materials and methods

In this study, the sisal fibre was used as a nonwoven. It was collected in Brazil and provided by Hamilton Rios Ltd., which employs sisal from the city of Conceição do Coité - Bahia. The nonwoven was formed by compression of the sisal fibers.

The gypsum plaster used in this study is coating plaster from Araripe, Pernanbuco. For the mixture of the coating plaster it was used an additive. It's a liquid superplasticizer additive, ready-to-use, presenting high fluidity and greater workability to the coating plaster, reducing the relation water-gypsum. It was made with a dosage of 1% which is mixture to the water before adding the plaster.

2.1 Composite preparation

The composite samples were prepared with four different compositions. The first sample was called GP and were prepared with 0,4 proportion of plaster/water and 1% of additive. The second sample was called GMG with one layer of nonwoven in the middle of the material. The third sample, called GMMG has two layers of fiber and one layer of plaster. And finally the fourth sample, called GMGMG, was made with one layer of sisal nonwoven, one of plaster, one layer of nonwoven and a final layer. Material control was performed in weight.

2.2 Thermal properties

2.2.1 Specific heat

Specific heat tests were conducted according to ASTM C 351 – 92b, NBR 15575, NBR 15220 and its supplementary standards, which investigate the amount of energy released by the mass of the sample. The composite were dried at 80°C until constant weight e temperature before specific heat experiments.

The values for the specific heat were calculated using the following formula:

$$Cp = Q/(m\ \Delta t) \quad (1)$$

Where Q is the heat flow (J), m is the mass of the sample (kg) and Δt which is the difference between the temperature of the sample and de temperature of the water (K).

2.2.2 Thermal resistance

Thermal resistance tests were carried out according to NBR 15575 and NBR 15220 which investigate the capacity of the material to resist the passage of heat.

The values for the specific heat was calculated using the following formula:

$$R = e/\lambda \quad (2)$$

Where e is the thickness of the sample (m) and λ is the thermal conductivity of the sample (W/mK).

2.2.3 Thermal transmittance

Thermal transmittance tests were carried out according to NBR 15575 and NBR 15220 which investigate the rate of heat through one square meter of the material according to the difference of temperature across of it.

The values for the specific heat were calculated using the following formula:

$$U = 1/R \quad (3)$$

Where R is the thermal resistance of the sample ($(m^3K)/W$).

2.2.4 Thermal delay

Thermal delay tests were conducted according to NBR 15575 and NBR 15220 and its supplementary standards which investigate the time elapsed between a thermal variation in the surface of a material and its manifestation on the opposite surface. The material is subjected to a periodic heat transmission.

The values for thermal delay in homogeneous samples were calculated using the following formula:

$$\varphi = 0{,}7284\ \sqrt{R_t + C_t} \quad (4)$$

Where φ is the thermal delay (h), Ct the heat capacity of the sample (J/K) and Rt is the thermal resistance of the sample ($(m^3K)/W$).

The values for thermal delay in heterogeneous samples were calculated using the following formula:

$$\varphi = 1{,}382\ R\sqrt{B_1 + B_2} \quad (5)$$

$$B_1 = 0{,}226\frac{B_0}{R_t} \quad (6)$$

$$B_2 = 0{,}205\left(\frac{(\lambda\rho c)ext}{Rt}\right)\left(\mathrm{Re}\,xt - \frac{Rt - \mathrm{Re}\,xt}{10}\right) \quad (7)$$

$$Bo = Ct - Ct\ ext \quad (8)$$

Where, φ is the thermal delay, (h) λ is the thermal conductivity of the composite (W/mK), p is the density of the sample (kg/m^3), C_t is the heat capacity of the sample (J/K), C_t ext is the heat capacity of the external layer of the sample (J/K), R_t is the thermal resistance of the sample ($(m^3K)/W$), e is the thickness of the sample and Rext of the external layer of the sample ($(m^3K)/W$).

2.2.5 Heat capacity

Heat capacity test were carried out according to NBR 15575 and NBR 15220 and its supplementary standards which investigate the amount of heat needed to vary the temperature of the material.

The values for thermal delay in heterogeneous samples were calculated using the following formula:

$$Ct = \sum_{i=1}^{n} \lambda_i R_i c_i \rho_i = \sum_{i=1}^{n} e_i c_i \rho_i \quad (9)$$

Where Ct is the heat capacity of the sample (J/K), λ_i is the thermal conductivity of the layer of the sample (W/mK), pi is the density of the layer of the sample (kg/m3), C_i is the specific heat of the layer of the sample J/(kgK), Ri is the thermal resistance of the layer of the sample ((m3K)/W)and e is the thickness of the layer.

3. RESULTS AND DISCUSSIONS

3.1 Specific heat

Specific heat of the composite is an important parameter mainly when natural fibre is applied. Fig. 1 presents the specific heat capacity of the gypsum (GP) and the three types of composite developed (GMG, GMMG and GMGMG)

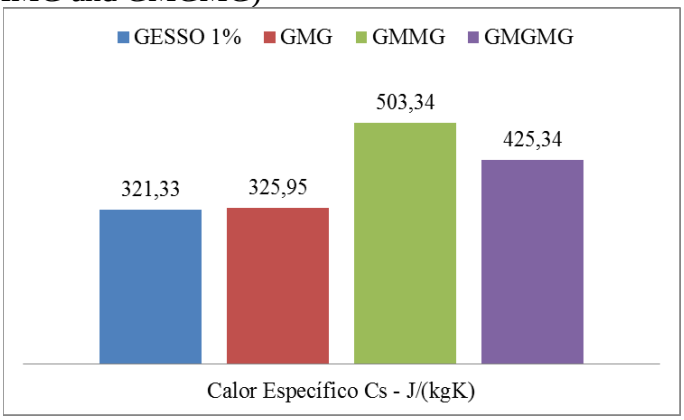

Figure 2: Specific heat values of the gypsum and the gypsum reinforced with sisal nonwoven composites.

We can clearly see that the increase of the fibres content induces a higher saturation time, reaching a temperature balance of 34,3°C at 14min, 15min, 22min, after 25 min. minutes for the GP, GMG, GMMG and GMGMG, respectively.

In Fig. 2 and 3 we notice that the heat exchange is important in the beginning of the process, occurring rapidly and allowing the increasing of the temperature in 27,27%, for the GP. However the evolution in the increasing of temperature in the composites is more significant than the GP with an increase of 26,89%, 32.52% and 45,16%, for the GMG, GMMG and GMGMG, respectively. However, after time, the heat exchange rate slows down until reaching the point of equilibrium. The velocity of the heat transfer in composites is related to the filling of the voids presented in the fibres, as well as the capacity of the fibres to absorb the heat without realising it.

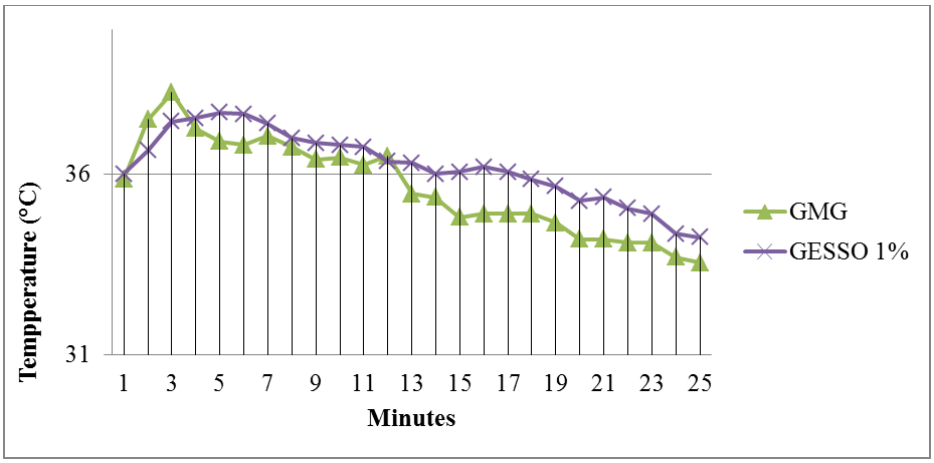

Figure 2: Heat exchange of the samples GP and GMG.

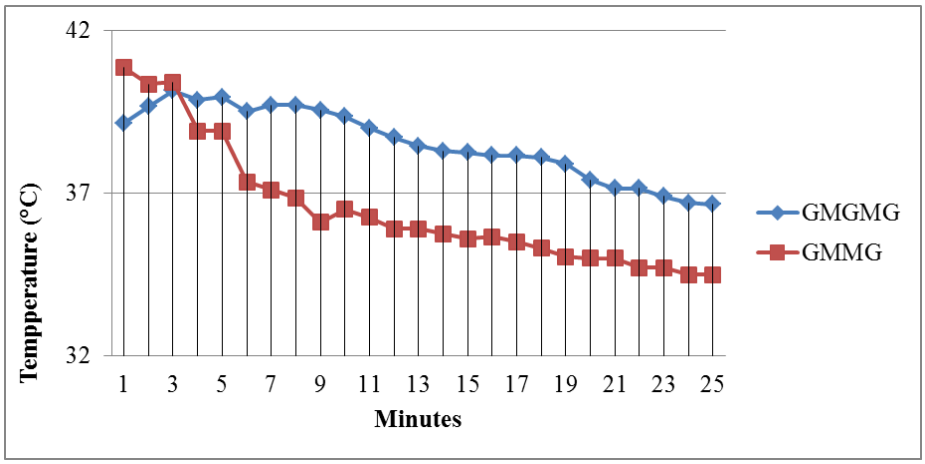

Figure 3: Heat exchange of the samples GMMG and GMGMG.

3.2 Thermal resistance

The thermal resistance measured for the GP is 0.02 m3K/W, compared to the GMG composite with 0.036 m3K/W. Also in table 1 we notice the values for GMMG with 0.076 m3K/W and GMGMG with 0.095 m3K/W. Therefore, the amount of fibres increased in the conformation of the composite allows us to improve the performance of the composite and retarding the trespassing of the heat flow inside the material. This could be related to the specific heat of each sample, for example, the GMMG composite is the material that presents the biggest values of specific heat and also the second best values for thermal resistance, next to GMGMG.

Table 1. Thermal properties values for the materials.

Material	Specific Mass g/cm^3	Fibre content %	Thermal Resistance m^{2}K/W	Thermal transmittance W//m^{2}K	Thermal delay h	Heat capacity KJ/m^{2}K
GP	157.051	0	0.020	48.06	91.4	756.99
GMG	131.944	0.84	0.036	27.61	93.64	645.10
GMMG	97.115	2.29	0.076	13.17	193.08	1222.06
GMGMG	110.576	2.019	0.095	10.46	234.08	1410.97

Thermal resistance is a properties that is related to the thickness of the material, GP and GMG are materials that have the same thickness, on the other hand GMMG and GMGMG presents a bigger thickness which also improve the thermal resistance of the material, without forgetting that they are the composites with more quantity of fibres in the composition.

3.3 Thermal transmittance

The samples revealed that the increasing of the fibres in the gypsum decreases the heat transfer in the plaster. As shown in table 1, the amount of heat flow radiated through the material decreases according with the amount of fibre of the composite. The thermal transmittance of the GP is 48.06 W/(m2K), GMG is 27.61 W/(m2K), GMMG is 13.71 W/(m2K) and GMGMG 10.46 W/(m2K),which represents the 20.45%, 35.89% and 37.6% of the values for GP, respectively.

3.4 Thermal delay

The thermal delay of the material is related to the composition of the composites in layers, defining the material as a homogenous or heterogeneous. As shown in table 1, for the homogenous material, GP, the heat flux crosses the material in 91.41hrs. In heterogeneous materials, GMG, GMMG and GMGMG, the values obtained are 93.64hrs, 193.08hrs and 234.08 hrs, respectively. Therefore, the composition of the layer will define the performance of the composite and its efficiency.

3.5 Heat capacity

The heat capacity of the materials is related to the density and thickness of the materials, therefore the composites with more layers and more quantity of gypsum shows higher values. Table 1 demonstrate that de GMGMG has the higher values followed by GMMG, GMG and GP, with 1410.97 KJ/m2K, 12222.06 KJ/m2K, 645.10 KJ/m2K, 756.99 KJ/m2K, respectively.

4. CONCLUSIONS

- The specific heat of the composites are related with the amount of fibre of the composite, the quantity of voids of the sisal nonwoven and the type and quality of gypsum used for the conformation of the composite. These elements will interfere with the adherence between the nonwoven of sisal and the gypsum, which will be related to the specific heat, thermal transmittance and resistance.
- The thermal transmittance, thermal resistance and thermal delay are related with the barriers that the layers of the composite create so the heat flux will not cross the material

easily. Also, in the heterogonous composite GMGMG the thermal delay increases because of the different types of materials that the heat flux must cross which is more difficult than the GMMG composite

- The heat capacity of the materials analysed shows the importance of the density of the nonwoven used in the conformation of the layers for each composite and the importance of the thickness of the layer made with gypsum that must be precise so it can be evaluated in the same condition each composite.

ACKNOWLEDGEMENTS

The authors would like to thank CAPES, Coordination of Improvement of Higher Level People, for their support and help through this work. The authors wish to express their gratitude to BASF and all the laboratories that provided the materials to develop this study.

REFERENCES

[1] Cherki, A.; Remy, B.; Khabbazi, A.; Jannot, Y.; Baillis, D. Experimental thermal properties characterization of insulating cork-gypsum composite. Construction and buildings materials. 2014. p.8. doi:10.1016/j.conbuildmat.2013.12.076

[2] Chikki, M.; Agoudjil, B.; Boudenne, A. and Gherabli, A. Experimental investigation of new biocomposite with low cost for thermal insulation. Energy and buildings. 2013. P.7. http://dx.doi.org/10.1016/j.enbuild.2013.07.019

[3] ORNAGHI, H.L.J. Thermal behaviour of vegetables fibres and dynamic-mechanical properties of polymeric sisal fiber composites. 2014. P. Dissertation (Doctorate in Mining, Metallurgical and Materials Engineering). Federal University of Rio Grande do Sul, Porto Alegre.

[4] Xu, J.Y; Widyorini, R.; Han, G.P. and Kawai, S. Manufacture and properties of low density binderless particleboard from kenaf core. Journal of Wood Science 50. 2004. p.62–67. https://doi-org.ez10.periodicos.capes.gov.br/10.1007/s10086-003-0522-1

[5] Walker, R. and Pavia, S. Thermal performance of a selection of insulation materials suitable for historic buildings. Building and Environment. 2015. p.6. https://doi.org/10.1016/j.buildenv.2015.07.033

ECO-FRIENDLY SODIUM BICARBONATE TREATMENT AND ITS EFFECT ON EPOXY/POLYESTER COIR FIBRE COMPOSITES

Lívia Á. de Oliveira[1,2], Júlio C. dos Santos [1,2], Luciano M. Gomes Vieira[3], Valdir Mano[2], Rodrigo S. Freire[1,2], Túlio H. Panzera[1,2]

(1) Centre for Innovation and Technology in Composite Materials - CIT^{e}C, Department of Mechanical Engineering, Federal University of São João del Rei-UFSJ, Brazil.

(2) Department of Natural Sciences, Federal University of São João del Rei-UFSJ, Brazil.

(3) Department of Production Engineering, Federal University of Minas Gerais-UFMG, Brazil.

https://doi.org/10.21452/bccm4.2018.10.04

Abstract: This work evaluates a new eco-friendly coir fibre surface treatment method based on sodium bicarbonate ($NaHCO_3$) solution. The fibres were treated with 10 wt.% $NaHCO_3$ solution at different periods (24, 96 and 168 h). A full factorial design $2^1 4^1$ was established to investigate the effect of the type of matrix (epoxy and polyester) and treatment time (24, 96 and 168 h) on the mechanical properties of coir fibre composites. Single fibre tensile test revealed a gradual increase in elastic modulus attributed to the treatment time factor. Epoxy and polyester composites led to higher strength and stiffness, respectively, in both tensile and flexural tests. The alkaline treatment did not affect the mechanical strength of the composites. Enhanced tensile and flexural moduli were obtained when the treatment time increased at 96 or 168 hours levels. Finally, the proposed treatment proved to be feasible and efficient in increasing the stiffness of coir fibre composites, besides being less damaging to the environment after disposal.

Keywords: sodium bicarbonate, coir fibre, epoxy, polyester, mechanical properties.

1. INTRODUCTION

Over the past decades, plant fibres including flax, hemp, jute, sisal, coir, kenaf and many others, have been receiving significant attention as reinforcing materials due to their advantages over synthetic fibres such as low cost, low density, biodegradability, renewability and considerate mechanical performance [1–7]. Composites made from natural fibres have been designed for extensive applications in areas such as consumer goods, civil structure, packaging, sports, automobiles and other mass production industries [8–10].

Among the numerous natural fibres, coir is an abundant, versatile, renewable, cheap and biodegradable lignocellulosic fibre extracted from coconut fruit (*Cocos nucifera*), which is

extensively cultivated in tropical regions [11–13]. In addition to conventional uses of coir fibre as cordage, cushion, floor-furnishing, mats, carpets, ropes, etc. [14-17], this natural raw material has shown great potential in the composite field due to its several valuable properties such as resilience, rigidity, wettability, elongation at break and resistance to weathering [17].

The main drawback of using natural fibre as reinforcement in polymeric composites is the incompatibility between the hydrophilic nature of the fibre and the hydrophobic nature of the matrix [18-21]. These features lead to poor fibre-matrix adhesion and undesirable mechanical properties to the material as a result of the low ability to transfer stress from the matrix to the fibre [22]. To overcome this problem, it is necessary to modify the surface of the fibres, either by physical or chemical methods [14].

Among methods for improving the adhesive character of the natural fibre, alkali treatment can be considered the most widely used technique because of its effectiveness in modifying the fibre surface, increasing the interfacial bond strength between the fibre and the matrix [22-24]. However, incorrect disposal of the chemical waste after treatment may be harmful to the environment [25]. In relation to this, a simple, economical and eco-friendly correct treatment, based on the use of an aqueous solution of sodium bicarbonate, was proposed by Fiore *et al.* [25], revealing remarkable improvements in the mechanical properties of the treated fibres and composites.

Based on the previous literature, this work investigates the effect of this eco-friendly sodium bicarbonate treatment on the properties of coir fibres in different treatment times through physical (density), mechanical (tensile) and microstructural (SEM) analyses. In addition, a design of experiment will be conducted to evaluate the compatibility of these fibres in epoxy and polyester polymers, through morphological analyses and tensile, flexural and Charpy impact tests.

2. MATERIALS AND METHODS

2.1 Materials

The composite materials were composed of two distinct polymer matrices: (i) unsaturated orthoftalic polyester resin/methyl-ethyl-ketone hardener (2 wt.%), supplied by Reichold, and (ii) Renlam M epoxy resin/Aradur HY956 hardener (5:1), supplied by Huntsman. The reinforcement phase consists of short coir fibres, supplied by *Deflor Bioengenharia* (Belo Horizonte – Brazil). Sodium bicarbonate ($NaHCO_3$, 99%) was supplied by Synth (Brazil). The treatment process of the fibres was similar to that reported by Fiore *et al.* [25]. Portions of coir fibres were soaked in 10 wt.% $NaHCO_3$ solution for 24, 96 and 168 hours at room temperature (~20^oC) into a sealed vessel, then immersed in fresh water for 30 min (without acid neutralization) and oven dried at 50 °C for 24 hours.

2.2 Statistical design

A full factorial design $2^1 4^1$ was established to investigate the effect of matrix type (epoxy; polyester) and treatment time (0 h; 24 h; 96 h and 168 h) on the tensile, flexural and impact properties of the composites, resulting in 8 experimental conditions (E.C.) (see Table 1). In replicate 1, thirty specimens (ten for each mechanical testing) were fabricated for each experimental condition. Two replicates were considered, running a total of 480 specimens. The statistical software Minitab v. 17 was used to perform the Design of Experiment (DoE) and Analysis of Variance (ANOVA) techniques.

Table 31. Full factorial design ($2^1 4^1$).

E.C.	Matrix Phase	Treatment Time	E.C.	Matrix Phase	Treatment Time
1	Epoxy	0 h	5	Polyester	0 h
2	Epoxy	24 h	6	Polyester	24 h
3	Epoxy	96 h	7	Polyester	96 h
4	Epoxy	168 h	8	Polyester	168 h

2.3 Characterization

The fibre microstructure was characterized by scanning electron microscopy (SEM) Hitachi T-3000.

The tensile properties of the fibres were determined following the recommendations of ASTM D3822-14 [25]. A single fibre was glued onto a paper and clamped on a universal testing machine. A constant cross-section was assumed for the estimation of tensile properties under a test speed of 2 mm/min. Fifteen samples for each treatment condition (0; 24; 96 and 168 h) were tested. The apparent density test of the coir fibres followed the principle of Archimedes and ASTM D276-12 [26].

The polyester and epoxy matrix phases were characterized via tensile, flexural and Charpy impact tests, conducted according to ASTM D638-14 [27], ASTM D790-15 [28] and ASTM D6110-10 [29], respectively. Five samples of each experimental condition were fabricated for each test and replicate. Two replicates were considered in the experiment.

The tensile and flexural properties of the composites were determined according to ASTM D3039/3039M [30] and ASTM D790-15 [28], respectively. The tests were conducted at 2 mm/min using a Shimadzu AG-X Plus testing machine, equipped with a 100 kN capacity load cell. The impact tests were performed on a Charpy Impact Tester XJJ Series, following the recommendations of ASTM D6110-10 [29]. A scanning electron microscopy (SEM) analyses was used to observe the microstructure of the composite cross section after the Charpy impact test.

2.4 Manufacturing process

The composites were manufactured via hand lay-up and cold uniaxial compaction, as shown in Figure 1a. The aluminium sheet (300 mm x 300 mm) covered with a thin layer of wax as the release agent was placed into a metallic mould. Subsequently, short coir fibres (30% v/v) were weighted according to the required grammage (900 g/m^2) and randomly distributed into the mould. The polymeric matrix (70% v/v) was prepared by hand-mixing the resin and the hardener for 5 minutes at room temperature, and then spread uniformly over the coir fibres. Another aluminium sheet, covered with wax, was placed on top and the mould was closed with a lid. A pressure of 654 kPa was applied for 12 hours in room temperature. Subsequently, the composite was released from the mould (Figure 1b) and sealed with a plastic bag to prevent moisture absorption for 14 days post-cure. Finally, the composite plate was cut according to the recommendations of ASTM standards and tested.

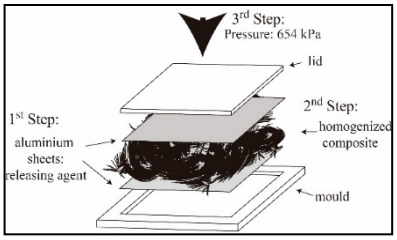

(a)

(b)

Figure 72. Manufacturing process: (a) cold compaction mechanism (b) composite plate.

3. RESULTS AND DISCUSSION

3.1 Coir fibre characterization

Table 2 shows the mean physical and mechanical properties of coir fibres at different treatment times. It is possible to note that the apparent density increased with longer treatment time. The Na^+ ions, released in the sodium bicarbonate solution, has a favourable diameter to widen the smallest pores in between the lattice planes and penetrate into them, which contributes to increase the apparent density [31, 32]. The rearrangement of cellulose fibrils, created by new hydrogen bonds between the chain, is attributed to the removal of hemicellulose, lignin and waxy substances to the external surface of the fibre [25, 33]. However, according to the SEM images shown in Figure 2, there was no significant change in the fibre surface roughness, evidencing that the sodium bicarbonate treatment is not very strong.

The mechanical properties of coir fibres are presented in a data range (Table 2), being attributed to the non-uniformity of this natural product. The tensile strength was not affected by treatment time factor. Otherwise, the modulus of elasticity presented a significant increase, as shown in Figure 3, which is attributed to the cellulose fibrils rearrangement, causing a decrease in the spiral angle and an increase in the molecular orientation [31].

Table 32. Coir fibre properties.

Property	Treatment Time			
	0 h	24 h	96 h	168 h
Apparent Density (g/cm^3)	0.83 ± 0.02	1.01 ± 0.02	1.02 ± 0.03	1.04 ± 0.03
Tensile Strength (MPa)	59 – 297	60 – 242	45 – 231	83 – 224
Modulus of Elasticity (GPa)	3.2 – 4.3	3.3 – 5.1	3.9 – 6.9	4.1 – 8.8

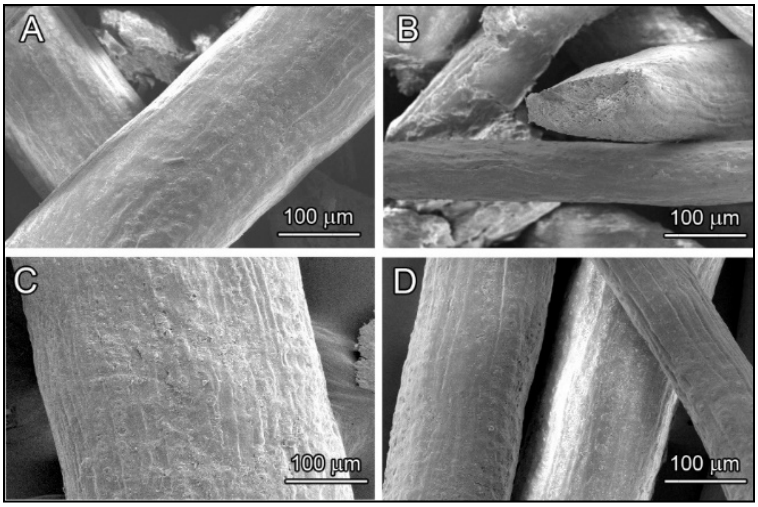

Figure 2. Coir fibre scanning electron micrographs at different treatment times: (A) 0 h, (B) 24 h, (C) 96 h and (D) 168 h.

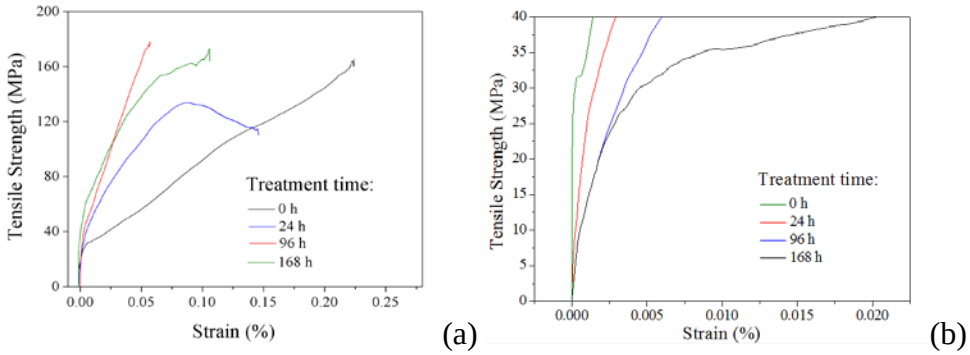

Figure 3. (a) Tensile testing of single filament of coir fibre, (b) Image zoom.

3.2 Matrix characterization

Table 3 shows the mechanical properties of the matrix phases in pristine conditions. It is noteworthy that the epoxy polymer is superior in strength, while the polyester is superior in modulus. The higher stiffness of the polyester polymer reflects on a lower impact resistance as shown in Table 3.

Table 33. Mechanical properties of the matrices.

Property (Unit)		Type of Matrix	
		Epoxy	Polyester
Tensile	Strength (MPa)	47.29 (±2.02)	39.80 (±3.05)
	Modulus (GPa)	2.24 (±0.11)	2.44 (±0.14)
Flexural	Strength (MPa)	69.26 (±3.96)	55.85 (±2.91)
	Modulus (GPa)	2.14 (±0.04)	2.19 (±0.08)
Impact	Resistance (kJ/m^2)	8.72 (±1.41)	5.81 (±0.31)

3.3 Composite design

Table 4 presents the DoE/ANOVA analysis. Significant effects (P-value ≤ 0.05) are underlined while those highlighted in bold will be interpreted via effect plots, which illustrate statistical analysis and provide variation of factors and levels. The R^2-adj values, ranging from 93.23% to 99.89%, indicate models of high predictive ability since they are close to 100%.

ANOVA was validated by the Anderson-Darling normality test, which exhibits P-values higher than 0.05 (0.145 – 0.999), implying that the data follow a normal distribution.

Table 34. Analysis of variance (ANOVA).

ANOVA		P-value ≤ 0.05				
	Experimental Factors	Tensile Strength (MPa)	Tensile Modulus (GPa)	Flexural Strength (MPa)	Flexural Modulus (GPa)	Impact Resistance (kJ/m²)
Main Factors	Matrix Phase	0.000	0.000	**0.000**	**0.000**	0.000
	Treatment Time	0.020	0.000	0.046	**0.000**	0.020
Interaction	Matrix Phase x Treatment Time	**0.047**	**0.003**	0.412	0.148	**0.013**
	R^2 - adj	98.98%	97.19%	93.23%	96.87%	99.89%
	Anderson-Darling (P ≥ 0.05)	0.145	0.824	0.551	0.606	0.999

3.3.1 Tensile test

Tensile strength data varied from 12.40 MPa to 18.77 MPa, while tensile modulus ranged from 2.32 GPa to 3.05 GPa, as shown in Figure 4, items a and b, respectively. As noted, coir fibres led to an increase in tensile modulus and a reduction in tensile strength compared to the neat polymer properties. The increased stiffness is attributed to the coir fibre characteristics, while the reduced strength is relative to the short length and the random orientation of thereof, which hinders the load distribution throughout the sample [25,34,35].

Figure 4, items c and d, shows the second order interaction effect plots for the tensile properties. The letters in blue represent the Tukey's comparison test, in which similar letters belong to the same grouping, i.e., equivalent means. Composite materials made with epoxy matrix phase present higher tensile strength (41.68%), as shown in Figure 4c. In contrast, polyester composites achieved higher tensile moduli (Figure 4d). These results are in accordance to the matrix characterization (Table 3). The strength is largely affected by fibre orientation and fibre-matrix interfacial adhesion [25,34]. Thus, higher strength values indicate that coir fibres have better compatibility with epoxy matrix composites.

The chemical treatments did not affect the tensile strength of the polyester composites, as observed by the same grouping A in the Tukey's test (see Figure 4c). A slight increase of 6% in tensile strength was obtained for epoxy composites when considering 96 hours of treatment. This behaviour can be attributed to a poor increase in surface roughness after treatment (see Figure 2), affecting physical fibre/matrix adhesion, as evidenced by the fibre pull-out mechanism of the fractured surface (Figure 5 - black arrows) especially when polyester matrix was considered. An opposite behaviour was observed for tensile modulus since this response is measured in small deformations, which are not affected by interfacial adhesion [25]. A gradual enhancement in composite stiffness is revealed in Figure 4d as treatment time increases. This effect is in agreement

with the fibre characterization (see Table 2), where the longer treatment time led to a higher stiffness of the fibre and composite.

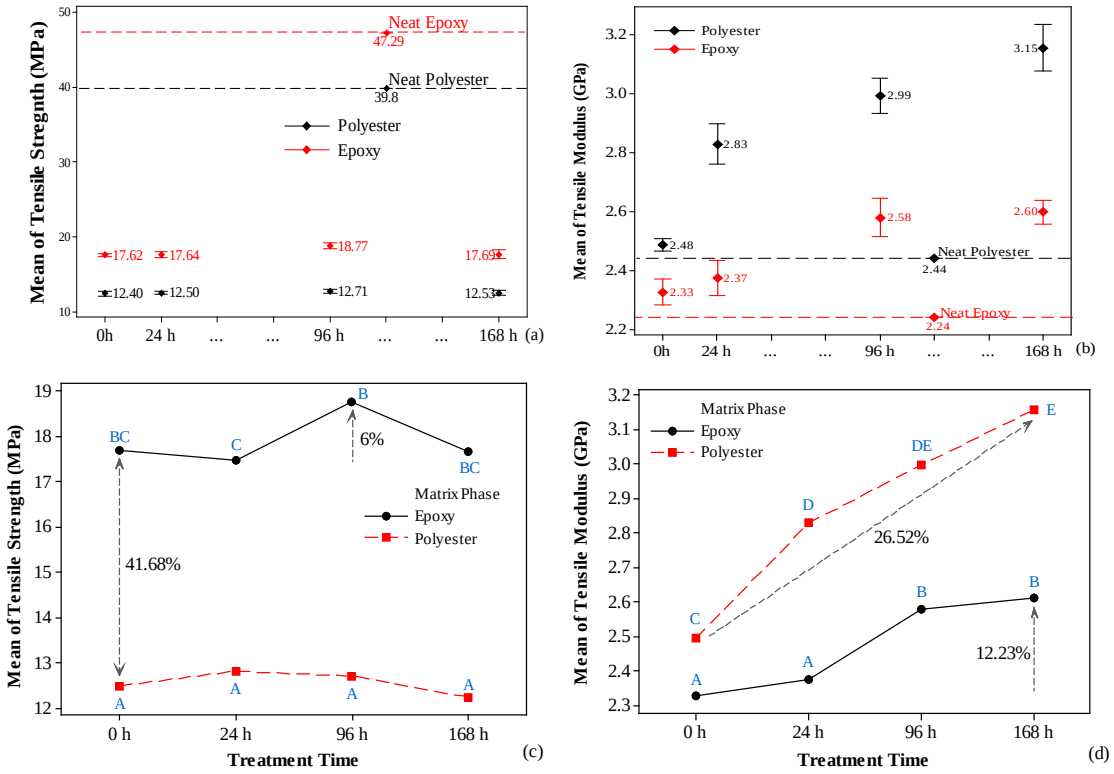

Figure 4. Tensile properties of coir fibre composites: (a) strength and (b) modulus. Second order interaction effect plot for the mean tensile (c) strength and (d) modulus.

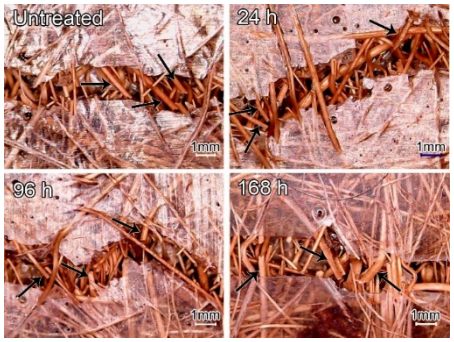

Figure 5. Fracture surface of the polyester matrix composite.

3.3.2 Flexural test

The flexural strength data varied from 24.73 MPa to 40.44 MPa, while the flexural moduli ranged from 2.27 GPa to 2.78 GPa, as shown in Figure 6, items a and b, respectively. Coir fibre reinforced polymers achieved higher flexural modulus and lower flexural strength compared to pure polymers. The similar effect was also identified for tensile properties, being attributed to the intrinsic characteristics of the coir fibres.

Figure 6, items c and d, shows the main effect plot for the flexural test. The epoxy composites presented higher strength (45.33%) and lower stiffness (-5.14%) in comparison to the polyester composites. These results are in accordance to the matrix characterization (see Table 3), implying that the matrix phase plays a role in the composite mechanical properties, in addition to that the epoxy polymer offers a better compatibility with the coir fibres [20,36].

The highest flexural modulus (Figure 6d) was reached for composites made with polyester matrix phase and treated coir fibres at 96h or 168h. This behaviour, also reported for tensile test, is attributed to the increase of coir fibre stiffness after treatment (see Table 2).

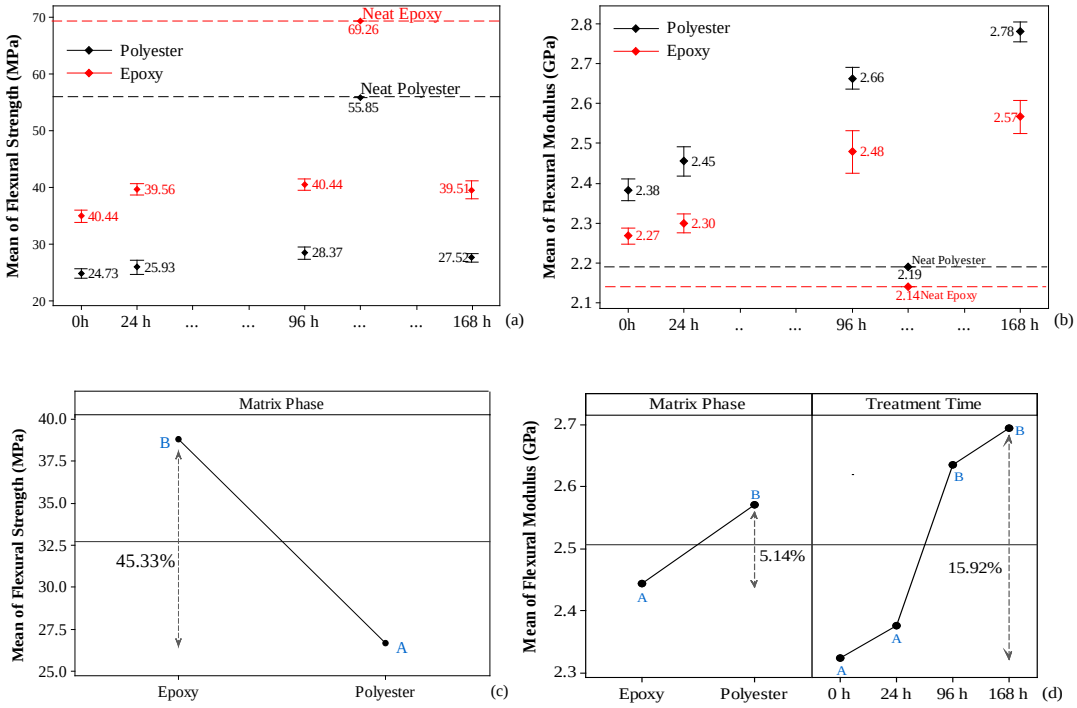

Figure 6. Flexural properties of coir fibre composites: (a) strength and (b) modulus. Main effect plot for flexural: (c) strength and (d) modulus.

3.3.3 Impact test

Figure 7a presents the impact resistance of the composites, which varied from 6.04 kJ/m^2 to 18.03 kJ/m^2. Although the polyester polymer has achieved low energy absorption, as shown in Table 3 and Figure 7a, an opposite behaviour was obtained for coir fibre reinforced composites, revealing a percent increase nearly at 194% in comparison to the neat polyester resin (Figure 7a). A substantial variation of 198% was identified between epoxy and polyester composites (Figure 7b). The impact resistance is largely affected by the level of bonding. While a significant part of the energy absorption during impact takes place through the fibre pull-out mechanism, very strong interfaces have a detrimental effect on the impact properties [37]. Thus, the high impact resistance achieved by the polyester composites can be attributed to the poor compatibility between the fibre and the matrix, resulting in a fibre pull-out mechanism, evidenced by SEM images obtained for the composite cross-section (Figure 8a).

The lower impact resistance obtained for epoxy composites (Figure 7a-b) is due to better fibre-matrix adhesion, resulting in a fibre fracture (Figure 8b) in the crack-plane with low fibre pull-out and, consequently, a reduction in energy dissipation [37-39].

The treatment time factor did not affect the impact resistance of the composites, as observed in Figure 7b by the same grouping A and B. This fact agrees with the tensile and flexural behaviours, which did not reveal significant changes in fibre-matrix compatibility after treatment.

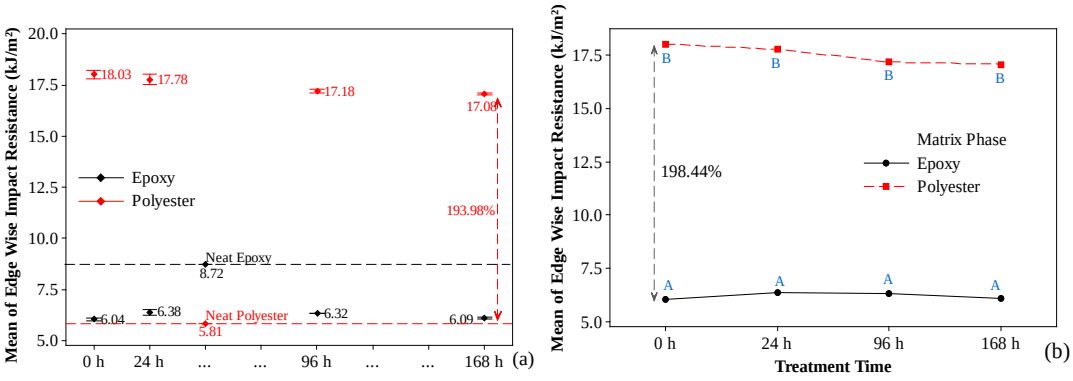

Figure 73. (a) Impact resistance values for coir fibre composites and neat matrices. (b) Second order interaction effect plot for the impact resistance.

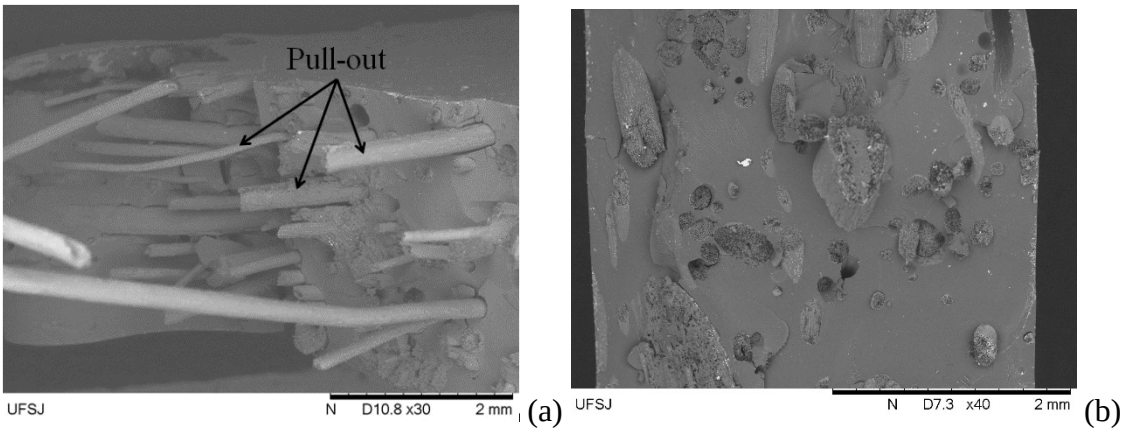

Figure 8. SEM images of the fractured surface of: (a) polyester and (b) epoxy composite after impact test.

4. CONCLUSIONS

The conclusions are described as follows:

i. A slight increase in coir fibre density of as a function of the treatment time was noted, being attributed to Na+ ions, which are able to enlarge smaller pores contributing to open the cellular structure. The treatment solution did not provide a significant increase in fibre roughness, as observed by the SEM images. The treatment time factor did not affect the tensile strength of the fibres; however, the modulus of elasticity was substantially increased.

ii. Coir fibre reinforced composites achieved enhanced stiffness and reduced strength when compared to the polymer in pristine condition. The epoxy composites achieved higher tensile and flexural strength while the polyester composites obtained a higher tensile and flexural modulus. It is noteworthy, the polymer matrices obtained similar

performance, revealing that the matrix phase substantially affects the mechanical properties of short-random coir fibre composites.

iii. The alkaline treatment did not affect the mechanical strength of the composites due to the presence of fibre pull-out mechanism. Enhanced tensile and flexural moduli were obtained when the treatment time increased at 96 or 168 hours levels.

iv. A higher impact resistance of polyester composites was attributed to the poor adhesion at the fibre/matrix interface.

Finally, although the proposed treatment is not as strong as the traditional one with sodium hydroxide, it proved to be feasible and efficient in increasing the coir fibre stiffness and its corresponding composites, besides being less harmful to the environment after disposal.

ACKNOWLEDGEMENTS

The authors would like to thank CAPES (MSc scholarship), CNPq (PP-306767/2016-3) and FAPEMIG (PPM-00075-17) for the financial support provided.

REFERENCES

[1] Brahmakumar, M., Pavithran, C. and Pillai, R.M., 'Coconut fibre reinforced polyethylene composites: Effect of natural waxy surface layer of the fibre on fibre/matrix interfacial bonding and strength of composites', *Compos. Sci. Technol.* **65** (2005) 563–569.

[2] Monteiro, S.N., Terrones, L.A.H. and D'Almeida, J.R.M., 'Mechanical performance of coir fiber/polyester composites', *Polym. Test.* **27** (2008) 591–595.

[3] Ramesh, M., Palanikumar, K. and Reddy, K.H., 'Plant fibre based bio-composites: Sustainable and renewable green materials', *Renew. Sustain. Energy Rev.* **79** (2017) 558–584.

[4] Ku, H., Wang, H., Pattarachaiyakoop, N. and Trada, M., 'A review on the tensile properties of natural fiber reinforced polymer composites', *Compos. Part B Eng.* **42** (2011) 856–873.

[5] Thakur, V.K. and Thakur, M.K., 'Processing and characterization of natural cellulose fibers/thermoset polymer composites', *Carbohydr. Polym.* **109** (2014) 102–117.

[6] Abdul Khalil, H.P.S., Bhat, A.H. and Ireana Yusra, A.F., 'Green composites from sustainable cellulose nanofibrils: A review', *Carbohydr. Polym.* **87** (2012) 963–979.

[7] Malkapuram, R., Kumar, V. and Singh Negi, Y., 'Recent development in natural fiber reinforced polypropylene composites', *J. Reinf. Plast. Compos.* **28** (2009) 1169–1189.

[8] Harish, S., Michael, D.P., Bensely, A., Lal, D.M. and Rajadurai, A., 'Mechanical property evaluation of natural fiber coir composite', *Mater. Charact.* **60** (2009) 44–49.

[9] Ezekiel, N., Ndazi, B., Nyahumwa, C. and Karlsson, S., 'Effect of temperature and durations of heating on coir fibers', *Ind. Crops Prod.* **33** (2011) 638–643.

[10] Akil, H.M., Omar, M.F., Mazuki, A.A.M., Safiee, S., Ishak, Z.A.M. and Abu Bakar, A., 'Kenaf fiber reinforced composites: A review', *Mater. Design.* **32** (2011) 4107–4121.

[11] Lecompte, T., Perrot, A., Subrianto, A., Le Duigou, A. and Ausias, G., 'A novel pull-out device used to study the influence of pressure during processing of cement-based material reinforced with coir', *Constr. Build. Mater.* **78** (2015) 224–233.

[12] Van Dam, J.E.G., Van Den Oever, M.J.A., Teunissen, W., Keijsers, E.R.P. and Peralta, A.G., 'Process for production of high density/high performance binderless boards from whole coconut husk. Part 1: Lignin as intrinsic thermosetting binder resin', *Ind. Crops Prod.* **19** (2004) 207–216.

[13] Saw, S.K., Sarkhel, G. and Choudhury, A., 'Surface modification of coir fibre involving oxidation of lignins followed by reaction with furfuryl alcohol: Characterization and stability', *Appl. Surf. Sci.* **257** (2011) 3763–3769.

[14] Rahman, M.M. and Khan, M.A., 'Surface treatment of coir (Cocos nucifera) fibers and its influence on the fibers' physico-mechanical properties', *Compos. Sci. Technol.* **67** (2007) 2369–2376.

[15] Geethamma, V.G., Thomas Mathew, K., Lakshminarayanan, R. and Thomas, S., 'Composite of short coir fibres and natural rubber: effect of chemical modification, loading and orientation of fibre', *Polymer.* **39** (1998) 1483–1491.
[16] Silva, G.G., De Souza, D.A., Machado, J.C. and Hourston, D.J., 'Mechanical and thermal characterization of native brazilian coir fiber', *J. Appl. Polym. Sci.* **76** (2000) 1197–1206.
[17] Zhang, L. and Hu, Y., 'Novel lignocellulosic hybrid particleboard composites made from rice straws and coir fibers', *Mater. Design.* **55** (2014) 19–26.
[18] Nam, T.H., Ogihara, S., Tung, N.H. and Kobayashi, S., 'Effect of alkali treatment on interfacial and mechanical properties of coir fiber reinforced poly(butylene succinate) biodegradable composites', *Compos. Part B Eng.* **42** (2011) 1648–1656.
[19] Mir, S.S., Nafsin, N., Hasan, M., Hasan, N. and Hassan, A., 'Improvement of physico-mechanical properties of coir-polypropylene biocomposites by fiber chemical treatment', *Mater. Design.* **52** (2013) 251–257.
[20] Kumar, S.M.S., Duraibabu, D. and Subramanian, K., 'Studies on mechanical, thermal and dynamic mechanical properties of untreated (raw) and treated coconut sheath fiber reinforced epoxy composites', *Mater. Design.* **59** (2014) 63–69.
[21] Rout, J., Misra, M., Tripathy, S.S., Nayak, S.K. and Mohanty, A.K., 'The influence of fibre treatment on the performance of coir - polyester composites', *Compos. Sci. Technol.* **61** (2001) 1303–1310.
[22] Fiore, V., Di Bella, G. and Valenza, A., 'The effect of alkaline treatment on mechanical properties of kenaf fibers and their epoxy composites', *Compos. Part B Eng.* **68** (2015) 14–21.
[23] Obi Reddy, K., Uma Maheswari, C., Shukla, M., Song, J.I. and Varada Rajulu, A., 'Tensile and structural characterization of alkali treated Borassus fruit fine fibers', *Compos. Part B Eng.* **44** (2013) 433–438.
[24] Gu, H., 'Tensile behaviours of the coir fibre and related composites after NaOH treatment', *Mater. Design.* **30** (2009) 3931–3934.
[25] Fiore, V., Scalici, T., Nicoletti, F., Vitale, G., Prestipino, M. and Valenza, A., 'A new eco-friendly chemical treatment of natural fibres: Effect of sodium bicarbonate on properties of sisal fibre and its epoxy composites', *Compos. Part B Eng.* **85** (2016) 150–160.
[25] ASTM D3822 - 12, Standard Test Method for Tensile Properties of Single Textile Fibers 1, (2012) 1–10.
[26] ASTM D276 - 12, Standard Test Methods for Identification of Fibers in Textiles, Astm. (2012) 1–14.
[27] ASTM International, Standard test method for tensile properties of plastics, ASTM Int. 8 (2014) 46–58.
[28] ASTM D790-15, Standard Test Methods for Flexural Properties of Unreinforced and Reinforced Plastics and Electrical Insulating Materials. D790, (2015) 1–12.
[29] P.M. Materials, Standard Test Method for Determining the Charpy Impact Resistance of Notched Specimens of Plastics 1, (2010) 1–17.
[30] ASTM D3039/D3039M − 14, Standard, Standard Test Method for Tensile Properties of Polymer Matrix Composite Materials1, (2014) 1–13.
[31] Van de Weyenberg, I., Chi Truong, T., Vangrimde, B. and Verpoest, I., 'Improving the properties of UD flax fibre reinforced composites by applying an alkaline fibre treatment', *Compos. Part A Appl. Sci. Manuf.* **37** (2006) 1368–1376.
[32] Gwon, J.G., Lee, S.Y., Doh, G.H. and Kim, J.H., 'Characterization of Chemically Modified Wood Fibers Using FTIR Spectroscopy for Biocomposites', *J. Appl. Polym. Sci.* **116** (2010) 3212–3219.
[33] Muensri, P., Kunanopparat, T., Menut, P. and Siriwattanayotin, S., 'Effect of lignin removal on the properties of coconut coir fiber/wheat gluten biocomposite', *Compos. Part A Appl. Sci. Manuf.* **42** (2011) 173–179.
[34] Yan, L., Chouw, N., Huang, L. and Kasal, B., 'Effect of alkali treatment on microstructure and mechanical properties of coir fibres, coir fibre reinforced-polymer composites and reinforced-cementitious composites', *Constr. Build. Mater.* 112. **112** (2016) 168–182.

[35] Oliveira, L.A., Santos, J.C., Panzera, T.H., Freire, R.T., Vieira, L.M.G. and Scarpa, F., 'Evaluation of Hybrid-Short-Coir-Fibre-Reinforced Composites via Full Factorial Design', *Compos. Struct.* (2018).
[36] Ebnesajjad, S. and Ebnesajjad, C. 'Surface treatment of materials for adhesive bonding', 2014.
[37] De Albuquerque, A.C., Joseph, K., De Carvalho, H.L. and D'Almeida, J.R.M., 'Effect of wettability and ageing conditions on the physical and mechanical properties of uniaxially oriented jute-roving-reinforced polyester composites', *Compos. Sci. Technol.* **60** (2000) 833–844.
[38] Dassios, K.G., 'A review of the Pull-Out Mechanism in the Fracture of Brittle- Matrix Fibre-Reinforced Composites', *Adv. Compos. Lett.* **16** (2007) 17–24.
[39] Wang, C., Ji, X., Roy, A., Silberschmidt, V.V. and Chen, Z., 'Shear strength and fracture toughness of carbon fibre/epoxy interface: effect of surface treatment', *Mater. Design.* **85** (2015) 800–807.

EVALUATION OF THERMAL BEHAVIOR AND CURE KINETICS OF A CURAUÁ FIBER PREPREG BY THE NON-ISOTHERMAL METHOD

Vilson Dalla L. Jr [(1)], Linconl A. Teixeira [(1)], Rosineide M. Leão [(1, 2)] and Sandra Luz [(1, 3)]

(1) Engineering Materials Integrity Program, University of Brasília, Brasília, Brazil

(2) Institute of Exact Sciences and Technology, Paulista University, Brasília, Brazil

(3) Department of Chemical and Materials Engineering, University of Alberta, Alberta, Canada

https://doi.org/10.21452/bccm4.2018.10.05

Abstract:

Curauá fibers have low-cost, low density, biodegradability and offer a relative high tensile strength level when applied in composites materials. The prepreg is a composite material constituted by fibers impregnated with a measured amount of resin matrix. Learning more about how the thermal properties of the matrix can be affected by curauá fibers, this work evaluated the thermal behavior and cure kinetics of a curauá fibers/ epoxy prepreg through Thermogravimetric Analysis (TGA) and Differential Scanning Calorimetry (DSC). The *in natura* or alkali treated (KOH or NaOH) curauá fibers blankets impregnated with epoxy resin were prepared using a manual rolling process. The prepreg samples containing 20 wt.% of fibers were analyzed when the matrix in the composite presented a semisolid tacky (B-stage). The prepreg cure kinetics was investigated by a non-isothermal isoconversional method, and the T_g was evaluate using the DSC data. The variables related to the curing kinetics were obtained on dynamic conditions with heating rates of 2.5, 5.0 and 10 °C/min. The prepreg activation energy was calculated at a given function of the extent of conversion. According to the dynamic runs, the prepreg T_g was higher for treated fibers than *in natura*. The 2.5 °C/min rate provided a curing cycle with a lower and controlled temperature when compared to the others heating rates and the humidity weight loss of prepreg amounted was ~2.8%. The KOH prepreg presents the highest activation energy and the *in natura* prepreg the lowest one. The kinetic conditions established will be used in further experiments to obtain natural fibers composites from prepregs.

Keywords: cure kinetics; prepreg; curauá fibers; epoxy; thermal analysis.

1. INTRODUCTION

The application of plant fibers in composites materials has increased because they have good mechanical properties regarding strength per weight, as well their renewability and relative low cost [1]. One of the greatest promising vegetable fibers is the curauá (*Ananas erectifolius*) planted in the Amazon Region in the north region of Brazil [2]. This natural fiber presents a

comparable cost to other fibers in Brazil, however, its strength is higher than sisal, coir or jute, and approximately accomplish the physical properties of high-cost flax or even glass fibers.[3].

Prepreg materials are becoming progressively common in the composites industry due to their ease of application, stable properties and high-quality surface completion [4]. The prepreg is a significant product in which fibers are impregnated with a measured amount of resin. The continuous fibers are responsible for the highest strength and modulus and discontinuous are cheaper and easy to process [5].

In prepregs, the resin used is staged or advanced (B-staged) to the point where the thermoset matrix in the composite is a tacky semisolid, which consents the layers to be layed up to procedure a laminate that can be cured. The thermal analysis is one of the experimental techniques that it has been used to monitor the curing reactions of thermosetting systems. Differential scanning calorimetry (DSC) and thermogravimetric analysis (TGA) permit to find the performance of polymer composites, as well as the glass transition temperature (T_g), the degree of cure and kinetics parameters of polymeric matrices [6]. The heat unconfined in the curing reaction is directly related to the conversion degree measured at a specific stage of the curing process [7]. The simplest way to quantify the cure degree of a partially reacted sample includes DSC measurement of a residual exotherm, comparing that to the heat of reaction measured on a completely unreacted sample. The conversion or extent of reaction α_{cure} can be calculated according to the Equation (1):

$$\alpha_{cure} = 1 - \frac{\Delta H_{res}}{\Delta H_{dyn}} \tag{1}$$

where ΔH_{res} is the residual heat of reaction measured from the sample, and ΔH_{dyn} is the heat of reaction measured by a dynamic scan of a "fresh" unreacted sample of the same prepreg [8]. The kinetic studies are essentially determined by the fundamental equation that governs the rate of reaction and can be expressed as a function of the temperature (T) and the extent of conversion (α) as following Equation (2):

$$\frac{d\alpha}{dt} = k(T)f(\alpha) \tag{2}$$

where $k(T)$ is the rate constant, t is the time, and $f(\alpha)$ is the reaction model. For epoxy cures, $f(\alpha)$ is usually taken in the form of $(1-\alpha)^n$ for n^{th} order or of $\alpha^m(1-\alpha)^n$ for autocatalytic reaction; where: α is the degree of conversion, n and m are the orders of the reaction [9-12]. The temperature dependence on the rate constant is presented by replacing $k(T)$ to the Arrhenius Equation (3):

$$\frac{d\alpha}{dt} = A \exp\left(-\frac{E_a}{RT}\right) f(\alpha) \tag{3}$$

where A is the pre-exponential factor, E_a the activation energy, and R is the ideal gas constant. When a constant rate is used to heat the sample, the temporal dependency showed in Equation (2) is excluded through the simple transformation, resulting in the Equation (4):

$$\frac{d\alpha}{dT} = \frac{A}{\beta} \exp\left(-\frac{E_a}{RT}\right) f(\alpha) \tag{4}$$

where $\beta = dT/dt$ is the heating rate. Used for both isothermal and non-isothermal conditions, the extent of conversion (α) is usually obtained by dividing the partial heat ΔH_p evolved at temperature T by the total heat ΔH_0 produced during the entire reaction, which gives the Equation (5):

$$\alpha = \frac{\Delta H_p}{\Delta H_0} \quad (5)$$

The kinetic parameters estimated from the non-isothermal DSC data are commonly different from those evaluated from isothermal DSC investigations [13]. A non-isothermal method is a more accurate measure to calculate the prepreg curing kinetics. In this method, the kinetic data can be obtained in a relatively short-period of time, which can make it very attractive. However, an isothermal method can lead to experimental errors because generally renders the destabilization of the DSC heat flow at the origin of the cure measurement [11].

The kinetic parameters *A* and E_a estimated experimentally are functions of the fundamental kinetic parameters of an individual step. For epoxy-based systems, thus, it is correct to call them the effective kinetic parameters. Since the influence of each step varies with the extent of conversion and temperature, the real activation energy will also vary intensely with these factors. In contrast, on the isoconversional method, the activation energy is calculated at a given function of conversion [10]. Furthermore, this method can be applied to evaluate both simple and complex chemical reactions [14,15]. Consequently, the rewards of using these monitoring techniques support the knowledge of the polymeric behavior of these materials, helping parameter processing control, which affects the mechanical properties and the morphological characteristics [16].

In the present work, we investigate the influence of fibers treatment on the thermal behavior and kinetics parameters of a curauá fiber prepreg. The curing kinetics and the curing cycle were based on an isoconversional method, which uses a non-isothermal and DSC data to determine these parameters.

2. EXPERIMENTAL

2.1 Materials

The curauá fibers used in this study were provided by the Center for Support to Community Action Projects (CEAPAC) from Santarém - PA. The fibers were available *in natura* with 80 cm length. Also, the polymer used as a matrix was a DGEBA epoxy resin based on Diglycidyl ether of bisphenol-A (DGEBA) with an amine-based curing agent.

2.2 Fibers treatment

The *in natura* fibers were chopped into small pieces of 4-6 cm and dried at 80 °C for 3 h. To improve the adhesion between matrix and reinforcement two different procedures for surface modification were applied to the curauá fibers: (1) The *in natura* fibers were soaked in distilled water at a ratio of 10:1 (water/fibers) for 1 h. The fibers were mercerized in 10% (w/v) potassium hydroxide solution (KOH), and the material was stirred at 150 rpm for 3 h at room temperature. Later, the fibers were washed in distilled water until pH neutralized and dried at room temperature for 48 h and at 80 °C for 3 h. (2) The *in natura* fibers were washed in distilled water at 80 °C for 2 h and dried at room temperature for 48 h. The fibers were mercerized in 5% (w/v) sodium hydroxide solution (NaOH) at 50 °C for 2 h with manual stirring. After the reaction time, the fibers were washed in distilled water until pH neutralized and dried at room temperature for 48 hours and at 80 °C for 3 h.

2.3 Prepregs Obtainment

Initially, curauá fibers blanket from each treatment was produced by discontinuous fibers. The matrix solution was prepared at room temperature by mixing proper quantities of DGEBA epoxy monomer and a specific hardener. The ratio used to produce the samples were 12 phr (parts per hundred) and corresponds to the stoichiometric composition. The fibers blanket (20 wt%) was impregnated with the matrix solution using a manual rolling process. The prepregs remained for 38 h curing at room temperature to a certain extent where the matrix in the composite presented a semisolid tacky (B-stage). To slow down the resin curing process, the prepregs were kept -18 °C for further analysis. The prepregs received a terminology according to the fibers treatment: *in natura*, KOH and NaOH prepregs.

2.4 Thermogravimetric Analysis (TGA) and Differential Scanning Calorimetry (DSC)

Thermogravimetric (TGA) and Differential Scanning Calorimetry (DSC) analysis were performed on a Q600 SDT equipment (TA Instruments, USA) under an inert atmosphere of nitrogen with a flow rate of 50 mL/min. The samples with 10 ± 0.5 mg were deposited in a sealed alumina pan. Two analysis configurations with different parameters and objectives were proposed: (1) In the dynamic study the analyses carry out under a heating rate of 5 °C/min from room temperature up to 600 °C; (2) In the cure kinetics study the analyses were performed under heating rates of 2.5, 5 and 10 °C/min from room temperature up to 300 °C.

3. RESULTS AND DISCUSSION

3.1 Thermogravimetric Analyses

The thermal stability and degradation of prepregs were determined by the thermogravimetric and its derivative thermogravimetric curves (TG – DTG). This characterization permitted not only to study the influence of fibers chemical modification but also to determine the limit of temperature application for this material.

The composites presented two-steps of degradation as we can see in Figure 1. Table 1 shows the data of humidity, degradation temperature and residue in the end of analysis. The first stage of prepregs weight loss occurs between 40 and 150 °C, and is related to the vaporization of the water present in the samples [17].

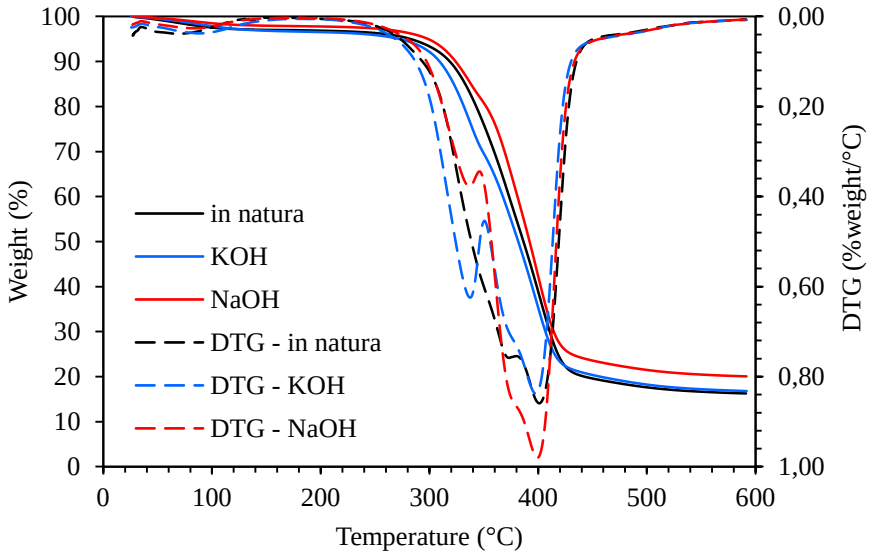

Figure 1: TG and DTG curves for curauá/ epoxy prepregs as a function of fiber treatment at the heating rate of 5 °C/min.

According to data, the NaOH prepreg present lower water vaporization (2.13%) and consequently better thermal stability at 150 °C. Although lignocellulosic fibers contain a significant level of water, the presence of the matrix influenced the vaporization and prevented the water from being released.

Table 1: TGA data for curauá fiber/ epoxy prepreg according to the fibers treatments.

Prepreg	Humidity (%)	T_{onset} (°C)	T_{peak} (°C)	T_{endset} (°C)	The residue at 600 ºC (%)
in natura	3.03	325.2	401.0	423.5	16.3
KOH	3.31	322.6	397.7	418.9	16.8
NaOH	2.13	341.5	399.4	421.2	20.1

According to Table 1, the T_{onset} of decomposition for the prepregs occurred between 322.6 and 341.5 °C, that is a higher temperature than the typical processing range (100–120 °C for curing). In the case of "thermal runaway", if a sufficient high temperature is reached during the curing process, the resin will begin to decompose, decreasing mechanical properties [18]. The second stage of weight loss showed thermal degradation peaks around 400 ºC. According Table 1, the NaOH prepreg exhibited the higher thermal stability at the beginning of the degradation (T_{onset}). In contrast, the *in natura* and KOH prepregs presented a decrease in T_{onset} degradation stage of 16.3 and 18.9 °C, respectively. All prepregs presented a residual weight between 16.3 and 20.06% at 600 ºC.

3.2 Differential Scanning Calorimetry Analyses

Figure 2 shows the DSC curves obtained from the non-isothermal runs for the uncured and cured prepregs. The thermal properties such as glass transition temperature (T_g), cure peak temperature ($T_{cure\ peak}$), enthalpy involved on the process (ΔH) and degree of cure (α_{cure}) are summarized in Table 2.

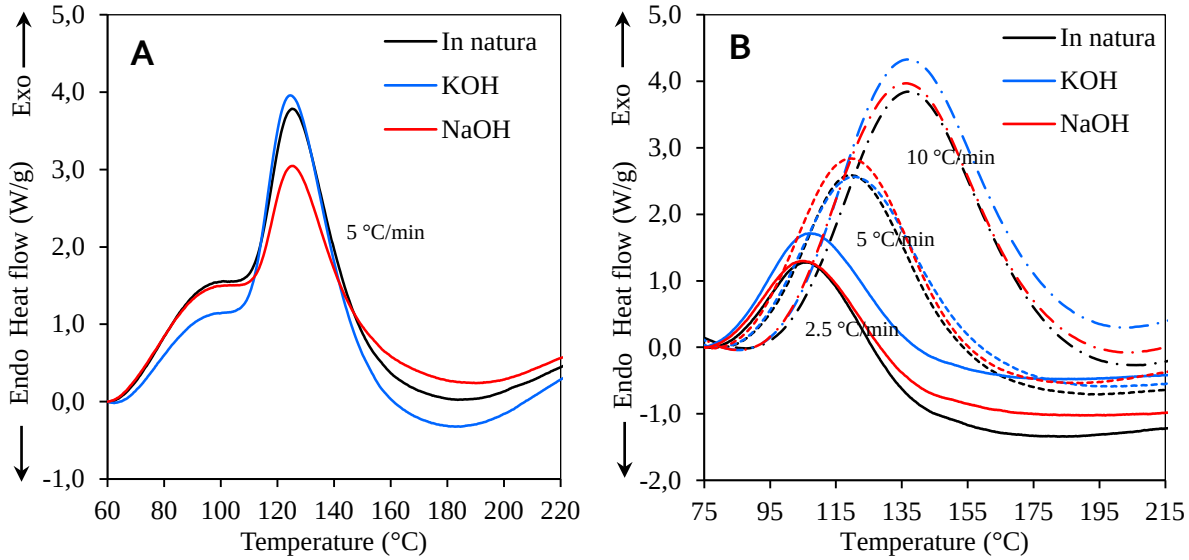

Figure 2: DSC curves of curauá fiber/ epoxy prepregs according to the different curing time: 0 hours (just prepared) (a) and 38 hours (semisolid tacky) (b).

The values of ΔH were obtained from DSC curves as exposed in Table 2 and corresponding to the heating rate of 5 °C/min. The glass transition temperature (T_g) for NaOH (59.9 °C) was higher than *in natura* and KOH prepregs (55.8 and 56.7 °C, respectively). The cured prepregs also present a higher T_g than the uncured samples (~6 °C). This growth in T_g can be explained by the fact that while the degree of crosslinking growths, the T_g of the epoxy resin also increases [16]. The curing peak for cured prepregs was found to be ~120 °C.

Table 2: DSC data of curauá fibers/ epoxy prepregs according to the different curing time.

Curing time	Sample	T_g (°C)	$T_{cure\ peak}$ (°C)	ΔH (J/g)	α_{cure} (%)
0 hours	neat resin	42.1	121.9	477.4	0
	in natura	49.9	125.1	184.3	0
	KOH	49.0	124.5	174.1	0
	NaOH	48.2	125.0	156.5	0
38 hours	neat resin	55.8	117.6	203.9	57.29
	in natura	55.8	119.7	142.9	22.46
	KOH	56.7	120.8	133.1	23.55
	NaOH	59.9	119.9	119.1	23.90

The average degree of curing (α_{cure}) was evaluated 57.29% for the neat resin. In prepregs, the α_{cure} was estimated ~23.3%, which is 34% lower concerning the neat epoxy. The reduction on the degree of curing can be associated to the addition of fiber on the matrix. A minor exothermic peak was also detected between 180 and 280 °C, which may be attributed to crosswise reactions, like homopolymerization and etherification of epoxide groups that usually take place at high temperatures [19].

3.4 Cure Kinetics

Non-isothermal DSC curves obtained at three different heating rates, 2.5, 5 and 10 °C/min for the curauá fibers/ epoxy prepregs was shown in Figure 2b, and it can be observed that all profiles have a single shape with a single exothermic peak at ~120 °C.

The total enthalpy involved in the curing process of the prepregs was obtained from the integration of the area under these DSC curves. The extent of conversion α was calculated by Equation 5 and is shown in Figure 3a.

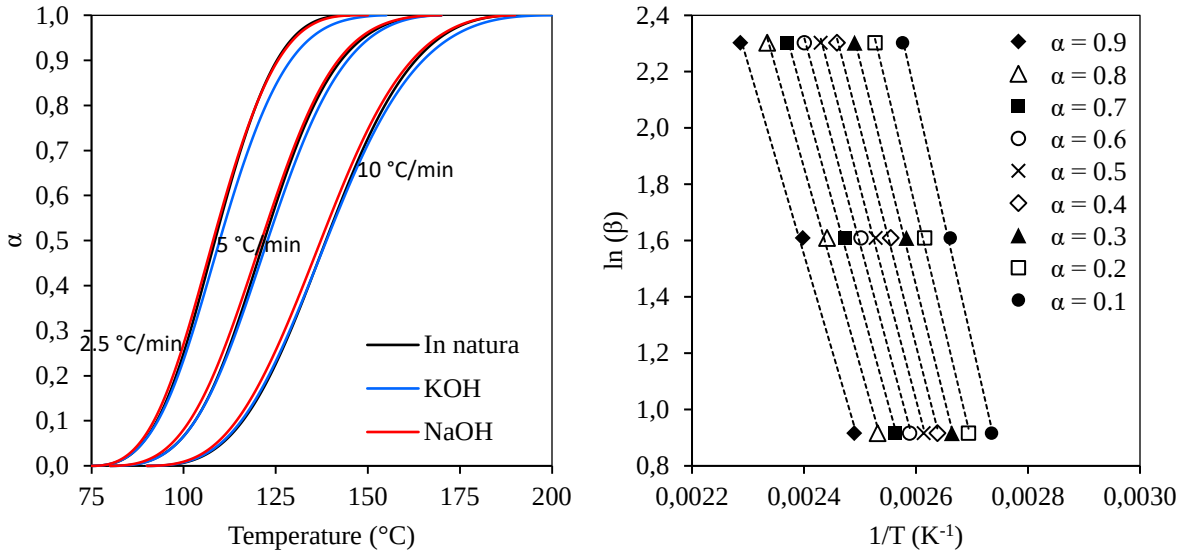

Figure 3: Reaction conversion profiles of the curauá fiber/ epoxy prepregs at different heating rates (a); Plots of ln (β) x 1/T (K^{-1}) for the *in natura* prepreg at different fractional conversions (b).

The application of the non-isothermal method was used to generate the conversion extension plot according to the different heating rates. From these curves, it was possible to extract the data relating the essential temperatures in different heating ratios (β) to reach the specific degree of conversion [10]. The plots of ln (β) against 1/T (K^{-1}) was generated from the conversion profiles and are present on the Figure 3b.

The activation energy (E_a) was calculated for each degree of conversion applying linear regression (Figure 4). The information about the E_a is presented in Table 3.

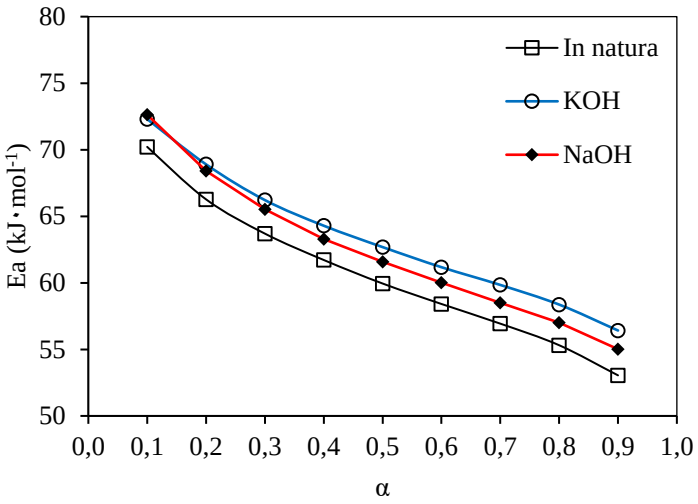

Figure 4: Activation energy of the curauá fiber/ epoxy prepregs as a function of the extent of conversion.

Table 3: Kinetics parameters obtained by the non-isothermal isoconversional method of the curauá fiber/ epoxy prepregs at α=0.5 extent of curing.

Prepreg	R^2	ln A (s^{-1})	Ea ($kJ \cdot mol^{-1}$)
in natura	0.9982	19.83	59.95
KOH	0.9985	20.64	62.69
NaOH	0.9985	20.38	61.57

The activation energy decreased with the progress of the curing extension for all samples, ranging from 72.63 to 53.05 $kJ \cdot mol^{-1}$. The KOH prepreg present the highest average activation energy (63.35 $kJ \cdot mol^{-1}$) and the *in natura* prepreg the lowest one (61.40 $kJ \cdot mol^{-1}$).

4 CONCLUSIONS

The fibers treatment influences on the thermal stability of the prepregs. The TG and DTG curves suggested the NaOH is the highest thermal stable prepreg between all samples and the T_{onset} was recorded at 341.5 °C. The decomposition of all composites mainly happened at ~400 °C and the residue at 600 °C was found between 16.28 and 20.06%. The NaOH treated fibers resulted in T_g higher than *in natura* and KOH prepregs, and the average degree of curing of prepregs was evaluated ~23.3%. An isoconversional method using the Arrhenius equation was developed and applied to analyze the curing kinetics, and the activation energy was calculated at a given function of the extent of conversion. The KOH prepreg presents the highest activation energy and the *in natura* prepreg the lowest one. The characterization of these prepregs was necessary to define the final processing conditions and to evaluate the cure cycle used to manufacture polymeric composite components.

ACKNOWLEDGEMENTS

This work was supported by Capes, CNPq, DPG-UnB and FAP-DF.

REFERENCES

[1] John, M.J. and Thomas, T., 'Biofibres and biocomposites', *Carbohydrate Polymers*. **71 (**2008) 343-364.

[2] Leão, A. L., Rowell, R., Tavares N., 'Applications of natural fibres in automobile industry in Brazil and thermo-forming process. Emerging technologies and business opportunities', In. 'Science and technology of polymers and advanced materials'. New York & London, Plenum Press, (1998) 755-761.

[3] Zah, R., Hischier, R., Leão, A.L., et al., 'Curauá fibers in the automobile industry e a sustainability assessment', *Journal of Cleaner Production.* **15** (2007) 1032-1040.

[4] Akbar S., Chen Y., Yousaf I., et al., 'E-glass/phenolic prepreg processing by solvent Impregnation', *Polymers and Polymer Composites*. **16** (2008) 19-26.

[5] Campbell, F.C. 'Structural Composite Materials'. ASM International, Cleveland, (2010).

[6] Saalbrink, A., Lorteije, A., Peijs, T., 'The influence of processing parameters on interphase morphology in polymer composites based on phase-separating thermoplastic/epoxy blends', *Composites Part A.* **29** (1998) 1243-1250.

[7] Costa, M.L., Rezende, M.C., Botelho, E.C., 'Estabelecimento de ciclo de cura de pré-impregnados aeronáuticos', *Polímeros: Ciência e Tecnologia.* **15** (2005) 224-231

[8] Gallagher, P.K. "Handbook of thermal analysis is and calorimetry: Applications to polymers and plastics', Elsevier Science, Amsterdam, (2002).

[9] Sbirrazzuoli, N., Vyazovkin, S., 'Learning about epoxy cure mechanisms from isoconversional analysis of DSC data', *Thermochimica Acta*, **388** (2016) 289-298.

[10] Mehdy Vafayana, M., Beheshtya, M.H., Ghoreishyb, M.H.R., et al., 'Advanced integral isoconversional analysis for evaluating and predicting the kinetic parameters of the curing reaction of epoxy prepreg', *Thermochimica Acta.* **557** (2013) 37-43.

[11] Ghumara, R.Y., Adroja, P.P., Parsania, P.H. 'Synthesis, characterization, and dynamic DSC curing kinetics of novel epoxy resin of 2,4,6-tris(4-hydroxyphenyl)-1-3-5-triazine', *Journal of Thermal Analysis and Calorimetry*. **114** (2013) 873-881.

[12] Costa, M.L., Botelho, E.C., Rezende, M.C., 'Monitoring of cure kinetic prepreg and cure cycle modeling', *Journal of Materials Science*. **41** (2006) 4349-4356.

[13] Vafayan, M., Beheshty, M.H., Ghoreishy, M.H.R, et al., 'The prediction capability of the kinetic models extracted from isothermal data in non-isothermal conditions for an epoxy prepreg', Journal of Composite Materials. **48** (2014) 1039-1048.

[14] Vyazovkin, S., Sbirrazzuoli, N. 'Isoconversional Kinetics of Thermally Stimulated Processes', Springer, New York. (2015).

[15] Vyazovkin, S., Chrissafis, K., Lorenzo, M.L., *et al*., 'ICTAC Kinetics Committee recommendations for collecting experimental thermal analysis data for kinetic computations', *Thermochimica Acta.* **590** (2014) 1-23.

[16] Costa, M.L., Paiva, J.M.F, Botelho, E.C., Rezende, M.C., 'Avaliação Térmica e Reológica do Ciclo de Cura do Pré-Impregnado de Carbono/Epóxi', *Polímeros: Ciência e Tecnologia*. 13 (2003) 188-197.

[17] Hoareaua, W., Trindadea, W.G., Siegmund, B., et al., 'Sugar cane bagasse and curaua lignins oxidized by chlorine dioxide and reacted with furfuryl alcohol: characterization and stability'. *Polymer Degradation and Stability*. **86** (2004) 567-576

[18] Chatterjee, A., 'Thermal degradation analysis of thermoset resins', *Journal of Applied Polymer Science*. **114** (3) (2009) 1417-1425.

[19] Sbirrazzuoli, N., Mija, A., Vincent, L., et al., 'Isoconversional kinetic analysis of stoichiometric and off-stoichiometric epoxy-amine cures', *Thermochimica Acta*. **447** (2006) 167-177.

WATER ABSORPTION STUDY IN COMPOSITES OF EPOXY MATRIX USING AS REINFORCEMENT FIBER: SISAL NATURAL, ACETYLATED AND MODIFIED WITH ALUMINIUM OXIDE HYDRATED

Pinheiro C. H.[1] (1), Pellucci L. A.(1) and Da Silva M. L. C. P (1)

(1) Chemical Engineering Department, Lorena School of Engineering, University of São Paulo, Lorena, São Paulo, Brazil

https://doi.org/10.21452/bccm4.2018.10.06

Abstract

Due to its eminent environmental concern, purely synthetic materials are being increasingly discouraged for application as dispersed phase in polymer matrix composites. Considering its mechanical properties, an ecological alternative for it is the use of Sisal fiber (Agave sisalana) as reinforcement. However, by reason of its hydrophilic nature, there is a necessity to improve the characteristics of the fiber in terms of decreased water absorption capacity, increased mechanical strength and improved thermal stability. The possible improvements currently studied are the surface modifications of plant fibers through physical and chemical treatments. This work has the objective of presenting two surface treatments of sisal fiber: acetylation and modification with hydrated aluminum oxide ($Al_2O_3.nH_2O$), which is called hybrid. The fibers were characterized by Fourier transform infrared spectroscopy (FTIR). The presence of 0.72% (w/w) aluminum was observed by using dispersive energy spectrometry (EDS) attached to a scanning electron microscope. The manual rolling process was used to prepare the composites. Tests of water absorption in the composites showed a decrease in 33% when the acetylated fiber was used as reinforcement and 28% when using the hybrid.

1. INTRODUCTION

Generally, a composite can be considered as any multiphase material that exhibits a significant proportion of properties of both constituent phases. For the biocomposites, at least one of the phases has organic origin[1][2]. Currently, there is a high demand for new materials that combine simplicity in production, high quality standard, large scale supply and low manufacturing cost. Additionally, with the growing environmental concern with residues and product lifetime, the use of pure synthetic materials in both matrices and reinforcements has been increasingly discouraged on the many engineering applications[3]. The sisal fiber (Agave Sisalana) stands out as a dispersed phase in biocomposites, due to its availability and mechanical resistance. Usually when the fiber

is hydrophilic, surface treatments are used to improve interfacial adhesion and consequently there is a significant increase in the mechanical properties of the material[4]. Acetylation is a chemical modification technique that decreases the hydrophilic tendency of natural fibers. The hydroxyl groups present in the hemicellulose or lignin constituting the sisal fibers are partially replaced by the acetyl functional group present in the acetic acid, thus it forms an ester. This type of modification shows a notable improvement in interfacial bonds, promoting changes in mechanical properties[5][6][7]. The hydrated aluminum oxide ($Al_2O_3.nH_2O$) is the inorganic component most used as flame retardant when applied to polymers[8]. As the temperature rises, the hydrated alumina oxide decomposes endothermally (about 220 ° C with an endothermic reaction of 1.17 KJ g -1). It absorbs energy and releases nonflammable water that dilutes combustible gases [9]. Group work has shown promising results regarding the thermal stability of lignocellulosic fibers treated with hydrated aluminum oxide[7][10][11]. Besides the optimization of mechanical and thermal properties, surface treatments of natural fibers seek to minimize water absorption[6]. The aim of the present work was to evaluate the amount of water absorption in epoxy matrix composites reinforced with modified sisal fiber through two surface treatments: acetylation and modification with hydrated aluminum oxide ($Al_2O_3.nH_2O$).

2. METHODOLOGY AND CHARACTERIZATION

First of all, the sisal fibers, which were bought from Sisalsul, were subjected to attack with 80% (v / v) acetic acid for 20 min at 120ºC whilst stirring, promoting their acetylation. In a second stage the acetylated fibers were placed in a reactor, where metal aluminum was solubilized in a solution of KOH (0.2 mol L^{-1}). Then, H_2SO_4 solution (1 mol L^{-1}) was added until pH ~ 9 for the precipitation of the hydrated aluminum oxide. The fibers were washed and dried at room temperature until constant weight. At that point The natural, acetylated and hybrid fibers were analyzed using Fourier Transform Infrared Spectroscopy (FTIR) techniques and scanning electron microscopy attached to a dispersive energy spectrometer (EDS). For this work three composites were prepared, one with natural sisal fiber as reinforcement, the second with acetylated fiber and the third with the hybrid. The conformation of the composite begins with the preparation of the reinforcement, which is the organization of the fibers in a continuous and parallel pattern. After preparation of the reinforcement, a blend of Araldite LY 1564 epoxy resin with Aradur 2963 hardener was added to the fibers at a ratio of 5.8 g of blend: 1g of fiber, using the manual laminating technique. After 24 hours the composites were submitted to the water absorption test according to ASTM D570. For this test, a pre-weighed 5cm x 5cm specimen was immersed in deionized water at 23 ° C (± 2). After 2h the specimens were dried and weighed. The tests were repeated every 24 hours until a significant mass variation was not observed. The test was done in triplicate.

3. RESULTS

Figure 1 shows the FTIR spectrum of the natural, acetylated and hybrid fibers. An axial strain C = O of ester is observed at 1740 cm-1, confirming the occurred esterification in the sisal fiber. It should be noted that the hybrid does not exhibit this vibration, that indicates a modification in the ester function of the structure. Figure 2 shows the results of the water absorption test between (a) natural, acetylated and hybrid fibers and (b) their respective composites. The test allows to say that the fibers maintained a different behavior and the treatment promoted significant changes in the capacity of absorption. Even though it was observed to increase in the fiber's water capacity after the treatment with aluminum oxide, the test with the composites shows a decrease of 33%

and 28% for those that used the reinforced fibers acetylated and hybrid, respectively.

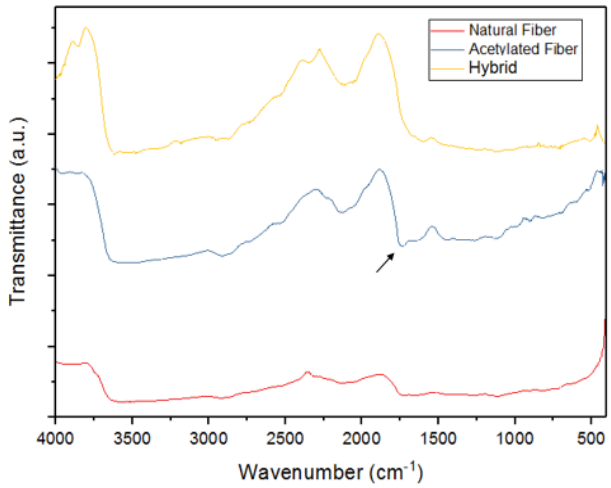

Figure 1 - FTIR spectre natural fiber, acetylated and hybrid

(a) (b)

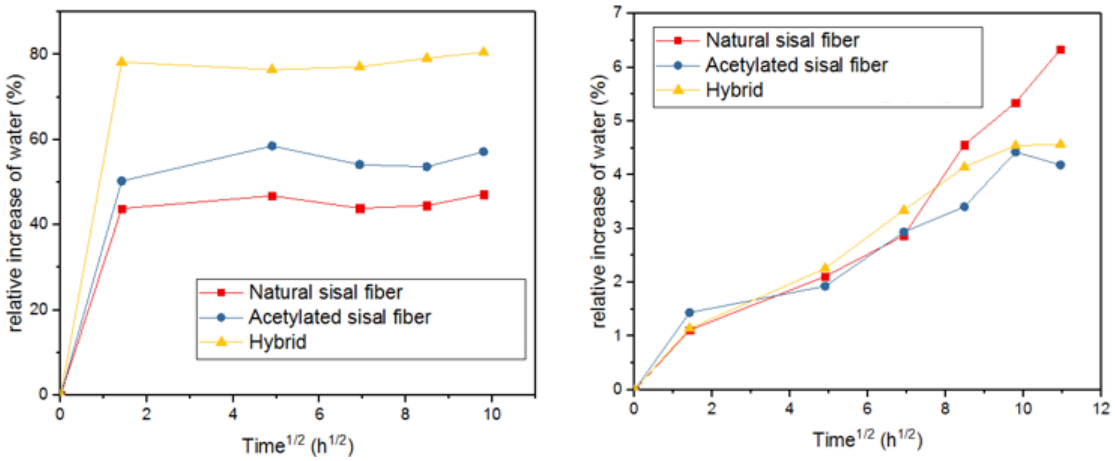

Figura 2 –water absorption (a) natural fiber, acetylated and hybrid (b) epoxy matrix composites with natural fiber, acetylated and hybrid

.

4. CONCLUSION

Esterification was verified by FTIR and generation of the hybrid by EDS. The treatments performed on the fiber promoted changes, resulting in a decrease in the water absorption capacity of the epoxy matrix composites studied.

REFERENCES

[1] CALLISTER, W. D.; RETHWISCH D.G. Ciência e engenharia de materiais uma introdução: 8. ed. Rio de Janeiro: LTC, 2012

[2] TICOALU, A.; ARAVINTHAN, T.; CARDONA, F. A review of current development in natural fiber composites for structural and infrastructure applications. n. **Southern Region Engineering Conference** November, p. 1–5, 2010.

[3] ASHIK, K. P.; SHARMA, R. S. A Review on Mechanical Properties of Natural Fiber Reinforced Hybrid Polymer Composites. **Journal of Minerals and Materials Characterization and Engineering**, v. 3, n. September, p. 420–426, 2015.

[4] SRISUWAN, S.; PRASOETSOPHA, N.; SUPPAKARN, N. The Effects of Alkalized and Silanized Woven Sisal Fibers on Mechanical Properties of Natural Rubber Modified Epoxy Resin. **Energy Procedia**, v. 56, p. 19–25, 2014.

[5] TSERKI, V. et al. A study of the effect of acetylation and propionylation surface treatments on natural fibres. **Composites: Part A** v. 36, p. 1110–1118, 2005

[6] SAHU, P.; GUPTA, M. K. Sisal (Agave sisalana) fiber and its polymer-based composites : A review on current developments. **Journal of Reinforced Plastics and Composites** Vol. 36(24) 1759–1780 2017

[7] SANTOS E. P. Dos. Síntese e caracterização de híbridos celulósicos modificados com óxidos metálicos hidratados para aplicação como aditivos em espumas rígidas de poliuretanos; Tese de doutorado; Instituto Nacional de Pesquisas Espaciais – INPE 2017

[8] XU, Z.; YAN, L.; CHEN, L. Synergistic flame retardant effects between aluminum hydroxide and halogen-free flame retardants in high density polyethylene composites. **Procedia Engineering**, v. 135, p. 630-636, 2016.

[9] GOUDARZI, M.; GHANBARI, D. Synthesis and Characterization of Al(OH)3, Al2O3 Nanoparticles and Polymeric Nanocomposites. **Journal of Cluster Science**, v. 27, n. 1, p. 25–38, 2016.

[10] CARVALHO, T. Preparação e caracterização de compósitos com matriz de poliuretano e híbridos fibrosos modificados com óxido de magnésio hidratado. 2016. 126 p. Dissertação (Mestrado em Ciências) - Escola de Engenharia de Lorena da Universidade de São Paulo. Lorena, 2016.

[11] OTTOBONI, F. S. Desenvolvimento de novos compósitos baseados em polietileno e híbridos gerados a partir de resíduos agrícolas modificados com óxido de nióbio. 2011. 121 p. Dissertação (Mestrado em Ciências) – Escola de Engenharia Lorena, Universidade de São Paulo, Lorena/SP, 2011.

EFFECT OF FIBERS ALKALI TREATMENT ON THERMAL BEHAVIOUR OF CURAUÁ/ POLYESTER COMPOSITES

Linconl A. Teixeira [(1)], Vilson Dalla L. Jr [(1)], Rosineide M. Leão [(1, 2)] and Sandra M. da Luz [(1, 3)]

(1) Engineering Materials Integrity Program, University of Brasília, Brasília, Brazil
(2) Institute of Exact Sciences and Technology, Paulista University, Brasília, Brazil
(3) Department of Chemical and Materials Engineering, University of Alberta, Alberta, Canada

https://doi.org/10.21452/bccm4.2018.10.07

Abstract:

The interaction between natural fibers and polymeric matrices can be the main disadvantage to expansion of natural fibers in industry application. Alkali treatments are usually applied on natural fibers to remove the lignin and extractives improving the adhesion between the reinforcement and matrix, and consequently, the thermal properties. The curauá, a typical plant from Amazon region, becomes very attractive since it presents high cellulose content, low density, and high strength. The primary objective of this work is to evaluate the thermal behavior and cure parameters of the curauá/ polyester composites through thermal analysis. The untreated curauá fibers and alkali treated by solutions of KOH 10% (w/v) or NaOH 5% (w/v) were mixed to polyester resin and a hardener (2 phr). Further, the curauá/ polyester composites were fabricated by hand lay-up method with fiber fraction of 10 or 20 wt% and cured for 24 hours. Thermogravimetry and its derivative curves (TG-DTG) and differential scanning calorimetry (DSC) analysis were used to determine composites thermal behavior as well its glass transition temperature (T_g). TG-DTG analysis revealed that the curauá treated with NaOH 20 wt%/ polyester composite presented the higher thermal stability compared to the neat matrix and other composites. Besides, the composites with both treated fibers presented higher T_g than the neat matrix, increasing with fiber content. The composite reinforced with curauá treated with NaOH 10 wt% shows the higher change in T_g, increasing to 11.3 °C. The DSC analysis showed that the second exothermic peak that appears in the curves is associated with the cure of composite between 117-119 °C. Finally, the composites with fibers treated with alkaline presented better thermal stability than composite reinforced with untreated fibers.

Keywords: Curauá fibers, polyester, composite, thermal properties.

1. INTRODUCTION

In recent years, the increasing interest of the industry in the use of natural fibers such as sisal, curauá, rami and buriti to replace synthetic fibers in polymeric composites has demanded studies on the performance of these materials. Natural fibers have been increasingly applied in polymeric composites due to its lower density and costs, and good mechanical strength concerning synthetic fibers [1-2]. The use of natural fibers as on the field of composites has become vital since they are renewable and biodegradable, as well as causing a lower risk to human health [2].

The curauá plant (*Ananas erectifolius*) is cultivated in the northern of Brazil, and its average chemical composition is 62% cellulose, 15% hemicellulose, 7% lignin and 0.9% ash [3]. The curauá fibers are extracted from their leaves and exposed to air to dry. Because of their excellent mechanical properties, curauá fibers are widely used as reinforcement of polymeric composites [3-5].

Achieving a fiber/matrix adhesion, the natural fibers are usually exposed to a chemical treatment to increase the fiber contact region with a polymer. Alkali, silane, acetylation, and benzoylation can be mentioned as chemical reagents most used to treat the surface of the natural fibers [6-7]. This increase in adhesion occurs due to the modification of the fiber structure and chemical composition. As a result, the hydrophilic nature of fiber is reduced, and its compatibility with the matrix increases once the surface roughness of the fiber also increases [5-7].

A wide variety of products to produce polymeric composites is commercially available, and the polyester resin is applied as the main material [9-10]. The polyester resin is a polymer matrix widely used by industry. The resin presents many attractive properties, such as excellent impact resistance, good adhesion properties and resistance to chemical corrosion [10]. The high crosslinking density, in which the binding of the macromolecules occurs, makes the polyester resins high thermally stable and mechanically harder. However, despite these advantageous properties, thermosetting resins are brittle and more predisposed to mechanical failure [12].

Thermogravimetry analyses (TG) is an important technique that is used to understand degradation that occurs in composite materials with the increase of temperature (TG), as well as to evaluate the thermal stability of materials. Its derivative thermogravimetric curves (DTG) provides data indicating the temperature at which specific thermal events occur and show the materials stages of degradation [12-13].

Another technique used to analyse the thermal behavior of composites is the differential calorimetry scanning (DSC), on this technique the physical property measured is the temperature difference between the sample and the reference material, as both are subjected to the same controlled variation of temperature. By this method it is possible to study the curing reaction in composites of thermosetting polymers, thus, determining the temperature at which the polymer curing takes place [14-15].

The objective of this work is to evaluate the thermal behavior of the curauá/ polyester composites, using the polyester resin as a matrix and the curauá fibers as reinforcement, comparing the treated fibers with different alkali to untreated curauá fibers. This comparison will allow a better understanding how the treatment and the fiber content will affect the thermal behavior.

2. EXPERIMENTAL

2.1 Materials

The curauá fibers used in work originated from Santarém - PA and were supplied by CEAPAC. The fibers were available untreated and long, with an average length of 80 cm. The AZ 14.0

infusion polyester resin of the E-composites brand was used as the polymer matrix with the Demelox 14.0 catalyst, both from *DML Produtos Químicos*.

2.2 Fibers chemical modification

The curauá fibers cut to a length of (5-6 cm) were submitted to two different alkali treatments. In the first treatment, the fibers were mercerized in a solution of sodium hydroxide 5% (w/ v) at ratio of 10: 1 (solution: fiber), at a temperature of 50 °C for 2 h under manual stirring. Finally, the fibers were washed with distilled water until neutralized pH, dried at room temperature for 48 h and in an oven for 24 h at 60 °C.

On the second treatment, the fibers were soaked at distilled water in a ratio of 10: 1 (water/ fiber) for 1 h at room temperature and then filtered. The fibers were immersed in a solution of potassium hydroxide 10% (w/ v). The mixture was mechanically stirred at a speed of 50 rpm and orbital agitation of 150 rpm simultaneously for 3 h at room temperature. Subsequently, the fibers were washed with distilled water until pH neutralized, dried at room temperature for 48 h and in an oven for 24 h at 60 °C.

2.3 Preparation of composites

The composites developed in this study were manufactured using the hand lay-up method. The polyester resin was forced through the fibers blankets by a hand roller. The composites with 3 x 5 x 0.2 cm dimensions was cured at room temperature for 24 h.

2.4 Thermogravimetric Analysis (TGA) and Differential Scanning Calorimetry (DSC)

The samples were analysed in a simultaneous (TGA-DSC) thermal analyser Q600 SDT equipment (TA Instruments, USA) under an inert atmosphere of nitrogen with a flow rate of 50 mL/min. The samples with 10 ± 0.5 mg were deposited in an alumina pan. The analyses were carried out under a heating rate of 5 °C/ min from 25 to 600 °C (fibers) and 25 to 300 °C (composites).

3. RESULTS AND DISCUSSION

3.1 Thermogravimetric Analyses

Figure 1 shows the thermal degradation curves of the untreated or treated curauá fibers, from the TG-DTG analysis. The thermal behavior of fibers is similar to each other, with a slight thermal stability for NaOH treated fibers. The thermal stability was found at the temperature range between 265 and 273 °C. Residues resulting from the fiber analysis (maximum TGA temperature of 600 °C) were around 12% - 15%. The residues content increases according to the treatments. The free ends of cellulose chains decompose at low temperature, increasing cellulose crystallinity and carbon ratio, resulting in waste content increases at the end of analysis [8, 19].

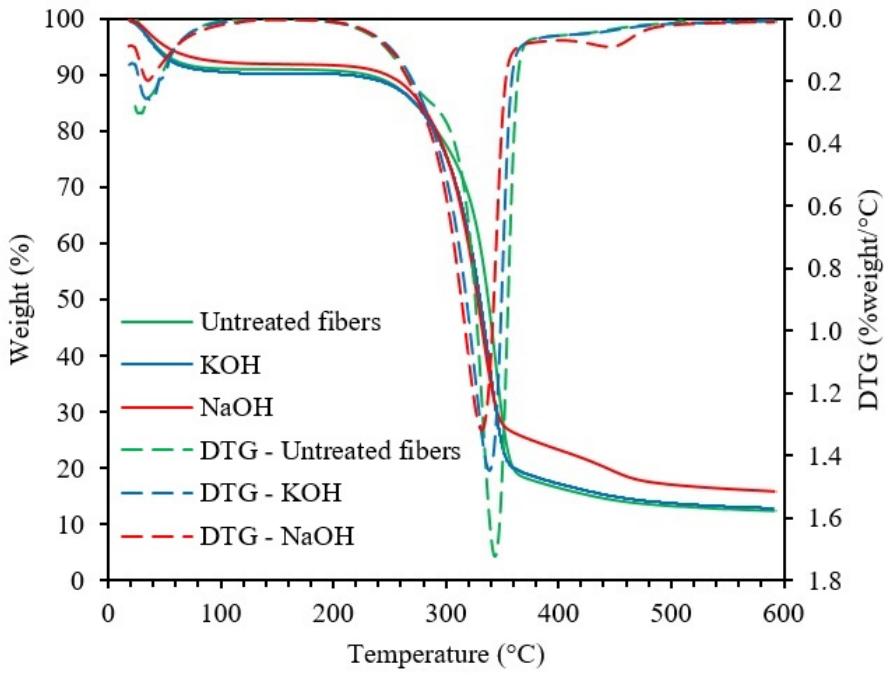

Figure 1: TG and DTG curves for untreated and treated curauá fibers

The DTG curves observed in Figure 1, presented two degradation peaks. The first peak corresponds to the moisture loss of fibers that can be observed at 100 ºC [17]. The second peak that occurs between 270 - 380 °C is attributed to the degradation of cellulose and hemicellulose [17]. The DTG curves also show that the untreated fibers present the maximum decomposition temperature, with T_{peak} around 343 °C and T_{onset} at 268 °C. The fibers treated with NaOH shows T_{peak} at 331 °C and T_{onset} at 273 °C, and the fibers treated with KOH shows T_{peak} of decomposition occurs at 338 °C and T_{onset} at 264 °C.

Table 1 shows the data from the TG-DTG curves for the curauá/ polyester composites. The composites treated with alkali presented the highest thermal stability compared to untreated fibers composites and polyester resin cured. The thermal stability of the composites was found at the temperature range between 251-254 °C.

Table 1: TG and DTG data of the curauá/ polyester composites

Sample	Moisture (%)	T_{onset} (°C)	The residue at 300 °C (%)
Untreated curauá 10 wt%/ polyester	2.97	247.86	81.36
Untreated curauá 20 wt%/ polyester	3.06	247.79	83.19
Curauá treated with KOH 10 wt%/ polyester	3.06	254.23	80.50
Curauá treated with KOH 20 wt%/ polyester	2.90	251.43	80.61
Curauá treated with NaOH 10 wt%/ polyester	2.97	251.95	79.88
Curauá treated with NaOH 20 wt%/ polyester	4.53	254.93	76.53
Polyester resin cured	-	228.17	81.75

3.2 Differential Scanning Calorimetry Analyses

Figure 2 presents the DSC curves of the curauá/ polyester composites. DSC analyses permit to find the glass transition temperature (T_g) and cure behavior of the composite as a function of treatment and fiber content.

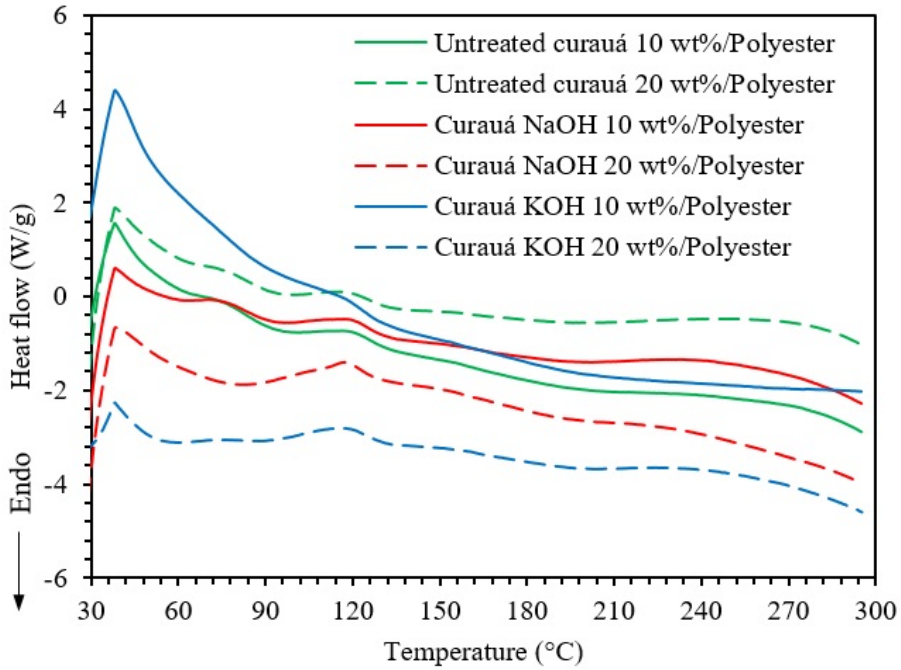

Figure 2: DSC data of the curauá/ polyester composites

Table 2 shows the data from the DSC curves of curauá/ polyester composites. The untreated curauá 10 wt%/ polyester composite showed the residual cure exothermic peak around 118 °C with *ΔH* of 3.19 J/g, while the curauá treated with KOH 20 wt%/ polyester presented the cure temperature at 116 ° C with enthalpy involved in this process of 6.80 J/g. The enthalpy involved in the curing process for alkali-treated composites increased compared to untreated fiber composites. This means that the higher the enthalpy energy could be given for the fiber/ matrix interaction [18].

Table 2: DSC data of the curauá/ polyester composites

Sample	T_g (°C)	T_{peak} cure (°C)	ΔH (J/g)
Untreated curauá 10 wt%/ polyester	91.44	118.69	3.19
Untreated curauá 20 wt%/ polyester	89.80	118.11	3.37
Curauá treated with KOH 10 wt%/ polyester	86.31	117.59	1.84
Curauá treated with KOH 20 wt%/ polyester	83.97	116.62	6.80
Curauá treated with NaOH 10 wt%/ polyester	90.62	119.03	4.44
Curauá treated with NaOH 20 wt%/ polyester	89.47	117.17	6.76
Polyester resin cured	79.32	118.18	3.06

According to the data obtained for enthalpy, the increase of fiber content on the composites decreases the T_{peak} cure of the material. The composites with 20 wt% fiber contents presented the highest enthalpy register on the residual cure stage, in this case, the material needed more energy to move. This is related to the presence of curauá fiber in composites. The bonds between the cellulose chains from fibers tend to increase the enthalpy values [18,19].

It was observed that there was an increase of T_g of composites concerning the T_g of the cured polyester. The increase in T_g is related to a reduction in molecular chain mobility and the increase in the formation of more efficient crosslinks. This phenomen reduces the volume of disordered molecular packaging, in this way, the increases in T_g occurs [20]. It is also noted that the composites with a lower content of fiber present the highest T_g. This is because the composites with lower fiber content have more resin and less crosslinks mobility, then a higher T_g is required for changes in the molecular structure of the composites [21]. The curing temperature of composites remained practically constant compared to the curing temperature of the polyester.

4. CONCLUSIONS

The alkaline chemical modifications promoted in the curauá fibers a best thermal stability for curauá fibers. The composites reinforced with NaOH and KOH treated fibers were also the most thermally stable when compared to composites untreated fibers. Noted that the T_g of the composites increased comparing to the polyester resin, which implies that a higher T_g is required to cause modification of the composite structure. Consequently, it was concluded that the alkali treatment is effective for curauá fiber to promote thermal stability increase in polymeric composites.

5. ACKNOWLEDGMENTS

This work was supported by Capes, CNPq, DPG-UnB, and FAP-DF.

6. REFERENCES

[1] Barreto, A. C. H., Rosa, D. S., Fechine, P. B. A., Mazzetto, S. E., ' Properties of sisal fibers treated by alkali solution and their application into cardanol-based biocomposites', *Composites Part A: Applied Science and Manufacturing.* **42** (2011) 492-500.

[2] Lavoratti, A., Romanzini, D., Amico, S.C., Zattera, A.J., 'Influence of fiber treatment on the characteristics of buriti and ramie polyester composites'. *Polymers & Polymer Composites*. **25** (4) (2017) 247-256.

[3] Spinacé, M. A.S., Lambert, C. S., Fermoselli, K. K.G., De Paoli, M.A.,'Curaua fiber reinforced high-density polyethylene composites: effect of impact modifier and fiber loading',*Carbohydrate Polymers Journal* **77** (2009) 47.

[4] Morais, J. A., Gadioli, R., De Paoli, M. A., 'Recycled polypropylene reinforced with curaua fibers by extrusion', *Journal of Applied Polymer Science*. **26** (2) (2016) 115-122.

[5] Nacas, A. M., Silva, R.L., De Paoli, M. A., Spinacé, M.A. S., 'Polypropylene composite reinforced with fibrillated curaua fiber and using maleic anhydride as coupling agent'. *Journal of Applied Polymer Science.* **113** (44913) (2017) 1-8.

[6**]** Kabir, M.M., Wang, H., Lau, K.T., Cardona, F., 'Chemical treatments on plant-based natural fibre reinforced polymer composites: an overview', *Composites Part B: Engineering*. **43** (2012) 2883-2992.

[7] Nimanpure, S., Hashmi, S.A.R., Kumar, R., Bhargaw, H.N., Kumar, R., Nair, P., Naik, A., 'Mechanical, electrical, and thermal analysis of sisal fibril/kenaf fiber hybrid polyester composites', *Polymer Composites.* (2017) 1-13.

[8] Harnnecker, F., Rosa, D.S., Lenz, D. M., 'Biodegradable polyester-based blend reinforced with curauá fiber: thermal, mechanical and biodegradation behaviour', *Journal of Polymers and the Environment.* **20** (2012) 237–244.
[9] Rossi, G., Giannakopoulos, I., Monticelli, L., Rostedt, N. K. J., Puisto, S.R., Lowe, C., Taylor,A. C., Vattulainen, I., T.A. Nissila., 'A martini coarse-grainedmodel of a thermoset polyester coating', *Macromolecules.* **44** (2011) 6198–6208.
[10] Wang, B., Qian,T., Zhanga, Q., Zhana, X., Chen, F., 'Heat resistance and surface properties of polyester resin modified with fluorosilicone', *Surface & Coatings Technology.* **304** (2016) 31–39.
[11] He, S., Petkovich, N. D., Liu, K., Qian, Y., Macosko, C. W., Stein, A,'Unsaturated polyester resin toughening with very low loadings of GO derivatives', *Polymer*. **110** (2017) 149-157.
[12] Mothé, C.G., Araújo C.R., 'Properties of polyurethane elastomers and composites by thermal analysis', *Thermochimica Acta*. **14** (2000) 357-358
[13] Jayaraman, K., Kok, M. V., Gokalp, I., 'Thermogravimetric and mass spectrometric (TG-MS) analysis and kinetics of coal-biomass blends', *Renewable Energy*. **101** (2017) 293-300.
[14] Kazilas, M. C., Partridge, I. K., 'Exploring equivalence of information from dielectric and calorimetric measurements of thermoset cure a model for the relationship between curing temperature, degree of cure and electrical impedance', *Polymer*. **46** (2005) 5868–5878.
[15] Papadopoulos, E., Markovic, M.G., Clarke, S., 'A Thermal and rheological investigation during the complex cure of a two-component thermoset polyurethane', *Journal of Applied Polymer Science*. **114** (2009) 3802–3810.
[16] Roman, M., Winter, W. T., 'Effect of sulfate groups from sulfuric acid hydrolysis on the thermal degradation behavior of bacterial cellulose', *Biomacromolecules*. (5) (2004) 1671-1677.
[17] Monteiro, S. N., Calado, V., Rodriguez, R. J.S., Margem, F. M., 'Thermogravimetric stability of polymer composites reinforced with less common lignocellulosic fibers', *Journal of Materials Research and Technology*. **1** (2) (2012) 117-126.
[18] Song, W., Zhao, F., Yu, X., Wang, C., Wei, W., Zhang, S., 'Interfacial characterization and optimal preparation of novel bamboo plastic composite engineering materials', *BioResources.* **10** (3) (2015) 5049-5070.
[19] Saw, S.K., Datta, C., 'Thermomechanical properties of jute/bagasse hybrid fibre reinforced epoxy thermoset composites', *BioResources* **4** (4) (2009) 1455-1476.
[20] Boey, F. Y. C., Lee, T. H., Sullivan, P. L., 'High-pressure autoclave curing for a thermoset composite: effect on the glass transition temperature', *Journal of Materials Science*. **29** (1994) 5985-5989.
[21] Bachtiar, D., Sapuan, S. M., Abdan, K., Zaman, K., 'The flexural, impact and thermal properties of untreated short sugar palm fihre reinforced high impact polystyrene (HIPS) composites', *Polymers & Polymer Composites*. **20** (5) (2012) 493-502.

PHOTOCHEMICAL APPROACH AS A STRATEGY TO RECYCLE RICE HUSK LIGNIN AND POST-CONSUMER POLYSTYRENE

Daniele G. Müller [(1)], Maria C. S. Bulhosa [(1)], Evelyn C. do C. Schenque [(1)], Marcelo P. da Rosa [(1)], Jessica S. da Silva [(1)], Paulo H. Beck [(1)] and Felipe Kessler [(1)]

(1) Photochemistry and Materials Chemistry Research Group. School of Chemistry and Food. Federal University of Rio Grande (FURG), Brazil

https://doi.org/10.21452/bccm4.2018.10.08

Abstract

The complete use of biomass and also the efficient management of waste materials are big challenges that must be overcome in this century. The work presented in this article uses lignin extracted from rice husk, using the organosolv method, as a filler in the residual expanded polystyrene (PS) matrix to obtain a PS/lignin composite. Two different carboxylic diacids (adipic acid and itaconic acid) were also employed as aditives. The initial materials and solvent were mixed and exposed to a medium pressure UV radiation source. The concentration of the lignin content was varied to evaluate its effect on the final material. The material was characterised using UV-Vis, FTIR, EDS, MEV, GPC, and mechanical assays. The spectroscopic and chromatographic data showed that 10 min of exposure was enough to promote changes in the polymeric chain. Due to the new spectroscopic features, a photo-grafting reaction occurred resulting in a stable PS/Lignin composite. Morphological analysis showed that even with a magnification of 40,000X some conditions result in films with great homogeneity. The mechanical tests showed a reduction in the tensile strength value with an increased lignin content, but in general, maintained the value of Young's modulus. Photochemical reactions were performed using a low complexity setup, in fast and mild reaction conditions, generating new uniform materials from polymeric residue and industrial waste.

1. INTRODUCTION

The increasing technological development of our society is leading to a serious imbalance between the environmental, economic, industrial, and social areas. Waste management has developed at different speeds throughout the world. Some parts of the world only recently in the past few decades, changed from waste being left in the streets to being treated and recycled using several methods and techniques and creating a very profitable industry. In the particular case of polymeric materials, some problems generated by the post-consumer polymers can be cited: i) the continuous increase in the amount of waste generated outstrips the collection, recycling, and

disposal capacities; and ii) synthetic polymers take a long time to degrade, needing management of the disposal sites for centuries.

General specifications have been developed, trying to achieve controlled degradation, like resins based on natural polymers[1], biopolymers[2], green polymers[3] .However, increasing oil production and the low cost of synthetic polymers make green material alternatives less attractive to industry. Natural polymers, especially those originating from biomass, are an interesting source for new materials. The renewable characteristic and the possibility to develop products free from carbon emissions agrees with the principles of green chemistry. Emerging countries produce large amounts of biomass due to their commodity-based economies. Rice husk is an example of an undervalued biomass resource generated by the food industry. On average the rice husk composes 22% of the grain**[4]**. The main components of the rice husk are polysaccharides (cellulose and hemicellulose), lignin and silicates, in proportions that vary slightly, depending on the plant and the soil that it grows in**[5]**. Lignin is a potential source of new materials due to its phenylpropanoids units. This random polymer is the second most abundant polymer in nature, present in almost all plant life. The chemical diversity, abundance, and its huge potential have motivated several studies to identify applications like polymeric precursors**[6]**, a carbon source for nanomaterials**[7]**, blends and composites**[8]**.

Photochemical methods are mainly based on photo-induced chemical processes. Chemical reactions can be induced if molecular groups show efficient reactivity once exposed to a light source. Depending on the chemical properties, specific reaction mechanisms can be achieved. Common chemical reactions like eliminations, additions, and dimerization in general, can induce the crosslink of macromolecule chains during UV exposure.[9] In addition, UV-assisted treatments usually have a simple experimental setup and low cost, being suitable for several industrial processes. Photochemical grafting has being used with success in composites, nanocomposites, biosensors[10]. Using a post-consumer PS and lignin extract from rice husk, the objective of this work was to synthesise Lignin/PS composite via the photochemical route. The results show that in a simple, fast, and low-cost synthesis route it is possible to obtain new polymeric materials, combining the strength of lignin and PS its versatility.

2. EXPERIMENTAL SECTION

2.1 Materials

Lignin extracted from rice husk using the organosolv method following the procedure of Rosa et al.[11] and was used as a macromolecule to be grafted. Expanded PS from discarded protective packaging was used without a purification process. Ethyl acetate (≥ 99%), hexane dioic acid (adipic acid), pureness ≥99%, and 2-methylidenebutanedioic acid (itaconic acid), pureness 99%, were purchased from Sigma-Aldrich, were used as received.

2.2 Synthesis of composites

All materials were synthesised using 1.0 g of PS, varying the lignin concentration in 2, 5, 10, 20 and 50% (w/w). 150 mL of ethyl acetate was added. Adipic acid (0.005 g) or itaconic acid (0.002 g) were used as the reaction controller. The system (PS–LO-dicarboxylic acid-solvent) was stirring at room temperature for 30 min. After this, the system was exposed to UV radiation using a medium pressure mercury lamp (400W) for 10 min, under magnetic stirring at room temperature. After the reaction, the polymer solution was poured into a petri dish and allowed to evaporate at ambient temperature and

pressure. All materials were named by the carboxylic acid used (AA or IA) followed by the percentage of LO (2, 5, 10, 20, and 50).

2.3 Analysis and characterization.

All precursors and products were characterised using spectroscopic analysis in the UV/visible region (UV-Vis) Infrared Fourier Transform Spectroscopy (FTIR-ATR) analysis were performed using a Shimadzu spectrophotometer - IR PRESTIGE 21. Gel Permeation Chromatography (GPC) were used to determinate the molecular weights of all samples (model Viscotek, VE 2001) equipped with one column (PS-DVB) and triple detector (refractive index, viscosimetric, and by light scattering). For the mechanical tests, five samples analysis were performed at room temperature, following the ASTM-D-88215 standard. The sample thickness was measured using a Mitutoyo micrometre (0.001 mm 0-25mm), and the cross-sectional area was calculated by the average of ten measurements. The maximum stress and the maximum elongation distance were measured by a texturometer, model TA XT plus, manufactured by Stable Micro Systems(UK). The Young's modulus was calculated by the relation between the initial distance and the distance at the break. Scanning Electron Microscopy (SEM) generated images, using a JEOL JSM-6610LV electronic microscope (Japan). Composition and semi-quantitative analysis of each element were performed by Energy Dispersive Spectroscopy (EDS) technique. Samples of each composite were analysed using a JEOL JSM-6610LV electronic microscope (Japan) using 15 KeV acceleration energy.

3. RESULTS AND DISCUSSIONS

The UV-Vis spectra of all samples (data not shown) present typical bands originating from pristine PS like the π–π^* transition of the C=C in the aromatic rings at 250-275nm.[12] It is also noted that this region matches with the lignin UV-Vis spectrum in that the majority have substituted aromatic rings and oxygenated groups in its structure, responsible for the π–π^* and n–π^* transitions. Oxygenated groups bonded to aromatic rings can increase the width of this band (220-280 nm), which allows lignin in natural environment to protect the plant from UV radiation.[13] After the reaction the structure of spectra changed.

FTIR-ATR analysis is presented in Figure 1, in both figure it is possible to compare the pristine PS spectrum with LO/PS composite with a load of 5% and 50%. When the pristine PS spectrum is compared with AA5 and AA50 samples spectra, the typical bands and peaks of PS remain, however, after the reaction some changes also are visible: symmetric and asymmetric aliphatic C-H stretch peaks have shifted from 2924cm^{-1} and 2852 cm^{-1} (PS), respectively, to 2922 cm^{-1} and 2848 cm^{-1} (AA5 and AA50). This shift is related to electron acceptor groups bonded to the main chain of PS.[8] A significant C-H stretch shift occurs for AI samples (Figure 1) indicating that the polymer chain changes more for samples with AI than AA. All composites show a wide C=O stretch band (~1718cm^{-1}) and seems to increase intensity when the lignin content increases. LO used in this study is rich in hydroxyl and carbonyl groups which we believe it was the main molecular group involved in the grafting onto some of the PS chain. It is important to observe the absence of hydroxyl peaks (3100-3600 cm^{-1}). The strong C-O-C stretch peaks present in all samples at 1265 cm^{-1} (Figure 1) indicate that a grafting reaction occurred. In this spectrum region also was identified C-O bending peaks at 1328 and 1217 cm^{-1} which are typical signals for syringyl and guaiacyl lignin groups.[14].

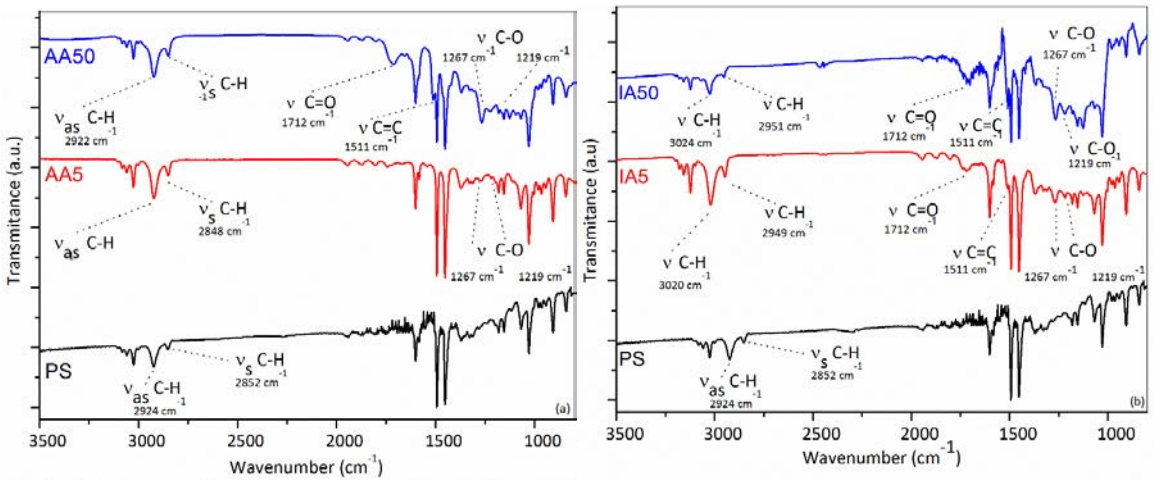

Figure 1. FTIR spectra for: (a) pristine PS (PS) and composites LO/PS prepared with adipic acid with 5% of lignin (AA5) and 50% of lignin (AA50); (b) pristine PS (PS) and composites LO/PS prepared with itaconic acid, with 5% of lignin (IA5) and 50% of lignin (IA50).

The UV-Vis data has revealed that after the photochemical reaction, the electronic transitions has suffered dramatical changes, showing new bands, yet maintaining the PS typical UV-Vis spectrum bands. The changes observed in FTIR-ATR spectra confirm the presence of lignin in the analysed samples and also some interesting features like the shift of aliphatic C-H peaks. Hydrogen abstraction mechanism is a common photochemical reaction, especially observed in polymers like PS when exposed to UV radiation.[9] During the UV irradiation, hydrogen atoms are abstracted from the main chain -CH_2 groups. The absence of -OH signals indicate that adipic acid and itaconic acid may are being decomposed during the irradiation, and responsible for the H-abstraction in the polymeric chain. This abstraction generates a reaction site, which in other conditions could lead to chain cleavage, but the presence of lignin during the irradiation leads to the grafting in the polymeric chain.

GPC analysis shows that in general, the polymeric chain does not suffer degradation due the UV radiation. GPC curves (data not shown) indicate that there is no formation of low weight products, which could justify PS chain cleavage.[15] In fact, the peak maximum is shifting to low retention time without any new bands or peaks. Table 1 shows the GPC data for PS, LO, and PS/LO samples. Is possible to observe that samples AA2, AA10, AA20, and AA50 showed a reduction in Mw and Mn values when comparing with pristine PS. The same samples slightly increased PDI value. This data could indicate that in those samples, the H-abstraction could lead to main chain cleavage, but the presence of lignin confirmed on the spectroscopic analysis, indicates that the cleavage is followed by the grafting of lignin units, which could also explain the low reduction of Mn and Mw values. AA5, AA50, IA2, IA10, IA20, and IA50 show the opposite behaviour. For these samples the values of Mw and Mn increase and the value of PDI decrease. For those samples, the cleavage is not evident in the GPC data, and the results also agree with the spectroscopic analysis. The grafting of LO units could lead to an increase in the Mw and Mn values. The presence of grafted lignin units could cause crosslinking between chains, which explains the decrease of PDI values.[16] The strain-stress data was obtained using an elongation test. The results of tensile strength (at breaking point) and the Young's modulus (E) are presented in Table 1. The tensile strength value of pristine PS was 21.78 MPa, and Young's modulus value was

2.33 GPa. All composites present a reduction in the tensile strength value. The tensile strength value of AA5, AA10, and AA20 composites do not suffer significant reduce (Table 1). A considerable reduction occurs with AA50. AA5, AA10, and AA50 showed a small increase in the value of Young's modulus.

Toriz et al. produced lignin/PP composites and reported that the effects of adding lignin to PP resulted in a decrease of the tensile strength value, proportional to the quantity of lignin added.[17] A reduction in the tensile strength is usually due to a partial interaction between load particles and the matrix. AA samples, in general, have little variation in the tensile strength value which can be correlated with the grafting of lignin macromolecules onto the polymeric chain. Once the PS/LO composite is formed the grafted lignin domains will stabilise non-grafted lignin domains. The better interaction reflects on the tensile strength results.[18] The tensile strength value of AA50 indicates that high concentration of lignin (50%) cannot be stabilised by the PS matrix, reducing the interaction between non-grafted lignin domains and composite chains. For IA samples, the tensile strength values decrease considerably.

Table 1. GPC data (Mn, Mw, and PDI) and mechanical test (tensile strength and Young's modulus for starting materials (PS and LO) and composites (AA and IA), and EDS data (carbon and oxygen) of starting materials (PS and LO) and all PS/LO composites.

Sample	Mn (Da)	Mw (Da)	PDI (a.u.)	Tensile Strenght (MPa)	E (GPa)	EDS analysis	
						Carbon (%)	Oxygen (%)
PS	93,126	221,063	2,3	21.78 (±0.02)	2.33	97.8	2.2
LO	1,222	2,067	1,6	-	-	50.6	49.4
AA2	89,061	216,421	2,4	18.65 (±0.05)	1.82	98.9	1.1
AA5	97,866	208,660	2,1	21.00 (±0.02)	2.57	88.6	11.4
AA10	79,816	186,097	2,3	19.65 (±0.02)	2.45	97.7	2.3
AA20	82,299	199,861	2,4	21.63 (±0.01)	1.95	96.6	3.4
AA50	92,511	219,125	2,3	6.18 (±0.03)	2.45	85.3	14.7
IA2	98,805	218,898	2,2	17.76 (±0.07)	2.41	90.3	9.7
IA5	85,340	208,354	2,4	16.93 (±0.06)	1.81	95.3	4.7
IA10	101,764	215,441	2,1	16.32 (±0.02)	2.48	71.5	28.5
IA20	105,796	223,164	2,1	17.06 (±0.02)	2.31	78.4	21.6
IA50	102,670	218,611	2,1	6.56 (±0.01)	1.54	96.5	3.5

When compared with PS data, with the exception of sample IA5, all IA samples show an increased Mn value and a decreased PDI value. The itaconic acid molecule has three chromophores groups. During the irradiation, the molecule could have a more efficient H-abstraction capability when compared with adipic acid. The IA composites could have a higher possibility of crosslinking between the polymeric chains than the AA coomposites, resulting in a superior hardness of the material. EDS and SEM analysis were performed on all samples. Table 1 shows the semi-quantitative data of carbon and oxygen percentage for pristine PS, LO and all composites prepared with adipic acid and itaconic acid. This comparison was possible due to the different carbon/oxygen ratio between LO and PS. As can be noted in Table 1, PS has in its composition 98.8% of carbon and 2.2% of oxygen. Post-consumer PS presents a low oxygen content due to the addition of plasticisers during

processing and manufacturing. On the other hand, LO presents in its composition 50.6% of carbon and 49.4% of oxygen.

After the photochemical reaction, for the AA samples, it is possible to observe an increase in the amount of oxygen, with the exception of AA2. AA5 was the smaple which presented the biggest oxygen content (11.4%). AA20 had a slight increase (3.4%) when comparing with pristine PS. Table 1 also shows the data for the IA composites which shows an increase in the oxygen percentage for all samples. IA2, IA10, and IA20 presented the highest values. IA5 and IA50 the lowest values, however, when compared with PS, the oxygen content still increased.

Comparing the EDS data with the previous discussion it is possible to observe some interesting correlations. The composites which presented the lowest oxygen content (AA2, AA10, IA5, and IA50), when compared with PS, also presented in the majority, a reduction in the Mn, Mw, tensile strength, Young's modulus and increase in PDI. Low presence of oxygen can be linked with the less grafting of lignin onto PS chains. It is likely that the number of grafted domains were not enough to provide stability for the non-grafted lignin. In those samples, there is the formation of pure lignin microdomains, leading to phase separation.

All samples with the highest oxygen content also presented an increase in the values of Mn, Mw, Young's modulus, and a small decrease in the tensile strength and PDI values. In those samples, the number of grafted lignin macromolecules were probably enough to stabilise the amount of non-grafted lignin.

The tendency observed above also repeats in SEM analysis. Figure 2 shows SEM images of the PS films, LO aggregates, and four composites (AA5, AA20, IA5, and IA50). As can be observed in Figure 2, PS films have a typical smooth surface, even at a magnification of 40.000x. LO does not form films, but particle aggregates. AA5 and AA20 keep the same smooth characteristic, with no sign of degradation, cracks, holes or particles. The same occurs for IA2, IA10, and IA20 (supporting information). This homogeneous appearance is related to mechanical properties and also with non-degraded chains[8] .

Wang et al., grafted chemical modified lignin in PS obtained films with great resemblance to the PS/LO films obtained in this work. The authors state that the smooth characteristic is due the good interaction between lignin monomers and grafted chains.[19]

Figure 2 also shows IA5 and IA50 images, which do not present the same film homogeneity. As can be observed, the IA5 image presents spots, particles, and dark marks (possible cracks) in the film surface. Similar features can be observed in the IA50 image (Figure 2) and in this case, a circular area corresponds to a lignin domain. EDS analysis reveals that inside the microdomain (circle) the carbon and oxygen percentage are very similar to the lignin values, while outside the microdomain the carbon and oxygen percentage matches with the composite IA50 values in Table 1.

These images confirm the spectroscopic, chromatographic, and mechanical data. In general, a short time of UV-radiation exposure in the presence of adipic acid and itaconic acid is enough to graft LO macromolecules into the PS polymeric chain.

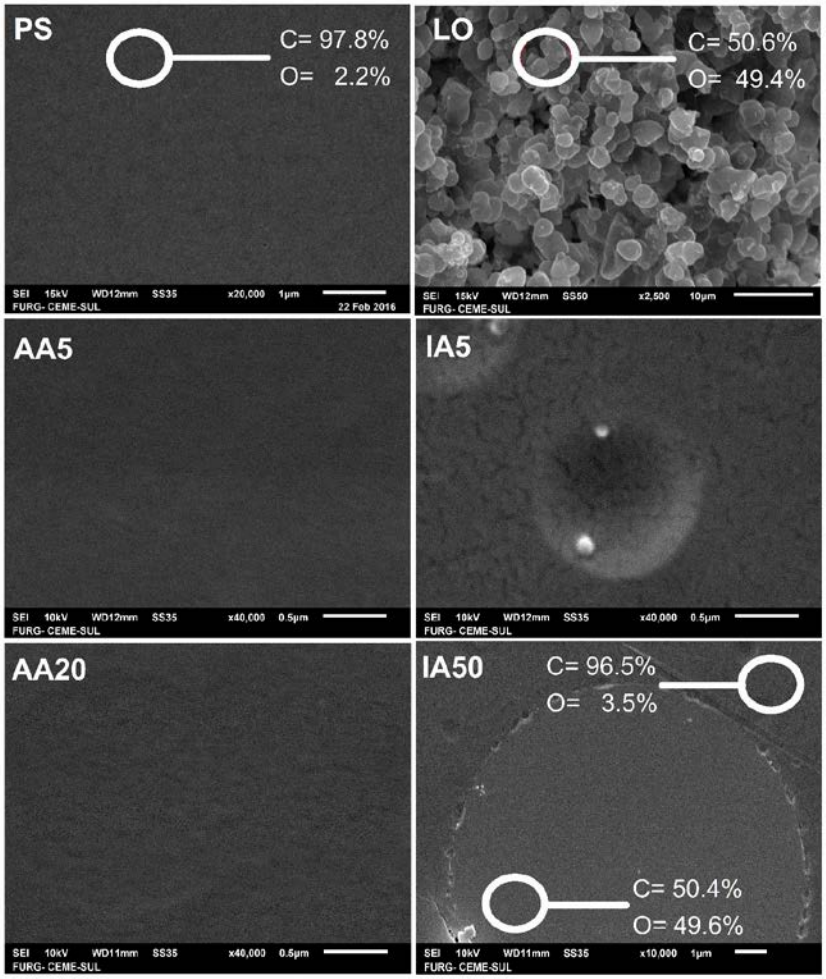

Figure 2. MEV images of PS, LO composite AA5, composite IA5, composite AA20, and IA50. PS, LO and IA50 presents carbon and oxygen composition provided by EDS analysis.

The formed films present spectroscopic data that confirm the presence and relative integrity of PS and LO macromolecules. The AA5 and AA20 composites results in uniform and transparent films that in overall maintain PS mechanical characteristics. Similar characteristics were obtained for IA2, IA10 and IA20 composites.

4. CONCLUSIONS

The changes observed in the FTIR-ATR spectra confirm the presence of lignin in the composites samples and also changes in the PS polymeric chain. GPC data presents changes in the molar mass, where it was possible to confirm the FTIR analysis. GPC data also relates to the mechanical tests, where for IA and AA samples, the tensile strength values decrease considerably, and discrete oscillation of the Young's modulus when compared with pristine PS. EDS data and MEV images showed that the samples have different oxygen contents, and it seems to be related to the mechanical properties. When the composites presented a low oxygen content, the mechanical properties seem to be worse than pristine PS. When the composite presented an increase in the oxygen content, the mechanical properties seem to be slightly improved. The methodology

described in this article could be applied to different post-consumer polymers and showed to be a very interesting green chemical route to generate new materials from polymeric residue and industrial waste.

ACKNOWLEDGEMENTS

The authors gratefully acknowledge the financial support from the Brazilian agencies CNPq and CAPES. The authors deeply thank Professor V. G. Carratu and L. Bresolin for providing their equipment, also the Electron Microscopy Center - FURG (CEME-SUL), the Analytical Center – UFRGS, and the Laboratory of Food Technology (LTA - FURG).

REFERENCES

[1] W. Yue, P. Yao and Y. Wei, *Polymer Degradation and Stability*, 2009, **94**, 851-858.
[2] J. Zhao, Q. Shi, S. Luan, L. Song, H. Yang, H. Shi, J. Jin, X. Li, J. Yin and P. Stagnaro, *Journal of Membrane Science*, **369**, 5-12.
[3] Z. Zhang, Y. Lai, L. Yu and J. Ding, *Biomaterials*, 2010, **31**, 7873-7882.
[4] N.-F. Chiu and T.-Y. Huang, *Sensors and Actuators B: Chemical*, 2014, **197**, 35-42.
[5] W. Dai, L. Yu, Z. Li, J. Yan, L. Liu, J. Xi and X. Qiu, *Electrochimica Acta*, 2014, **132**, 200-207.
[6] J. Gu, J. Du, J. Dang, W. Geng, S. Hu and Q. Zhang, *RSC Advances*, 2014, **4**, 22101-22105.
[7] H. Zhao, B. Zhu, J. Sekine, S.-C. Luo and H.-h. Yu, *ACS Applied Materials & Interfaces*, 2012, **4**, 680-686.
[8] I. Rodriguez, L. Shi, X. Lu, B. A. Korgel, R. A. Alvarez-Puebla and F. Meseguer, *Nanoscale*, 2014, **6**, 5666-5670.
[9] R. Rajajeyaganthan, F. Kessler, P. H. de Mour Leal, S. Kühn and D. E. Weibel, *Macromolecular Symposia*, 2011, **299-300**, 175 182.
[10] T. Zhang, X. Li and H. Gao, *Journal of the Mechanics and Physics of Solids*, 2014, **67**, 2-13.
[11] Rosa, M. P; Beck, P. H.; Muller, D. G.; Moreira, J. B.; Silva, J. S.; Durigon, M. M. . *Biological and chemical research*, v. 4, p. 87-98, 2017.
[12] Y. Yamada, K. Murota, R. Fujita, J. Kim, A. Watanabe, M. Nakamura, S. Sato, K. Hata, P. Ercius, J. Ciston, C. Y. Song, K. Kim, W. Regan, W. Gannett and A. Zettl, *Journal of the American Chemical Society*, 2014, **136**, 2232-2235.
[13] W. Zhang, L. Qin, R.-R. Chen, X.-W. He, W.-Y. Li and Y.-K. Zhang, *Applied Surface Science*, **256**, 3000-3005.
[14] W. Wang, R. M. T. Griffiths, A. Naylor, M. R. Giles, D. J. Irvine and S. M. Howdle, *Polymer*, 2002, **43**, 6653-6659.
[15] C. Zhijiang, H. Chengwei and Y. Guang, *Polymer Degradation and Stability*, 2011, **96**, 1602-1609.
[16] J. Zhou, Y. Hu, X. Li, C. Wang and L. Zuin, *RSC Advances*, 2014, **4**, 20226-20229.
[17] M. Zelzer, M. R. Alexander and N. A. Russell, *Acta Biomaterialia*, 2011, **7**, 4120-4130.
[18] H. Qin, Y. Xu, J. Kim, T. Hwang and T. Kim, *Materials Science and Engineering: B*, 2014, **184**, 72-79.
[19] L. Feng and B. I. Suh, *Macromolecular Chemistry and Physics*, 2007, **208**, 295-306.

HYBRID COMPOSITES BASED ON SILICA, GLASS AND SHORT SISAL FIBRES

Bruna T. Ferreira(1), Leandro J. Silva(1), Túlio H. Panzera(1), Júlio C. Santos(2) and Michael D. Naughton(3)

(1) Centre for Innovation and Technology in Composite Materials – CITeC, Department of Mechanical Engineering, Federal University of São João del Rei - UFSJ, Brazil.

(2) Centre for Innovation and Technology in Composite Materials – CITeC, Department of Natural Sciences, Federal University of São João del Rei - UFSJ, Brazil.

(3) Department of Mechanical and Automobile Engineering, Limerick Institute of Technology, Limerick, Ireland.

https://doi.org/10.21452/bccm4.2018.10.09

Abstract

Studies of composite materials in recent years have focused on the use of natural fibres as an alternative to synthetic fibres. The attractive mechanical properties, sustainability, low cost and low weight are potential factors that have leveraged research in this area, due to the variety of applications in the engineering sector. A full factorial design ($2^1 6^1$) was performed to identify the effect of silica inclusions and the stacking sequence of glass fibres and short sisal fibres. The response-variables, such as apparent density, tensile and flexural strength and modulus of elasticity, were assessed in this work. In general, the incorporation of silica particles improved the performance of composites containing larger amounts of sisal fibres. Hybrid composites with higher number of glass fibre layers achieved higher values of tensile and flexural strength (348 MPa and 663.28 MPa) and tensile and flexural modulus (22 GPa and 2.50GPa) and higher apparent density value (2.02 g/cm³).

1. INTRODUCTION

Natural fibre composite materials have been widely used because of their sustainable characteristics, moderate strength and low cost [1, 2]. One way that has been studied as an alternative to reduce the use of synthetic fibres is through hybridization of these fibres with natural fibres [3,4]. Hybridization is when the material has more than one type of reinforcement, either in the form of fibres or particles [2]Hybridization of sisal and glass fibres has been proposed in the literature specially to reduce final costs of composite materials [5, 6]. Moreover, another factor that significantly influences the mechanical properties of these composites is the form of stacking

of the fibers [7], having great importance in the final properties of the material. Fiber-reinforced composites and micro-nanoparticles have been investigated specifically to increase the thermal stability and the specific mechanical properties of laminated composites [8,9]. According to Silva *et al.* [10], the particles intercept the propagation of cracks, this effect retards the growth of cracks in the hybrid composites increasing their mechanical properties and preventing catastrophic failure. The incorporation of particles into laminates can increase the stiffness of matrix phase, in addition to promoting an interlocking effect between laminates [8-9, 11].
The types of fibers and particles and their arrangement affect the compatibility and interaction of these elements with the phase of the polymer matrix, being considered determinants in the final property of the material [12].

The present work studies hybrid composites with different stacking sequences of glass and sisal fibers and also investigates the efficiency of the use of silica particles as another type of composite reinforcement. A full factorial design was conducted to identify the effect of the sisal-glass fibre stacking sequences and inclusions of silica microparticles on the physical and mechanical properties of compacted hybrid composites.

2. MATERIALS AND METHODS

2.1. Materials

The hybrid composites were fabricated with five layers of sisal/glass fibres via compression molding. Random sisal short fibres were supplied by Sisalsul Company (Brazil). A cross-ply glass fibre fabric of 200 g/cm² was used in the experiment. Renlam M epoxy resin and HY Aradur 951 hardener were supplied by Hunstman Brazil. The silica micro particles were sourced by Omega Mining Company (Brazil).

2.2. Design of experiment

A full factorial design ($2^1 6^1$) was established to identify the effect of silica inclusions (0 and 5 wt%) and stacking sequence of short sisal fibres (S) and glass fibres (G) on the physical and mechanical properties of hybrid composites (see Table 1).

Table 1: Full Factorial Design ($2^1 6^1$).

Experimental Conditions	Layers Sisal/Glass	Silica inclusion (%)
1	5S	0
2	4S/1G	0
3	3S/2G	0
4	2S/3G	0
5	1S/4G	0
6	5G	0
7	5S	5
8	4S/1G	5
9	3S/2G	5
10	2S/3G	5
11	1S/4G	5
12	5G	5

The responses investigated in the experiment were apparent density, mechanical strength/modulus under tensile and flexural loads. Fifteen hybrid composite specimens (5 for physical tests, 5 for tensile, 5 for bending) were fabricated for each of the 12 experimental conditions. Two replicates were considered, running a total of 360 specimens. The replicate consists of the repetition of the experimental condition in order to estimate the experimental error of the individual response. A randomization procedure was adopted during sample manufacturing and experimental testing, avoiding uncontrolled factors from affecting responses [13]. Minitab 17 software was used to perform statistical analysis based on Design of Experiment (DoE) and Analysis of Variance (ANOVA).

2.3. Manufacturing process

The epoxy polymer was prepared by mixing the resin and the hardener at a ratio of 10:1 for 5 minutes. The particles were classified by sieving process in monomodal size of 0.037 mm. Subsequently, the silica particles were added to the epoxy polymer and hand-mixed for 5 minutes at room temperature (~21ºC). A fibre volume fraction of 20% was kept constant, being determined based on preliminary tests, in order to avoid resin leakage after compaction.

The composites were fabricated using a wood mould (200 x 200 mm) and a cold uniaxial pressure of 0.75MPa for 12 hours. After 7 days curing, the plates were cut to size according to ASTM standards [14-15] (Figure 1). The sisal fibres were replaced by glass fibres from the bottom to the top surfaces as shown in Figure 2. Each layer of glass fibre fabric weighed 7.0 g, while each layer of random sisal fibre weighed 3.4 g.

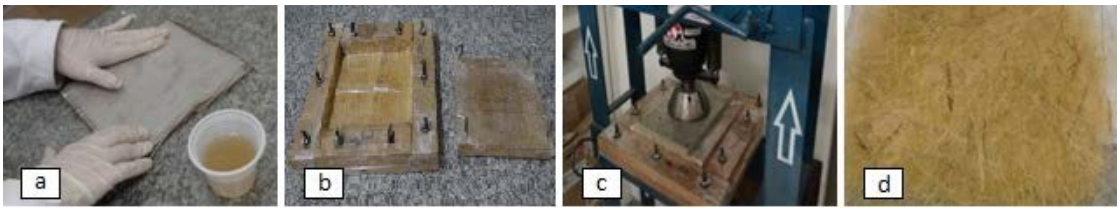

Figure 1: Manufacturing process of the hybrid composites: (a) lamination of the fibres, (b) wooden mould, (c) cold pressing, (d) material after compaction.

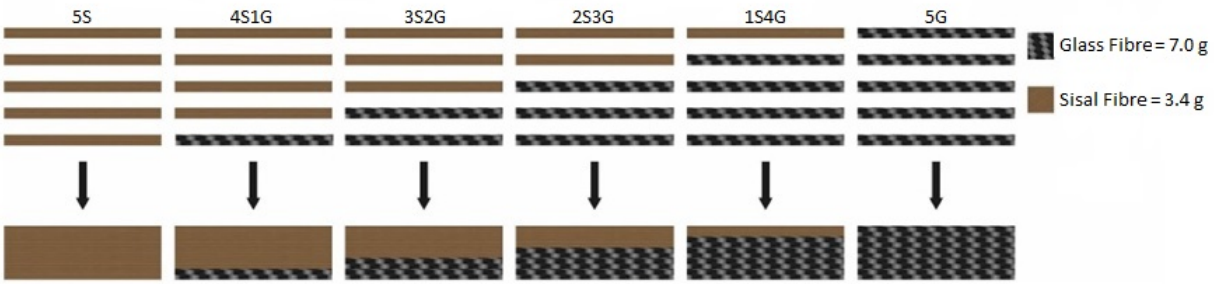

Figure 2: Stacking sequence of the fibres.

2.4. Testing

Tensile and flexural tests were carried out based on the recommendations of ASTM D3039-14 [14] and ASTM D790-15 [15], respectively. The Zwick /Roell Z020 test machine with a 20kN load cell was used to perform both tests, which were conducted at a test speed of 2 mm/min. The apparent density and apparent porosity were determined according to BS 10545-3 [16], based on the Archimedes principle using a precision balance (0.001g) and distilled water.

3. RESULTS

Table 2 shows the analysis of variance (ANOVA). P-values less or equal to 0.05 indicate the individual factor or the interaction significantly affect the response. When one or more interaction effects of superior order are significant, the interacting factors can be considered together [17]. The underlined P-values shown in Table 2 significantly affected the responses. P-values in bold show the presence of interaction effects. R^2 values close to 100% indicate that the model has higher predictive capacity [17]. To validate the ANOVA, a normality test (Anderson-Darling) was conducted based on the residual analysis for each response-variable. In this case, P-values must be greater than 0.05, as shown in Table 2.

Table 2. Analysis of Variance (ANOVA)

ANOVA		P-value ≤ 0.05				
	Experimental Factors	Apparent density (g/cm^3)	Tensile Strength (MPa)	Tensile Modulus (GPa)	Flexural Strength (MPa)	Flexural Modulus (GPa)
Main Factors	Silica Inclusion (SI)	0.442	0.000	0.951	0.000	0.115
	Glass fibre inclusion (GFI)	**0.000**	0.000	**0.000**	0.000	0.000
Interactions	SI x GFI	0.13	**0.000**	0.389	**0.000**	**0.029**
	R^2 – adj	99.13%	98.63%	98.49%	98.68%	98.28%
Anderson-Darling (P-value ≥ 0.05)		0.133	0.132	0.989	0.313	0.057

3.1. Apparent Density

The apparent density of the composites ranged from 1.15 g/cm³ to 2.02 g/cm³. The elastic properties of the composites were not affected or reduced in the presence of silica particles (Table 2). The glass fibres promoted an increase in mean apparent density as shown in Figure 3, due to their higher density relative to the sisal fibres.

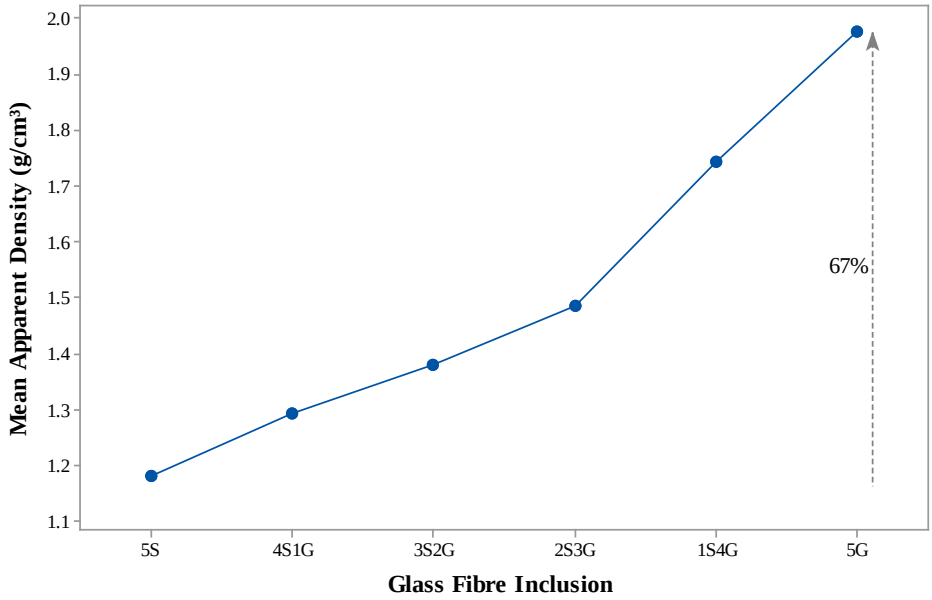

Figure 3. Main effect of glass fibre inclusions for mean apparent density of the composites

3.2. Tensile Strength

Figure 4 shows the interaction effect plot for mean tensile strength of the composites. The presence of silica led to reduced tensile strength values. This fact can be attributed to the non-efficiency of the particle-reinforced matrix under tensile load, followed by a possible reduction of interlaminar adhesiveness due to the silica incorporation. It was observed that the larger the amount of glass fibre, the greater the matrix phase volume expelled during the manufacturing process. Silica particles within laminated composites have a positive effect when the amount of matrix phase is maintained in the system [18]. As shown in Figure 4, tensile strength values are reduced when the amount of glass fibre layers is increased. This behaviour is related to the effect between the amount of matrix phase and silica particles. It is noteworthy that composites made with 4 layers of sisal and 1 of glass fibre (4S1G) without silica inclusions obtained an increase in tensile strength of 84% when compared to composites made with only natural fibres (5S). In contrast, significant percentage reductions were achieved when a glass fibre layer was replaced by the sisal fibre layer (1S4G), especially when no silica particle was added.

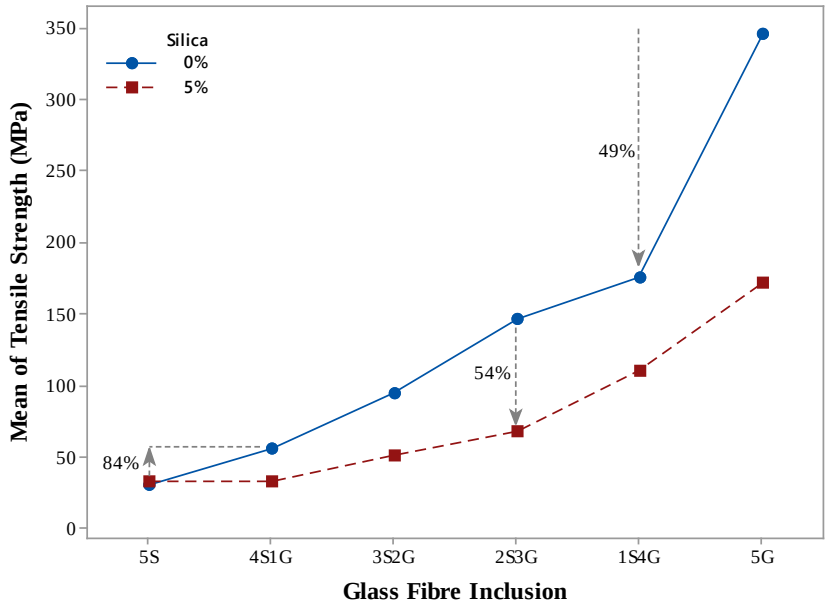

Figure 4. Interaction effect plot for mean tensile strength.

3.3. Tensile Modulus

Modulus of elasticity values ranged from 3.50 GPa to 22.00 GPa. Figure 5 shows the main effect plot for glass fibre inclusion factor. The treatments containing larger amounts of glass fibre layers obtained a higher tensile modulus, leading to a substantial increase of 477% from 5S to 5G. This behaviour was expected, considering that glass fibres exhibit superior mechanical performance to natural fibres.

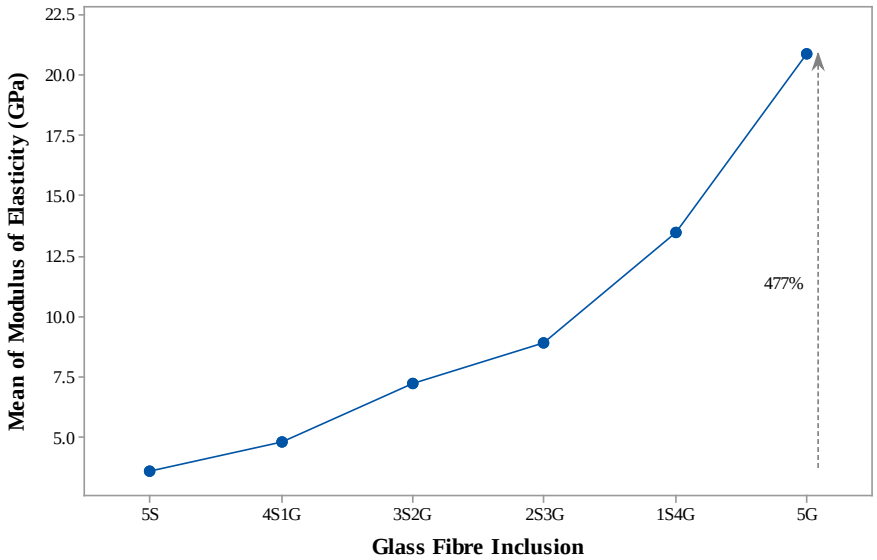

Figure 5. Main effect plot for mean modulus of elasticity.

3.4. Flexural Strength

Flexural strength values ranged from 51.36 MPa to 663.28 MPa. Figure 6 shows the interaction effect plot for mean flexural strength. The inclusion of particles led to reduced strength, except for composites made with 100% sisal fibres. The presence of silica particles provided a significant reduction (~30%) in the flexural strength of glass fibre reinforced composites (5G). A significant reduction was also observed when the glass fibres were replaced by one or more layers of sisal fibre. Otherwise, 2S3G composites without particles reached a percentage increase of 407% when compared to composites reinforced with sisal fibres (5S). The reduction of 25% in the 1S4G condition can be explained by the fact that the sisal fibres used in the upper part of the composite are short and arranged randomly in the matrix, which implies the possibility of the existence of regions without the presence of fibres reinforcement.

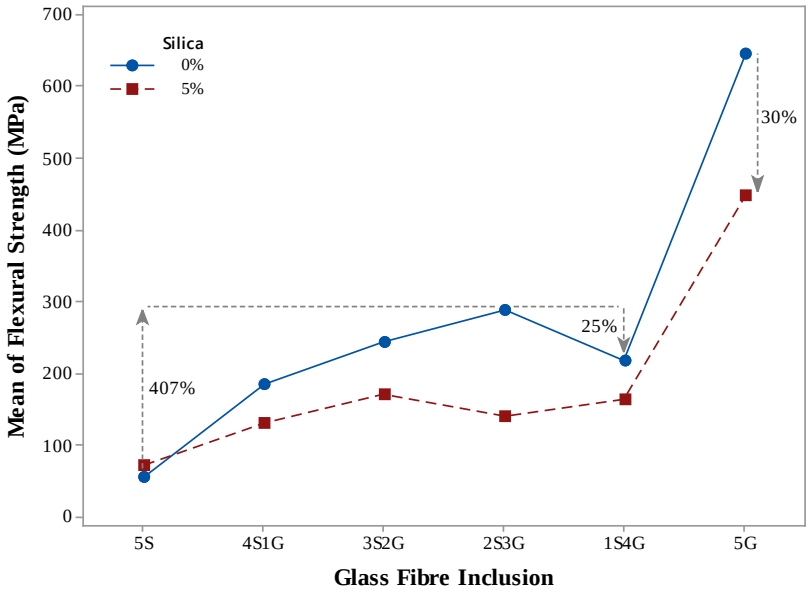

Figure 6. Interaction effect plot for mean flexural strength.

3.5. Flexural Modulus

The flexural modulus values varied between 1.61 GPa and 2.50 GPa. Figure 7 shows the interaction effect plot for mean flexural modulus. The highest flexural modulus was achieved when the composites were fabricated using five layers of glass fibre (5G) without silica inclusion. Silica particles promoted a positive effect only when a greater amount of sisal fibres was considered (5S and 4S1G). This behaviour suggests that the particles contribute more effectively to increase the matrix phase stiffness rather than the interlocking effect. In addition, the use of short random sisal fibres can lead to internal regions without fibre reinforcement, consequently, the particles can provide a mutually beneficial effect, increasing matrix phase stiffness and filling voids. A significant reduction (~70%) in the flexural modulus was evidenced when only a single layer of glass fibres (1S4G) was replaced by sisal. It is noteworthy that a significant increase of

approximately 324% in stiffness was achieved, compared to 5S composites, when three layers of glass fibre (2S3G) were incorporated.

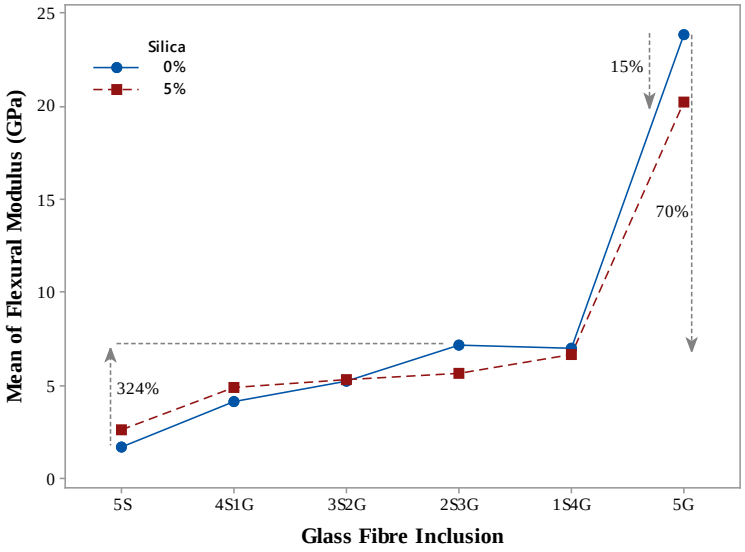

Figure 7. Interaction effect plot for mean flexural modulus.

3.6. Fracture Surface Analysis

The fracture analysis of the composites resulting from tensile and flexural tests was carried out using a scanning electron microscope. Among the different forms of fracture characteristics of the fibre-fibre composite are intralaminar fracture and interlaminar fibre fracture. Figure 8 shows the fracture surface of the glass fibre composites after the bending test. A fragile fracture containing some regions of failure by "fibre pull-out" is observed. The loss of matrix during the manufacturing process may have been the main responsible for the reduction of the mechanical properties of the material.

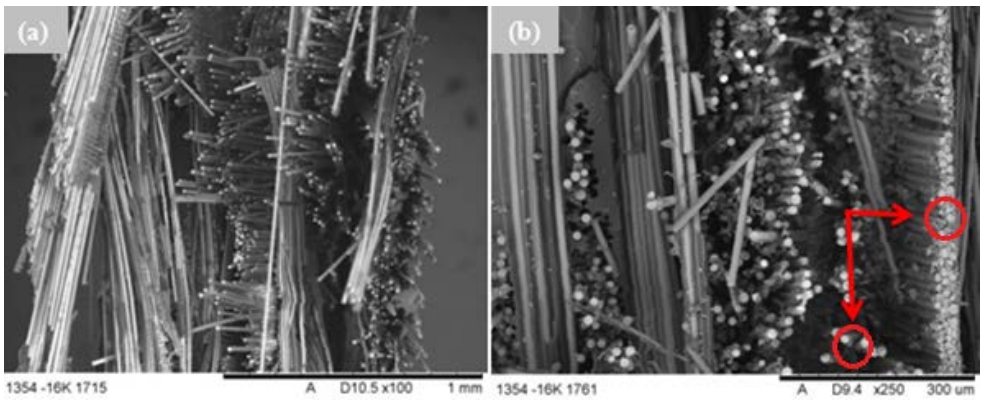

Figure 8. Fracture surface of the flexural test in glass fibre composites (5G).

Figure 9 shows the fracture section of composites reinforced with sisal fibres. The random distribution of fibres and the presence of macropores are observed, as well as the fibre pull-out failure characteristics.

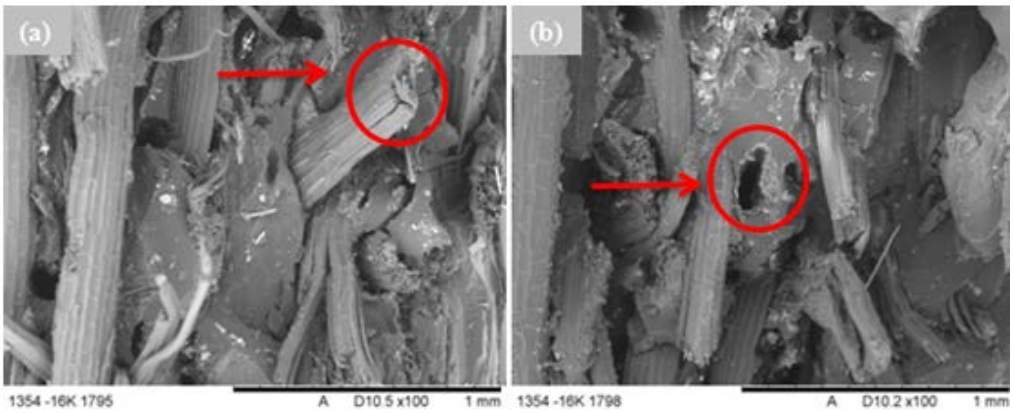

Figure 9. Fracture surface of the flexural test in sisal fibre composites (5S).

The delamination effect was more present in the hybrid composites due to the material difference and the mat structure (Figure 10). The structure of the sisal mat is formed by short and random fibres, while the glass fibre fabric has a cross-ply distribution. This variation along with the difference in the properties of each material leads to a combined behaviour at the time of fracture. Figure 10 shows that the characteristic fracture of sisal fibre is pull-out, while glass fibres break by fragile fracture.

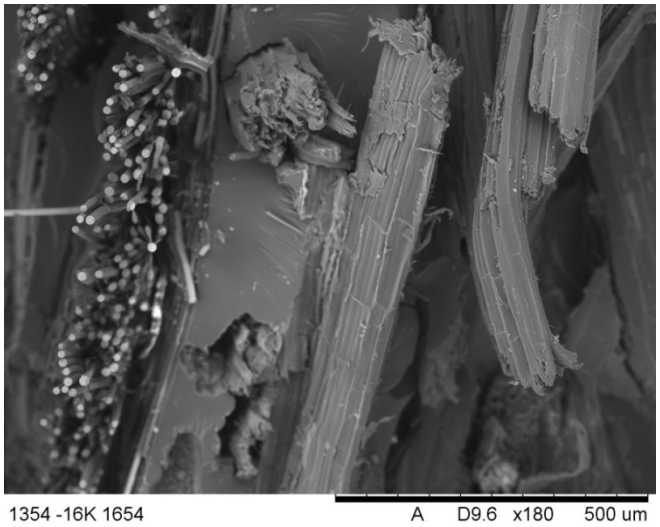

Figure 10. Fracture surface of the flexural test in hybrid composites (3S2G).

4. CONCLUSIONS

Hybridization of sisal/glass fibres and silica microparticles was assessed in this work. The main conclusions are described below:

- Replacement of sisal fibres by glass fibres led to significant effects on tensile strength, flexural strength, tensile modulus, flexural modulus and apparent density of the composites. Hybrid composites with higher number of glass fibre layers achieved higher mean values of tensile and flexural strength (348 MPa and 663.28 MPa, respectively), tensile and flexural modulus (22 GPa and 2.5 GPa, respectively) and apparent density (2.02 g/cm³).
- Silica microparticles significantly affected the responses: flexural strength, tensile modulus and flexural modulus. The presence of silica particles improved the mechanical performance of the composites especially when considering a larger amount of sisal fibres, i.e. 5S and 4S1G conditions.
- Finally, the 2S3G composites without silica particles achieved moderate strength and stiffness, being a promising alternative for secondary structural parts in projects with sustainable demands.
- The fracture analysis of the material presented as main types of fracture the pull-out effect and the delamination of the layers.

ACKNOWLEDGMENTS

The authors would like to thank CAPES, CNPq and FAPEMIG for the financial support.

REFERENCES

[1] Ashby, M.F., Bréchet, Y.J.M. Designing hybrid materials. Acta materialia, **51**, n. 19, pp. 5801-5821, 2003.
[2] Callister, W.D. Materials Science and Engineering: An Introduction. **7**th ed. New York: John Wiley & Sons, 2007.
[3] Jarukumjorn, K., Suppakarn, N. Effect of glass fiber hybridization on properties of sisal fiber polypropylene. Composites: Part B, **40**, pp. 623–627, 2009.
[4] Singh, B., Gupta, M., Verma, A. Mechanical behavior of particulate hybrid composite laminates as potential building materials. Construction and Building Materials, **9**, pp. 39-44, 1995.
[5] Venkateshwaran, N., Elayaperumal, A., Sathiya, G.K. Prediction of tensile properties of hybridnaturalfiber composites. Composites Part B: Engineering, **43**, n. 2, pp. 793-796, 2012.
[6] Nabi, S.D., Jog, J.P. Natural fiber polymer composites: a review. Advances in Polymer Technology, **18** (4), pp. 351-63, 1999.
[7] Mohan, T.P., Ramesh, M.K., Velmurugan, R. Thermal, mechanical and vibration characteristics of epoxy-clay nanocomposites. Journal Materials Science, **41**, pp. 5915-25, 2006.
[8] Santana, P.R.T., Panzera, T.H., Freire, R.T.S., Christoforo, A.L. Apparent shear strength of hybrid glass fibre reinforced composite joints. Polymer Testing, **64**, pp. 307-312, 2017.
[9] Cao, Y., Cameron, J. Flexural and shear properties of silica particle modified glass fiber reinforced epoxy composite. Journal of Reinforced Plastic and Composites, **25**, pp. 347-59, 2006.

[10] Silva, L.J., Panzera, T.H., Velloso, V.R., Rubio, J.C.C., Christoforo, A.L., Scarpa, F. Statistical design of polymeric composites reinforced with banana fibres and silica microparticles. Journal of Composite Materials, **47**, n. 10, pp. 1199-1210, 2012.
[11] Torres, R B., Santos, J. C., Panzera, T. H., Christoforo, A.L., Borges, P.H.R., Scarpa, F. Hybrid glass fibre reinforced composites containing silica and cement microparticles based on a design of experiment. Polymer Testing, pp. 87-93, 2016.
[12] Kickelbick, G. Introduction to hybrid materials. In: Kickelbick G, Editor. Hybrid mater synth charact appl. John Wiley & Sons; 2007.
[13] Wu, C.F.J., Hamada, M. Experiments: planning, analysis, and parameter design optimization, 2nd Edition, John Wiley & Sons, 2000.
[14] ASTM D3039 / D3039M-14, Standard Test Method for Tensile Properties of Polymer Matrix Composite Materials, ASTM International, West Conshohocken, PA, 2014, www.astm.org.
[15] ASTM D790-15e2, Standard Test Methods for Flexural Properties of Unreinforced and Reinforced Plastics and Electrical Insulating Materials, ASTM International, West Conshohocken, PA, 2015, www.astm.org.
[16] BRITISH STANDARD. BS EN ISO 10545-3. Ceramic Tiles - Part 3: Determination of water absorption, apparent porosity, apparent relative density and bulk density. 1997.
[17] Montgomery, D.C. Design and Analysis of Experiments. 6 ed. Hoboken: John Wiley e Sons, pp. 643, 2005.
[18] Detomi, A.C.; Santos, R.M., Ribeiro Filho, S.L.M., Martuscelli, C.C., Panzera, T.H., Scarpa, F. Statistical effects of using ceramic particles in glass fibre reinforced composites. Materials & Design, **55**, pp. 463-470, 2013.

ON THE MEASUREMENT OF CROSS-SECTIONAL AREA OF NATURAL FIBERS

Otavio da Fonseca Martins Gomes [1,2], Felipe Pinheiro Teixeira [3], Josimar Firmino de Lima [1] and Flavio de Andrade Silva [3]

(1) CETEM – Centre for Mineral Technology, Brazil

(2) Postgraduate Program in Geosciences, National Museum, Federal University of Rio de Janeiro, Brazil

(3) Department of Civil and Environmental Engineering, Pontifícia Universidade Católica do Rio de Janeiro, Brazil

https://doi.org/10.21452/bccm4.2018.10.10

Abstract

The measurement of cross-sectional area of natural fibers is fundamental in the determination of their mechanical properties. Several authors investigated the mechanical behavior of natural fibers and reported, for samples of same species, different values for tensile strength and elastic modulus. This variability can be due to many factors, such as plant variability, damage during processing or cutting, testing conditions and accuracy. This work presents a method for the measurement of cross-sectional area natural fibers that guarantees the dimensional integrity of the fiber and in which the measurement is performed on a plane perpendicular to its longitudinal axis. It comprises sample preparation, image acquisition on a reflected light microscope, and image analysis using the open source software Fiji/ImageJ. The method was applied to curaua, hemp, and sisal samples.

Keywords: natural fibers, materials characterization, quantitative microscopy, mechanical behavior, mechanical properties

1. INTRODUCTION

Several authors investigated the mechanical behavior of natural fibers and reported very different values for tensile strength and elastic modulus for fibers of same species [1]. This variability can be due to any one or more of many factors, including fiber type, fiber variability (the position of fiber in the stem, fiber maturity or harvesting), fiber damage during its processing in the laboratory or industry, testing conditions and accuracy [2]. Luna and Lizarazo-Marriaga [3] pointed out that the cross-section area measurement must be carried out on a plane perpendicular

to the longitudinal axis of the fiber and proposed a method to determine the cross-section area of Guadua angustifolia bamboo fibers. There are some papers in the literature [1,4-9] in which mechanical properties of natural fibers, like tensile strength and elastic modulus, were computed using cross-section measurements obtained through image analysis of SEM (scanning electron microscope) images. Besides not considering the slope of fibers with respect to the image plane, those papers do not take into account possible fibers crush and dismantling during cutting procedure and the fiber shrinking due to the high vacuum in the SEM.

The present work proposes a method that guarantees the dimensional integrity of the fiber and in which the measurement is performed on a plane perpendicular to its longitudinal axis.

2. METHOD

2.1 Sample preparation

The first preparation step is the treatment of fibers with hot water (70°C) for 1 h to eliminate impurities retained on the fibers surface. Thereafter, the fibers are air dried for 48 h.

A previously prepared epoxy resin block with 30 mm of diameter and 12 mm height is drilled with a 1.5 mm diameter drill to create 15 holes. The perforated block is placed on a Büchner funnel attached to a kitassato flask linked to a vacuum pump. A layer of filter paper between the Büchner funnel and the block separates it from the suction. Figure 1 shows this apparatus. It worth mentioning that it is possible to use a cheaper general-purpose epoxy resin to prepare the resin block to be perforated. The use of a high-cost epoxy resin for metallographic preparations, such as Struers Epofix, is required only for the fiber embedding in order to promote a good adhesion between fibers and surrounding resin and to mitigate the formation of bubbles.

One 10 mm length fiber sample is then carefully placed in each of the 15 holes of the block and subsequently the holes with fibers are filled with epoxy resin (Struers Epofix), as schematically illustrated in Figure 2. The vacuum is used to avoid fibers floating and to prevent the formation of bubbles during the 12 h of cold curing of resin.

After curing, the block is ground and polished in an automatic polishing machine (Struers Tegramin 20). Although, automatic polishing generally improves the quality of polished sections, it is not mandatory. Grinding and polishing tasks can be manually carried out with good results if they are carefully done. The grinding is carried out cooled with water using diamond impregnated metal discs with 125, 40, 9 and 6 μm sized particles, during 3, 4, 4 and 10 min respectively. After grinding, the block undergoes an ultrasonic bath to remove any possible residues, to prevent scratching during polishing. The polishing procedure employs cloths with diamond suspensions of 3 and 1 μm for approximately 20 min each, generating a highly polished section (Figure 3).

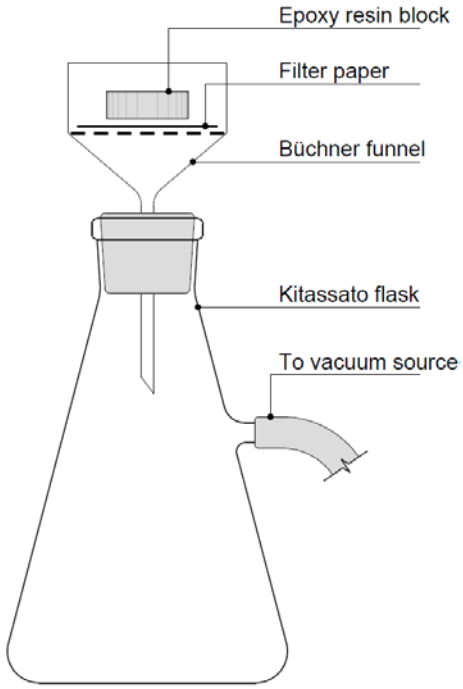

Figure 1: The resin embedding apparatus.

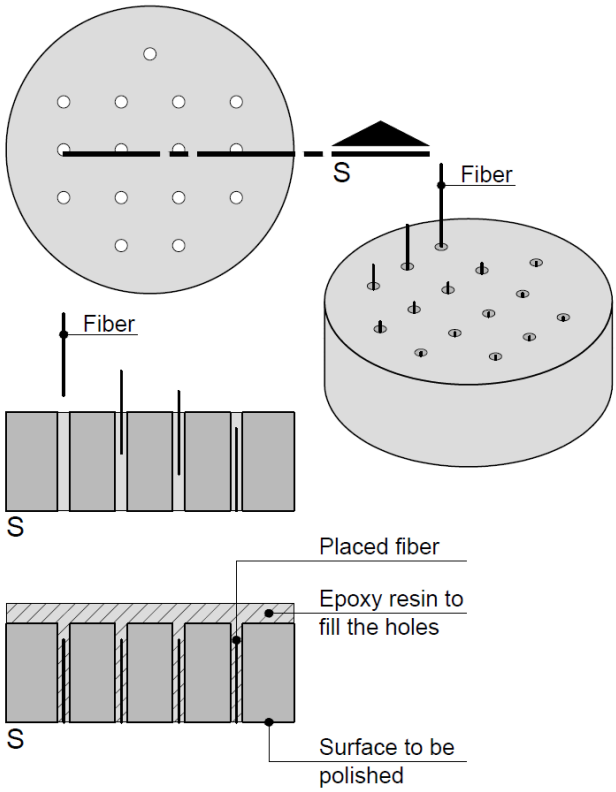

Figure 2: Schematic illustration of the block with 15 holes where fiber sample are placed and embedded with epoxy resin.

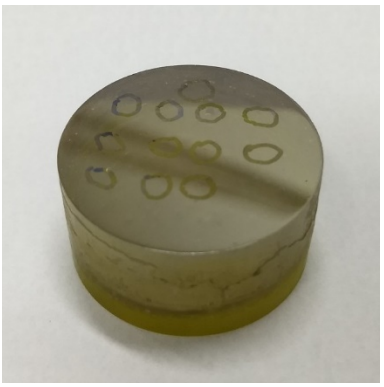

Figure 3: Block with fiber samples after curing and polishing. The fibers were circled with a marker pen to facilitate finding them at the microscope.

2.2 Image acquisition

A reflected light microscope with a digital camera (Zeiss Axioimager M2.m with Axiocam MRc) is used to generate an image of each fiber cross-section. Blank field contrast mode is employed. The magnification depends on each fiber type and plant species. Lamp voltage, exposition time and other operational parameters should be set to provide images with suitable brightness and contrast, avoiding intensity saturation in black or in white. Figure 4 shows images of fibers of: (a) sisal, (b) curaua, and (c) hemp, acquired using objective lenses of 20X, 50X, and 100X respectively.

(a) (b) (c)

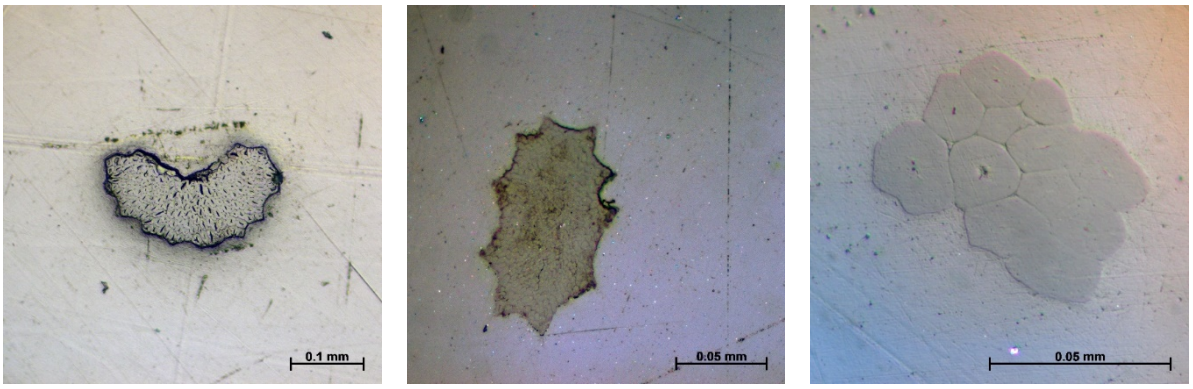

Figure 4: Images of fibers of: (a) sisal, (b) curaua, and (c) hemp, acquired using objective lenses of 20X, 50X, and 100X respectively.

3.3 Image analysis

The fiber cross-section is interactively segmented and then measured using Fiji/ImageJ. Fiji [10] is a free image processing package, a distribution of the popular open source software ImageJ [11] bundling a lot of plugins and different scripting languages.

At least before analyzing the first image, the scale (in microns/pixel, for instance) and the desired measurements (area, in the present case) must be set. This set-up can be made interactively accessing the functions **Set Scale** and **Set Measurements** in the **Analyze** menu or it can be done through the macro routine shown in Figure 5.

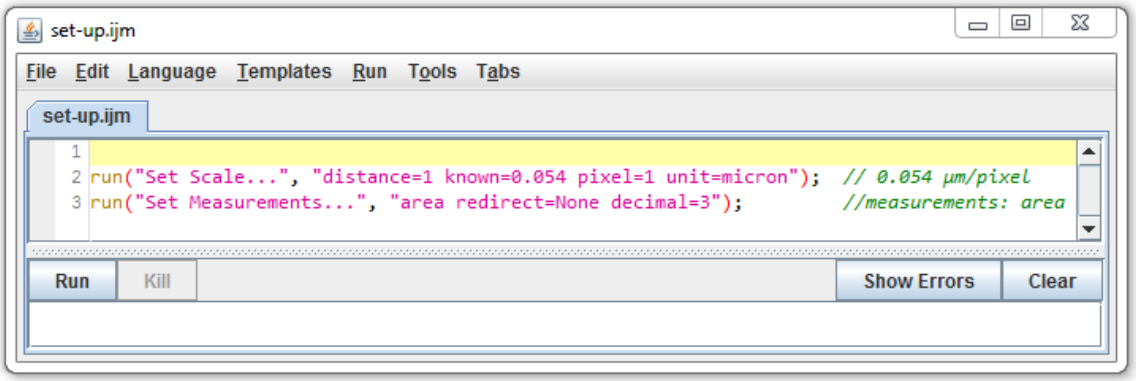

Figure 5: Macro routine to set scale and measurements.

The image analysis procedure follows this sequence:

(a) **Pencil Tool** is used to carefully freehand outline the fiber cross-section;

(b) **Wand Tool** (with parameters Tolerance = 0 and Mode = Legacy, which can be accessed through a double-click on the tool icon) is employed to create a selection from a click in the drawn outline;

(c) **Measure** (in **Analyze** menu) performs the previously set measurements in the outlined region.

Figure 6 presents the analysis of a fiber showing from top to bottom: the Fiji main window, the image of an outlined hemp fiber, and the results window with the obtained area value in μm^2.

In the image analysis field, segmentation is the technical term used for the discrimination of objects from the image background and among themselves. It is generally the critical step of an image analysis routine, since the measurements are done on the segmented objects. Segmentation is a complex task that tries to represent computationally a cognitive process that is inherent to the human vision. When we look at an image we use many different inputs to distinguish the objects, such as color, boundaries, shapes, textures, among others. Our brains process this information in parallel at high speed, using previous experience. Computers, on the other hand, do not have the same associative power yet [12]. Although we can easily recognize the cross-section of a natural fiber in an image obtained as described in the proposed method, its automatic segmentation is not easy. Natural fibers are non-opaque materials, as well as the epoxy resin, hence they present a poor contrast in images from reflected light microscopy. Moreover, natural fibers display a wide variability of size and shape, and their cross-sections present void lumens and lumens filled with resin. Therefore, we have opted to employ an interactive segmentation procedure in the proposed method.

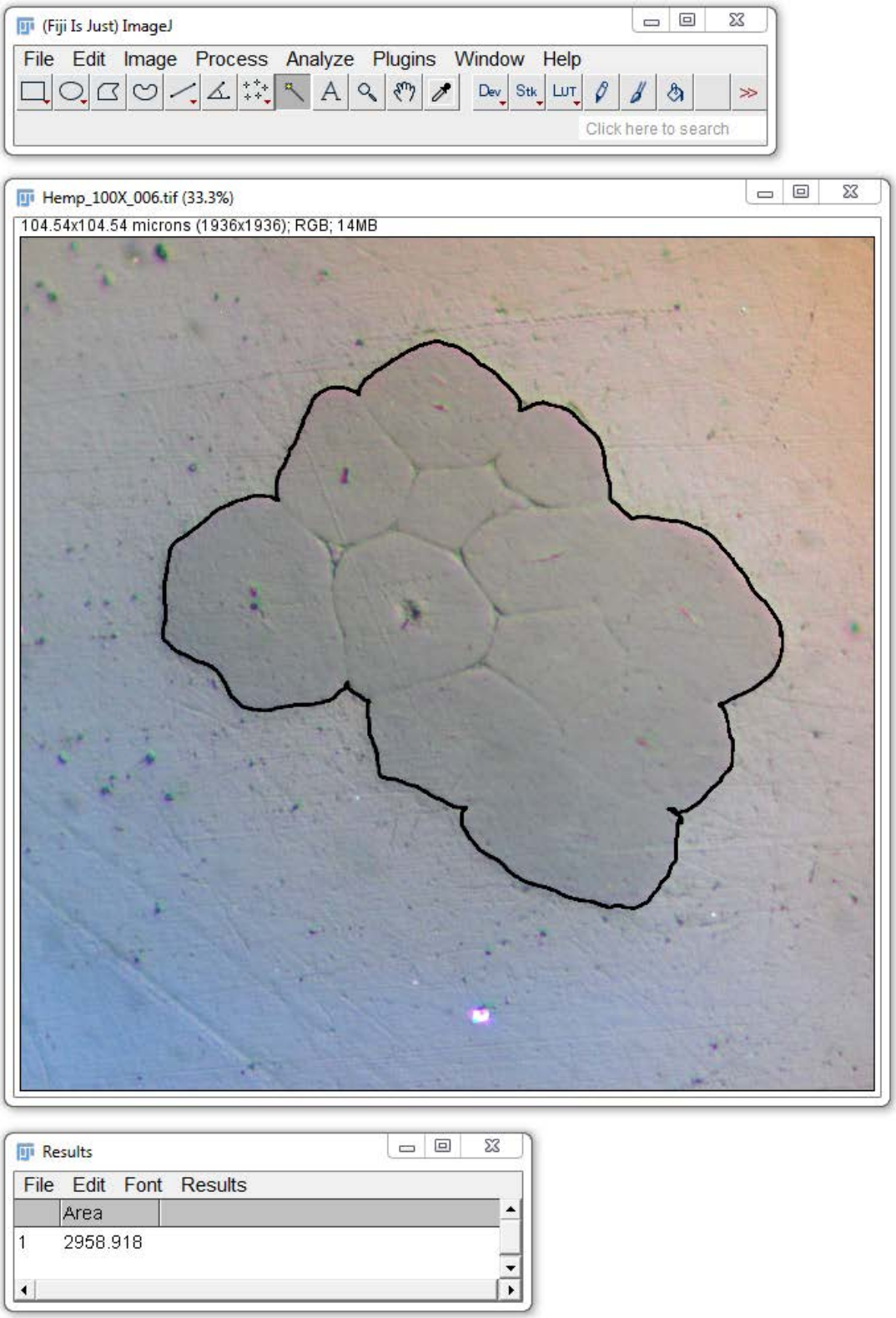

Figure 6: The analysis of a fiber, showing from top to bottom: the Fiji main window, the image of an outlined hemp fiber, and the results window with the obtained area value in μm^2.

The use of a SEM instead of a reflected light microscope can provide better images of natural fibers cross-sections that allow the automation of their image analysis. In back-scattered electrons images of polished (plane) specimens, materials present grey levels proportional to their average atomic numbers [12]. Thus, in such kind of image natural fibers can be easily discriminated from surrounding resin through their different grey levels by an automatic segmentation procedure. Nevertheless, besides its high cost, the use of a SEM has other disadvantages. An additional preparation step is required, the polished block should be coated (for instance, with evaporated carbon) to become conductive so that the SEM can provide high quality images. Furthermore, due to the high vacuum in the coater and in the SEM, natural fibers may shrink and detach from the resin, and their lumens may open, as one can see comparing the images in Figure 7 that shows the cross-section of a sisal fiber imaged by: (a) reflected light microscopy using the objective lens of 50X, and (b) SEM with the same optical resolution.

(a) (b)

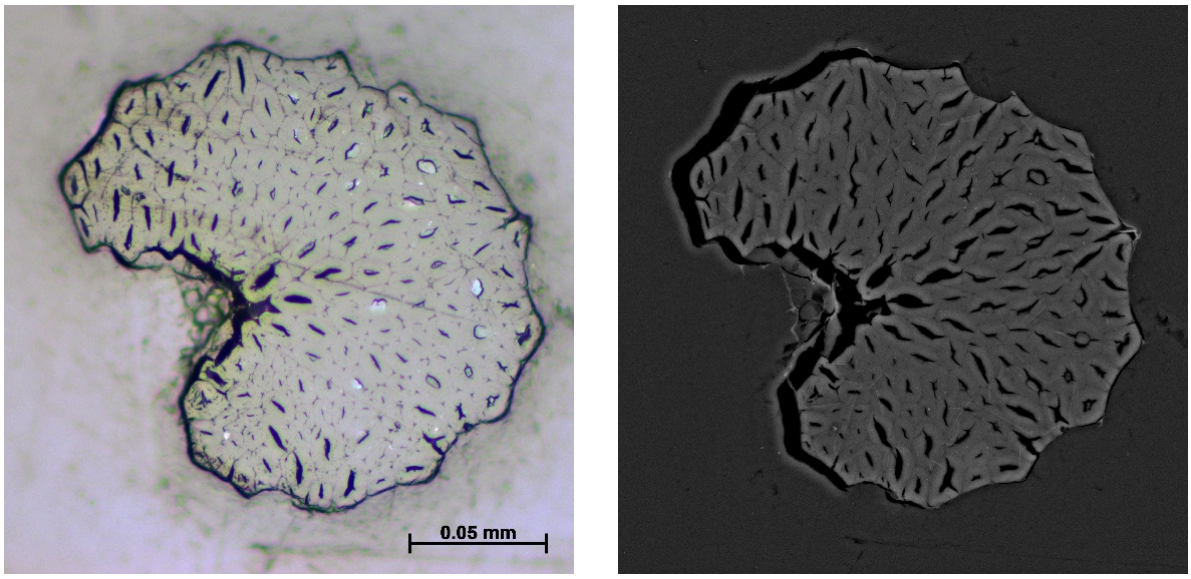

Figure 7: Cross-section of a sisal fiber imaged by: (a) reflected light microscopy (objective lens of 50X), and (b) SEM.

5. CONCLUSIONS

This work presents a method for the measurement of cross-sectional area natural fibers that comprises sample preparation, image acquisition on a reflected light microscope, and interactive image analysis using the open source software Fiji/ImageJ. The sample preparation procedure guarantees a clean perpendicular cut. The use a reflected light microscope avoids the fiber shrinking due to the high vacuum in the SEM.

Future works can focus on obtaining images through different microscopy techniques in order to provide images with a suitable contrast to allow natural fibers cross-section measurements through an automatic image analysis routine. Moreover, the image acquisition step may also be automatized, since the holes positions in the perforated block are known and the fibers can be located into them through image analysis.

ACKNOWLEDGEMENTS

The authors acknowledge the support from the Brazilian funding agencies CNPq, CAPES, FINEP, and FAPERJ. F.P. Teixeira thanks CAPES for the D.Sc. candidate scholarship number 88887.165362/2018-00.

REFERENCES

[1] Fidelis, M.E.A., Pereira, T.V.C., Gomes, O.D.M., Silva, F.A., Toledo-Filho, R.D., 'The effect of fiber morphology on the tensile strength of natural fibers', *J. Mater. Res. Technol.* **2** (2) (2013) 149-157.

[2] Hughes, M., 'Defects in natural fibres: their origin, characteristics and implications for natural fibre-reinforced composites', *J. Mat. Sci.* **47** (2) (2012) 599-609.

[3] Luna, P., Lizarazo-Marriaga, J., 'Proposed Method for Determining Cross-Sectional Area of Guadua angustifolia Bamboo Fibers', *J. Nat. Fibers* (2017).

[4] Silva, F.A., Chawla, N., Toledo-Filho, R.D., 'Tensile behavior of high performance natural (sisal) fibers', *Compos. Sci. Technol.* **68** (15-16) (2008) 3438-3443.

[5] Ramirez, F., Maldonado, A., Correal, J.F., Estrada, M., 'Bamboo-Guadua angustifolia kunt fibers for green composites', in Proceedings of 18th International Conference on Composite Materials, 2011 (The Korean Society of Composite Materials), 1-4.

[6] Diaz, J.P.V., Silva, F.A., D'Almeida, J.R.M., 'Effect of Peach Palm Fiber Microstructure on its Tensile Behavior', *BioResources* **11** (4) (2016) 10140-10157.

[7] Ferreira, S.R., Silva, F.A., Lima, P.R.L., Toledo-Filho, R.D., 'Effect of hornification on the structure, tensile behavior and fiber matrix bond of sisal, jute and curauá fiber cement based composite systems', *Construction and Building Materials* **139** (2017) 551-561.

[8] Ferreira, S.R., Pepe, M., Martinelli, E., Silva, F.A., Toledo-Filho, R.D., 'Influence of natural fibers characteristics on the interface mechanics with cement-based matrices', *Composites Part B: Eng.* **140** (2018) 183-196.

[9] Joshi, A., Mangal, R., Bhojak, N., 'Study of the mechanical properties of Ziziphus nummularia (ber) fibers for formation of fiber reinforced composites', *AIP Conference Proceedings* **1953** (2018).

[10] Schindelin, J., Arganda-Carreras, I., Frise, E., Kaynig, V., Longair, M., Pietzsch, T., Preibisch, S., Rueden, C., Saalfeld, S., Schmid, B., Tinevez, J.Y., White, D.J., Hartenstein, V., Eliceiri, K., Tomancak, P., Cardona, A., 'Fiji: an open-source platform for biological-image analysis', Nat. Methods 9 (7) (2012) 676-682.

[11] Schneider, C.A., Rasband, W.S., Eliceiri, K.W., 'NIH Image to ImageJ: 25 years of image analysis', Nat. Methods 9 (7) (2012) 671-675.

[12] Gomes, O.D.M., Paciornik, S., 'Multimodal Microscopy for Ore Characterization', in Kazmiruk, V. (ed.), 'Scanning Electron Microscopy' (InTech, Rijeka, 2012) 313-334.

[13] Goldstein, J.I., Newbury, D.E., Echlin, P., Joy, D.C., Lyman, C.E., Fiori, C., Lifshin, E., Sawyer, L., Michael, J.R., 'Scanning Electron Microscopy and X-ray Microanalysis', 3rd Edn (Springer, New York, 2003).

EFFECT OF CHEMICAL TREATMENTS ON THERMAL PROPERTIES OF *IMPERATA BRASILIENSIS* GRASS TO REINFORCE COMPOSITES WITH POLYMERIC MATRIX

Thiago de S. Dias (1), Kelly C. C. de C. Benini (2) and Maria O. H. Cioffi (2)

(1) Department of Materials and Technology, School of Engineering of Guaratinguetá-UNESP, Brazil.

https://doi.org/10.21452/bccm4.2018.10.11

Abstract

The development of new materials has been occurring in order to obtain solutions environmentally more effective. In this context, natural fibers have been used as reinforcement in polymer matrix composites, since they present low density and biodegradability. In the present work *Imperata brasiliensis* grass was chemically treated by acetosolv treatment using a solution of acetic acid 93 wt% at 110 °C, under reflux, using hydrochloric acid solution 0.3 wt% as catalyst, and bleached with a 1:1 solution of NaOH 4% (w/v) and H_2O_2 30% (v/v) at 70 °C for 3 h. Untreated and treated fibers were characterized by thermogravimetric analysis (TGA/DTG) and scanning electron microscopy (SEM) and also the color changes after each chemical treatment were considered. According to the results of TGA, the thermal stability of the fiber has increased, comparing untreated and bleached fibers. TGA results also showed the removal of some peaks which is related to the removal of amorphous constituents, a consequence that was also observed trough color analysis. Furthermore, SEM micrographs indicates a defibrillation of fiber after each chemical treatment, a result that can upgrade the anchorage between fiber and matrix and increase subsequent properties of the composite.

Key-words: Natural fibers. Composites. *Imperata brasiliensis*. Acetosolv. Bleaching

1. INTRODUCTION

The current development in materials area is seeking to assemble better properties to environmental issues with the view to perform material that are less harmful to the environment [1]. In this sense, natural fibers that were just used for traditional applications as in handicraft for example has been studied to be applied as reinforcement on composites and biocomposites with polymeric matrices [2,3]. Natural fibers show characteristics like low density, biodegradability, recyclable and require low energy consumption in production. On the other hand, they have been used as an alternative solution to the ever-depleting non-renewable materials and oil products like

plastics in general [4,5]. Many industries such as automotive industry is already using this idea in its products, since natural fiber polymer composites are being used in internal and external non-structural applications [6,7].

Natural fibers are mainly composed of cellulose, hemicellulose and lignin. These useful components are present inside plants' cell wall that is formed by fibrils compound of microfibrils. Nonetheless, other components as waxes, ash and extractives are also present in less quantity [8]. However, the union of natural fibers and polymeric matrices is hampered by hydrophilic character of natural fibers. This characteristic can be attributed to hydroxyl groups intra and intermolecular of fibers that combine to water molecules of atmosphere. The adhesion between natural fiber and polymer and characteristics like water absorption and low thermal stability of fibers have been aiming to study over last years [9].

For this reason, physical, thermal and chemical treatments were developed for fibers. Chemical treatments like acetylation, benzoylation, peroxide, etc., are extensively used in view of distending the crystalline region, eliminating the hydroxyl groups and removing impurities from the surfaces [10]. Furthermore, the most interesting component for composites is cellulose because its crystalline portion, which grant good mechanical properties in composites [11]. Chemical treatments as organosolv can also result in a fractionation of fiber components ant this one can be highlighted as a promising method because it uses an organic solvent [12]. Besides that, bleaching treatment is also carried out to remove the residual amorphous components obtaining a considerable white fiber, where cellulose is mostly present [13]. In this study, organosolv pulping with acetic acid and bleaching with sodium hydroxide and hydrogen peroxide were carried out for *Imperata brasiliensis* grass, an invasive native species of grass, with the aim of improving its thermal properties and surface aspect for later uses as a reinforcement to polymeric composites materials.

2. MATERIALS AND METHODS

2.1. Raw Materials

Imperata brasiliensis fibers were collected in Guaratingueta's countryside. The entire grass (root, stem and leaf) was cut into slices with random lengths using a Garthen GP-1500 AB machine. Subsequently, these grasses were milled using a Knife Mill Tecnal TE-650 and fibers separated through a sieve 8 mesh to obtain the powder that was used in this study. The fiber powder was dried in an oven at 60 ºC during 24 h.

2.2. Acetosolv treatment

With the milled and dry fiber, the chemical treatment of acetosolv pulping was first carried out with acetic acid solution 93 wt% at 110 °C under reflux, using hydrochloric acid solution 0.3 wt% as catalyst, performing with a fiber/solvent ratio of 1:10 (w/v). The system stayed under stirring for 180 min. and then the solid fraction (that was composed mainly by cellulose) was washed once with acetic acid to avoid lignin re-condensation on the fiber. Finally, the acetosolv pulp was washed with distilled water until reached a neutral pH and it was dried at 60 °C for 24 h to obtain the treated fiber.

2.3. Bleaching treatment

Treated fibers were bleached with a 1:1 solution of NaOH 4% (w/v) and H_2O_2 30% (v/v) at 70°C for 3h. Approximately 15g of fibers were added in 900 ml of NaOH/ H_2O_2 solution and stirred at 4000 rpm. Every hour until complete 3h of reaction it was added more 90 ml 4% (w/v) NaOH and 90 ml 30% (v/v) H_2O_2. Finally, the solution was washed until achieve neutral pH and then bleached fiber was also dried at 60 °C for 24 h.

2.4. Thermogravimetric Analysis

The untreated, treated and bleached fibers were characterized by TGA analysis using a TG/DTG SII Nanotechnology INC thermobalance (model 6200) with a heating rate of 10°C min^1, under nitrogen flow, using a temperature range from 25°C to 800°C. The initial degradation temperature was obtained from the first baseline deviation observed, based on ASTM E2550 [14]. Through this analysis, it was also possible to observe the mass losses within the temperature range for each thermal event.

2.5. Scanning Electron Microscopy (SEM)

The morphology of the untreated, treated and bleached fibers was analyzed in a Zeiss EVO 17 LS-15 scanning electron microscope with Oxford INCA Energy 250 EDS / EBDS system, operating from 15 to 20 kW and using secondary electron detector. It was used a self-adhesive carbon double-sided tape, the samples were fixed in a holder and coated with gold.

3. RESULTS AND DISCUSSIONS

3.1. Color analysis

The images of fibers before (Fig 1a) and after each chemical treatment are presented at Fig. 1. After carrying out acetosolv pulping the fibers became darker, according to Fig 1b. This fact may be justified by removing of hemicellulose from the constituents of the fiber, since hemicellulose which is more easily soluble in the organic solvent. Although lignin can be removed, it may have occurred less intensely because it is composed by a structure that is more complex [15]. The dark brown coloring can be explained by the presence of chromophore groups, molecules or parts of molecules, which excites an electron that emits the photons of the color in question, when these molecules are hit by light. These chromophore groups may be present in hexenuronic acids (hemicellulose), hydrated carbohydrates, extractives, transition metals, but mainly in residual lignin, present in the acetosolv pulp [16].

Fig. 1: Color modification on *Imperata brasiliensis* fibers after acetosolv and bleaching treatments.

After bleaching treatment, the fiber reached significant levels of whiteness (Fig. 1c), due to the removal of amorphous components such as mainly lignin, and metallic ions [17]. Using hydrogen peroxide to bleach the fiber, the hydroperoxide ion that is formed by the dissociation of the peroxide in the alkaline medium is responsible for the discoloration of the fiber, since these ions attack the remaining lignin and cellulose chromophores in the pulp [13].

3.2. Thermogravimetric analysis

Thermogravimetric curves of untreated, treated and bleached fibers are presented at Fig. 2. The main thermal parameters obtained from these results can be seen in Table 1.

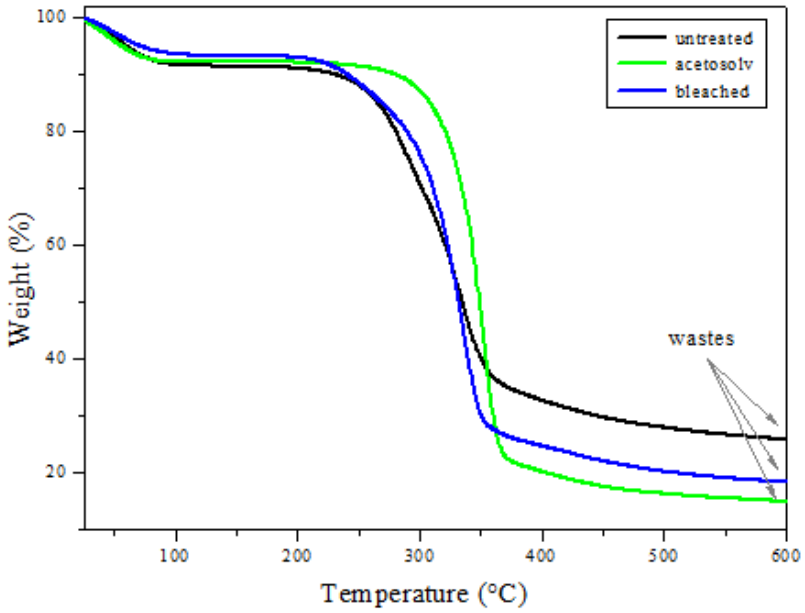

Fig.2: TG curves of untreated, treated and bleached *Imperata brasiliensis* fibers.

From TGA curves of all fibers it is possible to observe a first weight loss at around 10% up to 100 ºC, referring to the dehydration reactions of the water absorbed by the fiber, very common in analyzes of other lignocellulosic fibers [18]. It is also observed after acetosolv pulping, that the thermal stability of fiber increased from 152 °C to 168 °C. In the analysis of the curves referring to the bleached fiber it is possible to observe that the thermal stability of the fiber decreased in comparison to acetosolv pulp, going from 168 to 160 ºC. Although the thermal stability has decreased from acetosolv to bleaching, removing of the amorphous components can be observed by the high whiteness of the bleached fiber, which can improve the properties of the composites and may expand its using in several performing processes [1]. Regarding to the wastes, in untreated fiber there are approximately 25.8% at 600 °C due to carbonaceous residues and some part of non-degraded fiber [19].

In addition, it is possible to observe the degradation stages of the fiber through DTG curves that are shown in Fig.3. Regarding to untreated fibers, three degradation stages are observed, the first one related to water absorbed, the second one at about 300 °C corresponding to the degradation of the hemicelluloses, and the third one, between 300 and 375 °C, related to the degradation of mainly cellulose [1]. Lignin degradation occurs slowly throughout any thermal

event, between approximately 450 and 700 °C. Lignin is formed by aromatic rings and so its structure is more complex comparing to cellulose and hemicellulose [18]. One cannot observe a specific peak related to lignin degradation. However, the fourth stage of degradation in DTG curve (Fig. 3) can be associated to chemical reactions such as the breaking of lignin C-C bonds, releasing of water, CO and CO_2 during heat [20].

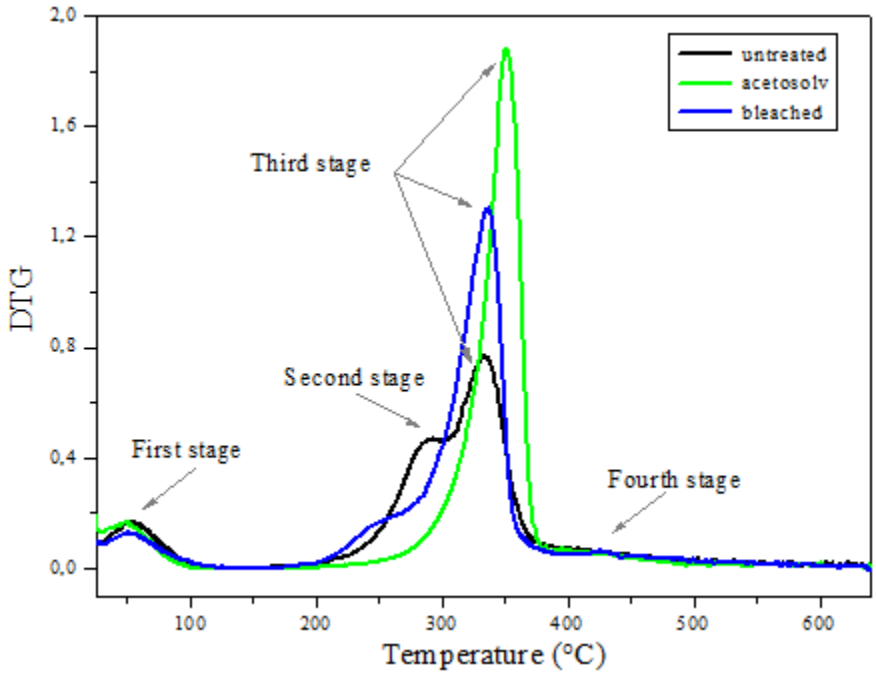

Fig.3: DTG curves of untreated, treated and bleached *Imperata brasiliensis* fibers. Nitrogen atmosphere (10 °C.min^{-1}).

Table 1 shows the TG/DTG parameters for all fibers and their degradations stages, which were already reported. According to *acetosolv* parameters, one cannot see a second stage, which must be associated by removing of hemicellulose of the fibers, as it was also observe by color analysis. Finally, analyzing TG of bleached fiber one can see a peak at about 250°C, this peak was not expected, since hemicellulose, which is degraded in this temperature range has been probably removed by acetosolv, so this shoulder may possibly be related to a contamination or bleaching residues.

Samples	Degradation stages	ΔT (°C)	T_{peak} (°C)	T_i (°C)	Weight loss (%)	Residue at 600ºC (%)
Untreated	1st	25-130	54	152	8.3	25.8
	2nd	185-300	290		20.3	
	3rd	310-400	334		33.2	
	4th	410-600	430		6.2	
Treated	1st	25-133	48	168	7.3	14.3
	3rd	190-380	351		71.4	

	4th	410-600	420		4.6	
Bleached	1st	25-128	48		6.5	
	3rd	273-415	336	160	60.3	18.4
	4th	420-600	423		5.3	

Table 1: TG/DTG data of untreated, treated and bleached *Imperata brasiliensis* fibers.

3.3. Scanning Electron Microscopy (SEM)

The morphology of fibers and the effect of treatments on the fibers surface was evaluated. The SEM micrographs of untreated fiber can be seen in Fig.4.

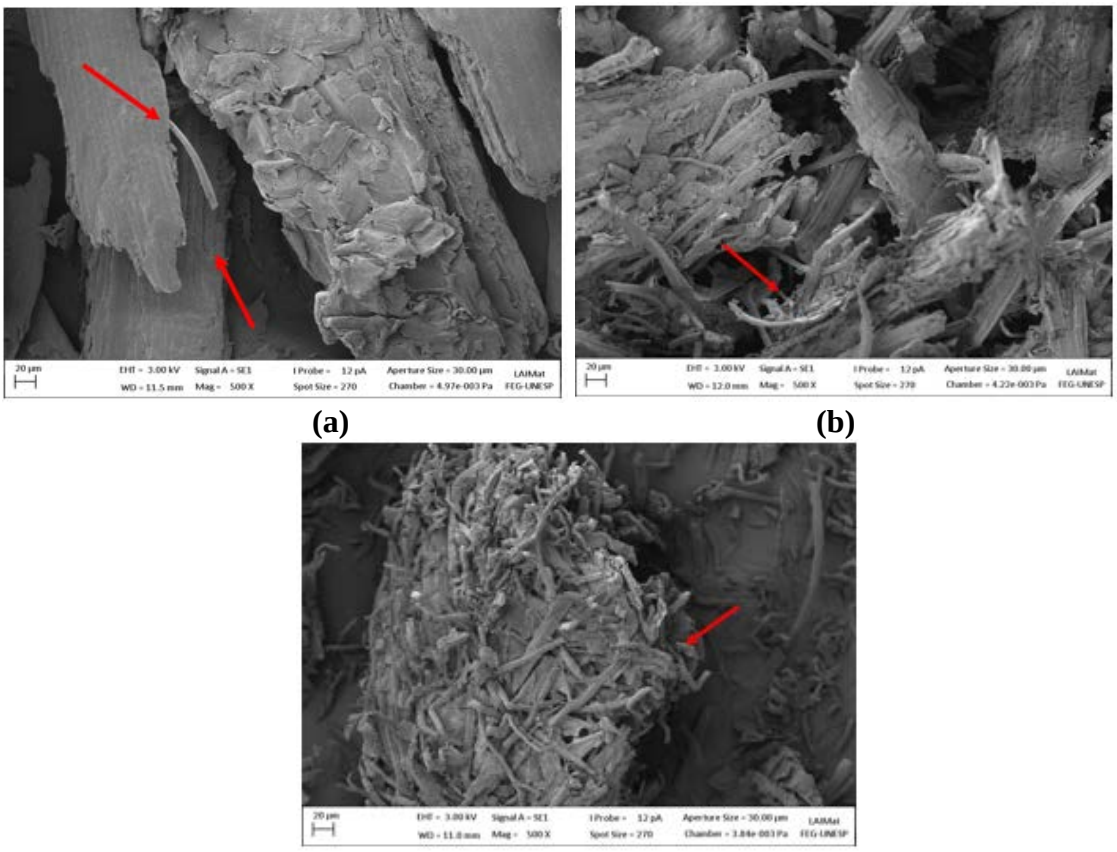

(a) **(b)**

(c)

Fig. 4 SEM micrographs of (a) untreated fiber, (b) *acetosolv* fiber, and (c) bleached fiber.

Analyzing the micrographs of Fig. 4a, it is possible to observe that untreated fiber surface is covered by several layers of substances like pectin, lignin and other impurities [21]. In addition, microfibrils that join to form the fiber bundle can be observed. The micrographs of acetosolv fibers can be seen in Fig.4b and because of this treatment there is the formation of lignin oligomers that

together with hemicellulose are solubilized in the solvent, remaining a portion of lignin, called residual [12]. These structural and surface modifications cause changes on the arrangement and the morphology of the fibers, which are defibrillated and therefore have a rougher surface, a good condition to reach a considerable adhesion between matrix and fibers in the composites [18,20].

After bleaching the defibrillation process (as shown in Fig. 4c) is more pronounced and the surface presents a greater number of recesses in the ending of treatment which may improve mechanical properties of the fibers and its posterior composites [20]. These reentrances caused by defibrillation are important for subsequent application in the composites as it facilitates mechanical anchoring with the polymer matrix and make easier the bonding with hydroxyl groups of the matrix [21].

4. CONCLUSIONS

The effect of two chemical treatments, acetosolv pulping and bleaching, on thermal properties and surface aspect of *Imperata brasiliensis* grass have been studied. It was demonstrated, according to thermogravimetric analyses, the improvement on thermal stability of the fibers. Nevertheless, the removing of non-crystalline constituents of fibers was also observed by the color after each treatment, which corroborated to degradation peak present in DTG curves.

One can also observe the surface modification after each treatment. Acetosolv and mostly bleached fibers presented a considerable defibrillation. Additionally, several reentrances were observed, a physical characteristic that improve the subsequent adhesion between fiber and polymeric matrix of composites.

5. ACKNOWLEDGMENTS

The authors acknowledge FAPESP (2017/15461-4) for fellowships and financial support.

6. REFERENCES

[1] PANDEY, P. *et al*. Performance of UV weathered HDPE composites containing hull fiber from DDGS and corn grain. **Industrial Crops & Products**. p. 1-11. jul. 2017.

[2] PICKERING, K.L.; EFENDY, M.G. A.; LE, T.M. A review of recent developments in natural fibre composites and their mechanical performance. **Composites Part A: Applied Science And Manufacturing**. S.i, p. 98-112. set. 2015.

[3] SANJAY, M.r. *et al*. Characterization and Properties of Natural Fiber Polymer Composites: A Comprehensive Review. **Journal Of Cleaner Production**. 09 out. 2017.

[4] NAIDU, D. S.; HLANGOTHI, S. P.; JOHN, M. J. Bio-based products from xylan: A review. **Carbohydrate Polymers**, [s.l.], v. 179, p.28-41, jan. 2018. Elsevier BV.

[5] STEFFENS, F.; STEFFENS, H.; OLIVEIRA, F. R. **Applications Of Natural Fibers On Architecture**. In: 3RD INTERNATIONAL CONFERENCE ON NATURAL FIBERS: ADVANCED MATERIALS FOR A GREENER WORLD, ICNF, 2017, Braga, Portugal. Peer-review. Braga, 2017. v. 200, p. 317 - 324.

[6] MOIGNE, N. Le *et al.* Study of the interface in natural fibres reinforced poly(lactic acid) biocomposites modified by optimized organosilane treatments. **Industrial Crops And Products**, [s.l.], v. 52, p.481-494, jan. 2014. Elsevier BV.

[7] OGUNSILE, B. O.; OLADEJI, Temitope Gbemi. Utilization of banana stalk fiber as reinforcement in low density polyethylene composite. **Matéria**, RJ , v.21, n.4, p. 953-963, Dez. 2016 .

[8] SILVA, R.; *et al*. **Aplicações de fibras lignocelulósicas na química de polímeros e compósitos**. Química Nova, v.32, p.661-67, 2009.
[9] POLETTO, M. *et al*. Thermal decomposition of wood: Influence of wood components and cellulose crystallite size. **Bioresource Technology**, [s.l.], v. 109, p.148-153, abr. 2012.
[10] KABIR, M.M. *et al*. **Chemical treatments on plant-based natural fibre reinforced polymer composites: An overview**. Composites Part B: Engineering. Australia, p. 2883-2892. Fev. 2012.
[11] FARUK, O. *et al*. Progress Report on Natural Fiber Reinforced Composites. **Macromolecular Materials And Engineering.** Kassel, p. 9-26. jan. 2014.
[12] HERNÁNDEZ-HERNÁNDEZ, H.M., et al. Acetosolv treatment of fibers from waste agave leaves: Influence of process variables and microstructural study. **Industrial Crops and Products,** v.86, p.163-172, 2016**.**
[13] BASAK, R.; CHOUDHURY, P.l.; PANDEY, K.M. Effect of Temperature Variation on Surface Treatment of Short Jute Fiber-Reinforced Epoxy Composites. **Materials Today**: Proceedings, [s.l.], v. 5, n. 1, p.1271-1277, 2018.
[14] AMERICAN SOCIETY FOR TESTING AND MATERIALS. **ASTM E2550**: Standard test method for thermal stability by thermogravimetry. United States, 2007.
[15] SALAPA, I.; TOPAKAS, E.; SIDIRAS, D.; Simulation and optimization of barley straw organosolv pretreatment. **Industrial Crops And Products**, [s.l.], v. 113, p.80-88, mar. 2018.
[16] GILLGREN, T.; HEDENSTRÖM, M.; JÖNSSON, L. J. Comparison of laccase-catalyzed cross-linking of organosolv lignin and lignosulfonates. **International Journal Of Biological Macromolecules**, [s.l.], v. 105, p.438-446, dez. 2017. Elsevier BV.
[17] FAVERO, C. *et al.* ASPECTOS GERAIS DO PROCESSO DE PRÉ-BRANQUEAMENTO DE CELULOSE. EnciclopÉdia Biosfera, Goiania, v. 10, n. 18, p.3696-3710, jul. 2014
[18] MARTIN, A. R. *et al*. Studies on the thermal properties of sisal fiber and its constituents. **Thermochimica Acta**, São Carlos, v. 506, p.14- 19, 25 jul. 2017.
[19] ROSA, I. M. de *et al*. Morphological, thermal and mechanical characterization of okra (Abelmoschus esculentus) fibres as potential reinforcement in polymer composites. **Composites Science And Technology**, [s.l.], v. 70, n. 1, p.116-122, jan. 2010. Elsevier
[20] BENINI, K. C. C. C. **Compósitos de nanocelulose/PHBV: manta microfibrílica por eletrofiação**. 2015. 166 f. Tese (Doutorado em Engenharia Mecânica) - Universidade Estadual Paulista. Faculdade de Engenharia de Guaratinguetá, 2015.
[21] KARGARZADEH, H. *et al*. Effects of hydrolysis conditions on the morphology, cristallinity, and thermal stability of cellulose nanocrystals extracted from kenaf bast fibers. **Cellulose**, *impress,* 2012.

NEW METHOD TO OBTAIN A NATURAL AND VERSATILE "CELLULOSE/SILICA HYBRID COMPOSITES" FROM RICE HUSK WASTE AND YOUR APPLICATION FOR ABSORPTIVE PROCESSES

Marcelo P. da Rosa (1), Paulo H. Beck (1), Felipe Kessler (1), Maria C. S. Bulhosa(1), Paulo M. T. Junior (1)

(1) School of Chemistry and Foods (EQA), Universidade Federal do Rio Grande, Brazil

https://doi.org/10.21452/bccm4.2018.10.12

Abstract

The synthetic hybrid composites formed by organics and inorganics molecules have potential to become important materials for many applications. The present study has objective to extract a "cellulose/silica" compound natural, directly from rice husk waste whose original structure is formed by lignin, cellulose, hemicellulose and silica. The obtaining of adsorbent (cellulose/silica composite) from rice husk was carried first by modified Organosolv method and the second step involved an agressive oxidative bleaching process. The samples were characterized by ash test, FTIR, SEM, XRD and BET. Tests was performed to verify the potential of the composite extracted as an adsorbent for dyes and metals in aqueous solutions and mycotoxins in barley. The results show the oxidative bleaching can be modified (increasing the cycles) to obtain different composites with different amounts of silica/cellulose. Besides that was possible to observe the "cellulose/silica hybrid composite" material have good capacity to remove different kinds of compounds in different matrix (liquid or solid phase). All adsorption tests performed presented maximum adsortions for the metals of until 92%; in other hand, the cellulose/silica composite removed 82% of crystal violet dye while the recoveries of mycotoxins show values between 64% and 74%. These results show great versatility for this hybrid material extracted from rice husk.

1. INTRODUCTION

Rice Husk (RH) is an abundant waste from agroindustry in south of Brazil, however most of this waste does not receive the proper destination. The main characteristic of RH is your resilience and resistance to chemical and biological attack. Besides RH is rich in natural compounds like cellulose, lignin and silica [1]. Cellulose shows interesting possibility to produce hybrid materials with inorganic compounds like the titanium and zinc oxides and silica, for instance [2]. The possibility of combining the properties of organic and inorganic compounds is very important and the researches have increased recently. Silica, for instance, can be incorporated into a wide variety of biopolymers such as cellulose, starch and chitin [3]. This combination of materials can result in

the possibility of promising applications for these composites like protective coatings, catalysis system, sensors and biological applications.

In the same way, the methodologies to produce hybrid (organic-inorganic) materials can be difficult and expansive, because involves many steps to make the linkage between two different materials. The nature have used frequently combinations of these compounds to form materials with better properties. Therefore, the extraction of a structure composed by part organic (cellulose) and inorganic (silica) to form a "cellulose/silica hybrid composite" with adsorbent properties can be important because two reasons, first; the recuperation of an abundant waste and second; the getting of a versatile and low cost adsorbent.

The process of adsorption is an important tool to remove contaminants or compounds presents in low concentration in aqueous solution mainly. In this way has become important the development of adsorbents "eco-friendly" and versatile to act in situations that go since water treatment until the quantitative analysis of contaminants in industrial products. This work was divided in two parts: the first is the extraction of a natural "cellulose/silica hybrid composite" from rice husk and your characterization, this step generated materials with different amount of silica and cellulose in your composition. The second part involves the application this composite obtained in the removal of copper, silver and Cristal Violet dye from an aqueous matrix. Your versatility and capacity of adsorption also has been tested against a solid matrix of barley in the recovery of three kinds of mycotoxins.

2. EXPERIMENTAL PROCEDURE

Firstly, to obtain the natural "cellulose/silica hybrid composite" adsorbent from Rice Husk (RH) was necessary make a delignification process, for this porpouse was carried the Organosolv process modified by Rosa et al. (2017) [4]. This process use Ethanol and Sulfuric acid under reflux conditions to remove most parte of Lignin from RH. After delignification process, the solid resulting presented in your structure cellulose, hemicellulose and silica with low amount of lignin. Than the RH was put in a flask with 100 ml with sodium hypochlorite (6% active chlorine) under acid pH and heating for 2 hours to remove residual lignin and hemicellulose by oxidative bleaching. The oxidative bleaching can be stopped when the Kappa Number be less than 5,0 (analysis to check the residual lignin at samples). After the oxidative bleaching the compounds obtained is dried and forwarded to characterization and tests of adsorptions.

Ashes test (ASTM D1102) was used to determine the silica amount. FTIR- Fourier Transform Infrared Spectroscopy (Shimadzu – IR PRESTIGE-21) determined the chemical structure. The investigation of surface morphology was made by scanning electron microscopy (SEM - Jeol JSM 6060). The same equipment carried the EDS. The surface areas was measured by N2 adsorption–desorption at 77K at Brunauer–Emmett–Teller (BET) method using a Quanta Chrome NOVA. A powder X-ray diffraction (XRD) method was used to determine the crystallinity by using a Rigaku - Miniflex 300 (Japan), this analysis was carried out with the generator settings of current of 30 mA and tension of 40 kV with Cu as an anode material at a temperature of 25°C with a step size (2h) of 0.033. An X-ray tube produced a monochromatic CuKa radiation of wavelength 0.154 nm, recorded between 10° and 80°.

The cellulose/silica composite obtained were tested like adsorbent for cationic dye (Crystal Violet) and two metals (Ag^{+1} and Cu^{+2}) to check the capacity and the best conditions to remove this compounds in aqueous solution. All assays were performed in batch mode, using a thermostated agitator (Marconi, MA 093, Brazil) at 220 rpm with volume of solution of 50 mL. In other hand the recovery of three mycotoxins (group of Trichothecene: nivalenol- NIV;

deoxynivalenol – DON; 3-acetyl- deoxynivalenol + 15-acetyl- deoxynivalenol - ADONS) was performed by matrix solid-phase dispersion (MSPD), but in this time the matrix was barley (solid matrix) and not water. The final recoveries was measured by Liquid chromatography–mass spectrometry.

3. RESULTS AND DISCUSSION

3.1 Characterization

The ashes test revealed if the number of cycles oxidative bleaching are increased, even after to remove residual lignin, that's results in a bigger degradation of cellulose and increase of silica amount. The exposure of composite to more than one cycles of bleaching resulted in two samples whose the amount of silica was increased from 30.01% to 42.26%. The FTIR spectrum (Figure 1) does not shows the lignin characteristic bands any more, but the stretch bands Si-O-Si (1080 cm^{-1}) and Si-H (469 cm^{-1}) are present. The O-H (3300 cm^{-1}), C-O-C and C-O (900-1200 cm^{-1}) stretch bands of the cellulose are observed for two samples. Another important characteristic about this spectrum is the similarity of the curves. This mean the reduction of cellulose amount at the samples do not result in significant chemistry change in the cellulose/silica hybrid composites extracted.

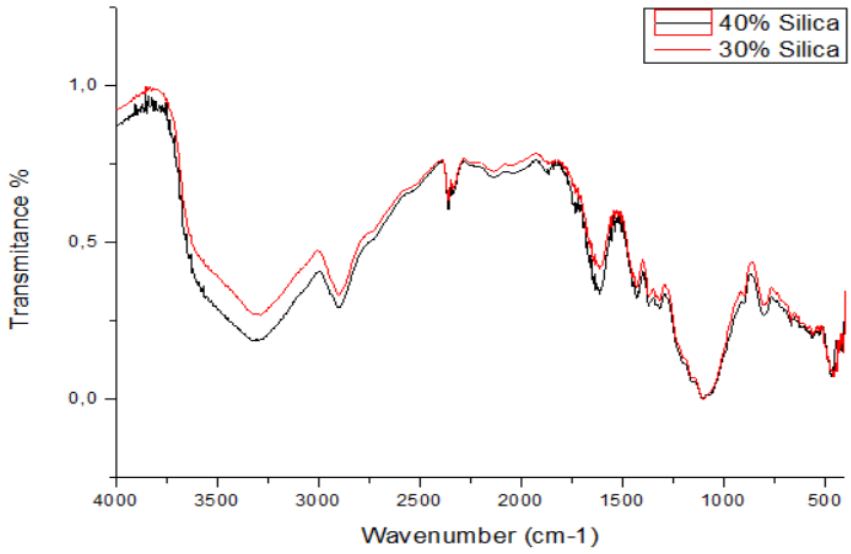

Figure 1: Spectrum of FTIR for two samples obtained the red line with 30% of silica and black line 40% of silica.

The Figure 2 (below) show that the more aggressive oxidative bleaching (more cycles) results beyond of decrease of cellulose amount by degradation in each sample, but also in reduction of particles size. In the future can be interesting try the obtantion of nanostructures by these methods.

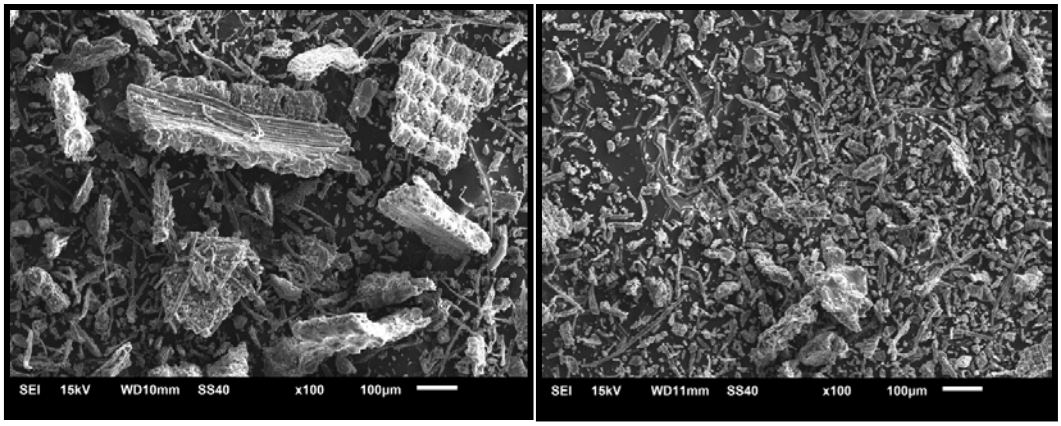

Figure 2: Image at left is sample with 30% silica, while the image at right is magnification of samples with 40% of silica.

The Figure 2 (left side less times bleaching cycles x right side more times bleaching cycles) show the difference of the morphological structures (reduction of particles size, mainly) between two samples of "cellulose/silica composite" adsorbent. The EDS analysis (Figure not shown), it was found that the "cellulose/silica composite" adsorbent surface is composed mainly by C, O and Si. Besides it is possible point some important characteristics. The EDS analysis (Figure not shown), it was found that the "cellulose/silica composite" adsorbent surface is composed mainly by C, O and Si. Besides it is possible point some important characteristics. The two composites analysed, with 30% and 40% of silica, showed heterogeneous surfaces on your composition. The most porous surfaces showed more amount of carbon and oxygen, while the smooth surfaces presented more quantity of silica than other elements.

The Rice Husk structure consists primarily of lignin, hemicellulose, cellulose and silica. The lignin and hemicellulose macromolecules are amorphous, but the cellulose, molecules are semi-crystalline. Furthermore the literature describe the silica present in rice husk like an amorphous silica distributed on their cell walls, forming silica-cuticle and silica-cellulose double layers on the surface of husks.

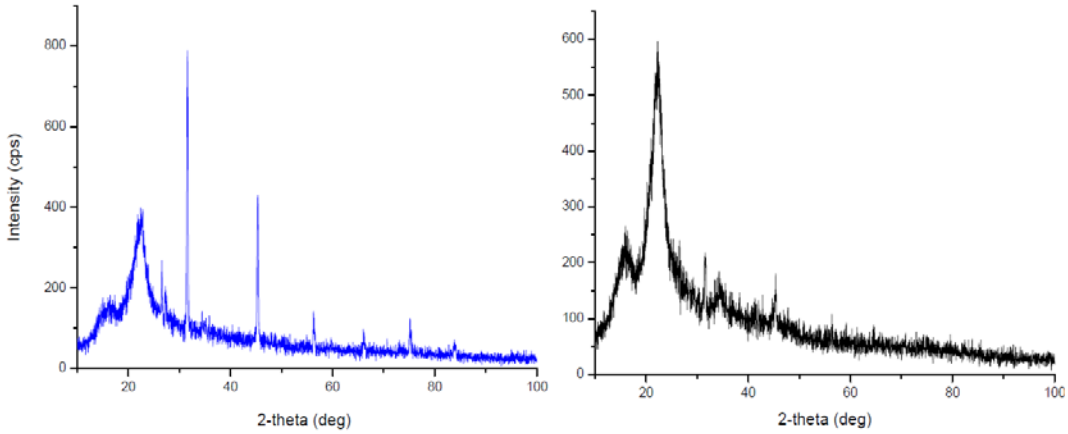

Figure 3: XRD plot of cellulose samples first (left) with more amount of silica (40%) and second (right) with less silica (30%).

The X-ray diffraction pattern of composite after oxidative bleaching is shown in Figure 3 for the two different amount of silica. The right side contains 30% of silica while left side is the sample with 40% of silica. The right side it shows two well-defined diffraction peaks at 2 theta = 15.9° and 2 theta = 22.5°, there are observed in cellulose natural fibers. These two peaks are attributed to the typical crystallographic plane of cellulose, which exhibits a monoclinic structure [5]. The spectrum at left side, show the reduction of cellulose peaks if compare the two XRD pattern, this was expected because the cellulose is attacked during the bleaching and your amount decrease. However the samples of "cellulose/silica composite" material that present more amount of silica (at left) revealed others important peaks (2 theta = 31,5; 45,3; 56,2 and 75.1). Although information about the silica structure in rice husk talked about kinds amorphous of silica, the peaks that appear at XRD open the possibility for existence of some structures of cristobalite in the samples after bleaching [6]. This structures are commonly observed in XRD patterns of rice husk ashes and depend of the conditions of burn to be able observed.

The surface area determined by BET method show values in the order of 18,422 m2/g (30% silica) and 9,534 m2/g (40% silica). That's values for surface area can be consider small if are compared with some kinds of active carbon, but this surface area is more than 10 times bigger than common cellulose powder and the same for cellulose nanocrystals obtained in other works [7]. The decrease of surface area on samples with 30% silica against the samples with 40% of silica opposes the result observed in SEM images where the size of particles reduce when de amount of silica increase. This result can be explained because the pores of silica particles in this case are filled by organic molecules resulting in a smaller surface area [8]. The removal of these structures from the pores in the silica particles can contributed very much to change these results. For now, probably the cellulosic amount of composite present bigger influence to increase or reduce the surface area.

3.2 Results of application tests

Table 1 shows the adsorption results for removal of Ag^{+1}, Cu^{+2} and Crystal Violet Dye in aqueous solution with adsorption times less than 30 minutes.

Table 1: Percentage of removal with two different composites of cellulose/silica.

	pH	30% Silica	40% Silica
Dye (Violet Crystal)	8,0	82,42%	79,49%
Ag^{+}	6,5	75,26%	92,01%
Cu^{+2}	6,5	51,10%	72,36%

These results present at Table 1 show that adsorbent can remove from aqueous solutions two different kinds of contaminants, metals e dyes. In other hand is possible to evaluate that the amount of silica and cellulose have great importance for the each kinds of substance (organic or inorganic) can be adsorbed. The copper and silver show better removal by the samples with more silica amount while the dye is adsorbed better in sample with more amount of cellulose.

The cellulose usually do not present god results for adsorption due your cristalinity. To compare with other results, in others works which used cellulose, modified cellulose and even chitosan, the results for silver adsorption showed maximum 64% of removing [9] while copper do not presented

results bigger than 50% of adsorption [10]. On the other hand for the Violet Crystal presented the best result around 70% of removal using pure cellulose [10]. However, the most important question about the "natural cellulose/silica composite", besides of your low cost, is your capacity of removal different kinds of substances (metal, dyes and mycotoxins). The others works use cellulose only for one purpose, metal or dyes.

Until now, the application of the composite cellulose/silica was to “purify” water samples. Now the next application involves the quantitative analysis of some contaminants (not desirable) present in feedstock of industrial use. The Table 2 show the results of recoveries for mycotoxins from the barley (here was used a solid matrix, not aqueous media). This time was used only the sample with 30% of silica and 70% of cellulose. The decision was made because the adsorbent with more amount of cellulose showed better results to remove organic compounds.

Table 2: values for recoveries of three kinds of mycotoxins by the composite with 30% of silica

Mycotoxin	Recoveries	RSD: relative standard deviations
NIV	64%	5,3%
DON	78%	3,5%
ADONS	72%	2,8%

The values considered acceptable by The Brazilian Health Regulatory Agency (ANVISA) is recoveries between 70 and 120% for trace compounds and a repeatability (RSD) lower than 20%. The importance of these results are the possibility for the use of theses “cellulose/silica hybrid composites” in quantitative analysis to help the quality control of barley. Today for this procedure is used C_{18} (octadecy-silica), this material show recovery between 80 to 90% for these mycotoxins. But we need higlight wich the problem about C_{18} is the hight cost of this material.

4. CONCLUSIONS

- The new procedure performed at rice husk make possible obtaining a natural composite formed by silica and cellulose (“cellulose/silica hybrid composites”), without lignin and hemicellulose.
- The process of bleaching show important to control the amount of silica in the samples by the increase of the cycles of oxidation.
- The material obtained from rice husk presented low cost and good properties to remove (by adsorption) different kinds of contaminants in aqueous solution or solid phase.
- The next step is the standard study of adsorption for all compounds removed to understand better this process proceed changes in chemical and physical structure of this composite.

ACKNOWLEDGEMENTS

To FURG, PPGQTA, LAMCA (FURG) and LAPAM (UFSM).

REFERENCES

[1] Laufenberg, G., Kunz, B. and Nystroem, M., "Transformation of vegetable waste into value added products", Bioresour. Technol. **87**(2) (2003) 167-198.

[2] Bobowska, I., Wojciechowski, P. and Halamus, T., "Organic–inorganic nanocomposites of (2-hydroxypropyl) cellulose as a precursor of nanocrystalline zinc oxide layers", Polymer. Adv. Tech. **19**(12) (2008) 1860-1867.

[3] He, X., Du, M., Li, H. and Zhou T., "Removal of direct dyes from aqueous solution by oxidized starch cross-linked chitosan/silica hybrid membrane", *Int. J. Biol. Macromolec.* **82** (2016) 174-181.

[4] Rosa, M.P., Beck, P.H., Müller, D.G., Moreira, J.B., Silva, J.S. and Durigon, A.M.M., "Extraction of Organosolv Lignin from Rice Husk under Reflux Conditions", *Biolog. and Chem. Res.* **4**(4) (2017) 87 – 98.

[5] Indran, S., R. Edwin Raj, and V. S. Sreenivasan. "Characterization of new natural cellulosic fiber from Cissus quadrangularis root." *Carbohy. Poly.* **110** (2014): 423-429.

[6] Yalcin, N., and V. Sevinc. "Studies on silica obtained from rice husk." *Ceramic. Inter.* **27.2** (2001): 219-224.

[7] Lu, P. and Hsieh, Y.-L., "Preparation and properties of cellulose nanocrystals: rods, spheres, and network", *Carbohydr Polym.* **82**(2) (2010) 329-336.

[8] Hu, S. and Hsieh, Y.-L., "Preparation of activated carbon and silica particles from rice straw", *ACS Sustain. Chem.* **2**(4) (2014) 726-734.

[9] Liu, P., Sehaqui, H., Tingaut, P., Wichser, A., Oksman, K. and Mathew, A. P., "Cellulose and chitin nanomaterials for capturing silver ions (Ag+) from water via surface adsorption", *Cellul.*, **21**(1) (2014) 449-461.

[10] Li, N. and Renbi B., "Copper adsorption on chitosan–cellulose hydrogel beads: behaviors and mechanisms", *Sep. and purify. Techn.*, **42.3** (2005) 237-247.

[11] Zhou, Y., Zhang, M., Wang, X., Huang, Q., Min, Y., Ma, T., and Niu, J., "Removal of crystal violet by a novel cellulose-based adsorbent: comparison with native cellulose", *Ind. & Eng. Chem. Res.*, **53**(13) (2014) 5498-5506.

11. NANOCOMPOSITES

REDUCED GRAPHENE OXIDE AS REINFORCEMENT IN ALUMINIUM NANOCOMPOSITES PREPARED BY POWDER METALLURGY

Andrada DM[1,2], Serodre TM[2], Santos AP[2], Furtado CA[2]

(1) Universidade Federal de Itajubá, Campus Itabira, Itabira, MG, Brasil

(2) Centro de Desenvolvimento da Tecnologia Nuclear, CDTN, Belo Horizonte, MG, Brasil.

https://doi.org/10.21452/bccm4.2018.11.01

Abstract

This study investigated the use of reduced graphene oxide (rGO) obtained by chemical route as a reinforcement phase in aluminium matrix nanocomposites (AMNCs) fabricated by powder metallurgy. Mechanical milling of a mixture of aluminium and rGO powders was able to form homogeneous and highly densified composites, allowing an effective interaction between matrix and reinforcement to establish. The effect of rGO content (ranging for 0.01 to 1.0 wt%) on the mechanical properties of rGO-AMNCs was investigated. Microhardness, elastic modulus and yield strength increase gradually up to 0.5 wt% with respective gains of 308%, 61% and 86%.

1. INTRODUCTION

Aluminium matrix nanocomposites (AMNCs) reinforced with carbon nanomaterials have attracted great attention in the last few decades due to their potential use in different areas such as the automotive and aerospace sectors, meeting specific demands currently fulfilled exclusively by metals and their alloys [1]. These nanocomposite materials offer a unique balance of the physical and mechanical properties of its constituents, such as ductility, tenacity, and thermal and electrical properties of the metallic matrix, together with the high elastic modulus, and high electrical and thermal conductivity of the graphenic materials. In addition, the proportions of the phases in the metal matrix composites (MMCs) are not directly limited by thermodynamic factors as in metallic alloys, offering great possibilities in terms of properties that can be designed, customized and adapted to a given application [2].

Among carbon nanomaterials, carbon nanotubes (CNTs) and, more recently, all graphene family compounds [2], i.e., graphene oxide (GO), reduced graphene oxide (rGO), few layer graphene (FLG), graphene nanosheets (GNS) and graphene nanoplatelets (GNPs) are considered to be the best candidates to provide AMNCs with better enhanced properties. Graphene materials seem to comprise the best choice for reinforcement in nanocomposites over other forms of carbon due to their relatively large surface area providing greater interaction with the matrix material, which implies an increased and more efficient transfer of electrons, phonons or mechanical [1]. Many researchers have focused in attempting to incorporate graphene materials into Al matrix in order to obtain AMNCs with desirable properties. Despite constant efforts, the reinforcing effects

are still notably lower than the theoretically predicted, due mainly to factors related with incorporation and dispersion efficiency of the graphene material in the Al matrix during processing [3]. In the face of the different processing methodologies like powder metallurgy, colloidal processing, molecular level mixing and nanoscale dispersion, powder metallurgy by ball milling processing (BM) is widely used due to its low processing temperature which is beneficial by avoiding or controlling the harmful reaction interface, allied to the relatively low cost, reproducibility and scalability that make this processing a common choice for obtaining AMNCs.

Bartolucci et al. [3] was one of the first to report obtaining an AMNC reinforced with graphene. The authors evidenced a remarkable decrease in mechanical properties of the AMNC, which was attributed to the formation of interfacial products. In the following studies, different methodologies showed promising results regarding a gain in mechanical properties of the AMNCs, mostly reinforced with GNPs [2,4–16]. A few approaches consider AMNCs reinforced with rGO, obtained in situ by thermal reduction (trGO) during the sinterization process [5,17–20]. Due to its graphene like nature allied with its own characteristics, such as the high degree of exfoliation and high-throughput production process, rGO is an important candidate as reinforcement in AMNCs. Herein, rGO previously obtained by low temperature chemical route was used as a reinforcement material in AMNCs prepared by powder metallurgy. SEM and TEM analysis was conducted to evaluate microstructural changes and help ensure the desirable material modifications. Furthermore, the influence of the rGO content in the mechanical properties of the composite, such as compressive strength and microhardness, were measured and compared with those reported in related works.

2. MATERIALS AND METHODS

2.1 - Materials

Atomized aluminium powder of globular particles with mean size of 6 μm (purity > 99.5%) was supplied by Alcoa®, Brazil, and used as received. Milled expanded graphite with average lateral size of 8 μm and thickness of 5-10 nm was supplied by Nacional de Graphite LTDA, Brazil. For simplification purposes this sample was labelled as GNP. All solvents and reagents were of analytic grade and used without further purification.

2.2 - Preparation of rGO

Firstly, a graphene oxide (GO) sample was obtained from natural graphite through an adapted Hummers method described by Abdolhosseinzadeh et al. [19]. The sample was washed with 1 $mol.L^{-1}$ HCl solution and distilled water for several times by centrifugation (Eppendorf, 5810-R) at 10000 rpm. The final solid precipitate was dried at temperatures below 40°C under vacuum for 48 hours and was manually ground until it passed through a sieve of 40# to obtain a homogenous powdered sample, which was chemically reduced to rGO. This reduction was carried out in one step under reflux treatment in pH 10 solution containing 0.45 $mol.L^{-1}$ L-ascorbic acid (LAA) as reducing agent (LAA:GO = 10:1). The solid product was separated by vacuum filtration and washed using deionized water and anhydrous ethanol. The final product was collected and dried in vacuum at temperature lower than 40°C for 24h.

2.3 - Preparation of AMNCs

The AMNC powders were prepared by ball milling at 250 rpm for 3 h in a 250 mL stainless steel jar with steel grinding balls of 2 mm in diameter, under inert atmosphere of ultrapure N_2, using a Retch PM 100 high energy (Germany) planetary ball mill. The ball to powder weight ratio was kept constant at 10:1. Methanol (CH_3OH) with purity of 99.99% was used as process control agent to avoid cold welding in a ratio of 0.8 wt% in relation to the aluminium content. At the end of the process, the jar with the powder blend was kept in a desiccator under vacuum to allow the passivation of the metallic powders for 24 h. Afterwards, each powder was placed in a die of 10 mm in diameter and cold compacted at a compaction pressure of 550 MPa in order to fabricate the billets. The obtained samples were placed in a tubular furnace with dry and inert gas atmosphere. The sintering conditions were: maximum temperature of 605°C, holding time of 180 min, and heating rate of 10 $C.min^{-1}$. Samples with different weight percent of the reinforcement ranging from 0.01, 0.05, 0.5 and 1.00 wt% were obtained. For comparison an Al sample was also prepared using the same method excluding the graphene material addition.

2.4 - Characterization

Morphology and structural characterizations were performed by optical microscopy (OM; Carl Zeiss–Axio Imager A2m, Gottingen, Germany), scanning electron microscopy (SEM) (SEM, TESCAN VEGA2) and transmission electron microscopy (Tecnai G2-20 Super Twin, FEI under the acceleration voltage of 200 KV). The relative density of the AMNC samples was measured by Archimedes' principle. The microhardness measurements were performed using a Vickers Wilson-402 MVD microdurometer with a load of 0.2 kgf and a time of 15 seconds. Compression tests were performed at room temperature on the basis of the monolithic cylindrical samples according to ASTM E9 using an Instron 2300 universal test machine with a 100 KN load cell with a speed of 0.5 $mm.min^{-1}$. Cylindrical samples with an aspect ratio (l/d) of ~ 1.5 were used in all assays. At least three samples for each composition were measured to ensure the accuracy.

3. RESULTS

3.1 - Morphology of the composite powders

Before ball milling dispersion, all mixtures resulted in a fine powder with a bright surface. In this condition, the resulting powders are still very reactive and need to be handled very carefully. SEM images of the powders obtained by manual mixing show aspects of both Al matrix and isolated reinforcement (Fig. 1 – a-b). Fig. 1-b clearly identifies a large flake of rGO attached to a non-deformed surfaces of Al particle before dispersion by ball milling.

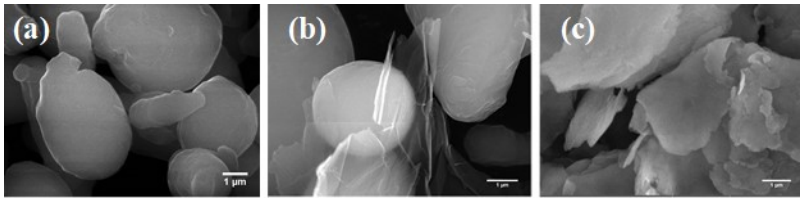

Figure 1. SEM images of Al particle(a), 1.0 wt% rGO-AMNC before dispersion (b) and 1.0 wt% rGO-AMNC after ball milling dispersion (c).

After milling it was not possible to distinguish the phases of carbon material from the metal matrix (Figure 1-c). Particles of irregular shape resulting from cold welding, deformation and fragmentation are observed in the image. Such a change in the morphology of the particles can be considered desirable from the point of view of compaction, since in thesis they provide a better packing than spherical particles allowing to obtain a higher densification. No rGO agglomerate was observed in representative SEM images of the milling composites.

3.2 - Density of AMNCs.

Calculated (ρ_c) and experimental (ρ_e) density values of sintered composites were evaluated for all AMNCs and are displayed in Table 1. Calculated densities were computed by the rule of mixtures, using the experimentally measured density of each constituent of the composite material, i.e. aluminium and rGO, found to be respectively 2.698±0.006 g.cm^{-3} and 1.651±0.019 g.cm^{-3}. Since rGO is less dense than aluminium, a slightly reduction in the density of the composites is expected in the range of the reinforcement concentration studied here. A significant reduction should just occur with incorporating large volumes of reinforcement.

For pure aluminium, a reduction of ~ 2% in the measured density after sintering (2.63±0.01) was observed in comparison to the one measured for Al powder. This reduction demonstrates the high level of densification that can be achieved by the proposed methodology, and is in accordance with the literature values [8,12]. For rGO-AMNCs composites, ρe values were 2.63±0.01, 2.63±0.01, 2.60±0.01 and 2.57±0.01 for 0.01, 0.05, 0.5 and 1.0 wt% rGO content respectively. Above the content of 0.5 wt%, the incorporation of reinforcement materials has a symptomatic effect in reducing the density, reaching ~96% in terms of relative ρ_e. A general difference between ρ_e and ρ_c can be expected due the mixing rule neglecting any effect related to morphological, textural changes such as porosity and / or product formation (agglomeration of the reinforcement) changes, interface between aluminium and carbon, etc. Similar results were obtained by Khan et al. [8], who used a similar methodology to that used in this work and in other studies using other processing methodologies [10,20].

In order to evaluate the densification of the composites by verifying of any significant porosity, the surface of rGO-AMNC was evaluated by optical microscopy (OM) and SEM. Figure 2 shows OM and SEM images for 1.0 wt% rGO-AMNC, respectively, revealing an effective compaction of aluminium powders after sintering without evidences of significant porosity or rGO agglomeration.

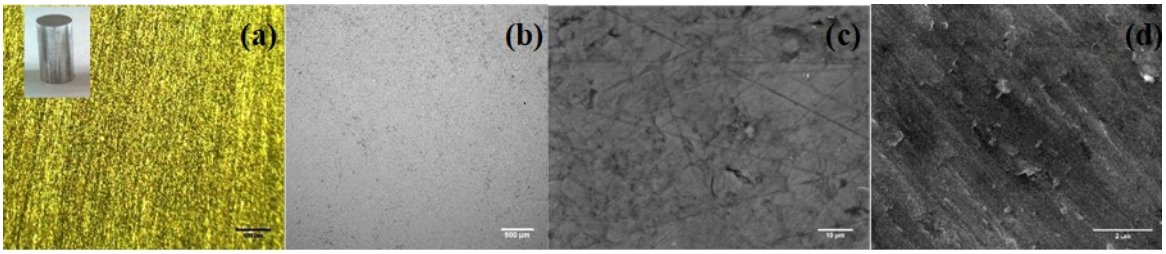

Figure 2 - Optical image of polished non-etched surfaces at 400x magnifications for 1.0 wt% rGO-AMNC (a) and SEM images under different magnifications (b-d) for 1.0 wt% rGO-AMNC.

3.3 - Microhardness and compression tests of the AMNCs

Table 1 displays the values of Vickers microhardness (HV) and the parameters of compression modulus (E), 0.2% yield strength (YS) and ultimate compressive strength (UCS) obtained from the stress-strain curves for the rGO-AMNC composites in different mass fractions. In general, it was observed that HV, YS and E gradually increases by increasing the reinforcement content until the limit of 0.5 wt% of rGO and then decrease at 1.0 wt%. The 0.2 % YS parameter is a measure of the resistance of the material to flow or to being submitted to plastic deformation. An increase of up to 86% in YS at 0.5% wt%. rGO agrees with the expectative of increase in mechanical resistance of the composite material. Furthermore, the increase of 61% of the elastic modulus reflects the synergetic combination of the elastic modulus of the matrix and the reinforcement, which can be reached when the material responds as a composite. Thus, we can consider that although we did not observe a clear trend or real gain in the UCS, in agreement with the results of Rashad et al [12], YS and E parameters provided evidences that rGO can act as an effective reinforcement in AMNCs. Similar behaviour was obtained in other studies reporting an enhancement in the mechanical properties of Al nanocomposites via favourable dispersion at low mass fraction up to 0.5 wt % of graphene material [3,13,20]. However, the gain of ~ 3 times (308%) in HV observed here for 0.5 wt% rGO-AMNC, from ~ 39 HV (382.5 MPA) for pure Al to ~ 120 HV (1177 MPA), had not been reported by now. Table 2 compares our result with the others reported in the literature. Few works have reached near the maximum gain observed in this work, despite using a relatively higher amount of reinforcement [9,15,21].

-

- Table 1 - Mean values of ρc, ρc, HV, 0.2% YS, E and UCS for the rGO-AMNC

wt%	ρ_c (g.cm^{-3})	ρ_e (g.cm^{-3})	HV	0.2% YS (MPa)	E (GPa)	UCS (MPa)
0	2.63±0.01	2.698	39 ± 2	57 ± 2	4.4 ± 0,2	299 ± 16
0.01	2.63±0.02	2.698	43 ± 3	57 ± 3	5.1 ± 0,5	305 ± 5
0.05	2.63±0.01	2.697	47 ± 3	71 ± 1	5.1 ± 0,4	255 ± 3
0.5	2.60±0.01	2.689	120 ± 4	106 ± 4	7.1 ± 0,2	284 ± 2
1.0	2.57±0.01	2.681	98 ± 2	99 ± 5	6.6 ± 1,0	274 ± 11

Table 2 – Comparison between the HV values reported here and in the literature for graphene content AMNCs

Reinforcement	Mass fraction	Microhardness variation	Reference
trGO	0-0.1% wt.	~1.2x increase in HV (0.1% wt.)	[4]
GNPs	0-3% wt.	~1.7x increase in HV (3.0% wt.)	[22]
GNPs	0-5% wt.	~1.6x increase in HV (5.0 % wt.)	[7]
GNPs	0-5% wt.	~3.0x increase in HV (1.0 % wt.)	[9]
GO	1.0% vol.	~2.4x increase in HV (1.0% vol.)	[15]
trGO	0-5% wt.	~1.2x increase in HV (0.5% wt.)	[17]
GNPs e trGO	0-5% wt.	~1.4x increase in HV (0.3 % wt.)	[16]
GNPs	0-5% wt.	~1.6x increase in HV (1.5 % wt.)	[3]
rGO	**0.5% wt.**	**~3.0x increase in HV (0.5 % wt.)**	**Present work**

3.4 - Microstructure of the AMNCs

In order to evaluate the interface and the phases present in the obtained composites, TEM analysis was carried out from thin sections obtained for the rGO-AMNCs sample. Figure 3 shows a sequence of images obtained for the 1 wt% rGO-AMNC sample in different magnifications. Initially it is possible to identify elongated Al grains (Figure 3 (a)), which are presented in this way because of the milling of the powders, which cause a deformation of the Al particles, changing their original rounded shape into elongated plates with a thickness of ~ 600 nm and with a higher

width of 6 μm (not shown). Regions of grain boundaries (GB) as well as the occurrence of some dislocations in the Al matrix ({D}) can be observed in Figure 3 (a). Pores or voids were not identified in the TEM images, again characterizing a well densified sample.

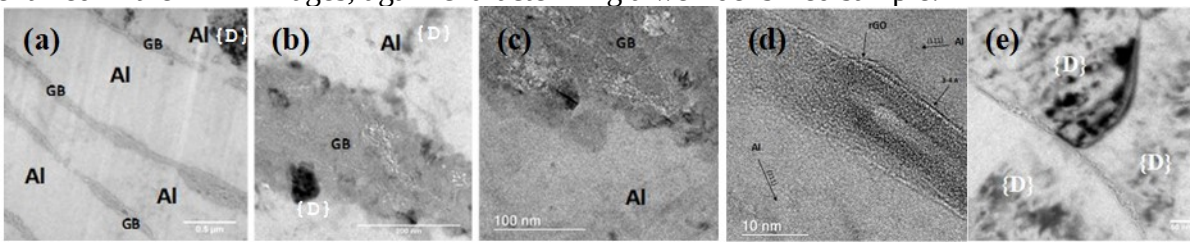

Figure 3 - TEM images under different magnifications for the 1 wt% rGO-AMNC sample.

GB are present as discontinuous phases in the Al matrix. Similar results were observed by Zhang et al. [23]. Due to its intrinsic characteristics as relative low crystallinity, high exfoliation degree, thin morphology, allied to its relative low mass fraction in the AMNCs, rGO phase becomes an object of difficult observation, mainly if it is intercalated between GB or surfaces of adjacent Al particles. However, in some specific regions of the sample outside the grain boundary region, it was possible to identify the rGO phase in the form of thin curved or folded layers (Figure 3 (c) e (d)), showing that the rGO phase was introduced into the Al matrix and does not occupy only the border regions between the metal particles. The reinforcement phase incorporated into the matrix reflects the conditions where stress transfer from the matrix to the reinforcement can be activated. Moreover, Figure 3 (d) illustrates the tendency of occurrence of discordances {D} pilling in the interface formed between the Al matrix and the rGO layer. These observations agree with the results obtained of increase in microhardness. The rGO act as a barrier to the movement of dislocations, thus controlling and restricting the plastic deformation of the matrix. Also, the rGO was found dispersed in the Al matrix and in suitable conditions to allow stress transfer phenomena to occur.

4. CONCLUSIONS

Chemical reduced GO (rGO) was employed as reinforcement in AMNCs. Composites with uniformly dispersed rGO in loadings of 0.01 to 1.0 wt% were successfully manufactured by powder metallurgy technique using the ball milling processes. Uniaxial pressing and pressureless sintering was used for the densification of mixed powders into compact composite bodies. The degree of densification of the sintered composites was of ~96%. Pores and voids were not identified by TEM, which also characterized the rGO phase acting as a barrier to the movement of dislocations and fully inserted into the metallic matrix in an appropriate condition for the phenomena of stress transfer. Additionally, intermetallic compounds like Al_4C_3 were not evidenced, signalling a good interaction between the reinforcement and the metal matrix. As a consequence, gains in mechanical properties of 61% in elastic modulus, 86% in yield strength and 308% in microhardness were reached for rGO-AMMCs at the limit of 0.5 wt% rGO content.

ACKNOWLEDGMENTS

This work was supported by the Brazilian Nanocarbon Institute, the SisNano Program, and the Brazilian agencies CNPq, CAPES, FAPEMIG, and CNEN. The authors would like to acknowledge Alcoa and Nacional de Grafite LTDA for the supply of samples, Dr. D.R. Miquita and Dr. H. Limborço from Center of Microscopy of UFMG for insightful work in TEM/FIB analysis.

REFERENCES

[1] A. Nieto, A. Bisht, D. Lahiri, C. Zhang, A. Agarwal, Graphene reinforced metal and ceramic matrix composites : a review, 6608 (2017). doi:10.1080/09506608.2016.1219481.

[2] A. Bianco, H.M. Cheng, T. Enoki, Y. Gogotsi, R.H. Hurt, N. Koratkar, T. Kyotani, M. Monthioux, C.R. Park, J.M.D. Tascon, J. Zhang, All in the graphene family - A recommended nomenclature for two-dimensional carbon materials, Carbon N. Y. 65 (2013) 1–6. doi:10.1016/j.carbon.2013.08.038.

[3] Z. Baig, O. Mamat, M. Mustapha, A. Mumtaz, M. Sarfraz, S. Haider, An Efficient Approach to Address Issues of Graphene Nanoplatelets (GNPs) Incorporation in Aluminium Powders and Their Compaction Behaviour, Metals (Basel). 8 (2018) 90. doi:10.3390/met8020090.

[4] S.F. Bartolucci, J. Paras, M.A. Rafiee, J. Rafiee, S. Lee, D. Kapoor, N. Koratkar, Graphene – aluminum nanocomposites, 528 (2011) 7933–7937. doi:10.1016/j.msea.2011.07.043.

[5] R. Pérez-bustamante, D. Bolaños-morales, J. Bonilla-martínez, I. Estrada-guel, Microstructural and hardness behavior of graphene-nanoplatelets / aluminum composites synthesized by mechanical alloying, J. Alloys Compd. 615 (2014) S578–S582. doi:10.1016/j.jallcom.2014.01.225.

[6] S.E. Shin, Y.J. Ko, D.H. Bae, Mechanical and thermal properties of nanocarbon-reinforced aluminum matrix composites at elevated temperatures, Compos. Part B Eng. (2016). doi:10.1016/j.compositesb.2016.09.017.

[7] A. Elghazaly, G. Anis, H.G. Salem, Effect of Graphene Addition on the Mechanical and Tribological Behavior of, Compos. Part A. (2017). doi:10.1016/j.compositesa.2017.02.006.

[8] M. Khan, M. Amjad, A. Khan, Microstructural evolution , mechanical pro fi le , and fracture morphology of aluminum matrix composites containing graphene nanoplatelets, (2017) 1–12. doi:10.1557/jmr.2017.111.

[9] L.K. Syed Nasimul Alamn, A Mechanical properties of aluminium based metal matrix composites reinforced with graphite nanoplatelets, Mater. Sci. Eng. A. 667 (2016) 16–32. doi:10.1016/j.msea.2016.04.054.

[10] G. Li, B. Xiong, Effects of graphene content on microstructures and tensile property of graphene-nanosheets / aluminum composites, J. Alloys Compd. 697 (2017) 31–36. doi:10.1016/j.jallcom.2016.12.147.

[11] S.J. Niteesh Kumar, R. Keshavamurthy, M.R. Haseebuddin, P.G. Koppad, Mechanical Properties of Aluminium-Graphene Composite Synthesized by Powder Metallurgy and Hot Extrusion, Trans. Indian Inst. Met. (2017). doi:10.1007/s12666-017-1070-5.

[12] M. Rashad, F. Pan, A. Tang, M. Asif, Effect of Graphene Nanoplatelets addition on mechanical properties of pure aluminum using a semi-powder method, Prog. Nat. Sci. Mater. Int. 24 (2014) 101–108. doi:10.1016/j.pnsc.2014.03.012.

[13] J.L. Li, Y.C. Xiong, X.D. Wang, S.J. Yan, C. Yang, W.W. He, J.Z. Chen, S.Q. Wang, X.Y. Zhang, S.L. Dai, Microstructure and tensile properties of bulk nanostructured aluminum/graphene composites prepared via cryomilling, Mater. Sci. Eng. A. 626 (2015) 400–405. doi:10.1016/j.msea.2014.12.102.

[14] Zan Li et al., Uniform dispersion of graphene oxide in aluminum powder by direct electrostatic adsorption for fabrication of graphene / aluminum composites, Nanotechnology. 25 (2014) 325601. doi:10.1088/0957-4484/25/32/325601.

[15] H. Kwon, J. Mondal, K. AloGab, V. Sammelselg, M. Takamichi, A. Kawaski, M. Leparoux, Graphene oxide-reinforced aluminum alloy matrix composite materials fabricated by powder metallurgy, J. Alloys Compd. 698 (2017) 807–813. doi:10.1016/j.jallcom.2016.12.179.

[16] J. Liu, U. Khan, J. Coleman, B. Fernandez, P. Rodriguez, S. Naher, D. Brabazon, Graphene oxide and graphene nanosheet reinforced aluminium matrix composites : Powder synthesis and prepared composite characteristics, JMADE. 94 (2016) 87–94. doi:10.1016/j.matdes.2016.01.031.

[17] Y. Sun, C. Zhang, B. Liu, Q. Meng, S. Ma, W. Dai, Reduced Graphene Oxide Reinforced 7075 Al Matrix Composites: Powder Synthesis and Mechanical Properties, Metals (Basel). 7 (2017) 499. doi:10.3390/met7110499.

[18] Z. Li, Q. Guo, Z. Li, G. Fan, D. Xiong, Y. Su, J. Zhang, D. Zhang, Enhanced Mechanical Properties of Graphene (Reduced Graphene Oxide)/Aluminum Composites with a Bioinspired Nanolaminated Structure, (2015). doi:10.1021/acs.nanolett.5b03492.

[19] S. Abdolhosseinzadeh, H. Asgharzadeh, H. Seop Kim, Fast and fully-scalable synthesis of reduced graphene oxide, Sci. Rep. 5 (2015) 10160. doi:10.1038/srep10160.

[20] A. Bisht, M. Srivastava, R. Manoj, I. Lahiri, D. Lahiri, Strengthening mechanism in graphene nanoplatelets reinforced aluminum composite fabricated through spark plasma sintering, Mater. Sci. Eng. A. (2017). doi:10.1016/j.msea.2017.04.009.

[21] A. El-Ghazaly, G. Anis, H.G. Salem, Effect of graphene addition on the mechanical and tribological behavior of nanostructured AA2124 self-lubricating metal matrix composite, Compos. Part A Appl. Sci. Manuf. 95 (2017) 325–336. doi:10.1016/j.compositesa.2017.02.006.

[22] F.H. Latief, E.M. Sherif, A.A. Almajid, H. Junaedi, Journal of Analytical and Applied Pyrolysis Fabrication of exfoliated graphite nanoplatelets-reinforced aluminum composites and evaluating their mechanical properties and corrosion behavior, J. Anal. Appl. Pyrolysis. 92 (2011) 485–492. doi:10.1016/j.jaap.2011.09.003.

[23] D. Zhang, Enhanced Mechanical Properties of Graphene (Reduced Graphene Oxide)/ Aluminum Composites with a Bioinspired Nanolaminated Structure, (2015). doi:10.1021/acs.nanolett.5b03492.

SIMPLE, ECONOMICAL, SCALABLE AND ENVIRONMENTALLY SUSTAINABLE ROUTE FOR FUNCTIONALIZATION BNNTS

SOUSA. A. A. (1), MEIRELES, M. G. A.(1), ANDRADA D. M.(1), SOUSA, E. M. B.(2) , GASTELOIS, P.L.(2) , MACEDO, W. A. A.(2), SILVA, W. M.(2).

https://doi.org/10.21452/bccm4.2018.11.02

Abstract

Boron nitride nanotubes (BNNTs) were synthesized at 1150 °C under atmosphere of NH_3/N_2 gas by chemical vapor deposition (CVD) technique. A simple mechanical method (ball milling in the presence of urea) is proposed for functionalization of BNNTs. FTIR results indicate that amine functional groups (N-H and -NH_2) were introduced on the nanotubes and the X-ray photoelectron spectroscopy showed that the obtained values for the B:N rates are slight different which may be an indication of the functionalization occurrence. TEM and MEV images after ball milling showed an evidence of small fragments of tubular particles by the parallel fringes corresponding to multiple stacked layers of h-BN sheets. Successful of functionalization of the BNNTs structure was evidenced by stability of the dispersions in water, DMF and acetone. Additionally, the result suggests that the amino termination of the functionalized BNNTs makes it possible to covalently bond to polymers for manufacturing nanocomposites.

1. INTRODUCTION

The fact that carbon nanotubes (CNTs) have unique properties motivated the search for other materials that could also present themselves in the form of nanotubes and bring with this morphology different properties [1,2]. Thus, after the assumption about the existence of boron nitride nanotubes (BNNTs) raised in 1994, research groups engaged and succeeded in the synthesis of this new type of nanomaterial [2]. Results from several studies described in the literature showed that BNNTs were as attractive as researchers imagined. These materials exhibit unique properties such as visible light transparency and electrically insulating nature associated with high thermal conductivity, high thermal and chemical stability and mechanical strength [3,4,5,6].

In addition, when compared to CNTs, BNNTs exhibited a greater homogeneity in their electronic properties, since these properties are not influenced by chirality and geometry [2, 7]. The properties cited above make BNNTs promising for applications in nanoelectronics devices, gas sensors, applications involving high temperature and aggressive environments, as well as in high performance and structural composites [8, 9].

Despite the remarkable properties, BNNTs present low solubility in solvents due to their low surface chemical reactivity (especially when they have a high degree of crystallinity) and a high tendency to self-aggregation [10]. Thus, its applicability is considerably reduced, especially when it becomes necessary to disperse them in a given solvent or even in a polymeric material [8, 11].

Functionalization is considered one of the solutions to overcome these problems. Experimentally, it was proved that different BN surfaces can be modified by $–NH_2$ and –NHR groups. In 2007, using NH_3 plasma, Zettl's group reported that $–NH_2$ groups could be covalently attached to BNNTs, followed by the amorphization of BNNTs' walls [12]. Furthermore, Liao and co-workers [13] found that BNNTs could be etched in ammonia solution under sonication. As a result, entangled and freestanding BN nanoribbons were detected in the products due to $–NH_2$ functionalization and unzipping. Lei and co-workers [14] synthesized NH_2- boron nitride nanosheets (NH_2-BNNSs) via ball milling and using urea and the resultant NH_2-BNNSs exhibited good solubility in water and formed colloidal solutions.

However, finding a process that is easy and effective to add functional groups to BNNTs' surface is not a trivial task, so functionalization is still seen as a challenge in the scientific environment. Thus, the aim of the present work was to develop a simple, economical, scalable, reproducible and environmentally sustainable route to functionalize BNNTs with urea so that it would be possible to disperse this nanomaterial in different solvents and polymeric matrices, promoting its applicability and allowing the scientific environment to profit from its outstanding properties. Urea is a low-cost reactant that was chosen to perform the functionalization of BNNTs. It acts as a chemical supply of nitrogen groups to perform the chemical modification of BNNT samples as well as the process control agent (PCA) of the high energy milling, since it protects the BNNTs from excessive mechanical damage, and minimize an extensive formation of lattice defects.

2 - MATERIALS AND METHODS

2.1 - Materials

The boron nitride nanotube samples that were used in this study were synthesized by CVD method using amorphous boron and iron oxide as a catalyst. This synthesis has been published in previous studies [15]. Acetone 99.5%, Ethyl alcohol 99.8%, Urea 99.0%, were of analytic grade obtained from Sigma Aldrich and were used without further purification.

2.2 - Chemical modification of Boron Nitride Nanotubes by high energy ball milling

The chemical modification of the BNNTs was obtained by high energy ball milling. BNNTs and urea were mixed together in a 1:60 weight ratio inside a stainless steel milling container (1.4435 vessel; 316L) using a planetary ball mill (PM 100, from Restch, Germany) at a rotation speed of 500 rpm for 10h under nitrogen atmosphere. The ball:powder ratio used was 1:100 and the ball size was 10 mm. The milling was stopped in the first half period of the process (after 5h), for 30 minutes, and rotated counterclockwise the second half period. At the end of the milling, the vessel was kept closed overnight for reducing internal temperature and pressure induced by the high energy ball milling.

2.3 - Purification of functionalized Boron Nitride Nanotubes

When the process was complete, the resulting loose powder as well as the material adhered to the grinding balls and reaction vessel were submitted to an exhaustive cleaning process with deionized water and vacuum filtration. At the end, the sample was washed with pure ethanol and submitted to vacuum filtration through a polytetrafluoroethylene membrane filter (47 mm diameter, 0.45 mm pore size, from Whatman) followed by drying at 60°C for 24 hours in a vacuum drying oven. To confirm the absence of any traces of urea as well as other degradation products, FTIR analysis was conducted in the purified functionalized boron nitride nanotubes (BNNTs-U2).

2.4 – Evaluation of the solubility behavior of the functionalized samples

In order to obtain a qualitative response of the change in chemical behavior of the samples due to the functionalization, the BNNTs-U2 sample was added in different solvents: distilled water, ethyl alcohol, acetone and dimethylformamide (DMF), in the proportion of 10mg/10ml and kept in an ultrasonic bath (from Elma) for 30 minutes to promote their dispersion. Dispersion stability was evaluated visually by photographs, which were taken one hour and one week after dispersion.

2.5 - Materials characterization

SEM analysis was performed using an electron microscope (model Sigma VP, from Carl Zeiss). The acceleration voltage used was 20-15kV. TEM analysis was performed in a Tecnai model G2 at 200 kV. FTIR analysis was conducted in a Frontier Single & Dual Range equipment (from PerkinElmer). The measurements were performed in the range of 4000 to 650 cm^{-1} with a resolution of 4 cm^{-1} and 64 scans min^{-1}. XPS spectra were obtained using monochromatic Al Kα radiation (1486.6 eV) and an electron energy analyzer (Specs, Phoibos-150).

3 - RESULTS AND DISCUSSION

3.1 –Visual, SEM and TEM characterization of the BNNTs after the high energy ball milling

When removing the resulting powder from the reaction between BNNTs and urea in the planetary ball mill, a change in color was observed, which also happened after washing it successively in distilled water. The white color of the pristine BNNTs changed to a greyish color after their removal from the planetary ball mill and finally, to a brownish color after their washing. This change in color readily suggests an evidence of change in chemical environment of BNNT sample due to functionalization. A similar result was obtained by Xie and co-workers [16] for BNNTs functionalized with amine-terminated oligomeric poly(ethyleneglycol).

Fig. 1 a-b shows a typical SEM image of the raw BNNT sample that was used in this work. It shows a web-like morphology and it is relatively rich in nanotubes. The sample consisted of nanotubes of tens of microns in length (Fig. 1c) with a large diameter distribution. Also, a soot material that consists of amorphous boron nitride is also present in the sample. The TEM image suggests that the nanotubes in the raw sample consist of thin hollow tubular particles with walls formed by multiple stacked layers of h-BN sheets. By the TEM high resolution mage (Fig. 1-d) it is also possible to calculate the interlayer spacing of the BNNT sample giving a mean value of the ≈ 0.34 nm that agrees with d(002) spacing in bulk h-BN (0.332 nm).

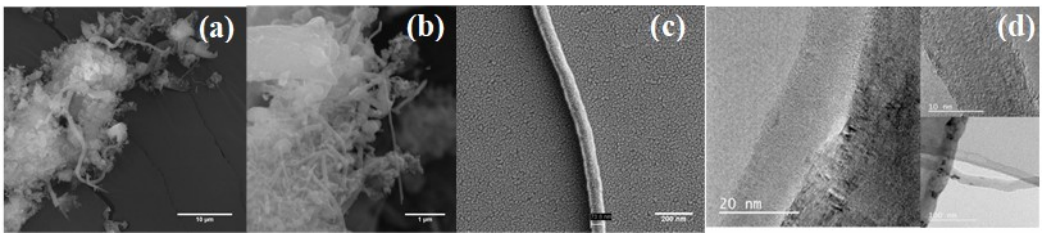

Fig. 1 - SEM (a-c) and TEM (d) images of raw BNNT sample.

After mechanical milling, BNNTs of relative large lengths and diameters disappear giving place to small compact particles (Fig. 2 a-b) and few small nanotubes can be found in some areas near the particle boundary (Fig. 2c). This modification suggests that the high energy of the milling can break the large nanotubes into small fragments and allow only the smallest nanotubes to be incorporated into these compact particles.

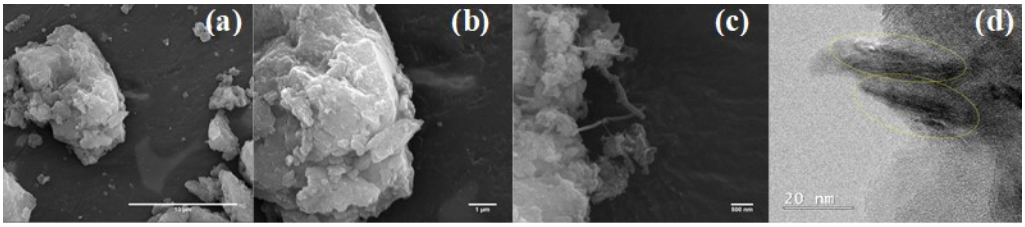

Fig. 2 - SEM (a-c) and TEM (d) images of BNNT sample after functionalization procedure in high energy mechanical milling.

The TEM image of BNNTs-U2 (Fig 2d) samples after ball milling shows evidences of small fragments of tubular particles by the parallel fringes corresponding to multiple stacked layers of h-BN sheets. These results agree with the SEM observations.

3.2 – Evaluation of the functionalization

3.2.1 - Fourier transform infrared spectroscopy (FTIR)

The FTIR spectra of the BNNTs, functionalized BNNTs before washing (BNNTs-U1), and after washing (BNNTs-U2) and urea are shown in Fig. 3a, 3b, 3c and 3d, respectively. It can be observed that bands at 1156, 1599, 1679, 3258, 3342 and 3437 cm^{-1}, assigned to functional group vibrations present in urea [17], are also identified in the FTIR spectrum of BNNTs-U1 (Fig. 3b). As the ratio used in this functionalization was 60:1 (urea/BNNTs), there was a high amount of urea in contact with the nanotubes, which explains the similarity between the BNNTs-U1 and urea spectra. After the successive washes in distilled water, all the adsorbed urea was removed (Fig. 3c), and a broad signal around 4000 and 2700 cm^{-1} can be observed which cannot be observed in the pristine BNNTs spectrum. This signal (inset in Fig. 3c) was attributed to the N-H and NH_2 stretch vibration modes by a peak-fitting procedure. Besides that, characteristic bands of urea, such as 1153 cm^{-1} (attributed to N-C-N) and 1683 cm^{-1} (attributed to C = O), are no longer present in the BNNTs-U2 sample after washing. Therefore, one can say that washing was efficient, removing all adsorbed urea on the walls of the nanotubes.

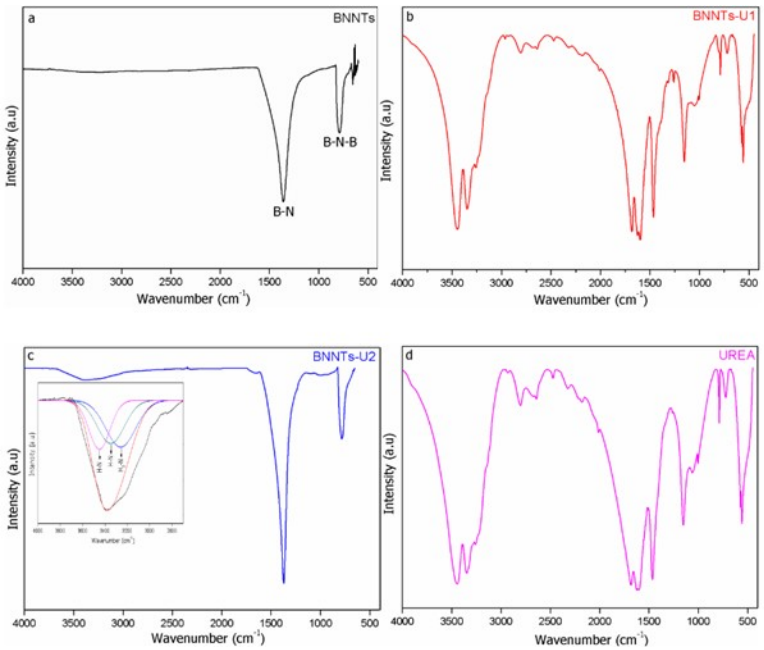

Fig. 3 – FTIR spectra for a) BNNTs, b) BNNTs-U1, c) BNNTs-U2 and d) urea.

Based on the results obtained in the spectroscopy analysis, where characteristic bands of the -NH and NH_2 bonds were found, it was inferred that functionalization occurred. It is thought that -NH or NH_2 groups have bounded to sites containing defects or on the walls of nanotubes.

3.2.2 - X-rays photoelectron spectroscopy (XPS)

XPS spectra were obtained in the regions of the main elements of interest (B, N, C and O). Fig. 4 shows the survey XPS spectra of the BNNTs and BNNTs-U2 samples. All samples show photoemission peaks for B 1s (~190.5 eV), N 1s (~198.8 eV), C 1s (~284.5 eV) and O 1s (~533.4 eV). The C, O and Si signals identified in the BNNT sample before chemical modification (Fig. 4a) are related to the surface contamination that generally occurs during the preparation process and to the exposure of the sample to air, as commonly observed in XPS measurements. The stoichiometry rate of boron to nitrogen atoms (B:N) is confirmed from the peak areas of the XPS survey spectra. The obtained values for the B:N rates are 1.05 for BNNTs and 0.96 for BNNTs-U2, indicating almost stoichiometric samples. Similar results were obtained by Li and co-workers [18]. However, for BNNTs-U2 sample a slight excess of N atoms was observed, which may be an indication of functionalization occurrence. Two additional peaks were identified in the Fig. 4b at 712.0 (Fe 2p) and 578.0 eV (Cr 2p). Both peaks are associated with the contamination from the stage of chemical modification carried out in the planetary mill.

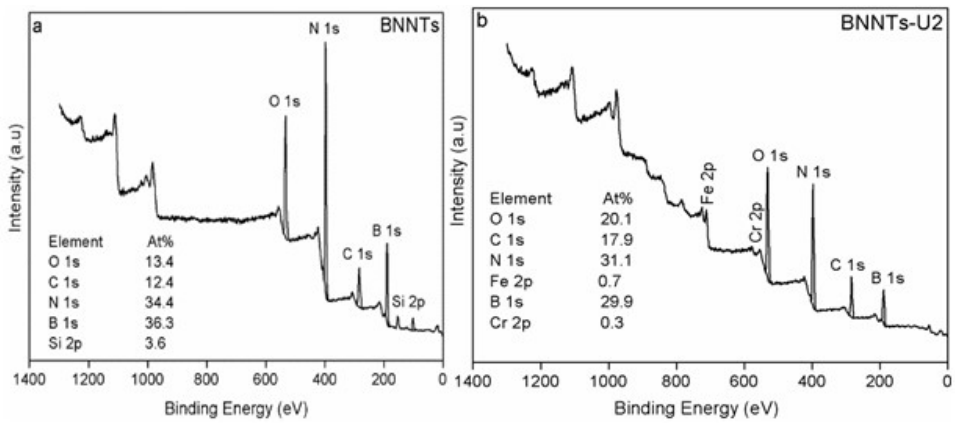

Fig. 4 – XPS spectra for a) BNNTs and b) BNNTs-U2.

3.2.3 - Evidence of the change in the chemical environment of the BNNTs-U2 sample

Fig. 5 shows BNNTs-U2 dispersed in distilled water, DMF, acetone and ethyl alcohol one hour and one week after the dispersion process. Visually, it is possible to observe that BNNTs-U2 showed better dispersibility in DMF, followed by acetone, water and ethyl alcohol. In all cases, BNNTs sedimentation was observed, but more noticeable in alcohol. The latter presented the least satisfactory result, since a short period of time after the dispersion process, it was possible to see a big quantity of sedimented BNNTs, which indicates the little interaction between the BNNTs-U2 and ethyl alcohol.

Tiano and co-workers [11] conducted a study of the dispersivity of BNNTs in several solvents and concluded that they did not disperse in water. To explain such behavior, the Hildebrand solubility parameter (δ^2_t) was used, which is a function of the Hansen parameters (δ^2_d,δ^2_h,δ^2_p), as one can see in Equation 1.

$$\delta^2_t = \delta^2_d,\delta^2_h,\delta^2_p \quad (1)$$

Where δ^2_t is the dispersion parameter, δ^2_h is the hydrogen interaction parameter, δ^2_p is the polar interaction parameter. Hansen parameters may explain why certain solutes can be dispersed in certain solvents and others cannot. Each solute and solvent have their own Hansen parameters and there is an optimal range in which the parameters of a given solvent must be contained in order to disperse certain solutes. Thus, all parameters will have a contribution that will permit the dispersion. Tiano and co-workers [11] observed that water was not able to disperse BNNTs, however in the present work, some dispersion was observed. This can be explained by the fact that the functionalization of BNNTs may have changed their Hansen parameters allowing water to disperse them.

These results are still preliminary for conclusions. Other ways to evaluate the dispersion of the functionalized nanotubes should be performed in the future, since in the present work focused on the visual aspect.

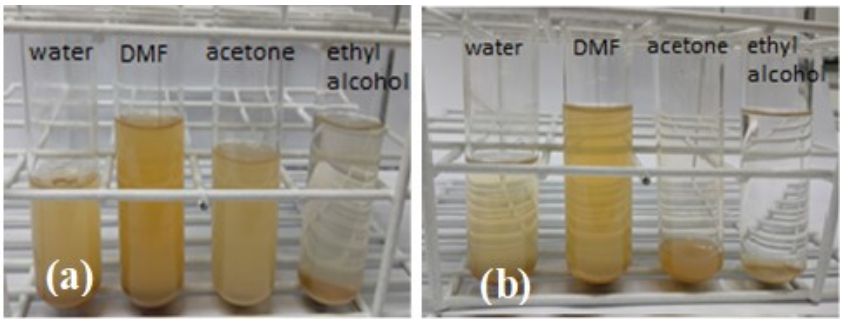

Fig. 5 - Dispersion of BNNTs-U2 in different solvents a) one hour after dispersion and b) one week after dispersion

4 - CONCLUSIONS

An efficient route for amino functionalization of BNNTs is proposed in this paper. The results clearly demonstrate that the urea induced functionalization is a good method for the successful functionalization of BNNTs with the advantages that functionalization can be carried out in a simple manner. Based on the results obtained in the FTIR spectroscopy, where characteristic bands of the -NH and NH_2 bonds were found it was inferred that functionalization occurred. It is thought that -NH or NH_2 groups have bound to sites containing defects or on the walls of nanotubes. Besides the X-ray photoelectron spectroscopy showed that the obtained values for the B:N rates are slight different which may be an indication of the functionalization occurrence. TEM and SEM images show that the high energy of the milling broke the large nanotubes into small fragments and possibly allowed only the smallest nanotubes to withstand the process. Successful of functionalization of the BNNTs structure was evidenced by stability of the dispersions in water, DMF and acetone. However, other ways to evaluate the dispersion of the functionalized nanotubes should be performed in the future.

ACKNOWLEDGMENTS

The authors is grateful to the Comissão Nacional de Energia Nuclear (CNEN) and Brazilian agencies CNPq, CAPES, FAPEMIG for financial support. We also acknowledge the support from the Microscopy Center of the Federal University of Minas Gerais Belo Horizonte, Brazil.

REFERENCES

[1] Iijima, S. ‘Helical microtubules of graphitic carbon’, Nature. 354, (1991) 56–58.
[2] Chopra, N., Luyken, R., Cherrey, K., Crespi, V., Cohen, M., Louie, S., and Zettl, A. ‘Boron Nitride Nanotubes.’ Science. 269, (5226) (1995) 966-967.
[3] Song, W., Wang, P., Cao, L., Anderson, A., Meziani, M., Farr, A., and Sun, Y. ‘Polymer/Boron Nitride Nanocomposite Materials for Superior Thermal Transport Performance’. Angewandte Chemie - International Edition. 51 (26) (2012): 6498-6501.
[4] Wattanakul, K., Manuspiya H. and Yanumet, N. “Effective Surface Treatments for Enhancing the Thermal Conductivity of BN-Filled Epoxy Composite”. Journal ofApplied Polymer Science. 119 (6) (2010) 3234–3243.
[5] Zhou, S. J., Ma, C.Y., Meng, Y.Y., Su, H.F., Zhu, Z., Deng S.L. and Xie, S.Y. ‘Activation of boron nitride nanotubes and their polymer composites for improving mechanical performance’. Nanotechnology. 23 (5) (2012).
[6] Zhi, C.Y., Bando, Y., Terao, T., Tang, C.C., Kuwahara, H. and Golberg, D. ‘Chemically Activated Boron Nitride Nanotubes’. Chemistry - An Asian Journal’. 4 (10) (2009): 1536–1540.

[7] Zhi, C.Y., Bando, Y., Tang, C.C., and Golberg, D. 'Boron nitride nanotubes'. Materials Science and Engineering R. 70 (3-6) (2010): 92-111.
[8] Thakur, V.K., Yan, J., Lin, M.F., Zhi C.Y., Golberg, D. Bando, Y., Simb R., and Lee, P.S. 'Novel polymer nanocomposites from bioinspired green aqueous functionalization of BNNTs'. Polymer Chemistry. 3 (4) (2012): 962-969.
[9] Golberg, D., Bando, Y., Tang, C.C and Zhi, C.Y. 'Boron Nitride Nanotubes'. Advanced Materials. 19 (18) (2007): 2413-2432.
[10] Zheng Z., Cox, M. and Li, B. 'Surface modification of hexagonal boron nitride nanomaterials: a review'. Journal of Materials Science. 53 (1) (2017): 66-69.
[11] Tiano A.L., Gibbons, L., Tsui, M., Applin, S.I., Silva, L., Park, C. and Fayd, C.C. 'Thermodynamic approach to boron nitride nanotube solubility and dispersion'. Nanoscale. 8 (7) (2016): 4348- 4359.
[12] Ikuno, T., Sainsbury, T., Okawa, D., Fréchet, J.M.J. and Zettl, A. 'Amine-functionalized boron nitride nanotubes'. Solid State Communications. 142 (11) (2007): 643–646.
[13] Liao Y., Chen, Z., Connell, J.W., Fay, C.C., Park, C., Kim, J.W. and Lin, Y. 'Chemical Sharpening, Shortening, and Unzipping of Boron Nitride Nanotubes'. Advanced Functional Materials. 24 (8) (2014): 4497-4506.
[14] Lei, W., Mochalin, V.N., Liu, D., Gogotsi, Y. and Chen, Y. 'Boron nitride colloidal solutions, ultralight aerogels and freestanding membranes through one-step exfoliation and functionalization'. Nature Communications. 6 (8849) (2015). 8p.
[15] Silva, W.M., Ribeiro, H., Ferreira, T.H., Ladeira, L.O. and Sousa, E.M.B. 'Synthesis of boron nitride nanostructures from catalyst of iron compounds via thermal chemical vapor deposition technique'. Physica E. 89 (2017): 177-182.
[16] Xie, S.Y., Wang, W., Shiral Fernando, K.A., Wang, X., Lin, Y. and Sun, Y.P. 'Solubilization of boron nitride nanotubes'. Chemical Communications. 29 (0) (2005): 3670-3672
[17] Socrates G. 2001. 'Infrared and Raman characteristic group frequencies'. 3rd Edn (Nova York, Wiley, 2010).
[18] Li J., Li, J., Yin, Y., Chen, Y. and Bi, X. 'Water-assisted chemical vapor deposition synthesis of boron nitride nanotubes and their photoluminescence property'. Nanotechnology. 24 (36) (2013): 365605-365612.

INFLUENCE OF SILANE TREATMENTS ON THE PROPERTIES OF GRAPHITE NANOPLATELET/EPOXY NANOCOMPOSITES

Alessandra Lavoratti [(1)], Ademir J. Zattera [(2)] and Sandro C. Amico [(1)]

(1) Postgraduate Program in Mining, Metallurgical and Materials Engineering (PPGE3M), Universidade Federal do Rio Grande do Sul (UFRGS), Brazil

(2) Postgraduate Program in Engineering of Processes and Technologies (PGEPROTEC), Universidade de Caxias do Sul (UCS), Brazil

https://doi.org/10.21452/bccm4.2018.11.03

Abstract

Epoxy resins are used in composite applications due to their good mechanical properties. To further enhance their performance, the use of nanofillers such as graphite nanoplatelets (GrNP) has been proposed, which can be surface treated for extra improvement. This study aims to evaluate the influence of GrNP content and treatment on the mechanical and dynamic-mechanical properties of GrNP/epoxy composites. GrNP was treated with (3-glycidyloxypropyl)trimethoxysilane and (3-aminopropyl)triethoxysilane, and later dispersed in epoxy resin aided by sonication. Composites reinforced with 0.25 wt% GrNP displayed increased tensile strength compared to the neat resin. Silane treated fillers showed an improvement in tensile strength and dynamic-mechanical properties compared to both neat resin and GrNP/epoxy composites at the same wt% of reinforcement, evidencing that the silane treatment was advantageous.

1. INTRODUCTION

Epoxy-based materials are widely employed as coating agents, structural adhesives, in microelectronics and as matrix for composites. Improvement in mechanical and thermal properties can be achieved by incorporating a number of different fillers in epoxy resins [1]. Recently, graphitic nanofillers have been introduced as a new class of material for reinforcing epoxy resins, such as carbon nanotubes and graphene oxide. Some of the limitations of these materials include the increase in viscosity of the systems, which could render epoxy resins difficult to use in liquid moulding processes such as resin infusion and resin transfer moulding. Moreover, they are difficult to disperse and often expensive [2].

Graphite nanoplatelets (GrNP) have been suggested as promising particles for reinforcing epoxy resins. They consist on several stacked platelet-like structures with a thickness of a few

nanometers and possess a good balance between mechanical and electrical characteristics due to their high surface area and platelet morphology. They have similar reinforcing potential to carbon nanotubes, for example, but with only moderate increase in viscosity of the systems, which makes them suitable for liquid moulding processes [2]. In addition, they can be functionalized with silanes to increase their compatibility with epoxy resins.

Some studies report the functionalization of carbon nanotubes and graphene oxide with (3-glycidyloxypropyl)trimethoxysilane (GPTMS) and (3-aminopropyl)triethoxysilane (APTES) [3], but few studies have addressed functionalization of GrNPs with silanes. As such, the aim of this study is to evaluate the dynamic-mechanical and tensile properties of GrNP/epoxy nanocomposites focusing on the effect of filler functionalization with silanes.

2. EXPERIMENTAL

2.1 Materials

Graphite nanoplatelets were purchased from Strem Chemicals (MA, USA). Bisphenol A diglycidyl ether (DGEBA) based epoxy resin and hardener grade HT1564/E150 were obtained from Advanced Vacuum (SP, Brazil). The resin had a viscosity of 1,200–1,400 mPa.s. GPTMS and APTES silanes were supplied by Sigma-Aldrich (MO, USA). Ethanol 99.5%, acetone and glacial acetic acid were purchased from Neon Química (SP, Brazil) and Anidrol (SP, Brazil). All reactants were used as received.

2.2 GrNP modification

GrNP (0.5 g) was dispersed into 50 mL of ethanol using a SONICS Vibracell VCX-505 (500 W) tip sonicator for 1 h, at 40% amplitude and net power output of 500 W. Hydrolysis of the silane was done using a 75:25 (v/v) ethanol:water solution. GPTMS or APTES silane (1.5 mL) was added to the solution, which was acidified with glacial acetic acid (pH 4-5). GrNP/ethanol was added to the silane and stirred for 4 h at 70 °C. Excess silane was removed by centrifugation (Novatecnica NT-820) at 4000 rpm for 5 min. The silane-functionalized GrNPs were dried in a vacuum oven for 12 h at 80 °C, and are named GrNP-G and GrNP-A after GPTMS and APTES treatment, respectively.

2.3 GrNP nanocomposites

GrNPs were studied at 0.25 wt% content. GrNPs were added to 50 mL of acetone and sonicated for 1 h in an ice bath. The acetone/GrNP suspension was added to 100 g of epoxy resin and sonicated for another hour. The mixture was magnetically stirred at 80 °C for 3 h to remove acetone. The remaining solvent was removed by placing the sample in a vacuum oven at 80 °C for 12 h. After cooling to room temperature, the hardener was added to the epoxy/GrNP mixture (15 parts of hardener to 100 parts of resin in weight). The hardener was manually mixed for 5 min and the mixture was degassed in a vacuum oven at -0.8 bar for 30 min.

The composites were casted into rubber silicone moulds, cured *in situ* for 48 h at room temperature and post-cured in an oven following 2 h at 70 °C, 2 h at 90 °C, 2 h at 120 °C and 15 h at 150 °C, according to the manufacturer's data. The composites were named after the wt% of GrNP and silane used, e.g. GrNP_0.25-G.

2.4 Characterization

X-ray diffraction (XRD) analyses were performed in a Shimazdu XRD-600 equipment (CuKα = 0.1542 nm, 30 mA, 40 kV, 2° ≤ 2θ ≤ 50°, 0.05°.2 s−1) for GrNP powders and for the nanocomposites. Morphology of GrNPs and their composites was evaluated by field emission gun scanning electron microscopy (FEG-SEM).

Dynamic-mechanical analysis was done in a TA instruments Q800 AT equipment, with clamp single cantilever from 30 °C to 200 °C, at 3 °C.min^{-1}, frequency of 1 Hz and deformation amplitude of 0.1%.

Tensile testing was performed according to ASTM D638 with Type I test specimens in an EMIC DL-3000 (200 kgf load cell) at 1 mm.min^{-1}, with a 50 mm extensometer. Five test specimens were used in each case. One-way statistical analysis of variance (ANOVA) of the results of tensile strength, modulus and strain at break was carried out, and a significance level of $p<0.05$ was adopted.

3. RESULTS AND DISCUSSION

The GrNPs were successfully functionalized with silanes, as demonstrated in previous studies [4]. XRD data obtained for GrNP is displayed in Figure 1 and shows a peak at 2θ = 26.4°, with a d-spacing of 0.3381 nm, associated with the stacked crystalline graphitic sheets. Functionalized GrNPs show a weaker and broader peak, possibly related to some intercalation of silane molecules, as reported in [3]. The crystallite size found for neat GrNP was L= 18 nm, and the calculated number of single sheets is ca. 41 layers, according to Pavoski et al. [5]. For the GrNP-G and GrNP-A, the crystallite size was smaller 15 nm, with 35 layers for both silanized GrNPs.

The peak at 2θ = 26.4° is present for GrNP_0.25 sample in Figure 1b, evidencing GrNP as restacked platelets in the nanocomposites. For functionalized GrNPs at similar content (0.25 wt%) this peak disappears, perhaps due to better exfoliation of GrNP-G and GrNP-A [6].

FEG-SEM micrographs in Figure 2 show the morphology of GrNPs. Both untreated and treated fillers display small stacks within the nanometric scale. GrNP-G are seemingly more exfoliated, in agreement with XRD results, which is advantageous in terms of dispersion in the epoxy resin.

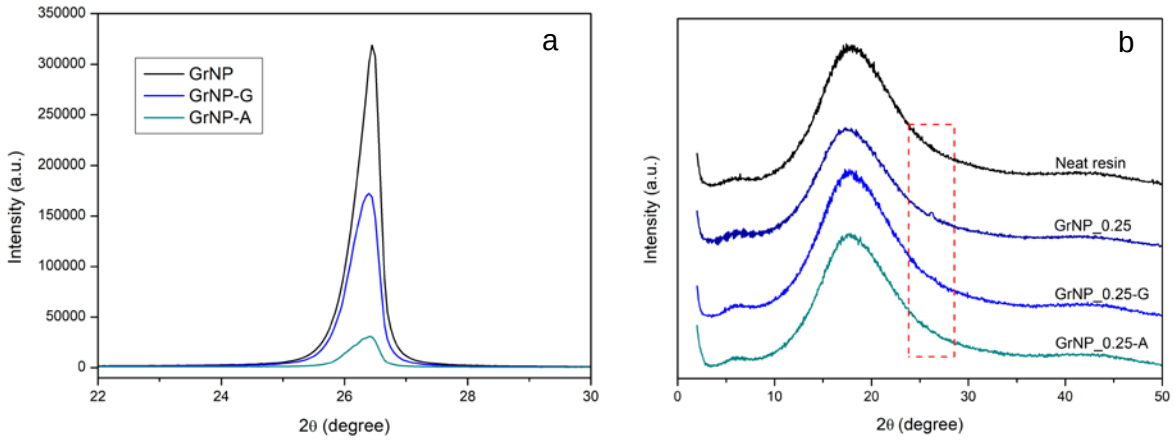

Figure 1: XRD spectra of GrNP powders (a) and GrNP nanocomposites (b).

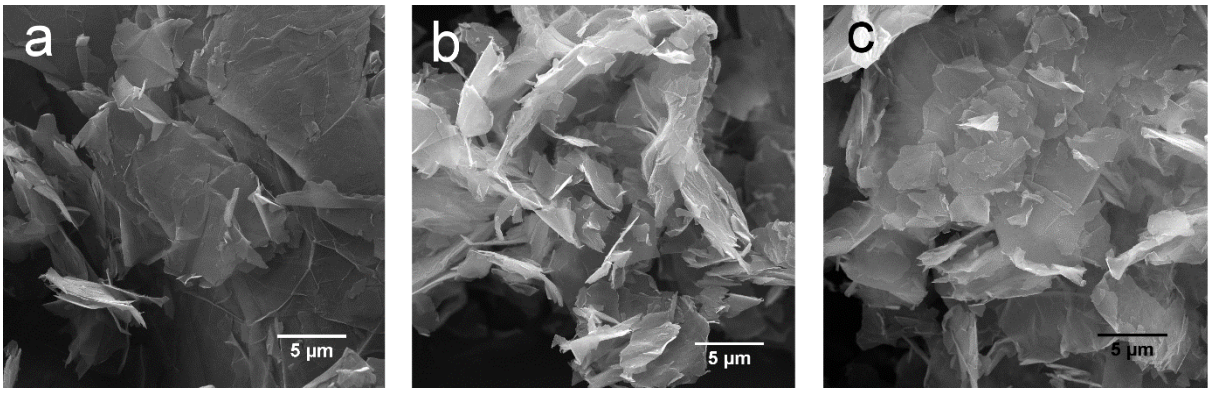

Figure 2: FEG-SEM micrographs of GrNP (a), GrNP-G (b) and GrNP-A (c) (×10.000).

The dynamic-mechanical results for neat epoxy and the nanocomposites are displayed in Figure 3. No significant difference was observed in modulus in the glassy region. But functionalization of GrNPs increased stiffness in the rubbery region, which could be an indicative of better adhesion at the interface due to the compatibility of the silanes with epoxy resin [7].

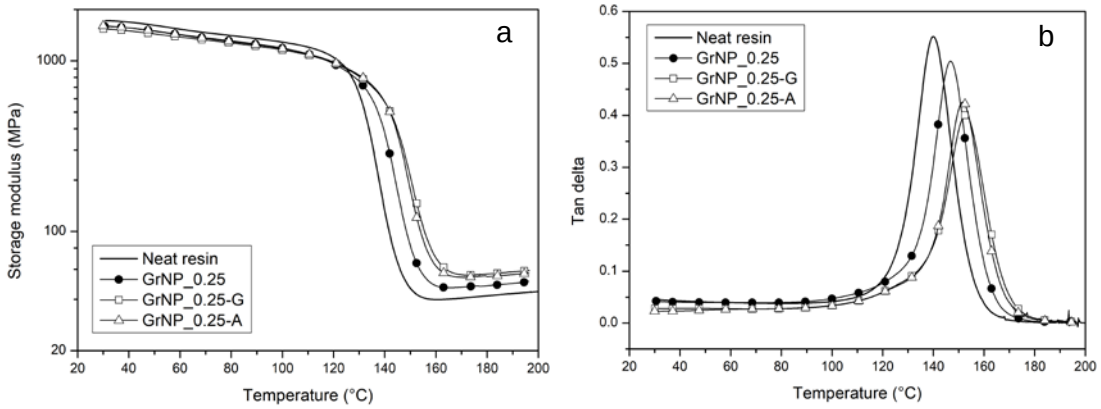

Figure 3: Storage modulus (a) and damping (tan delta) (b) of GrNP/epoxy nanocomposites.

Damping (tan delta) of the samples is shown in Figure 3b. Peak height of all nanocomposites is lower than that of the neat resin. The glass transition temperature (T_g) of the composites was 140 °C, 146 °C, 152 °C and 151 °C for the neat resin, GrNP_0.25, GrNP_0.25-G and GrNP_0.25-A, respectively. The shift to higher temperatures of the tan delta peak is related to the restriction of molecular mobility due to better adhesion [2].

The mean tensile strength, elongation at break and modulus results of the composites are listed in Table 1. Tensile strength increased with 0.25 wt% filler content, suggesting good interaction of the GrNP with the epoxy resin. An increase in tensile strength is noticed when using GrNP-G and GrNP-A compared to the GrNP_0.25. Treatment may improve stress transfer at the interface and increase interfacial area by facilitating dispersion, with a larger interfacial volume [8].

Elongation at break increased compared to the untreated GrNP, but not in relation to the neat resin considering the statistical results. Tensile modulus increased with the addition of untreated and treated fillers to the neat polymer due to the introduction of a rigid filler into the matrix. No increase in modulus can be observed within statistical significance for silanized nanocomposites. For intercalated structures, modulus increases with the degree of dispersion, exfoliation, for higher

aspect ratio and larger d-spacing [9]. As such, it is possible that an optimal dispersion was not yet achieved.

Table 1: Tensile strength, elongation at break and modulus of GrNP/epoxy nanocomposites.

Sample	Tensile strength (MPa)	Elongation at break (%)	Modulus (GPa)
Neat resin	52.8 ± 4.8^{a}	3.88 ± 0.15^{a}	2.09 ± 0.19^{a}
GrNP_0.25	59.3 ± 2.3^{b}	3.35 ± 0.39^{b}	2.75 ± 0.21^{b}
GrNP_0.25-G	64.3 ± 2.5^{d}	4.11 ± 0.42^{a}	2.65 ± 0.18^{b}
GrNP_0.25-A	63.5 ± 2.8^{d}	4.44 ± 0.50^{a}	2.60 ± 0.28^{b}

The FEG-SEM micrographs from the tensile fractured composites are shown in Fig. 4. Small platelets can be seen in all samples, especially for the treated samples, which is also in agreement with XRD results. Additionally, good adhesion at the interface can be seen for the silane treated GrNPs, which corroborates the dynamic-mechanical and tensile strength results.

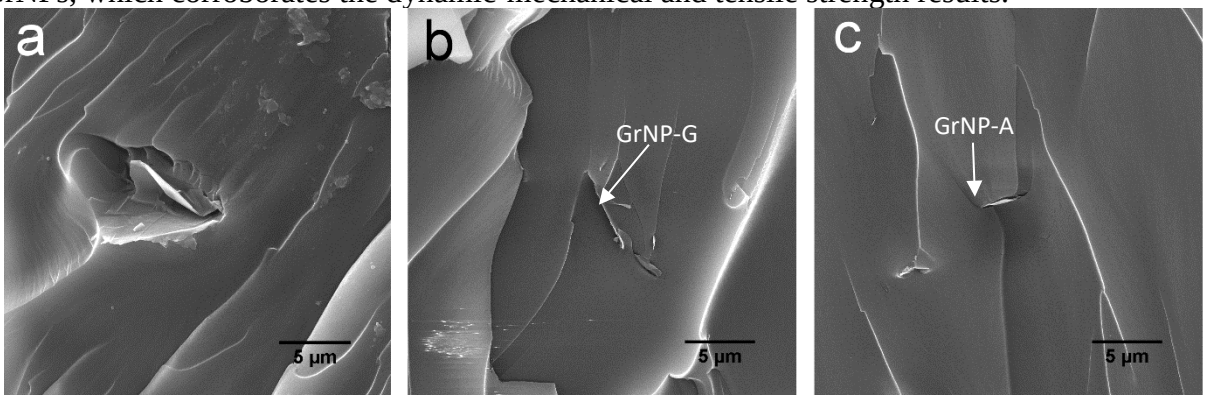

Figure 4: FEG-SEM micrographs of GrNP (a), GrNP-G (b) and GrNP-A (c) nanocomposites (×10.000).

4. CONCLUSIONS

GrNP/epoxy nanocomposites were successfully obtained using sonication only and the silane treatment promoted better dispersion of the GrNPs in the epoxy matrix;

Addition of untreated fillers was able to increased tensile strength, but better overall mechanical and dynamic-mechanical properties were obtained only after functionalization of GrNPs.

In conclusion, the silane treatment of GrNPs was favorable. Better dispersion and better overall properties could be achieved. Nevertheless, the nanocomposites could still benefit from further improvement in processing.

ACKNOWLEDGEMENTS

The authors would like to thank CNPq and CAPES for the financial support.

REFERENCES

[1] Kang, W. S., Rhee, K. Y. and Park, S. J., 'Influence of surface energetics of graphene oxide on fracture toughness of epoxy nanocomposites', *Compos. Part. B* **114** (2017) 175-183.

[2] Prolongo, S. G., Moriche, R., Jimenez-Suárez, A., Sánchez, M. and Ureña, A., 'Advantages and disadvantages of the addition of graphene nanoplatelets to epoxy resins', *Eur. Polym. J.* **61** (2014) 206-214.

[3] Li, Z., Wang, R., Young, R. J., Deng, L., Yang, F., Hao, L., Jiao, W. and Liu, W., 'Control of the functionality of graphene oxide for its application in epoxy nanocomposites', *Polymer* **54** (2013) 6437-6446.

[4] Lavoratti, A., Zattera, A.J. and Amico, S.C., 'Modificação de nanoplaquetas de grafeno com agentes de acoplamento silano para aplicação em nanocompósitos', in '14º Congresso Brasileiro de Polímeros', Águas de Lindóia, September, 2017.

[5] Pavoski, G., Maraschin, T., Fim, F. C., Balzaretti, N. M., Galland, G. B., Moura, C. S. and Basso, N. R. S., 'Few Layer Reduced Graphene Oxide: Evaluation of the Best Experimental Conditions for Easy Production', *Mater. Res.* **20** (2017) 53-61.

[6] Zhang. Y., Wang, Y., Yu, J., Chen, L., Zhu, J. and Hu, Z., 'Tuning the interface of graphene platelets/epoxy composites by the covalent grafting of polybenzimidazole', *Polymer* **55** (2014) 4990-5000.

[7] Jabbar, A., Militký, J., Wiener, J., Kale, B. M., Ali, U. and Rwawiire, S., 'Nanocellulose coated woven jute/green epoxy composites: Characterization of mechanical and dynamic mechanical behavior', *Compos. Struct.* **161** (2017) 340-349.

[8] Wan, Y. J., Tang, L. C., Gong, L. X., Yan, D., Li, Y. B., Wu, L. B., Jiang, J. X. and Lai, G. Q., 'Grafting of epoxy chains onto graphene oxide for epoxy composites with improved mechanical and thermal properties', *Carbon* **69** (2014) 467-480.

[9] Azeez, A. A., Rhee, K. Y., Park, S. J. and Hui, D., 'Epoxy clay nanocomposites – processing, properties and applications: A review', *Compos. Part. B.* **45** (2013) 308-320.

THE INFLUENCE OF MATRIX IMPREGNATION ON EFFECTIVE ELASTIC PROPERTIES OF A UNIDIRECTIONAL CARBON NANOTUBE BUNDLED COMPOSITE: A TOPOLOGY OPTIMIZATION APPROACH

Bruno G. Christoff[(1)], Humberto B. Santana[(1)], Eduardo L. Cardoso[(2)], Jandro L. Abot[(3)], Volnei Tita[(1)]

(1) Department of Aeronautical Engineering, São Carlos School of Engineering, University of São Paulo, São Carlos, Brazil

(2) Center of Technological Sciences, Santa Catarina State University, Joinville, Brazil

(3) Department of Mechanical Engineering, The Catholic University of America, Washington, DC, USA

https://doi.org/10.21452/bccm4.2018.11.04

Abstract

The present work aims to find the optimum distribution of a certain amount of matrix around a pack of fibers, which is the representative volume element of a bundle of carbon nanotubes, in order to maximize a linear combination of the effective properties of the media. The homogenization by asymptotic expansion is used to find the effective properties and a topology optimization procedure is conducted to find the optimal material distribution. In the adopted Representative Volume Element (RVE), the fibers are fixed in the domain, and the optimization is performed only at matrix, whose properties are parameterized by the Solid Isotropic Material with Penalization (SIMP) method. Three distinct linear combinations of the components of the fourth order stiffness tensor are chosen, as well as three distinct admissible volume fractions for the matrix. The numerical results are presented by both the optimal material distributions in the RVEs and the convergence plots of the objective functions. The results show which regions of the RVE play a significant role for the effective properties of the composite, and may be used for a careful manufacturing process guide.

KEYWORDS: Topology optimization, Fiber reinforced composites, Imperfect adhesion, carbon nanotube bundles.

1. INTRODUCTION

Fiber reinforced composites play an important role in aeronautical and aerospace industries, due to its excellent specific properties. However, the behaviour of this kind of material is not completely understood and the manufacturing processes are often unreliable. A new state-of-the-

art composite like material used as reinforcing component, developed in parallel by several research groups in the past years, consists of millions of bundles of carbon nanotubes. This kind of material is very flexible, have an easy handling and have mechanical and electrical properties that can be tuned by production conditions [1]. Despite of the advantages, the mechanical, electrical and thermal properties of the bundles carbon nanotubes are highly affected by the densification and polymer impregnation [2-3].

Thus, the objective of this work lies on analyzing the effect of matrix impregnation on the effective mechanical properties of the carbon nanotubes bundles. A topology optimization approach is used in order to obtain the optimum distribution of matrix around a pack of fibers, given a pre-defined volume of matrix, in order to maximize a linear combination of the components of the homogenized fourth order stiffness tensor of the media. The concept of representative volume element (RVE) is used to represent a periodic unidirectional fiber reinforced composite, playing the role of the bundles. The homogenization by asymptotic expansion is used in order to obtain the fourth order stiffness tensor of the media and the finite element method is used to discretize the RVE domain and solve the equilibrium problems in the microscale. The topology optimization is chosen since it is the most general form of structural optimization. The fibers are kept fixed in the RVE and the optimization is performed only in the matrix. The SIMP (Solid Isotropic Material with Penalization) is used to parameterize the matrix properties and the Optimality Criteria is used to solve the optimization problem. The optimization problem is stated as the maximization of a linear combination of the components of the fourth order stiffness tensor subjected to a volume constraint.

2. FORMULATION

2.1 Homogenization by asymptotic expansion

For the determination of the effective properties of the composite, the well-known homogenization by asymptotic expansion method is used. This method is based on the assumption that a representative volume element (RVE) represents the entire domain. In other words, there is a small part of the domain in which one can find a pattern of repetition.

In the linear elasticity context, three basic considerations are adopted. The first one requires that the displacement field of the media can be written as an asymptotic expansion. The second one is that two coordinate scales are used in the analysis, one at the macroscale level (or domain scale) and the other at the microscale level (or RVE scale). These coordinate systems are related to each other by a small scalar, that in the limit tends to zero, rendering both scales in different orders of magnitude. The third one is that kinematic constraints are imposed to the boundaries of the RVE, imposing that the displacement field must have the same values on opposite faces of the RVE (periodicity).

The mathematical background is well established in literature [4-5] and states that the effective fourth order stiffness tensor of the heterogeneous media can be found by

$$C^H_{ijkl}(\boldsymbol{x}) = \int_Y \left(C_{ijkl} - C_{ijpq} \frac{\partial \chi^{kl}_p}{\partial y_q} \right) dY \tag{1}$$

where $\boldsymbol{x}$ is the coordinate vector in the macroscale, $\boldsymbol{y}$ is the coordinate vector in the microscale, $\boldsymbol{Y}$ is the vector with the dimensions of the RVE and $\boldsymbol{\chi}^{kl}$ is the characteristic periodic displacement field of the RVE, given by the solution of the equilibrium equation

$$\int_Y C_{ijpq} \frac{\partial \chi^{kl}_p}{\partial y_q} \frac{\partial v_i}{\partial y_j} dY = \int_Y C_{ijkl} \frac{\partial v_i}{\partial y_j} dY \tag{2}$$

where $\boldsymbol{v}$ is a virtual displacement. The RVE for the present work is shown in figure 1, playing the role of a representative volume of the fiber bundles. The finite element method is used to solve Eq. 2.

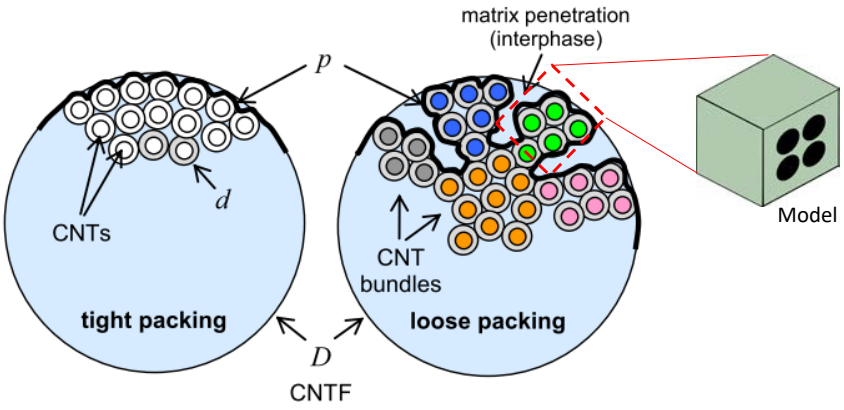

Figure 1: Illustration of Carbon Nano Tubes Fibers (CNTF) tight and loose packing and RVE model (adapted from [1])

2.2 Material parameterization

The main purpose of topology optimization is to determine the distribution of a set of materials within a certain fixed domain, in order to extremize an objective function, subjected to a set of constraints [6]. This is the most general form of structural optimization, allowing voids and new boundaries to be added to structure.

This work aims to find the optimal matrix distribution in the RVE in order to maximize a linear combination of the components of the homogenized fourth order stiffness tensor. A volume constraint is adopted in the matrix region, thus, a maximum matrix volume is allowed in the optimization procedure.

The design variables, for this case, play the role of the distribution of material. In a finite element method context, for each element of the mesh, a design variable, as known as relative-density, is associated to. If the value of the design variable is 0, there is no material associated to this particular region of the domain, conversely, if the value of the design variable is 1, this region contains material.

Let the RVE domain Ω to be formed by two sub domains, the fiber domain Ω_f and the matrix domain Ω_m. In addition, the matrix domain Ω_m is divided in two sub domains, the domain in which there is material Ω_m^{mat} and the domain in which there is no material, Ω/Ω_m^{mat}.It is considered that the fiber domain is fixed, and it is intended to find the distribution of material in Ω_m such that extremizes an objective function. It is desired to use the parameterization

$$C_{ijkl}(\boldsymbol{x}) = \begin{cases} C_{ijkl}^{f}, & \boldsymbol{x} \in \Omega_f \\ \kappa(\boldsymbol{x}) C_{ijkl}^{m}, & \boldsymbol{x} \in \Omega_m \end{cases}, \tag{3}$$

where $\boldsymbol{C}$ is the fourth order stiffness tensor in each point of the domain Ω, $\boldsymbol{C}^f$ and $\boldsymbol{C}^m$ are, respectively, the properties of fiber and matrix and κ is a discrete function, defined in all matrix domain, given by

$$\kappa(\boldsymbol{x}) = \begin{cases} 1, & \boldsymbol{x} \in \Omega_m^{mat} \\ 0, & \boldsymbol{x} \in \Omega / \Omega_m^{mat} \end{cases} \tag{4}$$

This approach is ill-posed, leading to numerical problems due to the non-existence of a solution, besides the fact that the function is non-differentiable. Therefore, a relaxation of the discrete problem is necessary, which allows the design variables to assume intermediary values between 0 and 1. However, at the end of the optimization procedure, it is desired that only discrete values remain. The SIMP method [7] is used in order to parameterize the matrix properties. Thus, the material properties in every point of domain are given by

$$C_{ijkl}(\boldsymbol{x}) = \begin{cases} C_{ijkl}^{f}, & \boldsymbol{x} \in \Omega_f \\ \rho(\boldsymbol{x})^P C_{ijkl}^{m}, & \boldsymbol{x} \in \Omega_m \end{cases} \tag{5}$$

where $\boldsymbol{\rho}$ is the vector containing the relative densities, or design variables, in every point of the matrix domain Ω_m. The relative densities are interpolated between $C_{ijkl}(\rho = 0) = 0$ and $C_{ijkl}(\rho = 1) = C_{ijkl}^{m}$, and it is required that, at the end of the optimization procedure, all relative densities assume either 0 or 1 as their values. Also, the penalization factor is chosen as $P > 1$ in order to render intermediate density values unfavorable, since the stiffness obtained is relatively small in comparison to the volume, or amount of material, involved.

2.3 Definition of the problem

The domain is divided in finite elements and, for every element representing the matrix, it is associated a design variable ρ_e, as known as the relative density. The objective function, Φ, is defined as the linear combination of each independent component of the homogenized fourth order stiffness tensor, weighted by scalars. In addition, a volume constraint is adopted, as well as side constraints applied directly in the design variables. Thus, the optimization problem is stated as

$$\begin{aligned} &Maximize\ \Phi(\boldsymbol{\rho}) = \sum_{i=1}^{21} \alpha_i C_i^H \\ &subject\ to \sum_{e=1}^{n} \rho_e v_e \leq V_m, \qquad \rho_e \in \Omega_m \\ &\qquad\qquad \rho_{min} \leq \rho_e \leq 1.0 \end{aligned} \tag{6}$$

where C_i^H is the i-th independent component of the homogenized fourth order stiffness tensor, α_i is an arbitrary scalar associated to it, V_m is the maximum allowed matrix volume, ρ_e and v_e are, respectively, the relative density and the volume associated to the e-th element of the mesh and ρ_{min} is the minimum allowed value for the e-th design variable, chosen in order to avoid numerical problems in the solution of the linear systems.

Due to the high number of design variables associated to a topology optimization procedure, a gradient-based optimization procedure is chosen. In addition, the computational effort associated to the equilibrium is high, thus, the derivatives of both objective function and constraint are obtained analytically. Several methods can be used in order to solve a topology optimization problem and, at this work, the Optimality Criterion (OC) [6] is used.

3. RESULTS AND DISCUSSION

An in-house software, written in Julia Language [8] containing all stages of the algorithm was developed. The visualization of topologies is performed in the software Gmsh [9].

For all cases, a unitary RVE is used, and the radius of each fiber is equal to 17% of RVE length, rendering the volume fraction of fibres in the RVE of approximately 36%. In addition, the domain shown in figure 1, which reinforcement is in the direction 3, is discretized by 60×60×60 regular trilinear isoparametric hexahedral elements with incompatible modes. The mechanical properties of fiber (S-glass fiber) and matrix (steel alloy) used in the simulations are shown in table 1. It is worth mentioning that if the mechanical properties are changed during the analysis, the qualitative results remain the same. Thus, the procedure can be extended to an analysis of the carbon nanotube bundle composites.

Table 1: Mechanical properties

E_f (GPa)	E_m (GPa)	ν_f	ν_m
303.0	110.3	0.21	0.3

A filtering radius of 0.07 is used, applied directly to the gradient of the objective function [10] and the minimum density adopted is equal to 10^{-3}. Three cases were chosen for the study. The objective functions of each one of the cases are given by, respectively, by
$\Phi = C^H_{1111} + C^H_{2222}$, $\Phi = C^H_{1212}$ and $\Phi = C^H_{1313} + C^H_{2323}$.

In addition, for each one of the cases, matrix volume fractions of 0.25, 0.50 and 0.75 were used. Three optimization problems are defined by using equation (6) alongside the three objective functions defined above and, for each one of the optimizations problems, three distinct volume fractions are used. Thus, 9 optimizations are carried out.

The initial distribution of relative densities in the matrix is homogeneous and with the value equal to the value of the volume constraint adopted in the procedure, thus, the volume constraint is satisfied in all iterations. Figures 2 to 4 show the convergence analysis for, respectively, cases 1, 2 and 3, for a volume fraction of 0.25. It can be noticed from figures 2 to 4 that all cases converge to a certain value of the objective function. In addition, the topologies obtained are mostly 0-1, in other words, voids and material.

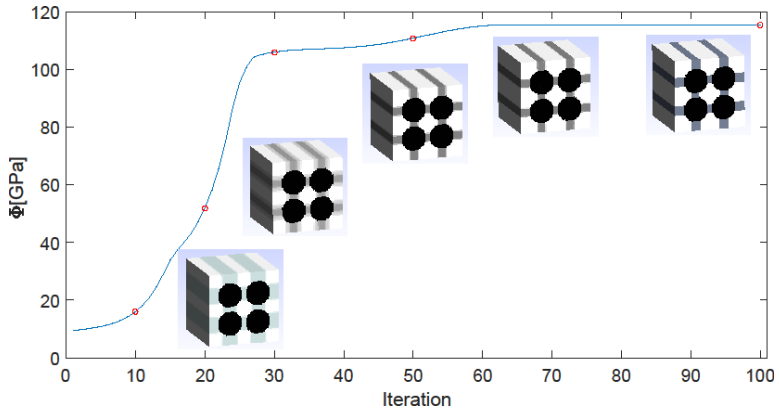

Figure 2: Convergence analysis of the objective function for case 1. Matrix volume fraction of 0.25. Topologies obtained for iterations 10, 20, 30, 50 and 100.

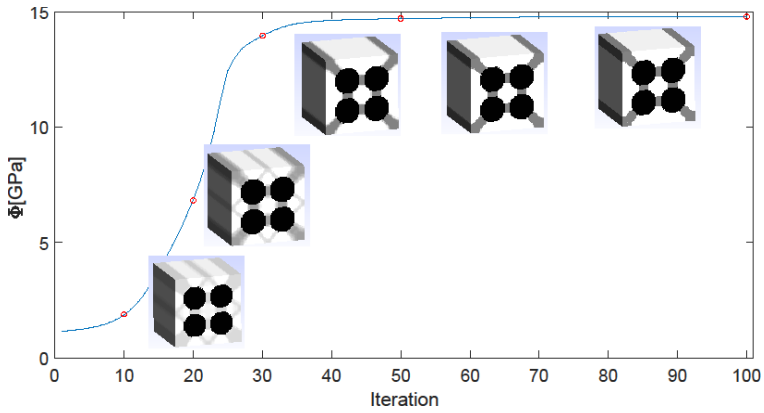

Figure 3: Convergence analysis of the objective function for case 2. Matrix volume fraction of 0.25. Topologies obtained for iterations 10, 20, 30, 50 and 100.

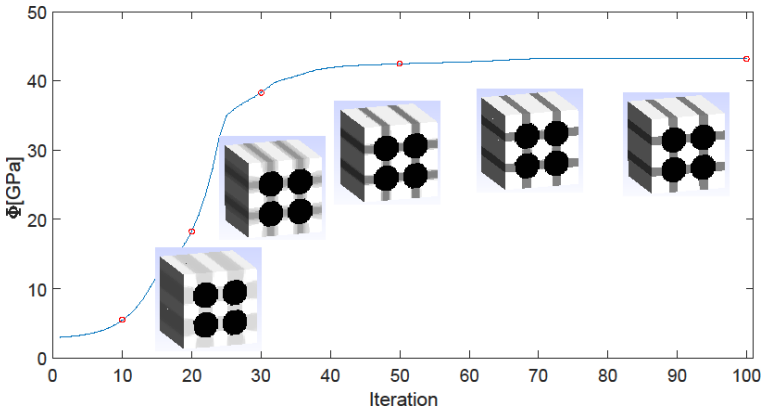

Figure 4: Convergence analysis of the objective function for case 3. Matrix volume fraction of 0.25. Topologies obtained for iterations 10, 20, 30, 50 and 100.

Only a few elements have intermediary relative densities in the final topologies. This behaviour is expected and shows that the approach adopted is consistent and that the filtering scheme is effective. Figures 5 to 7 show the optimal topologies obtained for, respectively, cases 1, 2 and 3, for volume fractions of, respectively, 0.25, 0.50 and 0.75.

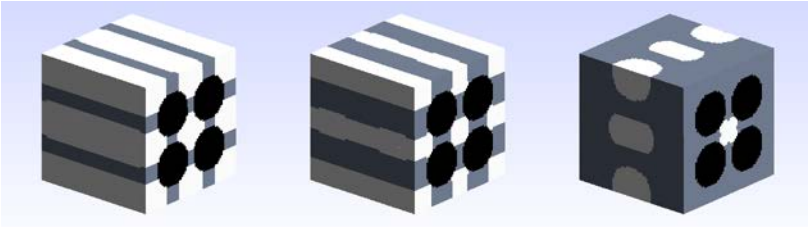

Figure 5: Optimal RVEs obtained for case 1. Matrix Volume fractions of 0.25, 0.50 and 0.75, respectively.

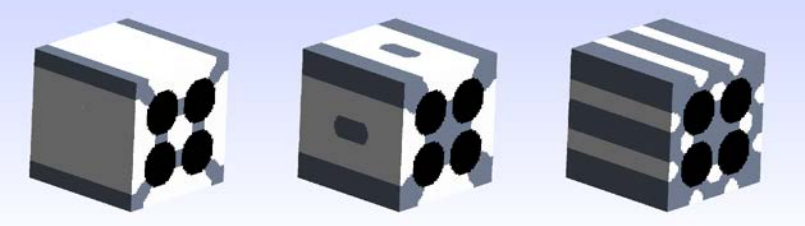

Figure 6: Optimal RVEs obtained for case 2. Matrix Volume fractions of 0.25, 0.50 and 0.75, respectively.

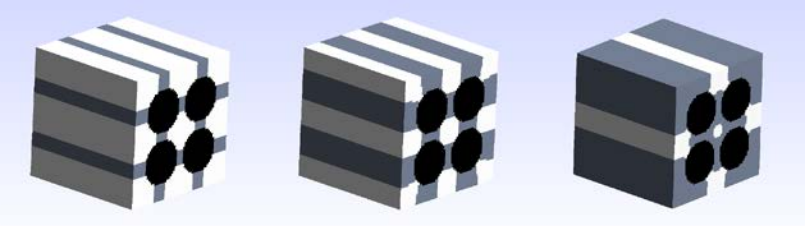

Figure 7: Optimal RVEs obtained for case 3. Matrix Volume fractions of 0.25, 0.50 and 0.75, respectively.

From figures 5 to 7 it can be seen the optimal distribution of matrix around the pack of fibers that maximizes the linear combination of the components of the homogenized fourth order stiffness tensor. The left-hand side, middle and right-hand side topologies in figures 5-7 represent, respectively, the optimal solutions for 25%, 50% and 75% of matrix. In the topologies with a relatively low volume of matrix, one can see the regions where the matrix has the most influence on the components of the effective stiffness tensor. For a low volume fraction, the algorithm adds material in crucial regions to maximize the objective function, shown as the dark gray regions. In the topologies with a relatively high volume of matrix, one can see the regions with the less influence in the effective properties of the media. In the topologies with a high volume fraction of matrix the white elements (lack of material) represent the regions that affect less the mechanical properties of the media.

Table 2 shows the numerical optimal results. It can be seen that a non-linear relation between the matrix volume fraction and the objective function is obtained. This is expected, since that for low volume fractions, only the most significant regions will have material and, as the volume fraction increases, regions that not play a significant role for the specific objective function will contain material as well.

Table 2: Optimal Solutions

	$\Phi = C^H_{1111} + C^H_{2222}$	$\Phi = C^H_{1212}$	$\Phi = C^H_{1313} + C^H_{2323}$
	Case 1	Case 2	Case 3
$V_m = 0.25$	116.2	14.8	43.3
$V_m = 0.50$	186.7	29.6	68.8
$V_m = 0.75$	288.1	41.8	93.6

4. CONCLUSIONS

In this work, numerical simulations regarding the behaviour of unidirectional fiber reinforced composites were carried out. A topology optimization approach was used in order to find the optimal distribution of a certain amount of matrix around a pack of fibers within a RVE. The results show a great consistency and that the implemented algorithm is very efficient. Also, this work can be seen as a guide in a controlled manufacturing process, since it shows the regions of matrix that most affect the effective properties of the media.

It can also be noticed that any combination of the components of the fourth order stiffness tensor can be used in the optimization. Thus, depending on the application, this approach can be used to optimize other linear combinations of the tensor. In time, this approach can be easily extended to other effective physical properties, such as thermal and electrical conductivity in composites. With the optimum topologies, an analysis regarding the effect of the matrix impregnation in a nanocomposite bundle can be made. Considering the effective fourth order tensor of the media, the loss of the properties can be foreseen with regard to the matrix impregnation and its distribution around the pack of fibers.

ACKNOWLEDGEMENTS

The authors are thankful to Coordination for the Improvement of the Higher Level Personnel (CAPES/PNPD) and National Council for Scientific and Technological Development (CNPq process number: 401170/2014-4 and 310094/2015-1).

REFERENCES

[1] Sui, Xiao Meng, Israel Greenfeld, Hagai Cohen, Xiao Hua Zhang, Qing Wen Li, and H. Daniel Wagner. "Multilevel composite using carbon nanotube fibers (CNTF)." Composites Science and Technology 137 (2016): 35-43.

[2] Vilatela, Juan J., Rupesh Khare, and Alan H. Windle. "The hierarchical structure and properties of multifunctional carbon nanotube fibre composites." *Carbon* 50, no. 3 (2012): 1227-1234.

[3] Jung, Yeonsu, Taehoon Kim, and Chong Rae Park. "Effect of polymer infiltration on structure and properties of carbon nanotube yarns." *Carbon* 88 (2015): 60-69.

[4] Sanchez-Palencia, E. "Homogenization in mechanics. A survey of solved and open problems." Rend. Sem. Mat. Univ. Politec. Torino 44, no. 1 (1986): 1-45.

[5] Hassani, Behrooz, and Ernest Hinton. "A review of homogenization and topology optimization I—homogenization theory for media with periodic structure." Computers & Structures 69, no. 6 (1998): 707-717.

[6] Bendsoe, Martin Philip, and Ole Sigmund. Topology optimization: theory, methods, and applications. Springer Science & Business Media, 2013.

[7] Bendsøe, Martin Philip, and Noboru Kikuchi. "Generating optimal topologies in structural design using a homogenization method." Computer methods in applied mechanics and engineering 71, no. 2 (1988): 197-224.

[8] Bezanson, Jeff, Stefan Karpinski, Viral B. Shah, and Alan Edelman. "Julia: A fast dynamic language for technical computing." arXiv preprint arXiv:1209.5145 (2012).

[9] Geuzaine, Christophe, and Jean-François Remacle. "Gmsh: A 3-D finite element mesh generator with built-in pre-and post-processing facilities." International journal for numerical methods in engineering 79, no. 11 (2009): 1309-1331.

[10] Sigmund, Ole. "Morphology-based black and white filters for topology optimization." Structural and Multidisciplinary Optimization 33, no. 4-5 (2007): 401-424.

NANOCELLULOSE FILLED BIOBASED POLYURETHANE FOAMS

Kerche E. F. (1), Delucis R. A. (2), Magalhães, W. L. E. (3) and Amico S. C.(1)

(1) Department of Materials Engineering, Federal University of Rio Grande do Sul, Brazil.

(2) Engineering Center, Federal University of Pelotas, Brazil.

(3) Brazilian Agricultural Research Corporation, Forest Research National Center, Brazil.

https://doi.org/10.21452/bccm4.2018.11.05

Abstract

In this paper, nanocellulose (NC) dispersed in glycerin was incorporated into polyurethane (PU) biobased foams, using castor oil and glycerin, in a ratio of 3:1, as a biopolyol, produced by free-rise pouring method. Firstly, the morphologicals properties, measureds by scanning electronic microscopy (SEM) images, were investigated and, after, the apparent density and compressives properties were measureds. The results indicated efficience in the preparation method for the biofoams and the filled foams presented a decrease in the cellular anisotropy and linear cell density and an increase in cell diameter, with a more homogenous cell structure. These morphologicals properties justify the modifications caused by the fillers in the biofoams, a larger cell, with less orientation, caused a decrease in the values of the apparent density and consequently lower values in compressive mechanical properties.

1. INTRODUCTION

Polyurethane (PU) foams are engineering materials dominant in several applications, such as industrial and domestic insulation, mattresses, upholstery, structural pieces, among others. Currently, expanded PU represents about a third of the whole PU market due to many advantages, including wide range of densities, low fragility, easy adhesion to coatings, and high versatility for production of complex shapes [1,2].

The insertion of cellulosic-based products into expanded polyurethanes may enhance some properties of these foams because of the natural affinity between NCO groups of isocyanates and OH groups from cellulose. Besides, the synthesis of PU foams with ingredients based on biological sources, such as plant fibers and lignocellulosic oils, has a great environmental appeal [3]. This materials was first studied in the paper of Aranguren et al. [4] in 2007, but since then, not many papers have been published. The materials already investigated as fillers include: individual fibers [5], cellulosic pulps [6,7] and wood flour [8,4].

Nanocellulosic materials have attracted considerable research attention in recent years [9] due to some exceptional properties and potential for a range of applications [10]. These nanocellulosic materials have many interesting features, such as nano dimensions (leading to high surface area per volume ratio), nontoxicity, biodegradability, biocompatibility, etc. Nanocellulose (NC) could be of interest in many fields, such as biomedical, energy, environment, reinforcement in polymer

composites [9]. Indeed, NC is often regarded as the next generation renewable reinforcement for the production of high performance biocomposites [11].

The present study aims at obtain and evaluate the mechanical and morphological properties of polyurethane foams, using a vegetable oil added with glycerine, and compare the properties obtained with those foams with NC fillers, obtained by a simpler physical method, compared to those found in the literature.

2. EXPERIMENTAL

2.1 Nanocellulose obtention

Nanofibrillated cellulose was obtained from a bleached cellulose pulp, which was dispersed in distilled water and homogenized in a laboratory blender. Then, this mixture (3% content) was processed between a static grindstone and a rotating grindstone, running at about 1500 rpm, and later milled (20 passes) in Super Masscoloider Masuko Sangyo mill. Through mechanical compression and shearing forces, the pulp is forced through the opening (0.10-0.15 mm) between the discs, and the cell wall is then individualized as a multilayer structure. Finally, the suspension in water was solvent exchanged with glycerin, using four successive centrifugations, at 3000 rpm and re-suspended in glycerine. The final weight percent of NC in glycerin was 4% with an aspect shown in Figure 1. The final percentage of humidity in the glycerin moisture was around 50% and it was used to manufacture the neat PU foams.

Figure 1: NC fibers (at 4%) dispersed in glycerin oil.

2.2 Biofoam preparation and characterization

Biobased PU foams were prepared via free-rise pouring method and the ingredients used are shown in Table 1. Castor oil and crude glycerin PA/with NC dispersed were used at a 3:1 weight ratio as a biobased polyol. The castor oil was purchased from Ecopol Reciclagem de Polimeros Ltda. (Farroupilha, Brazil). The moisture, remaining in the glycerin with NC, acted as the blowing agent for the foam.

Polyethylene glycol, purchased from Dinâmica Quımica Contemporânea Ltda. (Diadema, Brazil), was used as chain extender. Isotane DM, purchased from Polisystem Industria e Comércio de Poliuretano (Porto Alegre, Brazil), was used as polymeric methylene diphenyl diisocyanate (MDI). Tegoamin DMEA and Tegostab B8404, provided by Evonik Degusssa Brasil Ltda. (Americana, Brazil), were used as catalyst and surfactant, respectively. All foams were made with a NCO/OH index of 1.2, according to the literature [1]

Table 1: Formulation for the preparation of the biobased PU foams.

Component	Amount (g)
Castor oil	20.12
NC/glycerin	6.9
Chain extended	2.98
Surfactant	0.74
Catalyst	0.59
MDI	68.84

The ingredients were mechanically stirred at 1000 rpm for 180 s, with exception of the MDI, which was added later to the reaction mixture, followed by extra 120 s of stirring. This mixture was then poured into an open mould (4.3 liters) and, after 24 h, the resultant PU foam was removed from the mould and post-cured in an electric laboratory oven for 2 h at 60 ºC. The foams were then conditioned (65% RH; 20 ºC) for 2 weeks prior to characterization [12].

The added NC represented about 0.27% of the total foam mass. The evaluated morphological characteristics of the foam were: average cell diameter, anisotropic index (Equation 1) and linear cell density (Equation 2) [12]. The measurements were carried out using micrographs (taken parallel to the expansion direction) obtained by scanning electron microscopy (SEM) in a Jeol JSM 6060 equipment.

$$Anisotropic\ index = \frac{(Lcel - Wcel)}{Lcel} \quad (1)$$

$$LCD = \left(\frac{n.M^2}{A}\right)^{3/2} \quad (2)$$

Where: L_{CEL} = cell length; W_{CEL} = cell width; LCD = linear cell density; n = number of cells in the micrograph; M = magnification factor; A = micrograph area.

The apparent densities of 7 neat PU and 7 NC filled PU samples (dimensions: 50 × 50 × 25 mm^3, smaller size oriented in the expansion direction) were determined with the aid of a digital calliper (0.01 mm resolution) and an analytical scale (resolution of 0.01 g) according to ASTM D1622. Then, the same samples were tested under compression in a universal mechanical tests machine (Instron®), according ASTM D1621 standard. In these tests, an cross head speed of 2.5 $mm.min^{-1}$ was applied to obtain the elasticity modulus and compressive strength (read at 13% deformation, according to standard), calculated according to Equations 3 and 4, respectively.

$$Ec = \frac{L.T}{A.S} \quad (3)$$

$$\sigma c = \frac{L}{A} \quad (4)$$

Where: Ec= Elasticity Modulus in compression (Pa), σc= Compressive strength (kPa); L= Load 13% of strain (N); T= thickness of the sample (m); A= Cross sectional area (m^2); S = Extension (m).

3. RESULTS AND DISCUSSION

Appropriate surface quality, for the both foams, can be observed in the optical microscopy images (80×) (Figure 2). A stronger yellow color was also observed in the foams with NC, due to the incorporation of the filler, as already reported in the literature [1].

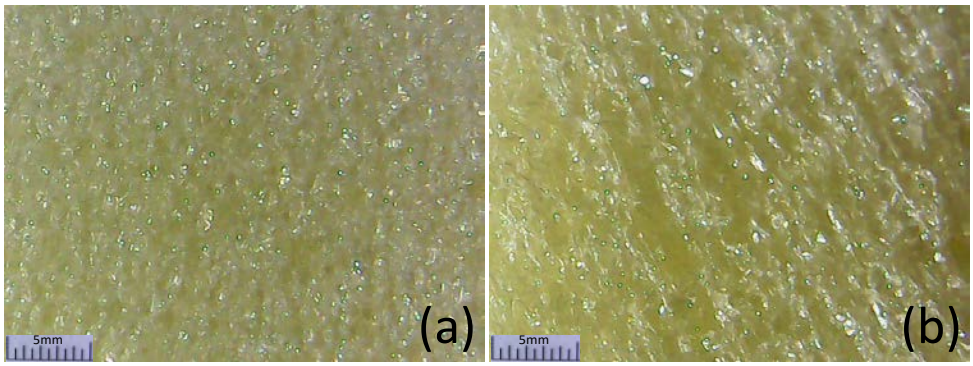

Figure 2: Images for neat PU (a) and NC-filled PU (b) biofoams.

According the micrographs, for the neat PU foam (Figure 3 (a)), can be observed a smaller and more heterogeneous microcellular structure, composed of smaller and an apparent greater number of open cells with a more elliptical shape, oriented in the direction of expansion. This greater number of open cells, of the neat PU, may be due to the more vigorous reaction of the foam, which may cause a higher degree of expansion and, consequently, disruption of adjacent cell walls. Comparatively, the PU-NC foam, shown in Figure 3(b), appears to have larger number of circular cells, probably due to the lower reactivity and expansibility, atributted to steric hindrance caused by the fillers, during polymerization. Besides, for PU-NC, there was slight deposition of the reinforcement inside the cellular wall, this effect indicates an optimal affinity of the NC-PU system, as reported in the literature for cellulose-filled foams [3].

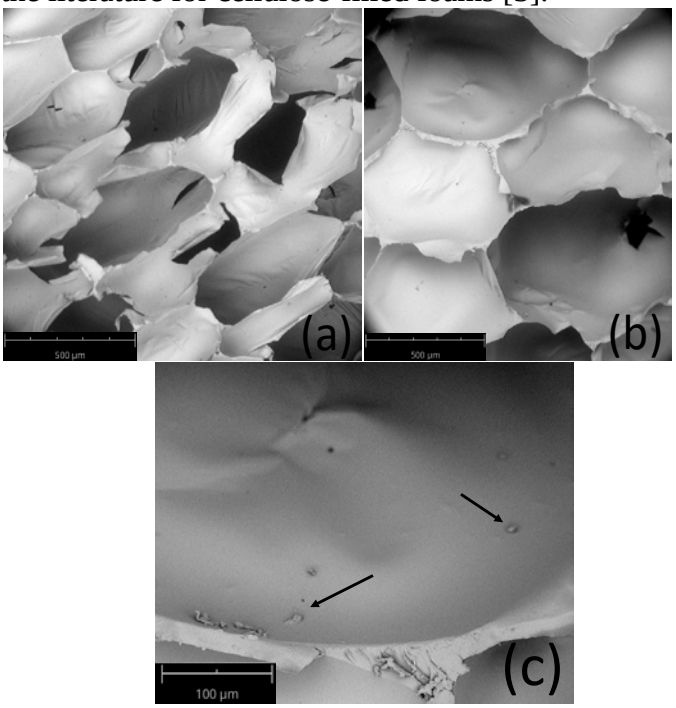

Figure 3: SEM microscopies for neat (a) (150×) and PU-NC filled (b) (145×), (c) (450x).

The filled foams presented a typical decrease (around 60%) in anisotropic index (Figure 4 (a)), attributed to the steric hindrance, caused by the presence of fillers, during polymerization. The filler increases viscosity and hampers flow of the foam, during expansion, as reported in the literature [7]. The PU-NC foam also presented a statistically significant increase in cell diameter (around 30%) (Figure 4 (b)) and a decrease in linear cell density (around 160%) (Figure 4 (c)). These results corroborate with those observed for the micrographs, where, for the foams with NC, a larger cell is observed and consequently fewer cells occupying the same space. This effect was contrary to previous studies on PU filled foams, with particles and vegetable fibers [7, 14], and can be attributed to the reduced filler dimensions, which may promote the formation of crosslinks, between NCO groups from isocyanate and OH groups from the cellulosic fillers.

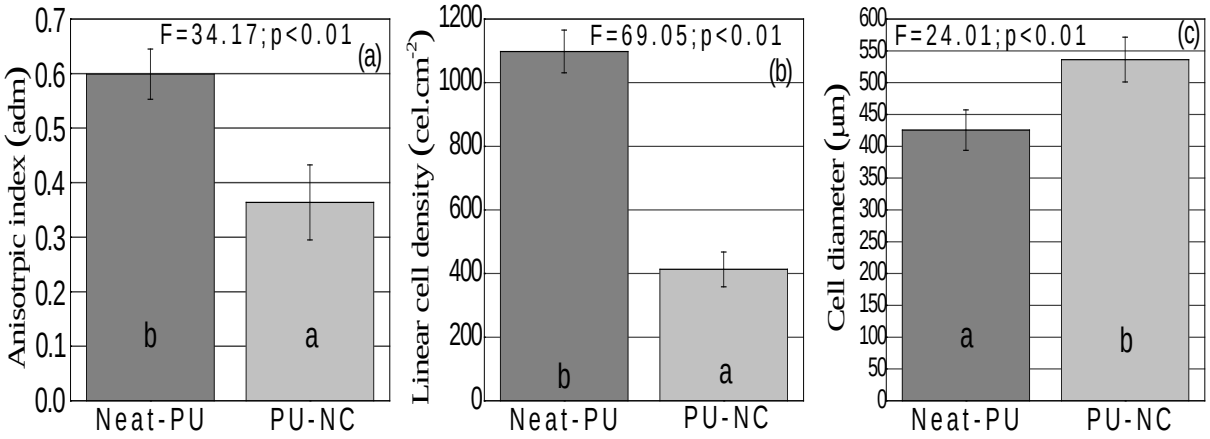

Figure 4: Morphological properties of neat-PU and PU-NC biofoams.

The larger cell size of the foams with NC, led to a smaller amount of material for the same volume and, therefore, there was a statistically significant decrease (around 100%) in the aparent density (Figure 5 (a)). The largest cell diameter of foams with NC has affected directly on this property, since larger and more voluminous pores carry greater volume of air, justifying, also, the lower values of resistance and modulus (Figure 5 (b), (c)). However, when the results on specific resistance (Figure 5 (d)) are observed, the properties for the neat and NC PUs are statistically the same. These results can be attributed to the higher structural stiffness, caused by the presence of the NC, that act as nucleation sites and enable a possible chemical tie with NCO groups of PU. Besides, factors that influence this property can be attribuated, including the filler content and type, wich provide competing and sometimes opposing polymerization mechanisms.

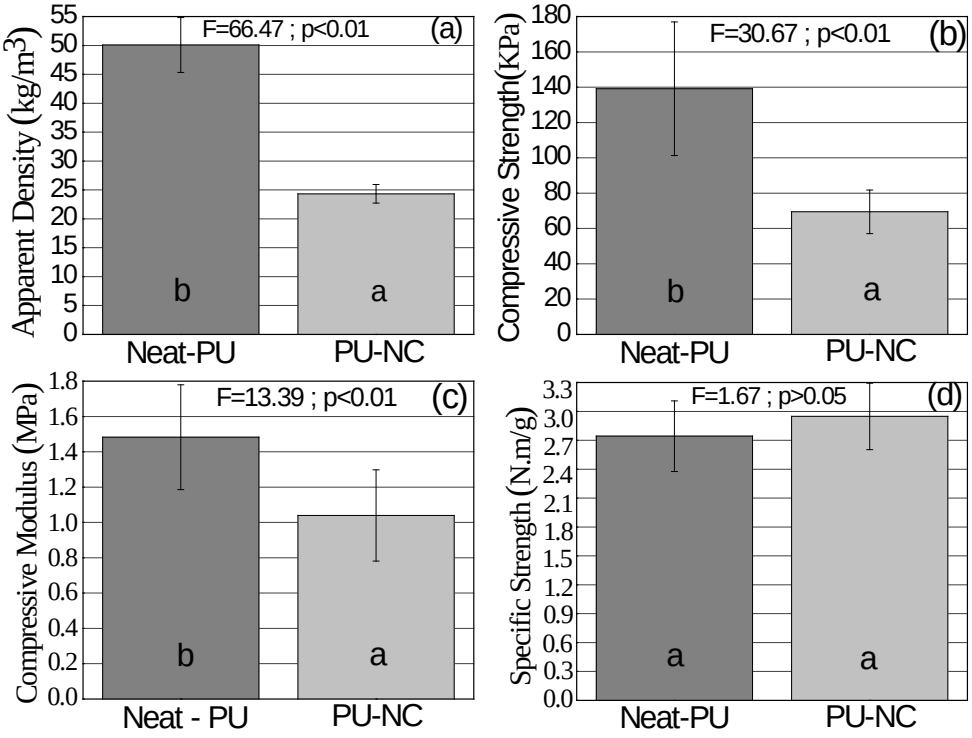

Figure 5: Apparent density and compressive mechanical properties of PU foams.

4. CONCLUSIONS

Rigid polyurethane foams were succefull obtained, utilizing a vegetable oil added to glinerine as biopolyol, presenting a good aesthetic surface. Besides, the NC fibers dispersed in glycerin oil were successfully used as fillers, presenting good compatibility with the PU system. Although the low rise of the fillers in the foam, there was a decrease in anisotropic index and formation of larger and more rounded cells with a filler accumulation on the polymer cellwall, according the SEMs images. These effects caused a decrease in the density, for the foam with fillers, and justify the lowers results in compressive strength and modulus. Besides, the results for specific properties did not present statistical alterations, probably related to the higher structural rigidity of the PU-NC. All results in this work follow those reported in the literature, for filled foams.

ACKNOWLEDGEMETS

The authors would like to thank CNPq for the doctorate grant.

REFERENCES

[1] DELUCIS, R.A.; MAGALHAES, L.W.E.; C.L. PETZHOLD; S.C.AMICO, 'Forest-based resources as fillers in biobased polyurethane foams', *Journal of Applied Polymer Science* **135** (3) (2018) 45684.

[2] DELUCIS, R. A.; MAGALHAES, W. L. E.; PETZHOLD, C. L.; AMICO, S. C., 'Thermal and combustion features of rigid polyurethane biofoams filled with four forest-based wastes', *Polymer Composites DOI 10.1002/pc.24784* .

[3] DELUCIS R. A.; PETZOLD C. L.; AMICO S. C., 'Resíduos florestais como reforço em espumas rígidas de poliuretâno' in '*Congresso Brasileiro de Engenharia e Ciência dos Materiais'*, Proceedings of a national conference, Natal, RN, Brasil, November, 2016, 4508-4519.
[4] ARANGUREN, M. I.; RÁCZ, I.; MARCOVICH, N. E., 'Microfoams based on castor oil polyurethanes and vegetable fibers', *Journal of Applied Polymer Science* **105** (5) (2007) 2791–2800.
[5] GU, R.; SAIN, M. M.; KONAR, S. K., 'A feasibility study of polyurethane composite foam with added hardwood pulp.', *Industrial Crops and Products* **42** (1) (2013) 273–279,.
[6] SILVA, M. C.; TAKAHASHI, J. A.; CHAUSSY, D.; BELGACEM, M. N.; SILVA, G. G. 'Composites of rigid polyurethane foam and cellulose fiber residue', *Journal of Applied Polymer Science* **117 (**6) (2010) 3665–3672.
[7] GU, R.; SAIN, M. M., 'Effects of Wood Fiber and Microclay on the Performance of Soy Based Polyurethane Foams', *Journal of Polymers and the Environment* **21** (1) (2013) 30–38.
[8] MOSIEWICKI, M. A.; DELL'ARCIPRETE, G. A.; ARANGUREN, M. I.; MARCOVICH, N. E. 'Polyurethane Foams Obtained from Castor Oil-based Polyol and Filled with Wood Flour', *Journal of Composite Materials* **43** (25) (2009) 3057– 3072.
[9] MONDAL, S; 'Preparation, properties and applications of nanocellulosic materials', *Carbohydrate Polymers* **163** (1) (2017) 301–316.
[10] DONIUS, A. E., LIU, A., BERGLUND, L. A., & WEGST, U. G. K. 'Superior mechanical performance of highly porous, anisotropic nanocellulose–montmorillonite aerogels prepared by freeze casting' *Journal of the Mechanical Behavior of Biomedical Materials* **37** (1) (2014) 88–99.
[11] K. Y. LEE, Y. AITOMÄKI, LARS A. BERGLUND, K. OKSMAN, A. BISMARCK 'On the use of nanocellulose as reinforcement in polymer matrix composites', *Composites Science and Technology* **105** (1) (2014) 15–27.
[12] ARANGUREN, M. I.; RÁCZ, I.; MARCOVICH, N. E. 'Microfoams based on castor oilpolyurethanes and vegetable fibers', *Journal of Applied Polymer Science* **105** (5) (2007) 2791–2800.
[13] ZIMMERMANN, M.V.G.; DA SILVA, M.P.; ZATTERA, A.J.; SANTANA, R.M.C. 'Effect of nanocellulose fibers and acetylated nanocellulose fibers on properties of poly(ethylene-co-vinyl acetate) foams', *Journal of Applied Polymer Science* **134** (1) (2017) 44760.
[14] NAR, M.; WEBBER, C.; ANNE D'SOUZA, N. 'Rigid polyurethane and kenaf core composite foams', *Polymer Engineering & Science* **55** (1) (2015) 132–144.

12. PROCESSING AND MANUFACTURING

PREPARATION AND CHARACTERIZATION OF EXTRUDED PBAT/ORGANOCLAY FILMS

L.H. de Carvalho [(1)], A.A. Nascimento Filho [(1)]

(1) Department Materials Science and Engineering, Federal University ofCampina Grande, Brazil

https://doi.org/10.21452/bccm4.2018.12.01

Abstract

Polymeric materials and their blends prepared from renewable and completely biodegradable resources are an important alternative to conventional synthetic materials. Produced by BASF, poly (butylene adipate) -co- (butylene terephthalate) (PBAT) commercially known as Ecoflex is a polymer with a good set of properties and low degradation during processing. The incorporation of additives, such as fillers, in plastics allows tailoring the properties of the polymer to specific applications and/or ease processing. In this paper, we investigate the influence of organoclay identity and content on the tensile properties, gas permeation characteristics and biodegradation of extruded PBAT/organophilic clay nanocomposite films. Cloisite C10A and C30B organoclays were used as fillers with loading levels of 0, 1 and 3%w/w. Processing was carried out in an internal mixer attached to a torque rheometer operating at 60rpm and 160 for 10 min. Extruded flat films of the processed materials were obtained and their tensile properties were determined. Biodegradation was determined by weight loss as a function of burial time in fertile soil. Biocomposites degraded more slowly than the matrix, which was attributed to organoclay antimicrobial properties. Torque rheometry indicated more intense degradation on the biocomposites with higher organoclay content, particularly C30B. Although the influence of clay identity on the tensile properties of the films was minimal, their thickness increased and permeability and biodegradation decreased with clay content, particularly for C30B modified films.

1. INTRODUCTION

Easy moulding and innovation potential, low cost and low density are the reason plastic materials have been replacing traditional materials such as ceramic and metals. Polymeric materials as well as their blends and composites can be obtained as films, profiled sheets or shaped and/or blown artefacts, serving different segments of the industry, according to the characteristics required by each application [1].

The substitution of conventional plastics for other materials less aggressive to the environment, such as biodegradable polymers, is one of the solutions to reduce the time that polymer residues

remain polluting and attacking the environment. Studies on the recycling of materials and the use of materials from renewable and / or biodegradable sources in the development of polymer products (composites or blends), especially for rapid disposal applications, are increasing and are being encouraged.

PHB (Poly (3-hydroxybutyric acid), Ecoflex ™ (synthetic biodegradable polyester copolymer) and Ecobras ™ (Ecoflex blend with thermoplastic starch) are examples of 100% biodegradable systems classified as biopolymer (PHB), synthetic polymer (Ecoflex) or polymer blends (EcobrasTM). These three materials completely degrade, in a short time, by microbial attack (fungi, bacteria and enzymes) under appropriate conditions in the environment [2]. However, these three materials have the same problem: they tend to degrade during processing, compromising their mechanical properties and, consequently, their applications [3] .

The properties of plastics can be significantly altered by blending and by additive incorporation. Fillers, particularly mineral fillers, are often added to polymers to increase their mechanical, thermal and barrier properties. Nanofillers cause these same changes at low loading levels (<10%) [4].

Considering the above, and that the packaging sector generates a large amount of plastic waste, responsible for environmental and visual pollution, the focus of this research lies in the development and characterization of flat films using a biodegradable polymer as the matrix and organoclays as fillers. The effect of clay identity and content on the mechanical properties, gas permeability and biodegradation of these systems are investigated, aiming to expand the range of possible applications of these films.

2. EXPERIMENTAL

2.1 Materials

The matrix employed was Ecoflex FC1200 manufactured by BASF. It is a synthetic aliphatic aromatic biodegradable copolyester which according to the manufacturer has a density of 1.26 g/cm^3 at ambient temperature, melt flow rate between 3 and 5 dg/min (ISO 1133, 190°C / 2,16 kg), glass transition temperature of –30°C, and melts at 110 to 120°C[5]. DSC measurements in our lab indicate a slightly higher melting point (completing the melting process at 135°C) and a low degree of crystallinity (10 to 15%). Two organoclays were used as fillers: Cloisite C10A and Cloisite C30B. The structures of C10A and C30B organoclays are shown in Figure 1. d001 values for C10A and C30B organoclays are 1.92 nm and1.85nm, respectively and the fatty acids used (T in Figure 1) to modify both clays are composed of 65% stearic acid (C18), 35% palmitic acid (C16) and 5% myristic acid (C14) [6].

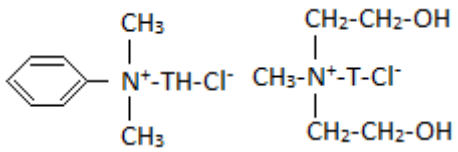

(a) (b)

Figure 1 – Chemical structures of (a) C10A and (b) C30B organoclays.

2.2 Methods

Processing took place in a Rheomix 3000 internal mixer fitted with roller type rotors, attached to a ThermoScientific torque Rheometer. The mixer chamber is 310cm^3 and the fill factor used was 75%. Operating conditions were: 60rpm, 160ºC, 10min.

After processing the products were cooled to room temperature, ground and fed into an AXPlastics Lab16 chill-roll single screw extruder operating with a coat hanger die at 180ºC, 45 rpm and rollers at 26 rpm and 15ºC to generate flat films.

Tensile testing was performed on an EMIC DL-10000 apparatus operating with a 20N cell at 50mm/min and room temperature. Samples were approximately 100x10mm^2 and grip separation was 50mm.

Gas permeability tests were conducted on a Brugger GDP-C apparatus operating according to ASTM D 1434 standard at 25ºC. The film area was 78,4cm^2.

Biodegradation (biodisintegration) took place on simulated soil according to ASTM G-160-03 standard. 20x20x3mm compression molded samples were weighted and buried in soil placed in an oven maintained at 40-60% air humidity and 35ºC. Samples were removed from the soil cleaned, pat dried and weighted weekly and their weight loss reported as a function of time.

3. RESULTS AND DISCUSSION

Torque and temperature curves as a function of processing time are shown in Figure 2.

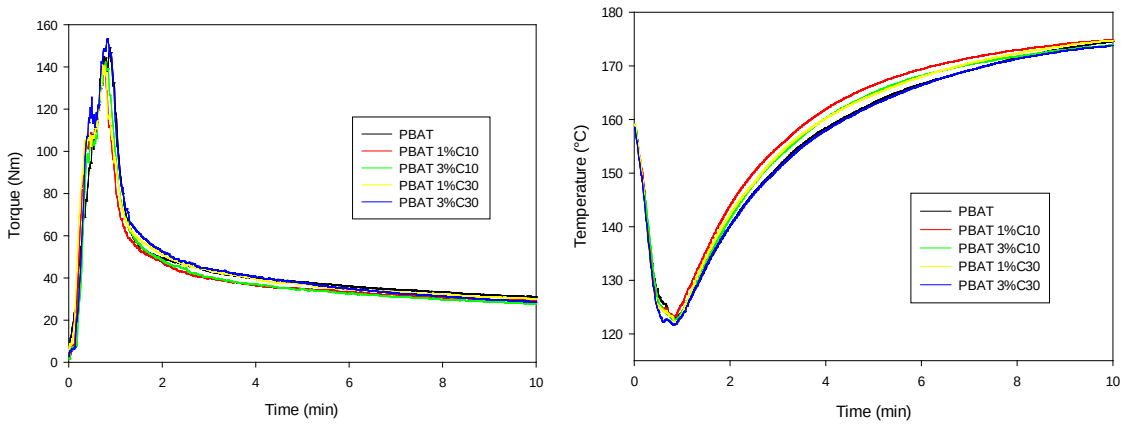

Figure 2 – Torque and temperature as a function of processing time in the internal mixer operating at 160ºC.

Temperature initially drops due to cold material feeding into the mixer and then increases by the combined effect of mechanical energy dissipation inside the chamber and heat transfer to/from the chamber wall. Torque increases by mechanical energy dissipation in the solids mix (friction and plastic deformation of the polymer particles), then decreases as the polymer melt. Polymer is molten after 4-5 min processing time. Neither torque nor temperature achieved a steady state plateau within the 10 min of processing employed here. Torque depends on polymer viscosity (and hence molecular weight) which strongly depends on temperature. Torque will decrease if polymers degrade during processing but it will also decrease if temperature rises. In order to eliminate temperature dependence on torque, the concept of adjusted torque (i.e., the torque expected for a given material to achieve at a fixed reference temperature) is used. A detailed description on the

fundamentals of this concept is presented elsewhere [7-9]. Applying this concept one can estimate the influence of filler incorporation on the rate of degradation at the final stages (8-10 min) of processing. Table 1 shows the average torque, temperature and average adjusted torque at the final stages of processing as well as the rate of torque decrease (dz*/dt) and the %rate of degradation RZ % (dz*/z*dt x100) of the systems investigated.

Table 1- Average toque, temperature, adjusted torque, torque decrease and % rate of degradation at the final stage (8-10 min) of processing as a function of film composition.

COMPOSITION	Z_{AVG}	T_{AVG}	Z^*_{AVG}	DZ*/DT	$R_{Z\ \%}$
PBAT	31,99	173,20	50,89	-0,20	-0,393
PBAT 1% C10A	29,96	174,04	48,44	-0,40	-0,826
PBAT 3% C10A	28,73	172,95	45,45	-0,66	-1,442
PBAT 1% C30B	31,01	173,70	49,81	-0,50	-1,002
PBAT 3% C30B	29,84	172,72	46,99	-1,02	-2,162

The data indicates that torque slightly decreases with filler incorporation, content and identity at the final stages of processing. This means that PBAT and its compounds, albeit not strongly, degrade during processing and that degradation is higher for C30B composites with higher filler content. It is believed that this results from the more polar structure of the C30B organoclay.

CO2 gas permeability data for the films investigated are reported in Table 2.

Table 2- CO2 gas permeability of PBAT and its nanocomposites processed at 160ºC.

Film	Thickness (µm)	Permeability (10^{-6}cm^{3}STP/cm-h-bar)
PBAT	110±21,6	688±40
1C10A 160	190±16,3	195,1±13,6
3C10A 160	143,3±4,7	136±21
1C30B 160	192,5±7,5	92,3±19,5
3C30B 160	191,7±11,8	88±14,4

As expected, the presence and concentration organoclay reduced film permeability, as fillers increase gas path tortuosity. Filler identity also seemed to play a role in this decrease as lower gas permeability was achieved with C30B modified films. It is likely that the somewhat more polar structure of the C30B clay has promoted a better interaction, dispersion or exfoliation of this filler, reducing the permeability of PBAT/C30B systems when compared to PBAT/C10A systems. XRD, SEM and MET analyses are necessary to confirm this hypothesis. Nonetheless, the addition of organophilic clay reduced the permeability of the systems to values comparable to those of premium packaging films (HDPE, LLDPE), which are much lower than the common LDPE film [10]. Biodegradation results are shown in Figure 3.

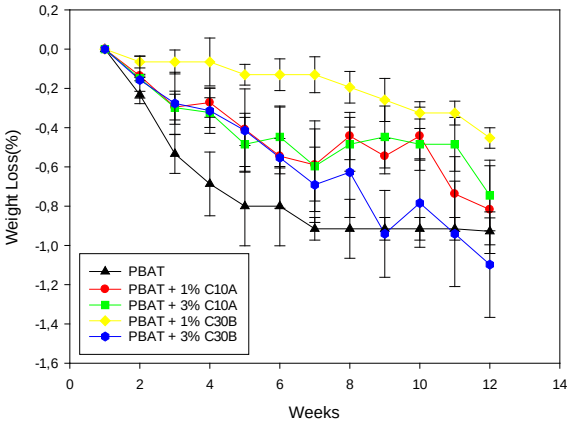

Figure 3 – Biodegradation of PBAT and PBAT/organoclay films.

Unexpectedly, biodegradation of all systems under investigation was very low (<1,5%) in the 12 weeks of the experiment. PBAT is reported to be 100% biodegradable polymer. Indeed, we have shown that if the polymer is UV exposed for as little as 5 days, it biodegrades in a few weeks and, if exposed for 20 days it disintegrates within one week, which indicates that it biodegrades very fast provided it is pre-oxidized[11]. The data also indicates that clay incorporation, particularly 1% C30B. This behavior was associated with possible antimicrobial characteristics of organoclays[12-13].

The tensile properties of some of the films investigated are displayed in Table 3.

Table 3 – Tensile properties of PBAT/organoclay films

	ε (%)	σ_{max} MPa	E MPa
PBAT	621,9 ± 56,13	13,2 ± 1,75	95,79 ± 3,37
3C10A 160	666,70 ± 66,43	12,56 ± 1,31	179,77 ± 31,84
3C30B 160	717,70 ± 63,77	16,27 ± 1,48	140,16 ± 3,55

As expected, organoclay incorporation caused an increase in the elastic modulus of PBAT films. Elongation at break and maximum tensile strength seem to be a little higher for the systems containing C30B organoclay. These increases, however, are within experimental error and further work needs to be done before conclusions can be made. The available data only allows one to state that organoclay incorporation led to stiffer materials with strength and deformations comparable to that of the neat polymer.

4. CONCLUSIONS

Results showed that, although degradation during processing was minimal, it slightly increased with organoclay incorporation. Our data also indicated that this degradation increases with the content and identity of the organophilic clay, being higher in the systems containing the C30B clay. It is believed that the somewhat more polar structure of this clay is responsible for this behavior. Extruded PBAT and PBAT/organoclay flilms were obtained and their thickness increases with clay content and identity, being larger for the PBAT/C30B system. Nanoclay incorporation led to stiffer films with elongation at break and tensile strength similar to that of neat

PBAT. The biodegradation of non-oxidized systems was quite low (<1.5%) and organoclay incorporation seemed to slow down biodegradation, which might be associated with antimicrobial activity of these clays. CO2 permeability of the nanocomposites was significantly smaller for the nanocomposites and that it was lower for PBAT/C30B systems. It is believed that this clay promotes better filler/matrix interaction. The low CO2 permeability of the nanocomposites recommends these materials for food packaging, where this property is a major concern. The permeability of PBAT/C10A and PBAT/C30B films are close to those of the materials ideal for this application, with the advantage of being fully biodegradable and processable by conventional methods.

ACKNOWLEDGEMENTS

The financial support of CNPq (grant #473622/2015-00 and Dr. Carvalho´s research fellowship) and CAPES (PNPD fellowship of Dr. Morais) are acknowledged.

6. REFERENCES

[1] Bastioli C (ed) - Handbook of biodegradable polymers, 2nd edn. Smithers Rapra Technology, Shawbury (2014).

[2] Mondal D, Bhowmick B, Maity D, Mollick MR, Rana D, Rangarajan V, Sen R, Chattopadhyay D - Investigation on sodium benzoate release from poly(butylene adipate-co-terephthalate)/organoclay/sodium benzoate based nanocomposite film and their antimicrobial activity. J Food Sci 80(2015) E602–E609.

[3] Ebnesajjad S (ed) - Handbook of biopolymers and biodegradable plastics. properties, processing (2013).

and applications. Elsevier, Amsterdam

[4] Utracki LA - Clay-containing polymeric nanocomposites. Rapra Technology, Sawbury (2004).

[5] BASF, A. G. Ecoflex®: biodegradable plastic. basf plastics - aplications, range, properties, processing **(**2003).

[6] Rhim JW, Park HM, Ha CS (2013) Bio-nanocomposites for food packaging applications. Progress in Polymer Science. 38,(2013),1629-1652

[7] Costa ARM, Almeida TG, Silva SML, Carvalho LH, Canedo EL - Chain extension in poly(butylene adipate-co-terephthalate). Inline analysis in a laboratory internal mixer. Polym Test 42, (2015), 115–121.

[8] Alves TS, Neto JES, Silva SML, Carvalho LH, Canedo EL - Process simulation of laboratory internal mixers. Polym Test 50 (2016), 94–100.

[9] Almeida TG, Neto JES, Costa ARM, da Silva AS, Carvalho LH, Canedo EL (2016) Degradation during processing in poly(butylene adipate-co-terephthalate)/vegetable fiber compounds estimated by torque rheometry. Polym Test 55:204–211.

[10] Van Krevelen DW, Te Nijenhuis K - Properties of polymers, 4th edn. Elsevier, Amsterdam (2009).

[11] Falcão GAM, Vitorino MBC, Almeida TG, Bardi MAG, Carvalho LH, Canedo EL - PBAT/organoclay composite films: preparation and properties, Pym. Bull 74, (2017),4423-4434.

[12] KHOSRAVI-DARANI K and BUCCI DZ - Application of Poly(hydroxyalkanoate)…, *Chem. Biochem. Eng. Q.*, **29** (2) 275–285 (2015);

[13] Moustafa H, El Kissi N, Abou-Kandil AI, Abdel-Aziz MS, Dufresne A - PLA/PBAT Bionanocomposites with Antimicrobial Natural Rosin for Green packaging - A*CS Appl. Mater. Interfaces* 9 (23) (2017) 20132-20141.

INFLUENCE OF SLIPPAGE COEFFICIENT ON THE NON-GEODESIC RETURN TRAJECTORY AT MANDRELS EXTREMITIES IN FILAMENT WINDING PROCESS

Ingo H. Dalibor [(1)], Tales V. Lisbôa[(2)], Rogério J. Marczak[(2)] and Sandro C. Amico [(1)]

(1) PPGE3M, Federal University of Rio Grande do Sul, Brazil

(2) Department of Mechanical Engineering, Federal University of Rio Grande do Sul, Brazil

https://doi.org/10.21452/bccm4.2018.12.02

Abstract

Filament Winding (FW) is a manufacturing process for composite materials that winds continuous tows on the surface of a mandrel at a predefined trajectory. This process is usually characterized by forward and backward strokes of a delivery eye that places the tow on the mandrel. Often, the tow's trajectory on the mandrel's surface in each stroke is geodesic, which is the shortest distance between two points on a surface. However, the return procedure at the extremities of the mandrel, since the process is continuous, must follow a non-geodesic path. Differently from the geodesic, which follows the Clairaut relation, non-geodesic trajectories depend on the friction besides on mandrel radius and the defined winding angle. A correct evaluation of such trajectory prevents slippage of the tow or waste of material and time, if the return path is excessively short or long, respectively. Based on differential geometry, the non-geodesic path is herein analytically deduced for a cylindrical surface and numerically determined for revolution surfaces. Examples of application regarding the pattern generation are provided and discussed.

1. INTRODUCTION

Filament winding (FW) is a widespread manufacturing process for composite materials that is usually chosen for the fabrication of revolution parts such as tubes, shafts and pressure vessels. Although simple, the optimal properties are not always obtained due to lack of detailed knowledge of the process. In FW of thermoset composites, a tow of filaments, pre-impregnated (dry) or just impregnated (wet) with a thermoset resin before winding is wound over a rotating mandrel. The tow is led by a delivery eye moving parallel, or near parallel, to the direction of the rotation axis of the mandrel, from one end of the mandrel to the other end, and returning again.

The FW process ends by curing the laminate, formed with the tows, in an autoclave or oven after which the mandrel is withdrawn from the wound part. This task is facilitated by the deposition of a release agent on the mandrel prior to fiber deposition, and this agent may influence the slippage coefficient between tow and mandrel.

The delivery eye positions the tow at a *winding angle*: angle between the tangent to the winding path and the rotational axis, determined through the ratio of the angular velocity of the mandrel and the longitudinal velocity of the delivery eye. Three winding modes are normally mentioned in the literature [1]: polar, hoop and helical winding. In polar winding, applied to manufacture vessels, the tow trajectory goes from one dome to the other, touching the polar opening at each side. In hoop winding, the tow is positioned side by side and the winding angle is near 90°, depending only on mandrel radius and tow width. Hoop winding may be done with a single stroke, which is the longitudinal movement of the delivery eye from one end to the other. The other winding modes must have at least two strokes – forward and backward. In case of helical winding, the tow is positioned at a defined winding angle forming a helix over the mandrel. The movements have to be repetitive in order to obtain uniform surface and thickness and, due to the continuity of the process (as the tow is continuous), a return procedure on the ends of the mandrel has to be adopted.

Many layers may be wound as needed to achieve the desired part thickness, and each layer has a slightly different constitution since the radius increases each time. In helical winding, two entangled layers are simultaneously wound, one at the winding angle $+\alpha$ and the other at $-\alpha$, thus the laminate is antisymmetric.

As aforementioned, the movements of the delivery eye in helical winding are defined by the forward and the backward strokes. Between them, a returning trajectory must be determined. Generally, the strokes follow a geodesic trajectory. i.e. the minimum distance between two points on a generic surface. Such paths are governed by Clairaut relation [3] and are independent of the mandrel-tow friction. In the return regions, however, the tow must follow a non-geodesic trajectory, which is governed by more complex equations that take friction into account.

The returning trajectory impacts product quality, productivity and cost. A short trajectory may generate some slippage, changing the tow's position close to the return region. Depending on the degree of slippage, the regular winding region may also be influenced, yielding a region where the layers are not with opposite winding angles and influencing the mechanical response of the component. On the contrary, a long trajectory reduces slippage but also the process' efficiency regarding cost and time.

Thus, this paper focuses on the analysis and understanding of the returning trajectory characteristics for a more adequate FW processing. The trajectory of tows on surfaces of revolution (both cylindrical and generic) using differential geometry concepts is presented. Analytical solutions are provided for a cylindrical surface and numerical procedures are described for generic surfaces of revolution.

2. ANALYTICAL FORMULATION

2.1 Non-geodesic trajectory for a returning tow on cylindrical surfaces

A generic curve on a surface of revolution is presented and its infinitesimal contribution is shown in Figure 1. L_m and L_p refer to the meridional and the parallel lengths, respectively, while α and θ correspond to the winding angle and the mandrel rotation (both considering the FW process), respectively. z is the direction of the axis of rotation.

Through differential geometry [1], one may define

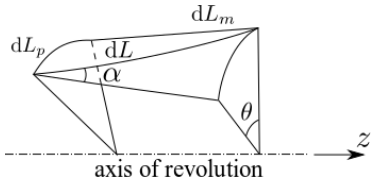

Figure 74- Infinitesimal rotational surface with tow path.

$$dL_m = \sqrt{E}\,dz \qquad dL_p = \sqrt{G}\,d\theta \tag{1}$$

where E and G are the first fundamental forms of the surface. For revolution geometries

$$E = \left(\frac{dr}{dz}\right)^2 + 1G = r^2 \tag{2}$$

where r denotes the radius of the surface of revolution. For cylinders, r is constant and thus

$$dL_m = dz \qquad dL_p = r\,d\theta \tag{3}$$

and, through trigonometric relations, one obtains

$$dL = \frac{dz}{\cos(\alpha(z))} = \frac{r\,d\theta}{\sin(\alpha(z))} \Rightarrow r\,d\theta = \tan(\alpha(z))\,dz \tag{4}$$

which implies in a relationship between the variation of the winding angle and the mandrel's rotation. From now on, the dependence of α on z is omitted.

The differential equation of the winding angle variation along the z axis which takes into account the slippage coefficient λ on a generic surface is written as [4,5]

$$\frac{d\alpha}{dz} = \lambda\left[\frac{\sin(\alpha)\tan(\alpha)}{r} - \frac{r''\cos(\alpha)}{1+r'^2}\right] - \frac{r'}{r}\tan(\alpha) \tag{5}$$

where r' and r'' correspond to the first and second derivative of the radius in term of the axis of revolution z, respectively. The slippage coefficient in eq. (5) is determined by the equilibrium condition [5] as

$$\lambda = \frac{K_g}{K_N} \tag{6}$$

where K_g and K_N denote the geodesic and normal curvatures, respectively. For cylindrical surfaces, eq. (5) may be simplified as

$$\frac{d\alpha}{dz} = \lambda\left[\frac{\sin(\alpha)\tan(\alpha)}{r}\right] \therefore \frac{d\alpha}{\sin(\alpha)\tan(\alpha)} = \lambda\frac{dz}{r} \tag{7}$$

Equation (7) describes a non-geodesic path on a cylindrical surface. A geodesic trajectory is obtained considering the slippage coefficient null. In this case, the solution of eq. (5) is the Clairaut relation, defined by

$$r\sin(\alpha) = c \tag{8}$$

where c is a constant. The solution of eq. (7) is

$$\frac{\sin(\alpha_f) - \sin(\alpha_i)}{\sin(\alpha_f)\sin(\alpha_i)} = \frac{\lambda}{r}(z_f - z_i) \Rightarrow \sin(\alpha_f) = \frac{\sin(\alpha_i)}{1 - \frac{\lambda(z_f - z_i)\sin(\alpha_i)}{r}} \tag{9}$$

where α_i and α_f are the initial and final winding angles with their respective position, z_i and z_f, respectively. By eq. (9), one can determine the position where the tow changes the stroke (forward to backward and *vice-versa*), z_f, considering $\alpha_f = 90°$. From a practical point of view, this information is important since it defines the required (minimum) mandrel length.

Another important information that can be extracted from eq. (9) is the rotation angle θ required for the return procedure. By inserting eq. (9) into eq. (4), one obtains

$$r\mathrm{d}\theta = \tan\left(\arcsin\left(\frac{\sin(\alpha_i)}{1 - \frac{\lambda(z_f - z_i)\sin(\alpha_i)}{r}}\right)\right)\mathrm{d}z \tag{10}$$

For integration purposes, let

$$a = \sin(\alpha_i) \qquad b = {}^{\lambda}/_{r} \qquad \mu = 1 - abz \tag{11}$$

As aforementioned, eq. (9) can be used to define the position on the z-axis where the tow changes its stroke by setting $\alpha_f = 90°$. Considering $z_i = 0$, this leads to

$$z_f = \frac{1 - a}{ab} \Rightarrow \mu_f = a \tag{12}$$

Equation (12) measures the required length of the return path at the z-axis. The integrations are carried out by μ, thus the Jacobian is

$$\frac{\mathrm{d}\mu}{\mathrm{d}z} = -ab \tag{13}$$

By inserting eq. (9) into eq. (4) in terms of cosine, one obtains

$$\mathrm{d}L = -\frac{1}{ab\cos\left(\arcsin\left({}^{a}/_{\mu}\right)\right)}\mathrm{d}\mu = -\frac{\mu}{ab\sqrt{\mu^2 - a^2}}\mathrm{d}\mu \tag{14}$$

Integration of eq. (14) yields

$$\int_0^{L(\mu)} \mathrm{d}L = -\int_{\mu_i}^{\mu} \frac{\mu}{ab\sqrt{\mu^2 - a^2}} \mathrm{d}\mu \;\Rightarrow L(\mu) = \frac{1}{ab}\left[\frac{(a^2 - \mu^2)}{\sqrt{\mu^2 - a^2}} - \frac{(a^2 - 1)}{\sqrt{1 - a^2}}\right] \tag{15}$$

where $\mu_i = 1$ $(z = 0)$. By replacing $\mu = a$ into eq. (15), one obtains an indeterminate, since close to the turning point, $\tan(\alpha) \to \infty$.

Applying the L'Hopital rule, one determines the limit of the function with $\mu \to a$, obtaining

$$L(a) = \frac{(1 - a^2)}{ab\sqrt{1 - a^2}} \tag{16}$$

Equation (16) defines the half-length of the returning path (until α=90°). Two limits may be defined: if the initial angle is close to 90°, as in hoop winding, the length is the smallest possible since a ≈ 1, and if α ≈ 0°, the half-length required to the return trajectory tends to infinity.

Another important parameter is the required rotation angle θ for the half-length. It may be obtained analogously to L. Firstly, one considers eq. (4) along with eq. (9), thus

$$r \int \mathrm{d}\theta = -\frac{1}{ab} \int \tan\left(\arcsin\left(\frac{a}{\mu}\right)\right) \mathrm{d}\mu \tag{17}$$

which results in

$$\theta(\mu) = \frac{1}{\lambda} \ln \left| \frac{\sqrt{\mu^2 - a^2} - \mu}{\sqrt{1 - a^2} - 1} \right| \tag{18}$$

An interesting point of eq. (18) is that the half-dwell, which is independent on the mandrel radius, is defined as

$$\theta(\,\mu_f = a) = \frac{1}{\lambda} \ln\left(\frac{a}{1 - \sqrt{1 - a^2}}\right) \tag{19}$$

and, it strongly depends on the winding angle (in a nonlinear fashion), being inversely proportional to the slippage coefficient.

2.2 Non-geodesic trajectory for returning tow on generic surfaces

In order to determine non-geodesic trajectories on generic surfaces, a position vector, $\boldsymbol{d}$, is defined as

$$\boldsymbol{d}(z) = \{r\cos(\theta) \quad r\sin(\theta) \quad z\}^{\mathrm{T}} \tag{20}$$

where both r and θ depend on z. Differentiating $\boldsymbol{r}$ with respect to z, one obtains

$$\frac{\mathrm{d}\boldsymbol{d}}{\mathrm{d}z} = \boldsymbol{d}' = \{r'\cos(\theta) - r\sin(\theta)\,\theta' \quad r'\sin(\theta) - r\cos(\theta)\,\theta' \quad 1\}^{\mathrm{T}} \tag{21}$$

The angle between the vectors $\boldsymbol{r'}$ and $\boldsymbol{\kappa}$ (unit vector in z direction) is the winding angle α.Thus

$$\boldsymbol{d'} \cdot \boldsymbol{\kappa} = |\boldsymbol{d'}||\boldsymbol{\kappa}| \cos(\alpha) \;\Rightarrow\; \cos(\alpha) = \frac{\boldsymbol{d'} \cdot \boldsymbol{\kappa}}{|\boldsymbol{d'}||\boldsymbol{\kappa}|} = \frac{1}{|\boldsymbol{d'}|} \tag{22}$$

Considering that the norm of $\boldsymbol{d'}$ is determined as

$$|\boldsymbol{d'}| = \sqrt{r'^2 + r^2\theta' + 1} \tag{23}$$

One defines the mandrel's rotation by the following differential equation

$$\theta' = \frac{\sqrt{\tan^2 \alpha - r'^2}}{r} \tag{24}$$

which is obtained by algebraic manipulation of eqs. (22) and (23). Equation (24), along with eq. (5), defines the mandrel's rotation and the winding angle through a generic revolution surface. One defines

$$\boldsymbol{H}(z) = \begin{Bmatrix} \theta(z) \\ \alpha(z) \end{Bmatrix} \Leftarrow \boldsymbol{H'}(z) = \begin{Bmatrix} \theta'(z) \\ \alpha'(z) \end{Bmatrix} \tag{25}$$

Due to the characteristics of $\boldsymbol{H'}(z)$, θ and α can be only obtained by a numerical procedure, noting that the last (α) may be solved before the first (θ). Thus, the non-geodesic path over a generic surface of revolution may be determined.

3. RESULTS AND DISCUSSION

Trajectories, winding angle and mandrel's rotation at the return region on cylindrical and surfaces of revolution are presented and discussed in this section. Firstly, concerning cylindrical surfaces, Equation (18) is plotted for four different slippage coefficients ($\lambda = 0.1$, $\lambda = 0.2$, $\lambda = 0.3$ and $\lambda = 0.4$), considering a mandrel with $r = 25$ mm and winding angle of $60°$ in Figure 2. The curves should be analyzed as at bound to the trajectories. For example, if the slippage coefficient of the mandrel is 0.1, in order to avoid any unwanted displacement of the tow in the return path, the shortest trajectory is presented by the curve with solid circles. Consequently, greater mandrel's rotation and longer trajectories are needed, i.e. a longer mandrel is required.

Figure 2 also implies that the greater the slippage coefficient, the lower the mandrel's rotation and the required size of the return region. Moreover, eq. (18) estimates the minimum required size for the mandrel. For $\lambda = 0.1$, ca. 40-mm long return size is required, while for $\lambda = 0.2$, this length drops to ≈ 20 mm.

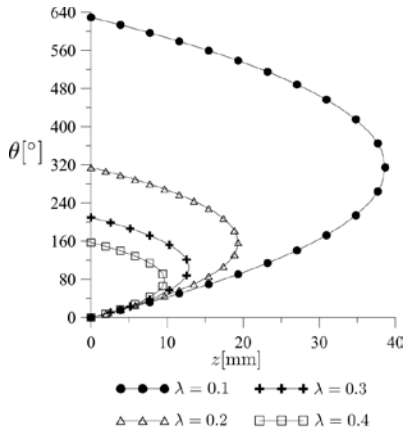

Figure 75 – Slippage coefficient at the returning path: mandrel's rotation and max. z.

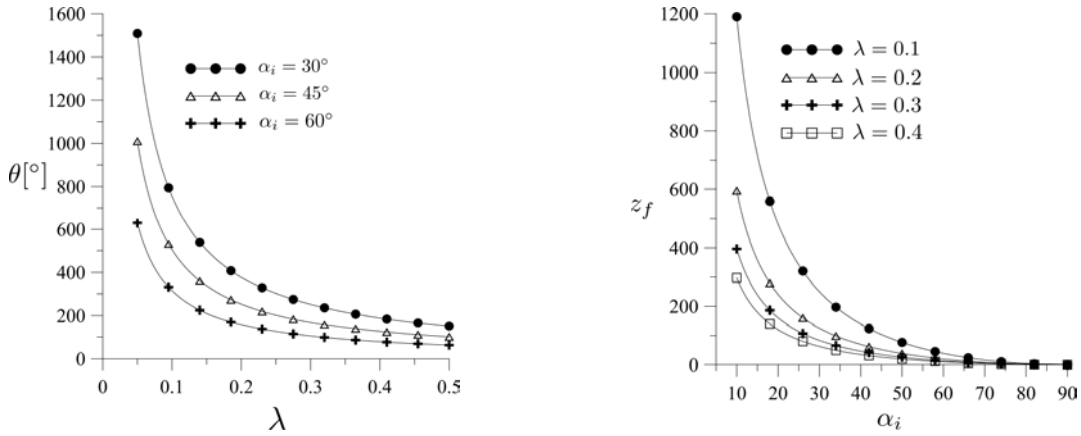

(a) (b)

Figure 76 – Bounds for the return region: (a) return angle × slippage coefficient for different winding angles and (b) length of return stroke × winding angle for different slippage coefficients.

The two plots in Figure 2(a)-(b) show the correlation between mandrel's rotation, slippage coefficient and stroke at the return region. Figure 2 also presents the bounds for these parameters and the mandrel's rotation and the final stroke are inversely proportional to the slippage coefficient and the initial winding angle, respectively. As $\lambda \to 0$, the required mandrel's rotation tends to infinity (Figure 3(a)). A similar trend is noted as the winding angle tends to 0°, as mentioned before in the discussion of eq. (16). Also, the closer the winding angle is to 90°, the shorter is the return path.

Figure 4 depicts the winding angle and the mandrel's rotation in a non-cylindrical revolution surface governed by

$$r = 5.5731.10^{-6}z^3 - 0.00226208z^2 + 0.480329z + 17.9 \text{ [mm]} \quad (26)$$

where $z_i = 0$ [mm] and $z_f = 108$ [mm]. Moreover, the winding angle at z_i is 55°. Equation (25) is solved with a Runge-Kutta algorithm – RK4 – with 1500 points. Five slippage coefficients are evaluated. Interestingly, the winding angle for $\lambda = 0.4$ decreases until $\approx 40°$ and then increases to the initial winding angle. The same trend is found for $\lambda = 0.5$, but due to the high friction between the tow and the mandrel, the trajectory has a return ($\alpha = 90°$) before the end of the

mandrel, at $z \approx 72$ mm. This behavior is similar to the non-geodesic trajectories in cylindrical surfaces previously shown in Figure 2.

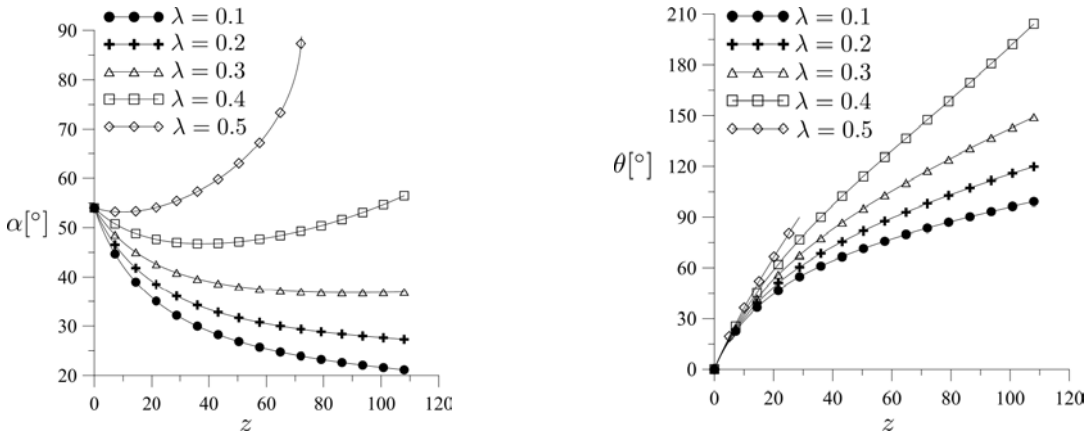

Figure 77 – Winding angle and mandrel's angle × stroke at the return region for a non-cylindrical revolution surface.

4. CONCLUSIONS

The return region in helical FW is mostly disregarded in published literature work on FW. The return procedure influences process economics, processing time and waste generation, and the pattern formation during regular winding. Through equations α(z) and θ(z) presented in this work, the non-geodesic path for the return procedure is fully described on a cylindrical surface and also on a generic surface of rotation. The effect of mandrel radius, slippage coefficient and initial winding angle on maximum z and total rotation angle θ was presented, being useful for parameters selection in the FW process.

ACKNOWLEDGEMENTS

The authors would like to acknowledge CAPES (Coordination for the Improvement of Higher Educational Personnel) and CNPq (National Council for Scientific and Technological Development) for the financial support.

REFERENCES

[1] Peters, S.T. Composite Filament Winding. ASM International. 2011
[2] Beukers A., Koussios S., Bergsma O. Composite pressure vessel design: integral determination of winding patterns. 16th international conference on composite materials. 2007.
[3] Gray A. Modern differential geometry of curves and surfaces. CRC Press. 1993.
[4] Zu L., Koussios S., Beukers A. Design of filament-wound isotensoid pressure vessels with unequal polar openings. Comp. Struct. 2010.
[5] Koussios, S. Filament Winding: A Unified Approach. IOS Press. 2004.

13. PHYSICAL AND MECHANICAL PROPERTIES

NUMERICAL AND EXPERIMENTAL ANALYSES ON THE CURING OF A THICK THERMOSETTING POLYMER MATRIX

Vivianne M. Bruère (1), Nadège Bouchonneau (1) and Christian Jochum (2)

(1) Department of Mechanical Engineering, Universidade Federal de Pernambuco, Brazil

(2) Service de Recherche en Mécanique des Structures Navales ENSTA Bretagne / IRDL-UMR CNRS 6027, Brest, France.

https://doi.org/10.21452/bccm4.2018.13.01

Abstract

In the present work, the curing process of a thick thermosetting polymer matrix was investigated through experimental and Finite Element analyses. The study was carried out on COMSOL Multiphysics® software considering coupled thermal and chemistry phenomena involved in an epoxy's polymerization process. The curing parameters of two single-step and one two-step curing were investigated, denoting defective samples from the two first cases due to thermal degradation and a defect-free sample from the last one. Numerical results were in good agreement with experimental records, and thus reveal the potential of this COMSOL® FE simulation.

Keywords: Curing; Finite Element; COMSOL Multiphysics®; Epoxy; Thermal degradation.

1. INTRODUCTION

The appearance of synthetic fiber-reinforced composites in late 19th century, due to the development of resin polymerization and fiber fabrication processes, and their subsequent popularity increase after World War II, led to our current extensive composite industry. The growing mastery of fabrication processes and the development of designed materials with combinations of superior properties encourages the enlargement of the composites field, which can be seen in sectors such as aerospace, marine, construction and energy.

As a result, composite materials are currently the focus of several studies, aiming the achievement of a better control and optimization of the manufacturing process. Namely, fiber-reinforced thermosetting polymer matrix composites show superior strength capabilities and are increasingly used in high performance applications to improve load capacity and reduce energy costs. The manufacturing of those composites, nevertheless, generally represents one of the main obstacles for their use. As the matrix undergoes a curing process, there is a chemical reaction, both

thermoactivated and exothermic, as well as the coupling of several physics phenomena. The final properties of the material depend, therefore, on the curing.

Nonetheless, during curing internal stresses were already expressed in literature to be generated [1,2], which can induce quality defects such as bubbles, cracks and fiber waviness, depreciating the material's mechanical performance [3-7]. These defects become more relevant as the material's thickness increases since mass effects amplifie the exothermic factor of the curing. This is a central investigation point in thick laminates, whose use is constantly expanding in naval and offshore applications, as well as in components which withstand severe loads [8,9]. Another phenomenon associated with the cure of a thermosetting polymer matrix (TPM) is thermal degradation, triggered by internal overheat from the exothermic reaction. Particularly in thick laminates, temperature gradients are more intense, and lead to a high temperature profile and a more heterogeneous final material.

The knowledge and prediction of the material's internal state at the end of cure becomes essential and strategic for the industry, to identify the mechanical properties of the resulting product. Optimization studies of TPM curing cycle and manufacturing process have been carried out experimentally [1,10,11], ensuring better mechanical properties to the composites. The downside of this knowledge is its approach of experimental origin and the materials being often intended for very specific use, which limit their applicability to a wider field. It is required, hence, to combine experimental analysis with another type of investigation.

For the laminate quality evaluation and determination of residual internal stresses, as well as solving of the implemented multiphysics couplings, the use of the Finite Element Method (FEM) is a very promising approach [8,9,12-16]. The execution and validation of 3D models of the material's curing process, considering chemical, thermal and mechanical coupled phenomena, is a key point to the elaboration of reliable predictive models. Studies with the use of this numerical tool are more and more present, and the constant evolution of FE software and computer speed increase are an additional impulse for its use in such analyses.

In this context, this work highlights the numerical modeling of curing of a thick thermosetting polymer matrix, more specifically, an epoxy resin. Epoxies are known to be widely used in high-performance applications for their excellent mechanical properties, dimensional stability and greater resistance to humidity. The purpose of this paper is, thus, to evaluate the curing cycle involving several physics, for a reliable and realistic prediction of the material's behavior in the composite's manufacturing process. COMSOL Multiphysics® software was used considering the coupled physics of thermal and chemistry as a means to develop fast, realistic and reliable predictive modeling approaches and simulations able to describe the epoxy behavior and to represent changes in material properties and gradients occurring during cure. In addition, a fully thermal-chemical-mechanical coupled model is in progress and is to be presented in future publications. Experimental tests were also performed to collaborate in the developing and validation of the models, for different curing processes.

2. NUMERICAL METHODOLOGY

As the curing consists of an exothermic reaction, the heat produced helps its activation, leading to a coupling of two physics: thermal and chemistry. A simple coupling of them was taken as an additional heat flow equivalent of that released by chemistry into the heat transfer equation, as the focus remains on the evolution of degree of cure and temperatures instead of how chemical species are reacting. Hence, the heat transfer equation used is:

$$\rho C_p \, dT/dt = \text{div}\{k[\mathbf{grad}\ T]\} + q + \rho \Delta H_r \, d\alpha/dt - T\{(3\kappa + 2\mu)\, \alpha_T\}\, tr\, \dot{\boldsymbol{\varepsilon}} \quad (1)$$

where ρ, C_p, k and α_T stand for the density, specific heat, thermal conductivity and coefficient of thermal expansion of the forming matrix, while q and ΔH_r are the heat imposed by the oven and the reaction's enthalpy, respectively, where $\rho \Delta H_r \, d\alpha/dt$ denotes the heat flow produced by the chemical reaction. Bulk and Shear moduli are given by κ and μ, the second-order strain tensor is $\dot{\boldsymbol{\varepsilon}}$ and T and α are the temperature and degree of cure. The last term of Equation (1) can be neglected for the heat induced from mechanics is low compared to the others.

2.1 Cure kinetics

The degree of cure was expressed by Kamal and Sourour's phenomenological model [17], considering both catalytic and auto-catalytic reaction effects. Diffusion phenomenon was added, since as curing evolves the polymerization reaction becomes more and more controlled by reactive species diffusion and more reduced in molecule mobility, slowing the reaction rate. Thus, Kamal and Sourour's model extended by Fournier et al. [18] was applied:

$$d\alpha/dt = (K_1 + K_2 \alpha^m)(1 - \alpha)^n f_d(\alpha) \quad (2)$$

Exponent m is the order associated with the auto-catalytic reaction, and n, with the catalytic one. Rate constants K_1 and K_2 from the catalytic and auto-catalytic processes, respectively, follow the Arrhenius Law, given in terms of pre-exponential constants A_1 and A_2, activation energies E_1 and E_2, universal constant of perfect gases R and temperature T:

$$K_1 = A_1 \exp[-E_1/(RT)] \quad (3)$$

$$K_2 = A_2 \exp[-E_2/(RT)]$$

Diffusion factor $f_d(\alpha)$ is expressed by

$$f_d(\alpha) = -1 + 2/\{1 + \exp[(\alpha - \alpha_f)/b]\} \quad (4)$$

where α_f is the conversion that could be reached at the end of a corresponding isothermal cure performed at T, and b is an empirical material diffusion constant. Rabearison et al. [19] defined cure kinetics parameters for a LY 556 epoxy system, with HY 917 hardener and DY 070 accelerator in a 100:90:2 mass ratio. The used parameters are presented in Tables 1 and 2.

Table 1: Cure Kinetics parameters

A_1 [1/s]	A_2 [1/s]	E_1 [kJ/mol]	E_2 [kJ/mol]	m	n	R [J/(mol K)]
1339879.17	21042820.69	69.14	72.62	1	2	8.314

Table 2: Diffusion factor parameters

α_f :	$4.0646*10^{-3}\, T[K] - 8.2434*10^{-1}$	b:	$7.1588*10^{-4}\, T[K] - 2.2816*10^{-1}$

Parameters α_f and b were defined for temperature ranges between 360 K and 420 K. As the final degree of cure cannot exceed 100%, physically speaking, for temperatures above 448.8 K α_f remains constant. Limitation of b consists of not achieving zero – indeterminacy in $f_d(\alpha)$'s denominator –, and so this parameter remains constant at temperatures below 319 K.

2.2 Glass transition temperature

As epoxy undergoes structural and phase changes – liquid to rubbery solid, and then to glassy solid –, which directly affects material's properties, the glass transition temperature, T_g, had to be properly described by DiBenedetto's equation [20], the most common model:

$$T_g = T_{g0} + [\lambda\alpha(T_{g\infty} - T_{g0})]/[1 - (1 - \lambda)\alpha] \quad (5)$$

where T_{g0} and $T_{g\infty}$ are the glass transition temperatures for uncured and fully cured resin, and λ is an adjustable parameter, assuming the values 236 K, 409 K and 0.57, respectively [21].

2.3 Epoxy's material properties

The epoxy system's density has a small variation throughout the curing process – less than 10%. Thus, its density was taken as constant and equal to 1170.6 kg/m^3. The material's specific heat capacity, thermal conductivity and coefficient of thermal expansion vary according to the Rules of Mixtures [9] as $C_p(\alpha,T) = (1 - \alpha)\, C_p(0,T) + \alpha\, C_p(1,T)$, $k(\alpha,T) = (1 - \alpha)\, k(0) + \alpha\, k(1,T)$ and $\alpha_T(\alpha,T) = (1 - \alpha)\, \alpha_T(0,T) + \alpha\, \alpha_T(1,T)$, where:

$$C_p(0,T) = 1.8500 + 0.002625*T[^oC] \ \ [J/(g\ ^oC)] \quad (6)$$

$$C_p(1,T) = 1.3125 + 0.004437*T[^oC],\ T < T_{g\infty} \text{ or } C_p(1,T) = C_p(0,T),\ T \geq T_{g\infty} \ \ [J/(g\ ^oC)]$$

$$k(0) = 0.188 \text{ and } k(1,T) = -2.727\ 10^{-4}*T[^oC] + 3555.529*10^{-4} \ \ [W/(m\ ^oC)] \quad (7)$$

$$\alpha_T(0,T) = 5*10^{-4} \ \ [1/\ ^oC] \quad (8)$$

$$\alpha_T(1,T) = 450*10^{-6},\ T < T_g \text{ or } \alpha_T(1,T) = 450*10^{-6} + 4.1*10^{-6}*(T - T_g),\ T \geq T_g \ [1/\ ^oC]$$

The epoxy system is inserted into a steel mold, with a density of 7800 kg/m^3, thermal conductivity and specific heat capacity of 24 W/(m K) and 460 J/(kg K), respectively, at 293 K, and of 29 W/(m K) and 540 J/(kg K) at 773 K.

2.4 Heat flow from chemical reaction and from the oven

This is represented by term $\rho\, \Delta H_r\, d\alpha/dt$ in Equation (1). From previous DSC experiments [19], we could express this term as:

$$\rho\, H_U\, d\alpha/dt = 1170600*330*d\alpha/dt,\ T < T_g \quad (13)$$

$$\rho\, H_U\, (H_T/H_U)\, d\alpha/dt = 1170600*330*(0.00243*T[K] - 0.158)*d\alpha/dt,\ T \geq T_g$$

H_T and H_U are the enthalpy of the reaction at a given temperature and the total enthalpy for the complete reaction, respectively, where H_U was found to be 355 ± 25 J/g [19]. As for the heat imposed by the oven, only the convection was considered, since the dimensions of the oven relative to the epoxy sample were considerably larger. Therefore,

$$q = h(T - T_e) \quad (14)$$

Coefficient of convection h was previously calculated [22], and T_e is the oven temperature.

2.5 COMSOL Multiphysics® Implementation

In the software, all varying parameters were added as interpolation, piecewise or analytic functions. The program allowed an easy implementation with simple logical expressions, exempting the need of an associated programming language. Cure kinetics equation was solved inside COMSOL® [23] itself with *Domain ODEs DAEs* module; *Heat Transfer* module governed

the thermo-chemical coupling. The investigated geometry consisted of a 32 mm-diameter and 60 mm-height of the epoxy inside a steel mold of overall 45 mm-diameter and 65 mm-effective height. The 2D-axisymmetric geometry mesh was had quadrilateral (for the epoxy) and coarser triangular elements (for the mold), with a total of 645 elements.

3. EXPERIMENTAL METHODOLOGY

Curing at three different temperatures were carried out, all of them with heating and cooling rates of 3ºC/min, based on manufacturing practices. The investigated temperatures were: single-step curing at 140ºC with a 2h isothermal plateau; single step-curing at 110ºC, also with a 2h plateau; and the manufacturer's recommendation – a two-step curing at 80ºC for 4h, followed by a 4h plateau at 120ºC. Thermocouples registered the temperatures on the mold's wall and inside the oven. For the 140ºC case, it was also possible to record the temperature in the epoxy sample's center. Samples were prepared respecting the mass ratio of 100:90:2 for a LY 556 epoxy system, with HY 917 hardener and DY 070 accelerator. As the resin preparation led to the appearance of bubbles, the samples were placed before curing in a vacuum chamber to remove these bubbles and reduce sources of defects.

4. RESULTS ANALYSIS

The resulting samples (Figure 1) for the single-step curing processes evidenced the presence of cracks. Although all the bubbles might not be removed before curing, a likely motive is thermal degradation: high temperatures achieved during curing provoke the phenomenon, leading to loss of mass, followed by the formation of gases and bubbles, which increases the epoxy's internal pressure and, consequently, induces cracks in the material.

(a) (b) (c)

Figure 1: Epoxy samples for the (a) 140ºC and (b) 110ºC single-step and (c) two-step curing.

The color gradients – darker coloration in the center, better detected at Figure 1c – indicate the degree of cure gradients and its higher values inside the geometry. This is a reflex of the curing temperature – which the greater it is, the higher the temperature peaks due to difficulty in heat getting transferred out of the resin. The two-step curing, based on manufacturer's recommendation, showed no signs of defects, proving to be a safe procedure.

Numerical simulations from COMSOL® and experimental data provided similar results. For the 140ºC curing (Figure 2), recorded temperatures on the center (Center Exp from the experiment and T1 from simulation) agree on the peak from the intense exothermic reaction.

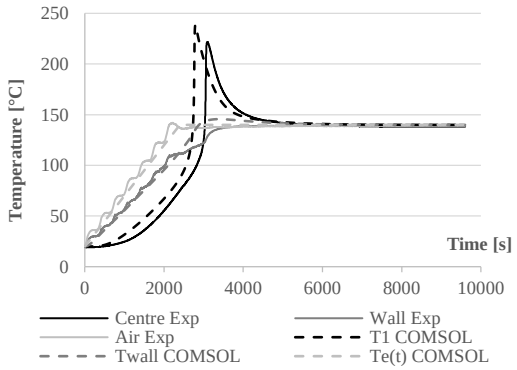

Figure 2: Temperature evolution Experiment x Simulation: 140ºC.

The wall temperatures, however, distant themselves a little at the temperature peak duration in the epoxy's center. A possible reason could be the coefficient of convection h, added to the model from previous works. The peak in center's temperature rises the wall's as well, probably leading to changes in h. These dissimilarities also occur for the 110ºC and the two-step curing (Figure 3). This denotes improvements to be made in this aspect of the model.

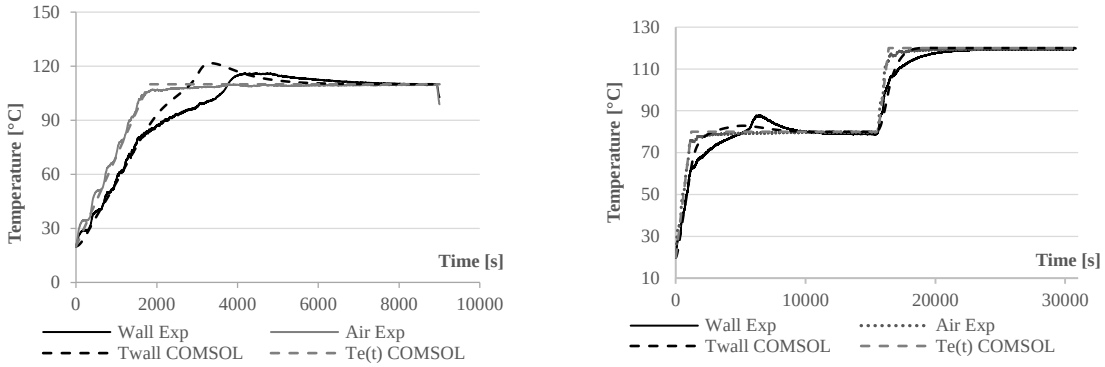

(a) (b)

Figure 3: Temperature evolution Experiment x Simulation: (a) 110ºC and (b) two-step curing.

The evolutions of degree of cure and temperatures at the center (maximum values; index 1) and the outer edge (minimum values; index 4) are presented for the three simulated cases: single-step curing at 140ºC and 110ºC and the two-step curing at 80ºC + 120ºC (Figure 4). A higher curing temperature, as expected, led to higher degree of cure rates as the curing agent is concentrated on the faster crosslinking reactions, resulting in a more heterogeneous material. Peak temperatures were found to be 238°C (140ºC curing), 199ºC (110ºC curing) and 121ºC (80ºC + 120ºC curing). As thermal degradation starts around 160ºC and becomes more intense after 200ºC for the LY 556 epoxy system, we detect the degradation phenomenon for the single-step cases, which indeed provided cracked samples. The manufacturer's recommendation (80ºC + 120ºC curing), on the other hand, proved to be appropriate for giving a more homogeneous material, and exempting it from thermal degradation, especially for the studied geometry, in which mass effects occur from its larger thickness. Nevertheless, the final degree of cure reached is below 80% and highlights the need of a third curing stage (post-cure) to achieve a higher level of degree of conversion.

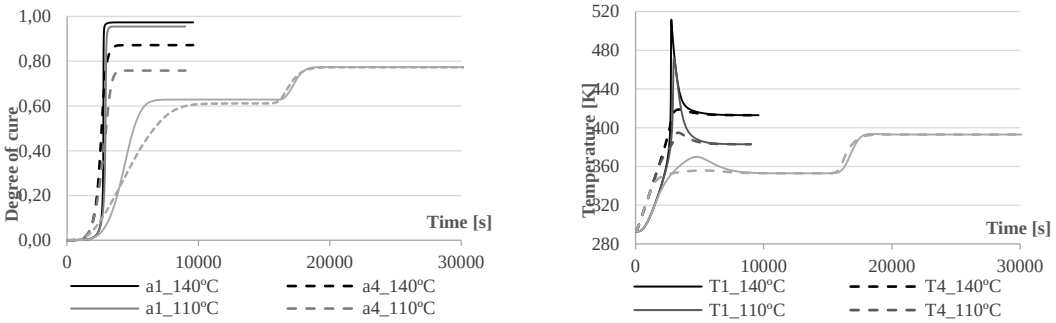

(a) (b)

Figure 4: Maximum [index 1] and minimum [index 4] (a) degree of cure [a] and (b) temperature [T] evolutions for the investigated curing processes.

5. CONCLUSIONS

A finite element modeling of the curing process of an epoxy resin matrix was presented. The chosen software, COMSOL Multiphysics®, provided coupled thermo-chemical predictions of curing parameters in accordance to experiments, with an implementation using the own program resources. Results reveal the importance of curing temperature on the final material in terms of homogeneity and of it being subjected to thermal degradation, which may interfere on its quality. For thick epoxies, mass effects strongly influence the material's final state, since lower heat diffusion to the outside causes the appearance of higher temperatures and gradients and, hence, giving rise to thermal degradation, impairing the product. Improvements are yet to be accomplished for oven convection and the fully coupled thermo-chemical-mechanical model, already in investigation. Thereby, this works highlights the importance of knowledge on the curing of an epoxy resin, in which the achievement of good final properties and material quality derives from control and optimization of manufacturing processes, and exposes the great potential of the FEM for reliable curing quality predictions.

ACKNOWLEDGEMENTS

The authors would like to thank ENSTA Bretagne, for providing the infrastructure to perform the experimental tests. The authors also wish to thank CNPq (MCTI/CNPq/Universal 14/2014 - Process number: 460973/2014-2) for the financial support.

REFERENCES

[1] Jochum, Ch., Grandidier, J.-C., Smaali, M., 'Experimental study of long T300 carbon fibre undulations during the curing of LY556 epoxy resin', *Compos. Sci. Technol.* **67** (2007) 2633-2642.

[2] Jochum, Ch., Grandidier, J-C., Smaali, M.A.,'Proposal for a long-fibre microbuckling scenario during the cure of a thermosetting matrix'. *Compos. Part A* **39** (2008) 19-28.

[3] Adams, D.O., Hyert, M.W., 'Effects of layer waviness on the compression fatigue performance of thermoplastic composite laminates'. *Fatigue* **16** (1994) 385-392.

[4] Hsiao, H.M., Daniel, I.M, 'Effect of fiber waviness on stiffness and strength reduction of unidirectional composites under compressive loading'. *Compos. Sci. Technol.* **56** (1996) 581-593.

[5] Drapier, S., Grandidier, J-C., Potier-Ferry, M.,'A non-linear numerical approach to the analysis of microbuckling'. *Compos. Sci. Technol.* **58** (1998) 785-790.

[6] Stecenko, T., Piggott, M.R., 'Fiber waviness and other mesostructures in filament wound materials'. *J. Reinf. Plast. Compos.* **16** (1997) 1659-1674.
[7] Drapier, S., Grandidier, J-C., Potier-Ferry, M., 'A structural approach of plastic microbuckling in long fibre composites: comparison with theoretical and experimental results'. *Int. J. Solids Struct.* **38** (2001) 3877-3904.
[8] Balvers, J.M., Bersee, H.E.N., Beukers, A., Jansen, K.M.B, 'Determination of cure dependent properties for curing simulation of thick-walled composites'. 49th AIAA/ASME/ASCE/AHS Structures, Structural Dynamics, and Materials Conference. Schaumburg, April, 2008 (American Institute of Aeronautics and Astronautics, 2008-2035) 1-15.
[9] Rabearison, N., Jochum, Ch., Grandidier, J-C. 'A FEM coupling model for properties prediction during the curing of an epoxy matrix'. *Comput. Mater. Sci*. **45** (2009) 715-724.
[10] Ruiz, E., Trochu, F., 'Multi-criteria thermal optimization in liquid composite molding to reduce processing stresses and cycle time'. *Compos. Part A* **37** (2006) 913-924.
[11] Grandidier J.-C., Casari P., Jochum Ch., 'A compressive failure criterion for long fibre laminates based on laminate thickness effect and stacking sequence'. Proceedings of the ICCS 2016 - International Conference on Computational Science. San Diego, June, 2016.
[12] Lord, S., Stringer, L.G., 'A modelling approach for predicting residual stresses and distortions in polymer composites'. 17th International Conference on Composite Materials. Edinburgh, July, 2009.
[13] Zhang, J., Xu, Y.C., Huang, P., 'Effect of the cure cycle on curing process and hardness for epoxy resin'. *Express Polym. Lett.* **3** (2009) 534-541.
[14] Msallem, Y.A., Jacquemin, F., Poitou, A., 'Residual stresses formation during the manufacturing process of epoxy matrix composites: resin yield stress and anisotropic chemical shrinkage'. *Int. J. Mater. Form.* **3** (2010) 1363-1372.
[15] Shevtsov, S.N., Axenov, V.N., Alekseeva, O.D., Vetrova, T.I., 'Cure kinetics of epoxy resin and distributed thermal control of polymeric composite structures moulding. 3rd International Conference Physics and Control. Potsdam, September, 2007.
[16] Jochum, Ch., Arrigoni, M., Boustie, M., Grandidier, J.-C., 'A cut-off fracture approach for residual stress estimation in thick epoxies'. *Materwiss. Werksttech.* **47** (5-6) (2016) 530-538.
[17] Kamal, M.R., 'Thermoset characterization for moldability analysis'. *Polym. Eng. Sci.* **14** (1974) 231-239.
[18] Fournier, J., Williams, G., Duch, C., Aldridge, G.A., 'Changes in molecular dynamics during bulk polymerization of an epoxyde-amine system as studied by dielectric relaxation spectroscopy'. *Macromolecules* **29** (1996) 7097-7107.
[19] Rabearison, N., Jochum, Ch., Grandidier, J.-C., 'A cure kinetics, diffusion controlled and temperature dependent, identification of the Araldite LY556 epoxy'. *J. Mater. Sci.* **46** (2011) 787-796.
[20] DiBenedetto, A.T., 'Prediction of the glass transition temperature of polymers: a model based on the principle of corresponding states'.*J. Polym. Sci., Part B: Polym. Phys.* **25** (1987) 1949-1969.
[21] Rabearison, N., Jochum, Ch., Grandidier, J.-C., 'A finite element coupling model for internal stress prediction during the curing of thick epoxy composites'. International Conference on Flow Processes in Composite Materials. Montreal, July, 2008.
[22] Rabearison, N. 'Elaboration d'un outil numérique dédié à la simulation du procédé de fabrication des matériaux composites à résine thermodurcissable - prédiction des contraintes internes'. Université de Bretagne Occidentale, Brest, 2009.
[23] COMSOL Multiphysics® v. 5.1. www.comsol.com. COMSOL AB, Stockholm, Sweden.

STUDY OF MECHANICAL PROPERTIES OF COMPOSITE WITH SILICONE MATRIX TO MIMETIZATE BIOLOGICAL TISSUE

Marcio Gabriel Moura Netto, Luiz Carlos da Silva Nunes(1)

(1) Departament of Mechanical Engineering (PGMEC), Universidade Federal Fluminense, Brazil

https://doi.org/10.21452/bccm4.2018.13.02

Abstract

It is of scientific interest to know the mechanical properties of biological materials so they can be reproduced in synthetic materials, since the study in living tissues is often arduous. Silicone is one of the synthetic materials most used to mimic the properties of biological tissues. The present study has as objective to verify the relationship between the orientation of the fibers arranged in a silicone matrix composite. A relationship was found between the orientation of the fibers and the mechanical properties of the material, since when the force is applied in the same direction of the fibers, there is an increase in the mechanical strength and a decrease in the elasticity of the material. It was possible to observe that the mechanical behavior of the material was similar to that found in the literature, being possible to conclude that the work was successful in its objective.

Keywords: Silicone, composites, mechanical properties

1. INTRODUCTION

It is of scientific interest to know the mechanical properties of biological materials in such a way that they can be reproduced in synthetic materials, since the study in living tissues is arduous and often conflicts with ethical and legal principles. With the help of the principles of mechanical engineering it is possible to understand the normal functions of organisms, to predict changes and to propose artificial methods of interventions [1].

Among the synthetic materials most used to mimic the properties of biological tissues there is the silicone [2,3]. Both living and synthetic tissues are referred to as hyperelastic materials or elastic materials of Green, and the stress components are obtained through the deformation energy of the body [4].

The mechanical behavior of real materials can be described through constitutive equations [5-10]. In the comparison between the main mathematical models that describe hyperelastic materials for the characterization of different biological tissues, it was possible to affirm that synthetic silicone rubber fabrics are better characterized by these equations than the living tissues [11].

The present work consists in the mechanical characterization of a sample of silicone matrix, in order to predict the behavior of living tissues. For this purpose, the deformation data obtained

through the digital image correlation technique during the tensile tests are used in the constitutive equations of hyperelastic materials.

2. OBJECTIVE

2.1 General Objetive

Verify the relationship between the orientation of the fibers arranged in a silicone matrix composite.

2.2 Specific Objetive

To manufacture polymeric composite samples of silicone matrix with cotton fibers in different orientations;

Testing the specimens produced in a traction machine;

Obtain the experimental behavior of these materials from tensile tests;

Apply the technique of correlation of digital images for acquisition of displacement field;

Apply mathematical model based on the concept of strain energy, to determine the mechanical properties of these composites;

3. MATERIALS AND METHODS

For this work were used bi-component vulcanized silicone rubber RTV-2 model 4-150 RTV of the brand Moldflex and fibrous cotton fabric. From the fabrication of the composite material, samples were obtained with the same dimensions and with fibers oriented at 0º, 45º and 90º and also produced test pieces consisting only of silicone.

Initially, fiber-free silicone rubber was manufactured and a mold with dimensions 220 mm long, 160 mm wide and 3.8 mm high was used to contain the liquid silicone to be used in the experiment. To facilitate removal of the final material, traditional model of the Grand Prix molding wax was used on a glass plate containing the mold.

The production of the silicone rubber was carried out according to the manufacturer's instructions. For complete cure the T-40 catalyst was added to this material in a proportion equivalent to 3% of the mass of silicone used. From the mold volume and the silicone density provided by the manufacturer, it was possible to know the total mass of silicone and catalyst to be produced. This mixture was poured onto level glass plate evenly spreading through the mold. Figure 1 shows materials and utensils used and the polymer being manufactured.

Figure 1: Materials used (left) and fabricated silicone rubber (right).

Subsequently, composite materials consisting of layers of silicone rubber interspersed with cotton fibers were fabricated. As well as for the manufacture of pure silicone, a glass plate previously treated with a release agent, height regulating support and level ruler was used, but there was no need to use a mold, since the rubber was applied with the help of a roll of foam.

Figure 2 shows the manufacturing process that resulted in composites formed by four silicone matrix slides and three cotton fibers slides.

Figure 2: Manufacturing process of composite materials.

After the curing process, the excess silicone was removed and the fabricated composites were sectioned in the shape of specimens.

From each material were obtained specimens of same dimensions, and for the composites there was differentiation as to the orientation of the fibers. Afterwards, these materials were randomly painted with spray of black paint, according to figure 3 and tested in a traction machine.

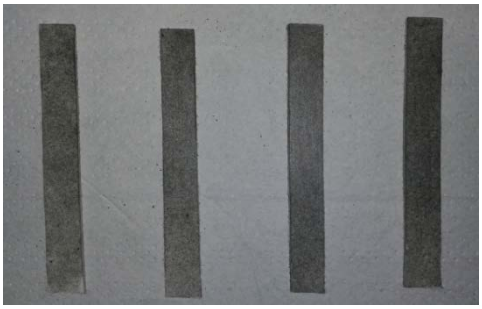

Figure 3: Specimens.

In order to obtain the mechanical properties of the materials produced, tensile tests were carried out. Figure 4 shows the apparatus used, which has in its center the specimens connected to the traction machine through two jaws that hold the lower and upper ends of this specimens. Between the upper claw and the traction machine there is a 100kgf load cell, responsible for measuring the force applied throughout the process. The high-resolution Sony XCD-SX900 camera associated with the Digital Image Correlation (DIC) system positioned perpendicular to the samples is responsible for capturing images of the specimen during the test. The obtained data were processed, thus obtaining the fields of material displacement.

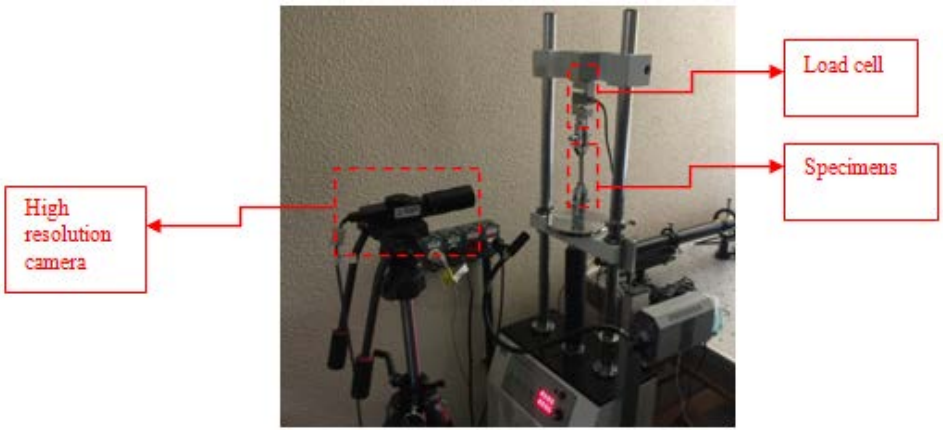

Figure 4: Test Apparatus.

4. MATHEMATICAL METHOD

The developed model considers that the silicone rubber, when submitted to the uniaxial traction, presents behavior similar to that of incompressible hyperelastic materials [11].

Figure 5 is the schematic representation of an infinitesimal element in the reference configuration, with coordinates $\boldsymbol{X} = (\boldsymbol{X}_1, \boldsymbol{X}_2, \boldsymbol{X}_3)$ while $\boldsymbol{a}_0$ is the unit vector that defines the direction of the fiber in that configuration.

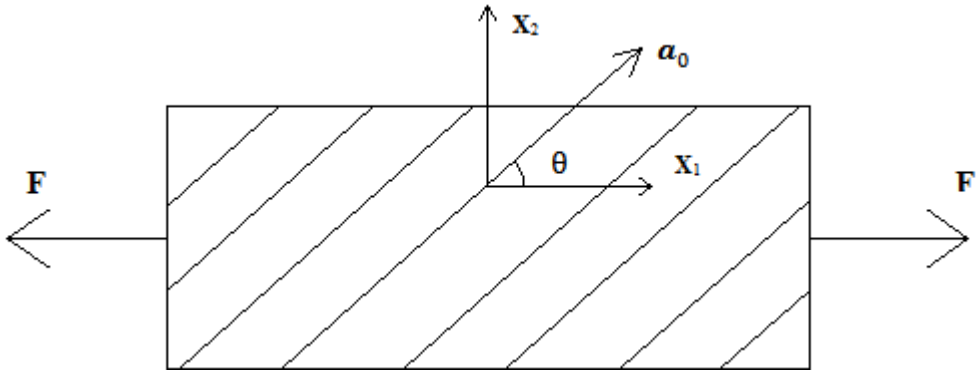

Figure 5: Infinitesimal element.

From the stretching (λ), which is the scalar value responsible for relating the configuration change of the body, it is possible to obtain the second-order tensor (F) called the strain gradient.

$$\mathbf{F} = \frac{\partial \mathbf{x}}{\partial \mathbf{X}} = \begin{bmatrix} \lambda_1 & 0 & 0 \\ 0 & \lambda_2 & 0 \\ 0 & 0 & \lambda_3 \end{bmatrix} \tag{1}$$

With this result the Cauchy-Green deformation tensor on the left is calculated, $\boldsymbol{B} = \boldsymbol{F}\boldsymbol{F}^T$, and the invariants $I_1 = tr(\boldsymbol{B})$, $I_2 = \frac{1}{2}\left[(tr\boldsymbol{B})^2 - tr\boldsymbol{B}^2\right]$, $I_3 = det\boldsymbol{B}$, in addition to the pseudo-invariant $I_4 = \boldsymbol{a}.\boldsymbol{a} = \boldsymbol{a}_0$.

For the study of incompressible composites composed of non-linear isotropic matrix and reinforced by unidirectional fibers, one of the most aborted mathematical models in the literature [12] is the so-called standard reinforcement model, in which the strain energy is given by:

$$\Psi = \frac{\mu}{2}[I - 3 + \gamma(I-2)^2] \quad (2)$$

Let μ be the shear modulus of the composite matrix, while γ is the constant that provides a measure of the reinforcing force in the direction of the fiber.

The constitutive equation of the Cauchy stress for transversely isotropic incompressible hyperelastic materials subjected to uniaxial traction is given, according to [13], by:

$$\boldsymbol{\sigma} = -p\boldsymbol{I} + 2\frac{\partial \Psi}{\partial I_1}\boldsymbol{B} - 2\frac{\partial \Psi}{\partial I_2}\boldsymbol{B}^{-1} + 2\frac{\partial \Psi}{\partial I_4}\boldsymbol{a} \otimes \boldsymbol{a} \quad (3)$$

In which p is the arbitrary hydrostatic pressure resulting from the incompressibility hypothesis. The components of this Tensor are given below.

$$\sigma_{11} = -p + \mu\lambda_1^2 + 2\mu\gamma(\lambda_1^2 cos^2\theta + \lambda_2^2 sen^2\theta - 1)\lambda_1^2 cos^2\theta \quad (4)$$
$$\sigma_{22} = -p + \mu\lambda_2^2 + 2\mu\gamma(\lambda_1^2 cos^2\theta + \lambda_2^2 sen^2\theta - 1)\lambda_2^2 sen\theta$$
$$\sigma_{33} = -p + \mu\lambda_3^2$$

If the load is uniaxial, then σ_{22}=σ_{33}, and the material is incompressible $(\lambda_1\lambda_2\lambda_3 = 1)$ it is possible to determine the value of σ_{11} when the test is performed in the fiber direction, according to equation (5).

$$\sigma_{11} = -\frac{\mu}{\lambda} + \mu\lambda_1^2 + 2\mu\gamma\lambda_1^4 - 2\mu\gamma\lambda_1^2 \quad (5)$$

For composites with fibers oriented at 45 ° and 90 °, it is assumed that $\lambda_2 = \alpha\lambda_1$ and $\lambda_2 = \beta\lambda_1$, respectively. So, in the case of fibers oriented at 45 °, the stress σ_{11} is given by equation (6).

$$\sigma_{11} = \mu\lambda_1^2(\alpha^2 + 2\gamma\alpha^2\lambda_1^2 + 2\gamma\alpha^4\lambda_1^2 - 2\gamma\alpha^2 + 1 + 2\gamma\lambda_1^2 + 2\gamma\alpha^2\lambda_1^2 - 2\gamma) \quad (6)$$

For the case of fibers oriented at 90 °, the stress σ_{11} is given by equation (7)

$$\sigma_{11} = \mu\lambda_1^2(\beta^2 + 2\gamma\beta^4\lambda_1^2 - 2\gamma\beta^2 + 1) \quad (7)$$

5. RESULTS AND DISCUSSIONS

Figure 6 shows the relationship between the stretches undergone by the fiber test specimens in different orientations and the real or applied Cauchy stress. It is possible to notice that the smaller the angle between the direction of the fiber and the direction of application of the force, the greater the tension generated during deformation of the

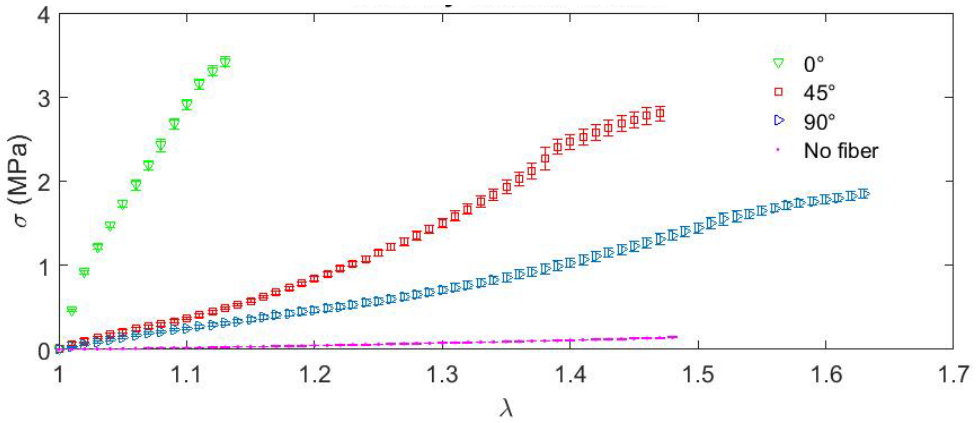

Figure 6: Cauchy stress curve.

Figure 7 shows a comparison between the Cauchy voltages and the Piola-Kirchhoff engineering voltages (or nominal voltages). It is possible to observe that for small deformations there is a coincidence between the applied stresses, however, as expected, for large deformations the real tensions are greater than the Piola-Kirchhoff tensions, since, the real tension considers the decrease of the cross section of the body of evidence.

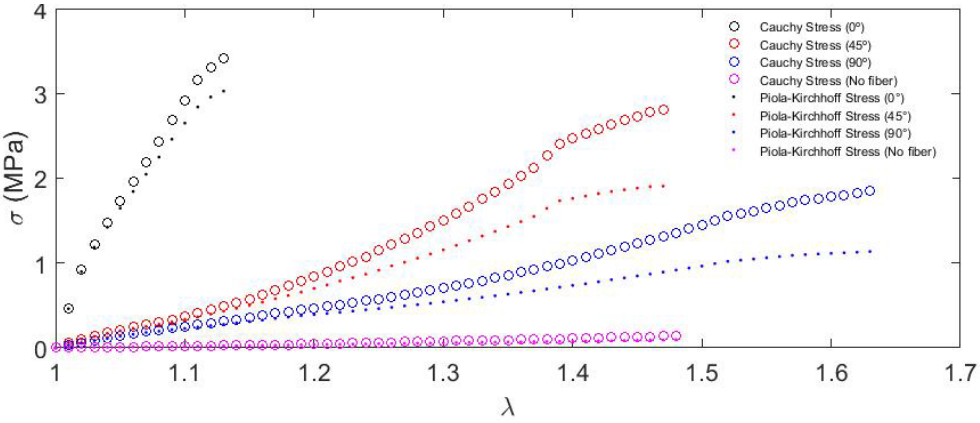

Figure 7: Real and engineering stress versus stretching.

In analyzing Figures 6 and 7 it is possible to notice that the results are in agreement with those found by other authors [14,15], being visible the change of the behavior initially linear to non-linear, when the specimens are submitted to great deformation and increasing the strength of the material according to the arrangement of the fibers, as shown in Table 1.

Table 1: relation on the resistance of materials.

Fiber angle	Tensile strength
0°	3,42
45°	2,8
90°	1,85
No fiber	0,14

Figure 8 shows the comparison between the results obtained experimentally and those obtained through the application of the standard reinforcement model, while the correlation coefficient (R^2) between these results and the values of the constants of the materials are presented in table 2. It is possible to perceive that the theoretical model adopted presents a good correlation with the experimental results, but this model does not consider changes in the structure of the material, which justifies the lack of correlation with the final phase of the experiment, at which moment the rupture is initiated of the reinforcing fibers.

The values of γ found are in agreement with the expected one, since this constant is related to the degree of reinforcement that the fiber grants to the material. The value of μ is the same for all materials, since this constant belongs to the matrix [12].

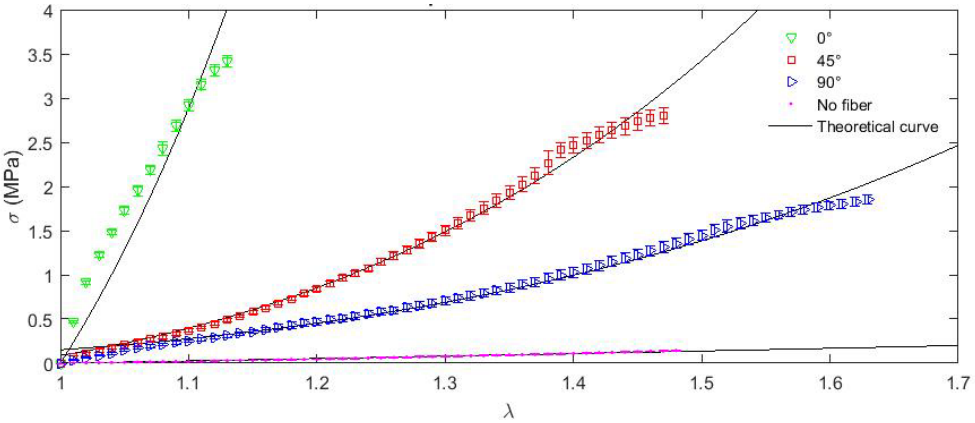

Figure 8: Comparative chart between experimental and theoretical results.

Table 2: Material constants and correlation coefficients.

Fiber angle	Values		
	μ	γ	R^2
0°	0,08699	64,65	0,8891
45°	0,08699	6,59	0,9937
90°	0,08699	2,37	0,9889
No fiber	0,08699	-	0,9861

6. CONCLUSION

It was possible to observe that the mechanical behavior of the material was similar to that found in the literature. In addition, its strength is directly related to the orientation of the fibers constituting the composite material.

The equations of the mathematical model used generated similar theoretical results to the experimental results and the values of the constants found are within the expected, being the value of γ increasing according to the rigidity of the composite. Therefore, it was possible to conclude that the work was successful in its objective.

8. ACKNOWLEDGEMENTS

The financial support of Rio de Janeiro State Funding (FAPERJ), and Research and Teaching National Council, CNPq, are gratefully and acknowledged.

9. REFERENCES

[1] FUNG, Yuan-cheng. Biomechanics: mechanical properties of living tissues. Springer Science & Business Media, 2013.

[2] SAAGER, Rolf B. et al. Multilayer silicone phantoms for the evaluation of quantitative optical techniques in skin imaging. In: Design and Performance Validation of Phantoms Used in Conjunction with Optical Measurement of Tissue II. International Society for Optics and Photonics, p. 756706, 2010.

[3] SPARKS, Jessica L. et al. Use of silicone materials to simulate tissue biomechanics as related to deep tissue injury. Advances in skin & wound care, v. 28, n. 2, p. 59-68, 2015.

[4] KULKARNI, S. G. et al. A transversely isotropic visco-hyperelastic constitutive model for soft tissues. Mathematics and Mechanics of Solids, v. 21, n. 6, p. 747-770, 2016.

[5] SASSO, M. et al. Characterization of hyperelastic rubber-like materials by biaxial and uniaxial stretching tests based on optical methods. Polymer Testing, v. 27, n. 8, p. 995-1004, 2008.

[6] MARCKMANN, Gilles; VERRON, Erwan. Comparison of hyperelastic models for rubber-like materials. Rubber chemistry and technology, v. 79, n. 5, p. 835-858, 2006.

[7] DIANI, Julie et al. Directional model for isotropic and anisotropic hyperelastic rubber-like materials. Mechanics of Materials, v. 36, n. 4, p. 313-321, 2004.

[8] HORGAN, Cornelius O.; SMAYDA, Michael G. The importance of the second strain invariant in the constitutive modeling of elastomers and soft biomaterials. Mechanics of Materials, v. 51, p. 43-52, 2012.

[9] HOLZAPFEL, Gerhard A.; GASSER, Thomas C.; OGDEN, Ray W. A new constitutive framework for arterial wall mechanics and a comparative study of material models. Journal of elasticity and the physical science of solids, v. 61, n. 1-3, p. 1-48, 2000.

[10] DESYATOVA, Anastasia; MACTAGGART, Jason; KAMENSKIY, Alexey. Constitutive modeling of human femoropopliteal artery biaxial stiffening due to aging and diabetes. Acta biomaterialia, v. 64, p. 50-58, 2017.

[11] MARTINS, P. A. L. S.; NATAL JORGE, R. M.; FERREIRA, A. J. M. A comparative study of several material models for prediction of hyperelastic properties: Application to silicone-rubber and soft tissues. Strain, v. 42, n. 3, p. 135-147, 2006.

[12] MERODIO, J.; OGDEN, R. W. Mechanical response of fiber-reinforced incompressible non-linearly elastic solids. International Journal of Non-Linear Mechanics, v. 40, n. 2-3, p. 213-227, 2005.

[13] Holzapfel, G. A., Nonlinear Solid Mechanics, John Wiley & Sons LTD, pp. 205-304, 2000.

[14] KIM, Beomkeun et al. A comparison among Neo-Hookean model, Mooney-Rivlin model, and Ogden model for chloroprene rubber. International Journal of Precision Engineering and Manufacturing, v. 13, n. 5, p. 759-764, 2012.

[15]NERURKAR, Nandan L.; ELLIOTT, Dawn M.; MAUCK, Robert L. Mechanics of oriented electrospun nanofibrous scaffolds for annulus fibrosus tissue engineering. Journal of orthopaedic research, v. 25, n. 8, p. 1018-1028, 2007.

EVALUATION OF MOISTURE ABSORPTION EFFECTS ON MECHANICAL BEHAVIOR OF HYBRID GLASS/CARBON FIBERS EPOXY MATRIX COMPOSITES

L.M. Ottolini (1), **J.R.M. d'Almeida** (1)

(1) Chemical and Materials Engineering Department, Pontifical Catholic University of Rio de Janeiro, Brazil.

https://doi.org/10.21452/bccm4.2018.13.03

Abstract

This study aimed to evaluate the water absorption behavior and its effects on the Young's modulus and damping coefficient of three different types of laminated epoxy resin composites reinforced with glass and carbon fibers. The Young's modulus and the damping factor were evaluated as a function of the immersion time by a non-destructive sonic test, and their variation was correlated with the mass gain of the samples. The diffusion coefficient of water in the composites was evaluated using Fick's Law. The results showed that the water absorption increased rapidly and stabilized after 5 months of immersion. Young's modulus and damping factor values changed abruptly in the first hours of aging in water and remained constant after that. The Young's modulus decreased at first while the damping factor increased in the first hours. Plasticization of the polymer matrix seems to be the cause of the variation of these properties. The microstructure of the composites was also analyzed by both optical and scanning electron microscopy. Internal defects, such as pores and voids, were observed and their quantities affected the amount of water absorbed by each type of composite.

Keywords: Composite, moisture absorption, sonic test, mechanical behavior.

1. INTRODUCTION

The use of polymer matrix composites reinforced with fibers is continuously increasing over the past decades in the industry, to replace conventional engineering materials such as carbon steel. The main characteristics of these composites are high mechanical strength, chemical stability, low cost and low specific weight [1-3]. Laminated composites are the most used ones in aerospace and naval facilities as well as on many sport goods [3]. These composites present the best compromise between specific weight-mechanical resistance and resistance to crack propagation [2].

Under service conditions composites can be subject to damage from mechanical loading, but they are also susceptible to degradation and loss of their mechanical properties due to chemical or

physical interaction with aqueous or gaseous environments [4]. The most common elements to which composites are in contact during their service lives are temperature and moisture [4, 5].

The moisture absorption by the polymeric matrix composites causes swelling/dilation of the polymer matrix generating cracks and microcracks in the microstructure of the material [6]. Sometimes, depending on the constituent materials of the composite, hydrolysis can occur in the interfacial region between the matrix/fiber phases. This weakens the bond strength between the matrix and the reinforcement and, consequently, reduces the mechanical resistance [4-6]. The plasticization of the polymer matrix can also occur as a function of the water absorption, which reduces the modulus of elasticity and increases the deformation of the material [4, 7].

Studies on fiberglass composites performed by Ashbee et al. [8] showed that the water diffusion led impurities into the microstructure of the material, which created small zones of high pressure and, finally lead to the appearance of internal cracks.

The kinetics of moisture absorption depends on factors such as temperature, fiber volumetric fraction, fiber affinity with water, contact surface and internal defects (pores and voids). Water absorption can occur either diffusely, according to Fick's law, or by capillarity [6, 9]. The type of absorption mechanism will depend mainly on the composite material, on the wettability of the matrix phase with the fiber, on the interfacial adhesion between matrix and fiber and the presence of internal defects [4-7].

The objective of this work was to evaluate the effect of moisture on the mechanical behavior of fiber-reinforced epoxy matrix laminated composites. To reach this goal, samples of laminated composites were immersed in tap water, simulating the environment conditions to which these materials are usually exposed during their life time. The water absorption behavior and the amount of water absorbed were correlated with the microstructure of the composites.

2. MATERIALS AND METHODS

Three types of epoxy matrix laminated composites plates reinforced with fiberglass and carbon fiber were analyzed. All laminates were manufactured with twelve laminas and unidirectional fibers. All the samples have the same number of layers of glass fiber and carbon fibers. The fibers were aligned parallel to the longitudinal axis of the laminate. TABLE 1 presents the dimensions, mass and lamina configuration of the samples machined from the plates.

Table 4: Characteristics of the laminated composites.

	Dimension (mm)			Weight (g)	Configuration
	Length	Width	Thickness		
Sample 1	98.15	25.50	2.05	9.19	$[1G/2C/6\bar{G}]_s$
Sample 2	103.64	25.52	2.01	9.59	$[2C/8\bar{G}]_s$
Sample 3	101.64	25.77	2.15	10.01	$[4G/4\bar{C}]_s$

G – Represents the layer of glass fiber.
C – Represents the layer of carbon fiber.

The samples were immersed in a glass with tap water at room temperature (22°C). No type of seal was applied to the samples edges. This implies that water diffusion occurs in all directions. The glass was capped to prevent external contamination, and the total aging period was around 5 months. Samples were taken at regular intervals to measure water absorption and to evaluate the Young's modulus (E) and damping factor (ζ). In the first week of aging, the interval between measurements was 4 hours. After this, the interval was extended to one measurement every week

and finally one measurement every three weeks. The adjustments in the intervals between measurements was necessary to avoid experimental errors due to small mass variation after a long time of aging.

The procedure for removing excess of water from the samples to mass measurement was performed in accordance to ASTM D570-98 standard. The weight of the samples was measured using a balance with an accuracy of ±0.0001g.

The moisture absorption of the samples (M_p) was calculated using Equation 1, where M_t represents the mass of the laminate measured at time "t" and M_d is the initial mass of the dried laminate at $t = 0$ [9]:

$$M_p(\%) = \frac{M_t - M_d}{M_d} \times 100 \quad (1)$$

The experimental data adjustment was performed following Equation 2, adapted to describe the moisture absorption model in accordance to the first Fick's law, both for short and long absorption periods. In Equation 2, M_p is the percentage moisture absorption at a given time "t", M_∞ is the maximum moisture absorption at the saturation point, h is the laminates thickness and D is the diffusion coefficient [10]:

$$\frac{M_p}{M_\infty} = \tanh\left(\frac{4}{h} \times \left(\frac{D \times t}{\pi}\right)^{\frac{1}{2}}\right) \quad (2)$$

Young's modulus and damping factor were evaluated by a non-destructive sonic test. This test consists in capturing with a microphone the propagation of the sound generated by a mechanical impulse at the edge of the sample. FIGURE 1 shows the configuration of the sonic test for one sample. After the mechanical impulse, the sound is captured by an electret microphone and the signal is processed by a software incorporated into the device (Sonelastic®). Young's modulus and damping factor values are automatically obtained from the device [11]. The calculations involved in the determination of these both parameters are based on ASTM E1878 standard. Although the sound test uses the premise that the analyzed material is homogeneous and isotropic, studies performed show that it is possible to use the technique in heterogenous materials. However, the results must be analyzed according to the boundary conditions used in the test and the geometry of the samples [11, 12]

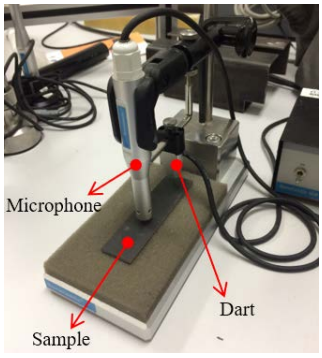

Figure 12: Apparatus for the sonic tests of the specimens

The microstructure of the composites was analyzed by optic microscopy (OM) and scanning electron microscopy (SEM). Both methods were necessary due to the characteristics of the

laminates. In the SEM, the carbon fibers do not show a sufficient contrast in relation to the epoxy matrix, because both contain carbon and, therefore, they exhibit similar average values of atomic number [13]. Thus, carbon fiber characterization was performed by OM. Fiberglass and the voids are easily detected and segmented from the images obtained by SEM. The complete characterization of the microstructures was performed from mosaics obtained in both microscopy techniques with 500x magnification. To reach the goal to determine the volumetric fractions of matrix, fibers and voids, the mosaic images were submitted to steps of preprocessing, segmentation and post processing. A FIJI software was used to quantify the volumetric fraction of the phases.

3. EXPERIMENTAL RESULTS AND DISCUSSION

The experimental results and the fitted curve of water absorption versus the square root of time are represented in FIGURE 2. TABLE 2 shows the values obtained from Equation 2 of the water absorption at the saturation point (M_∞), the diffusion coefficient (D) and the correlation coefficient of the fitted curve (r^2). It is possible to note that the experimental points adhered satisfactorily to the experimental points of the proposed Fick's law model. The correlation coefficient "r^2" ratifies this statement [14]. However, it is important to note that all composites exhibit Type I deviations of the experimental points in relation of theoretical model. Hahn [4] associates this deviation to the absorption of water molecules in two distinct phases. One phase is associated to the polymeric matrix. The water molecules are bounded to the matrix, and thus contribute to the swelling of the composite due to water absorption. The other is associated with the occupation by water molecules of the free volume, with no correlation to the composite's swelling.

Studies performed by Pritchard et al. [15] on unsaturated polyester resin laminated composites reinforced with fiberglass presented values of 1.1% and 8.1×10^{-7} mm²/s for M_∞ and D, respectively. The fibers of the laminate were oriented at 10° and the aging temperature was 30°C. Imaz et al. [16] found values of 1.2% and 1.04×10^{-7} mm²/s for M_∞ and D, respectively, in studies with epoxy resin laminated composites reinforced with carbon fibers at 20°C.

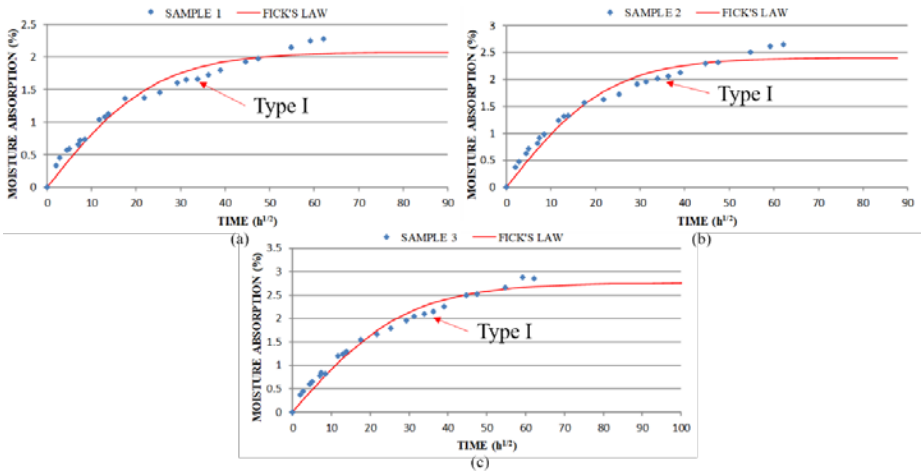

Figure 13: Results of moisture absorption versus square root of aging time for samples (a) 1; (b) 2 and (c) 3.

Table 5: Water absorption parameters.

SAMPLE	M_∞ (%)	D (10^{-7} mm²/s)	r²
1	2.07	4.33	0.95
2	2.41	4.15	0.96
3	2.75	2.66	0.97

The results of the sonic test for the Young's modulus, obtained for aging times corresponding to the linear region of the graphs of FIGURE 2 and before the Type I deviation, are shown in FIGURE 3. In a comparative way, it was possible to observe that the Young's modulus of the samples 1 and 2 decrease at the first measurement after the beginning of aging. After that, the Young's modulus values remain almost constant until the end of the test. The sample 3 also shows a decrease in the Young's modulus as a function of aging time, but there was no systematic variation on the behavior. Therefore, for this sample the data are not conclusive and only shows a decreasing tendency, as seen in FIGURE 3c.

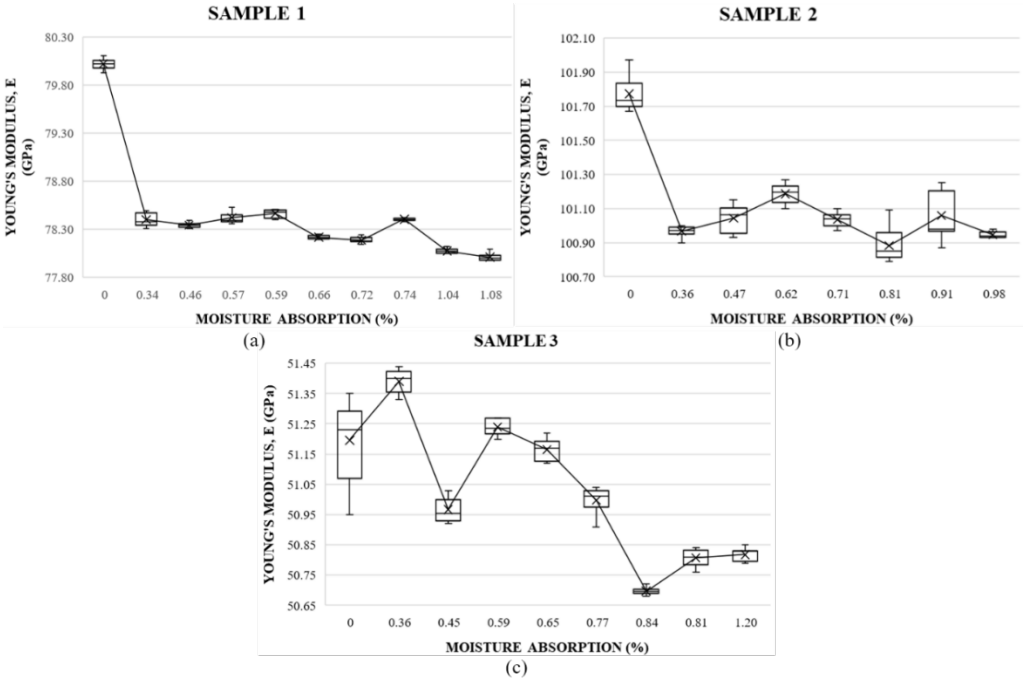

Figure 14: Results of Young's modulus of samples (a) 1; (b) 2 and (c) 3.

The damping factor of the samples are shown in FIGURE 4. It was possible to observe an increase of damping factor values for all samples in the first hours of aging time. After that, and throughout the aging period, the values tend to be constant. Again, sample 3 presented only a tendency, but without a systematic variation.

The Young's modulus and damping factor variations observed in this work are in line to those reported for a polyester-sponge gourd composite [17]. That is, both properties changed while water absorption did not reach the saturation point. The Young's modulus of polyester-sponge gourd composite decreased in the first hour of the aging while the damping factor value followed the opposite direction, increasing at the first hours of aging, as was also observed in this work.

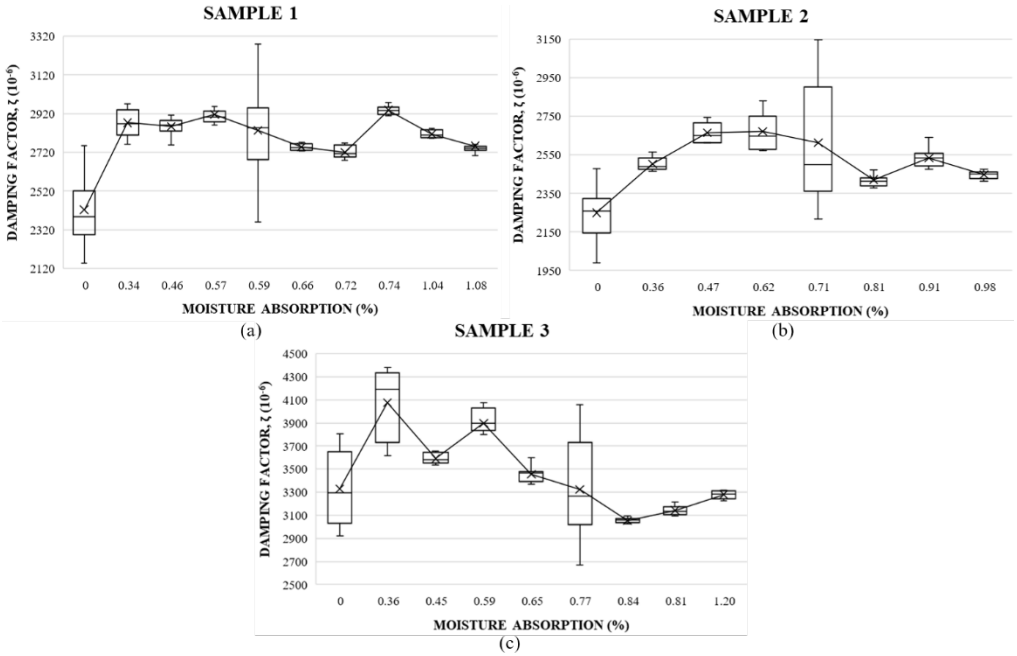

Figure 15: Results of damping factor of samples (a) 1; (b) 2 and (c) 3.

FIGURES 5 to 7 show the mosaics obtained by SEM from the cross section of the composite samples. The laminas of each sample are identified and it was possible to observe that the laminates have many internal defects (pores and voids). From the images obtained by optical microscopy, it was possible to identify that the carbon fiber layers do not have constant thickness along the width of the composite. TABLE 3 shows the values of the volumetric fractions of epoxy matrix, fibers and voids of the samples.

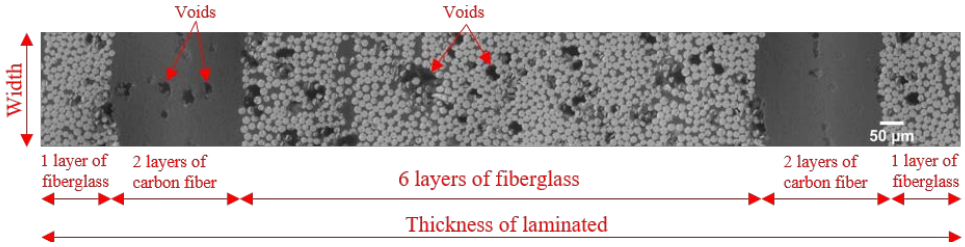

Figure 16: Image of SEM showing voids and internal defects on sample 1.

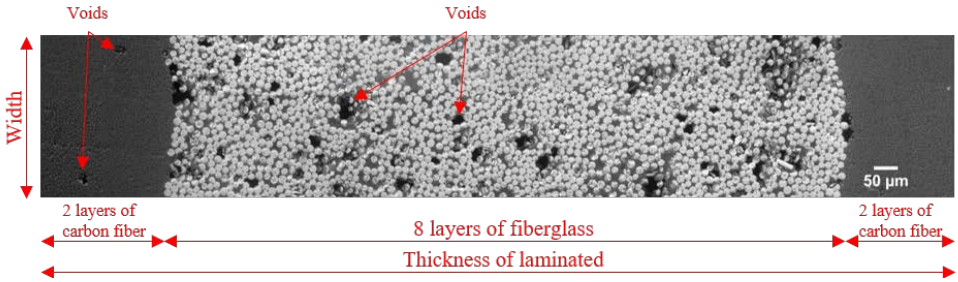

Figure 17: Image of SEM showing voids and internal defects on sample 2.

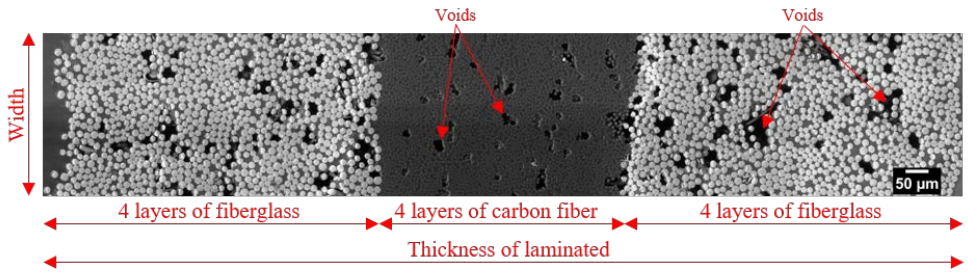

Figure 18: Image of SEM showing voids and internal defects on sample 3.

Table 6: Volume fraction of fibers, matrix and voids from SEM images.

SAMPLE	V_m (%)	V_{cf} (%)	V_{fg} (%)	V_v (%)
1	39.75	11.94	43.49	4.82
2	45.89	10.45	40.29	3.38
3	36.71	12.90	44.11	6.28

TABLE 3 illustrates that all samples have similar volumetric fractions of fibers and resin. Thus, it is important to note that the absolute values of the Young's modulus of the samples showed in FIGURE 3 should be similar too, according to the rule of mixtures describing the behavior of composites reinforced with unidirectional fibers [1,2]. However, the results of the unaged samples showed distinct Young's modulus values. The possible reason for this behavior is associated to differences of the type of fiber placed at the top surface of the laminate, hit by the dart (FIGURE 1).

In fact, the results shown at FIGURE 3 show a decrease of Young's modulus from laminate 2 to 1 and to 3. Regarding the lamina stacking sequence for these laminates, it can be seen from TABLE 1 that composite 2 has carbon fiber placed at the outer laminas, composite 1 has once glass fiber lamina followed by one carbon fiber lamina, and composite 3 has four glass fiber laminas at their outer laminas. Thus, sample 3 should have a lower Young's modulus value than sample 2.

It seems, therefore, that the configuration used at this non-destructive test was not able to measure the bulk response of the composite, but only the response of the outer layers. It has to be pointed out, however, that the sonic test can be used to follow the variation of the properties with time, since comparative values can be accurately measured.

4. CONCLUSION

From the experimental results in this work, it was possible to conclude that the moisture absorption by the laminated composites followed the Fickian model and the values of the diffusion coefficient are in line to other similar studies.

The analysis of the microstructures showed a high volumetric fraction of voids, which may be the probable cause for high water absorption of the composites at the saturation point.

The values of Young's modulus as well as the damping factor of the samples were affected by the moisture absorption, indicating that there was plasticization of the polymeric resin. The stabilization of damping factor and Young's modulus along with the aging time seems to indicate that the aging of the composites due to water absorption was mainly of the physical type.

The absolutes values of the sonic test were influenced by the surface of the laminates and do not represent the properties of the bulk. Thus, the values found should be used only in a comparative way.

ACKNOWLEDGEMENTS

The authors acknowledge the support from the Brazilian Agency CNPq.

REFERENCES

[1] Chawla, K.K., 'Composite Materials', 3rd Edn (Springer Science & Business Media, New York, 2013).
[2] Kaw, A.K., 'Mechanics of Composite Materials', 2nd Edn (Taylor & Francis Group, New York, 2006).
[3] Mahieux, C.A., 'Environmental Degradation in Industrial Composites', 1st Edn (Elsevier Science, Oxford, 2006).
[4] Hahn, H.T., 'Hygrothermal damage in graphite/epoxy laminates', *Journal of Engineering Materials and Technology*. **109** (1987) 3-11.
[5] Ray, B.C., 'Temperature effect during humid ageing on interfaces of glass and carbon fibers reinforced epoxy composites', *Journal of Colloid and Interface Science*. **298** (2006) 111-117.
[6] Costa, M.L., Rezende, M.C. and Almeida, S.F.M., 'Effect of void content on the moisture absorption in polymeric composites', *Polymer-Plastics Technology and Engineering*. **45** (2006) 691-698.
[7] d'Almeida, J.R.M., Almeida, R.C. and Lima, W.R., 'Effect of water absorption of the mechanical behavior of fiberglass pipes used for offshore service waters', *Composite Structures*. **83** (2008) 221-225.
[8] Ashbee, K.H.G. and Wyatt, R.C., 'Water damage in glass fibre/resin composites', *Proc. Roy. Soc. A.* **312** (1969) 553-564.
[9] Shen, C.H. and Springer, G.S., 'Moisture absorption and desorption of composites materials', *Journal of Composite Materials*. **10** (1976) 2-20.
[10] McKague, Jr.E.L., Reynolds, J.D. and Halkias, J.E., 'Moisture diffusion in fiber reinforced plastics', *Journal of Engineering Materials and Technology*. **98** (1) (1976) 92-95
[11] Otani, L.B. and Pereira, A.H.A., 'Caracterização dos módulos elásticos de compósitos utilizando a técnica de excitação por impulso', *Informativo Técnico-Científico ITC-06/ATCP*. (2014).
[12] Otani, L.B., Pereira, A.H.A., Segundinho, P.G.A and Morales, E.A.M., 'Caracterização dos módulos elásticos de madeiras e derivados utilizando a técnica de excitação por impulso', *Informativo Técnico-Científico ITC-05/ATCP*. (2015).
[13] Goldstein, J.I, Newbury, D.E., Echlin, P., Joy, D.C., Fiori, C. and Lifshin, E., 'Scanning Electron Microscopy and X-Ray Microanalysis', 1st Edn (Plenum Press, New York, 1981).
[14] Devore, J. L., 'Probabilidade e Estatística para engenharia e ciências', 2nd Edn (Cengage Learning, São Paulo, 2014).
[15] Pritchard, G. and Speake, S.D., 'The use of water absorption kinetic data to predict laminate property changes', *Composites*. **18** (3) (1987) 227-232.
[16] Imaz, J.J., Rodriguez, J.L., Rubio, A. and Mondragon, I., 'Hydrothermal environment influence on water diffusion and mechanical behavior of carbon fibre/epoxy laminates', *Journal of Materials Science Letters*. **10** (1991) 662-665.
[17] Feiferis, S. and d'Almeida, J.R.M., 'Evaluation of water absorption effects on the mechanical properties and sound propagation behavior of polyester matrix-sponge gourd reinforced composite', *Journal of Composites and Biodegradable Polymers*. **4** (2016) 26-31.

DEVELOPMENT AND CHARACTERIZATION OF CARBON FIBER REINFORCED THERMOPLASTICS – PART A: PROCESSING, THERMAL AND RHEOLOGICAL PROPERTIES

Bruno J. Lopes (1), José Roberto M. d'Almeida (1)

(1) Department of Chemical and Materials Engineering, Pontifícia Universidade Católica do Rio de Janeiro, Brazil

https://doi.org/10.21452/bccm4.2018.13.04

Abstract

Carbon fiber reinforced ABS (Acrylonitrile Butadiene Styrene) was produced via extrusion with varying fiber content and length. Samples were prepared from neat ABS and mixtures containing 5% and 16.7% of carbon fiber with two different initial lengths (3 mm and 6 mm). In this initial study, the challenges of processing the material were investigated along with the determination of rheological and thermal properties of the final composite. For material characterization and property evaluation, Fourier-Transform Infrared Spectroscopy (FTIR), Thermogravimetric Analysis (TGA) and capillary rheology were used. Matrix degradation was observed at low processing temperatures. Results showed correlation between process additives and composite properties, mainly in thermal stability and actual fiber content. Increasing fiber content showed positive effects on thermal stability. Process additives and longer fiber lengths resulted in higher actual fiber contents. Rheological properties seemed largely unaffected mostly due to poor fiber/matrix interfaces.

Keywords: Composites; Carbon fiber; ABS; Extrusion, Additive Manufacturing.

1. INTRODUCTION

Much has been developed in the field of composite materials in the last decades. Researchers have found ways to make structural components faster and cheaper than ever before [1–4]. The development of thermoplastic matrix fiber reinforced composites broadens the range of applications and processing techniques for composite materials borrowing much from the know-how developed for polymers.

The benefits of advanced fibers reinforced in common thermoplastics, such as ABS, are very attractive. These benefits are especially attractive to novel processes like additive manufacturing, which usually rely on polymers as feedstock, limiting its breadth of ability. The change to fiber reinforced composite feedstock has been already proven to revolutionize the additive manufacturing industry [5–8]. The continued development of even more capable materials will only make this revolution come faster.

The objective of this paper was to produce carbon fiber reinforced ABS, identify the challenges of processing this composite via extrusion and characterize its thermal and rheological properties and how they vary with two different fiber contents and lengths.

2. EXPERIMENTAL

2.1. Material processing

For the initial material processing, pellets were produced mixing chopped carbon fiber (Tenax®-J HT C261, from Toho Tenax America, Inc.) in two different lengths (3 mm and 6 mm) and ABS GP-35 (Terluran® GP-35, from INEOS Styrolution) at two weight percentages (% wt). The 5% wt mixtures were initially processed as tests for setup and the 16.7% wt mixtures were processed based on previous works from Love et al. [6] and Tekinalp et al. [7] that indicates the ideal content of carbon fiber in ABS for 3D printing is between 13% and 20%. In some mixtures, grape seed oil was added during mixing for improved processability, as seen in Table 1.

Each mixture was extruded using a twin-screw extruder (Leistritz ZSE 18 MAXX) at 200°C, 500 RPM and kg/h. The subsequent filaments were then water cooled and chopped to produce pellets.

For mechanical testing, filaments were extruded from each mixture's pellets using a micro extruder (Xplore Micro Compounder MC5) at 160 RPM and maximum force of 700 N. Three different zones were used to create a temperature ladder, at 230°C (entry), 210°C and 200°C (exit).

Table 35: Composition of each of the produced mixtures and its nominal % wt of fibers.

Mixture	ABS	Carbon Fiber (CF)	CF length	% wt CF
I	1000 g	-	-	-
II	500 g	25 g	3 mm	5%
III	207.2 g	10.6 g	3 mm	5%
IV	1000 g	200 g	3 mm	16.7%
V	1000 g	200 g	6 mm	16.7%

2.2. Fourier Transform Infrared Spectroscopy (FTIR)

The main goal with the FTIR analysis was to evaluate the possibility of degradation occurring in the polymeric matrix during processing. Initially, samples of neat ABS were extruded in two different temperatures (180°C e 220°C) and the resulting pellets, tested. The data obtained was then used to define extrusion temperatures.

Afterwards, a sample from each mixture was analyzed. At this point, the objective was to determine if the presence of carbon fiber caused any abnormal effects on the materials' behavior.

All analysis were performed in a Perkin Elmer 100 FT-IR absorption spectrophotometer in the medium infrared region, with data collected in the range of 4000 to 450 cm^{-1} using ATR sampling at room temperature.

2.3. Rheology

A capillary rheometer was used to verify the effects of different contents and lengths of carbon fiber to the viscosity of the composite.

All tests were performed using a Göttfert Rheograph 25 with capillary dimensions of 30 mm (length) by 2 mm (constant section diameter). Test conditions were of 240°C and shear rate ranging from 12 to 1000 s^{-1}.

2.4. Thermogravimetric Analysis (TGA)

Thermogravimetric analysis served two main purposes. Firstly, it was used to determine actual carbon fiber content (% wt) in the extruded pellets of each mixture. Secondly, using different cooling rates, it was possible to observe the decomposition kinetics occurring in each mixture at high temperature as well. Additionally, grape seed oil was also tested to evaluate its degradation at high temperatures.

For determination of actual carbon fiber content and grape seed oil degradation, a fixed cooling rate of 10°C/min. from room temperature up to 700-900°C under Nitrogen atmosphere was used.

For the decomposition kinetics, three cooling rates were used: 10, 20 and 30°C/min. Runs were performed from 50°C to 750°C, also under Nitrogen atmosphere. Then, for each mixture, a graph relating heating rates with degradation temperature at defined decomposition levels, was plotted. The decomposition levels analyzed were: 0.5%; 1.0%; 2.5%; 5.0%; 10.0% and 20.0%.

In each graph, a trend line representing the best fit for the data points for each decomposition level was plotted. From each trend line, the angular coefficient was extracted via linear regression and used to calculate the activation energy for each decomposition level. This calculation used the Flynn-Wall method [9] (Equation 1), using the table presented in Doyle [10].

$$E = \frac{-R}{b}\left[\frac{d\log\beta}{d\left(\frac{1}{T}\right)}\right] \quad (1)$$

where E is the activation energy (J/mol), R is ideal gas constant (8,314 J/mol K), T is the decomposition temperature (K), β is the heating rate (°C/min) and b is a constant determined via the iterative process described in detail in [9] and [10]. The derivative term inside the brackets is the angular coefficient of the trend lines.

3. RESULTS AND DISCUSSION

3.1. Matrix Degradation

FTIR spectra showed signs of degradation of the ABS polymer at temperatures over 200°C. This can be observed by the presence of a peak, meaning lower transmittance, in the region between 1690 cm^{-1} and 1800 cm^{-1} (Figure 1). This region is related to the stretching of C=O bonds, typically associated with carbonyl. The presence of this group in the spectrum of the material indicates that an oxidation reaction occurred, since no oxygen is present in the molecular structure of ABS.

Based on these results, extrusion temperature was set at 200°C for all mixtures. This temperature was set as a compromise between polymer degradation and viscosity, to make mixing of all components possible inside the extruder with few property losses.

Further analysis of the spectra showed that neither fiber content nor length significantly influenced degradation of the matrix.

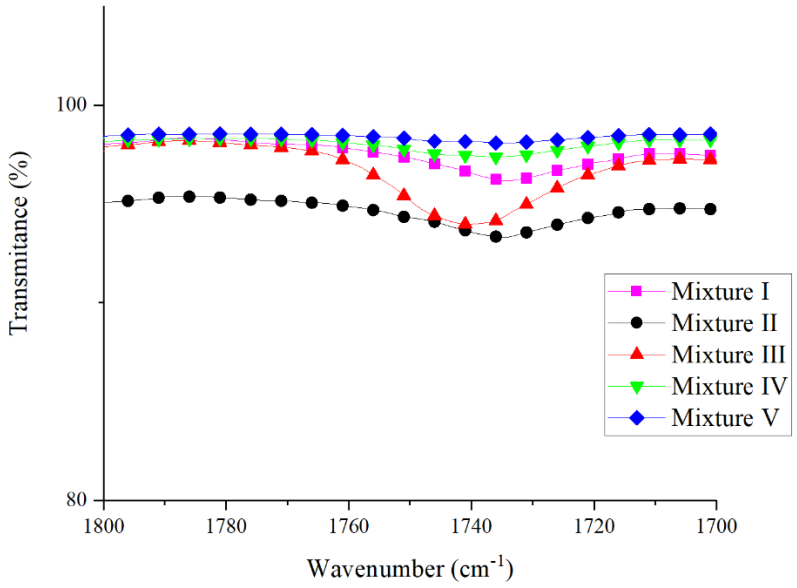

Figure 78: Comparison between mixtures in the range of the spectra associated with degradation

3.2. Thermogravimetric Analysis

Table 2 shows the results for the thermogravimetric analysis performed on each sample, including the grape seed oil. Results show no significant variation between mixtures but shows that the grape seed oil has lower onset and temperature at the inflection point, indicating a lower degradation threshold.

Table 36: Results of the TGA analysis for the mixtures and the grape seed oil

Mixture	Sample weight (mg)	Onset X (°C)	Onset Y (%)	Temperature at inflection point (°C)	Rate at the inflection point (%/min)
I	22.313	419.36	976.672	469.98	-155.786
II	20.773	426.15	970.366	476.17	-149.419
III	12.632	419.37	961.493	450.95	-141.667
IV	17.874	420.94	979.978	459.2	-131.275
V	13.801	428.98	964.327	474.85	-156.269
Oil	2.18	399.86	81.722	428.42	-15.426

3.2.1. Thermal Stability

For low degradation levels, possible multiple reaction mechanisms make it inadequate to use the Flynn-Wall method for calculating the activation energy. This can be due to humidity evaporation or volatile loss during early stages of degradation. In higher degradation levels, other phenomena occur and also indicate the presence of multiple simultaneous reaction mechanisms. For these reasons, only the 5.0% and 10.0% degradation levels were used for activation energy calculations.

From the values calculated (Table 3), it is possible to observe that the thermal stability is slightly affected by the contents of the mixtures. All values are in the same order of magnitude of what can be found in the literature [11].

However, if analyzed closely, it is possible to identify a trend in activation energy variation among the five mixtures (Figure 2). Once carbon fiber is introduced, in mixture II, activation

energy increases indicating improved thermal stability. With mixture III, which has grape seed oil in its composition, activation energy falls to its lowest. Then, with a major increase in carbon fiber % wt, activation energy increases again, remaining relatively stable even with the longer fibers in mixture V.

Table 37: Activation Energies for each mixture at the 5% and 10% degradation levels

	Activation Energy *E* (kcal/mol)				
	Mixture				
Degradation level (%)	I	II	III	IV	V
5.0	33.1	53.4	25.7	37.5	34.8
10.0	33.4	44.0	29.6	35.0	33.7

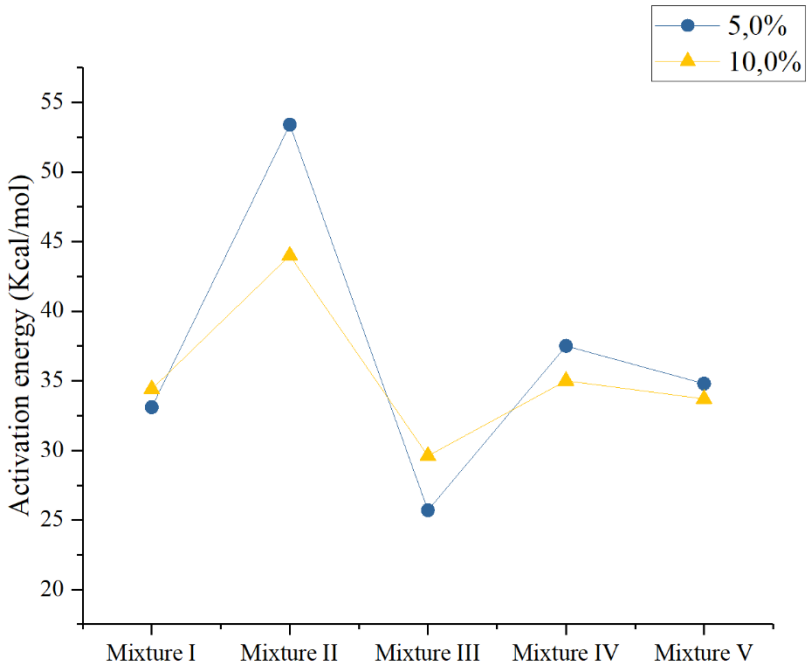

Figure 79: Activation energy plot for each mixture at the 5% and 10% degradation levels

3.2.2. Actual Fiber Content

As seen in Hull et al. [12], actual fiber content can vary from the estimated value due to process losses. The actual fiber content in each mixture was determined as the residual mass at the end of each TGA run. For neat ABS, the residual mass was zero, as seen in Figure 3, hence any remaining material can be related to the presence of carbon fiber.

It can be observed in Table 4 that the introduction of grape seed oil greatly improved the actual carbon fiber content. Fiber length also improved fiber content, with mixture V almost reaching its nominal value.

Mixture III showed a value higher than nominal. A possible explanation lies in the fact that the addition of grape seed oil acted as a lubricant, loosening fibers stuck to the feeding tube of the extruder, causing more fibers to enter the mixture.

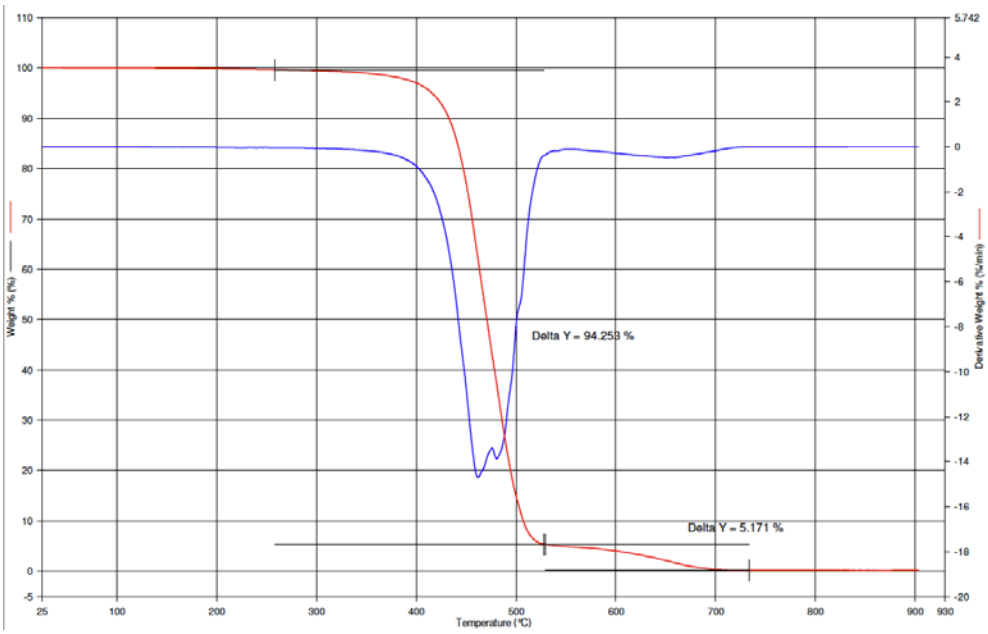

Figure 80: TGA thermogram for neat ABS showing zero residual weight

Table 38: Comparison between nominal fiber content and actual fiber content after processing for each mixture

Mixture	Grape seed oil % wt (%)	Carbon Fiber length (mm)	Nominal % wt CF (%)	Actual % wt CF (%)
I	-	-	0	0
II	-	3	5	3.1
III	1	3	5	5.2
IV	1	3	16.7	13.2
V	1	6	16.7	16.5

3.3. Viscosity

From Figure 4, it is possible to observe that viscosity was largely unaffected by the presence of carbon fibers and/or grape seed oil. Small variations do occur, as expected, but they do not represent a major change in absolute viscosity value and on its behavior with increasing shear rates. Ajinjeru et al. [13] found variations up to 50% in viscosity values in similar composites. The difference in results in this case can be attributed to a poorer interface between matrix and fibers in the present material, which has been previously observed for similar materials [14].

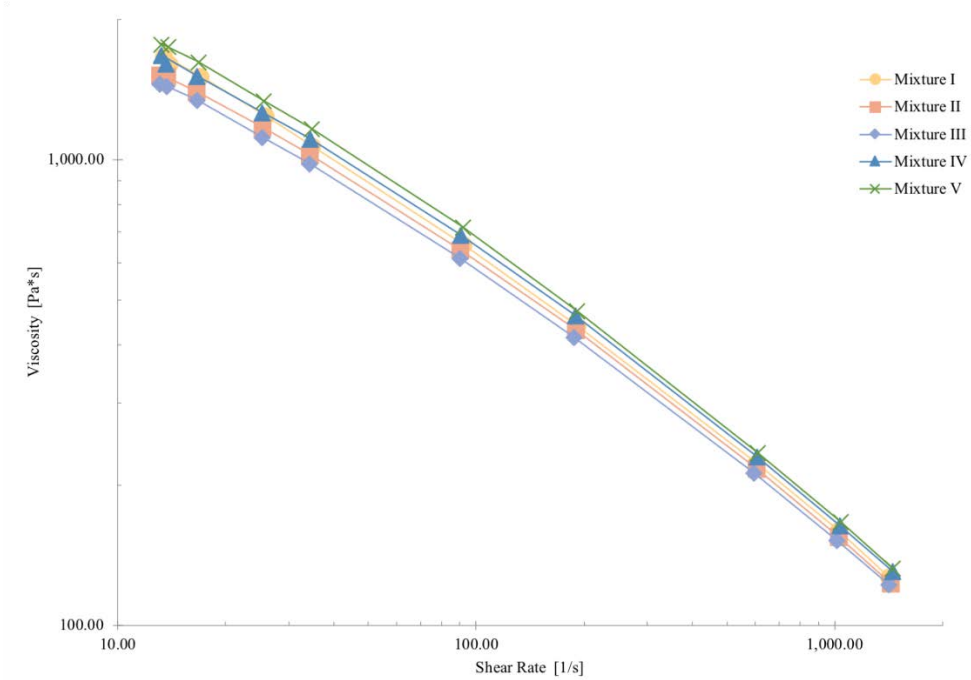

Figure 81: Graph showing the behavior of viscosity values with increasing shear rate

4 CONCLUSIONS

Carbon fiber reinforced ABS was successfully produced with varying fiber content and fiber length via extrusion. Degradation of the polymeric matrix was detected at temperatures as low as 220°C during processing, below manufacturer's recommended temperatures. Thermogravimetric analysis (TGA) showed that the composite's thermal stability is influenced by the % wt of carbon fiber and presence of processing additives, such as the grape seed oil used. Thermal stability increased with the increase in carbon fiber content, whereas the presence of grape seed oil caused a decrease in activation energy. Also, with the aid of TGA, the actual post processing fiber content was found to be dependent on the presence of grape seed oil and fiber length, with mixtures processed with this additive and longer fibers showing higher actual fiber contents. Viscosity seemed largely unaffected by the introduction of carbon fiber, indicating a poor interface between the matrix and reinforcement phase.

From a processing perspective, results show a strong dependence of parameters such as temperature during initial compounding of the material on the final properties. Also, for mechanical mixing processes, additives that act as lubricants are paramount for avoiding waste of material and low actual fiber content in the final composite. That said, however, the properties of additives can and most likely will affect the properties of the material being processed. The negligible effect of the fiber content on the rheological behavior shows that no special consideration is needed when applying high shear rates on the composite, when compared to neat ABS.

ACKNOWLEDGEMENTS

The authors acknowledge the support from the National Council for Scientific and Technologic Development (Conselho Nacional de Desenvolvimento Científico e Tecnológico - CNPq).

REFERENCES

[1] P. Feraboli, E. Peitso, F. Deleo, T. Cleveland and P. B. Stickler, 'Characterization of Prepreg-Based Discontinuous Carbon Fiber/Epoxy Systems,' Journal of Reinforced Plastics and Composites, vol. 28, no. 10/2009, pp. 1191-1214, May 2008.

[2] P. Feraboli, E. Peitso, T. Cleveland, P. B. Stickler and J. C. Halpin, 'Notched behavior of prepreg-based discontinuous carbon fiber/epoxy systems,' Composites , vol. Part A, no. 40, pp. 289-299, March 2009.

[3] P. Feraboli, E. Peitso, T. Cleveland and P. B. Stickler, 'Modulus Measurement for Prepreg-based Discontinuous Carbon Fiber/Epoxy Systems,' Journal of Composite Materials, vol. 43, no. 19/2009, pp. 1947-1965, August 2009.

[4] P. Feraboli, F. Gasco, B. Wade, S. Maier, R. Kwan, A. Masini, L. DeOto and M. Reggiani, 'Lamborghini Forged Composite technology for the suspension arms of the Sesto Elemento,' in ASC Conference, Montreal, 2011.

[5] L. J. Love and C. Duty, 'Cincinnati Big Area Additive Manufacturing (BAAM),' Oak Ridge, TN, 2015.

[6] L. J. Love, V. Kunc, O. Rios, C. E. Duty, A. M. Elliot, B. K. Post, R. J. Smith and C. A. Blue, 'The importance of carbon fiber to polymer additive manufacturing,' J. Mater. Res., vol. 29, no. 17, 14 Sep 2014.

[7] H. L. Tekinalp, V. Kunc, G. M. Velez-Garcia, C. E. Duty, L. J. Love, A. K. Naskar, C. A. Blue and S. Ozcan, 'Highly oriented carbon fiber-polymer composites via additive manufacturing,' Composites Science and Technology, vol. 105, pp. 144-150, 16 Oct 2014.

[8] The Boeing Company, 'One For The Record Books,' 26 August 2016. [Online]. Available: http://www.boeing.com/features/2016/08/record-books-08-16.page. [Accessed 30 November 2016].

[9] J. H. Flynn and L. A. Wall, 'A quick, direct method for the determination of activation energy from thermogravimetric data,' Polymer Letters, vol. 4, no. 5, pp. 323-328, May 1966.

[10] C. D. Doyle, 'Kinetic Analysis of Thermogravimetric Data,' Journal of Applied Polymer Science, vol. V, no. 15, pp. 285-292, May/June 1961.

[11] M.-H. Yang, 'The thermal degradation of acrylonitrile-butadiene-styrene terpolymer under various gas conditions,' Polymer Testing, vol. 19, no. 1, pp. 105-110, February 2000.

[12] E. Hull, W. Grove, M. Zhang, X. Song, Z. J. Pei and W. Cong, 'Effects of Process Variables on Extrusion of Carbon Fiber Reinforced ABS Filament for Additive Manufacturing,' in ASME 2015 International Manufacturing Science and Engineering Conference, Charlotte, North Carolina, 2015.

[13] C. Ajinjeru, V. Kishore, X. Chen, J. Lindahl, Z. Sudbury, A. A. Hassen, V. Kunc, B. Post, L. Love and C. Duty, 'The Influence of Rheology on Melt Processing Conditions of Amorphous Thermoplastics for Big Area Additive Manufacturing (BAAM),' in Proceedings of the 27th Annual International Solid Freeform Fabrication Symposium - An Additive Manufacturing Conference, Austin, TX, 2016.

[14] F. Ning, W. Cong, Z. Hu and K. Huang, 'Additive manufacturing of thermoplastic matrix composites using fused deposition modeling: A comparison of two reinforcements,' Journal of Composite Materials, vol. 51, no. 27, pp. 3733-3742, 1 November 2017.

DEVELOPMENT OF PARTIALLY BIODEGRADABLE FOAMS FROM PP/HMSPP BLENDS WITH NATURAL AND SYNTHETIC POLYMERS

Cardoso, E. C. L.(1), Scagliusi, S. R.[1], Parra, D.F.[1]and Lugão, A. B.[1]

(1) Center for Chemical and Environmental Technology (CQMA), Nuclear and Energy Research Institute, S. Paulo, Brazil

https://doi.org/10.21452/bccm4.2018.13.05

Abstract

Polymers are used in various applications and in different industrial areas providing enormous quantities of wastes in environment. Among diverse components of residues in landfills are polymeric materials, including Polypropylene, which contribute with 20 to 30 % of total volume of solid residues. As polymeric materials are immune to microbial degradation, they remain in soil and in landfills as a semi-permanent residue. Environmental concerning in litter reduction is being directed to renewable polymers development for manufacturing of polymeric foams. Foamed polymers are considered future materials, with a wide range of applications; high density structural foams are specially used in civil construction, in replacement of metals, woods and concrete with a final purpose of reducing materials costs. At present development, it was possible the incorporation of PP/HMSPP polymeric matrix blends with sugarcane bagasse and PHB in structural foams production. Gamma radiation degradation, at 50, 100, 150, 200 and 500 kGy showed effective for biodegradability induction. Irradiated bagasse blends suffered surface erosion, in favor of water uptake and consequently, a higher biodegradation in bulk structure.

Keywords: PP/HMSPP; PHB; sugarcane bagasse; gamma-radiation; biodegradability

1. INTRODUCTION

Foamed polymers are future materials, with a comprehensive application field; they are especially used to improve structures appearance or to reduce costs of involved material, besides their applications in construction market. In summary, structural foams (high density foams with density higher than 320 kg/m^3), have major applications in automotive industry, in heavy equipment and in civil construction, where they can replace wood, metals and even concrete. Most of thermoplastics can be extruded in order to obtain structural foams and commercial activities are concentrated in thermoplastic of lower cost, as Polypropylene (PP) [1]. PP suffers simultaneously chain-scission and crosslinking, when subjected to ionizing radiation; both chemical phenomena are able to induce changes capable to enhance its use in various applications and in different processes. PP is a linear hydrocarbon polymer, originated from a cheap petrochemical material

and shows an easy processing for obtaining various products. Consequently, the enormous production and further use lead to an accumulation in environment, because they are not easily degraded by microorganisms and present a serious pollution risk to flora and fauna. In general, polymers fossil based are very bio-resistant, once they have just carbon atoms in backbone chain with non-hydrolysable functional group. Non-degradable plastics accumulate in environment at a rate of 25 million per year. A few possibilities have been considered in order to minimize environmental impact caused by the use of conventional polymers [2,3,4].

When transforming structural foams in biodegradable ones two concepts are fundamental to know: Biodegradation: physical or chemical change, caused by microorganisms action, under heat, moisture, light, oxygen, organic nutrients and Biodegradable Polymers: polymers where degradation results from the action of microorganisms of natural occurrence, as: bacteria, fungus and algae, able to be consumed in weeks or months, under biodegradation favorable conditions [2,3,4]. Biodegradable materials can be originated from natural resources or raw-materials, such as: starch, corn, sugarcane bagasse or even oil [5]; biodegradable polymers are provided with some properties as non-toxic and capable to keep an effective mechanical integrity up to their degradation. This paper aims to the assessment of biodegradability characteristics shown by foams from PP/HMSPP with synthetic and natural polymers blends. PP is a semi-crystalline thermoplastic, isotactic, with low melt strength; in order to impart a higher melt strength to PP, it was subjected to gamma-radiation, 12.5 kGy dose, acetylene environment. 50 % PP/HMSPP mixture is the ideal base for preparing structural foams [6]. Synthetic polymer involved in this study comprised Poli(hydroxybutirate) – PHB and sugarcane bagasse, as raw-material of agricultural origin.

The present work aimed to investigate the influence of gamma radiation on biodegradability of PHB and sugarcane bagasse PP/HMSPP based foams, in terms of thermal behavior by TG/DTG, mass loss via soil burial test and mechanicals assessments.

2. EXPERIMENTAL PROCEDURE

Materials

Polypropylene (PP): H-503 from Braskem, 3.5 g.(10 min)$^{-1}$ melt index.

High Melt Strength Polypropylene (HMSPP): PP subjected to gamma irradiation, at 12.5 kGy, under acetylene environment.

PP/HMSPP, 50 %.

PHB: Poli(hydroxibutirate), aliphatic polyester, from renewable source: PHB Industrial S/A, Biocycle®, dried at 60 ºC for 12 h before processing.

Sugarcane bagasse: Caçapava, in S.Paulo state; previously washed in tap water, outdoor dried but protected from bad weather, for 2 months. Dried in air-circulating oven, at 60ºC, for 24 h; further crushed in a blender and kept at 60 ºC in oven, for more 4 h, before segregation in 150 µm molecular sieves.

Carbon dioxide): eco-friendly gas, used as physical blowing agent (PBA), to produce a cellular structure by foaming process [7,8].

Blends preparation

Blends were prepared according to Table 1. PP/HMSPP was used as base for PHB and sugarcane bagasse, by varying both contents from 10, 15, 30 and 50%.

Blends were first processed by melting extrusion process, using a twin-screw extruder Haake Rheomex L/D-25.Temperature profile from feed zone to die was 175 to 200 ºC, 100 rpm screw speed. After exiting die, the extrudates were air-cooled before being granulated in a Primotecnica pelletizer.

Table 1: Designation and composition of blends

Materials	PP/HMSPP (wt %)	PHB (wt %)	SCB* (vol %)
PP/HMSPP	100.0	---	---
PP/HMSPP – PHB	90.0	10.0	---
PP/HMSPP – PHB	85.0	15.0	---
PP/HMSPP – PHB	70.0	30.0	---
PP/HMSPP – PHB	50.0	50.0	---
PP/HMSPP – SCB	90.0	---	10.0
PP/HMSPP – SCB	85.0	---	15.0
PP/HMSPP – SCB	70.0	---	30.0
PP/HMSPP – SCB	50.0	---	50.0

*SCB: Sugarcane Bagasse

Foaming

Processed samples presented in Table 1 were foamed by using CO_2 as Physical Blowing Agent (PBA),within 175 to 200 ºC profile temperature, 4 mm circular die, 30 rpm and 30 bar pressure. Samples were collected directly from die to be further investigated.

3. CHARACTERIZATION

Thermogravimetry (TG/DTG): It was used Thermogravimetric Analyzer TGA/SDTA 851 Mettler-Toledo, with thermo-balance, for evaluating sample mass variation in function of temperature, according to ASTM E1641 [9] method. Tests were programmed according to: nitrogen environment, 50 $mL.min^{-1}$ flow rate, within 25 to 600 ºC, 10 $ºC.min^{-1}$ heating rate. Samples were inserted in aluminum pan, 40 µL capacity, 99.999 % purity degree nitrogen and oxygen level lower than 1 ppm (White Martins). Thermogravimetric analyzer was used to obtain thermal degradation and mass loss (residue).

Tensile force and elongation at break: Mechanical essays were accomplished in a TA-HDi (Stable Micro Systems Texture Analyzer) texturometer, 5 kg (50 N) load cell, operating with a 10 mm/sec deformation rate, at room temperature. The specimen dimension was 80 x 10 mm^2 denoting respectively the length and breadth for tensile evaluations.

Soil burial test: Soil burial test methods in plastics were established and standardized for assessing plastics resistance to microorganisms, in function of mass change [10,11,12]. The material is buried under controlled conditions of temperature (24º C) and relative humidity (80 %); typical analysis accomplished after soil burying is the evaluation of mass loss. Foamed samples aliquots were buried in 1,000 ml capacity beckers containing gardening specific inoculum with water content approximately 20 %, wt %. Recipients were kept in specific conditions of temperature and humidity (24º C ± 1º C/80 % relative humidity). Evaluations were accomplished

after 12 month soil burying, with samples carefully cleaned with brush and towel, before weighing in analytical digital balance BP210D Sartorius AG, RFA model. Mass variation rate was assessed in function of time, according to equation (1):

$$T(\%) = \frac{m_o - m_t}{m_o} \times 100 \quad (1)$$

Where m_o is sample initial mass, at t_o time, and m_t is sample mass at t time, after soil burying.

4. RESULTS AND DISCUSSION

Thermogravimetry (TG/DTG):

Sugarcane bagasse foams:

TG and DTG curves for bagasse foams presented in Table 1 are shown in Figures 1(a) and 1(b), respectively:

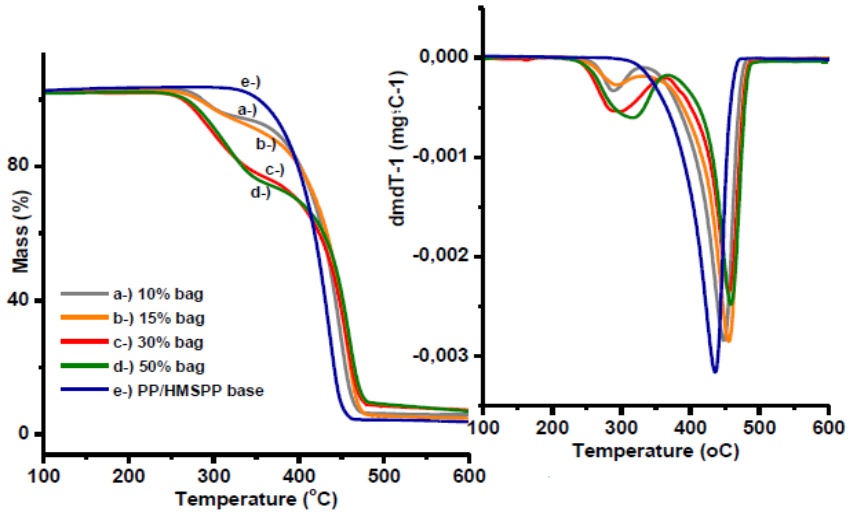

Figure 1(a): TG for sugarcane bagasse foams **Figure 1(b): DTG for sugarcane bagasse foams**

It occurs a first mass loss within room temperature and 250 °C, attributed to absorbed water or water bound to vegetal fiber, corresponding to approximately 4 % mass loss. Within 250 and 460 °C it occurs a mass loss attributed to thermal degradation of organic compounds, especially cellulose, hemicelluloses and lignin [13,14,15]. Hemicellulose is the component with lower thermal stability, within 200 to 260 °C degradation temperature followed by cellulose, within 240 to 350 °C. Lignin presents a higher thermal stability and it is thermally degraded within 280 to 500 °C. So, medium degradation temperature for sugarcane bagasse foams attained 460 °C, superior to that one found for PP/HMSPP polymeric base: 420 °C.

PHB foams:

TG and DTG curves for PHB foams presented in Table 1 are shown in Figures 2 (a) and 2(b), respectively:

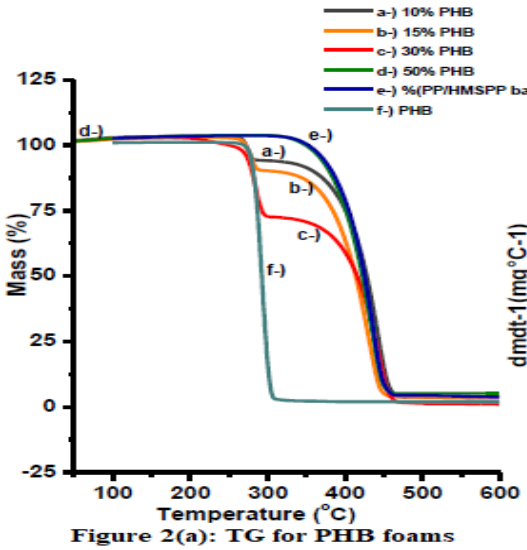

Figure 2(a): TG for PHB foams

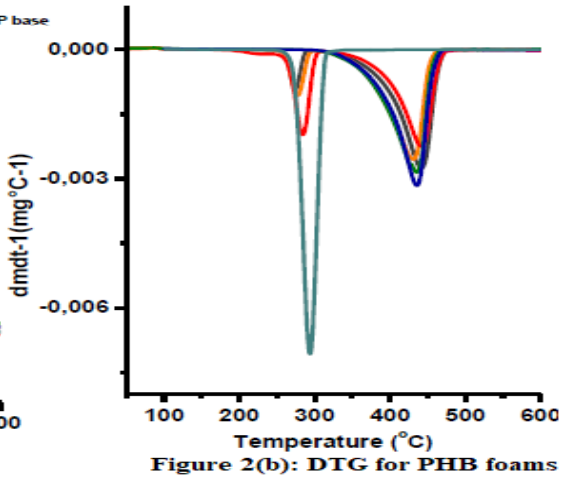

Figure 2(b): DTG for PHB foams

PHB appears to have two main overall degradation steps while compounds degradation is complex constituting of several processes. Whilst these results are suggestive that the addition of PHB to PP/HMSPP basis promotes PHB degradation, it does not, however, give a quantitative assessment of the overall stability of blends. As shown in Figure 2 (a), degradation of pure PHB is complete at 300 ºC. The lower weight loss is an indication that the blends are thermally more stable than PHB over a wider temperature range [16,17,18]. Thermal degradation of pure PHB and PP/HMSPP basis occurs through one step, characterised by a single peak on Figure 2(b).

Tensile force and elongation at break:

Sugarcane bagasse foams:

Mechanicals assessments for sugarcane bagasse foams are shown in Figure 3:

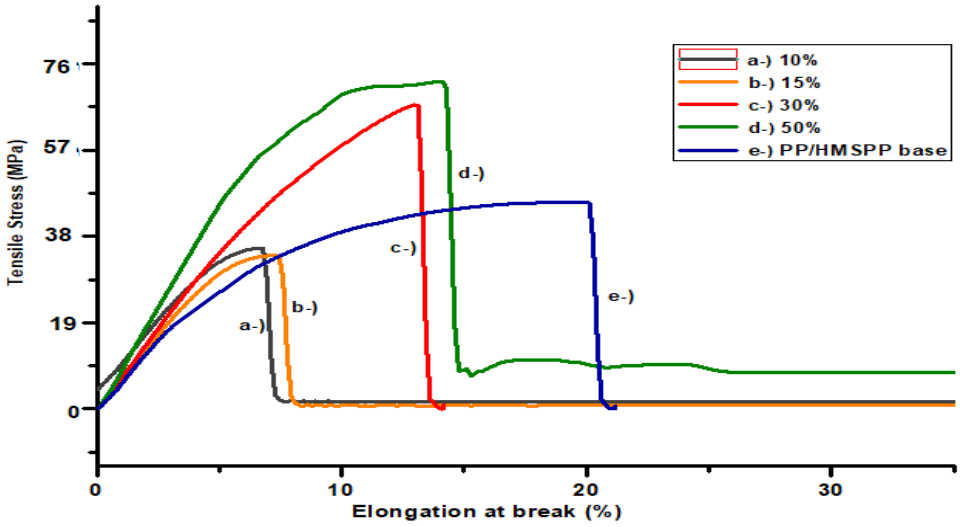

Figure 3. Mechanical behavior of sugarcane bagasse foamed compositions.

All sugarcane bagasse foamed compositions exhibited tensile stress values higher than that one presented by PP/HMSPP polymeric base, proportionally on increasing bagasse contents. So, it was ratified that sugarcane bagasse plays the role of reinforcing agent. Nevertheless, elongation at break for all sugarcane bagasse foamed compositions showed lower values when compared to PP/HMSPP base.

PHB foams

Mechanicals assessments for PHB foams are shown in Figure 4:

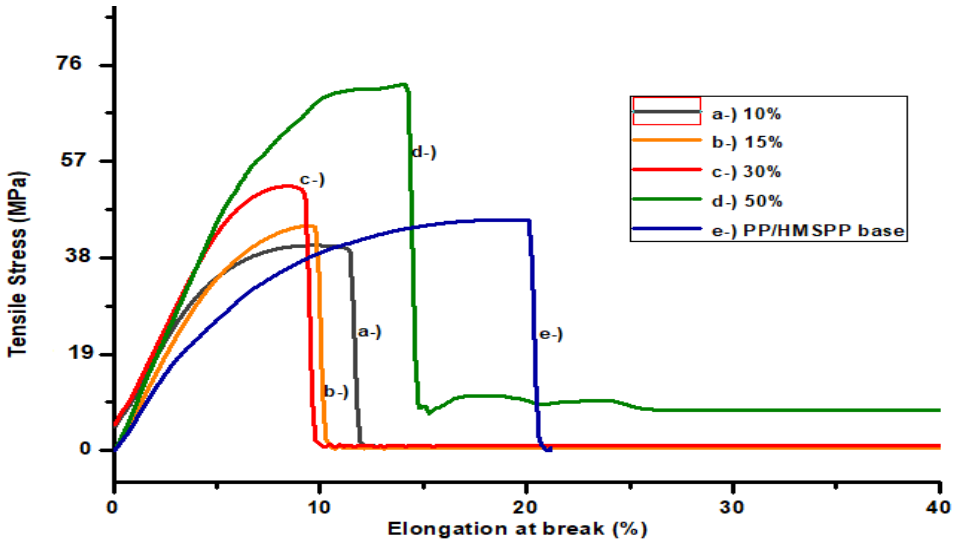

Figure 4. Mechanical behavior of PHB foamed compositions.

30 % and 50 % PHB foamed compositions showed tensile higher than that one found for PP/HMSPP base; elongation at break for all foamed PHB compositions presented values lower than that one found for PP/HMSPP base.

Soil burial test:

Prior to gamma-radiation treatment to induce biodegradability:

In Table 2 are shown mass loss for foamed compounds after 12 month – period of soil buried:

Table 2. Mass variation index for foamed compounds after 12 month-period soil buried

	Sugarcane bagasse foams	PHB foams
%		
10 %	21.30	0.10
15 %	22.50	0.12
30 %	29.20	0.16
50 %	32.40	0.19

Results shown in Table 2 indicate that just foamed sugarcane bagasse foams were susceptible to soil burial test after 12 months. PHB foamed compounds showed negligible results for soil burial test.

Gamma-radiation treatment:

All foamed samples were subjected to gamma radiation within 50, 100, 150, 200 and 500 kGy. At first, there were performed mechanicals tests, prior to soil burial tests, according presented in Figures 5 and 6, respectively.

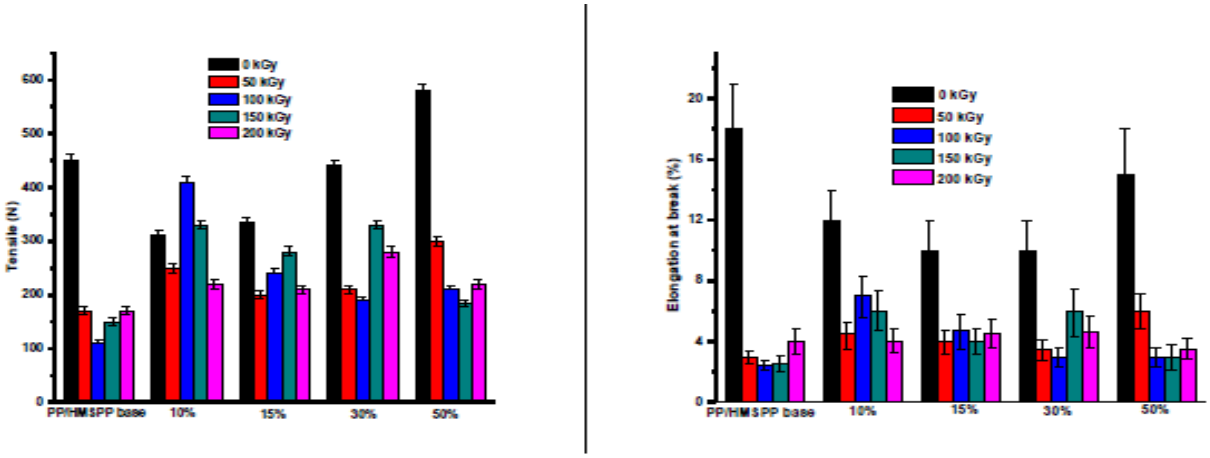

Figure 5.Tensile and Elongation at break for sugarcane bagasse foams after gamma- radiation at: 50, 100, 150 and 200 kGy.

Results presented in Figure 5 indicated that PP/HMSPP base showed susceptible to gamma radiation, with a visible reduction in tensile and elongation at break, when compared to sugarcane bagasse foams. It should be emphacized that 100 to 600 N range for Tensile Load corresponds to 12 to 75 MPa for Tensile Stress.

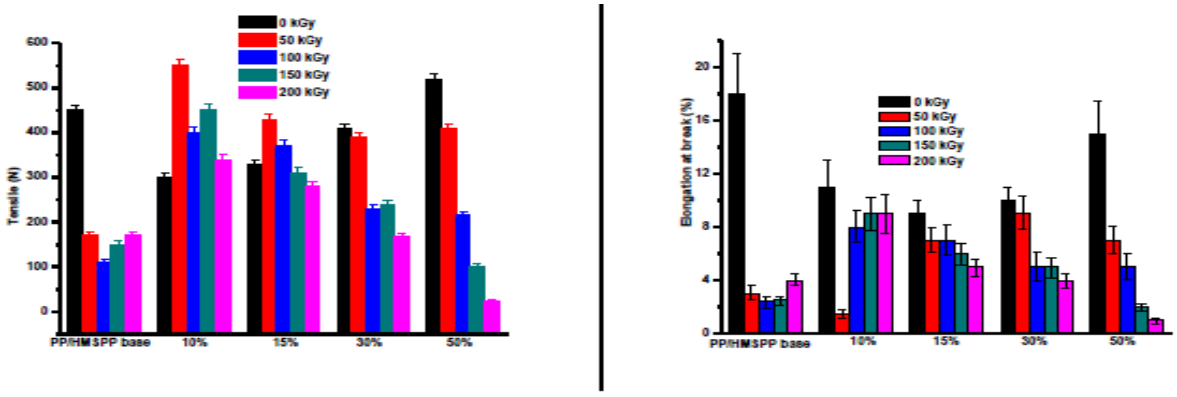

Figure 6. Tensile and Elongation at break for PHB foams after gamma-radiation at: 50, 100, 150 and 200 kGy.

Results presented in Figure 6 indicated that PP/HMSPP base showed susceptible to gamma radiation, with a visible reduction in tensile and elongation at break, when compared to PHB foams. It should be emphacized that 100 to 600 N range for Tensile Load corresponds to 12 to 75 MPa for Tensile Stress.

Soil burial tests in irradiated sugarcane bagasse and, PHB foams presented mass loss according depicted in Table 3:

Table 3. Mass variation index for foamed compounds gamma irradiated at 200 kGy and 500 kGy, after 12 month-period soil buried

%	Sugarcane bagasse foams 200 kGy	500 kGy	PHB foams 200 kGy	500 kGy
10	***	***	4.80	10.30
15	***	***	5.20	11.60
30	***	***	6.90	15.90
50	***	***	7.40	20.10

*** assessments prejudiced due to water uptake.

Sugarcane bagasse irradiated foams presented final values higher than initial ones due to surface erosion caused by gamma radiation; even impossible to quantify mass loss due to water uptake, the biodegradability will be imparted in these samples by micro- organisms action. Non irradiated PHB foams presented negligible values for mass loss, according to Table 2 ; even within 200 and 500 kGy doses PHB foams showed a slight biodegradability development. Nevertheless, PHB foams showed a higher mass loss when compared with PP/HMSPP polymeric base that showed a negligible mass loss equal to 1.9 %, even at 500 kGy and after one year of soil buried.

5 CONCLUSIONS

It is possible the incorporation of sugarcane bagasse and PHB in structural foams PP/HMSPP base and further turn them into partially biodegradable ones. Thermogravimetric tests presented expected results for sugarcane bagasse and PHB PP/HMSPP base foams. Mechanical essays proved that either natural polymer (sugarcane bagasse) as synthetic PHB one acted as reinforcing agent even after gamma-radiation imparted on them. PP/HMSPP polymeric base presented a expected negligible result of mass loss after one year of soil buried even after gamma-radiated at 500 kGy, proving non-biodegradable characteristic of fossil polymers. Non-irradiated sugarcane bagasse foams presented better biodegradability efficiency when compared to PHB foams, after one year of soil burial, even with soil burial measurements prejudiced due to water-uptake fostered in damaged surfaces; nevertheless, hydrolysis favored water inlet through damaged surfaces and consequently biodegradability by microorganism action.

ACKNOWLEDGEMENTS

The authors thank to Braskem, Nature Works, PHB Industrial and Celanese by raw- materials supply, IPEN/CNEN-SP and CNEN for their financial support through 0134.000411/2013-20 post doctorate process.

REFERENCES

[1] C. Longo, M.Savaris, M. Zani, R. M. Brandalise, A. M. C. Gris, ´Degradation Study of Polypropylene (PP) and Bi-oriented Polypropylene (BOPP)`. *Environment Materials Research* **14** (4)**, (**2011) 442-448.

[2] J. Arutchelvi; M. Sudhakar; A. Arkatkar; M. Doble; S. Bhaduriandp; V.Uppara, *Indian Journal of Biotechnology*, **7,** (2008) 9 – 22.

[3] Chandra, R; Rustgi, R., *Polym. Degrad. Stab.* **56, (**1997) 185.

[4] Y.Tokiwa, B. P. Calabia, C. U. Ugwu and S. Aiba, *Int. J. Mol. Sci*,**10**, (2009) 3722-3742.

[5] E. Chiellini; P. Cinelli; R. Solaro; M. Laus, `Thermomechanical Behavior of Poly(vinyl alcohol) and Sugarcane Bagasse Composites`, *Journal of Applied Polymer Science*, **92**, (2004) 426-432,.

[6] Lugão et al, `Process for preparing high melt strength polypropylene and crosslinked prepared therewith`, *U. S. Patent 20040171712***,** (2004).

[7] Ademar B. Lugão; Elizabeth C. L.Cardoso, Luis Filipe C. P. Lima, Beatriz Hustzler, Shinichi Tokumoto, `Characterization study of gamma-irradiated, high melt strength polypropylene`, *Nuclear Instruments and Methods in Physics Research, Section B: Beam interactions with materials and atoms, Ionizing Radiation and Polymers*, **208**, (2003) 252-255.

[8] Cardoso, E.C.L., `Desenvolvimento de espumas a partir de misturas poliméricas de PP linear e HMSPP`, *Thesis (MSC) – IPEN/CNEN, SP*, (2010).

] ASTM E 1641 – 07, *Standard Test Method for Decomposition Kinetics by Thermogravimetry.*

[10] Natalia Naime, `Embalagens ativas de fonte renovável`, *Dissertação, IPEN – Instituto de Pesquisas Energéticas e Nucleares, São Paulo,* (2010).

11] N. Lardjane et al, `Soil burial degradation of new bio-based additives`, *Journal of Vinyl and Additive Technology* **7 (2)**, (2011) 98-104.

[12] N. Vogelsager Jr et al, `Acompanhamento da Biodegradação em Solo por Propriedades Térmicas e Morfológicas`, *Revista Matéria*, **9**, **n.4**, (2004) 370 – 377.

[13] Seung-Hwan Lee, Siqun Wang, `Biodegradable polymers/bamboo fiber biocomposite with bio-based coupling agent`, *Composites: Part A***, 37, (**2006) 80 – 91.

[14] E. Chiellini, P. Cinelli, R. Solaro, M. Laus, `Thermomechanical Behavior of Poly(vinyl alcohol) and Sugar Cane Bagasse Composites`, *Journal of Applied Polymer Science,* **92**, (2004) 426-432.

[15] Amir Hooman Hemmasi, Ahmad Samariha, Asghar Tabei, Mohammad Nemati and Alireza Jkhakifirooz, `Study of Morphological and Chemical Composition of Fibers from Iranian Sugarcane Bagasse`, *American-Eurasian J. Agric. & Environ. Sci*., **11** (4): (2011) 478-481.

[16] Haffar, A.M.E.A., `Development of a biodegradable material based on Poly(3-hydroxybutyrate) PHB`, *Ph.D. Thesis, Martin-Luther University, Wittenberg, Germany*, (2002).

[17] Mochizuki, M.; Hirami, M., `Structural effects on biodegradation of aliphatic polyesters`, *Polym. Adv. Technol*. **8**, (1997), 203.

[18] E. Bugnicourt, P. Cinelli; A. Lazzeri; V. Alvarez, `Review of synthesis, characteristics, processing and potential application in packaging`, *Express Polymers Letters*, **18**, nr. 11, (2014) 791 – 801.

EFFECTS OF SILICA MICROPARTICLES IN GLASS FIBRE/EPOXY LAMINATES

Aluizio Heleno Ribeiro Junior [(1)], Juan Eduardo Gomez [(2)], Devin Wayne Hale [(2)], Maikson Luiz Passaia Tonatto [(1)] and Tulio Hallak Panzera[(1)]

(1) Centre for Innovation and Technology in Composite Materials, Department of Mechanical Engineering, Federal University of São João del Rei-UFSJ, Brazil

(2) Whitacre College of Engineering, Texas Tech University, United States

https://doi.org/10.21452/bccm4.2018.13.06

Abstract

Composites have been widely used in engineering applications due to high strength to weight ratios. A large amount of materials used in aeronautics is based on composite materials. This provides motivation to improve the mechanical properties of the existing composite materials. When a glass fibre laminate is subjected to bending stresses, maximum compressive and tensile stresses are generated at its sides of the surface beam. Rigid particles have been added into laminate composites specially to enhance their bending performance attributed to the matrix stiffness and interlaminar shear resistance increases. In order to better assess the enhancement mechanism provided by particle inclusions, this work investigates the incorporation of micro-sized silica on the top, bottom and both surfaces of glass fibre laminates, mitigating the interference of the interlocking effect. Three-point bending and impact test were performed to evaluate hybrid glass fibre composites containing 5, 7.5 and 10% by weight silica. Although the silica particles lead to increased compressive modulus of epoxy polymers, their positive effect on glass fibre composite under flexural loads was more evident on the bottom beam side subjected to maximum tensile stress. The incorporation of 7.5wt% silica microparticles on the bottom surface of the laminates achieved higher flexural behaviour and lower impact resistance.

1. INTRODUCTION

Composites have been used in a variety of applications in many sectors, especially in the aeronautical industry, due to the need to have strong mechanical properties in a lightweight material [1]. It is common knowledge that the aeronautic industry uses glass fibre composites on aircraft, and therefore this study focuses on glass fibre composites and the incorporation of silica particles on the surface of the laminate composites. The primary cause of delamination in composites that are in-service now is impact damage, involving reductions of residual strength by up to 60%. In fact, low impact tolerance is what limits the use of composite laminates.

Improvements have been made with the inclusion of micro/nano-particles into Glass Fibre Reinforced Composites (GFRCs) [2].

Some important reasons why glass fibre composites are being used in many fields today are because of their favourable mechanical properties and the low relative cost if used in mass production. Glass fibre composites also have unfavourable mechanical properties that can affect the integrity of the entire component. A simple way to improve the properties of glass fibres is adding multiple types of reinforcements such as particles. Any composite containing more than one type of reinforcement is called 'Hybrid Composite'. A hybrid composite has equally important mechanical properties such as flexural strength and impact toughness [3]. When epoxy polymers are used as adhesives, they tend to add useful mechanical properties, including high modulus, failure strength, and good performance at high temperatures. However, this accompanies a negative side effect, which causes the material to become relatively brittle [4]. These properties lead engineers to try to remove or strengthen these negative properties by adding rigid particles within the matrix phase and creating a stronger bond between the matrix and fibre phases; which allows a stiffer and durable material for specific applications.

Failure due to the impact loading creates the motivation to strengthen composite materials. The inclusion of silica microparticles in HGFRCs creates a Hybrid Glass Fiber Reinforced Composite (HGFRCs); which is generally done to enhance the impact strength without losing the flexural strength. There is evidence that the inclusion of silica microparticles to the compressive side of the laminate GFRC has shown a significant increase in specific flexural strength. The mean impact strength was increased by 9.8% with the inclusion of 5wt% of silica particles in GFRCs [5]. Experimental and computational efforts have been addressed to try to understand the strengthen mechanism involved [6]. However, in most of the models and tests, the laminates have been reinforced between each layer. In the present work, the particles were added only on the upper and lower surfaces of the laminates, where the compressive and tensile stresses are maximal under three-point bending test. The motivation of using micro rather than nanoparticles is the ability to easily spread the microparticles along large surface areas with a constant concentration. The process that nanoparticles must undergo is much more complex and the time that prevents the constant concentration within GFRCs takes days, whereas the process of the microparticles can be completed in minutes [7].

This study investigates the influence of silica microparticles (0, 5, 7.5, and 10wt%) and the silica inclusion site (top, bottom and whole sample) on the flexural modulus, flexural strength and impact resistance of hybrid with glass fibre reinforced composites. To better assess the findings for the hybrid composites, the epoxy polymers reinforced with particles at 5, 7.5 and 10wt% were evaluated under tensile and compressive tests.

2. MATERIALS AND METHODS

2.1 Materials and sample preparation

Renlam M epoxy resin and Ren HY 956 hardener used at 5:1 ratio was supplied by Huntsman (Brazil). The glass fibre material was provided by *Resinplast* (Brazil). The silica microparticles were obtained from *Moinhos Gerais* Company (Brazil). A particle size range of 325-400 (44-37μm) were considered. Ten cross-ply fabrics of glass were laminated considering a 70% matrix volume fraction to reach 2 mm thickness recommended by the ATSM D790 [8] and ATSM D6110 [9] standards for flexural and impact tests, respectively.

The silica particles were hand mixed with the epoxy resin for 5 minutes, then the hardener was combined and mixed for another 5 minutes. Three different levels of particle amount were considered: 5wt%, 7.5wt%, or 10wt%. The particulate reinforced matrix phase was placed at three different sites: the top surface, the bottom surface and thorough the sample, leading to 9 experimental conditions and a non-particulate reference (see Table 1). A constant pressure of 10kPa was applied to the laminate for 24 hours, then left for another 7 days to cure at room temperature (≈21±1°C). Two replicates were considered in the experiment. Five samples for each test and condition were fabricated, running the total of 200 specimens.

Table 1: Full factorial design (3^2).

Condition	Particle site	Silica inclusion (wt.%)
1	Top	5
2	Top	7.5
3	Top	10
4	Bottom	5
5	Bottom	7.5
6	Bottom	10
7	Both	5
8	Both	7.5
9	Both	10
10	Reference	0

Tensile and compressive samples were manufactured based on epoxy polymer and silica particles only. The particles were hand-mixed with epoxy polymer for 5 minutes and then poured into silicone moulds fabricated according to the ASTM standards [10, 11].

2.2 Mechanical tests

The samples with 50×12.7×2 mm were tested at 2mm/min under three-point bending using a Shimadzu AG-X plus test machine equipped with 100 kN load cell. The flexural strength and modulus were calculated based on ATSM D790 [8]. Charpy impact testing was carried out using XJJ-50 pendulum machine. The samples with 80×10 mm were tested according to ASTM D6110 standard [9]. The impact resistance was calculated. Minitab 18 software were used to perform the Design of Experiment (DoE) and Analysis of Variance (ANOVA) [12, 13].

In order to better evaluate the findings for the hybrid composites, the epoxy polymers reinforced with particles at 5, 7.5 and 10wt% were characterize under tensile [10] and compressive tests [11].

3. RESULTS

3.2 Effect of silica on matrix phase

Table 2 shows the mechanical properties of the epoxy polymer with silica microparticles. Although a reduction in tensile stiffness at levels of 5 and 7.5wt% by silica was evidenced, a slight

increase was found in 10wt%. In contrast, the compressive modulus increased as much as the amount of silica particles. Tensile strength data were slightly reduced, while the mean values of the compressive strength were enhanced by the incorporation of silica. Ferreira [14] studied the incorporation of micro-sized silica into epoxy polymer at 2.5, 5, 7.5 and 10wt%. The compressive modulus and strength values presented in this work were 11.3% and 3.7% higher than those obtained by Ferreira [14]. The strength of micro-particulate composites relies on the effectiveness of stress transfer between resin and fillers, which are associated due to the interplay between of three factors: particle size, particle/matrix interfacial adhesion and particle loading, which cannot always be separated [15].

Table 2: Mechanical properties for particulate reinforced epoxy polymer

Silica inclusion (wt. %)	Tensile Modulus (GPa)	Tensile strength (MPa)	Compressive modulus (GPa)	Compressive strength (MPa)
0%	2.10 ± 0.13	39.50 ± 0.97	2.20 ± 0.09	68.70 ± 4.34
5%	2.02 ± 0.21	39.21 ± 0.51	2.35 ± 0.08	71.15 ± 1.34
7.5%	1.98 ± 0.22	38.98 ± 1.77	2.43 ± 0.10	71.57 ± 2.18
10%	2.20 ± 0.14	37.88 ± 1.67	2.53 ± 0.06	73.60 ± 0.53

3.3 Flexural and Impact behaviour of HGFRCs

Table 3 shows the results of the analysis of variance (ANOVA) for the mean flexural and impact data. P-value values less than 0.05 (5%) are considered significant at a 95% confidence level. Drumond *et al.* [16] emphasized that the effects of interaction between factors are more important than individual factors, because they had better explain the behaviour of responses when considered significant. The effects of second-order interaction were significant for all responses, as shown by the P-values underlined in Table 3. R^2 values close to 100% indicate well-fitted data to the statistical model.

Figure 1 shows the interaction effect plots for the mean flexural strength (a) and modulus (b). Higher flexural strength values were achieved when silica particles were incorporated, especially on the bottom beam side, followed by the top sample surface (Figure 1a). The inclusion of particles on the top surface did not provide greater flexural strength as expected. It is noteworthy that the inclusion of particles on both sides led to reduced strength compared to the reference condition. The silica amount levels did not substantially change the strength of the composites. In contrast, 7.5wt% silica achieved higher stiffness values for all added sites (Figure 1b). The highest flexural modulus was reached when 7.5wt% of silica was added to the bottom surface of the laminate. Hybrid composites only achieved a modulus larger than the reference condition when fabricated with 7.5wt% of silica on the bottom or top sides of the beam.

The bending test combines tensile (bottom beam side), compressive (upper beam side) and shear loadings [1]. Considering the particles were added on the laminate surfaces, there is no interlocking effect in the interlaminar region to be considered. Based on the findings presented in Table 2 for the reinforced matrix phase, it was expected to have greater flexural behaviour for samples reinforced especially on the upper surface under compressive loads. The incorporation of particles on only one side of the laminate can affect the normal load distribution generated by the bending. The presence of silica on the bottom surface may also contribute to retard crack

propagation, as reported in the open literature [2,4,6], which may be responsible for increasing the flexural performance of hybrid composites.

Table 3: ANOVA

Experimental factor	P-value ≤ 0.05		
	Flexural Strength	Flexural Modulus	Impact Strength
Percent	0.045	0,000	0.000
Position	0.000	0,000	0.000
Percent*Position	**0.030**	**0,003**	**0.014**
R^2-adjusted (%)	98.86%	96.96%	98.97%

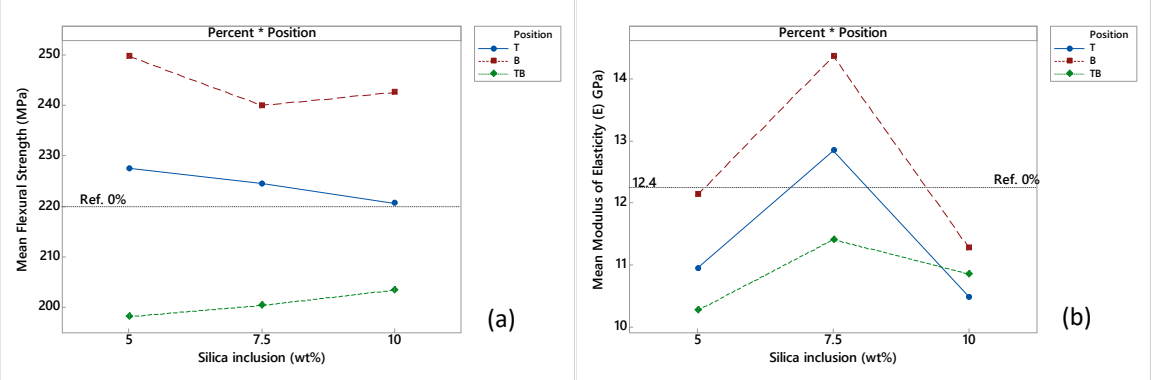

Figure 1: Interaction effect plots (a) for mean flexural strength and (b) mean flexural modulus

Figure 2 shows the interaction effect plot for the mean impact resistance. Since the inclusion of silica increased the stiffness of the composites, an opposite behaviour for the impact resistance was expected, as shown in Figure 2. It should be noted that the reference condition (without particles) achieved the highest impact resistance at 135 kJ/m^2. Cao and Cameron [6] have attributed positive effects on impact response by adding micro particles in the interlaminar region of glass fibre composites due to the presence of fibre pull-out mechanism and increased interlocking effect. However, such a mechanism cannot be considered in the present work since the particles were added on the surfaces of the laminate and not in the interlaminar regions.

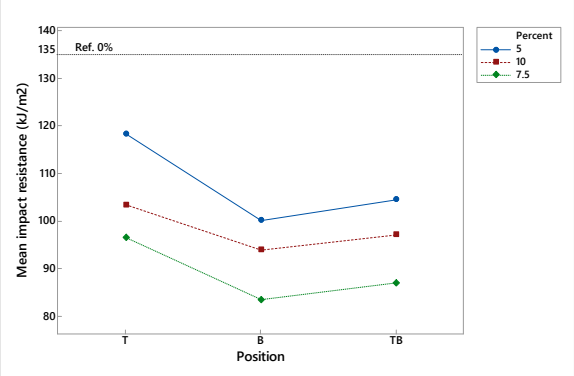

Figure 2: Interaction effect plot for mean impact resistance.

4. CONCLUSION

The main conclusions are following described:

- The inclusion of silica particles in the epoxy polymer led to increased compressive modulus (2.53GPa) and strength (73.60MPa). However, no substantial change was verified for the tensile behaviour.
- The inclusion of particles on both sides of glass fibre composites led to reduced flexural strength and stiffness compared to the reference condition.
- Hybrid glass fibre composites only achieved a modulus larger than the reference condition (without particles) when fabricated with 7.5wt% of silica on the bottom or top sides of the laminate.
- The incorporation of 7.5wt% silica microparticles on the bottom surface of the laminates achieved higher flexural behaviour and lower impact resistance.
- The highest impact resistance (135kJ/m^2) was achieved by the reference condition without particles, followed by hybrid laminates made with 5wt% of particles added in the top surface.

ACKNOWLEDGEMENTS

The authors would like to thank Texas Tech University, CNPq (PP-306767/2016-3) and FAPEMIG (PPM-00075-17) for the financial support provided.

REFERENCES

[1] Santos, J. C. and Panzera, T. H., 'Hybrid silica micro and PDDA/nanoparticles-reinforced carbon fibre composites', (Journal of Composite Materials, vol. 51, Published June 17, 2016) 783-795.

[2] Torres, R. B. and Santos, J.C., 'Hybrid glass fibre reinforced composites containing silica and cement microparticles based on a design of experiment', (Polymer Testing, vol. 57, 2017) 87-93.

[3] Hasan, I., Qingtao, W., Ahmed, A., and Wei, L., 'Effect of Hybrid Ratio and Laminate Geometry on Compressive Properties of Carbon/Glass Hybrid Composites', (Fibers and Polymers 2016, Vol.17, No.1), 117-129.

[4] Kinloch, A. J., Masania, K., Taylor, A. C., Sprenger, S., 'The fracture of glass-fibre-reinforced epoxy composites using nanoparticle-modified matrices', (Journal of Materials Science, vol. 43, Published February, 2008) 1151-1154

[5] Silva, L. J., Panzera, T. H., Christoforo, A. L., 'Micromechanical Analysis of Hybrid Composites Reinforced with Unidirectional Natural Fibres, Silica Microparticles and Maleic Anhydride', (Materials Research, vol.15 no.6 São Carlos December, 2012).

[6] Cao, Y. and Cameron, J., 'Impact Properties of Silica Particle Modified Glass Fiber Reinforced Epoxy Composite', (Journal of Reinforced Plastics and Composites, May 1, 2006).

[7] Cao, Y. and Cameron, J., 'The Effect of Curing Conditions on the Properties of Silica Modified Glass Fiber Reinforced Epoxy Composite', (Journal of Reinforced Plastics and Composites, January 1, 2007).

[8] American Society for Testing and Materials. ASTM D790-15. Standard - Test Methods for Flexural Properties of Unreinforced and Reinforced Plastics and Electrical Insulating Materials. 2015.

[9] American Society for Testing and Materials. ASTM D6110-10. Standard Test Method for Determining the Charpy Impact Resistance of Notched Specimens of Plastics.

[10] American Society for Testing and Materials. ASTM D3039-14. Standard Test Method for Tensile Properties of Polymer Matrix Composite Materials. 2014.

[11] American Society for Testing and Materials. ASTM D695-15. Standard Test Method for Compressive Properties of Rigid Plastics. 2015.
[12] ISO 179-1:2010. Plastics – Determination of Charpy impact properties Part 1: Determination of Charpy impact properties.
[13] ISO 179-1:2010. Plastics – Determination of Charpy impact properties Part 2: Instrumented impact test.
[14] Ferreira, B. T., 'Compósitos Híbridos Reforçados com Fibras de Sisal/Vidro e Micropartículas de Sílica'. 2017. Dissertação do Programa de Pós-Graduação em Engenharia Mecânica. UFSJ.
[15] Fu, S. Y., Feng, X. Q., Lauke, B., and Mai, Y. W., 'Effects of Particle Size, Particle/Matrix Interface Adhesion and Particle Loading on Mechanical Properties of Particulate Polymer Composites', (Composite Part B, Vol. 39, No. 6, 2008, pp. 933–961).
[16] Drumond, F. B. et al. 'Metodologia de otimização de processos. Departamento de Estatística da UFMG', (Departamento de Tecnologia Mineral do CDTN/CNEM, Belo Horizonte, Minas Gerais, 1993).

DEVELOPMENT AND CHARACTERIZATION OF CARBON FIBER REINFORCED THERMOPLASTICS – PART B: MECHANICAL PROPERTIES AND MICROSTRUCTURAL ANALYSIS

Bruno J. Lopes (1), José Roberto M. d'Almeida (1)

(1) Department of Chemical and Materials Engineering, Pontifícia Universidade Católica do Rio de Janeiro, Brazil

https://doi.org/10.21452/bccm4.2018.13.07

Abstract

Mechanical and microstructural properties of carbon fiber reinforced ABS (Acrylonitrile Butadiene Styrene) were analyzed and compared to neat, commercial ABS. Pellets of neat ABS and mixtures with varying fiber content (5% and 16.7%) and length (3 mm and 6 mm) were submitted to mechanical testing and SEM (Scanning Electron Microscopy). Mechanical testing showed increases of up to 38% in tensile strength and 90% in modulus at the cost of loss of ductility. Surface analysis of pellets and fractured specimens carried out by SEM showed poor interface between fibers and matrix as well as a random distribution of the reinforcement phase along the composite.

Keywords: Composites; Carbon fiber; ABS; Extrusion, Additive Manufacturing.

1. INTRODUCTION

Much has been developed in the field of composite materials in the last decades. Researchers have found ways to make structural components faster and cheaper than ever before [1–4]. The development of thermoplastic matrix fiber reinforced composites broadens the range of applications and processing techniques for composite materials borrowing much from the know-how developed for polymers.

The benefits of advanced fibers reinforced in common thermoplastics, such as ABS are very attractive. These benefits are especially attractive to novel processes like additive manufacturing, which usually rely on polymers as feedstock, limiting its breadth of ability. The change to fiber reinforced composite feedstock has been already proven to revolutionize the additive manufacturing industry [5–8]. The continued development of even more capable materials will only make this revolution come faster.

The objective of this paper was to evaluate the mechanical properties of a carbon fiber reinforced ABS thermoplastic and to observe its microstructure looking for characteristics that may influence the final properties of the composite.

2. EXPERIMENTAL

2.1. Background: Material processing

For the initial material processing, pellets were produced mixing chopped carbon fiber (Tenax®-J HT C261, from Toho Tenax America, Inc.) in two different lengths (3 mm and 6 mm) and ABS GP-35 (Terluran® GP-35, from INEOS Styrolution) at various weight percentages (% wt). Each mixture was then extruded using a twin-screw extruder (Leistritz ZSE 18 MAXX) and chopped to produce pellets. For mechanical testing, filaments were extruded from each mixture's pellets using a micro extruder (Xplore Micro Compounder MC5).

More details regarding the processing stages, along with the calculation of the actual fiber content for each mixture can be seen in a previous work from the authors [9] and in Part A of this paper. Table 1 lists each mixture's characteristics.

Table 39: Composition of each analyzed mixture including nominal and actual fiber content verified via TGA

Mixture	Grape seed oil % wt (%)	Carbon Fiber length (mm)	Nominal % wt CF (%)	Actual % wt CF (%)
I	-	-	0	0
II	-	3	5	3.1
III	1	3	5	5.2
IV	1	3	16.7	13.2
V	1	6	16.7	16.5

2.2. Mechanical Testing

Mechanical testing was conducted to investigate properties such as tensile strength, Young's modulus and ductility. All tests were done using a universal testing machine (Oswaldo Filizola AME-2kN) with a constant rate of 50 mm/mm.

As extensometers were not used for these tests, Young's modulus values were obtained from the following equation, which takes into account the rigidity of the test rig:

$$\frac{1}{K_S} = \frac{1}{K_m} + \frac{1}{E} \cdot \frac{L_0}{A_0} \quad (2)$$

where E is the Young's modulus, L_0 is the distance between grips and A_0 represents the test specimen's cross section area. K_m is the rigidity of the test rig, determined by Novoa [10], to be 546.4 MPa. K_S is related to the non-corrected Young's modulus value. This value can be achieved from a pair of coordinates extracted from the linear region of the load vs. deformation (P x Δl) plot.

2.3. Microstructural Analysis

Pellet cross section and the fracture surface of tested specimens were observed using a JEOL JSM-6510LV Scanning Electron Microscope (SEM) at 20 kV and high vacuum. Samples were metallized with gold, via sputtering in a Balzers SCD 050 Sputter Coater.

Magnifications ranging from 100x to 5000x were used and are indicated in each image.

3. RESULTS AND DISCUSSION

3.1. Mechanical Properties

The mechanical properties are shown in the box plots below, Figures 1(a) to (c). For each plot, the top and bottom of the box represent the 3rd and 1st quartiles of the data distribution, respectively, and the line in the middle of the box represents the median. The whiskers represent the maximum and minimum values within 1.5 interquartile range, whereas the crosshead marks represent the maximum and minimum values obtained. The square inside de boxes represents the mean of the data for each particular mixture.

Tensile strength, Figure 1(a), showed oscillating results. Initially, the introduction of carbon fiber to the ABS polymer (Mixture II) seemed to improve the tensile strength values reaching up to 14% increase. Mixture III, with the introduction of grape seed oil, showed a decrease back to neat ABS values. Since fiber content is very similar, the influence of the oil seems to be relevant to the final properties of the composite. Mixture IV, with a much greater % wt of carbon fiber, showed a stark increase in tensile strength, reaching a maximum of 62.1 MPa (38% increase over neat ABS) but with large variance. This value is higher than what was found by Ning et al. [11, 12], who in their work used carbon fiber powder as reinforcement instead of fibers, but below what can be found in literature [5, 7, 13].. Mixture V, with the same % wt of fibers, but with longer initial lengths, once again showed values similar to neat ABS. This oscillating behavior can be traced to poor fiber/matrix interface and also to the random distribution of the reinforcement along the composite, which will be investigated in more detail in subsequent item 3.2.

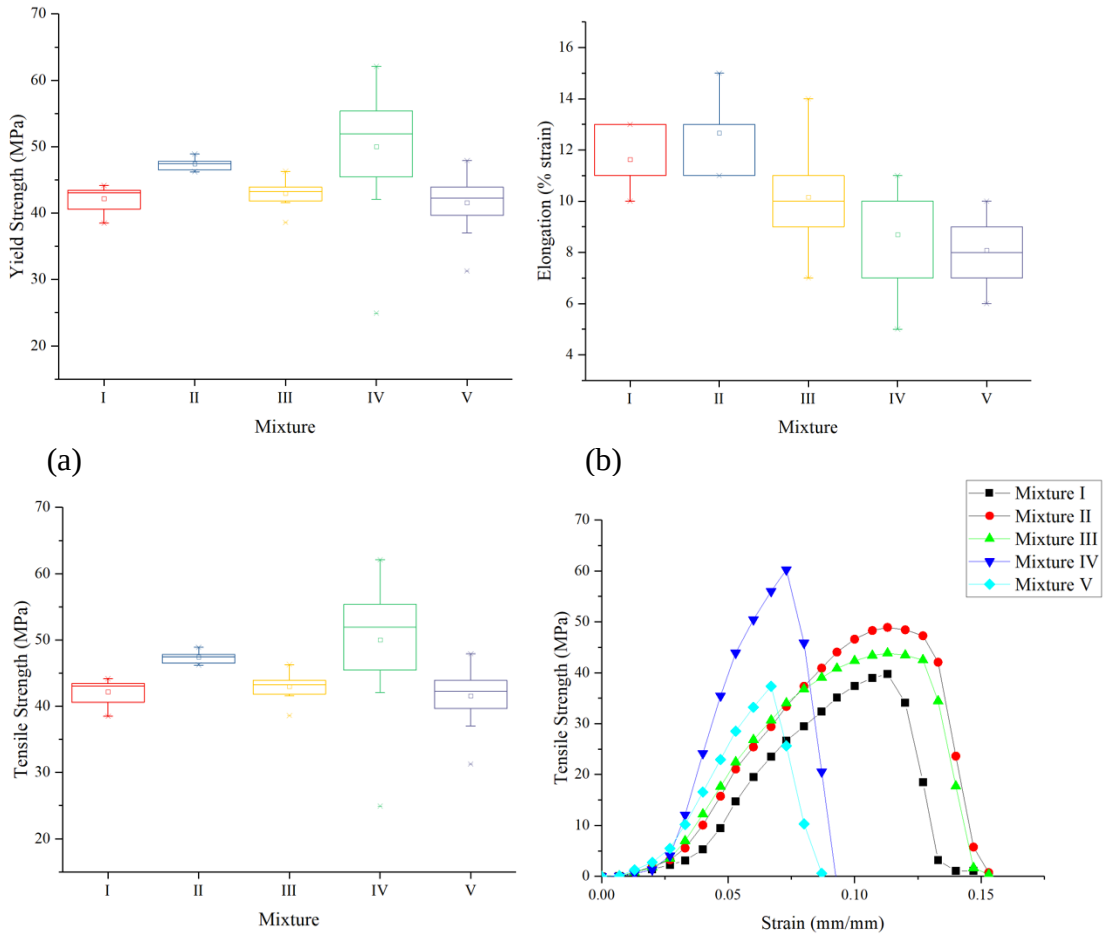

(c) (d)

Figure 82: Box plot comparison of (a) Tensile strength; (b) Ductility (using elongation as a parameter); (c) Young's modulus; (d) A representative sample of each mixture during tensile testing

Ductility, Figure 1(b), showed a clear downward trend, as seen also in Ning et al. [12], despite large variations and small differences between each mixture. This is mostly due to the introduction of a high modulus and brittle material, such as carbon fiber, in the polymeric matrix. Greater % wt of fibers caused a decrease between 25% and 30% over neat ABS.

Young's modulus, Figure 1(c), was the most affected property. Modulus increase followed the increase in carbon fiber content, reaching its peak at mixture IV, with a maximum of approximately 4.0 GPa (90% increase over neat ABS). Once again, this value is higher than what was found by Ning et al. [12], but lower than some of the values that can be found in the literature [5, 7, 13]. Mixture V, with its longer initial carbon fiber length showed a decrease of 5% over mixture IV, which was statistically relevant (t-Student test) despite relatively large variances.

Figure 1(d) shows the results of tensile testing for one sample from each mixture plotted together. The lower strains at rupture for mixtures with higher carbon fiber content are indicative of reduced ductility, showing a more brittle behavior.

3.2. Microsctructure

In the cross-section area of the pellets, Figures 2(a) and 2(b), it is possible to observe a large number of voids, as expected and seen in the literature [11]. With increasing % wt of carbon fibers, more voids can be seen. These voids are formed during the cooling stages of the extrusion process by temperature gradients and are mostly constituted of entrapped air. The presence of voids is mainly due to sub-optimal process parameters, which were set to avoid matrix degradation [9].

In the fracture surface of tested specimens, Figures 2(c) and 2(d), the voids are completely eliminated. Due to the second extrusion process, the entrapped air was allowed to escape resulting in void-free microstructures. Also, it is possible to observe that the fracture initiation mechanism changed between neat ABS and reinforced samples. Neat ABS showed a very localized initiation site (indicated with an arrow), whereas reinforced samples had no clear initiation site. This difference confirms the transition from a more ductile behavior in neat ABS samples to more brittle in the carbon fiber/ABS mixtures, as observed in Figure 1(d).

In both the pellets and the fractured specimens, the interface between fibers and matrix is weak. Empty spaces can be seen around fibers, indicating poor adhesion. This can be further confirmed by the amount of holes left by pulled-off fibers. Higher magnifications show that the fibers do not damage the matrix while being pulled-off, thus reinforcing the poor adhesion observed.

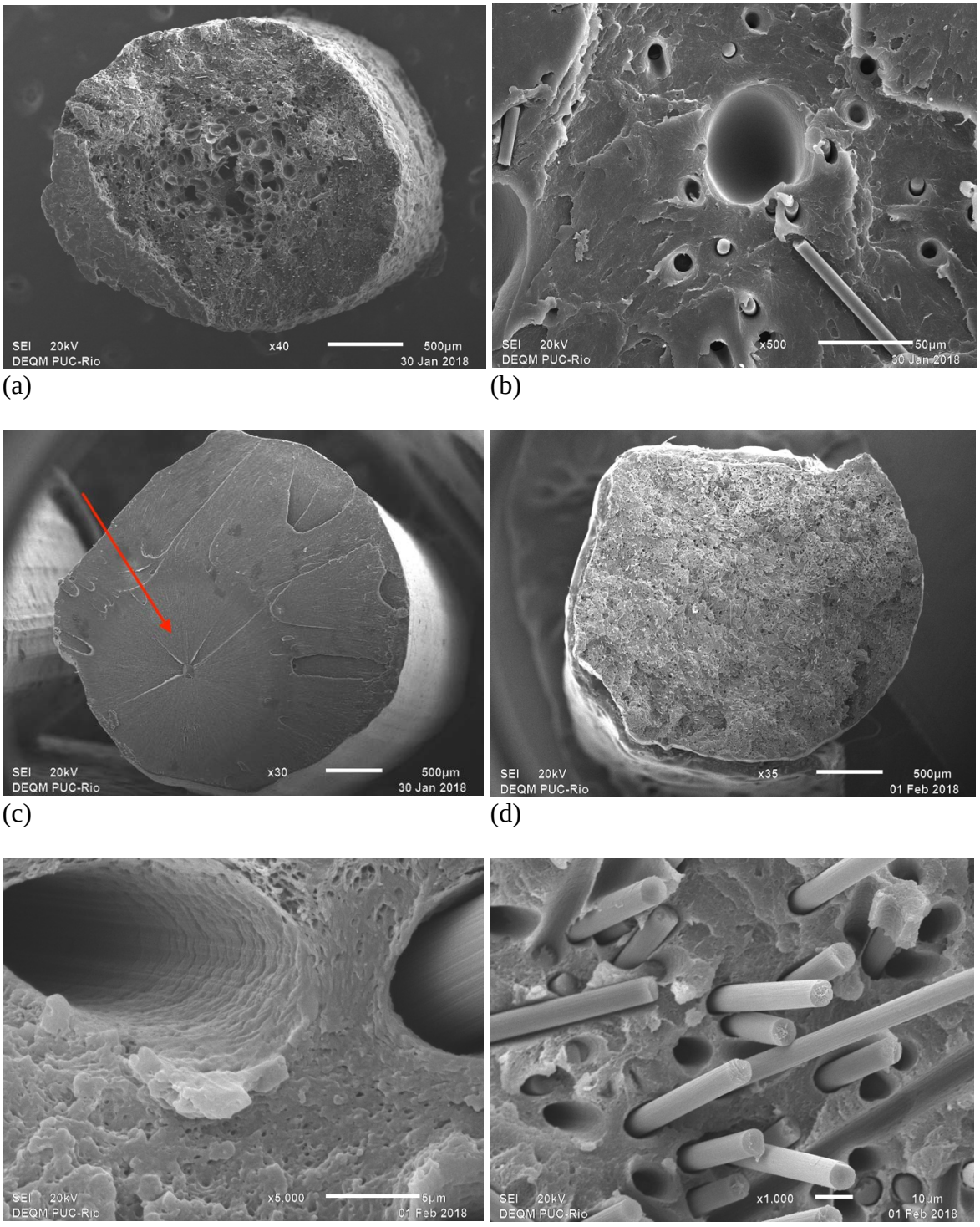

Figure 83: (a) Surface of a pellet (Mixture V); (b) Surface of a pellet at high magnification (Mixture II); (c) Surface of a fractured neat ABS (Mixture I) sample with an arrow indicating where failure begun; (d) Fractured surface of a sample with high % wt CF (Mixture V); (e) Hole left from a pulled-off fiber and empty space around a fiber (Mixture V); (f) Random fiber distribution and interaction (Mixture V).

4. CONCLUSIONS

The effects of the introduction of carbon fiber as reinforcement for neat ABS were successfully analyzed. Increases of up to 38% in tensile strength and 90% in modulus were achieved over neat ABS. Although these results highlight the great potential of mechanical properties enhancement that carbon fiber can cause to for thermoplastics, the randomness of distribution and poor interface caused large variations in results, thus making it difficult to predict the actual structural performance of a final composite component. Furthermore, the effects of process additives, such as the grape seed oil, on the final characteristics of the composite should be more thoroughly investigated.

ACKNOWLEDGEMENTS

The authors acknowledge the support from the National Council for Scientific and Technologic Development (Conselho Nacional de Desenvolvimento Científico e Tecnológico - CNPq).

REFERENCES

[1] P. Feraboli, F. Gasco, B. Wade, S. Maier, R. Kwan, A. Masini, L. DeOto and M. Reggiani, 'Lamborghini Forged Composite technology for the suspension arms of the Sesto Elemento,' in ASC Conference, Montreal, 2011.

[2] P. Feraboli, E. Peitso, T. Cleveland and P. B. Stickler, 'Modulus Measurement for Prepreg-based Discontinuous Carbon Fiber/Epoxy Systems,' Journal of Composite Materials, vol. 43, no. 19/2009, pp. 1947-1965, August 2009.

[3] P. Feraboli, E. Peitso, T. Cleveland, P. B. Stickler and J. C. Halpin, 'Notched behavior of prepreg-based discontinuous carbon fiber/epoxy systems,' Composites , vol. Part A, no. 40, pp. 289-299, March 2009.

[4] P. Feraboli, E. Peitso, F. Deleo, T. Cleveland and P. B. Stickler, 'Characterization of Prepreg-Based Discontinuous Carbon Fiber/Epoxy Systems,' Journal of Reinforced Plastics and Composites, vol. 28, no. 10/2009, pp. 1191-1214, May 2008.

[5] H. L. Tekinalp, V. Kunc, G. M. Velez-Garcia, C. E. Duty, L. J. Love, A. K. Naskar, C. A. Blue and S. Ozcan, 'Highly oriented carbon fiber-polymer composites via additive manufacturing,' Composites Science and Technology, vol. 105, pp. 144-150, 16 Oct 2014.

[6] L. J. Love and C. Duty, 'Cincinnati Big Area Additive Manufacturing (BAAM),' Oak Ridge, TN, 2015.

[7] L. J. Love, V. Kunc, O. Rios, C. E. Duty, A. M. Elliot, B. K. Post, R. J. Smith and C. A. Blue, 'The importance of carbon fiber to polymer additive manufacturing,' J. Mater. Res., vol. 29, no. 17, 14 Sep 2014.

[8] The Boeing Company, 'One For The Record Books,' 26 August 2016. [Online]. Available: http://www.boeing.com/features/2016/08/record-books-08-16.page. [Accessed 30 November 2016].

[9] B. J. Lopes, 'Desenvolvimento e Caracterização de Compósitos Termoplásticos Reforçados por Fibra de Carbono,' PUC-Rio, Rio de Janeiro, 2018.

[10] D. M. C. Novoa, 'Avaliação físico-química do polietileno de alta densidade processado pelo método de impressão 3D por modelagem por fusão e deposição FDM,' Rio de Janeiro, 2014.

[11] F. Ning, W. Cong, Z. Hu and K. Huang, 'Additive manufacturing of thermoplastic matrix composites using fused deposition modeling: A comparison of two reinforcements,' Journal of Composite Materials, vol. 51, no. 27, pp. 3733-3742, 1 November 2017.

[12] F. Ning, W. Cong, J. Wei, S. Wang and M. Zhang, 'Additive Manufacturing of CFRP Composites Using Fused Deposition Modeling: Effects of Carbon Fiber Content and Length,' in ASME 2015 International Manufacturing Science and Engineering Conference, Charlotte, North Carolina, 2015.

[13] C. E. Duty, V. Kunc, B. Compton, B. Post, D. Erdman and R. Smith, 'Structure and mechanical behavior of Big Area Additive Manufacturing (BAAM) materials,' Rapid Prototyping Journal, vol. 23, no. 1, pp. 181-189, January 2017.

NIOBIUM OXIDE (Nb_2O_5) FILLED HIGH-MODULUS POLYETHYLENE EXTRUDABLE (HMPEX) COMPOSITES: TENSILE PROPERTIES

João Pedro Coré Pinto [(1)], Nancy Isabel Alvarez Acevedo [(1)], Marisa Cristina Guimarães Rocha [(1)] and Noemi Tatizawa [(2)]

(1) Polytechnic Institute, Rio de Janeiro State University, UERJ, Nova Friburgo, RJ, Brazil

(2) Petrobras Research & Development Center, CENPES, Rio de Janeiro, RJ, Brazil

https://doi.org/10.21452/bccm4.2018.13.08

Abstract

The present study reports the development of composites of high-modulus polyethylene extrudable (HMPEX) filled with niobium oxide (Nb_2O_5) for using in therapeutic applications. The effect of filler content on mechanical properties of composites processed with Nb_2O_5 contents in the range of 5-30 wt% was evaluated. Tensile strength tests were performed according to ASTM D 638. The tensile modulus values of composites increased significantly at high filler contents (15, 20, 25 and 30 wt%), where the modulus increased 18, 16, 14 and 24%, respectively, compared with the modulus of neat HMPEX. The yield strength showed slight improvement with the increase of filler content up to 20 wt%. At this concentration, it reached the maximum value, 10% higher than the value of HMPEX. The values of elongation at break and tensile strength decreased with the increase in filler content. All properties presented by the composites processed by extrusion were inferior to those of the composites prepared by compression molding. The neat HMPEX and the HMPEX composites processed with 5 wt% of Nb_2O_5 obtained by compression molding exhibited properties matching those required for medical grade UHMWPE resins, according to ASTM F648-00, making them potential candidates for medical applications.

Keywords: High modulus polyethylene extrudable, niobium pentoxide, biomaterial, therapeutic applications, tensile properties.

1. INTRODUCTION

Polymeric biomaterials, in the form of dental and medical implantable devices or implants, are widely used in the medical field for therapeutic applications. Examples of these applications are orthopedic implants, implantable cardiac defibrillators, coronary stents, and dental prosthetics or intraocular lenses [1 - 3]. Ultra-high-molecular-weight polyethylene (UHMWPE) is widely used to manufacture hip and knee implants for total joint arthroplasties [3 - 5]. Woven ribbons of UHMWPE fibers are one the reinforcing materials most often used in dental composite resins for

applications such as prosthodontics, restorations or periodontics [6 - 8]. In addition to its excellent biocompatibility, this polymer has an excellent combination of physical and mechanical properties, such as self-lubrication, low coefficient of friction, high impact resistance, high stress resistance, making it suitable for these applications [4, 5]. However, its processing is rather cumbersome compared with other grades of polyethylene. Generally, techniques based on the powder casting method are used. Usually, compression molding and ram extrusion are the techniques often used for consolidating forms [5, 9, 10], and gel spinning is used for obtaining fibers [11]. Thus, there is a need to develop less complex transformation processes, while maintaining the characteristic properties of this polymer [12 - 16].

The Petrobras Research & Development Center has developed a novel type of polyethylene, named high-modulus polyethylene extrudable (HMPEX) [17]. HMPEX has interesting characteristics, which make it a potential alternative material to UHMWPE for some applications. Its modulus is similar to the modulus of UHMWPE, but its processing properties are better than those presented by this polymer. Therefore, the production costs associated with HMPEX must be lower than those of UHMWPE.

Abrasion wear has a significant impact on the useful life of any implant. Wear debris accumulated at the interface of contact can accelerate the implant's mechanical failure. Those that migrate to peripheral tissues, when interacting with these tissue, can cause loosening of the implant, forcing its removal [18 -22]. Development of composites is one of the methods used to improve the wear resistance of polymeric materials [18]. Different type of fillers such as alumina [23], graphite, molybdenum disulfide, [24]; carbon nanofibers and nanotubes [25,26] have been added to biopolymers.

Niobium oxide, Nb_2O_5, is a mineral filler that is abundant in Brazil. It is commonly used in the preparation of dielectric ceramic materials, acoustic and electro-optic materials and optical glass, while in catalysis it is used as support phase or as promoter of chemical activity [27]. In recent years, many published reports describe its uses as biomaterial. Due to its properties of biocompatibility, high corrosion resistance, high mechanical strength and thermodynamic stability, it has been used as coating material for metallic biomaterials [28 - 30]. Nb_2O_5 filled titanium composites exhibit excellent biocompatibility and cell adhesion, and high mechanical strength, making it a promising material for use in orthopedic implants [31]. Besides being biocompatible, it is also a bioactive material. This property enables its use in the production of bioglass or ceramic glass for using as bone filler material or substitute material for bone tissues [30 - 34]. Some studies have shown the feasibility of using Nb_2O_5 as radiopacifying agent in the production of luting agents for endodontic treatment [35, 36]. Studies of Nb_2O_5 as a mineral filler in polymer composites for production of biomaterials are more recent. Leitune et al. [37] presented Nb_2O_5 as a novel filler for dental adhesive resin. These researchers developed Nb_2O_5 filled adhesive resins with improved tissue-resin bond strength compared with that of original resin. Young et al. [38] developed a Nb_2O_5-polydimethylsiloxane hybrid composite for application in coating on dental implants. Their results showed that tissue/implant interfaces could be optimized by adjusting the oxide content in the composite.

In this context, the aim of this study was to develop Nb_2O_5 filled HMPEX composites for using in biomedical applications. Since there is a relation between processing method, mechanical properties and wear resistance, the effect of filler content on mechanical properties of composites obtained by compression molding were compared with the properties obtained by extrusion.

2. EXPERIMENTAL

2.1 Materials

The matrix material used in this study was the high-modulus polyethylene extrudable (HMPEX) powder (Petrobras Research & Development Center, Rio de Janeiro, Brazil) (Melt Flow Index (21.60 kg, 190°C) = 0.84 g/10 min. Niobium pentoxide powder from Companhia Brasileira de Metalurgia e Mineração - CBMM) was used as filler. The α-tocopherol (E-vitamin) from Fagron was used as antioxidant.

2.2 Preparation of HMPEX/Nb_2O_5 composite samples by compression molding

Initially, the raw materials were dried in an oven with air circulation at 70ºC for 24 h. Then, different concentrations (5, 10, 15, 20, 25 or 30 wt%) of Nb_2O_5 were mixed with HMPEX by manual stirring, followed by ultrasonic agitation for 30 minutes. Finally, the mixtures were consolidated in the form of rectangular plates (109 mm x 107 mm x 4 mm), by using a press (Carver, 3851-OC) at 210ºC with force of 10 tons, warm-up time of 5 min, residence time of 7 min, and cooling at room temperature for 40 min.

2.3 Preparation of HMEPX/Nb_2O_5 composite samples by extrusion

Initially, HMPEX was mixed with 3 wt%, of vitamin E (VE) to prevent the polymer degradation by oxidation during processing. This mixture was introduced in a 500 ml flask and then an alcohol solution containing 72.4% absolute ethyl alcohol was added. The flask was immersed in a water bath maintained at 70°C with continuous stirring at 200 rpm, during 6 hours. After this period, the stirrer was turned off, and the temperature was maintained at 70°C until total evaporation of the residual alcohol solution. In the subsequent step, VE-doped HMEXP was pre-mixed with Nb_2O_5 (15 wt%) and, then, processed in a twin-screw extruder (Leistritz ZSE 18 MAXX) using a temperature profile, from feed to die of 180/190/200/210/220/230/240/250/260/270°C at 500 rpm screw speed and 2.0 kg/h feed rate.

2.4 Determination of tensile mechanical properties of the HMEPX/Nb_2O_5 composites

The tensile properties of neat HMPEX and reinforced HMPEX composites were determined according to ASTM D 638, using V-type test specimens, seven for each composition, obtained by machining with a milling machine (Roland, Desktop Engraver GX-350). The test was carried out in a Universal testing machine (Shimadzu, AGX-Plus 100 kN), at a crosshead speed of 50 mm/min with load of 5 kN.

3. RESULTS AND DISCUSSION OF RESULTS

Table 1 presents the results of tensile test of neat HMPEX (0% Nb_2O_5) and Nb_2O_5 filled HMPEX composites with different filler contents.

Table 1 shows that the elastic modulus and yield strength of composites increased with the increasing in filler content, while elongation at break and tensile strength decreased. This result matches the mechanical behavior generally observed in particle-filled polymeric composites [39 - 44]. The elastic modulus values of composites increased significantly at high filler contents (15, 20, 25 and 30 wt%) where the modulus increased 18, 16, 14 and 24%, respectively, compared with the neat HMPEX.

Table 1 - Tensile properties of HMPEX/ Nb_2O_5 composites obtained by compression molding.

Nb_2O_5 (wt%)	Elastic Modulus (MPa)	Yield Strength (MPa)	Elongation at Break (%)	Tensile Strength (MPa)
0	1095.90±66.81	19.86±0.65	456.37±34.92	39.66±2.72
5	1063.22±33.95	19.89±1.12	371.81±37.33	31.08±3.28
10	1104.36±89.19	20.38±1.59	207.73±72.16	20.46±5.71
15	1293.92±47.76	21.09±0.17	139.67±88.08	18.85±2.30
20	1270.56±137.37	22.07±1.04	18.79±8.13	18.16±0.846
25	1247.99±80.98	19.34±1.09	34.99±3.99	6.63±2.76
30	1358.91±58.434	18.94±0.56	35.71±9.17	9.056±3.16

Figure 1 (a) illustrates the effect exerted by Nb_2O_5 content on the elastic modulus of each composite: for low filler content, the addition of Nb_2O_5 reduces the matrix cohesion, while for high contents, the reinforcing effect of the filler predominates [25]. The increment of elastic modulus value represents an increment in the stiffness of the composite [39]. Nb_2O_5 is a rigid filler, so it restricts the mobility of the polymer chains when inserted between them, so the stiffness increases [25, 42 - 46].

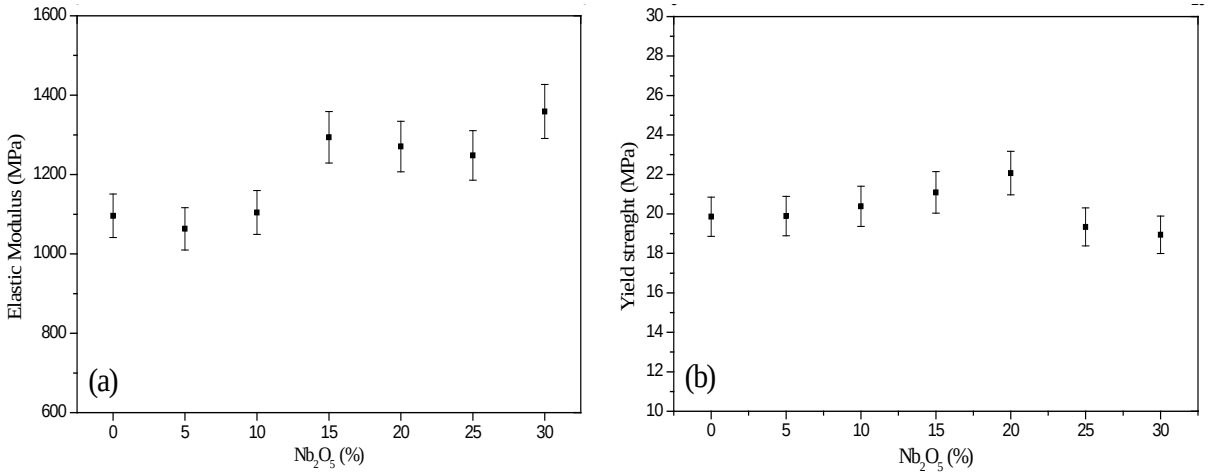

Figure 1 – The effect of filler content on the (a) elastic modulus, and (b) yield strength of HMEXP/Nb_2O_5 composites obtained by compression molding

Yield strength values of composites increased gradually, when the Nb_2O_5 content was increased, until a maximum value of 22.07 MPa for the composite filled with 20 wt % of Nb_2O_5 (Figure 1-b). This means an increase of 11% compared with that of neat HMPEX. For concentrations higher than 20 wt%, the yield strength values decrease gradually with the increase of Nb_2O_5 content. The minimum yield strength value reached 18.94 MPa, 4.6% below that of HMPEX. All composites, with the exception of that containing 30% of Nb_2O_5, exhibited values compatible with the minimum values of yield strength specified by ASTM F648-00 for medical grade UHMWPE resins (21 MPa for type 1 and 19 MPa for type 2).

The elongation at break of the composites decreased suddenly from 18% at 5 wt% of Nb_2O_5 to 96% at 20 wt% of Nb_2O_5 and remained practically constant above this filler content (Figure 2-a). Similar results were reported by Berçot [45] for niobium oxide filled polypropylene composites, and by Tavman [44] for aluminum-powder filled HDPE composites. The decreasing of elongation

at break values is linked to the increment in stiffness promoted by the filler [39]. The HMPEX/5 wt% Nb_2O_5 and the neat UHMWPE present elongation at break values higher than the minimum required by ASTM F648-00 for medical grade UHMWPE resins (300%).

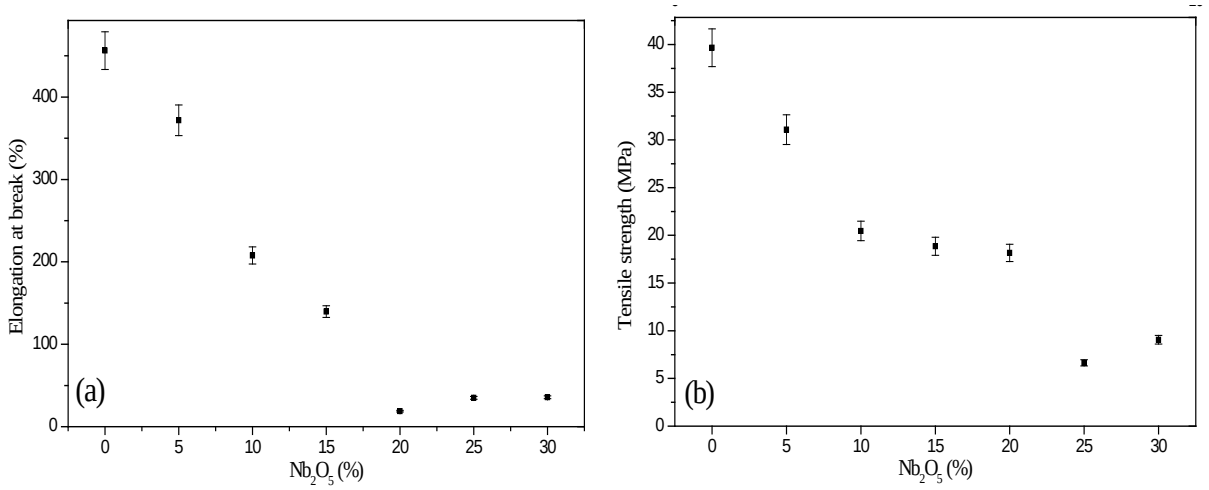

Figure 2 – The effect of filler content on the (a) elongation at break, and (b) tensile strength of HMEXP/ Nb_2O_5 composites.

The tensile strength decreased gradually with the increasing of filler content until 20 wt% content (Figure 2-b). However, there was an abrupt decrease at higher filler content. The maximum decrease, 83%, occurred at 25 wt% of Nb_2O_5 content. The reduction in tensile strength indicates the formation of filler particle agglomerates [40, 41]. This effect was stronger when a higher filler content (25 and 30 wt%) was introduced into the polymer. Formation of agglomerates, insertion of discontinuities with reduction of effective cross-sectional area of continuous phase and irregular distribution of particles can occur with increasing of the filler content. These effects account for the decrease in the tensile strength of composites [46]. The minimum tensile stress required for medical grade UHMWPE, for type 1 resin, is 35 MPa, and for type 2 is 27 MPa. According to these requirements, only neat UHMWPE and the composite processed with 5 wt% of Nb_2O_5 can be used for medical applications.

Table 2 shows the tensile properties of HMPEX/ 15% Nb_2O_5 composites prepared by the extrusion process (EP), compared to the values obtained for the composites prepared by compression molding (CM).

Table 2 shows that all tensile mechanical properties decreased in comparison to the corresponding values for composites obtained by compression molding. The standard deviation of elongation at break did not allow a reliable assessment of its value. This result suggests that there is a polymer degradation, when the composites are submitted to the extrusion process. This behavior should be investigated in depth.

Table 2 – Tensile properties of composites HMPEX/(15%)Nb_2O_5processed by compression molding (CM) and by extrusion process (EP)

Processing by	Elastic Modulus (MPa)	Yield Strength (MPa)	Elongation at Break (%)	Tensile Strength (MPa)
CM	1293.92 ± 47.76	21.09 ± 0.17	139.67±88.08	18.85±2.30
EP	839.31 ± 32.63	15.13 ± 1.12	474.20±364.22	11.96±8.61

4. CONCLUSIONS

Both neat HMPEX and the HMPEX/ 5% Nb2O5 exhibit properties suitable for medical grade UHMWPE resins according to ASTM F648-00.

The mechanical properties of HMPEX/ Nb2O5 composites prepared by compression molding are superior to those obtained by the extrusion process.

REFERENCES

[1] Banoriya, D, Purohit, R. and Dwedi, R.K, 'Advanced application of polymer base biomaterials, Mater Todar-Proc. 4 (2) (2017) 3534 – 41. https://doi.org/10.1016/j.matpe.2017.02.244

[2] Wei, H. and Benson, R., 'Polymeric Biomaterials', in Handbook of Biopolymers and Biodegradable Plastics (Plastics Design Library, W . A. Publishing, Boston, 2013) 87-107.

[3] Rodrigues, L.B., 'Aplicações de biomateriais em ortopedia', *Estud. Tecnol. Eng.* **9** (2) (2013) 63-76. doi: 10.4013/ete.2013.92.02

[4] Sobieraj, M.C. and Rimnac, C.M., 'Ultra high molecular weight polyethylene: Mechanics, morphology, and clinical behavior', *J. Mech. Behav. Biomed. Mater.* **2** (5) (2009): 433–443.

[5] Farias, J.X.N. de, Sanson F.K. and Calumby R.B. R. 'Polietileno de ultra alto peso molecular (PEUAPM): Propriedades, processamento e aplicações', Anais 9° Congresso Brasileiro de Polímeros, Campina Grande, PB, October, 2007 (Associação Brasileira de Polímeros, 2007).

[6] Agrawal M. 'Applications of ultrahigh molecular weight polyethylene fibres in dentistry: A review article'. *J Adv Med Dent Scie*. **2**(2) (2014) 95-99.

[7] Strassler, H.E., 'Fiber-reinforcing material for dental resins', *Inside Dent.*, **4** (5) (2008).

[8] Deliperi, S., Bardwell, D.N. and Coiana, C., 'Reconstruction of devital teeth using direct fiber-reinforced composite resins: a case report. *J. Adhes. Dent.* **7** (2) (2005): 165-71.

[9] Wiebeck, H. and Harada, J., 'Plásticos de Engenharia: Tecnologia e Aplicações', 1st Ed. (Artibler, São Paulo 2005) Cap. 2, 37-50.

[10] Sangeeta H. and Jog, J.P., 'Sintering of ultra-high molecular weight polyethylene', *Bull. Mater. Sci.* **23** (3) (2000) 221–226.

[11] Xu, H., An, M., Lv, Y. et al.. 'Strutural development of gel-spinning UHMWPE fibers through industrial hot-drawing process analyzed by small/wide-angle X-ray scattering', *Polym. Bull.* **74** (3) (2017) 74: 721. https://doi.org/10.1007/s00289-016-1742-z

[12] Fang, X., Wyatt, T., Hong, Y. et al., 'Gel spinning of UHMWPE fibers with polybutene as a new spin solvent', *Polym. Eng. Sci.* **56** (2016) 697-706. doi:10.1002/pen.24296

[13] Rajput, A.W., Aleem, A.ul and Arain, F.A., 'An environmentally friendly process for the preparation of UHMWPE as-spun fibres', *Int. J. Polym. Sci*., **2014** Art ID 480149, 5 pages, 2014.

[14] Souza M. Carvalho et al., 'Processamento de polietileno de ultra alta massa molar (PEUAMM) por moagem de alta energia', Anais 10º Congresso Brasileiro de Polímeros, Foz do Iguaçu, PR, 2009 (Associação Brasileira de Polímeros, 2009).

[15] Bala, A.S., Wahab, M.S., Ahmad, M., Soon, C.F. and Ramli, M.S., 'Processability and thermal properties of ultra-high molecular weight polyethylene/polypropylene blends', *ARPN J. Eng. Appl. Sci.* **11** (8) (2016) 5481-86. ISSN 1819-6608.

[16] Yilmaz, G., Ellingham, T. and Turngm, L., 'Improved injection molding of ultra-high molecular weight polyethylene using supercritical nitrogen', in SPE ANTEC Anaheim, May, 2017 ()1496

[17] Alvares, D.R.S; Silva, J.C.; Tatizawa, et al., 'Desenvolvimento de Polietileno de Ultra Alto Peso Molecular para Processamento Convencional', *Polímeros.* **5** (1) (1995) 34-36.

[18] Tsujimoto, A., Barkmeier, W.W., Fischer N.G. et al., 'Wear of resin composites: Current insights into underlying mechanisms, evaluation methods and influential factors', *Jpn. Dent. Sci. Rev.* **54** (2) (2018) 76-87. ISSN 1882-7616. https://doi.org/10.1016/j.jdsr.2017.11.002.

[19] Nine, Md J., Choudhury, D., Hee A.C. et al., 'Wear debris characterization and corresponding biological response: artificial hip and knee joints', *Materials* **7** (2) (2014) 980-1016.

[20] Brandão, A., Lucas, F., Joaquim, G. et al., 'Partículas de polietileno e osteólise periprotética da anca: aspetos biológicos e tribológicos' in ORT - Publicações Pedagógicas (Coimbra, Serviço de Ortopedia, Centro Hospitalar e Universitário de Coimbra, 2013) 1-17.
[21] Rodrigues, A.M., Vanzillotta, P.S., Figuereido, C.M.S., et al., 'Avaliação in vitro da resistência à abrasão de dois dentes de resina acrílica melhorada utilizados na confecção de próteses removíveis'. *Rev. Bras. Odontol*. **68** (1) (2011) 25-28.
[22] Ho, S. P., Caldwell, R. A. and LaBerge, M., 'Polymers for dental and orthopedic applications', ed. Shalaby, Sh.W. and Salz, U. (CRC Press, Boca Ratón, FL, USA, 2007) Cap 10, 303-336.
[23] Teixeira, R.P., Influência da adição de alumina nas propriedades de compósitos de matriz polimérica para restaurações provisórias dentais. Dissertation (Master's degree in Science), Instituto Militar de Engenharia, IME. Rio de Janeiro, 2008
[24] Panin, S.V, Kornienko, L.A., Suan, N. T., Poltaranin, M.A. and Ivanova, L.R., 'Increasing the wear resistance of ultra-high molecular weight polyethylene by adding solid lubricating fillers', 2014, *AIP Conf. Proc.,* **1623** (1) (2014) 471-474, doi: 10.1063/1.4898984.
[25] Brostow W., Lobland, H.E.H., Hnatchuk N. and Perez, J.M., 'Improvement of scratch and wear resistance of polymers by fillers including nanofillers'. *Nanomaterials,* **7** (66) (2017) 1-12.
[26] Wannasri, S., Panin, S.V., Ivanova et al., 'Increasing wear resistance of UHMWPE by mechanical activation and chemical modification combined with addition of nanofibers', *Procedia Eng.,* **1** (1) (2009) 67–70. ISSN: 1877-7058.
[27] Gupta, C.K. and Suri, A.K., 'Extractive metallurgy of niobium' (CR Press, Boca Ratón, FL, USA, 1994). ISBN: 0-8493-6071-4.
[28] Rodrigues, P.E.P., Terada, M., Junior, O.R.A. et al., 'Niobium pentoxide coating replacing zinc phosphate coating', *Matéria (Rio J.)* **19 (**2) (2014) 105-116.
[29] Ramírez, G., Rodil, S.E., Arzate, H., Muhl, S. and Olaya, J.J.,'Niobium based coatings for dental implants', *Appl. Surf. Sci.* **257** (7) (2011) 2555-59. ISSN 0169-4332.
[30] Olivares-Navarrete, R., Olaya, J.J., Ramirez, C. et al., 'Biocompatibility of niobium coatings', *Coatings* **1** (1) (2011) 72-87; doi:10.3390/coatings1010072
[31] Li, Y., Munir, K.S., Lin, J. and Wen, C., 'Titanium-niobium pentoxide composites for biomedical applications', *Bioact. Mat.* **1** (2) (2016) 127-131. ISSN 2452-199X,
[32] Bonadio, T.G.M., 'Biocompósitos de pentóxido de nióbio, hidroxiapatita e β- fosfato tricálcico: produção, caracterização e estudos in vivo como suportes ósseos denso e poroso', Thesis (Doctor's degree in Physics), Universidade Estadual de Maringá, Maringa, PR. 2014.
[33] Silva, M.H.P. da, Ramirez, M., Granjeiro, J. et al., 'In vitro assessment of new niobium phosphate glasses and glass ceramic', *Key Eng. Mater*. **361-363** (1) (2008) 229-232. ISSN: 1662-9795. doi: 10.4028/www.scientific.net/KEM.361-363.229.
[34] Lopes, J. H., 'Biovidros derivados do 45S5: Os efeitos do Nb_2O_5 ou da modificação da superfície com Ca^{2+} sobre a estrutura e bioatividade'. Thesis (Doctor's degree in Science), Universidade Estadual de Campinas, UNICAMP, Instituto de Química, Campinas, SP, 2015.
[35] Silva, G.F., Tanomaru-Filho, Bernardi, M.I.B. et al, 'Niobium pentoxide as radiopacifying agent of calcium silicate-based material: evaluation of physicochemical and biological properties', *Clin. Oral Invest*. **19** (8) (2015) 2015-25. ISSN 1432-6981**.** https://doi.org/10.1007/s00784-015-1412-9
[36] Farias, Í. de L., Silva, F.N. da, Araujo, P.M.A.G.de, et al., 'Caracterização do óxido de nióbio (Nb_2O_5) para atuar como radiopacificador em produtos odontológicos', Anais I Congresso Nacional de Pesquisa e Ensino em Ciências. Campina Grande, PR, Junho, 2016. (UFCG/UEPB) .
[37] Leitune, V.C.B., Collares, F.M., Takimi, A. et al., 'Niobium pentoxide as a novel filler for dental adhesive resin', *J. Dent*. **41** (2) (2013) 106 - 113. ISSN 0300-5712.
[38] Young, M. D., Tran, N., Tran, P.A. et al., 'Niobium oxide–polydimethylsiloxane hybrid composite coatings for tuning primary fibroblast functions'. *J. Biomed. Mater. Res. Part A*, **102** (5) (2014) 1478-1485. https://doi.org/10.1002/jbm.a.34832
[39] Khalaf, M.N., 'Mechanical properties of filled high density polyethylene', J Saudi Chemical Society, **19** (2015) 88-91. ISSN: 1319-6103.

[40] Tasdemir, M. and Ersoy, S., 'Mechanical, morphological and thermal properties of HDPE polymer composites filled with talc, calcium carbonate and glass spheres'. *Rev Rom. Mater.* **45** (2) (2015) 147-154.

[41] Taşdemir, M., 'Relation between microstructure and tribological properties of high density polyethylene hibrid composites filled with untreated glass spheres,talc and calcium carbonate', *Key Eng. Mater.* **592-593** (2014) 655-659, doi:10.4028/www.scientific.net/KEM.592-593.655.

[42] Parvin, N; Ullah, S., Mina, F. and Gafur, A. 'Structures and mechanical properties of talc and carbon black reinforced high-density polyethylene composites: effects of organic and inorganic fillers', Journal of Bangladesh Academy of Sciences, 37 (1) (1) (2013) 11-20.

[43] Akinci, A., 'Mechanical and structural properties of polypropylene composites filled with graphite flakes', *Arch. Mater. Sci. Eng*. **35** (2) (2009) 91-94. ISSN: 1897-2764.

[44] Tavman, I.H. 'Thermal and mechanical properties of aluminum powder filled high density polyethylene composite', J App. Polym. Sci. **62**(12)(1996)2161–2167.

[45] Berçot, C.J. and Rocha, M.C.G., 'Avaliação do efeito da adição de óxido de nióbio nas propriedades do polipropileno', Anais 22º Congresso Brasileiro de Engenharia e Ciência dos Materiais, Natal, RN, Novembro, 2016. (UFERSA). ISBN 978-85-93068-02-7

[46] Chang, B.P. Akil, H. Md., Nasir, R. Md. and Nurdijati, S.,'Mechanical and antibacterial properties of treated and untreated zinc oxide filled UHMWPE composites', *J. Thermoplast. Compos*., **24**(2011)653-667.

NANOCELLULOSE-COATED CARBON FIBERS TOWARDS DEVELOPING HIERARCHICAL POLYMER MATRIX COMPOSITES

Braian E.B. Uribe, Alessandra C. Soares-Pozzi, José R. Tarpani*

Sao Carlos School of Engineering (EESC-USP), 13.566-590, Sao Carlos-SP, Brazil

*Corresponding author: jrpan@sc.usp.br

https://doi.org/10.21452/bccm4.2018.13.09

Abstract: 0.1, 0.25 and 0.5 wt% microfibrillated cellulose (MFC) aqueous suspensions were used to impregnate carbon fiber fabric via aspersion and immersion to build cost-effective hierarchical polymer matrix composite laminates with enhanced load carrying capacity. Mechanical performance improvements of 28 and 21% were obtained in terms of ultimate tensile strength for 0.1 wt% MFC suspension via aspersion and immersion routes, respectively. The same impregnation conditions provided increments in tensile toughness of 52 and 31%, respectively, showing the positive role of the nanostructure as a strong interfacial agent. MFC solution aspersion was determined as the best impregnation procedure towards strengthening and toughening of the final product.

Keywords: Carbon fibers; Microfibrillated cellulose; Interphase, Mechanical properties.

1. INTRODUCTION

In recent years there has been strong interest in developing polymer matrix composites presenting at least one of their main phases on the nanometric scale [1]; Such materials offer advantages compared to micro- and macro-scale composites that depend not only on the properties of each individual constituent, but also on their morphological and interfacial characteristics [2]. The use of aqueous suspensions to coat continuous fibers with cellulose-based nanofillers has been shown to be an accessible alternative method to improve the mechanical performance of cost-effective polymer composites [3,4]. In the present work an attempt is made to coat carbon fibers with MFC using two different impregnation methods, namely aspersion and immersion, followed by resin infusion under flexible tooling (RIFT) as the manufacturing technique [5,6]. Additionally, an unexplored route based on the use of phosphotungstic acid (PTA) for the selective positive staining of hydroxyl groups [7] was carried out to contrast the nanocellulose interphase via backscattering electron microscopy. This work thus presents information of interest to both academic research and industrial application of polymer composites, with its focus in the field of hierarchical structures.

2. MATERIALS AND METHODS

MFC was synthesized from eucalyptus and was provided by Suzano Pulp and Paper™, Brazil, in the form of water suspension. Continuous PAN-based unsized carbon fiber in the form of 0.30 mm-thick bidirectional plain-weave fabric with areal weight of 200 g/m^2, 5 bundles/cm in both the warp and weft directions, and 3K filaments per bundle, as provided by Fibertex Brazil™, was employed as the main reinforcing structure. A liquid system composed of Araldite LY 5052 epoxy resin and Aradur 5052 hardener purchased from Huntsman™ Brazil was selected as the polymer matrix.

2.1 COMPOSITE PREPARATION

2.1.1 MFC impregnation of carbon fiber fabric (CFF)

Unsized CFF dry preforms were coated using immersion and aspersion coating processes. Immersion was carried out by dipping the fabrics in aqueous MFC suspension (0.1, 0.25 and 0.5% MFC by weight) for 60 seconds. The spray process was developed using the above-mentioned MFC concentrations and a Western Spray-Gun™ equipped with a 1.5 mm diameter nozzle. Pressure and application distance were maintained constant at 300 kPa and 250 mm, respectively, to impregnate the fabrics. Coated fabrics were subsequently dried in an oven for 3 h at 102 °C until weight loss stopped.

2.1.2 Manufacture of composite laminates

Five plies with in-plane dimensions of 300 x 300 mm^2, each comprising an unsized CFF covered with MFC, were piled up according to the quasi-isotropic sequence [(0/90),(45),(0/90),(45),(0/90)]. The resin system was degassed at -93 kPa for 8 minutes at an ambient temperature of 25 °C and vacuum assisted liquid resin infusion was then carried out using the same set of pressure and temperature given above. A period of 10 min was spent infusing each composite plaque, giving rise to 1.5 mm-thick laminates. Initial curing was carried out for 24 h under vacuum bagging pressure of -50 kPa at ambient temperature. Post curing was performed in an electric oven for 1 h at 90 °C. The same conditions were applied to build baseline laminates comprising unsized CFF. To differentiate each composite condition, laminates were designated as follows:

CF: Baseline composite laminate (neat CF fibers), I1: 0.1wt.% MFC suspension deposited by immersion, I2: 0.25wt.% MFC suspension deposited by immersion, I5: 0.5wt.% MFC suspension deposited by immersion, A1: 0.1wt.% MFC suspension deposited by aspersion), A2: 0.25wt.% MFC suspension deposited by aspersion, A5: 0.5wt.% MFC suspension deposited by aspersion

2.2 CHARACTERIZATION

2.2.1 Scanning Electron Microscopy (SEM)

Inspection of the topology and morphological features of coated CF surfaces was carried out using a low vacuum, high-resolution FEI Inspect F50™ Field Emission SEM, with the examined surfaces previously sputter-coated with electrically conductive ultra-thin layers of carbon to improve imaging quality. Secondary electron imaging mode was employed at low accelerating voltages ranging from 2 to 10 kV. To assess the interphase, SEM backscattering mode was used at a voltage of 15 kV. Samples were subjected to selective staining of Hydroxyl groups with PTA.

2.2.2 Atomic Force Microscopy (AFM)

Surface assessment of each type of coated CF sample was carried out using an NX-10 Park Systems™ AFM. Silicon probes provided by NCHR Nanoworld™ with a resonance frequency of 320 KHz and a spring constant of 42 N/m were employed to scan the respective surfaces. To perform the measurements, CF and MFC as isolated phases, as well as the CFF/MFC arrangements were mounted onto a metallic stub with a flat Mica lamella surface. Whenever necessary, fast-curing Araldite™ adhesive was used to attach each sample to the lamella. Finally, the images were processed in the open platform software Gwyddion™.

2.2.3 Stereoscopy

CF surface was observed before and after coating with MFC using a Zeiss Discovery™ V8 stereoscope at 5x magnification. Image acquisition was carried out using an AxioCam Erc™ 5s integrated camera, and subsequent image analysis in the open platform software ImageJ™.

2.2.4 Transmission electron microscopy (TEM)

TEM studies were performed using FEI Titan Low-Base™ microscope working at 80 kV and equipped with a CESCOR Cs™ probe corrector, an ultra-bright X-FEG™ electron source and a monochromator. TEM imaging was performed with the high-angle annular dark field (HAADF) detector. Composite sections with ~60 nm in thickness were produced via focused ion beam (FIB).

2.2.5 Contact angle measurements

The produced materials were analyzed at room temperature with KSV CAM101™ equipment. Measurements were performed for each composite condition as well as for neat CF and epoxy resin, examining three samples of each type of material and taking three measurements per sample. The method used for the contact angle assessment was based on the measurement of the contact angle of a drop of water deposited onto the surface of treated and untreated fiber bundles.

2.2.6 Mechanical testing

Mechanical testing was performed in an EMIC™ model 23-100 electromechanical universal testing machine equipped with a 10 kN load cell and an axial extensometer with an original gauge length of 25 mm. In tensile mode, five test coupons with in-plane dimensions 250 x 22 mm^2 were used for each class of composite laminate. Tests were carried out according to the ASTM-D3039-08 standard under displacement-controlled conditions, with the test speed fixed at a speed of 2 mm/min.

3. RESULTS AND DISCUSSION

3.1 Comparison of impregnation routes

The amount of MFC deposited onto CF by immersion and aspersion, respectively, are plotted in Figure 1. The aspersion method was more efficient for nanostructure deposition within the entire range of MFC concentrations studied, attaining the peak at 0.25wt% MFC suspension in water.

Interesting to note that the water dependency of each impregnation method is crucial to optimize the deposition process.

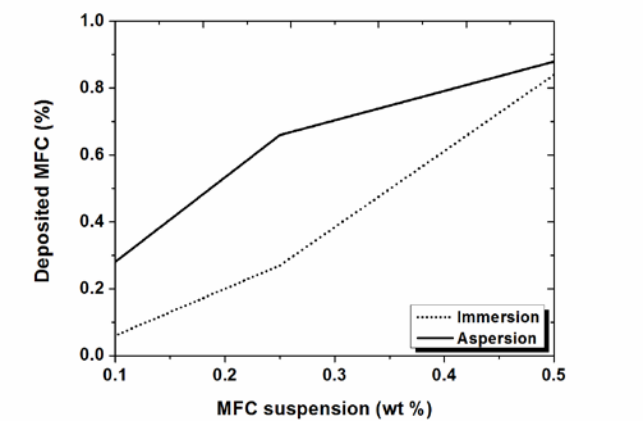

Fig. 1: Amount of deposited MFC onto CF as a function of the MFC concentration for immersion and aspersion impregnation routes.

3.2 Phase morphology

Isolated carbon microfibers and MFC nanofibers, as well as their assembling, were observed via different microscopy techniques at increasing image magnification, as shown in Figure 2.

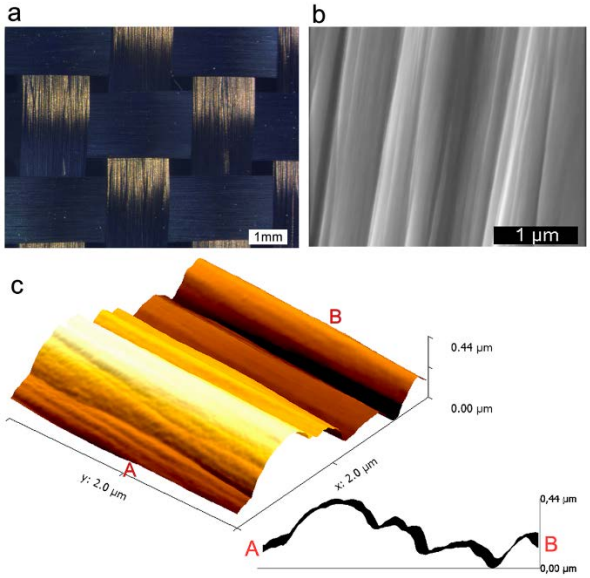

Fig. 2: Three distinct views of CF surface: (a) Stereoscopy, (b) FEG-SEM, and (c) AFM (inset corresponds to the height profile measured along the segment AB).

The irregular surface topography (12 nm roughness) suggests the possibility of mechanical interlocking between the main constituents of the composite.

MFC was also analyzed via AFM as shown in Figure 3, with shape and size features being revealed. The main nanofibres are < 75 nm in height, which are linked to minor substructures of ~30 nm, therefore forming a hierarchical array. This complex nanostructure trends to provide efficient load transfer and distribution along the whole nanophase element, resulting in cooperative dynamics of the thinner nanofibrils acting as an energy dissipater for the thicker ones. The compatibility of carbon micro fiber / MFC nanofiber is based upon mechanical anchoring mechanism [8,9]. However, previous studies have also shown the generation of hydroxyl and

carbonyl groups on the CF surface when exposed to atmospheric oxygen [10], thus suggesting that Van der Waals interactions might cooperate to MFC / CF interaction owing to the reactivity of the OH- groups present on the MFC surface [11].

Roughness of MFC / CF array was determined as 79.5 nm. This substantial increase in surface roughness (700%), when compared to neat CF, gives rise nano- and microcavities, creating multiple points of mechanical anchorage for the solid resin after infusion process, leading to strong and efficient matrix / reinforcement interplay.

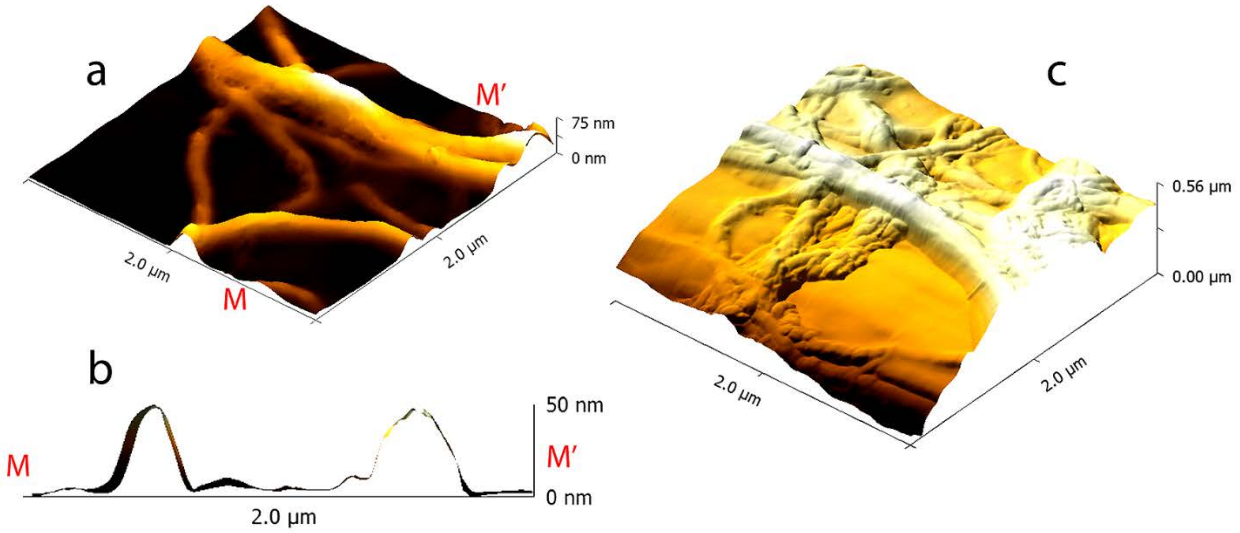

Fig. 3: (a) AFM micrograph of MFC structure; (b) Height profile measured along the segment MM'; (c) MFC deposited onto a CF filament.

3.3 MFC-impregnated CF

Stereoscopic analysis produced the images displayed in Figure 4, where the insets correspond to FEG-SEM secondary electron images of MFC impregnated-CF regions. Immersion process trends to induce nanostructure coalescence with increasing MFC suspension concentration, leading to greater heterogeneity as compared to the aspersion method. By contrast, the latter process trends to generate thinner coatings with evenly MFC distribution and higher solid content.

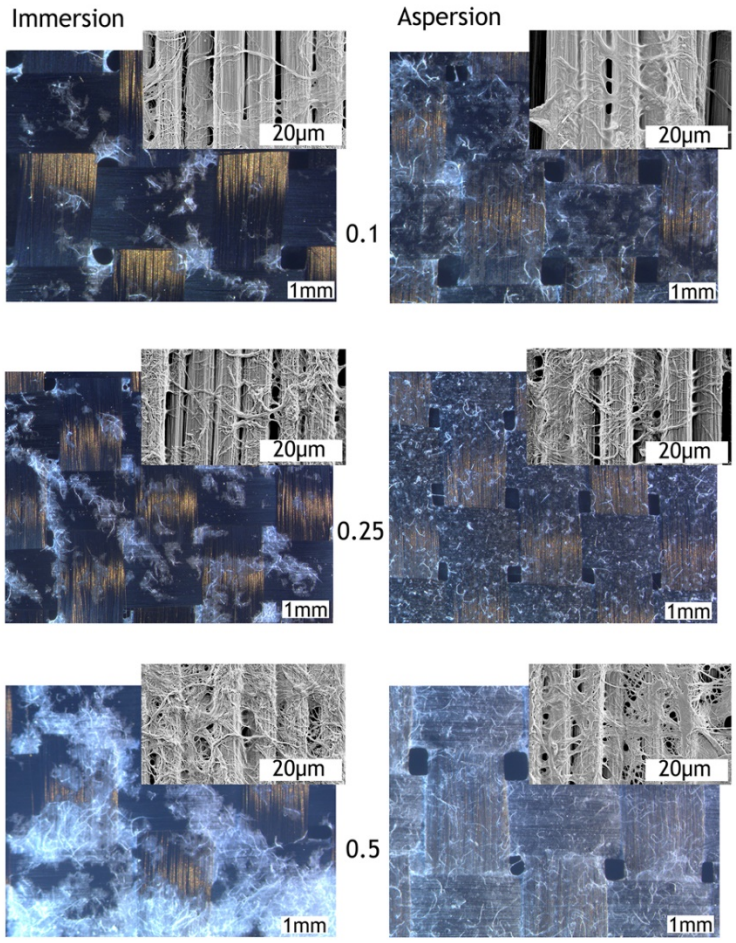

Fig. 4 Stereoscopic and FEG-SEM images of MFC-coated CF via immersion and aspersion routes, respectively. MFC solution concentration are indicated.

3.4 Interphase analysis

HAADF secondary electrons micrographs referring to the minimum interphase thickness of A1 sample are presented in Figure 5.

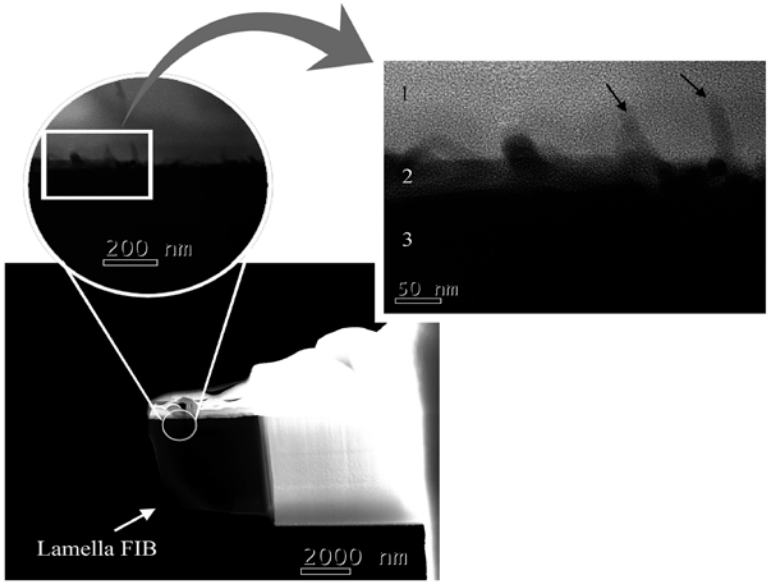

Fig. 5 HAADF STEM micrographs displaying matrix / fibre interphase in composite A1.

MFC coating resulted in an interphase with visible nanofibres (black arrows) and orthogonally aligned towards the main CF. The average widths of the nanofibres and interphase were 20 ± 6 nm and 40 ± 1 nm, respectively. FC / MFC aspect ratio equals 175. Figure 6 displays FEG-SEM micrographs of the composite interphase in arrangement A1, where the inhomogeneous nature of the microfibrillated cellulose, due to its defibrillation during the synthesis process, is seen [12].

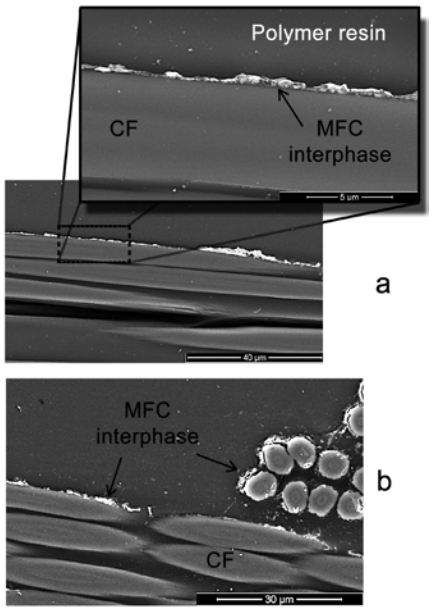

Fig. 6 Composite interphase aspect as seen via BSE-FEG for CF directions: (a) 0°, (b) 45° and 90°. MFC treated with phosphotungstic acid (PTA) as the selective staining agent.

Minimum and maximum interphase widths were calculated at 150 and 2.0 μm, with an increasing trend to wider interphase for CF oriented from 0° to 90°.

3.5 Contact angle measurement

Figure 7 shows that the epoxy resin matrix presents low water wettability (hydrophobic character). By contrast, unsized CF displays intermediate value, which was further reduced with the deposition of MFC, denoting increasing adhesion potential [13,14]. This indicates that MFC can be recommended for use in composite systems having polar resin matrices.

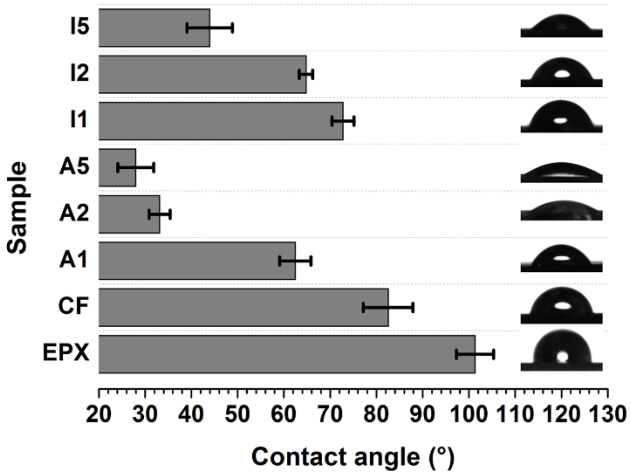

Fig. 7 Contact angle measurements.

As shown in Figure 7, aspersion MFC deposition provides the lowest contact angle, therefore evidencing its high potential for generating wettable CF surfaces for MFC contents lower than 0.28% on a CF weight basis.

3.6 Mechanical properties

Figure 8 shows tensile stress-strain curves for the studied composites. For the aspersion process, the most favorable result was verified in CF impregnated with 0.1wt% aqueous suspension, leading to an increase of 28% in ultimate strength as compared to the baseline condition (neat CF). By contrast, the same impregnation route using MFC concentrations of 0.25 and 0.5wt% impacted negatively that mechanical tensile property.

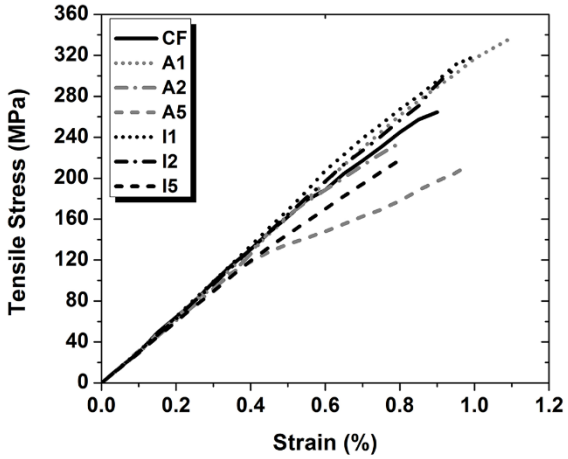

Fig. 8 Stress-strain curves obtained from tensile testing.

For the immersion rout, whereas conditions of 0.1 and 0.25wt% MFC suspension resulted in increased tensile strength of 21 and 16%, respectively, the mechanical response of CF coated with 0.5wt% MFC was impaired by 18%. The tensile strength improvement in sample I1 is similar to values reported in the literature [3]. From the results, it can be hypothesized that lower MFC amounts provides more effective hydrogen bonding between hydroxyl groups present in both phases, i.e., optimized water absorption level [15]. Tensile stiffness was practically the same for all composites formulations, indicating that at lower strains the role of MFC in restraining polymer chain movement is negligible. In previous study [3], the authors found MFC improving tensile modulus by 28% for non-post-cured composites This point needs further study and clarification. Toughness at ultimate load, corresponding to the area underneath the stress-strain curve, was discovered to increase from 31 to 52% for I1 and A1 samples, respectively, permitting one to conclude that aspersion process is substantially more efficient than immersion route in providing toughening via fiber bridging [16].

3.7 Fractographic analysis

Figure 9a presents the composite structure of sample A1 after tensile fracture, which portrays well-adhered and consolidated interlayers (white arrow). Propagation of cracks in the middle zone resulted in catastrophic failure, possibly associated with a high local concentration of nanofibrils. As shown in Figure 9b, nanocellulose-rich region (black arrow) acts as a bridge joining solid blocks of resin to the CF reinforcement. This micrograph also shows the surrounding nanophase regarding the CF surface. Several thicker fibrils can be observed in Figure 9c, indicating the saturation of the CF surface with MFC, which decreased the adhesion of the main composite constituents due the remarkable difference in surface energy between the resin and the treated CF surface (see Figure 7 referring to A5 sample). microfracture displayed in Figure 9d reveals a catastrophic interphase rupture, indication that deposited MFC can act as a stress concentration region as well. By contrast, Figure 10 portrays a web-like MFC structure firmly attached to the main composite constituents, indicating the vital role of appropriate control of MFC´s branch size and spatial distribution, beside naturally the deposited amount onto CF.

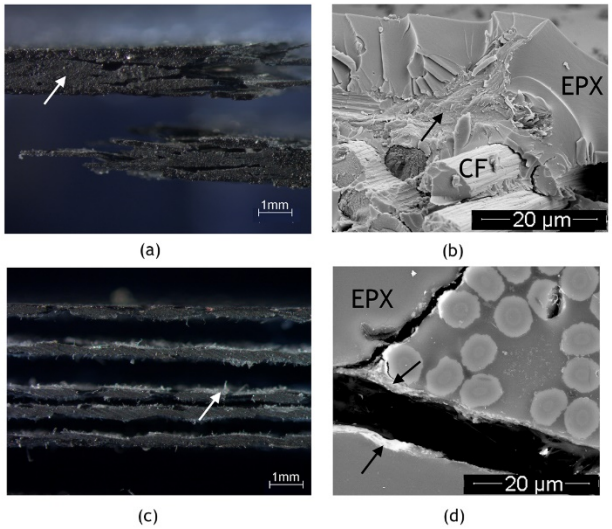

Fig. 9 Fracture surfaces after tensile testing displaying: (a,b) Micro-failure in best-performing sample A1; (c,d) Macro- and micro-failure in worst-performing sample A5.

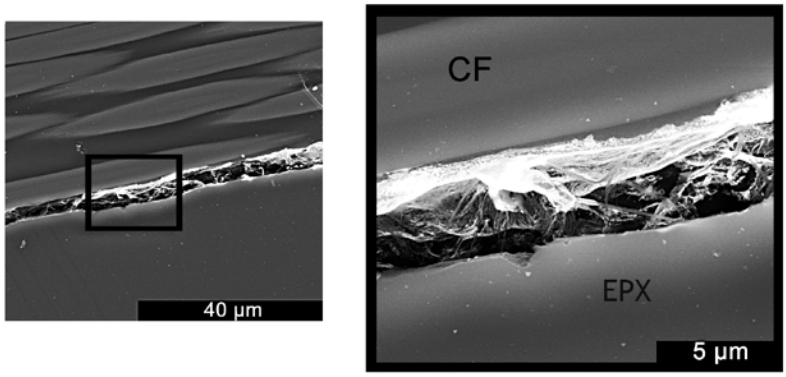

Fig. 10 Composite interphase after tensile fracture.

4. CONCLUSIONS

In this paper, maximum improvement on tensile strength and fracture toughness of hierarchical composite laminates were reached for an MFC concentration in water of 0.1% (0.28% MFC in terms of CF weight), with the aspersion method shown as the more promising MFC / CF impregnation method. Nanocellulose interphase evaluation via electron microscopy techniques was enhanced by selective PTA staining, which provided high contrast for observation in backscattering electron mode.

Acknowledgements: To CNPq-Brazil (Process 140339/2015-9), Dr. Antonio Carvalho and M.Sc. Emanoele Chiromito (SMM-EESC-USP São Carlos, Brazil), Dr. Raul Arenal (Instituto de Nanosciencia de Aragon, Universidad de Zaragoza, Spain) and Suzano Pulp and Paper™, Brazil.

5. REFERENCES

[1] Hussain F. Polymer-matrix nanocomposites, processing, manufacturing, and application: An Overview. J. Compos. Mater. 2006, 40, 1511–1575.
[2] Zhang Q, Liu J, Sager R, Dai L, Baur J. Hierarchical composites of carbon nanotubes on carbon fiber: Influence of growth condition on fiber tensile properties. Compos. Sci. Technol. 2009, 69, 594–601.
[3] Uribe BEB, Chiromito EMS, Carvalho AJF, Tarpani JR. Low-cost, environmentally friendly route for producing CFRP laminates with microfibrillated cellulose interphase. Express. Polym. Lett. 2017, 11, 47–59.
[4] Asadi A, Miller M, Moon RJ, Kalaitzidou K. Improving the interfacial and mechanical properties of short glass fiber/epoxy composites by coating the glass fibers with cellulose nanocrystals. Express. Polym. Lett. 2016, 10, 587–597.
[5] Williams C, Summerscales J, Grove S. Resin infusion under flexible tooling (RIFT): a review. Compos. Part A Appl. Sci. Manuf. 1996, 27, 517–524.
[6] Summerscales J, Searle TJ. Low-pressure (vacuum infusion) techniques for moulding large composite structures. J. Mater. Des. Appl. 2005, 219, 45–58.
[7] Sawyer, L, Grubb, D, Meyers, GF, Eds., Polymer Miscroscopy, 3rd ed., Springer-Verlag: New York, 2008.
[8] Shi Y, Wang B. Mechanical properties of carbon fiber/cellulose composite papers modified by hot-melting fibers. Prog. Nat. Sci. Mater. Int. 2014, 24, 56–60.
[9] Song W, Gu A, Liang G, Yuan L. Effect of the surface roughness on interfacial properties of carbon fibers reinforced epoxy resin composites. Appl. Surf. Sci. 2011, 257, 4069–4074.

[10] Yip PW, Lin SS. Effect of surface oxygen on adhesion of carbon fiber reinforced composites. MRS Proc. 1989, 170.
[11] Romanzini D, Ornaghi-Junior HL, Amico SC, Zattera AJ. Preparation and characterization of ramie-glass fiber reinforced polymer matrix hybrid composites. Mater. Res. 2012, 15, 415–420.
[12] Chinga-Carrasco G. Cellulose fibres, nanofibrils and microfibrils: The morphological sequence of MFC components from a plant physiology and fibre technology point of view. Nanoscale Res. Lett. 2011, 6, 417.
[13] Ma L, Meng L, Wang Y, Wu G, Fan D, Yu J, et al. Interfacial properties and impact toughness of dendritic hexamethylenetetramine functionalized carbon fiber with varying chain lengths. RSC Adv. 2014, 4, 39156–39166.
[14] Ma L, Meng L, Wu G, Wang Y, Zhao M, Zhang C, et al. Improving the interfacial properties of carbon fiber-reinforced epoxy composites by grafting of branched polyethyleneimine on carbon fiber surface in supercritical methanol. Compos. Sci. Technol. 2015, 114, 64–71.
[15] Chen J, Nakamura T, Aoki K, Aoki Y, Utsunomiya T. Curing of epoxy resin contaminated with water. J. Appl. Polym. Sci. 2001, 79, 214–220.
[16] Philippidis TP, Theocaris PS, Roupakias GS. Delamination prevention in composites by interleaving techniques. Int. J. Damage. Mech. 1993, 2, 349–363.

14. RECYCLING AND SUSTAINABILITY

THERMAL PROPERTIES STUDY OF RECYCLED ESPRESSO COFFEE CAPSULES FOR BIOCOMPOSITE APPLICATION

Anne Shayene Campos de Bomfim(1), Herman Jacobus Cornelis Voorwald(1), Maria Odila Hilário Cioffi(1) and Kelly Cristina Coelho de Carvalho Benini(1)

(1) Department of Materials and Technology, São Paulo State University (UNESP), School of Engineering, Guaratinguetá, São Paulo, Brazil (12516-410). Fatigue and Aeronautical Materials Research Group.

https://doi.org/10.21452/bccm4.2018.14.01

Abstract

Solid plastic waste has been an environment problem with a lot of discussions in literature. The humanity needs to think about the future and be aware about its residues because only with this thinking will be possible to decrease environmental impacts and conserve natural resources. Espresso coffee capsules waste have grown in the last years because espresso machines provide an easily and quickly way to have a coffee time. This residue is difficult to recycling because it is composed of various materials. However the needs to decrease the impact caused by this waste influenced the thinking of researchers about applied this recycled polymer as matrix in polymeric biocomposites. In this context, the present work has the main objective of to separate the polypropylene (PP) that is the main component of the capsules, and carried out the mechanical recycling of this material to use it as a matrix of a biocomposites reinforced with natural fibers. In order to understand thermal degradation, melting point and crystallization point, the recycled material was characterized before and after recycling process by thermogravimetric (TGA) and differential scanning calorimetry (DSC) analysis and compared with a virgin PP. TGA shows no significant thermal stability loss with PP thermal degradation beginning at 280 ºC for virgin PP and 275 ºC for capsules and recycled material. DSC shows melting point and crystallization point respectively at 163 ºC and 114 ºC for virgin PP, 163 ºC and 116 ºC for capsules and 163 ºC and 114 ºC for recycled material. These results demonstrate the viability of mechanical recycling of plastic capsules for future reuse in new products.

1. INTRODUCTION

The need to decrease the environment impacts has increased the solutions in recycling and reuse of materials. The plastic solid waste is one of the major environmental problems because of the large production and the degradation time [1]. Plastics are the major contributor to municipal and

industrial residues and their recycling is a sustainable way to improve the humanity future through its reuse in new products avoiding the amount of waste in sanitary landfills [2].

The recycling process can be mechanical, chemical or across to the recover energy by incineration [3]. Mechanical recycling allows direct material recuperation to reuse in new products manufacturing [2], the waste is separated, washed and grinding to become a new raw material [4].

The espresso coffee capsules is an emerging solid waste because the advantage of their practicality with coffee variations done in a quickly way and the decrease price of espresso domestic machines. The research of Consórcio Pesquisa Café (2015) shows that between 2014 and 2019 the coffee capsules market can almost triple with a volume of 6 thousand tons to 16 thousand tons [5]. However, these wastes cannot be recycling in whatever place because the materials variation like plastic, coffee grounds and aluminium, influencing the sanitary landfills overcrowding [6]. Then this residue needs more attention, like selective collection to material separation and recycling.

Nowadays there are studies about environment friendly polymers to be used as polymeric matrix in biocomposites with non-structural applications [7]. These biocomposites can have biodegradable polymers [8], natural fibers [9] or recycled polymers [10] to be considered a sustainable material. Composites with recycled polymeric matrix are getting more attention in literature because the use of waste materials help the environmental preservation [1].

In this context, the objective of this work was the recycling of espresso coffee capsules plastic waste and analysed the thermal properties through thermogravimetric analysis (TGA) and differential scanning calorimetry (DSC) to apllication in a biocomposite reinforced with natural fibers. This results were compared to virgin PP and the capsules before recycling to ensure plastic recycled thermal stability as a polymeric matrix.

2. EXPERIMENTAL

Materials

The plastic waste used was Dolce Gusto espresso coffee capsules. All varieties of capsules were collected after consumption, like coffee varieties, cappuccino, chocolates and tea. After that, they were opened to components separation and washing. The plastic package is composed by a laminated sheet sealing the package, a plastic film (only in coffee capsules), coffee powder or other variety and aluminium foil on a plastic filter. In this work only the plastic package and the filter were recycled because both are made of polypropylene (PP).

The polypropylene Homopolymer H103 manufactured by Braskem was also characterized as a control and used just as a base to compare the PP behaviour on the capsules and after recycling. The follow three samples were analysed: virgin polypropylene homopolymer H103 (PP), polypropylene capsules (PPC) and polypropylene capsules recycled (PPR).

Mechanical recycling methodology

Cleaned plastic package and plastic filter were firstly ground in a knife mill model RONE then the material was grounded again in a mill model WILLYE in order to obtain small granules. After that, the granules were dried in an oven at 60 ºC for 24 h. The dried granules were melted in a thermokinetic mixer with the objective to carry out the same process which will be used for the biocomposites obtaining.

Thermogravimetric analysis (TGA)

Approximately 10 mg of PP, PPC and PPR samples were analysed in a SII Nanotechnology INC equipment, model Exstar 6000, TG/DTA 6200 series, using a temperature range from 30 ºC to 800 ºC, at a 10 ºC/min heating rate, operating with a nitrogen flow of 100 mL/min.

Differential scanning calorimetry (DSC)

Approximately 7 mg of PP, PPC and PPR samples were analysed in a DSC Q20 TA Instruments equipment, using dual scan technique with a temperature range from -30 ºC to 250 ºC, at a 10 ºC/min heating rate and a 20 ºC/min cooling rate, operating with a nitrogen flow of 40 mL/min.

3. RESULTS AND DISCUSSION

3.1 TGA

TGA and DTG curves of PP, PPC and PPR samples are presented at Figure 1 and the thermal parameters determined from this curves are presented at Table 1.

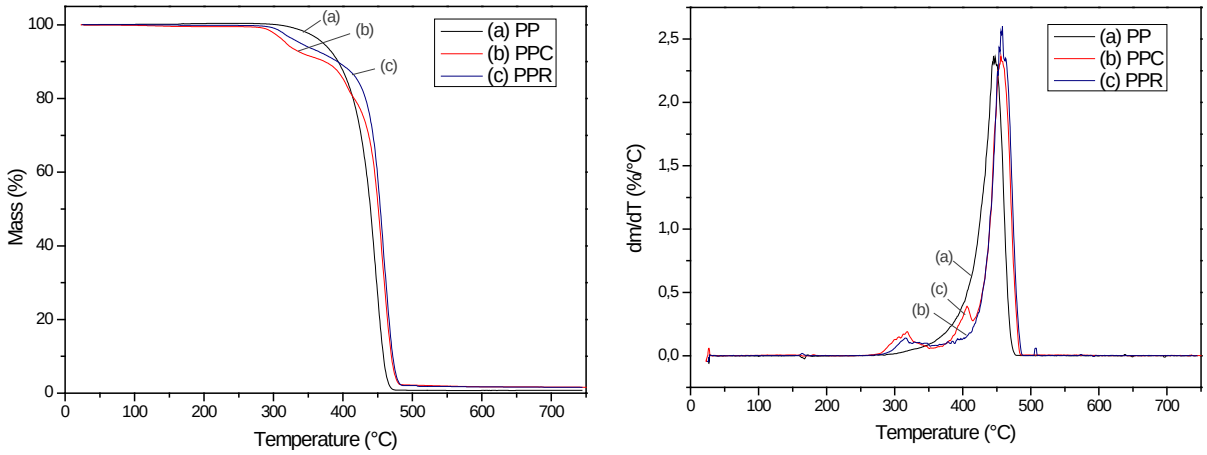

(a) (b)

Figure 84 : (a) TGA and (b) DTG curves of PP, PPC and PPR samples.

According to presented results it is possible to observe that PP presents only one thermal event with a degradation temperature beginning at 280 ºC, T_{onset} at 402 ºC and no significant residue at 700 ºC. This similar behaviour of PP thermal degradation was observed by GOLEBIEWSKI and GALESKI [11], and PARPARITA et al. [12]. On the other hand, PPC presents tree thermal events, probably because the capsules manufacturing process. Degradation temperature beginning at 275 ºC, T_{onset} at 289 ºC and 1.6 % of residue at 700 ºC was observed probably due to fixed carbons and additives, like stabilizers, pigments and antioxidants. The presence of two more peaks in PPC samples indicates there is another material degrading with the original polymer (PP), suggesting that the capsules may have some contaminant, like other polymer or substance.

Table 1: TGA parameters for PP, PPC and PPR samples

Samples	ΔT (ºC)	T_{onset} (ºC)	T_{peak} (ºC)	Weight loss (%)	Residue at 700 °C (%)
PP	280-480	402	446	99.2	0.8
PPC	275-360	289	317	9.0	1.6
	360-415	386	405	10.0	
	415-488	439	456	78.0	
PPR	275-360	294	315	7.0	1.6
	360-490	433	457	91.0	

Recycling process probably caused some thermal changes in polymers. PPR sample presents two thermal events beginning at 275 ºC, T_{onset} at 294 ºC and also 1.6 % of residue at 700 ºC. This result suggest that the second event presents in PPC specimen disappear after recycling, probably because the material was exposed to thermo-mechanical degradation due to submission to high shear forces and high temperatures during recycling [1,14].

3.2 DSC

DSC curves of second heating and cooling for PP, PPC and PPR samples are presented at Figure 2 and Figure 3, respectively. The parameters determined from this curves are presented at Table 2. In the present work only the second heating and cooling were considered to determine the melting and crystallization points since the first heating is carried out in order to cleaning the thermal history of the samples [15].

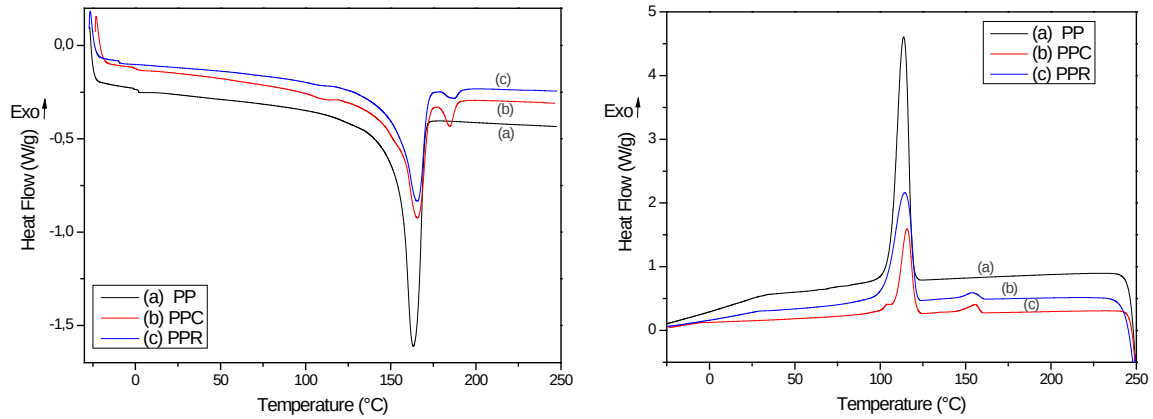

(a) (b)

Figure 85 – (a) Second Heating and (b) Colling curves for PP, PPC and PPR samples.

According to data, PP sample presents one endothermic peak with melting temperature (T_m) at 163 ºC and glass transition temperature (T_g) at 1.8 ºC, and one exothermic peak with crystallization temperature (T_c) at 114 ºC. In literature, a commercial polypropylene presents the same behaviour [15–17]. On the other hand, PPC sample presents two endothermic peaks (T_{m1} and T_{m2}) and T_g at

0.4 ºC during the second heating, and three exothermic peaks (T_{c1}, T_{c2} and T_{c3}) at the cooling, but T_{c3} is just a shoulder suggesting some PP crystal needed a little more temperature to crystalize. This difference between PP and PPC, such as the presence of one more melting and crystallization peaks suggest there is a polymer mixture in the capsule package, as observed in TGA analysis. The other polymer could be polyamide 11with melting temperature between 180-200 ºC and thermal degradation 439-451 ºC [18,19].

Table 2: DSC parameters for PP, PPC and PPR samples

Samples	T_{m1} (ºC)	ΔH_1 (J/g)	T_{m2} (ºC)	ΔH_2 (J/g)	T_{c1} (ºC)	ΔH_{c1} (J/g)	T_{c2} (ºC)	ΔH_{c2} (J/g)	T_{c3} (ºC)	ΔH_{c3} (J/g)	T_g (ºC)
PP	163	98	-	-	114	-97	-	-	-	-	1.8
PPC	165	58	185	4	155	-6	116	-52	99	-5	0.4
PPR	165	59	187	2	154	-3	114	-64	-	-	-9.6

After recycling process is possible to observe that PPR sample presents the same PPC endothermic peaks, at the same temperature, but a significant decrease in the values of T_g. During the cooling only two exothermic peaks were observed at the same temperatures of the first two crystallization peaks of PPC, indicating that the shoulder presents in PPC sample disappears after recycling process, confirming it was some PP crystal taking more temperature to crystalize.

4. CONCLUSION

Thermal analysis shows espresso coffee capsules plastic waste can be mechanical recycled to biocomposites application. There is not significant thermal stability loss, difference melting and crystallization temperatures comparing with virgin PP. Degradation temperature and melting temperature proves that the recycled material can be injected to obtain tensile and impact specimens to mechanical studies and future application in new products.

As a plastic residue it is not possible to known all properties of this polypropylene package. This fact is emphasis in the TGA and DSC curves with the presence of non-expected peaks probably due to contaminants of capsules manufacturing. But it not interferes in the good result of capsules recycling and biocomposites manufacturing.

REFERENCES

[1] SINGH, N. et al. Recycling of plastic solid waste : A state of art review and future applications. **Composites Part B**, v. 115, p. 409–422, 2017.

[2] HAMAD, K.; KASEEM, M.; DERI, F. Recycling of waste from polymer materials: An overview of the recent works. **Polymer Degradation and Stability**, v. 98, n. 12, p. 2801–2812, 2013.

[3] SPINACÉ, M. A. DA S.; DEPAOLI, M. A. A tecnologia da reciclagem de polímeros. **Química Nova**, v. 28, n. 1, p. 65–72, 2005.

[4] RAGAERT, K.; DELVA, L.; VAN GEEM, K. Mechanical and chemical recycling of solid plastic waste. **Waste Management**, v. 69, p. 24–58, 2017.

[5] EUROMONITOR. **Tendências do Mercado de CaféAssociação Brasileira da Indústria de Café (ABIC)**. [s.l: s.n.]. Disponível em:

<http://consorciopesquisacafe.com.br/arquivos/consorcio/consumo/Tendencia_do_Mercado_de_Cafe_-_2015_1.pdf>. Acesso em: 4 set. 2017.
[6] OGLOBO. **Pesquisas inéditas mostram que reciclagem de cápsulas de café é problemática no Brasil**. Disponível em: <https://oglobo.globo.com/sociedade/ciencia/meio-ambiente/pesquisas-ineditas-mostram-que-reciclagem-de-capsulas-de-cafe-problematica-no-brasil-20660567>. Acesso em: 29 ago. 2017.
[7] MANCINO, A.; MARANNANO, G.; ZUCCARELLO, B. Implementation of eco-sustainable biocomposite materials reinforced by optimized agave fibers. **Procedia Structural Integrity**, v. 8, n. 2017, p. 526–538, 2018.
[8] GURUNATHAN, T.; MOHANTY, S.; NAYAK, S. K. A review of the recent developments in biocomposites based on natural fibres and their application perspectives. **Composites Part A**, v. 77, p. 1–25, 2015.
[9] LEMOS, A. L. DE et al. Biocomposites reinforced with natural fibers : thermal, morphological and mechanical characterization. **Revista Matéria**, p. 8–10, 2017.
[10] LAADILA, M. A. et al. Green synthesis of novel biocomposites from treated cellulosic fibers and recycled bio-plastic polylactic acid. **Journal of Cleaner Production**, v. 164, p. 575–586, 2017.
[11] MEI, L. H.; OLIVEIRA, N. Caracterização de um compósito polimérico biodegradável utilizando Poli (ε -caprolactona) e borra de café. **Polímeros**, v. 27, p. 99–109, 2017.
[12] GOLEBIEWSKI, J.; GALESKI, A. Thermal stability of nanoclay polypropylene composites by simultaneous DSC and TGA. **Composites Science and Technology**, v. 67, n. 15–16, p. 3442–3447, 2007.
[13] PARPARITA, E. et al. TG/FT-IR/MS study on thermal decomposition of polypropylene/biomass composites rp a rit. **Polymer Degradation an Stability**, v. 109, p. 13–20, 2014.
[14] SANCHEZ, F. A. C. et al. Polymer Recycling in an Open-Source Additive Manufacturing Context: Mechanical Issues. **Additive Manufacturing**, v. 17, p. 87–105, 2017.
[15] AMINTOWLIEH, Y. et al. Effects of processing variables on polypropylene degradation and long chain branching with UV irradiation. **Polymer Degradation and Stability**, v. 104, n. 1, p. 1–10, 2014.
[16] MAJEWSKY, M. et al. Determination of microplastic polyethylene (PE) and polypropylene (PP) in environmental samples using thermal analysis (TGA-DSC). **Science of the Total Environment**, v. 568, p. 507–511, 2016.
[17] OLIVEIRA, R. A. DE. **Comportamentos, térmico e mecânico, de compósitos de polipropileno e resíduo da hidrólise enzimática do bagaço de cana de açúcar**. 2014. São Paulo State University (UNESP). 2014.
[18] OLIVER-ORTEGA, H. et al. Evaluation of thermal and thermomechanical behaviour of bio-based polyamide 11 based composites reinforced with lignocellulosic fibres. **Polymers**, v. 9, n. 10, 2017.
[19] HOCKER, S. J. A. et al. Graphene oxide reduces the hydrolytic degradation in polyamide-11. **Polymer (United Kingdom)**, v. 126, p. 248–258, 2017.

A NOVEL RECYCLING ROUTE FOR POLYETHYLENE BOTTLE CAPS AS CIRCULAR HONEYCOMB CORE

Murilo Monteiro de Jesus(1), Pablo Resende Oliveira(1), Sergio Luiz Moni Ribeiro Filho(1), Maikson Luiz Passaia Tonatto(1) and Tulio Hallak Panzera(1).

Centre for Innovation and Technology in Composite Materials, Department of Mechanical Engineering, Federal University of São João del Rei-UFSJ, Brazil

https://doi.org/10.21452/bccm4.2018.14.02

Abstract

The disposal of plastic wastes in the environment has been an urgent issue due to pollution of the soil and the sea. The incorporation of polymeric residues into innovative and sustainable structural composites can be considered a promising recycling route. This work investigates the use of disposed polyethylene (PE) caps from drinking water bottles as a sustainable honeycomb core with circular cell geometry. A full factorial design was conducted to identify the effect of bottle caps orientation (single and alternated directions), polymeric adhesive (epoxy and polymer), and aluminium roughness (smooth and rough surface) on the mechanical properties of sandwich panels. The use of epoxy polymer contributes significantly to enhance panel strength and stiffness. Smooth aluminium skins lead to increased panel strength, suggesting a limited effect of roughness increase to enhance aluminium and skin bonding. Finally, single directed caps in the core achieve better mechanical performance than alternated caps. The results evidence the feasibility of alternative uses for bottle caps into structural and sustainable applications.

1. INTRODUCTION

In recent years, issues related to sustainability have motivated a significant amount of material´s research involving a new pro-ecological perspective. This green concept can be obtained either by designing the recycling of the material after its useful life [1] or by using industrial waste as its structural components [2,3]. In this way, recycled wastes have awakened a new interest to the development of innovative materials which can alleviate the impact from global warming [4-6].

Several wastes are of interest for their reuse in structural components. One of them is the disposable bottle caps. The production of PET bottles in Brazil was approximately of 562 thousand tons in 2012 [7], while more than 56 million tons of PET were annually consumed in 2010 around the globe. From this total, 18.9 million tons consisted of PET bottles [8]. Although PET is considered an easy-recycled material, its bottle caps made of polyethylene (PE) do not have a mutual processing with the PET bottle, bringing high processing costs. In the United States, while

PET bottles have a 25% recycling rate, their caps represent only 9% of the total plastic components available for recycling [9]. The critical scenario is also found in Brazil, where the recycling rate of high density polyethylene is around 23%, while PET represents 42% of the total of plastics recycled [10].

Sandwich panels are characterized by a three-layer structure, in which the external facings are stiff and resistant, consisting of a dense material. Its core, on the other hand, is composed of a less rigid and ultra-low-density material, which may be arranged in several configurations or even be made up of foam [11]. The bond between the core and the external skins can be ensured by means of an adhesive film or resin injection in its interface [12]. The honeycomb core is the most common core type in sandwich panels. This structure is based on a biaxial support of the facings. The most used honeycomb cell geometry is the hexagonal cells. However, the use of an innovative cell geometry based on circular tubes as cells core has been reported as a promising configuration by recent researches. Oruganti and Ghosh [13] have compared the circular and hexagonal cell honeycombs under fatigue and shear loads. Circular honeycombs have exhibited enhanced strength due to wall restrictions to buckling. The results were later confirmed by Lin, Cheng and Huang [14]. In addition, a sustainable panel based on bottle caps and aluminium skins was proposed by Oliveira et al. [15] in order to reduce the impact of disposing of PP wastes in the environment. These panels achieved acceptable mechanical strength and stiffness for secondary structural applications, revealing a new recycling route for plastic bottle caps.

Considering that PE is the most consumed plastic in Brazil between 2008 and 2012 [16], those results evidence a viable method to address the large disposal of polyethylene caps. In addition, the divergent properties of polyethylene when compared to polypropylene [17] create further challenges in their utilization in structural applications. Therefore, this work investigates a recycled circular honeycomb core in sandwich panels made by polyethylene (PE) caps from drinking water bottles and aluminium facings. A full factorial design (DoE) was carried out to verify the effects of the following factors, type of adhesive, geometric position of the caps, and aluminium faces roughness on the core shear stress, core shear stiffness, facing stress, flexural stiffness and flexural strength of the sandwich panels.

2. MATERIALS AND METHODS

2.1. Sandwich panel

The sandwich structures were manufactured by manual lamination at room temperature (~25oC) consisting of aluminium sheets as facing and polyethylene water bottle as core material. Aluminium sheets (type 1200 H14 [18] with dimensions 243 x 91 x 0.5mm) were supplied by Alumiaço (Brazil) in two types of surface finishes: smooth and brushed. Epoxy (Huntsman type M, Amine-based hardener type HY951) and polyester (Huntsman type Polylyte, Organic Peroxide-based hardener type MEK) polymers were used as adhesive bonding between the adjacent facings and the core and were sourced by MaxiEpoxi (Brazil). The disposed caps were collected from water PET bottles. The recycled caps were washed and dried at room temperature for 24h.

2.2. Experimental planning and testing

The Design of Experiment (DoE) is a methodology involving of a collection of statistical techniques that offers a robust method for planning and analysing the experiments [19-20]. A full factorial design 2^3 was performed to investigate the effect of the factors, orientation of the bottle

caps (caps placed along the same direction or in an alternated pattern – see Figure 1), type of adhesive (epoxy and polyester) and surface roughness of aluminium facings (smooth and rough surface) on the mechanical properties of the panels. The experimental factors are summarised in Table 1. The following factors were kept constant: type of aluminium (Type ISO 1200), type of bottle cap (from water bottles), adhesive volume fraction (equivalent to 1 mm of thickness), resin-hardener mixture time (5 min), drain direction of rough aluminium surfaces (longitudinal direction), and cure time (7 days at approximately 23ºC). Preliminary tests pointed out the use of longitudinal drains promoted higher mechanical performance under flexural loadings. Four test samples were fabricated for each one of the 8 (eight) experimental conditions from 2^3 factorial (see Table 2). Two replicates were considered in the experiment, running the total of 64 samples. Minitab$^{T\ M}$ v.17 [21] was used to manipulate the data. Table 2 exhibits the experimental matrix design.

Table 1. Factor analysed in the 2^3 full factorial design

Fators	**Experimental levels**
Bottle caps orientation	Same direction
	Alternated direction
Type of adhesive	Epoxy
	Polyester
Surface roughness	Smooth surface
	Rough surface

Table 2 – Experimental matrix design

Condition	**Bottle caps orientation**	**Surface roughness**	**Type of adhesive**
C1	Single direction	Smooth surface	Polyester
C2	Single direction	Smooth surface	Epoxy
C3	Single direction	Rough surface	Polyester
C4	Single direction	Rough surface	Epoxy
C5	Alternated direction	Smooth surface	Polyester
C6	Alternated direction	Smooth surface	Epoxy
C7	Alternated direction	Rough surface	Polyester
C8	Alternated direction	Rough surface	Epoxy

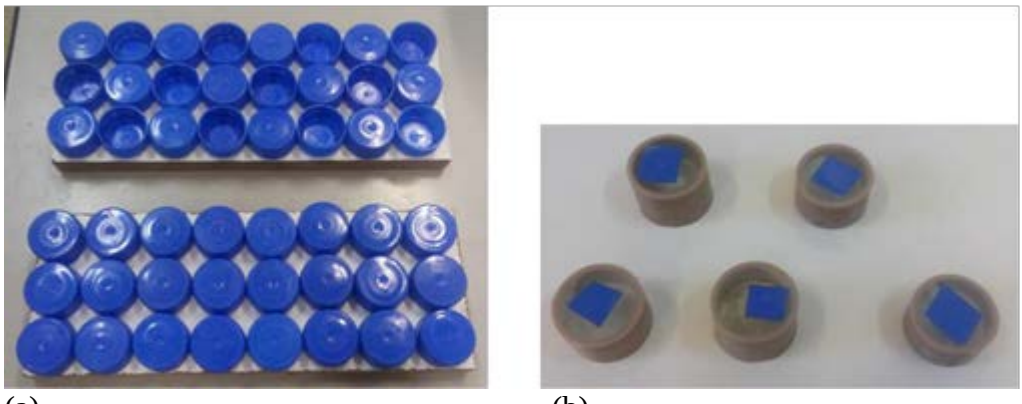

(a) (b)

Figure 1: Alternated (above) and single directed (below) bottle caps configurations (a) and micro-hardness bottle caps samples (b).

The bottle caps were characterised using micro-hardness test in square samples of 10 mm size (see Figure 1.b). The test was conducted in a Mitutoyo MVK -G1 machine, which determined the Vickers hardness (HV) of the material. Elastic modulus, tensile strength and shear strength were then obtained by Equations (1) to (3), as summarised by Oliveira et al. [15].

$$\sigma_{max} = \frac{H_V}{3} \quad (1)$$

$$\tau_{max} = \frac{H_V}{6} \quad (2)$$

$$E = H_V * 20 \quad (3)$$

The sandwich panels were characterized using three-point bending test following the ASTM C393 protocol [22]. The mechanical tests were performed in a Shimadzu universal testing machine (AG-X model) with a load cell of 100 kN. The 3P flexural loading had a cross-head rate of 6 mm/min and span length of 150 mm. Tests were performed at room temperature (~23°C) at a humidity level of 58%.

The mechanical properties (responses) evaluated via DoE were: the core shear modulus (G_f, calculated according to ASTM 7250 [23]), the core shear ultimate and facing stresses (F^{ult} and σ, respectively, determined via ASTM C393 [22]), and the flexural stress and the flexural stiffness (σ_f and E_f, following the ASTM D790 protocol [24]). The core shear modulus was calculated following the set of equations (4) - (7):

$$D = \frac{E_{facing}*(d^3 - c^3)*b}{12} [N.mm^2] \quad (4)$$

$$U_i = \frac{P_i*(S - L_1)}{4*\left(\Delta - \left(\frac{P_i}{96*D}*(2*S^3 - 3*S*L_1^2 + L_1^3)\right)\right)} [N] \quad (5)$$

$$G_i = \frac{U_i*(d - 2*t)}{(d-t)^2*b} [MPa] \quad (6)$$

$$G_f = \frac{\sum_{i=1}^{10} G_i}{10} [MPa] \quad (7)$$

Equations (4) - (7) can be used only if the elastic stiffness of both facings are identical and can be previously determined (ASTM D7250 [23]). D is the flexural stiffness, with Efacing being the elastic moduli of the facing. The shear rigidity (Ui) and the core shear modulus (Gi) are calculated based on flexural stiffness (D) for a series of ten applied forces evenly spaced up to the maximum force. Pi is the force level considered (in N), d is the sandwich thickness, t is the nominal facing thickness, b is the sandwich width, L1 is the load span length (for 3-point loading configuration, L1 = 0), S is the support span length, and Δ is the beam mid-span deflection (in mm) at each force level considered. If the response of the sandwich structure is linear, then the overall core shear modulus (Gf) can be calculated using the values from all forces level (Eq. (7). The core shear ultimate stress and the facing stress can be calculated based on Eqs. (8) and (9) (ASTM C393 [22]):

$$F_s^{ult} = \frac{P_{max}}{(d+c)*b} [MPa] \quad (8)$$

$$\sigma = \frac{P_{max}*S}{2*t*(d+c)*b} [MPa] \quad (9)$$

Pmax is the maximum force and c is the core thickness (calculated from c = d – 2*t). Finally, the flexural strength σf and modulus can be described as Eqs. (10) and (11) (ASTM Ef D790 [24]).

$$\sigma_f = \frac{3*P_{max}*S}{2*b*d^2}\ [MPa] \quad (10)$$

$$E_f = \frac{S^3*m}{4*b*d^3}\ [MPa] \quad (11)$$

The additional parameter m in Eq. (11) is the slope coefficient of the initial straight-line portion of the load deflection curve.

2.3 Fabrication

The sandwich panels were fabricated under manual uniaxial compaction (3.5 kPa) at room temperature (~23°C) for 24h. All aluminium sheets (with smooth and rough surfaces) were washed and cleaned by sandpapering and acetone to remove possible oxides formed on the metallic surface see Figure 2.a). This treatment has been used to eliminate poor adhesion between the polymer and the substrate surface [25]. Subsequently, a mixture containing Wash Primer Phosphate 045 and Catalyst 051 in a 2:1 ratio was uniformly spread on the aluminium surfaces. The Wash Primer is based on phenolic compounds to improve the adhesion between metal surfaces and polymer films. After 21 minutes cure interval of the Wash Primer, the sheets were covered by a PVC plastic film to avoid resin leakage (Figure 2.b). The covered facings were then introduced into the moulds lined with release fabric (Armalon). The polymer resin used was then prepared according to the ratio specified by the manufacturer and spread uniformly within the prismatic mould, forming an adhesive layer of approximately 1 mm of thickness. Finally, the bottle caps were hand inserted within the mould as defined orientation (Figure 2.c). After the 24-hour compaction time, the second aluminium skin was attached considering an analogous procedure. A curing time of 7 days was adopted to obtain the resulting sample (Figure 2.d).

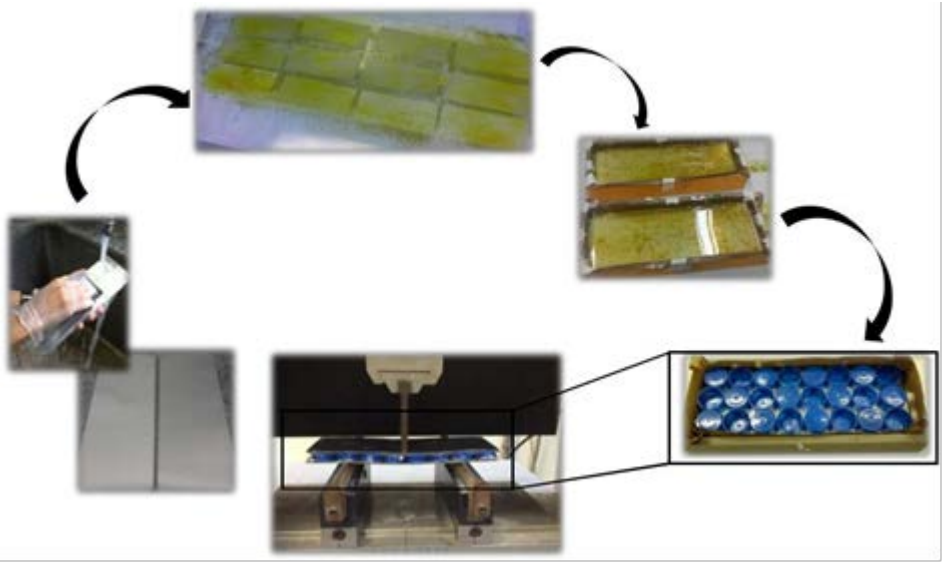

Figure 2: Sample manufacturing process based on surface treatment (a), preparation of the mould (b), bottle caps allocation (c), and finished sample during test (d).

3. RESULTS

The Analysis of Variance (ANOVA) is shown in Table 3, exhibiting the P-Values for each factor and interactions. When a P-Value is equal or less to 0.05 (see bold values in Table 2), it indicates that the factor or interaction significantly affects the response within a confidence interval of 95%. Superior order interactions are preferably analysed instead of individual factors when considered significant. In this case, P-Values are highlighted in italic and underlined. Table 3 also reports the results of R^2(adj), which indicates the adjustment of the experimental data over the statistical model. Higher values of R^2 (near 100%) indicate a greater predictability of the statistical model. ANOVA results reveal R2 varying from 98.82 to 99.89%, which demonstrate excellent adjustments of the data to the model.

A mean micro-hardness of polyethylene was 4.06±0.02 HV. The converted value for micro-hardness in MPa and the results obtained from Equations (1) to (3) for polyethylene elastic modulus, tensile and shear strength are presented in Table 4. The results are in agreement with the literature [17].

Table 3: ANOVA, P-Values for the analysed mechanical responses.

	Factors	Core Shear Stress (MPa)	Facing Stress (MPa)	Core Shear Stiffness (MPa)	Flexural Stiffness (MPa)	Flexural Strength (MPa)
Main	**Bottle Caps Orientation (BO)**	**0.000**	**0.000**	**0.000**	**0.000**	**0.000**
	Surface Roughness (SR)	**0.000**	**0.000**	**0.000**	**0.000**	**0.000**
	Type of Adhesive (TA)	**0.000**	**0.000**	**0.000**	**0.000**	**0.000**
Interaction	**BO*SR**	**0.000**	**0.000**	**0.000**	**0.000**	**0.000**
	BO*TA	**0.000**	**0.000**	**0.000**	0.303	**0.000**
	SR*TA	**0.000**	**0.000**	0.354	0.144	**0.000**
	BO*SR*TA	***0.000***	***0.000***	***0.001***	***0.008***	***0.000***
	R^2 (adj) (%)	**99.89**	**99.89**	**97.27**	**98.82**	**99.60**

Table 4: Characterisation of core material by micro-hardness test.

Parameters	Values
Hardness (MPa)	**39.8**
Elastic Modulus (MPa)	**795.6**
Tensile strength (MPa)	**13.3**
Shear Strength (MPa)	**6.3**

3.1. Flexural Stress, Core Shear Stress and Facing Stress

The flexural stress, core shear stress and facing stress provided similar mechanical behaviour, since they are directly dependent on the maximum flexural load and geometrical parameters, as shown in Equations (5) to (7). For this reason, these response-variables were analysed together. The flexural stress varied from 5.69 to 10.29 MPa. Core shear stress results were between 0.209

and 0.378 MPa. Finally, the results for skin stress ranged between 31.31 and 56.75 MPa. Third order interaction effects were identified for these responses (see Table 2), which are presented in Figures 3(a) to 3(c). The use of aluminium skins with smooth surface led to enhanced mechanical performance compared to the rough surface. In contrast, Oliveira et al. [15] revealed a reduction in bonding when smooth aluminium surface was used without any treatment. In this case, however, a surface treatment based on sandpapering, full cleaning with acetone, and WashPrimer pulverisation was more effective when applied to smooth aluminium skins, reaching moderate roughness values. As shown in plot (i) of Figures 3(a), 3(b), and 3(c), the smooth treated surface achieved higher response values when the bottle caps were placed in a single direction, revealing increases between 18 and 18.6%. The type of adhesive factor had major influence on the panel strength, in which epoxy polymer provided higher stresses under flexural loads, as seen in Figures 3(a), 3(b) and 3(c), plots (ii) and (iii). The enhancement in strength by the use of epoxy polymer varied from 34.8 to 38.9% for single directed caps, which had the most favourable configuration, and from 57.2 to 58% for caps in alternated directions. Caps in alternated directions led to reduced strength compared to the configuration of single directed caps when associated with the polyester adhesive (Figures 3(a) to 3(c), plot ii). An opposite behaviour was found in a previous study [15], which used polypropylene bottle caps. In this case, alternated caps presented a better distribution of the surface contact area between the caps and the skins, enhancing the adhesion and the panel strength. In the present study, however, the flat geometry of bottle caps and their reduced elastic properties may have affected the alternated configuration reinforcement parameters. In alternate configuration, it was identified that the flat-closed surface of PE cap expels the excess resin into the adjacent open cells when pressed against aluminium skin, which creates a weak connection between the skin and the core. This process was favoured by the lower viscosity of the polyester polymer, which flowed easily between the caps during manufacture. In the single direction configuration, although the pressure of the flat surface was also present, the resin could not be expelled into the adjacent cells. It resulted in a greater peripheral contact between the adhesive and the caps, besides greater thickness of the adhesive layer. On the other hand, the caps orientation had almost no significant influence when associated with epoxy adhesive. Finally, the aluminium smooth surface promoted a positive effect on the type of polymer, showing significant improvements between 52.9 and 53.5% when considering the epoxy polymer (Figures 3(a) to 3(c), plot iii). This behaviour suggests less interaction between the polyester resin and the other components. In addition, higher strength of samples with a smooth surface indicates a limited surface roughness effect to promote better bonding between the skin and the adhesive.

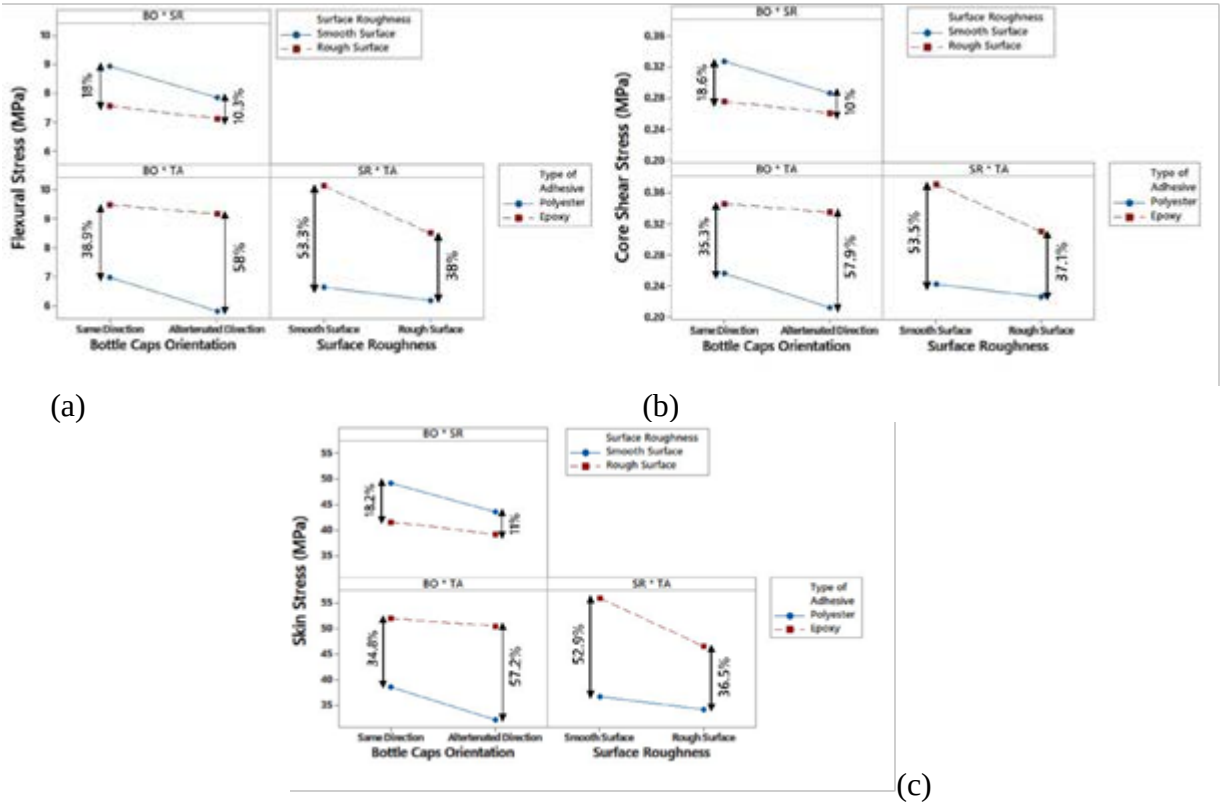

Figure 3: Interaction plot for flexural stress (a), core shear stress (b) and skin stress (c).

3.2 Flexural and Core Shear Stiffness

In general, the sandwich panel stiffness relates to the facing-core interface, the core and facing elastic behaviour and the inertial effect between the core and the facing constituents [26-27]. Besides, the stiffness of the structure is directly dependent on the configuration and topological parameters (Eq. (6) and Eq. (11)). The flexural stiffness of the sandwich structure varied from 991.90 MPa to 1437.47 MPa, while the core shear stiffness ranged from 12.73 MPa to 16.70 MPa. A third order interaction effect was significant for both responses. The interaction effect plots are shown in Figures 4(a) and 2(b). The flexural modulus and core shear stiffness reveal similar behaviour to the responses previously mentioned. In this way, the sandwich panel stiffness is predominately dependent on the type of adhesive. Epoxy polymer presented further enhanced flexural and core shear stiffness values when compared with polyester adhesive. The type of adhesive provided reduced interaction with the remaining factors for the flexural modulus. However, the adhesive led to significant enhanced stiffness (about 17.1%) when associated with single directed caps configuration, and a slight increase for smooth aluminium skins. Finally, the aluminium roughness presented divergent behaviour depending on the bottle caps configuration. The use of alternated caps led to similar and reduced results for both types of aluminium surfaces. On the other hand, caps in a single direction achieved superior stiffness for smooth and treated aluminium surfaces, with an increase of 10.6% when compared with rough skins.

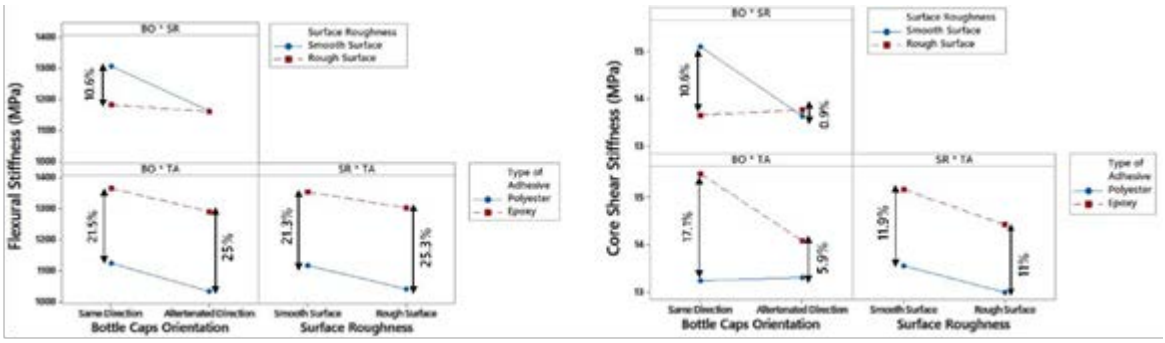

(a) (b)

Figure 4: Interaction effect plot for flexural stiffness (a) and core shear stiffness (b).

3.3 Results comparison

The results obtained in this research were compared with those of a previous research with PP bottle caps honeycomb developed by Oliveira et al. [15] and the sustainable honeycomb developed by Cabrera, Alcock, and Pejis [1], which consisted of a sandwich panel made of polypropylene tubular honeycomb. The most favourable experimental condition based on epoxy adhesive, aluminium smooth skin and single directed caps (Condition 2) was considered for comparison, which is shown in Table 3. The sandwich panel presented in this work obtained reduced mechanical properties compared to the similar bottle caps panel manufactured by Oliveira et al. [15]. This can be explained by the reduction of the mechanical strength and stiffness presented by the polyethylene caps, in addition to the low interaction between the PE caps and the polymer. However, C2 panels led to enhanced absolute and specific properties when compared to the sustainable panel designed by Cabrera, Alcock, and Pejis [1], despite their higher core density. This comparison evidences the feasibility of the proposed panel as a lightweight and low-cost component for secondary structural applications in engineering.

Table 3: Comparison between mechanical properties for PE and PP based panels [1, 15]

Responses	PP Bottle Caps Composite (C2)	PP Bottle Caps Composite [15]	PP composite [1]
Composite Bulk density (g/cm³)	0.418 (0.003)	0.532 (0.104)	0.195
Shear stress (MPa)	0.38 (0.02)	0.77 (0.07)	0.27
Specific Shear Stress (N-m/g)	**0.91 (0.01)**	**1.45 (0.12)**	**1.3**
Skin Stress (MPa)	56.75 (2.98)	115.38 (9.69)	24
Specific Skin stress (N-m/g)	**135.76 (1.53)**	**216.87 (18.22)**	**123.08**

4. CONCLUSIONS

A new concept of circular sandwich panel based on aluminium facings and disposed bottle caps as core were investigated in this work. The structures were evaluated under three-point bending test. The main conclusions are described as follows:

i. The statistical analysis (ANOVA) revealed that a third order interaction between 'Bottles Caps Orientation', 'Surface Roughness' and 'Type of adhesive' significantly affected the core shear stress, facing stress, core shear stiffness, the flexural stiffness and flexural strength;
ii. The type of adhesive was the most relevant factor in the mechanical properties. The epoxy polymer led to enhanced mechanical performance when compared to the polyester adhesive;
iii. Bottle caps oriented along to the same direction achieved superior mechanical properties;
iv. The smooth surface of the aluminium facings promoted a further increase in the shear stresses, maximum force and stiffness;
v. Finally, this sustainable composite design featured a viable route to reuse discarded bottle caps in a lightweight panel for secondary structural applications.

ACKNOWLEDGEMENTS

The authors would like to thank the Brazilian Research Agencies CAPES and FAPEMIG for the financial support provided

REFERENCES

[1] Cabrera, N., Alcock, B. and Peijs, T. 'Design and manufacture of all-PP sandwich panels based on co-extruded polypropylene tapes'. *Composites Part B: Engineering*, **39** (7-8) (2008) 1183-1195.
[2] Durão, L.M.P., Panzera, T.H., Scarpa, F., Ribeiro Filho, S.L.M. and Oliveira, P.R. 'Damage Assessment of Fibre Reinforced Laminates'. *Composite Structures*, **133** (2015) 939-946.
[3] Oliveira, P.R., Ribeiro Filho, S.L.M., Panzera, T.H., Scarpa, F. and Brandao, L.C. 'Sustainable hybrid composites based on sugarcane bagasse and rubber wastes'. *Proceedings of the Brazilian Conference on Composite Materials*, 1 (2014) 1-7.
[4] Ramesh, M., Palanikumar, K. and Reddy, K.H. 'Plant fibre based bio-composites: Sustainable and renewable green materials', *Renewable and Sustainable Energy Reviews*, **79** (2017) 558-584.
[5] Ottele, M., Perini, K., Fraaij, A.L.A, Haas, E.M., Raiteri, R. 'Comparative life cycle analysis for green facades and living wall systems'. *Energy Build* **43** (3) (2011) 419–29.
[6] Cetiner, I., and Shea, A.D. 'Wood waste as an alternative thermal insulation building material solution', *Energy and Buildings*, Available from: https://doi.org/10.1016/j.enbuild.2018.03.019. (Accessed 11 March 2018)
[7] Hendges, A.S. 'Produção, utilização, descarte e reciclagem do PET no Brasil'. EcoDebate. Available from: http://www.revistaecologica.com/producaoutilizacao-descarte-e-reciclagem-do-pet-no-brasil. (Accessed 28 March 2017).
[8] Bartolome, L., Imran, M., Cho, B.G., Al-Masry, W.A., Kim, D.H. 'Recent developments in the chemical recycling of PET'. In: Achilias D, editor. *Material Recycling – Trends and Perspectives*. Dr. Dimitris Achilias (Ed.), InTech, DOI: 10.5772/33800. Available from: https://www.intechopen.com/books/material-recycling-trends-and-perspectives/recent-developments-in-the-chemical-recycling-of-pet.
[9] Seaver, K. '360: Bottle Caps'. Earth911. Available from: http://www.earth911.com/food/360-bottle-caps/. (Accessed 28 March 2017)
[10] CEMPRE - COMPROMISSO EMPRESARIAL PARA A RECICLAGEM. Pesquisa Ciclosoft – 2016 (in Portuguese). Available from: <http://cempre.org.br/ciclosoft/id/8>. (Accessed 20 March 2018)
[11] Qi, G., Ma, L., 'Experimental investigation of composite pyramidal truss core sandwich panels with lightweight inserts', *Composite Structures* (2017) doi: https://doi.org/10.1016/j.compstruct.2017.12.071.
[12] Bitzer, T. 'Honeycomb Technology: materials, design, manufacturing, applications and testing'.

(London: Chapman & Hall, 1997).
[13] Oruganti, R.K. and Ghosh, A.K. 'FEM analysis of transverse creep in honeycomb structures'. *Acta Materialia*, **56** (4) (2008) 726–735.
[14] Lin, T., Chen, T. and Huang, J. (2012). 'In-plane elastic constants and strengths of circular cell honeycombs'. *Composites Science and Technology,* **72** (12) (2012) 1380-1386.
[15] Oliveira, P.R., Bonaccorsi, A.M.S., Panzera, T.H., Christoforo, A.L. and Scarpa, F. 'Sustainable sandwich composite structures made from aluminium sheets and disposed bottle caps'. *Thin-Walled Structures* **120** (2017) 38-45.
[16] Zanin, M, Mancini, S. D. 1Resíduos plásticos e reciclagem: aspectos gerais e tecnologia'. (SciELO - EdUFSCar, 2015).
[17] Engineering ToolBox, (2003). Young's Modulus - Tensile and Yield Strength for common Materials. [online] Available from: https://www.engineeringtoolbox.com/young-modulus-d_417.html (Accessed 23 March 2018).
[18] International Organization for Standardization, Aluminium and Aluminium Alloys – chemical composition (ISO 209), (2007).
[19] Montgomery. D. C. Design and analysis of experiments. 6a edition. Arizona: John Wiley & Sons, Inc., 2005.
[20] Wu C.F.J. and Hamada M. 'Experiments: planning, analysis, and parameter design optimization'. New York: John Wiley & Sons, 2000.
[21] Minitab 17 Statistical Software, [Computer software], Minitab, Inc, State College, PA, 2010. ⟨www.minitab.com⟩.

RECYCLED GLASS FIBRE/POLYESTER RESIN SYSTEM – INTERFACE CHARACTERIZATION

R.T. Durai Prabhakaran (1), James Thomason (2), and Liu Yang (2)

(1) The BioComposites Centre, Bangor University, Gwynedd, UK

(2) Advanced Composites Group, Department of Mechanical and Aerospace Engineering, University of Strathclyde, Glasgow, G11XJ

https://doi.org/10.21452/bccm4.2018.14.03

Abstract

Polymer composites are finding substantial application in the most diverse engineering fields. Use of polymers and synthetic fibres in large structural composite developments consume several tonnes of material. End-of-life scenarios of composite structures is a major issue in the composite industry due to current norms of environmental policies and impending waste management legislation. Scientist are evaluating new methods and techniques to recycle structural composites. Current article addresses the recycling of glass fibres from a composite structure and regenerating glass fibre functionality through surface treatments. In the present study, bonding between recycled glass fibre and polyester resin are evaluated through experiment approach called micro-droplet test. Results demonstrate strong effect on fibre properties due to various surface treatments used for regenerating recycled glass fibre surface.

Keywords

Glass fibre, Thermal conditioning, Tensile strength, Strength recovery, Interface strength

1. INTRODUCTION

Environmental protection is a growing concern for many industries today, with emphasis on the reduction of carbon dioxide and other poisonous emissions like carbon monoxide -CO, nitrogen oxides- NO_x to mitigate climate change. European Union and major countries in the world demanding solutions for end-of-life scenarios of used materials and structures, hence put more pressure on the industry to address the options available for dealing with FRP waste. Annually around 35% of the total production of FRP are used by transportation and construction industries in Europe. As a raw material, glass fibre accounts for about 90% of the reinforcements used in composite consumption globally. Excluding composites, glass fibres usage is high in other sectors

of product developments targeting properties - good insulation, strong heat resistance, and better in corrosion resistance.

Glass fibre with high strength and modulus can be achieved by adding sizing chemicals modifying fibre surface. Fibre manufacturers develop their own sizing know-how and apply it to the fibre to best suit the needs of targeted composite structures or products. Sizing is essential to glass fiber manufacture and critical to several key fiber characteristics that determine both how fibers will handle during processing and how they perform as part of a composite. Most commonly used polymers for composite structural developments are unsaturated polyester resin and epoxy resin. Interface properties of virgin glass fibre with polyester/epoxy resin are well known in composites community, which are experimentally studied by several scientists using micro-droplet, fibre pull out tests.

From the past decade, composites recycling gained much importance in industry and academic scientists derive methods to recycle thermoplastic polymers and fibre reinforcements (glass and carbon fibres). The academic research slowly moving to industry by knowledge transfer for possible future developments in the areas of end-of-life of composites structures. From the literature [1-4], Pickering [1] demonstrated experimental methods to recycle carbon fibres and reuse the carbon fibre for several product developments. Thomason and co-workers [2-4] developed methods to recreate functionality to recycled glass fibres and generate fibre strength and modulus. Durai Prabhakaran [4] discussed the property enhancements obtained for the recycled glass fibres and studied recycled glass fibre/polyester resin composite performance. Few articles discussed the methods to evaluate interface properties of recycled glass fibre with polymer, articles highlighting the steps of surface treatment which affect of the performance are not many in the literature.

In this article, recycled glass fibres are chosen to study tensile properties and its interface properties with polyester resin. The microdroplet test is carried out under optimal testing conditions, established from our previous work, in order to study debonding and interfacial shear stress analysis of the recycled glass fibre-polyester resin. Glass fibre as received in chopped strand mat (CSM), heat-treated (silane removed), silane coated without prewashed heat treated glass fibres, silane coated after prewashed heat treated glass fibres are chosen to investigate the influence of washing glass fibre surface on the fibre/matrix bond.

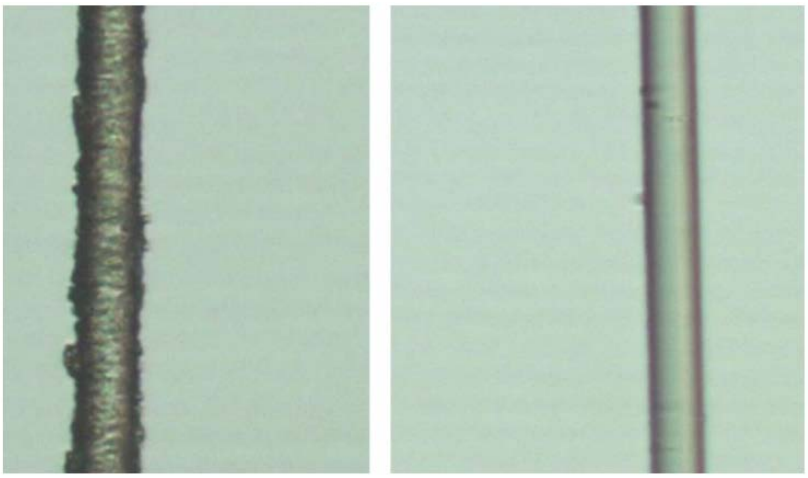

Figure 1: Heat-treated glass fibre surface without wash and with a water wash

2. EXPERIMENTAL WORK

2.1 Materials

CRYSTIC 701 PAX polyester infusion resin and its associated catalyst (methyl ethyl ketone peroxide) were acquired from East Coast Fibreglass Supplier. The chopped strand mat 92 was provided by PPG industries with average fibre diameter of 13μm.

2.2 Pyrolysis

The recycling was made through burn-off process, in a Carbolite Furnace. A sample was placed in the centre of an aluminium tray and then put into the furnace, at room temperature (25°C). The furnace heats up to 500°C and stays at this temperature until the end of the experiment. The sample stays inside the furnace until the entire polymer is burned-off and only clean fibres remain, this time may vary according to the sample conditions. Glass fibres from pyrolysis are observed under optical microscope to study fibre surface, see Figure 1.

2.3 Single Fibre Tensile Test

Single fibre tensile tests were chosen to evaluate the fibre properties [2]. The fibre strength was determined by using the single fibre tensile test based on ASTM D2256. Gauge length of the test specimen is critical in single fibre tensile test, where single fibre strength was highly dependent on the specimen length. Due to difficulties in separation of single glass fibre from fibre bundle of CSM and specimen preparation issues, the tests are performed for only 20 mm gauge length. Individual fibres were glued onto card tabs with a central cut-out that matched the gauge length chosen for the test as shown in Figure 2. Then the tab ends were gripped by the universal testing machine (Instron® Model 3342) with a 10N load cell. Tests were performed with a gauge length of 20mm and strain rate of 1.5%. All samples were photographed with a microscope lens of 500x, and then the diameter was obtained using ImageJ software with a scale of 113.5 pixel/μm. The mechanical performance of single fibres taken from CSM of well-defined sizing and binder and heat treated E-glass fibre samples, heat treated, heat treated and silane treated, heat treated and washed glass fibre with silane sized were investigated at room temperature after thermal conditioning at temperatures upto 500°C.

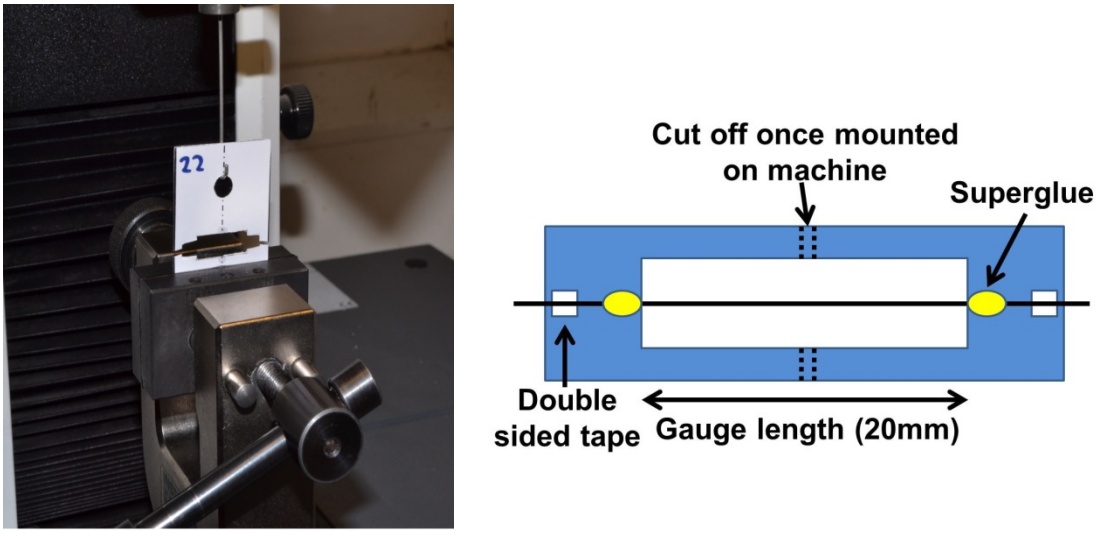

Figure 2: Single fibre tensile test setup: glass fibre glued in a card tabs

2.4 Microdroplet Test

The microdroplet test is a simple experiment technique designed to study interface between fibre and polymer. Where fibre is embedded in a drop of resin and subsequently pulled out while the drop is being supported by two knife-edges, resulting in either debonding of the droplets from the fibres as shown in Figure 3, or breakage of the fibres before debonding can occur. An in-house experimental set-up is designed for the microdroplet test were used to study recycled glass fibre interface properties with polyester resin, refer Figure 4. Specially designed fixture [2-3] with two movable knife edges controlled by a pair of micrometer heads with resolution to 1μm. The microbond tests were conducted with a free distance between fibre and knife edge of 20μm. A stereo-microscope was utilised to aid the positioning of knife edges and monitor the testing process. The same testing machine used in the single fibre tensile test with 10N load cell was employed to carry out the test with the rate of fibre end displacement set to 0.1mm/min. The fibre with bonded resin droplets was mounted in the machine. Some card frame was left taped to the bottom of the fibre to keep it under tension (~0.5mN). The fibre was pulled out of the droplet while the droplet was constrained by the knife edges. Where the load-extension from the sample is recorded and noted the peak load to estimate the Interfacial Shear Strength (IFSS).

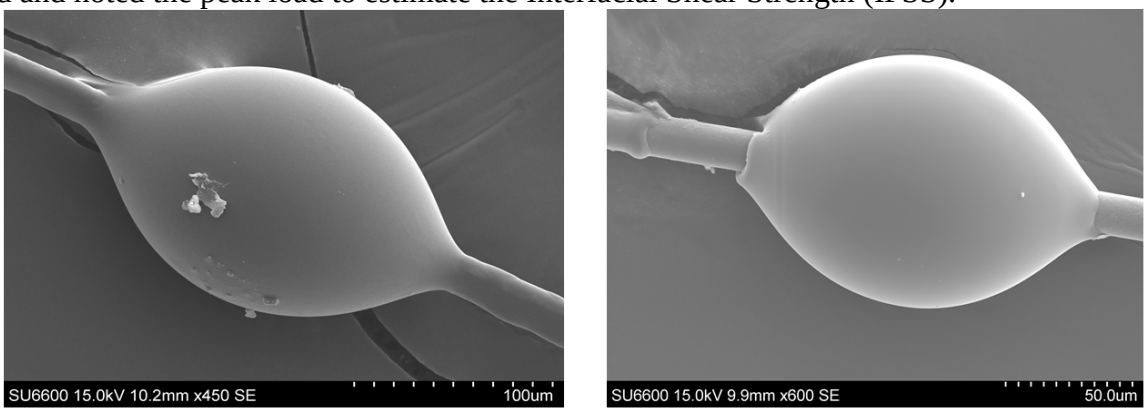

Figure 3: Polyester droplets on glass fibre surface (before and after micro-droplet test)

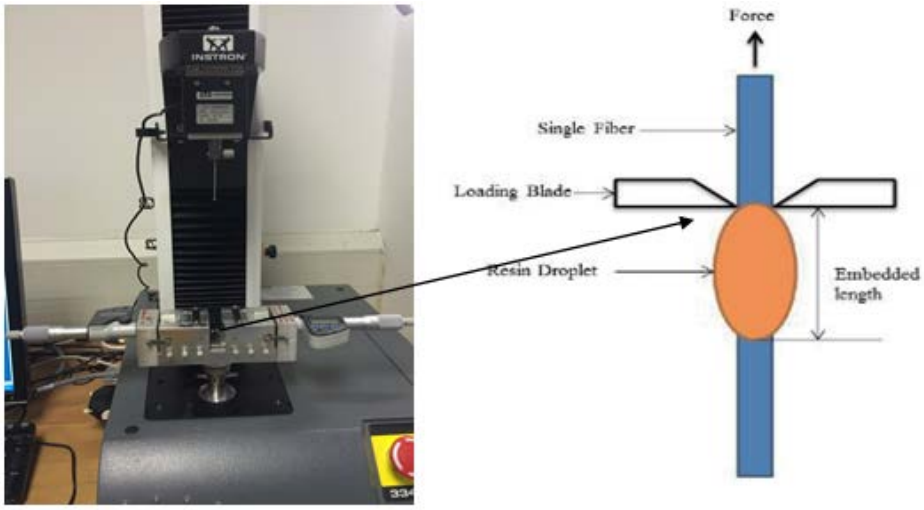

Figure 4: Experimental setup to characterize the interface of recycled glass fibre/polyester

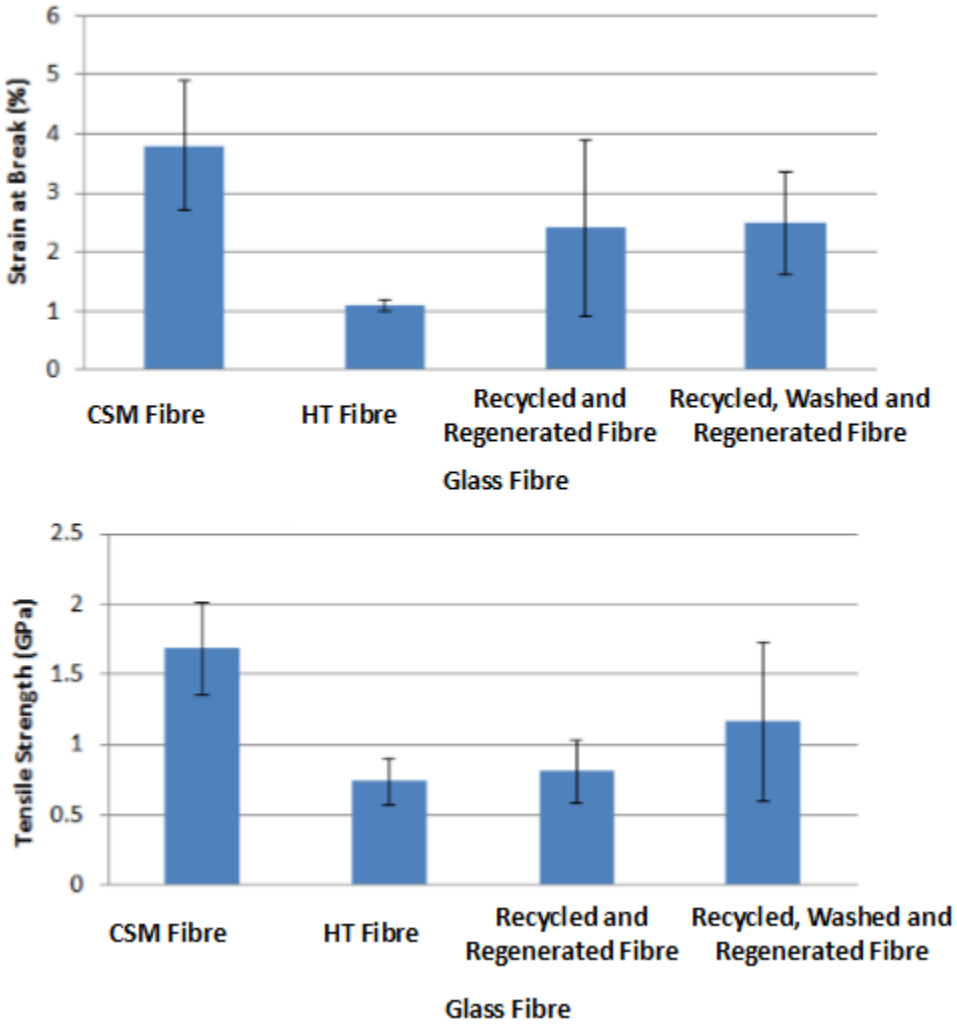

Figure 5: Single Glass Fibre Tensile Properties Before and After Heat Treatment

Table 1. Tensile Properties – Recycled Glass Fibres

Fibre Type	Diameter (μm)	Force Peak (N)	Strain Peak (%)	Stress at fibre break (GPa)	Youngs Modulus (GPa)
CSM Fibre	14.0 ± 0.9	0.26 ± 0.03	3.8 ± 1.1	1.687 ± 0.330	59.3 ± 8.30
HT fibre (500deg C @30min)	13.6 ± 1.4	0.11 ± 0.02	1.1 ± 0.1	0.739 ± 0.162	63.3 ± 17.2
Recycled and Regenerated Fibre	12.6 ± 0.8	0.11 ± 0.03	2.4 ± 1.5	0.810 ± 0.226	57.5 ± 11.3
Recycled, Washed @70deg C and Regenerated Fibre	11.6 ± 0.9	0.15 ± 0.05	2.5 ± 0.9	1.376 ± 0.401	67.6 ± 10.0

4. RESULTS AND DISCUSSIONS

4.1 Fibre Strength

Recreating fibre functionality and regenerating fibre strength is a major task in composites recycling. This involves sizing chemistry and requires series of experiments to study sizing chemical compatibility with fibre surface and with the polymer. The results for the average single fibre strength (at 20mm testing gauge length) of CSM fibre with standard sizing's, CSM fibres after heat treatment, and heat treated fibres and regenerated with silane sized, heat treated fibres and regenerated with a hot water wash and silane sized are shown in Figure 5. The results indicate that thermal conditioning can cause a considerable strength reduction for fibre samples after heat treatment, with a loss of over half of the original strength in the case of 30 minutes at 500°C. It can be seen that heat-treated glass fibre types reduce in strength, with the silane-sized glass falling by a greater percentage of its original strength. In general glass fibres can be extracted after thermal conditioning 500°C and above. Above this threshold temperature the average fibre strength is seen to decrease rapidly.

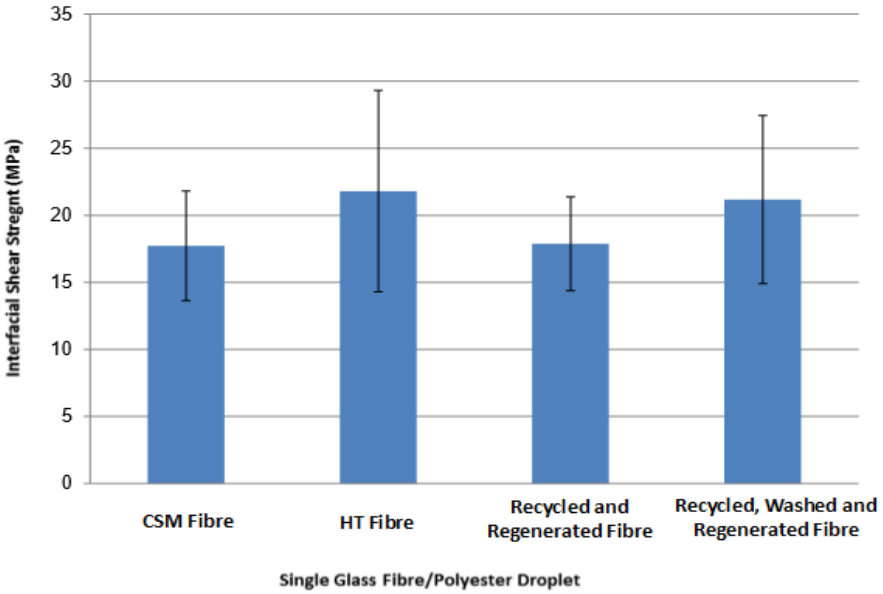

Figure 6: Single Glass Fibre/Polyester Resin Interface Properties

Comparison with the results in Figure 5 indicates that the single fibre tensile strength results of recycled washed and regenerated/sized fibres recover its strength around 83% compared to fibre strengths of CSM glass fibres. Diameter of fibres used in the study are given in Table 1 shows fibre after heat treatment have polyester particles resulting diameter similar to CSM. After hot water washing of heat treated fibres and silane treated the fibre diameter reaches to 11.6 μm forming better coating surface for glass fibres. The CSM fibres and fibres taken after heat treatment or during sizing treatments are having greater potential for damaging due to bundle-bundle interactions while separating from the fabrics (also damaging due to fibre-fibre interactions within the fibre bundles) taken from CSM (fibres separating from bundles are extremely difficult). In some cases the fibres after separating from the fibre bundles seems extremely difficult to handle or fixing single fibres on card frame which can also damage the fibres. The results shown in Figure 5, indicates recycled-washed-and-regenerated fibres can recover strain-to-failure around 66%

compared to CSM fibres, which is a good sign of tensile property improvement. Whereas the modulus measured for the four fibre types show different trend. Fibres taken from CSM gave 60GPa, whereas for the heat-treated fibres the modulus is a bit higher than the modulus of CSM (63GPa). The recycled and regenerated fibres shown better performance and the modulus recorded is 57.5GPa lesser than the recycled-washed-regenerated fibres (68GPa). Therefore, fibre washing is an important step in regenerating fibre strength and modulus. In addition, the results demonstrate the strength of glass fibres is strongly influence by thermal conditioning at temperatures and times, which may commonly be experience in the processing of such fibres in engineering composite materials.

4.2 Interfacial Shear Strength (IFSS)

Interface strength for single glass fibre/polyester can been determined by using fibre pull-out and microbond methods. In the current study, microbond test is chosen to evaluate the interfacial properties. The apparent IFSS is an adequate quantitative parameter which can characterise the mechanism of interfacial failure in any fibre reinforced polymer composites. Sample preparation is one difficult task to use single fibres from CSM fabrics. To replicate the composite processing technique, microbond test specimens are prepared exactly similar to vacuum infusion technique used for laminate trials (i.e. droplets are formed under vacuum for 24 hours and then dried over an oven at 80°C for 4 hours). The average fibre tensile strength of CSM fabrics is 1.69±0.33GPa at 20 mm gauge length was obtained by the single fibre tensile test. The tests are conducted for 30 specimens each, and the average interfacial shear strength for each case is shown in Figure 6.

Different failure modes are observed during the microdroplet test: (a) fully debonded droplet, (b) partially debonded (broken) droplet and (c) mixed mode of the previous two modes. SEM pictures shown in Figure 3 demonstrates fully debonded droplet for a glass fibre (CSM) having silane sizing interface with polyester. Fibres taken from CSM and recycled-washed-regenerated fibres were able to perform good interfacial tests i.e. shown constant interfacial friction after debonding. Whereas the heat-treated fibres, as the fibre surface is not coated and the surface is damaged due to thermal conditioning to 500°C, where the droplets formed on the fibre surface could not show good bond strength with polyester and debonding similar to previous case. This indicates the specimens fail before droplet able to initiate debond and also observed specimen to encounter fibre breakage rather than fibre pull-out from the polyester droplet.

The results shown in Figure 6 demonstrate washing of glass fibre surface after heat treatment plays major role. Hot water with 70°C were used to clean the glass fibre surface after heat treatment. Figure 1 shows the polyester particles after burn off still stick to the fibre surface resulting into partial bonding with polyester resin. Washed glass fibre after heat treatment and then silane sized showed better bonding and hence better IFSS value compared as received CSM case (refer Figure 6). In general the reference case (as received CSM) have sizing on glass fibre surface and binders to keep the fibre bundles to form a fabric structure. Therefore the IFSS values recorded in the microbond test for reference case shown less values compared to heat treated glass fibre cases. The IFSS values recorded are in the range of 18-22 MPa, the values agrees well with the IFSS-range published in the literature for glass fibre-thermoset polymer interface (evaluated by the single fibre pullout technique).

5. CONCLUSIONS

In this paper, experimental work is conducted to evaluate recycled glass fibre performance under tensile and microdroplet test. Single fibre tensile properties and single fibre/polyester interface properties are determined experimentally. Summary of the results are as follows :

1. Single fibre testing presented here clearly show that the thermal conditioning (heat treatment at 500°C) likely cause damage to glass fibres and can potentially show decrease in the fibre properties compared to the room temperature fibre strength (i.e. CSM glass fibres).
2. The washed fibre after heat treatment and coated with silane sizings show nearly full recovery of interfacial shear strength as shown in Figure 6.
3. SEM micrographs reveal poor interface bonding can cause damage to microdroplet under loading and can move down after debonding occurs.
4. Hot water washing for a heat treated glass fibres before silane treatment, play key role in regenerating recycled glass fibre strength and modulus.

Theoretical and numerical models will be developed in the future work to find reasonable correlation between measured data and the predictions of interface properties through finite element models.

ACKNOWLEDGEMENTS

This work is part of the EPSRC grant ‘Towards Affordable, Closed-Loop Recyclable Future Low Carbon Vehicle Structures’ (TARF-LCV). The financial support by the EPSRC is gratefully acknowledged. The authors would also like to thank the Advanced Materials Research Laboratory (AMRL) for the use of the mechanical testing machines and the SEM. Special thanks to Fiona Sillars for her support and useful discussions during the research study.

The authors of the paper would like to acknowledge the financial support provided by the Welsh Government and Higher Education Funding Council for Wales through the Sêr Cymru National Research Network for Low Carbon, Energy and Environment.

REFERENCES

[1] Pickering, S.J. 'Recycling technologies for thermoset composite materials – current status', *Composites Part A: Applied Science and Manufacturing*, **37** (8) (2006) 1206-1215.

[2] Thomason, J., Kao, C-C., Ure, J.M. and Yang, L. 'The strength of glass fibre reinforcement after exposure to elevated composite processing temperatures', *Journal of Materials Science*, **49** (1) (2014) 153-162.

[3] Yang, L. and Thomason, J.L. 'Interface Strength in glass fibre-polypropylene measured using the fibre pull-out and microbond methods', *Composites Part A: Applied Science and Manufacturing*, 2010, **41**(9) (2010) 1077-1083.

[4] Durai Prabhakaran, R.T., Thomason, J., 'Recycled glass fibre/polyester composites – Processing and Mechanical Characterization', Proceedings of an International Conference on Composite Materials, Copenhagen, Denmark, 2015 (ICCM, Denmark 2015).

EPOXY POLYMERS REINFORCED WITH CARBON POWDER WASTES

Thaís da Costa Dias[1], Túlio Hallak Panzera[1], Rodrigo Teixeira Santos Freire[12], Carlos Thomas Garcia[3], Júlio César dos Santos[2]

(1) Centre for Innovation and Technology in Composite Materials, Department of Mechanical Engineering, Federal University of São João del Rei, Brazil.

(2) Centre for Innovation and Technology in Composite Materials, Department of Natural Sciences, Federal University of São João del Rei, Brazil.

(3) Laboratory of Materials Science and Engineering - LADICIM, University of Cantabria. E.T.S. de Ingenieros de Caminos, Canales y Puertos, Av/Los Castros 44, 39005 Santander, Spain.

https://doi.org/10.21452/bccm4.2018.14.04

Abstract

This paper investigates the incorporation of recycled carbon micro fibres obtained from the cutting process of laminate composites into epoxy polymers at different mass fractions (0, 2.5, 5, 7.5 and 10%). The elastic modulus and strength under tensile, compressive, flexural and impact loadings were investigated via Analysis of Variance (ANOVA). The tensile (compressive) modulus progressively increases up to 36.6% (28.6%) with the inclusion of carbon powder wastes. The inclusion of 5% mass fraction waste resulted in an increase of 27% (19%) in tensile (compressive) strength. The flexural strength also increased 28.6% when 10wt% carbon powder wastes were added. Carbon powder waste led, however, to a dramatic decrease (approx. 50%) in impact resistance attributed to the increase in stiffness.

Keywords: recycled, epoxy polymers, carbon powder waste, mechanical tests.

1. INTRODUCTION

The demand for composite materials has progressively increased in various technological applications due to their low density and improved mechanical performance compared to conventional materials. However, the fabrication of such materials generates waste that may lead to environmental damage if improperly disposed of. Landfills are the most common strategy, but several countries have already limited or banned the disposal of composites in landfills due to environmental issues [1,2,3]. Polymeric composites, especially thermosets, dominate the global market and, owing to their long-life cycle, alternatives to landfills need to be sought and boosted. Mechanical, thermal and chemical recycling have been developed in order to address this problem.

Mechanical recycling involves shredding and grinding and the subsequent separation of the fibre-rich fractions for reuse [4]. Mechanically recycled composites are usually reincorporated into new composites as fillers or reinforcement [1]. Thermal processes have also been developed for

energy recovery (combustion of the composite waste) or selective material recovery for reuse (fluidized beds and pyrolysis). In pyrolysis, for example, a large amount of thermal energy is required in order to remove the matrix phase. Chemical recycling involves the decomposition of the polymeric structure and the high-quality end products (monomers, hydrocarbon molecules, gases and chemical intermediates for polymerization) are reused to produce new components [5].

The literature suggests that wastes from the manufacture of composites can also be reused in recycled composites. The CarbonTek S.L.® company (Spain) has recently used powder waste resulting from the cutting process of carbon fibre-based products as polymeric matrix reinforcements for the fabrication of carbon fins, as well as to reduce the volume of waste generated [6]. The residue is composed of carbon microfibres coated with epoxy polymer, sometimes with pigment particles used to produce fins. Thomas *et. al.* [6] evaluated the effect of micro carbon fibres wastes inclusions at three different mass fractions (0, 10 and 20 wt%) on the thermal and mechanical properties of epoxy composite materials. These authors report an increase in compressive and flexural strength and impact resistance proportional to the mass fraction of residues. Although less significantly, hardness and erosion resistance also increased with waste inclusion. The use of waste at 10 wt% (20 wt%) increased the compressive strength by 6% (20%) relative to the pure polymer, being attributed to the additional energy expended by the cracks to overcome the micro fibres and particles.

Compared to most recycling processes, the methodology proposed by Thomas *et. al.* [6] is economically more feasible. Therefore, this work further investigates the effect of different mass fractions of carbon powder residues on the mechanical properties of the materials, extending the analysis to tensile modulus and strength.

2. MATERIALS AND METHODS

Carbon powder, supplied by CarbonTek S.L. ®, Spain, was obtained from the cutting process of laminated composites used in the manufacture of fins. These wastes were incorporated into an epoxy matrix phase. Figure 1a shows a pair of carbon fins from CarbonTek S.L., after the cutting and assembly processes. Figure 1b presents the cutting process leftovers. The fin-cutting process generates a powder that can be considered as carbon microfibres enveloped by a polymer matrix (Figure 2).

Figure 1 - a) Fins and b) Remains from the cutting process
Source: Thomas *et al*. (2014) [6].

Figure 2 - Powder collected after the cutting process

The particle size distribution of the carbon microfibres was performed by sieving at the range of 100-200 US TYLER. These particles were incorporated into the epoxy polymeric matrix (Resin MX-14 and hardener ARADUR HY 951, resin/hardener proportion of 10:1). The wastes were mixed to the epoxy matrix phase in the following mass fractions: 0; 2.5; 5; 7.5; 10%. For each condition 5 specimens were fabricated for each type of test (tensile, compression, flexural and impact) and later replicated. The components were mixed for 5 minutes and left for a curing period of 2 weeks to finally undergo mechanical testing.

2.1. Mechanical tests

Tensile, compressive and flexural tests were performed in a SHIMADZU AG-X Plus testing machine (Figure 3a) equipped with a 100 kN load cell, at a crosshead speed of 2 mm/min, according to ASTM D638-14 [7], ASTM D695 [8], ASTM D790 [9] standards. The elongation of the specimens was measured using a digital video-extensometer. Impact tests were performed in an XJJ series impact testing machine with a 15 J hammer (Figure 3b) according to ASTM D6110 [10].

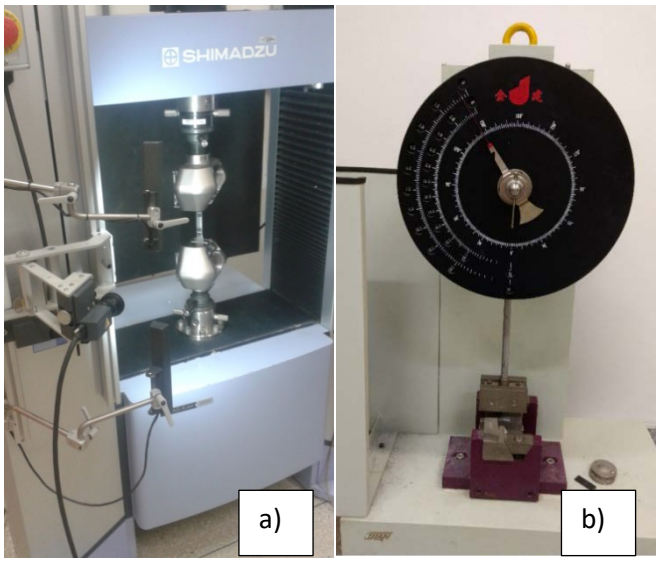

Figure 3 - a) SHIMADZU ® AG-X Plus Universal Testing Machine b) XJJ series impact testing machine

2.2. Scanning Electron Microscopy

A TM3000 Hitachi Analytical Microscope apparatus was used to investigate the morphological aspects of the carbon powder waste as well as the surface of the fractured samples. The images were obtained in secondary electron mode at 15kV.

2.3. Statistical Analysis

The experimental data was analysed via Analysis of Variance (ANOVA) and Tukey's test using Minitab 17, within a 95% confidence interval.

3. RESULTS AND DISCUSSIONS

Table 1: P-value ANOVA

Test	P-value
Mean Elasticity Modulus in Tensile	0.000
Mean Tensile Strengh	0.002
Mean Elasticity Modulus in Compression	0.000
Mean Compressive Strengh	0.000
Mean Flexural Strengh	0.000
Mean Impact Resistance	0.000

There are P-values of ANOVA in Table 1. The mean values of tensile modulus varied from 1.42 to 1.94 GPa (Figure 4a). Tukey's test indicates that carbon powder waste inclusions increased the stiffness at all levels. In particular, for 10 wt%, the tensile modulus was 36.6% higher relative to the reference level (non-particulate samples). Tensile strength ranged from 28.83 to 36.87 MPa (Figure 4b). Based on Tukey's test, waste inclusions increase the tensile strength at all levels, especially at 5 wt% (30% above the reference level).

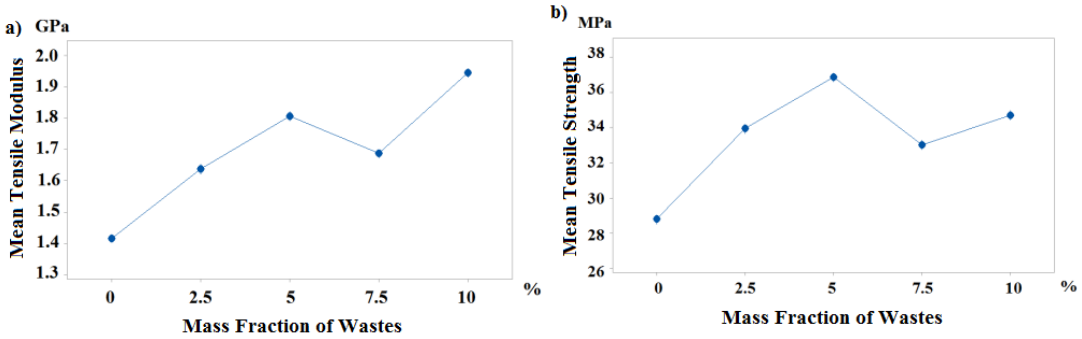

Figure 4 - Main effect plot for mean tensile (a) modulus and (b) strength.

The mean compressive modulus varied from 1.47 to 1.89 GPa (Figure 5a). According to Tukey's test, the incorporation of 7.5 wt% and 10 wt% resulted similar, exhibiting a significant increase of 28.6% relative to the reference. The mean compressive strength ranged from 50.06 to 59.64 MPa (Figure 5b), with an enhancement of approximately 19% when 5 wt% wastes are added. Such behaviour can be attributed to the microfibres, which inhibit crack proliferation by the bridging effect. Behind the crack front, bridging fibres stretch freely along the separating crack faces and in analogy to Hook's law, absorb energy that will otherwise be available at the crack tip.

In addition, as discussed below (microscopical analyses), particles are present in the carbon powder waste and also prevent the propagation of cracks.

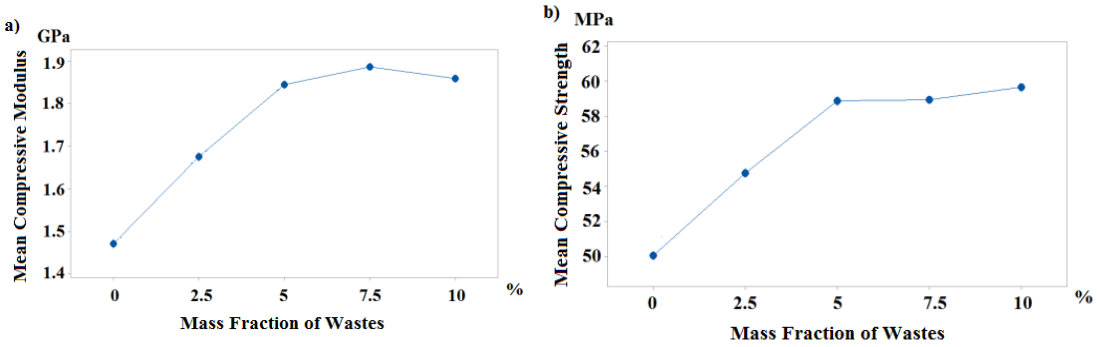

Figure 5 - Main effect plot for mean compressive (a) modulus and (b) strength.

The flexural strength ranged from 30.11 to 36.94 MPa (Figure 6a). According to Tukey's test, the effect of 7.5 and 10 wt% waste inclusions was similar, with an increase of approximately 23% relative to the reference. The impact resistance varied from 6.53 to 15.64 kJ /m^2 (Figure 6b). All levels of particle inclusions led to a dramatic reduction of the impact resistance (approx. 55%). This behaviour may be attributed to the increased stiffness of the reinforced composites, which makes the material more brittle and consequently reduces the impact resistance.

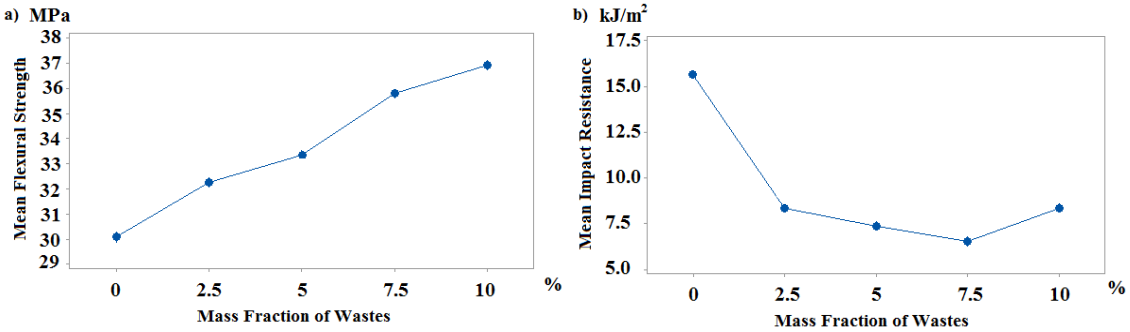

Figure 6 – Main effect plot for (a) mean flexural strength and (b) impact resistance.

The scanning electron microscopic analysis of the carbon particle waste (Figure 7) also reveals spherical particles among carbon microfibre residues. Such particles are metal oxides used as pigments during the fabrication of fins. Figure 8a presents the fractured surface of a specimen after the tensile test with 10 wt% waste inclusions, magnified 100 times.

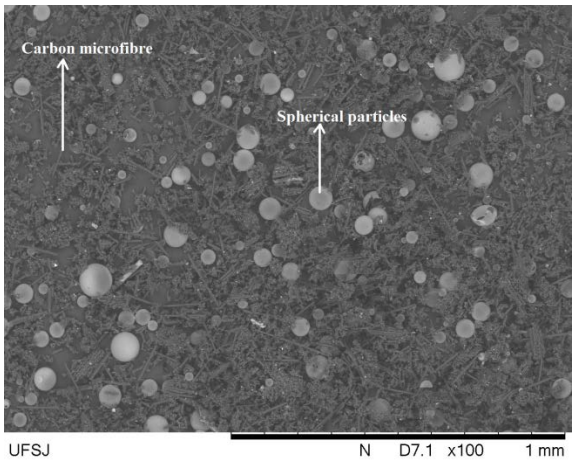

Figure 7 – BSE images of the carbon wastes obtained from the cutting process.

Figure 8b shows the same region with 500-fold magnification, where it is possible to observe the crack propagation along a spherical particle. During crack propagation, such rigid particles may function as barriers along the interface due to their high strength, inhibiting crack growth with subsequent enhancement of mechanical properties [9,15,16]. Thomas *et al.* in fact reported that the inclusion of these wastes generally improved the stiffness and strength of the epoxy polymer composites, including under impact loadings [6]. However, a substantial reduction in impact resistance was observed in this study, as discussed above. According to Dassios [16] fibre pull-out is the most important mechanism of impact energy dissipation in fibre-reinforced composites. It is worth noting that no evidence of fibre pull-out was observed here. However, such mechanism is present in the fractographic analysis presented by Thomas *et al.* [6] and may therefore explain the increase in impact resistance.

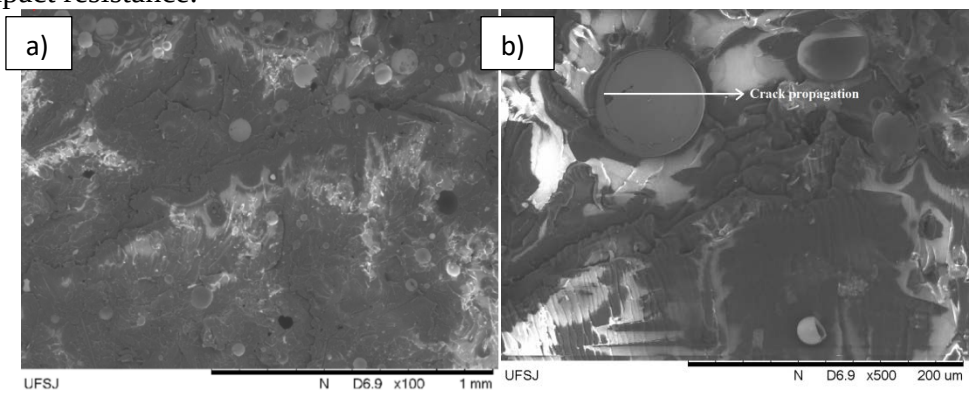

Figure 8 - BSE image: a) Fractured region of tensile test specimen with 10% waste incorporation, magnified 100 times. b) Tensile test fracture surface of a specimen with 10% of waste, magnified 500 times.

4. CONCLUSIONS

The incorporation of carbon powder waste into epoxy polymer promotes an increase in tensile modulus and strength, which increases with the waste mass fraction within the range considered. Results indicate an increase in tensile modulus (strength) up to 36.6% (30%) for 10 wt% (5 wt%) waste inclusions. Similar results were observed for compressive modulus and strength and for flexural strength. The compressive modulus (strength) increased up to 28.6% (19%) for 7.5 wt%

or more (5 wt%) of waste inclusions. The flexural strength increased up to 22% for 7.5 wt% or more of waste inclusions. In contrast, the increased stiffness renders the material more brittle and therefore dramatically reduces the impact strength in 55% for all waste mass fraction levels considered. Carbon fibre wastes derived from the cutting process of laminated composites can therefore be employed as epoxy polymeric matrix reinforcement so as to promote significant enhancements of stiffness and strength. In addition, this low-cost recycling process prevents improper waste disposal with environmental and economic benefits.

ACKNOWLEDGMENTS

The authors would like to thank CarbonTek S. L. ® for the carbon powder waste used in this work and also CAPES (MSc scholarship), CNPq (PP-306767/2016-3 & PDE-205255/2017-5) and FAPEMIG (PPM-00075-17) for the financial support provided.

REFERENCES

[1] S. J. Pickering, Recycling technologies for thermoset composite materials – current status. Compos Part A: Appl Sci Manuf 2006;37(8):1206-15.

[2] D. Khale, R. Chaudhary, Mechanism of geopolymerization and factor influencing its development: a review. J Mater Sci 2007;42:729-46.

[3] S. Feih, E. Boiocchi, G. Mathys, Z. Mathys, A. G. Gibson, A. P. Mouritz, Mechanical properties of thermally-treated and recycled glass fibres. Compos Part B: Eng 2011;42(3):350-8. 4.

[4] Y. Yang, R. Boom, B. Irion, D. van Heerden, P. Kuiper, H. de Wit. Recycling of composite materials. Chem Eng Process: Process Intensification 2012;51(0):53-68.

[5] S. Manrich, Identificação de Polímeros: Uma ferramenta para a Reciclagem. São Carlos. EDUFSCAR, 1997.

[6] C. Thomas, P. H. R. Borges, T. H. Panzera, A. Cimentada, I. Lombillo, Epoxy composites containing CFRP power wastes. Composites: Part B 59 (2014) 260- 268.

[7] ASTM Standard D638-14. 2014. “Standard Test Method for Tensile Properties of Plastics”. ASTM International.

[8] ASTM Standard D695-15. 2015. “Standard Test Method for Compressive Properties of Rigid Plastics”. ASTM International.

[9] ASTM Standard D790. 2015. “Standard Test Methods for Flexural Properties of Unreinforced and Reinforced Plastics and Electrical Insulation Materials1”. ASTM International.

[10] ASTM Standard D6110-10. 2010. “Standard Test Method for Determing the Charpy Impact Resistance of Notched Specimens of Plastics”. ASTM International.

[11] Y. Cao, J. Cameron, Impact Properties of Silica Particle Modified Glass Fiber Reinforced Epoxy Composite, J. Reinf. Plast. Compos. 25 (2006) 761–769. doi:10.1177/0731684406063536.

[12] U. Szeluga, B. Kumanek, B. Trzebicka, Synergy in hybrid polymer/nanocarbon composites. A review, Compos. Part A Appl. Sci. Manuf. 73 (2015) 204–231. doi:10.1016/j.compositesa.2015.02.021.

[13] Y. Cao, J. Cameron, Flexural and shear properties of silica particle modified glass fiber reinforced epoxy composite, J. Reinf. Plast. Compos. 25 (2006) 347–359. doi:10.1177/0731684405056450.

[14] K.G. Dassios, a Review of the Pull-Out Mechanism in the Fracture of Brittle- Matrix Fibre-Reinforced Composites, Adv. Compos. Lett. (2007) 17–24.

ANALYSIS OF POLYACRILONITRILE/LIGNIN BLENDS BY SEM AND FT-IR AS AN ALTERNATIVE PRECURSOR FOR CARBON MATERIALS

Katia S. D. Nunes (1) Nilton P. Alves(2) and Luiz C. Pardini (3)

(1) Instituto Tecnológico de Aeronáutica - ITA
(2) IGTPAN
(3) Departamento de Ciência e Tecnologia Aeroespacial - DCTA - Instituto de Aeronáutica e Espaço-IAE, Divisão de Materiais (AMR)

https://doi.org/10.21452/bccm4.2018.14.05

Abstract

Lignin has been investigated as a promising feedstock for production of low-cost carbon materials. The kraft lignin was studied in this work since it is a waste from a production process at pulp and paper factory. Currently fibers from polyacrylonitrile (PAN) are precursors for obtaining carbon fiber, but at very high costs. In the first step of this work, blends with polyacrylonitrile and kraft lignin were investigated. The methodology employed was the extrusion process at temperature of 200°C. Extrusion process is an economically viable and technologically robust process for the production of low-cost carbon materials from lignin precursors. The low cost and high availability of lignin have brought interest on its use as precursor of carbonaceous materials like activated carbons, carbon catalysts or composite materials. Copolymerization with conventional commodity plastics, particularly polyacrylonitrile (PAN), has gaining attention. This can be accomplished by an innovative technology for polyacrylonitrile-based precursors for carbon fibers, where lignin is mixing with the PAN in appropriate amounts to produce a polymer blend through a conventional extrusion process. The investigation revealed the production of good blends without disconnectedly phases inter polymers, based on the results of Scanning electron microscopy (SEM). FTIR analysis were also used to investigate the interaction inter polymer in the blend after the extrusion process.

1. INTRODUCTION

New carbon materials produced directly from biomass have gained a lot of interest on last years [1]. Biomass is an important feedstock for the renewable production of fuels, chemicals, and energy [2]. Recently, it has been shown that lignin is potentially a suitable precursor material for the production of carbon fiber and composites [3, 4]. Lignin is an aromatic heteropolymer that is mainly found in the secondary wall of wood cells and, after cellulose, it is the most abundant and important polymeric organic substance in the plant kingdom [5]. In Brazil there is large availability

of many industrial wastes with high potential for lignin production. Industrial wastes deeply studied as raw material for carbon fiber precursors are the black liquor (from pulp and paper), sugarcane bagasse and Brazil nut shell waste. The production in 2012 of black liquor was 21,461 ton [6]. According to the MAPA [7] the industrial production of sugarcane bagasse during harvest from April 2015 to January 2016 was 186,214,322.08 t [7]. The production of Brazil nut is being increased every year and it is becoming a new line of research of great potential in the production of lignin in Brazil. Lignin-blends, like PAN-lignin (PAN = polyacrylonitrile), were a step ahead in this direction. In this work, new method to produce precursors to carbon materials containing lignin it was investigated. The methodology to obtain copolymer PAN-Lignin fibers evaluated herein is the extrusion process. It worth to mention that as a solvent free process it has great economic and ecological prospects. Lignin contains both hydrophilic and hydrophobic groups in its composition and PAN is the macromolecule with –CN dipole group to be preferably attracted by substances with hydrogen dipole interactions. The formation of cooperating bonds with neighbor carbons and formation of a copolymer PAN-lignin were tested. Glycerol, which is a by-product of biodiesel production and was used in the preparation of the blend samples, is a natural organic plasticizer to PAN-lignin blends. A key issue is the interaction of glycerol with PAN-lignin that exhibits high compatibility owed to chemical characteristics of interaction of the hydrogen dipole [9]. The objective of this study was to investigate a PAN-co-styrene (10%) / lignin blends as a possible precursor material suitable for production of carbon fiber, using an environmentally friendly process, since no organic toxic solvents are required.

2. EXPERIMENTAL PROCEDURE

2.1 Extrusion Process

The copolymer PAN-co-styrene (10%) / lignin blend was obtained by melt spinning process with glycerol as a plasticizer. The process was based in two stages: (1) formation of pellets of PAN-lignin plasticized with glycerol and additives through extrusion and, (2) PAN-lignin tapes production in extrusion equipment. The basic methodology was developed and the respective basic procedure will be following described. Proportions of 5%, 10%, 15% and 20% of lignin were used with PAN-co-styrene (10%) to manufacture the blends.

In stage 1: It was produced pellets of blend PAN-co-styrene (10%) / lignin plasticized with glycerol in the extruder. Various proportions PAN-co-styrene (10%) / lignin blends were tested to obtain formulations of the PAN-co-styrene (10%) / lignin blends. Figure 1 shows a schematic representation of the first extrusion step for copolymer precursors. The compound was prepared by mixing PAN-co-styrene (10%) and lignin powders, glycerol and other additives in appropriate amounts. The pre-extrusion compound was homogenized and fed in the extruder equipment to obtain polymer blend pellets. Afterwards, the polymer was thrown into feed hopper of the extruder equipment. The molten copolymer was compressed up a die with circular duct of diameter of 6 mm to conform in the shape of polymer blend tape. Then, the tape passed to a pelletizer that cut, through a rotary knife, the material that turned into pellets of plasticized PAN-co-styrene (10%)/lignin. These pellets were collected and stored.

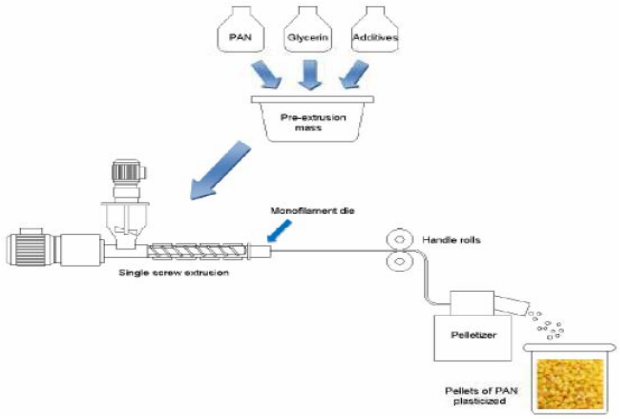

Fig.1. Stage 1: Illustrative scheme for obtaining the co-polymer PAN-lignin plasticized with glycerol in an extruder to produce pellets [4].

The next step was the production of PAN-co-styrene (10%) / lignin tapes by extrusion. It was comprised by a system that extends from the extrusion of pellets to the PAN-co-styrene (10%) / lignin blend winding tapes [9].

At the Stage 2: The pellets undergo melting and begin to flow at the screw extruder. Figure 2 shows scheme of the extrusion equipment to obtain the PAN-co-styrene (10%) / lignin tape. The dissipation of gases occurs during this event.

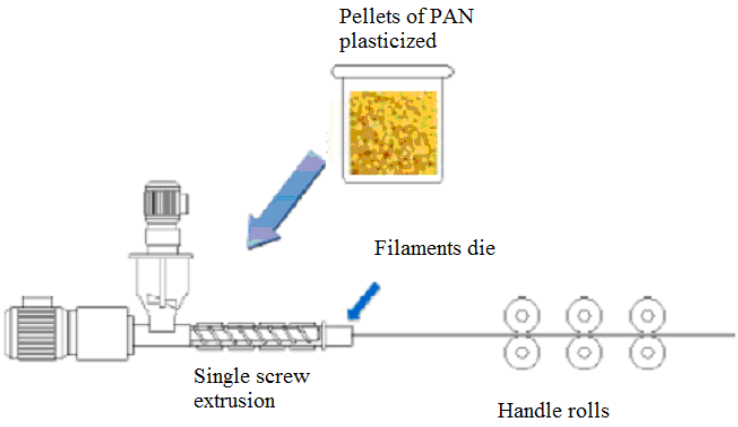

Fig.2. Stage 2: Illustrative scheme for obtaining PAN-co-styrene (10%) / lignin tapes in the extrusion equipment.

This work discusses the study that is undergoing using an environmentally friendly process. Since no organic toxic solvents were used, by using renewable and cheap sources of carbon (lignin). For the characterization of blends, instrumental methods were used, i.e., Fourier Transform Infrared (FTIR) and Scanning Electron Microscopy (SEM).

2.2 SEM micrographs

SEM micrograph analyses were done in room temperature after the gold sputter coating application on the surface of tape samples. The analyses parameters were: SEM High Voltage -

HV: 20kV, Wavelength Dispersive - WD: 9.85 mm, SEM Magnitude - MAG: 3.00 kx, and view filed on 69.2 um. This equipment is located in the Micrograph Laboratory at Dep. Mechanical Engineering, Instituto Tecnologico de Aeronautica - ITA.

2.3 FTIR

FTIR analyses were performed on Spectrum One - PerkinElmer, in the medium infrared (MIR) region by obtaining reflection spectra with universal attenuated total reflection accessory (UATR), 120N torque, 20 scans, in room temperature, without any previous preparation of the samples. This equipment is located at laboratory of Instrumental Analyses (LAAI), Division of Chemistry (AQI), Institute of Aeronautics and Space (IAE).

2.4 MATERIALS

Hardwood kraft lignin was provided by Fibria. Lignin was blended with PAN-co-styrene (10%) using the procedure described by Quimlab [Alves 2007; 2011]. PAN-co-styrene (10%) is named henceforth as PAN. Glycerol was used as plasticizing agent. The employed extrusion equipment was domestic homemade equipment developed by Quimlab.

3. RESULTS AND DISCUSSION

The SEM micrographs blends manufactured by extrusion process are shown in Fig. 3. The mixing ratios used were 5% lignin / 95% PAN; 10% lignin / 90% PAN; 15% lignin / 85% PAN; and 20% lignin / 80% PAN. Despite the presence of small particles dispersed in the images, likely from the lignin, the analyses by SEM did not give any evidence of phase separation, which is an indication of very good miscibility between the materials involved.

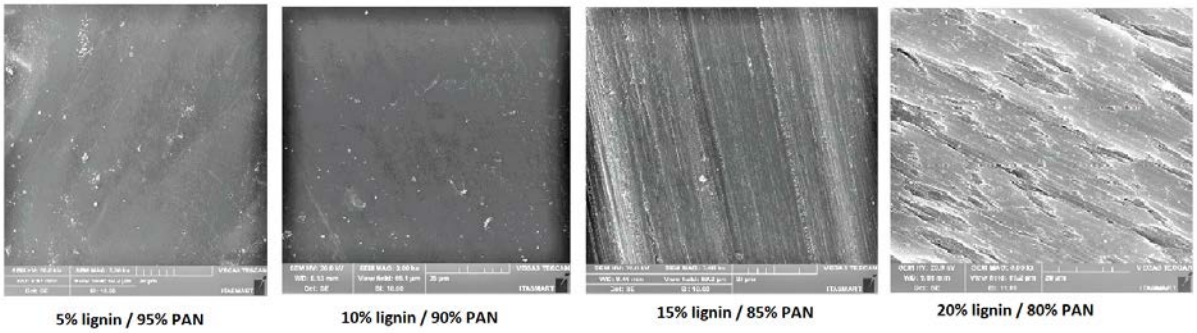

Figure 3: SEM micrographs from extruded blends with kraft lignin and PAN

The quality of the extruded blend can be compared by their miscibility, where different levels of interaction between PAN and lignin can exist. Lignin is powder filler. Therefore, lower amounts of lignin in the formulation can provide better mixing with PAN. So, it is possible to observe that formulations containing 5% lignin in the composition shows better homogeneity, as no phase separation is observed. The same consideration can be drawn for the blends having 10%, 15% and 20% of kraft lignin, which resulted in a more homogeneous structure, having no observed phase separation. However, from 15% and up of lignin in its composition, the pieces of produced samples of the blends demonstrated, by simple handling the material, to be slightly brittle. At the same way, blends with 20% lignin were evidently the most brittle mixture.

In the FTIR analyses shown in figure 4, the relative transmittances were used to characterize the effects of functional groups of the PAN-co-styrene blended with hardwood lignin (Brazilian eucalyptus) over the analyzed samples. When comparing both FTIR spectra, after (1) and before (2) the extrusion process, they show a very high level of similarity. The assignments of the FTIR analysis spectra represent the formulations of PAN/lignin (A, B, C and D) posted with one analysis done for kraft lignin alone (E). In all spectra it is possible to observe an increase in the absorption (∗) at 1601cm^{-1} (ν C-C), 1516 cm^{-1} (aromatic ring), 1211 cm^{-1} (ν C=O) and 1111 cm^{-1} to (ν C-O), in assignments related to lignin component in blend PAN/lignin.

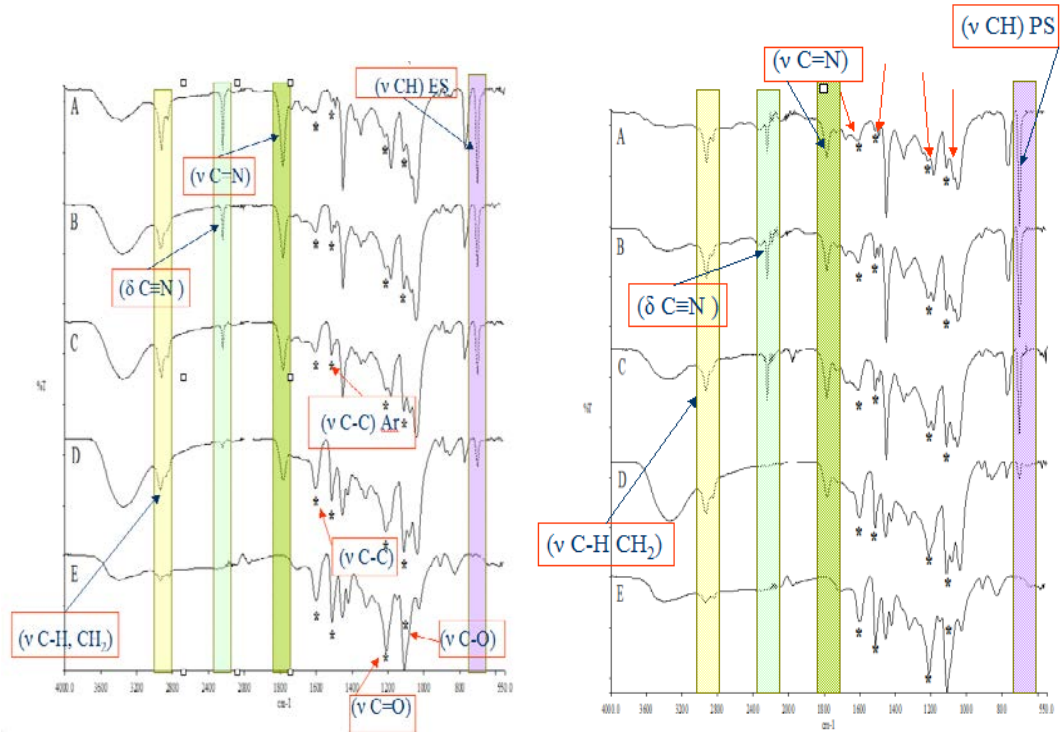

1) After process extrusion

2) Before process extrusion

Figure 4: 1) and 2): A) 95% PAN + 5% lignin; B) 90% PAN + 10% lignin; C) 85% PAN + 15% lignin; D) 80% PAN + 20% lignin; E) 100% Kraft lignin. The color-highlighted ranges of the plot are relative to PAN-co-styrene. The signals marked with (*) are relative to kraft lignin on the blend.

Also, the assignments relative to PAN in blend PAN-lignin showed the signal intensity decreasing as the amount of lignin in the blend increases, regardless the action of heat during the extrusion process. The assignments like: stretching (ν C-H, CH_2), deformation (δ C≡N), stretching (ν C=N) and stretching relative to styrene (ν C-H) from PAN underwent a signal attenuation for higher proportions of lignin in the blend. And, as it would be expected, the assignments relative to kraft lignin on spectra, including stretching (ν C=O), (ν C-O), (ν C-C) and aril (ν C-C), intensified as the amount of lignin increases [10].

So, the results of spectrum analyses suggest that the production of blend PAN-lignin by extrusion process did not cause chemical inter-polymeric reactions among the components of the

blend. The results characterize only molecular physical interactions like mechanical anchorage and electrostatic connections.

4. CONCLUSIONS

This work studied the formation of PAN/lignin blends prepared by conventional extrusion process. The materials were analyzed by SEM micrographs and FTIR. By the use of SEM micrographs, it was possible to conclude that blends with composition up to 10% in mass with lignin and 90% with PAN showed good homogeneity, exhibiting no phase separation. Blends having kraft lignin at proportions of 15% and 20% in relation to PAN-co-styrene (10%) exhibited a rough surface aspect, however still without phase separation. When comparing the FTIR spectra from blend samples before and after extrusion, no significant differences were observed. So, based on the performed analyses, no degradation or chemical reactions among the components of the blend have occurred as a result of the heat in which the components were exposed during the extrusion process. It means that the process is appropriate to produce PAN/lignin blends with lignin concentration up to 20%/mass.

ACKNOWLEDGMENTS

This work was main possible due to the support from FIBRIA, CAPES, QUIMLAB and DCTA.

REFERENCES

[1] Xie, X.; Goodell, B.; Zhang, D.; Nagle, D.C.; Qian, Y.; Peterson, M.L.; Jellison, J.; "Characterization of carbons derived from cellulose and lignin and their oxidative behavior". Bioresource Technology, 100, (2009) 1797-1802.
[2] Zakzeski, J.; Bruijnincx, P.C.A.; Jongerius, A.L.; Weckhuysen, B.M.; "The catalytic valorization of lignin for the production of renewable chemicals" Chem. Rev. 110, 3552-3599 (2010) DOI: 10.102/cr900354u.
[3] Luo, J.; "Lignin-based carbon fiber" Thesis of Degree of Master of Science. M.S. The Graduate School The University of Maine (2010). Braun, J.L., Holtman, K.M.;
[4] Kadla, J.F.; Lignin-based carbon fibers: Oxidative thermostabilization of kraft lignin. Carbon. 43 (2005) 385-394.
[5] Awal, A.; Sain, M.; "Spectroscopic studies and evaluation of thermorheological properties of softwood and hardwood lignin". Journal of Applied Polymer Science, Vol. 122, 956-963, 2011.
[6] EPE, 2013, p. 51
[7] <http://www.udop.com.br/download/estatistica/institucional_economia/11mar16_analise_comparativa_safra_atual_anterior_2015a16_acumulado.pdf >
[8] [<http://www.tecnologiademateriais.com.br/portal/noticias/composites/2013/setembro/piche.html>].
[9] Nunes, K.S.D.; Pardini, L.C.; Alves, N. P. "Pan/lignin copolymer by extrusion process". 2nd Brazilian Conference on Composite Materials - BCCM2, september 15-18, 2014.
[10] Cateto, C.A.B.; "Lignin-based polyurethanes: Characterisation, synthesis and applications", Faculdade de Engenharia da Universidade do Porto (FEUP), to obtain degree of Doctor in Biological and Chemical Engineering. December 2008.

[11] ALVES, N. P. Acrylic and modacrylic polymer fusion process, acrylic and modacrylic polymer: acrylic and modacrylic polymer composition and acrylic and modacrylic polymer usage. W.O Patent 147 224, 2007.
[12] ALVES, N. P.; Thermoplastic polyacrylonitrile production process. United States Patent Application Publication. Pub. No.: US 2011/0024939A1. Pub. Date: Feb. 3, 2011.

KRAFT LIGNIN FROM PAPER MILL LIGNOBOOST® PROCESS - A PROMISE TO LOW COST GREEN CARBON FIBER

Katia S. D. Nunes [(1)] **and Luiz C. Pardini** [(2)]

(1) Departamento de Química dos Materiais em Ciências e Tecnologias Espaciais (CTE-Q) -ITA - Instituto Tecnológico de Aeronáutica - São José dos Campos, Brazil
(2) Departamento de Ciência e Tecnologia Aeroespacial - DCTA - Instituto de Aeronáutica e Espaço-IAE, Divisão de Materiais (AMR) - São José dos Campos, Brazil

https://doi.org/10.21452/bccm4.2018.14.06

ABSTRACT

The application of lignins in biodegradable/biobased materials is receiving increasing attention as the world looks for alternatives to petrochemicals. A new industrial method used to obtain higher purity and low cost lignin is now possible by the LignoBoost® process. The kraft lignin from this process has high carbon content level and opened a new research line for the production of products with high economic value like low cost carbon fiber. Kraft lignin is a paper mill waste with very low production costs that could open new possibilities for the lignin applications. In this work, three different types of lignin were compared with a regular carbon fiber precursor in order to verify their potential as alternative low cost precursor materials. The key aspect to be considered in the assessment of potential use of the material in the production of precursors is the carbon content level since it is the foremost constituent element of carbon-based materials.

1. INTRODUCTION

The use of biologically derived polymers (bio macromolecules) is emerging as an important component for economic development. By transforming forest and agricultural feedstock's, a new class of renewable, biodegradable and biocompatible materials (biomaterials) is being introduced [1, 2]. Emerging applications for bio macromolecules range from packaging and industrial chemicals, to producing 'green' materials with unique physical and functional properties, the processes used to create bio-based materials lead to new manufacturing opportunities that minimize energy consumption and waste [1]. Recently, environmental concerns have sparked interest in utilizing biodegradable and bio-derived materials in various industrial fields. Particularly, the utilization of plant-derived materials such as agricultural residues and forest products has received increasing attention. Biomass based fuels have found renewed interest

because of the rising cost of oil. Common sources of biomass include wood, agricultural crops and their residues. Although more research is being done on wood as a fuel, there is a growing interest in alternatives [2, 4].

Particularly, lignin has gained interest as a source of fuel and new materials. The main reason for this trend is a growing concern for more sustainability, which results in an increased usage of renewable materials to replace petrochemicals [7]. Lignin is one of the most abundant bio macromolecules existing in the plant kingdom. An enormous amount of lignin is produced as a by-product of the pulp and paper industry. As a result, a number of systems have been proposed for the utilization of lignin as a renewable polymeric material. However, lignin utilization is still limited, with less than 2% of the lignin produced being used in high value commercial applications. Lignin is a relatively inexpensive and as a precursor for low cost carbon fibers could be very attractive. Lignin is a high molecular weight polyaromatic macromolecule with a reported total worldwide production of approximately 26 million tons/year. This by-product of 'wood-free' paper making, it is predominately burnt in a chemical recovery process as a fuel source. However, as a fuel it is relatively inefficient, producing less than about 1/2 as much energy per kilogram as middle distillate (diesel, jet and boiler) fuels. Nonetheless, lignin combustion plays a critical role in the papermaking chemical recovery process and it is vital to that industry. However, an ever-increasing number of paper mills have become chemical recovery limited; if paper production is to maximize, the by-product lignin can no longer be used in its traditional role as a fuel [2, 3, 7]. Biodegradability of biopolymers is the base for their applications, however, their processability, performance and in particular price as compared to synthetic petrochemical-based polymers are of extreme importance. To this end, materials such as agricultural residues and/or bioprocessing by-products are obvious sources of low cost biomacromolecule materials [1, 7].

1.1 LIGNIN STRUCTURE

Lignin is a complex three-dimensional network polymer, as showed in Figure 2. Lignin behaves as a continuous matrix component in plant cell walls, providing mechanical strength and structural support [1]. The lignin binds fibers together to form a strong and tough matrix of plants and provides mechanical support to the plant vessels for the transportation of water and nutrients [6]. Depending on the wood species, e.g., softwood (conifers) or hardwood (angiosperms), lignins can contain predominately glycerol-aryl ether linkages, but there are several types of C-C bonds which likely serve as crosslinks between relatively short, linear chains of phenyl propane units [5, 9]. There is no method to isolate lignin from plants in the native form, chemical and physical modifications are unavoidable during lignin isolation. Therefore, the chemical structure and thermal behaviour of lignin is strongly dependent on the isolation method used. Isolated lignin displays both thermoplastic and thermosetting behaviour. The thermal properties of lignin are usually explained in association with its chemical structure, i.e., molecular weight, degree of condensation, and chemical modification during the preparation process. However, noncovalent interactions, such as hydrogen bonding, will also affect the thermal properties of lignin; strong interactions will reduce the thermal molecular motion of the lignin molecules [5, 7, 9].

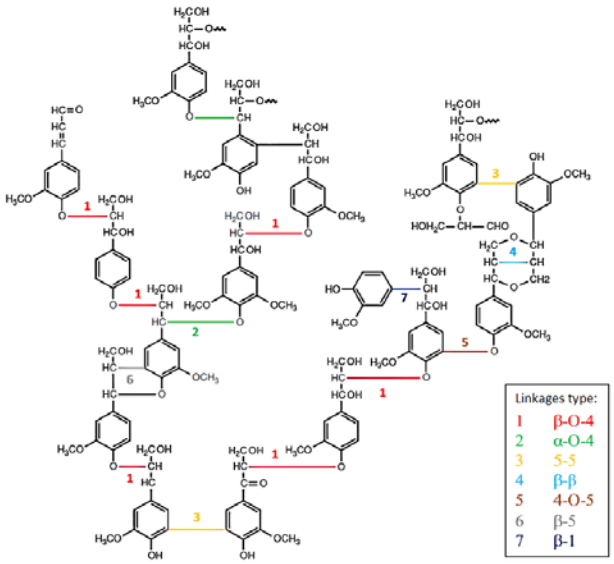

Figure 1: Model structure from hardwood lignin [9]

The traditional process of lignin precipitation and separation from kraft black liquors causes severe problems, related to complete or partial plugging of the filter cake and/or of the filter medium. Plugging of these types of filter cakes results in an extremely low level of the washing liquor flow through the cake and, consequently, to the need for extremely large filter areas. Partial plugging of the filter cake also leads to high levels of impurities in the lignin. It has been shown that these negative effects on the filtration process are caused by changes in lignin solubility, due to an excessive pH level and to the ionic strength gradients in the lignin filter cake during the washing process. Such changes result in restructuring the lignin particles, e.g. returning to a colloidal state, or in dissolution and reprecipitation of lignin in the filter medium [8, 14].

1.3 THE LIGNOBOOST® PROCESS

The development of the LignoBoost® process was carried out to reduce costs and impurities from kraft lignin [3]. Furthermore, full-scale combustion trials were carried out to evaluate the effects of firing the lignin bio fuel product in two different types of boilers and in a limekiln generation. One way of exploiting the energy surplus of a modern kraft pulp mill is to extract lignin from the black liquor. This gives the pulp mill a great opportunity to develop new economical revenues when the new by-product, lignin, is commercialised or used within the pulp mill to reduce production costs [8]. Lignin extraction has the additional advantage of providing an incremental capacity in the chemical recovery area, so that it can be used to off-load the recovery boiler or to avoid expansion, when pulp production is increased [7, 8]. The LignoBoost® process therefore makes it possible to extract lignin efficiently from the black liquor in kraft mills. The major advantages, compared to the previous technology, are the following: 1- the filter area and the volume of acidic washing water can be kept at lower values, resulting in lower investment costs, 2- the addition of sulfuric acid can be also kept at a lower level, resulting in lower operational costs, 3- the yield of lignin is higher, 4- the lignin has a lower ash and carbohydrate content, 5- the lignin has a higher content of dry solids [7]. The main idea is that kraft lignin processing, precipitated from black liquor produce a solid biofuel with high energy density and low ash

content, to use the dry lignin powder as a biofuel in the lime kiln and swap fossil fuel. So, a lignin without chlorides and lower ash content could be use in other burners/boilers, where fossil fuel is normally used, boilers in which corrosion from chlorides is a problem or, generally, in fluidised bed boilers frequently used for biomass combustion [8].

In the LignoBoost® Process, a stream of black liquor is taken from the black liquor evaporation plant (Fig. 2), then lignin is precipitated by acidification (the preferred acid is CO_2) and filtered ("chamber press filter 1", Fig. 2). Instead of washing lignin immediately after filtration, as in traditional processes, the filter cake is re-dispersed and acidified ("cake re-slurry", Fig. 2) [8].

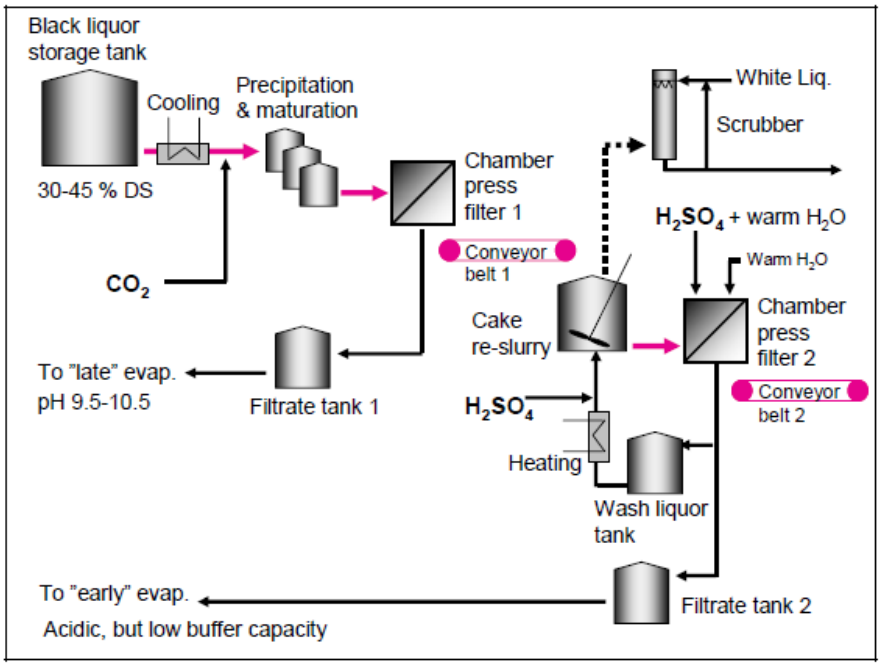

Figure 2: General layout of the LignoBoost® lignin removal process (post-treatment, drying and pulverizing are excluded) [8].

The resulting slurry is then filtered and washed by means of displacement washing ("chamber press filter 2", Fig. 2). When the filter cake is re-dispersed in a liquid, at pH level and temperature values approximately equal to those of the final washing liquor, the concentration gradients during the washing stage will be low. The change in the pH level, most of the change in ionic strength and any change in lignin solubility will then take place in the slurry, and not in the filter cake or in the filter medium during washing [8].

1.4 LIGNIN AS A CARBON FIBER PRECURSOR

Today approximately 95% of all carbon fiber uses polyacrylonitrile (PAN) as a precursor [10]. The high cost of carbon fiber production limits its widespread use. The basic difficulty is to combine precursor cost, yield and processing cost. Efforts to decrease the costs of carbon fiber and environmental concerns production are ongoing and kraft lignin is an attempt on this way due to being a biodegradable and bio-derived waste residue [3, 10].

With the development of the LignoBoost® process and the obtation of higher quality kraft lignin, the possibility of a new line of lignin use was opened. The kraft lignin contains more carbon compared to any other bio fuels showing great potential in the manufacture of carbon fiber precursor [8].

Due to the great potential as a precursor for carbon fiber, a lot attempts are being made with lignins. The domestic paper industry, could annually yield sufficient precursor for the present worldwide carbon fiber production needs without affecting paper mill operations. Carbon fibers have been manufactured from lignin. Kayacarbon lignin carbon fiber, was first developed and made commercially available by Nippon Kayaku Co. on a pilot scale. The process involved carbonization of dry spun fibers from lignin dissolved in alkali solution with poly(vinyl alcohol) added as a plasticizer. Sudo and co-workers showed that lignin could be converted into a molten viscous material with suitable properties for thermal spinning by hydrocracking, phenolation, or hydrogenolysis followed by heat treatment in vacuum. These modification methods seem to induce flow by remove as possible hydroxyl and hydroxy methyl functional groups from the lignin. The resulting carbon fibers showed superior properties to those of the Kayacarbon. More recently, Sano et al. have produced carbon fibers with properties suitable for midrange markets from organosolv lignin obtained by aqueous acetic pulping. Unfortunately in each of previous systems utilizing lignin, concerning production costs exists. Either plasticization or lignin modification was required, or no commercially available carbon fibers from commercially available lignins were used [3].

2. EXPERIMENTAL PROCEDURE

Kraft Lignin from LignoBoost® process was analyzed by elementary analyses. For content quantification of C, N, H, S and O in lignin samples it was used a calibration curve with minimum requirements for the correlation coefficient (r^2) greater than 0.99 for the reference analytical standard. The detection mode for N was thermal conductivity and to S, C and H the detection mode was IR. Oxygen gas was used to burning all the raw materials and Helium was used as gas drag. To elementary analysis of C, N and H was done by weighting 0.100 g of raw materials and completely incinerated at 1050 ^{o}C. The oxygen content was obtained by difference according to the guidelines of Bech et al. and Protásio et al. [11, 12]. The elementary analysis for sulfur was done weighting ± 0.1000 g of the sample in a porcelain crucible by complete incineration of the sample at 1450 ^{o}C. Detection was accomplished by IR mode.

3. MATERIALS

The kraft lignin used in this work is a hardwood lignin obtained from eucalyptus, by using *LignoBoost*® process [13], from Fibria S.A.

A Sigma Aldrich lignin was analysed for comparation. It is a commercial kraft lignin obtained from Sigma Aldrich Brasil.

The analytical standard used for quantification level of the elements was EDTA (LECO, USA), with the following contents: carbon (%): 41.07±0.13; hydrogen (%): 5.5±0.03; nitrogen (%): 9.56±0.02. The analytical standard used for quantification level of contained sulfur was petroleum coke (LECO, USA), with the following contents: sulfur (%): 5.67±0.14; volatile (%): 13.0±0.70; ash (%): 0.27±0.06; were conduced on a CHN 628 (LECO) for Module S and 628S (LECO) for module CHN.

4. RESULTS AND DISCUSSION

The results from elementary analyses for the samples of different lignins and PAN polymer are shown in Table 1. The comparison between carbon content shows that kraft lignin from LignoBoost® process has very high percentage of carbon in its chemical constitution. It is also possible to observe that the level of carbon content from kraft lignin is very close to the level found in PAN, which is the main and widely employed material for the production of carbon fiber. Elementary analysis of kraft lignin obtained by INVENTIA, also exhibits similar results with the ones found in this work [8]. On the other hand, the carbon content for a lignin available from Sigma Aldrich shows values lower than the ones from INVENTIA lignins. Most probably Sigma Aldrich lignin is also obtained by the kraft process, which in this case, resulted in low carbon content. The sulphur content at the analysed lignins are close, 1% - 3%, which is typical for paper mill plants [8]. Sigma Aldrich lignin shows slightly higher levels of sulphur when compared to the other lignins. Still for the Sigma Aldrich lignin, the level of oxygen content is remarkably higher than the other presented samples. High oxygen content on lignin brings problems on the next production processes due to molecular interaction driven by oxygen and hydrogen bonds. It gives lower mobility and higher Tg to lignin. Many attempts have been described to eliminate hydroxyl (-OH) and hydroxyl methyl functional groups (-CH2-OH) from lignin. These studies on lignin processes are intended to produce carbon fibers with superior properties, with target on midrange markets [3].

Table 1: Elementary analyses to lignin and PAN.

Sample	N (%)	C (%)	H (%)	O (%)	S (%)
INVENTIA lignin*	0.10	65.10	5.80	26.10	2.50
kraft lignin	0.15	62.74	5.86	26.90	2.19
Sigma Aldrich lignin	0.12	46.7	5.21	44.36	3.61
PAN (Radici Fibras)	26.3	66.4	5.80	1.4	0.10

* Source: [8].

5. CONCLUSION

This work focused on the review of one relevant chemical characteristic of the lignin as a raw material for carbon based precursors. The results of the elementary analyses for kraft lignin from FIBRIA and Sigma Aldrich and for PAN were reviewed and compared with available data from literature. Values of carbon content in the range of 60-65% are typical from the LignoBoost® process. It was shown that its carbon content is close to the carbon content of PAN polymer, which is the classical and most important industrial precursor used to obtain carbon fiber. The carbon content from kraft lignin obtained from FIBRIA meets the standard quality for use as a carbon based precursor.

ACKNOWLEDGEMENTS

This work was main possible due to the support from FIBRIA, CAPES, Quimlab and DCTA.

REFERENCES

[1] Kadla, J. F. and Kubo, S., 'Lignin-based polymer blends: Analysis of intermolecular interactions in lignin - synthetic polymer blends', *Composites: Part A*, **35** (2004) 395-400.
[2] Kubo, S. and Kadla, J. F., 'Lignin-based carbon fibers: Effect of synthetic polymer blending on fiber properties', *Journal of Polymers and the Environment*, **13** no. 2 (2005) 97-105.
[3] Kadla, J. F., Kubo, S., Venditti, R. A., Gilbert, R.D., Compere, A.L., Griffith, W., 'Lignin-based carbon fibers for composite fiber applications', *Carbon*, **40** (2002) 2913-2920.
[4] Chandrasekaran, S.R., Hopke, P.K., Kinetics of switch grass pellet thermal decomposition under inert and oxidizing atmospheres", *Bioresource Technology*,**125** (2012) 52-58.
[5] Kubo, S., and Kadla, J.F., 'Hydrogen Bonding lignin: A Fourier transform infrared model compound study', *Biomacromolecules*, **6** (2005) 2815-2821.
[6] Pan, X., Saddler, J.N., 'Éffect of replacing polyol by organosolv and kraft lignin on the property and structure on rigid polyuretane foam' *Biotechnology for Biofuels*, **6**:12 (2013) 1-10.
[7] Brodin, I., 'Chemical Properties and thermal behaviour of kraft lignins' Thesis, KTH Royal Institute of Technology, School of Chemical Sciences and Engineering, Division of Wood Chemistry and Pulp Technology, (Stockolm 2009).
[8] Tomani, Peter, 'The LignoBoost process', *Cellulose Chemistry and Technology*, **44**(1-3), (2010) 53-58.
[9] Laurichesse, S., Averus, L., 'Chemical modification of lignins. Towards biodased polymers.' *Progress in Polymer Science*, **39**, 7, (2014) 1266-1290.
[10]Huson, M.G., Church, J.S., Kafi, A.A., Woodhead, A.L., Khoo, J., Kiran, M.S.R.N., Bradly, J.E., Fox, B.L., 'Heterogeneity of carbon fibre', *Carbon*, **68**, (2014) 240-249.
[11]T. P. Protásio, et all., 'Braziliam Journal of Forest Research - Pesquisa Florestal Brasileira', *Colombo 31*, **66**, 113 (abr./jun. 2011).
[12]N. Bech, P. A. Jensen, K. Dam-Johansen, *Biomass and Bioenergy* **33**, Issue 3, (March 2009) 534-537.
[13]http://compositesmanufacturingmagazine.com/2016/01/state-of-the-composites-industry-lucintel-2016/6/
[14]Patent applications 1794363, 1797236 and PCT/SE 2008/000142

15. REPAIR AND JOINING TECHNIQUES

ANALYSIS OF A NOVEL INTERLOCKING ADHESIVE JOINING TECHNOLOGY FOR COMPOSITE-METAL STRUCTURES

Michael C. Corbett (1) and Conor T. McCarthy (1)

(1) Bernal Institute, School of Engineering, University of Limerick, Limerick, Ireland

https://doi.org/10.21452/bccm4.2018.15.01

Abstract

The incorporation of composite materials in the future's lightweight vehicle structures depends on the availability of suitable joining techniques. A novel joining concept is presented herein. It employs interlocking morphology formed on the surfaces of composite (female) and metal (male) adherends that are coupled with a layer of adhesive to interlock in shear. This acts to increase load transfer in the central region of the joint overlap. In the present work, the concept is investigated with a sophisticated finite element model, incorporating: adhesive damage through a cohesive zone model (CZM), composite intralaminar damage through a continuum damage model, composite interlaminar damage through a CZM, and metallic damage through Abaqus' ductile damage model. The concept demonstrates impressive improvements in performance compared to a standard adhesive joint. Its maximum applied load is increased by 33.7%, while the work to failure is 582.9% greater than the standard joint. These improvements are achieved as the interlocking geometry prevents the propagation of damage in the adhesive and damage develops in the composite adherend prior to failure.

Keywords: joining, continuum damage model, cohesive zone model, finite element analysis

1. INTRODUCTION

The demand to minimise the environmental impact of the transportation industry is motivating the lightweighting of vehicles. Research shows that the future's lightweight vehicle structures will be multi-material constructions, incorporating high-strength metallic alloys and composite materials. Adhesive bonding is a primary technique for the joining of composite to metal. However, it presents a number of inherent weaknesses that have restricted its uptake in load bearing applications. This research considers a novel, hybrid, mechanical-adhesive technique for joining materials. The technique employs interlocking bond-surface morphology formed on the surfaces of male (metallic) and female (composite) adherends that are coupled with a layer of adhesive to mechanically interlock in shear. The interlocking surfaces serve to activate the central overlap region of the adhesively bonded joint, which is known to typically be relatively inactive for load transfer in comparison to the overlap ends. Thus, the weight penalty and stress concentration associated with mechanical fastening are negated, while an additional, mechanical

loading mechanism is presented in the adhesive joint to improve durability. The concept has previously been investigated for a metal-metal joining configuration [1] and shown compelling improvements in joint strength and toughness. Herein, the concept is investigated, with finite element analysis, in a multi-material, composite-metal joining configuration. Detailed dimensions of the joint geometry are not provided herein and the performance attributes of the concept are non-dimesionalised with respect to a standard adhesive joint, modelled with equivalent material properties, to protect the nobility of the concept. It was also necessary to hide the interlocking geometry in the images presented herein in order to protect the intellectual property of the authors at the present time.

2. JOINT SPECIFICATION AND MATERIALS

The single-lap joint (SLJ) is one of the most commonly occurring joining configurations and is that most often used for testing adhesives and for characterising mechanically fastened joints. It is therefore an effective starting point to investigate the efficacy of a new, hybrid joining concept. The joint geometry, shown in Figure 1, was selected in consideration of the American Society for Testing and Materials (ASTM) standards: ASTM D 1002 and ASTM D 5868. The joint was loaded in quasi-static, displacement controlled tension, as shown in Figure 1.

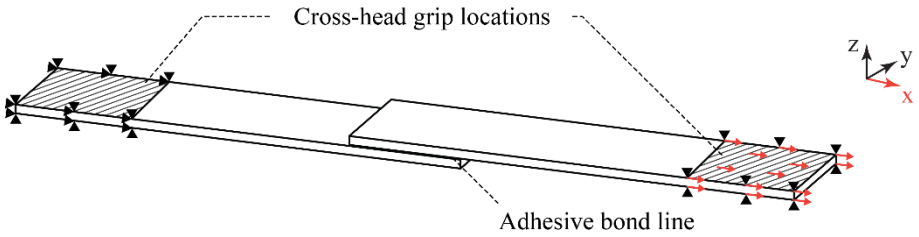

Figure 86: Single lap joint geometry and boundary conditions.

The interlocking adaptation of the SLJ is comprised of *male* and *female* adherends, as shown in Figure 2, which had interlocking geometry formed on their surfaces. The female adherend, which was a laminated composite material, HTA/6376, was characterised by depressions in its surface corresponding to the interlocking morphology. A symmetric, quasi-isotropic laminate stacking sequence was employed, $[45/0/-45/90]_{2s}$. The male adherend, which was an aluminium alloy, AA5754-H111, was distinguished by protruding profiles which are defined to fit the female adherend with a constant clearance to accommodate the adhesive, which was an epoxy resin from Nagase ChemteX, XNR6823 [2].

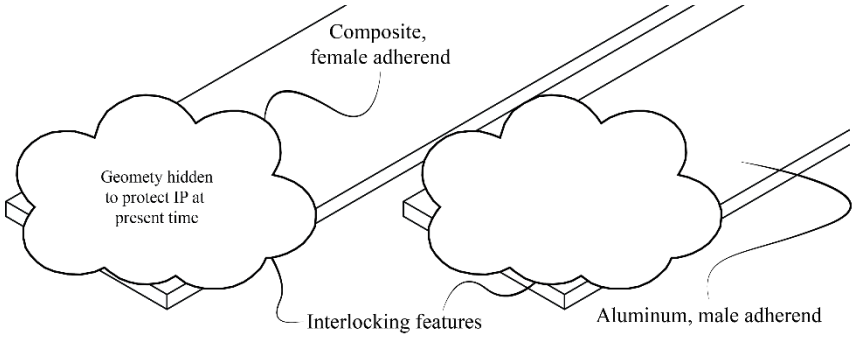

Figure 87: Male and female adherends, with interlocking morphology dimensions.

3. FINITE ELEMENT JOINT MODEL

A three-dimensional finite element (FE) model of the joint was developed in Abaqus®. It incorporated separate parts for each of the male adherend, the female adherend, and the adhesive. Partitioning was applied to each part to facilitate structured meshing with solid hexahedral elements. Layered partitioning was applied to the composite adherend and each ply was discretised by a single layer of elements, which were orientated according to the laminate stacking sequence. First-order, reduced integration elements (C3D8R in Abaqus®) with hourglass control were used to discretise the adherends, and the adhesive in models that considered its elastic response (six elements through thickness). In models considering adhesive damage it was discretised by a single layer of 8-node cohesive elements (COH3D8 in Abaqus®). ®).

3.1 Material Models

The mechanical response of the aluminium alloy, AA5754-H111 was characterised by elastic-plastic behaviour, incorporating von Mises yield criterion and isotropic strain hardening defined through Swift's law:

$$\sigma = A(\varepsilon_o + \varepsilon_p)^n, \quad \text{Eq. 5}$$

where σ is the true stress, A is a strength coefficient, ε_o is the true strain at the onset of yielding, ε_p is the true plastic strain, and n is the strain hardening exponent. The stress-strain response was produced from experiments; salient properties are summarised in Table 1. Damage initiation in the metal was considered through the ductile criterion in Abaqus® [3]. This is a phenomenological model for predicting damage onset as a function of stress triaxiality and the third invariant of deviatoric stress, which is related to the Lode angle [3]. The experimental data for this criteria was obtained from literature [4], which shows that ductile fracture of AA5754 shows significant dependence on these parameters. Linear damage evolution based on effective plastic displacement was applied to approximate the behaviour observed during experiments.

In models considering the stress distribution in the adhesive prior to the onset of damage, the adhesive was considered an elastic material. Subsequently, to determine the influence of damage and fracture on performance of the joint, the adhesive was represented by the uncoupled, mixed-mode cohesive zone model (CZM) in Abaqus® [3], which simplifies the macroscopic response of the adhesive layer into a bi-linear traction-separation law. The elastic response of the cohesive law was governed by the elastic properties of the adhesive, equal to the Young's modulus, E in the normal direction, and the shear modulus, G in shear [2]. The quadratic stress criterion was used to determine a damage initiation,

$$\left(\frac{\langle t_n \rangle}{t_n^o}\right)^2 + \left(\frac{t_s}{t_s^o}\right)^2 + \left(\frac{t_t}{t_t^o}\right)^2 = 1 \quad \text{Eq. 6}$$

where t_n, t_s and t_t, are tractions in the normal, and first and second shear directions, respectively, and t_n^o, t_s^o and t_t^o are critical traction values for damage initiation in each mode. Once damage initiates, the stiffness of the cohesive elements softens progressively according to a scalar damage parameter, which evolve monotonically from zero to one upon further loading. The evolution of damage is controlled by the linear energetic criterion,

$$\left(\frac{G_n}{G_n^c}\right)^\alpha + \left(\frac{G_s}{G_s^c}\right)^\alpha + \left(\frac{G_t}{G_t^c}\right)^\alpha = 1 \quad \text{Eq. 7}$$

where G_n, G_s, and G_t are the normal and tangential fracture energy release rates, respectively, G_n^c, G_s^c, and G_t^c are critical fracture energies in each modes, and $\alpha = 1$ for the linear criterion. Once this criterion is satisfied, the damage parameter is set to 1, the element may no longer carry load and is deleted from the model, allowing fracture to propagate. The properties of the adhesive were taken from [2] and are provided in Table 2.

Table 40: Mechanical properties of AA5754-H111.

E	ν	σ_y	A	n
68 MPa	0.33	90 MPa	371.72 MPa	0.2085

Table 41: Mechanical properties of XNR6823 [2].

E	G	t_n^o	t_s^o	G_n^c	G_s^c
2600 MPa	1000 MPa	57 MPa	32.9 MPa	1.18 N/mm	1.5 N/mm

The constitutive behaviour of the composite material, HTA/6376, was represented by an intra-laminar damage model, developed by [5], implemented through a VUMAT. It includes in-plane non-linear shear and features an innovative treatment of load reversals. The maximum stress criteria is employed for the prediction of tensile and compressive fibre failures. Puck's criteria is incorporated in order to predict tensile and compressive intralaminar matrix failure by checking for damage initiation on multiple potential fracture planes. Subsequent to initiation, damage evolves irreversibly through a non-linear softening law and the crack band model is used to mitigate mesh sensitivity by adjusting the final failure strain of each element based on its characteristic length and fracture energy. Once an element has been fully degraded it is subject to deletion based on a shear criterion. Experiments were previously conducted by O'Higgins [6] to determine the material properties and describe the damage development laws of HTA/6376, relevant damage model properties are outlined in Table 3. To account for interlaminar damage, zero-thickness layers of cohesive elements were included at each ply boundary. The uncoupled, mixed-mode CZM in Abaqus® [3] defined the mechanical behaviour of these elements through a bi-linear traction-separation law with linear softening. The initial stiffness of the cohesive elements was governed by a penalty parameter, K. The initiation of damage was determined by the quadratic stress damage initiation criterion (Eq. 2), while damage evolution was controlled by the linear fracture energetic criterion (Eq. 3). The CZM properties, corresponding to [7], are provided in Table 4.

Table 42: Damage model properties for HTA/6376 [6].

X_T	X_C	Y_T	S_{12}	S_{nt}	μ_t	μ_l	G^f
2170 MPa	1600 MPa	73.3 MPa	82.6 MPa	94.2 MPa	0.29	0.37	40 N/mm

Table 43: Cohesive zone model properties for delamination of HTA/6376 [7].

K	t_n^o	t_s^o	G_n^c	G_s^c
$1e^5$ N/mm^3	30 MPa	58.89 MPa	0.26 N/mm	1.002 N/mm

4. RESULTS AND DISCUSSION

4.1 Elastic stress distribution

The elastic stress distribution in the adhesive of the interlocking joint was examined by applying a constant load corresponding to linear deformation of the joint. The resulting distributions of normal and tangential stress are shown in Figure 3, and compared to a standard adhesive joint in Figure 4. To discuss the influence of the interlocking morphology on the stress distribution, the joint overlap is described by its *female end*, i.e. the end of the overlap closest to the constraint of the female adherend (x = 0) and vice versa, its *male end* (x = 1).

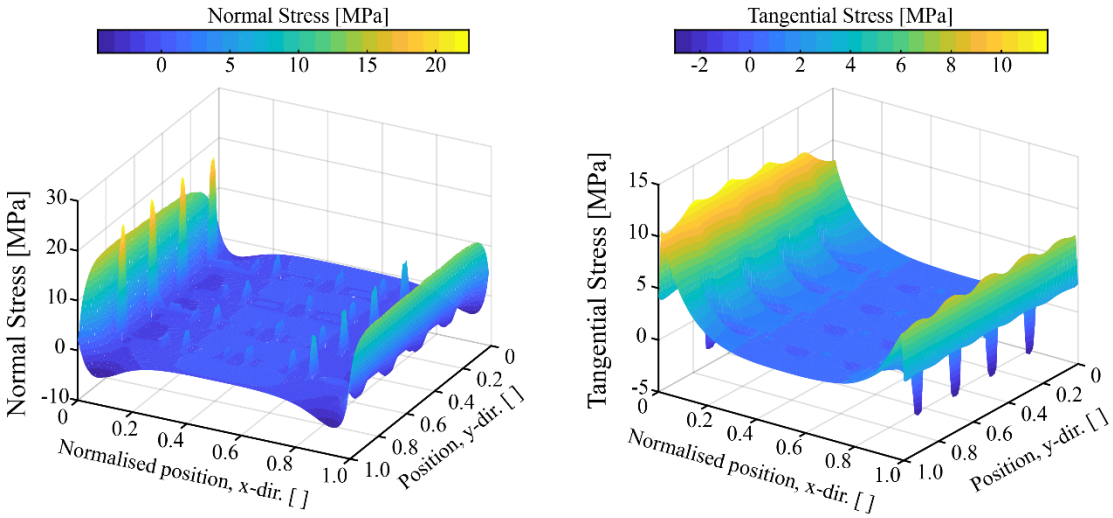

Figure 88: Normal (left) and tangential (right) stress in the adhesive of the interlocking joint.

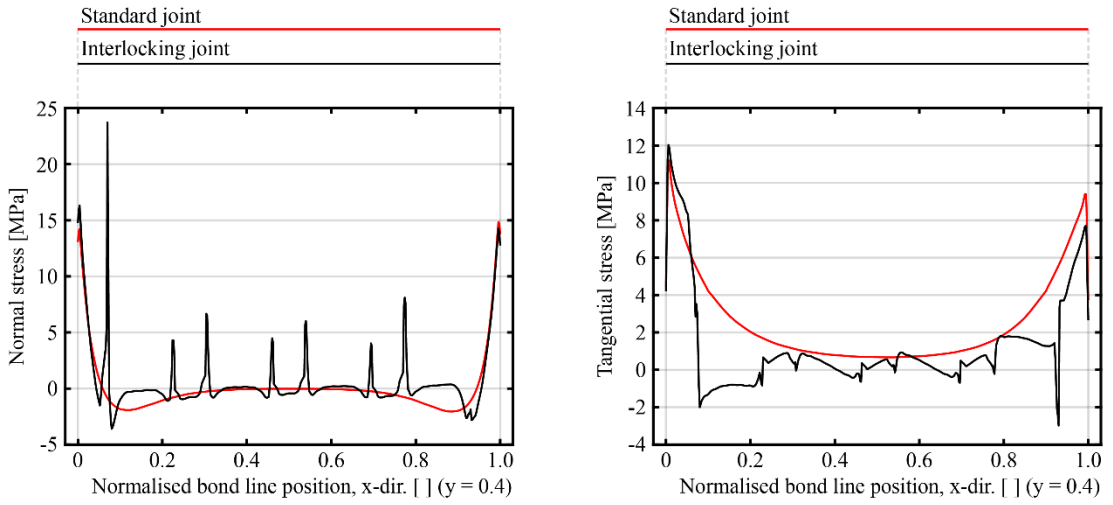

Figure 89: Normal (left) and tangential (right) stress in a section (at y = 0.4) of the adhesive of the interlocking joint compared to a standard joint.

The normal and tangential distributions of stress in the adhesive at the ends of the interlocking joint overlap correspond closely that observed in the standard joint. Peaks in tensile normal stress at the female and male ends of the interlocking joint are slightly higher and lower, respectively,

than the standard joint. Concentrations in tensile normal stress also exist acting on the interlocking features (x-dir). Similarly, peaks in tangential stress at the female and male ends of the joint are slightly higher and lower, respectively, than the standard joint. This indicates that damage may initiate at the female end of the overlap. Minimal tangential stress is observed in the adhesive in the central part of the overlap of the interlocking joint.

4.2 Progressive damage and failure

The mechanical response of the interlocking adhesive joint is compared to that of a standard adhesive joint (without interlocking geometry), which has been modelled with equivalent material properties, in Figure 5; important performance characteristics are summarised in Table 5. The interlocking joint achieves a significantly greater displacement than the standard joint prior to failure. Accordingly, the maximum applied load of the interlocking joint is 33.7% greater than that of the standard joint, and more remarkably, the work required to fracture the interlocking joint is 582.9% greater. The response curves exhibit highly nonlinear response, with decreasing stiffness as the joint extension increases. This is most apparent for the interlocking joint and is indicative of plastic deformation of the aluminium adherend.

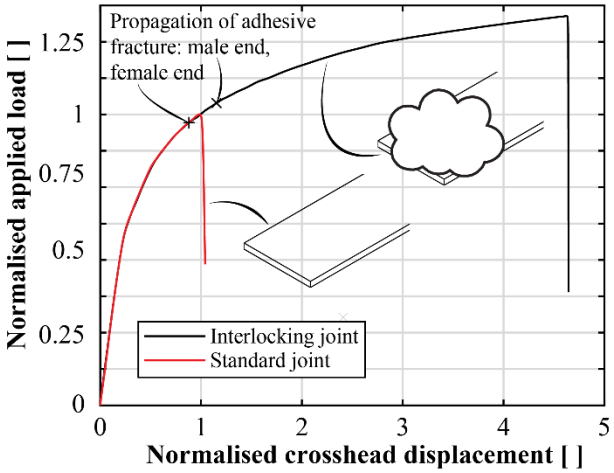

Figure 90: Mechanical response of the interlocking joint compared to a standard joint.

Fracture initiated and began to propagate almost simultaneously from both ends of the standard joint's overlap at the point of its maximum load; after which, fracture propagated rapidly through the remaining adhesive, resulting in failure. In contrast to this, the points at which the fracture began to propagate in the adhesive from each of the female and male ends of the overlap of the interlocking joint are indicated in Figure 5. Fracture initiated in the adhesive at the female end of the interlocking joint, corresponding to the increased adhesive stress discussed in Section 4.1. It subsequently initiated in the adhesive at the male end of the overlap. However, the interlocking geometry prevented adhesive fracture from propagating across the remaining adhesive by restricting the relative displacement of the adherends as load was transferred mechanically through the interlocking features. The progress of damage in the adhesive is illustrated in Figure 6. A delamination also initiated at the female end of the overlap following the initiation of adhesive fracture, as shown in Figure 7a.

Table 44: Normalised performance of the interlocking adhesive joint.

	Interlocking joint	Standard joint	Difference
Max. applied load	1.337	1	+33.7%
Work to failure	6.829	1	+582.9%

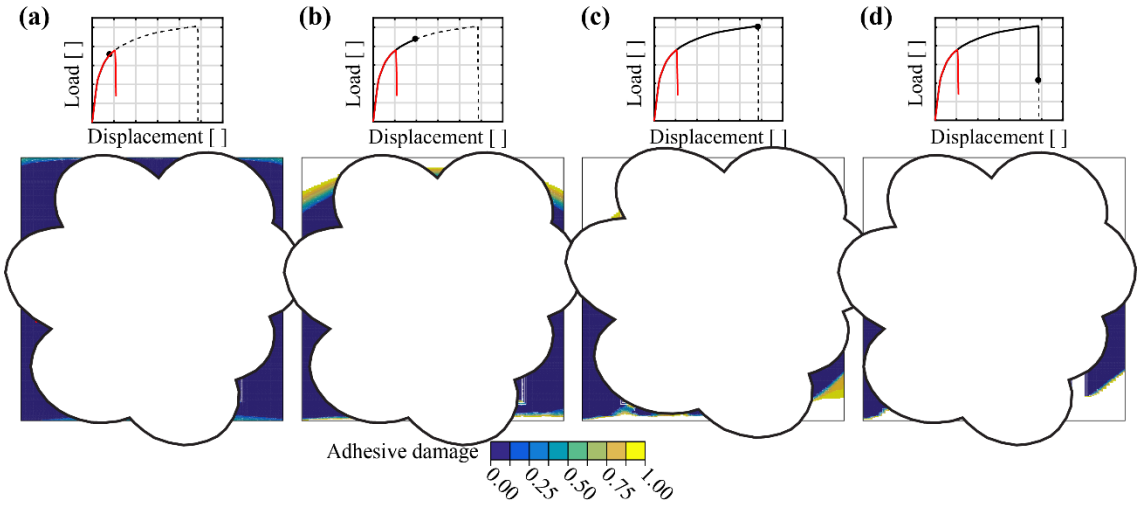

Figure 91: Damage in the adhesive of the interlocking joint at four points in the load history.

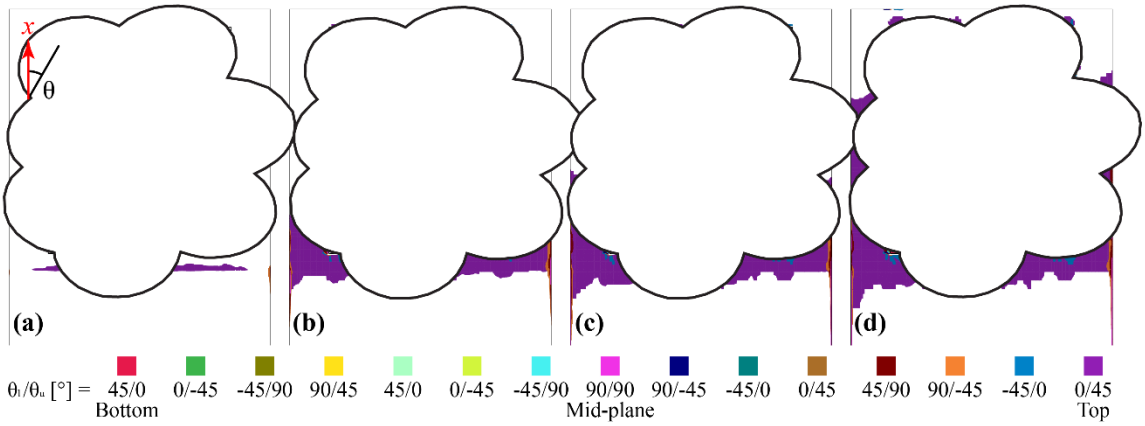

Figure 92: Delamination in the composite, female adhered of the interlocking joint at four points in the loading history (points correspond to a-d in Figure 6).

The interlocking joint subsequently sustained increasing load as damage developed in the adhesive and in the composite adherend. Compressive stress was induced on the adhesive at the male end of each interlocking profile as load was transferred mechanically through these features. Minor delaminations developed around the profiles closest to the female end of the overlap, while the large delamination propagated between the two plies closest to the joint's bonding plane at the female end of the overlap (Figure 7b,c). Failure of the joint was ultimately a result of this

delamination propagating across the overlap region while some adhesive remained in-tact, adhering the top ply of the composite to the male adherend.

5. CONCLUSIONS

The interlocking adhesive joint demonstrates significant increases in performance compared to a standard adhesive joint, with a 33.7% improvement in the maximum applied load and 582.9% in work to failure. These improvements are achieved as the interlocking morphology of the joint prevents the propagation of adhesive fracture across the central region of the joint overlap. Once fracture initiates at the ends of the joint overlap, the interlocking geometry assumes load transfer mechanically across the joint interface. This prevents relative displacement of the adherends which prevents further damage to the adhesive. Thus, significant plastic deformation occurs in the metal and damage develops in the composite prior to failure, which ultimately occurred through delamination. Importantly, this presents a shift in failure mode from adhesive/cohesive failure observed in the standard adhesive joint, while the additional deformation mechanisms engaged in the interlocking joint are central to increasing the work required to fracture the joint. The developments suggest that the interlocking adhesive joint would find suitable applications in automotive crash structures of lightweight, composite-metal vehicles, where the work to failure is a critical performance criterion.

ACKNOWLEDGEMENTS

The authors acknowledge the financial support of Science Foundation Ireland under Grant No. 13/IA/1833 and the Irish Research Council (IRC) for funding under their Government of Ireland Postgraduate Scheme through Grant No. GOIPG/2014/945. The authors also wish to acknowledge the DJEI/DES/SFI/HEA Irish Centre for High-End Computing (ICHEC) for the provision of computational facilities and support.

REFERENCES

[1] M. C. Corbett, P. A. Sharos, M. Hardiman, and C. T. McCarthy, “Numerical design and multi-objective optimisation of novel adhesively bonded joints employing interlocking surface morphology,” *Int. J. Adhes. Adhes.*, **78**, pp. 111–120, (2017).

[2] T. E. A. Ribeiro, R. D. S. G. Campilho, L. F. M. da Silva, and L. Goglio, “Damage analysis of composite-aluminium adhesively-bonded single-lap joints,” *Compos. Struct.*, **136**, pp. 25–33, (2016).

[3] Abaqus, “User’s Manuals, Version 6.14,” Providence, RI, USA, (2014).

[4] M. R. Millán, “Análisis experimental y numérico de la influencia del estado tensional en la deformación de fallo de elementos estructurales de aluminio,” Charles III University of Madrid, (2013).

[5] B. Egan, M. A. McCarthy, R. M. Frizzell, P. J. Gray, and C. T. McCarthy, “Modelling bearing failure in countersunk composite joints under quasi-static loading using 3D explicit finite element analysis,” *Compos. Struct.*, **108**, no. 1, pp. 963–977, (2014).

[6] R. M. O’Higgins, “An Experimental and Numerical Study of Damage Initiation and Growth in High Strength Glass and Carbon Fibre-Reinforced Composite Materials,” University of Limerick, (2007).

[7] C. Wang and X. Xu, “Cohesive element analysis of fatigue delamination propagation in composite materials with improved crack tip tracking algorism,” *Compos. Struct.*, **134**, pp. 176–184, (2015).

THE EFFECT OF ALUMINIUM SURFACE TREATMENTS ON THE APPARENT SHEAR STRENGTH OF HYBRID EPOXY SINGLE-LAP JOINTS

Francisco M. Dos Santos [(1)], Tulio H. Panzera [(1)], Alysson H. S. Bueno [(1)], Rodrigo T. S. Freire [(1,2)] and Cody Campsey [(3)]

(1) Centre for Innovation and Technology in Composite Materials – CITeC, Department of Mechanical Engineering, Federal University of São João Del-Rei, Brazil.

(2) Department of Natural Sciences, Federal University of São João Del-Rei, Brazil.

(3) Department of Mechanical Engineering, Texas Tech University, United States of America.

https://doi.org/10.21452/bccm4.2018.15.02

Abstract

Adhesive bonding in aluminium plates has been used for some time in aeronautical and automotive applications in order to replace rivets or welding. Surface preparation of aluminium prior to bonding is an important step that guarantees the strength of the joint. The use of silica micro-inclusions in the adhesive layers, and wash primers can improve the adhesion strength by some degree. In this study, an experimental characterisation was conducted in order to verify the influence of the surface treatment and silica micro-inclusions in the epoxy adhesive layers as well as the use of wash primer on the apparent shear strength of single-lap joints by tensile loading. Scanning electron microscopy (SEM), surface energy and *Ra* roughness measurements were conducted to characterize the aluminium surface. The results showed that the use of wash primer decreased the overall apparent shear strength of the joints in 55%. However, the inclusion of silica microparticles in the adhesive layers caused an increase of 24% in the shear strength. The surface treatment carried out with NaOH for one minute without the use of wash primer and with silica microinclusions provided the most resistant joint with mean apparent shear strength of 7.39 MPa. Cohesive break of the wash primer was the main cause of the decrease in strength. The joints without wash primer presented a mixture of cohesive and adhesive failure modes.

Keywords: Aluminium surface treatment, silica micro-inclusion, apparent shear strength.

1. INTRODUCTION

Aluminium is commonly used by numerous transportation industries for its durability, light weight, and cost-effectiveness. Bonding structural aluminium components with adhesives offer many advantages over conventional mechanical fasteners like lower structural weight and better appearance [1]. The surface of aluminium alloys contains a natural oxide layer that provides low quality bonding capabilities [2]. Surface pre-treatments such as mechanical abrasion and alkaline

etching can be used to remove this natural layer and provide a more homogeneous surface, thereby increasing the strength of the bond. Furthermore, the relationship between roughness and adhesion strength is not very simple. Xu *et al.* [3] showed that the surface energy decreases with the increasing of surface roughness resulting in low wettability of the substrate.

Incorporating silica micro- or nanosized particles to adhesives is a simple and reliable method for increasing the bonding capabilities between adhesives and adherents [4]. Liu *et al.* [5] concluded that the incorporation of silica microparticles to the adhesive increases both the impact critical stress and strain of polymers. The use of surface treatments on aluminium adherents, along with the incorporation of silica micro or nanoparticles to the adhesive, has been used to increase the overall shear and fatigue strength of bonded joints [6].

The use of low viscosity wash primers usually increases the shear strength of the joint. This increase in strength is the result of better-filled aluminium surfaces, owing to a larger interface area between the adhesive and the wash primer. Also, wash primers have corrosion-inhibiting additives that further improve chances of providing long-term bonding strength in harsh environments [7].

In this study, the effects of surface treatments, silica microparticle enhanced epoxy, and the use of wash primer on the apparent shear strength of single-lap joints were analysed using a Full Factorial Design.

2. MATERIALS AND METHODS

2.1 Materials

Rectangular plates (178 x 103 x 0.5 mm) of the aluminium alloy AA 1200 were used in the experiments according to the standard ASTM D1002 [8]. The aluminium was supplied by Belmetal (Belo Horizonte – MG). The polymeric adhesive used was the epoxy Renlam® M-1 and hardener Ren® HY 956, both supplied by Huntsman®. The selected wash primer was the Lazzuril phosphate agent 045 along with the Lazzuril catalyst 051. The silica microparticles were classified in the mesh 325 - 400 US Tyler with size range between 37 and 44 μm.

2.2 Surface treatments

The aluminium plates were initially washed under tap water with soap and then paper wiped with acetone to remove remaining grease and oil. Degreasing is effective in removing contaminants from the surface and this process is normally used as reference condition. However, according to Xu *el al.* [3], it does not provide acceptable surface conditions for bonding adhesives and additional appropriate treatments are necessary.

Three different surface treatments were carried out. The first was mechanical abrasion using sandpaper (grit 600) followed by acetone cleaning. The second and third treatments were alkaline cleaning of the surface by immersing the plates in a solution of 100 g/l of NaOH for 1 and 5 minutes at 60°C respectively, followed by desmutting in a nitric acid solution of 50 % (v/v) for 30 seconds at room temperature (~23°C). After all the treatments, the plates were rinsed with tap water followed by hot blow drying.

2.3 Surface morphologies

The Hitachi model TM-3000 scanning electron microscopy (SEM) equipped with energy dispersive spectroscopy (EDS) model Quantax 70 was used to analyse the treated surfaces. The *Ra* roughness of the treated surfaces was measured using a Form Talysurf 50 profilometer (Taylor Honson®). The contact angle (θ) was measured with an optical microscope Easyover 800x using

water and ethylene glycol drops (35 µl) as probe liquids. Since their surface energies components are known it is possible to calculate the surface energy of the treated surfaces, as follows. The work of adhesion (W_a) is calculated according to Equation 1, then Young's equation (Eq. 2) is used to get Equation 3, where γ_{SV}, γ_{LV}, γ_{SL} are the surface energies of the substrate, the liquid and the interface substrate/liquid respectively [3].

$$W_a = \gamma_{SV} + \gamma_{LV} - \gamma_{SL} \tag{1}$$

$$\gamma_{SV} = \gamma_{SL} + \gamma_{LV} cos\theta \tag{2}$$

$$W_a = \gamma_{LV}(1 + cos\theta) \tag{3}$$

The work of adhesion includes the polar component and the dispersion component (Eq. 4), where γ_{SV}^{d} and γ_{LV}^{d} are the dispersion components of the solid and the liquid surface energies respectively and γ_{SV}^{p} and γ_{LV}^{p} are the polar components of the solid and the liquid surface energies, respectively. Therefore, the apparent surface energy of the substrate is calculated according to the Equation 5 [3].

$$W_a = 2\sqrt{\gamma_{SV}^{d}\gamma_{LV}^{d}} + 2\sqrt{\gamma_{SV}^{p}\gamma_{LV}^{p}} \tag{4}$$

$$\gamma_{SV} = \gamma_{SV}^{d} + \gamma_{SV}^{p} \tag{5}$$

2.4 Fabrication of single-lap specimens

The plates were coated with epoxy modified and non-modified with silica microparticles. The wash primer was used in order to analyse its influence on the adhesion. According to Oosting [2], primers play an important function in protecting the aluminium substrate prior to the adhesive bonding. The wash primer was applied on the edges of the aluminium surface in an area of at least ten times the overlapping as showed in Figure 1a using an air coating applicator and the curing was held for 4 hours at room temperature.

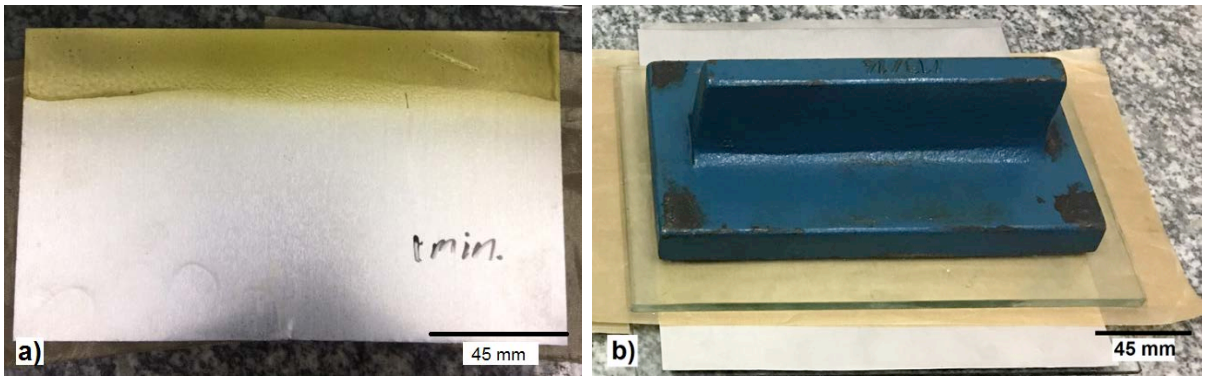

Figure 1: Plate with wash primer layer (a) and plates glued together (b).

The fabrication of the single-lap specimens was performed by pasting two plates with an overlapping area of 180 x 5 mm and subsequent compaction by a 3 kg weight for 24 hours as shown in Figure 1b. The total curing process (7 days at room temperature) followed the recommendations of the epoxy polymer manufacturer. After curing, the plates were cut into seven specimens (Figure 2a) according to the Figure 2b with a width of 25.4 mm, and the two specimens

from the borders were discarded due to chance of adhesive failure as recommended by ASTM D1002 [8].

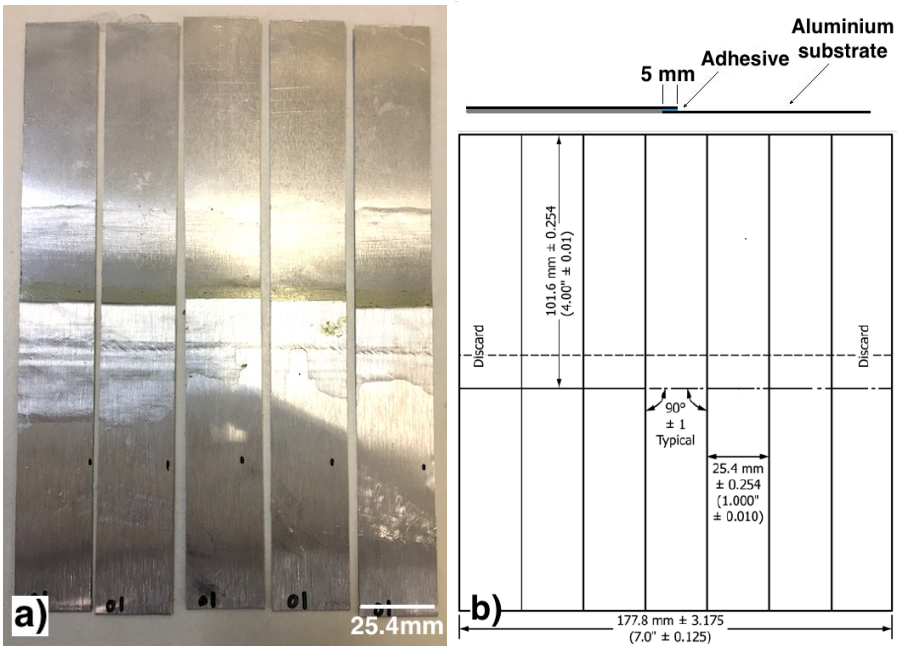

Figure 2: Single-lap test specimens (a) and standard panel (b) (Adapted from [8]).

2.5 Apparent shear strength of the single-lap joints

The apparent shear strength tensile tests were performed in a Shimadzu AG-X Plus testing machine with a testing speed of 1.3 mm/min according to ASTM D1002-10, (2010). Minitab v. 17 software was used to create the DoE scheme presented in Table 1, providing a $4^1 2^2$ Full Factorial Design, resulting in 16 conditions. The factors analysed were the surface treatment, the use of wash primer and the inclusion of silica microparticles in the adhesive layers.

Table 1: Experimental conditions.

Condition	Surface treatment	Wash primer	Silica inclusion (wt. %)
1	Degreased	With	0
2	Degreased	With	10
3	Degreased	Without	0
4	Degreased	Without	10
5	Mechanical Abrasion	With	0
6	Mechanical Abrasion	With	10
7	Mechanical Abrasion	Without	0
8	Mechanical Abrasion	Without	10
9	NaOH 1 min	With	0
10	NaOH 1 min	With	10
11	NaOH 1 min	Without	0
12	NaOH 1 min	Without	10
13	NaOH 5 min	With	0
14	NaOH 5 min	With	10

15	NaOH 5 min	Without	0
16	NaOH 5 min	Without	10

3. RESULTS AND DISCUSSION

3.1 Surface morphology

Figure 3 shows the SEM images of the different aluminium surfaces. Table 2 shows the EDS analysis of those surfaces. Figure 3a shows the degreased only aluminium surface, the red arrows indicate organic contaminants, degreasing is not effective in removing all contaminants. The surface treated with mechanical abrasion showed a common characteristic of grooves caused by sandpaper as shown in the Figure 3b. The mechanical abrasion enhances surface roughness and increases the contact area with the adhesive. promoting mechanical interlocking, which can improve the shear strength. The aluminium surfaces etched with sodium hydroxide presented characteristic pits (black dots in Figures 3c and 3d) generated by the alkaline solution. It can be noted that the number of pits in the sample treated for 5 minutes (Figure 3d) are higher than those treated for 1 minute, probably due to the longer immersion time in the alkaline solution. The small white dots in Figures 3c and 3d are intermetallic particles presented in the alloy, such as magnesium and iron that were revealed after the removal of the oxide layer by the sodium hydroxide.

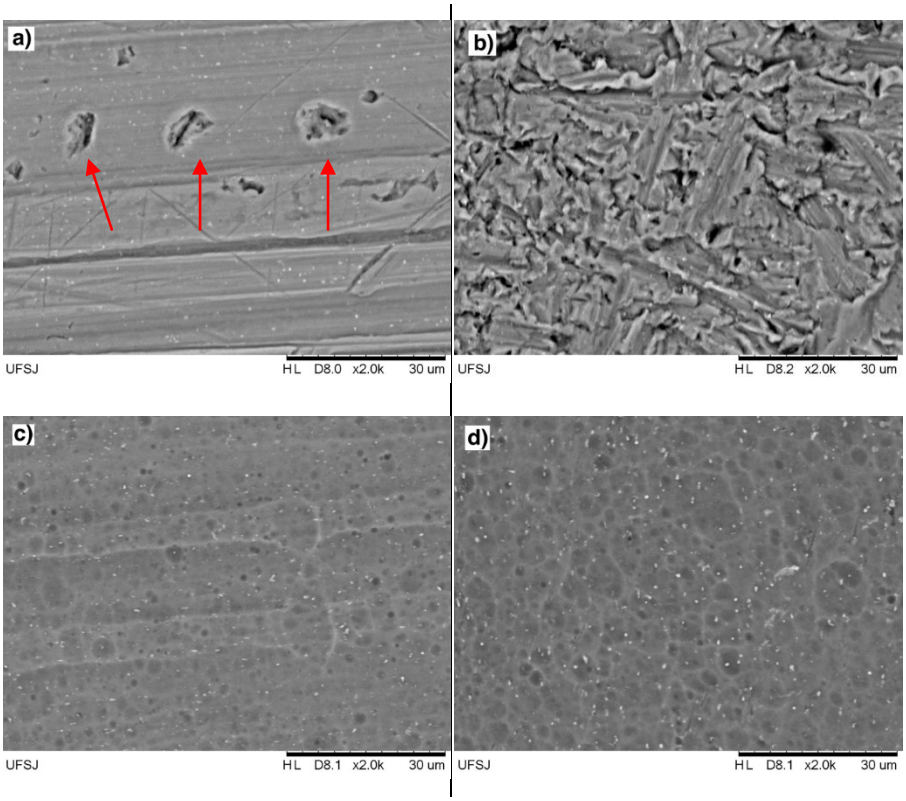

Figure 3: SEM images of aluminium surfaces degreased (a), pretreated by sandpaper (b), NaOH for 1 min (c) and NaOH for 5 min (d).

Table 2: Composition of the treated aluminium surfaces obtained from EDS.

Element (wt.%)	Al	C	O	Fe	Mg
Degreasing	92.78	4.76	1.81	0.10	0.11
Mechanical abrasion	83.76	7.46	8.00	0.11	0.17
NaOH for 1 min	94.48	3.65	0.97	0.28	0.62
NaOH for 5 min	94.44	4.04	0.77	0.43	0.32

Figure 4 shows the contact angles of the probe liquids for the degreased only aluminium surface. The contact angles of the surfaces subjected to the others treatments were measured the same way and the values of the their angles along with the calculated surface energies and *Ra* roughness are in the Table 3. The lower the contact angle of the drop with the surface, the greater the surface energy, indicating good wettability of the surface, which provides good adhesion properties [5].

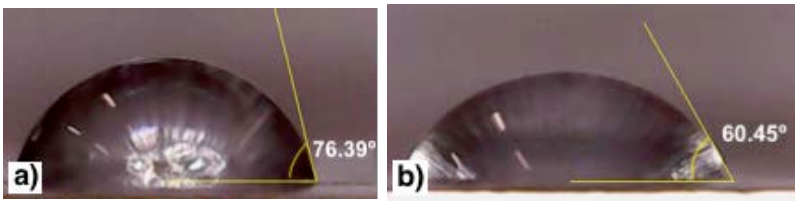

Figure 4: Contact angles for the water (a) and ethilete glycol (b) drops of the degreased sample.

Table 3: Contact angles, surface tension and roughness of the treated surfaces.

Condition	Contact angle (deg.)		Dispersive component (mJ/m^2)	Polar component (mJ/m^2)	Surface energy (mJ/m^2)	*Ra* Roughness (nm)
	Water	Ethylene Glycol				
1	76.39	60.45	11.30	16.80	28.10	398.4 ± 4,4
2	80.81	51.42	27.51	6.16	33.67	501.9 ± 8,9
3	73.36	41.79	28.06	9.57	37.63	358.9 ± 4,5
4	64.34	39.13	18.57	20.13	38.70	368.7 ± 3,2

Condition: Degreased (1), Mechanical abrasion (2), NaOH for 1 min (3) and NaOH for 5 min (4).

3.2 Apparent shear strength of the joints

Figure 5a shows the SEM image of the thickness layer of the adhesive in the joint, which had an average value of 0.126 mm. The apparent shear strength of the joints varied between 2.93 MPa and 7.39 MPa. Table 4 shows the analysis of variance (ANOVA) of the results. P-values lower or equal to a α-level of 0.05 imply significance of the factor effect on the variable response with a 95% of reliability [9]. The underlined P-values shown in Table 4 indicate the significant factors that affected the response. The adjusted R^2 value indicates whether the statistical model behaved appropriately. This means that the variance of the properties is explained by the variance of the factors analysed, the closer from 1 (100%) is the R^2, better is the predictive ability of the model. When one or more interaction effects are significant, the factors that interact should be considered together [10]. The R^2 value given in Table 4 is 86.60% showing good predictability of the model. The Anderson-Darling normality test was used to validate the ANOVA. In this case, the P-value must be equal or superior to 0.05 to follow a normal distribution configuration. The data followed a normal distribution with a P-value of 0.984 with the plot of residues shown in Figure 5b.

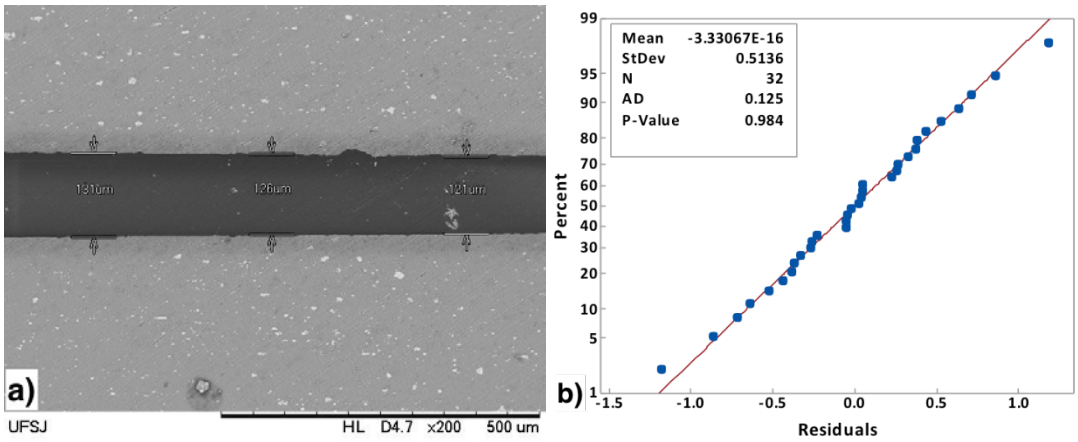

Figure 5: SEM image of the thickness layer of the adhesive (a), probability plot (b).

Table 4. P-values of the Analysis of variance

Experimental factor	**P-value**
Surface pre-treatment	0.385
Wash primer	**0.000**
Silica inclusion	**0.002**
Surface treat.*Wash primer	**0.004**
Surface treat.*Silica	0.783
Wash primer*Silica	0.163
Surface treat.*Wash primer*Silica	0.168
P-value And. Darling > 0.05	**0.984**
R^2-adjusted (%)	**86.60%**

Figure 6 shows the main effect plot for the use of wash primer and silica inclusion on the mean apparent shear strength. The wash primer decreased the apparent shear strength of the joints in 55%. According to Oosting [2], wash primer can improve the interface adhesion, but its cohesive strength is sometimes very weak, compromising the strength of the joint. Figure 7a shows a failure mode by wash primer cohesive break and Figure 7b a mixture of cohesive and adhesive failure modes of the conditions with neat epoxy. The silica inclusion improved the shear strength of the joints in 24%. Similar results were found by Liu *et al.* [6], who reported that silica inclusions may decrease crack growth rates increasing the apparent shear strength. Figure 8 shows the interaction plot between the factors of surface treatment and the use of wash primer. It can be noted that all conditions without wash primer presented better results of apparent shear strength, and the surface pre-treated by NaOH for 1 min provided the highest apparent shear strength, 45.9% higher compared to the mechanical abrasion condition. This is probably due to the better infiltration of the epoxy in the aluminium surface, owing to the higher surface energy compared to mechanical abrasion and degreased conditions. The mechanical abrasion condition showed the best result in the condition with wash primer, 32% higher than NaOH for 1 min condition. This is probably due

the mechanical interlocking with the wash primer and the larger area of contact with the resin caused by the surface high roughness.

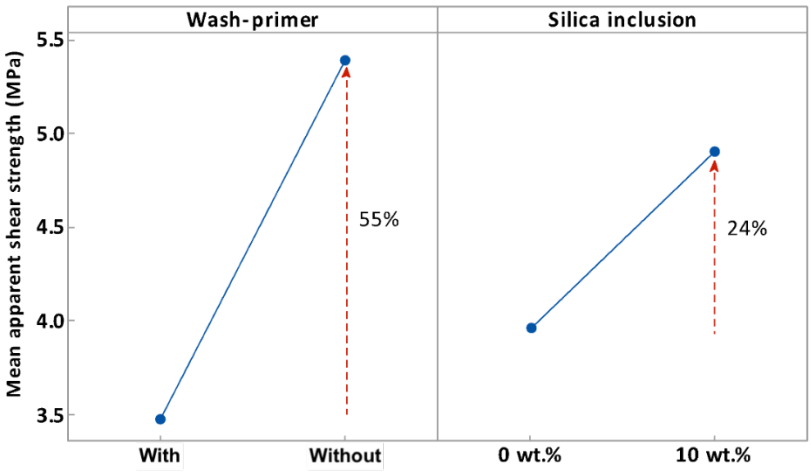

Figure 6: Main effect plot for the use of wash primer and micro-silica inclusion on the mean apparent shear strength.

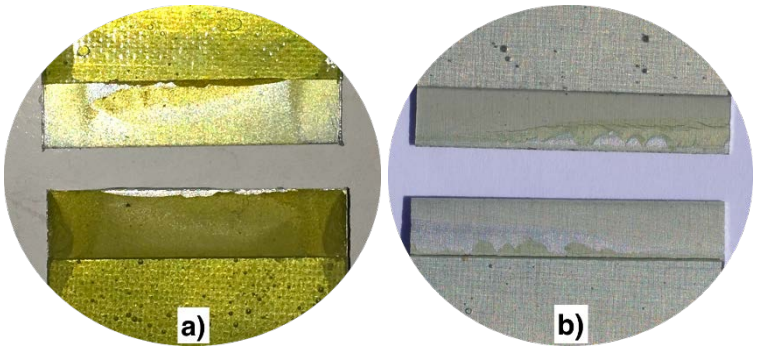

Figure 7: Failure mode by wash primer cohesive break (a), mixture of cohesive and adhesive failure mode of the epoxy adhesive (b).

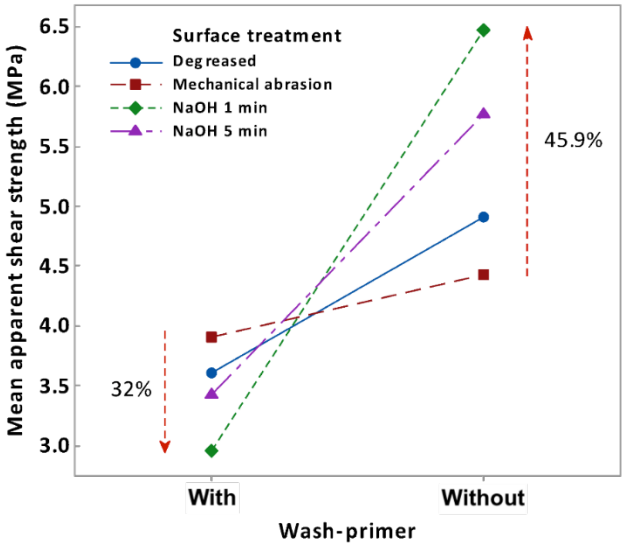

Figure 8: Interaction effect plot for the mean apparent shear strength.

4. CONCLUSION

This paper investigated the effect of aluminium surface treatment, micro-silica inclusion into epoxy polymer and the use of wash primer on the apparent shear strength of single-lap joints. A full factorial design was conducted to identify the effects of individual factors and interactions on the responses. The use of wash primer reduced the apparent shear strength of the joints in 55%. The micro silica inclusion was able to increase the overall shear strength of the joints in 24%. The failure mode of the joints with wash primer was mainly cohesive break and the failure mode of the joints without wash primer was a combination of cohesive break of the epoxy and adhesive break of the interface aluminium/epoxy. The use of accelerated aging of the joints by high humidity and temperature will be the scope of future works.

ACKNOWLEDGMENTS

The authors would like to thank CAPES, CNPq and FAPEMIG for the financial support provided.

REFERENCES

[1] T. Sinmazçelik, E. Avcu, M. Ö. Bora, and O. Çoban, "A review: Fibre metal laminates, background, bonding types and applied test methods," *Mater. Des.*, vol. 32, no. 7, pp. 3671–3685, 2011.

[2] R. Oosting, "Towards a New Durable and Environmentally compliant Adhesive Bonding Process for Aluminium Alloys," Delft University of Technology, 1995.

[3] Y. Xu, H. Li, Y. Shen, S. Liu, W. Wang, and J. Tao, "Improvement of adhesion performance between aluminum alloy sheet and epoxy based on anodizing technique," *Int. J. Adhes. Adhes.*, vol. 70, pp. 74–80, 2016.

[4] Q. Meng *et al.*, "Nanosilica-toughened polymer adhesives," *J. Mater.*, vol. 61, pp. 75–86, 2014.

[5] H. Y. Liu, G. Wang, and Y. W. Mai, "Cyclic fatigue crack propagation of nanoparticle modified epoxy," *Compos. Sci. Technol.*, vol. 72, no. 13, pp. 1530–1538, 2012.

[6] H. Zhou, H. Liu, H. Zhou, Y. Zhang, X. Gao, and Y. Mai, "On adhesive properties of nano-silica / epoxy bonded single-lap joints," *JMADE*, vol. 95, pp. 212–218, 2016.

[7] S. Technology, "Bonding of aluminum," 2016. [Online]. Available: https://goo.gl/dNBSI0. [Accessed: 15-Feb-2017].

[8] ASTM D1002-10, "Standard Test Method for Apparent Shear Strength of Single-Lap-Joint Adhesively Bonded Metal Specimens by Tension Loading (Metal-to-Metal)," 2010.

[9] D. C. Montgomery, *Design and Analysis of Experiments*, Eighth Edi. John Wiley & Sons, Inc., 2013.

[10] M. C. C. Werkema and S. Aguiar, *Planejamento e Análise de Experimentos: Como identificar as principais variáveis influentes em um processo*. Belo Horizonte: Fundação Christiano Ottoni, 1996.

16. SIMULATION IN COMPOSITES

COMPUTATIONAL ANALYSES FOR CARBON-EPOXY PLATES DAMAGED BY LOW-VELOCITY IMPACT

Gregório Felipe Oliveira Ferreira [1], Marcelo Leite Ribeiro [1], António Joaquim Mendes Ferreira [2], Volnei Tita [1]

(1) [a] *Department of Aeronautical Engineering, São Carlos School of Engineering, University of São Paulo, Av. João Dagnone, 1100, 13573-120, São Carlos, SP, Brazil.*

(2) *Department of Mechanical Engineering, Faculty of Engineering of University of Porto, Rua Dr Roberto Frias s/n, 4200-465, Porto, Portugal.*

https://doi.org/10.21452/bccm4.2018.16.01

Abstract

The usage of composite materials on new design structures is still very conservative, mainly due to its very complex failure behavior. Therefore, the prediction of these mechanisms requires computational analysis. Thus, a damage model based on CDM concepts is applied in order to predict intra-ply failure mechanisms in impacted carbon-epoxy laminate structures. The damage model was implemented as VUMAT (User Material Subroutine for explicit integration analyses) and linked to ABAQUS™. Several numerical analyses were performed, and the results were compared to experimental tests in order to evaluate the potentialities and limitations of the damage model application.

Keywords: composite materials, damage model, progressive failure analyses, low velocity impact, Finite Element Analyses.

1. INTRODUCTION

In the last decades, fiber reinforced polymer (FRP) composite materials have aroused great interest within the aircraft and aerospace industry where the design of structures requires optimal stiffness/weight and strength/weight ratio. Composite materials enable the reduction of the structural weight of aircrafts, increasing payload and aircraft range. In spite of the designers' efforts to use composites within the aircraft industry, the application of those materials on civil aircraft structures is still limited due to the certification process and prediction of behavior in service life [1]. Regarding the aircraft life cycle, composite structures are subjected to different impact loads such as airplane ground contact, debris launched from the take-off lane, bird strike, hail and tools that falls during the service and maintenance phase. Based on the investigated literature, composite structures are more susceptible to the impact damage than that similar metallic ones. In addition, the dynamic behavior of composite laminates is more complex, considering their anisotropy and heterogeneity which many failure mechanisms occur

simultaneously and randomly. The combination of fiber rupture, delamination, matrix fracture, inelastic deformations due to the contact forces and high displacement values can produce catastrophic failure of the structure.

Continuous Damage Mechanics (CDM) is one good approach to formulate intra and interlaminar damage models. This can be confirmed by a list of published works: Abrate [2]; Maio, L. et al. [3]; Zhang et al. [4]; Camanho et al. [5], Shi et al. [6]; Kim et al. [7], Puck & Shurmann [8]; Feng and Aymerich [9]; Ferreira et al. [10].

Thus, considering the presented scenario, this manuscript shows an application of a new damage model to predict intralaminar failure mechanisms in impacted carbon-epoxy laminate structures. The damage model was implemented as VUMAT (User Material Subroutine for explicit simulations) and linked to ABAQUS™. After that, several numerical analyses were performed, and the results were compared to experimental tests in order to evaluate the potentialities and limitations of the damage model application.

2. DAMAGE MODEL: MATHEMATICAL FORMULATION

The proposed material model is based mainly on the models developed by Ribeiro [11] and Ladevèze & Le Dantec [12]. Based on CDM concepts, it considers the behavior of fiber and matrix in a meso-mechanical scale (for a homogenized ply) in a plane stress state. Fiber failure under tension and compression, as well as matrix failure under tension, compression and shear are considered in the formulation. Thus, the present model can predict only intralaminar failure, but cannot delamination. Moreover, it was assumed the hypothesis that the failure modes are independents. In this way, matrix failure does not contribute directly to the fiber failure and vice versa. Nevertheless, after failure identification, degradation process of the properties for the failure plies will happen, affecting matrix damage evolution in fiber damage and vice versa. This can be explained through the constitutive matrix modified by damage variables shown by Equation 1.

$$D = \frac{1}{K}\begin{bmatrix} (1-d_1)E_{11} & (1-d_1)(1-d_2)\nu_{21}E_{22} & 0 \\ (1-d_1)(1-d_2)\nu_{21}E_{22} & (1-d_2)E_{22} & 0 \\ 0 & 0 & K(1-d_6)G_{12} \end{bmatrix} \quad (1)$$

with $K = \left[1-(1-d_1)(1-d_2)\nu_{12}\nu_{21}\right]$

The behavior of carbon/epoxy laminate under tensile load σ_{11} was considered elastic linear and brittle. According to this characteristic, there is not yielding phenomenon, and failure occurs abruptly. Thus, this behavior can be simulated by using the Maximum Stress Criterion, and the internal variable damage d_1 (related to the degradation in this direction) is considered equal to value "1", when the failure is detected; so it is assumed the complete damage of the reinforcements.

However, in order to model fiber behavior under compression, a linear behavior until a specific value X_{C0} was assumed. When $\sigma_{11} \geq X_{C0}$, a non-linear elastic behavior was considered. Thus, elastic modulus from X_{C0} is not represented by E_{11_0} (initial elastic modulus), but by secant modulus E_{11}. Linear tensile, compression and shear limits were considered to simulate the matrix behavior. Those limits were taken from 90º and [+45º/-45º] tests. Based on those results, it was possible to propose a damage surface for the matrix (Figure 1), considering transversal (σ_{22}) and shear stresses (τ_{12}).

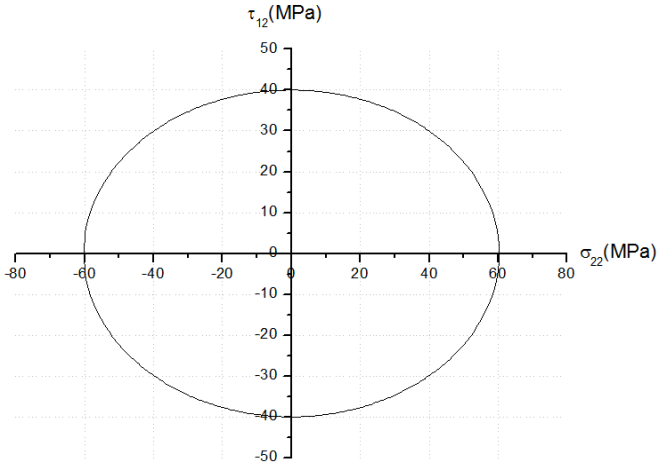

Figure 1- Damage surface for matrix.

The proposed damage surface is represented by Equation 2, and it has as parameters Y_{C0} and, S_{12_Y} both the compression and shear elastic limits.

$$f = 1 - \left(\frac{{\tau_{12}}^2}{{S_{12_y}}^2} + \frac{{\sigma_{22}}^2}{{Y_{co}}^2} \right) \tag{2}$$

The proposed material model is presented in Table 1 and is modified from Ribeiro's [11], since it does not use degradation law as a function of fiber orientation angle. Although it is similar to the model presented by Ladevèze & Le Dantec [12], it differs totally in fiber and matrix compression behaviors.

Table 1- Proposed material model.

Failure Criteria	Failure Mechanism	Degradation Law	Damage Evolution
$\frac{\sigma_{11}}{X_T} \geq 1$	Fiber failure under tensile stress ($\sigma_{11} > 0$)	$E_{11} = E_{11_0}(1 - d_1)$	$d_1 = 1$
$\frac{\lvert\sigma_{11}\rvert}{X_{C0}} \geq 1$	Fiber failure under tensile stress ($\sigma_{11} < 0$)	$E_{11} = \frac{X_{C0}}{\lvert\varepsilon_{11}\rvert}(1 - f(\varepsilon_{11})) + f(\varepsilon_{11}) \cdot E_{11_0}$	
$f \geq 0$	Matrix under tensile stress ($\sigma_{22} > 0$)	$E_{22} = E_{22_0}(1 - d_2)$	$d_2 = \frac{\left\langle \sqrt{\hat{\underline{Y}}} - \sqrt{Y_0'} \right\rangle}{\sqrt{Y_c'}}$
$f \geq 0$	Matrix under tensile stress ($\sigma_{22} < 0$)	$E_{22} = \frac{Y_{C0}}{\lvert\varepsilon_{22}\rvert}(1 - g(\varepsilon_{22})) + g(\varepsilon_{22}) \cdot E_{22_0}$	
$f \geq 0$	Matrix under shear stress ($\tau_{12} > 0$)	$G_{12} = G_{12_0}(1 - d_6)$	$d_6 = \frac{\left\langle \sqrt{\hat{\underline{Y}}} - \sqrt{Y_0} \right\rangle}{\sqrt{Y_c}}$

3. IMPACT TESTS: EXPERIMENTAL AND COMPUTATIONAL ANALYSES

Impact tests on 120 mm composite square plates made of prepreg M10 were carried out by Tita et al. [14]. Considering FD (Falling Dart) method [15], the impactor had a hemispheric shape (Figure 1) and is made of aluminum which is added to the frame mass and the load cell. Thus, the total impact mass is around 1.205 kg. Finite Element (FE) models developed in ABAQUS™ with

the VUMAT subroutine were used to simulate the carbon-epoxy laminate $[+45^o/-45^o/+45^o/0^o/90^o]_S$ and $[0^o/90^o/0^o/90^o/0^o]_S$ behavior under impact loading.

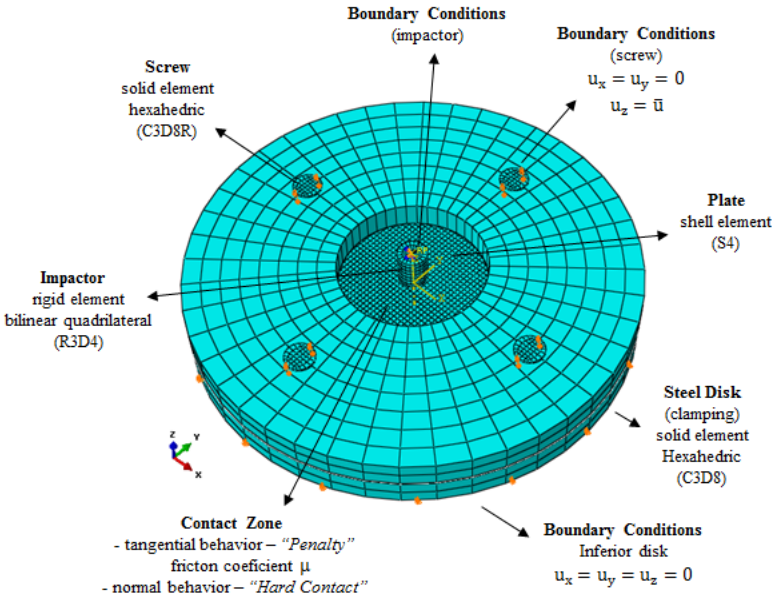

Figure 2- Finite Element model to simulate the impact test

The clamping steel discs and the screws were modeled by full integration eight nodes linear hexahedral solids (C3D8) and reduced integration solid (C3D8R), respectively (Figure 2). The composite plate was modeled by full integration shell elements (S4). Moreover, four nodes quadrilateral rigid bilinear elements (R3D4) were used to simulate the impactor, which has impact mass equal to 1.205 kg and final velocity of impact around 3.13 m/s that corresponds to 5.91 J of impact energy.

Regarding the boundary conditions used in the FE model, all translations of the bottom disc were restricted ($u_x=u_y=u_z=0$), and a prescribed displacement ($u_z = \bar{u}$ = 1.57 mm) equivalent to the torque in-situ was used. The impactor displacement was limited to the z-direction, applying $u_x=u_y=0$ and $u_z \neq 0$. It highlights that the contact between the discs and the composite plate was simulated by using Coulomb Friction Law. Moreover, the contact between the impactor and plate was simulated, considering the tangential penalty algorithm with friction factor equal to 0.15, and hard contact algorithm for normal behavior.

4. RESULTS AND DISCUSSION

First, it was performed mesh convergence tests in order to find "the most adequate" one for the simulations. Different tests of mesh convergence with 3600, 6400 and 14400 elements were handle. Although the mesh with 14000 elements has shown the best response, that with 6400 elements was chosen because of the high computational time simulation of 14400.

So, from the 6400 elements mesh it was possible to analyze the behavior of the two composite plates under impact. Figure 3-a) shows the force vs. displacement curves for the laminate $[+45^o/-45^o/+45^o/0^o/90^o]_S$ under 5.91 J of impact energy. It is possible to observe a high oscillation region between 0.0 ms and 1.2 ms. At 1.8 ms, there are small oscillations of high frequency. These oscillations are related to the dynamic behavior of the impact event as well as to failure process in

the composite material. It is important to noteworthy that matrix rupture and delamination drive failure mechanisms as shown by Tita et al. [14], and these mechanisms reduce the structure global stiffness. However, the maximum force value provided by the numerical analyses with damage model (3313.39 N) is closer to the maximum experimental force (3217.77 N) than without damage (3470.37 N). Besides, the duration of the impact event was around 4.0 ms for the experimental test, and numerical analysis with damage model predicted 3.7 ms, which was very close to the value provided by FE analysis without damage model (3.6 ms).

In the Figure 3-b), the FE model simulated about 50% of the absorbed energy by the real structure (2.0 J). It is important to observe that the absorbed energy predicted by the FE model is entire related to matrix damage mechanism, which is shown by the damage parameters d_2 and d_6.

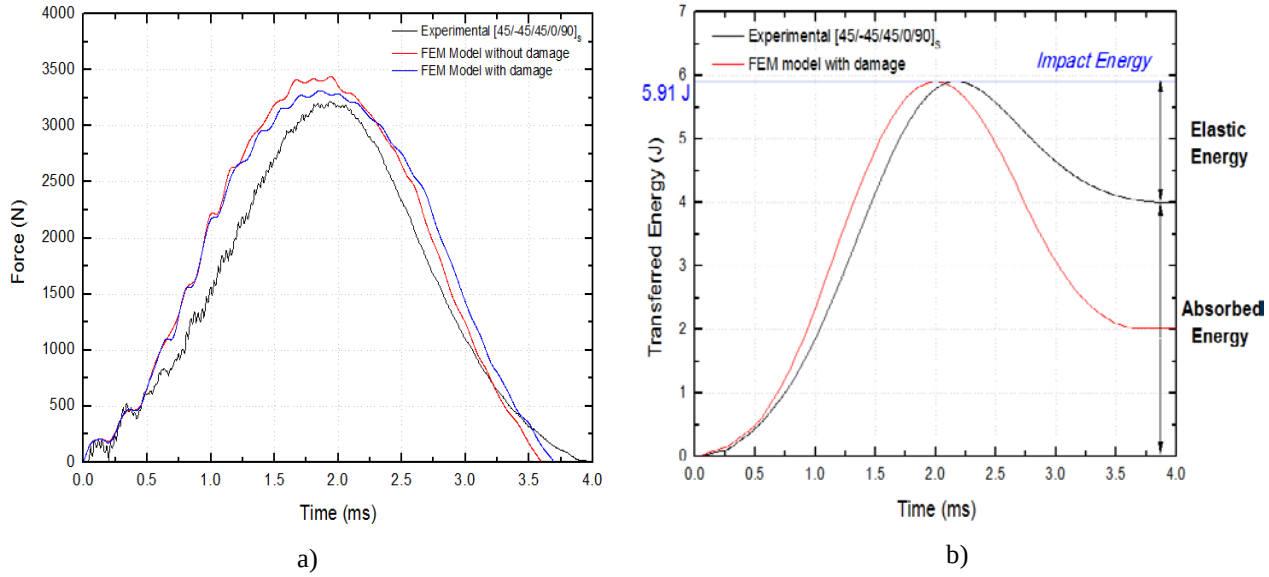

a) b)

Figure 3- Comparison between experimental and numerical results for the $[+45^o/-45^o/+45^o/0^o/90^o]_S$ laminate under 5.91 J. a) Force x time b) Energy transferred vs. time

In other hand, from Figure 4-a), it is observed qualitatively, that the damage variable d_2 was activated until the 6th layer, which is oriented at 90º, while d_6 showed a discontinuity in the 7th layer, but it is verified in 8th, 9th and 10th layers. The damage evolution along the laminate thickness close to the impact point is represented by the Figure 4-b). At the final of 5.91 J impact event, the damage caused in the matrix due to shear stress in 2nd and 4th layers was complete, i.e. d_6=1. For the 8th, 9th and 10th layers, the damage is caused by shear stress, and the parameter d_6 is respectively equal to 0.0001, 0.08 and 0.18. However, the parameter d_2 associated to tensile transversal stress on matrix reaches the maximum in first three layers. It is verified that there is no damage in matrix caused by tensile transversal stress from 7th until 10th layers, once the parameter d_2 is equal "0"for those layers.

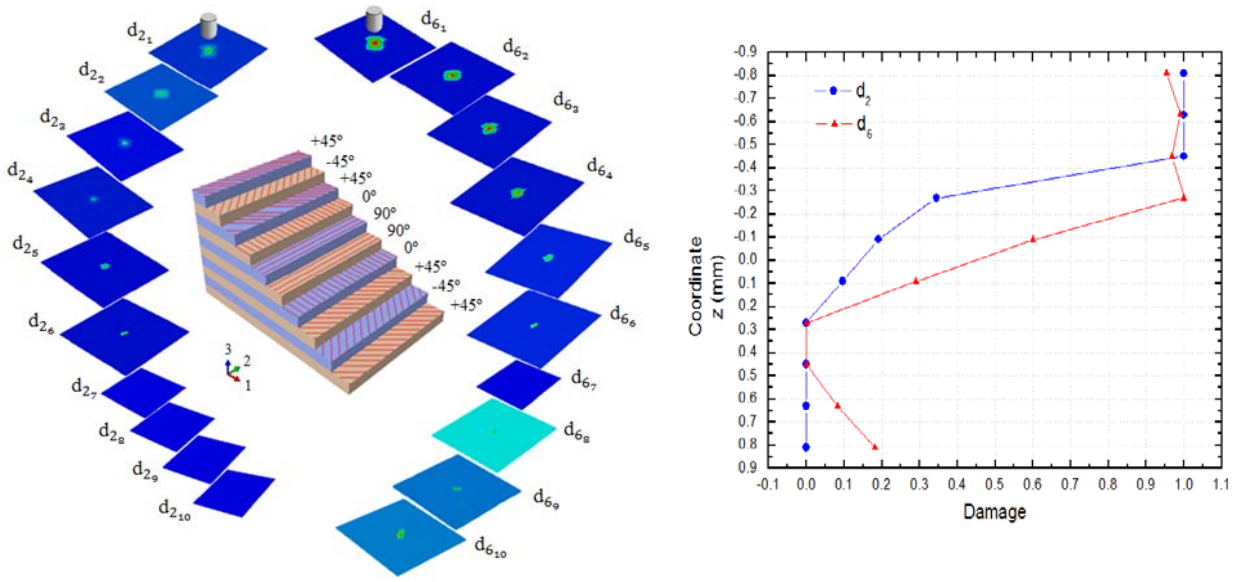

Figure 4- Qualitative and quantitative analysis for the laminate $[+45^o/-45^o/+45^o/0^o/90^o]_S$ at the final of impact event. a) Damage variables d_2 and d_6 for the layers of laminate b) Damage evolution along the laminate thickness

Figure 5-a) shows the force vs. time curve for the laminate $[0^o/90^o/0^o/90^o/0^o]_S$ under 5.91 J of impact energy. In the experimental results, a high frequency oscillation region between 0.0 ms and 1.2 ms can be observed. In this laminate, the main failure mechanisms are matrix rupture and delamination, which reduce the global structural stiffness, as well. FE analysis using the proposed damage model was able to simulate the impact high frequency oscillations from 0.0 ms until 0.25 ms and between 0.75 ms and 1.25 ms. On the other hand, the FE analysis using only the elastic model was able to simulate the oscillations beginning from 0.0 ms until 0.25 ms and the maximum force equal to 3072.81N. However, it is observed that the maximum force simulated by using the damage model was equal to 2847.63 N, which was lower than the force predicted by elastic model. Moreover, in the Figure 5-a), it is observed that after 2.0 ms, FE analysis with damage model (blue curve) diverges of the experimental curve, while FE analysis with elastic model (red curve) approaches to the experimental result (black curve). This was expected due to the absence of a delamination model to simulate the separation between 0º and 90º layers. From Figure 5-b), FE analyses with damage model predicted about 50% of the absorbed energy by the cross ply laminate sample, i.e. about 1.98 J. Thus, the absorbed energy predicted by FE analysis was totally related to the matrix damage mechanism. This can be verified in the Figure 6-a) monitoring the damage parameters d_2 and d_6. The damage variable d_2 was activated from the 1st layer until the 5th layer, while for the damage variable d_6, the damage is verified not only from the 1st layer until the 5th layer, but also in 8th, 9th and 10th layers. By the Figure 6-b), it is shown the damage evolution along the laminate thickness close to the impact point. The damage caused by the shear stresses in the matrix was relevant as confirmed by the damage parameter d_6, which was close to "1" in the first three layers. Moreover, it was verified the damage caused by transversal tensile stresses in the matrix reached the maximum value ("1") only in the 1st layer. It is observed that from the 6th layer, there was not damage caused by transversal tensile stress in the matrix, only damage caused by shear stress. And, the values of d_6 are 0.1, 0.15 and 0.2 for the 8th, 9th and 10th layers, respectively.

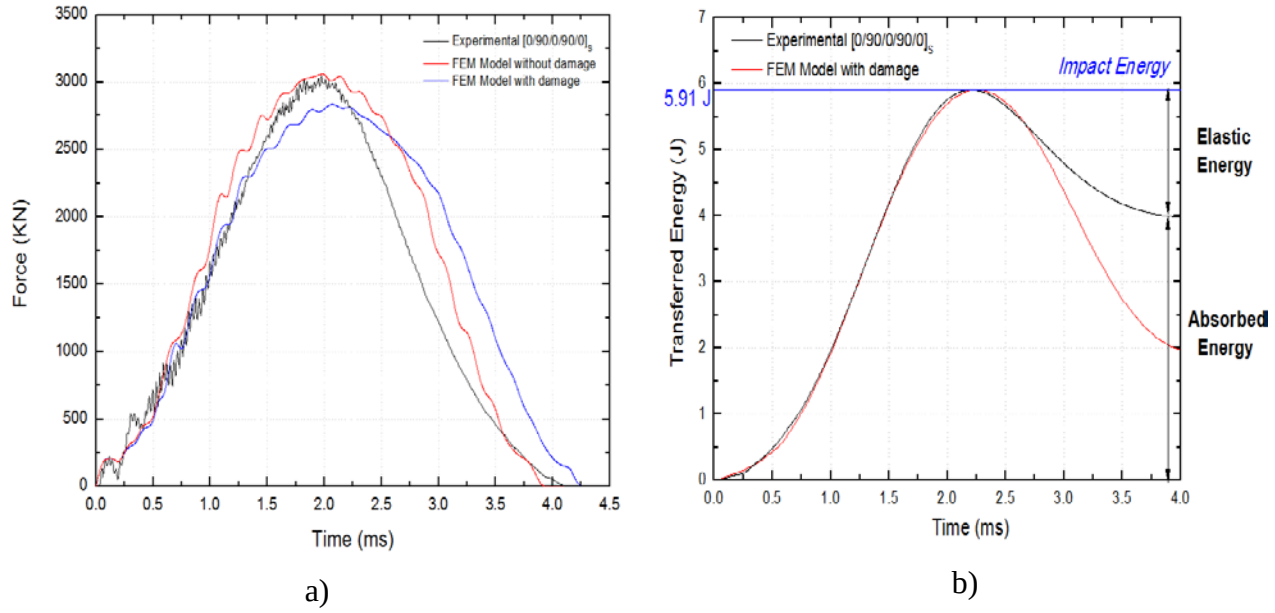

Figure 5- Comparison between experimental and numerical results for the $[0^o/90^o/0^o/90^o/0^o]_S$ laminate. a) Force x time b) Energy transferred vs. time

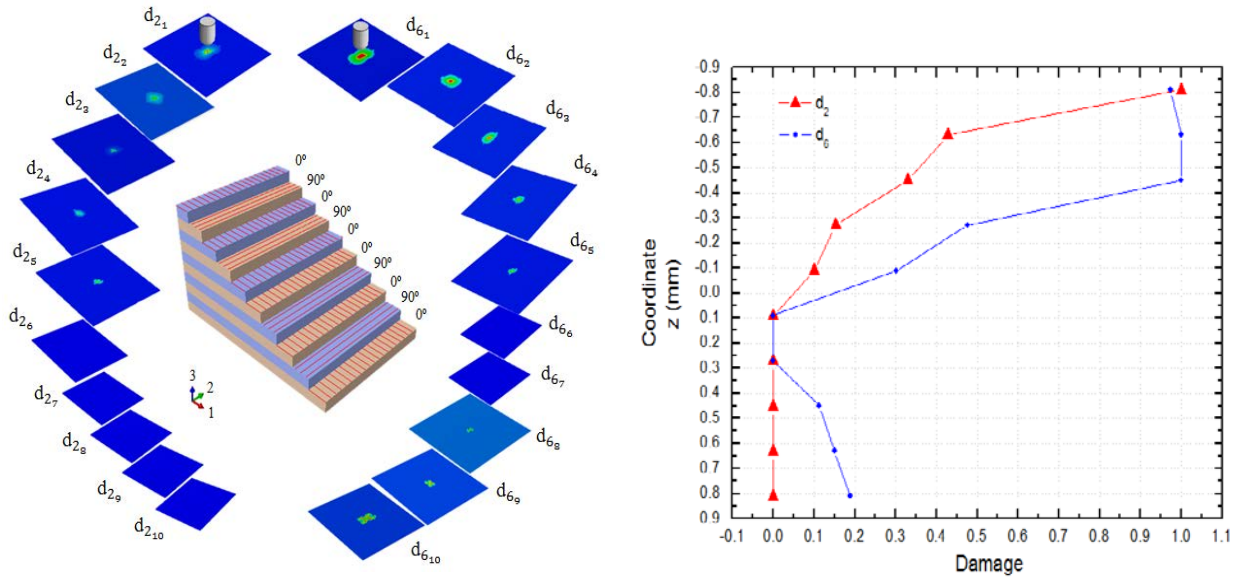

Figure 6- Qualitative and quantitative analysis of laminate $[0^o/90^o/0^o/90^o/0^o]_S$ at the final of impact event. a) Damage variables d_2 and d_6 for the layers of laminate b) Damage evolution along the laminate thickness

5 CONCLUSIONS

A new damage model was applied for simulating impact problems on composite structures. This damage model was implemented as an explicit subroutine (VUMAT) and linked to software ABAQUS™. Thus, based on the implemented damage model, intra-ply failure mechanisms in carbon-epoxy plates were investigated considering low velocity impact load for two different laminate configurations. Due to the proposed formulation, including damage evolution laws, as well as the strategy for implementation, the FE analyses were performed with a reasonable computational cost and no convergence problems occurred during simulations. Moreover,

acceptable results for Force vs. time are showed in the simulation, although delamination phenomenon was not considered in the analyses. The simulation of delamination process requires a much more complicated and complex model, generating numerical issues such as high computational cost and convergence problems.

Therefore, the present computational analyses can provide an alternative way in order to obtain good predictions of Force vs. time graphics with low computational cost, which can help conceptual and preliminary design of composite structures under impact loadings.

Acknowledgements

The authors acknowledge the financial support of the Coordination for the Improvement of the Higher Level Personnel (CAPES/PROEX) and National Council for Scientific and Technological Development (CNPq process numbers: 401170/2014-4 and 310094/2015-1). Volnei Tita acknowledges the financial support of Air Force Office of Scientific Research – AFOSR (Grant FA9550-16-1-0222).

REFERENCES

[1] Zhou, W. X.; Gao, X., Damage and failure of a laminated carbon fiber reinforced composite under low velocity impact, Journal of Aerospace Engineering 27: 308-317, 2012.

[2] Abrate, S. Modeling of impacts on composite structures, Composite Structures 51: 129-138. 2001.

[3] Maio, L., Monaco, E., Ricci, F., Lecce. L., Simulation of low velocity impact on composite laminates with progressive failure analysis, Composite Structures 103: 75-85, 2013.

[4] Zhang, Yan; Zhu, Ping; Lai, Xinmin. Finite element analysis of low-velocity impact damage in composite laminated plates, Materials & Design. 27, 513–519, 2006.

[5] Camanho PP, Miamí P, Dávila CG. Prediction of size effects in notched laminates using continuum damage mechanics. Compos Sci Technol; 67 (13):2715–27, 2007.

[6] Shi, Y., Swait, T., Soutis, C., Modelling damage evolution in composite laminates subjected to low velocity impact, Composite Structures 94:2902-2913, 2012.

[7] Kim, E., Rim, M., Lee, I., Hwang, T., Composite damage model based on continuum damage mechanics and low velocity impact analysis of composite plates, Composite Structures 95: 123-124, 2013.

[8] Puck, A.; Schürmann, H., Failure analysis of FRP laminates by means of physically based phenomenological models, Composites Science and Technology 62: 1633-1662, 2002.

[9] Feng, D., Aymerich, F., Finite element modelling of damage induced by low-velocity impact on composite laminates, Composite Structures 108: 161-171, 2014.

[10] Ferreira, G.F.O., Medeiros, R.M., Ogea, J.L., Tita, V. Damage simulation in composite structures considering friction and sliding effect. In Fifth International Symposium on Solid Mechanics - MECSOL2015, Belo Horizonte, Brazil. Proceedings of MECSOL, 2015.

[11] Ribeiro M.L.; Tita V.; Vandepitte D., A new damage model for composite laminates, Composite Structures 94: 635-642, 2012.

[12] Ladevèze, P.; Le Dantec, E., Damage modelling of the elementary ply for laminated composites, Composites Science and Technology 43: 257-267, 1996.

[13] Matzenmiller A, Lubliner J, Taylor RL. A constitutive model for anisotropic damage in fiber-composites. Mech Mater; 20 (2):125–52, 1995.

[14] Tita, V., Carvalho, J., Vandepitte, D., Failure analysis of low velocity impact on thin composite laminates: experimental and numerical approaches, Composite Structures 83: 413-428, 2008.

[15] American Society for Testing and Materials. ASTM D5628-96. Standart test method for impact of flat, rigid plastic specimens by means of falling dart (Tup or falling mass). West Conshoken, 2001.

ARTIFICIAL NEURAL NETWORKS APPLYING TO DETECT DAMAGE IN CARBON FIBER/EPOXY COMPOSITES.

Luísa R. Völtz, Eduardo L. Cardoso and Ricardo De Medeiros.

Department of Mechanical Engineering, Santa Catarina State University, Brazil.

https://doi.org/10.21452/bccm4.2018.16.02

Abstract

Artificial Neural Networks (ANNs) have emerged as one of the most useful tools in Artificial Intelligence (AI), being used in the most applications, such as engineering, economics, and health. Due to their great capacity for learning, adaptation, and generalization, ANNs can handle linear and nonlinear models that other methods are not capable to solve. Composite materials are increasingly used in critical and demanding applications, mainly due to its high specific strength and stiffness. However, the challenging of the current Structural Health Monitoring (SHM) methodologies includes identification, detection, and quantification of the damage and, also the prediction of the residual resistance/life of the structure. Therefore, this work proposes a methodology based on ANNs to detect damage in composite structures. Initially, the vibration-based method was applied using Frequency Response Functions (FRFs) along with Principal Component Analysis (PCA). This tool seeks to reduce the dimensionality of the original data while maintaining its characteristics. Next, a multi-layer neural network was developed for detecting damage in composite plates made of Carbon Fiber Reinforced Polymer (CFRP). Finally, it is discussed the potentialities and limitations of the methodology for use in damage detection systems.

Key-words: Artificial Neural Networks (ANNs), composite materials, damage detection, Principal Component Analysis (PCA).

1. INTRODUCTION

Composite material, which combines high performance with low weight, are constantly used in many applications, such as the automotive, sporting and aerospace industries, replacing conventional materials due to their excellent mechanical properties, such as high stiffness and corrosion resistance. The advantages of composite materials are many, including fatigue strength and good design practices [1]. However, they have disadvantages due to their micromechanical interactions and their particular failure modes, such as matrix cracking, fiber rupture, interfacial debonding and delamination [2]. Therefore, as any structure, the monitoring of material condition must be performed to ensure its integrity. Many techniques of damage detection use structure vibration responses, including FRFs, natural frequencies and vibration modes [3]. The main idea

behind damage detection techniques based on dynamic changes is the fact that these variables are all functions of mass, stiffness, and damping and therefore it is reasonable to assume that the existence of damages leads to change of such properties [4]. On the other hand, ANN is a processor made up of processing units that has the natural tendency to store knowledge acquired from its environment through a learning process and makes it available when required for use [5]. After the learning process, the network is then able to generalize the acquired knowledge, making it possible to estimate solutions that were unknown [6]. Brito et al. [7] used ANN to predict the dynamic-mechanical behavior of epoxy resin with carbon fiber composites. The input parameters for the ANN were fiber orientation and response time measured by vibration tests and the output represented the amplitude. Al-Assaf and Kadi [8] predict the fatigue life of glass fiber epoxy composites with a range of fiber orientation using ANN and the network was able to give accurate results when comparing with experimental data.

Although many studies have been carried out using neural networks in damage detection, fatigue studies or prediction of mechanical behavior, few studies are related to composite materials [8]. Therefore, this work aims to present a methodology, based on the use of neural networks and dynamic characteristics of the structure, to be sought for the damage detection in composite plates made of epoxy resin reinforced by carbon fiber.

2. MATERIALS AND METHODS

Sixteen composite plates produced from carbon fibers with epoxy resin through the filament winding process were studied. The carbon fiber composites were divided into two groups: eight plates with twelve layers and stacking orientation $[0/15/-15/0/15/-15]_S$ and eight plates with eight layers and stacking orientation $[0]_8$. The average thickness for the first group was 3.39 mm (standard deviation = 0.07) and for the second 2.23 mm (standard deviation = 0.02). The experimental procedure was carried out by Medeiros [9] and is shown in Fig 1.

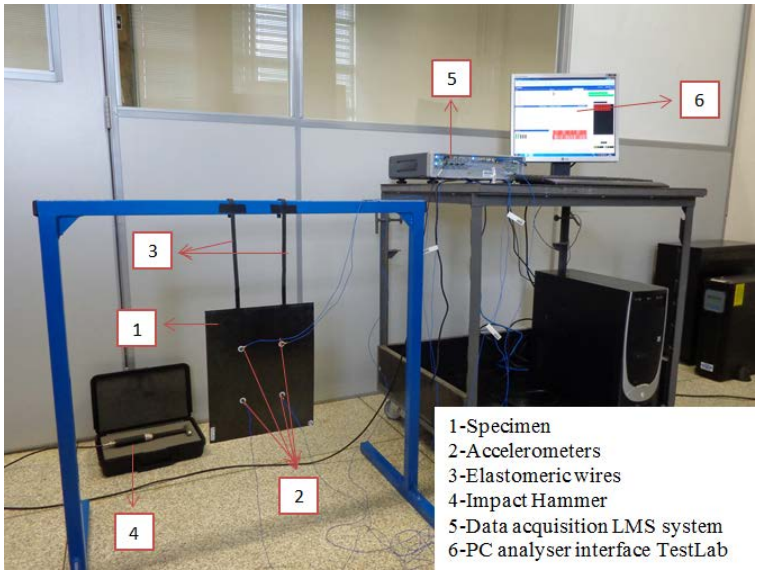

Figure 1: Experimental procedure [9].

Initially, the dynamic response of each healthy laminated plate was obtained by using accelerometers in free-free boundary conditions. The impulse input by impact hammer was applied on a fixed point on the back side of the plate. In the vibration tests, the analyzed frequency range was 0-1024 Hz, in a total of 2048 spectral points. Each FRF was obtained through an average of five samples, aiming to reduce the effects of variation [9].

The second stage consists of the damage test phase. For the $[0]_8$ orientation group, five plates were damaged by impact loading, one was damaged by drilling a center hole and other two kept undamaged. For the $[0/15/-15/0/15/-15]_S$ plates, four were damaged by impact loading, two by delamination and other two kept undamaged. The damaged plates were analyzed again through the use of vibration methods monitored by accelerometers. In total 56 FRFs for $[0]_8$ orientation plates were obtained, 32 FRFs for healthy cases and 24 FRFs for damaged cases. For $[0/15/-15/0/15/-15]_S$ plates, a total of 48 FRFs was obtained, 24 for undamaged cases and 24 for damaged cases.

Recently, methods involving ANNs have been considered state-of-the-art to predict a behavior of a system. The intention is to establish a multidimensional and non-linear correlation between the input data and the corresponding output neuron. Each neuron, in each layer, interconnects through synaptic weights, and thus the information crosses from one layer to another until the exit of the network [7]. In this way, a forward neural network was developed to classify patterns of vibration responses of intact and damaged composite plates. Due to a large number of inputs associated with each FRF and the consequently large number of connections required to form a suitable ANN topology, it was studied a methodology to reduce the dimension of the experimental data, called PCA. It is a statistical technique that uses an orthogonal projection, transforming a set of correlated variables into a set of uncorrelated variables, called principal components (PCs). The aim of the PCA is a dimensional reduction and elimination of the noise present in the original data [4].

The ANN was implemented in Julia language [10] using steepest descent with backtracking line search algorithm and automatic differentiation to evaluate the gradients. A moment term was used to accelerate the gradient descent in direction of the error function [5]. For each stack orientation, a new ANN was created to achieve the best result according to each case. After using the PCA, the data were split into three data sets: training, validation, and testing. The training set was used as input into the neural network, and an error calculation was performed by using feedforward propagation and square-root or cross-entropy functions. The validation set was then used to monitor the behavior of the network simultaneously with the training set during the learning phase, to monitor the best values of the hyperparameters and topology. After the learning phase, the network was then tested using the last set of data, that it wasn't used during training.

The confusion matrix is a very useful technique for evaluating the errors distributed across the classes. Tab. 1 shows an example of the confusion matrix. TP means true positive that is the samples of the damaged class were correctly classified as damaged. FP means false positive, is the number of samples not belonging to damaged class but misclassified into damaged class. FN, false negative, is the number of samples of damaged class misclassified as an undamaged class. TN, true negative, is the number of samples of undamaged class that were classified correctly. The accuracy can be calculated as the trace of the matrix divided by the total number of the samples [11]. Recall (R), or sensitivity, is the proportion of positive cases that were correctly identified, defined as

$$R = TP/(TP + FN). \quad (1)$$

Precision (P) is the proportion of the predicted positive cases that were correct, defined as

$$P = TP/(TP + FP). \quad (2)$$

Table 7: Confusion Matrix.

		Actual class	
		Yes	**No**
Predict class	**Yes**	TP	FP
	No	FN	TN

3. RESULTS AND DISCUSSION

Each stacking orientation group was studied separately, due to the large differences in dynamic behavior among them.

3.1 Composite plates with stacking orientation [0/15/-15/0/15/-15]s

Figure 2 shows the experimental real, imaginary and magnitude graphs for one plate with stacking orientation [0/15/-15/0/15/-15]s, considering undamaged and damaged cases. It is possible to observe that the differences between undamaged and damaged are very subtle. In addition, comparing the damage and undamaged FRFs, the differences in amplitude are more perceptible in both the imaginary part and magnitude.

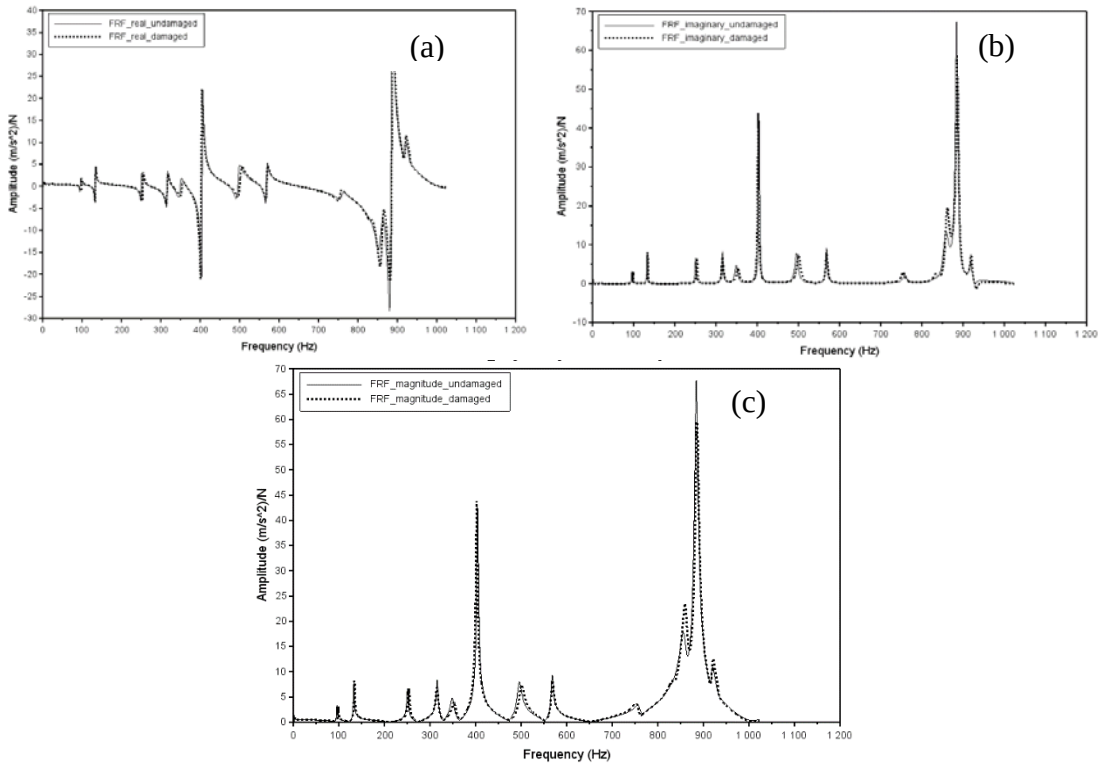

Figure 2: (a) real part, (b) imaginary part and (c) magnitude FRFs.

The data dimensionality was reduced using the PCA, and for the first 30 PCs, the total variance was 98.85%, using only real values of the FRFs. The data were split into 62% for the training set, 21% for the validation set and 17% for the testing set. The resulting 30 variables were introduced

as input in the ANN. Different topologies and values of parameters were taken. The best topology was 30 inputs, 20 neurons in the first hidden layer, 10 neurons in the second hidden layer and 1 output (0 for healthy and 1 for damaged conditions). The moment term used was 0.1. The learning rate was kept fixed with 0.1. The logistic function as activation function was applied. The cross-entropy cost function was used and in 400 iterations the network reached 100% of accuracy in the training set, 80% in the validation set and 87.7% in the testing set. Table 2 shows the confusion matrix for the testing set with 87.5% of accuracy, 100% for precision and 75% for recall.

Table 2: Confusion matrix for [0/15/-15/0/15/-15]s testing set, considering the real part.

		Actual Class		
		Damaged	**Undamaged**	*TOTAL*
Predict Class	**Damaged**	TP=3	FP=0	*3*
	Undamaged	FN=1	TN=4	*5*
	TOTAL	*4*	*4*	***8***

After performing the first analysis, it was observed that the influence of the imaginary part in the $[0/15/-15/0/15/-15]_s$ stacking sequence could be important. A new simulation using magnitude values of FRFs was then studied. After pre-processing using PCA, new 20 PCs was calculated with 98.10% of the total variance. The resulting 20 variables were introduced as input in the new ANN. After some simulations, the best result was found. The topology was 20 inputs, 12 neurons in the hidden layer and 1 output. The value of 0.7 for the moment term was used and backtracking line search. The logistic function and the L_2 cost function were applied. After 150 iterations the network reached 100% of accuracy in the training set, 90% in the validation set and 100% in the testing set, showing good generalization. The best ANN results were obtained by using only magnitude values. Figure 3 shows the ANN errors and accuracy curves during the training and the validation phases. The continuum lines are error curves, and the dot lines are the accuracy curves for [20/12/1] topology, the final error for the training phase was 0.0009.

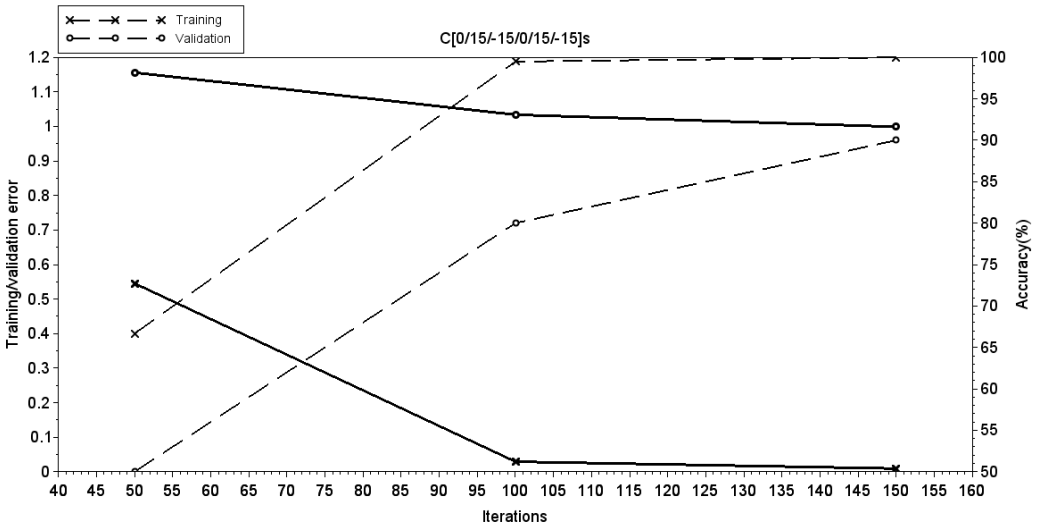

Figure 3: ANN Error and Accuracy for $[0/15/-15/0/15/-15]_s$ plates.

3.2 Composite plates with orientation $[0]_8$

Figure 4 shows the experimental real, imaginary and magnitude graphs for one plate with stacking orientation of $[0]_8$, considering undamaged and damaged cases. The differences between

undamaged and damaged are very clear, with changes in the natural frequencies, amplitude, and phases, especially on imaginary part.

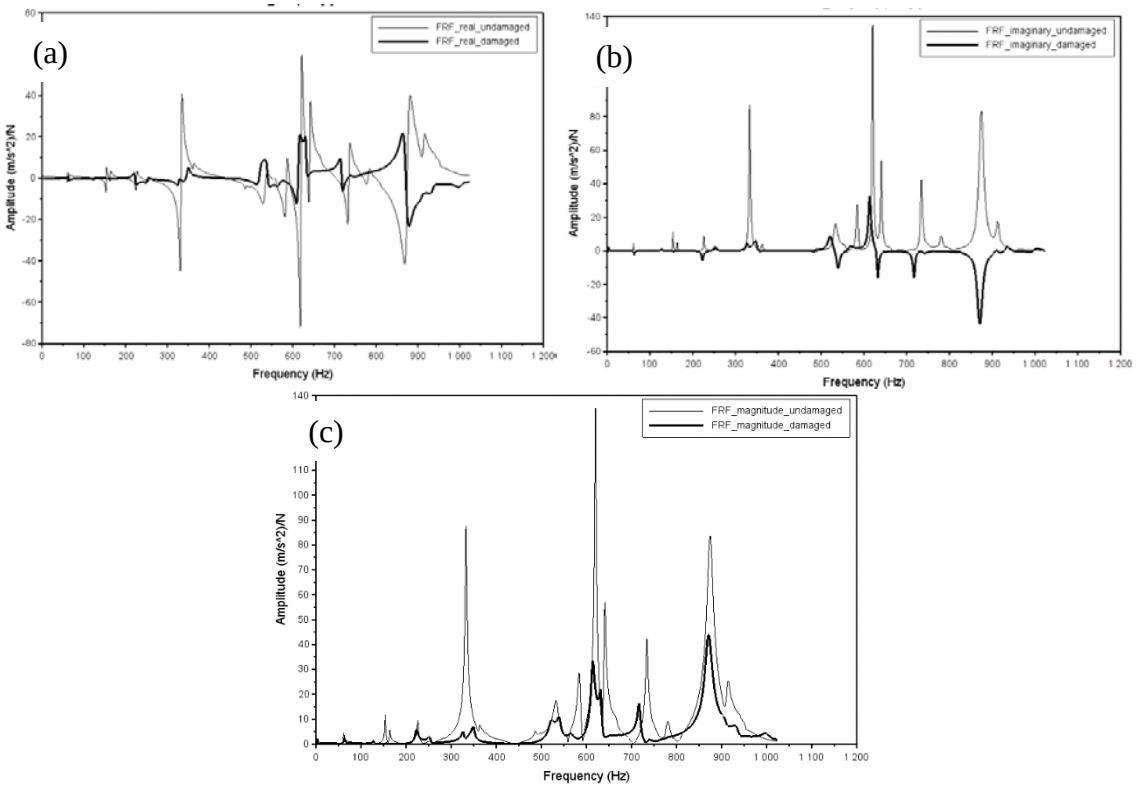

Figure 4: (a) real part, (b) imaginary part and (c) magnitude FRFs.

After dimension reduction, the first 20 PCs were evaluated with 98.55% of total variance using only real values of the FRFs. The data were split into 61% for the training set, 21% for the validation set and 18% for the testing set. The resulting 20 variables were introduced as input and different topologies, and values of parameters were considered until reaching the best solution. The best topology was 20 inputs, 6 neurons in the hidden layer and 1 output (0 for healthy and 1 for damaged conditions). The moment term used was 0.7 and the backtracking line search. Logistic and L_2 cost functions were applied, and in just 150 iterations the network reached 100% of accuracy in training, validation and testing sets.

To evaluate the influence of the imaginary part in the 0° orientation the same procedure was done. The magnitude values were calculated and passed through PCA, and the first 20 PCs were taken with 99.19% of total variance. The best result was achieved with 20 inputs, 9 neurons in the first hidden layer, 2 neurons in the second hidden layer and 1 output. The moment term was 0.7, backtracking line search, and the logistics and the L_2 cost functions were used. After 300 iterations the network reached 100% of accuracy in the training set, 83.3% in the validation set and 90% in the testing set. Table 3 shows the confusion matrix for the testing set, with 90% for accuracy, 66.7% for recall and 100% for precision.

After comparing the results using real and magnitude values, the best ANN result was obtained by using only real part of the FRF for stacking orientation $[0]_8$. Figure 5 shows the curves between errors and accuracy during the training and the validation phases. The continuum lines are error curves, and the dot lines are the efficiency curves for [20/6/1] topology. The final error for training was 0.009 and 100% of accuracy for both sets.

Table 3: Confusion matrix for $[0]_8$ testing set, considering magnitudes values.

		Actual Class		
		Damaged	**Undamaged**	*TOTAL*
Predict Class	**Damaged**	TP=2	FP=0	*2*
	Undamaged	FN=1	TN=7	*8*
	TOTAL	*3*	*7*	***10***

Finally, as observed, all the ANNs showed good learning and generalization. The best result for each orientation agreed to what was observed in the originals FRFs. Large differences can be observed in real, imaginary and magnitude values for $[0]_8$ stacking orientation. During ANN simulations it was verified that when using only real values as input the behavior of the network was better than when using magnitude values. It was probably due to the fact that in the real part of the FRF there are inversions of the phases in almost all the modes between intact and damaged plates. This situation was hidden when working with magnitude values, as seen in Fig. 4(c). The inversion of the phase, differentiating the intact from the damaged ones, can contribute to feature extraction during the learning and then to the classification performed by the network. The network accuracy using real values was 100%, for all the three sets, and for testing set the ANN precision and recall were 100% either. It means that ANN can correctly classify all the classes studied.

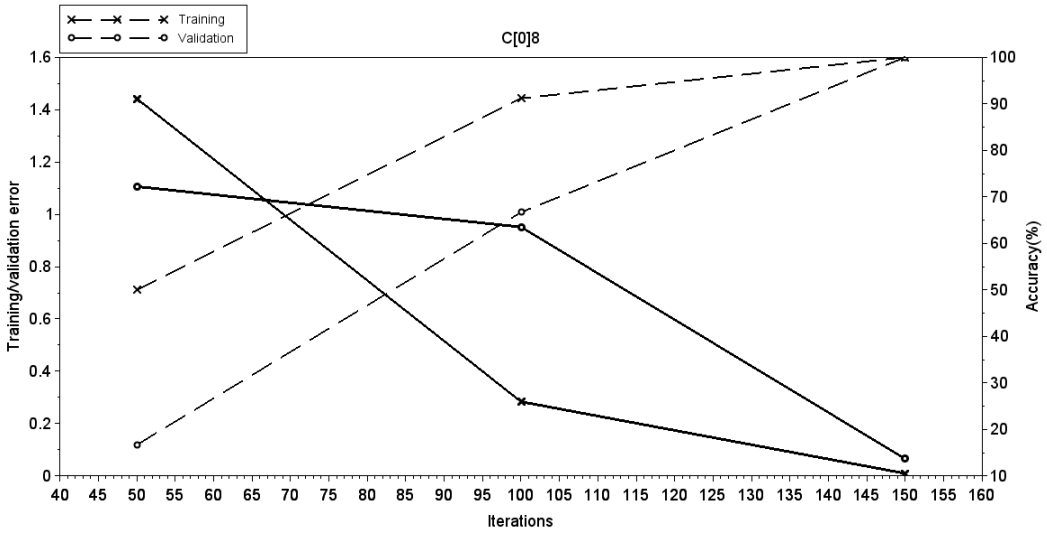

Figure 5: ANN Error and Accuracy for $[0]_8$ plates.

For $[0/15/-15/0/15/-15]_S$ laminates the best result was obtained when the magnitude values were used. This is probably due to the fact that values in magnitude carry more information about each integrity condition. As the FRFs are similar, the features acquired only by the real part created a more complex decision boundary between healthy and unhealthy cases. Adding the features acquired by the imaginary part, the curves changed differentiating the dynamic behavior between them. Due to this feature addition, the network began to rank better and evaluate the presence or not of the damage and thus make its decision correctly. The network accuracy was 100% for the training, 90% for the validation set and 100% for the testing set, showing very good precision (100%), which means the network didn't classify any samples that shouldn't be classified.

4. CONCLUSIONS

In this work, ANNs combined with vibration-methods and PCA were used to detect damages in epoxy/carbon reinforced composites. Several architectures and hyperparameters values were evaluated to find the best solution to classify each integrity class. A confusion matrix was used to evaluate the accuracy, recall, and precision of the ANN and its effectiveness for pattern recognition. The best result showed that for real values of the FRF the ANN performed better with $[0]_8$ orientation, with 100% of accuracy in the training, the validation, and the testing sets. Opposite, laminates plates with orientation $[0/15/-15/0/15/-15]_S$ the ANN generalized better when using magnitude values of the FRFs, with an accuracy of 100% for the training and the testing sets, showing good generalization and 90% for the validation set. Therefore, this methodology can help in the development of SHM systems and, consequently, in the damage detection.

ACKNOWLEDGMENTS

The authors acknowledge the financial support of the State Research Founding Agency (FAPESC process number: 2017TR1747 and 2017TR784). As well as, Sao Paulo State Research Foundation (FAPESP process number: 2012/01047-8 and 2015/15221-8), Coordination for the Improvement of the Higher Level Personnel (CAPES process number: 011214/2013-09), National Council for Scientific and Technological Development (CNPq process number: 401170/2014-4 and 310094/2015-1). The authors also would like to thank Navy Technological Centre (CTM – Brazil) for manufacturing specimens.

REFERENCES

[1] Campbell, F.C. 'Structural composite materials'. ASM International. (Ohio, EUA, 2010).

[2] Montalvão, D., Maia, N.M.M. and Ribeiro, A.M.R. 'A review on vibration-based structural health monitoring with special emphasis on composite materials'. *Shock and Vibration Digest*, **38** (4) (2006) 295 - 324.

[3] Bandara, R.P., Chan, T.HT. and Thambiratnam, D. P. 'Structural damage detection method using frequency response functions'. *Structural Health Monitoring*. **13** (4) (2014). 418 - 429

[4] Li, J., Dackermann, U., Xu, Y.L. and Samali, B. 'Damage identification in civil engineering structures utilizing PCA-compressed residual frequency response functions and neural networks ensembles'. *Structural Control Health Monitoring*. **18** (2011) 207-226.

[5] Haykin, S. 'Neural networks: a comprehensive foundation'. Translate by Paulo Engel. 2nd Edn. (Bookman, Porto Alegre, 2001).

[6] Silva, I.N, Spatti, D.H. and Flauzino, R. 'Artificial neural networks'. 2nd Edn. (Artliber, São Paulo, 2016).

[7] Brito, Jr et al. 'Redes Neurais Artificiais aplicadas para a predição do comportamento dinâmico-mecanico de compositos de matriz epóxi reforçados com fibras de carbono'. *Revista Matéria* **12** (1) (2007) 346-357.

[8] Al-Assaf, Y. and Kadi, El. 'Fatigue life prediction of unidirectional glass fiber/epoxy composite laminae using neural networks'. *Composite Structures* **53** (2001) 65-71.

[9] Medeiros, R. 'Development of a criterion for predicting residual strength of composite structures damaged by impact loading'. São Carlos University (2016).

[10] Bezanson, J., Edelman, A., Karpinski, S. and Shah, V.B. 'Julia: A fresh approach to numerical computing'. *CoRR*, abs/1411.1607 (2014). Disponível em: <http://arxiv.org/abs/1411.1607>. Acess: march 15th, 2018.

[11] Kuncheva, L. 'Combining Pattern Classifiers: Methods and Algorithms'. (John Wiley & Sons, New Jersey, 2004).

DIFFERENT METHODS OF THREE-POINT BENDING ANALYSIS OF POLYMER EPOXY REINFORCED WITH FIBERGLASS LAMINATED FACES.

João Pedro Monteiro Cheloni (1), Marcio Eduardo Silveira (1), Leandro Jose da Silva (2)

(1) Applied Numerical Simulation Laboratory, Federal University of São João Del Rei-UFSJ, Mechanical Engineering Department, São João Del Rei, MG, Brazil

(2) Center of Technological Innovation in Composite Materials, Federal University of São João Del Rei-UFSJ, Mechanical Engineering Department, São João Del Rei, MG, Brazil

https://doi.org/10.21452/bccm4.2018.16.03

Abstract

The purpose of this paper is the study of mechanical behavior in three-point bending of polymer epoxy using different amount of glass fibers laminated faces as reinforcement. Therefore, it was used experimental method, numerical simulation using linear and non-linear method and analytical method of composite beams analysing force, displacement and normal stress. The specimens were prepared using hand lay-up process and vacuum bag compaction. It was realized tensile and flexural tests in the specimens obtaining mechanical properties used in numerical simulation and analytical method. The numerical simulation was performed using linear and non-linear method with 3D solid elements. The materials were considered isotropic. The results showed similar values between methods with emphasis for the non-linear simulation that most approached the experimental results.

1. INTRODUCTION

Composite materials comprise from polymers reinforced with fibers, structural concretes, others that use ceramic and metal materials [1,2]. The polymer composites may exhibit excellent properties due to use great possibility of fibers combinations and orientations, forming optimized and specific structures for different types of loading [3]. The basic characteristic of a composite is to combine at macroscopic level, at least two distinct phases called matrix and reinforcement [4].

The use of glass fibers as reinforcements in laminated composites provide advantages like great cost/benefit ratio between the reinforcements offered for manufacturing polymer composites. Commonly glass fibers are used in applications that require some increase in strength because its properties as high weight-strength ratio, high tensile strength and low cost. However, there are

some limitation in this material for example, short fatigue life and temperature sensitivity, mainly comparing with carbon fibers [5,6]

Nowadays, fiberglass laminates are being used at the top and bottom (as faces) of some types of materials, as well as in sandwich structures, to improve resistance under flexural loads [7-9]. There are some methods for bending analysis of composite materials that help understand the behavior and identify values of the stresses which the material is subjected. One of the most commonly used methods is numerical simulation by finite elements [10,11].

In this paper, it is shown the three-point static bending behavior of epoxy resin reinforced with different amount of glass fibers laminated using four different methods, experimental procedure, linear and non-linear numerical simulation and analytical method of composite beams. The loads, displacement and stress were obtained by methods and a comparison was made among them.

2. MATERIALS AND METHODS

To accomplish the study, three different materials with the same thickness were analysed. It was performed specimens of polymer epoxy, specimens of polymer epoxy reinforced with 3 layers of fibers glass laminated at the top and bottom (PE3L) and specimens of polymer epoxy reinforced with 5 layers of fibers glass laminated at the top and bottom (PE5L). The conception of materials used is shown in Figure 1.

The polymer epoxy used in this paper was Renlan M with hardener HY 951 provided by Huntsman-Brazil. The material used as reinforcement was plain weave glass fibers cloth (200 g/m^2) supplied by Owens Corning-Brazil.

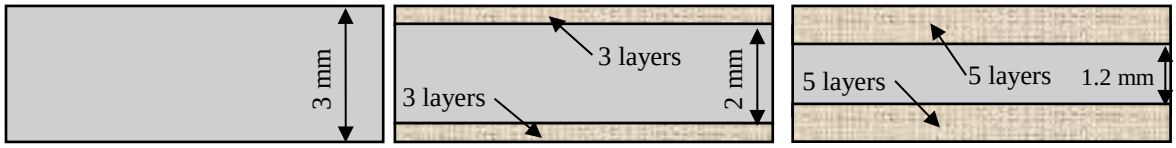

Figure 1: Sample illustration: (a) polymer epoxy, (b) PE3L and (c) PE5L

2.1 Manufacturing of specimens

Firstly, both laminates used as reinforcement of polymer epoxy were performed, one of them using three layers and the other using five layers. These laminated were created by manual lamination manufacturing (hand lay-up) which the epoxy resin mixed with hardener (10:1 ratio), was homogeneous spread over each layer obtaining volumetric fraction 40% fibers. Soon after, the vacuum bag lamination process was performed, to provide better resin compaction and distribution. The cure process occurred at room temperature, 25°C. After seven days curing, a part of the laminate was separated to obtain at least five specimens for mechanical tests and the other part to use as face reinforcement of polymer epoxy. Using specific molds for each material to obtain the same total thickness, the specimens of polymer epoxy with and without glass fibers laminated faces were formed.

2.2 Tensile and Flexural tests

The uniaxial tensile tests were performed in each material individually using Universal Mechanical Test Machine SHIMADZU AG-X Plus. It was created, five specimens of glass fibers laminated according to ASTM D3039[23] Standard [12]. It was used cross-head speed 2 $mm.min^{-1}$ with room temperature 25ºC. It was created five specimens of polymer epoxy were analyzed according to ASTM D638[24] Standard [13]. The three-point bending test was performed according BS EN 2562[25] Standard [14] for polymer epoxy with and without glass fibers laminates faces. It was used the Universal Mechanical Test Machine SHIMADZU AG-X Plus at cross-head speed 2 $mm.min^{-1}$. Five specimens for each material were analyzed with dimensions: 100 mm length, 10 mm width and 3 mm total thickness.

2.3 Numerical Simulation

Finite Elements Model was used to analyse the behavior of three types of specimens in this paper during bending tests. It was realized two types of simulation, using linear static solution and dynamic non-linear solutions.

The numerical simulations were performed using 3D solid elements. The linear methods were performed for three-point bending with constrain located below the specimen not allowing z axis movement. The simulation was accomplished resorting to the OptStruct Solver and a displacement of 2 mm was applied in the center through rigid elements, used to distribute the load along section. Non-linear simulation methods were carried out using Radioss Solver. It was created contact surface between laminated faces and cylindrical support surface using coefficient of friction 0.3. A displacement of 2 mm was applied in the central support. All rollers (fixed and mobile) were considered rigid (non-deformable).

In all simulations, both cross-ply glass fibers laminated and polymer epoxy were considered isotropic. The Figure 2 shows the discretization of the specimens made by finite elements. The Figure 3(a) shows the linear model with rigid elements used and Figure 3(b) shows the non-linear model with cylindrical support surfaces.

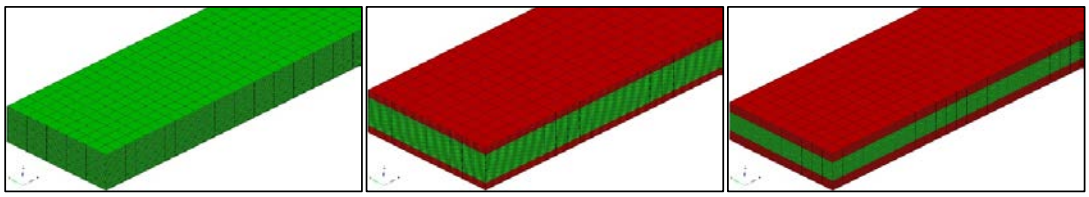

(a) (b) (c)

Figure 2: Discretization by finite elements of (a) polymer epoxy, (b) PE3L and (c) PE5L

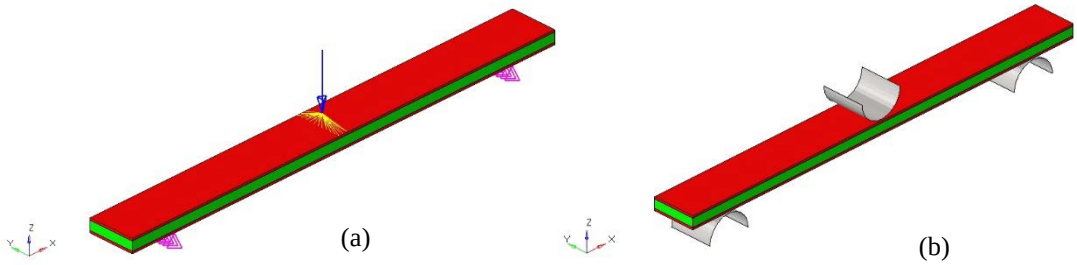

(a) (b)

Figure 3: (a) Rigid elements and constrains used in linear simulation and (b) cylindrical support surface used in non-linear simulation

2.4 Analytical method of composite beams

The analytical method performed in this study were based on the theory of composite beams. Since the polymer epoxy reinforced with laminated glass fibers faces is not homogeneous materials, it is necessary to modify the cross section of the beam into a section made of a single material. Therefore, the flexural stress can be given as:

$$\sigma_f = n\frac{Mc}{I} \qquad \text{with} \qquad n = \frac{E_1}{E_2} \tag{1}$$

where M is the bending moment, c is the perpendicular distance of the neutral axis, I is the transformed moment of inertia, E_1 is the Elasticity Modulus of material 1 and E_2 is the Elasticity Modulus of material 2. During the three-point bending loading the maximum deflection δ can be estimated by:

$$\delta = \frac{FL^3}{48EI} \tag{2}$$

where F is the force and L is the span distance.

3. RESULTS AND DISCUSSION

3.1 Mechanical properties - tensile and flexural tests

The mechanical properties related to tensile tests of polymer epoxy and glass fibers laminated, as well as the mechanical properties related to flexural tests of PE3L and PE5L are shown in Table 1.

Table 1: Mechanical properties of tensile and flexural tests

Materials	Tensile		Flexural	
	Strength[MPa]	Modulus[GPa]	Strength[MPa]	Equivalent Modulus[GPa]
Laminates	329.15 ± 30.07	16.14 ± 2.09	-	-
Epoxy	19.08 ± 2.02	1.60 ± 0.20	18.45 ± 1.55	-
PE3L	-	-	292.76 ± 5.30	12.70 ± 1.10
PE5L	-	-	293.43 ± 5.80	17.14 ± 0.83

The Elasticity Modulus using 5 layers as reinforcement is higher 34,96 % when compared using 3 layers. It can be seen from the flexural strength analyses that equivalent moment of inertia of the polymer epoxy reinforced with 5 layers is largest, but the moment generated by the force during the test is also largest, which makes the maximum flexural strength, equivalent in both materials using the method of composite beams.

Some failure modes were observed in the specimens during the flexural tests. The polymer epoxy without reinforcement, presented a fragile and sudden fracture. However, as shown in the Figure 4 (a) and (b), the polymer epoxy using 3 and 5 layers as reinforcement presented, due to compression on the top face, some broken fibers. Another failure occured was delamination between the faces and polymer epoxy.

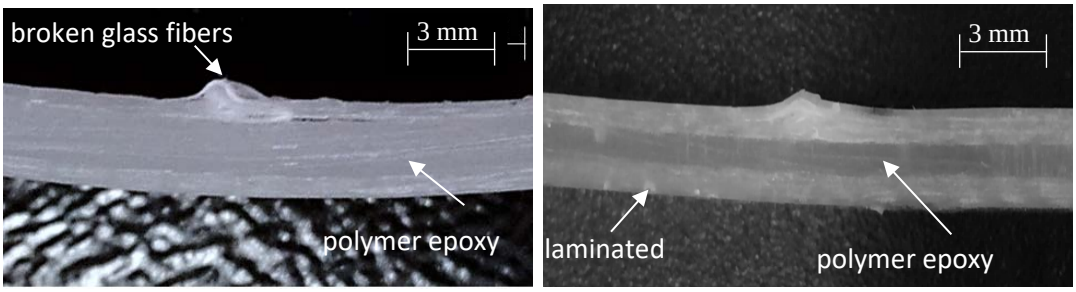

(a) (b)

Figure 4 : Failure modes in the polyer epoxy reinforced with (a) 3 and (b) 5 layers of glass fiber laminated

3.2 Numerical Simulation

The specimens behavior in the linear and non-linear simulation of flexural tests are shown in Figure 5. It is noticed that in the linear simulations the values of the compression stresses were affected by the rigid elements, due to the impossibility of displacements imposed by type of elements.

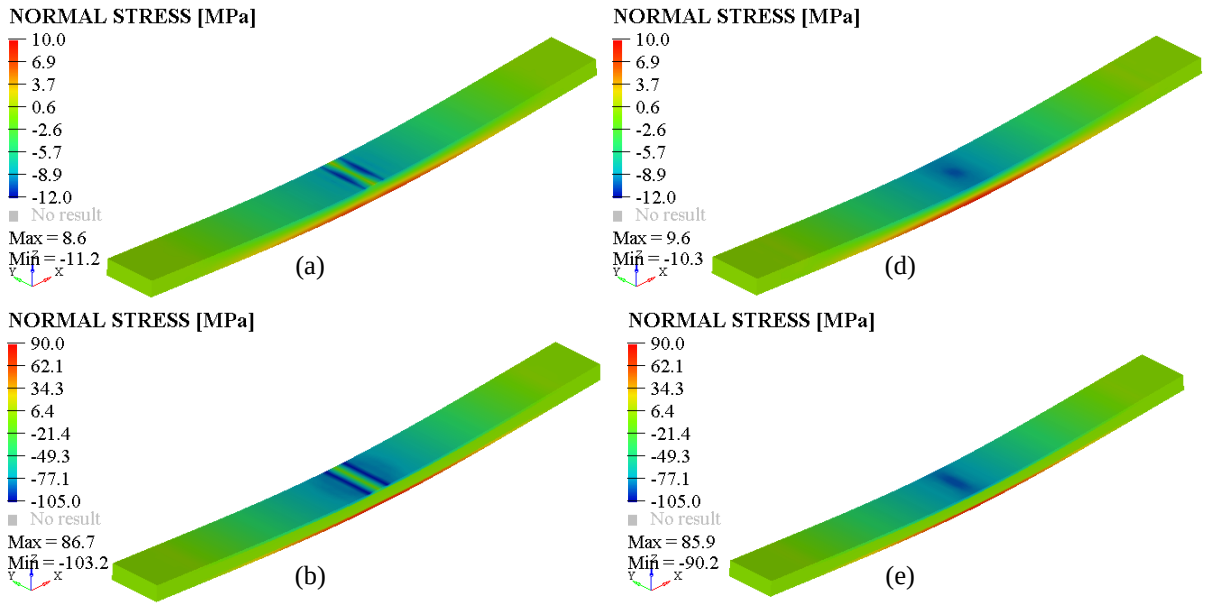

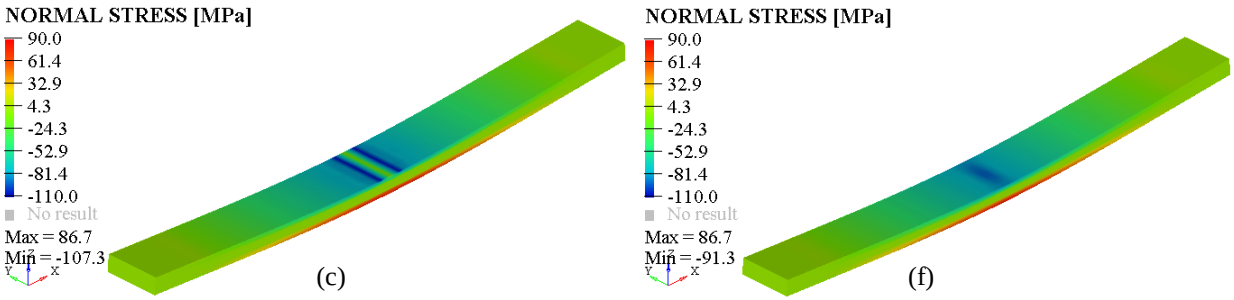

Figure 5: Linear simulation results of (a) polymer epoxy (b) PE3L and (c) PE5L. Non-linear simulation results of (d) polymer epoxy (e) PE3L and (f) PE5L.

The Figure 6 shows load x displacement diagram among non-linear simulation and experimental methods. Through this analysis it can be observed similar values between the methods.

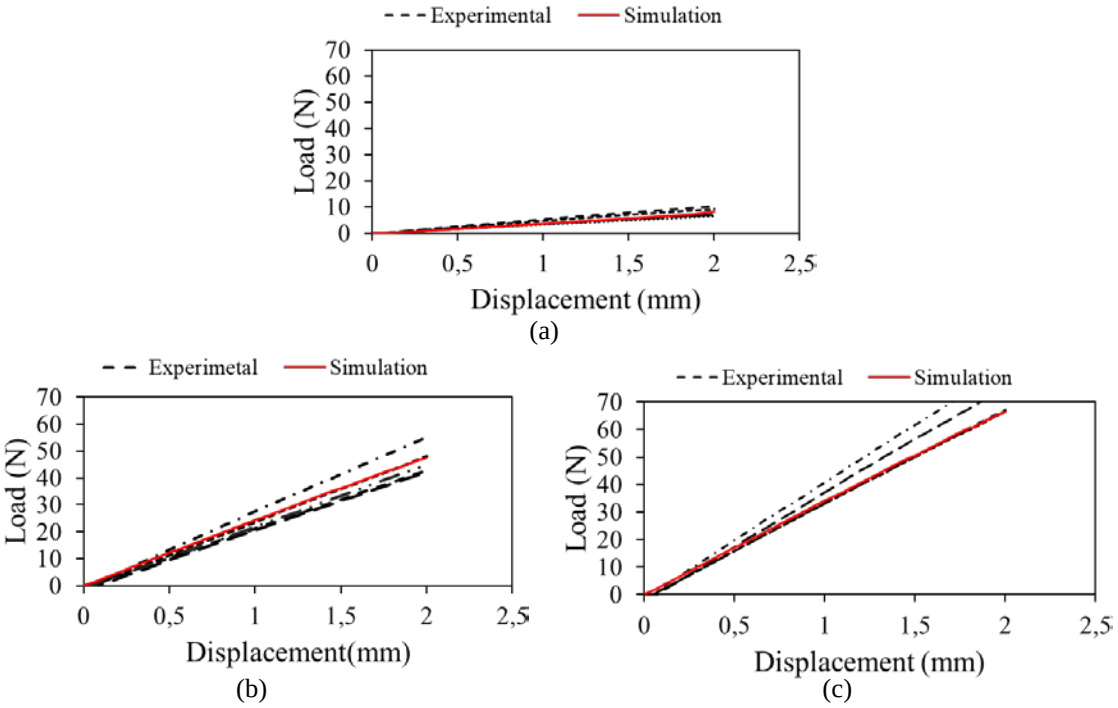

Figure 6: Load x Displacement diagram of flexural tests by experimental and numerical simulation: (a) Polymer Epoxy, (b) PE3L and (c) PE5L

3.3 Analytical Method

The results of the Analytical Method, Experimental average and Numerical Simulation are shown in Table 3. Considering maximum displacement of 2 mm, observed values of loading and normal stress in the specimens. With respect to the force values, it can be noted that the results of the non-linear simulations are closer to the experimental results.

However, the results of the linear simulations were closer to the analytical results, probably because these two methods have the same simplifications (used to small deformations and to disregard the contact conditions). The tensile stresses on the faces of the laminate showed similar results among the three methods. Compression stresses were not analysed due to the influence of the rigid elements in the linear simulation results. Observing the epoxy resin, the nonlinear simulation results were slightly closer to the analytical results.

Table 3: Experimental, Numerical Simulation and Analytical results.

Methods	Experimental	Linear Simulation	Non-Linear Simulation	Analytical Method
Polymer Epoxy				
Load [N]	7.97	6.85	8.20	6.75
Max Stress Faces[MPa]	-	-	-	-
Max Stress Epoxy [MPa]	-	8.60	9.50	9.00
PE3L				
Load [N]	46.63	49.80	47.50	49.50
Max Stress Faces[MPa]	-	86.70	85.90	90.00
Max Stress Epoxy [MPa]	-	5.00	4.00	3.60
PE5L				
Load [N]	69.80	63.90	64.00	63.60
Max Stress Faces[MPa]	-	86.70	85.80	90.00
Max Stress Epoxy [MPa]	-	4.00	3.00	3.00

4. CONCLUSIONS

In this paper, it was evaluated the behavior in three-point bending of polymer epoxy reinforced with glass fiber laminated faces through four different methods. The values of load, displacement and stress were obtained and compared. It was possible to observe that, despite the considerably lower computational cost, linear simulation should be used with caution because the small displacements limitations and rigid elements influence, mainly in compress stress. Non-linear dynamic analysis with contact simulation has a higher computational cost, however the results can be more reliable.

ACKNOWLEDGEMENTS

The authors thank to FAPEMIG, CAPES and CNPq for the support in this paper.

REFERENCES

[1] Felipe, R.C., Felipe, R. N., Melo, A.C., Batista, C., Aquino, E.M. 'Polymer Composites Reinforced with Hybrid Fiber Fabrics', Materials Research, 20 (2) (2017) 555-567.

[2] Tamilarasan, U., Karunamoorthy, L., Palanikumar, K., 'Mechanical Properties Evaluation of the Carbon Fibre Reinforced Aluminium Sandwich Composites', Materials Research, 18 (5) (2015) 1029-1037.

[3] Zenkert, D., Industrifond, N., 'The Handbook of Sandwich Construction', Emas publishing; 1997.

[4] Levy Neto, F., Pardini, L.C. 'Compósitos Estruturais: Ciência e Tecnologia', (Edgard, Blücher, 2006).

[5] Daniel, I.M., Ishai, O., 'Engineering mechanics of composite materials', (Oxford University Press, New York, 1994).

[6] Santos, J.C., Vieira, L.M., Panzera, T.H., Shiavon, M.A., Christoforo, A.L, Scarpa, F., 'Hybrid glass fibre reinforced composites with micro and poly-diallyldimethylammonium chloride (PDDA) functionalized nano sílica inclusions.' Materials and Design: 65 (2015) 543-549.

[7] Chemami, A., Bey, K., Gilgert, J., Azari, Z., 'Behaviour of composite sandwich foam-laminated glass/epoxy under solicitation static and fatigue', Composites Part B: Engineering, 43 (3) (2012) 1178–1184.

[8] Borrego L.P., Costa J.D.M., Ferreira J.A.M., Silva H., 'Fatigue behaviour of glass fibre reinforced epoxy composites enhanced with nanoparticles', Composites Part B Engineering, 62, (2014) 65–72.

[9] Bey, K., Tadjine, K., Khelif, R., Chemami A., Benamira, M., Azari, Z., 'Mechanical Behavior of Sandwich Composites Under Three-Point Bending Fatigue. Mechanics of Composite Materials', 50 (6) (2015) 747–756.

[10] Mantari, J.I., Soares, C.G., 'Generalized layer wise HSDT and finite element formulation for symmetric laminated and sandwich composite plates. Composite Structures', 105 (2013) 319-331.

[11] Cheloni, J.P.M., Silveira, M.E., 'Analytical and numerical analysis of laminated composite tubes. Brazilian Conference on Composite Materials' Proceedings of Brazilian Conference on Composite Materials-BCCM3, 2016 Aug 28-31 Gramado, RS Brazil.

[12] American Society for Testing and Materials. ASTM D3039-14. 'Standard Test Method for Tensile Properties of Polymer Matrix Composite Materials', 2014.

[13] American Society for Testing and Materials. ASTM D638-14. 'Standard Test Method for Tensile Properties of Plastics', 2014.

[14] British Standards Institution BS 2562: 1997; 'Carbon fibre reinforced plastics-Unidectional laminates-Flexural test parallel to the fibre direction', London, 1997.

NUMERICAL MODELLING OF HELICAL CABLES USING BEAM ELEMENTS

Eduardo A. W. de Menezes [(1)], Rogério J. Marczak [(1)] and Sandro C. Amico[(2)]

(1) Department of Mechanical Engineering, Federal University of Rio do Sul, Brazil

(2) Department of Materials Engineering, Federal University of Rio do Sul, Brazil

https://doi.org/10.21452/bccm4.2018.16.04

Abstract

Due to the complex geometry of helical cables and wire ropes, the available analytical models have a series of simplifications, assumptions and a limited capacity in reproducing their mechanical behavior, and 3D numerical models are often costly and time-consuming due to interwire contact. Both methods are not viable when dealing with long cables, as in cable-stayed bridges and offshore platforms applications, where they can reach more than 1500 m (ultra-deep waters). The purpose of this work is to incorporate a new 1D beam element in a commercial finite element (FE) software. A 3D FE model, previously verified by experiments, was used to calibrate the 1D element, which carries the information provided by the 3D model in its stiffness matrix. The result is a 2-node beam element with six degrees of freedom per node which is able to simulate long cables, combining both the practical implementation of an analytical model with the accuracy of a 3D FE model. The adjusted beam model fitted the 3D model with a coefficient of determination (R^2) above 0.90.

Keywords: Cables, Finite element modelling, beam element.

1. INTRODUCTION

A cable or a wire rope is a structural element made of a layup of strands and wires or fibers helically wrapped around a central straight core [1]. Their applications include prestressing of concrete, stays for guyed masts [1], deployable structures for satellite transportations [2] bridging applications [3] and mooring of offshore platforms [4]. In all these applications, carbon-fiber reinforced polymer (CFRP) cables are replacing traditional materials due to their high specific strength and stiffness compared to metallic and synthetic fiber cables [5], outstanding fatigue behavior [3], no-magnetism, corrosion resistance [2] and low thermal expansion, being also superior to steel in critical mechanical aspects as creep and relaxation [6]. Their disadvantages, however, include lack of ductility, high cost, and difficulties related to connections [6].

The first mathematical models created to predict its mechanical behavior considered the cable as a set of bars, neglecting torsion and bending stiffness, such as the model proposed by Hruska [7]. In the 70's and 80's different authors applied Love's rod theory [8] to model cables, as in Costello's model for the tensile and bending behavior of single and multi-layered cables [9]. These models, however, made many assumptions, including linear elastic infinitesimal elasticity, isotropic material, neglection of contact forces, and limited applicability to a few boundary conditions [10]. Ghoereishi [1] compared classical analytical models and a finite element (FE) model and showed that for low helix angles (low pitch cables), analytical and numerical models diverge substantially.

More recently, different models were reported to tackle some of these assumptions. Elata [11] proposed a model to accurately capture stress distribution along the wires of multi-layered cables, which has been reported to be poorly predicted by most analytical models like Costello's [12], while Argatov [13] attempted to model interwire friction and Crossley [14] created a model for a transversally isotropic material. Nevertheless, none of them could overcome all hypotheses, which is desirable for a trustworthy model for structural cables.

Regarding numerical solutions, a good correlation can be achieved between FE models and experimental tests (tensile or bending), even for helical composite cables [15]. However, it has been shown that the required computational time to simulate helical cables with 3D hexahedral elements greatly increases as a function of the cable length. For dynamic simulations of an in-service cable in offshore platforms, for instance, it is recommended to simulate its full length, whose value for ultra-deep water is greater than 1500 m.

This work proposes a methodology to model a helical cable using Euler-Bernoulli beam elements in order to combine the accuracy of 3D FE models with the quickness of analytical models. The process consists in numerically evaluating the stiffness matrix of a transversally isotropic cable and then apply the least square method to compute coefficients that could adjust an Euler-Bernoulli stiffness matrix to the stiffness of the 3D model.

2. METHODOLOGY

2.1 Beam element

Beams are the most common type of structural components, widely used in civil and mechanical engineering. Since a 3D body is modeled as a 1D body, several assumptions and approximations to the underlying physics are made [16]. Classical beam theory of Euler-Bernoulli, which is eligible for slender beams [17], involves the following assumptions [18]: (i) one dimension is considerably larger than the other two; (ii) plane cross-sections perpendicular to the axis of the beam remain plane and perpendicular to the axis after deformation; (iii) shear deformation is neglected; (iv) deformations are infinitesimal; (v) the Poisson effect is neglected; (vi) symmetric cross-sectional area, with the neutral axis coincident with the centroid; (vii) linear-elastic material. Since the focus here is on long composite cables, usually CFRP (with ultimate strain ca. 2%), hypotheses (i-vi) are valid, whereas hypothesis (vii) must be further investigated.

In order to evaluate the beam element stiffness matrix, a two-node element is considered, with six degrees of freedom (DOF) per node (namely, axial displacement, transverse displacement in *y*-direction, transverse displacement in *z*-direction, and rotation about *x*, *y* and *z*-axis) depicted in Figure 1, where u are displacements and θ rotations, with subscripts indicating node number and direction, respectively.

For DOF 1 (axial displacement), considering a beam with length L, constant cross-section area A and Young's modulus E, the stiffness is as follows:

$$K_{ij} = EA\int_{x_1}^{x_2} \frac{d\,\psi_i\,(x)}{d\,x} \cdot \frac{d\,\psi_j\,(x)}{d\,x}\, d\,x \tag{8}$$

where i and j are stiffness coefficients (for indices 1 and 7), and ψ represents the interpolation functions:

$$\psi_1 = 1 - \frac{x_2 - x_1}{L}, \tag{9}$$

$$\psi_7 = \frac{x_2 - x_1}{L}$$

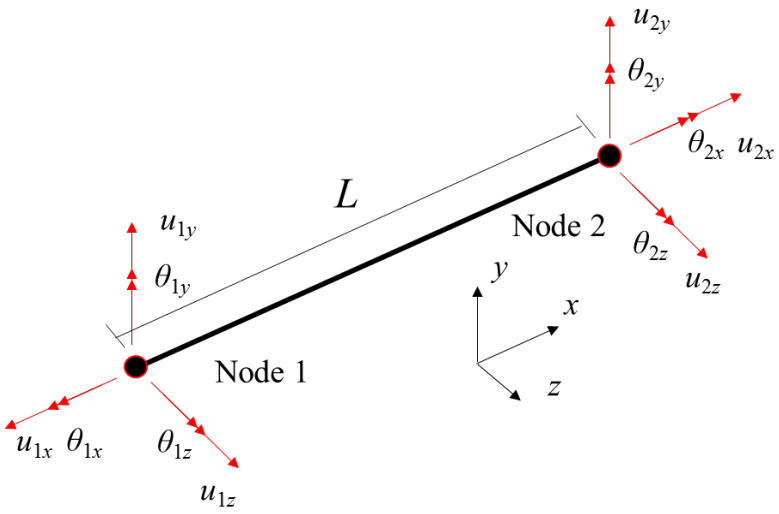

Figure 93 – Illustration of the beam element and coordinate system**.**

Regarding DOFs 2 and 5 (deflection in y and rotation around the z-axis, respectively), Hermite interpolation functions were applied, and the stiffness is given by:

$$K_{ij} = EI_z\int_{x_1}^{x_2} \frac{d\,\psi_i^2\,(x)}{d\,x^2} \cdot \frac{d\,\psi_j^2\,(x)}{d\,x^2}\, d\,x \tag{10}$$

for (11)

$$\psi_2 = 1 - 3\left(\frac{x_2 - x_1}{L}\right)^2 + 2\left(\frac{x_2 - x_1}{L}\right)^3$$

$$\psi_6 = (x_2 - x_1)\left(1 - \frac{x_2 - x_1}{L}\right)^2$$

$$\psi_8 = 3\left(\frac{x_2 - x_1}{L}\right)^2 - 2\left(\frac{x_2 - x_1}{L}\right)^3$$

$$\psi_{12} = (x_2 - x_1)\left[\left(\frac{x_2 - x_1}{L}\right)^2 - \frac{x_2 - x_1}{L}\right]$$

where *i* and *j* are indices 2, 6, 8 and 12 and I_z is the moment of inertia about *z*-axis. Analogously, DOFs 3 and 6 (deflection in *z* and rotation around the *y*-axis, respectively) are obtained with the same interpolation functions of Equation (4), but changing I_z for I_y in Equation (3). DOF 4 (torsion around the *x*-axis) is achieved by substituting *E* for *G* (shear modulus) and *A* for *J* (polar moment of inertia) in Equation (1), through the interpolation functions of Equation (2). The complete stiffness matrix is obtained as:

$$K = \begin{bmatrix}
\frac{EA}{L} & 0 & 0 & 0 & 0 & 0 & -\frac{EA}{L} & 0 & 0 & 0 & 0 & 0 \\
0 & \frac{12EI_z}{L^3} & 0 & 0 & 0 & \frac{6EI_z}{L^2} & 0 & -\frac{12EI_z}{L^3} & 0 & 0 & 0 & \frac{6EI_z}{L^2} \\
0 & 0 & \frac{12EI_y}{L^3} & 0 & -\frac{6EI_y}{L^2} & 0 & 0 & 0 & -\frac{12EI_y}{L^3} & 0 & -\frac{6EI_y}{L^2} & 0 \\
0 & 0 & 0 & \frac{GJ}{L} & 0 & 0 & 0 & 0 & 0 & -\frac{GJ}{L} & 0 & 0 \\
0 & 0 & -\frac{6EI_y}{L^2} & 0 & \frac{4EI_y}{L} & 0 & 0 & 0 & \frac{6EI_y}{L^2} & 0 & \frac{2EI_y}{L} & 0 \\
0 & \frac{6EI_z}{L^2} & 0 & 0 & 0 & \frac{4EI_z}{L} & 0 & -\frac{6EI_z}{L^2} & 0 & 0 & 0 & \frac{2EI_z}{L} \\
-\frac{EA}{L} & 0 & 0 & 0 & 0 & 0 & \frac{EA}{L} & 0 & 0 & 0 & 0 & 0 \\
0 & -\frac{12EI_z}{L^3} & 0 & 0 & 0 & -\frac{6EI_z}{L^2} & 0 & \frac{12EI_z}{L^3} & 0 & 0 & 0 & -\frac{6EI_z}{L^2} \\
0 & 0 & -\frac{12EI_y}{L^3} & 0 & \frac{6EI_y}{L^2} & 0 & 0 & 0 & \frac{12EI_y}{L^3} & 0 & \frac{6EI_y}{L^2} & 0 \\
0 & 0 & 0 & -\frac{GJ}{L} & 0 & 0 & 0 & 0 & 0 & \frac{GJ}{L} & 0 & 0 \\
0 & 0 & -\frac{6EI_y}{L^2} & 0 & \frac{2EI_y}{L} & 0 & 0 & 0 & \frac{6EI_y}{L^2} & 0 & \frac{4EI_y}{L} & 0 \\
0 & \frac{6EI_z}{L^2} & 0 & 0 & 0 & \frac{2EI_z}{L} & 0 & -\frac{6EI_z}{L^2} & 0 & 0 & 0 & \frac{4EI_z}{L}
\end{bmatrix} \quad (12)$$

2.2 3D FE Model

The cable was modelled in the FE commercial platform Abaqus using the C3D8R element (hexahedral linear eight-node with reduced integration) [19]. The geometry adopted, 1×7, is shown in Figure 2 (a). Hard and tangential contacts (penalty method) were inserted between external wires and between wires and core (Figure 2 (b)). Since the material is considered transversally isotropic, a local coordinate system was used to keep the wires' properties aligned in the correct orientation.

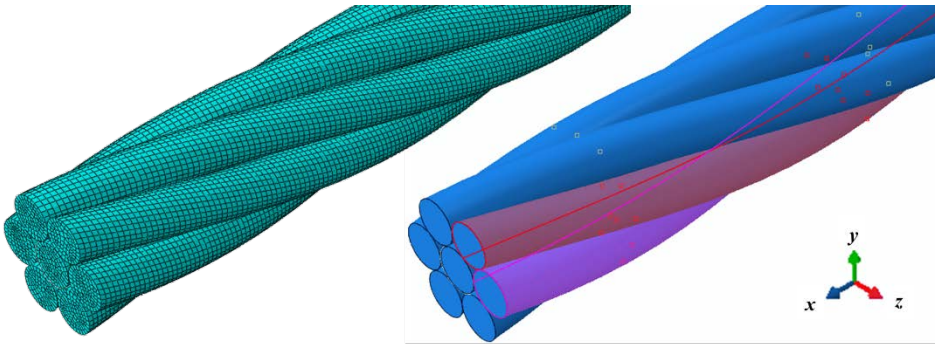

Figure 94 – (a) 1×7 cable meshed with the C3D8R elements and (b) one of the 12 contact pairs inserted in the model.

The procedure to obtain the stiffness components is illustrated in Figure 3 and consists in clamping the cable in the left end and allowing 1 DOF free in the right end. The stiffness is obtained by measuring the reaction forces or moments after applying the prescribed displacements or rotations. Since the I_y and I_z values are equal, DOFs 2 and 6 are equal to 3 and 5, respectively. For the DOF 4, rotation was applied clockwise and anti-clockwise since for a helical cable torsion stiffness is expected to be higher when twisting it in a direction opposite to the wires initial orientation. The other terms of the beam stiffness matrix were omitted due to matrix symmetry and assumption of $I_y = I_z$.

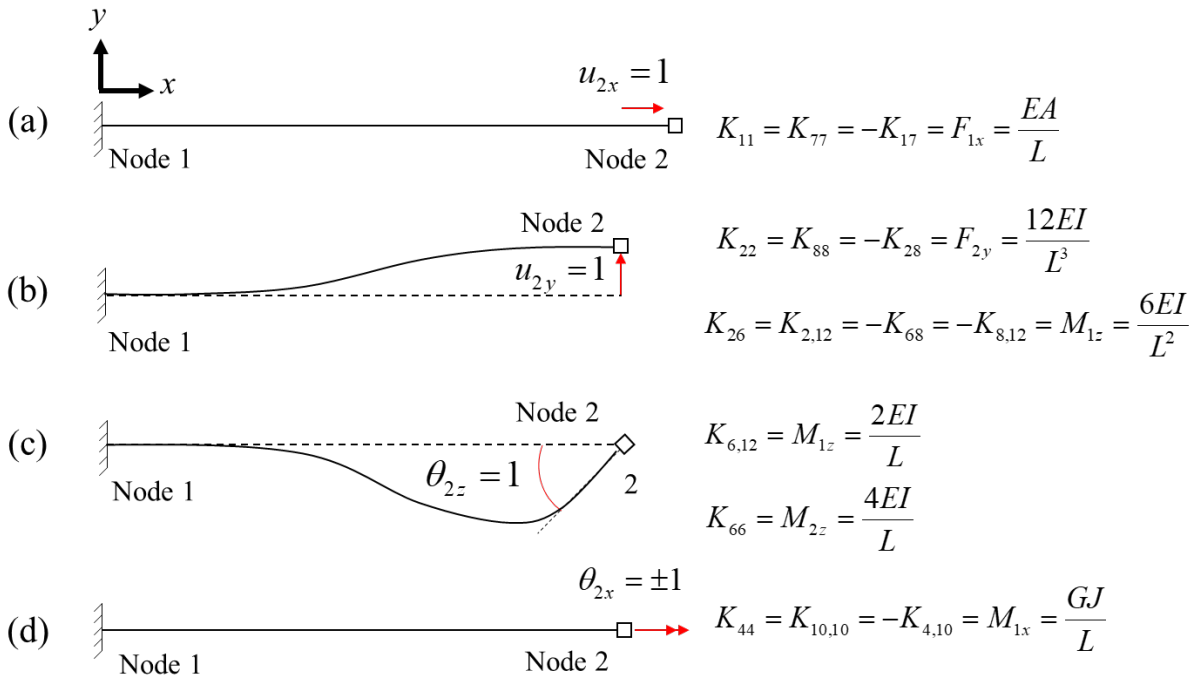

Figure 95 – Procedure adopted to obtain six terms of the beam stiffness matrix.

2.3 Regression procedure

The factorial design allows the simultaneous consideration of many variables at different levels, as well as the interaction between them [20]. In order to define the required level for each variable, a sensitive analysis was performed involving all parameters that significantly impact the cable behavior. Considering the material as transversally isotropic, engineering constants $\nu_{12}=\nu_{13}$, ν_{23}, G_{23}, $E_2=E_3$ and the friction coefficient μ play a small role in the cable behavior [15], therefore, the sensitivity analysis focused on wire diameter D, longitudinal Young's modulus E_1, in-plane shear modulus $G_{12}=G_{13}$, helix angle α and length L. The variables were individually studied.

After defining the factorial design, coefficients to adjust the cable stiffness to the beam stiffness matrix of Equation (5) were numerically evaluated through finite-differences method [21]. Different function families were tried to maximize the coefficient of determination (R^2).

3. RESULTS AND DISCUSSION

The values used as input in the 3D model to evaluate cable stiffness are reported in Table 1, while the ranges of the sensitivity analysis are reported in Table 2. Relative to shear modulus, its influence was only significant in DOF 4, and for a long cable, the difference in stiffness considering rotation applied clockwise and anti-clockwise was negligible. Its influence in DOF 4 (torsion term) was approximately linear ($R^2>0.999$).

Regarding the Young's modulus, its influence in the torsion stiffness was negligible and approximately linear for all the other stiffness matrix terms (average value of R^2 above 0.98). Relative to length and diameter, linear behavior was observed in all DOFs. However, while the linearity in L increases with cable length, the opposite occurred for the diameter. For the analysis of α, a review in scientific and technical literature was carried out to identify the angle range for real cables, which was found to be within 62°-82°. As the helix angle increases, all stiffness terms increase, but at distinct and non-linear rates.

Table 45 – Values adopted for the numerical model.

Property	Value
Geometry	1×7 (6 wires+core)
$E_2=E_3$ (MPa)	180000
G_{23} (MPa)	69231
$\nu_{12}=\nu_{13}=\nu_{23}$	0.30
μ	0.65

Table 46 – Ranges of the analyzed variables.

Parameter	Minimum	Maximum
E_1 (MPa)	90000	270000
G_{12} (MPa)	34615	103846
D (mm)	2.12	3.67
L (mm)	50	150
α (°)	62	82

Based on the aforementioned results, two levels were adopted for E, G, and L, three for D and five for α. Considering the four cases (a-d) mentioned in Figure 3, the total number of simulations

was (2×2×3×5)×4=240. These simulations were performed considering the ranges exposed in Table 2, except for the length, whose value was the largest possible within the convergence range, aiming to achieve a better fitting for the proposed application. The applied lengths and updated stiffness coefficients are reported in Table 3, along with the R^2 values, which were greater than 0.9 in all cases.

Considering that all terms in the stiffness matrix of the beam element were adjusted with relative good accuracy, this beam model is expected to satisfactory reproduce a 1×7 cable behavior under different load conditions, with an extremely low computational time in comparison to 3 D models with contact between wires, since this feature is incorporated in the updated beam model.

Table 47 – Updated values of stiffness after the adjustment process, along with the respective coefficients of determination.

Length Range	Adjusted Stiffness	R^2
100 - 150 mm	$K_{11} = -2.641\frac{EA}{L} + 3.598\frac{EA}{L}\sin(\alpha)$	0.9994
100 - 200 mm	$K_{22} = 3.041\frac{12EI}{L^3} - 2.756\frac{12EI}{L^3}\sin(\alpha) - 1.184\frac{12EI}{L^3}\cos(\alpha)$	0.9547
100 - 200 mm	$K_{26} = 2.756\frac{6EI}{L^2} - 2.492\frac{6EI}{L^2}\sin(\alpha) - 1.077\frac{6EI}{L^2}\cos(\alpha)$	0.9423
100 - 150 mm	$K_{66} = 0.012\frac{4EI}{L} - 0.015\frac{4EI}{L}\tan(\alpha)$	0.9117
100 - 150 mm	$K_{6,12} = -0.002\frac{2EI}{L} + 0.020\frac{2EI}{L}\tan(\alpha)$	0.9006
100 - 200 mm	$K_{44} = -0.035\frac{GJ}{L} + 0.060\frac{GJ}{L}$	0.9180

4. CONCLUSIONS

A methodology for the simulation of cables using 3D beam elements was presented. Higher coefficients of determination were obtained when comparing the beam stiffness with the stiffness of a 3D cable, indicating that the beam mechanical behavior will accurately simulate the behavior of the 3D cable. This model is able to simulate long cables much faster than 3D models. The use of trigonometric functions in the stiffness terms that account for the helix angle is justifiable since the cable is composed of one straight (core) and six helical wires.

The influence of the ratio between core and external wires diameter on the updated stiffness must be further investigated, as well as the application of this methodology for multi-layered cables. And the proposed methodology still needs to be validated to verify the implications of neglecting non-linearities and the coupling between tension and torsion.

ACKNOWLEDGEMENTS

The authors gratefully acknowledge the National Council for Scientific and Technological Development (CNPq).

REFERENCES

[1] Ghoreishi, S. R., Messager, T., Cartraud, P., Davies, P., 'Validity and limitations of linear analytical models for steel wire strands under axial loading, using a 3D FE model', *Int. J. of Mech. Sci.***49** (2007) 1251-1261.

[2] Motoyama, H., Ohta, T., Ohno, T., Moriya, K. 'Dynamic Tensile Properties of CFRP Cables Subjected to High-speed Loads', *Mem of Fac of Eng.* **62** (3) (2002) 113-127.

[3] Meier, U., 'Carbon Fiber Reinforced Polymer Cables: Why? Why Not?', *Arab. J. Sci. Eng.* **37** (2012) 399-411.

[4] Sparks, C., Zivanovic, I., Luyckx, J., Hudson, W., 'Carbon Fiber Composite Tendons for Deepwater Tension Leg Platforms', in 'Offshore Technology Conference', Houston, Texas, USA, May, 2003.

[5] Jackson, D. et. al., 'Carbon Fiber Composite Tendons for Deepwater Tension Leg Platforms', in 'Offshore Technology Conference', Houston, Texas, USA, May, 2005.

[6] Xie, X., Li, X., Shen, Y., 'Static and Dynamic Characteristics of a Long-Span Cable-Stayed Bridge with CFRP Cables', *Materials* **7** (2014) 4854-4877.

[7] Hruska, F. H., 'Calculation of stresses in wire ropes', *Wire and Wire Prod.*, **26** (9) (1951) 766-767.

[8] Love, A. E. H., 'A Treatise on the Mathematical Theory of Elasticity', 4th Edn (Dover Publications, New York, 2011).

[9] Costello, G. A., 'Theory of Wire Rope', 1st Edn (Springer-Verlag, New York, 1990).

[10] Cardou, A., Jolicoeur, C., 'Mechanical models of helical strands', *Appl Mech. Rev.*, **50** (1) (1997) 1-14.

[11] Elata, D., Eshkenazy, R., Weiss, M. P., 'The mechanical behavior of a wire rope with an independent wire rope core', *Int. J. of Sol. and Str.*, **41** (2004) 1157-1172.

[12] Menezes, E. A. W., et. al., 'Numerical and Experimental Analysis of the Tensile and Bending Behavior of CFRP Cables', *Pol. and Pol. Comp.* **25** (9) (2017) 643-650.

[13] Argatov, I., 'Response of a wire rope strand to axial and torsional loads: Asymptotic modelling of the effect of interwire contact deformations', *Int. J. of Sol. and Str.*,**48** (2011) 1413-1423.

[14] Crossley, J. A., Spencer, A. J. M., England, A. H., 'Analytical solutions for bending and flexure of helically reinforced cylinders', *Int. J. of Sol. and Str.*, **40** (2003) 777-806.

[15] Menezes, E. A. W., Silva, L. V., Marczak, R. J., Amico, S. C., 'Numerical model updating applied to the simulation of carbon fiber-reinforced polymer cables under bending and tensile stress', *J. of Strain Analysis*, **52** (6) (2017) 356-364.

[16] Felippa, C. A., 'Introduction to Finite Element Methods', (University of Colorado, 2004).

[17] Lee, S. J., Park, K. S., 'Vibrations of Timoshenko beams with isogeometric approach', *Applied Math. M.*, **37** (2013) 9174-9190.

[18] Han, S. M., Benaroya, M., Wei, T., 'Dynamics of transversely vibrating beams using four engineering theories', *J. of Sound and Vib.*, **225** (5) (1999) 935-988.

[19] Abaqus 2016, SIMULIA Academic Research, Dassault Systèmes Americas Corp, Waltham, Massachusetts, USA, 2016.

[20] Berrios, M., Gutiérrez, M. C., Martín, M. A., Martín, A., Application of the factorial design of experiments to biodiesel production from lard', *Fuel Pro. Tech.*, **90** (12) (2009) 1447-1451.

[21] MATLAB R. version 8.0.0.783 (R2012b), The MathWorks Inc., Natick, Massachusetts, USA, 2012.

SIMULATION OF FLEXURAL STRESSES ON LAYERED NATURAL FIBRE/EPOXY COMPOSITE BEAMS

R.T. Durai Prabhakaran [(1)], G.A. Ormondroyd [(1, 3)] and Guan Zhongwei [(2)]

(1) The BioComposites Centre, Bangor University, Gwynedd, UK

(2) School of Engineering, University of Liverpool, Liverpool, UK

(3) Department of Architecture and Civil Engineering, University of Bath, Bath, UK

https://doi.org/10.21452/bccm4.2018.16.05

Abstract

Biobased fibre reinforcements (hemp, jute, flax) derived from agricultural waste and forestry are increasing its potential towards advanced composites promoting environmental benefits and thermal recycling (including a reduction in CO2 emissions and the fossil fuel depletion). Currently, there is a growing interest of natural fibres due to its lower density, and higher modulus-to-density ratios compared to glass and carbon fibre reinforcements. The present work was intended to understand how the flax fibre layups and oreintation affect the behavior of laminated composites in bending. Unidirectional $[0^0]_{2S}$, cross-ply $[0/90]_S$, and angle-ply $[+45/-45]_S$ laminates made up of flax fibre reinforced epoxy composites are considered to study flexural stresses and mid-span deflections. Basic principles of the classical beam theory (CBT) are applied for obtaining analytical solutions, which were also compared with the finite element simulation results.

Keywords

Natural fibre, Epoxy, Flexural Loads, Cross/Angle-ply, Classical Beam Theory, FE analysis

1. INTRODUCTION

Recent state-of-the-art reviews on bio-based composites showed a rapid growth in research and innovation in the natural fibre composite area **[1-4]**. Polymer and fibres derived from fossil fuel resources are mostly non-biodegradable leading to a potential increased environmental burden. Scientists from academic and industries have shifted their focus toward bio-based materials, which are more eco-friendly (low environmental impact and low cost) and hence improving commercialization of biobased industrial products **[5]**. Fibres derived from agricultural waste/forestry as reinforcements have grown importance and their performance by implementing advanced chemistry and processing techniques. Henceforth bio-based composites are increasing

their applications in replacing conventional composites by hybridization methods in aviation, wind, aerospace, defence and automotive areas **[6]**.

Heterogeneous materials having two or more constituents (multi-phase) comprised of a matrix, fibre reinforcements (one or more fibres types), and nanoparticles require a thorough understanding to tailor the composite properties. Due to complex architecture, the materials have a large number of design variables. Selection of the right constituents, manufacturing methods and layups from endless combinations require modelling tools to design lightweight composites **[7]**. When designing such composites, the characteristics of layers should be known beforehand. FEM as an numerical method offers the possibility to quickly examine and evaluate laminate design at early stages of design long before a prototype is built.

From the literature review **[8-12]**, it is clear to note that some experimental investigations were conducted to understand stresses in a layered flax/epoxy composite. Cerbu **[10]** studied mechanical behaviour of flax/epoxy and flax/glass/epoxy composites, where bidirectional flax woven fabrics are considered. Performance of bidirectional eight layered flax/epoxy composites showed higher mechanical properties in weft direction when compared to warp direction. Young's modulus in tensile (33.84%)/bending (13.44%) and normal tensile stress (40.63%)/bending stress (12.69%) is greater for weft direction compared to warp direction of the specimen. Similarly, Durai Prabhakaran et. al. **[11-12]** studied flexural performance of biaxial ($\pm 45^0$) non-crimp glass and flax fabrics with super-sap epoxy resin. Symmetrical laminates with layered configuration are produced to demonstrate the effect of hybridization of flax/glass layups on bending properties. Limited research carried out to demonstrate the flexural performance comparison of flax/epoxy laminates with unidirectional, cross-ply, and angle-ply layups with symmetric configuration, as shown in Figure 1.

Theoretical and numerical analysis has been undertaken to determine stresses and mid-span deflections in layered composites in this study. Classical beam theory and finite element simulation have been used to examine the stress distribution in the symmetric laminates of flax/epoxy composites under flexural loading conditions. For the simulation of stresses, Solidworks® version 2018 software (Dassault Systems, UK) was used.

2. SYMMETRIC LAMINATES AND LAYUPS

In the present paper, laminates with varying fibre orientations are considered to understand how the fibre orientation and layup sequence in a symmetric configuration affects the performance of laminated composites in bending. The laminates are shown in Figure 1, with $[0^0]_{2S}$, $[0/90]_S$, $[+45/-45]_S$ having constituent properties i.e. flax fibre and epoxy resin are described in Table 1. The four independent elastic properties for flax/epoxy lamina considered for analytical and simulation analysis are also given in Table 1.

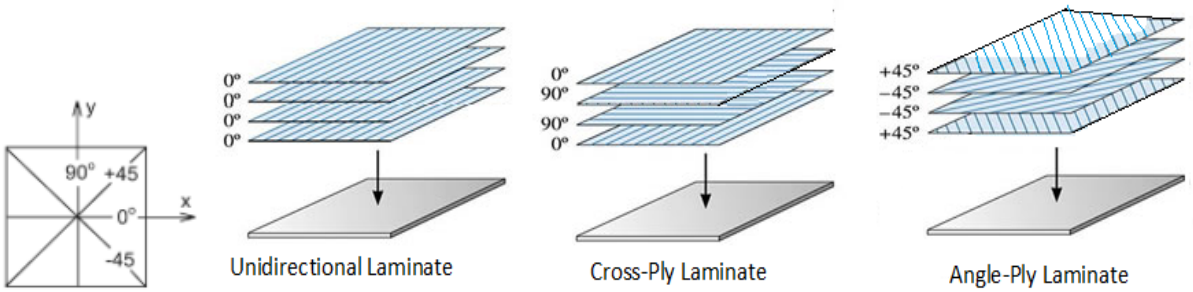

Figure 1: Symmetric laminates: layup's with varying lamina fibre orientations

Table 1: Material properties of fibre, matrix and lamina **[11-12]**

	Fibre – Flax fibre					
Symbol	V_f (%)	E_{1f} (GPa)	E_{2f} (GPa)	G_f (GPa)	ϑ_f	ρ_f (g/cm^3)
Value	0.275	39.0	5.44	3.46	0.11	1.516
	Matrix – Epoxy resin					
Symbol	V_m (%)	E_m (GPa)	-	G_m (GPa)	ϑ_m	ρ_m (g/cm^3)
Value	0.725	3.70	-	1.37	0.35	1.152
	Lamina – Flax/Epoxy single ply					
Symbol	-	E_1 (GPa)	E_2 (GPa)	G_{12} (GPa)	ϑ_{12}	ρ_c (g/cm^3)
Value	-	13.4	4.45	1.74	0.284	1.2794

3. THEORETICAL APPROACH

In many applications, deflection of a beam plays a key role in the structure. This can happen when the beam is subjected to either static or dynamic loading conditions. It can cause durability concerns and hence, deflection and stress analysis for composite beams need to be thoroughly understood. In the present study, composite beams with dimensions of 80mm x 15mm x 4mm are considered for three point bending analysis. Loading and supporting conditions as described in standards ISO 14125: 1998 are shown in Figure 2 used for the beam theory and finite element simulations.

According to the classical beam theory (CBT), the beam made of several layers of either same or different materials are placed either symmetrically or non-symmetrically to the median surface. In the current study symmetric layers with the same thickness and same material are considered to define a composite laminate (Figure 2). Laminates $[0^0]_{2S}$, $[0/90]_S$, $[+45/-45]_S$ are defined as symmetric transversely orthotropic laminated conditions. The stresses in a laminate vary from layer to layer, as well strains vary linearly across the beam thickness in spite of having laminae with different directional properties **[7]**.

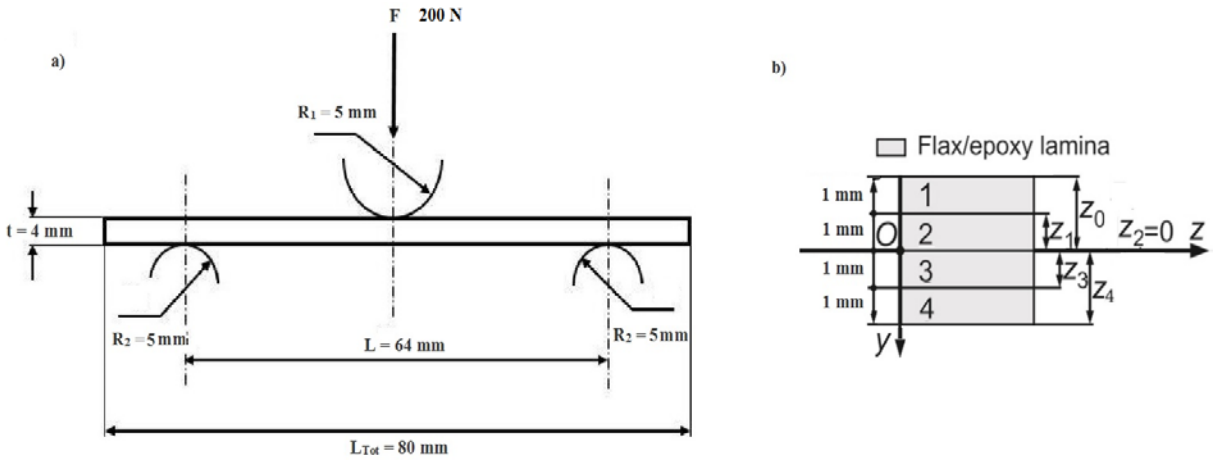

Figure 2: a) Load configuration of 3 point bending b) Thickness and coordinates of the lamina

From Table 1, using the constituent properties of fibre and matrix, stiffness matrix for a lamina can be defined as:

$$\text{Stiffness Matrix [S]} = \begin{bmatrix} Q_{11} & Q_{12} & 0 \\ Q_{21} & Q_{22} & 0 \\ 0 & 0 & Q_{66} \end{bmatrix} \quad (1)$$

where $Q_{11} = \frac{E_L}{1-\vartheta_{LT}\vartheta_{TL}}$; $Q_{22} = \frac{E_T}{1-\vartheta_{LT}\vartheta_{TL}}$; $Q_{12} = \frac{\vartheta_{TL}E_L}{1-\vartheta_{LT}\vartheta_{TL}}$; $Q_{66} = G_{LT}$; (2)

$$\vartheta_{LT}E_T = \vartheta_{TL}E_L \quad (3)$$

According to beam theory [7], total plate constitutive equation of a multi-layered laminate is used to calculate force and moment resultants

$$\begin{bmatrix} N \\ M \end{bmatrix} = \begin{bmatrix} A & B \\ B & D \end{bmatrix} \begin{bmatrix} \varepsilon_0 \\ k \end{bmatrix} \quad (4)$$

where strains and plate curvatures are estimated by using

$$\varepsilon_0 = \frac{\partial u_0}{\partial x} \qquad k = -\frac{\partial^2 w}{\partial x^2} \quad (5)$$

The elements of matrix [A], [B], and [D] are defined by equation (6), as shown below :

$$A_{ij} = \sum_{k=1}^{n} \left(\bar{Q}_{ij}\right)_k (h_k - h_{k-1}) \qquad B_{ij} = \frac{1}{2}\sum_{k=1}^{n} \left(\bar{Q}_{ij}\right)_k \left(h_k^2 - h_{k-1}^2\right)$$
$$D_{ij} = \frac{1}{3}\sum_{k=1}^{n} \left(\bar{Q}_{ij}\right)_k \left(h_k^3 - h_{k-1}^3\right) \quad (6)$$

Using equation (4) and equation (6), stress-strain relation for an orthotropic lamina referred to arbitrary axes can be determined by using equation (7)

$$\begin{Bmatrix} k_x^0 \\ k_y^0 \\ k_{xy}^0 \end{Bmatrix} = \begin{bmatrix} \delta_{11} & \delta_{12} & \delta_{16} \\ \delta_{21} & \delta_{22} & \delta_{26} \\ \delta_{61} & \delta_{62} & \delta_{66} \end{bmatrix} \begin{Bmatrix} M_x \\ M_y \\ M_{xy} \end{Bmatrix} \quad (7)$$

Considering the beam section shown in Figure 2, assuming beam subjected to 3-point bending, the differential equation of deformed section of beam is derived from the classical beam theory as

$$\frac{d^2 w_0}{dx^2} = -\frac{M}{E_x I} \quad (8)$$

Applying simply supported beam boundary conditions and solving the above equation leads to the following **[7]**:

$$E_x = \frac{12}{h^3 \delta_{11}} \quad (9)$$

$$w_0 = -\frac{Fl^2}{48E_xI}x\left[3-\left(\frac{2x}{l}\right)^2\right] \qquad w_{0\,max} = \frac{Fl^3}{48E_xI} \tag{10}$$

$$\left(\sigma^f_{max}\right) = \frac{3F_{max}l}{2bh^2}\left(1+6\left(\frac{w_{max}}{l}\right)^2-3\left(\frac{w_{max}h}{l^2}\right)\right) \tag{11}$$

[A], [B], [D] matrices for the four layered symmetric laminates $[0^0]_{2S}$, $[0/90]_S$, $[+45/-45]_S$ can be estimated from the lamina (or each ply) transformed stiffness matrix elements as given in Table 2. Stresses in each lamina and the mid-span deflections of the composite beam are estimated for flax/epoxy symmetric laminates are given in Table 3 and Table 4.

Table 2: Transformed Stiffness Matrix of Laminates with 0, 90, 45, -45 orientations

Lamina number and fibre angle θ		$\bar{Q}_{11}$	$\bar{Q}_{22}$	$\bar{Q}_{12}$	$\bar{Q}_{66}$	$\bar{Q}_{16}$	$\bar{Q}_{26}$
		MPa					
Unidirectional Laminates $[0^0]_{2S}$							
1st, 2nd, 3rd, 4th Ply	0^0	13769	4572	1298	1740	0	0
Cross-Ply Laminate $[0/90]_S$							
1st Ply, 4th Ply	0^0	13769	4572	1298	1740	0	0
2nd Ply, 3rd Ply	90^0	4572	13769	1298	1740	0	0
Angle-Ply Laminate $[+45/-45]_S$							
1st Ply, 4th Ply	$+45^0$	6975	6975	3495	3936	2299	2299
2nd Ply, 3rd Ply	-45^0	6975	6975	3495	3936	-2299	-2299

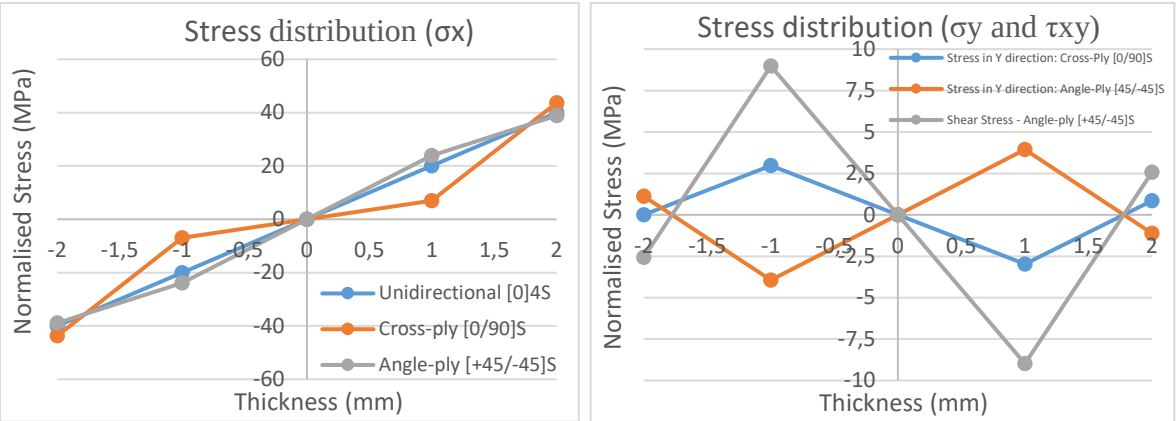

Figure 3: The axial and shear stress variations along the thickness of flax/epoxy laminate

Table 3: Stress distribution along the thickness of the laminate subjected to 3 point bending

Lamina No	Angle/fibre orientation	Stress (σ_x) MPa	Stress (σ_y) MPa	Shear Stress (τ_{xy}) MPa
Unidirectional Laminates $[0^0]_{2S}$				
Ply #1	0^0	-40	0	0
Ply #2	0^0	-20	0	0
Ply #3	0^0	20	0	0
Ply #4	0^0	40	0	0
Cross-Ply Laminate $[0/90]_S$				
Ply #1	0^0	-43.7	-0.85	0
Ply #2	90^0	-6.94	2.97	0
Ply #3	90^0	6.94	-2.97	0
Ply #4	0^0	43.7	0.85	0
Angle-Ply Laminate $[+45/-45]_S$				
Ply #1	$+45^0$	-38.9	1.12	-2.57
Ply #2	-45^0	-23.9	-3.94	8.98
Ply #3	-45^0	23.9	3.94	-8.98
Ply #4	$+45^0$	38.9	-1.12	2.57

4. NUMERICAL SIMULATION

Finite element models were developed using SOLIDWORKS® version 2018 (Dassault Systems, UK) to help understand flexural behaviour (analysis of stresses, strains and displacements) of a symmetric laminate in bending. To simulate the real material behaviour it was necessary to define density and mechanical properties of the material in solidworks as given in Table 1. For any simulation, geometry, material, and boundary conditions are defined. The flax/epoxy specimens considered in the study have symmetry and therefore, unidirectional and cross-ply will have symmetry in the ply sequence, material, and geometrical symmetry, whereas the angle-ply has no through thickness plane of symmetry for material orientation.

To simulate 3 point bending with the “simply supported” assumption, the load and deflection follows linear relationship. In the current study, comparison of three symmetric laminates are analysed for bending assuming load applied at centre of beam as 200N. The sum of reaction forces acting at supports are equal to 200 N in reverse direction to load applied. Specimen geometry is 80 x 15 x 4 mm^3, where span (L) were set as 64 mm as shown in Figure 2. SolidWorks used the directions X, Y, and Z of the global Cartesian system of coordinates having mixed mesh with high quality having total nodes 23208, and elements 14628.

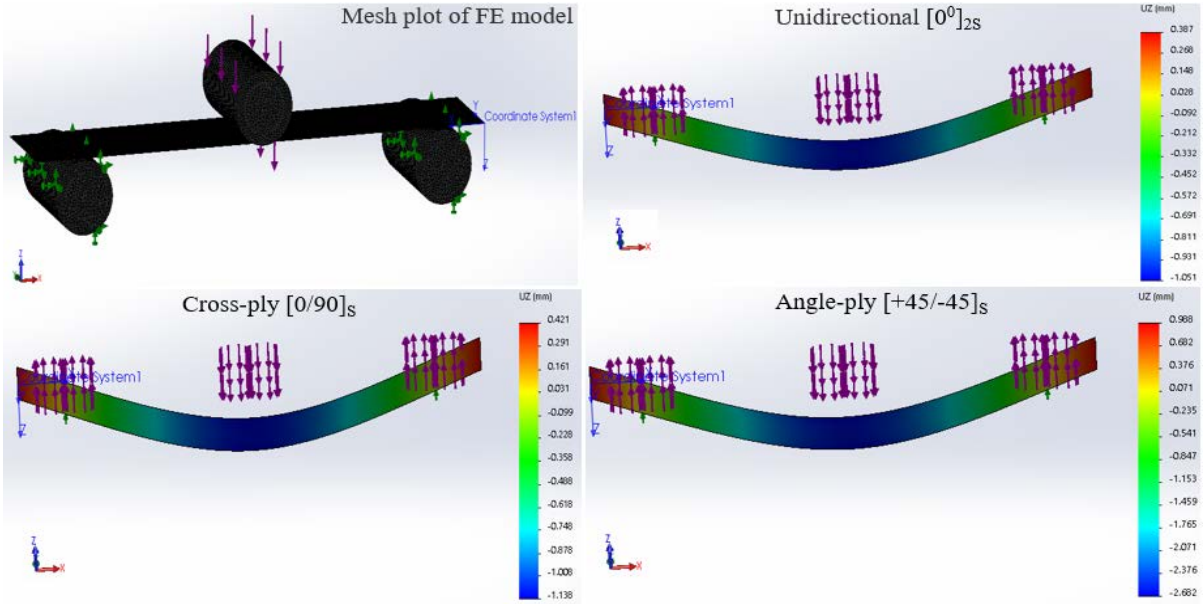

Figure 4: Finite Element Model and Mid-span Deflection of Symmetric Flax/Epoxy Laminate

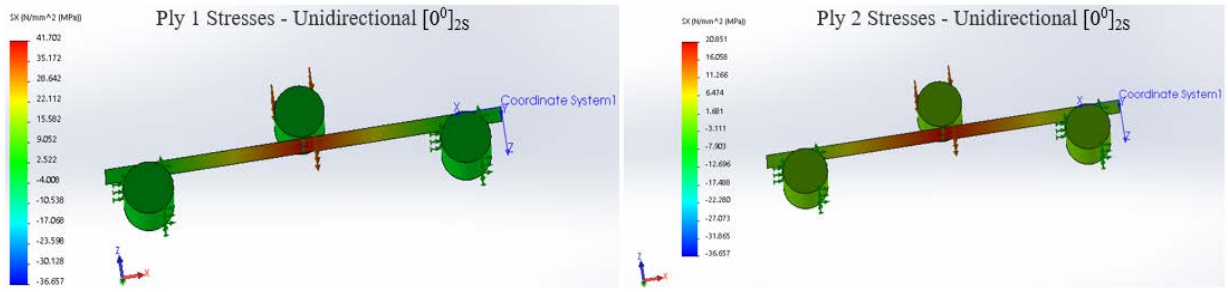

Figure 5: Ply Stresses for Unidirectional $[0]_{2s}$ Flax/Epoxy Composite

5. RESULTS AND DISCUSSIONS

The symmetry or asymmetry of a laminate based on angle, material, and thickness of plies, may cancel out some elements of the extensional stiffness [A], coupling stifness [B], and bending stiffness [D] matrices. In the current work, laminates $[0^0]_{2S}$, $[0/90]_S$, $[+45/-45]_S$ are considered as symmetry therefore elements of [B] matrix is zero and elements of Q matrix for unidirectional and cross-ply i.e. $[Q_{16}]$ and $[Q_{26}]$ are zero. According to CBT, symmetric laminates subjected to forces only have zero midplane curvatures reducing or zeroing out the coupling of forces and bending moments, normal and shear forces, or bending and twisting moments. Laminates having angle/symmetry, and number of plies the same but change the stacking sequence influences the interlaminar stresses.

For the current study, three point bending configuration has been adopted to study flax/epoxy laminates. To compare the laminate performance under load F (200 N) is applied at centre of beam, which is subjected to resultant moment M_x (213.3 N.m/m), M_y, M_{xy} equal to zero. As no other forces acting on beam, resultant forces N_x, N_y, N_{xy} are defined as zero, whereas the fibre direction coincides with the global axis for unidirectional and cross-ply laminates. Table 3 lists the individual ply stresses when a load is acting at centre of beam. For unidirectional and cross-ply, shear stress and midplane strains are zero because there are no in-plane forces acting and the laminate is symmetric. The state of stress through the thickness of the laminate (due to bending) results into laminate stiffness (estimated using eqn. (9). Figure 3 demonstrates the normal stress

and shear stress variations across the thickness of laminates. Similarly, strain distribution through thickness of laminate is linear and plies used as outer contribute more to stiffness than inner layers of the laminate. Therefore bending stiffness for unidirectional is higher than cross-ply and angle-ply as given in Table 4. From the analytical results, it has been shown that shear stress (τ_{xy}) in angle-ply is higher than the normal stress (σ_y), and this leads to laminate twisting under bending loads. Shear stress for the unidirectional and cross-ply laminate are computed as zero, resulting no twisting.

Using SolidWorks, the distribution of the normal stress ($\sigma_x = S_{11}$) across the thickness of the unidirectional laminate (ply 1 and ply 2) are shown in Figure 5. The stress values shown in the plots are in the first and fourth ply as 41.7MPa and in the second and third ply as 20.8 MPa, nearly matches with the analytical (CBT) solution computed for each lamina, refer Table 3. The distribution of vertical displacement (mid-span deflection) of the laminate W_{0max} in the direction of the Z-axis are plotted in all three cases of laminate, as shown in Figure 4 and Table 4. The deflection obtained for the load (200 N) applied at centre of beam demonstrates unidirectional and cross-ply have better performance compared to angle-ply (deflection higher than $[0]_{2S}$ and $[0/90]_S$).

Table 4: Bending Properties of Unidirectional, Cross-ply, & Angle-ply Flax/Epoxy Laminates

Composite Plate Type	Bending Modulus E_x	Bending Stress σ_{fb}	Mid-Span Deflection W_{0max}	
	Theoretical (GPa)	Theoretical (MPa)	Theoretical (mm)	Numerical (mm)
Unidirectional $[0]_{2S}$	13.4	77.9	1.02	1.05
Cross Ply $[0/90]_S$	12.3	78.0	1.11	1.13
Angle Ply $[+45/-45]_S$	5.01	84.2	2.72	2.68

6. CONCLUSIONS

The work reports results obtained in numerical modelling of flexural behaviour (in bending) of flax/epoxy composites with symmetrical layups (unidirectional, cross-ply, and angle-ply) and these results are validated analytically using the classical beam theory. Based on the work, some conclusions may be drawn as follows :

- Flexural stiffness for the unidirectional laminates is greater than cross-ply and angle-ply flax/epoxy laminates.
- From the results, it has been shown that shear stress (τ_{xy}) in angle-ply is higher than the stress (σ_y), and this leads to laminate twisting under bending loads.
- The laminate (angle-ply) presents much higher mid-span deflection than symmetric unidirectional and cross-ply flax/epoxy laminates.

Future experiments are planned to study bending properties for the three symmetrical layups of flax/epoxy composites and evaluate theoretical/numerical results presented in the article.

ACKNOWLEDGEMENTS

The authors of the paper would like to acknowledge the financial support provided by the Welsh Government and Higher Education Funding Council for Wales through the Sêr Cymru National Research Network for Low Carbon, Energy and Environment.

REFERENCES

[1] Pickering, K., 'Properties and performance of natural –fibre composites', 1st Edition (Woodhead Publishing, Cambridge, 2008).

[2] Edgars, S., 'Mechanical Properties of flax fibers and their composites', *Licentiate thesis* (Luleå University of Technology, Sweden, 2006).

[3] Aslan, M., Sørensen, B.F. and Madsen, B. 'Characterization of flax fibres & flax fibre composites: Bending cellulose based sources of materials', *PhD Thesis* (DTU Wind Energy, Denmark, 2012).

[4] Pickering, K.L., Aruan Efendy, M.G., Le, T.M., 'A review of recent developments in natural fibre composites and their mechanical performance', *Composites: Part A*, **83** (2016) 98-112.

[5] Yan, L., Chouw, N. and Jayaraman, K., 'Flax fibre and its composites – A Review', *Composites Part B: Engineering*, **56** (2014) 296 – 317.

[6] Durai Prabhakaran, R.T., 'A critical review on future materials for wind turbine blades', *International Journal of Materials Engineering Innovation*, **5** (2) (2014) 81-99.

[7] Agarwal, B.D., Broutman, L.J. and Chandrashekhara, K., 'Analysis and performance of fiber composites', 3rd Edition (John Wiley & Sons, Inc., New Delhi, 2006).

[8] Meng, M., Le, H.R., Rizvi, M.J. and Grove, S.M., '3D FEA modelling of laminated composites in bending and their failure mechanisms', *Composite Structures*, **119** (2015) 693 – 708.

[9] George, J., Ivens, J. and Verpoest, I., 'Mechanical properties of flax fibre reinforced epoxy composites', *Die Angewandte Makromolekulare Chemie*, **272** (1999) 41-45.

[10] Cerbu, C., 'Practical solution for improving the mechanical behaviour of the composite materials reinforced with flax woven fabric', *Advances in Mechanical Engineering*, **7** (2) (2015) 01 – 11.

[11] Durai Prabhakaran, R.T., Madsen, Bo., Toftegaard, H. and Markussen, C.M., 'Flexural Properties of Hybrid Natural Composite: Micromechanics and Experimental Assessment', Proceedings of an International Conference, New Delhi, December, 2012 (ACMFMS, IIT Delhi, 2012) 469 – 472.

[12] Durai Prabhakaran, R.T., Toftegaard, H., Markussen, C.M. and Madsen, Bo., 'Experimental and Theoretical Assessment of Flexural Properties of Hybrid Natural Fibre Composites', *Acta Mechanica*., **225** (10) (2014) 2775 – 2782.

DYNAMIC ANALYSIS OF COMPOSITE STRUCTURES USING KRIGING MODEL APPLIED TO MANUFACTURING DESIGN TOLERANCES

Luiz Fernando Dos Santos Souza [(1)], Volnei Tita [(2)] and Ricardo De Medeiros [(1)]

(1) Department of Mechanical Engineering, Santa Catarina State University - UDESC, Brazil

(2) Department of Aeronautical Engineering, São Carlos School of Engineering, University of São Paulo - EESC/USP, Brazil

https://doi.org/10.21452/bccm4.2018.16.06

Abstract

Dynamic model updating is an effective means of damage identification, and surrogate modeling has attracted considerable attention for saving computational cost in finite element (FE) model updating, especially for large-scale structures. On the other hand, composite materials are very complex in terms of manufacturing and testing. Due to the manufacturing process, the properties of a component are very hard to control. As many damage detection methods are based on the comparison of intact and damaged plates, the definition of the intact plate must be clearly defined. This paper shows a methodology to define a frequency range to characterize a composite plate as intact structure. Using a model update process, with Kriging metamodel based on natural frequencies, the updated variables allowed to obtain the Frequency Response Function (FRF) by Finite Element Method (FEM). A set of five plates with a stacking sequence of [0/15/-15/0/15/-15]s were analyzed. The applicability of the methodology is presented using one of the known plates. The presented analysis shows that it is possible to make a preliminary study to improve the manufacturing design tolerances.

1. INTRODUCTION

Composite materials are becoming widely applied in the industry. Many times, as an alternative, to save weight on structural components. Employing this new kind of materials, it is necessary to develop new methodologies for maintenance. On the other hand, the study of structural dynamic behavior can give enough information to evaluate components and better planning the maintenance interventions [1-3]. On the way of combining the analysis of structural behavior with strategies to monitor the structure, several Structural Health Monitoring (SHM) systems are becoming in evidence [4-5]. Dynamic analyses have shown high potential to evaluate damage on structures [6-7]. Different methods have been already presented in the literature using natural frequencies and

FRFs to detect damages on composite structures [8-9]. Several damage detection methods assume that damages cause changes in the mass and stiffness matrix [10]. However, to make this assumption, it is necessary to have a good definition of the undamaged state of the component. A usual methodology is to proceed nondestructive testing on all the components, just before and after the manufacturing process in order to verify its state [11]. This is required because it is well known that the characteristics of a composite component are not easy to control. The manufacturing process has several variables that can affect the final properties of the component. Therefore, depending on the manufacturing process and the design tolerances for the structure, it is possible to define a method to provide information about the acceptability of the components based on a set of specimens, reducing the time and cost of the non-destructive evaluations.

Thus, in this work, the dynamic behavior of composite plates is evaluated in order to propose a methodology to allow a preliminary study about the acceptability of the intact state of a component. This is made based on the assessment of the structural dynamic behavior of a set of composite plates. To support this study, a numerical model is updated using a Kriging based methodology. Therefore, numerical and experimental results are used to compose a range of possibilities for the FRF that can be used to verify the state of other composite plates.

2. METHODOLOGY

The methodology consists of a hybrid approach using experimental and numerical data. First, a set of manufactured plates are analyzed, using modal analysis in order to get the natural frequencies and the damping factors. A range of natural frequencies is established based on the experimental data to represent a set of specimens. These experimental data are used as a reference to carry out a model update process, aiming to obtain the design variables that better represent the experimental data. Finally, using the updated design variables it is possible to obtain the FRF, which represents the entire set of composite plates. Therefore, these FRFs can be used to rank new specimens that have been manufactured with the same characteristics. In this work, a set of plates with a stacking sequence of $[0/15/-15/0/15/-15]_s$ is evaluated. The FRFs were obtained using lightweight structure accelerometers (Bruel & Kjaer model 352A24), the sensitivity of 102.34 mV/g, attached to the plates. An impact hammer PCB Model 0860C3 (Piezotronics) was used to apply the impulse signal, providing the required excitation on a wide frequency spectrum. The experimental set-up used in the experiments consists of a plate hanged by elastomer wires to simulate free-free boundary conditions. Accelerometer and the impact hammer are connected to an LMS SCADAS Mobile equipment controlled by the Test.Lab software (LMS Test.Lab). Figure 1 shows the complete setup used.

Evaluating the experimental data and defining the frequency range, the model update is applied to obtain the design variables. Thus, a strategy using metamodel Kriging is implemented aiming to reduce the computational time consuming of the model update process. This strategy consists of using few numbers of FEM (Finite Element Method) simulations to train the metamodel. After that, it uses only the metamodel in the optimization process, which is required to update the model. A detailed methodology used can be found in [12].

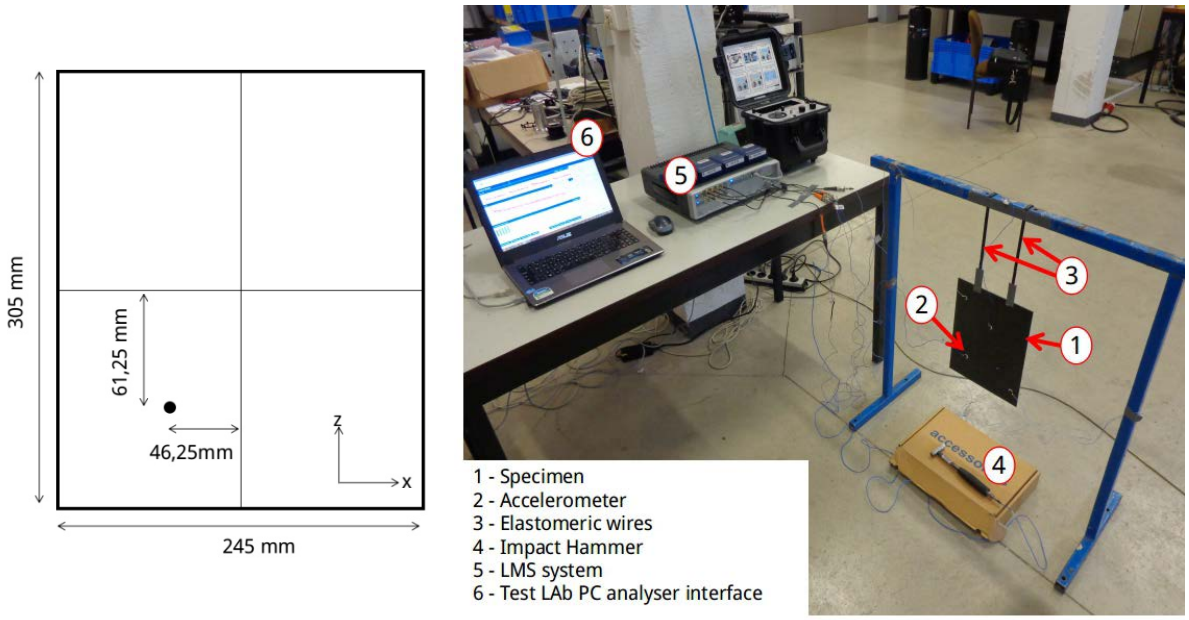

(a) (b)

Figure 1: (a) Schematic representation of the plate and accelerometer position and (b) Experimental setup.

Achieved the updated design variables, the FEM simulation is used to obtain the FRF of the structure. The dynamic structure response is used to define the range of the intact plates. Finally, this range can aid engineers to detect out of tolerance structures and as a reference for the manufacturing process.

3. EXPERIMENTAL INPUT DATA

The intact plates have been submitted to modal analysis, and the natural frequencies were obtained. Table 1 presents the experimental results for the plates $[0/15/-15/0/15/-15]_s$, including the natural frequencies, the average, and the standard deviation.

Table 1: Experimental natural frequencies obtained experimentally for composite plates with stacking sequence $[0/15/-15/0/15/-15]_s$.

	f_1 [Hz]	f_2 [Hz]	f_3 [Hz]	f_4 [Hz]	f_5 [Hz]	f_6 [Hz]
P09	95.379	132.911	250.645	316.229	349.436	405.460
P10	104.152	139.884	261.091	320.690	367.079	411.455
P11	106.412	144.506	265.334	332.630	377.859	424.862
P12	107.616	146.244	268.219	332.774	381.241	426.971
P13	102.961	139.202	258.850	320.595	365.101	412.746
P14	99.628	136.840	258.484	324.150	361.405	414.755
Average	103.557	139.543	259.971	322.420	366.090	413.751
St. Dev	4.542	4.902	6.119	6.824	11.525	8.280

Furthermore, Table 2 presents the minimum and maximum values for each mode. Those values were obtained using the experimental average and the standard deviation, which was chosen to exemplify the problem.

Table 2: Minimum and maximum natural frequencies to characterizes the composite plates with stacking sequence $[0/15/-15/0/15/-15]_s$.

Boundaries fo 1 standard deviation						
	f_1 [Hz]	f_2 [Hz]	f_3 [Hz]	f_4 [Hz]	f_5 [Hz]	f_6 [Hz]
Min	99.014	134.641	253.852	315.596	354.565	405.471
Max	108.099	144.445	266.089	329.244	377.615	422.030

4. NUMERICAL MODEL

Finite element models of the laminated composite plates are used to train the Kriging model, and also to obtain the FRF curves. Abaqus™ software and Python subroutines were used to build the computational models. Based on previous studies [13], quadrilateral 8-node shell elements are used (defined as S8R5 – Abaqus nomenclature). In addition, 5640 elements and 8784 nodes are used to mesh the plate domain. This mesh size (3 mm) is defined after a refinement analysis to obtain the six first modes, considering the Nyquist theorem.

The numerical analyses are done considering quasi-free-free boundary conditions. In fact, the elastic wires have a very low stiffness (10 N/m). with fixed translation (U_x, U_y, U_z) and rotations (U_{rx}, U_{ry}, U_{rz}) in the extremities non-attached to the plates. The excitation force is applied in the same position as in the experimental tests (Figure 2).

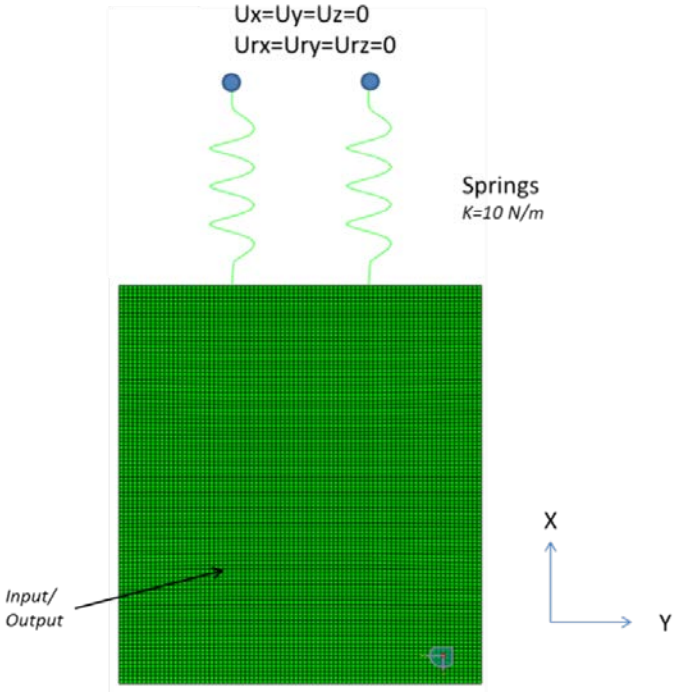

Figure 2: Finite element model

The damping coefficients were extracted experimentally from all plates, using the Peak Picking method [13]. Table 3 shows the mean and the standard deviation of the damping ratios in terms of modes.

Table 3: Damping ratios for the six first mode shapes

[0/15/-15/0/15/-15]s		
Mode	**Damping Ratios**	
	Mean	**Std. dev.**
1	0.63%	0.09%
2	0.58%	0.03%
3	0.57%	0.06%
4	0.66%	0.12%
5	1.08%	0.25%
6	0.44%	0.03%

5. KRIGING BASED MODEL UPDATE

A typical model update process consists of an optimization algorithm aiming to reduce the difference of the model results from the experimental results. Thus, the updated model is to obtain the design variables by using a FEM model, which returns the natural frequencies of the plates that better reproduce the experimental data. Therefore, a Particle Swarm Optimization (PSO) algorithm is used to search the most appropriate design variable values for each case. The strategy using the metamodel Kriging can significantly reduce the computational time of this process [12]. The model update is used to obtain the design variables that can result in the natural frequencies for the boundaries found in the experimental data. Table 4, shows the results obtained for plates $[0/15/-15/0/15/-15]_s$, considering the case of standard deviation.

Table 4: Maximum and minimum frequencies for plates $[0/15/-15/0/15/-15]_s$ considering standard deviation

	Boundaries for standard deviation					
	f1 [Hz]	*f2 [Hz]*	*f3 [Hz]*	*f4 [Hz]*	*f5 [Hz]*	*f6 [Hz]*
	Maximum					
Experimental	107.39	145.65	267.42	333.62	380.40	426.84
Kriging	108.56	146.77	264.59	333.62	380.40	423.67
Difference	1.09%	0.77%	-1.06%	0.00%	0.00%	-0.74%
	Minimum					
Experimental	103.17	138.74	259.01	319.70	364.53	410.76
Kriging	103.17	140.01	251.91	319.70	364.55	404.44
Difference	0.00%	0.92%	-2.74%	0.00%	0.00%	-1.54%

The design variables resulted from this model update process are presented in Table 5.

Table 5: Updated design variables

Boundaries for standard deviation				
	E_{11} [GPa]	E_{22} [GPa]	G_{12} [GPa]	t [mm]
Minimum	137.72	10.13	4.73	3.24
Maximum	135.92	10.03	4.79	3.41

Figure 3 shows the convergence of the PSO for the two cases previously studied.

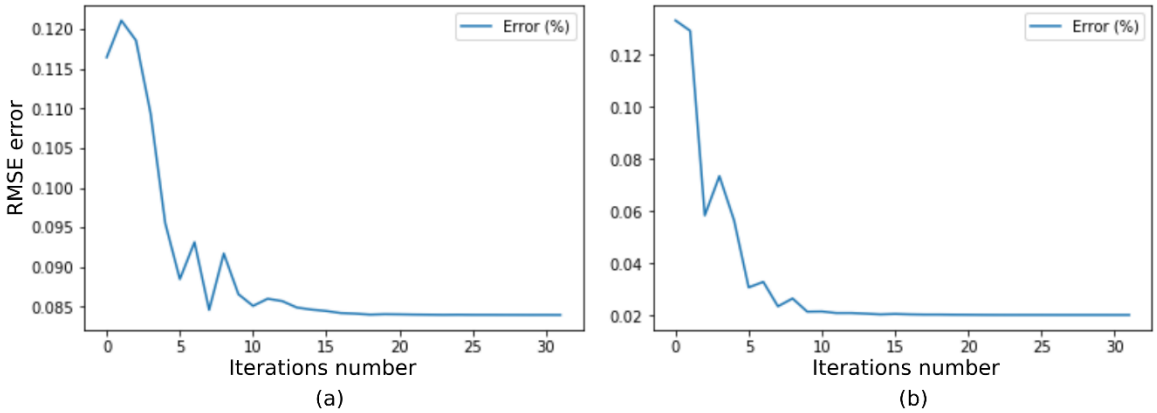

Figure 3: PSO convergence (a) maximum, (b) minimum

6. FRF ANALYSES

The FRFs show the global dynamic response of the system, and they are very useful on dynamic analysis. From the design variables determined via Kriging model update, it is possible to use a numerical model via FEM to obtain the correspondent FRF. Using the maximum and minimum values, the range of FRFs is created, and it can be compared to the experimental data of the plates in order to evaluate the admissibility of a project. Figure 4 shows the FRF for the minimum and maximum limits obtained.

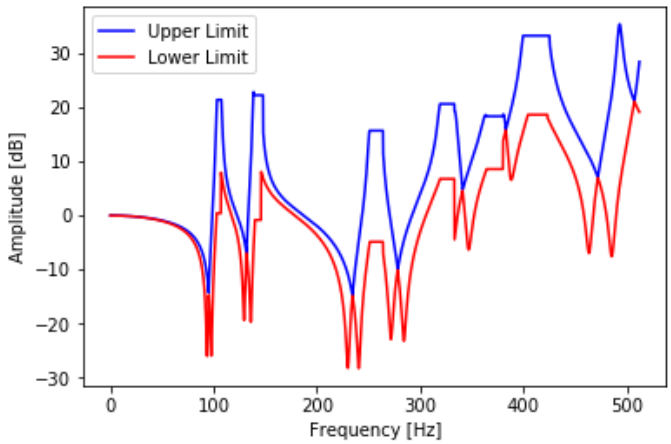

Figure 4: FRF obtained on FEM using the updated design variables

Figure 5 presents the FRF limits and the experimental FRF of Plate 09 and Plate 10. It is possible to see that Plate 09 has a higher deviation than Plate 10. Calculating the percentage of the points in the limits, it is possible to note that Plate 09 has 33.28% of its points inner the limits, and Plate 10 has 48.16%. Despite this, looking only for the positive part of the FRFs, it is possible to note that 48.10% of the FRF from Plate 09 is in the limits, whereas Plate 10 has 74.2% of its points within the limits. In addition, looking to the graphic Plate 09 is always on the left of the boundary limits, meaning that this component has a lower stiffness. This could be resulted by some problem on the manufacturing process as a lower thickness, high concentration of resin or even cracks and delaminations.

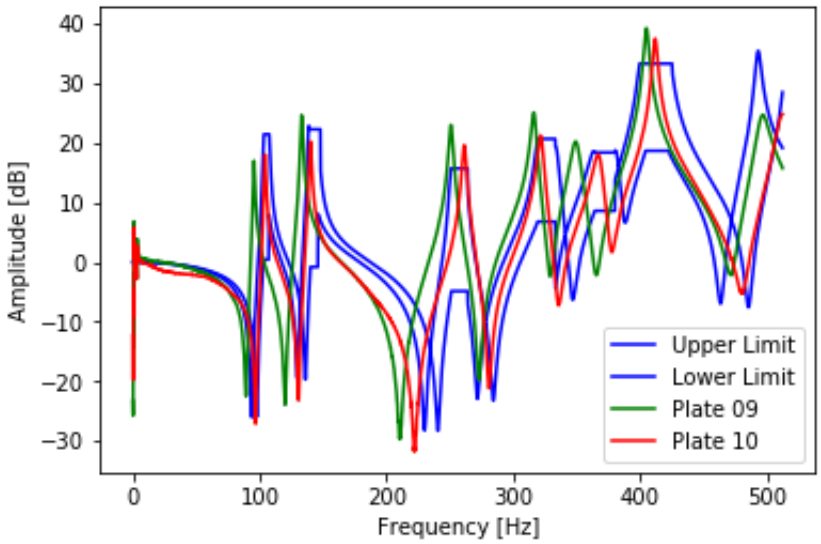

Figure 5: FRF limits and experimental FRF from Plate 09 and Plate 10

Therefore, Plate 09 should be not considered admissible to use as an intact plate in a monitoring system. It means that considering the tolerance of standard deviation from the analyzed set of plates, this plate does not match with the requirements, and should be verified about some manufacture imperfection.

7. CONCLUSIONS

This paper assesses the dynamic behavior of composite plates aiming to better identify the conditions after manufacturing. The experimental analysis shows clearly the variability on dynamic behavior for components manufactured with the same conditions, once the standard deviation for the natural frequency is about 4 to 8 Hz. A model update process using Kriging Metamodel was used to obtain the extreme values of the dynamic behavior. This metamodel allows a reduction of the computational time during the model update, approximately from 1 hour to 10 minutes when compared with a pure Finite Element Analysis-based model update (desktop computer, memory: 4Gb, processor: Intel i5). The envelope generated on the case presented shows the identification of the admissible components that have more than 70% of its FRF inner the envelope. Therefore, these results show that it is possible to identify components with the required specifications in terms of dynamic behavior.

ACKNOWLEDGMENTS

The authors acknowledge the financial support of the State Research Founding Agency (FAPESC process number: 2017TR1747 and 2017TR784). As well as, Sao Paulo State Research Foundation (FAPESP process number: 2012/01047-8 and 2015/15221-8), Coordination for the Improvement of the Higher Level Personnel (CAPES process number: 011214/2013-09), National Council for Scientific and Technological Development (CNPq process number: 401170/2014-4 and 310094/2015-1). The authors also would like to thank Navy Technological Centre (CTM – Brazil) for manufacturing specimens and Prof. Joel Martins Crichigno Filho (Santa Catarina State University - Brazil) for kindly providing the use of the ABAQUS™ license.

REFERENCES

[1] Alaswad, S., & Xiang, Y. (2017). A review on condition-based maintenance optimization models for stochastically deteriorating system. Reliability Engineering & System Safety, 157, 54-63.

[2] Rastegari, A., Archenti, A., & Mobin, M. (2017, January). Condition based maintenance of machine tools: Vibration monitoring of spindle units. In Reliability and Maintainability Symposium (RAMS), 2017 Annual (pp. 1-6). IEEE.

[3] Peeters, C., Guillaume, P., & Helsen, J. (2018). Vibration-based bearing fault detection for operations and maintenance cost reduction in wind energy. Renewable Energy, 116, 74-87.

[4] De Medeiros R, Vandepitte D, Tita V. Structural health monitoring for impact damaged composite: a new methodology based on a combination of techniques. Structural Health Monitoring, v17, n.2, p.185-200, 2018.

[5] Sohn H, Farrar CR, Hemez FM, Czarnecki J. A review of structural health monitoring literature. Report, Los Alamos, NM: Los Alamos National Laboratory, 2003.

[6] Sinou J. A review of damage detection and health monitoring of mechanical systems from changes in the measurement of linear and non-linear vibrations, Robert C. Sapri. Mechanical Vibrations: Measurement, Effects and Control, Nova Science Publishers, Inc., pp.643-702, 2009, 978-1-60692-037-4.

[7] Farrar CR, Doebling SW, Nix DA. Vibration based structural damage identification. Philosophical Transactions of the Royal Society A, 2001(359):131149.

[8] Montalvo D, Maia MMN, Ribeiro AMR. A review of vibration-based structural health monitoring with special emphasis on composite materials. Shock and Vibration, 2006(38):295-324.

[9] Kim JT, Ryu YS, Cho HM, Stubbs N. Damage identification in beam-type structures: frequency-based method vs mode-shape-based method. Engineering Structures, 2003(25):57-67.

[10] Kessler SS, Spearing SM, Atalla MJ, Cesnik CE, Soutis C. Damage detection in composite materials using frequency response methods. Composites Part B: Engineering, 2002(33):87-95.

[11] De Medeiros R, Lopez H, Guedes R, Vaz M, Vandepitte D, Tita V. A new approach for SHM system: Combination of vibration based method and shearography speckle. In: 5th International Symposium on Solid Mechanics (MecSol2015), Belo Horizonte, Brazil, 2015.

[12] Magalhães F, Cunha A, Caetano E. Vibration based structural health monitoring of an arch bridge: From automated OMA to damage detection. Mechanical Systems and Signal Processing, 2012(28):212-228.

[13] Souza L F S, Tita V, De Medeiros R. Composite Plates Model Update using Kriging Method. In: 24th ABCM International Congress of Mechanical Engineering (COBEM2017), Curitiba, Brazil, 2017.

DESIGN OPTIMIZATION OF A COMPOSITE PRESSURE VESSEL USING FEA AND DERIVATIVE BASED METHOD

Luiz G. Oliveira [(1)], Rafael B. Leite [(1)], Pablo A. Munõz-Rojas [(1)] and Ricardo De Medeiros [(2)]

(1) Department of Mechanical Engineering, Santa Catarina State University, Brazil.

https://doi.org/10.21452/bccm4.2018.16.07

Abstract

This paper presents a design optimization, in a thin wall elliptical-headed pressure vessel, considering 2:1 axis rate. The aim is the thickness optimization of the layers of fiber composite material, made of carbon fiber and epoxy resin, using the derivative-based method. It is considered the layup orientation as design variables. Also, the Tsai-Wu failure criterion, evaluated from the stresses calculation by the classical laminate theory, which uses the membrane forces obtained by FEA (Finite Element Analysis), is taken as a constraint for the optimization. In order to reduce computational cost, there is no interaction of the optimization algorithm with the FEA. The stiffness is changed during optimization using constant membrane forces. At the end of the optimization, the membrane forces are recalculated by FEA considering the current rigidity of the structure. The procedure is repeated iteratively until the stress matches the stop criteria. Finally, the safety factor established by ASME is verified, considering a certain class of pressure vessel.

Key-words: Design optimization, Composite materials, Finite element method, Tsai-Wu failure criterion.

1. INTRODUCTION

High-pressure vessels are widely used in commercial and aerospace industries, such as fuel tanks, portable oxygen storage, and compressed natural gas (CNG) pressure vessels for transportation vehicles [1]. On the other hand, the use of fiber reinforced, and polymer-based composites have been increasing. Various numbers of applications have also been flourishing with this development. Parnas and Katirci [2] developed an analytical procedure to design and predict the behavior of fiber-reinforced composite pressure vessels under combined mechanical and hygrothermal loading. Liang *et al.* [3] investigated the optimum design of dome contours for filament-wound composite pressure vessels, subjected to the Tsai–Wu failure criterion and involving problems of the maximum shape factor. The stress field is modeled using classical lamination theory. Pelletier and Vel [4] described a methodology for the multi-objective optimization of fiber reinforced composite materials for strength, stiffness and minimal mass via

the layerwise tailoring of fiber orientations and fiber volume fractions. Vafaeesefat [1] presented a new strategy to optimize composite pressure vessels with metallic liners using an adaptive response surface method. The finite analysis is used to evaluate the fitness function and constraints. Romeo *et al.* [5] used a genetic algorithm to optimize the laminate layup to reduce the weight of the tank and ensure that it can resist without at failing catastrophically.

In this paper, a new methodology is proposed for design optimization of complex structures such as a composite pressure vessel. The Finite Element Analysis (FEA) and derivative-based method are used to analyze the pressure vessel. The Tsai–Wu yield criteria are used as a failure criterion for the composite section. The stiffness is modified using constant membrane forces after it is updated and refined optimization. The procedure is repeated iteratively until the stress matches the design criteria. Finally, the safety factor established by ASME is verified, considering a certain class of pressure vessel.

2. MATERIAL AND METHOD

2.1 Material

The composite laminated is symmetrical and quasi-isotropic, with 20 layers and stacking orientation of $[0/45/-45/90/0/45/-45/90/45/-45]_S$. Also, the thickness of 0.6 mm per layer (*i.e.* total thickness of 12 mm). The used material is carbon fiber and epoxy resin H3501 [6], with the properties, shown in Table 1.

Table 1: Material properties of carbon-epoxy H3501 [6].

Elastic properties		**Strength values**	
E_{11} = 138,0 GPa	$\nu 12$ = 0,3	X_t = 1447,0 MPa	Y_c = -206,0 MPa
E_{22} = 8,96 GPa	G_{12} = 7,1 GPa	X_c = -1447,0 MPa	S_{12} = 93,0 MPa
$\nu 12$ = 0,3	G_{13} = 7,1 GPa	Y_t = 51,7 MPa	

2.2 Optimization Method

The optimization project is divided into external iterations, pre-optimization, and internal optimization. The external iterations aim to update the membrane forces through FEA (finite element analyze) considering the current condition. The pre-optimization, improve the current critical region and aims to reveal another region that becomes critical. Thus, it was considered both regions simultaneously during optimization. Finally, the internal iterations are intended to optimize a laminated composite that meets multiple types of loads. Figure 1(a) illustrates the pressure vessel section analysis, where the Tsai-Wu critical criteria regions are located. The project starts from the minimum thickness required to withstand the internal pressure using an arbitrary prescribed fiber's orientation with a fixed number of layers. The considered pressure vessel in this study has a 1-meter diameter and, it is submitted to an internal pressure of 4.0 MPa. The mesh used for FEA is shown in Figure 1(b). The geometry was modeled with shell elements, the quadrilateral of 8 nodes, with 6 degrees of freedom per node (rotation in x, y and z-axis, and translation in x, y, and z-axis) in the APDL software, the element is called Shell281 (Ansys nomenclature). At the end of the project, in addition to checking the Tsai-Wu failure criterion, the safety factor is evaluated by the quadratic stress interaction criterion established by [7]. The minimization is done using the method of the conjugate gradients. For this, the information of the first derivative is necessary. The objective function is modeled by the internal penalty method,

$$\begin{aligned} &\boldsymbol{minimize}\ f(\boldsymbol{x}) \\ &\textbf{such that}\ g(\mathbf{x}) \geq 0, j = 1, \ldots, n_g, \end{aligned} \tag{1}$$

where $g_j(x)$ is the j-nth constraints and n_g is the total number of constraints. The optimization problem with penalty function [8] is,

$$\textbf{minimize}\ \phi(x,r) = f(\mathbf{x}) + r\sum_{j=1}^{n_g} 1/g_j(\mathbf{x}), \qquad r = r1, r2, \ldots, r_i \to 0, r_i > 0 \tag{2}$$

where r is the penalty parameter. The constraints are from the Tsai-Wu failure criterion,

$$f_{TW_j}\left(\boldsymbol{\sigma}_{A_j}\right) < 1, \qquad j = 1, \ldots, 20 \tag{3}$$

where $\boldsymbol{\sigma}_{A_j}$ are the stresses in the section A, of the j-nth layer. Thereby,

$$g_j = -f_{TW_j}\left(\boldsymbol{\sigma}_{A_j}\right) + 1 > 0, j = 1, \ldots, 20. \tag{4}$$

The optimization has the thickness of the laminate as the cost function. Setting the equations (4) and the cost function in (2), it is possible to obtain the penalty function.

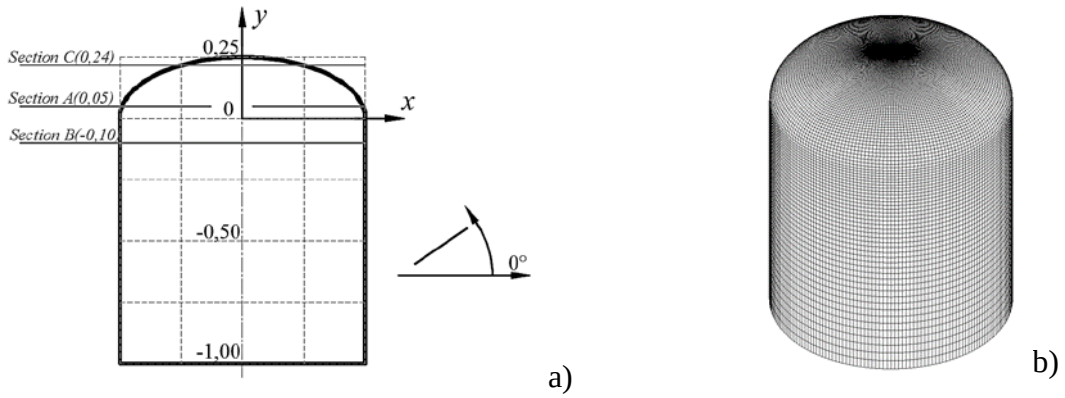

a) b)

Figure 1: Pressure vessel geometry: a) Arrangement of the vessel in the coordinate system and approximate position of the analyzed sections, b) finite element mesh.

2.3 Failure Criteria

The Tsai-Wu failure criterion represents a factor from the quadratic combination of stresses. In addition, it takes into account the different behavior of resistance in traction and compression [9]. The expression for an orthotropic plane [10] in-plane stress state can be represented by,

$$f_{TW} = F_1\sigma_1 + F_2\sigma_2 + F_{11}\sigma_1^2 + F_{22}\sigma_2^2 + F_{66}\sigma_{12}^2 + 2F_{12}\sigma_1\sigma_2 < 1 \tag{5}$$

where,

$$\begin{aligned} &F_1 = \frac{1}{X_t} + \frac{1}{X_c}, F_{11} = -\frac{1}{X_cX_t}, F_2 = \frac{1}{Y_t} + \frac{1}{Y_c}, \\ &F_{22} = -\frac{1}{Y_tY_c}, F_{66} = \left(\frac{1}{S_{12}}\right)^2, F_{12} = -\frac{1}{2}\sqrt{F_{11}F_{22}} \end{aligned} \tag{6}$$

The Quadratic Interaction Strength Criterion designed by [7] is equal to the Tsai-Wu failure criterion and establishes R as a safety factor used in the design methodology by discontinuity analysis. Where must meet R > 1,

$$\mathrm{R}^2(F_{11}\sigma_1^2 + 2F_{12}\sigma_1\sigma_2 + F_{22}\sigma_2^2 + F_{66}\sigma_{12}^2) + R(F_1\sigma_1 + F_2\sigma_2) - 1 = 0 \tag{7}$$

where σ_{ij} are the stress in the local coordinate system of the layer.

3. RESULTS AND DISCUSSION

The mesh convergence is based on the interest variable, *i.e.* the membrane forces. Figure 2 shows the convergence of the main membrane forces by the division number in the circumference. The division's number adopted is 200.

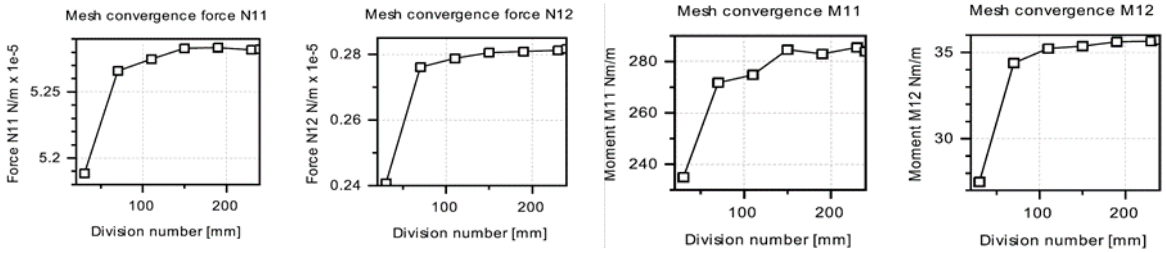

(a) (b) (c) (d)

Figure 2: Mesh convergence for forces: a) N_{11}, b) N_{12}, c) M_{11}, d) M_{12}.

3.1 Preliminary optimization results

When evaluating the Tsai-Wu criterion for the pressure vessel along the axial coordinate, the critical region can be identified. Figure 3(a), illustrates this region marked in the graph as section A, on coordinate y = 0.05 m. The critical value, therefore, occurs on the layer 20. In Figure 3(b), it is illustrated the failure criterion for the layer 20 and its symmetrical layer 1, both at 0°, where loads effect due to the shape transition cylindrical-head can be noted, which justifies the difference of the curves for layers 20 and 1.

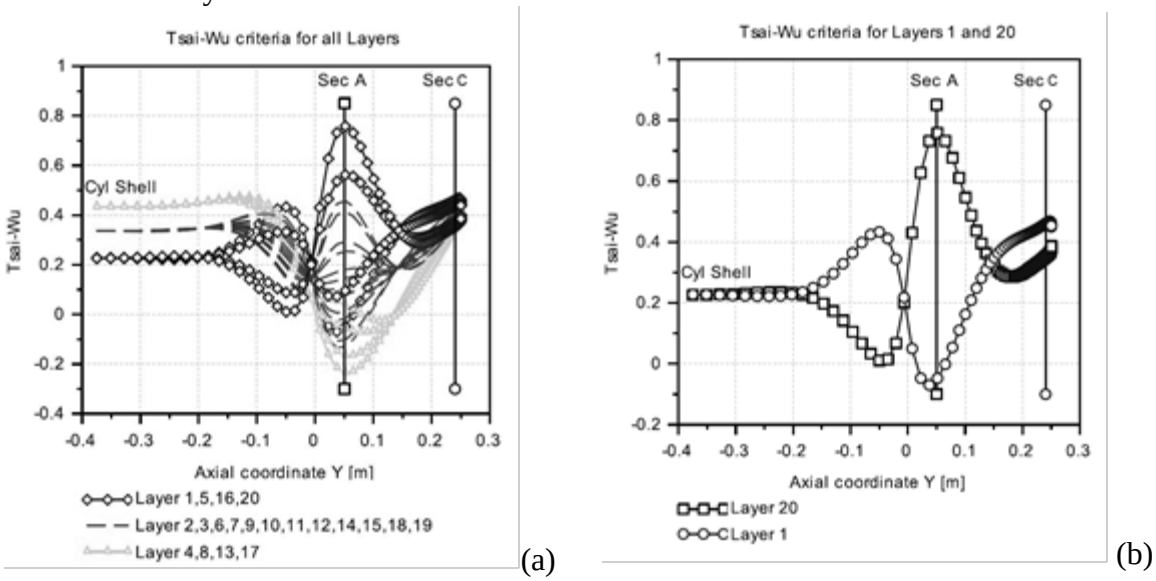

(a) (b)

Figure 3: Tsai Wu criteria along the axial coordinate before any optimization: a) Projection of the 20 layers overlapping. b) Projection of the layer 20 and layer 1.

Based on this preliminary analysis, the pre-optimization of the laminate is carried out, taking in consideration the membrane loading that acts in section A. The result of the pre-optimization allows identifying a new critical region, which must be considered simultaneously in the optimization.

3.2 Approximation of the optimal result from constant forces

The failure criterion is evaluated along the pressure vessel for the pre-optimized structure, given that it is possible to identify the new region to be considered. The Figure 4(a), illustrates this region demarcated by section B. With the knowledge of the new critical section, the objective function is modified and the constraints in the eq. (2) become,

$$g_j = \begin{cases} -f_{TW_j}\left(\boldsymbol{\sigma}_{A_j}\right) + 1 > 0 \\ -f_{TW_j}\left(\boldsymbol{\sigma}_{B_j}\right) + 1 > 0 \end{cases} \qquad j = 1, \ldots, 20. \tag{8}$$

Since the starting point must be in the feasible domain, the optimization is restarted with the modified objective function. The result of the multi-objective optimization is shown in Figure 4(b).

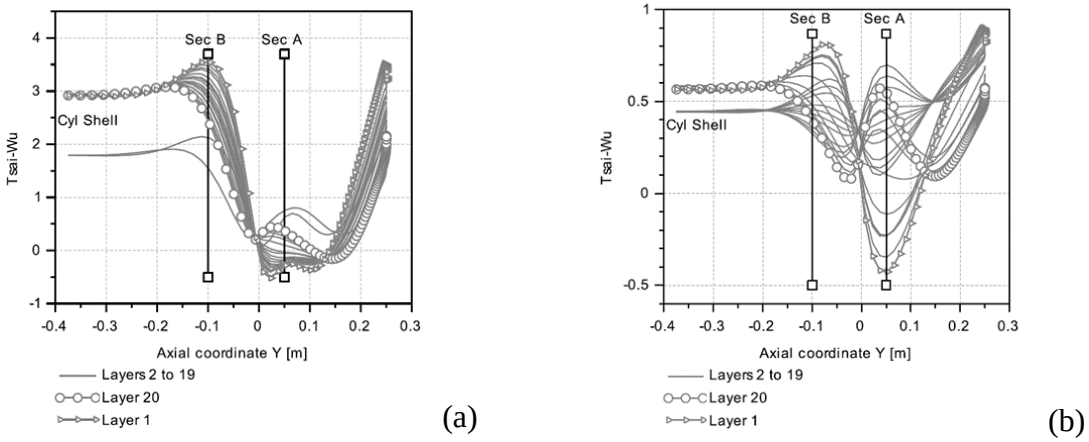

(a) (b)

Figure 4: First optimization step, a) single optimized critical region, b) two critical optimized regions simultaneously.

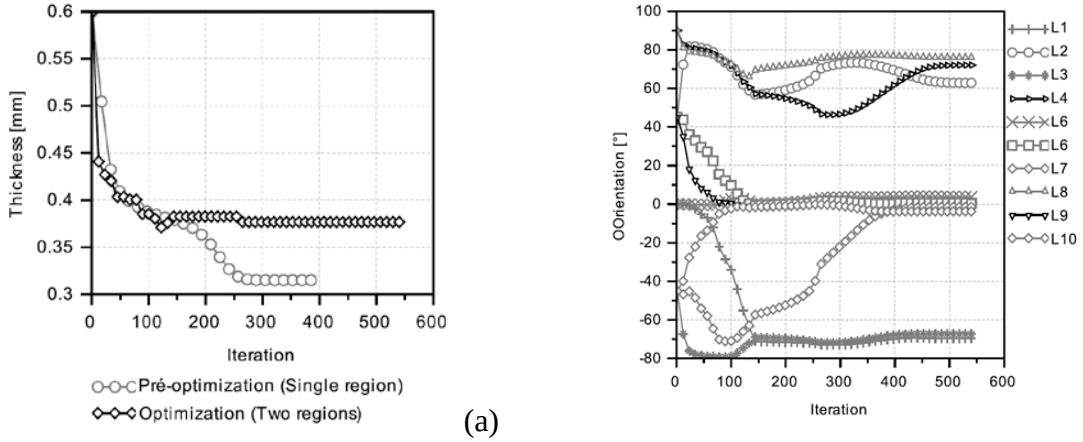

(a) (b)

Figure 5: Convergence, a) of thickness for a single region and two regions, b) convergence of the orientations considering both regions.

The stopping criterion is taken from the convergence of the thickness. When only a single critical section is considered, the found thickness is less than when two regions are considered. This is evident since it is easier to satisfy the failure criterion for only one loading condition than for two simultaneously. Figure 5(a) shows the convergence of the thickness for one region and two simultaneously and, Figure 5(b) shows the convergence of slopes as design variables. The result of the first step of the optimization was a total thickness of 7.53 mm or 0.376 mm for each layer with orientation [-70/64/-67/71/5/0/-2/75/-4/4]s. With this result, the geometric properties of the

finite element problem were updated, and the membrane forces were obtained for the new structure to refine the optimization.

3.3 Optimization using updated membrane forces

At this stage, the same systematics of the previous step is adopted. Therefore, it is started from the orientations obtained from the current result [-70/64/-67/71/5/0/-2/75/-4/-4], with a thickness of 0.5 mm per layer (10mm in total thickness) and with updated membrane forces. Figure 6(a) shows the Tsai-Wu failure criterion for the optimized structure indicating the two sections A and C, considered simultaneously for the optimization. Figure 6(b) shows the behavior of the thickness' convergence for the pre-optimization and the final optimization. The final total thickness found is 8.15 mm and orientations of [-74/22/-74/69/-2/-2/-2/70/-3/74]s. Finally, the structural problem of finite elements is again updated, where the membrane forces are extracted to the current configuration.

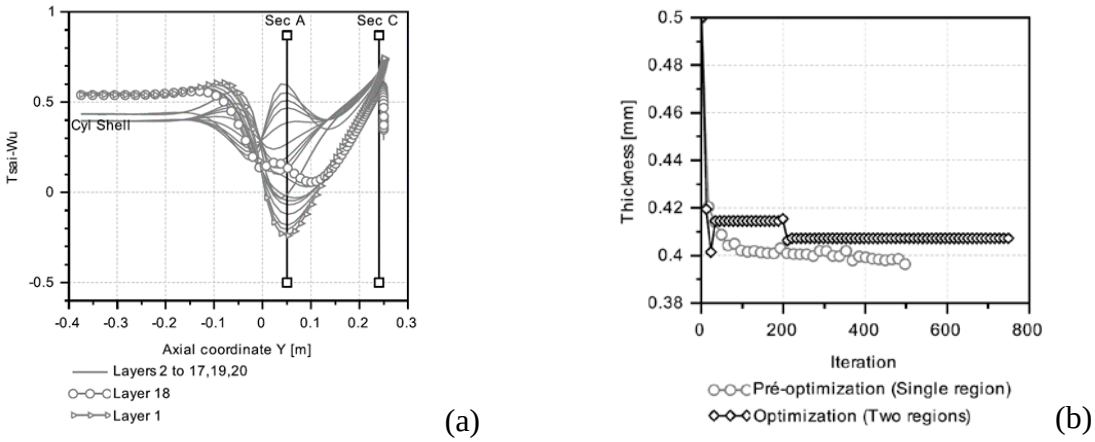

Figure 6: Results of the second stage of optimization. a) Projection of the 20 layers overlapping for Tsai Wu criteria along the y coordinate. b) Convergence of the pre-optimization and optimization.

3.4 Solution analysis

Figure 7 illustrates the convergence for global optimization. Membrane forces N_{11}, N_{22}, N_{12}, and M_{11} have undergone minor changes, on the other hand, the membrane moments M_{22} and M_{12} are in general more sensitive to modification in the structural rigidity. Figure 8 shows the difference between moments M_{22} and M_{12}, for initial and optimized structure. However, the membrane forces used to make the last optimization iteration, are close to the actual forces for the optimized structure except for the moment M_{22} and M_{12}. However, this difference was not enough to make the result unfeasible. This can be verified through the Figure 9, with the new configuration of the laminate and the convergence of the membrane forces verified, the criterion of Tsai-Wu failure is verified for the mesh of the pressure vessel. In addition, it is possible to verify the Quadratic Interaction of Stress Criterion established by [7]. Figure 9 illustrates the failure criteria for the optimal structure, where the two most critical layers 2 and 19 are highlighted. Finally, no section of the vessel exceeds the failure criterion. With this, we have the optimized layup and thickness.

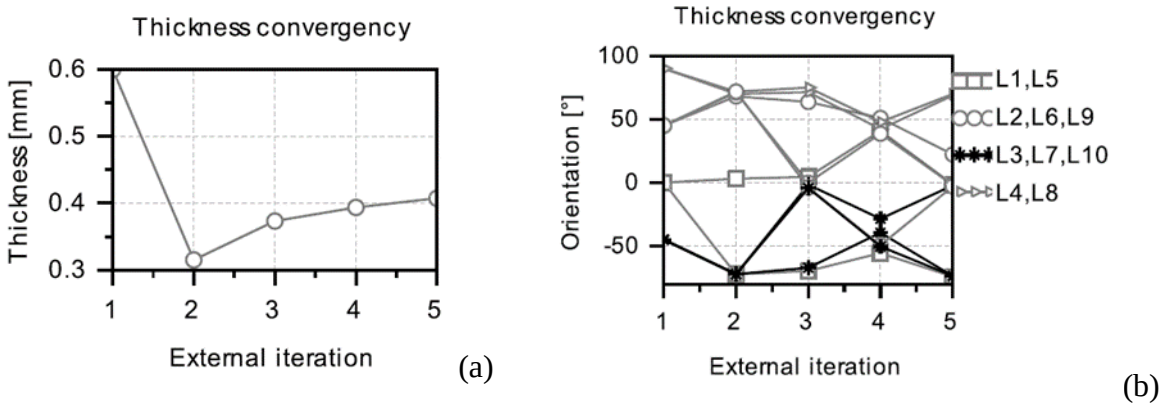

(a) (b)

Figure 7: Failure criterion for the optimum design, a) Tsai-Wu, b) Safety factor R by [7].

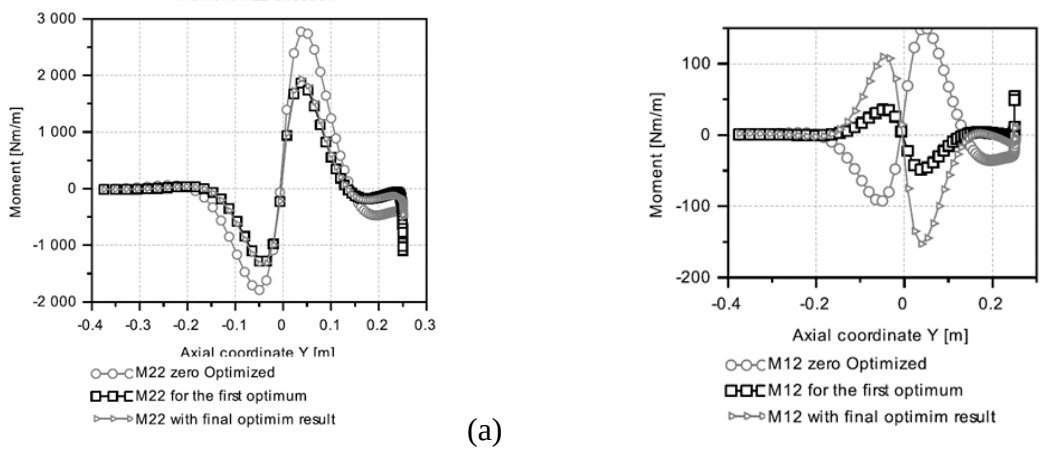

(a) (b)

Figure 8: Membrane forces along the optimization: a) Moments M_{22} and b) Moments M_{12}.

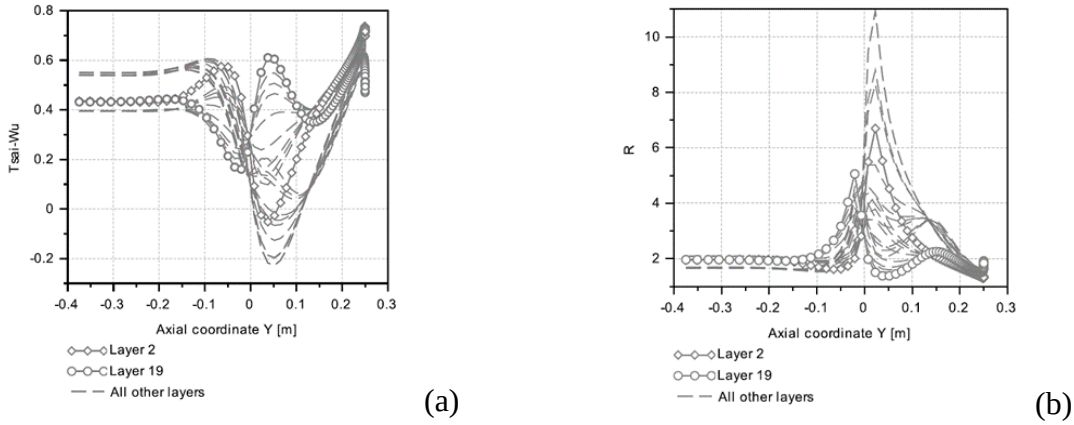

(a) (b)

Figure 9: Failure criterion for the optimum design: a) Tsai-Wu, b) Safety factor R by [7].

4. CONCLUSIONS

This paper presented an optimization design in a thin wall pressure vessel under internal pressure. The internal optimization iterations without updating the membrane forces by finite elements bring great advantage due to the substantial reduction of computational cost. Although this procedure, for the time being, is more amenable to restricted problems, where normal

membrane stresses N_{xx} is predominant with respect to M_{xx} membrane moments, typical cases of pressure vessels. The agreement with a failure criterion established by a design standard provides credit to evaluate and adjust the study to be used as a methodology for pressure vessel design by analysis. The advantage of using the internal penalty method is that the whole optimization project takes place within the feasible domain, it is, at any time that the optimization is interrupted, there is a feasible optimized result. On the other hand, it impairs the convergence to the global optimum, especially when it is under active constraints. This is a limitation of the internal penalty method. The use of the derivative method yields a future comparison with stochastic optimization methods for this problem nature. The starting point was a lay-up of 0.6 mm per layer or 12.0 mm total thickness, no reduction [0/45/-45/90/0/45/-45/90/45/-45]s, of significant thickness was possible without changing the orientation of the fibers. After optimization, the stacking orientation variables found are [-74/22/-74/69/-2/-2 /-2 /70/-3/74]s and thickness of 0,408 mm per layer or 8,15 mm total, *i.e.* 3.85 mm of total thickness was reduced from the initial laminate. Therefore, this methodology can help in the development of the design of composite pressure vessel.

ACKNOWLEDGMENTS

The authors acknowledge the financial support of the State Research Founding Agency (FAPESC process number: 2017TR1747 and 2017TR784).

REFERENCES

[1] Vafaeesefat, A., 'Optimization of composite pressure vessels with metal liner by adaptive response surface method', *J Mech. Sci. Technol.* **25 (**11) (2011) 2811-2816.
[2] Parnas, L., Katirci, N., 'Design of fiber-reinforced composite pressure vessels under various loading conditions', *Compos. Struct.* **58 (**1) (2002) 83-95.
[3] Liang, C.-C., Chen, H.-W., Wang, C.-H., 'Optimum design of dome contour for filament-wound composite pressure vessels based on a shape factor', *Compos. Struct.* **58 (**4) (2002) 469-482.
[4] Pelletier, J.L., Vel, S.S., 'Multi-objective optimization of fiber reinforced composite laminates for strength, stiffness and minimal mass', *Comput. Struct.* **84 (**29-30) (2006) 2065-2080.
[5] Romeo, G., Danzi, F., Cestino, E., Borello, F., 'Design and optimization of a composite vessel for hydrogen storage subject to internal pressure and in-flight loads for UAVs', *Int. J. Aerospace Sci.* **2 (**3) (2013) 124-137.
[6] Agarwal, B.D., Broutman, L.J., Chandrashekhara, K., 'Analysis and performance of fiber composites', 3rd Ed (New York, John Wiley & Sons, 2006).
[7] ASME Boiler and Pressure Vessel Code, Fiber Reinforced Plastic Pressure Vessels, NY, 2015.
[8] Haftka, R.T., Gürdal, Z., 'Elements of structural optimization', 3rd Ed (New York, Springer-Verlag, 1991).
[9] Jones, R.M., 'Mechanics of Composite Materials', 2nd Ed (Philadelphia: Taylor & Francis, Inc., 1998).
[10] Barbero, E.J., 'Introduction to composite materials design', 2nd Ed (New York: Taylor & Francis Group, 2010).

MULTIOBJECTIVE OPTIMIZATION OF COMPOSITE RISERS

Marina A. Maia (1) **and Evandro Parente Jr.** (1)

(1) Laboratório de Mecânica Computacional e Visualização, Universidade Federal do Ceará, Fortaleza, Brazil.

https://doi.org/10.21452/bccm4.2018.16.08

Abstract

Use of fiber-reinforced laminated composites has proved itself as a valuable option in the manufacturing of risers, particularly for deepwater applications, a scenario where its lightweight related properties and good fatigue resistance are most needed. In addition, its use allows these structures to be tailored to meet specific manufacturing, safety, and stability criteria. This paper proposes an optimization model to composite risers in a free-hanging catenary configuration that considers multiple load cases and two objective functions. The optimization is carried out using a modified version of the Nondominated Sorting Genetic Algorithm II (NSGA-II). The riser structural analysis is performed by an inextensible cable model that accounts for the vertical static loads, floater offset and current loads in a fast and efficient way. The proposed algorithm is validated using a benchmark problem and applied to obtain the Pareto Front of a composite riser.

Keywords: Multiobjective optimization, Catenary risers, Composite materials.

1. INTRODUCTION

In the last few years, offshore projects have been set aside and onshore investments, particularly on tight oil, played a major role in the oil industry, forcing deepwater projects to be even more competitive. At the heart of this discussion are the risers, which work as a physical connection between the subsea wells and the floating production facility and are usually made of steel. An important alternative to help reduce cost is the replacement of steel risers by composite risers, especially in projects with water depths over 2000 m, when the pipeline thickness increases significantly to sustain the higher hydrostatic pressure and the harsh environment and the weight reduction enabled by the composite use is most needed [1].

Composite materials have several others important advantages over metals (e.g. low thermal conductivity, good corrosion resistance and high specific strength and stiffness) and, more importantly, fiber-reinforced laminated composites allow risers to be tailored to meet specific manufacturing, safety, and stability constraints under several different loading conditions by choosing adequate design variables [2]. Using optimization technics in this type of problem could also enable the decision maker to consider features in the project that could be impracticable to do by trial and error, such as the consideration of multiple objective functions. It is important to note

that the balance between better structural performance and cost has always been a major engineering concern.

This paper proposes a methodology to the multiobjective optimization of a composite catenary riser subjected to multiple load cases and constraints. A modified version of the Nondominated Sorting Genetic Algorithm II (NSGA-II), an algorithm proposed by [3] that proved itself as a useful tool for composite structures optimization [4, 5], is used for multiobjective optimization. The riser analysis is performed at two stages as suggests the global-local philosophy and the design variables considered are the ply thickness and fiber angle orientation.

2. COMPOSITE CATENARY RISER

The catenary (or free-hanging catenary) is one of the simplest configurations employed in deepwater offshore exploration and, basically, the riser rests on the seabed, which can significantly reduce the installation and operation costs due to minimal subsea equipment if compared to configurations that demand floating elements to shape their final forms (e.g. Lazy-S and Lazy-Wave). Composite Catenary Risers (CCRs) generally consist of several segments assembled together by its connections, these segments are called joints and they are generally composed by outer and/or inner liner, the composite tube itself and terminations, properly connected to each other. In this work, connections and terminations are only accounted to the riser weight; any other contribution is not addressed since the major concern is to optimize the design of the composite tube. Typical positions of a CCR considering the floater offsets and the riser cross-section are depicted in Figure 1.

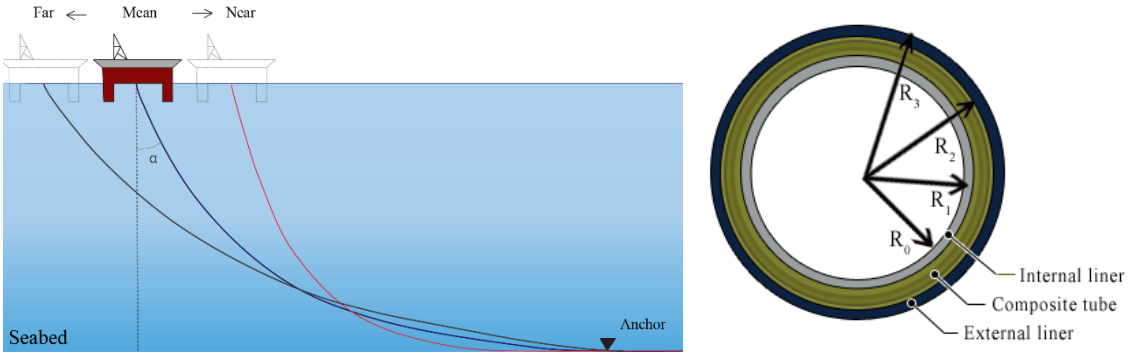

(a) (b)

Figure 96 : (a) Catenary riser scheme (b) Composite riser cross-section

The riser structural analysis is performed in two stages, global and local, this methodology is employed to flexible risers, but also recommend to composite risers [6]. At the global step, an inextensible cable model [7] performs the analysis considering the entire riser system in order to obtain axial forces acting on it and global displacements (bending and torsional moments are neglected); these data are the input for the next stage of the analysis, when stresses and strains at each lamina are evaluated locally by the Classical Laminated Theory (CLT) in several sections of the riser.

2.1 Global Analysis

In order to obtain the riser axial forces, the structure was assumed to behave as inextensible cable - that is, infinite axial stiffness and zero bending stiffness - subjected to vertical static loads

(weight and buoyancy), horizontal (marine currents) and to the offset of the Floating Production Unit (FPU). The first step is to evaluate the dry weight, which consists of the sum of the riser components (internal liner, composite tube, external liner and terminations), next, the internal fluid per length unit (w_{fl}) is calculated and added to the dry weight, while the buoyancy weight is subtracted from it, which leads to the effective weight per unit of the riser (w_{ef}) [8].

2.2 Local Analysis

The CLT is employed to local analysis in several sections of the riser. At this point, internal liner and composite tube are considered as perfectly bound and, therefore, can be analysed as one single structural system, neglecting the external liner, which works only as a protective layer during transport and operation. The riser is subjected to the effective axial force (evaluated at the global analysis), internal and external pressure. Each layer thickness is represented by h_k and the total thickness of the tube by h_t, the structure is, then, modelled as a cylindrical structure composed by N layers, where the first one corresponds to the internal liner and the rest of them to the layers of the composite tube, as shown in Figure 1 (b). To evaluate in-plane forces on the riser wall, the thin-walled tube theory is used, considering load factors recommended by [6, 9]:

$$N_x = \frac{N_{tw}}{2\pi R} = \frac{\gamma_F N_{ef}^{Mean} + \gamma_E(\beta N_{ef} - N_{ef}^{Mean}) + (p_i \pi R_0^2 - p_e \pi R_2^2)}{2\pi R} \qquad (1)$$

$$N_y = p_i R_0 - p_e R_2$$

where N_{tw} is the true wall tension, R is the average radius of the structure composed by the composite tube and the internal liner, β is the dynamic amplification factor, γ_F is the functional load factor and γ_E is the environmental load factor. In this work, N_{xy} is taken as zero, once torsion is not considered, and hydrostatic pressures are computed from:

$$p_i = p_0 + \gamma_{fl}\, h \qquad (2)$$

$$p_e = \gamma_{wat}\, h$$

where p_0 is the pressure on the top of the riser, h is the depth of the riser section where the forces are evaluated and p_i and p_e are the internal and external pressure, respectively.

2.3 Failure Criteria

To compute the composite safety factor, the First-Ply Failure methodology is applied. In this approach, the lowest safety factor evaluated for each layer (SF_k), which is evaluated using Tsai-Wu criterion, is assumed to be the composite safety factor (SF^c), that is, when the first layer fails, the whole structure supposedly fails too. This is a conservative approach, but simple and easy to implement and yield good results. The von Mises criterion is used to evaluate the internal liner resistance (SF^{il}).

2.4 Buckling

In order to assure the structural integrity of the riser, the structure is analysed considering the buckling due to external pressure. Collapse pressure of cylindrical orthotropic shells (P_{col}) is estimated using the CLT and to evaluate the buckling safety factor (SF^{bck}), collapse pressure is divided by the external pressure (P_e), as shown in Eq. (3).

$$SF^{bck} = \frac{P_{col}}{P_e} \tag{3}$$

$$P_{col} = k_p \frac{3}{{R_m}^3}(D_{22} - \frac{{B_{22}}^2}{A_{22}})$$

where k_p is the knock-down factor, a factor that aims to correct the difference between theory and empirical results and to long tubes is worth 0.75, R_m is the medium radius of the riser and D_{22}, B_{22} and A_{22} are coefficients obtained in the $\boldsymbol{A}$, $\boldsymbol{B}$ and $\boldsymbol{D}$ matrices given by the CLT. External pressure is evaluated at the touchdown point (TDP), point where the riser first touches the seabed, since this is where P_e is maximum.

3. DESIGN METHODOLOGY

This section describes the main aspects considered to the composite riser design, starting on with the design variables, which consist of the thickness of each layer (h_k) and the fiber orientation (θ_k). Thus:

$$\mathrm{x} = \{\mathrm{h}_1\ \mathrm{h}_2\ \mathrm{h}_3\ \ldots\ \mathrm{h}_{N_p}\ \theta_1\ \theta_2\ \theta_3\ \ldots\ \theta_{N_p}\}^t \tag{4}$$

where N_p is the maximum number of plies. By imposition, the stacking sequence is the same for all sections of the riser. Typically, thickness and fiber orientations are characterized as discrete variables, since their allowable values belong to a finite set of values due to manufacturing constraints.

The composite tube thickness minimization and buckling safety factor maximization are the criteria selected for the optimization. It is important to notice that, as the stacking sequence is constant and only one material was used, minimization of the composite tube thickness corresponds to the minimization of its cost. Constraints considered in present work are either related to the strength of the composite material and liner or related to the riser stability. Having that in mind, SF_{ij}^l and SF_{ij}^c correspond to the safety factors of the liner and the composite evaluated for load case *i* at section *j* of the riser and SF_{req}^l and SF_{req}^c are the required safety factors to the liner and the composite tube according to [6], respectively. That way, safety requirements of resistance are guaranteed if the following relations are assured:

$$g_{ij}^l(x) = \frac{SF_{req}^l}{SF_{ij}^l} - 1 \leq 0 \tag{5}$$

$$g_{ij}^c(x) = \frac{SF_{req}^c}{SF_{ij}^c} - 1 \leq 0$$

where i = 1, 2, 3, ..., N_{lc}, j = 1, 2, 3, ..., N_{vs}, N_{vs} is the number of sections considered in the riser and N_{lc} is the number of load cases considered. In this work, the buckling safety factor (SF^{bck}) is evaluated at the worst scenario, which corresponds to the empty riser at the TDP and neglecting the resistance of the internal liner. This factor is compared to the required buckling safety factor (SF_{req}^{bck}).

The riser is subjected to internal and external pressure, floater offsets and marine currents. Table 1 summarizes the load cases selected to the numerical example shown later on. It is worth noting that waves are not considered since this would require dynamic analysis that could significantly

increase computational cost and present work aims to present a simple and efficient optimization methodology for the preliminary design of composite risers.

Table 48 : Load cases

Description	Offset (% of WD)	Position	Fluid density (kg/m³)	Pressure on top (MPa)	Marine current profile	
	Δ_{os}		ρ_{fl}	p_0	Vertical coordinates (m)	Current velocity (m/s)
Max. production	8.5	*Far*	880.0	30.0	(0; WD)	(0; 1.0)
Max. production	8.5	*Near*	880.0	30.0	(0; WD)	(0; -1.0)
Empty riser	8.5	*Far*	0.0	0.0	(0; WD)	(0; 1.0)
Empty riser	8.5	*Near*	0.0	0.0	(0; WD)	(0; -1.0)
Hydrotest	3.0	*Far*	1006.0	37.5	(0; WD)	(0; 0.30)
Hydrotest	3.0	*Near*	1006.0	37.5	(0; WD)	(0;-0.30)

WD: Water depth.

The NSGA-II is as a fast and elitist multiobjective optimization algorithm that evolves its population of solutions through many processes of sorting [3]. The main modifications made in this work are related to how the algorithm deals with composite laminated problems, especially when it comes to the encoding of the variables and specific operators. Here, the encoding of the design variables is made using a correspondence of the *n* allowable thickness values to a list of numbers from 1 to *n*, in which each value of that list corresponds to a design variable, the same process is done to the fiber orientation. This is especially useful for the algorithm operations such as crossover and mutation. Another important feature implemented, particularly for hybrid composite laminated problems, is the modification of a small number of solutions (randomly selected) in a way that these solutions are modified to be composed by only one material, which could take many generations for the algorithm to generate by itself. Computational implementation was done in an in-house software written in C++.

4. NUMERICAL EXAMPLES

In order to validate the algorithm implementation, a benchmark named TNK is selected. Once this verification is done, a numerical example of a CCR is illustrated.

4.1 Validation

The benchmark objective functions are $f_1 = x_1$ and $f_2(x) = x_2$, the two continuous variables have bounds $[0, \pi]$ and two constraints, $g_1(x) = -x_1^2 - x_2^2 + 1 + 0.1\cos[16\arctan\left(\frac{x_1}{x_2}\right)] \leq 0$ and $g_2(x) = (x_1 - 0.5)^2 + (x_2 - 0.5)^2 \leq 0.5$. The number of optimizations, population size, mutation probability, crossover rate and the maximum number of generations were set as 10, 100, 5%, 100% and 500, respectively. Results are presented in Figure 2·

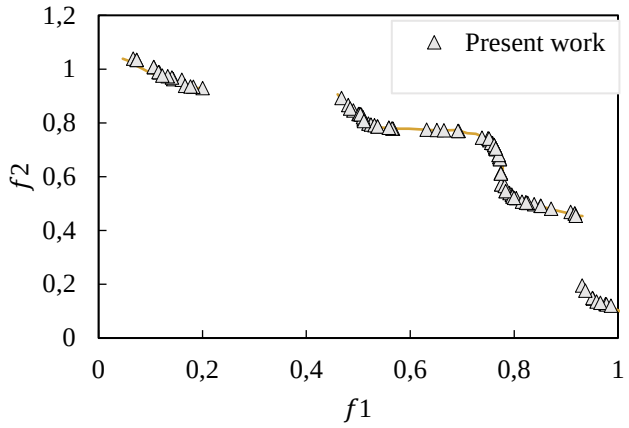

Figure 97 :Results for TNK problem

Results show great agreement between the Pareto Front found by [3] and present work, proving the good functioning of the algorithm.

4.2 Composite catenary riser

In this example, water depth is considered as 1500 m, riser length is taken as 4500 m, the internal liner has 0.125 m of thickness, top angle (α) is 17° and the maximum number of plies is 30. The thicknesses of the internal and external liner are set as 0.005 and 0.003 m, respectively. Terminations are taken as 5% of the joint length and are made of steel. When it comes to the load factors, the following values for the functioning load factor (γ_F), environmental load factor (γ_E) and amplification factor (β) were considered: 1.1, 1.3 and 1.5. Required SFs considering [6, 9] were found to be: 1.3 for the internal liner (SF_{req}^{il}), 2.1 for the composite tube (SF_{req}^{c}) and 3.0 for the buckling (SF_{req}^{bck}). The drag coefficient is set as 1.0 and load cases presented previously on the design methodology section are used. The properties of the composite material (γ_{comp}= 15.69 kN/m³) are shown in Table 3, degraded properties, that is, when the matrix of the composite material is considered as failed, were evaluated according to [9], the FPF analysis, then, becomes equivalent to a First-Fiber Failure (FFF) analysis, once fibers are the only ones resisting. To the internal liner manufacturing steel API X65 was selected, which has a yield stress of 203 MPa and Poisson's coefficient of 0.3, for the external liner a polymeric material of weight 9.04 kN/m³ was used.

Table 49 : Composite material properties

$\boldsymbol{E_1}$ (GPa)	E_2 (GPa)	$\boldsymbol{G_{12}}$ (GPa)	ϑ	F_{1t} (MPa)	F_{1c} (MPa)	$\boldsymbol{F_{2t}}$ (MPa)	F_{2c} (MPa)	$\boldsymbol{F_{3t}}$ (MPa)	$\boldsymbol{F_{3c}}$ (MPa)	S (MPa)
135.00	10.00	5.00	0.30	1500.00	1200.00	50.00	250.00	50.00	250.00	70.00

The following algorithm parameters were set: 100 generations, 100 individuals, 5% of probability of mutation, 100% of crossover rate and 3 optimizations. The allowable values for ply thickness vary from 1 mm to 5 mm in steps of 1 mm, while the allowable angles vary from 0º to 90º in steps of 5º. Only symmetrical and balanced lay-ups are allowed. Results are shown in Figure 4, followed by Table 3, which presents one stacking sequence for each curve.

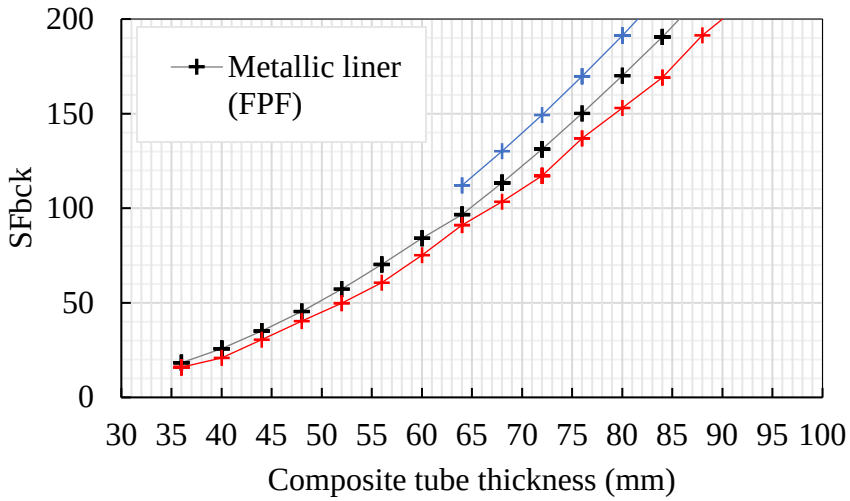

Figure 98 : Nondominated solutions for different combinations of liner and composite material

Table 50 : Lay-ups for different combinations of liner and composite material

Liner/Composite		Lay-up	Constraints		Objective functions	
			SF^{il}	SF^{c}	SF^{bck}	h_t
Metallic/Intact (FPF)	h (mm)	[1, 1, 1, 1, 1, 1, 1, 1, 1, 1, 2, 2, 2, 2]s	1.37	2.33	18.31	36
	$\boldsymbol{\theta}$ (º)	$[\pm 85, \pm 80, \pm 65_2, \pm 15, \pm 20_2]$s				
Metallic/Degraded (FFF)	h (mm)	[1, 1, 1, 1, 1, 1, 2, 2, 1, 1, 2, 2, 1, 1]s	1.30	4.67	16.61	36
	$\boldsymbol{\theta}$ (º)	$[\pm 75, \pm 85, \pm 80, \pm 10, \pm 55, \pm 15]$s				
No liner/Intact (FPF)	h (mm)	[4, 4, 3, 3, 2, 2, 1, 1, 1, 1, 4, 4, 1, 1]s	-	2.29	112.04	64
	$\boldsymbol{\theta}$ (º)	$[\pm 85_5, \pm 15_2]$s				

It can be seen that the consideration of the matrix failure does not directly affect the composite tube thickness optimization when the liner is considered in the project. However, different stacking sequences for the same tube thickness do change the buckling safety factor. Naturally, when the composite is considered intact, SFs were higher. When no internal liner was considered, the composite tube was 78% thicker and presented a much higher SF^{bck}. However, this is a tricky conclusion, once the global cost of the structure considering its assemble and manufacturing cost may increase with the use of an internal liner.

5. CONCLUSION

The main purpose of this work is to present a methodology to the multiobjective optimization of catenary risers, which is a powerful tool to help the decision maker choose between solutions obtained from criteria that are often a trade-off. A benchmark from the literature was used to validate the algorithm. In the numerical example of a composite riser, solutions obtained showed that either FPF or FFF analysis led to the same minimum composite tube thickness when the

internal liner is considered (although with different safety factors). On the other hand, the absence of such component showed a high impact on the chosen optimization criteria. Finally, it is important to highlight that the objective functions can be easily modified in order to represent other criteria that need to be optimized.

ACKNOWLEDGEMENTS

The financial support by CNPq (Conselho Nacional de Desenvolvimento Científico e Tecnológico) and FUNCAP (Fundação Cearense de Apoio ao Desenvolvimento Científico e Tecnológico) are gratefully acknowledged.

REFERENCES

[1] U.S. Energy Information Administration, 'Trends in U.S. Oil and Natural Gas Upstream Costs', Report, March, 2016.
[2] Ochoa, O. O., 'Composite Riser Experience and Design Guidance', Offshore Technology Research Center Library, Technical Report, Texas, 2006.
[3] Deb, K., Pratap, A., Agarwal, S. and Meyarivan T., 'A Fast and Elitist Multiobjective Genetic Algorithm', *IEEE Transactions on Evolutionary Computation*. **6** (2) (2002) 182–197.
[4] Kalantari, M., Dong, C. and Davies, I. J., 'Multi-objective robust optimisation of unidirectional carbon/glass fibre reinforced hybrid composites under flexural loading', *Composite Structures*. **138** (2016) 264–275.
[5] Vo-duy, T., Duong-gia, D., Ho-huu, V., Vu-do, H. C. and Nguyen-thoi, T., 'Multi-objective Optimization of Laminated Composite Beam Structures Using NSGA-II Algorithm', *Composite Structures.* **168** (2017) 498–509.
[6] Det Norske Veritas, 'DNV-RP-F202 Composite Risers', October, 2010.
[7] Alves, J. C., Parente Junior, E., 'Análise numérica de risers utilizando um modelo de cabo inextensível' in Iberian Latin American Congress on Computational Methods in Engineering, Brasília, Brazil, 2016.
[8] Silva, R. F., Teófilo, F. A. F., Parente Junior, E., Melo and A. M. C., Holanda, A. S., 'Optimization of composite catenary risers', *Marine Structures.* **33** (2013) 1-20.
[9] Det Norske Veritas, 'DNV-OS-C501 Composite Components', November, 2013.

ISOGEOMETRIC ANALYSIS OF FGM PLATES

Samir P. Auad [(1)], Jamires S. C. Praciano[(1)], Elias S. Barroso[(1)], João B. M. Sousa Jr. [(1)] and Evandro Parente Jr. [(1)]

(1) Departamento de Engenharia Estrutural e Construção Civil, Universidade Federal do Ceará, Brazil

https://doi.org/10.21452/bccm4.2018.16.09

Abstract

This work presents an isogeometric formulation for the geometrically nonlinear analysis of functionally graded material (FGM) plates. FGM plates are made of a mixture of two components (ceramic and metal) whose volume fractions vary smoothly along the thickness. The kinematic model is based on the Reissner-Mindlin theory for bending and shear strains and the von Kármán theory for nonlinear membrane strains. Non-Uniform Rational B-splines (NURBS) are used as basis functions for the isogeometric formulation. The formulation is applied to study the buckling and post-buckling of FGM plates.

1. INTRODUCTION

In light of technological development, especially within the spectrum of engineering applications, the search for new materials, which can perform well under the most diverse and rigorous conditions, plays an important role.

Functionally Graded Materials (FGM) are advanced materials of the composite family. These materials consist of two or more different components, forming a continuous and smooth varying spatial profile. In the preferred orientation, FGM properties (such as Young's modulus and Poisson's ratio) have superior performance in comparison with the isolated constituents and possess mechanical and thermal advantages, such as toughness and a high degree of temperature resistance [1,2].

Due to its thermo-mechanical properties, FGM have a vast application in the manufacture of structural components, in particular, plate elements. Thus, the mechanical behavior of FGM plates has received considerable attention [3-12]. In these studies, nonlinearity and shear effects are some important factors and need to be taken into account.

The Isogeometric Analysis (IGA) is a numerical method proposed by Hughes et al. [13] in order to integrate the numerical analysis and Computer Aided Design (CAD). In IGA, the same basis functions (e.g. NURBS) functions are used for geometric modeling and approximation of the displacement field. Therefore, the geometry is exactly represented in the structural analysis,

independent of the discretization level. In addition, the analysis model can be easily refined using standard geometric modeling algorithms, as knot-insertion and degree-elevation [14].

This work presents an accurate and efficient isogeometric formulation for geometrically nonlinear analysis of FGM plates and shallow shells based on the Reissner-Mindlin plate theory and von Kármán strains. This formulation will be applied in the stability analysis of perfect FGM plates, including the evaluation of the buckling load and post-buckling paths.

2. FUNCTIONALLY GRADED MATERIALS

FGM are obtained by mixing two distinct material phases, as a ceramic and a metal. The manufacture techniques allow a smooth variation of the volume fraction along the thickness direction. Thus, FGM do not present the high stress discontinuities present in conventional laminates.

The ceramic volume fraction (V_c) is assumed to vary in the thickness direction (z) according to a simple power law:

$$V_c(z) = \left(\frac{1}{2} + \frac{z}{h}\right)^n \tag{1}$$

where n is the volume fraction index and h is the plate thickness. The effective material properties can be evaluated by the rule of mixtures [15]:

$$\begin{aligned} E(z) &= E_m + (E_c + E_m)V_c(z) \\ \nu(z) &= \nu_m + (\nu_c + \nu_m)V_c(z) \end{aligned} \tag{2}$$

where E represent Young's modulus, ν represents the Poisson's ratio, and the subscripts m and c represent metal and ceramic, respectively.

3. ISOGEOMETRIC ANALYSIS

The model adopted in this work is based on the Reissner-Mindlin theory for bending and transverse shear strains and the von Kármán theory for nonlinear membrane strains. Thus, the displacement field at any point of the shell is given by:

$$u_x(x,y,z) = u(x,y) + z\theta_y; \;\; u_y(x,y,z) = v(x,y) - z\theta_x; \qquad u_z(x,y,z) = w(x,y) \tag{3}$$

where u, v and w are the midsurface displacements in the x, y, and z directions, respectively.

Using the von Kármán theory, the in-plane strains are given by:

$$\boldsymbol{\varepsilon} = \begin{Bmatrix} \frac{\partial u}{\partial x} \\ \frac{\partial v}{\partial x} \\ \frac{\partial u}{\partial y} + \frac{\partial v}{\partial x} \end{Bmatrix} + \begin{Bmatrix} \frac{1}{2}\left(\frac{\partial w}{\partial x}\right)^2 \\ \frac{1}{2}\left(\frac{\partial w}{\partial y}\right)^2 \\ \left(\frac{\partial w}{\partial x}\right)\left(\frac{\partial w}{\partial y}\right) \end{Bmatrix} + z \begin{Bmatrix} \frac{\partial \theta_y}{\partial x} \\ -\frac{\partial \theta_x}{\partial x} \\ \frac{\partial \theta_y}{\partial x} - \frac{\partial \theta_x}{\partial x} \end{Bmatrix} = \boldsymbol{\varepsilon}^m + z\boldsymbol{\kappa} \tag{4}$$

where $\boldsymbol{\varepsilon}^m$ are the membrane strains and $\boldsymbol{\kappa}$ are the curvatures. According to the Reissner-Mindlin theory, the transverse shear strains are given by:

$$\boldsymbol{\gamma} = \begin{Bmatrix} \gamma_{xz} \\ \gamma_{yz} \end{Bmatrix} = \begin{Bmatrix} \frac{\partial w}{\partial x} + \theta_y \\ \frac{\partial w}{\partial y} - \theta_x \end{Bmatrix} \tag{5}$$

where θ_x and θ_y represents the rotations about the y and x axes, respectively.

Considering a linear elastic behavior:

$$\begin{Bmatrix}\sigma_x\\ \sigma_y\\ \tau_{xy}\\ \tau_{xz}\\ \tau_{yz}\end{Bmatrix}=\begin{bmatrix}Q_{11} & Q_{12} & 0 & 0 & 0\\ Q_{12} & Q_{22} & 0 & 0 & 0\\ 0 & 0 & Q_{66} & 0 & 0\\ 0 & 0 & 0 & Q_{44} & 0\\ 0 & 0 & 0 & 0 & Q_{55}\end{bmatrix}\begin{Bmatrix}\varepsilon_x\\ \varepsilon_y\\ \gamma_{xy}\\ \gamma_{xz}\\ \gamma_{yz}\end{Bmatrix} \tag{6}$$

where:

$$Q_{11}=\frac{E}{1-v^2} \qquad Q_{12}=vQ_{11} \qquad Q_{22}=Q_{11} \qquad Q_{44}=Q_{55}=Q_{66}=\frac{E}{2(1-v)} \tag{7}$$

The membrane (**N**), bending (**M**) and shear ($\mathbf{Q}_s$) stress resultants are given by:

$$\mathbf{N}=\begin{Bmatrix}N_x\\ N_y\\ N_x\end{Bmatrix}=\int_{-h/2}^{h/2}\begin{Bmatrix}\sigma_{xx}\\ \sigma_{yy}\\ \sigma_{xy}\end{Bmatrix}dz \qquad \mathbf{M}=\begin{Bmatrix}M_x\\ M_y\\ M_{xy}\end{Bmatrix}=\int_{-h/2}^{h/2}\begin{Bmatrix}\sigma_{xx}\\ \sigma_{yy}\\ \sigma_{xy}\end{Bmatrix}z\,dz$$
$$\mathbf{Q}_s=\begin{Bmatrix}Q_{xz}\\ Q_{yz}\end{Bmatrix}=\int_{-h/2}^{h/2}\begin{Bmatrix}\tau_{xz}\\ \tau_{yz}\end{Bmatrix}dz \tag{8}$$

The stress resultants can be written in terms of the generalized strains as:

$$\begin{Bmatrix}\mathbf{N}\\ \mathbf{M}\\ \mathbf{Q}\end{Bmatrix}=\begin{bmatrix}\mathbf{A} & \mathbf{B} & \mathbf{0}\\ \mathbf{B} & \mathbf{D} & \mathbf{0}\\ \mathbf{0} & \mathbf{0} & \mathbf{G}\end{bmatrix}\begin{Bmatrix}\boldsymbol{\varepsilon}^m\\ \boldsymbol{\kappa}\\ \boldsymbol{\gamma}\end{Bmatrix} \tag{9}$$

where **A**, **B**, **D** and **G** are the extensional, membrane-bending coupling, bending and shear stiffness matrices, respectively, given by:

$$\left(A_{ij},B_{ij},D_{ij}\right)=\int_{-h/2}^{h/2}Q_{ij}(1,z,z^2)dz \qquad G_{ij}=k_s\int_{-h/2}^{h/2}Q_{ij}dz \tag{10}$$

where k_s denotes the transverse shear correction coefficient and the value 5/6 is adopted. It is important to note that **A**, **B** and **D** are defined for *i*,*j* = 1,2,6 and **G** is defined for *i*,*j* = 4,5.

3.2 NURBS

Non-Uniform Rational B-splines (NURBS) are widely used by CAD systems to model complex geometries. This item provides only the basics required for the present paper and the interest in the reader is referred to [14].

The B-spline basis functions are defined by the recursive Cox-de Boor formula:

$$N_{i,0}(\xi)=\begin{cases}1, & \xi_i\le\xi\ge\xi_{i+1}\\ 0, & otherwise\end{cases}$$
$$N_{i,0}(\xi)=\frac{\xi-\xi_i}{\xi_{i+p}-\xi_i}N_{i,p-1}(\xi)+\frac{\xi_{i+p+1}-\xi}{\xi_{i+p+1}-\xi_{i+1}}N_{i+1,p-1}(\xi) \tag{11}$$

However, B-Splines may be insufficient to exactly model curved geometries, as circles and cylinders. In this case, they can be exactly represented by non-uniform rational B-splines (NURBS) functions. The NURBS functions can be defined as:

$$R = \frac{w_{ij} N_{i,p}(\xi) N_{j,q}(\eta)}{W} \qquad W = \sum_{\hat{\jmath}=1}^{m} \sum_{\hat{\imath}=1}^{n} w_{\hat{\imath}\hat{\jmath}} N_{\hat{\imath},p}(\xi) N_{\hat{\jmath},q}(\eta) \tag{12}$$

where ξ and h are two parametric dimensions and p and q are the B-splines basis of degrees in these dimensions, respectively.

A tensor product NURBS surface of degree (p x q) is defined by a linear combination of bivariate rational blending functions (R) and a matrix of control points **p**:

$$\mathbf{S}(\xi, \eta) = \sum_{i=1}^{m} \sum_{j=1}^{n} R_{ij} \mathbf{p}_{ij} \tag{13}$$

In this work, the plate geometry described by a bivariate NURBS surface given by:

$$x = \sum_{k=1}^{nn} R_k x_k \qquad y = \sum_{k=1}^{nn} R_k y_k \tag{14}$$

In the isogeometric formulation presented here, the same NURBS basis are also employed to approximate the membrane and transverse displacements and rotations of the shell:

$$\mathbf{u} = \mathbf{R}\mathbf{u}_e \qquad \mathbf{R} = [\mathbf{R}_1 \ \mathbf{R}_2 \ \cdots \ \mathbf{R}_{\mathrm{nn}}] \qquad \mathbf{R}_k = \mathrm{R}_k \mathbf{I}_{5\mathrm{x}5} \tag{15}$$

where $\mathbf{u} = [u \ v \ w \ \theta_x \ \theta_y]$ is the displacement vector of the midsurface, $\mathbf{u}_e$ is the control points displacements, **R** is the matrix of shape functions and *nn* is the number of control points. Using Equations (4) and (15), the strains can be written as:

$$\boldsymbol{\varepsilon} = \begin{Bmatrix} \boldsymbol{\varepsilon}^m \\ \boldsymbol{\kappa} \\ \boldsymbol{\gamma} \end{Bmatrix} = \begin{Bmatrix} \boldsymbol{\varepsilon}_0^m \\ \boldsymbol{\kappa} \\ \boldsymbol{\gamma} \end{Bmatrix} + \frac{1}{2} \begin{Bmatrix} \boldsymbol{\varepsilon}_L^m \\ \mathbf{0} \\ \mathbf{0} \end{Bmatrix} = \left(\mathbf{B}_0 + \frac{1}{2} \mathbf{B}_L \right) \mathbf{u}_e = \mathbf{B}\mathbf{u}_e \tag{16}$$

where the sub-matrices of **B** for each control point are given by:

$$\mathbf{B}_0^m = \begin{bmatrix} R_{k,x} & 0 & 0 & 0 & 0 \\ 0 & R_{k,x} & 0 & 0 & 0 \\ R_{k,x} & R_{k,x} & 0 & 0 & 0 \end{bmatrix} \qquad \mathbf{B}_0^b = \begin{bmatrix} 0 & 0 & 0 & 0 & R_{k,x} \\ 0 & 0 & 0 & -R_{k,y} & 0 \\ 0 & 0 & 0 & -R_{k,x} & R_{k,y} \end{bmatrix}$$

$$\mathbf{B}_L^m = \begin{bmatrix} 0 & 0 & W_x R_{k,x} & 0 & 0 \\ 0 & 0 & W_y R_{k,x} & 0 & 0 \\ 0 & 0 & W_y R_{k,x} + W_x R_{k,x} & 0 & 0 \end{bmatrix} \qquad \mathbf{B}_0^s = \begin{bmatrix} 0 & 0 & R_{k,x} & 0 & R_k \\ 0 & 0 & R_{k,y} & R_k & 0 \end{bmatrix} \tag{17}$$

with

$$W_x = \sum_{k=1}^{nn} R_{k,x} w_k \qquad W_y = \sum_{k=1}^{nn} R_{k,y} w_k \tag{18}$$

The internal forces vector **g** is derived from the Principle of Virtual Work using the Total Lagragian approach:

$$\mathbf{g}(\mathbf{u}) = \int_{A_0} \overline{\mathbf{B}}^T \hat{\boldsymbol{\sigma}} dA_0 \, , \overline{\mathbf{B}} = (\mathbf{B}_0 + \mathbf{B}_L) \tag{19}$$

The tangent stiffness matrix ($\mathbf{K}_T$) is given by:

$$\mathbf{K}_T = \frac{\partial \mathbf{g}(\mathbf{u})}{\partial \mathbf{u}} = \int_{A_0} \overline{\mathbf{B}}^T \frac{\partial \widehat{\boldsymbol{\sigma}}}{\partial \mathbf{u}} dA_0 + \int_{A_0} \frac{\partial \overline{\mathbf{B}}^T}{\partial \mathbf{u}} \widehat{\boldsymbol{\sigma}} dA_0 \tag{20}$$

where the first term is the material stiffness matrix $\mathbf{K}_L$ and the second term corresponds to the geometric stiffness matrix $\mathbf{K}_\sigma$, given by:

$$\begin{aligned} \mathbf{K}_L &= \int_{A_0} \overline{\mathbf{B}}^T \frac{\partial \widehat{\boldsymbol{\sigma}}}{\partial \mathbf{x}} dA_0 = \int_{A_0} \overline{\mathbf{B}}^T \frac{\partial \widehat{\boldsymbol{\sigma}}}{\partial \boldsymbol{\varepsilon}} \frac{\partial \boldsymbol{\varepsilon}}{\partial \mathbf{u}} dA_0 = \int_{A_0} \overline{\mathbf{B}}^T \mathbf{C}_T \overline{\mathbf{B}} dA_0 \\ \mathbf{K}_\sigma &= \int_{A_0} \frac{\partial \overline{\mathbf{B}}^T}{\partial \mathbf{u}} \widehat{\boldsymbol{\sigma}} dA_0 = \int_{A_0} \frac{\partial \overline{\mathbf{B}}^T}{\partial \mathbf{u}} \mathbf{N} dA_0 = \int_{A_0} \mathbf{G}^T \mathbf{S} \mathbf{G} dA_0 \end{aligned} \tag{21}$$

where:

$$\mathbf{G} = \begin{bmatrix} 0 & 0 & R_{k,x} & 0 & 0 \\ 0 & 0 & R_{k,y} & 0 & 0 \end{bmatrix} \qquad \mathbf{S} = \begin{bmatrix} N_x & N_{xy} \\ N_{xy} & N_y \end{bmatrix} \tag{22}$$

The equilibrium equations for displacement independent loads can be written as:

$$\mathbf{r}(\mathbf{u}, \lambda) = \mathbf{g}(\mathbf{u}) - \lambda \mathbf{f} = \mathbf{0} \tag{23}$$

where $\mathbf{f}$ is the reference vector for external loads, λ is load factor, and $\mathbf{r}$ is the residual vector. The nonlinear equilibrium paths (i.e. load-displacement curves) can be traced using appropriate path-following methods, as the Displacement Control or Arc-Length Method [15].

For stability analysis, critical points (limit or bifurcation) along the equilibrium path can be determined solving the nonlinear system:

$$\begin{bmatrix} \mathbf{r}(\mathbf{u}, \lambda) \\ \mathbf{K}(\mathbf{u}, \lambda)\boldsymbol{\varphi} \\ \|\boldsymbol{\varphi}\| - \mathbf{1} \end{bmatrix} = \mathbf{0} \tag{24}$$

The numerical algorithms presented in [16] can be used to the stability analysis of perfect and imperfect structures, including the branch-switching to secondary paths at bifurcation points.

4. NUMERICAL RESULTS

Simply supported (SS) and a clamped (C) FGM plates under uniaxial compressive loading were analyzed using the proposed IGA formulation. The plates are square with length a = 2m and thickness h = 0.02m (h/a = 1/100). The materials properties are: E_m = 70 GPa (metal) and E_c = 380 GPa (ceramic). Poisson's ratio is considered constant and chosen as $\nu = 0.3$. The volume fraction variation along the thickness is illustrated in Figure 1a.

The load is applied at *x*-direction (Figure 1a). In the simply supported (SS) case are all edges fixed in *z*-direction. The nodes at the middle point of loaded and transverse edges are fixed in *y* and *x* directions, respectively. In addition, when all edges are clamped, the rotations about *y* and *x* axes are fixed along the loaded and transverse edges, respectively. These boundary conditions are illustrated in Figure 1a. The IGA model used in the analysis of the FGM plates has 8x8 elements with cubic basis functions (p = 3).

The results are compared with Finite Elements Method (FEM) solution obtained using Abaqus software [17]. Since Abaqus does not have FGM in the materials options, the stiffness matrices **A**, **B**, **D**, and **G** were evaluated in an external routine and given as input data. The analysis was carried out using a 16x16 mesh of quadratic S8R elements.

Several studies about the influence of boundary conditions in FGM plates have been presented in the literature. These works showed the inexistence of bifurcation buckling in simply supported (SS) plates subjected to in-plane compressive edge loads [18], as also occurs for non-symmetric

laminated plates. Therefore, only the clamped (C) case was considered in the bifurcation analysis (linearized buckling), since plates with all edges clamped exhibit bifurcation buckling [19].

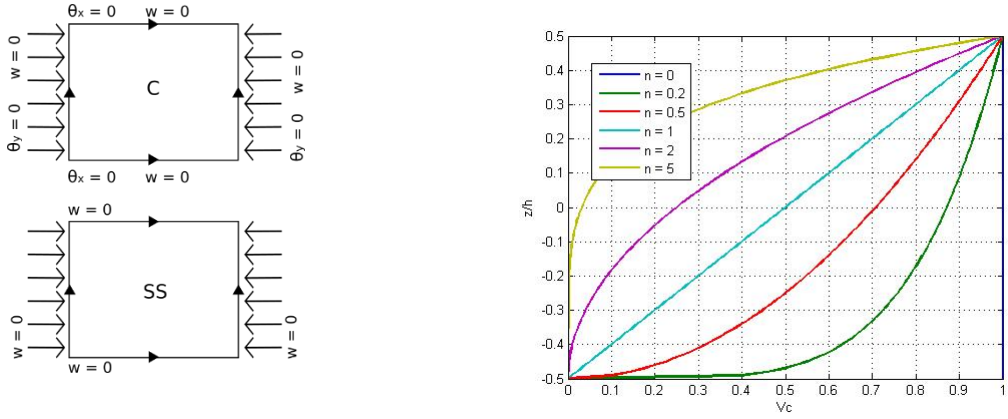

(a) (b)

Figure 1: Boundary conditions and volume fraction along the thickness.

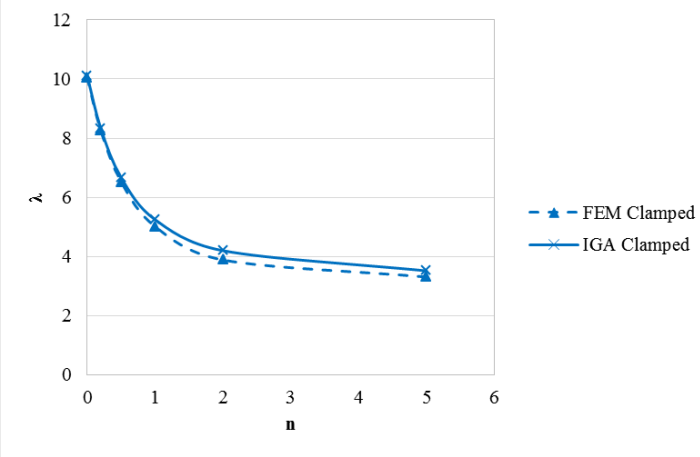

Figure 2: Buckling loads for different exponents.

The obtained results are given in Figure 2, where the normalized buckling coefficient is defined as $\lambda = N_{cr}a^2/\pi^2 D_0$, where $D_0 = Eh^3/12(1-v^2)$. Good agreement is obtained between the IGA and FEM results. The results clearly show that the buckling load decreases with the volume fraction exponent (n).

4.2 Nonlinear analysis

The proposed IGA formulation is used for geometrically nonlinear analysis of FGM plates. The obtained results for simply supported plates are presented in Figure 3a. The load factor is normalized as $\lambda = N_{cr}/N_c$, where N_c is the buckling load of the plate with homogeneous ceramic section (n = 0).

The results show that bifurcation buckling occurs only for $n = 0$ (isotropic plate), since $n > 0$ results in a non-symmetric stiffness distribution leading to stable equilibrium paths, similar to the behavior of imperfect plates. In addition, the results show that increasing the volume fraction exponent (n) decreases the plate strength.

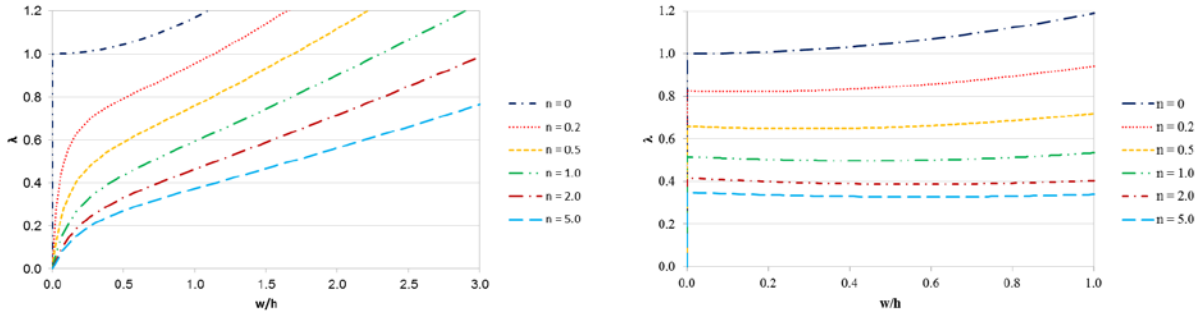

(a) Simply Supported. (b) Clamped.

Figure 3: Nonlinear paths.

The results obtained for clamped plates are presented in Figure 3b. The results show that clamped FGM plates present bifurcation buckling, unlike simple supported ones. In addition, increasing the volume fraction exponent (n) not only decreases the buckling load, but also decreases the post-critical strength reserve of FGM plates, leading to post-buckling behavior characterized by small imperfection sensitivity. This imperfection sensitivity increases with the volume fraction exponent (n).

5. CONCLUSIONS

In this paper, the buckling and post-buckling behavior of FGM plates under uniaxial loading were studied using a NURBS-based isogeometric formulation. Plate kinematics is based on Reissner-Middlin plate theory with the geometrically nonlinear effects considered using the von Kármán theory.

FGM plates with simply supported and clamped boundary conditions were analyzed. The linearized buckling loads for clamped FGM plates computed by the IGA formulation are in good agreement with FEM results. The buckling loads decrease with the volume fraction exponent.

The nonlinear equilibrium paths confirmed that FGM plates with simply supported boundary conditions do not present bifurcation buckling and display a stable nonlinear behavior similar to imperfect homogeneous and laminated plates. On the other hand, clamped FGM plates present bifurcation buckling, but display a slight imperfection sensitivity, which increases with the volume fraction exponent.

ACKNOWLEDGEMENTS

The financial support by CNPq and CAPES is gratefully acknowledged.

REFERENCES

[1] Jha, D. K., Kant, T., & Singh, R. K. (2013), 'A critical review of recent research on functionally graded plates', *Composite Structures*, **96**, (2013) 833-849.

[2] Udupa, G., Rao, S. S., & Gangadharan, K. V., 'Functionally Graded Composite Materials: An Overview', *Procedia Materials*, **5**, (2014) 1291-1299.
[3] Arciniega, R. A., & Reddy, J. N., 'Large deformation anlysis of functionally graded shells', International Journal of Solids and Structures, **44** (6), (2007) 2036-2052.
[4] Lee, Y. Y., Zhao, X., & Reddy, J. N., 'Postbuckling analysis of functionally graded plates subject to compressive and thermal loads', *Computer Methods in Applied Mechanics and Engineering*, **199** (25-28), (2010) 1645-1653.
[5] Woo, J., Meguid, S.A., Stranart, J. C., & Liew, K. M., 'Thermomechanical postbuckling analysis of moderately thick functionally graded plates and shallow shells', *International Journal of Mechanical Sciences*, **47** (8), (2005) 1147-1171.
[6] Yang, J., & Shen, H.-S., 'Non-linear analysis of functionally graded plates under transverse and in-plane loads. *International Journal of Non-Linear Mechanics*', **38** (4), (2003a) 467-482.
[7] Yang, J., & Shen, H. S., 'Nonlinear bending analysis of shear deformable functionally graded plates subjected to thermo-mechanical loads under various boundary conditions', *Composites Part B: Engineering*, **24** (2), (2003b) 103-115.
[8] Zhao, X., Lee, Y. Y., & Liew, K. M., 'Mechanical and thermal buckling analysis of functionally graded plates', *Composite Structures*, **90** (2), (2009) 161-171.
[9] Kim, N. Il, & Lee, J., 'Geometrically nonlinear isogeometric analysis of functionally graded plates based on first-order shear deformation theory considering physical neutral surface', *Composite Structures*, **153**, (2016) 804-814.
[10] Nguyen-Xuan, H., Tran, L. V., Thai, C. H., Kulasegaram, S., & Bordas, S. P. A., 'Isogeometric analysis of functionally graded plates using a refined plate theory', *Composites Part B: Engineering*, **64**, (2014) 222-234.
[11] Yin, S., Hale, J. S., Yu, T., Bui, T. Q., & Bordas, S. P. A., 'Isogeometric locking-free plate element: A simple first order shear deformation theory for functionally graded plates', *Composite Structures*, **118** (1), (2014) 121-138.
[12] Yu, T. T., Yin, S., Bui, T. Q., & Hirose, S., 'A simple FSDT-based isogeometric analysis for geometrically nonlinear analysis of functionally graded plates', *Finite Elements in Analysis and Design*, **96** (C), (2015) 1-10.
[13] Hughes, T.; Cottrell, J.; Bazilevs, Y., 'Isogeometric analysis: CAD, finite elements, NURBS, exact geometry and mesh refinement', *Computer Methods Applied Mechanics and Engineering*, v. **194**, (2005) p. 4135−4195.
[14] Piegl, L.; Tiller, W., 'The NURBS Book'**,** 2nd ed (Germany: Springer, 1997).
[15] Shen, H.S., 'Functionally graded materials: nonlinear analysis of plates and shells' (Boca Raton: CRC Press, 2009).
[16] Parente, E.; Holanda, A. S.; Silva, S. M. B. A., 'Tracing nonlinear equilibrium paths of structures subjected to thermal loading', *Computational Mechanics*, vol. **38**, pp. (2006) 505-520.
[17] SIMULIA. 'ABAQUS/Standard user's manual', Version 6.12 (Providence, RI, USA, 2012).
[18] Shen, H.S., 'Postbuckling Behavior of Plates and Shells', 1st ed (Singapore: World Scientific, 2017)
[19] Bateni, M., Kiani, Y. & Eslami, M. R., 'A comprehensive study on stability of FGM plates', *International Journal of Mechanical Sciences*, **75**, (2013) 134-144.

SEQUENTIAL APPROXIMATE OPTIMIZATION OF COMPOSITE STRUCTURES USING RADIAL BASIS FUNCTIONS

David S. Balreira (1), Luana A. G. Moura (1) and Evandro Parente Jr. (1)

(1) Departamento de Engenharia Estrutural e Construção Civil, Universidade Federal do Ceará, Brazil

https://doi.org/10.21452/bccm4.2018.16.10

Abstract

The use of optimization techniques is necessary in order to explore the full potential of laminated composite structures. Unfortunately, the computational cost of the optimization process can be very high when numerical methods are used to carry out the structural analysis. This work addresses the use of surrogate models to reduce the computational cost to optimize composite structures. The PSO algorithm is used for optimization and a sequence of surrogate models, based on the use of Radial Basis Functions, is used to approximate the structural responses. The accuracy of the proposed approach is assessed using a set of laminate optimization problems and very good results were obtained.

1. INTRODUCTION

Fiber reinforced composite (FRC) materials present high resistance/weight and stiffness/weight ratios, corrosion and fatigue resistance, and other interesting properties for high performance structural applications. These composites are formed from high strength fibers embedded in a polymeric matrix, resulting in an orthotropic composite material. Typically, several layers with different fiber orientations are stacked to obtain more efficient designs, leading to a laminated structure. Due to their complex mechanical behavior, the analysis of laminate structures requires the use of numerical methods, as the Finite Element Method (FEM) and Isogeometric Analysis (IGA).

The design of laminated structures requires the determination of the number of layers and the characteristics of each layer (material, thickness and fiber orientation). Since there are a large number of possibilities, the use of optimization techniques is necessary in order to explore the full potential of laminated composite structures. However, the optimization of laminated composite structures has a high computational cost, especially when heuristic methods, as Genetic Algorithm or Particle Swarm Optimization (PSO), are applied. An alternative to reduce the processing time is to use surrogate models to approximate the structural responses.

Surrogate models build an approximation of the structure behavior based on the structure responses evaluated by the numerical methods at a set of selected sampling points. Artificial

Neural Networks (ANN), Radial Basis Functions (RBF), Support Vector Regression (SVR) and Kriging are some surrogate models widely used (Wang and Shan, 2007; Forrester *et al*., 2008). The RBF approach is used in this work, since it stands out for its simplicity, accuracy and robustness, when compared with other options (Jin et al., 2001).

The PSO algorithm is used for optimization since it is simple, efficient and can easily handle discrete variables (Barroso et al., 2017). A Sequential Approximate Optimization (SAO) approach is presented, where a sequence of RBF models is used to approximate the laminate responses. The accuracy of the proposed approach is assessed using a set of laminate optimization problems and very good results were obtained.

2. RADIAL BASIS FUNCTIONS

RBF models where proposed by Hardy (1971) to interpolate geographic data. Nowadays, this technique is widely used as a surrogate model (Jin et al., 2001; Forrester *et al*., 2008; Kitayama *et al*., 2011; Amouzgar and Strömverg, 2016). An RBF model can be written as:

$$\hat{f}(\mathbf{x}) = \sum_{i=1}^{n} w_i \varphi(\left|\left|\mathbf{x} - \mathbf{c}_i\right|\right|) \tag{1}$$

w_i are known as weights, φ are the Radial Basis Functions, $\mathbf{c}_i \in \mathbb{R}^m, i = 1, 2, \dots, n$ are the basis centers, which can be taken from the sampling points by different techniques (Haykin, 2008; Amouzgar and Strömberg, 2016). In this work, all the sampling points are RBF centers.

The RBF herein used was the Gaussian function

$$\varphi(r) = \exp\left(-\frac{r^2}{\sigma^2}\right) \tag{2}$$

where $r = ||\boldsymbol{x} - \boldsymbol{c}||$ is the radial distance and σ is a parameter which controls the RBF shape. This parameter can be evaluated by cross-validation (Forrester *et al*., 2008) or by closed-form expressions depending on the distance between the sampling points (Kitayama *et al*., 2011).

The simplest way to create an RBF model is by interpolating the sampling points $f(\mathbf{x}_i) = \mathbf{y}_i$:

$$\begin{bmatrix} \varphi_{11} & \varphi_{12} & \dots & \varphi_{1n} \\ \varphi_{21} & \varphi_{22} & \dots & \varphi_{2n} \\ \vdots & \vdots & \vdots & \vdots \\ \varphi_{n1} & \varphi_{n2} & \dots & \varphi_{nn} \end{bmatrix} \begin{bmatrix} w_1 \\ w_2 \\ \vdots \\ w_n \end{bmatrix} = \begin{bmatrix} y_1 \\ y_2 \\ \vdots \\ y_n \end{bmatrix} \Rightarrow \mathbf{H}\,\mathbf{w} = \mathbf{y} \tag{3}$$

where $H_{ij} = \varphi\left(\left|\left|\mathbf{x}_i - \mathbf{x}_j\right|\right|\right), i, j = 1, 2, \dots, n$. The interpolation matrix is nonsingular provided that the sampling points ($\mathbf{x}_i$) are distinct (Forrester *et al*., 2008). However, this matrix tends to become bad conditioned when the sampling points are close to each other (Haykin, 2008). In addition, overfitting, in which the model only represents well the points included in the sampling points, can occur when many points are used (Forrester *et al*., 2008). Both problems can be avoided by finding the weights w_i using the least squares approach considering a regularization parameter (λ) (Kitayama *et al*., 2011):

$$E = \sum_{i=1}^{n} \left(\mathbf{y}_i - \hat{f}(\mathbf{x}_i)\right)^2 + \sum_{j=1}^{n} \lambda\, w_j^2 \tag{4}$$

The error (E) minimization yields the linear system:

$$(\mathbf{H}^{\mathrm{T}}\mathbf{H} + \lambda\mathbf{I})\mathbf{w} = \mathbf{H}^{\mathrm{T}}\mathbf{y} \tag{5}$$

whose solution yields the weight vector ($\mathbf{w}$). The value $\lambda = 10^{-3}$ was adopted in this work.

3. SEQUENTIAL APPROXIMATE OPTIMIZATION

The simplest approach to surrogate based optimization is to build a fixed surrogate model based on an initial sampling plan. Different Design of Experiments (DoE) techniques, as the Latin Hipercube Sampling and Hammersley Sequence Sampling (HSS), can be used to generate this sampling plan (Forrester *et al*., 2008; Amouzgar and Strömberg, 2016). The fixed surrogate is used to in all optimization iterations (or generations in GA). This approach has been successfully applied to several problems, but it requires a large sampling plan, which can be costly for problems with many design variables. Since the optimum solution is not known, costly numerical analysis are carried out to build an accurate surrogate model in regions far away from the optimum.

A better alternative is to use the Sequential Approximate Optimization (SAO) approach (Schmit and Farshi, 1974; Haftka and Gürdal, 1991; Jones *et al.,* 1998; Kitayama *et al*., 2011; Pan *et al*., 2014; Chung *et al.,* 2018). In this approach, an initial surrogate model is built based on a small sampling plan. This initial model is updated after each iteration of the optimization algorithm, including the optimum solution found in this iteration and possibly other new sampling points. This approach naturally generates more sampling points, and a better approximation, in the region close to the optimum. However, it can be shown that including only the optimum solution found at each iteration is not sufficient to find the global optimum solution and different infill strategies have been proposed to update the surrogate model (Forrester *et al*., 2008).

In this work, the initial sampling is generated by the Hammersley Sequence Sampling (Amouzgar and Strömberg, 2016), the design optimization is carried-out is a Hybrid PSO-GA algorithm including special laminate operators (Barroso et al., 2017) and the surrogate model is updated using the infill strategy proposed by Kitayama *et al*. (2011).

In order to balance the local and global approximation aspects, after each iteration not only the current optimal solution, but also new sampling points are evaluated using numerical methods and used to update the surrogate model. These points are found minimizing the density function (Kitayama *et al*., 2011) in order to include new sampling points where the model is poorly approximated. It is expected that adding new sampling points in sparse regions of the design space will lead to convergence to the global optimum (Kitayama *et al.,* 2011).

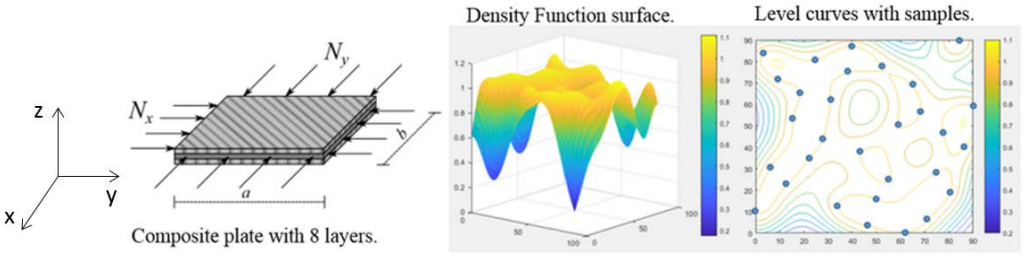

Figure 19. Density Function surface and level curves.

The density function is approximated by a RBF model whose weights ($\mathbf{w}^{\mathrm{DF}}$) are evaluated using Equation (*5*) with $\mathbf{y}^{\mathrm{DF}} = [1, 1, 1, \dots, 1]^{T}_{m\mathrm{x}1}$. This function is illustrated in Figure 1 for a sampling plan composed 30 points (blue circles) used to approximate the buckling load of a simply support square plate with balanced and symmetric layup subjected to a biaxial load. The plate has 8 plies

corresponding to two design variables (θ_1, θ_2). It can be noticed that minimizing this function results in the insertion of the point **x** = [90, 0] in the sample.

In this work, the minimum of the density function is found using the standard PSO algorithm. The number of infill points to be included at each iteration is taken as *n*/2 (Kitayama *et al*., 2011). The general SAO algorithm used in this work is presented in Figure *2*. For practical problems, the costlier step is the evaluation of the sampling points, since it involves the analysis of the composite structure by numerical methods.

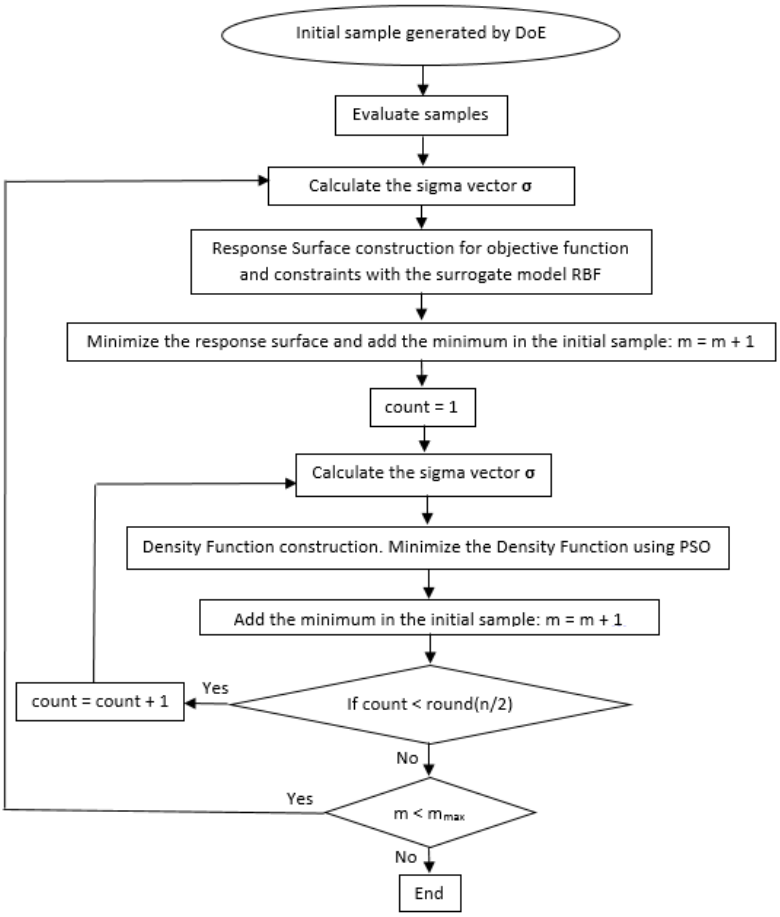

Figure 20. SAO flowchart.

4. RESULTS

The first example consists on a square laminated plate, with 8 plies, simply supported and subjected to biaxial loading (Figure 1). The design variables are the fiber orientation of each ply. Since the layup is symmetric and balanced, there are only two design variables ($0 \leq \theta_1, \theta_2 \leq 90$). The objective is to find the fiber orientations ($\mathbf{x} = [\theta_1, \theta_2]$) that maximize the buckling load (λ_b):

$$\begin{aligned} &\text{Find} && \mathbf{x} = [\theta_1, \theta_2] \text{ that} \\ &\text{maximize} && \lambda_b \\ &\text{with} && 0° \leq \theta_i \leq 90° \end{aligned} \tag{6}$$

Table 1 presents the geometrical parameters and material properties. Reddy (2004) presents a closed-form expression for the buckling load, which is exact for cross-ply laminates and give accurate results for angle-ply laminates with several plies. This solution will be adopted as the exact structural response to build the surrogate model.

Table 8. Geometry and properties of Example 1.

Geometry (m)			Material: Carbon-Epoxy			
a	*b*	thickness	$E_1(GPa)$	$E_2(GPa)$	$G_{12}(GPa)$	ν_{12}
0.508	0.508	1.272e-4	130.71	6.36	4.18	0.32

An initial sample with 9 points was generated using the Hammersley Sequence Sampling. The optimization was carried out using 5 iterations and a swarm composed of 100 particles. The final sample has 19 points due to the addition of 2 points at each iteration. The results presented in Table *2* show that the same optimum layup was obtained by the exact and SAO approaches, with the former requiring 500 structural analysis and the latter only 19.

Table 9. SAO optimization results.

Approach	Layup	λ_b
Exact	$[\pm 45\ \pm 45]_s$	462.63
SAO	$[\pm 45\ \pm 45]_s$	462.63

The second problem corresponds to a simply support rectangular plate under biaxial loading (Figure 1) with N_x/N_y = 0.125 (Barroso et al., 2017). Table 3 presents the geometry and properties of this plate. Since a symmetric and balanced layup with 48 plies is adopted, the problem has 12 design variables. The objective is to find the best layup ($\mathbf{x} = [\theta_1, \theta_2, \dots, \theta_{12}]$) that maximize the plate strength, considering buckling (λ_b) and material failure (λ_f) according to the Maximum Strain Criterion (Daniel and Ishai, 2004). The number of contiguous plies (N_{cp}) is limited to 4.

$$\begin{aligned} &\text{Find} && \mathbf{x} = [\theta_1, \theta_2, \dots, \theta_{12}] \ \text{that} \\ &\text{maximize} && \lambda_b, \lambda_f \\ &\text{subjected to} && 1 - \frac{N_{cp}}{cp_{max}} \leq 0 \\ &\text{with} && 0° \leq \theta_i \leq 90° \end{aligned} \tag{7}$$

Table 10. Plate properties and geometry.

Geometry (m)			Engineering properties				Ultimate strain		
a	*b*	*thickness*	$E_1(GPa)$	$E_2(GPa)$	$G_{12}(GPa)$	ν_{12}	ε_1^u	ε_2^u	γ_{12}^u
0.508	0.127	1.27e-4	138	9.0	7.1	0.3	0.008	0.029	0.015

The initial sample used in SAO has 137 points. This problem was optimized initially using 100 particles and 20 iterations. Since the problem has 12 variables, 7 points were added to the sample at the end of each iteration, resulting in a final sample with 277 points. The obtained results are

presented in Table *4*. It can be noted that exact and SAO layups are not the same, but the difference in the buckling load (λ_b) was only -2.11%, on the other hand the difference in failure criterion was 12.18%.

Table 11. Optimization results for 20 and 50 iterations.

Approach	Layup	λ_b	λ_f
Kogiso et al. (1994)	$[\pm 45_5\ 0_4\ \pm 45\ 0_4\ 90_2\ 0_2]_s$	14659.58	13518.66
SAO (20 iterations)	$[\pm 45_5\ 0_2\ \pm 45\ 0_2\ 90_2\ 0_4\ \pm 45]_s$	14969.50	11871.10
SAO (50 iterations)	$[\pm 45_5\ (\ 0_4\ \pm 45)_2\ 0_2]_s$	14680.00	13458.30

Better results were obtained optimizing the problem using 50 iterations, as shown in Table *4*. The exact and SAO layups are still different, but the buckling load difference decreases to only 0.13% and the failure load difference decreases to only 0.44%. Therefore, SAO results can be improved increasing the number of iterations, since more sampling points are included, leading to a better surrogate model. Obviously, the computational cost also increases due to the additional structural analysis.

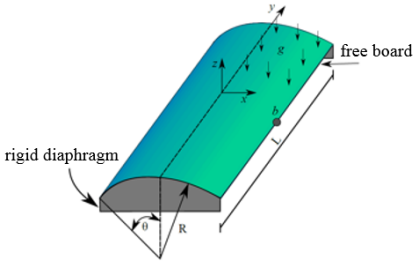

Figure 21. Laminated cylindrical shell.

The third problem consists in the stiffness maximization of a laminated cylindrical shell (Figure 3) with 40 plies (Barroso, 2015). Table 5 presents the shell properties. The problem has 10 design variables since a symmetric and balanced layup was adopted. The shell stiffness can be maximized by minimizing the vertical displacement (w) of point b. In addition, the required safety factor (SF) is equal to 1.5. The number of contiguous plies (N_{cp}) is limited to 4. The optimization problem is written as:

$$\begin{aligned} &\text{Find} && \mathbf{x} = [\theta_1, \theta_2, \ldots, \theta_{10}] && \text{that} \\ &\text{minimize} && w_b \\ &\text{subjected to} && \frac{N_{cp}}{cp_{max}} - 1 \leq 0 \\ & && 1 - \frac{S_{TW}}{SF} \leq 0 \\ &\text{with} && 0° \leq \theta_i \leq 90° \end{aligned} \tag{8}$$

The Isogeometric Analysis (IGA) was used to evaluate the displacements and stresses considering a 3D model. The Tsai-Wu criterion was adopted to evaluate the safety factor against material failure (S_{TW}).

Table 12. Geometrical and engineering properties.

g (kN/m²)	R (m)	L (m)	θ (°)	t (cm)	N_{lam}	t_{lam} (cm)	E_1 (GPa)
45	3.0	6.0	40	3.0	40	0.075	147
E_2 (GPa)	E_3 (GPa)	ν_{12}	ν_{13}	ν_{23}	G_{12} (GPa)	G_{13} (GPa)	G_{23} (GPa)
10.3	10.3	0.27	0.27	0.54	7.0	7.0	3.7

The reference solution, where all designs were analyzed using IGA, was obtained using 49 particles and 30 iterations. The SAO method used the same number of particles, but considered initially only 20 iterations. The initial sample had 99 points. Since the problem has 10 variables, 6 points were added to the sample at the end of each iteration, resulting in a final sample with 219 points. The results are presented in Table 6.

Different layups were obtained by the exact and SAO approaches, but the differences were negligible for the displacement and safety factor. Increasing the number of SAO iterations to 30 lead to even closer results. In this case, the use of SAO leads to a reduction of 82.77% in the elapsed time. Therefore, SAO makes feasible the use of optimization techniques in the design of complex laminated structures.

Table 13. SAO optimization results.

Approach	Layup	Time	w_b	S_{TW}
IGA (30 iterations)	$[(90_4\ \pm 45)_2\ 0_4\ \pm 45\ 0_2]_s$	12306 s	11.58	2.12
SAO (20 iterations)	$[\pm 45\ 90_4\ \pm 45_3\ 0_4\ \pm 45\ 0_2]_s$	1342 s	12.09	2.05
SAO (30 iterations)	$[90_2\ (90_2\ \pm 45)_2\ \pm 45\ 0_4\ \pm 45\ 0_2]_s$	2120 s	11.63	2.10

5. CONCLUSION

This work studied the use of Sequential Approximate Optimization (SAO) to laminate composite structures. In this SAO approach, the HSS sampling technique was used to generate the initial sample and Radial Basis Functions (RBF) were used as a surrogate model. The surrogate model is updated at each iteration including the iterative optimum solution and additional points in regions sparsely sampled of the design space. The additional sampling points are found minimizing a RBF density function using the PSO algorithm.

Optimization problems with both small and large number of design variables were solved and very good results were found. The efficiency of the SAO was demonstrated by the large reduction in the optimization time obtained when numerical methods are required for structural analysis. The accuracy of SAO results can be increased using a large number of optimization iterations. Therefore, the obtained results depend on the available computer resources and project schedule constraints. Thus, SAO is a promising technique to allow the design optimization of real-world laminated composite structures.

ACKNOWLEDGEMENTS

The support given by Elias Barroso in the implementation of the Isogeometric Analysis problem, the help provided by Guilherme Mendes in the use of the program BIOS, the Laboratório de Mecânica Computacional e Visualização infrastructure to perform this work, and the financial

support by CAPES (Coordenação de Aperfeiçoamento de Pessoal de Nível Superior) are gratefully acknowledged.

REFERENCES

[1] Wang, G. G. and Shan, S., 'Review of Metamodeling Techniques in Support of Engineering Design Optimization' *The American Society of Mechanical Engineers* **129** (2007) 370-380.
[2] Forrester, A. I. J., Sóbester, A. and Keane A. J., 'Engineering Design via Surrogate Modelling: A Practical Guide' (John Wiley and Sons, 2008)
[3] Jin, Ruichen, Wei Chen and Timothy W. Simpson, 'Comparative studies of metamodelling techniques under multiple modelling criteria' *Structural and multidisciplinary optimization* **23** (1) (2001) 1-13.
[4] Barroso, E. S., Parente Jr., E. and Melo, A. M. C. de, 'A hybrid PSO-GA algorithm for optimization of laminated composites', *Structural and Multidisciplinary Optimization* **55** (2017) 2111-2130.
[5] Hardy, R. L., 'Multiquadratic equations of topography and other irregular surfaces' *Journal of geophysical research* **76** (1971) 1905-1915.
[6] Kitayama, S., Arakawa, M. and Yamazaki, K. 'Sequential Approximate Optimization using Radial Basis Function network for engineering optimization', *Optimization and Engineering* **12** (2011) 535-557.
[7] Amouzgar, K. and Strömberg, N., 'Radial basis functions as surrogate models with a priori bias in comparison with a posteriori bias', *Structural and Multidisciplinary Optimization* **55** (2016) 1453-1469.
[8] Haikyn, S., 'Neural Networks and Learning Machines' (Prentice Hall, 2008)
[9] Schmit, L. A., Farshi, B., 'Some Approximation Concepts for Structural Synthesis', *AIAA Journal* **12** (1974) 692-699.
[10] Haftka, R. T. and Gürdal, Z., 'Elements of Structural Optimization' 3rd ed (Kluwer Academic Publishers, 1991)
[11] Jones, D. R., Schonlau, M. and Welch, W. J., 'Efficient Global Optimization of Expensive Black-Box Functions', *Journal of Global Optimization* **13** (1998) 455-492.
[12] Pan, G., Ye, P., Wang, P. and Yang, Z., 'A Sequential Optimization Sampling Method for Metamodels with Radial Basis Functions', *The Scientific World Corporation* (2014)
[13] Chung, I., Park, D. and Choi, D., 'Surrogate-based global optimization using an adaptive switching infill sampling criterion for expensive black-box functions', *Structural and Multidisciplinary Optimization* **57** (2018) 1443-1459.
[14] Reddy, J. N., 'Mechanics of Laminated Composite Plates and Shells: Theory and Analysis' 2nd ed (CRC PRESS , 2004)
[15] Daniel, I. M. and Ishai, O, 'Engineering mechanics of composite materials' 1st ed. (Oxford University Press, 1994)
[16] Kogiso, N., Watson, L., Gürdal, Z. and Haftka R, 'Genetic algorithms with local improvement for composite laminate design', *Structural Optimization* **7** (4) (1994) 207-218.
[17] Barroso, E. S., 'Análise e Otimização de Estruturas Laminadas Utilizando a Formulação Isogeométrica' (2015) 163p. *Dissertação (Mestrado em Engenharia de Estruturas) – Universidade Federal do Ceará, Fortaleza*

COMPOSITE STRUCTURAL BEHAVIOUR PREDICTION WITH THE SURROGATE MODEL AND TRACE-BASED APPROACH

Eduardo Gerhardt [(1)], Rogério J. Marczak [(2)] and Sandro C. Amico [(3)]

(1) SENAI Institute for Innovation in Polymers Engineering, Brazil.

(2) Department of Mechanical Engineering, Federal University of Rio Grande do Sul, Brazil.

(3) Department of Materials Engineering, Federal University of Rio Grande do Sul, Brazil.

https://doi.org/10.21452/bccm4.2018.16.11

Abstract

An approach for the prediction of a composite tube structural behavior is presented. An estimate of the elastic properties of the material is accessed by the development of a knowledge-based surrogate model and the use of a trace-design approach, which is compared with experimental tests. The estimate is applied to a finite element model simulation for buckling analysis using both linear and non-linear methods. Buckling simulation results are then compared with the result of an experimental hydrostatic pressure test. It is demonstrated that this methodology can be a valuable tool in the early stages of a structural design.

1. INTRODUCTION

Filament winding process produces high quality composite polymer tubes and vessels. Because of its peculiar features, this technique is most suitable to produce surfaces of revolution [1]. However, most standardize procedures for characterizing composite materials demand flat coupons. Flat coupons when made by filament winding will not represent the real state of that material in a revolution shape due to differences in compaction influencing the void and fiber content, for example [1]. Some standard methods for tubular specimen characterization are available, although requiring laborious and time-consuming tasks.

Pursuing the reduction in effort required for composite characterization, Tsai and co-workers have proposed the trace-based approach [2]. They proposed the use of a master-ply for carbon-epoxy composites that corresponds to a statistical relation with the stiffness parameters of that material system. With the master-ply, the elastic properties of a ply can be estimated after measuring the elastic modulus in the fiber direction only [3]. Recently, it was proposed that a structure designed by the trace approach could have its material properties scaled by coupons taken from that structure for predicting its behavior [4].

Buckling of composite cylinders is a critical issue since it represents the loss of structural stability leading to premature collapse. Buckling predictions of composite structures is affected by

several factors, among them geometrical imperfections, actual mechanical properties of the material, over-simplified numerical model assumptions, and sensitivity to internal defects [5].

This study focuses on composite tube structural behavior prediction. The material elastic properties are assessed by a surrogate model and using the trace-based approach, which are applied to radial ring compression test. Finite element model simulation for buckling analysis using both linear and non-linear methods is performed and compared with experimental hydrostatic pressure test results.

2. METHODS

2.1 Trace-based approach

From the linear stress-strain relation of a unidirectional ply, the trace is defined as an invariant equal to the sum of diagonal elements of the stiffness matrix [Q]. The trace value is obtained in the form of Equation (1) in the principal directions of the ply [6].

$$Tr(Q) = Q_{11} + Q_{22} + 2Q_{66} = Q_{xx} + Q_{yy} + 2Q_{ss} \tag{1}$$

With the trace value it is possible to obtain the master-ply which is given by the trace-normalized stiffness parameters [Q_{ij}^*] and the trace-normalized modulus [E_x^*] using Equations (2) and (3), respectively.

$$[Q_{ij}^{\ *}] = \frac{[Q_{ij}]}{Tr(Q)} \tag{2}$$

$$[E_x^{\ *}] = \frac{E_x}{Tr(Q)} \tag{3}$$

The flexural laminate stiffness trace $Tr(D^*)$ can also be obtained and has the same value of $Tr(Q)$. Thus, the flexural stiffness parameter D_{22}^* can be calculated by Equation (4) and the trace-normalized flexural stiffness parameter D_{22}^{**} by Equation (5).

$$[D_{22}^{\ *}] = \frac{12[D_{22}]}{t^3} \tag{4}$$

$$[D_{22}^{\ **}] = \frac{D_{22}^{\ *}}{Tr(Q)} \tag{5}$$

2.2. Material properties scaling

Two composite tubes were manufactured by filament winding with a carbon/epoxy towpreg (Toray T700-12K-50C / UF3369 epoxy resin) using a MF Tech robotic system. The stacking sequence adopted was $[90/-90/60/-60/90/-90]_T$. From these cylinders, a ring section was cut and subjected to radial compression between parallel plates on a universal testing machine, at 5 mm/min and 23 °C, to obtain force-displacement curves (Figure 1a). One test was run in a monotonic way until failure. Another test was run in a cyclic way, loading and unloading the sample at ever-higher loads in an attempt to monitor damage evolution in the specimen. These tests were necessary to validate the linear elastic behaviour of the material.

The unidirectional ply elastic properties of this material were also characterized [7] from flat coupons produced by filament winding. As already commented, these material properties may

differ from those obtained when the towpreg is wound over a cylindrical mandrel. To overcome this, material properties scaling procedure was developed, as follows. A monotonic test was simulated with the finite element method applying the original elastic properties (Figure 1b). The simulation was modelled in ABAQUS software [8] using quadratic shell elements, large displacement field hypothesis, ring section dimensions (thickness, radius and width) equal to the actual test specimen, and the mesh size was defined after a mesh sensitivity analysis study.

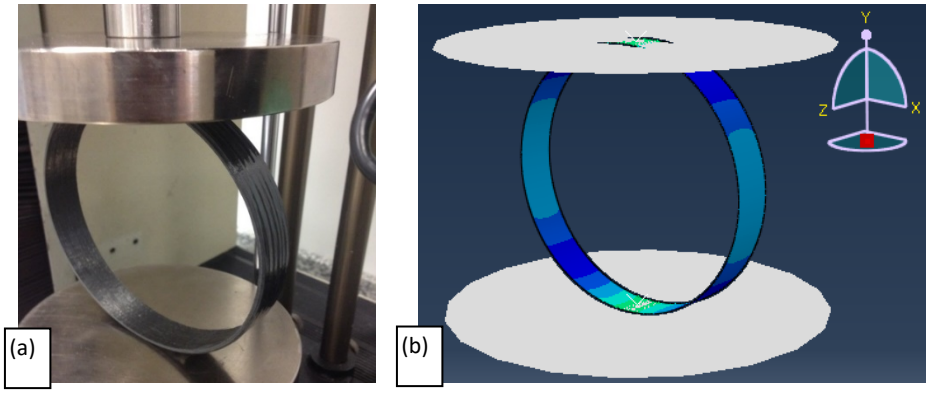

Figure 1 – Preliminary experimental (a) and simulated (b) ring compression test.

With the experimental and numerical curves, a knowledge-based surrogate model was developed based on the analytical solution found in reference [9] and shown as Equation (6). This analytical solution refers to the displacement of a ring compressed by a point load and does not take into account the contact between the compression plates and the ring or the large displacements hypothesis.

$$w = \frac{PR^3}{4EI}\left(\frac{\pi}{2} - \frac{4}{\pi}\right) \tag{6}$$

where w is half the displacement on the compressed ring, P is the applied force, E is the elastic modulus of an isotropic material and I is the section moment of inertia.

From the moment-curvature equations [9], it is possible to combine the laminate bending-stiffness parameter D_{22}, defined in Equation (7), with Equation (6) to obtain the force-displacement relation as a function of D_{22}, as shown in Equation (8).

$$D_{22} \approx \frac{EI}{b} \tag{7}$$

$$P = 13.4428\frac{bw}{R^3}D_{22} \tag{8}$$

where D_{22} is the bending parameter of the ABD matrix, b is the width of the ring section.

From Equation (8), the knowledge-based surrogate model, Equation (9), was obtained implementing an unknown function parameter determined through a numerical procedure for error minimization between the experimental and the simulated force-displacement curves.

$$P = 13.4428\frac{bw}{R^3}D_{22}(1 + f_{(w)}) \tag{9}$$

where $f_{(w)}$ is the unknown parameter, which depends on the radial displacement *w*.

2.4. Buckling analysis

The manufactured cylinders were dimensioned to collapse by buckling prior to material failure, that is, the radius to thickness dimensional ratio was lower than 20 (i.e. R/t < 20). The mean cylinder nominal dimensions were: 136.2 mm internal diameter, 200 mm length, and 2.6 mm thickness. The tube ends were closed using steel flanges with O-rings for sealing, respecting the simply-supported boundary condition. The tube was tested in a hydrostatic water chamber (Figure 2a-b) at the Subsea Technology Laboratory/UFRJ at room temperature and using a pressure increase rate of 0.4 MPa/min until the pressure dropped in the chamber.

Finite element analysis (FEA) was used to predict buckling of the composite tube when subject to an external hydrostatic pressure, using simply-supported boundary conditions on the tube edges, quadratic shell elements, and mesh size defined after conducting a mesh sensitivity analysis. For comparison purposes, FEA buckling analyses were performed using the linear bifurcation method to extract the eigenvalues of deformation modes (i.e. a linear buckling analysis) and the incremental RIKS method with geometric imperfections implementation (i.e. a non-linear buckling analysis) [8].

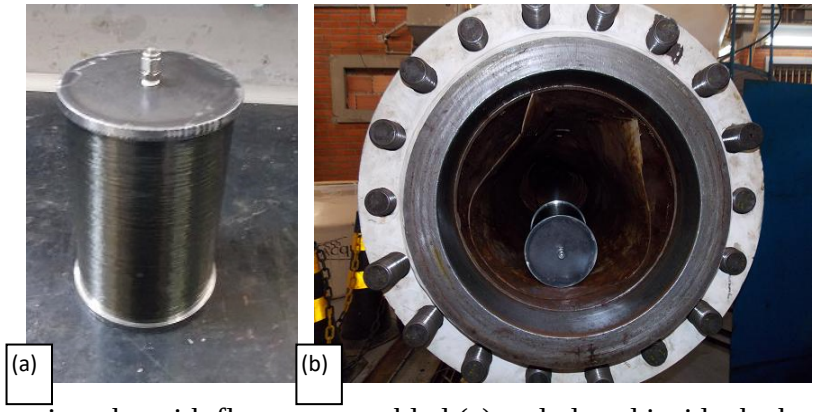

Figure 2 – Composite tube with flanges assembled (a) and placed inside the hydrostatic chamber (b).

3. RESULTS AND DISCUSSION

Results from the monotonic and cyclic ring compression test are shown in Figure 3. Averaged measured ring specimens dimensions were 136.2 mm internal diameter, 20.0 mm width and 2.5 mm thickness for the monotonic test, and 136.2 mm internal diameter, 21.5 mm width, and 2.25 mm thickness for the cyclic test. The differences on width and thickness of the tests specimens resulted in force-displacement curves with distinct inclinations as seen on Figure 3. The cyclic curve does not show any evidence of progressive damage until the first failure and validates the linear elastic behavior of the material within that range of displacement. This condition was considered in the surrogate model.

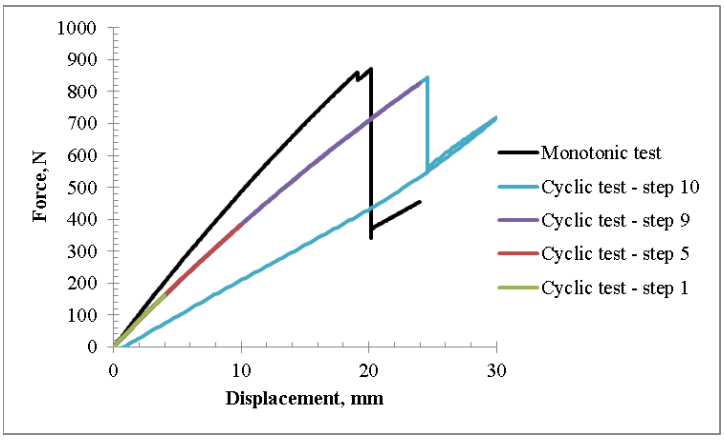

Figure 3 – Monotonic and cyclic ring compression test results.

Applying the previous characterized ply elastic properties (presented in Table 1) in the FEA simulation of the ring compression test, the force-displacement curve was obtained. The composite stiffness parameter D_{22} was determined by classical laminate theory and the surrogate model developed for this study was fitted according to Equation (9). Ring dimensions used in the calculations were 136.2 mm internal diameter, 20.0 mm width and 2.5 mm thickness. This solution is presented in Figure 4a, which shows that the surrogate model represents well the physical behaviour. The unknown function $f_{(w)}$ is presented in Figure 4b.

Table 1: Elastic properties from flat coupons and calculated trace parameters.

E_x	E_y	ν_{xy}	G_{xy}	Q^*_{xx}	Q^*_{yy}	Q^*_{xy}	Q^*_{ss}	Tr
MPa	MPa	-	MPa	-	-	-	-	MPa
129300	9110	0.32	5440	130181	9172	2843	5440	150233

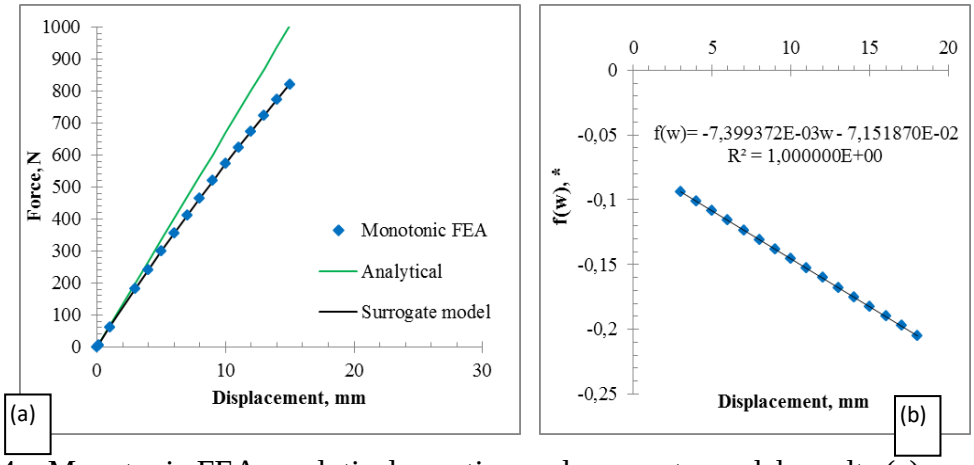

Figure 4 – Monotonic FEA, analytical equation and surrogate model results (a), and $f_{(w)}$ (b).

The surrogate model was applied to calculate the actual bending-stiffness parameter D_{22} of the compression test results by fitting the experimental curves, as presented in Figure 5.

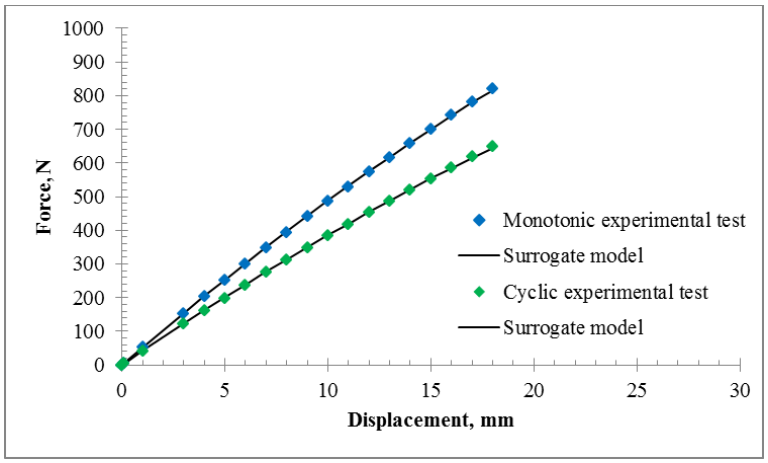

Figure 5 – Fitted surrogate model for the ring compression experimental test results.

For scaling the elastic properties, the trace-design parameters were calculated based on the estimated material properties of Table 1 to allow prediction of the as built ply material properties. These results are presented in Table 2.

Table 2: Trace flexural parameters and scaled properties of ring specimens.

	D_{22} N.mm	D_{22}^{*} MPa	D_{22}^{**} -	Tr MPa	E_x MPa	E_y MPa	ν_{xy} -	G_{xy} MPa
FEA	167098	128331	0.8542	150233	-	-	-	-
Monotonic	142583	109504	0.8542	128193	110331	7773	0.27	4642
Cyclic	104753	110357	0.8542	129192	111190	7834	0.27	4678
				Mean values	110760	7804	0.27	4660

In fact, the modulus defined with the ring compression test are an apparent modulus since due to bending we have tensile and compression regions, and a composite polymer laminate have different modulus on tensile and compression directions [10].

The mean values of the estimated elastic properties (Table 2) were used in the linear and non-linear buckling FEA model for comparison with the hydrostatic test. For the non-linear buckling FEA, percentiles of the first buckling mode shape were applied as initial imperfection in the geometry of the cylinder. Figure 6 presents the failed sample after hydrostatic test and the FEA results. Good correlation was observed between numerical and actual test results for linear as well as non-linear analysis, with 1% and 5% initial imperfections based on the first linear buckling mode.

As expected, the linear analysis resulted in a buckling load above of that of the non-linear analysis because a perfect cylindrical geometry is in general less sensitive to the load case and this is observed in the Figure 6c where higher imperfection percentiles resulted in lower buckling pressure, although in some cases an imperfection may act as reinforcement. Moreover, a 5% imperfection based on the calculated first linear buckling mode represents here approximately an oscillation on the thickness plane of 0.125 mm amplitude that we can realize as a geometric deviation in the diameter consistent with manufacturing practices. Non-linear buckling result with 5% imperfection is very close to the experimental result. Geometrical imperfections must always

be considered in a structural analysis since it is impossible to produce an exactly perfect component and moreover these imperfections affect their structural response. The ratio between experimental and linear results (knockdown-factor [10]) is 0.97 showing the accuracy of the prediction provided by the estimated material elastic properties. A linear buckling analysis with the elastic properties (Table 1) measured with the flat coupons specimens result in a buckling load of 4.88 MPa and thus a knockdown-factor of 0.83, almost 20% far from the experimental result against only 3% of the presented methodology.

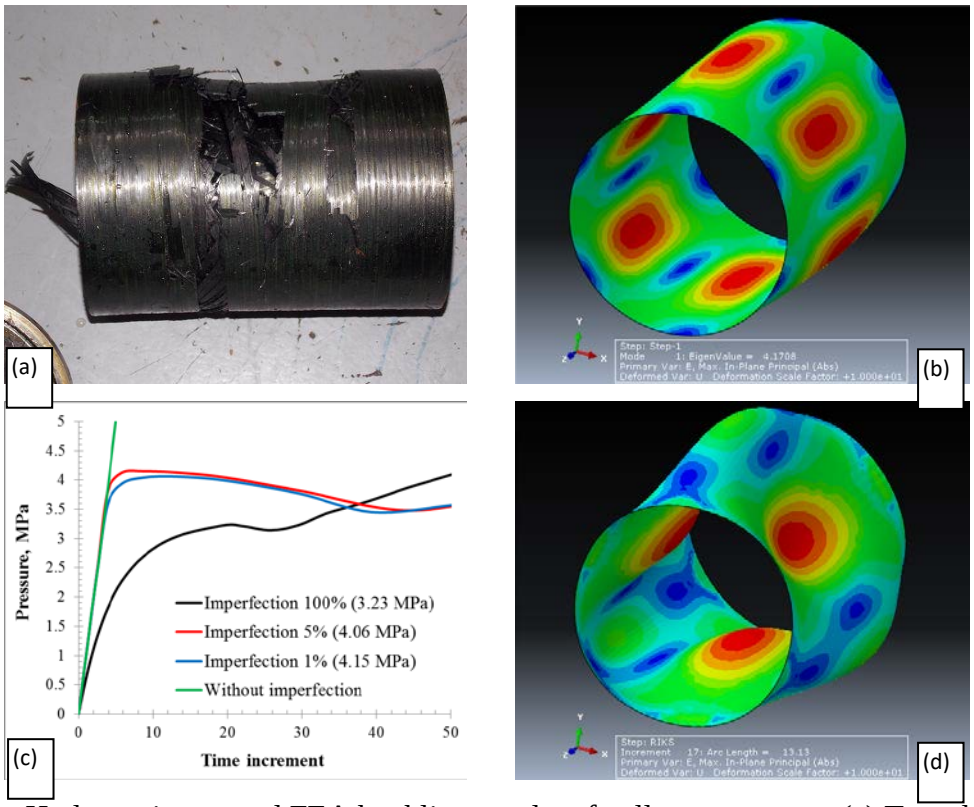

Figure 6 – Hydrostatic test and FEA buckling results of collapse pressure: (a) Tested tube (4.07 MPa), (b) Linear FEA result (4.17 MPa - first mode), (c) Non-linear FEA results for imperfect geometry, (d) Non-linear buckling mode with 5% initial imperfection (4.06 MPa).

4. CONCLUSIONS

The developed surrogate model has overcome the lack of accuracy of the referenced analytical model in representing the physical behaviour of the radial ring compression (parallel-plate) test. Moreover, it has simplified calculations in the fitting procedure, avoiding time-consuming FEA routine and supporting the trace-based approach. The developed scaling procedure for the elastic properties using the trace approach was validated by the ring compression test and by the experimental and FEA buckling analysis since good agreement was found in the results. This methodology was may be a valuable tool in the early stages of structural design since it minimizes the required material characterization efforts and saves time. Further investigations on the trace-design approach will enlighten its statistical basis and its correlation with composite material physical constitutive laws.

ACKNOWLEDGEMENTS

We would like to thank the testing support of the Subsea Technology Laboratory of UFRJ, and the Composite Materials Group/LAPOL/UFRGS for cylinder manufacturing.

REFERENCES

[1] PETERS, S.T., 'Composite Filament Winding'. ASM International, 2011.

[2] TSAI, S.W., MELO, J.D.D., 'An invariant-based theory of composites'. Composites Science and Technology, v. 100, p. 237-243, 2014.

[3] HA, S.K., CIMINI JR, C.A., 'Theory and validation of the master ply concept for invariant-based stiffness of composites'. Journal of Composite Materials, DOI: 10.1177/0021998317728782, 2017.

[4] TSAI, S.W., SIHN, S., MELO, J.D. D., 'Trace-based stiffness for a universal design of carbon-fiber reinforced composite structures'. Composites Science and Technology, v. 118, p. 23-30, 2015.

[5] CHOQUEUSE, D., DAVIES, P. 'Durability of Composite Materials for Underwater Applications'. In: Durability of Composites in a Marine Environment. Springer, Dordrecht, 2014. p. 195-207.

[6] MELO, J.D., BI, J., TSAI, S.W., 'A novel invariant-based design approach to carbon fiber reinforced laminates'. Composite Structures, v. 159, p. 44-52, 2017.

[7] ALMEIDA JR, J.H.S., RIBEIRO, M.L., TITA, V., AMICO, S.C., 'Damage and failure in carbon/epoxy filament wound composite tubes under external pressure: Experimental and numerical approaches'. Materials & Design, v. 96, p. 431-438, 2016.

[8] SYSTEMES, Dassault. ABAQUS 6.7-1 FEA software, ABAQUS. 2007.

[9] TIMOSHENKO, S.P., 'Theory of Elastic Stability', McGraw-Hill Book Company, 1936.

[10] GERHARDT, E., AMICO, S., MARCZAK, R., 'Numerical and computational analysis regarding buckling knockdown factor of composite cylinders'. In: MACMS - Meeting on Aeronautical Composite Materials and Structures, Brazil, 2017. Available at: http://soac.eesc.usp.br/index.php/macms/macms2017/paper/view/820. Accessed: 19 Feb. 2018.